NanoScience and Technology

Ion Tiginyanu
Pavel Topala
Veaceslav Ursaki *Editors*

Nanostructures and Thin Films for Multifunctional Applications

Technology, Properties and Devices

NanoScience and Technology

Series editors

Phaedon Avouris, Yorktown Heights, USA
Bharat Bhushan, Columbus, USA
Dieter Bimberg, Berlin, Germany
Cun-Zheng Ning, Tempe, USA
Klaus von Klitzing, Stuttgart, Germany
Roland Wiesendanger, Hamburg, Germany

The series NanoScience and Technology is focused on the fascinating nano-world, mesoscopic physics, analysis with atomic resolution, nano and quantum-effect devices, nanomechanics and atomic-scale processes. All the basic aspects and technology-oriented developments in this emerging discipline are covered by comprehensive and timely books. The series constitutes a survey of the relevant special topics, which are presented by leading experts in the field. These books will appeal to researchers, engineers, and advanced students.

More information about this series at http://www.springer.com/series/3705

Ion Tiginyanu · Pavel Topala
Veaceslav Ursaki
Editors

Nanostructures and Thin Films for Multifunctional Applications

Technology, Properties and Devices

Editors
Ion Tiginyanu
Academy of Sciences of Moldova
Chisinau
Moldova

Veaceslav Ursaki
Laboratory of Nanotechnologies
Academy of Sciences of Moldova
Chisinau
Moldova

Pavel Topala
Alecu Russo Balti State University
Balti
Moldova

ISSN 1434-4904 ISSN 2197-7127 (electronic)
NanoScience and Technology
ISBN 978-3-319-30197-6 ISBN 978-3-319-30198-3 (eBook)
DOI 10.1007/978-3-319-30198-3

Library of Congress Control Number: 2016932857

© Springer International Publishing Switzerland 2016
This work is subject to copyright. All rights are reserved by the Publisher, whether the whole or part of the material is concerned, specifically the rights of translation, reprinting, reuse of illustrations, recitation, broadcasting, reproduction on microfilms or in any other physical way, and transmission or information storage and retrieval, electronic adaptation, computer software, or by similar or dissimilar methodology now known or hereafter developed.
The use of general descriptive names, registered names, trademarks, service marks, etc. in this publication does not imply, even in the absence of a specific statement, that such names are exempt from the relevant protective laws and regulations and therefore free for general use.
The publisher, the authors and the editors are safe to assume that the advice and information in this book are believed to be true and accurate at the date of publication. Neither the publisher nor the authors or the editors give a warranty, express or implied, with respect to the material contained herein or for any errors or omissions that may have been made.

Printed on acid-free paper

This Springer imprint is published by Springer Nature
The registered company is Springer International Publishing AG Switzerland

This book is dedicated to the 55th anniversary of the inauguration of the Academy of Sciences of Moldova

Preface

Thin films, nanostructures, and nanocomposite materials, owing to the ability to tune their properties by controlling the size, represent a basis for the development of electronic device components for a wide range of interdisciplinary high-tech industries such as microelectronics, nanoelectronics, optoelectronics, spintronics, photonics, plasmonics, and fine mechanics. The wide implementation of low-dimensional structures is based on their unique physical–chemical properties that cannot be attained in a bulk material, this feature being crucial for satisfying the basic needs of industries in the modern world. Moreover, the combination of thin films, nanostructures, and nanocomposite materials on a common platform provides even more unique physical and multifunctional characteristics, which further stimulate their development and implementation in various fields.

Many efforts have been undertaken in the past decades to develop nanotechnologies for creating nanomaterials with determined structure and functionalities. Due to applications in spintronics, magnetic sensing, and ultrahigh-density magnetic recording, the rapidly progressing field of nanomagnetism is of particular importance. Development of new nanocomposite and nanostructured materials with novel optical, magnetic, transport, and magneto-optical properties is a key issue in this rapidly growing field. More interesting properties, effects, and possibilities for applications arise when combining the magnetism with superconductivity.

This book provides a collection of review articles from experts working in the field of nanotechnology and nanomaterials structured into 18 chapters to give an overview of recent advances in the development of thin films, nanostructured and nanocomposite materials with a detailed analysis of technologies for preparation, properties, and various applications of materials and device structures. Most chapters contain in-depth studies related to a particular nanomaterial issue, the book being therefore targeted at researchers. However, it can be useful also for Ph.D. students, graduate and undergraduate students specializing in disciplines related to solid-state nanotechnologies and nanomaterials. The chapters are grouped into three parts: the first part focuses on preparation and characterization of thin films, the

second concentrates on magnetic nanomaterials, and the third deals with nanostructured and composite materials.

The first part involves five contributions on metal/alloy-based films, nanometer oxide and hydroxide pellicles, graphite coatings, and semiconducting films of A^2B^6 compounds, including CdS, CdSe, CdTe, and ZnS_xSe_{1-x}.

In the first chapter, Cesiulis et al. present the capabilities and advantages of Electrochemical Impedance Spectroscopy (EIS) as a useful and nondestructive technique for investigating various types of thin films such as metal/alloy films, oxide films produced by anodization of metals, and organic films onto metals. The approach is overviewed from the point of view of theoretical basics and practical applications of EIS, as for instance for the characterization of biosensing surfaces and in evaluation of bioanalytical signals generated by biosensors.

In the next two chapters, Topala et al. describe the advantages, importance, and prospects of producing nanometer oxide, hydroxide, and graphite films on metal surfaces by electrical discharge pulse technologies with focus on their applications as anticorrosive coatings, for surface passivation in chemical industries, and in applications in micro- and nanoelectronics.

The contribution of Popa provides results related to the preparation and characterization of ZnS_xSe_{1-x} thin films with various x values produced by vacuum evaporation technique on glass substrates, while that of Potlog gives a review on technological methods for growing II–VI thin films and their application in four types of photovoltaic devices based on CdS/CdTe, ZnSe/CdTe, TiO_2/CdSe, and TiO_2/CdTe heterostructures.

The second part, composed of four contributions, focuses on the development of magnetic nanomaterials. Recent developments in the field of magnetoelectric effects occurring due to coupling between the ferroelectric and ferromagnetic orders, notably as a strain-mediated phenomena in piezoelectric/magnetostrictive composite materials, are presented in two chapters by Vidal et al., with special emphasis on direct and converse magnetoelectric effects in trilayers of metglas and lead-free piezoelectrics and their extensive promising applications in *AC* and *DC* vector-magnetic field sensors, current sensors, transducers, spintronic, microwave, and read/write devices. The basis for most theories related to the magnetoelectric effect in composites is described, and the experimental methods for measuring the magnetoelectric effect are identified with particular emphasis on the dynamical techniques.

Physical properties of narrow-bandgap semimagnetic semiconductors and their practical applications are reviewed in the contribution of Gheorghitza et al., while exchange bias diluted ferromagnetic alloys are described by Sidorenko et al. in the final chapter of this second part as an essential building block of spintronic devices, particularly for superconducting spintronics. In particular, the influence of a cobalt sublayer on a conventional exchange bias $CoO_x/Cu_{41}Ni_{59}$ interface is identified, and its advantages for application in superconductor-ferromagnet spin-valve heterostructures are analyzed.

Through nine chapters of the third part of this book, the reader will be familiarized with various types of nanostructured and nanocomposite materials, among

which TiO_2/WO_3 bi-layers are reviewed in the contribution from Macovei et al. by bringing new details of the local atomic ordering at the TiO_2–WO_3 interface and their relevance in designing oxidic semiconductor heterostructures for applications with enhanced photocatalytic performances.

The optical and photoelectrical properties of composite nanostructures with intercalated $A^{III}B^{VI}$ lamellar semiconductors are analyzed in three chapters by Evtodiev et al. with respect to technologies for intercalating of atoms (molecules) into $A^{III}B^{VI}$ semiconductors, polymorphism, crystal structure, electronic band structure, and prospects of their applications in photodetectors and photovoltaics.

Various manufacturing methods for obtaining nanoreliefs are reviewed in a chapter by Slatineanu, such as mechanical, electrochemical, thermal, and hybrid processes. Methods of characterization and possible applications of the produced nanoreliefs are analyzed.

Recent advances in template assisted production of nanocomposite materials with especial emphasis on the production of metal nanotubes by means of ion-track membranes, alumina templates, and semiconductor templates are reviewed in the contribution of Tiginyanu et al. with the analysis of advantages and drawbacks of different templates. Prospects of applications of metal nanotubes and nanotube-based materials in the fabrication of microelectronic and photonic devices, magnetic recording media, biomagnetics, etc., are analyzed.

The contribution of Nica et al. presents a review of phonon thermal properties of segmented nanowire with a focus on theoretical results for Si and Si/Ge structures with constant and periodically modulated cross-sections. Possible practical applications of segmented nanowires in thermoelectric energy generation are also discussed.

The results obtained in the past few years regarding THz devices based on carbon nanomaterials, such as graphene, are reviewed by Dragoman with the purpose of estimating the prospects of covering the famous THz gap by means of further development of research in the field of two-dimensional materials. Different devices and circuits based on graphene and carbon nanotubes are discussed, such as antennas operating at terahertz frequencies, generators, detectors, and mixers of terahertz electromagnetic waves.

Some elements related to abrasive flow machining (AFM), specifically state-of-the-art elements of technological systems, and equipment fabrication and characterization are presented in the chapter by Ionescu et al.

We are grateful to all the contributors who made special efforts to prepare their respective chapters, and we hope that this book will be an essential reference tool for a wide scientific community, and for libraries at universities and research institutions.

Chisinau — Ion Tiginyanu
Balti — Pavel Topala
Chisinau — Veaceslav Ursaki

Contents

Part I Preparation and Characterization of Thin Films for Optoelectronic and Sensoric Applications

1 The Study of Thin Films by Electrochemical Impedance Spectroscopy 3
H. Cesiulis, N. Tsyntsaru, A. Ramanavicius and G. Ragoisha
1.1 Introduction 4
1.2 Basics of EIS 4
1.3 EIS Responses During Cathodic Metals and Alloys Films Deposition 12
1.4 Anodization of Metals: Characterization of Oxide Films and Their Growth by EIS 17
1.5 The Study of Underpotential Deposition of Metals by EIS 23
1.6 Characterization of Organic Films onto Metals by EIS 26
1.7 Electrochemical Impedance Spectroscopy (EIS) in Development of Biosensors and Biofuel Cells 29
1.8 Conclusions 34
References 34

2 Nanostructures Obtained Using Electric Discharges at Atmospheric Pressure 43
Pavel Topala, Alexandr Ojegov and Veaceslav Ursaki
2.1 Introduction 43
2.2 Physical Model of Nano-Pellicle Formation by Applying Pulse Electrical Discharge Machining 46
2.3 Processes of Dissociation, Ionization and Synthesis in the Plasma and on the Electrode Surfaces 49
2.4 Diffusion Processes at Oxide Nano-Pellicle Formation by Applyind PEDM 51
2.5 Technology Development 54

2.6 Results of Experimental Investigations and Their Analysis 60
2.6.1 Results of Technological Investigations on Film Formation 60
2.6.2 *Phase Composition of Nano-Oxide Films* 68
2.6.3 Morphology and Chemical Composition of Nano-Oxide Films 69
2.6.4 Surface Electrical Resistance 71
2.6.5 *Resistance to Corrosion* 74
2.7 Conclusions........ 78
References 79

3 Graphite Films Deposited on Metal Surface by Pulsed Electrical Discharge Machining 85
Pavel Topala, Vitalie Besliu and Laurentiu Marin
3.1 Introduction........ 85
3.2 Technology of Graphite Film Forming 86
3.3 Physical Model of Graphite Film Formation by Applying Pulsed Electrical Discharge 88
3.4 Scanning Electron Microscopy Analysis of the Graphite Films 91
3.5 XPS Spectroscopy 96
3.6 Thermal Gravimetric Analysis (TGA) of Graphite Film....... 97
3.6.1 TGA Tests on Reference Samples 97
3.6.2 TGA Tests on Experimental Sample by 10/1,5/600/250 Deposition 98
3.7 Solubility of Graphite Films Formed by PED Method on Metal Surfaces 100
3.8 Functional Properties of Graphite Films 102
3.8.1 Anti Socket........ 102
3.8.2 Antiblocking Properties of Graphite Films........ 103
3.8.3 Resistance to Wear for the Graphite Films........ 106
3.8.4 Corrosion Resistance of the Graphite Films........ 108
3.9 Conclusions........ 110
References 111

4 Structural and Physical Properties of ZnS_xSe_{1-X} Thin Films...... 115
Mihail Popa
4.1 Introduction........ 115
4.2 Preparation of ZnS_xSe_{1-X} Thin Films by Thermal Evaporation Method in Vacuum, in Quasi-Closed Volume 116
4.3 The Structure and Surface Morphology of ZnS_xSe_{1-X} Thin Films 117
4.4 The Electrical Properties of ZnS_xSe_{1-X} Thin Films 120
4.5 The Optical Properties of ZnS_xSe_{1-X} Thin Films........ 126

4.6 The Luminescent Properties of ZnS_xSe_{1-X} Thin Films 133
4.7 Conclusions 140
References 141

5 Thin-Film Photovoltaic Devices Based on A^2B^6 Compounds 143
Tamara Potlog
5.1 Introduction 143
5.2 Historical Development of the CdS/CdTe Photovoltaic Devices 144
5.3 Technology Development Trends by Companies in CdS/CdTe Photovoltaic Market 146
5.4 Comparison of Moldova State University CdS/CdTe Photovoltaic Device with Manufacturing Target 147
5.5 Deposition Processing and Photovoltaic Device Fabrication 147
5.6 Analysis of Efficiency Loss Mechanism in MSU CdS/CdTe Photovoltaic Devices 150
5.6.1 Current-Voltage Characteristics of the CdS/CdTe Photovoltaic Devices 150
5.6.2 Quantum Efficiency 155
5.7 Characterization of ZnSe/CdTe Photovoltaic Devices 155
5.7.1 Morphological and Structural Studies of Glass/SnO_2/ZnSe Interface 155
5.7.2 Optical Properties of ZnSe Thin Films Deposited on SnO_2/Glass Substrates 161
5.7.3 Current-Voltage Characteristics of the ZnSe/CdTe Photovoltaic Devices 163
5.8 Comparison of CdTe Photovoltaic Devices with Different Buffer Layers 166
5.9 Photovoltaic Devices Based on TiO_2/CdTe and TiO_2/CdSe Structures 167
5.9.1 Morphological and Structural Studies of TiO_2 Nanostructured Thin Films 168
5.9.2 XPS Analysis 171
5.9.3 Optical Properties 176
5.9.4 Electrical Properties 179
5.10 TiO_2/*p*-CdTe and TiO_2/*n*-CdSe Photovoltaic Devices 180
5.11 Conclusions 182
References 184

Part II Magnetic Nanomaterials for Spintronic and Sensoric Applications

6 Engineering the Magnetoelectric Response in Piezocrystal-Based Magnetoelectrics: Basic Theory, Choice of Materials, Model Calculations 189
João V. Vidal, Andrey A. Timopheev, Andrei L. Kholkin and Nikolai A. Sobolev
6.1 Introduction 190
6.1.1 The Magnetoelectric Effect 190
6.1.2 Magnetoelectric Composites 191
6.2 Theory of the Magnetoelectric Effect 199
6.2.1 Piezoelectricity and Magnetostriction 199
6.2.2 Presentation of the Averaging Quasi-Static Method. . . . 202
6.2.3 Estimation of the Quasi-Static Transversal ME Voltage Coefficients in Magnetostrictive/ Piezocrystalline/Magnetostrictive Tri-Layers. 209
6.3 Conclusions. 218
References 219

7 Dynamic Measurements of Magnetoelectricity in Metglas-Piezocrystal Laminates. 227
João V. Vidal, Andrey A. Timopheev, Andrei L. Kholkin and Nikolai A. Sobolev
7.1 Introduction. 228
7.2 Magnetoelectric Measurement Techniques 230
7.2.1 Dynamic Magnetoelectric Technique. 230
7.2.2 Experimental Dynamic Magnetoelectric Measurement Setup 234
7.3 Experimental Results 242
7.3.1 Comparative Study of the Direct and Converse Magnetoelectric Effects in Tri-Layered Composites of Metglas with $LiNbO_3$ and PMN-PT Single Crystals. 242
7.3.2 Comparison of the Anisotropic Magnetoelectric Effects in Tri-Layered Composites of Metglas with LiNbO3 and GaPO4 Single Crystals 250
7.4 Conclusions. 260
References 261

8 Peculiarities of Physical Properties of Semimagnetic Semiconductors and Their Practical Application 267
E.I. Gheorghitza, V.I. Ivanov-Omskii and I.T. Postolaki
8.1 Introduction. 267
8.2 Structure and Parameters of the Energy Bands 268

8.3 Electrical Properties of $Hg_{1-x}Mn_xTe$ and $Hg_{1-x-y}Cd_xMn_yTe$ Semimagnetic Semiconductors 273
8.4 Photoelectrical Properties. 278
8.4.1 Photoelectrical Properties of $Hg_{1-x}Mn_xTe$ and $Hg_{1-x-y}Cd_xMn_yTe$ in the Absence of Magnetic Field. 279
8.4.2 Photoelectrical Properties in a Magnetic Field 281
8.5 Photoluminescence Properties 284
8.5.1 Photoluminescence Properties in the Absence of Magnetic Field. 284
8.5.2 Photoluminescence Properties in a Magnetic Field 285
8.6 Magneto-Optical Properties 290
8.7 ODMR in Semimagnetic Semiconductors. Optical Orientation 294
8.8 Photoreceivers Based on $Hg_{1-x}Mn_xTe$, $Hg_{1-x-y}Cd_xMn_yTe$ 295
8.9 Conclusions. 295
References 296

9 Cobalt/Cobaltoxide Exchange Bias System for Diluted Ferromagnetic Alloy Films in Superconducting Spin-Valves 301
A.S. Sidorenko, D. Lenk, V.I. Zdravkov, R. Morari, A. Ullrich, C. Müller, H.-A. Krug von Nidda, S. Horn, L.R. Tagirov and R. Tidecks
9.1 Introduction. 301
9.2 Sample Preparation and Characterization 303
9.3 Results of Magnetic Measurements and Discussion. 306
9.4 Conclusion 310
Appendix 310
References 311

Part III Nanostructured and Composite Materials

10 Local Ordering at the Interface of the TiO_2-WO_3 Bi-Layers 317
Dan Macovei, Vasile Dăscăleanu, Cristian M. Teodorescu and Dumitru Luca
10.1 Introduction. 317
10.2 Materials and Methods 319
10.3 Results and Discussion 320
10.3.1 XRD Analysis 320
10.3.2 XPS Analysis 321
10.3.3 Ti K-Edge XANES 323
10.3.4 EXAFS Measurements 324
10.3.5 XPS Analysis of the Interface 328
10.4 Conclusions. 329
References 330

11 Crystalline Structure and Surface Morphology of $A^{III}B^{VI}$ Type Lamellar Semiconductor Nanocomposites Obtained by Heat Treatment in *Cd* and *Zn* Vapor 333
Igor Evtodiev, Iuliana Caraman, Valeriu Kantser, Dumitru Untila, Irina Rotaru, Liliana Dmitroglo, Silvia Evtodiev and Mihail Caraman
11.1 Introduction 333
11.2 Growth of Single Crystals of $A^{III}B^{VI}$ Lamellar Compounds 335
11.3 Crystal Structure of *GaS*, *GaSe*, *GaTe* and *InSe* Single Crystals 336
11.4 Electrical Properties of the $A^{III}B^{VI}$ Compounds (*GaS*, *GaSe*, *InSe*, and *GaTe*) Undoped and Doped with Group I, II and IV Elements 342
11.4.1 Electrical Properties of $A^{III}B^{VI}$ Compounds 342
11.4.2 Structure and Some Physical Properties of *Cd* and *Zn* Chalcogenides Thin Films 346
11.5 Crystal Structure and Composition of the Material Obtained by Treatment in *Zn* Vapors of *GaS*, *GaSe*, *GaTe* and *InSe* Lamellar Single Crystals 346
11.5.1 Crystal Structure and the Morphology of the Surface and Interface of the Composite Obtained by Heat Treatment of Single Crystal *GaS* Lamellas in *Cd* and *Zn* Vapors 349
11.5.2 The Crystal Structure and the Surface Morphology of Nanolamellar *GaSe*–Intrinsic Oxide Composites and Composites Prepared by Heat Treatment of ε–*GaSe* Single Crystal Plates in *Cd* and *Zn* Vapors 353
11.5.3 Crystal Structure and the Surface Morphology of the Interface Between the Packets of the Composite Obtained by Heat Treatment of *GaTe* Single–Crystal Lamellas in *Cd* and *Zn* Vapors 365
11.5.4 Crystal Structure and the Morphology of the Surface and Interfaces Between the Packets of the Composite Prepared by Heat Treatment of InSe Single-Crystal Lamellas in *Cd* and *Zn* Vapors 372
11.6 Conclusions and Generalities 376
References 377

12 Optical and Photoelectric Properties of *GaS*, *GaSe*, *GaTe* and *InSe* Semiconductors and Nanocomposites Obtained by Heat Treatment in *Cd* and *Zn* Vapor 381
Igor Evtodiev, Iuliana Caraman, Valeriu Kantser, Dumitru Untila, Irina Rotaru, Liliana Dmitroglo, Silvia Evtodiev and Mihail Caraman
12.1 Introduction 382

12.2 Optical and Photoluminescence Properties of Oxide—$A^{III}B^{VI}$ Structures 382
12.3 Dispersion of the $n_{\perp}$ and $n_{\parallel}$ Refractive Indices 384
12.4 Light Absorption in Undoped *GaSe*, *GaS*, *GaTe* and *InSe* Single Crystals, Doped and Intercalated with *Cd* and *Zn* 386
12.4.1 Absorption at the Edge and Depth of Fundamental Band ($h\nu \geq E_g$) 386
12.4.2 Light Absorption of *GaSe* and *GaSe* Doped with *Cd* in the Region of $h\nu < E_g$ 404
12.5 Photoelectrical Properties of Nanolamellar Structures with *GaS*, *GaSe*, *GaTe* and *InSe* Semiconductors 406
12.5.1 *Photosensitive Elements on GaTe Semiconductor* 406
12.5.2 *GaSe–CdSe* Heterojunctions 406
12.5.3 *InSe–CdSe* Heterojunctions 409
12.6 Conclusions and Generalities 410
References 411

13 Photoluminescence of Nanocomposites Obtained by Heat Treatment of *GaS*, *GaSe*, *GaTe* and *InSe* Single Crystals in *Cd* and *Zn* Vapor 415
Igor Evtodiev, Iuliana Caraman, Valeriu Kantser, Dumitru Untila, Irina Rotaru, Liliana Dmitroglo, Silvia Evtodiev and Mihail Caraman
13.1 Introduction 415
13.2 Photoluminescence of Nanocomposites with *GaS* Lamellar Semiconductors 416
13.2.1 Undoped *GaS* and *GaS* Doped with *Mn* 416
13.2.2 *GaS* Intercalated with *Zn* from Vapor Phase 419
13.2.3 *GaS* Intercalated with *Cd* from Vapor Phase 421
13.3 Photoluminescence of Nanocomposites with *GaSe* Lamellar Semiconductors 421
13.4 Photoluminescence of Nanocomposites with *GaTe* Lamellar Semiconductors 436
13.5 Photoluminescence of Nanocomposites with *InSe* Lamellar Semiconductors 439
13.5.1 InSe 439
13.5.2 *InSe* Intercalated with *Cd* 440
13.5.3 *InSe* Intercalated with *Zn* 441
13.6 Conclusions and Generalities 444
References 445

14 Nanoreliefs Obtained by Various Machining Methods 447
Laurenţiu Slătineanu, Oana Dodun, Margareta Coteaţă and Irina Beşliu
14.1 Introduction 447
14.2 Possibilities of Characterizing Nanoasperities/Nanoreliefs 449
14.3 Nanoreliefs Obtained by Mechanical Processes 451

14.3.1 General Aspects Concerning the Cutting Process and Its Capacity to Generate Nanoreliefs 451
14.3.2 Nanoreliefs Obtained by Turning 452
14.3.3 Nanoreliefs Obtained by Abrasive Processes 456
14.4 Nanoreliefs Obtained by Electrochemical Processes 461
14.5 Nanoreliefs Obtained by Thermal Machining Processes 464
14.6 Nanoreliefs Obtained by Hybrid Machining Processes 466
14.7 Conclusions 470
References 470

15 Template Assisted Formation of Metal Nanotubes 473
Ion Tiginyanu, Veaceslav Ursaki and Eduard Monaico
15.1 Introduction 473
15.2 Porous Templates for Nanofabrication 474
15.3 Production of Metal Nanotubes in Ion-Track Membranes 479
15.4 Metal Nanotubes in Porous Alumina Templates 482
15.5 Semiconductor-Metal Nanocomposites on the Basis of Metal Nanotubes Deposited in Semiconductor Templates 490
15.6 Applications 493
15.7 Conclusions 501
References 503

16 Thermal Conductivity of Segmented Nanowires 507
Denis L. Nika, Alexandr I. Cocemasov and Alexander A. Balandin
16.1 Introduction 507
16.2 Phonons in Segmented Nanowires 509
16.2.1 Face-Centered Cubic Cell Model of Lattice Dynamics in Bulk Crystals 510
16.2.2 Born-von Karman Model of Lattice Dynamics in Bulk Crystals 512
16.2.3 Lattice Dynamics in Segmented Nanowires 513
16.3 Phonon Engineered Heat Conduction of Segmented Nanowires 518
16.4 Conclusions 528
References 528

17 THz Devices Based on Carbon Nanomaterials 533
Mircea Dragoman and Daniela Dragoman
17.1 Introduction 533
17.2 Graphene Antennas at THz Frequencies 539
17.3 THz Generation Based on Graphene 543
17.4 THz Detection Based on Graphene and Carbon Nanotubes 545
17.5 Conclusions 547
References 548

18 Abrasive Flow Machining 551
N. Ionescu, D. Ghiculesc, A. Visan and V. Avramescu
18.1 Introduction 551
18.2 Elements of Technological System at Abrasive Flow Machining 552
18.3 Conceptual Design of the AFM Equipment 553
18.4 Detailed Design of the AFM Equipment 555
18.5 Experimental Results 561
18.6 Conclusions 566
References 567

Index 569

Contributors

V. Avramescu SC ICTCM SA—Mechanical Engineering and Research Institute, Bucharest, Romania

Alexander A. Balandin Department of Electrical and Computer Engineering and Materials Science and Engineering Program, University of California, Riverside, Riverside, CA, USA

Vitalie Besliu Alecu Russo Balti State University, Balti, Moldova

Irina Beşliu "Ştefan cel Mare" University of Suceava, Suceava, Romania

Iuliana Caraman "Vasile Alecsandri" University of Bacau, Bacau, Romania

Mihail Caraman Laboratory of Photonics and Physical Metrology, Department of Physics and Engineering, Moldova State University, Chisinau, Moldova

H. Cesiulis Department of Physical Chemistry, Faculty of Chemistry, Vilnius University, Vilnius, Lithuania

Alexandr I. Cocemasov "E. Pokatilov" Laboratory of Physics and Engineering of Nanomaterials, Department of Physics and Engineering, Moldova State University, Chisinau, Moldova

Margareta Coteaţă "Gheorghe Asachi" Technical University of Iaşi, Iasi, Romania

Vasile Dăscăleanu Alexandru Ioan Cuza University, Iasi, Romania

Liliana Dmitroglo Laboratory of Photonics and Physical Metrology, Department of Physics and Engineering, Moldova State University, Chisinau, Moldova

Oana Dodun "Gheorghe Asachi" Technical University of Iaşi, Iasi, Romania

Daniela Dragoman University of Bucharest, Bucharest-Magurele, Romania; Academy of Romanian Scientists, Bucharest, Romania

Mircea Dragoman National Institute for Research and Development in Microtechnology, Bucharest-Voluntari, Romania

Igor Evtodiev Laboratory of Photonics and Physical Metrology, Department of Physics and Engineering, Moldova State University, Chisinau, Moldova; Institute of Electronic Engineering and Nanotechnologies "D. Ghitu", Academy of Sciences of Moldova, Chisinau, Moldova

Silvia Evtodiev Laboratory of Photonics and Physical Metrology, Department of Physics and Engineering, Moldova State University, Chisinau, Moldova

E.I. Gheorghitza Tiraspol State University, Chisinau, Moldova

D. Ghiculesc University Politehnica of Bucharest, Bucharest, Romania

S. Horn Institut für Physik, Universität Augsburg, Augsburg, Germany

N. Ionescu University Politehnica of Bucharest, Bucharest, Romania

V.I. Ivanov-Omskii Physical-Technical Institute A. F. Ioffe RAN, St. Petersburg, Russia

Valeriu Kantser Laboratory of Photonics and Physical Metrology, Department of Physics and Engineering, Moldova State University, Chisinau, Moldova; Institute of Electronic Engineering and Nanotechnologies "D. Ghitu", Academy of Sciences of Moldova, Chisinau, Moldova

Andrei L. Kholkin Departamento de Física and CICECO, Universidade de Aveiro, Aveiro, Portugal; Institute of Natural Sciences, Ural Federal University, Ekaterinburg, Russia

D. Lenk Institut für Physik, Universität Augsburg, Augsburg, Germany

Dumitru Luca Alexandru Ioan Cuza University, Iasi, Romania

Dan Macovei National Institute of Materials Physics, Măgurele-Ilfov, Romania

Laurentiu Marin National Institute for Research and Development in Chemistry and Petrochemistry, Bucharest, Romania

Eduard Monaico National Center for Materials Study and Testing, Technical University of Moldova, Chisinau, Moldova

R. Morari Institute of Electronic Engineering and Nanotechnologies "D. Ghitu", Academy of Sciences of Moldova, Chisinau, Moldova; Institut für Physik, Universität Augsburg, Augsburg, Germany; Solid State Physics Department, Kazan Federal University, Kazan, Russia

C. Müller Institut für Physik, Universität Augsburg, Augsburg, Germany

Denis L. Nika "E. Pokatilov" Laboratory of Physics and Engineering of Nanomaterials, Department of Physics and Engineering, Moldova State University, Chisinau, Moldova

Alexandr Ojegov "Alecu Russo" Balti State University, Balti, Moldova

Mihail Popa "Alecu Russo" Balti State University, Balti, Moldova

I.T. Postolaki Tiraspol State University, Chisinau, Moldova

Tamara Potlog Department of Physics and Engineering, Moldova State University, Chisinau, Moldova

G. Ragoisha Research Institute for Physical Chemical Problems, Belarusian State University, Minsk, Belarus

A. Ramanavicius Laboratory of Nanobiotechnology, Department of Materials Science and Electronics, Institute of Semiconductor Physics, State Scientific Research Institute Centre for Physical Sciences and Technology, Vilnius, Lithuania

Irina Rotaru Laboratory of Photonics and Physical Metrology, Department of Physics and Engineering, Moldova State University, Chisinau, Moldova

A.S. Sidorenko Institute of Electronic Engineering and Nanotechnologies "D. Ghitu", Academy of Sciences of Moldova, Chisinau, Moldova

Laurenţiu Slătineanu "Gheorghe Asachi" Technical University of Iaşi, Iasi, Romania

Nikolai A. Sobolev Departamento de Física and I3N, Universidade de Aveiro, Aveiro, Portugal; National University of Science and Technology "MISiS", Moscow, Russia

L.R. Tagirov Solid State Physics Department, Kazan Federal University, Kazan, Russia; Institut für Physik, Universität Augsburg, Augsburg, Germany

Cristian M. Teodorescu National Institute of Materials Physics, Măgurele-Ilfov, Romania

R. Tidecks Institut für Physik, Universität Augsburg, Augsburg, Germany

Ion Tiginyanu Institute of Electronic Engineering and Nanotechnologies "D. Ghitu", Academy of Sciences of Moldova, Chisinau, Moldova; National Center for Materials Study and Testing, Technical University of Moldova, Chisinau, Moldova

Andrey A. Timopheev Departamento de Física and I3N, Universidade de Aveiro, Aveiro, Portugal

Pavel Topala Alecu Russo Balti State University, Balti, Moldova

N. Tsyntsaru Department of Physical Chemistry, Faculty of Chemistry, Vilnius University, Vilnius, Lithuania; Institute of Applied Physics, Academy of Sciences of Moldova, Chisinau, Moldova

A. Ullrich Institut für Physik, Universität Augsburg, Augsburg, Germany

Dumitru Untila Laboratory of Photonics and Physical Metrology, Department of Physics and Engineering, Moldova State University, Chisinau, Moldova; Institute of Electronic Engineering and Nanotechnologies "D. Ghitu", Academy of Sciences of Moldova, Chisinau, Moldova

Veaceslav Ursaki Institute of Electronic Engineering and Nanotechnologies D. Ghitu, Academy of Sciences of Moldova, Chisinau, Moldova

João V. Vidal Departamento de Física and I3N, Universidade de Aveiro, Aveiro, Portugal

A. Visan University Politehnica of Bucharest, Bucharest, Romania

H.-A. Krug von Nidda Institut für Physik, Universität Augsburg, Augsburg, Germany

V.I. Zdravkov Institute of Electronic Engineering and Nanotechnologies "D. Ghitu", Academy of Sciences of Moldova, Chisinau, Moldova; Institut für Physik, Universität Augsburg, Augsburg, Germany

Part I
Preparation and Characterization of Thin Films for Optoelectronic and Sensoric Applications

Chapter 1
The Study of Thin Films by Electrochemical Impedance Spectroscopy

H. Cesiulis, N. Tsyntsaru, A. Ramanavicius and G. Ragoisha

Abstract The capabilities and advantages of electrochemical impedance spectroscopy (EIS) as a useful and non-destructive technique are discussed. EIS provides the time dependent quantitative information about the electrode processes. The description of EIS is given in comprehensive way beginning from the theoretical basics of EIS and data interpretation in the frames of various equivalent electric circuits. The practical applications of EIS are described for the following thin film types: (i) cathodic metals/alloys films deposition; (ii) anodization of metals and characterization of oxide films and its growth by EIS including information provided by Mott-Schottky plots; (iii) underpotential deposition of metals; (iv) characterization of organic films onto metals; (v) application in development of biosensors and biofuel cells. The original data of EIS on cathodic electrodeposition of Co and Co-W are provided and reduction mechanisms involving adsorbed intermediates are discussed. The advantages of EIS in the oxide films characterization and their electrochemical properties are shown. EIS can be successfully applied for the characterization of biosensing surfaces and/or in evaluation of bioanalytical signals generated by biosensors. The glucose oxidase (GOx) based biosensor could be successfully analyzed by merged scanning electrochemical microscopy (SECM) and EIS techniques. Such combining study by SECM and EIS could be very attractive in order to evaluate the biofuel cell efficiency and in the

H. Cesiulis (✉) · N. Tsyntsaru
Department of Physical Chemistry, Faculty of Chemistry, Vilnius University, Vilnius, Lithuania
e-mail: henrikas.cesiulis@chf.vu.lt

N. Tsyntsaru
Institute of Applied Physics, Academy of Sciences of Moldova, Chisinau, Moldova

A. Ramanavicius
Laboratory of Nanobiotechnology, Department of Materials Science and Electronics, Institute of Semiconductor Physics, State Scientific Research Institute Centre for Physical Sciences and Technology, Vilnius, Lithuania

G. Ragoisha
Research Institute for Physical Chemical Problems, Belarusian State University, Minsk, Belarus

© Springer International Publishing Switzerland 2016

I. Tiginyanu et al. (eds.), *Nanostructures and Thin Films for Multifunctional Applications*, NanoScience and Technology,
DOI 10.1007/978-3-319-30198-3_1

modeling of biosensor action, because it is unavailable to obtain by other convenient electrochemical methods.

1.1 Introduction

Electrochemical impedance spectroscopy is a recent and powerful tool in corrosion and solid-state laboratories. Electrochemical Impedance Spectroscopy (EIS) also is called AC Impedance or just Impedance Spectroscopy. The usefulness of impedance spectroscopy lies in the ability to distinguish the dielectric and electric properties of individual contributions of components under investigation. Impedance spectroscopy is a non-destructive technique and so can provide time dependent quantitative and time-dependant information about the electrode processes and complex interfaces, extract some characteristics of materials including high resistance materials (e.g. paintings, oxide coatings). There are number of books devoted to the theory, terminology and definitions, and experimental setup of EIS in details, and some of them we recommend for young researchers [1–6]. The aim of this review is to provide information for users about variety of thin films study by EIS in view of general principles of the method.

1.2 Basics of EIS

The electrochemical impedance method consists in measuring the response of an electrode to a sinusoidal potential modulation at different frequencies. Often these *ac* modulations are superimposed either onto applied anodic or cathodic potential, or onto open circuit potential. The mathematical approach of electrochemical impedance data is based on the Ohm's law, i.e. on the linear interdependency between potential perturbation and current response or vice versa. However, the potential-current dependencies of electrochemical systems in general are non-linear. On the other hand, it is possible to extract a small fraction of this dependence, where the mentioned dependence can be approximated as linear, e.g. in the range of 5–10 mV. Therefore, the measurements of impedance are performed under sinusoidal potential modulation with amplitude 5–10 mV. The sinusoidal perturbations of potential $E(t)$ induces a sinusoidal current $I(t)$ of the same frequency (ω) superimposed onto the steady state current with the phase shift ϕ with the respect to the potential. As for physical electric circuits, the electrochemical impedance of electrode reaction (Z) is defined analogous to Ohm's law as:

$$Z(\omega) = \frac{E(t)}{I(t)} = \frac{|E_0|\sin(\omega t)}{|I_0|\sin(\omega t - \phi)} = Z_0 \frac{\sin(\omega t)}{\sin(\omega t - \phi)} \tag{1.1}$$

here: E_0 and I_0 is amplitude of potential and current, respectively, $\omega = 2\pi f$ is the radial frequency in rad/s (f is a frequency expressed in Hz).

Here we follow methodology of the description of EIS basic conception provided in [7]. In polar coordinates these functions are represented by vectors of length $|E_0|$ and $|I_0|$ rotating counter clockwise at the radial frequency ω. These functions are most easily described by using complex numbers. With the mathematical identity,

$$\exp(jx) = \cos x + j \sin x \tag{1.2}$$

it is obtained

$$E(t) = |E_0| \exp(j\omega t) \tag{1.3}$$

$$I(t) = |I_0| \exp(j\omega t - j\varphi) \tag{1.4}$$

here j is a complex unit $j = \sqrt{-1}$.

Thus, (1.1) can be rewritten to define the electrochemical impedance as a sum of real (Z_{Re}) and imaginary parts (Z_{Im}) at certain ω:

$$Z(\omega) = |Z_0| \exp(j\phi) = |Z_0|(\cos \varphi + j \sin \varphi) = |Z_0| \cos \varphi + j|Z_0| \sin \varphi = Z_{\mathrm{Re}} + jZ_{\mathrm{Im}} \tag{1.5}$$

Note, that in the electrochemical literature real and imaginary parts of electrochemical impedance often are marked as Z' and Z'', respectively.

Using theory of complex functions the modulus of impedance, tanϕ, and ϕ are expressed by a following equations:

$$|Z(\omega)| = \sqrt{Z_{\mathrm{Re}}^2 + Z_{\mathrm{Im}}^2} \tag{1.6}$$

$$\tan \phi = \frac{Z_{\mathrm{Im}}}{Z_{\mathrm{Re}}} \tag{1.7}$$

$$\phi = \arctan \frac{Z_{\mathrm{Im}}}{Z_{\mathrm{Re}}} \tag{1.8}$$

One popular format for evaluating electrochemical impedance data, consists on plotting the imaginary impedance component (Z″) against the real impedance component (Z′) at each excitation frequency the Nyquist plot. This format is also known as a Cole-Cole plot or a complex impedance plane plot. The Nyquist plot has several advantages. The primary one is that the plot format makes it easy to see the effects of the ohmic (uncompensated) resistance (see the text below). If data are taken at sufficiently high frequencies, it is easy to extrapolate the obtained curve toward the left, down to the x axis to read the ohmic resistance. The shape of the curve (often a semicircle) does not change when the ohmic resistance changes.

Another advantage of this plot format is that it emphasizes circuit components that are in series. The Nyquist plot format also has some disadvantages. For example, frequency does not appear explicitly. Secondly, although the ohmic resistance and polarization (charge transfer) resistance can be easily read directly from the Nyquist plot, the electrode capacitance can be calculated only after the frequency information is known.

Another format for evaluating electrochemical impedance data known as Bode plots, and consists of the plotting $|Z(\omega)|$ and ϕ versus logω, i.e. lets to examine these values as a function of frequency. The Bode plot has some distinct advantages over the Nyquist plot. Since frequency appears as one of the axes, it is easy to understand from the plot how the impedance depends on the frequency. The plot uses the logarithm of frequency to allow a very wide frequency range to be plotted on one graph, but with each decade given equal weight. The Bode plot also shows the magnitude ($|Z|$) on a log axis so that you can easily plot wide impedance ranges on the same set of axes. This can be an advantage when the impedance depends strongly on the frequency, as is the case with a capacitor (see text below). The Bode plot is a useful alternative to the Nyquist plot. It lets you avoid the longer measurement times associated with low frequency determinations of polarization resistance, because the log $|Z|$ versus log ω plot sometimes allows a more effective extrapolation of data from higher frequencies. The Bode plot also has some disadvantages. The greatest one is that the shape of the curves can change if the circuit values change, e.g. uncompensated resistance.

Therefore, usually EIS are analyzed both Nyquist and Bode plots. EIS data is commonly analyzed by fitting it to an equivalent electrical circuit model consisting of passive elements that do not generate current or potential such as resistors (R), capacitors (C), and inductors (L). To be useful, the elements in the model should have a physical meaning in the physical electrochemistry of the system. As an example, most models contain a resistor that models the cell's solution resistance.

The alternating current response of circuit elements are following. A sinusoidal voltage applied to an ohmic resistance induces as alternating current that is in phase with applied voltage, and the impedance of ohmic circuit element is therefore equal to its resistance R:

$$Z_r = \frac{E(t)}{I(t)} = \frac{|E_0|\sin(\omega t)}{|I_0|\sin(\omega t)} = R \tag{1.9}$$

Notice that the impedance of a resistor is independent of frequency and has no imaginary component.

The impedance of a capacitor can be calculated based on the relation:

$$I(t) = C\frac{dE(t)}{dt} \tag{1.10}$$

that yields to the expression of capacitance impedance, it's modulus and phase shift:

$$Z_c = -\frac{j}{\omega C} \tag{1.11}$$

$$|Z_c| = \frac{1}{\omega C} \qquad \phi = -\frac{\pi}{2} \tag{1.12}$$

A capacitor's impedance decreases as the frequency is raised. Capacitors also have only an imaginary impedance component. As follows from the detailed derivation of (1.11), the current through a capacitor is phase shifted by 90° with respect to the voltage.

For the inductance, it can be written:

$$E(t) = L\frac{dI(t)}{dt} \tag{1.13}$$

that yields to the expression of inductance impedance, it's modulus and phase shift:

$$Z_l = j\omega L \tag{1.14}$$

$$|Z_l| = \omega L \qquad \phi = \frac{\pi}{2} \tag{1.15}$$

The impedance of an inductor increases as frequency increases. Inductors have only an imaginary impedance component. As a result, the current through an inductor is phase-shifted by −90° with respect to the voltage.

The interpretation of EIS data is built upon reaction model (or equivalent circuit) consisting on passive elements connected in some order. Regardless the variety of electrode processes (deposition and corrosion of metals, electroreduction of ions, oxide film formation, adsorption phenomena, and etc.) they contain the similar stages and comprises similar processes such as formation of double electric layer, the presence of ohmic resistance, charge transfer resistance of electrochemical reaction, adsorbed layers formed by intermediates of complex electrochemical reactions either by protective films, diffusion (transport phenomena) in solutions and in the organic or polymeric films, and etc. Therefore, the same equivalent circuits but with some different physical meaning of passive elements can simulate different processes occurred on the electrode. With the equations of the model it is then possible to calculate the electrochemical impedance as a function of frequency and check conformity experimental data to theoretical model using commercial software, for example ZVIEW® or Autolab® with frequency response analyzer (FRA).

Notably, the reactions occurring consequently are modeling by elements or circuits connected in series, whereas simultaneously occurring processes are modeling by elements or circuits connected in parallel. Mostly used equivalent circuit describing electrode processes are provided in Fig. 1.1. The simplest equivalent circuit can model the electrical behavior of electrode-solution interface is shown in Fig. 1.1a. In this case R_1 simulates ohmic resistance (solution, wires and

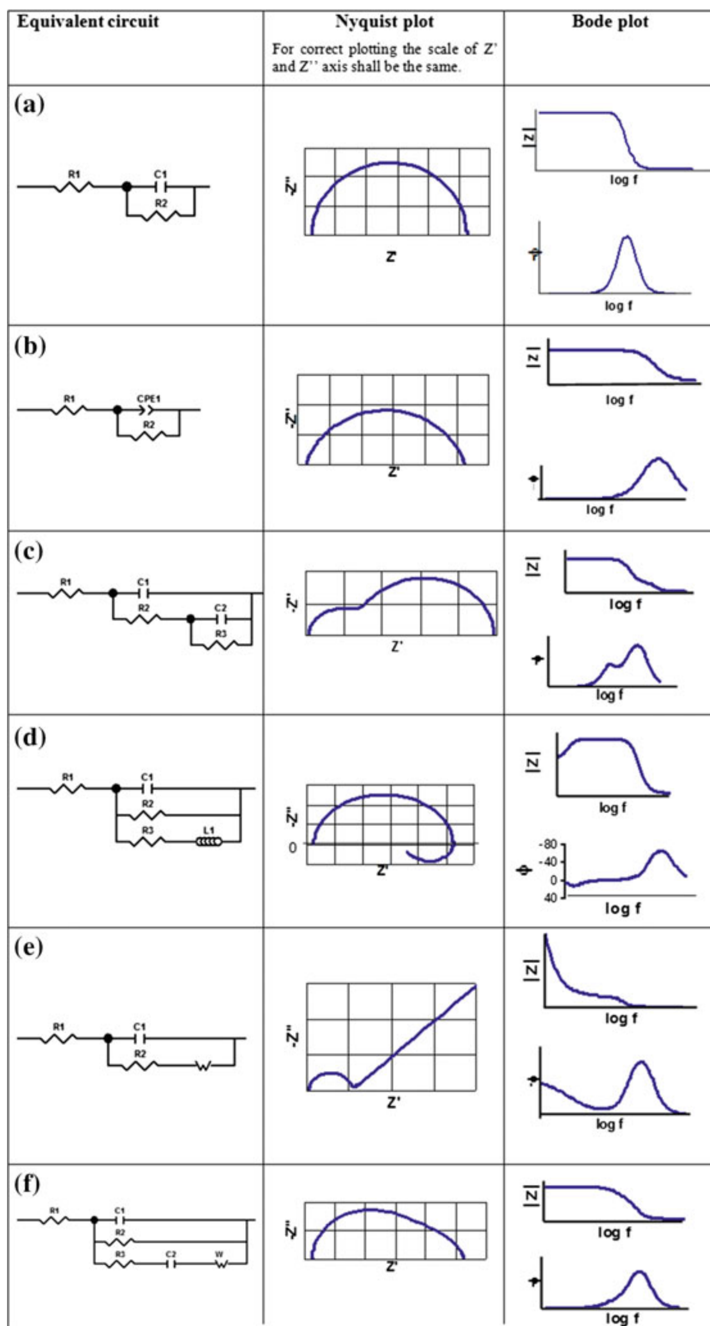

Fig. 1.1 Often used equivalent circuits to describe electrode processes, typical shapes of Nyquist and Bode plots of ones. For details, see the text

other uncompensated resistances), C_1 simulates the capacity of double electric layer which is charged simultaneously with the occurring electrochemical reaction; the charge transfer resistance (R_p) of one is simulated by R_2. The Nyquist plot represents a semi-circle of radius $R_2/2$ whose center is located on the real axis at the distance $R_1 + ½R_2$ from the origin.

The physical interpretation of the distributed elements in an equivalent circuit modeling solid electrodes is somewhat more complicated than predicted by this model. They are, however, essential in understanding and interpreting most impedance spectra. There are two types of distributions which we need to concern. Both are related, but in different ways, to the finite spatial extension of any real system. The first one is associated directly with nonlocal processes, such as diffusion, which can occur even in a completely homogeneous material, one whose physical properties, such as charge mobilities, are the same everywhere. The other type, exemplified by the constant-phase element (CPE), arises because microscopic material properties are themselves often distributed. For example, the solid electrode–solid electrolyte interface on the microscopic level is not the often presumed smooth and uniform surface. It contains a large number of surface defects such as kinks, jags, and ledges, local charge inhomogeneities, two- and three-phase regions, adsorbed species, and variations in composition and stoichiometry. Reaction resistance and capacitance contributions differ with electrode position and vary over a certain range around a mean, but only their average effects over the entire electrode surface can be observed. The macroscopic impedance, which depends, for example, on the reaction rate distribution across such an interface is measured as an average over the entire electrode [3]. Consequently, in the Nyqist plot the semicircle becomes flattened (Fig. 1.1b). To account for this effect, it has become current practice, especially in corrosion science and engineering, to replace the double layer capacitance (and other capacitances) in the equivalent circuits by a constant phase element (CPE). The impedance of constant CPE is given by:

$$Z(\omega) = \frac{1}{Q}(j\omega)^{-n} \tag{1.16}$$

here $0 < n < 1$, and Q is a constant.

The case $n = 1$ recovers a perfect capacitor.

If electrochemical impedance measurements are performed under reversible potential it is possible to calculate apparent value of exchange current density, i_0, and rate of constant of electrochemical reaction, k_0 from the charge transfer resistance extracted from the EIS data. If one takes Butler-Volmer equation under the reversible condition, i.e. that in which the overpotential, η, tends to zero, then [8]

$$\frac{\partial i}{\partial \eta} = \frac{1}{R_p} = i_0 \frac{F}{RT} \tag{1.17}$$

The relation of the exchange current density to the rate constant at equilibrium is

$$i_0 = zF\chi k_0 c_i \tag{1.18}$$

here χ is the thickness of the reaction ion layer

On some electrochemical processes, there is more than one rate-determining step. Each step represents a system impedance component and contributes to the overall reaction rate constant. The electrochemical impedance experiment can often distinguish among these steps and provide information on their respective rates or relaxation times. In such cases, the equivalent circuit contains more elements. For example, if electrochemical reaction involves intermediate stage with one adsorption of reacting intermediate, the equivalent circuit for this case is shown in Fig. 1.1c. The physical meanings for R_1, C_1, and R_2 are the same as in Fig. 1.1a, b. The elements C_2 and R_3 represent capacitance and resistor of adsorbed layer, respectively. However, this equivalent circuit describes also other processes, such as the presence of non-conductive films (lubricants, paints etc.), therefore passive elements have other physical meanings, and they are noted in the corresponding chapters below.

In fact, the analysis provided in [5] shows that in the simple case of one adsorbed intermediate various complex plane plots may be obtained, depending on the relative values of the system parameters. These plots are described by various equivalent circuits, which are only the electrical representations of the interfacial phenomena. In fact, there are no real capacitances, inductances or resistances in the circuit (faradaic process). These parameters originate from the behavior of the kinetic equations and they are functions of the rate constants, transfer coefficients, potential, diffusion coefficients, concentrations, etc. Besides, all these parameters are highly nonlinear, that is they depend on the electrode potential. It seems that the electrical representation of the faradaic impedance, however useful it may sound, is not necessary in the description of the system. The system may be described in a simpler way directly by the equations describing impedances or admittances.

When transport phenomena play a role, the faradaic impedance can be separated into two terms, the kinetic impedance (Z_t) and the diffusion impedance (Z_d), and $Z_F = Z_t + Z_d$.

Z_t represents impedance in the absence of concentration overpotential. In some simple cases it can be represented by charge transfer resistance (see Fig. 1.1a), in more complicated cases it may include several circuit elements, e.g. impedance of consequently occurring charge transfer reactions (Fig. 1.1c). Z_d describes the contribution of concentration overpotential to the faradaic impedance, and therefore depends on transport phenomena in the solution. In the absence of convection, it is referred as Warburg impedance Z_W. The Warburg impedance is equal to:

$$Z_W = \frac{\sigma}{\sqrt{\omega}} - j\frac{\sigma}{\sqrt{\omega}} \tag{1.19}$$

$$\sigma = \frac{RT}{C_{st} n^2 F^2 A \sqrt{2D}}$$

As follows from (1.19):

$$\tan\phi = \frac{Z_{\mathrm{Im}}}{Z_{\mathrm{Re}}} = -1 \tag{1.20}$$

Therefore, the phase shift is equal to $\phi = -45°$, and in the Nyquist plot the Warburg impedance is represented by a straight line at 45° angle. If charge transfer is represented only by one resistance (R_p = R2), the total impedance of the electrode corresponds to that of the Randles equivalent circuit, as it is shown in Fig. 1.1e. In this figure Nyquist diagram consists of two distinct domains: at high frequency, a semicircle shows that the transfer resistance determines the impedance, while at low frequencies diffusion dominates and Warburg impedance is observed. However, in some cases, the kinetics of electrode processes is more complicated [9], because of the adsorption of intermediates and components of solutions (e.g. ligands) coupled with charge transfer and diffusion processes. Therefore, it is impossible to distinguish frequencies ranges at those the kinetics or mass transfer controls electrode processes based on the experimental EIS data (some of these were published for ex. in [10, 11]).

Analysis of the ac impedance spectra in the presence of specific adsorption revealed that the complex plane show formation of deformed semicircles, that might be described by introducing into equivalent circuit CPE. Authors [12] proposed an electrical equivalent model, in which instead of the CPE there is a double-layer capacitance in parallel with a series connection of the adsorption resistance and capacitance, R_{ad} and C_{ad} (R3 and C2 in Fig. 1.1f), and the semi-infinite Warburg impedance (W) connected with the diffusion of adsorbing species. This equivalent circuit allows describing various shapes of Nyquist plots, such as 2 semicircles, depressed one semicircle, and other.

Other more specific equivalent circuits are provided in the corresponding chapters of this paper below.

The impedance technique is often applied to various electrochemical systems that were never studied before. The Nyquist and Bode plots obtained often display shapes that had never been encountered previously. Before starting the analysis and modeling of the experimental results, it should be confirmed that the impedance data are valid. There is a general mathematical procedure, which allows for the verification of the impedance data. It was introduced by Kramers in 1929 and Kronig, 1926 further developed by Bode in 1945 and later applied to EIS [13]. The impedance derived is valid provided that the following four criteria are met: (i) linearity (a system is linear when its response to a sum of individual input signals is equal to the sum of the individual responses); (ii) causality (the response of the system must be entirely determined by the applied perturbation, that is the output depends only on the present and past input values); (iii) stability (a stable system remains stable unless excited by an external source and it should return to its original state once the perturbation is removed and the system cannot supply power to the output irrespective of the input); and (iv) finiteness (the real and imaginary components of the impedance must be finite-valued over the entire frequency range

$0 < \omega < \infty$, i.e. the impedance must tend to a constant real value for $\omega \rightarrow 0$ and $\omega \rightarrow \infty$. Unfortunately, the Kramers-Kronig transform requires integration over a range of frequency from zero to infinity. Since no one can measure spectral data over that range, evaluating the K-K relations via integration always involves assumptions about the behavior of a spectrum outside the frequency over which it was measured. The transformation procedure is described in details in for ex. [3–5, 13]. In practice, the Kramer-Kronig transformation is possible to perform using built in the EIS recording devices corresponding software, e.g. Gamry Echem Analyst or Autolab® with FRA. When you select Kramers- Kronig on an impedance menu a model of the type is fit to the selected region of the spectrum. If the fit is poor, you can assume that the data is not transformable and is therefore of poor quality. There is little point fitting non-Kramers-Kroning compliant data to an equivalent circuit model.

1.3 EIS Responses During Cathodic Metals and Alloys Films Deposition

Electrochemical impedance spectroscopy (EIS) responses during electrodeposition have gained the interest last decades due to possibility to determine several parameters of the systems e.g. double-layer capacitance, to characterize the electrode processes and to determine the kinetics of the electrochemical systems. The use of this technique in metals/alloys electrodeposition in the presence of complexes or additives has also high impact since adsorption phenomena strongly influence the electrochemical impedance [14–18]. One of its advantages is the possibility of investigation the relaxation of the electrode surface from adsorbed species and growth of layers. The impedance spectra of the deposition processes of metals/alloys usually show one or several relaxations (capacitive or inductive) [19, 20]. Thus, using electrochemical impedance spectroscopy, the electrodeposition of Co and Co-W were studied by authors in order to compare the differences of the deposition and codeposition of Co with tungsten and the effect of the pH on these processes.

The cobalt and cobalt alloys are investigated for their magnetic and corrosion resistant properties by many groups of researchers, including [21]. The interest in tungsten and its alloys has been driven by its outstanding properties and multiple possible applications overviewed by E. Lassner and W.D. Schubert [22] and recently by N. Tsyntsaru and others [9]. The first commercial Co-W alloy electrodeposition process was reported by Schwartz [23], indicating the role of citrate species as an important factor to achieve the desirable morphology and structure of deposits. Complexing is used as a method to approach the electrode potentials of different metals by reducing the concentration of "free" Me^{2+}" ions and increasing the solubility of Me(II) salts in baths containing OH^-, WO_4^{2-} and PO_4^{3-} [24, 25]. Several common electrolytes are known and used for the electrodeposition of

tungsten alloys with iron-group metals but the number of complexing agents used is limited (citrates, pyrophosphates [26, 27], tartarates [28, 29], gluconates [30, 31]). The presence in such electrolytes the species with high molecular weight [32, 33] is the particular feature of the given systems which influence the mechanism of electrodeposition.

However, some difficulties to describe the mechanism and kinetics of tungsten codeposition with iron group metals (Fe, Co, Ni) are related with rare data about the mechanism and kinetics of pure iron group metal complexes electroreduction and identification of the electrochemically active complex of metal that participates in the electrochemical charge transfer reaction in complex solutions. Even in the "simple" case of cobalt electrodeposition, the process actually is complex and multistaged, caused by transfer of two electrons for cobalt reduction to metal state and by the parallel process of hydrogen evolution. This secondary process increases the pH of the near-electrode layer and induced the formation of $CoOH^+$ on electrode surface [34], effect on the kinetics and mechanism of cobalt electrodeposition [35–38].

As an example, data on Co electrodeposition from various solutions are discussed below. The polarization curves at the same total Co(II) concentration in the electrolyte are presented in Fig. 1.2. The differences are caused by the different ionic content of solution due to the formation of ionic pairs (sulphate electrolyte) and complexes (citrate electrolyte). However, from the first view, the shape of these curves is similar to the shapes obtained for the processes of mixed kinetics (charge transfer and diffusion). In this case the plateau evident on the curves should be linked to limiting diffusion current. On the other hand, it is not expected such big differences in diffusion coefficients of various Co(II) compounds. Moreover, if this plateau is linked to limiting diffusion current, in accordance with equation describing the Warburg impedance Z_W shall be equal to infinity when concentration at the electrode surface ($c_{st,s}$) becomes equal to zero in according to (1.19).

Therefore, the whole impedance of electrode process shall become infinitive too.

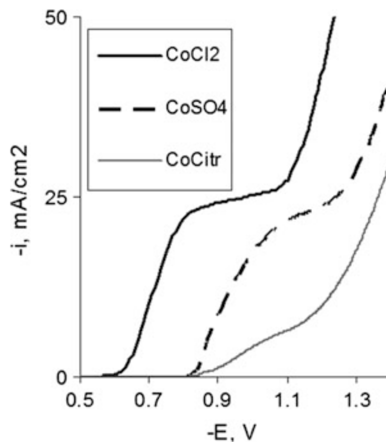

Fig. 1.2 Polarization of Co electrode in the various electrolytes: chlodide: 0,25 mol/l $CoCl_2$ + 0.4 mol/l NaCl + 0.25 mol/l H_3BO_3 pH 6; sulphate: 0.25 mol/l $CoSO_4$ + 0.5 mol/l Na_2SO_4 + 0.65 mol/l H_3BO_3 pH 6; citrate: 0.25 mol/l $CoCl_2$ + 0.4 mol/l H_3BO_3 + 0.4 mol/l $Na_3C_6H_5O_7$ pH 6

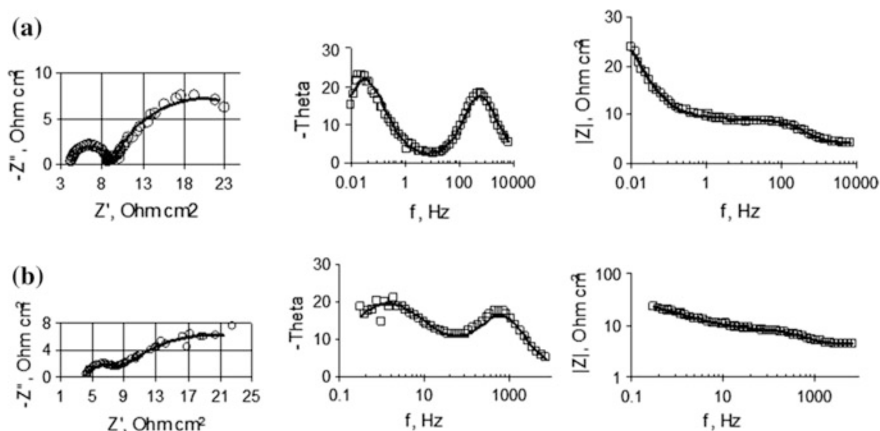

Fig. 1.3 EIS (Nyquist and Bode plots) obtained in the sulphate solution (content as in Fig. 1.2) on Co and fitting results to the equivalent circuit (Fig. 1.1c) at the potentials: **a** E = −1.00 V, **b** E = −1.20 V

The EIS data obtained in the sulphate electrolyte on Co at the "plateau" potentials presented in Fig. 1.3 show relatively small values of real and imaginary parts and spectra fit well to the equivalent circuit containing elements simulating stage of intermediate adsorbed compound (Fig. 1.1c), probably of $CoOH^+$, similarly to the case of Ni and Fe electrodeposition [39, 40]. Also, the analogous EIS data were obtained in [41] for the cases of Ni electrodeposition from chloride, sulphate and citrate solutions. In addition, this point of view is confirmed by EIS data obtained also in citrate solutions for Co-Cu alloys electrodeposition [42], where was shown that the reduction of Cu(II)-citrate and Co(II)-citrate is divided into two steps. The Cu(II)-citrate and Co(II)-citrate are first reduced to an intermediate state and then to Cu^0 and Co^0. Adsorption exists at the surface of the electrode at the potential of about −1.0 V.

The polarization curve for Co-W electrodeposition and corrected for ohmic drop are shown in Fig. 1.4. It is similar as for the processes with the ionic mass transfer determining step.

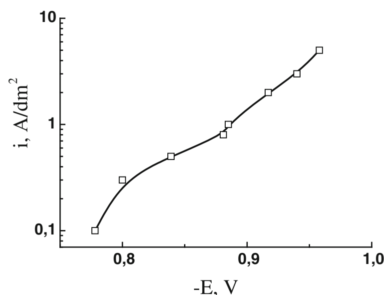

Fig. 1.4 Polarization curves of Co-W electrodeposition obtained under natural convection and subtracted of ohmic drop

The results obtained by us [10] suggest that the process under study is more complex than the classical process of mixed kinetics (slow charge transfer plus slow convective diffusion). The first complexity lies in the fact that, due to the complex formation at pH > 4, the concentration of the electroactive particles significantly differs from the analytical value; hence, the respective diffusion currents and the diffusion coefficients that are determined on their basis decrease. The second complexity is due to the possibility of the formation of intermediates (in the bulk solution or on the electrode surface) and their reduction is a multistage process that includes intermediate adsorption and interaction in the adsorption stage. One of the methods for determining the role of the ionic mass transfer (the diffusion in the solution) in this process can be electrochemical impedance spectroscopy, which was applied by us.

The data presented in Fig. 1.5 show that the shape of the impedance spectra does not imply a slow diffusion stage. The presence of two peaks in the Bode diagram excludes a single slow stage of charge transfer. Also note that, if in the case of the deposition of Co-W at pH = 6.7 at low cathode potentials the electrochemical impedance spectrum is described without separate adsorption component (Fig. 1.5a), then an increase in the potential leads to an increase in the hydrogen evolution and hence in the alkalization of the near electrode layer, which results in the appearance of an adsorption component at potentials above –0.7 V (Fig. 1.5b).

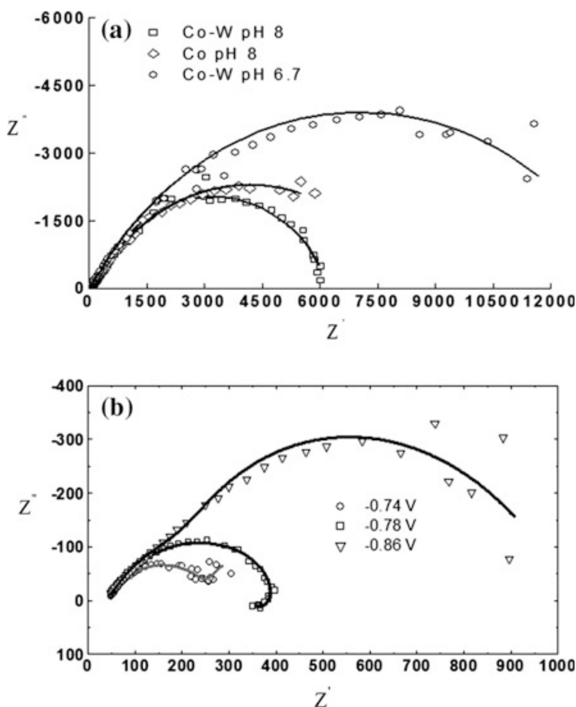

Fig. 1.5 Comparison of the experimental electrochemical impedance spectra for Co and Co-W obtained from citrate electrolytes and the results of fitting in Nyquist and Bode coordinates to the equivalent circuit shown in Fig. 1.1c

Meanwhile, at a higher value of the pH (equal to 1.8), electrochemical impedance spectrum is described by the equivalent circuit with separate adsorption at low and high cathode potentials. The presence of an adsorption complex at high pH values also plays a fundamental role in the deposition of a simpler system, such as the electrodeposition of cobalt (Fig. 1.5a).

Thus, these experimental data are adequately described by an equivalent electric circuit characteristic of the processes that include the adsorption of an intermediate compound, the double layer capacity and the adsorption capacity are replaced by the respective constant phase elements. Applied to the electrodeposition of iron group metals with tungsten/molybdenum the following sequence of reactions can be attributed to this process:

$$\mathrm{M(II)L} + e^- \rightarrow \mathrm{M(I)L_{ads}} \quad (1.21)$$

$$\mathrm{M(I)L_{ads}} + e^- \rightarrow \mathrm{M(s)} + \mathrm{L} \quad (1.22)$$

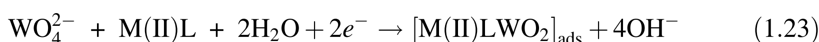

$$\mathrm{WO_4^{2-}} + \mathrm{M(II)L} + 2\mathrm{H_2O} + 2e^- \rightarrow [\mathrm{M(II)LWO_2}]_{\mathrm{ads}} + 4\mathrm{OH^-} \quad (1.23)$$

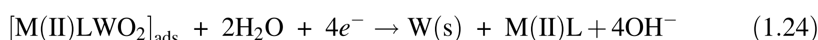

$$[\mathrm{M(II)LWO_2}]_{\mathrm{ads}} + 2\mathrm{H_2O} + 4e^- \rightarrow \mathrm{W(s)} + \mathrm{M(II)L} + 4\mathrm{OH^-} \quad (1.24)$$

Thus, the equivalent circuit shown in Fig. 1.1c is not the only one describing the impedance spectrum of a process with the adsorption of an intermediate compound. Depending on the ratio of the rates of the reactions of the total process (1.21–1.24), which also depend on the potential, a situation can occur when the resulting phase shift will correspond to the inductance; that is, so called pseudoinductance will take place and is modelled by equivalent circuit shown in Fig. 1.1d. In this case the inductance simulates the situation when the adsorption layer is not constant under cyclic changes in the low frequency potential [43]. The similar equivalent circuits are also obtained in [40].

Thus, the data of the impedance measurements show the presence of adsorption processes in the systems under study and the impedance does not specify the chemical composition of the adsorbed layer or the number of adsorption stages. It only shows the presence of a slow adsorption stage that follows from the data. Regardless of the complexes used for the codeposition of Co and W (individual or mixed cobalt–tungsten), the reduction of Co(II) and W(VI) requires a certain number of electrons (two for cobalt and six for tungsten). The simultaneous transfer of this number of electrons is hardly probable; therefore, a partially reduced complex is apparently held on the surface, in particular, by adsorption forces. The data for the impedance also suggest that the stirring of the electrolyte has an effect on the state of its surface rather than on the mass transfer from the solution to the electrode. It follows from the results of [44] that, at pH ≤ 4, the electrochemically active particles are an aquatic complex of Co^{2+}; therefore, the calculated value of the diffusion coefficient is “unsual” in this case.

At higher pH values, the electrochemically active particles will be both cobalt hydroxocomplexes [40, 43] and citrate complexes of cobalt as well as (possibly)

mixed cobalt–tungsten citrate complexes. As the pH increases, their concentration changes and the adsorbed citrate complexes undergo a structuring. It is also known (see, e.g., [45]) that the concentration of the cobalt aquatic complexes in the solution and the current density of the electrodeposition decrease at pH > 5. The hydrogen evolution on the electrode favors a local increase in the pH. With the rotation of the electrode, the local increase in the pH sharply slows down, which leads to a decrease in the concentration of the adsorbed complexes and an increase in the electrodeposition current's density. In a galvanostatic mode, at a constant current density, this results in an increase in the current efficiency; a lowering of the electrodeposition potential; and a decrease in the concentration of tungsten in the coating [46], which, in turn, is one of the causes of changes in its structure [47] and hence properties [48].

1.4 Anodization of Metals: Characterization of Oxide Films and Their Growth by EIS

Anodization, because of its nature-friendly properties and low cost, has become a point of interest in the last century. Anodizing is an electrochemical process which is performed to form a protective oxide layer on the surface of a metal. Other methods such as evaporation or plasma enhanced chemical vapor deposition (PECVD) are known to be used also for oxidation. But among these, advantages of anodizing make it more attractive. Low cost, more precise thickness control and easier handling of process can be given as examples to these advantages [49]. Anodization can be used in different fields or for different applications. Protection of a surface against corrosion, decorative metal finish, architectural and nanotechnology applications, electrolytic capacitors, humidity sensors, self-lubricating systems and aerospace structures can be given as examples [50–53].

Anodic film formation of various thickness and structure is mostly applied on titanium (Ti) and aluminium (Al). However, zinc, magnesium, niobium, tantalum and iron can also be anodized [52]. For valve metals such as Al, Ti, Ta, or Zr, anodization has been extensively explored and, by a controlled variation of the electrochemical parameters used, the thickness, morphology e.g., compact or porous layers or crystal structure of the anodic films can be tailored to achieve the desired functionality [54]. Either a thick non-porous oxide or a film consisting of pores in nano-scale can be achieved by anodizing [49].

The porous structure of the anodic layers provides the oxides with absorbent characteristics which increase their applications. Nevertheless, in those applications where the oxides are atmospherically exposed, sealing of the anodic layers is required because porosity decreases the corrosion resistance [55]. The sealing process achieves an important reduction in the porosity of the anodic layer. Atmospheric exposure of the oxide produces significant changes in the anodic layer (due to the autosealing process) increasing the material corrosion resistance

[56, 57]. The corrosion resistance depends on layer thickness and especially on the sealing quality, so good quality control on both parameters has maximum significance. There are many different experimental evaluation techniques which offer interesting information, but all of them have their limitations [57]. The application of electrochemical impedance spectroscopy to the oxide films characterization has many advantages. The results show that EIS is a powerful tool able to provide tiny pieces of information on the films electrochemical properties, and not least in which way atmospheric exposure can modify the anodized samples properties [57–61]. Hoar and Wood [62] were first proposing an impedance bridge to describe oxide films; they suggested ECs to model unsealed and partially sealed anodized films [55]. Lorenz and other authors proposed the "passive pit model" (where it is assumed that pits have penetrated only the outer porous layer without damaging the barrier layer) and the active pit model (where it is assumed that pits have penetrated both the porous and barrier layer) [60, 61, 63, 64]. As pointed out by Mansfeld and Kendig [60], the passive pit model can also be used to interpret the sealing mechanism.

Electrochemical impedance spectroscopy has been used to characterize oxide films on titanium surface [65–71]. Thus, in [71] the surface treatment consisted of an etching followed by an anodising procedure of titanium and sample sealing. Anodic oxide films were grown electrochemically on titanium surface using modulated potential, in hydrofluoric acid solution aiming for the production of a porous film. It is assumed that the oxide film is a two-layer film, consisting of one inner barrier layer and an outer porous layer The effect of surface etching before anodising, oxide film sealing is analyzed using the equivalent electrical circuit proposed by Pan and et al. [65] and Aziz-Kerzzo et al. [67] to simulate EIS data for an anodic oxide titanium film. This equivalent circuit is similar to shown in Fig. 1.1c, only in this R1 = Rs, which is electrolyte resistance, C1 = C_{pr}, which CPE of porous layer, R2 = R_{pr}, which is porous layer resistance, C2 = C_b, which CPE of barrier layer and R3 = R_b, which barrier layer resistance.

By evaluating R_{pr} value at different anodizing potentials it gives data on the oxide film formed and namely if the R_{pr} value is smaller than the pores produced should be larger. At the same time, Ti etching procedure before anodizing did not show any influence on Rpr values, but sealing of the oxide film increased R_{pr} values [71]. This fact can be expected because R_{pr} is associated to the outer porous layer resistance and sealing closes partially the film pores promoting a better behaviour of the anodised samples in terms of corrosion resistance. Etching of Ti surface and oxide film sealing instead increase R_b values of samples. These facts could be an indication that the inner layer is also porous. Chemical etching causes a rougher Ti surface that might improve the barrier characteristic of the inner layer. Sealing in boiling deionized water converts amorphous Ti oxide into a more stable crystalline form. Thus, if the inner layer has pores the sealing process can improve the R_b value, hence increases the inner layer corrosion resistance.

Over the years, fluoride containing electrolytes have been utilized to develop TiO_2 nanotubes of varied dimensions [72–74] in order to increase surface area for various applications. Based on EIS measurements in NaCl solution the presence of

inner barrier and outer porous TiO_2 nanotube layer was detected [75]. TiO_2 nanotubes showed two time constants at different frequency ranges and this can be due to the change in surface morphology and thickness changes with increasing anodization time. The decrease in phase angles at the high-frequency region may be related to the porous nature of the outer layer. Nyquist plots for as-formed and annealed TiO_2 nanotubes display a semicircle, which indicates near capacitive response and the presence of two time constants, can also be identified. Surface anodized for longer duration showed a larger capacitive loop which can be related to increase in thickness of the oxide layer. At high frequency, semicircles show that the transfer resistance dominates the impedance and at lower frequencies, Warburg impedance is observed which is due to diffusion of titanium ions to the porous layer. It has been reported that upon immersion in bio-fluids, Warburg impedance tends to decrease at earlier stages and finally it reaches a constant value. This behavior is due to the increase in the buildup of titanium ions in the electrolyte such that the diffusion of titanium ions back into the porous layer takes place.

More complex case is present by Suay et al. [55] which by means of electrochemical impedance spectra investigated composite process of aluminum porous anodizing, in the view of the sealing quality and the anodic films changes, and the ageing process produced by atmospheric exposure, which is important from the point of view of corrosion reliability of those oxides. To oversee the alumina porous film properties, it is a need to understand its nature. The hexagonal cells and barrier layer are made from anhydride alumina with different sulphate ions $Al_2(SO_4)_3$ from the anodizing bath. On the other hand, the porous layer is full of hydrate alumina (mono- or trihydrate or a mixture) plus absorbed water [55, 57]. Finally, there is one last layer (the intermediate layer), which is formed by diffusion from the exterior, especially in the sealing process, and slowly in atmospheric exposure [76]. Can be expected that significant changes in the porous layer will appear due to the atmospheric exposure (water absorption and the transformation of anhydride alumina to hydrate alumina inside the cells), and in the intermediate layer.

In order to fit the EIS experimental results of the anodic aluminum layer multipart equivalent circuit was proposed (Fig. 1.6). The parameter R_{sol} represents

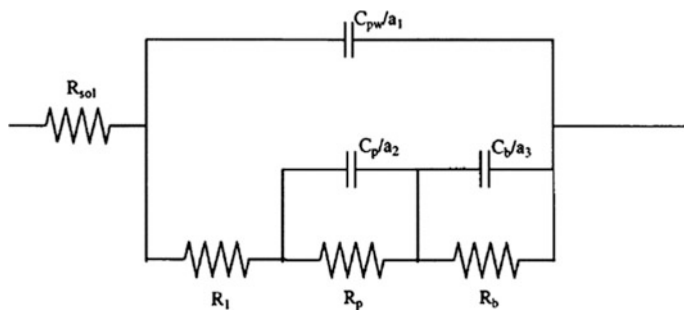

Fig. 1.6 The proposed EC to model the impedance spectra of the sealed anodized aluminium layer

electrolyte used, R_1 simulates the presence of electrolyte in the pores and faults of the intermediate layer. One of the parallel branches which are present in the circuit is formed by the resistance R_{pw} and the associate capacitance C_{pw}—they represent the walls of the hexagonal cells with uniform or nearly uniform dielectric properties. Taking into account that R_{pw} is usually so high that it prevents the passage of current, so in equivalent circuit only a capacitance C_{pw} in this branch is present. The other branch is formed by the resistance R_1 of the electrolyte in the pores and defects of the intermediate layer, in series with the pores as a whole (the pore and the barrier layers). The electrochemical properties of the pore filling are represented by R_p and C_p, while the properties of the barrier layer are represented by R_b and C_b.

Resistance R_1 is directly related to the intermediate layer changes as result to atmospheric exposure. R_1 vary markedly with the extent of sealing and the growing of the intermediate layer thickness (both processes are closely related and depend on ageing time) [55]. R_1 doubles in size for all types of atmospheres when the samples have been exposed up to 39 months. This change can be due to a better sealing of pores because hydroxides precipitation increases with exposure time and/or to an intermediate layer thickness increment. As exposure time increases precipitate particles start covering the alumina layer surface making cavities disappear and finally forming after years of exposure a homogeneous anodic layer surface, so anodized and sealed aluminum anticorrosion performance is increased due to sealing and natural ageing process.

A special case in the view of oxide films characterization by EIS is attributed to oxides formed on the metal/alloys surfaces. Here, we would like to point out oxides formed on nickel-based alloys, which are extensively used as component materials in nuclear power plants or in other aggressive corrosion environments due to its superior corrosion resistance that is attributed to the passive film formed on alloy surface. As surface metal oxide films exhibit a capacitive behavior, because of the dielectric nature of oxide films; therefore, it is convenient to study the structure of ones by EIS. During study of oxide films formed on the Ni-based superalloys in NaCl solutions was revealed a complex structure of ones that was reflected in EIS: there are three capacitance arcs in Bode plots [77]. The interfacial processes in the solutions were modeled by the equivalent circuit shown in Fig. 1.7. The values of the circuit element such as the solution resistance (Rs), the porous oxide capacitance (CPE1), the porous resistance (R1), the double layer capacitance (CPE2), the

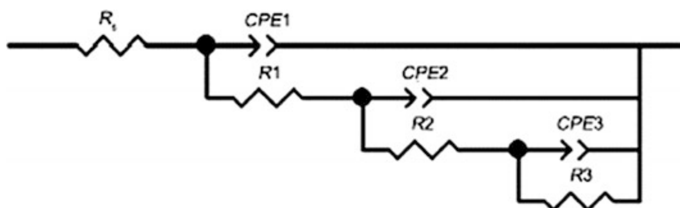

Fig. 1.7 Equivalent circuit model employed in analysis of electrochemical impedance data of oxide films

compact resistance (R2), the compact oxide capacitance (CPE3) and polarization (the chloride ions transport) resistance (R3) were used to characterize the performance of the oxide film in the corrosive environment. Based on the changes in values of elements the following dynamics of processes was proposed. Diffusion of ions into micro-pores in the oxide film experienced difficulties because of the large resistance to charge transfer. Accordingly, the fitted resistance was very large. Under this condition, the changes of CPE3 with exposure time could be used to determine water/ions uptake of the oxide film. With increasing the immersion time, the oxide film capacitance (CPE3) increased, indicating that chloride ions had penetrated into the oxide film. After then, some interconnected micro-pores were filled with the electrolyte solution, which enables further measurements of the pores resistance reasonable.

The close dependence between breakdown of a passive film and its defective nature has been directly connected with its ionic and electronic conductivity characteristics [78]. Acquisition of Mott-Schottky plots is a usual way for semiconductor materials electrochemical characterisation such as semiconducting properties of the oxide film, such as the electronic type, the effective donor density and the flat band potential by measuring the electrode capacitance (C) as a function of the electrode potential (E). The capacitance as a function of the electrode potential (E) can be expressed as follows:

$$\frac{1}{C^2} = \frac{2}{\varepsilon\varepsilon_0 A^2 q N_q}\left(-E + E_{FB} + \frac{kT}{q}\right) \quad (1.25)$$

here ε and ε_0 is the dielectric constant of the passive film and permittivity vacuum, respectively, q is the elementary charge ($-e$ for electron and $+e$ for holes), N_q is the doping density which represents the donor N_d or acceptor N_a densities for and n- or p-type semiconductor; q is the elementary charge ($-e$ for electron and $+e$ for holes), k is the Boltzmann constant; E_{FB} is the flat band potential; A is area of electrode.

Therefore, a plot of $1/C^2$ against applied potential E should yield a straight line from which E_{FB} can be determined from the intercept on the E axis, and the slope of line is equal to $\frac{2}{\varepsilon\varepsilon_0 A^2 q N_q}$ The value of N_q can also be conveniently found from the slope knowing ε and A. Example of Mott-Schottky plot for passive film formed on stainless steel [79] in Fig. 1.8, and graph explaining how to extract parameters is presented in Fig. 1.9. Electrochemical determination of these parameters is simple when energy band edges are pinned at the surface and ac response of space charge layer capacitance can be separated in frequency range from other interfacial structures and processes, which is a usual case for stationary ideally polarisable semiconductor-electrolyte interface. Complications come with surface states and Faradaic processes that require frequency response analysis by impedance spectroscopy for extraction of space charge layer capacitance from the total ac response [80]. In this case the capacity can be extracted based on analysis of EIS data employed equivalent circuits containing capacity of double electric layer. The

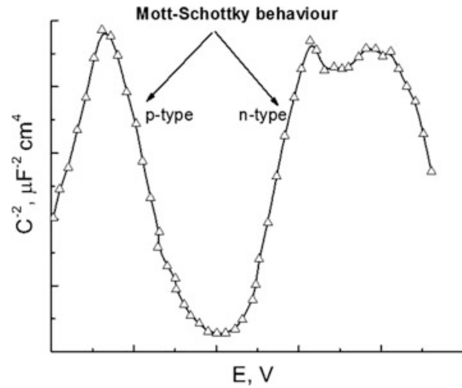

Fig. 1.8 An example of Mott-Schottky plot for passive film

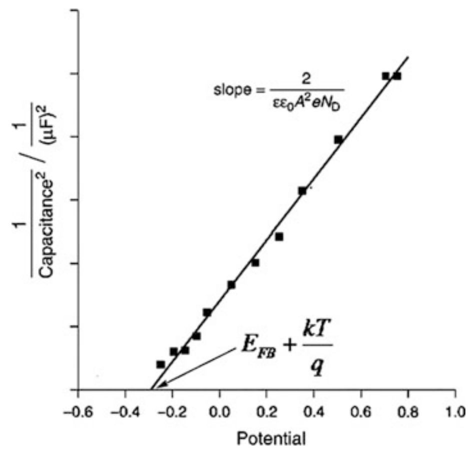

Fig. 1.9 Determination parameters from Mott-Scottky plot

mentioned procedure using Randles equivalent circuit (see Fig. 1.1b) is described in [81].

As was shown in the case of Ni-based alloy [82], the slopes of straight lines in Mott-Schootky plots is tightly depended on the measured frequency, the slopes decrease with decreasing frequency, i.e., the capacitance decreases with increasing frequency. The source of the frequency dispersion is a matter of debate and various points of view is provided in this work. The main reason probably consists in frequency dispersion in Mott-Schottky tests aroused from surface roughness and inhomogeneous current flow. In some cases [75], the Mott-Schottky plot may show a wide variation in data with frequency for porous and defective oxide structures and makes it difficult to choose a frequency value for analysis. It has been recommended by authors [83, 84] that, a frequency greater than 1 kHz with relatively higher scan rate can be used to performMott Schottky analysis, where the ionic conductivity is negligible and the response is only due to electronic conductivity. The above equation shows a linear dependence between C^{-2} and E. However,

non-linearity was observed experimentally, which according to Tomkiewicz [85] is due to oxidation of the electrode itself by holes in the depletion region, non-homogeneous doping and deep doping levels. Despite the existence of non-linear behavior, it has been shown that N_D and E_{FB} values can be determined fromthe slope and the intercept of the linear portion.

1.5 The Study of Underpotential Deposition of Metals by EIS

Underpotential deposition (UPD) is the phenomenon of electrochemical deposition of typically a monolayer of a metal on a foreign metal substrate at potentials higher than the reversible Nernst potential $E(Me^{n+}/Me)$, i.e. the deposition at "less negative" potential than that predicted from Nernst equation. In the wider sense, the UPD is not limited to the deposition of metals on metals; e.g. electrochemical adsorption of hydrogen atoms on platinum above $E(H^+/H_2)$ is also an example of UPD. The essence of the UPD phenomenon is in the surface limited character of the deposition. The UPD is controlled by the first atomic layer of the deposited material specific interaction with atoms of a substrate, which determines the intrinsic limit of the deposited material amount, typically a monolayer. Due to the surface limited character, the UPD is an efficient instrument for creating atomic layer building blocks for nanostructured materials assembly [86–91]. The UPD is also an important stage in the mechanisms of electrodeposition of semiconductor materials, mainly metal chalcogenides [92]. The difference between the reversible UPD potential, E_{UPD} (or quasi-reversible potential in the case of irreversible UPD) and $E(Me^{n+}/Me)$ is called the UPD shift, ΔE_{UPD}. The UPD shift correlates with differences of work functions of the substrate and the deposited metal in many UPD processes [93], though the correlation with work functions is not universal [94], e.g. in UPD of metals on tellurium ΔE_{UPD} shows correlation with free energies of formation of the corresponding tellurides rather than work function differences [95]. The dependences of the UPD shift on different physical quantities disclose possible differences in the nature of the interactions that control the underpotential deposition in different systems.

The surface limited character of the UPD determines the choice of electrochemical methods for investigation and monitoring of the underpotential deposition. The stationary electric current in the UPD is equal to zero, but the potentiodynamic profiles of the current and few other electrochemical variables obtained by potential sweep methods are typically very expressive (Fig. 1.10). The decay of the current at a steady potential under the potentiostatic control may affect essentially the frequency response acquired in impedance spectroscopy, due to the following reasons. First, the metal cation concentration profile which controls the impedance of diffusion decays along with the current. Second, many UPD processes are irreversible, i.e. the cathodic deposition and anodic oxidation of the

adlayer may proceed in different regions of potential, as shown in Fig. 1.10 for Pb UPD on tellurium. In the irreversible UPD, neither the forward, nor back reaction can respond to a small perturbation of the potential, when impedance spectrum is acquired at the steady state after the UPD current decay. So, the requirement of stationarity in the classical version of impedance spectroscopy appears to be in conflict with the essential properties of the object. The way out of this trouble is the same as in the case of voltammetric response acquisition in the UPD. Instead of measuring stationary frequency response which may lack essential contribution of the UPD, one can acquire the frequency response in the potential sweep, keeping in mind that the potential sweep itself causes a low-frequency limit in the frequency response acquisition [96]. Thus, the optimal solution in the UPD investigation by alternating current frequency response analysis lies in the use of potentiodynamic electrochemical impedance spectroscopy [96–98]. The latter is applicable both to reversible and irreversible UPD processes.

Interestingly, different equivalent electric circuits were derived from analysis of impedance spectra of reversible and irreversible UPD (Fig. 1.11) [96]. The equivalent circuit that represents typical reversible UPD processes (Fig. 1.12a) contains the charge transfer resistance R_{ct}, adsorption capacitance C_a and Warburg impedance Z_W in the Faradaic branch of the circuit, the latter is connected in parallel with double layer capacitance C_{dl} and the two parallel branches are

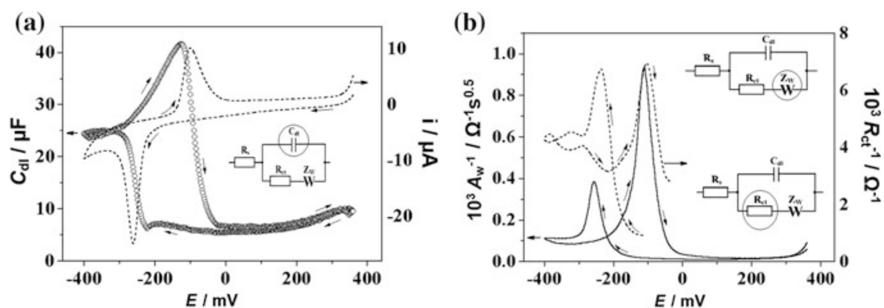

Fig. 1.10 Potentiodynamic profiles of **a** electric current i and double layer capacitance C_{dl}; **b** Warburg coefficient A_W and charge transfer resistance R_{ct} in Pb UPD on tellurium in 6 mM Pb $(NO_3)_2$ + 0.1 M HNO_3 at potential sweep rate 2.35 mV/s. The insets show equivalent electric circuits from which the frequency response parameters of the UPD were derived, with the corresponding elements of the circuit highlighted

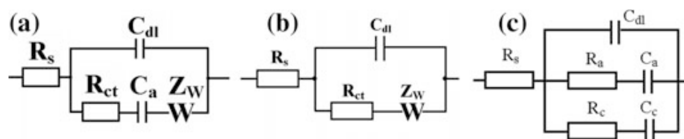

Fig. 1.11 Basic equivalent electric circuits of **a** reversible, **b** irreversible UPD, and **c** the reversible UPD with anion coadsorption

altogether connected in series with the active resistance of solution R_s. The equivalent circuit of irreversible UPD contains the same elements except C_a (Fig. 1.11b). The adsorption capacitance, which is characteristic only of the reversible UPD, results from oscillation of metal adatom coverage at the periodic perturbation of the potential. The adatom coverage does not oscillate in the absence of the back reaction; therefore, the irreversible UPD processes of the kind shown in Fig. 1.10 do not show this parameter.

The most informative parameter of the UPD derived from EIS is the double layer capacitance. This parameter discloses alterations of the interface status during the cathodic deposition and anodic oxidation of the adlayer (Fig. 1.10a). The two parameters of the Faradaic branch of the equivalent circuit, charge transfer resistance R_p and Warburg coefficient σ, characterize, correspondingly, kinetic and diffusional contributions to the Faradaic impedance. The inverses of these two parameters show peaks at the potentials of adlayer deposition and oxidation (Fig. 1.10b).

In the case of a reversible UPD, the steady state coverage of the adatoms oscillates with the potential perturbation [99], so both versions of impedance spectroscopy can give informative frequency response which corresponds to either circuit *a*, or circuit *c* shown in Fig. 1.11. The circuit *c* characterises the UPD with coadsorption of anions, such as Bi [98, 99] or Cu [97] UPD on Au. The circuit *c* was first derived in the analysis of impedance spectra of hydrogen UPD on platinum [100]. The pseudocapacitances that result from UPD and also from anion coadsorption, when the latter affects the UPD, can be much higher than the double layer capacitance; however, their contribution to the total capacitive response of the electrode is graded by the charge transfer resistance that stands in series with the corresponding capacitance in the equivalent circuit. The adsorption capacitances can be also a valuable source of information about the UPD. Figure 1.12 shows the variation of the adsorption capacitance of lead UPD on gold in the cyclic scan and also the cyclic voltammograms of Pb UPD on bare gold and gold electrode covered with atomic layer of selenium [101]. The sharp peak in $C_a(E)$ plot in Fig. 1.12b discloses the phase transition in Pb monolayer in the final stage of UPD. This

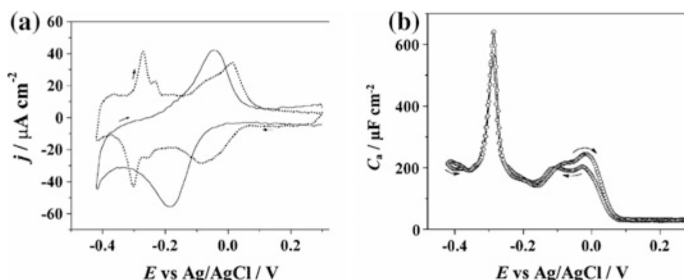

Fig. 1.12 **a** Cyclic voltammograms of bare Au electrode (*dotted*) and Au electrode coated with selenium atomic layer (*solid*) in 1 mM $Pb(ClO_4)_2$ + 0.1 M $HClO_4$ and **b** the variation of lead adsorption pseudocapacitance in the cyclic scan that corresponds to the *dotted line* in *a*

element disappeared from the equivalent circuit of Pb UPD, after the gold electrode was covered electrochemically with atomic layer of selenium, which was due to the transition from reversible to irreversible UPD (see Fig. 1.12a).

Thus, impedance spectroscopy can be a very informative source of information about underpotential deposition when it is applied adequately with the account of the surface limited character of the UPD processes.

1.6 Characterization of Organic Films onto Metals by EIS

The base purpose of protective organic films is to prevent the corrosion of metal structures. New films are developed that could be more successfully resist the versatile aggressive environments to which metals are exposed during processing. In order to assist the development and characterization of new films formulations, the early evaluation of their performance is of greatest importance. This evaluation is possible by using electrochemical impedance spectroscopy (EIS).

The first works on the EIS characterization of organic films were published by Epelboin et al. [102] and Mansfield et al. [103], and it also suggested a general model of an equivalent electrical circuit from which a large number of other models can be derived. This circuit is composed of the electrolyte resistance, followed by a capacitance (coating capacitance *C*) in parallel with a resistance (the coating or pore resistance) and finally an element Z which represents the electrochemical impedance *Z* of the process at the metal interface. One of the simplest circuit describing *Z* is composed of a capacitance, which represents the double electric layer capacitance in parallel with a resistance representing charge transfer resistance, which describes the electrochemical reaction under activation control (Fig. 1.1c). This model "as is" (Fig. 1.1c) and with some modifications still is very popular and useful to investigate various systems containing organic films on the metallic surface, such as conducting polypyrrole film on Pt [104], fluor-polymer and oligomer coated steel [105–107], industrial lubricants on stainless steel [108], organic films and corrosion inhibitors [109–114].

One of the examples of such films can be used of organic films for steel protection. Interesting cases in this view presents the use of different "films-paints" [114–116]. Thus, research by EIS of the corrosion resistance of a water-based paint system applied on carbon steel is well documented [115, 116]. Epoxy-polyamine, epoxy-amine and epoxy-acrylic resins as primer films, and acrylic-polyurethane and acrylic paints as top films, were investigated both in single layer and double-layer applications. The best protection was provided by the epoxy-amine resin, whereas acrylic-polyurethane exhibited the poorest characteristics and signs of corrosion could be observed since the initial moments of immersion onwards. Even more efficient protection against corrosion can be provided by the acrylic polymer containing zinc phosphate pigments when it was applied as a multilayer system. In this way, the high density of pores produced in the polymer matrix during the curing process could be avoided to become direct ionic pathways for the transport of

aggressive species from the environment towards the surface of the underlying metal substrate [116].

Another case is use of oil lubricant films for steel protection. Fully formulated lubricant or organic films can be viewed as a non-aqueous colloidal polymeric system with low, primarily ionic electrical conductivity. Typical lubricating oil is composed of a combination of mineral or synthetic base oils and specialized additives designed to improve long-term stability and enhanced performance in aggressive environments. The dipolar nature of components of the lubricant permits investigation of their properties using electrochemical impedance spectroscopy. EIS presents an opportunity to resolve a complicated non-aqueous colloidal system both spatially and chemically, and to analyze specific parts of that system based on relaxation frequencies using small potential (5–10 mV) for the excitation of electrochemical activity of the system metal/coated film/solution. The final purpose of the EIS characterization of the protected organic coatings is to obtain information about the system properties such as presence of defects in films, reactivity of the interface, adhesion, barrier properties [113, 117].

Thus, one of the "oil films" which will be described here is barrier properties of the films of mineral oil SAE 10 with antioxidant as well as contained Fe particles were investigated [113]. The 3 cases of steel corrosion were investigated: (a) the steel corrosion without lubricant; (b) and (c)—oil film with and without suspended Fe particles, respectively. The oil film was formed on the active area of steel rod by dropping of fixed amount (5 μl) of oil. Such amount of oil allows forming of oil film with thickness 200–250 μm. As corrosive media for such kind of measurements usually NaCl solution is used.

The value of open circuit potential (OCP) is a parameter determined by the rates of cathodic reaction and anodic reaction of a corroding device. In the studying case, the cathodic reaction is hydrogen evolution reaction, and the anodic reaction is the active electrolytic dissolution of metal [118]. At the open circuit potential, the rates of these reactions are equal. The rates of both reactions depend on the corrosion media, chemical composition of electrode material. Furthermore, the hydrogen evolution reaction depends on the state of the surface. If oil film does not participate in any chemical interaction with steel, the OCP values should be close to each other both in the presence and absence of oil film. The data presented in Fig. 1.13 confirm this statement as settled values of OCP are in the range of ~50–70 mV. The more positive values of OCP obtained for steel covered by film containing iron particles might be caused by contacting Fe particles whose surfaces are partially oxidized due to high specific area and activity. The OCP of oxidized entirely or in part surface is more positive than that for metallic surfaces. EIS is particularly well suited to evaluating corrosion behavior and insulator film characterization of materials whose surfaces have been coated with isolator films, because the EIS method in contrary to voltammetry is non-destructive method.

In Fig. 1.13 also Nyquist plots are presented for variously modified electrodes by oil films. To interpret data and physical meanings of the studied electrochemical system the equivalent circuit shown in Fig. 1.1c was used. This model is used in consideration that isolator film builds always on the metal surface in a corrosive

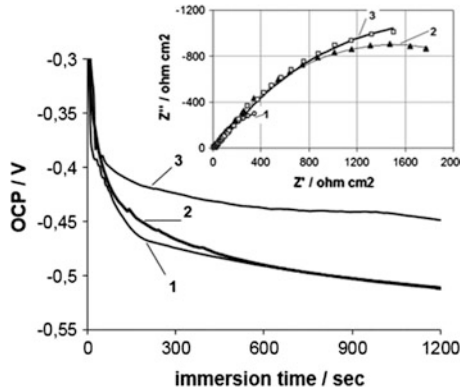

Fig. 1.13 OCP versus time in 0.5 M NaCl solution and Nyquist plots of modified electrodes (*inset figure*). In both figures: *1*—bare steel electrode; *2*—steel covered with mineral oil film; *3*—steel covered with mineral oil + 0.1 % Fe film. *Inset figure* points—experimental data, solid lines—fitting results using equivalent circuit shown in Fig. 1.1c with values of elements presented in Table 1.1 and physical meaning as in [113])

environment. Thus, an equivalent circuit model for the metal-film-solution interface requires inclusion of the film parameters: R1 = R_{sol}, C1 = $\mathrm{CPE_{film}}$, R2 = $\mathrm{R_{pores}}$, C2 = CPE, R3 = R_{corr}, resistor, R_{sol}, is the bulk solution resistance [113]. This equivalent circuit is often used to interpret data obtained for metallic electrode coated by various organic films [110–113, 118–121]. The film resistor, R_{pores}, has been interpreted as the film resistance due to the electrolyte penetration through the porous film formed by fluor-oligomer. The film capacitor, CPE_{film}, has been interpreted as the capacitance of the electric capacitor consisting of film and the solution inside. R_{corr} is the charge transfer resistance for the electrochemical reactions and in this case has a meaning of corrosion resistance. CPE in the real system is attributed to the non-ideal double layer capacitance separating the metal-electrolyte interface.

Resistances are more useful values to evaluate the corrosion behavior because charge transfer resistance (R_{corr}) which is inversely related to corrosion rate. As it follows from the data presented in Table 1.1, corrosion resistance is higher in the presence of oil ($\sim$2 times) and Fe particles in oil ($\sim$3 times). The film resistor R_{pores} also is higher in the presence of oil films. The effectiveness of inhibition (*IE*) can be calculated from the values of charge transfer (corrosion) resistance by [113, 118]:

$$IE = \frac{R_{corr}^{film} - R_{corr}^{bare}}{R_{corr}^{film}} \cdot 100\,\%, \qquad (1.26)$$

where: R_{corr}^{film} is the charge transfer resistance in test with oil film; R_{corr}^{bare} is the charge transfer resistance for bare electrode.

Table 1.1 Values of elements used to fit experimental data with equivalent circuit shown in Fig. 1.1c

Element	Bare steel	Steel covered with mineral oil film	Steel covered with mineral oil + 0.1 % Fe film
R_{sol}, Ω cm^2	3.84	4.97	4.28
R_{pores}, Ω cm^2	63.99	278.6	490.4
R_{corr}, Ω cm^2	1263	2683	3394
CPE_{film}, μF cm^{-2}	19.40	21.35	34.92
	n = 0.61	n = 0.700	n = 0.63
CPE, μF cm^{-2}	53.20	15.20	21.24
	n = 0.815	n = 0.724	n = 0.725

The IE in the 0.5 M NaCl of mineral oil film on steel is 53 %, and of mineral oil film containing Fe particles is 62 %. These results means that oil films are moderate corrosion inhibitors.

1.7 Electrochemical Impedance Spectroscopy (EIS) in Development of Biosensors and Biofuel Cells

EIS is has been successfully applied for the characterization of biosensing surfaces [122] and/or in evaluation of bioanalytical signals generated by biosensors [104].

Electrochemical biosensors could be divided into two principally different classes: (i) catalytic (which are mostly based on enzymatic catalysis) biosensors [123] and (ii) affinity sensors [124]. The application of EIS in both types of biosensors is significantly different, because in the most of enzymatic sensors variations that can be detected by EIS are mostly accumulated in bulk solution in the form of changing concentrations of reactants and/or reaction products, at the same time the changes on the enzyme-modified electrode are mostly not well detectable by EIS, therefore here other some electrochemical methods such as constant potential amperometry [125] or cyclic voltammetry are applied [126]. In this respect EIS is mostly applied during the formation of enzymatic and other materials based sub-layers, which are essential for function of the sensor, e.g. in our recent researches we have shown that EIS could be successfully applied for the evaluation of separateed multilayers in glucose sensors based on multi-layered structure [127, 128]. The EIS is mostly used in order to determine the double electric layer capacity and resistance of various modifiers, which carry the charge from electrolyte to electrode and also for the estimation of ion diffusion in solution towards the studied electrode [129]. Because of these abilities the EIS provides detailed information on some electrochemical characteristics of the electrochemical system. During our preliminary evaluation of 1,10-phenanthroline-5,6-dione and glucose oxidase modified electrode basic $R_{\Omega}(R_{A}C_{A})$ circuit was applied [128],

however the circuit well fitted with experimental results only in very narrow frequency range from 1390 Hz to 14.37 mHz. Therefore, the aim of advanced research was advanced EIS-based evaluation of 1,10-phenanthroline-5,6-dione and glucose oxidase deposited on graphite electrodes, in order to adjust most suitable equivalent circuit, which is describing this electrochemical system [127]. It was determined that equivalent circuit $R_{\Omega}(R_{F2}C_2)(C[R_F W])$ most optimally describes this electrochemical system.

There are also some other studies on the application of EIS for the characterization of enzyme-modified surfaces [130]. Some other researches illustrated that EIS could be applied in glucose concentration measurements based on bio-electrochemical systems on GOx-modified electrodes [131].

Very different situation is observed in affinity sensors, because during the application of these sensors there are almost no observable changes in bulk solution, which could be easily detected by EIS. But differently from enzymatic biosensors in affinity sensors changes on electrode surface are very different since affinity sensors are not able to generate constant flow of electrons or significantly change the concentration of redox compound, therefore analytical signal in affinity sensors can be only indirectly detected by constant potential amperometry, e.g. such detection is possible when secondary antibodies labelled by horseradish peroxidase are applied [132]. However, surface changes in affinity sensors are significant therefore they could be determined and relatively well evaluated by various potentiodymic methods, such as cyclic voltammetry [133, 134], differential pulse voltammetry [134], square wave voltammetry [135], pulsed amperometric detection [136] and EIS techniques [134]. We have demonstrated that among here mentioned techniques EIS is providing the most useful set of data, which is required for the evaluation of analytical signal [134]. The EIS is based on electrochemical response of a system towards perturbations applied at different frequencies [104]. Using other electrochemical methods, such as amperometry or potentiometry there is always a problem of the measured system being non-linear because of changing electrochemical conditions, due to relatively high variation of electric current or voltage, and in this way influencing measured results. In potentiostatic EIS, which is based on constant electrode polarization voltage, a small sinusoidal perturbation of potential is usually applied. The amplitude of such perturbation usually is in the range of 5–20 mV. Such perturbation does not disturb the system's linearity and in this way it enables to acquire results, which are also linear in time and suitable for further analysis [129, 130]. Hence the EIS is one of the most informative out of many recently available electrochemical methods in development of affinity sensors and biosensors [135].

Especially well the EIS is applied in the sensors based on electrodes modified by semiconducting polymer based layers [137]. Especially well EIS is suitable for affinity sensors based on molecularly imprinted conducting polymers (MIPs) such as polypyrrole, which could be imprinted by low molecular mass molecules such as theophylline [138], caffeine [139, 140] or by large molecules such as proteins [141] and even DNA [142]. In a number of our research we have demonstrated that the EIS is the most efficient electrochemical signal detection technique in sensors where

here mentioned MIPs [138, 139, 142] or some other affinity towards analyte exhibiting structures are applied for creation of affinity sensors [143]. If correct equivalent circuit is applied the EIS has advantages over other electrochemical methods, (e.g. pulsed amperometric detection [136]).

It should be noted that conventional EIS based techniques represents only averaged response of the entire electrochemical system. Therefore, if advanced evaluation of affinity sensor signals is required during various stages of creation of affinity sensors [122, 139, 143, 144]. In such investigations combination of EIS with quartz crystal microbalances [139, 144], surface plasmon resonance [145], scanning electrochemical microscopy [122] and other techniques are applied.

In order to get more advanced mapping of electrochemical system the EIS could be merged with scanning electrochemical microscopy (SECM) this marged technique is named scanning electrochemical impedance spectroscopy (SEIM). In SEIM based technique localized impedance measurements could be performed in the range of frequencies when the surface of interest is scanned by ultramicroelectrode (UME) [122]. Dependingly on requerments the result of SEIM could be visualized by mapping one of calculated parameters, e.g. charge transfer resistance or double layer capacitance as a function of 3D coordinates [146, 147]. It was demonstrated that the combination of SECM and EIS is providing information about local corrosion phenomena, which could help to identify the location of defects induced by corrosion [147]. In addition, comparison of conventional EIS with localized EIS was done during the investigation of degradation of polyester coil-coated galvanized steel [148] and in the evaluation of the degradation of some coatings, which were based on deposited organic compounds or polymeric layers [149, 150].

During the development of enzymatic biosensors, it was demonstrated that the glucose oxidase (GOx) based biosensor surfaces could be sucessfully analyzed by merged scanning electrochemical microscopy (SECM) and EIS techniques [122]. This advancement of SECM by EIS could provide additional electrochemical information on electrochemical properties and concentrations gradients of electrochemically active and even not active materials in selected 3D volume of solution [122]. Such EIS data based information could be very atractive in the evaluation of biofuel cell efficiency [151] and in the modelling of biosensor action [152] because it is hardly available by other electrochemical methods.

The evaluation of enzymatic reaction intensity could be estimated by conventional SECM techniques [153, 154]. However, in conventional SECM the most commonly used electrochemical method is based on faradaic response when fixed potential is applied to the UME in order to register the concentration of electrochemically active enzymatic reaction products [155, 156]. Moreover, it should be noted, that the potential applied to the electrode drives the electrochemical system far from the equilibrium, and then the response to this perturbation is observed as disturbing signal. In order to avoid this problem, the applicability of technique based on SECM in which the UME is modulated by selected frequency alternating current (AC-SECM) can be applied. The AC-SECM based technique also allows to study local corrosion processes in the entire solution volume without any redox

mediator [157]. Using AC-SECM method the approach curves were recorded at several different frequencies and they demonstrated negative feedback behavior while the UME was approaching an insulating surface [158]. This phenomenon is similar to that observed in faradaic SECM based methods, however, different approach curves were observed when different frequencies were applied [159]. In order to advance this technique, the entire electrochemical impedance spectra can be registered at every measurement point and then the electrochemical system can be evaluated using the most suitable and informative equivalent circuits. This technique is called scanning electrochemical impedance microscopy (SEIM). In the case of SEIM conventional approach curves, which represent ohmic resistance and/or other equivalent circuit parameters vs distance are plotted. The concept of SEIM was described recently in the evaluation of localized corrosion processes by Schuhmann's group [147, 160]. When SEIM was applied for localized evaluation of corrosion processes the sample was minimally influenced by UME, which was applied as a scanning probe, and it was demonstrated that domains, which have different electrochemical properties, could be easily distinguished by SEIM even if they have similar topography and/or morphology [147]. In another research, impedance dependence on UME distance from insulating sample was revealed at feedback mode SEIM [161]. The spherical diffusion, which has most significant influence far from insulating surface, was evaluated by Cole-Cole impedance evaluation method, and the radial diffusion, which has most significant influence when the UME is approaching insulating surface, was evaluated by Cole-Davidson impedance evaluation method. It was determined that the low-frequency part of the EIS in a thin-layer between UME and surface of interest is controlled by both above mentioned types of diffusion. Moreover, it was also demonstrated that the SEIM in feedback mode is suitable for constant-height based imaging. When SEIM was acting in feedback mode the local information on both topography and surface reactivity was obtained from the simultaneous analysis of the current and electrolyte-resistance variations [162]. Fundamental aspects of SEIM were investigated comparing UME responses while it was approaching to different surfaces e.g.: (i) insulator surface, (ii) conducting surface not-connected to electric circuit, and (iii) conducting surface, which was connected to electric circuit and was held at constant potential [163]. By this research it has been shown that the admittance of the UME located at relatively small distance from the surface of interest mostly depends on the distance between UME and the surface and on interfacial properties of the surface. Therefore, the SEIM based imaging is informative even without any redox mediators. When AC-SECM and SECM methods are compared, it should be noted that the AC-SECM is performed at single frequency, while the SEIM is performed in broad range of frequencies what enables to select the most suitable equivalent circuit and to calculate number of EIS parameters. Therefore, parameters, which are derived from SEIM evaluations, better describe an electrochemical system than the parameters that are derived from AC-SECM data. We believe that the SEIM could be suitable for the investigation of biosensor and biofuel cell surfaces in order to evaluate localized activity of immobilized enzymes and/or to perform advanced evaluation of the diffusion of enzymatic reaction products.

Some researches were based on the EIS application for the evaluation of enzymatic reaction when the enzymes were immobilized on surfaces of electrodes [127, 128]. In addition, it was determined that conventional SECM is very suitable for the investigation of enzyme-modified insulating surfaces while applying constant potential to UME [153–156]. Therefore, by the assumption of previous achievements we have expected that it is possible to merge the EIS technique with SECM in order to get efficient SEIM system, which will be suitable for the evaluation of enzyme-modified surfaces [122]. The main aim of here mentioned research was to merge EIS with SECM into efficient SEIM system and, using developed SEIM for the investigation of solution conductivity at different positions, to demonstrate the suitability of SEIM for the evaluation of reaction product diffusion from enzyme-modified surface in real time [22]. The working electrode in this research applied SEIM equipment was an UME. This electrode was scanning in all three directions and therefore it was applied for the investigation of selected 3D space of solution. The obtained data were analyzed using randles equivalent circuit. Actually the SEIM is used more rarely, than the AC-SECM, because scanning at one desired frequency takes less time. But the advantage of SEIM is that the EIS measurements are performed in wide range of frequencies at each point of the UME position. Such measurements allow to evaluate the response of the electrochemical system, to develop 3D model of the system, also to determine the most suitable equivalent circuit and their parameters, which in the most optimal way to describe the system [125]. What is the most important, such measurements allow to find the values of equivalent circuit parameters in selected volume of the electrochemical cell. Reaction products, which affect solution's conductivity, diffuse from the active sites of GOx-modified surface into the solution; therefore, the SEIM with moving UME is one of the best choice to study the diffusion of formed reaction products in selected volume of electrochemical cell. Due to the fact that the EIS measurements take a long time, the conductivity changes in time were also evaluated and this issue was taken into account.

Another alternative technique, which is used for the determination of localized EIS data, is an impedance imaging combined with atomic force scanning electrochemical microscopy (AFM-SECM) [164]. In this technique the AFM-based topography and alternating current SECM (AC–SECM) based signals are recorded simultaneously with ring-shaped microelectrode, which is integrated on the AFM probe. In one AC–SECM-based research structured glass/gold substrate was evaluated by such advanced AFM probe and significant increase of current was registered when the probe was placed over spots consisting of gold [164].

However, according to our best knowledge, up to now complex research in the area of application of EIS for the investigation of biosensors and biofuel cells is still missing. Therefore, despite of high number of researches based on various EIS applications in biosensorics and biofuel cell development, further developments in these areas are required especially in those directions where the combination with other surface characterization techniques is leading towards advanced phenomena of complex interactions between biomolecules and modified electrode.

1.8 Conclusions

1. Electrochemical impedance spectroscopy (EIS) is a recent and powerful tool in corrosion and solid state laboratories. The basics of EIS and data presentation formats (Nyquist, Cole-Cole, Bode) are described and discussed.
2. The described interpretation of EIS data is built upon equivalent circuit. Regardless the variety of electrode processes its contain the similar stages and comprises similar processes such as formation of double electric layer, the presence of ohmic resistance, charge transfer resistance of electrochemical reaction, and etc. Therefore, the same equivalent circuits but with some special physical meaning of passive elements of equivalent circuit can simulate the various processes occurred on the electrode, such as cathodic metals/alloys films deposition; anodization of metals, under potential deposition of metals; characterization of organic films onto metals, application in development of biosensors and biofuel cells. With the equations of the model it is then possible to calculate the electrochemical impedance as a function of frequency and check conformity experimental data to theoretical model using commercial software.
3. Combining study by scanning electrochemical microscopy and EIS could be very attractive in order to evaluate the biofuel cell efficiency and in the modeling of biosensor action as it is unavailable to obtain by other convenient electrochemical methods.

Acknowledgments The authors acknowledge funding from FP7 Oil&Sugar project (295202), from the Research Council of Lithuania (MIP-031/2014) and Moldavian national projects (15.817.02.05A), (14.819.02.16F). Also, A.Ramanavicius is grateful to LaMeTech program project No.VP1-3.1-SMM-08-K-01-004/KS-120000-1756 for financial support.

References

1. M. Sluyters-Rehbah, Impedances of electrochemical systems: terminology, nomenclature and representation. Part 1. Cells with metal electrodes and liquid solutions. Pure Appl. Chem. **66** (9), 1831–1891 (1994)
2. A.J. Bard, L.R. Faulkner, Electrochemical methods. *Fundamentals and Applications* (Wiley, New York, 2001), 829 pp
3. E. Barsoukov, J.R. Macdonald (ed.), *Impedance Spectroscopy Theory, Experiment, and Applications* (Wiley, New York, 2005), 595 pp
4. M.E. Orazem, B. Tribollet, *Electrochemical Impedance Spectroscopy* (Wiley, New York, 2008), 523 pp
5. A. Lasia, in *Electrochemical Impedance Spectroscopy and its Applications*, ed. by B.E. Conway, J.O'M. Bockris, R.E. White, Modern Aspects of Electrochemistry, vol. 32 (Kluwer Academic Publishers, New York), pp. 143–248
6. A. Lasia, *Electrochemical Impedance Spectroscopy and its Applications* (Springer, New York, 2014), 367 pp
7. D. Landoldt, *Corrosion and Surface Chemistry of Metals* (EPFL Press, Lausanne, 2007), 622 pp

8. J.O'M Bockris, A.K.N. Reddy, M. Gamboa-Aldeco, *Modern Electrochemistry*, vol. 24. Fundamentals of Electrodics (Kluwer Academic Publishers, New York, 2002)
9. N. Tsyntsaru, H. Cesiulis, M. Donten, J. Sorte, E. Pellicer, E.J. Podlaha-Murphy, Modern trends in tungsten alloys electrodeposition with iron group metals. Surf. Eng. Appl. Electrochem. **48**(6), 491–520 (2012)
10. S.S. Belevskii, H. Cesiulis, N. Tsyntsaru, A.I. Dikusar, The role of mass transfer in the formation of the composition and structure of CoW coatings electrodeposited from citrate solutions. Surf. Eng. Appl. Electrochem. **46**(6), 570–578 (2010)
11. Y. Liu, W. Wangz, Investigation on the Cu(II) and Co(II) electrochemical reduction process in citrate solution by CV and EIS. J. Electrochem. Soc. **159**(6), D375–D381 (2012)
12. T. Pajkossy, Th Wandlowski, D.M. Kolb, Impedance aspects of the anion adsorption on gold single crystal electrodes. J. Electroanal. Chem. **414**, 209–220 (1996)
13. J.R. Macdonald, *Impedance Spectroscopy Emphasizing Solid Materials and Systems* (Wiley, New York, 1987)
14. C. Cachet, B. Saidani, R. Wiart, A model for zinc deposition in alkaline electrolytes: inhibition layer and activation mechanism. Electrochim. Acta **34**, 1249 (1989)
15. C. Cachet, B. Saidani, R. Wiart, The kinetics of zinc deposition at low overpotentials in alkaline electrolytes. Electrochim. Acta **33**, 405 (1988)
16. C. Cachet, B. Saidani, R. Wiart, The behavior of zinc electrode in alkaline electrolytes I. A kinetic analysis of cathodic deposition. J. Electrochem. Soc. **138**, 678 (1991)
17. C. Cachet, Z. Chami, R. Wiart, The behavior of zinc electrode in alkaline electrolytes II. A kinetic analysis of anodic dissolution. J. Electrochem. Soc. **139**(3), 644–654 (1991)
18. T. Chengyu, C. Hang, H. Wei, L. Yu, Z. Ziqiao, Influence of Nano-Al_2O_3 particles on nickel electrocrystallization at initial stage. Rare Metal Mat. Eng. **39**, 10–16 (2010)
19. C. Cachet, C. Gabrielli, F. Huet, M. Keddam, R. Wiart, Electrochim. Acta **28**, 899 (1983)
20. I. Danaee, Theoretical and experimental studies of layer by layer nucleation and growth of palladium on stainless steel Chemija. **24**(2), 128–136 (2013)
21. E.M. Garcia, T. Matencio, R.Z. Domingues, L.M. Garcia, J.A. Figueiredo dos Santos, N. Ribeiro, H.A. Tarôco, V. F.C. Lins, Study of cobalt electrodeposition onto stainless steel using electrochemical impedance spectroscopy (IES) J. Phys. Sci. Appl. **2**(10), 409–413 (2012)
22. E. Lassner, W.D. Schubert, *Tungsten—Properties, Chemistry, Technology of the Element, Alloys, and Chemical Compounds* (Springer, New York, 1999), 422 pp
23. M. Schwartz, N.V. Myung, K. Nobe, Electrodeposition of iron group-rare earth alloys from aqueous media. J. Electrochem. Soc. **151**, C468–C477 (2004)
24. H. Cesiulis, A. Baltutiene, M. Donten, M.L. Donten, Z. Stojek, Increase in rate of electrodeposition and in Ni(II) concentration in the bath as a way to control grain size of amorphous/nanocrystalline Ni-W alloys. J. Solid State Electrochem. **6**, 237–244 (2002)
25. H. Cesiulis, E.J. Podlaha-Murphy, Electrolyte considerations of electrodeposited Ni-W alloys for microdevice fabrication. Mater. Sci. (Medziagotyra) **9**, 324–327 (2003)
26. H. Cesiulis, M. Donten, M.L. Donten, Z. Stojek, Electrodeposition of Ni-W Ni-Mo and Ni-Mo-W alloys from pyrophosphate baths. Mater. Sci. (Medziagotyra) **7**, 237–241 (2001)
27. P. Andricacos, S.H. Boettcher, S.G. Malhotra, M. Paunovic, C. Ransom, Structure comprising a barrier layer of a tungsten alloy comprising cobalt and/or nickel. U.S. Patent Application Publication 6 pp. US 2004108136 A1 20040610 (2004)
28. M. Svensson, U. Wahlstrom, G. Holmbom, Compositionally modulated cobalt–tungsten alloys deposited from a single ammoniacal electrolyte. Surf. Coat. Technol. **105**, 218–223 (1998)
29. G.Y. Wei, J.W. Lou, H.L. Ge, Y.D. Yu, L. Jiang, L.X. Sun, Co–W films prepared from electroplating baths with different complexing agents. Surf. Eng. **28**, 412–417 (2012)
30. D.P. Weston, S.J. Harris, P.H. Shipway, N.J. Weston, G.N. Yap, Establishing relationships between bath chemistry, electrodeposition and microstructure of Co-W alloy coatings produced from a gluconate bath. Electrochim. Acta **55**, 5695–5708 (2010)

31. D.P. Weston, S.J. Haris, H. Capel, N. Ahmed, P.H. Shipway, J.M. Yellup, Nanostructured Co-W coatings produced by electrodeposition to replace hard Cr on aerospace components. Trans. Inst. Metal Finish. **88**, 47–56 (2010)
32. A.I. Shul'man, S.S. Belevskii, S.P. Yushchenko, A.I. Dikusar, Role of complexation in forming composition of Co-W coatings electrodeposited from gluconate electrolyte. Surf. Eng. Appl. Electrochem. **50**(1), 9–17 (2014)
33. S.S. Belevskii, S.P. Yushchenko, A.I. Dikusar, Anomalous electrodeposition of Co-W coatings from a citrate electrolyte due to the formation of multinuclear heterometallic complexes in the solution. Surf. Eng. Appl. Electrochem. **48**, 97–98 (2012)
34. J.S. Santos, F. Trivinho-Strixino, E.C. Pereira, Investigation of Co(OH)2 formation during cobalt electrodeposition using a chemometric procedure. Surf. Coat. Technol. **205**, 2585–2589 (2010)
35. P. Vermeiren, R. Leysen, H. Vandenborre, Study of hydrogen evolving reaction in alkaline medium at nickel and cobalt based electrocatalysts. Electrochim. Acta **30**, 1253 (1985)
36. D.R. Gabe, The role of hydrogen in metal electrodeposition processes. J. Appl. Electrochem. **27**, 908 (1997)
37. J.T. Matsushima, F. Trivinho-Strixino, E.C. Pereira, Investigation of cobalt deposition using the electrochemical quartz crystal microbalance Electrochim. Acta **51** (2006)
38. J.S. Santos, R. Matos, F. Trivinho-Strixino, E.C. Pereira, Effect of temperature on Co electrodeposition in the presence of boric acid Electrochim. Acta **53**, 644 (2007)
39. W.C. Grande, J.B. Talbot, Electrodeposition of thin films of nickel-iron. 1. Experimental. J. Electrochem. Soc. **140**(3), 669–674 (1993)
40. W.C. Grande, J.B. Talbot, Electrodeposition of thin films of nickel-iron. 2. Modelling. J. Electrochem. Soc. **140**(3), 675–681 (1993)
41. A. Budreika, The study of the electrodeposition of Ni, Co and their alloys with tungsten and molybdenum. Doctoral dissertation, 2010, Vilnius
42. Yan Liu, Wei Wang, Investigation on the Cu(II) and Co(II) electrochemical reduction process in citrate solution by CV and EIS. J. Electrochem. Soc. **159**(6), D375–D381 (2012)
43. H. Cesiulis, G. Baltrunas, The study of surface passivity and blocking by the electrochemical technique. Physicochem. Mech. Mater. **5**, 11–17 (2006)
44. M.I. Jeffrey, W.L. Choo, P.L. Breuer, The effect of additives and impurities on the cobalt electrowinning process. Miner. Eng. **13**(12), 1231–1241 (2000)
45. S.S. Belevskii, S.P. Yushchenko, A.I. Dikusar, Electrodeposition of nanocrystalline Co–W coatings from citrate electrolytes under controlled hydrodynamic conditions: Part 1. Co electrodeposition. Surf. Eng. Appl. Electrochem. **45**(6), 446–454 (2009)
46. S.S. Belevskii, N.I. Tsyntsaru, A.I. Dikusar, Electrodeposition of nanocrystalline Co–W coatings from citrate electrolytes under controlled hydrodynamic conditions: part 2. The electrodeposition rate and composition of the coatings. Surf. Eng. Appl. Electrochem. **46**(2), 91–99 (2010)
47. N. Tsyntsaru, H. Cesiulis, E. Pellicer, J.-P. Celis, J. Sort, Structural, magnetic, and mechanical properties of electrodepositedcobalt–tungsten alloys: intrinsic and extrinsic interdependencies. Electrochim. Acta **104**, 94–103 (2013)
48. S.A. Silkin, S.S. Belevskii, A.S. Gradinar, V.I. Petrenko, I.V. Yakovets, N.I. Tsyntsaru, A.I. Dikusar, Electrodeposition of nanocrystalline Co–W coatings from citrate electrolytes under controlled hydrodynamic conditions: part 3. The micro_ and macrodistribution of the deposition rates, the structure and the mechanical properties. Surf. Eng. Appl. Electrochem. **46**(3), 206–214 (2010)
49. L.M. Hagelsieb, Anodic aluminum oxide processing, characterization and application to DNA hybridization electrical detection. PhD. thesis, Universite Catholique de Louvain, Louvain-La-Neuve, Belgique (2007)
50. C.X. Jiang, J.P. Tu, S.Y. Guo, M.F. Fu, X.B. Zhao, Friction properties of oil-infiltrated porous AAO film on an aluminium substrate. Acta Metallurgica Sinica (English Letters) **18**, 249–253 (2005)

51. W. Lee, The anodization of aluminium for nanotechnology applications. JOM **62**, 57–63 (2010)
52. J. Choi, Fabrication of monodomain porous alumina using nanoimprint lithography and its applications. PhD. thesis, Martin-Luther-Universitat Halle, Wittenberg, Germany (2004)
53. I.U. Khan, P. John, S.T. Sheikh, N. Gulzar, A.U. Rehman, Anodizing of aluminum with improved corrosion properties. J. Chem. Soc. Pak. **32**, 46–51 (2010)
54. T.D. Burleigh, P. Schmuki, S. Virtanen, Properties of the nanoporous anodic oxide electrochemically grown on steel in hot 50 % NaOH. J. Electrochem. Soc. **156**(1), C45–C53 (2009)
55. J.J. Suay, E. Gimenez, T. Rodrıguez, K. Habbib, J.J. Saura, Characterization of anodized and sealed aluminium by EIS. Corros. Sci. **45**, 611–624 (2003)
56. M.R. Kalantary, D.R. Gabe, D.H. Ross, A model for the mechanism of nickel fluoride cold sealing of anodized aluminium. J. Appl. Electrochem. **22**(3), 268–276 (1992)
57. J.A. Gonzalez, S. Feliu, J.A. Bautista, E. Otero, Changes in cold sealed aluminum oxide films during ageing. J. Appl. Electrochem. **29**, 843–852 (1999)
58. V López, E. Otero, A. Bautista, E. Escudero, J.A. González, Changes in the morphology of porous anodic films formed on aluminium in natural and artificial ageing. Rev Metal Madrid Vol Extr, 104–109 (2003)
59. F. Mansfeld, M.W. Kendig, Spectroscopy as quality control and corrosion test for anodized aluminum alloys. Corrosion **41**, 490 (1985)
60. F. Mansfeld, M.W. Kendig, W.J. Lorenz, Corrosion inhibition in neutral, aerated media. J. Electrochem. Soc. **132**, 290 (1985)
61. J. Hizing, K. Juettner, W.J. Lorenz, W. Paatsch, AC-impedance measurements on porous aluminium oxide films. Corros. Sci. **24**, 945 (1984)
62. T.P. Hoar, G.C. Wood, The sealing of porous anodic oxide films on aluminium. Electrochim. Acta **7**, 333 (1962)
63. K. Juettner, W.J. Lorenz, W. Paatsch, The role of surface inhomogeneities in corrosion processes-electrochemical impedance spectroscopy (EIS) on different aluminium oxide films. Corros. Sci. **29**, 279–288 (1989)
64. F. Mansfeld, Electrochemical impedance spectroscopy (EIS) as a new tool for investigating methods of corrosion protection. Electrochim. Acta **35**, 1533 (1990)
65. J. Pan, D. Thierry, C. Leygraf, Electrochemical impedance spectroscopy study of the passive oxide film on titanium for implant application. Electrochim. Acta **41**(7–8), 1143 (1996)
66. J.R. Birch, T.D. Burleigh, Oxides formed on titanum by polishing, etching, anodzng, or thermal oxidizng. Corrosion **56**(12), 1233 (2000)
67. M. Aziz-Kerrzo, K.G. Conroy, A.M. Fenelon, S.T. Farrell, C.B. Breslin, Electrochemical studies on the stability and corrosion resistance of titanium-based implant materials. Biomaterials **22**, 1531 (2001)
68. S. Piazza, G. Lo, Biundo, M.C. Romano, C. Sunseri, F. Di Quarto, In situ characterization of passive films on al-ti alloy by photocurrent and impedance spectroscopyfn1. Corros. Sci. **40** (7), 1087 (1998)
69. J.R. Macdonald, *Impedance Spectroscopy* (Wiley, New York, 1987)
70. M.J. Esplandiu, E.M. Patrito, V.A. Macagno, Characterization of hafnium anodic oxide films: an AC impedance investigation. Electrochim. Acta **40**(7), 809 (1995)
71. M.E.P. Souza, M. Ballester, C.M.A. Freire, EIS characterisation of Ti anodic oxide porous films formed using modulated potential. Surf. Coat. Technol. **201**, 7775–7780 (2007)
72. J.M. Macak, L.V. Taveira, H. Tsuchiya, K. Sirotna, J. Macak, P. Schmuki, Influence of different fluoride containing electrolytes on the formation of self-organized titania nanotubes by Ti anodization. J. Electroceram. **16**, 29–34 (2006)
73. N.K. Shrestha, J.M. Macak, F. Schmidt-Stein, R. Hahn, C.T. Mierke, B. Fabry, P. Schmuki, Magnetically guided titania nanotubes for site-selective photocatalysis and drug release. Angew. Chem. **120**, 1–5 (2008)

74. H. Cesiulis, T. Maliar, N. Tsyntsaru, F. Wenger, P. Ponthiaux, E. Podlaha, Anodic titanium oxide films: photoelectrochemical and tribocorrosion behavior. J. Nanoelectron. Optoelectron. **9**, 1–6 (2014)
75. Balakrishnan Munirathinam, Lakshman Neelakantan, Titania nanotubes from weak organic acid electrolyte: Fabrication, characterization and oxide film properties. Mater. Sci. Eng. C **49**, 567–578 (2015)
76. A.W. Brace, *The Technology of Anodizing Aluminium* (Tecnicopy Ltd., Stonenhouse, Gloucesterhire, Great Britian, 1979), pp. 1–19
77. H. Bai, F. Wang, Protective properties of high temperature oxide films on Ni-based superalloys in 3.5 % NaCl solution. J. Mater. Sci. Technol. **23**(4) (2007)
78. P. Schmuki, H. Bohni, Semiconductive properties of passive films and susceptibility to localized corrosion. Werkstoffe und Korrosion Mater. Corros. **42**(5), 203–207 (1991)
79. N.E. Hakiki, S. Boudin, B. Rondot, M. Da Cunha, Belo. The electronic structure of passive films formed on stainless steels. Corros. Sci. **37**(11), 1809–1822 (1995)
80. A.S. Bondarenko, G.A. Ragoisha. Variable Mott-Schottky plots acquisition by potentiodynamic electrochemical impedance spectroscopy. J. Solid State Electrochem. **9** (12), 845–849 (2005)
81. K. Gelderman, L. Lee, S.W. Donne, Flat-band potential of a semiconductor: using the Mott-Schottky equation. J. Chem. Educ. **84**(7), 685–688 (2007)
82. D. Li, D. Chen, J. Wang, H. Chen, Chemical composition and Mott-Schottky analysis of passive film formed on G3 alloy in bicarbonate/karbonate buffer solution. Acta Metall. Sin. (Engl. Lett.). **23**(6), 461–472 (2010)
83. E. Sikora, J. Sikora, D.D. Macdonald, A new method for estimating the diffusivities of vacancies in passive films. Electrochim. Acta **41**(6), 783–789 (1996)
84. Z. Jiang, X. Dai, H. Middleton, Investigation on passivity of titanium under steady-state conditions in acidic solutions. Mater. Chem. Phys. **126**(3), 859–865 (2011)
85. M. Tomkiewicz, Impedance spectroscopy of rectifying semiconductor-electrolyte interfaces. Electrochim. Acta **35**(10), 1631–1635 (1990)
86. B.W. Gregory, D.W. Suggs, J.L. Stickney, Conditions for the deposition of CdTe by electrochemical atomic layer epitaxy. J. Electrochem. Soc. **138**, 1279–1284 (1991)
87. F. Forni, M. Innocenti, G. Pezzatini, M.L. Foresti, Electrochemical aspects of CdTe growth on the face (111) of silver by ECALE. Electrochim. Acta **45**, 3225–3231 (2000)
88. A.S. Bondarenko, G.A. Ragoisha, N.P. Osipovich, E.A. Streltsov, Multiparametric electrochemical characterisation of Te-Cu-Pb atomic three-layer structure deposition on polycrystalline gold. Electrochem. Commun. **8**, 921–926 (2006)
89. G.A. Ragoisha, A.S. Bondarenko, N.P. Osipovich, S.M. Rabchynski, E.A. Streltsov, Multiparametric characterisation of metal-chalcogen atomic multilayer assembly by potentiodynamic electrochemical impedance spectroscopy. Electrochim. Acta **53**, 3879–3888 (2008)
90. I. Sisman, U. Demir, Electrochemical growth and characterization of size-quantized CdTe thin films grown by underpotential deposition. J. Electroanal. Chem. **651**, 222–227 (2011)
91. J. Stickney, in *Encyclopedia of Applied Electrochemistry*, ed. by G. Kreysa, R.F. Savinell, K. Ota (Springer, New York, 2014), pp. 1447–1453
92. M. Bouroushian, *Electrochemistry of Metal Chalcogenides* (Springer, Heidelberg, 2010)
93. D.M. Kolb, M. Przasnysky, H. Gerischer, Underpotential deposition of metals and work function differences. J. Electroanal. Chem. **54**, 25–38 (1974)
94. E. Budevski, G. Staikov, W.J. Lorenz, *Electrochemical Phase Formation and Growth* (VCH, Weinheim, 1996)
95. P.V. Chulkin, Y.M. Aniskevich, E.A. Streltsov, G.A. Ragoisha, Underpotential shift in electrodeposition of metal adlayer on tellurium and the free energy of metal telluride formation. J Solid State Electrochem. **19**, 2511–2516 (2015). doi:10.1007/s10008-015-2831-x
96. G.A. Ragoisha, Potentiodynamic electrochemical impedance spectroscopy for underpotential deposition processes. Electroanalysis **27**, 855–863 (2015)

97. G.A. Ragoisha, A.S. Bondarenko, Potentiodynamic electrochemical impedance spectroscopy. Copper underpotential deposition on gold. Electrochem. Commun. **5**, 392–395 (2003)
98. G.A. Ragoisha, A.S. Bondarenko, Potentiodynamic electrochemical impedance spectroscopy. Electrochim. Acta **50**, 1553–1563 (2005)
99. J.E. Garland, K.A. Assiongbon, C.M. Pettit, S.B. Emery, D. Roy, Kinetic analysis of electrosorption using fast fourier transform electrochemical impedance spectroscopy: underpotential deposition of Bi^{3+} in the presence of coadsorbing ClO^{4-} on Gold. Electrochim. Acta **47**, 4113–4124 (2002)
100. S. Morin, H. Dumont, B.E. Conway, Evaluation of the effect of 2-Dimensional geometry of Pt single-crystal faces on the kinetics of UPD of H using impedance spectroscopy. J. Electroanal. Chem. **412**, 39–52 (1992)
101. G.A. Ragoisha, A.S. Bondarenko, N.P. Osipovich, E.A. Streltsov, Potentiodynamic electrochemical impedance spectroscopy of lead upd on polycrystalline gold and on selenium atomic underlayer. Electrochem. Commun. **7**, 631–636 (2005)
102. L. Beaunier, I. Epelboin, J.C. Lestrade, H. Takenouti, Electrochemical and scanning microscope study of pained Fe. Surf. Technol. **4**, 237 (1976)
103. F. Mansfield, M. Kendig, S. Tsai, Evaluation of corrosion behavior of coated metals with AC impedance measurements. Corrosion **38**(7), 478–485 (1982)
104. A. Ramanavicius, A. Finkelsteinas, H. Cesiulis, A. Ramanaviciene, Electrochemical impedance spectroscopy of polypyrolle based immunosensor. Bioelectrochemistry **79**(1), 11–16 (2010)
105. P.L. Bonora, F. Deflorian, L. Fedrizzi. Electrochemical impedance spectroscopy as a tool for investigating underpaint corrosion. Electrochimica Acta **41**(7–8), 1073–1082 (1996)
106. J. Padgurskas, R. Rukuiza, H. Cesiulis, A. Amulevicius, A. Daugvila, R. Davidonis, C. Sipavicius, The properties and physicochemical interactions in the system iron-fluoroligomer. Physicochem. Mech. Mater. **45**(5), 81–90 (2009)
107. J. Padgurskas, R. Rukuiza, A. Amulevicius, C. Sipavicius, K. Mazeika, R. Davidonis, A. Daugvila, H. Cesiulis, Influence of fluor-oligomers on the structural and tribological properties of steel surface at the rolling friction. Ind. Lubr. Tribol **60**(5), 222–227 (2008)
108. V.F. Lvovich, M.F. Smiechowski, Non-linear impedance analysis of industrial lubricants. Electrochim. Acta **53**(25), 7375–7385 (2008)
109. D. Hallam, D. Thurrowgood, V. Otieno-Alego, D. Creagh, An EIS Method for assessing thin oil films used in museums, in *Proceedings of Metal 2004 National Museum of Australia Canberra ACT*, 4–8 October 2004 ABN 70 592 297 967, pp. 388–399
110. L. Jianguo, G. Gaoping, Y. Chuanwei, EIS study of corrosion behaviour of organic coating/Dacromet composite systems. Electrochimica Acta **50**(16–17), 3320–3332 (2005)
111. Y.J. Tan, S. Balley, B. Kinsella, An investigation of the formation and destruction of corrosion inhibitor films using electrochemical impedance spectroscopy (EIS). Corros. Sci. **38**(9), 1545–1561 (1996)
112. S. González, M.A. Gil, J.O. Hernández, V. Fox, R.M. Souto, Resistance to corrosion of galvanized steel covered with an epoxy-polyamide primer coating. Prog. Org. Coat. **41**, 167–170 (2001)
113. H. Cesiulis, N. Tsyntsaru, Non-destructive method for assessing thin oil films, in *Proceedings of the International Conference BALTTRIB'2009* (2009), pp. 59–64
114. J.J. Santana, J.E. González, J. Morales, S. González, R.M. Souto, Evaluation of ecological organic paint coatings via electrochemical impedance spectroscopy. Int. J. Electrochem. Sci. **7**, 6489–6500 (2012)
115. N. Hammouda, H. Chadli, G. Guillemot, K. Belmokre, The corrosion protection behaviour of zinc rich epoxy paint in 3 % NaCl solution advances in chemical. Eng. Sci. **1**, 51–60 (2011)
116. B.M. Fernández-Pérez, J.A. González-Guzmán, S. González, R.M. Souto, Electrochemical impedance spectroscopy investigation of the corrosion resistance of a waterborne acrylic coating containing active electrochemical pigments for the protection of carbon steel. Int. J. Electrochem. Sci. **9**, 2067–2079 (2014)

117. P.L. Bonora, F. Deflorian, L. Fedrizzi. Electrochemical impedance spectroscopy as a tool for investigating underpaint corrosion. Electrochimica Acta **41**(7–8), 1073–1082 (1996)
118. H. Cesiulis, G. Baltrūnas, J. Padgurskas, The effect of FOLEOX thin films on the corrosion behaviour of Armco iron. Mater. Sci. (Medziagotyra) **8**(4), 392–395 (2002)
119. G.W. Walter, A review of impedance plot methods used for corrosion performance analysis of painted metals. Corros. Sci. **26**(9), 681–703 (1986)
120. Y.J. Tom, S. Bailey, An investigation on the formation and destruction of corrosion inhibitor films using electrochemical noise analysis (ENA). Corros. Sci. **38**(9), 1545–1561 (1996)
121. A. Banu, O, Radovici, M. Marcu, T. Spataru, S. Jurcoane, Electrochemical synthesis and characterization of a polipyrrole/lipase composite film. Roum. Biotechnol. Lett. **13**(1), 3551–3556 (2008)
122. I. Morkvenaite-Vilkonciene, P. Genys, A. Ramanaviciene, A. Ramanavicius, Scanning electrochemical impedance microscopy for investigation of glucose oxidase catalyzed reaction colloids and surfaces. B-Biointerfaces **126**, 598–602 (2015)
123. I. Lapenaite, A. Ramanaviciene, A. Ramanavicius, Current trends in enzymatic determination of glycerol. Crit. Rev. Anal. Chem. **36**, 13–25 (2006)
124. A. Ramanavicius, A. Ramanaviciene, A. Malinauskas, Electrochemical sensors based on conducting polymer—polypyrrole (Review). Electrochim. Acta **51**, 6025–6037 (2006)
125. Y. Oztekin, A. Ramanaviciene, Z. Yazicigil, A.O. Solak, A. Ramanavicius, Direct electron transfer from glucose oxidase immobilized on polyphenanthroline modified-glassy carbon electrode. Biosens. Bioelectron. **26**, 2541–2546 (2011)
126. N. German, A. Ramanaviciene, A. Ramanavicius, Electrochemical deposition of gold nanoparticles on graphite rod for glucose biosensing. Sens. Actuators B: Chem. **203**, 25–34 (2014)
127. A. Ramanavicius, P. Genys, A. Ramanaviciene, Electrochemical impedance spectroscopy based evaluation of 1,10-Phenanthroline-5,6-dione and glucose oxidase modified graphite electrode. Electrochim. Acta **146**, 659–665 (2014)
128. A. Ramanavicius, P. Genys, Y. Oztekin, A. Ramanaviciene, Evaluation of the redox mediating properties of 1,10-Phenanthroline-5,6-dione for glucose oxidase modified graphite electrodes. J. Electrochem. Soc. **161**, B31–B33 (2014)
129. D.D. Macdonald, Reflections on the history of electrochemical impedance spectroscopy. Electrochim. Acta **51**, 1376–1388 (2006)
130. R.K. Shervedani, A.H. Mehrjardi, N. Zamiri, A novel method for glucose determination based on electrochemical impedance spectroscopy using glucose oxidase self-assembled biosensor. Bioelectrochemistry **69**, 201–208 (2006)
131. T. Hoshino, S. Sekiguchi, H. Muguruma, Amperometric biosensor based on multilayer containing carbon nanotube, plasma-polymerized film, electron transfer mediator phenothiazine, and glucose dehydrogenase. Bioelectrochemistry **84**, 1–5 (2012)
132. B. Kurtinaitiene, D. Ambrozaite, V. Laurinavicius, A. Ramanaviciene, A. Ramanavicius, Amperometric immunosensor for diagnosis of BLV infection. Biosens. Bioelectron. **23**, 1547–1554 (2008)
133. Y. Oztekin, A. Ramanaviciene, N. Ryskevic, Z. Yazicigil, Z. Ustundag, A.O. Solak, A. Ramanavicius, 1,10-Phenanthroline modified glassy carbon electrode for voltammetric determination of cadmium(II) ions. Sens. Actuators B: Chem. **157**, 146–153 (2011)
134. Y. Oztekin, Z. Yazicigil, A. Ramanaviciene, A. Ramanavicius, Polyphenol-modified glassy carbon electrodes for copper detection. Sens. Actuators B: Chem. **152**, 37–48 (2011)
135. Y. Oztekin, Z. Yazicigil, A. Ramanaviciene, A. Ramanavicius, Square wave voltammetry based determination of copper (II) ions by polyluteolin- and polykaempferol-modified electrodes. Talanta **85**, 1020–1027 (2011)
136. A. Ramanaviciene, A. Ramanavicius, Pulsed amperometric detection of DNA with an ssDNA/polypyrrole modified electrode. Anal. Bioanal. Chem. **379**, 287–293 (2004)
137. A. Ramanavicius, Y. Oztekin, A. Ramanaviciene Electrochemical Formation of Polypyrrole-based layer for immunosensor design. Sens. Actuators B: Chem. **197**, 237–243 (2014)

138. V. Ratautaite, S.D. Janssens, K. Haenen, M. Nesládek, A. Ramanaviciene, I. Baleviciute, A. Ramanavicius, Molecularly imprinted polypyrrole based impedimentric sensor for theophylline determination. Electrochim. Acta **130**, 361–367 (2014)
139. V. Ratautaite, D. Plausinaitis, I. Baleviciute, L. Mikoliunaite, A. Ramanaviciene, A. Ramanavicius, Characterization of caffeine-imprinted polypyrrole by a quartz crystal microbalance and electrochemical impedance spectroscopy. Sens. Actuators B: Chem. **212**, 63–71 (2015)
140. A. Ramanaviciene, A. Finkelsteinas, A. Ramanavicius, Basic electrochemistry meets nanotechnology: Electrochemical preparation of artificial receptors based on a nanostructured conducting polymer, polypyrrole. J. Chem. Educ. **83**, 1212–1214 (2006)
141. A. Ramanaviciene, A. Ramanavicius, Molecularly imprinted polypyrrole-based synthetic receptor for direct detection of bovine leukemia virus glycoproteins. Biosens. Bioelectron. **20**, 1076–1082 (2004)
142. V. Ratautaite, S.N. Topkaya, L. Mikoliunaite, M. Ozsoz, Y. Oztekin, A. Ramanaviciene, A. Ramanavicius, Molecularly imprinted polypyrrole for DNA determination. Electroanalysis **25**, 1169–1177 (2013)
143. A. Ramanaviciene, A. Ramanavicius, Application of polypyrrole for the creation of immunosensors. Crit. Rev. Anal. Chem. **32**, 245–252 (2002)
144. D. Plausinaitis, V. Ratautaite, L. Mikoliunaite, L. Sinkevicius, A. Ramanaviciene, A. Ramanavicius, Quartz crystal microbalance based evaluation of electrochemical formation of aggregated polypyrrole particle based layer. Langmuir **31**(10), 3186–3193 (2015)
145. A. Ramanaviciene, N. German, A. Kausaite-Minkstimiene, J. Voronovic, J. Kirlyte, A. Ramanavicius, Comparative study of surface plasmon resonance, electrochemical and electroassisted chemiluminescence methods based immunosensor for the determination of antibodies against human growth hormone. Biosens. Bioelectron. **36**, 48–55 (2012)
146. A.S. Bandarenka, K. Eckhard, A. Maljusch, W. Schuhmann, Localized electrochemical impedance spectroscopy: Visualization of spatial distributions of the key parameters describing solid/liquid interfaces. Anal. Chem. **85**, 2443–2448 (2013)
147. V. Kuznetsov, A. Maljusch, R.M. Souto, A.S. Bandarenka, W. Schuhmann, Characterization of localised corrosion processes using scanning electrochemical impedance microscopy. Electrochem. Commun. **44**, 38–41 (2014)
148. L. Philippe, G. Walter, S. Lyon, Investigating localized degradation of organic coatings comparison of electrochemical impedance spectroscopy with local electrochemical impedance spectroscopy. J. Electrochem. Soc. **150**, B111–B119 (2003)
149. K. Darowicki, M. Szociński, A. Zieliński, Assessment of organic coating degradation via local impedance imaging. Electrochim. Acta **55**, 3741–3748 (2010)
150. M. Szociński, K. Darowicki, K. Schaefer, Identification and localization of organic coating degradation onset by impedance imaging. Polym. Degrad. Stab. **95**, 960–964 (2010)
151. A. Ramanavicius, A. Kausaite-Minkstimiene, I. Morkvenaite-Vilkonciene, P. Genys, R. Mikhailova, T. Semashko, J. Voronovic, A. Ramanaviciene, Biofuel cell based on glucose oxidase from Penicillium funiculosum 46.1 and horseradish peroxidase. Chem. Eng. J. **264**, 165–173 (2015)
152. A. Ramanavicius, Y. Oztekin, A. Ramanaviciene, Electrochemical formation of polypyrrole-based layer for immunosensor design. Sens. Actuators B: Chem. **197**, 237–243 (2014)
153. M.V. Mirkin, W. Nogala, J. Velmurugan, Y. Wang, Scanning electrochemical microscopy in the 21st century. Update 1: five years after. Phys. Chem. Chem. Phys. **13**, 21196–21212 (2011)
154. M. Ciobanu, D.E. Taylor, J.P. Wilburn, D.E. Cliffel, Glucose and lactate biosensors for scanning electrochemical microscopy imaging of single live cells. Anal. Chem. **80**, 2717–2727 (2008)
155. D.T. Pierce, P.R. Unwin, A.J. Bard, Scanning electrochemical microscopy. 17. Studies of enzyme-mediator kinetics for membrane- and surface-immobilized glucose oxidase. Anal. Chem. **64**, 1795–1804 (1992)

156. B.R. Horrocks, D. Schmidtke, A. Heller, A.J. Bard, Scanning electrochemical microscopy. 24. Enzyme ultramicroelectrodes for the measurement of hydrogen peroxide at surfaces. Anal. Chem. **65**, 3605–3614 (1993)
157. K. Eckhard, T. Erichsen, M. Stratmann, W. Schuhmann, Frequency-dependent alternating-current scanning electrochemical microscopy (4D AC-SECM) for local visualisation of corrosion sites. Chem. Eur. J. **14**, 3968–3976 (2008)
158. K. Eckhard, C. Kranz, H. Shin, B. Mizaikoff, W. Schuhmann, Frequency dependence of the electrochemical activity contrast in AC-scanning electrochemical microscopy and atomic force microscopy-AC-scanning electrochemical microscopy imaging. Anal. Chem. **79**, 5435–5438 (2007)
159. P.M. Diakowski, Z.F. Ding, Novel strategy for constant-distance imaging using alternating current scanning electrochemical microscopy. Electrochem. Commun. **9**, 2617–2621 (2007)
160. B. Ballesteros, A. Katemann, E.J. Schulte, M. Calvo, W. Koudelka-Hep, Schuhmann, Localised electrochemical impedance spectroscopy with high lateral resolution by means of alternating current scanning electrochemical microscopy. Electrochem. Commun. **4**, 134–138 (2002)
161. C. Gabrielli, M. Keddam, N. Portail, P. Rousseau, H. Takenouti, V. Vivier, Electrochemical impedance spectroscopy investigations of a microelectrode behavior in a thin-layer cell: experimental and theoretical studies. J. Phys. Chem. B **110**, 20478–20485 (2006)
162. C. Gabrielli, F. Huet, M. Keddam, P. Rousseau, V. Vivier, Scanning electrochemical microscopy imaging by means of high-frequency impedance measurements in feedback mode. J. Phys. Chem. B **108**, 11620–11626 (2004)
163. A.S. Baranski, P.M. Diakowski, Application of AC impedance techniques to scanning electrochemical microscopy. J. Solid State Electrochem. **8**, 683–692 (2004)
164. K. Eckhard, H. Shin, B. Mizaikoff, W. Schuhmann, C. Kranz, Alternating current (AC) impedance imaging with combined atomic force scanning electrochemical microscopy (AFM-SECM). Electrochem. Commun. **9**, 1311–1315 (2007)

Chapter 2
Nanostructures Obtained Using Electric Discharges at Atmospheric Pressure

Pavel Topala, Alexandr Ojegov and Veaceslav Ursaki

Abstract The results of theoretical and experimental investigations of physical phenomena that accompany the formation of oxide and hydroxide nano-metric pellicles on metal surfaces by applying pulsed electrical discharge machining (PEDM) are presented. The chemical composition of the processed surface determined by Energy Dispersive X-ray analysis (EDX) attests the presence of oxygen that reaches the abnormal ammounts (up to 60 % at.) for all investigated alloys. The surface phase analysis using X-ray Photoelectron Spectroscopy (XPS) allows one to affirm that the oxygen in film forms three basic structures: $–O^{2-}$ (oxides), $–OH^{-}$ (hydroxides) and structures of C–O and O–C=O types. Experimental investigations have shown that the surface active resistance of these pellicles increases by about 10^7 times, the potential of corrosion increases to positive values and the speed of corrosion decreases in the chemically active media. Oxide pellicle formation occurs on flat, round and combined interior and exterior piece surfaces made of metal materials. It can be applied in oxide pellicle formation on piece surfaces aiming at providing anticorrosive protection; in surface passivation of construction pieces used in the chemical industry; in manufacturing active resistances of high values (10^6 Ω) and small dimensions (1 × 1 × 0.01 mm) used in microelectronics; in the production of elements with electronic emission surfaces.

2.1 Introduction

In recent decades, great attention is given to research related to the technologies of manufacturing low-dimensional objects such as nano-films, nano-particles, nano-wires and nano-tubes. With the reduction in size of new structures formed

P. Topala (✉) · A. Ojegov
"Alecu Russo" Balti State University, Balti, Moldova
e-mail: pavel.topala@gmail.com

V. Ursaki
Institute of Electronic Engineering and Nanotechnologies D. Ghitu,
Academy of Sciences of Moldova, Chisinau, Moldova

© Springer International Publishing Switzerland 2016

I. Tiginyanu et al. (eds.), *Nanostructures and Thin Films for Multifunctional Applications*, NanoScience and Technology,
DOI 10.1007/978-3-319-30198-3_2

using novel technologies, some new electrical, mechanical, optical and chemical properties are formed and this is mainly the result of surface and quantum confinement effects. Low-dimensional objects represent a class of multifunctional materials very promising for application in machine and equipment building technology, microelectronics, photonics, medicine, chemical and biological sensors, etc. [1–4]. To emphasize the importance of low-dimensional objects it is sufficient to refer to nano-pellicles [2] and nano-wires which, as demonstrated recently [1, 5, 6], have unique thermal and electrical properties.

The formation of nano-metric oxide pellicles [7] on the active piece surfaces has found a rather wide application aiming at increasing resistance to wear and corrosion in pieces used in machine building, as well as at changing electrical conductivity properties for pieces in electronics and microelectronics.

Surface oxidation methods that use concentrated sources of energy such as plasma get, ion beam, electron beam, photon beam [8–19] have low efficiency of energy use and require the use of complicated equipment which is very costly. In case of formation of oxide layers in the electrolytic plasma, [9, 10] before anodizing, pieces subjected to processing require prior cleaning, degreasing and washing of the work surface. The thickness of oxide strata in the case of using this method is between units of micrometers to hundreds of micrometers. Harmful aqueous solutions of acids are used. The formed oxide pellicles possess porosity within the limits of 10–40 %. When the oxide pellicles are formed via the electric arc [20–23], the plasma get directed towards the processing surface causes partial melting of the surface layer; the oxide films are fragile and have poor adhesion with the base material subjected to machining; the process requires large expenditures of energy (for gas ionization, thermal and light radiation). All these methods do not solve the problem of nano-metric pellicle formation; the formed layers are fragile, spongy and develop roughness; further processing is necessary and special processing environments are required, etc.

The method of oxide nano-pellicle formation by applying pulsed electrical discharge machining (PEDM) is currently less known. The abnormal dissolution of oxygen in piece surfaces made of steel was attested for the first time [23], after which a series of works [7] attested the possibility of oxide and hydroxide pellicle formation in the amorphous state on metal surfaces.

An analysis of works [24–27] made it possible to conclude that generators of RC type with parallel priming can be successfully used for micro- and nano-oxidation of piece surfaces made of electrically conductive materials. Research on the interaction of PEDM plasma channel with electrode surfaces has shown that two types of interactions are characteristic of the electro-erosion phenomenon: type I—the appearance of “cold” electrode spots on the electrode surfaces which appear on the asperities and impurities from them [24–27] and cause surfaces clean of impurities, as well as thermal interaction with them, causing structural changes in the surface layers at small depths (in terms of nano- and micrometers); type II—after the “cold” electrode spots, the “hot” electrode spots are formed on the electrode surfaces; this causes essential melting of the processed surfaces, accompanied

by the phenomenon of vaporization and removal of electrodes' material in the form of drops [7, 25].

By analyzing the results obtained by the author of works [28, 29] it was stated that to obtain an interaction of type I with the plasma channel on the piece surface it is necessary that the energy density on the machined surface to be lower than the specific heat of material melting, and the latter can be expressed by the relation [28–35]:

$$\frac{4W}{\pi d_c^2 \cdot S} < Q_{melt} = q\rho, \tag{2.1}$$

where q and ρ are the heat of fusion and the density of piece material respectively; W is the energy emitted in the gap, d_c is the diameter of the plasma channel and S is the gap value.

As can be seen from (2.1), in the case when the energetic processing regime, the size of the gap and the thermo-physical properties of the piece material are known, it is possible to determine the diameter of the plasma channel which coincides with the size of its trace on the machined surface.

If we name the coefficient of trace overlap k = 0.5–0.1.0 and the frequency of pulsed electrical discharges f, then the technological process productivity may be determined by the relation:

$$\eta = \frac{k\pi d_c^2 f}{4} \tag{2.2}$$

It was demonstrated in [35, 36] that when applying PEDM for superficial processing, the erosion processes combined with melting and explosive vaporization of the electrode material occur for the most studied metals and alloys at durations of current pulses of 10^{-6} s. It follows that to achieve the expected effects it is necessary to ensure discharge pulses of relatively short duration.

The effects that take place on the electrode surfaces depend on the way of piece connection in the discharge circuit (as cathode (direct) or as anode (inverted)). These desiderates have been studied in [32] and it was established that for short duration pulses they are "cathode" and for long duration pulses they are "anode"—so in the case of superficial thermal treatment the piece will be included as circuit cathode. In the case of thermal treatment of steel pieces, their hardness increases by 2–0.3 times and in those of titanium surfaces it increases by 2–0.5 times at the depths of the formed layers from a few micrometers up to several tens of micrometers. The depth of these layers achieves the maximum value after three passes for steel and after five passes for titanium alloys [37, 38].

The interaction of plasma channel with the piece-electrode surface does not always have a pure thermal character, but often the work piece surface is enriched with elements from the environment where plasma forms and with the content of anode-tool material.

The depth of penetration of these elements in the piece surface layer depends on both the pulse energy and the size of the gap and can be expressed by the relation [29]:

$$h = \frac{kW_S}{AS}, \tag{2.3}$$

where $W_S = \int_0^\tau U(t)I(t)dt$ is the energy emitted in the gap at a solitary discharge; U and I are the voltage on the gap and the current intensity in it respectively; τ is the pulse duration; A is the area of the surface attacked at a discharge; S is the gap value; k is a constant that depends on the thermo-physical properties of the processed material.

It has been experimentally proven that the surface oxidation is more effective when the work piece is connected in the discharge circuit as cathode (direct connection), because there are craters on the anode surface that are formed when the dielectric is pierced at its interaction with PEDM plasma.

An oxide film of a certain thickness, stable and adherent to the surface of the metal of origin, compact, continuous and free of pores or cracks can considerably slow down the development of the corrosion process. The condition for the film protection can be expressed by the coefficient of expansion [29–33] indicating the ratio between the volume of oxide and the volume of metal in the machined surface [39]:

$$\frac{V_{oxide}}{V_{metal}} > 1. \tag{2.4}$$

Surface oxidation is easy to achieve by applying PEDM. The materials subjected to processing can be conductive materials (metals and alloys), as well as semiconductor surfaces. The thickness of the oxide layer is counted in terms of nanometers, the environment is not contaminated and the ozone is formed, but the research concerning the functional properties of formed films made by the authors of works [32–36, 40–50] only scientifically ascertained the new effects.

2.2 Physical Model of Nano-Pellicle Formation by Applying Pulse Electrical Discharge Machining

Since the application of *PEDM* in technological purposes for dimensional machining [9, 19], the formation of deposits from compact and powder materials [7], as well as the micro-metallurgical processes that occur in the surface layer of the work piece were studied both in liquid and solid state. It was established that the formation of a new alloy in the machined surface is accompanied by convective

mixing of the components in the liquid phase and by the diffusion of elements in substrate from solid phase of deposition. It was shown that for the gaps bigger than 0.03 mm the interaction of PEDM plasma channel with the machined surface is manifested by the appearance of a trace consisting of a central zone that presents a crater with liquid phase and a zone of thermal influence of the freshly pickled metal color [22]. The central zone disappears for certain values of the gap and the machined surface presents only the zone of thermal influence, where phenomena of hardening and enriching the piece material with elements from the active media occur.

The priming voltage of pulsed electrical discharges depends on the gap value *S* and the pressure of gas *P*, and it is described by the relation of Paschen [7] that can be interpreted on the basis of Taundsen theory of breakdown. According to this law, the minimal value of the priming voltage in the air at normal pressure, depending on the electrode material, is about 250–0.300 V. At the same time, in the case of deposit formation from compact materials with contact breaking, the range of used voltages constitutes 15–0.200 V, which is below the minimum of Paschen's curve. Thus, the results of several researches show that at priming voltage of 100–0.200 V the size of the gap can reach the values of 5–0.10 μm [22].

According to Nemoshkalenco et al. [22], at processing by electro-erosion in the conditions when the priming voltage constitutes $U_{pr} \leq 300$ V, the gap beakdown cannot be explained on the basis of ionization avalanche for two reasons: absence of necessary voltage in the gap (for accelerating electrons which would ionize the molecules and atoms at collision) and insufficiency of a required number of collisions of electrons with molecules and atoms in the gap.

By analyzing the priming of electrical discharges due to the current of self-emission, it was noted that, in this case, it is necessary to take into account the primordial action of the electrostatic field, which can cause considerable mechanical tensions that may exceed the limit of resistance of the electrode material [24, 25]. For example, for gap breakdown voltages, the mechanical tension on the surfaces of the electrodes (calculated by the relation [25]: $\tau = \frac{E^2}{8\pi}$) constitutes about 450 MPa.

When using pulsed electrical discharges in a sub-excitation regime at surface processing, it is important to apply a pulse of small power but high voltage (12–0.24 kV) on the gap, which is responsible for the conductibility channel formation, through which the energy stored in the condenser battery of the pulse generator releases. This type of pulses is applied in the case of metal powder layer deposition [7, 37, 38]. To form deposition layers from metal powder they are introduced in the gap near the anode zone [7], in order to provide a longer duration for interaction with the plasma channel of pulsed electrical discharges.

For micrometer and millimeter sizes of the gap, it is difficult to observe and to record phenomena that are born and devolve in the gap and on electrode surfaces during PEDM. It was hypothesized that the electrode spots through which the PEDM plasma channel interact with machined surfaces are responsible for the effects that are produced on the electrode surfaces [25]. The plasma formations at

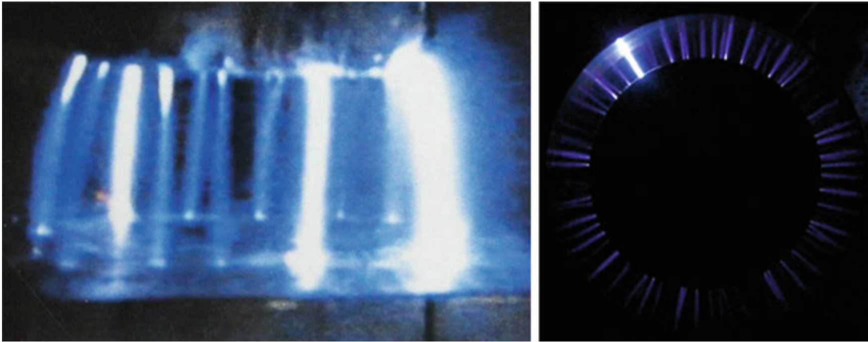

Fig. 2.1 Electrode spot and plasma channel formation at machining by applying PEDM [53]

PEDM for gaps of 10–25 mm and the charging voltage of the condenser battery of 28 kV are presented in Fig. 1 [51, 52].

From Fig. 2.1 it is clearly seen that plasma formations (of spherical shape) are born at electrodes surfaces (obvious spherical bright areas) which then develop a plasma channel mainly from the cathode to the anode. It follows that the electrode spots are responsible not only for electrical and thermal effects that occur on the electrode surfaces, but also for the effects that occur in the gap formed by their surfaces.

The supersaturated dissolution of oxygen in the construction steel was detected in the previously performed experimental research [22]. This phenomenon cannot be explained on the basis of Lazarenko's theory of interaction of electrical discharge plasma channel with electrode surfaces. The authors of several works in the field called its formation as "the condensed plasma" [40]. We propose to investigate phenomena in the gap for pulsed electrical discharges as follows: gap breakdown, emergence of the anode and cathode electrode spots, and formation of plasma channel under their action (Fig. 2.2). If such a model is accepted, the results of plasma interaction with electrode surfaces can be explained. For instance, it was suggested that electrode spots are point sources of high electric field and of heat [40]. In this case, the electric field with an intensity of 10^6–10^7 V/m arises at the cathode and anode surfaces, while the summary intensity of electric field on the gap constitutes only 10^4 V/m.

As mentioned above, the films that are formed are in amorphous state, or the amorphization process can be produced either at films' deposit from vapor or liquid state on cold surfaces or by very fine melting at depths of nanometers on the surface under the action of electrode spots. Probably, under our conditions of processing, very fine surface melting occurs at depths of nanometers of machined surface and amorphization is due to rapid cooling of the film located on the massive (in relation to the dimensions of the interaction zone) metal surface.

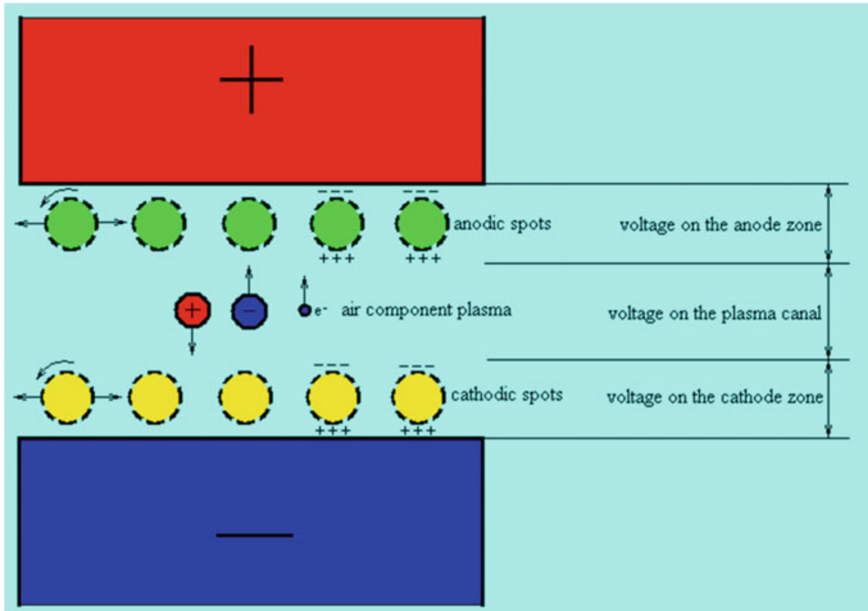

Fig. 2.2 Physical model of oxide nano-pellicle formation by applying PEDM [53]

2.3 Processes of Dissociation, Ionization and Synthesis in the Plasma and on the Electrode Surfaces

In the case of using of pulsed electrical discharges under a sub-excitation regime at the surface processing, it is important to apply a low power pulseon the gap with an electric field intensity on the gap within 6–0.12 × 10^6 V/m, which is responsible for the formation of a conductive channel through which the energy stored in the condenser battery of the pulse generator releases. A series of phenomena are produced in the gap both at the priming phase and at the power discharge phase: electron emission, ionization, production of light radiation, thermal and sound waves, etc. We considered that the gap breakdown occurs according to Townsend mechanism and the electrons play a primordial role in all that follows.

Electrons are accelerated in the electric field of the interstice; they collide with gas molecules and atoms from the work area and produce their ionization according to the reactions [32–36, 53]:

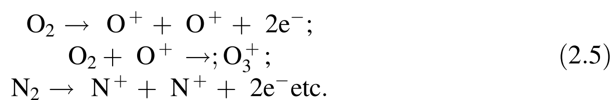

$$\begin{gathered} O_2 \rightarrow O^+ + O^+ + 2e^-; \\ O_2 + O^+ \rightarrow; O_3^+; \\ N_2 \rightarrow N^+ + N^+ + 2e^- \text{etc.} \end{gathered} \tag{2.5}$$

Parallel dissociation and recombination occur in the interstitial area [32–36, 53]:

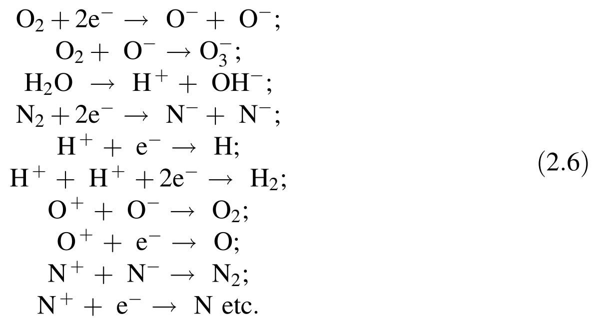

$$\begin{array}{c} O_2 + 2e^- \rightarrow O^- + O^-; \\ O_2 + O^- \rightarrow O_3^-; \\ H_2O \rightarrow H^+ + OH^-; \\ N_2 + 2e^- \rightarrow N^- + N^-; \\ H^+ + e^- \rightarrow H; \\ H^+ + H^+ + 2e^- \rightarrow H_2; \\ O^+ + O^- \rightarrow O_2; \\ O^+ + e^- \rightarrow O; \\ N^+ + N^- \rightarrow N_2; \\ N^+ + e^- \rightarrow N \text{ etc.} \end{array} \quad (2.6)$$

The following chemical reactions are produced on the surface of the electrodes [32–36, 53]:

- On the anode:

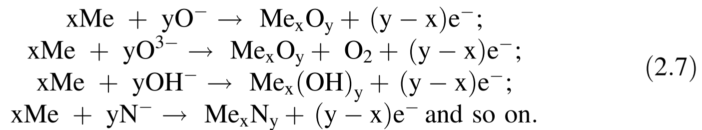

$$\begin{array}{c} xMe + yO^- \rightarrow Me_xO_y + (y-x)e^-; \\ xMe + yO^{3-} \rightarrow Me_xO_y + O_2 + (y-x)e^-; \\ xMe + yOH^- \rightarrow Me_x(OH)_y + (y-x)e^-; \\ xMe + yN^- \rightarrow Me_xN_y + (y-x)e^- \text{ and so on.} \end{array} \quad (2.7)$$

- On the cathode:

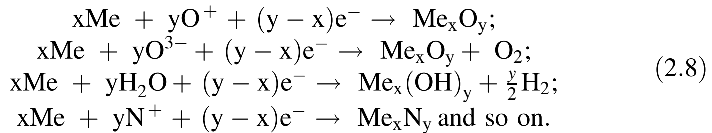

$$\begin{array}{c} xMe + yO^+ + (y-x)e^- \rightarrow Me_xO_y; \\ xMe + yO^{3-} + (y-x)e^- \rightarrow Me_xO_y + O_2; \\ xMe + yH_2O + (y-x)e^- \rightarrow Me_x(OH)_y + \frac{y}{2}H_2; \\ xMe + yN^+ + (y-x)e^- \rightarrow Me_xN_y \text{ and so on.} \end{array} \quad (2.8)$$

The reactions described above attest that all plasma components influence the effects occurring in the electrode surfaces, but a special role is played by the ozone synthesis process that possibly plays the most important role in the pellicle formation, being one of the chemically unstable formations of oxygen.

One can try to speculate that the process of introduction of oxygen, hydrogen and nitrogen from the air into the machined surface is similar to the magnetron cathodic sputtering system [18, 26]. However, such kinds of specullations are inadmissible for several reasons. Firstly, the electric field at PEDM constitutes 10^6–10^8 V/m, while at cathodic sputtering it is 10^3–10^5 V/m. Secondly, the gas ions at cathodic sputtering serve as energy particles to spray the target material, while in the case of PEDM they are the working agent and the medium of the surface enrichment with oxygen, hydrogen and nitrogen. It is known that in ordinary atmosphere nitrogen constitutes about 70 %, while oxygen constitutes about 27 %. In spite of this, a supersaturated dissolution of oxygen is attested.

From what has been said, we can notice that the surface oxidation occurs at the anode surface too. That is why it can function in the steady state only if its active surface is protected by one or another method, or if permanent regeneration is ensured.

2.4 Diffusion Processes at Oxide Nano-Pellicle Formation by Applyind PEDM

The determination of the diffusion coefficient and the thickness of the oxidized or hydro-oxidized surface layer also present interest in the thermal or thermochemical piece treatment by unipolar PEDM. According to the obtained results [46], and those mentioned above, we can say that, in the case of applying unipolar pulses, each cycle of thermal or thermochemical treatment develops in several steps: the step of high-temperature plasma when the discharge channel of the electrical pulse interacts with the sample surface through "cold" electrode spots with the life time of 0.2–0.0.5 μs [40]; and the low-temperature step, due to the break between the repeated action of "cold" electrode spots, as well as during the pause between two consecutive electrical discharges.

The life time of "cold" electrode spots depends on the maximum current density in the gap, and can be determined experimentally by ultrafast filming or theoretically by the relation:

$$T_{es} = \tau / N_{es}, \tag{2.9}$$

$$N_{es} = A / A_{es}, \tag{2.10}$$

where τ is the duration of the discharge pulse; N_{es} is the number of electrode spots existing during a solitary discharge; A is the area of the machined surface at a solitary electrical discharge and A_{es} is the area of the machined surface by an electrode spot.

In calculating the formed oxide film thickness we will take into account the experimental relation (2.3) obtained by Nemoskalenko [22, 29].

This paper highlights the influence of the specific energy density emitted in the gap and the properties of processed material on the process of oxide and hydroxide film formation, and can be applied for the estimation of the integral actions of plasma on the processed surface without emphasizing the real phenomena which arise in the gap and on the electrode surfaces.

Actually, the "cold" electrode spots have a migratory and selective character, as it has already been mentioned [40]. They move on the machined surface with the speed of 70–0.100 m/s and are born on its asperities and impurities. Taking into account the traces made by them on the machined surface, then for a solitary discharge, the trace made by the electrode spots is a branched one, demonstrating both their migratory nature and the fact that once the micro-oxidation takes place

the surface active resistance increases and the conditions for current flowing are aggravated. It was noticed that the character of continuity of surface processing increases when the electrical discharges were repeated. This is due to the fact that some of the asperities have been vaporized, and some impurities were subjected to volatilization. Further processing (after n cycles) demonstrates that the pellicle has a continuous character and the surface roughness constitutes Ra = 0.2–1 μm [7, 28, 29] which corresponds to the traces of "cold" electrode spots.

The processing was performed on the piece surfaces made of construction steel, titanium, aluminum and copper alloys. It was found that both the quantity of dissolved oxygen (up to 60 % at. for iron alloys, 50 % at. for copper alloys, 35 % at. for titanium alloys and 20 % at. for aluminum alloys), and its penetration depth in the sample surface differs depending on the properties of the material used. In conditions of PEDM application for surface oxidation, the most active from this point of view is the steel, followed by the alloys of Al, Ti and Cu. The above-mentioned confirms, by one or another way, the behavior of these materials in nature. If we take into account the size of atoms of each element and the compactness of crystal lattice, then the results can be described by a normal distribution [29].

The analysis of those described in the mentioned work allows one to determine the effective coefficient of elements diffusion D_{ef} by the relation:

$$D_{ef}t = N(D_1t_1 + D_2t_2 + \cdots + D_nt_n + D_it_i) \tag{2.11}$$

where N is the number of thermal or thermo-chemical treatment cycles; D_1 is the diffusion coefficient at the first interaction; D_2 is the diffusion coefficient during the interval between the two interactions with the electrode spot; D_n is the diffusion coefficient at the interaction number n; D_i is the diffusion coefficient during the interval between two consecutive interactions; t_1, t_3, …, t_n are the durations of the interaction time of machined surface with the electrode spot during one pulsed electrical discharge; t_i is the duration of intervals between two consecutive interactions; t is the total time of thermal or thermo-chemical treatment.

Quantitatively the number of thermal or thermo-chemical treatment cycles corresponds to the number of pulsed electrical discharges on the work piece surface. Considering that each pulsed electrical discharge on the work piece surface leaves a circle shaped trace with diameter d_0, the area A_0 for which the concentration of elements is determined can be calculated by: $A_0 = \pi d_0^2/4$, If the treated surface presents a square with the side of a, then the treated surface area is $A_d = a^2$. Taking into account the fact that $A_d \geq A_0$ at the thermal or thermo chemical surface treatment by applying PEDM, it follows that the number of cycles of thermal or thermo-chemical treatment can be determined by the relation:

$$N = k(A_d/A_0)f\tau \tag{2.12}$$

where k represents the overlapping coefficient of elementary treatment zones; f is the frequency of pulsed electrical discharges; τ is the duration of thermal or thermo chemical treatment of the sample surface.

During the time interval that constitutes the pause between two consecutive electrical discharges, the redistribution of the elements in the layer deposition does not occur because the temperature is low. As a result, the speed of diffusion in this period is much smaller. It was demonstrated that the layers formed by applying PEDM are composed of two zones: the first is the substantially uniform distribution of alloying elements—called the mixing zone; and the second zone is called diffusional zone [46, 54, 55]. In the first zone complicated metallurgical processes are produced due to vaporization, melting and mixing the liquid phases of the alloying material and the matrix material part, while in the second the diffusion processes take place, caused by the thermal processes in the solid phase, at considerable depths of the work piece material. The results analyzed and presented in this chapter were obtained in the case when the machined surface was subjected to a preponderant action under the regime of diffusion of the active media elements into the work piece surface.

To describe the proposed mechanism, in accordance with previous works [46, 56–62], the one-dimensional equation of the elements diffusion from a layer of thickness h could be applied (as the original layer thickness is considered cathode strata thickness, i.e. the thickness of air between the cathodic spot and the machined workpiece surface) for a semi-infinite body:

$$\frac{\partial C_j}{\partial t} = D\frac{\partial^2 C_j}{\partial x^2}, (j = 1, \ldots, N) \tag{2.13}$$

The initial conditions for the first cycle of thermal or thermo-chemical treatment (the first interaction of the "cold" electrode spot with the machined surface) are as follows:

$$C_1(x,0) = \begin{cases} C_0, & \text{if} \quad 0 \le x \le h; \\ 0, & \text{if} \quad x > h. \end{cases} \tag{2.14}$$

where C_0 represents the initial concentration of the piece material from the surface layer deposited on the sample's surface.

When the processed surface interacts with the "cold" electrode spots it bears a multiple character, and a portion with modified composition exists already on the surface at every consecutive interaction. For the following cycles the initial conditions are determined from the distribution of element concentration from the preceding cycle, taking into account the thickness of the formed layer:

$$C_j(x,0) = \begin{cases} C_0, & \text{if} \quad 0 \le x \le h; \\ C_{j-1}(x-h), & \text{if} \quad x > h. \end{cases} \; j \ge 2. \tag{2.15}$$

According to this, the thickness h is considered constant for each cycle of thermal or thermo-chemical treatment, and it is determined separately for each case, taking into account the balance equation of the substance quantity, by the relation:

$$h = \frac{\int_0^\infty C(x)dx}{C_0 N} \tag{2.16}$$

From this analysis, we can affirm that the effective diffusion coefficient can be determined experimentally, as described previously for the case of unipolar pulses [46]. By applying the previously described mathematical model, we can determine the formed thickness. It has been shown experimentally that the thickness of the oxide strata formed on the metal surfaces doesn't exceed micrometer order at the multiple interactions of "cold" electrode spots. In solitary interactions it doesn't exceed nanometer order.

2.5 Technology Development

As it was already mentioned [22], the effect of supersaturation of metal surfaces with atmospheric oxygen at normal pressure was detected and documented for the first time in 1990 by Nemoshkalenko et al. Then it was demonstrated that the surface oxidation with plasma is accompanied by a wide range of structural and phase modifications [22, 23, 25, 28]. Phase transformations are conditioned by the appearance of the liquid phase and deposited particle vapors that interact with the discharge channel, the surrounding environment, the cathode material and are due to the mass transfer processes in liquid and solid phase. As it was highlighted above, due to the electro-erosion processes, the cathode material can be in the "liquid-vapor" state and can interact with the environment, that's why, beside oxides, nitrides and intermetallic components, the cathode material and its other phases can usually enter the layer formed of powder [7, 29, 37, 63–69]. These conditions have been achieved in Roentgen research of the phasic superficial component for steel (steel 3, steel 45) and titanium (BT 1-0) [25, 38].

The interaction with plasma was obtained at continuous processing regime (without the inclusion of powder in the processing), when the areas of interaction were partially or multiply superposed (number of passes i was varied for the same surface portion) [25, 38]. The electrode-anode was of cylindrical form made of graphite [25, 42, 56]. The value of the gap varied between 0.15 and 2 mm, and the other parameters had the following values: the voltage on the condenser battery U_C = 240 V and the frequency of electrical discharges f = 40 Hz [51, 52].

The analysis of the phasic change in the composition of machined surfaces (steel 45, titanium BT 1-0) demonstrated that the basic role in these changes is not played only by the accelerated heating and cooling, but also by their interaction with the environment during processing [25, 38].

The intensity of these changes depends on the material properties and on the processing conditions, as well as on the size of the gap (which varied during the experiments, but the energy released in the gap W was constant) [25, 29].

During the processing of titanium all possible phases of its interaction with oxygen and nitrogen in the air were detected on its surface (Fig. 2.3a) [25, 29].

Oxides (TiO, TiO_2) and titanium nitride (TiN) are formed more intensively for the gap $S < 1$ mm. Only traces of TiO and TiN were recorded for a higher value gap ($S \approx 2$ mm) [29]. At the multiple action of plasma, even for large values of the gap, the same phasic composition is formed on the titanium surface [29], i.e. TiO, TiO_2, TiN appear again on the surface. In this regard, the steel surfaces are less active, and the phasic composition is changed insignificantly by increasing the processing time (Fig. 2.3b) [25, 29, 38].

After the action of electrical discharge plasma on the steel surface, beside the characteristic lines of ferrite phase, the appropriate lines of austenite phase appear. The maximum amount of austenite is obtained for $S \leq 0.5$ mm, i.e. when the attacked surface is practically covered with liquid sample material. Some of the diffractogram lines can be identified as characteristic lines of iron carbide (Fe_3C) and nitride (Fe_3N-Fe_4N) (see Fig. 2.3) [25, 29].

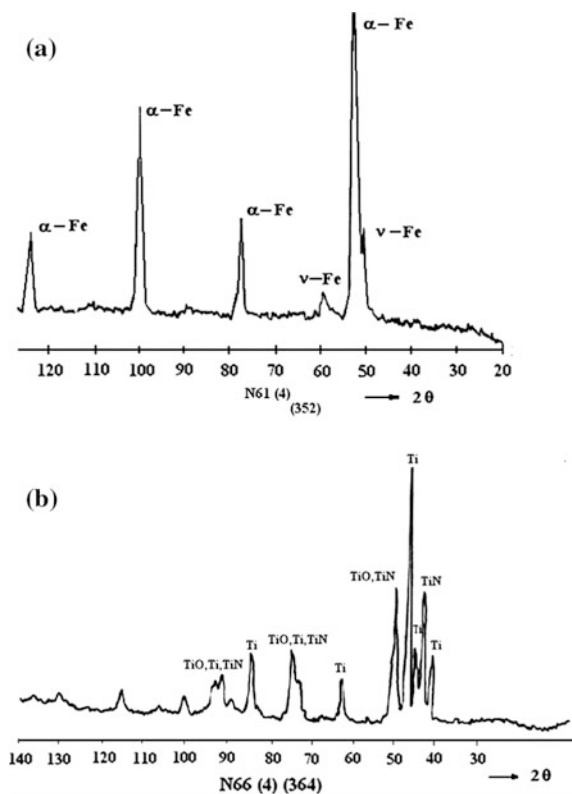

Fig. 2.3 Roentgenogram of superficially treated steel 45 (**a**) and titanium BT-1-0 (**b**) in the regime of "cold" electrode spots [25, 29, 38]

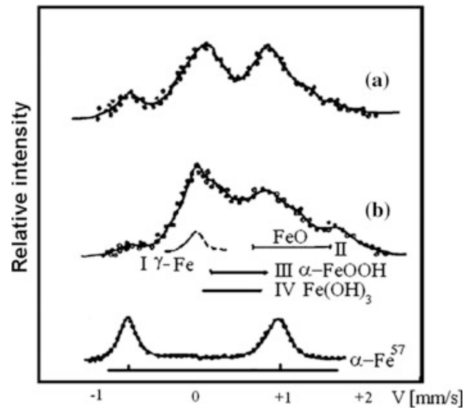

Fig. 2.4 Mössbauer spectra of steel 3 samples after machining by applying spark discharges: S = 2 mm (**a**); S = 0.5 mm (**b**) [7, 25, 29]

The presence of austenite and cementite lines in steel 3 processing is determined by the transfer through the gap of the anode material (graphite) on the cathode surface. The absence of oxides at studied regimes, according to the Roentgenogram, at the first assessment (under ordinary conditions), confirms that "colder" spots burn oxides and impurities from the surface strata [22, 25, 29], i.e. the discharge channel "migrates", in principle, on these surface defects, that, finally, leads to their removal through vaporization (this is valuable for the solitary passes). Due to this phenomenon the process of steel surface cleaning by arc-discharge in vacuum can be explained [8].

Detailed researches [23, 29] of machined surfaces by analyzing the Mossbauer spectra of steel samples (Fig. 2.4) have revealed the evidence of both spectra and represent an evasive superposition of doublets of iron oxides and hydroxides, that confirm the presence of γ-Fe phase for S = 0.5 mm. The distribution of iron, oxygen, carbon and nitrogen is shown in Fig. 2.5, a, from which it is noted that carbon is concentrated especially at the surface.

Carbon concentration decreases sharply with the increase of the surface layer depth, and the oxygen concentration reaches up to 30 % at. [25, 29]. This increased concentration of oxygen is due to the formation of hydroxides in the superficial layer of the sample. The nitrogen concentration reaches up to 5–6 % at. at layer depths up to 300 nm (Fig. 2.5) [25, 29].

For the gap of S = 2 mm, the basic components of the superficial layer are iron and oxygen, and the secondary are, respectively, carbon and nitrogen (Fig. 2.5b) [25, 29]. Oxygen concentration reaches up to 60 % at. at the surface and decreases with the increase of the sample depth. This can be explained by the fact that the hydroxides are formed at the surface and the metastable oxides are formed at depth. From the obtained roentgenograms it is seen that FeO (unique paramagnetic iron oxide at room temperature) is missing in the sample surface.

Thus, we may admit the meta-stability of some thin layers of Fe_2O_3 and Fe_3O, a fact that is well known in literature [29]. The possibility of formation of iron hydroxides in the amorphous state should not be excluded [29]. The complexity of Mossbauer

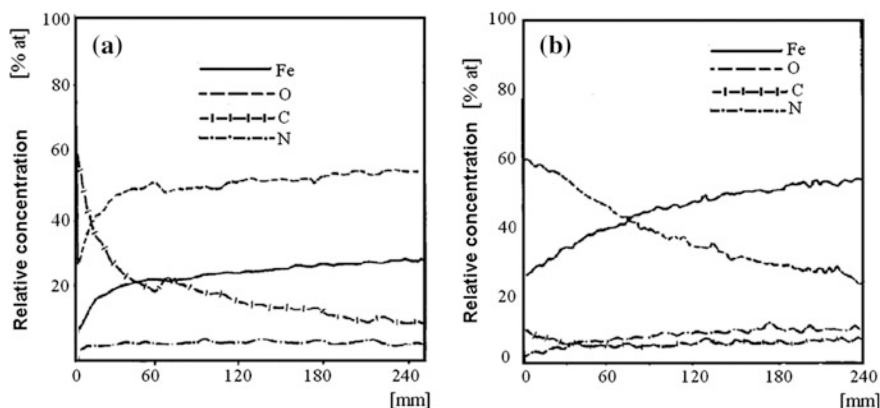

Fig. 2.5 The distribution of elements in steel 3 after PEDM for: S = 0.5 mm (**a**); S = 2 mm (**b**); *1* Fe; *2* O; *3* C; 4—N [7, 25, 29]

spectra shows that the univocal identification of amorphous hydroxides is very difficult.

The phasic composition of titanium and steel superficial layers after removal by rectification of a layer whose thickness is 5–0.10 μm changes insignificantly: the amount of oxides decreases on the titanium surface while that of nitrides decreases on the steel surface. The change of the energy regime does not cause significant qualitative changes, only quantitative changes occur (for $S = const$) [25, 29].

Thus, the study of diffractograms has shown that the most important technological parameters which influence the phase composition of the surface are the value of the gap and the duration of the interaction with the plasma (the number of passes), respectively.

Recently, a number of works [32–36, 42–46, 53–56] have been published, where the results on electro-discharge oxidation of metal surfaces under ordinary conditions are presented. Coatings obtained by this method usually have a dual structure. It consists of an inner base layer at the edge of the metal-coating and an external outer layer.

The base layer is fine-porous, has a crystalline structure and constitutes 60–90 % of the coating thickness. The outer layer coating is less hard, more porous, has an amorphous state and takes on 40–10 % of the thickness.

The coating under the oxidation process is able to germinate in metals in about 10–60 % of the total thickness of the coating in depth and consists mainly of oxides of the elements contained in the machined alloy and elements from the interstice.

The PEDM method allows to form coatings on pieces of complex shapes and of any configuration [70], including the internal surface of pipes [35].

In order to develop the technology of oxide film formation, the duration and the form of the pulse, the energy and the power released in the gap at a singular discharge, the size of the gap and the frequency of pulses were chosen as input

parameters of the technological process, and the thickness of the oxide films, the width of oxidation strips, the productivity of the technological process, the micro hardness of the processed surface layer, the surface electrical resistance, and the corrosion resistance were chosen as output parameters.

To perform the experimental research aiming at the appreciation of the oxidation strip width depending on the sample material and the processing energy regime we used the current pulse generator with priming from a block of high voltage of 12 kV and of 0.3 μA current [29], the laboratory setup that ensures the positioning, fixing and rotating of the samples in the process of machining with the rotation frequency adjustable within 0 and 150 rot/min.

The used tool-electrode was made in the form of cylindrical bar rounded at the working end of the hemispheric shape and made of the same material as the work piece to avoid the appearance of foreign phases in the machined surface as a result of electrical erosion. The cathode work piece presents a cylinder of Ø11.28 mm. The anode tool-electrode is a Ø6 mm cylinder with a semicircular end.

The generator for the formation of oxide films on metal piece surfaces by applying PEDM contains the following blocks: the power pulse generator, the priming block (intended to initiate electrical discharges) and the control block whose role is to synchronize the power and priming pulses [29, 45, 53].

The pulse current generator [29, 45, 53] with a voltage block for interstice pre-ionization was used as a source of energy. The discharge energy emitted in the interstice constitutes 1–6 J. Thus, by establishing the generator energy regime, the superficial piece oxidation for indicated materials without melting the processed surface can be produced. The superficial piece oxidation for indicated materials without melting the processed surface can be produced to establish the generator energy regime.

The thickness of the oxide pellicle subjected to the condition of the energy balance and according to Palatnik's criterion [29, 45, 53] is directly proportional, respectively, to the quantity of heat and the energy emitted on the electrode surfaces:

$$\begin{aligned} \delta &\sim Q; \\ \delta &\sim W_s. \end{aligned} \tag{2.17}$$

The power of electrical discharge:

$$P = \frac{dW_s}{dt} = \frac{W_s}{\tau} \tag{2.18}$$

where τ is the duration of electrical discharge.

From the other point of view, the thickness of the oxide pellicle depends on the physical properties of the processed surface material [29]:

$$\delta \sim \sqrt{\rho \cdot c \cdot \lambda}, \tag{2.19}$$

where ρ is material density; c is specific thermal conductibility; λ is specific melting heat.

Thus the thickness of the oxide pellicle is directly proportional to the power of electrical discharge emitted in the interstice and depends on the physical properties of the processed surface material.

The technological schemes used in the formation of the oxide pellicles by applying PEDM are shown in Fig. 2.6. The work-piece was connected in the discharge circuit as a cathode, and the tool-electrode—as an anode.

The direct determination of operating properties that affect the functionality of pieces has required intensive investigations. Therefore, this task has been addressed in a manner that does no require the use of lengthy and expensive techniques and equipment.

Following the analysis of literature [29, 45, 53] we concluded that the RC type generators with parallel priming can be successfully used for micro- and nano-oxidation of the conductive piece surface. The measurement of the oxidation strip size was performed in a continuous processing regime at solitary zones of plasma channel interaction with surface samples with overlap coefficient $k_{sp} = 0.5$, and the rotational frequency was established according to the frequency of PEDM taking into account the value of k_{sp}. The width of the strips was appreciated for various materials and processing technological regimes.

The strip width of the oxide films was measured with a microscope of the type METAM with measurement accuracy of ±0.025 mm.

Because the oxide films have small thickness, the current exceeding mA should not pass through them. Therefor, it is necessary to measure the resistance with the use of a bridge that should divide the current from the ohmmeter source. The oxide film having high electrical resistance R_p (of the order of MΩ) is shunted by a much smaller ohmic resistance, R_{sh} (of the order of tens of kΩ), and then the maximum of the total current should pass through the shunt resistor.

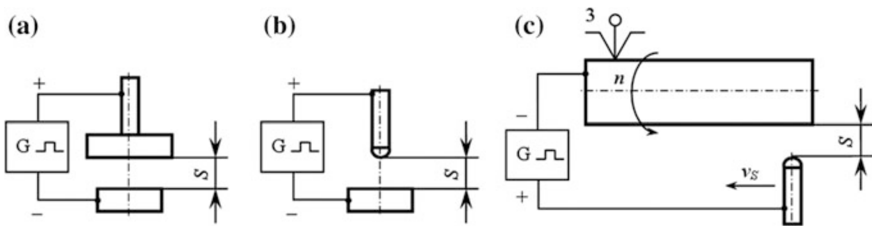

Fig. 2.6 The technological schemes of the oxide pellicle formation by applying PED: **a** on the plane surface with plane tool-electrode; **b** on the plane surface with a semi circular tool-electrode; **c** on the exterior cylindrical surfaces [53]

The measurement of electrical resistance of samples before processing is done using a digital ohmmeter with a measurement limit of tenths or hundredths of Ω, because the metallic samples are good electrical conductors.

Electrolytes made of chemical agents dissolved in distilled water at room temperature having a certain concentration were prepared to perform investigations on resistance to chemical corrosion of processed samples (with oxide films formed on the active surface by applying PEDM). The oxide films were formed by applying PEDM with optimal energy parameters for each investigated material.

The samples were fixed in the developed device so that only a circular portion of the machined surface was subjected to dissolution. It was included in the circuit of anodic dissolution as anode. The investigations were performed in DC regime with step-by-step changing of the applied voltage of 0.1 V.

The speed of corrosion is determined by weighing the samples before and after the investigations using the analytical balance of type VL-200 with an accuracy of 10^{-4} g.

The index of the corrosion speed is determined by the relation [53]:

$$K = \frac{\Delta m}{S \cdot t}; \tag{2.20}$$

where K is the speed of corrosion (the mass index), g/m^2·h; S is the area of the work piece surface, m^2; t is the duration of investigation (working time), h; Δm is the loss (or the addition) in the work piece mass, g;

$$\Delta m = m_i - m_f; \tag{2.21}$$

where m_i is the initial mass of the sample, g; m_f is the final mass of the sample, g.

The conditions under which the investigations were performed for experimental determination of corrosion speed are as follows: the sample—anode; the voltage between the electrodes U = 2 V; the distance between the electrodes d = 10 mm; the electrolyte is composed of aqueous solution of 3 % NaCl at room temperature for samples made of construction steel, or of 30 % H_2SO_4 at the temperature of 80 °C for titanium alloy samples; the processing time at each measuring step t = 0.5 h; the work piece surface area (the area of contact with the electrolyte) S = 50.24 mm^2.

2.6 Results of Experimental Investigations and Their Analysis

2.6.1 Results of Technological Investigations on Film Formation

Next we will present the results of experimental research on the formation of oxide films on metal surfaces by applying PEDM. It has been experimentally established

that the surface oxidation is more effective when the work piece is connected in the discharge circuit as cathode (direct polarity). Below are presented the dependencies of the output parameters upon the input ones with their approximation by mathematical modeling. The productivity of oxide films formation is optimized. The next results show the interdependence between the chemical and phase composition of the formed films and their properties. It was found that the micro hardness of the processed surface layer increases by 30–100 HV units, the surface electrical resistance increases by about 10^7 times, the corrosion speed decreases by at least 2 times for construction steels and by 100 times—for titanium alloys compared with the unprocessed surface.

The dependence of oxide layer thickness δ on the power dissipated in the gap at a solitary discharge is shown in Fig. 2.7, while its dependence on the gap size is presented in Fig. 2.8.

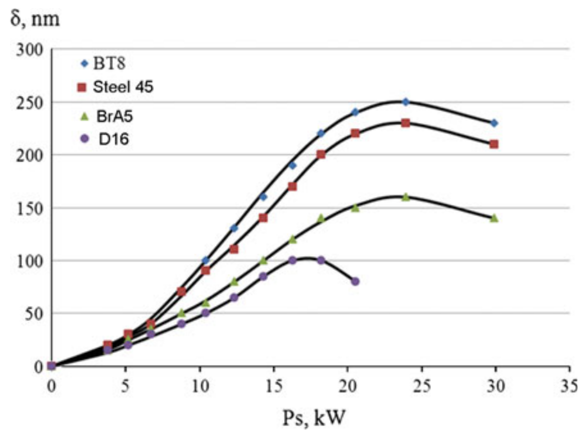

Fig. 2.7 The dependence of the oxide film thickness on the power dissipated in the gap [53]. The work piece-cathode and the tool-electrode material: ♦—titanium alloy BT8; ■—steel 45; ▲—BrA5 copper alloy; ●—aluminum alloy D16. The processing scheme according to Fig. 2.6a

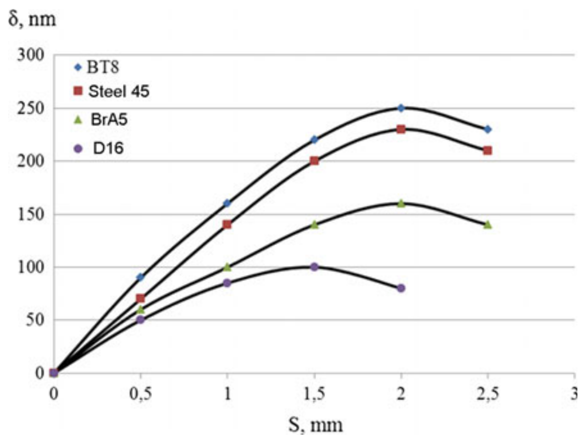

Fig. 2.8 The dependence of the oxide film thickness on the gap size [53]. The work piece-cathode and the tool-electrode material: ♦—titanium alloy BT8; ■—steel 45; ▲—BrA5 copper alloy; ●—aluminum alloy D16. The processing scheme according to Fig. 2.6a

By analyzing the curves shown in Figs. 2.7 and 2.8 we can see that the thickness of the oxide strata increases exponentially with the value of input energy parameters regardless of the physico-mechanical properties of the piece material. This can be explained by the fact that the efficiency of the energy and, respectively, the power dissipated in the gap becomes higher with the increase of their values. At the same time, the increase of the gap active resistance is attesting and the greater amount of energy is spent on such secondary effects as brightness and sound intensity increase created by the shock wave.

When applying the pulsed electrical discharge power greater than that of critical value (for titanium, iron and copper alloys this value is 30 kW and for aluminum alloys it is 20 kW) the intensity of evaporation of the work piece surface layer enhances, which leads to the decrease of the oxide film thickness.

The optimum value of the pulse power for the surface oxidation of the metal surface is P_S = 20–0.30 kW at the gap sizes of S = 1.5–0.2 mm for iron, titanium and copper alloys, and P_S = 15–0.20 kW at S = 1.0–0.1.5 mm for aluminum alloys, respectively.

The experimental research results on the determination of oxidizing strip width dependence on the energy processing regime are shown in Fig. 2.9.

Referring to Fig. 2.9 we can see that the dependencies of the processed strip width on the work piece-cathode surface upon the power dissipated in the gap represents an exponential dependence for all processed materials. The process is conducted more intensively on the sample surfaces made of titanium alloy, than on those made of steel, copper alloy, and the last one is the aluminum alloy. These effects can be explained on the basis of thermo-physical properties, of electron emission for these materials, and of the avidity of their constituent elements to oxygen.

Technological dependencies obtained after mathematical processing according to the described methodology [36, 45, 53, 54] can be approximated by the equations:

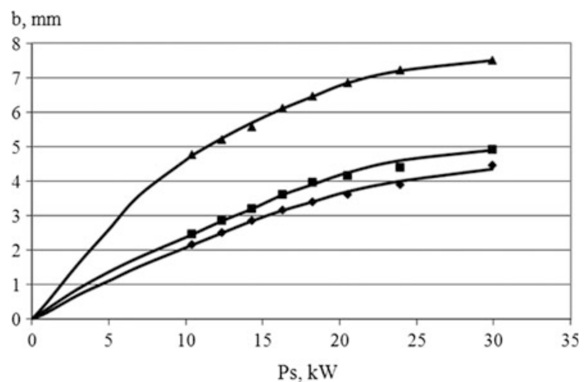

Fig. 2.9 Dependence of the oxidizing strip width on the pulse power dissipated in the gap [53] for samples made of: ♦—D16; ■—steel45; ▲—BT8. The processing scheme according to Fig. 2.6c

(1) The film thickness on the gap size:

$$\delta_{Ti} = \frac{373 \cdot S^{1.53}}{e^{0.77 \cdot S}};\ \delta_{Fe} = \frac{379 \cdot S^{1.82}}{e^{0.91 \cdot S}};\ \delta_{Cu} = \frac{231 \cdot S^{1.46}}{e^{0.73 \cdot S}};\ \delta_{Al} = \frac{213 \cdot S^{1.51}}{e^{1.01 \cdot S}}; \tag{2.22}$$

(2) The film thickness on the power dissipated in the interstice:

$$\delta_{Ti} = \frac{0.12 \cdot P_S^{3.52}}{e^{0.15 \cdot P_S}};\ \delta_{Fe} = \frac{0.08 \cdot P_S^{3,67}}{e^{0.15 \cdot P_S}};\ \delta_{Cu} = \frac{0.05 \cdot P_S^{3.66}}{e^{0.15 \cdot P_S}};\ \delta_{Al} = \frac{0.01 \cdot P_S^{5,08}}{e^{0.28 \cdot P_S}}. \tag{2.23}$$

(3) The oxide film strip on the power dissipated in the interstice:

$$b_{Al} = 0.46 \cdot P_S^{0.68}; b_{Fe} = 0.55 \cdot P_S^{0.66}; b_{Ti} = 1.66 \cdot P_S^{0.46}. \tag{2.24}$$

For quantitative assessment of productivity, the specific processing time T (s/cm^2) or (min/cm^2) was measured, which presents the processing time of a surface with the area A = 1 cm^2. As it has already been mentioned the electrode spots are migratory and they scan the machined surface depending on the impurities presented on it or on its roughness "seeking" the place with the lowest electrical resistance of the gap. The electrode spot can randomly migrate on the surface, but by adjusting or setting the priming voltage pulse we can organize desired surface machining without breaking the formed film. Figure 2.10 shows the photos of unprocessed surface and of the work piece surface consecutively processed by one and several solitary discharges.

The technological scheme applied to such processing corresponds to Fig. 2.6a, i.e. electrical discharges occur between two flat parallel surfaces. The traces of plasma channel interaction with the machined surface confirm the migratory character of the electrode spots and the hypothesis that the electrical discharges occur in the gap zones with the lowest active resistance.

In the case when the tool-electrode dimensions and the geometric shape are different from those of the machined surface the situation changes in the gap, and the electric discharge can only develop along the radius vector of the electric field that corresponds to the intensity necessary for dielectric environment breakdown. It follows that by setting a certain value of priming voltage applied to the gap and its certain size we can manage the sequence of plasma (electrode spots) interactions with the machined surface, and, thus, we can elaborate the nano-oxidation technology of surfaces with a large area and a complicated geometry. Figure 2.11 can serve as an example.

Thus, by applying PEDM, we can process conjugated surfaces of different shapes (e.g. flat surface with flat tool-electrode) with the formation of continuous oxide films, or we can form discrete oxide stripes using a rounded bar tool-electrode. The oxidation strip width will depend on the tool-electrode geometry and processing energy regime.

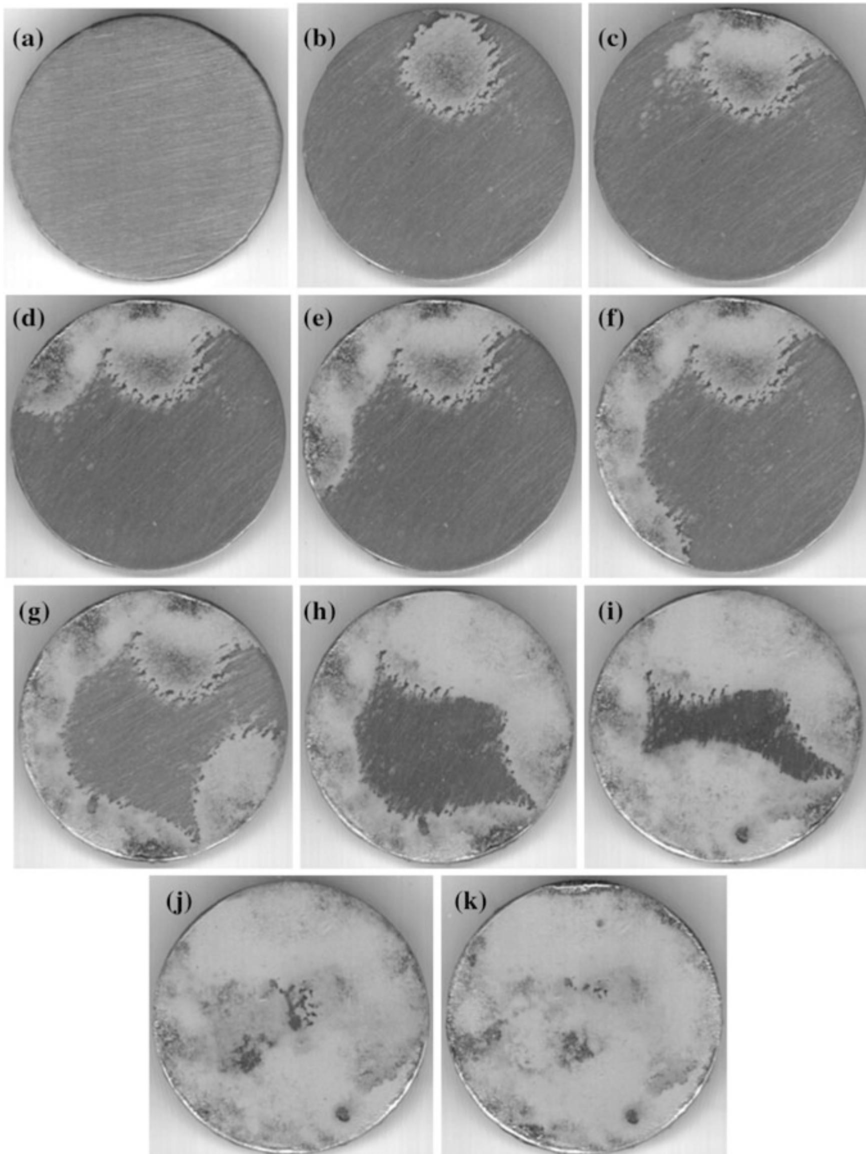

Fig. 2.10 A general view of unprocessed and processed flat surface by applying PEDM with flat tool-electrode, × 4 [53]. Energetic processing regime: the size of the gap S = 2 mm; charging voltage of the condenser battery U_C = 240 V; its capacity C = 600 μF; the energy released in the gap W_S = 5.27 J; the duration of the power pulse τ = 220 mS. The number of solitary pulses, *i*: **a** 0 (unprocessed surface); **b** 1; **c** 2; **d** 3; **e** 4; **f** 5; **g** 10; **h** 15; **i** 20; **j** 25; **k** 30. Work piece and tool-electrode material—titanium alloy BT-8

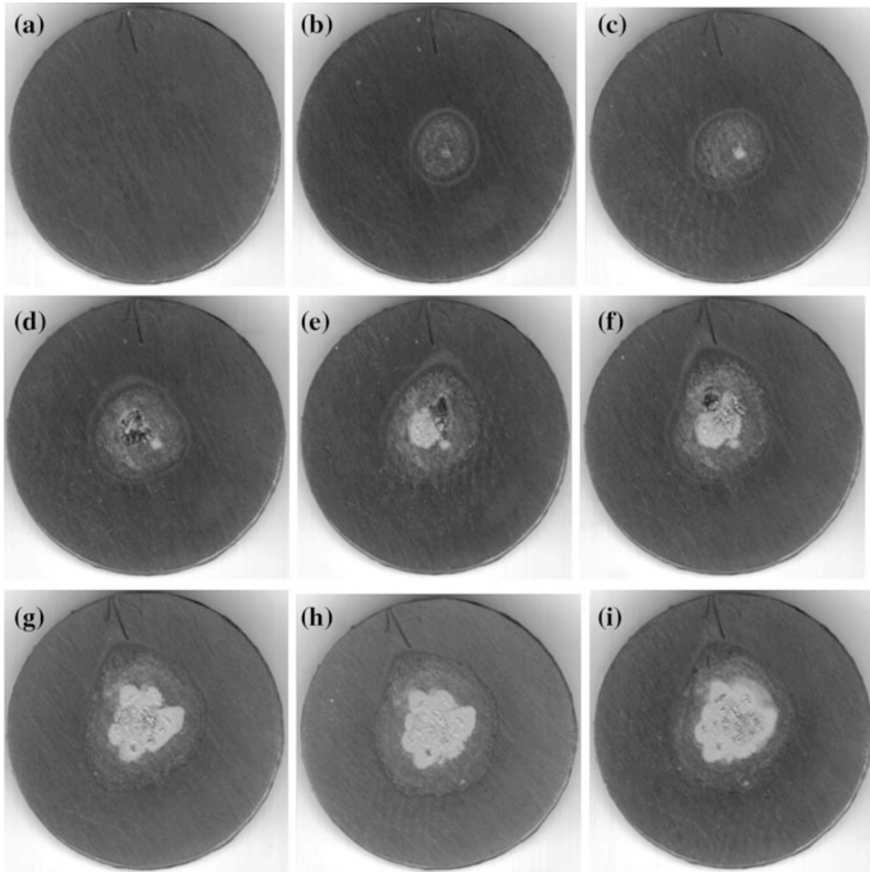

Fig. 2.11 A general view of unprocessed and processed flat surface by applying PEDM with semi-circular (Ø6 mm bar) tool-electrode, × 4 [53]. Energetic processing regime: the size of the gap S = 1.5 mm; charging voltage of the condenser battery U_C = 140 V; its capacity C = 600 μF; the energy released in the gap W_S = 3.15 J; the duration of the power pulse τ = 220 mS. The number of solitary pulses, *i*: **a** 0 (unprocessed surface); **b** 1; **c** 2; **d** 3; **e** 4; **f** 5; **g** 10; **h** 15; **i** 20. Work piece and tool-electrode material—titanium alloy BT-8

The end of processing is recorded at the time when no discharge occurs between the examined samples, which indicates that a continuous oxide film is formed on the surface with the active surface resistance that exceeds the initial parameters of the processing regime.

The productivity is calculated as the inverse value of the specific processing time [53, 58]:

$$\eta = \frac{1}{T}\left(\mathrm{cm}^2/\mathrm{min}\right). \tag{2.25}$$

The research results of the dependence of the film formation productivity on the input parameters (the pulse frequency, the energy released in the gap, and the size of the gap) are presented in Figs. 2.12, 2.13 and 2.14.

With the increase of the pulse discharge frequency (from 0 to 15 Hz) the productivity increases, reaching the maximum value $\eta \approx 2.14\ \mathrm{cm}^2/\mathrm{min}$ for f = 15 Hz. For the values f > 15 Hz the productivity decreases hyperbolically (Fig. 2.12).

The decrease of productivity of oxide films formation is due to the fact that the condenser battery does not succeed in loading totally, and the work environment from the gap does not restore completely. Therefore, the energy discharge decreases, which leads to the constriction of the plasma channel, and, as a result, to the decrease of the chemico-thermal influence of the zone of the work piece surface. To annihilate the undesirable effect, we propose to decrease the value of the ballast resistance (or the ballast resistance is to be replaced by an electronic key) in

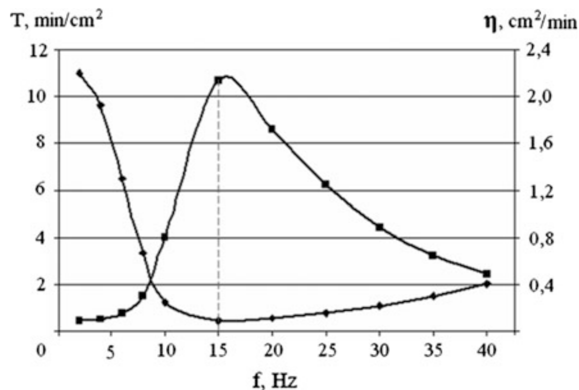

Fig. 2.12 Dependence of the specific processing time (♦) and of the productivity of oxide films formation (■) for steel 45 mating surfaces of the electrodes on the pulse frequency: the gap size S = 2 mm; the capacity of the condenser battery C = 600 μF; the charging voltage of the condenser battery Uc = 240 V. Processing scheme according to Fig. 2.6a [53]

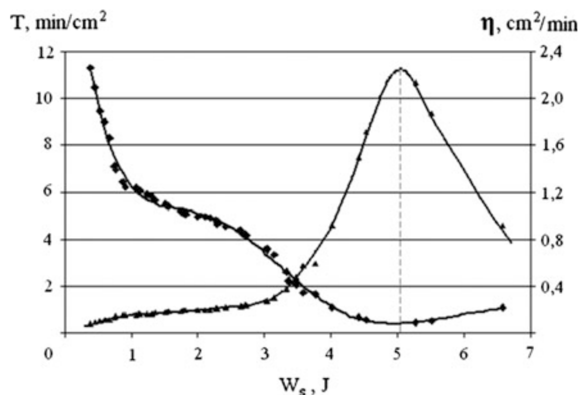

Fig. 2.13 Dependence of the specific processing time (♦) and of the productivity of oxide films formation (▲) for steel 45 mating surfaces of the electrodes on the energy released in the gap: The pulse frequency f = 15 Hz. Processing scheme according to Fig. 2.6a [53]

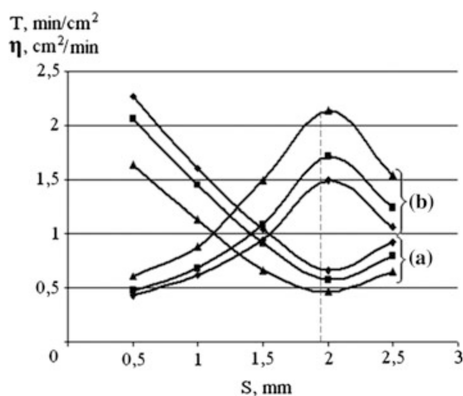

Fig. 2.14 Dependence of the specific processing time (♦) and of the productivity of oxide films formation (▲) for steel 45 mating surfaces of electrodes on the gap size: the energy released in the gap Ws: ♦—3.5–4 J; ▲—4–4.5 J; ■—4.5–5 J; the capacity of the condenser battery C = 600 μF; the pulse frequency f = 15 Hz. Processing scheme according to Fig. 2.6a [53]

order to decrease the loading time of the condenser battery of the pulse generator, to provide additional oxygen supply for the gap, and to restore the interstitial environment. Considering the optimal value of the pulse frequency, for which the maximum of productivity is obtained, the further researches on the influence of other parameters on the productivity of oxide films formation were made for f = 15 Hz.

The observed maximum in the dependence of the productivity of oxide film formation on the energy released in the gap (Fig. 2.13) (for $W_S \approx 5$ J, the capacity of the capacitor C = 600 μF, the charging voltage of the condenser battery $U_C = 240$ V, and the gap size S = 2 mm) can be explained by the fact that at higher energies released on the surface layer of the sample, beside the "cold" electrode spots, "hot" electrode spots are functioning, causing material melting and vaporization of the machined surface (together with the film rich in oxides) in the interaction zone with the plasma channel, which leads to its renewal and, therefore, to the possibility of gap breakdown.

As it was previously established [29], the dependence of the volume of the hot central zone of the plasma channel upon the size of the gap gets a maximum for S = 1.5–2 mm when the energy released in the gap is $W_S = 3.5$–6 J. The maximum of heat quantity in the plasma channel corresponds to the maximum of productivity from Fig. 2.14 (for all 3 cases (Ws = 3.5–4 J, Ws = 4–4.5 J and Ws = 4.5–5 J) the maximum was obtained for S = 1.5–2 mm).

Thus, taking into account the influence of PEDM parameters on the intensity of oxide film formation on the conjugated surfaces of pieces made of structural steel, the optimal processing regime was set: the pulse frequency f = 15 Hz; the gap size S = 1.5–2 mm; the capacity of the condenser battery of the power generator C = 600 μF; the charging voltage of the condenser battery $U_c = 240$ V (the average value of the energy released in the gap for these values Ws = 5.27 J). The specific processing time in this case does not exceed 0.5 min/cm^2 and the productivity is $\eta \approx 2.14$ cm^2/min.

2.6.2 Phase Composition of Nano-Oxide Films

An example of high-resolution XPS oxygen spectrum is shown by curve 1 in Fig. 2.15. The spectra were obtained using XPS and PHI SUMMIT processing—by using PHI Multipack 8.2 C. The standard procedure is described in details elsewhere [46], based on the characteristics of the Versa Probe 5000 equipment.

The signal analysis revealed the presence of oxygen O−1 s in three types of chemical bonds (called components). These are as follows: (a) the component O^{-2} (which contains oxygen atoms of metal oxides, in the sample labeled number 3 in Fig. 2.15), with the specific energy 529.6 EV; (b) the component of OH^{-} with EV 531.5 (indicated by the numeral 2 in Fig. 2.15c) the component of type O–C and O–C=O with EV 533.4 (indicated by 4 in Fig. 2.15).

The chemical analysis showed the concentration of each of the three components (C) (a): (C) (b): C (c) = 0.89: 1.00: 0.50. Additional studies have shown a possible existence of a fourth component of oxygen within the context of type O-H_2. However, the relative concentration of this component value is assumed to be not greater than 0.15.

Studies have proven that virtually there is no change in the geometry of the original surface when applying the PEDM method for the formation of oxide coatings. This makes it possible to recommend this method for surface processing of completed parts. The thickness of films is between 10–240 nm [32, 35, 53], i.e. it corresponds to the field of nanotechnology.

The abnormal dissolution of oxygen in metals is observed when processing metal surfaces by this method [53]. For instance, when processing samples made of structural steel, the dissolution of oxygen reaches 59 % at., while this value is around 34, 19, and 39 % at. for samples made of titanium alloys, aluminum alloys, and copper alloys, respecively.

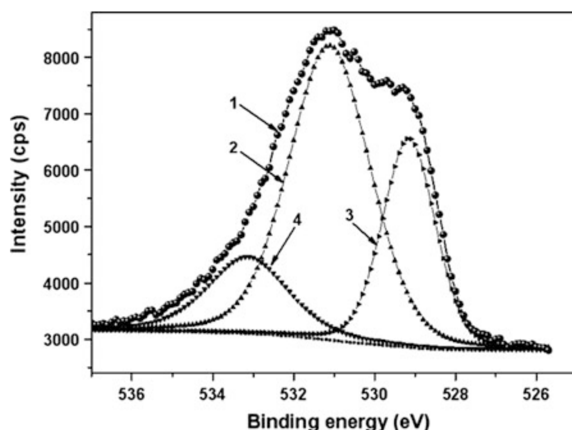

Fig. 2.15 XPS spectrum of oxygen of oxide pellicles on samples of steel 45: *1* total spectrum; *2* OH^{-} component; *3* O^{2-} component; *4* components of O–C and O C=O types

The metal oxides in the pellicle are in amorphous state. This probably explains why the surface resistance for steel pieces increases up to 10^6 Ω/mm^2 [32, 53], the potential to corrosion increases by 10 or more times, and the corrosion speed is reduced by 2–0.4 times [32, 34, 53].

2.6.3 Morphology and Chemical Composition of Nano-Oxide Films

The results of SEM and EDX analysis of investigated sample surfaces are presented in Figs. 2.16, 2.17, 2.18, 2.19, 2.20 and 2.21 and in Table 2.1.

As we can see from these results, the abnormal dissolution of oxygen in metals is observed while processing metal surfaces by this method [22, 53, 56, 59]. It is

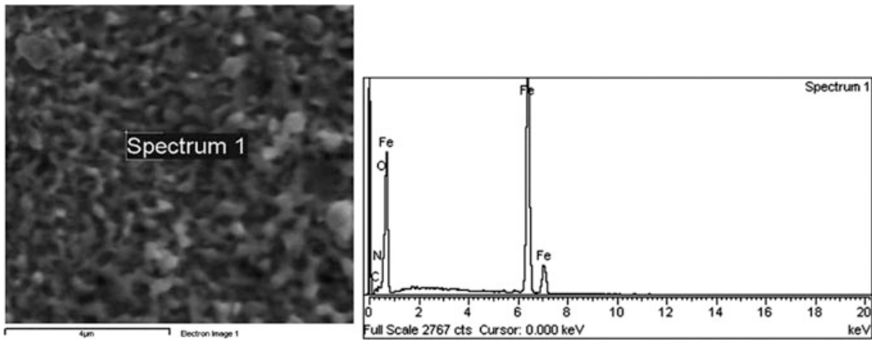

Fig. 2.16 SEM and EDX analysis of steel 45 sample surface [53]

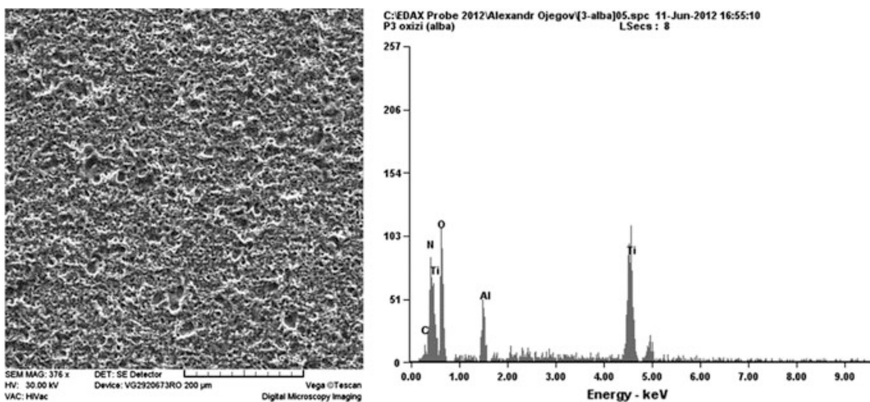

Fig. 2.17 SEM and EDX analysis of BT8 titanium alloy sample surface [53]

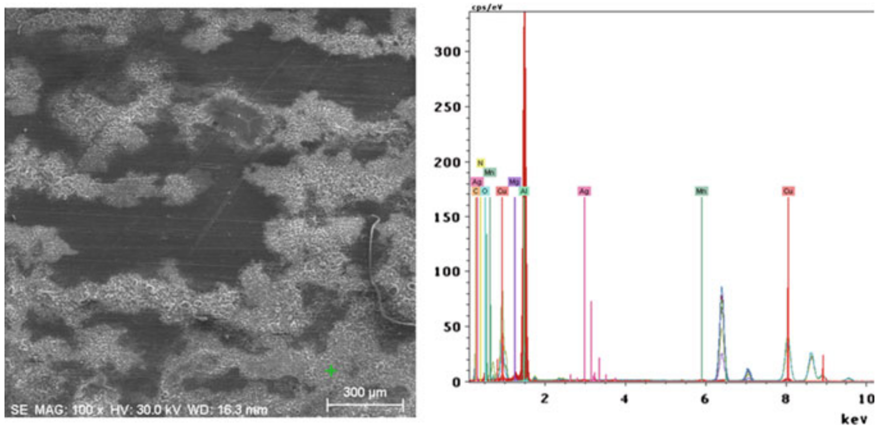

Fig. 2.18 SEM and EDX analysis of D16 aluminum alloy sample surface [53]

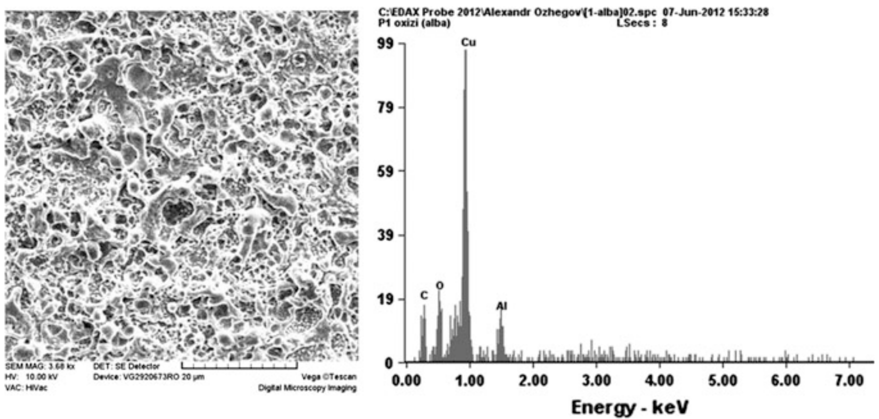

Fig. 2.19 SEM and EDX analysis of M0 copper alloy sample surface [53]

demonstrated that the dissolution of oxygen when processing the samples made of construction steel reaches 60 % at., while this value is around 30–35, 20, and 50 % at. for samples made of titanium alloys, aluminum alloys, and copper alloys, respectively. The superficial layer of steel and titanium alloy surfaces contains nitrogen, besides oxygen.

Still in one of the first works dedicated to the surface processing by applying PEDM in the regime of its maintenance on the "cold" electrode spots [29] it was demonstrated that the reduction of the initial surface roughness is attested in all the cases. If we analyze the images shown in Fig. 2.22b, hich represents the morphology of the processed surface layer, we find that the quality of the surface with the oxide film (Ra ≈ 0.1–0.2 μm) is increased as compared to the mechanically machined surface (Ra ≈ 0.63 μm, Fig. 2.22a). This phenomenon can be explained

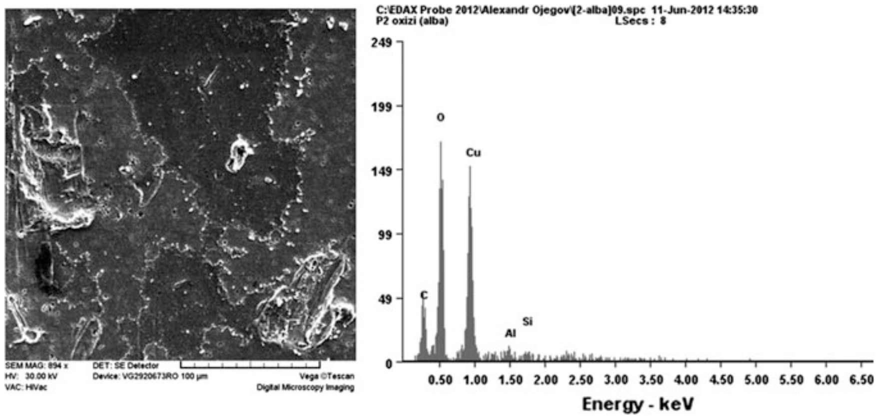

Fig. 2.20 SEM and EDX analysis of brass L63 sample surface [53]

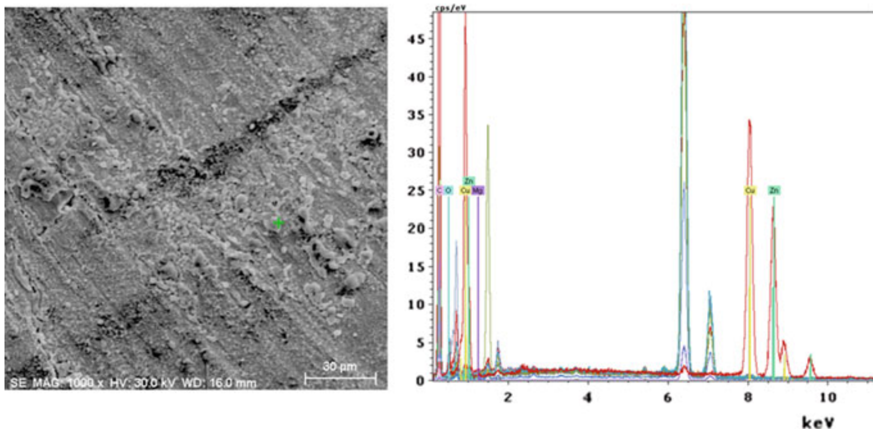

Fig. 2.21 SEM and EDX analysis of bronze BrA5 sample surface [53]

by the fact that the asperities formed on the surface of the sample as a result of mechanical machining are subjected to vaporization and electrical erosion in the solid, liquid and vapor state under the action of strong electric fields and of PEDM plasma.

2.6.4 Surface Electrical Resistance

The results of investigations of surfaces subjected to the oxidation process under the maintenance of PEDM by "cold" electrode spots are presented in Fig. 2.23. It is seen that for the cathode–work piece (Fig. 2.23a) the processing has taken place

Table 2.1 The EDX analysis of sample element content [53]

Basis material of the sample	EDX element content of processed surface		
	Element	(norm. wt%)	(norm. at.%)
Steel 45 (C45)	Carbon	1.89	4.32
	Nitrogen	7.82	12.43
	Oxygen	29.77	58.74
	Iron	60.52	24.51
Titanium alloy BT8 (TiAl6Mo4)	Carbon	00.41	01.38
	Oxygen	30.33	33.27
	Nitrogen	03.38	09.56
	Aluminum	05.84	08.57
	Titanium	60.04	47.22
Aluminum alloy D16 (AlCu4Mg1)	Aluminum	66.84	55.68
	Oxygen	13.95	19.60
	Magnesium	2.49	2.30
	Carbon	1.82	3.40
	Copper	2.42	0.86
	Manganese	0.55	0.23
	Silver	0.86	0.18
Technically pure copper M0	Copper	59.5	25.55
	Oxygen	29.53	50.50
	Carbon	10.22	23.20
	Aluminum	0.75	0.76
Bronze BrA5 (Cu95Al5)	Copper	52.97	21.18
	Oxygen	26.66	42.34
	Carbon	14.83	31.38
	Aluminum	02.66	02.50
	Silicate	02.87	02.60
Brass L63 (Cu63Zn37)	Copper	42.30	23.25
	Zinc	32.89	17.57
	Oxygen	16.72	36.50
	Carbon	7.52	21.86
	Magnesium	0.57	0.82

over the entire surface, while on the anode-surface sample (Fig. 2.23b) traces of plasma channel migration are clearly observed (areas with more light color), and among these areas darker color areas are observed (where the electrode surface interacts with the peripheral plasma channel).

For the first time, the surface electrical resistance was measured in the samples made of steel 45 processed by applying PEDM (Table 2.2) both for the anode-tool-electrode and for the cathode-work piece surfaces. The surface electrical resistance of the unprocessed samples is comprised within the limits of 0.05–0.09 Ω/mm^2. By analyzing the results presented in Table 2.2 we can attest a substantial

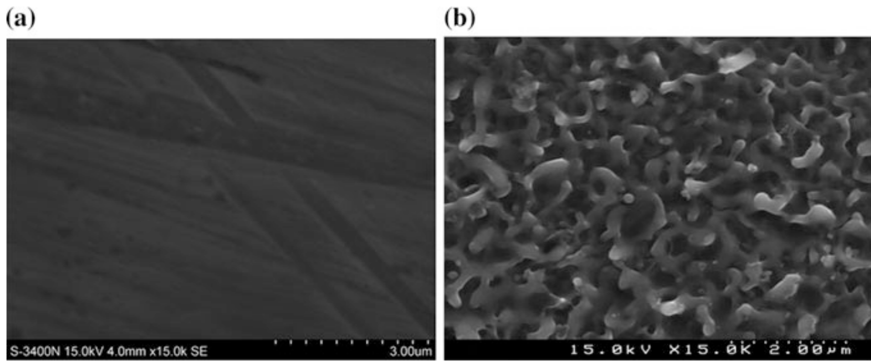

Fig. 2.22 Morphology of the superficial strata of the work pieces: **a** unprocessed surface; **b** surface processed by applying [53]

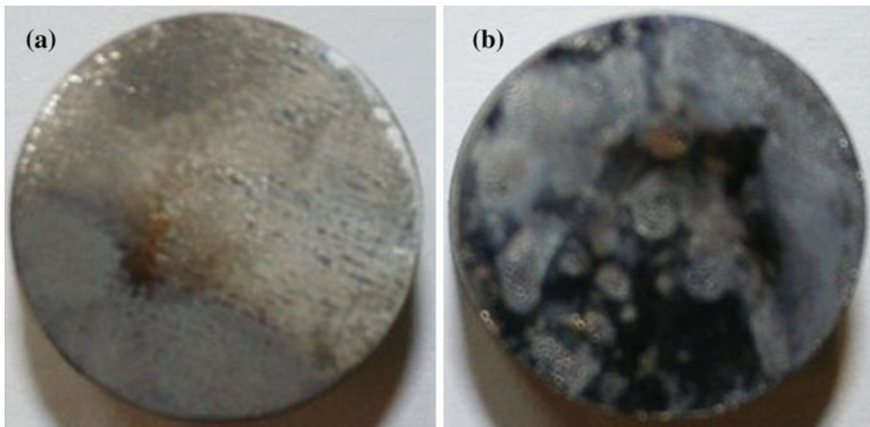

Fig. 2.23 General view of the samples made of steel 45 processed by applying PEDM (the capacity of the condenser battery C = 600 μF, the charging voltage of the condenser battery U_c = 160 V, the distance between electrodes (the gap size) S = 1.5 mm, the pulse frequency f = 15 Hz, the energy accumulated on the condenser battery W_C = 7.68 J, the energy released in the gap W_S = 3.58 J): **a** sample—cathode; **b** sample—anode [53]

increase of the surface electrical resistance of the electrodes that have participated in the PEDM process in all cases. However, the active surface resistance of the anode-electrode is about 3 times lower than that of the cathode. This latter finding can be explained by the fact that, under the same conditions, a larger amount of energy is released on the anode surface, and it is possible that more intense vaporization process occurs. That is why the oxide film formation is slower.

Next, the surface electrical resistance of the surerficial stratum for cathode-samples made of titanium, aluminum and copper alloys was measured (Table 2.3).

Table 2.2 Surface electrical resistance of oxide pellicles on samples of steel 45 [53]

Sample	Surface electrical resistance ($\times 10^6$ Ω/mm^2)				
	Experimental data				Average value
Cathode	0.88	0.72	1.46	0.71	0.98
	0.97	1.52	0.68	0.72	
	0.73	1.09	0.76	0.83	
	1.33	1.10	1.04	0.73	
	1.07	0.88	1.21	0.78	
Anode	0.81	0.26	0.46	0.31	0.33
	0.11	0.14	0.56	0.34	
	0.29	0.11	0.62	0.38	
	0.87	0.38	0.11	0.15	
	0.12	0.13	0.27	0.17	

Table 2.3 Surface electrical resistance of the oxide pellicles formed on the surfaces of cathode—samples [53]

Base material of the processed samples	Average value of the surface electrical resistance ($\times 10^6$ Ω/mm^2)
Titanium alloy BT8	1.6
Duralumin D16	0.25
Technically pure copper M0	0.15
Bronze BrA5	0.17
Brass L63	0.19

As one can see from the results presented in Tables 2.2 and 2.3, the surface electrical resistance depends on the investigated sample material, and it has higher values for materials with lower electrical conductivity.

2.6.5 Resistance to Corrosion

The sufficient and necessary conditions were established for avoiding the appearance of the liquid phase on the surface of processed samples [32–36, 42–46, 53–56]. Avoiding the emergence of a liquid phase is necessary for two reasons: to omit the erosion process of the processed surface and the crater formation, and, as a result, to avoid the increase of the final processed surface roughness.

The microscopic surface investigation of two identical samples made of steel 45 (Fig. 2.24a—the surface with oxide films, Fig. 2.24b—the unprocessed surface) after 3 years of their storage in air in ordinary conditions shows that rust appeared on the unprocessed surface. As for the machined surface, no interaction with the environment was noticed.

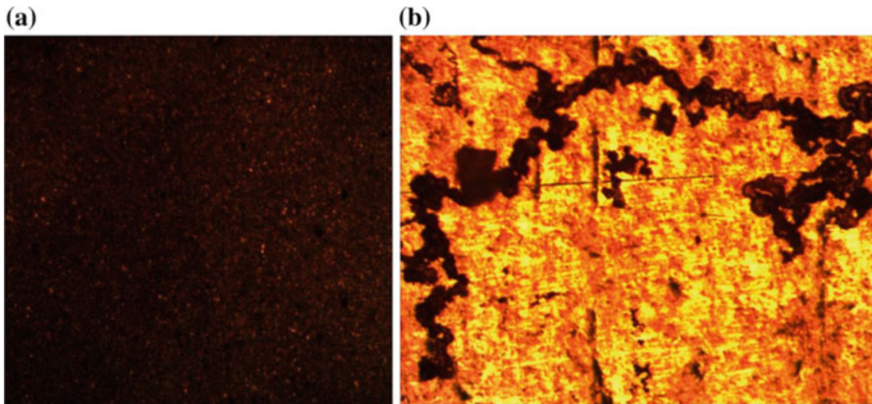

Fig. 2.24 General view of surface of samples made of steel 45 after 3 years of storage in air in ordinary conditions: **a** sample surface with oxide films; **b** unprocessed surface [53]

The research of the piece surfaces (Fig. 2.25a) and of the tool-electrode (Fig. 2.25b) allowed to establish that the latter is also subjected to oxidation. The layer formed on the tool-electrode is discontinuous, with obvious signs of melting and electroerosion. The tool-electrode loses its electrical conductivity properties, changes its original geometry character and requires renewing or cleaning of the active surface during its functioning. For these reasons, the tool-electrode must be made of a material resistant to both electroerosion and oxidation.

The study of the piece surfaces made of steel 45 machined under the oxidation regime by applying PEDM and the analysis of their chemical content allowed to

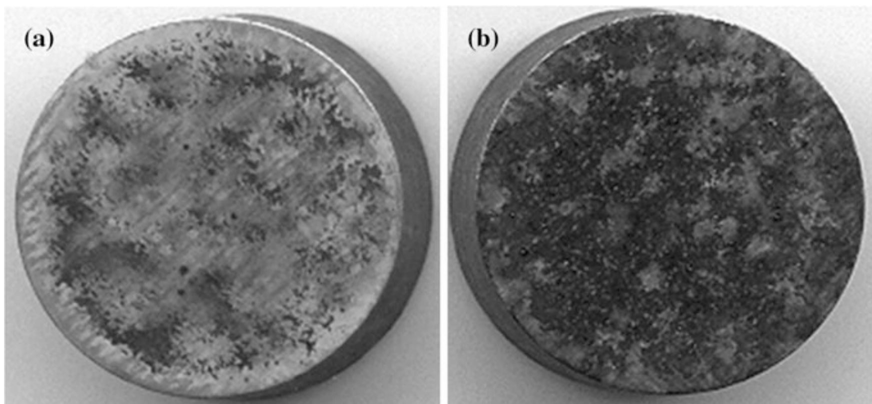

Fig. 2.25 General view of surface of samples made of steel 45 after processing by PEDM (parameters of the processing regime: the charging voltage of the condenser battery U_c = 140 V; the capacity of the condenser battery C = 600 μF; the gap size S = 1.5 mm; the pulse frequency f = 15 Hz): **a** cathode- work piece; **b** anode—tool electrode [53]

establish that a considerable percentage of C, N, O, Fe is attested in them (Figs. 2.16, 2.17, 2.18, 2.19, 2.20 and 2.21, Table 2.1). Among the detected elements, Fe and C are presented in the base material of the work piece, but O and N are implanted into the work piece material from the work environment (air). At the same time, we can say that the result of the surface oxidation processing via PEDM does not show any significant deterioration of the machined surface. Only sub-micrometer asperities are attested on it (Fig. 2.22b). The formation of iron oxides and hydro-oxides in amorphous state was previously attested [32–36, 42, 46, 53–56]. This will be confirmed by corrosion investigations.

The volt-ampere characteristics were plotted for samples with oxidized surfaces and for those with non-oxidized surfaces based on the investigations of resistance to corrosion (Fig. 2.26).

If we compare the results presented in Fig. 2.26 we can see that the potential of anodic dissolution of the sample material has increased to positive values as compared to the raw sample. With the increase of the voltage applied to the electrodes, the anodic dissolution process of the investigated samples changes. For instance, for a voltage U = 2 V the current in the circuit for the raw piece is 300 mA, while for the sample with oxide films it is about twice lower—161 mA (Fig. 2.27).

Figure 2.27 shows that the volt-ampere characteristics for raw and processed sample in the range of 1.5–2.5 V are practically similar, which points to the presence of an isolating film on the surface of the processed sample, that enhances its active resistance.

Taking into account the previous results [43, 44, 53] aimed at the measurement of surface active resistance, we might conclude that oxide layers formed on the surfaces of samples do not have a total continuity. Due to this, their anodic dissolution is more intense than it is expected.

In order to determine the corrosion speed, 5 pairs of raw and processed samples were investigated under the same anodic dissolution (3 % NaCl aqueous solution at room temperature for steel surfaces, and 30 % H_2SO_4 at the temperature of 80° for

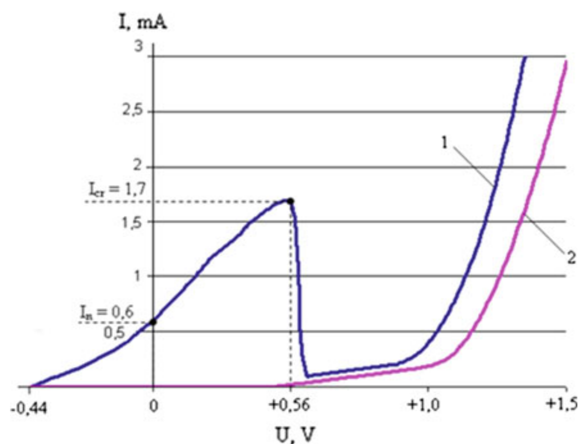

Fig. 2.26 Volt-ampere characteristics of the corrosion process of samples made of steel 45 in electrolyte (3 % NaCl aqueous solution): *1* unprocessed surface; *2* surface with oxide films [53]

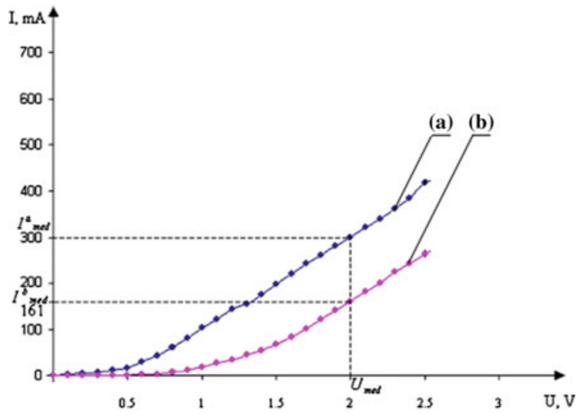

Fig. 2.27 Volt-ampere characteristic of the electro-chemical corrosion process: (*a*) unprocessed surface, (*b*) surface with oxide films [53]

titanium alloy surfaces). The results of measurements are presented in Tables 2.4, 2.5, 2.6 and 2.7.

If we analyze the obtained results, we can conclude that for the processed steel samples the corrosion speed is about twice lower than for unprocessed samples, and it is by about 100 times lower for titanium surfaces.

If we take into account the fact that the natural corrosion potential is tens and hundreds times smaller than in the case of the performed tests, then we can suppose that the efficiency of oxide film application will significantly increase. For instance, if we return to Fig. 2.26, then we can affirm that for applied voltages within 0 and 0.4 V there is no current in the circuit formed by the work piece. Therefore, the

Table 2.4 Speed of anodic dissolution of unprocessed surfaces of samples made of steel 45 [53]

No.	Initial mass of the sample m_i (g)	Final mass of the sample m_f (g)	Δm (g)	Speed of corrosion K (g/m^2 h)
1	12.8441	12.8237	−0.0204	812.10
2	13.1458	13.1254	−0.0204	812.10
3	13.3225	13.3025	−0.0200	796.17
4	14.0610	14.0417	−0.0193	768.31
5	13.0248	13.0031	−0.0217	863.85

Table 2.5 Speed of anodic dissolution of oxidized surfaces of samples made of steel 45 [53]

No.	Initial mass of the sample m_i (g)	Final mass of the sample m_f (g)	Δm (g)	Speed of corrosion K (g/m^2 h)
1	12.8569	12.8441	−0.0128	509.55
2	13.1605	13.1458	−0.0147	585.19
3	13.3338	13.3225	−0.0113	449.84
4	14.0717	14.0610	−0.0107	425.95
5	13.0366	13.0248	−0.0118	469.74

Table 2.6 Speed of anodic dissolution of unprocessed surfaces of samples made of titanium alloy BT8 [53]

No.	Initial mass of the sample m_i (g)	Final mass of the sample m_f (g)	Δm (g)	Speed of corrosion K (g/m^2 h)
1	1.6803	1.6700	−0.0103	103
2	1.6700	1.6599	−0.0101	101
3	1.6599	1.6466	−0.0133	133
4	1.6466	1.6324	−0.0142	140
5	1.6324	1.6198	−0.0126	126

Table 2.7 Speed of anodic dissolution of oxidized surfaces of samples made of titanium alloy BT8 [53]

No.	Initial mass of the sample m_i (g)	Final mass of the sample m_f (g)	Δm (g)	Speed of corrosion K (g/m^2 h)
1	1.9582	1.9578	−0.0004	4
2	1.6615	1.6613	−0.0002	2
3	1.8829	1.8828	−0.0001	1
4	1.8325	1.8324	−0.0001	1
5	1.7648	1.7647	−0.0001	1

corrosion speed is zero. However, a considerable current is attested in the same conditions for unprocessed pieces. Therefore, the speed of corrosion is also significant. Finally, we can admit that the application of oxide films on metal surfaces via PEDM is beneficial for enhancing their active resistance, as well as for anticorrosion protection.

2.7 Conclusions

1. The physical model of the plasma channel interaction with the work piece surface via "cold" electrode spots explains the nanometer diffusion processes in the processed surface strata and can provide a substantial scientific contribution to developing new technologies for the modification of chemical composition of surfaces with their amorphization at nanometer depths;
2. The abnormal diffusion of oxygen in the metal piece surfaces accompanied by the oxide and hydroxide phase formation is due to ozone synthesis in the PEDM plasma, and also to high intensity of the electric field in the anodic and cathodic zones of 10^6–10^8 V/m, high temperatures of 10^4K in the electrode spots, and their short lifetime;
3. During surface machining of samples made of alloys of iron, copper, aluminum and titanium by applying PEDM under ordinary conditions, the surface oxidation is more effective when the workpiece is connected in the discharge circuit

as cathode; this is due to lower voltage drops in this situation and less intensive processes of vaporization of machined surfaces in this technological variant;

4. The layer thickness obtained at surface oxidation via PEDM for samples made of metal alloys depends on the physico-mechanical properties of the base material, on the energy density released in the gap, on the duration of PEDM, and on the number of discharges per unit of the machined surface;
5. The nanometer thickness of the oxide and hydroxide films places this process among nanotechnologies, ensuring simplicity of technology realization and possibilities of processing various materials from the class of metals and semiconductors;
6. The developed technology ensures the increase of the active surface resistance of pieces made of metal alloys by about 10^7 times, the increase of the corrosion potential to positive values (for iron alloys from −0.44 to +0.4 V; for titanium alloys from −0.56 to +0.22 V) and the decrease of the corrosion speed in the chemically aggressive solutions (for iron alloys by about 2 times and for titanium alloys by about 10^2 times).

Acknowledgments **The authors wish to thank**: The National Center of Materials Study and Testing, Technical University of Moldova, Chisinau, Republic of Moldova; CARPATH Center for Applied Research in Physics and Advanced Technologies, A.I. Cuza University of Iasi, Romania; The National Institute for Research and Development in Microtechnologies IMT, Bucharest, Romania; Nano Science and Surface Research, Christian-Albrechts University from Kiel, Germany; Center of Surface Study and Analysis from the Department of Physics, University of Aveiro, Portugal and Professor Petru Stoicev from the Technical University of Moldova—for their assistance in the SEM and EDX research, for logistical support and for fruitful discussions of the work.

References

1. E. Monaico, I. Tiginyanu, Nanowires and nanotubes: technologies and perspectives for their use. Phys. Mod. Technol. **10**(1–2), 4–12 (2012)
2. M. Enachi, O. Lupan, T. Braniste, A. Sarua, L. Chow, Y.K. Mishra, D. Gedamu, R. Adelung, I. Tiginyanu, Integration of individual TiO_2 nanotubes in the chip: nanodevice for hydrogen sensing. Phys. Status Solidi: Rapid Res. Lett. **9**(3), 171–174 (2015)
3. M. Enachi, O. Lupan, T. Braniste, A. Sarua, R. Adelung, I. Tiginyanu, Hydrogen nanosensor based on a single nanotube of TiO_2, in *International Conference on Microelectronics and Computer Science*, October 22–25 Oct 2014, Chisinau, Moldova (2014)
4. O. Lupan, T. Pauporte, I.M. Tiginyanu, V.V. Ursaki, V. Sontea, L.K. Ono, B.R. Cuenya, L. Chow, Comparative study of hydrothermal treatment and thermal annealing effects on the properties of electrodeposited micro-columnar ZnO thin films. Thin Solid Films **519**(22), 7738–7749 (2011)
5. A.I. Hochbaum, R. Chen, R.D. Delgado, W. Liang, E.C. Garnett, M. Najarian, A. Majumdar, P. Yang, Enhanced thermoelectric performance of rough silicon nanowires. Nature **451**, 163–167 (2008)
6. A.I. Boukai et al., Silicon nanowires as efficient thermoelectric materials. Nature **451**, 168–171 (2008)

7. P. Topala, Research on obtaining deposit layers of metal powder by applying pulsed electrical discharge machining. Summary of PhD thesis, Bucharest, University Politehnica (1993), 32 pp
8. V.E. Bulat, M.H. Esterliv, Cleaning metal articles from scale, oxided pellicle and soiling by electro arc discharge in vacuum. FHOM **3**, 49–53 (1987)
9. B.A. Artamonov et al., *Electro-physical and electrochemical methods of material processing*, vol. 1 (Vyssaia Shkola, Moscow, 1983)
10. P.S. Gordienko et al., RF Patent No. 2283901. Technique of electrolytic oxidation of valvular metals and their alloys. Publ. 20.09.2006. Bulletin of inventions No. 28 (2006)
11. Sh Ramanathan, *Thin Film Metal-Oxides. Fundamentals and Applications in Electronics and Energy* (Springer, New York, 2010). 337 p
12. J. Wu, J. Cao, W.-Q. Han, et al., *Functional Metal Oxide Nanostructures* (Springer, New York, 2012), 368 pp
13. Ph Avoris et al., AFM-tip-induced and current-induced local oxidation of silicon and metals. Appl. Phys. A **66**, 659–667 (1998)
14. IYa. Mittova, Ya., Pshestanchik V. R. The chemistry of processes which create dielectric layers with functional group substituents on semiconductors by impurity thermo-oxidation. Russ. Chem. Rev. **60**(9), 967–979 (1991)
15. K. Kushida-Abdelgafar et al., Integr. Ferroelectr. **13**, 113 (1997)
16. K. Shoji, et al., *Symposium on VLSI Technology Digest of Technical Papers* (Widerkehr and Associates, Gaithersburg, 1996), p. 28
17. K. Kushida-Abdelgafar et al., Mechanism of TiN barrier-metal oxidation in a ferroelectric random access memory. J. Mater. Res. **13**(11), 3265–3269 (1998)
18. B. Schmidt, K. Wetzig, *Ion Beams in Materials Processing and Analysis* (Springer, 2013), 418 pp
19. L. Slatineanu, *Non-Conventional Technologies in Machine Building* (Tehnica Info, Chisinau, 2000), p. 252
20. S.S. Ushakov, et al., *Micro-Arc Oxidation of Pipes and Shipbuilding Components Made of Titanium Alloys* (Manual RD5. AEIS. 2459-2006. Saint-Petersburg: FSUE CRI KM "Prometey", 2006), 242 pp
21. I.I. Chernenko, L.A. Snejko, I.I. Papanova, Getting coating by means of anode-spark electrolysis, L. Himia (1991), 128 pp
22. V.V. Nemoshkalenco, et al., Peculiarities of surface strata formation at spark discharge. Kiev: Metal-Phys. **12**(3), 132–133 (1990)
23. P. Levitz, G. Calas, D. Bonin, Etude par spectroscopie Mösbauer du fer (III) dans verres silicates multicomposants d'intérêt géologique. Phys. Appl. **15**, 1169–1173 (1980)
24. P.S. Gordienko et al., Formation of coatings on valvular metals and alloys in electrolytes with capacitive energy control at micro-arcwise oxidation. Prot. Met **42**(5), 500–505 (2006)
25. P. Topala, P. Stoicev, Technologies of conductible material processing by applying pulsed electrical discharge machining. Chisinau: Edition Tehnica-Info (2008), 265 pp
26. I.A. Chapligina (ed.), *Nano technologies*. (Tehnosphere, Moscow, 2013)
27. J. Martin, *The Concise Encyclopedia of Materials Processing* (Elsevier, New York, 2009), 854 pp
28. P. Topala, *Condidions of Thermic and Thermo-Chemical Superficial Treatment Innards with the Adhibition of Electric Discharge in Impulses. Nonconventional Technologies Review* (Editura BREN, Bucureşti, 2005), pp. 27–30
29. P. Topala, Research on obtaining deposit layers of metal powder by applying pulsed electrical discharge machining. PhD thesis, Bucharest, University Politehnica (1993), 161 pp
30. I.I. Safronov, P.A. Topala, A.S. Gorbunov, *Electro-Erosive Processes on Electrodes and the Microstructural and Phase Composition of the Alloy Stratum* (Tehnica-Info, Chisinau, 2009)
31. P.V. Gavrilo,v et al., Microarc oxidation of the working surface of technologically equipped elements made of aluminium alloys. Technologies of repairing, restoration and consolidation of machine pieces, mechanisms, equipment, instruments and technological equipping. Part 2, in *Materials of 9th International Practical Conference*, 10–13 April 2007. Polytechnical University Publishing House, (2007), pp. 77–79

32. P. Topala, A. Ojegov, *Formation of Oxide Thin Pellicles by Means of Electric Discharges in Pulse*. Annals of the Oradea University. Fascicle of Management and Technological Engineering, vol. VII (XVII) (CD-ROM Edition. Editura Universităţii din Oradea, România, 2008), pp. 1824–1829. ISSN 1583-0691, CNCSIS Clasa B+
33. P. Topala, A. Ojegov, *Formation of oxide Thin Pellicles by Means of Electric Discharges in Pulse* (Buletinul Institutului Politehnic Iaşi. Tomul LIV (LVIII), 2008), pp. 121–128
34. P. Topala, A. Ojegov, *Formation of Oxide Thin Pellicles by Means of Electric Discharges in Pulse*. Annals of Oradea University. Fascicle of Management and Technological engineering, vol. VII (XVII) (2008), p. 309
35. P. Topala, A. Ojegov, Protection the *Interior Cylindrical Surfaces of Industrial Pipes with Oxide Films Obtained by Applying Pulsed Electrical Discharge Machining*, vol. 21 (State Agrarian University from Moldova. Scientific Papers, Chisinau, 2008), pp. 171–174
36. P. Topala, P. Stoicev, A. Ojegov, Experimental investigations on microoxidation of surfaces by means of applying electrical discharges in impulse under ordinary conditions, in *Creativity Management International Conference—New Face of TCMR*. 21–23th May 2009 (Culegeri de lucrări ştiinţifice. Ediţia XIII-a. Editura U.T.M., Chişinău, 2009), pp. 172–175
37. L.P. Kornienco et al., Electro-chemical and corrosive behaviour of titanium with electro-spark coating Pd и Cr-Pd. Metal Protect. Moscow **29**(3), 351–358 (1991)
38. P. Topala et al., The influence of tempering on the corrosive behaviour of titanium with electro-spark coating. Metal Protect. Moscow **26**(3), 433–437 (1990)
39. S. Gutt, G. Gutt, *Chemistry of Electro-technical Materials*. Course. University Ştefan cel Mare, Suceava. Romania, (1992), 304 pp
40. M.K. Mitskevich et al., *Electro-erosion Processing of Metals* (Science and Technics, Minsk, 1988), p. 216
41. P. Topala, *The Energy Distribution in the Gap at the Gap Tehnological Appling of the Electrical Discharges in Impulses*. Nonconventional Tehnologies Review, vol. 1. (Editura PIM, Iaşi, 2007), pp. 129–132
42. V. Besliu, P. Topala, A. Ojegov, Predicting the thickness of the surface layer subjected to applying EDI using modeling through the method of neuronal model. Machine building and tehno-sphere of XXI century, in *Materials of XVIth International Scientifico-Technical Conference*, Sebastopol, September 14–19 2009, Donetsk: DonNTU, vol. 4 (2009), pp. 30–34
43. P. Topala, P. Stoicev, A. Ojegov, N. Pinzaru, E. Monaico, Analysis of processes occurring on the tool and piece electrode surface during the formation of by applying electrical discharges in impulse, in *ModTech 2010*, 20–22 May 2010. Slănic-Moldova, România, (2010), pp. 631–634
44. P. Topala, P. Stoicev, A. Ojegov, N. Pinzaru, Effects of abnormal dissolving of oxygen in metals under the influence of electrical discharges in impulse plasma. Int. J. Mod. Manuf. Technol. **2**, 95–102 (2010). ISSN 2067-3604
45. A. Ojegov, *The Action Of Electrical Discharges in Impulse Plasma on Structure and Properties of Steel 45 Surface Strata*. Engineering Meridian, vol. 4. Edition U.T.M. (2010), pp. 44–47
46. P.A. Topala, P. Vizureanu, A.V. Ojegov, P.N. Stoichev, M.K. Perju, Some results of metal surface microoxidation by means of electropulsed discharges, in Materials of 13th Scientifico-Practical Conference Technologies of Repairing, Restoration and Consolidation of Machine Pieces, Mechanisms, Equipment, Instruments and Technological Equipping, St. Petersburg, 12–15 April 2011, pp. 1087–1094
47. C.C. Kao, J.A. Shih, Sub-nanosecond monitoring of micro-hole electrical discharge machining pulses and modeling of discharge ringing. Int. J. Mach. Tools Manuf. **46**, 1996–2008 (2006)
48. P. Pecas, E. Henriques, Electrical discharge machining using simple and powder-mixed dielectric: the effect of the electrode area in the surface and topography. J. Mater. Process. Technol., 1–9 (2007)
49. Y. Li et al., Micro electro discharge machine with an inchworm type of micro feed mechanism. J. Int. Soc. Precis. Eng. Nanotechnol. **26**, 7–14 (2002)

50. Y. Uno et al., A new polishing method of metal mold with large-area electron beam irradiation. J. Mater. Process. Technol. **187–188**, 77–80 (2007)
51. A. Hirbu, P. Topala, A. Ojegov, Auto-ionization laboratory plasma, in *ModTech International Conference "Modern Technologies in Industrial Engineering*, Book of abstracts, June 27–29, 2013, Sinaia, Romania (2013), p. 359
52. A. Hirbu, P. Topala, A. Ojegov, Laboratory plasma formation without preventive ionisation of the active medium, in *The 17th International Salon of Research and Technological Transfer* "INVENTICA 2013", (2013), pp. 721–722
53. A. Ojegov, Obtaining thin oxide films on metal surfaces of iron, copper, aluminum and titanium alloys, by applying pulsed electrical discharge machining. Summary of PhD thesis in technique. Edition "Tehnica UTM", Chisinau (2014), 32 pp
54. P. Topala, A. Hirbu, A. Ojegov, New directions in the practical application of electro erosion, in *Annual Session of Scientific Papers IMT* Oradea—2011, Oradea, Felix Spa, May 26–28th, 2011, sect. Tehnologia Construcţiei de Maşini. Annals of the Oradea University. Fascicle of Management and Technological Engineering (2011)
55. P. Topala, A. Hirbu, A. Ojegov, *New Directions in the Practical Application of Electro Erosion*. Nonconventional Technologies Review, vol. 1 (2011), pp. 49–56
56. P. Topala, V. Besliu, V. Rusnac, A. Ojegov, N. Pinzaru, Structural modification of the chemical composition and microgeometry of the piece surfaces by applying pulsed electrical discharge machining. *Physics and Technics: Processes, Models, Experiments*, vol. I. (Balti University Press, Balti, 2011), pp. 36–42
57. P. Topala, V. Rusnac, V. Beşliu, A. Ojegov, N. Pînzaru, Physical and chemical effects of EDI processing. Int. J. Eng. Technol. **2**(1), 6 http://www.i-jet.eu/journal_ijet/c_p_ijet1112.pdf
58. A. Ojegov, The influence of pulsed electrical discharge machining parameters on the intensity of oxide films formation on steel 45 surface. Phys. Mod. Technol. **10**(3–4), 18–24 (2012)
59. P. Topala, A. Ojegov, About chemical and phase content of nano-pellicles formed on metal surfaces by applying electrical discharges in impulse, in *Proceedings of International Scientific Conference* "*10 years of Nanotehnology Development in the Republic of Moldova*", 22—23 Oct 2012, Balti, (2012), p. 21
60. P. Topala, V. Besliu, P. Stoicev, A. Ojegov, Application of electric discharges in impulse in micro and nano-technology, in *Proceedings of the 16th International Conference Modern Technologies, Quality and Innovation—New face of TMCR,* vol. II, 24–26 May, 2012, Sinaia, Romania, (2012), pp. 969–972
61. P. Topala, D. Luca, A. Ojegov, P. Stoicev, N. Pinzaru, Results on metal surface nano-oxidation by electrical discharges in impulse, in *ICCCI 2012. The Fourth International Conference on The Characterization and Control of Interfaces for High Quality Advanced Materials. Kurashiki, Japan*, 2–5 Sept 2012. (2012), p. 85
62. P. Topala, A. Ojegov, V. Besliu, Oxygen diffusion during the formation of thin pellicles by applying EDI, in *ModTech International Conference "Modern Technologies in Industrial Engineering"*, Book of abstracts, June 27–29, 2013, Sinaia, Romania, (2013), 356 pp
63. M. Yang, et al., Scanned probe oxidation on an octadecyl-terminated silicon (111) surface with an atomic force microscope: kinetic investigation in line patterning. Nanotechnology **17**, 330–337 (2006)
64. Ph Avoris et al., Atomic force microscope tip-induced local oxidation of silicon: kinetics, mechanism, and nanofabrication. Appl. Phys. Lett. **71**(2), 285–287 (1997)
65. W. Mönch, *Semiconductor Surfaces and Interfaces* Springer (Ser. Surf. Sci.), vol. 26, Chap. 17, (1993), 276 pp
66. Y. Nishioka, et al., *Proceedings of 1995 International Electron Devise Meeting* (1995), p. 903
67. A.V. Ancudinov, et al., Nano-relief of the oxidated surface of the railings of alternated heterostrata $Ga_{0.7}Al_{0.3}As$ и GaAs. Phys Technol. Semicond. **33**(5), 594–597 (1999)
68. S.A. Kovaleva, et al., Morphology and structure of silicon oxide anodic pellicles obtained by means of probe oxidation using the atomic power microscope. Nano Technologies Popnano RU/HIOKR/ Investigations (2008)

69. D.V. Sokolov, Mechanisms of n-In GaAs nano-oxidation with the use of atomic force microscope. JTPh **72**(1), 60–65 (2002)
70. P. Topala, A. Ojegov, V. Besliu, A. Hirbu, N. Pinzaru, MD Patent No. 4325. Multi-electrode tool for surface pulsed electrical discharge machining. Natalia. Publ. 28 Feb 2015

Chapter 3
Graphite Films Deposited on Metal Surface by Pulsed Electrical Discharge Machining

Pavel Topala, Vitalie Besliu and Laurentiu Marin

Abstract The paper presents the results of experimental research on the physics of natural graphite film formation, the establishment of chemical composition and functional properties of the graphite films, formed on metal surfaces, as a result of the action of plasma in the air environment, at a normal pressure, under the pulsed electrical discharge (PED) conditions. The continuity of the formed film, the thickness of the layer, the diffusion depth, the micro-hardness of the surface layer, the potential of corrosion, and the wear resistance are investigated. It is shown that the use of electrode tool made of pyrolytic graphite improves the mechanical properties at the microscopic level, such as tensile strength. The behaviour of films in an exceptional manner with reference to solubility in different environments is highlighted and the hypothesis that they could contain space structures such as fullerenes and carbon nanotubes are emphasized. Testing studies, using three processing regimes, have proved that the maximum breaking force of samples made from graphite-coated steel-3 increases essentially as compared to the untreated sample. It is demonstrated that the graphite films made by PED method have similar characteristics to those of fullerene or carbon nanotubes.

3.1 Introduction

The formation of graphite films at micrometric and nanometric scale on the surfaces of alloys-made parts causes their diffusion in the surface layer accompanied by the formation of high hardness carbides, and, as a result, the wear resistance of this layer increases [1–5].

P. Topala (✉) · V. Besliu
Alecu Russo Balti State University, Balti, Moldova
e-mail: pavel.topala@gmail.com

L. Marin
National Institute for Research & Development in Chemistry and Petrochemistry, Bucharest, Romania

© Springer International Publishing Switzerland 2016

I. Tiginyanu et al. (eds.), *Nanostructures and Thin Films for Multifunctional Applications*, NanoScience and Technology,
DOI 10.1007/978-3-319-30198-3_3

The process of formation of graphite films, in all cases, leads to a decrease in surface roughness of the processed surface. According to the results obtained by the authors [4, 6–9], the application of films on the surfaces of the components that work in cinematic couples, leads to a decrease of the friction coefficient of at least 3 times.

Experimental tests on the adherence effect of threaded joints have shown that this effect, caused by the mutual diffusion of constituent materials of the joint parts, is prevented by the presence of graphite films. Even if the couple is maintained in furnaces at temperatures framed within 400–800 °C it was demonstrated that the adherence effect between couple parts, made of construction steel, does not take place [4].

The formation of films on the internal surfaces of pipes allows eliminating the adherence effect for paraffin plugs, which represents a real problem for petroleum transporting pipelines. Experimental research and industrial tests are aimed at demonstrating that the deposits are formed more efficiently if the processed piece is included in the discharge contour of the current pulse generator used as anode. The formed films can reach up to 7 μm in thickness, increasing, at least twice, the operating durability of the casting molds components, due to their solid lubricant and anti-refractory properties [5, 10, 11].

From the above-mentioned facts, it results that developing an efficient technology of graphite deposit formation on active piece surfaces of machinery manufacturing industry would allow a successful solution for a number of issues such as: ensuring surfaces refractory properties, obtaining wear resistant surfaces, reducing the friction coefficient of the part surfaces that function in cinematic couples, forming buffer films at the interface between two surfaces of a couple, partial or total elimination of the adherence effect, etc.

3.2 Technology of Graphite Film Forming

Experimental tests of forming graphite deposits on metal surfaces were performed in normal working environment—air. To achieve this technology a special installation was applied and it was further thoroughly described as a construction and as an operating system in the paper [6]. To achieve this, electrical discharges in impulse were applied, which interacted with the electrodes surfaces in electrode patches maintenance regime “cold” in order to avoid melting, vaporization and removal of material from them. Bars, made of technical graphite, were used as electrode tools, having a cylindrical form and the cross-sectional area of 5–7 mm^2.

In order to maximally approach the attained results to the producing firm’s interests, as pieces were chosen: screw nuts and bolts with metric fillet M16, plungers applied to pouring the pack bottles, component-pieces of glass molding forms, segments of pipes, plane boards made of different materials with the size of 20 × 20 × 5 mm, etc. These pieces were connected in the contour discharge current

impulse generator as anodes. Their made-of materials were relatively diverse, including the group of steels (Steel 45 and Steel 37), alloyed cast iron and bronze.

With the aim of forming graphite deposits, without melting and vaporising the treated surface of the work piece serving as the energy source, the current impulse generator is applied, whose design and operating principle are described in work [6]. This ensures the formation of current impulses with duration ranging between 10^{-6}–10^{-7} s, which corresponds to life duration of "cold" electrode spots. Generator offers the formation of current impulses with the following parameters: gap released energy W_S = 0–4,8 J, accumulated energy on the capacitor W_c = 0–12 J, at the voltage applied to the charging capacitor U_c = 0–250 V, for its capacity comprised within C = 100–600 μF with 100 μF pace. This ensures the priming of electrical discharges in impulse at the gap values of S = 0,01–2,5 mm, with the discharge frequency f = 0–50 Hz.

The morphology of the treated surfaces was studied by means of SEM method, and the EDX and XPS phase methods were used to study the its chemical composition.

The adherence of the formed film to the treated surface was made by attempts of shearing on a HECKERT FPZ 100 dynamometer type. To identify the emerged changes in adhesion properties, as a result of applying graphite films, a comparative measurement was performed, related to the detachment forces of the assemblies, made with the help of a strong adhesive−polyurethane−between a set of samples treated with graphite and non-treated samples. A set of 3 graphite-treated samples and a set of 3 non-treated samples are glued; the treated samples with graphite film at the end, as it was shown in the paper [3]. After bonding, the samples are overlapped on top of an area of 25 × 25 mm, and afterwards, when the adhesive hardens, they are subjected to traction.

To measure the wear-grade of graphite films deposited on the plungers of the molding glass the УИМ-21 universal microscope was used, which allows the measurement with an error of 1 μm as described in the paper [8]. The component pieces of molding glass were subjected to wear process in glassy mass at 44625 cycles (85 h) for sample 19 and 39900 cycles (75 h) for sample 23. The speed of cycles was v = 8.75 cycles/min, the temperature of the glass drop constituted 1129 ° C, the glass for food packaging was used.

In order to determine the anti-socket properties, 6 pairs of pin joints were selected, three pairs of which deposited graphite films on the bolt and the other three were kept intact. They jointed under the action of one and the same torque. Thus, there were established 3pairs for attempts; each of these had 2 couples with and without the presence of graphite film. The studied pairs were placed in the NaCl solution with a concentration of 3 % for 24 h, after which they were inserted into the oven at temperature of 800 °C, where they were kept for 10 h, and then the torque at the termination of the couplings was measured, according to [4, 7].

The concept of technology is developed. The experimental investigations and technology installation model are executed and performed. A patent was obtained. The practical realization of the proposed technology can be demonstrated.

3.3 Physical Model of Graphite Film Formation by Applying Pulsed Electrical Discharge

The formation efficiency of the graphite deposits on the processed surface is also determined by the fact that, while subduing the plasma to electric discharges in impulse according to [6], the temperature in the plasma jet reaches values up to 10^4 K, which is more than sufficient for graphite vaporization and its polar transfer to the piece surface.

The physical model, offered below, refers to the transfer of electrode tool material made of graphite from the processed piece surface, through impulse electrical discharges under a sub-excitement regime. It is worth mentioning that the electro-erosion of the graphite is a special one, with regard to metallic and semi-conductor materials.

The concept of physical model is based on the analysis of experimental results, previously obtained by the authors [11, 12], where, it was established that, a more evident erosion of the graphite occurs when connecting the electrode to the discharge circuit of electric impulse generator, functioning as cathode.

While concerning the general case of processing electrically conductive materials in work [12] it was established that the amount of material collected from the surface of the electrode subdued to electric discharges in impulse can be determined by the following relationship:

$$m = k\rho U_e \int_0^{\tau} i(t)dt \tag{3.1}$$

where: k—is the proportionality coefficient; ρ—is the density of the electrode material; U_e —is the voltage drop at the electrode surface; i—is the actual value of the electric discharge in impulse; τ—is the duration of the electric discharge in impulse.

For the same formation conditions of the deposit and for the thermal or thermochemical treatment, the following relation can be written, in accordance with the work [11, 12]:

$$\frac{m_a}{m_c} = \frac{U_a}{U_c} \tag{3.2}$$

where: m_a and m_c are the mass of collected material from the anode and cathode surfaces correspondingly, but U_a and U_c are voltage drops at the anode and cathode surfaces. If we consider the fact that the electrode erosion from the graphite is higher when connecting it as a cathode, then it follows that the voltage drop at its surface is higher:

$$U_c > U_a \tag{3.3}$$

With the increasing of the voltage drop at the electrode-cathode surface, the amount of electric power, released from its surface, increases as well. It is equal to:

$$W_c = U_c \int i(t)dt \tag{3.4}$$

In accordance with the theory of electro-erosion, the material collected from the surface of the anode constitutes positive ions, while that from the cathode constitutes emitted electrons. These judgments are not valid for graphite-made electrode, used as a cathode. Considering that the process of electro-erosion is, actually, an electrochemical one, arising at high temperatures, we can assume that recombining and dissociative processes occur at the anode-electrode surface, at the electrode-cathode surface and that of the plasma channel.

Summarizing the above mentioned facts in work [8, 13] and considering the distributed processes, we suggest the following physical model of the formation of graphite deposits under the action of the plasma subdued to electric discharges in impulse: in the initial phase (a) (see Fig. 3.1) the priming of electrical discharge occurs according to Townsend mechanism and to the formation of conductive channel; in phase (b) there take place a whole range of dissociation of atmospheric components in separate atoms, ions of oxygen, hydrogen and nitrogen, and, definitely, the electrons from the previous phase are present in the plasma; in phase (c) they interact one with each other and with electrode surfaces, producing surface activation and causing their erosion; both in phase (c) and in phase (d) there are many series of intensive oxidation reactions of the surface of the graphite electrode, as well as there is a dissociation of the product in oxygen and carbon, with a further transfer on the treated surface, both under the action of the electric field gap and under the action of the plasma component atoms (e); the process ends with film

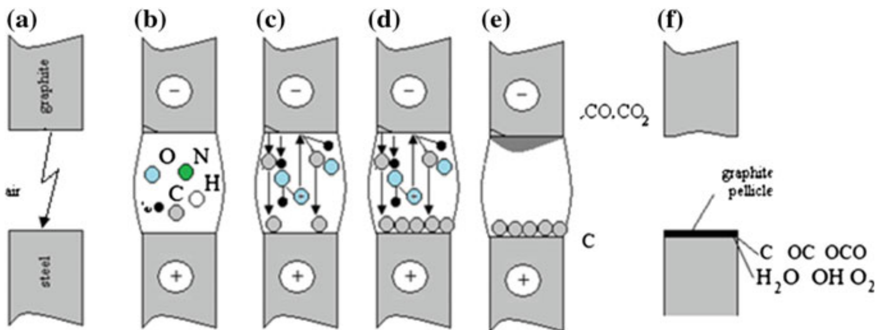

Fig. 3.1 Physical model of forming the graphite film on the piece surface under the influence of electric discharges in impulse

synthesis, which contains carbon of various crystallization forms and phases formed from component elements of plasmagene gas.

Proceeding from concrete conditions (air working environment, at the atmospheric pressure), we might assume the following.

Due to the fact that the oxygen, in the plasma channel, interacts more intensively with the cathode-electrode surface, the oxidation reactions take place, accompanied by the release of carbon oxide CO, complemented by additional discharge of heat Q on the cathode surface and accompanied probably by the formation of carbon dioxide CO_2, according to the reactions:

$$\begin{aligned} C + O &\rightarrow CO + Q \\ C + 2O &\rightarrow CO_2 \end{aligned} \tag{3.5}$$

As a result of these phenomena, occurring on the cathode surface, its released energy increases respectively, together with the energy released from the intensive oxidation. In addition, the summary energy from its surface may be expressed by means of the relationship:

$$W_c = U_c \int i(t)dt + \mathrm{W_Q} \tag{3.6}$$

As a confirmation of the processes of graphite oxidation at the cathode surface can serve the obtained results by work authors [14] in the process of formation of oxides film on metal parts surfaces, with the application of electric discharges in impulse. Carbon oxide in the plasma of electric discharges in impulse is negatively electrified through capturing an electron and it is made to move towards the surface of the piece-anode.

Due to the fact that the released energy at the anode surface is greater than the one in the gap, the gas molecule dissociates into carbon and oxygen ions. Those from the oxygen return to plasma channel and perform again the surface oxidation of the cathode; in addition, the carbon ions recombine on the anode surface, forming the graphite film. Further, the graphite film formed on the work-piece surface, under the action of the released heat at the interface with the plasma channel, is subdued to the diffusion processes from the work-piece surface, with the formation of the hardened layer. The erosion of a quantity of graphite is not excluded from this surface, in the last phase.

Meanwhile, the plasma processes occurring in the air are accompanied by the dissociation of molecules of oxygen, hydrogen and nitrogen, forming ions and free electrons. The ions of the work environment elements present heavy accelerated particles in the electric field gap. They serve as spraying particles of the cathode surface, causing the scattering of its surface, similar to the process of sputtering in radio frequency [15–18]. In this situation, some of the listed items could, in some way, interact with the graphite deposit from the treated surface and alter both, its composition and structure, and, as a result, they can influence the functional properties.

3.4 Scanning Electron Microscopy Analysis of the Graphite Films

Many scanning electron microscopy (SEM) researches were done to unravel the phenomena occurring at the surface of the processed piece and at the surface of the electrode tool.

Thus, in Figs. 3.2 and 3.3, the morphology, as well as the chemical composition of the deposition electrode tool is presented. We can observe the mosaic block surface of the electrode-tool, magnified on micrometric scale and applied for deposing accomplishment, its chemical composition consisting of 100 % carbon.

A significant line of modifications of the surface morphology occur as the result of electric discharges in impulse under plasma action and bombarding ions of plasma generate gas. The globular formations with nanometric size are confirmed on this surface (Fig. 3.2). The globular formations, observed on the electrode tool

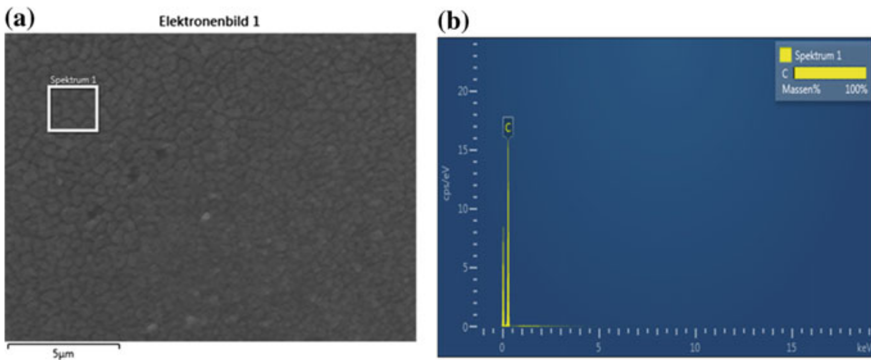

Fig. 3.2 General view of electrode tool surface (**a**) and its chemical composition (**b**)

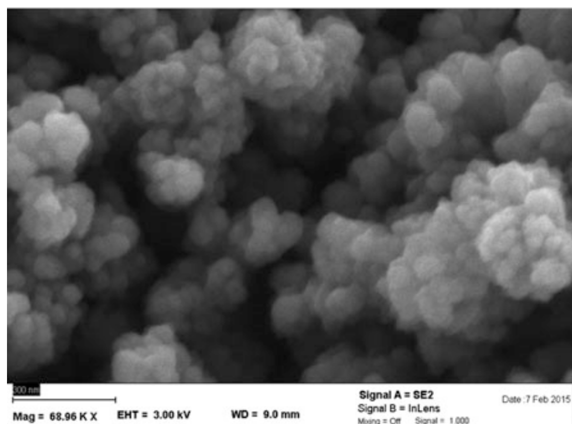

Fig. 3.3 Surface morphology of cathode pyrolytic graphite made on electrode tool after the plasma PED (electrical discharge in impulse) influence

surface, may be explained as the result of two concurrent phenomena, have simultaneous manifestation: heating, melting and graphite recrystallization under the influence of the plasma energy, on one side, and ions bombarding generating plasmagene gas, on the other side.

At the SEM of pyrolytic graphite, investigated on the electrode tool, show the formation of macro formations (Fig. 3.2) on their surface, assembled by the discovered nanostructures (Fig. 3.3). This leads to the conclusion that a chain of specific erosion phenomena occurs.

These phenomena are similar to cathode disintegration with the dissipation of the atoms and ions (nitrogen, oxygen, hydrogen and electrons, of course) of the working environment.

The difference between these phenomena and the cathode dissipations consists in the fact that additional oxidation reactions on the pyrolytic graphite from the electrode tool surface occur, and they develop into additional energy sources. All these above mentioned facts, serve as arguments for explaining a more substantial erosion of pyrolytic graphite from the electrode tool, used as cathode in the discharging impulse generator circuit.

According to the physical frame, described in paragraph II, as well as the conditioning technology, presented in paragraph III, the graphite film deposition, transfer and diffusion in the superficial layer were accomplished on the working samples surfaces [19–21].

The experimental researchers, carried out on graphite film, formed on the treated samples surfaces, have demonstrated that the depth of the graphite layer has a micrometric size. Excluding initial components of the treated materials, a large part of carbon (more than 90 %) in atomic percentage is detected (Fig. 3.4).

From the EDX analysis (Fig. 3.4) the presence of iron was attested, that in conditions of graphite deposition formation serves as catalyser for 3D structures (of fullerene or nanotube types) synthesis.

The carbon displacement on the working piece surface crystallizes in characteristic structures and a deep diffusion of the carbon in the superficial layer is established.

The impregnated carbon in the depth of the metallic structure cannot exist in a free state. It ensures chemical links in the metallic structure, forming metallic carbides and, furthermore, separating graphite structures.

Analysing the submitted facts in Fig. 3.4 we can notice in what way a part of carbon is transferred to the piece surface and is impregnated up to a micrometer depth. This leads to the conclusion that both phases of carbide formation are possible and carbon has separate structures.

The following results of the experimental research on the formation of graphite deposits on metal surfaces in the form of films, by means of applying electric discharges in impulse, are presented below [22].

These discharges resulted in obtaining black spots on the sample surfaces. Their size is a result of the released energy function and amount in the interstitial gap.

Spectrum processing:
No peaks omitted

Processing option: All elements analyzed (Normalised)
Number of iterations = 4

Standard:
C CaCO3 1-Jun-1999 12:00 AM
O SiO2 1-Jun-1999 12:00 AM
Fe Fe 1-Jun-1999 12:00 AM

Element	Weight%	Atomic%
C K	86.53	90.28
O K	11.99	9.39
Fe K	1.47	0.33
Totals	100.00	

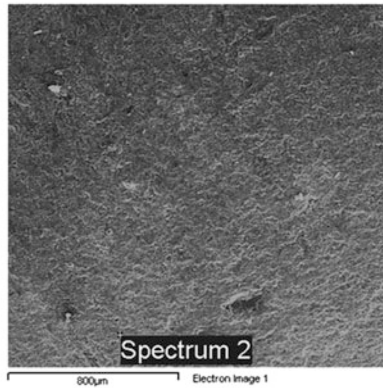

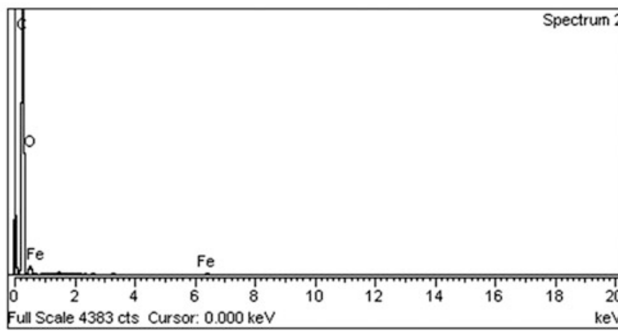

Fig. 3.4 EDX of the workpiece surface

Figure 3.5a–e presents the image of treated surfaces at different energy regimes, for a number of electric discharges n = 90.

The images were perceived with the help of an optical microscope of MBC-9 type, magnifying 14 times the observed area.

Figure 3.5f presents the oscillogram of the current pulse shape, applied to the gap in the process of electrical discharge in impulse.

The oscillograms show that the maximum current in discharge circuit is comprised within the range of 240–1066 A, for the situations shown on Fig. 3.5a–e.

Assuming that the total voltage drop on the electrode surfaces has a constant magnitude, as it was experimentally recognized the overall size of the current active resistance decreases, due to the gap intensification [21–23]. In this situation the amount of the released energy is reduced proportionally with the electrode surface.

If we consider the magnitude of the released energy in the plasma channel gap, we can see that it increases proportionally with its size, i.e. the size of the gap active resistance.

These assumptions are demonstrated by increasing the brightness and the intensity of the sound, produced by the shock wave, increasing the size of the gap to one and having the same amount of energy, accumulated in the capacitor.

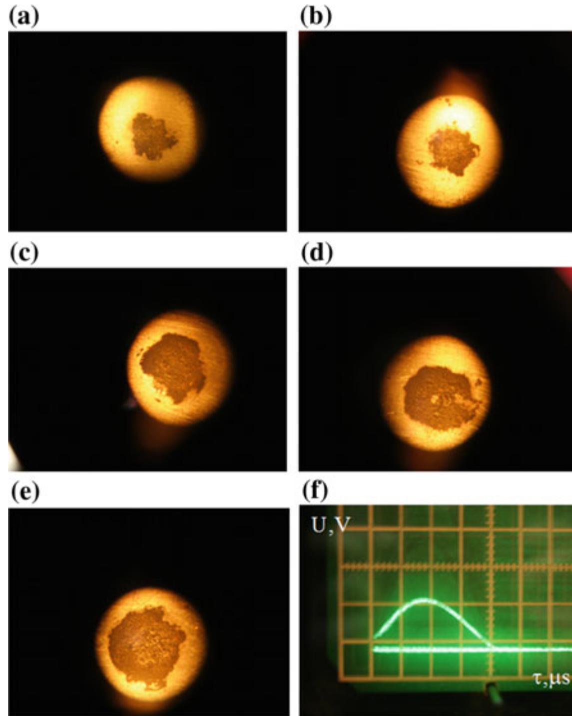

Fig. 3.5 Deposits of graphite (S = 1,5 mm, C = 100 μF, n = 90); **a** W = 0,23 J; **b** W = 0,53 J; **c** W = 0,94 J; **d** W = 1,46 J; **e** W = 2,12 J; magnification × 14; **f** pulse shape image: W = 0,23 J

Taking into consideration the fact that the accumulated energy in the capacitor battery is directly proportional to its capacity and to the square of the charging voltage, we can say that with an energy increase in the capacitor, the gap released energy will increase as well. As it is experimentally observed, an increase of the brightness and sound, caused by the wave power testing shock [20], causes a growth in the size of the black spots from the piece surface (Fig. 3.5).

Figure 3.6 shows a steel-45 graphite-coated workpiece surface, the surface morphology of which is photographed with the help of QUANTA-200 (FEI Filips) scanning electron microscope.

This image shows that the achieved area of a graphite film is accompanied by a change in the surface layer structure of figure white areas.

Analysing the offered experiments, in the conditions when electrodes serve as cathode tools, we can conclude that, in these particular situations, the graphite deposits from the work piece surface are created by electrical discharges in impulse and, as a result, graphite thin films are formed.

The formation of these deposits can be explained by the fact that the electrode tool material is not made from a metal, but from graphite, with higher erosion as of

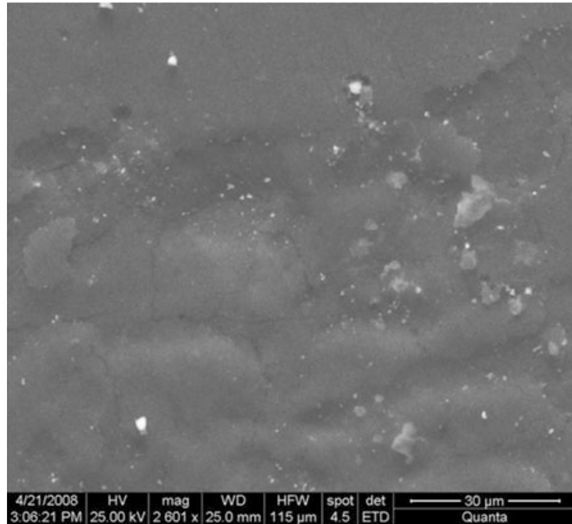

Fig. 3.6 Workpiece surface covered with graphite film, (W = 0,53 J; S = 1,5 mm; C = 100 µF, n = 90)

the cathode. In addition, the discharge impulse processes occur particularly if the metallic deposits are compact and if they conform to the developed physical model.

Figure 3.7 represents the above described technology, able to obtain sufficiently homogeneous graphite films, composed of mosaic blocks.

The mosaic blocks are composed of nanometre-sized spherical particles. These structures can embed the phases, comprising the elements from the working environment (air), as well as the elements formed while accomplishing the material of the work piece.

If we analyze the shown data in Fig. 3.7, we can see that the film is composed of clusters of nanometer configurations. Between these clusters and between their formations there are attested blank spots (pores), fact that can explain a number of their properties.

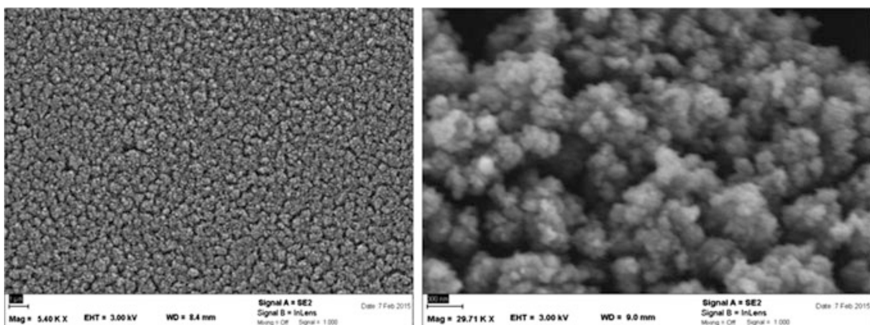

Fig. 3.7 SEM morphology of graphite films on the surface of samples made of steel

3.5 XPS Spectroscopy

It has been recorded the wide range of X-ray Photoelectron Spectroscopy (XPS) spectra (survey) around the range of energies (0–750 EV), with step 0.5 EV, that interests us, as well as a wide spectrum of oxygen (orbit O 1s) carbon (C 1s), iron ($2p_{1/2}$, $2p_{3/2}$) and silicon (Si 2p, 2s). A typical survey studied the surface presented in Fig. 5.8a, and shows the above elements, and the next element composition of subsurface: 60.7 % of carbon, oxygen—22.9 %, iron—6.2 %, 6.2 % of silicon and nitrogen 2.7 %, others—1.3 %. It is worth pointing out the high value of atomic carbon. Carbon peak resolution emphasizes its presence mainly (about 80 %) as an element in adsorbed surface (BE = 285.3 eV) and, to a lesser extent (approximately 20 %), in structures of the type C–O (BE = 286.6 eV), O–C=O (BE = 288.9 EV).

The example of XPS oxygen spectrum of high-resolution is shown at curve 1 in Fig. 3.8b, in which some experimental points on the graph of visibility were ignored. Spectra were obtained using XPS and PHI SUMMIT processing−by using PHI Multipack 8.2 C. The standard procedure was followed and described in detail in papers [9, 10, 24], based on the characteristics of equipment Versa Probe 5000 use [25].

Signal analysis revealed the presence of oxygen O-1 s in three types of chemical bonds (collectively called components). These are (a) component O^{-2} (which contains oxygen atoms of the metal oxides, in the sample is labeled number 3 in Fig. 3.8b, with the specific energy 529.6 EV; (b) component of OH^{-} energy relation EV 531.5 (indicated by the numeral 2 in Fig. 3.8b; (C) the component of type O–C and O–C=O (EV 533.4, curve 4 in Fig. 3.8b.

The chemical analysis showed the concentration of each of the three components C(a):C(b):C(c) = 0.89:1.00:0.50. Additional studies have shown the possibility of the existence of the fourth component of oxygen within the context of type $O–H_2$, however, the relative concentration of the component value is assumed to be not greater than 0.15.

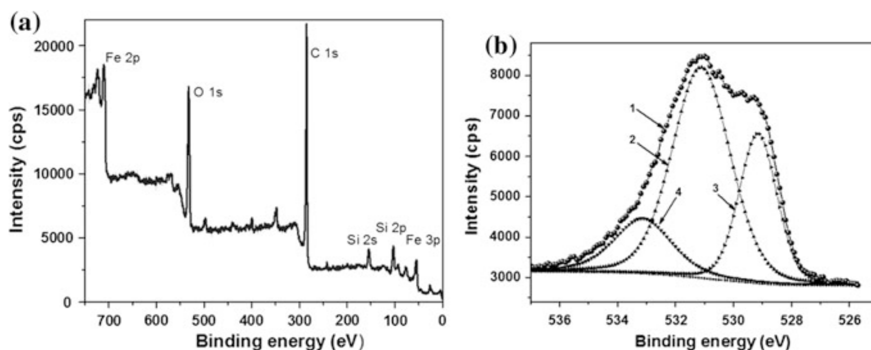

Fig. 3.8 The phase composition of oxide pellicles on samples of steel 45: **a** total surface spectral composition; **b** spectrum of oxygen on the surface: *1* total spectrum; *2* OH^{-} component; *3* O^{2-} component; *4* components of O–C and O–C=O types

The presence of phases that contain groups of –OH, –O–C and O–C=O types is possible for 3D structures formation and especially for single wall nanotubes (SWNT) [26] at iron atoms presence [27].

3.6 Thermal Gravimetric Analysis (TGA) of Graphite Film

TGA tests on graphite films were conducted on a Du Pont Instruments 951 device. In order to avoid errors—due to the oxidative process that takes place at high temperature and results in a weight increase—TGA tests on graphite films were carried out in nitrogen atmosphere. Graphite powder was collected from three conditioned samples and, further, introduced in the platform unit. Afterwards, it is placed on the platform and the sample is inserted into the heating chamber.

The following parameters were set for the reference sample and for the graphite deposit material on the surface of the work piece: 20–800 °C temperature range; 10 °C/min heating rate; medium N_2 analysis at a working pressure of 760 mm Hg. Thermo-gravimetric analysis began with samples that showed the highest level of water.

3.6.1 TGA Tests on Reference Samples

First of all, TGA tests were done on a pure graphite sample, which was thought to be the reference sample. About 5 mg of powdered graphite reference sample was inserted into the device platform. TGA adsorption curve of reference sample is given in Fig. 3.9.

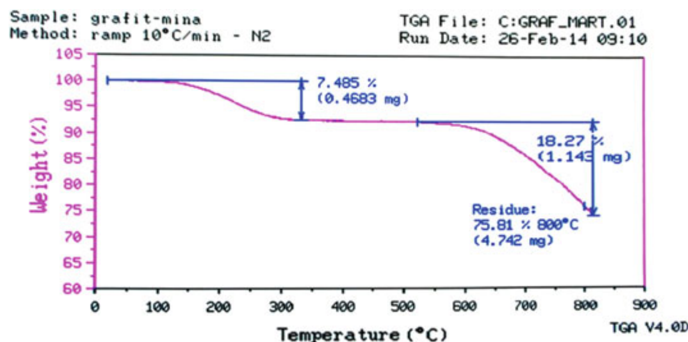

Fig. 3.9 TGA curve corresponding to pure graphite reference sample

The following features are observed from Fig. 5.9: up to 100 °C—the curve shape does not reveal any unusual thermal behaviour for graphite; within the temperature range of 100–280 °C a weight loss of 7.485 % (0.4683 mg) occurs as a result of volatiles and water evaporation; between 280–600 °C no weight loss occurs which shows a high thermal stability of graphite; some non-significant decomposition (of about 18 % of baseline) occurs within the temperature range of 650–800 °C, caused by decomposition of tars and heavy hydrocarbons that are found in most varieties of graphite and, finally, considerable amount of graphite is found in the residue—more than 75 %, at the end of determination 800 °C. These aspects are characteristic for graphite behavior, a compound well-known for its particularly high chemical and thermal stability.

3.6.2 TGA Tests on Experimental Sample by 10/1,5/600/250 Deposition

A similar procedure was used to analyse the graphite films, deposited on the experimental samples. Since the available amount was extremely low, the graphite powder was collected from 3 of the 4 samples of each alternative. The collection process was done by the mechanical graphite scraping, without contacting the sample. The registration of the tested sample weight change versus the temperature is presented in Fig. 3.10.

TGA curve of 10/1.5/600/250 sample (Fig. 3.10) shows a completely different allure from that characteristic of pure graphite. The graph shows a number of very interesting aspects suggesting that the graphite film, deposited by electrical discharge in impulse, has a completely different structure from that of pure graphite or that, besides graphite, other chemical compounds of carbon are formed. From Fig. 3.10, one may notice that within 200–300 °C temperature range (at 222.99 °C) a significant weight increase (of 1.999 %) occurs, showing that the graphite sample gains

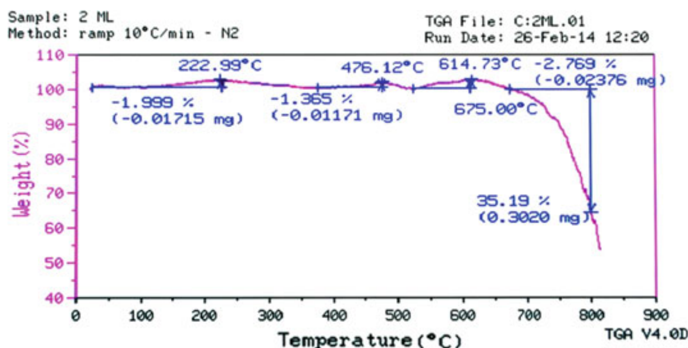

Fig. 3.10 TGA curve corresponding to 10/1,5/600/250 sample

weight, instead of losing it due to decomposition or loss in volatiles—showing a material adsorption in graphite film structure (as the adsorbed material cannot be anything but nitrogen from the atmosphere in which the tests are run). The phenomenon is reversible—at about 300 °C the weight does not increase anymore, which may be the result of substance volatilization at this evaporation temperature.

Within the temperature range of 450–550 °C (476.12 °C) a new significant increase in weight (of 1.365 %) may be observed, suggesting that, as a sample of graphite increases its weight instead of losing weight due to decomposition or loss in volatiles, a material adsorption occurs in the graphite film structure. Predominantly, a high temperature denies the assumption of a device error; the phenomenon of weight increases, being concrete and real. The phenomenon becomes reversible again at about 550 °C and a weight increase does not occur anymore.

Within the temperature range of 600–750 °C (614.73 °C), a new weight increase occurs in a significant percentage of 2.769 %, showing that the graphite sample weight increases instead of decreasing due to volatile decomposition or loss of weight gain−showing a material adsorption within the graphite film structure. Particularly, high temperature denies the assumption of a device error, the phenomenon of weight increase being concrete and real.

Reversible weight increase occurs within temperature ranges of 200–300, 450–550, 600–700 °C having enough increased values, that cannot be assigned to device errors (permissible error being of max. 0.1 %). The phenomenon of adsorption/desorption (reversibility) is very similar to the one occurring in zeolites, which presents spatial molecular structures made of atoms of Si, O, Al, able to close smaller molecules within them and to release them later. A similar phenomenon occurs also in graphite film, showing that besides graphite, spatial structures are also synthesized, in this example consisting of carbon atoms, which are known as fullerenes. These structures are made up of spatial molecules of 40–70 carbon atoms and have 20–40 nm in size. Because TGA tests were carried out under N_2 atmosphere, the chemical oxidation process, that could eventually bring mass intake, is excluded. The only scientific explanation consists of the presence of spatial structures able to store small molecules (N_2) and release them later. The emergence of the adsorption/desorption phenomenon at different temperatures and different percentages also shows that the potential spatial structures of carbon atoms have different sizes.

It is noteworthy that within the 20–750 °C temperature range graphite film does not suffer any changes arising from thermal degradation.

In literature it is mentioned that spatial structures, containing fullerenes-type carbon atoms, could be found in carbon particles, resulting from incomplete combustion of hydrocarbons and, generally, in everything that involves violent combustion—combustion in internal combustion engines.

It is also stated that spatial structures of these molecules, consisting of carbon atoms, can embed—without reacting to them—small molecules (H_2, N_2, monatomic inert gas molecules, HOH) inside their spatial structure (Fig. 3.11). These scientific literature [28–30] explanations provide a plausible elucidation on weight increase

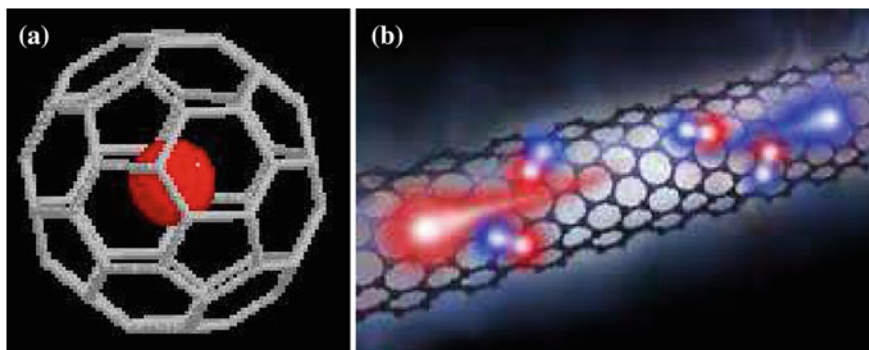

Fig. 3.11 Graphical representation of the properties of sapatial structures formed of nitrogen atoms

phenomena, which were observed in TGA tests on 10/1.5/600/250 sample and nearly double the proportion in which the sample absorbs water—compared to other samples under investigation.

These scientific results support the assertion of Mr. Professor Topala that after treating the metal surfaces with electrical discharge in impulse, using graphite electrode, i.e. carbon, other interesting structures composed of carbon atoms can be also achieved [30].

These possible spatial structures could be responsible for the double percentage of adsorbed water (0.12–0.15 % instead of 0.053–0.006 %) as compared to other samples.

Based on these scientific work data and on extremely fair observation [30], scientifically substantiated by Prof. Topala, further specific research was carried out to elucidate and demonstrate the assertion that after the treatment by electrical discharges in impulse, other structures are obtained apart from the graphite film.

3.7 Solubility of Graphite Films Formed by PED Method on Metal Surfaces

The results on solubility of graphite films formed by PED method on metal surfaces in the interaction with different solvents are presented in Table 5.1 [7, 8].

Scientific research results, presented in Table 3.1, lead to the conclusion that other susceptible chemical species are dissolved after the treatment with a suitable solvent. Initial suppositions, attributable to analysed electronic microscopy presented in Fig. 3.7, have stated that after treating the metallic surface with graphite films by PED, other chemical formations are also obtained—probably some spatial carbon structures of fullerenes and nanotubes type. In the paper [31–37] it was specified that the fullerenes are black, opaque solids, with low hardness and low

Table 3.1 The solubility of carbon spatial formations of C60 fullerene and nanotubes type in different organic solvents [7, 8]

Solvent	Solubility
1-chloronaphthalene	51
1-methylnaphthalene	33
1,2-dichlorobenzene	24
1,2,4-trimethylbenzene	18
Tetrahydronaphthalene	16
Carbon disulfide	8
1,2,3-tribromopropane	8
Xylene	5
Bromoform	5
Cumene	4
Toluene	3
Benzene	1.5
Carbon tetrachloride	0.447
Chloroform	0.25
n-hexane	0.046
Cyclohexane	0.035
Tetrahydrofuran	0.006

heat and electricity conductivity. The behaviour of the samples, treated with a specific fullerenes and nanotubes [17, 18, 38, 39, 41–44] solvent offer the first indication for the assumption, according to which, after treating the graphite films with PED, the same atom C spatial-composed formations are obtained.

Chemical reactivity of the formed deposition leads to the hypothesis that they contain single wall nanotubes (SWNT) too, that can be compared with reactivity of generating graphite strip that is grown as direct result of lateral surface curvature. This is explained by mixing of π-orbitals done by lateral surface curvature of SWNT that leads to a difference between reactivity of the lateral wall and reactivity of nanotube “caps”. The literature of speciality indicates the fact that a nanotube with smaller diameter has higher reactivity due to more pronounced mixing of π-orbitals [45].

The recent study in the field of carbon nanostructures [46–48] marks a keen interest in sub-nanometer nanotubes category (nanotubes diameters ranging in limits 3–7 Å). Sub-nanometer nanotubes were discovered inside of multi wall nanotubes (MWNT) gained by electric arc method [46, 48], as well as inside of zeolite crystal channels [47] that impose certain conditions for SWNT diameters during their formation due to their very small dimensions.

If these nanotubes are isolated they possess a very high mechanical stability at 1100 °C [49]. Theoretical investigations confirm the fact that the nanotubes with diameters lower than 3 Å are stable from the energetic point of view and that the sub-nanometer nanotubes of semiconductor type has a bandgap up to 3 eV [50].

3.8 Functional Properties of Graphite Films

Carbon and its allotropic forms in which it crystallizes, shows a particular interest for researchers both as material and in particular as functional properties for technical applications in contemporary technologies. Following are presented a number of functional properties of graphite films deposited on active surfaces of the various types of pieces of machinery and equipment industry.

3.8.1 Anti Socket

In order to broaden the applicability of the practical domain related to the scientific elaborations and, particularly, to graphite films deposited on metal surfaces, with the help of PED method, a number of attempts, on the timing of screw driving—unscrewing of threaded joints (bolt-nut), were made by the authors [51, 52]. Measurements were made concerning the value of screwing moment in bolt couplers—screw nut with the formation of deposits on its front surface and the second solution—on the surface of the thread bolt (see Table 3.2).

If we compare the results shown in Table 3.2, we can see that the moment of screwing is increasing, being variable and dependent on the number of tracers (surface processing with PED). It would seem that the deposit formation is not beneficial and leads to an increase of the screwing moment value. This unimportant increase of the screwing moment is also caused by increasing the size of the pieces that form the couple. In contrast to the reverse—the unscrewing was not registered, together with the outlet effect for parts of couplings with graphite film on the active surface (also in case of keeping them at high temperatures, ad in case of placing mounted joints in solutions presenting active chemical environments).

Table 3.2 Values of the unscrewing moment of screw nuts, covered with a graphite film, M_{des}, Nm

Number of passes	Screwing force, kN			
	0.5	1	1.5	2
2	2	6	9.9	13
3	2.2	5.8	9.5	12.5
4	2.5	4.5	8.2	10.15
5	3	6.1	10.2	14
6	2.9	8	12	16
8	3.5	6.2	11	14.1
10	3.5	5.9	11	13.2

3.8.2 *Antiblocking Properties of Graphite Films*

Graphite films deposited by pulsed electrical discharges with 7–8 μm thickness, react physico-chemical as theoretical model, with metallic surface which leads to a high adhesion of graphite film [52–54].

A first method of verifying the theory on the creation of an anti-adhesive film on the metal surface as a result of treatment with graphite, achieved by electrical discharges, it consisted in achieving of a set of specimens made of two metal plates bonded by an structural adhesive to verify the shear forces.

According to the valid standardization, structural adhesives are the adhesives used to create structures- assemblies of components—which can not be removed only with the destruction of the structure. It follows that adherence achieved with this type of adhesive is stronger than the resistance of the glued components. Structural adhesives are used to achieve structures that no longer can be sold in parts. Therefore, a permanent structure is produced.

In these conditions the adhesives that made the structure should have excellent bonding characteristics and excellent resistance. Assemblies made with structural adhesive obtained were subjected to shear stress test. As the result, the values presented in Table 3.3 were obtained for the shear test.

From the shear stress test results table it can be observed that the untreated specimens have the higher values about 85 daN/cm^2. Mixed treated specimens are averages of shear stress values about 60 daN/cm^2, which proves that the graphite film, deposited on one of specimens, reduces the adherence between the adhesive and the metal surface.

The last version where both specimens are treated with graphite tension the shear stress values diminishes up to the approximate value about 50 daN/cm^2, which represents a decrease of approximately 40 % compared to untreated specimens [55, 56] (version 1) (Fig. 3.12).

In this context, it is also observed that the shear occurs in two ways as it is shown in Fig. 3.13.

In the first version breakage occurs in the adhesive mass Fig. 3.13b which is characteristic of specimens that were not subjected to the treatment of electrical discharges with graphite tool-electrode.

In the second version breakage occurs at interface graphite pellicle and adhesive surface which is characteristic of specimens that were subjected to the treatment of electrical discharges with graphite electrode too.

As a confirmation of this goal comes the surface morphology research for PED treated and untreated specimens after the shear.

Table 3.3 Shear stress values for different ways of gluing the specimens

Both specimens untreated daN/cm^2			Mixed treated specimens daN/cm^2			Both specimens treated with graphite daN/cm^2		
86.4	85.80	83.7	62.1	58.6	62.0	49.6	51.2	50.4

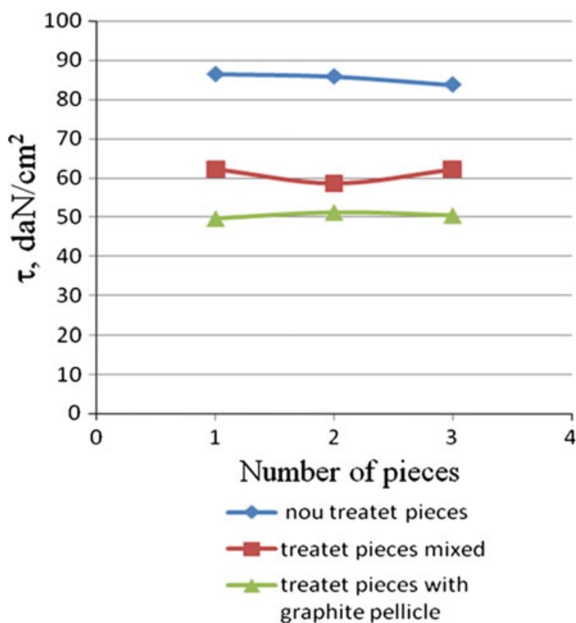

Fig. 3.12 The dependence of the shearing stress on the way of conditioning the test pieces

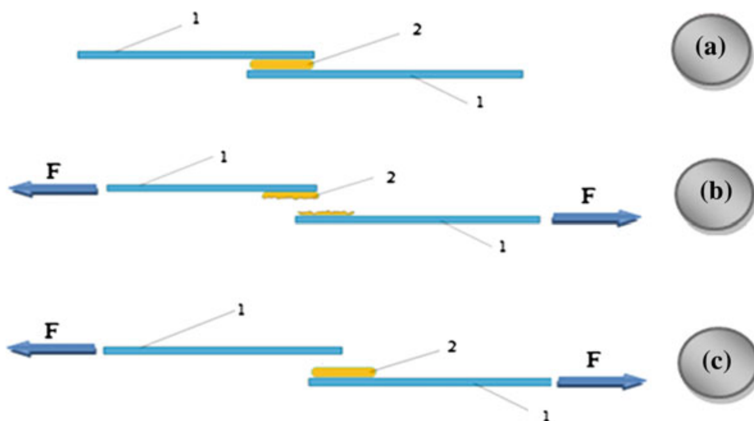

Fig. 3.13 Main scheme shear rupture assemblies: *a* initial state; *b* final state for untrated specimens; *c* final state for PED trated specimens; *1* metallic sheets, *2* structural adhesive

In the case of the specimens which do not have been subjected to electrode-position treatment, all assemblies cleavage occurred in the adhesive mass, which is demonstrated by the pictures shown in Fig. 3.14. This shows strong adhesion to metal substrates of the adhesive.

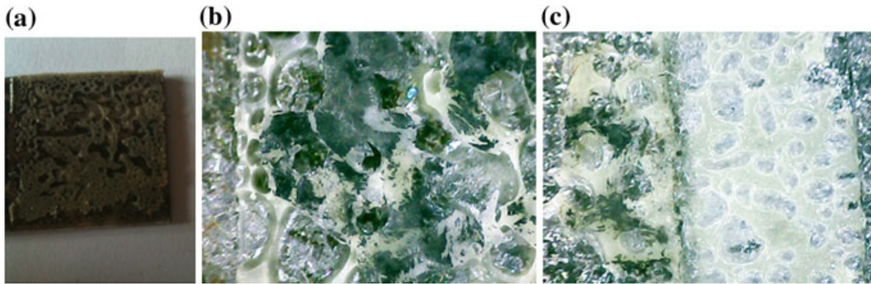

Fig. 3.14 Component of the assembly without surface treatment after shearing: **a** general view; **b, c** microscope image, ×80

It can be seen from Fig. 3.14 that breaking assembly occurred in adhesive mass. This is noticed by the presence of adhesive on whole active surface of the specimen (dark coloured zone).

In this case the higher shear forces have been observed (over 80 daN/cm^2). In the case of the specimens treated with graphite by electrical discharges pulse treatment PED breaking structure if they applied a tangential force occurs at the adhesive support interface (Fig. 3.15). So the whole mass of the adhesive or much of it will remain on one of the supports. It says in this case that the inner resistance of the adhesive is greater than adherence to the metal support, the structure is not destroyed as a result of unbundling in parts, and i.e. the adhesive cannot works as structural adhesive. Determined share forces in this case are only to half (50 daN/cm^2) compared with the superficial untreated specimens.

It can be seen from Fig. 3.15, that the existence of large stretching dark area, means that breaking assembly occurred at adhesive graphite film interface.

In Fig. 3.15, a may also be better observed, an area where film deposition of graphite treatment was not performed properly with a continuity 100 %—area with a lighter colour—where there was a breakage in the adhesive mass, and in other areas where electro-deposition treatment of graphite was performed properly with a

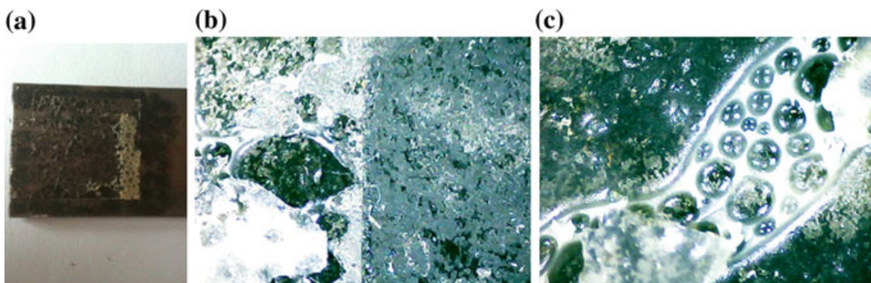

Fig. 3.15 Component of the assembly with PED surface treatment after shearing: **a** general view; **b, c** microscope image, ×80

continuity 100 % assembly rupture occurred at the graphite adhesive interface—area with a dark colour.

These images taken under the microscope demonstrate these statements. In Fig. 3.15c is observed really well the area where the adhesive remains—area with a lighter colour—in contrast with the dark area, where the cleavage occurred at the interface adhesive—graphite film from the metallic surface.

All these observations allow asserting that the graphite films deposited by pulsed electrical discharge—PED—determine non-adherence properties, which confirm the assumptions made in previous papers [57].

3.8.3 Resistance to Wear for the Graphite Films

As a result of the film formation on the surface of graphite parts, the effective diameter of the piece increased by approximately 14 μm in diameter compared to initial diameter, thus, as a result, we have graphite deposits with a corresponding size on the surface such as continuous film.

Thus the application of films on the surfaces of constituent parts of molding glass forms has enabled their efficient functionality. The sustainability of the pieces increased at least twice compared to the factory pieces [2, 5]. This can be explained by the fact that graphite has a solid ointment and prevents the glass adherence to the workpiece surface, and its grip wear process, as well as the fact that graphite film possesses anti refraction properties and serves as an insulator heat from the surface of metal parts and liquid glass.

The above mentioned facts can be confirmed by authors' achieved results [51], which tested the plungers in real exploitation conditions. Consequently it was determined that the plungers of the molding forms on active surface of which there were formed graphite films, which functioned at 57600 cycles without changing their shape and size. In this regard, to compare the usage of plungers of the glass molding forms experimental research in technological cycle was performed [52–54]. Two plungers underwent testing, one was coated with graphite through electrical discharge in impulse, and other was unprocessed.

If we research (Fig. 3.16a) the untreated piece with PED before functioning in technological cycle and after functioning, we can observe that its diameter decreases in some spots to approximately 11 μm. Sample (Fig. 3.16b) is studied from three points of view, at the initial phase, then after applying electrical discharge in impulse and, finally, after it was subjected to the wear process. After the sample was subjected to the PED processing, the diameter of the plunger increases, within acceptable limits, due to deposits of graphite on surface. The research of the piece after functioning in above prescribed regimes track a decrease in the diameter of the work piece at the sizes tens of micro-meters, as indicated in Fig. 3.17.

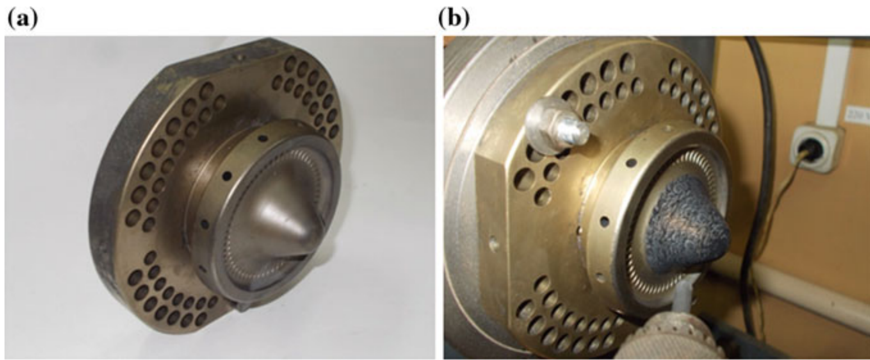

Fig. 3.16 General view of the finishing edges: **a** in normal conditions, **b** after covering with a graphite film

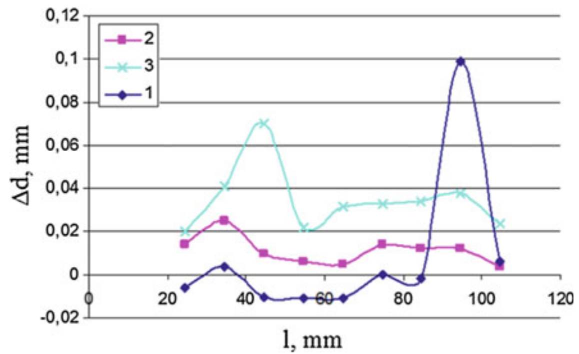

Fig. 3.17 The dependence difference of the diameter of the piece upon the length of its active assets for: *1* sample 19 after functioning in technological cycle; *2* sample 23 after functioning in technological cycle; *3* sample 23 after applying PED

Besides decreasing the piece diameter, in some cases, we can observe its increase, explained by the adherence of the glassy mass to its active surface. This phenomenon is practically unnoticed for parts not covered with graphite film which could confirm that graphite serves as a good ointment at high temperatures and reduces considerably the friction forces between the glass mass and work piece surface.

To confirm or to contest the adherence of various materials to piece surface, they were subjected to tests, according to the methodology described in [52–54], the couplings consisting of graphite film pieces by sticking them through the adhesive surface area. As a result of traction of glued assembled pieces, we can see that untreated samples have higher values of shear stress and the other is about 85 daN/cm^2 mixed treated samples have an average of 60 daN/cm^2 which tells us that graphite film deposited on one of the samples reduces the adhesion between the adhesive and the metal surface. The last variant, in which both surfaces are coated with graphite film, the shear stress is reduced to approximately 50 daN/cm^2, which is a reduction of the adhesion by 40 % compared to untreated samples. Further

experimentation of untreated samples shows that shear occurs within the adhesive, as compared to those treated where shearing takes place the separation of the adhesive surface with graphite film. This effect can be explained by the fact that the formed film is pored, and respectively the adhesive penetrates into its pores. One might assume that one of the reasons of the absorption component adhesive substances is that the graphite film formations present nanotubes and they have the ability to absorb certain components of the work environment [42–44].

3.8.4 Corrosion Resistance of the Graphite Films

For the determination of corrosion resistance of the graphite films it was chosen the method of electrochemical research. This method was used because it allows the acceleration of corrosion process which is nothing more than anodic dissolution and thus shortens the study of a sample

The electrochemical installation is composed of an electrolysis cell containing a 1 % de NaCl solution in which two electrodes are placed, a steel cathode and anode also steel or steel coated with graphite film, and they are merged by a voltmeter and an ampermeter at an adjustable continuous current source in 0–40 V domain.

Also, a set of samples were studied in 30 % HNO_3 solution.

Corrosion rate was determined by the relation:

$$K_m = \frac{\Delta m}{A\tau} \tag{3.7}$$

where Δm—metal mass difference in the time τ after removal of corrosion products, A—area subjected to the corrosion.

To determine the value for potential of the electrochemical dissolution is necessary to build the characteristic voltage intensity, for the sample anode steel 45 and for the sample anode steel 45 covered with graphite. Cathode material in both cases is steel 45.

For the beginning, the samples are polished and rinsed with distilled water, then placed in the electrolyte solution at a distance of 10 mm to one another. A DC voltage with an 0.4 V increments is applied and a holding time of 3 min (Fig. 3.18). Values for electric currents are recorded by the ampermeter and they are presented in the chart 1.

When samples are placing in electrolyte, in the absence of external electric current a stationary potential is established.

In the case where both electrodes are made from the same type of steel stationary potential is almost zero and in the case where the anode is covered with graphite the stationary potential is 0.1 V.

When an external potential it is applied, curves in Fig. 3.18 are obtained (curve 2).

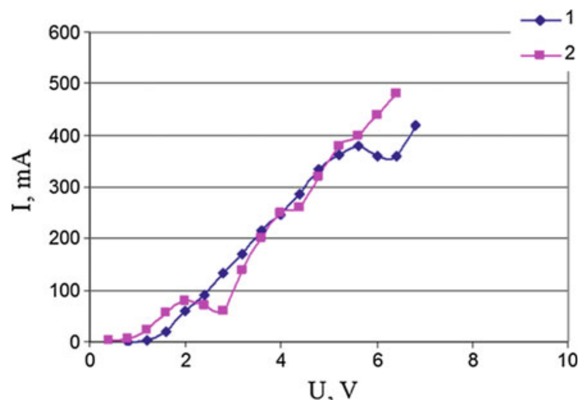

Fig. 3.18 Characteristic voltage intensity for electrochemical process: *1* steel 45 covered with graphite; *2* steel 45

It is observed that for the steel sample, with the potential increasing, current intensity increase occurs too until to a value of. 2 V, followed by an area where a decrease of intensity occurs until to a value of 2.9 V. This effect may be due to oxidation and hydroxidation chemical reactions that lead to the steel surface passivation, in the absence of the graphite film.

After this value, as shown in the chart, with increasing the potential difference the corrosion current decreases and the corrosion process takes place at low speed, i.e. appeared passive film which does not allow anodic dissolution.

Passive state is maintained until the potential of 2.8 V, then the current intensity increases considerably accelerating the corrosion process.

An analogue behaviour is found at the research of graphite coated steel sample, except that the passivation area appears almost to value 5.6 V.

In the field of 5.6–6.2 V is observed the destruction of the graphite film deposed, followed by an increase of corrosion currents.

The behaviour of sample covered with graphite film (Fig. 3.19, curve 1) demonstrates that the presence of carbon significantly enhances the surface potential of passivation approx. 3.2 V.

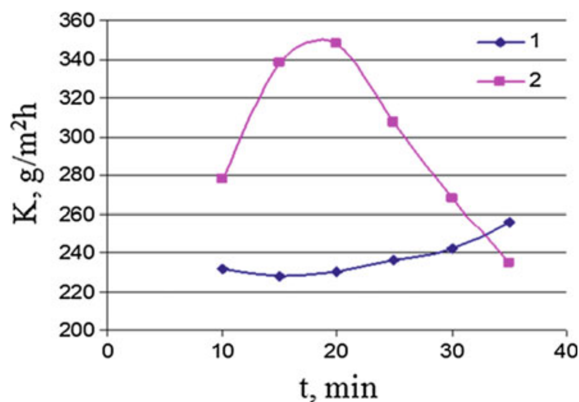

Fig. 3.19 Corrosion rate variation depending on the time of immersion: *1* steel 45 covered with graphite; *2* steel 45 unprocessed

It is possible that the presence of graphite on metallic electrode surface to generate deoxidation reactions, and porosity of graphite film ensures the electrical contact between electrolyte environment and sample surface.

In Fig. 3.19 corrosion rate variation depending on the time of immersion is shown for samples processed with graphite tool-electrode.

From the analysis results relating to corrosion speed variation depending on the duration of exposure of samples (Fig. 3.19) in aggressive environment, it finds essentially higher corrosion rates for initiation stage corrosive process in the case of unprocessed Steel 45 without graphite pellicle (Fig. 3.19, curve 2).

Over time, the process of corrosion is attenuated; the determined corrosion rate is with so small when the time of immersion is longer [58–60].

Over time also the nature of the corrosion product is modified, probably are formed oxides with low oxygen content that are more stable (Fe_3O_4) ($FeO{\cdot}Fe_2O_3$) [60, 61].

At the same time it is acceptable that corrosion products form on the metal surface films that insulate the metal from corrosive agent, for this reason the curves showing the variation of corrosion rate time show the trend of flattening.

These films are adherent and also compact enough so that the corrosion process to diminish in time but not annihilate.

It should be noted that determinations were made in static regime. In dynamic conditions, formed oxide film can probably be detached from the metal surface and, in this case, the corrosion process to be conducted with higher corrosion rates.

In the case of steel coated with graphite film, lower corrosion rates are found, after, they begin to rise due to degradation of graphite film and then as a result of its destruction.

Experimental was established that in acid solution 30 % HNO_3, over 3 min, the amount of dissolved electrochemically uncovered with graphite steel, was 1.4 times greater, than steel coated with graphite, and 1.3 times greater over 10 min. In salt solution 1 % NaCl, the amount of dissolved electrochemically uncovered with graphite steel, was 1.2–1,4 times greater, than steel coated with graphite deposited by electrical discharges in pulse.

3.9 Conclusions

From the above mentioned are drawn the following conclusions:

The erosion of the graphite and its transfer on the metal surfaces with deposition film formation by the action of electrical discharges in impulse is more effective when the tool electrode made of pyrolytic graphite is connected in the discharge circuit of the current impulse generator as cathode. The erosion process in ordinary conditions (air at atmospheric pressure and room temperature) is one complex, of electro-physical and electro-chemical nature that devolves at high temperatures.

The presence of the sample made of steel containing an important amount of the iron stimulates the formation on its surface of 3D type formations (fullerenes or

nanotubes). These goals are confirmed by the behaviour of depositions at thermo-gravimetric actions (stating mass increase under the influence of nitrogen at the temperature of 222.99, 476,12 and 614.73 °C) and by solubility tests in different environments: it varies from 51 for chloronaphthalene down to 0,006 for tetrahydrofuran).

The graphite films formed by applying electrical discharges in impulse possess a set of beneficial functional properties, such as: decrease the surface adherence by 1.4 times, decrease the wear coefficient from 4 down to −0.1, increase the wear resistance of piece components of glass molding forms, condition the increase of corrosion resistance in chemically aggressive media by 1.5 times.

Functional properties of the graphite depositions, their chemical composition and morphology indicate the fact that they presents 3D structures and in particular fullerene and carbon nanotubes. The presence of iron in the sample, graphite purity of the tool-electrode, as well as energetic parameters of electrical discharges in impulse provide sufficient and necessary conditions for carbon nanotubes synthesis.

References

1. V.P. Luneva, A.D. Verhoturov, A.V. Coziri, T.V. Glabet, V.N. Brui, Using the Cr-Ni alloys for the electric discharge deposition forming of. EPI, Nr 4, 11–18 (2005)
2. F.H. Burumculov, P.P. Lezin, P.V. Senin, V.I. Ivanov, *The Electric Discharge Tehnology Aimed at Retreading and Hardening of the Machining Pieces and Tools*.(USM “Ogareva”, Saransk, 2003)
3. P. Topala, The transfer of mass and diffusion processes on surface layers of engoine parts during electrosparkle processing. The materials of international conference: the technologies of maintaining, retreading and hardening of engine parts. Saint-Petersburg. **2**, 234–242 (2007)
4. S.I. Sidorenco, E.V. Ivaschenco, V.F. Mazanko, G.F. Lobachva, D.V. Mironov, E.N. Khranovskaia, *Forming of Ferrous Alloys Surface Layer by Combination of Nitriding and Electrospark Alloying by Chrome and Titanium and Certain Properties of the Afore-Mentioned Layer*. 6th International Conference “Interaction of Radiation with Solids”, Minsc, Belarus, pp. 430-432, Sept 28–30, 2005
5. B. Vitalie, Structure and properties of surface layers of pieces cemented when interacting with the plasma channel of electric discharges in pulse. the annals of „dunărea de jos university of galaţi. Fascicle V, Technol. Mach. Build **1**, 24–30 (2008)
6. P. Topala, P. Stoicev, *Technologies of Conductible Material Processing by Applying Pulsed Electrical Discharge Machining* (Edition Tehnica-Info, Chisinau, 2008), p. 265
7. P. Topala, B. Vitalie, P. Stoicev, A. Ojegov, Structural modifications—properties of surface micro-strata with graphite depositions. Int. J. Mod. Manuf. Technol. vol II, 97–102 (2013)
8. P. Topala, L. Marin, B. Vitalie, in Applying graphite micropellicles to decrease the coefficient of superficial adhesion. Advanced Manufacturing Technologies 2013, 7th International Seminar Advanced Manufacturing Technologies (Sozopol, Bulgaria, p. 97–104 (2013)
9. Y. Kurochkin, Y. Demin, Technology for surface hardening of parts by treatment with concentrated energy flux. Chem. Pet. Eng. **37**, 404–408 (2001)
10. A. Mihaliuc, The roughness reduction of electrosparkle Co rings during the following processing with graphite electrode. EPI. Nr.3, 21–23 (2003)
11. P. Topala, Condition of thermic treatment and chemico-superficial innards, with the adhibition electric discharge in impulses. Nonconventional Technol. Rev. Nr.1, 129–132 (2007)

12. P. Topala, B. Vitalie, Graphite deposits formation on innards surface on adhibition of electric discharges in impulses. *Bulletin of the Polytehnic Institute of Iassy, T.LIV*, pp.105–111 (2008)
13. B. Vitalie, *Structure and Properties of Surface Layers of Pieces Cemented when Interacting with the Plasma Channel of Electric Discharges in Pulse.* The annals of ``Dunărea de Jos" University of Galaţi, Fascicle V, Technologies in Machine Bulding, vol.1, Year XXIV (XXIX), p.75–82 (2008)
14. P. Topala, P. Stoicev, A. Epureanu, B. Vitalie, The hardening of steel surfaces on the sections for electrosparkle alloyage. International Scientific and Technical Conference Machinebulding and Technosphere of the XXI Century. Donetk, pp. 262–266 (2006)
15. B. Ekmekci, O. Elkoca, A. Erden, A comparative study on the surface integrity of plastic mold steel due to EDM, metallurgical and materials transactions. ProQuet Sci. J. Feb 36B, 117–124 (2005)
16. P. Topala, B. Vitalie, Graphite deposits formation on innards surface on adhibition of electric discharges in impulses. Bulletin of the Polytechnic Institute of Iasi, vol. LIV, pp. 105–111 (2008)
17. P. Sigmund, Mechanisms and theory of physical sputtering by particle impact. Nucl Instr Meth Phys Res B **27**, 1 (1987)
18. N. Laegreid, G.K. Wehner, Sputtering yields of metals for ArC and NeC ions with energies from 50 to 600 eV. J. Appl. Phys. **32**, 365–369 (1961)
19. P. Topala, V. Rusnac, B. Vitalie, A.Ojegov, N. Pînzaru, Physical and chemical effects of EDI processing. International Conference NewTech 2011, Brno, Czech Republic. 14–15 September, 2011. Part. Advances in non-traditional manufacturing, rapid prototyping and reverse engineering (2011)
20. P. Topala, S. Mazuru, B. Vitalie, P. Cosovschii, A. Ojegov, Application of EDI in increasing durability of glass moulding forms poansons. ModTech-2011. 25–27 May, Vadul lui Voda-Chisinau, Republic of Moldova, pp. 1093–1096 (2011)
21. V.V. Nemoshkalenco et al., Peculiarities of surface strata formation at spark discharge. Kiev: Metal-physics, t. 12, No 3, pp. 132–133 (1990)
22. P. Topala, Research on obtaining deposit layers of metal powder by applying pulsed electrical discharge machining. Summary of PhD thesis, Bucharest, University Politehnica, p. 32 (1993)
23. M.K. Mitskevich et al., *Electro-erosion processing of metals* (Science and Technics, Minsk, 1988), p. 216
24. B. Vitalie, Research on the thermal and thermo-chemical treatment of piece surfaces by means of electrical discharges in impulse/ Summary of the Doctoral Thesis, Galaţi, p.56 (2008)
25. P. Topala, Condition of thermal treatment and chemical-superficial innards, with the adhibition electric discharge in impulses. Non-conventional Technol. Rev. Nr.1, 129–132 (2007)
26. G. Ruxanda, M. Stancu, S. Vizireanu, G. Dinescu, D. Ciuparu, J. Optoelectron. Adv. Mater. **10**(8), 2047–2051 (2008)
27. W. Vogelsberger, H.G. Fritcsche, E. Muller, Phys. Stat. Sol. (B) **148**, 155 (1988)
28. B. Howard Jack, J.T. McKinnon, Y. Makarovsky, L. Arthur, M. Johnson Elaine, Fullerenes C_{60} and C_{70} in flames. *Nature* **352** (6331), 139–41 (1991). Bibcode:1991Natur.352..139H. doi:10.1038/352139a0. PMID 2067575
29. J. Howard, A. Lafleur, Y. Makarovsky, S. Mitra, C. Pope, T. Yadav, Fullerenes synthesis in combustion. Carbon **30**(8), 1183 (1992). doi:10.1016/0008-6223(92)90061-Z
30. H.W. Kroto, J.R. Heath, S.C. O'Brien, R.F. Curl, R.E. Smalley, C_{60}: Buckminsterfullerene. *Nature* **318** (6042), 162–163 (1985). Bibcode:1985Natur.318..162 K. doi:10.1038/318162a0
31. Y. Zhao, Y.-H. Kim, A.C. Dillon, M.J. Heben, S.B. Zhang, Hydrogen storage in novel organometallic buckyballs. Phys. Rev. Let. **94** (15), 155504 (2005). Bibcode: 2005PhRvL..94o5504Z. doi:10.1103/PhysRevLett.94.155504. Retrieved 24 September 2012
32. A. Hirsch, C. Bellavia-Lund (eds.), *Fullerenes and Related Structures (Topics in Current Chemistry)* (Springer, Berlin, 1993). ISBN 3-540-64939-5
33. F.N. Diederich, Covalent fullerene chemistry. Pure Appl. Chem. **69**(3), 395–400 (1997). doi:10.1351/pac199769030395.edit

34. A. Hirsch, C. Bellavia-Lund (eds.), *Fullerenes and Related Structures (Topics in Current Chemistry)* (Springer, Berlin, 1993). ISBN 3-540-64939-5
35. F.N. Diederich, Covalent fullerene chemistry. P Appl. Chem. **69** (3): 395–400 (1997). doi:10.1351/pac199769030395.edit
36. D.R. Mitchel et al., The synthesis of megatubes: new dimensions in carbon materials. Inorg. Chem. **40** (12), 2751–5 (2001). doi:10.1021/ic000551q.PMID11375691
37. Y. Li et al. Structures and stabilities of C_{60}-rings. Chem. Phys. Lett. **335** (5–6), 524 (2001). Bibcode:2001CPL…335..524L. doi:10.1016/S0009-2614(01)00064-1
38. B.H. Hong, P. Joshua Small, S. Purewal Meninder, A. Mullokandov, Y. Matthew Sfeir, F. Wang, J.Y. Lee, F. Tony Heinz, E. Louis Brus, P. Kim, S. Kwang Kim, Applied physical sciences. PNAS **102**(40), 14155–14158 (2005)
39. J.M. Moon, K.H. An, Y.H. Lee, Y.S. Park, D.J. Bae, G.S. Park, Synthesis and characterization of carbon nanostructures. J. Phys. Chem. B **105**(24), 5677–5681 (2001)
40. K.S. Kim, Y.S. Park, K.H. An, H.J. Jeong, W.S. Kim, Y.C. Choi, S.M. Lee, J.M. Moon, D.C. Chung, D.J. Bae, S.C. Lim, Y.S. Lee, Y.H. Lee, Carbon Sci. **1**(2), 53–59 (2000)
41. G. Ruxanda, M. Stancu, S. Vizireanu, G. Dinescu, D. Ciuparu, Investigation of transport and deposition of species in an arc discharge reactor with carbon electrodes, 14th International Conference on Plasma Physics and Applications, Braşov (2007)
42. G. Andrievsky, V.K. Klochkov, A.B. Bordyuh, G.I. Dovbeshko, Comparative analysis of two aqueous-colloidal solutions of C_{60} fullerene with help of FTIR reflectance and UV–Vis spectroscopy. Chem. Phys. Lett. **364**(8) (2002). Bibcode:2002CPL…364….8A. doi:10.1016/S0009-2614(02)01305-2
43. G. Andrievsky, V. Klochkov, L. Derevyanchenko, Is the C 60 fullerene molecule toxic?! Fullerenes, Nanotubes, Carbon Nanostruct. **13**(4), 363 (2005). doi:10.1080/15363830500237267
44. X. Blase, L.X. Benedict, E.L. Shirley, S.G. Louie, Phys. Rev. Lett. **72**, 1878 (1994)
45. X. Zhao et al., Carbon **35**, 775 (1997)
46. N. Wang, Z.K. Tang, G.D. Li, J.S. Chen, Nature, vol. 408, p. 51 (2000)
47. L.-C. Qin, X. Zhao, K. Hirahara, Y. Miyamoto, Y. Ando, S. Iijima, Sinteza şi caracterizarea unor nanostructuri cu atomi de carbon 70. Nature **408**, 50 (2000)
48. L.-M. Peng, Z.L. Zhang, Z.Q. Xue, Q.D. Wu, Z.N. Gu, D.G. Pettifor, Phys. Rev. Lett. **85**, 3249 (2000)
49. I. Cabria, J.W. Mintmire, C.T. White, Phys. Rev., B 67, 121406(R)
50. P. Topala, S. Mazuru, B. Vitalie, P. Cosovschii, A.Ojegov, Application of EDI in increasing durability of glass moulding forms poansons. Proceedings of the 15th International Conference, Modern Technologies, Quality and Innovation. Vadul-lui-Vodă, Chişinău, V.II, 1093–1096 (2011). ISSN 2069-6736
51. P. Topala, B. Vitalie, L. Marin, *Decreasing Theadhesion Effect of Surfaces Using Graphite Pellicle Deposition Through Electric Discharges in Pulse.* Advanced Materials Research, vol. 1036 (Trans Tech Publications, Switzerland, 2014), pp. 172–177. doi:10.4028/www.scientific.net/AMR.1036.172
52. P. Topala, B. Vitalie, A. Ojegov, (2011). Application of pulsed electrical discharges with graphite tool-electrode. Machine building and techno-sphere of XXI century Proceedings of xviii International Scientific-Technical Conference, Donetsk, 2011, pp. 240–245
53. P. Topala, S. Mazuru, B. Vitalie, P. Cosovschii, P. Stoicev, Increasing the durabilitz of glass moulding forms applying graphite pillicles. Proceedings of the 14th International Conference, Modern Technologies, Quality and Innovation. Slănic-Moldova, 2010, pp. 635–638. ISSN 2066-3919
54. L. Marin, P. Topala, P. Stoicev, B. Vitalie, A. Ojegov, *Application of Graphite Micro-Pellicles for Superficial Adhesion Coefficient Decrease*. Engineering meridian, no.1, 2014, pp. 39–44
55. B. Vitalie, P. Topala, P. Stoicev, A. Ojegov, A. Hîrbu, D. Guzgan, *Some Experimental Investigations on the Corrosion of the Graphite Pellicles Formed by Pulsed Electrical Discharge Machining*. Engineering meridian, no.3, 2015, pp. 40–46

56. Y. Li, M. Guo, Z. Zhou, H. Min, Micro electro discharge machine with an inchworm type of micro feed mechanism. J. Int. Soc. Precis. Eng. Nanotechnol. **26**, 7–14 (2002)
57. P. Topala, V. Rusnac, B. Vitalie, A. Ojegov, N. Pînzaru, Physical and Chemical Effects of EDI Processing. Proceedings of International Conference NewTech 2011, Brno, Czech Republic. 14–15 septembrie, 2011. Part. Advances in non-traditional manufacturing, rapid prototyping and reverse engineering. p. 15
58. P. Topala, A. Hirbu, A. Ojegov, New directions in the practical application of electro erosion. Nonconventional Technol. Rev. no. 1/2011, 49–56. ISSN 1454-3087
59. P. Topala, V. Rusnac, B. Vitalie, A. Ojegov, N. Pînzaru, Physical and chemical effects of EDI processing. Internet J. Eng. Technol. vol. II, No. 2, Is.1. 6 p (2011). ISSN 1338–2357. http://www.i-jet.eu/journal_ijet/c_p_ijet1112.pdf
60. P. Topala, B. Vitalie, P. Stoicev, A. Ojegov, Application of electric discharges in impulse in micro and nano-technology. Proceedings of the 16th International Conference *Modern Technologies, Quality and Innovation−New* face of TMCR, vol. II, 24–26 May 2012, Sinaia, Romania, pp. 969-972. ISSN 2069-6736
61. P. Topala, D. Luca, A. Ojegov, P. Stoicev, N. Pinzaru, Results on metal surface nano-oxidation by electrical discharges in impulse. ICCCI 2012. The Fourth International Conference on the Characterization and Control of Interfaces for High Quality Advanced Materials. Kurashiki, Japan. September 2–5, 2012. p. 85

Chapter 4
Structural and Physical Properties of ZnS_xSe_{1-X} Thin Films

Mihail Popa

Abstract ZnS_xSe_{1-x} thin films with various x values in the range from 0 to 1 were prepared by vacuum evaporated technique on glass substrates using powders of ZnS and ZnSe. The structure, surface morphology and composition of thin films have been investigated by XRD, SEM and EDAX techniques. The composition analysis and the diffraction patterns revealed that ZnS_xSe_{1-x} thin films are nearly stoichiometric and have a cubic zinc blende type structure, with a strong orientation of the crystallite along the crystalline plane (111). The temperature dependence of electrical conductivity measured in a temperature range of 300–500 K demonstrated that the films are of n-type conductivity. The thermal activation energy was evaluated from electrical measurements, and the transparency of films in the wavelength range of 380–1100 nm has been demonstrated from oprical measurements. The lifetime of nonequilibrium charge carriers was determined from the relaxation curves of photoconductivity and photoluminescence, and the energy levels of recombination and trapping centers have been determined from the spectral dependence of photoluminescence and thermoluminesce.

4.1 Introduction

The materials for the contemporary optical systems for the visible and infrared wavelength range must have high values of mechanical strength, hardness, high transmission coefficient, optical homogeneity, erosion resistance and thermal stability.

$A^{II}B^{VI}$ wide band gap semiconductor compounds are attractive due to many applications in electronic and optoelectronic nanostructured devices. ZnS and ZnSe polycrystalline semiconductors are perspective materials, which have found many applications in preparing of optical elements working in the visible and infrared. The solid solutions of ZnS_xS_{1-x} ($0 < x < 1$) are much less studied. The interest for

M. Popa (✉)
"Alecu Russo" Balti State University, Balti, Moldova
e-mail: miheugpopa@yahoo.com

© Springer International Publishing Switzerland 2016

I. Tiginyanu et al. (eds.), *Nanostructures and Thin Films for Multifunctional Applications*, NanoScience and Technology,
DOI 10.1007/978-3-319-30198-3_4

the preparation and investigation of physical properties of zinc sulfurselenides is determined by the possibility to vary their physical properties by changing their composition. ZnS_xSe_{1-x} semiconductor materials should combine the high optical characteristics of ZnSe and the mechanical resistance of ZnS. It is interesting to use zinc sulfurselenides as materials for gradient optics.

In the specialized literature there is some information about the use of ZnS_xSe_{1-x} polycrystalline thin films in a variety of optoelectronic applications, such as lasers or laser diodes functioning in the blue spectral range [3] as well as heterojunctions of solar cell [4, 5]. As concerns the environmental protection, ZnS_xSe_{1-x} nanostructured composites are alternative materials for the production of window-layers and buffer-layers for photovoltaic applications, replacing the CdS which is a toxic material [1, 6].

The purpose of this paper is to present the results of research on the structure and surface morphology, electrical, optical and luminescent properties of ZnS_xSe_{1-x} thin films obtained by thermal vacuum evaporation in quasi-closed volume.

4.2 Preparation of ZnS_xSe_{1-X} Thin Films by Thermal Evaporation Method in Vacuum, in Quasi-Closed Volume

Glass substrates of different dimensions (1.5 × 1.5 cm, 1.5 × 3.5 cm and 2.0 × 4.0 cm) were used for the preparation of thin films. During the evaporation they were maintained at different temperatures (300–500 K). For cleaning, the substrates were immersed into a chromic mixture for 24 h. Then, they were removed and rinses with distilled water for several times. To remove traces of salts, the substrates were also rinsed in ethyl alcohol (98 %) and distilled water, and were left to dry.

As a starting material we used powders of ZnSe (with purity 99.9 %) and ZnS (with purity 99.9 %) which were mixed at various concentrations (x = 0, 0.2, 0 4; 0.5; 0.6; 0.8; 1.0).

An automatic installation for thermal vacuum evaporation of UVH-70A-1 type was used for the preparation of thin films. The powder mixtures were poured into tungsten evaporators made in form of a tray. ZnSe and ZnS crystals were deposited onto the substrate by vaporisation (sublimation) of the source material by heating.

ZnS_xSe_{1-x} thin layers with various values of x have been obtained. The substrate-evaporator distance has been modified between 70 and 120 mm. The substrate temperature during deposition varied between 300 and 500 K, and the evaporator temperature varied between 1000 and 1500 K. There were obtained films with thickness between 0.2 and 1.0 μm.

Measurement cells with electrodes in the form of thin films with thicknesses of 1–2 μm were used for the study of temperature dependence of the electrical conductivity (Fig. 4.1a, b). The distance between the electrodes varied between 2–5 mm.

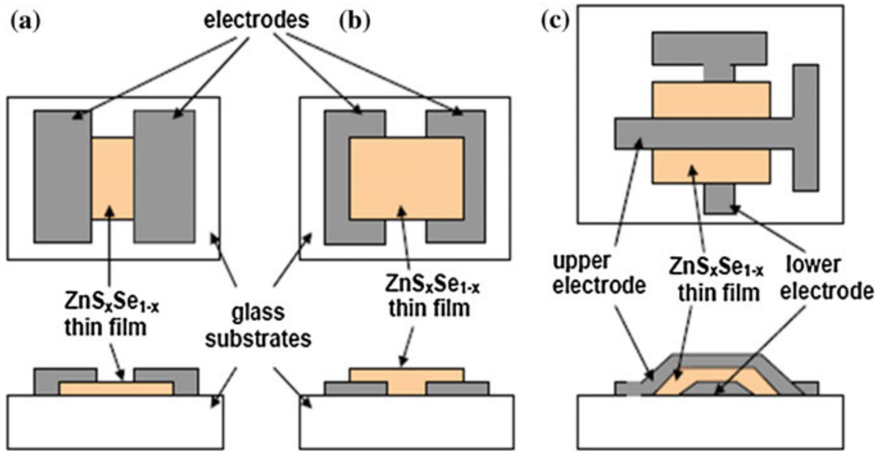

Fig. 4.1 Surface type cells (**a**, **b**) and sandwich type (**c**)

A device with sandwich type cells was used for the study of current-voltage characteristic features (Fig. 4.1c). The sandwich cells were prepared by the deposition of the first In electrode on a glass substrate, followed by the deposition of ZnS_xSe_{1-x} thin films, and finally by the deposition of the second electrode in the direction perpendicular to the first electrode.

4.3 The Structure and Surface Morphology of ZnS_xSe_{1-x} Thin Films

The crystalline structure of the ZnS_xSe_{1-x} thin films was studied by X-ray diffraction using CuK_α radiation (λ = 1.5418 Å). It was found that the layers are polycrystalline and have a cubic structure of zinc blende type, with a strong orientation of the crystallites of the planes (111) parallel to the support surface (Figs. 4.2 and 4.3). The position of this peak deviates from $2\theta = 27{,}297^0$ (for $x = 0$) to the $2\theta = 28{,}612^0$ (for $x = 1$) (Table 4.1).

The parameter of cubic lattice for ZnS_xSe_{1-x} thin films was determined by the relationship [2]

$$a = \frac{\lambda}{2\,sin\,\theta}\sqrt{(h^2 + k^2 + l^2)}, \tag{4.1}$$

where λ is the wavelength of CuK_α radiation (λ = 1.5418 Å) and h, k, l are the Miller indices of the plane (111). The values obtained are in the range a = 5.658 Å (for $x = 0$) and a = 5.406 Å (for $x = 1$) (Table 4.1). Venkata Subbaiah and Ramakrishna Reddy [3] reported similar values of the crystal lattice parameter for similar layers.

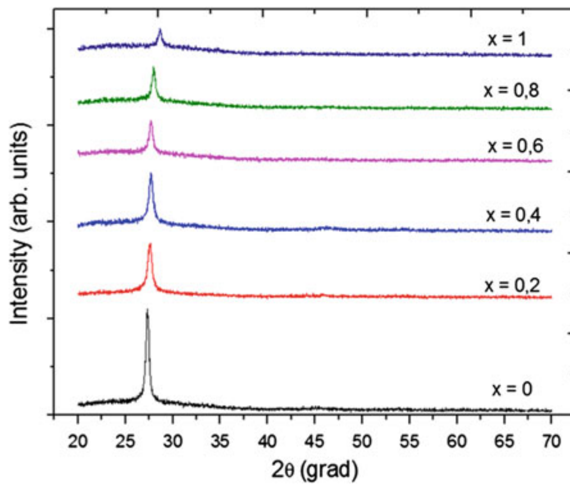

Fig. 4.2 The evolution of diffractograms for ZnS_xSe_{1-x} thin films

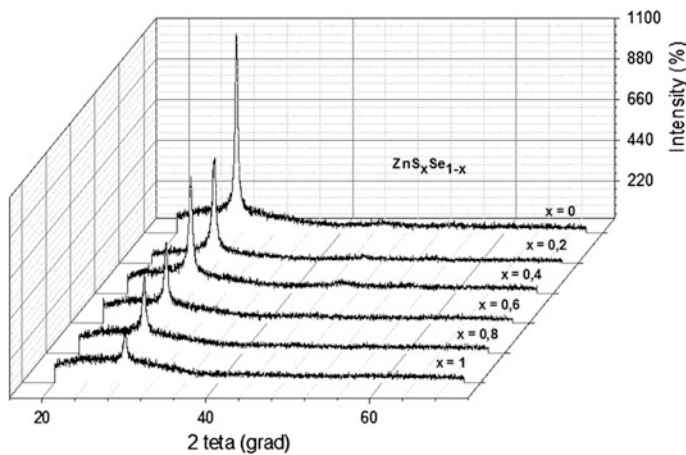

Fig. 4.3 *XRD* analysis for ZnS_xSe_{1-x} thin films

The formula for calculating of the distance between parallel and equidistant planes that have Miller indices (*hkl*) is [2]

$$d_{hkl} = \frac{n\,\lambda}{2\,sin\,\theta}. \quad (4.2)$$

The interplanar distance value for ZnS_xSe_{1-x} thin films was determined using this relationship. The values obtained are in the range of $d_{hkl} = d_{111} = 3.267$ Å (for $x = 0$) and $d_{111} = 3.121$ Å (for $x = 1$) (Table 4.1).

Table 4.1 The experimental values of the cubic structure of ZnS_xSe_{1-x} thin films

x	2*θ*, grad	*FWHM*	*a*, nm	d_{111}, nm (*form.* 2)	d_{111}, nm (*form.* 3)
0	27.297	0.4092	5.658	3.267	3.27
0.2	27.423	0.4336	5.634	3.253	3.25
0.4	27.658	0.4654	5.586	3.226	3.23
0.5	27.801	0.4977	5.559	3.209	3.21
0.6	27.952	0.5290	5.529	3.192	3.19
0.8	28.273	0.5663	5.473	3.160	3.16
1.0	28.612	0.6143	5.406	3.121	3.12

The interplanar distance can be calculated directly using the formula for the cubic system [2]

$$d_{hkl} = \frac{a}{\sqrt{h^2 + k^2 + l^2}} \quad (4.3)$$

For the plane (111), we obtain $d_{111} = a/(1^2 + 1^2 + 1^2)^{1/2} = a/3^{1/2}$. By using cubic lattice parameter values, calculated according to the (4.1) we have obtained interplanar distance values between $d_{111} = 3.270$ Å (for $x = 0$) and $d_{111} = 3.120$ Å (for $x = 1$). Venkata Subbaiah et al. [3], Ambrico et al. [4] obtained similar values of interplanar distances for the respective thin films.

The SEM image of ZnS_xSe_{1-x} thin film surface is shown in Fig. 4.4. It is noted that the sample shows small crystallites, and their shape and dimensions are similar. The image indicates the growth of a "columnar" layer (column-shaped crystallites have grown perpendicularly to the support). The roughness of layers determined by scanning electron microscopy is between 2 and 6 nm. The average crystallite size as determined by scanning electron microscopy varied between 3.60 and 2.20 Å.

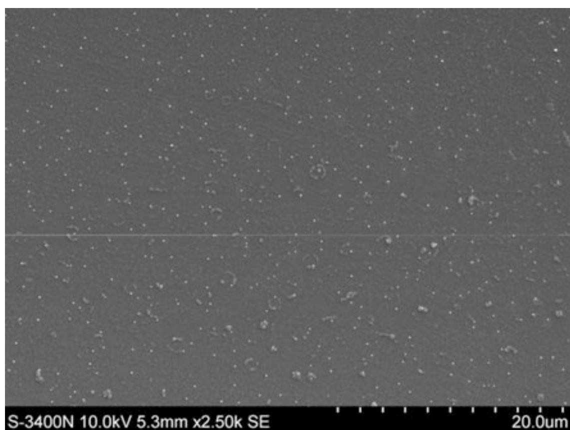

Fig. 4.4 SEM image of $ZnS_{0.2}Se_{0.8}$ thin film

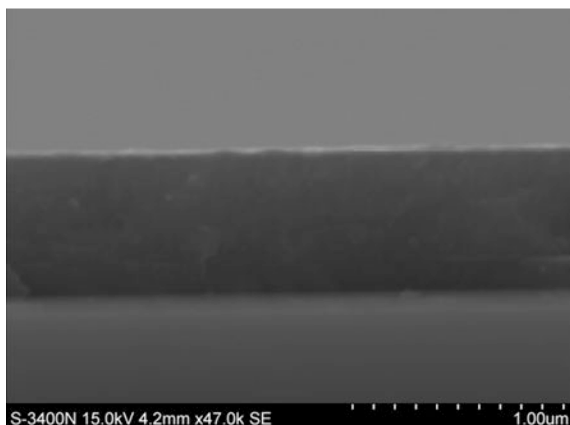

Fig. 4.5 SEM image of fractionated $ZnS_{0.2}Se_{0.8}$ thin film

Figure 4.5 presents the cross-section view of a thin ZnS_xSe_{1-x} layer. It notes that the layer structure is uniform and compact. The thickness of the thin film was determined from this figure.

The EDAX diagrams for ZnS_xSe_{1-x} thin layers are presented in Fig. 4.6, while the initial and the final atomic percentage of chemical elements in the obtained thin layers are shown in Table 4.2. The composition of chemical elements of ZnS_xSe_{1-x} semiconductor compounds is confirmed with an error of about 2–4 %. The presence of a small amount of carbon impurity in the obtained structures is probably due to the amorphous glass substrates which contain this element in their structure.

4.4 The Electrical Properties of ZnS_xSe_{1-X} Thin Films

The study of the influence of temperature on the electrical conductivity of the semiconductor thin films provides information about the conduction mechanisms as well as about possible structural changes that may occur in the layer during the heating process.

The temperature dependence of the electrical conductivity of ZnS_xSe_{1-x} thin films was studied during a thermal treatment consisting of a series of successive heating and cooling processes (temperature rate of 6 K/min) performed in the temperature range of 300–500 K.

The dependencies $ln\sigma = f(10^3/T)$ for some ZnS_xSe_{1-x} polycrystalline thin films (d = 0.15–0.99 μm) are shown in Figs. 4.7, 4.8 and 4.9. The films were prepared by vacuum evaporation method on unheated glass substrate (T_{sub} = 300 K), with the rate of deposition r_d = 1.3–1.6 nm.

A sharp increase of electrical conductivity takes place during the first heating process. During the first cooling and the next cycle of heating and cooling, the curves become reversible and present two distinct parts:

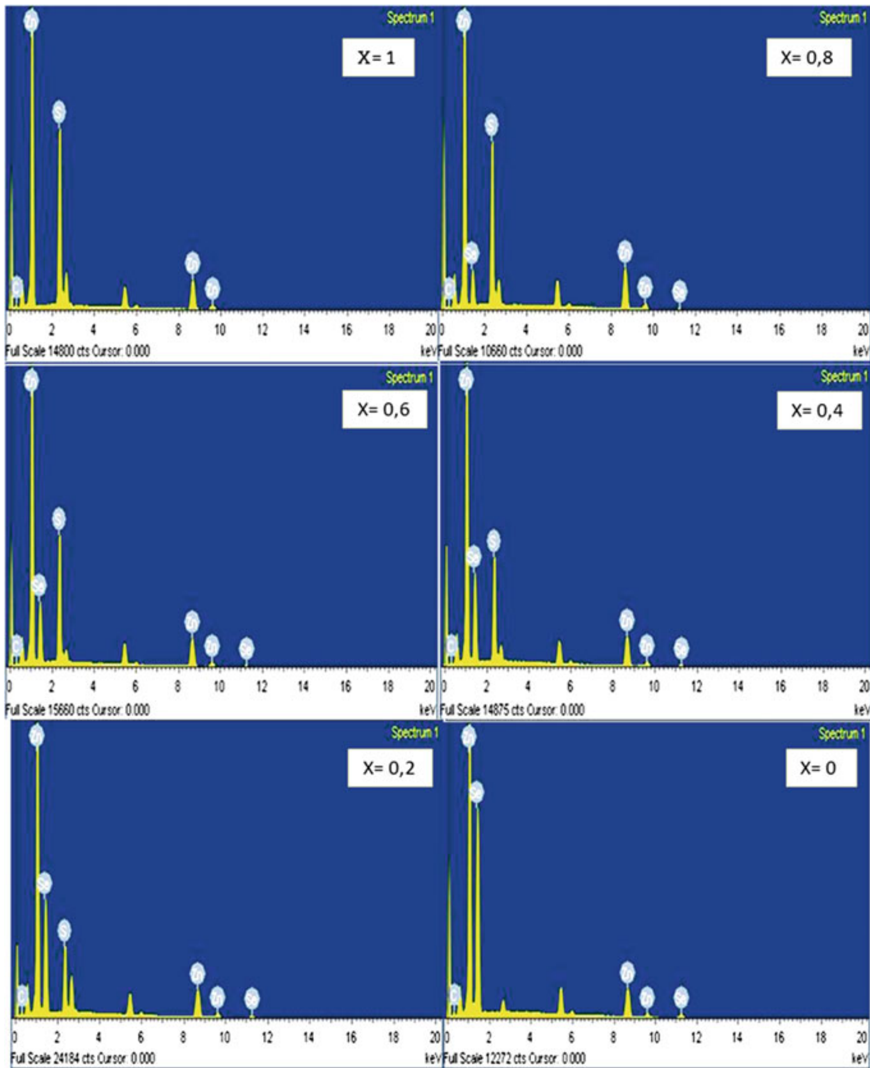

Fig. 4.6 EDAX images for ZnS_xSe_{1-x} thin films

- the first part in the range of low temperatures suggests that the films exhibit extrinsic conduction;
- the second part in the range of high temperatures corresponds to intrinsic conduction.

Figure 4.10 presents the dependencies $ln\ \sigma = f\ (10^3/T)$ (second heating) for all the films with the values of x = 0; 0.2; 0.4; 0.5; 0.6; 0.8; 1.0. It is observed that with increasing x the conductivity moves to lower values and the slope of this

Table 4.2 Atomic percentage of the elements of EDAX analysis

ZnS_xSe_{1-x}	Zn (%)		S (%)		Se (%)		C (%)
	Teoretic	Exper.	Teoretic	Exper.	Teoretic	Exper.	Experimental
ZnS	50	52.2	50	46.0	–	–	1.8
$ZnS_{0.8}Se_{0.2}$	50	52.0	40	35.9	10	10.1	2.0
$ZnS_{0.6}Se_{0.4}$	50	51.6	30	27.7	20	18.9	1.8
$ZnS_{0.5}Se_{0.5}$	50	51.5	25	22.8	25	23.2	2.5
$ZnS_{0.4}Se_{0.6}$	50	50.9	20	19.1	30	28.2	2.4
$ZnS_{0.2}Se_{0.8}$	50	50.6	10	9.6	40	37.8	2.0
ZnSe	50	50.3	–	–	50	47.1	2.0

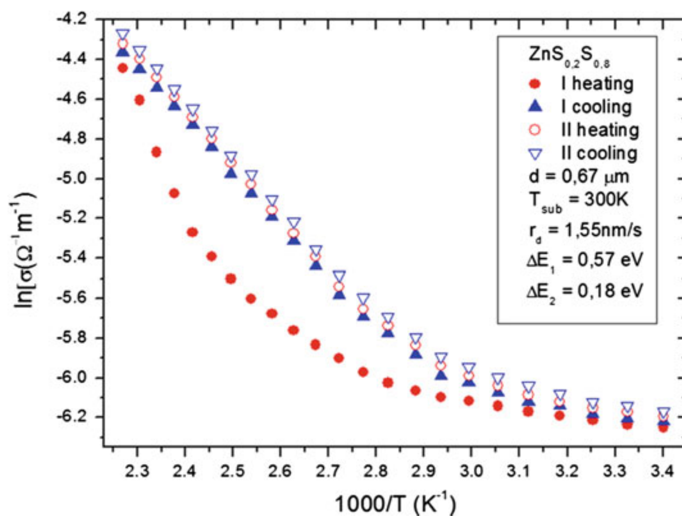

Fig. 4.7 The temperature dependence of the electrical conductivity for $ZnS_{0.2}Se_{0.8}$ sample

dependence increases. The thermal activation energy can be determined from the slope of the curves $ln\ \sigma = f\ (10^3/T)$ in the intrinsic and extrinsic conductivity acording to the relation

$$\Delta E = 0{,}1725 \frac{\lfloor ln\,\sigma_2 - ln\,\sigma_1 \rfloor}{\left(\frac{10^3}{T_1} - \frac{10^3}{T_2}\right)}\ \text{eV}. \tag{4.4}$$

The values of ΔE_1 determined in the field of intrinsic conduction (the temperature range T > 300 K) (Fig. 4.10) vary from 0.43 eV (for x = 0) up to 1.89 eV (for x = 1) (Table 4.3). These values are in good agreement with those found by other authors [3–6].

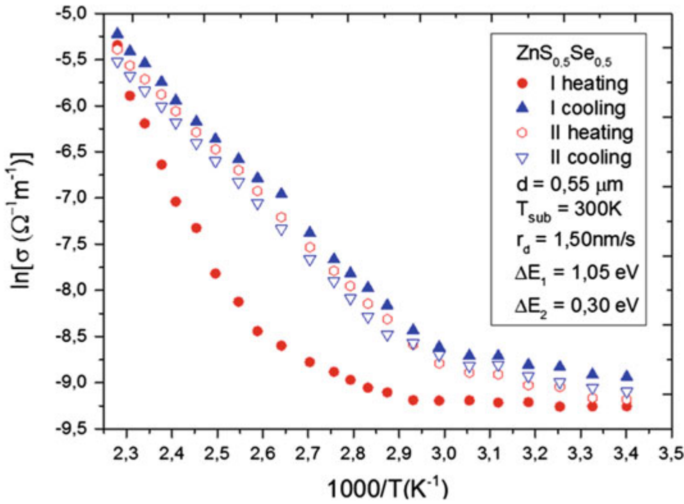

Fig. 4.8 The temperature dependence of the electrical conductivity for $ZnS_{0.5}Se_{0.5}$ sample

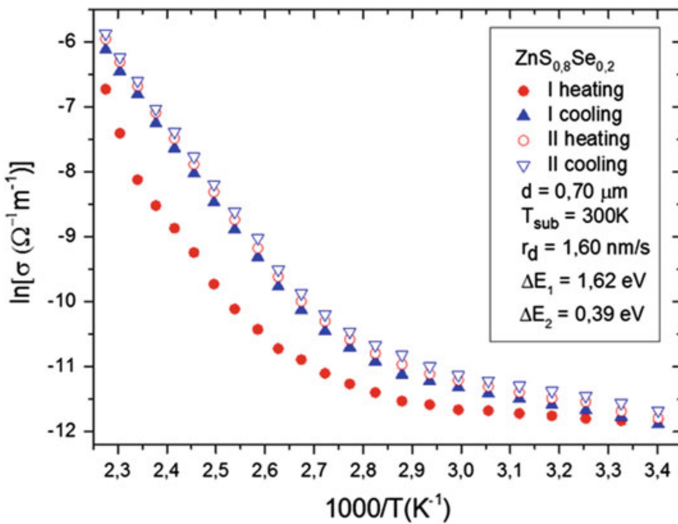

Fig. 4.9 The temperature dependence of the electrical conductivity for $ZnS_{0.8}Se_{0.2}$ sample

The presence of the part related to the extrinsic conduction in the dependencies $ln\sigma = f(10^3/T)$ suggests that additional energy levels located deep within the band gap are present in the studied layers. Interstitial zinc atoms (Zn_i) and selenium vacancies (V_{Se}) are native defects in ZnSe crystals. The energy levels of the Zn_i donor are located below the botom of conduction band ($\Delta E_d = 0.90$ eV) [7], and acceptor levels of V_{Se} are located above the top edge of the valence band

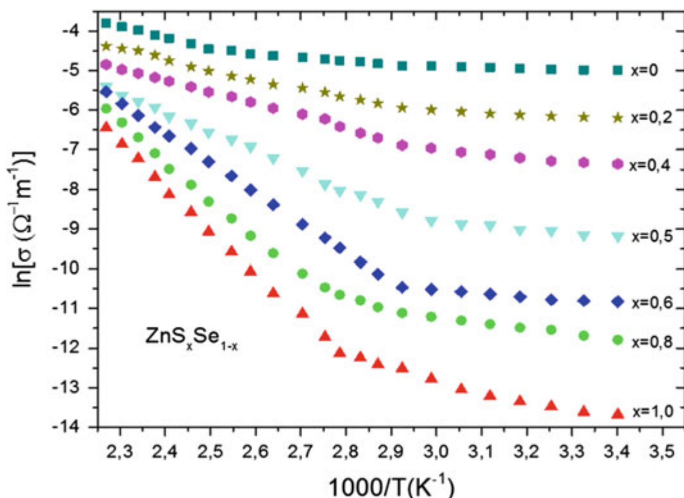

Fig. 4.10 The dependence type lnσ = 10^3/T (II heating) of ZnS_xSe_{1-x} thin films

Table 4.3 The values of thermal activation energy of ZnS_xSe_{1-x} thin films

x	0	0.2	0.4	0.5	0.6	0.8	1.0
ΔE_1, eV	0.43	0.57	0.74	1.05	1.34	1.62	1.89
ΔE_2, eV	0.13	0.18	0.24	0.30	0.34	0.39	0.43

($\Delta E_a = 0.01$ eV) [8, 9]. The shallow impurities (donors and acceptors) are ionized in the temperature range $k_BT = 0.026$–0.043 eV [8, 9], and the Fermi level is located near the middle of band gap.

From the slopes of the curves $ln\sigma = f(10^3/T)$ in the range of extrinsic conduction (Fig. 4.10), the values of thermal energy activation were determined, ΔE_2, which ranges from 0.13 and 0.43 eV, in the temperature range of T < 300 K (Table 4.3). Probably, these values can be attributed to a complex defect—impurity of the type Zn_i-V_{Se} [7].

Very low values of the thermal activation energy ΔE_2, obtained at low temperature, indicate that the hopping conduction mecanism can be the dominant in these layers, and conduction can be explained on the basis of the Efros-Shklovskii and Mott models for hopping transport in thin layers with high resistance at low temperature [10].

To get new information about the nature of electrical conduction mechanism of thin ZnS_xSe_{1-x} layers, current-voltage characteristics of sandwich systems metal—semiconductor—metal were studied for a large number of samples prepared under different experimental conditions (Fig. 4.1c).

The current-voltage characteristics of the In–$ZnS_{0.5}Se_{0.5}$–In system are shown in Fig. 4.11. Two distinct parts can be distinguished in these charcteristics:

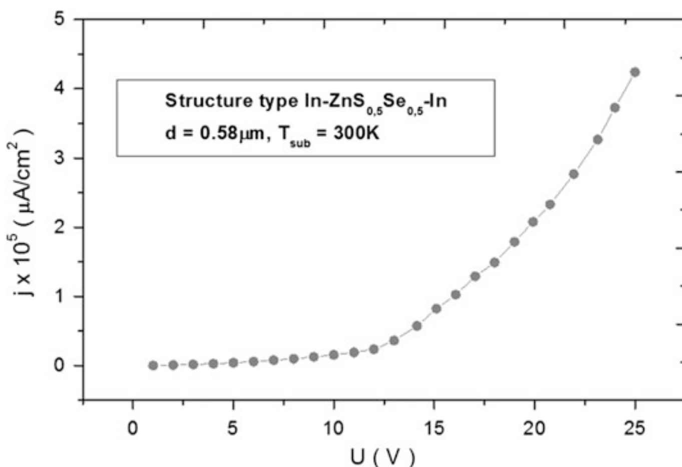

Fig. 4.11 The current-voltage characteristics of structure type In–$ZnS_{0.5}Se_{0.5}$–In

- the first part, which is characterized by a linear dependence of the current intensity upon the applied voltage, and which complies Ohm's law;
- the second part, which has a nearly exponential increase in the intensity of the current with increasing the applied voltage.

If the conduction mechanism is Richardson-Schottky type, current density is expressed by the relationship (4.8, 4.9)

$$I_{RS} = AT^2 \left[exp\left(-\frac{\Phi_0}{k_B T} \right) \right] exp\left[\frac{1}{k_B T} \left(\frac{e^3 U}{4\pi\varepsilon_0\varepsilon_r d} \right)^{1/2} \right]. \tag{4.5}$$

where A is the Richardson Dushman "effective" constant

$$A = \frac{4\pi m_\theta e k_B^2}{h^2}, \tag{4.6}$$

and Φ_0 is the potential barrier height at the metal-semiconductor interface and m_e is the effective mass of charge carriers.

Logarithm of expression (4.5) gives

$$lnJ_{RS} = ln\left(AT^2\right) - \left(-\frac{\Phi_0}{k_B T} \right) + \left[\frac{1}{K_B T} \left(\frac{e^3 U}{4\pi\varepsilon_0\varepsilon_r d} \right)^{1/2} \right]. \tag{4.7}$$

The current-voltage characteristics for the investigated samples, represented in the Schottky coordinates (lnJ, $U^{1/2}$), are also linear. By extrapolating the linear

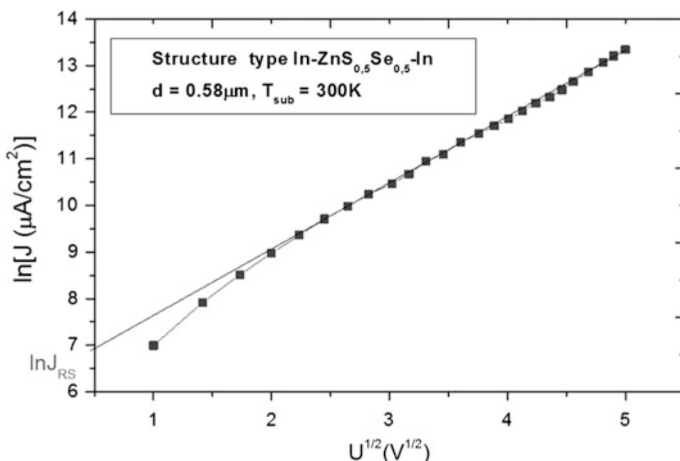

Fig. 4.12 Dependence lnJ = f ($U^{1/2}$) of sandwich system type In–$ZnS_{0.5}Se_{0.5}$–In

segment of the curve $lnJ = f(U^{1/2})$ (Fig. 4.12) for $\sqrt{U} \to 0$, one can determine the height of the potential barrier at the metal-semiconductor interface

$$\Phi_0 = k_B T \left[ln(AT^2) - lnJ_{RS} \right]. \tag{4.8}$$

Table 4.4 shows some values of Φ_0 calculated for several In–$ZnS_{0.5}Se_{0.5}$–In samples. The values found for Φ_0 correlate well with those found for ZnSe and ZnS crystals [7–9]. This can be explained by the fact that the electrical conduction mechanism is less affected by the contact between crystallites in sandwich systems.

4.5 The Optical Properties of ZnS_xSe_{1-x} Thin Films

The transmission spectrums of the ZnS_xSe_{1-x} thin films have been recorded in the spectral range of 330–1750 nm, using a spectrophotometer Hitachi U-3400.

Table 4.4 The values of potential barrier height of systems type In–ZnS_xSe_{1-x}–In

x	d (μm)	lnJ_{RS} (μA/cm^2)	Φ_0 (eV)
0	0.55	6.20	0.677
0.2	0.67	7.50	0.677
0.4	0.77	8.75	0.678
0.5	0.55	8.50	0.678
0.6	0.50	9.10	0.678
0.8	0.60	8.90	0.679
1.0	0.80	9.30	0.679

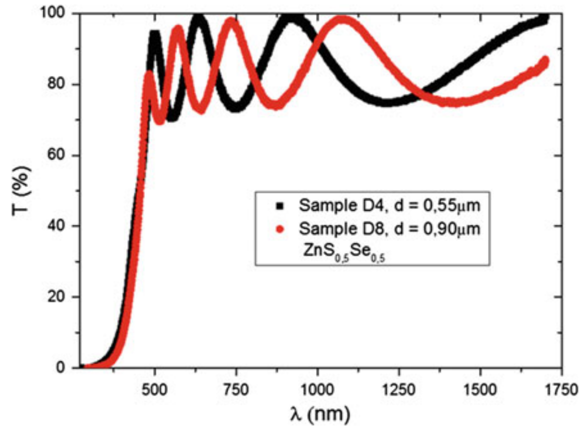

Fig. 4.13 Evolution depending on the thickness of the transmission spectra of $ZnS_{0.5}Se_{0.5}$ thin films

The transmission spectra for two $ZnS_{0.5}Se_{0.5}$ thin films with different thicknesses are shown in Fig. 4.10. The transmission of samples D4 and D8 (Fig. 4.13) increases sharply to a peak value and then decreases slowly in the range of 500–600 nm, after which the evolution of spectra depends on the thickness of samples. Three interference maxima appear in the sample D4 with thickness d = 0.5 µm (Fig. 4.13), while in the sample D8 with thickness d = 0.9 µm there are five maxima. The transmission spectra for the samples with thicknesses greater than 1 µm are formed of a combination of maxima and minima, and the difference between the maximum and minimum transmission decreases with the increase of thin films thickness.

The presence in the transmission spectra of maxima and minima due to the interference of beams reflected at the layer surfaces is an indication that the samples are uniform from the point of view thickness and the layer surfaces are flat. This was also highlighted by the scanning electron microscopy studies (Figs. 4.3 and 4.4), which showed that the roughness of the free surface of the layer is small. A high roughness or irregularity of thickness would lead to the disappearance of interference, namely to the disappearance of minima and maxima in the transmission spectra.

Another analysis was based on the increased concentration of S and the decreased concentration of Se (Fig. 4.14). It is observed that edge transmission spectrum is moving in the lower wavelength region from 420 to 300 nm with increasing the *x* value.

The reflection spectra of ZnS_xSe_{1-x} thin films were measured in the spectral range of 330–1100 nm, using the Hitachi spectrophotometer U-3400. The reflection spectrum of $ZnS_{0.5}Se_{0.5}$ thin films is presented in Fig. 4.12. One can observe that the reflection does not exceed 0.5 % in the wavelength range of 380–1080 nm, while the transmission is between 75–97 % (Fig. 4.15). This tells us that the layers are transparent and the absorption of electromagnetic waves in these layers is also quite small. It is also found that the transmission maxima coincide with the reflection minima, which demonstrates the presence of the interference in the respective films.

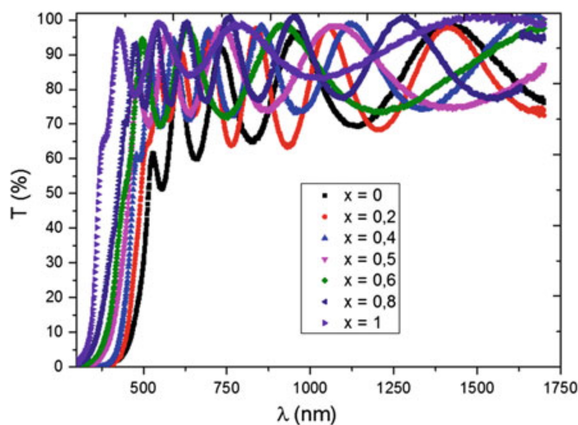

Fig. 4.14 Evolution depending on x of transmission spectra of ZnS_xSe_{1-x} thin films

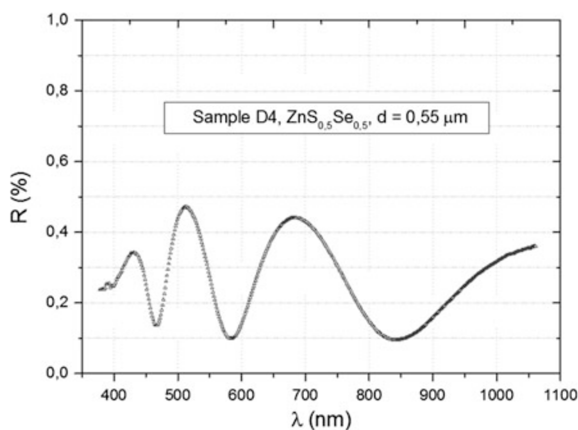

Fig. 4.15 The reflectance spectra of $ZnS_{0.5}Se_{0.5}$ thin films

The absorption coefficient of the ZnS_xSe_{1-x} thin film was calculated from the transmission spectrum (considering the very low reflection of layers) using the formula:

$$\alpha = \frac{1}{d} ln \frac{1}{T}. \tag{4.9}$$

Figure 4.16 presents the absorption spectra of seven polycrystalline ZnS_xSe_{1-x} thin films. It is observed that the absorption edge moves to higher energies from 2.25 up to 3.35 eV with increasing of x value.

In the range of low photon energies, the absorption coefficient has a value different from zero, which can be attributed to the light absorption at the boundaries between crystallites [11]. The high values of the absorption coefficient at photon energies below the fundamental absorption edge may be due to structural defects,

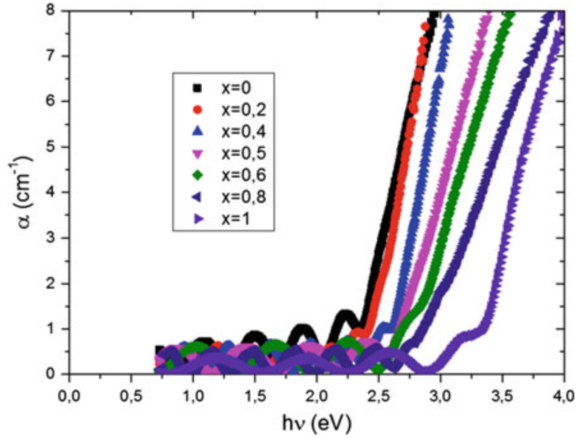

Fig. 4.16 The absorption spectra of ZnS_xSe_{1-x} thin films

which determine the appearance of localized levels in the band gap, leading to electronic transitions as a result of the absorption of incident radiation.

The authors of the paper [11] have explained the form of the absorption spectra by small roughness of the thin film, which leads to the idea of small crystallite size and high degree of crystallization.

For materials with direct band gap we can write the Tauc relationship [11]:

$$\alpha h\nu = A(h\nu - E_g)^{1/2}, \tag{4.10}$$

where A is a constant which is different for different transitions. The presentation of data in coordinates $(\alpha h\nu)^2 = f(h\nu)$ gives a linear dependence. By extrapolating this dependence to $(\alpha h\nu)^2 \rightarrow 0$ one can determine the width of the band gap (E_g) at the given temperature.

The dependencies $\alpha^2(h\nu)^2 = f(h\nu)$ for seven ZnS_xSe_{1-x} thin films are shown in Fig. 4.17. The increase of the thickness of samples leads to increasing the optical absorption and, respectively, the optical band gap deduced from the linear dependence $\alpha^2(h\nu)^2 = f(h\nu)$. The found values of E_g = 2,68–3,50 eV are in good agreement with those established for ZnSe and ZnS crystals [7–9].

Similarly, one can plot the graph

$$\left[h\nu \cdot ln\left(\frac{R_{max} - R_{min}}{R - R_{min}}\right)\right]^2 = f(h\nu), \tag{4.11}$$

where R_{max} and R_{min} are the maximum and minimum of the reflectance spectrum. For the ordinate null value $\left[h\nu \cdot ln\left(\frac{R_{max}-R_{min}}{R-R_{min}}\right)\right]^2 \Rightarrow 0$, the intersection of extrapolated straight line with the ordinate gives the band gap width E_g.

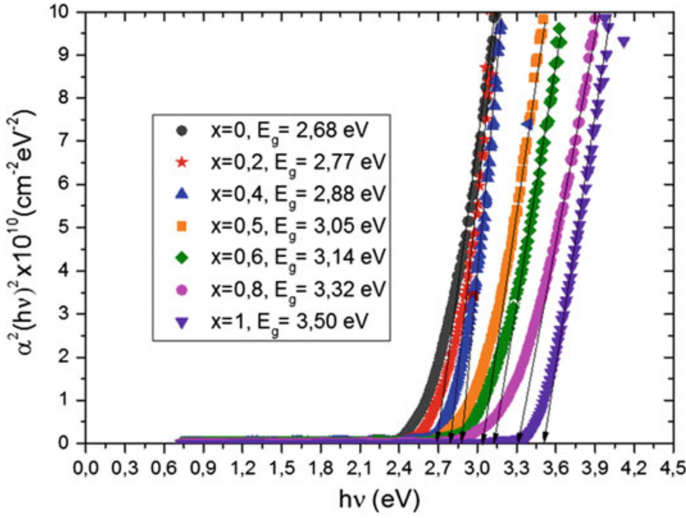

Fig. 4.17 Dependencies $a^2(h\nu)^2 = f(h\nu)$ of ZnS_xSe_{1-x} thin films

The dependencies $\left[h\nu \cdot ln\left(\frac{R_{max}-R_{min}}{R-R_{min}}\right)\right]^2 = f(h\nu)$ for six ZnS_xSe_{1-x} thin films are presented in Fig. 4.18a–f. The values of the band gap between 2.65 and 3.50 eV were obtained by using the method described above.

For comparison, in Table 4.5 are shown the E_g values determined from the reflectance spectra, from absorption spectra and the theoretical values. We note that these values are in good agreement.

The refractive index of the thin film was determined from the transmission spectra using the "envelope" method [12, 13] proposed by R. Swanepoel. The steps of calculating the index of refraction for ZnS_xSe_{1-x} thin films were the following:

(a) Calculation of the refractive index of the substrate, n_s, from its transmission spectrum, $T_{sub} = f(\lambda)$ using the relations [12, 13]

$$n_S = \frac{1}{T_{sup}} - \left(\frac{1}{T_{sup}^2} - 1\right)^{1/2}; \quad (4.12)$$

(b) Plotting windings of interference minima and maxima of the transmission spectrum of a thin film $T = f(\lambda)$ and determining the wavelength for each pair of values T_M and T_m;

(c) Calculation of the coefficient N using the relationship:

$$N = 2n_S \cdot \frac{T_M - T_m}{T_M \cdot T_m} + \frac{n_S^2 + 1}{2}. \quad (4.13)$$

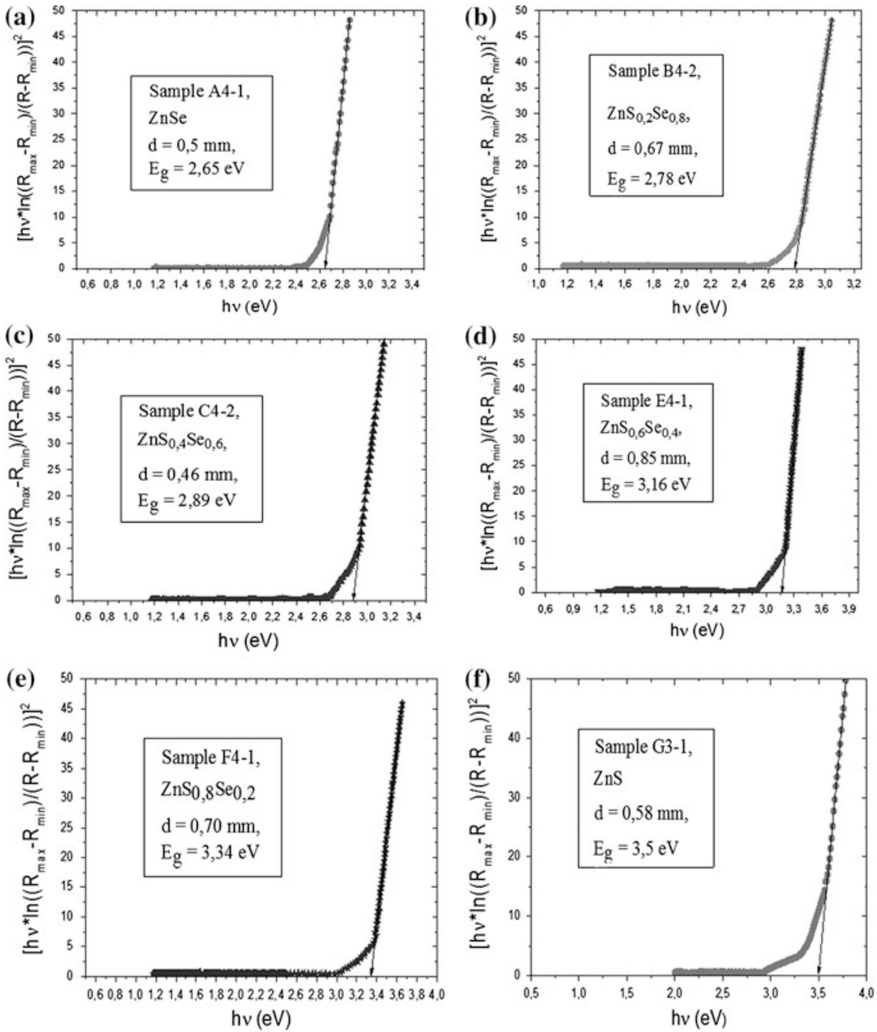

Fig. 4.18 The evolution of width of band gap Eg depending on x for ZnS_xSe_{1-x} thin films

(d) Calculation of n values, using the formula:

$$n = \left[N + \left(N^2 - n_s^2\right)^{1/2}\right]^{1/2}, \tag{4.14}$$

The dispersion of the refractive index of ZnS_xSe_{1-x} thin films is presented in Fig. 4.19. Depending on the increase of concentration of S and the decrease of concentration of Se, the refractive index of the respective layers decreases from 2.95

Table 4.5 Comparison of theoretical and experimental values of E_g

Type of semiconductor	Energy band gap, E_g		
	Theoretical	Determined from absorption spectra	Determined from reflection spectra
ZnSe	2.7	2.68	2.65
$ZnS_{0.2}Se_{0.8}$		2.77	2.78
$ZnS_{0.4}Se_{0.6}$		2.88	2.89
$ZnS_{0.5}Se_{0.5}$		3.05	3.06
$ZnS_{0.6}Se_{0.4}$		3.14	3.16
$ZnS_{0.8}Se_{0.2}$		3.32	3.34
ZnS	3.5	3.50	3.50

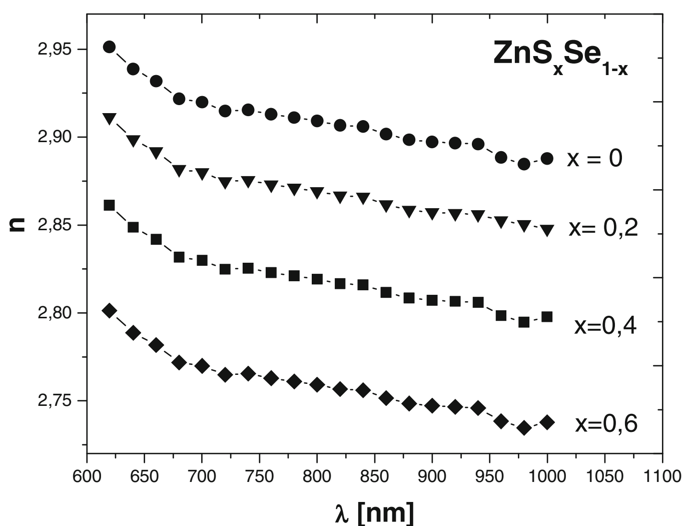

Fig. 4.19 The dispersion of refractive index for ZnS_xSe_{1-x} thin films

(for the sample with $x = 0$) to 2.80 (for the sample with $x = 0.6$). These values are in good agreement with those reported in literature for ZnSe and ZnS crystals [7, 8].

In the frame of a single oscillator model [14], the dispersion of the refractive index in the region of transparency (for photon energies lower than the width of the band gap) can be described by the equation

$$n^2 - 1 = \frac{E_0 E_d}{E_0^2 - (h\nu)^2}, \quad (4.15)$$

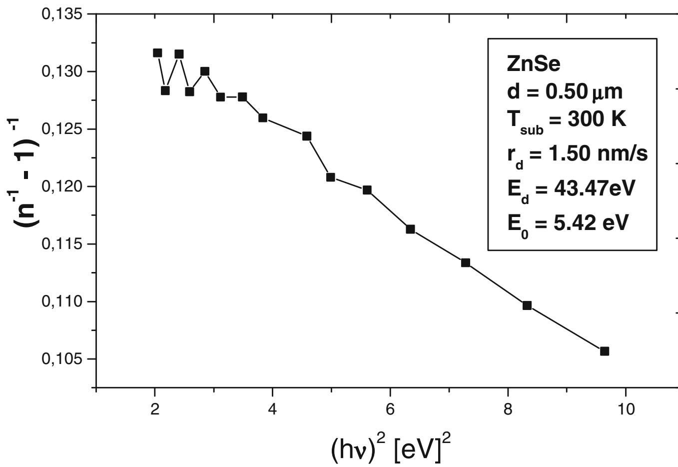

Fig. 4.20 The dependence type 1/(*n*-1 – 1) = *f*(*hν*)2 for ZnSe sample

Table 4.6 Parameters a single oscillator model

ZnS_xSe_{1-x}	Thickness of films d (μm)	Substrate temperature T_{sub} (K)	Deposition rate r_d (nm/s)	E_d (eV)	E_0 (eV)
0	0.50	300	1.50	43.47	5.42
0.2	0.67	300	1.43	45.90	5.56
0.4	0.25	300	1.50	47.35	5.80
0.6	0.50	300	1.60	50.06	6.32
0.8	0.15	300	1.55	52.83	6.70
1	0.50	300	1.55	55.58	6.93

where E_0 is a parameter which value is equal to about double the width of the band gap ($E_0 \cong 2E_g$) and E_d is a dispersion parameter.

Figure 4.20 presents the dependence $1/(n^{-1} - 1) = f(h\nu)^2$ for ZnSe thin films on the glass. The respective values of E_d and E_0 are obtained from the slope of the linear dependence. The values for other ZnS_xSe_{1-x} thin layers are summarized in Table 4.6.

4.6 The Luminescent Properties of ZnS_xSe_{1-X} Thin Films

In direct band gap semiconductors, such as ZnSe and ZnS crystals, the band to band electronic transitions are vertical and, therefore, for the emergence of intrinsic photoconductivity the incident photon energy *hν* should be equal or larger than the width of the band gap.

For an n-type semiconductor, electrical conductivity caused by the nonequilibrium carriers (photoconductivity) is written as:

$$\Delta\sigma = e\mu_n \Delta n. \tag{4.16}$$

where Δn is the nonequilibrium electron concentration, μ_n is the electron mobility, e is the electron charge.

The decay of the photoconductivity after the light is turn off is desribed for the case of linear recombination by the formula

$$\Delta\sigma = \Delta\sigma_{st} e^{-\frac{t}{\tau}}, \tag{4.17}$$

where $\Delta\sigma_{st}$ is the stationary photoconductivity, τ is the carrier lifetime.

The lifetime characterizes the decrease in the concentration of non-equilibrium carriers, and it is an important parameter in describing the phenomenon of photoconductivity.

Figure 4.21a–e presents the relaxation curves of photoconductivity of $ZnS_{0.5}Se_{0.5}$ thin films measured at different temperatures. Note that the stationary photoconductivity $\Delta\sigma_{st}$ decreases with increasing the sample temperature. This is explained by the fact that the recombination probability ($R \sim \alpha$) is higher at higher temperatures.

The dependencies of $\ln(\Delta\sigma/\Delta\sigma_{st}) = f(t)$ calculated from the relaxation curves of the $ZnS_{0.5}Se_{0.5}$ sample measured at various temperatures are presented in Fig. 4.22. Note that these dependencies are linear. From the slope of these dependencies, the lifetime (τ) of non-equilibrium charge carriers was calculated using the relationship

$$\tau = \frac{t_2 - t_1}{\left(\ln\frac{\Delta\sigma_1}{\Delta\sigma_{st}}\right) - \left(\ln\frac{\Delta\sigma_2}{\Delta\sigma_{st}}\right)}, \tag{4.18}$$

One can see that the value of τ decreases with increasing the sample temperature.

Specialized studies [15] have revealed that the photoconductivity with large relaxation time can be attributed to the presence in the sample of collective potential barriers related to different types of inhomogeneities. The electric field of these barriers produces a separation of the nonequilibrium charge carriers generated by illumination. In such a case, the recombination rate is low, since the probability that an electron will reache a region which contains holes is very low. The phenomenon was revealed in a series of semiconductor $A^{II}B^{IV}$ materials [15, 16].

Figure 4.23 presents the spectral characteristic of photoconductivity for a $ZnS_{0.5}Se_{0.5}$ thin films. The value of $\Delta\sigma/\Delta\sigma_{st}$ is called relative spectral sensitivity and it is given in relative units. This characteristic presents a curve with two peaks localized at 2.33 and 2.54 eV respectively.

The photoluminescence relaxation curve represents the variation with time of the intensity of luminescence, $J_{FL} = f(t)$, after the sample illumination is switched off. It follows the exponential decay law of the form

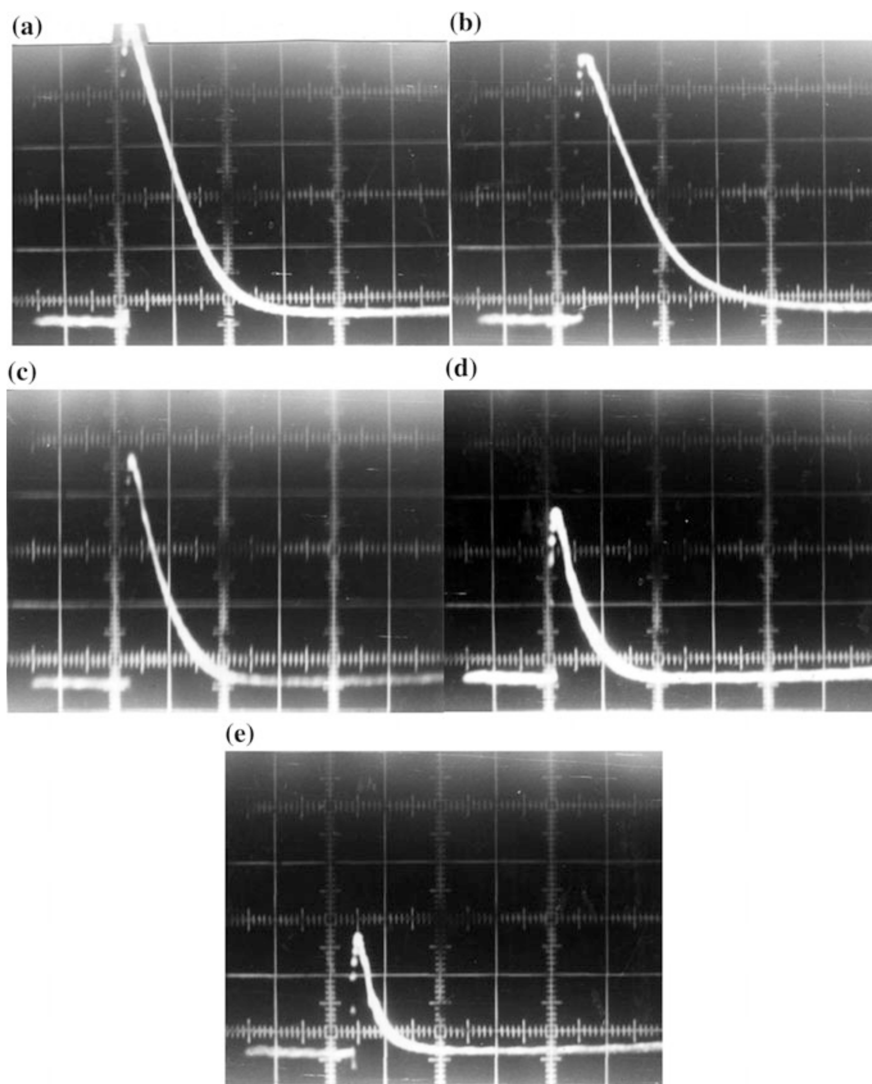

Fig. 4.21 Relaxation curves of the photoconductivity a thin film of $ZnS_{0.5}Se_{0.5}$ (d = 0.55 μm, T_{sub} = 300 K, r_d = 1.50 nm/s) at sample different temperatures (in ordinate indicates $\Delta\sigma = \sigma_L - \sigma_0$ in relative units): **a** T = 81 K (1 cm = 0.1 μs); **b** T = 175 K, (1 cm = 0.2 μs); **c** T = 225 K, (1 cm = 0.2 μs); **d** T = 262 K (1 cm = 0.4 μs); **e** T = 300 K (1 cm = 0.4 μs)

$$J_{FL}(t) = J_{FL}(0) exp\left(-\frac{\mathbf{t}}{\tau}\right), \tag{4.19}$$

where J_{FL} is the luminescence intensity at the momentum of illumination switching off (t = 0), and τ is the lifetime of non-equilibrium carriers.

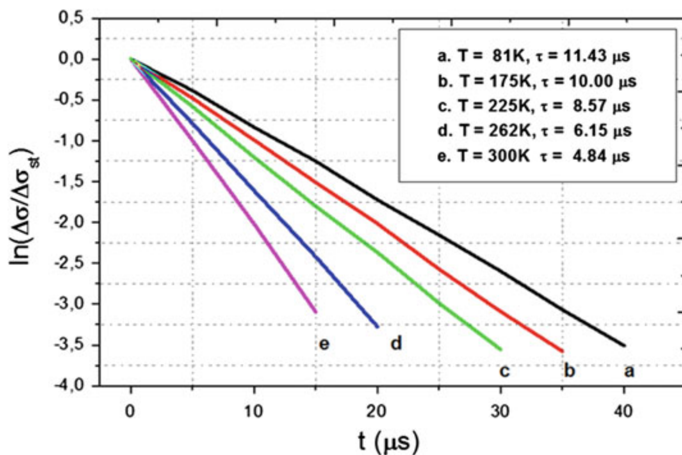

Fig. 4.22 The dependencies $\ln(\Delta\sigma/\Delta\sigma_{st}) = f(t)$ obtained at different temperatures of $ZnS_{0.5}Se_{0.5}$ thin films (d = 0.55 μm, T_{sub} = 300 K, r_d = 1.50 nm/s)

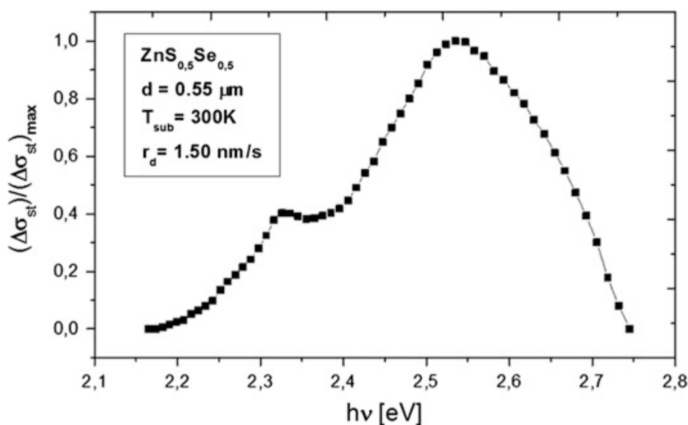

Fig. 4.23 Spectral dependence of photoconductivity of $ZnS_{0.5}Se_{0.5}$ thin films (T = 300 K, R_s = 47 MΩ, U = 180 V, ν = 12.5 Hz)

Figure 4.24 presents the photoluminescence relaxation curve of a $ZnS_{0.5}Se_{0.5}$ thin films. Excitation was performed with a molecular N_2 laser (λ_{ex} = 0.337 μm, P = 1.60 kW, $\Delta t = 10^{-8}$ s, f = 25 Hz) at the temperature of 78 K. The $J_{FL}(0)$ value is called stationary value of photoluminescence and the $J_{FL}(rem)$ is the residual value of luminescence.

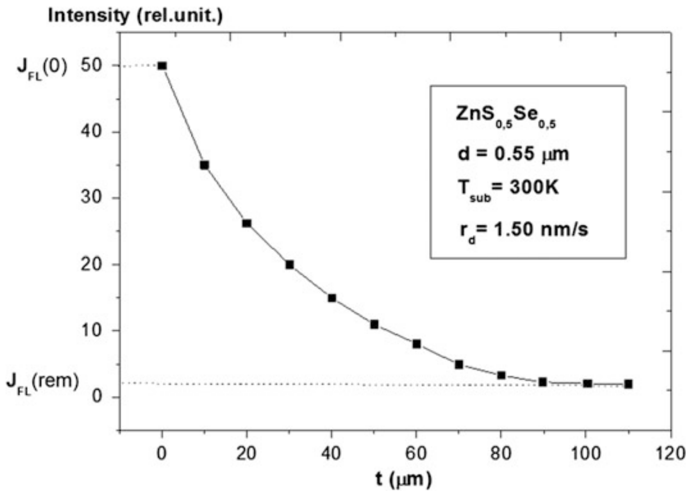

Fig. 4.24 Photoluminescence relaxation curve a $ZnS_{0.5}Se_{0.5}$ thin film

The lifetime of charge carriers can be determined according the relationship

$$\tau = \frac{t_2 - t_1}{ln\frac{J_{FL1}}{J_{FL}(0)} - ln\frac{J_{FL_2}}{J_{FL}(0)}}, \tag{4.20}$$

where J_{FL1} represents the stationary photoluminescence of the sample at time point t_1 and J_{FL2} is the stationary photoluminescence of the sample at time point t_2.

The dependence $ln(J_{FL}/J_{FL}(0)) = f(t)$ plotted for the same $ZnS_{0.5}Se_{0.5}$ sample si shown in Fig. 4.25. The relaxation time calculated from the slope of the linear

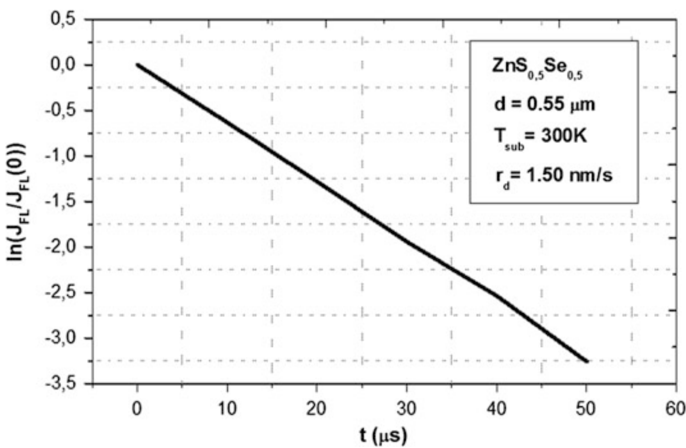

Fig. 4.25 Dependence $\ln(J_{FL}/J_{FL}(0)) = f(t)$ for a $Zn_{0.5}Se_{0.5}$ thin film

segment is equal to 15.38 μs. This value, as well as those obtained from of photoconductivity relaxation curves (Fig. 4.22) are in good agreement with those obtained by Şeikman and Şik [17] for ZnSe crystals.

The photoluminescence spectra of ZnS_xSe_{1-x} thin films were also investigated at the temperature of 78 K. The layers were obtained by vacuum thermal evaporation on glass substrates. $AuCl_2$ electrodes were deposited on layers at 1 mm distance from each other, and the samples were cooled to liquid nitrogen temperature. The photoluminescence excitation density was around 10^5 W/cm^2. The photoluminescence spectral dependence of $ZnS_{0.5}Se_{0.5}$ thin film measured at 78 K is presented in Fig. 4.26. The quantity Σ_{fL} is called relative spectral sensitivity of photoluminescence. The curve has a single peak, which is located approximately at 2.01 eV. Taking into account this value, we can determine the position of recombination centers as the difference between the width of the band gap (E_g = 3.05 eV) [3–6] and the value of 2.01 eV. Thus, one can conclude that the energy level of recombination centers in the $ZnS_{0.5}Se_{0.5}$ thin films is localized at a distance of 1.04 eV from the top edge of valence band.

Gaşin et al. [18] observed a respective peak in ZnSe crystals annealed in a Zn melt and then cooled to liquid nitrogen temperature. They assumed that the appearance of this band is related to $Zn_i^+ \rightarrow V_{Zn}$ radiative transitions. The activation energy of zinc vacancies is about 0.93 eV.

Other results are related to thermoluminescence of ZnS_xSe_{1-x} thin films. The excitation of luminescence centers was performed by ultraviolet radiation at T < 77 K. The excited electrons and holes are trapped at different energy levels in the band gap. With increasing temperature, release of “thermal” electrons from traps occurs. After a certain period of time, the free electrons either recombine on levels of recombination or are captured again in traps. Both processes are accompanied by emission of light radiation, called thermoluminescence.

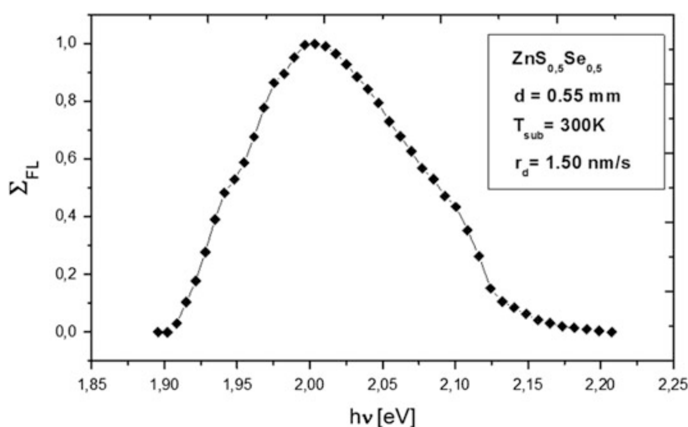

Fig. 4.26 Photoluminescence spectral dependence of a $ZnS_{0.5}Se_{0.5}$ thin film (λ_{ex} = 0.337 μm, T = 77 K, ν = 25 Hz)

The thermoluminescence parameters are [18]:

(a) the temperature at which thermoluminescence intensity is maximum (T_{max});
(b) the half-width of the thermoluminescence band (δ), equal to the difference $T_2 - T_1$ for which thermoluminescence intensity is equal to half the maximum value;
(c) the surface area (S) limited by the curve $J_{TL} = f\ (T)$and the axis of temperatures.

Vaksman and Serdiuk [19] deduced a formula for calculating the ionization energy of traps by using the parameters listed above. One can distinguish two cases:

(a) the case of *linear kinetics*

$$E_t = \frac{2k_B T_{max}}{\delta} \tag{4.21}$$

(b) the case of *quadratic kinetics*

$$E_t = \frac{4k_B T_{max}}{\delta}, \tag{4.22}$$

where $k_B = 8.6172 \times 10^{-5}$ (eV/K) is the Boltzmann constant.

Figure 4.27 presents the spectral dependence of thermoluminesce an ZnS_xSe_{1-x} thin films. The curve has two peaks: the first, most intense one, appears at

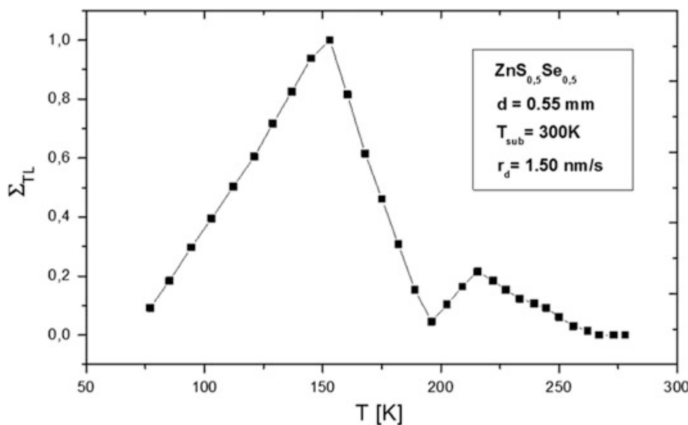

Fig. 4.27 Spectral dependence of thermoluminescence a $ZnS_{0.5}Se_{0.5}$ thin film (λ_{ex} = 0.337 μm, T = 77 K, ν = 25 Hz)

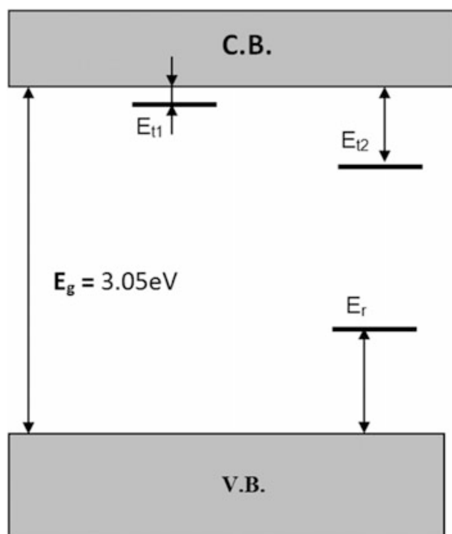

Fig. 4.28 Trapping levels and the level of localization of recombination centers from the band gap of $ZnS_{0.5}Se_{0.5}$ thin films

T_{max} = 153 K, and the second is situated at T_{max} = 216 K. One can observe that the low temperature part is higher than the high temperatures part for the first maximum (*linear kinetics*), while it is vice versa for the second maximum (*kinetic quadratic*). The E_t values calculated according to (4.18) and (4.19) equal to 0.062 and 0.44 eV for the frist and the second maximum, respectively.

A model can be proposed for the location of recombination and trapping levels in the band gap of of $ZnS_{0.5}Se_{0.5}$ thin films (Fig. 4.28) on the basis of thermoluminescence (Fig. 4.27) and photoluminescence (Fig. 4.26) spectra. The trapping levels are situated at 0.062 eV (E_{t1}) and 0.44 eV (E_{t2}) below the bottom of the conduction band, while the recombination centers are locallized at 0.93 eV (E_r) above the top edge of the valence band.

4.7 Conclusions

1. ZnS_xSe_{1-x} thin films (x = 0, 0.2, 0.4, 0.5, 0.6, 0.8, 1.0) with a thickness between 0.2 and 1.0 μm were prepared by thermal evaporation using the quasi closed volume technique.
2. The crystalline structure of layers was investigated by X-ray diffraction. It has been found that the layers are polycrystalline and have a cubic structure of zinc blende type with a large crystallite orientation of the planes (111) parallel to the surface of the substrate.
3. The cubic lattice parameter calculated from diffractograms is between a = 5.658–5.406 Å, the interplanar distance equals d_{111} = 3.270–3.120 Å, and the crystallite size is D = 3.750–2.435 Å. These values are in good agreement with prevuiously reported data.

4. The surface morphology of the polycrystalline ZnS_xSe_{1-x} thin films has been studied by scanning electron microscopy. The average crystallite size determined from the SEM images ranges between 3.6 and 2.2 Å.
5. The thermal activation energy determined from the dependencies $ln\sigma = f\,(10^3/T)$ is between 0.43–1.89 eV (for $T > 300$ K) and 0.132–0.403 eV (for $T < 300$ K). The mechanism of electron transport in polycrystalline ZnS_xSe_{1-x} thin films is explined on the basis of Efros-Shklovskii and Mott models.
6. The current-voltage characteristics of the In–ZnS_xSe_{1-x}–In systems plotted in Schottky coordinates proved to be linear. By extrapolating the linear segment of the $lnJ = f(U^{1/2})$ curve for $\sqrt{U} \to 0$, the height of the barrier potential at the metal-semiconductor interface was determined. The determined values for the Φ_0 are in agreement with those found for the ZnSe and ZnS crystals.
7. Transmission, reflection and absorption spectra have been investigated for polycrystalline ZnS_xSe_{1-x} thin films. It has been found that in the wavelength range of 380–1100 nm the reflectance does not exceed 0.5 %, and the transmission coefficient is in the range of 75–97 %.
8. The band gap width values determined from the reflection and absorption spectra (E_g = 2.65–3.5 eV) are in good agreement with the respective values for the bulk crystals.
9. The refractive index of polycrystalline ZnS_xSe_{1-x} thin films was determined from transmission spectra using the "envelope" method proposed by Swanepoel. It was found that the refractive index decreases with increasing the layer thickness, and it increases after the thermal treatment. A single oscillator model was used for explanation of the normal dispersion of the refractive index.
10. The lifetime (τ) of nonequilibrium charge carriers was calculated from the relaxation curves of photoconductivity and photoluminescence of ZnS_xSe_{1-x} of thin films. It was established that the value of relaxation time decreases with increasing the sample temperature.
11. The location of energy levels of recombination centers was determined from photoluminescence spectra, and the ionization energy of traps was calculated from the thermoluminescence spectra of ZnS_xSe_{1-x} thin films.

References

1. M.S. Shinde, P.B. Ahirrao, I.J. Patil, R.S. Patil, Studies of nanocristalline ZnSe thin films prepared by modified chemical bach deposition method. Indian J. Pure Appl. Phys. **49**, 765–768 (2011)
2. Y. Sirotin, M. Shaskolskaya, *Fundamental of Crystal Physics* (Mir Publishers, Moscow, 1982)
3. Y.P. Venkata Subbaiah, K.T. Ramakrishna Reddy, Structural behaviour of ZnS_xSe_{1-x} films deposited by close-spaced evaporation. Mater. Chem. Phys. **92,** 448–452 (2005)
4. M. Ambrico, G. Perna, D. Smaldone, C. Spezzacatena, V. Stagno, V. Capozzi, Structural and optical parameters of ZnS_xSe_{1-x} films deposited on quartz substrates by laser ablation. Semicond. Sci. Technol. **13**, 1446–1455 (1998)

5. Y.P. Venkata Subbaiah, P. Prathap, K.T.R. Reddy, D. Mangalaraj, K. Kim, Yi. Junsin, Growth and characterization of ZnS_xSe_{1-x} films deposited by close-spaced evaporation. J. Phys. D Appl. Phys. **40**, 3683–3688 (2007)
6. A. Ganguly, S. Chaudhury, A.K. Pal, Synthesis of ZnS_xSe_{1-x} ($0 < \mathbf{x} < 1$) nanocrystalline thin films by high-pressure sputtering. J. Phys. D Appl. Phys. **34**, 506–513 (2001)
7. D.D. Nedeoglo, A.V. Simaşkevici, *Elektriceskie i liuminisţentnâe svoistva selenida ţinka*, Chişinău, (ed.) "Ştiinţa", 1984
8. R. Bhargava (ed.), *Properties of Wide Bandgap II–VI Semiconductors* (Inspection, London, 1997)
9. M. Jain (ed.), *II–VI Semiconductor Compounds* (World Scientific, Singapore, 1993)
10. B.I. Shklovsky, A.L. Efros, *Electronic Properties of Doped Semiconductors* (Nauka, Moscow, Russia, 1979)
11. H.E. Bennett, J.M. Bennett, in *Physics of Thin Films* vol. 4, eds. by G.Hass, R.E.Thun (Academic Press, New York, 1987), p.1–96
12. R. Swanepoel, Determination of the thickness and optical constants of amorphous silicon. J. Phys. E: Sci. Instrum. **16**, 1214–1222 (1983)
13. R. Swanepoel, Determination of the surface roughness and optical constants of inhomogeneous amorphous silicon films. J. Phys. E: Sci. Instrum. **17,** 896–903 (1984)
14. L. Meng, M. Andritschky, M.P. dos Santos, The effect of substrate temperature on the properties of d.c. reactive magnetron sputtered titanium oxide films. Thin Solid Films **223**, 242–247 (1993)
15. T.S. Moss, in *Handbook on Semiconductors, Optical Properties of Semiconductors*, vol.2, ed. by M.Balkanski (Elsevier, Amsterdam, 1994)
16. G. Harbeke, *Polycrytalline Semiconductors: Physical Properties and Applications* (Springer, Berlin, 1985)
17. М.Я. Шейнкман, А.Я. Шик, Долговременные релаксации и остаточная проводимость в полупроводниках. Физика и техника полупроводников **10**(2), 209 (1976)
18. Гашин, П.А., Иванова, Г.Н., Матвеева, T.JI. и др. *Фотолюминесценция монокристаллов ZnSe: Al*, Физ. и техн. Полупроводников, 1981, т.15, №9, с. 1841–1844
19. V.V. Serdiuk, Iu.F. Vaksman, *Liuminisţenţia poluprovodnikov*, Kiev-Odessa, Izd-vo "Vâsşaia şkola", 1988

Chapter 5
Thin-Film Photovoltaic Devices Based on A^2B^6 Compounds

Tamara Potlog

Abstract This review gives a brief description of four types of photovoltaic devices based on A_2B_6 thin film semiconductors. Among A_2B_6 semiconductors CdTe is widely researched due to its near ideal band gap energy of 1.45 eV for the achievement of the theoretical maximum photovoltaic conversion efficiency of 31 %. The first part of the paper highlights the history of CdS/CdTe thin-film photovoltaic devices. It also describes the basic physics and design of CdS/CdTe and ZnSe/CdTe thin film heterojunction photovoltaic devices prepared by close spaced sublimation method at Moldova State University. The second part of this paper discusses the physical properties of novel TiO_2 oxide as a partner in heterojunction with CdSe and CdTe thin films. This section also describes the physics, design, and fabrication process of thin film photovoltaic devices based on TiO_2/CdSe and TiO_2/CdTe structures.

5.1 Introduction

The highest efficiency of conversion of solar light into electricity has been demonstrated in photovoltaic devices made from single-crystal semiconductor wafers. Traditional single-crystal solar cells, such as Si and GaAs [1–5], demonstrate very high efficiencies (20–30 %), but the production is expensive. Thin film solar cell technology offer the best hope for obtaining photovoltaic devices with low price and reasonable efficiency. Thin-film crystalline-silicon (c-Si) solar cells are considered to be one of the most promising alternatives to bulk silicon solar cells [6]. Thin films significantly decrease the silicon wafer cost, which accounts for about half of the total cost of standard silicon solar modules. Thin-films

T. Potlog (✉)
Department of Physics and Engineering, Moldova State University,
Chisinau, Moldova
e-mail: tpotlog@gmail.com

© Springer International Publishing Switzerland 2016

I. Tiginyanu et al. (eds.), *Nanostructures and Thin Films for Multifunctional Applications*, NanoScience and Technology,
DOI 10.1007/978-3-319-30198-3_5

crystalline-silicon (c-Si) solar cells are made a few μm thick, as opposed to at least several hundred μm for most Si wafers. Since such little amount of semiconductor is used, material cost is greatly reduced with respect to crystal substrate cells, making even relatively low efficiency thin-film solar panels cost-competitive with Si modules. Today crystalline silicon (c-Si) still accounts for 85 % of the market though the cost of manufacturing remains higher. Recently, Morales-Vilches, A. group has obtained a remarkable conversion efficiency of 17.2 % on 1 cm^2 hydrogenated amorphous silicon (a-Si:H) layers deposited at low temperature on crystalline silicon (c-Si) substrates [7, 8]. Amorphous silicon shows long term-stability issues. Significant thin-film PV production levels are also being set up for CdTe [9] and copper-indium-gallium-di-selenide (CIGS) [10]. CIGS requires expensive elements such as indium, gallium, and careful proportioning of the component elements. Representative examples of high-efficiency A_2B_6 thin films PV devices are the *n*-CdS/*p*-CdTe heterojunction [11]. These PV devices feature many of the technologies that provide high efficiency in this type of PV cell. Cadmium telluride has been identified as the principal candidate for low cost thin film photovoltaic applications because of the direct band gap and the ability to be doped both *n*-and *p*-type, allowing the formation of a variety of junction structures. The CdTe thin film photovoltaic devices have shown long-term stable performance [12] and high efficiency under AM1.5 illumination for terrestrial application. In many respects, CdTe resembles CIGS solar cells and can be produced with similar techniques, though much easier.

The main purpose of this overview is to demonstrate the possibility to manufacture other types of A_2B_6 photovoltaic devices based on CdTe with high efficiency in order to form multijunctions to push efficiencies beyond the Schockley-Queisser limit for single band-gap PV devices. This review will give a brief general discussion on the characterization of the ZnSe/SnO_2 interface. Then, the review will continue with the characterization of the ZnSe/CdTe photovoltaic devices and the comparison with the CdS/CdTe devices fabricated at Moldova State University. Finally, a brief description on *n*-TiO_2 nanostructured thin films for photovoltaic applications and a characterization of the TiO_2/CdTe, TiO_2/CdSe photovoltaic devices will be given.

5.2 Historical Development of the CdS/CdTe Photovoltaic Devices

Research in CdTe began in the 1950s and Loferski [13] first proposed the CdTe PV technology. CdTe with a band gap of 1.45 eV (300 K), high absorption coefficient ($\sim 10^5$ cm^{-1}) and a high chemical stability perfectly matched to the distribution of photons in the solar spectrum in terms of optimal conversion to electricity.

The most commonly used CdTe thin film photovoltaic devices are the *p-n*-heterojunction devices. Standard CdTe-based photovoltaic devices employ a "superstrate" and "substrate" designs. In the "superstrate" design, sunlight enters through the transparent substrate, which is usually glass or a transparent plastic. The insulating substrate needs a conducting layer, which is typically a "transparent conductive oxide" (TCO) such as SnO_2. The p-n-heterojunction is fabricated by the successive deposition of the *n*-type window layer (CdS), the *p*-type CdTe absorber, and finally the back metal contact is applied. Superstrate design of the device was first demonstrated in 1969 by Adirovich et al. with an efficiency >1 % with evaporated CdTe on a CdS/SnO_2/glass substrate [14]. In the "substrate" configuration, sunlight enters the p-n heterojunction before it reaches the substrate. Starting with the substrate, the cell is fabricated in the reverse order compared to the superstrate design: first a back contact, then the p-n heterojunction layers (starting with an n-type layer), and finally a TCO layer to act as an electrode to the window layer of the p-n HJ. In 1972 Bonnet and Rabenhorst [15] first proposed CdTe/CdS thin-film photovoltaic device in the "substrate" configuration. They reached 5–6 % efficiency in the substrate design of CdS/CdTe/Mo made by chemical vapor–deposited CdTe and vacuum-evaporated CdS thin films. These two configurations permit a very wide range of applications for CdTe photovoltaic devices. The "superstrate" design can be integrated as architectural element in buildings. The "substrate" configuration has been developed using stainless steel substrates. Attempts were made to develop CdTe/CdS solar cells in a "substrate" configuration with efficiencies in the range 3.5–8 % by Enrıquez et al. in 2004 on metal foils [16], Matulionis et al. [17], Vijay et al. [18], Mathew et al. [19]. One of the obstacles in the development of CdTe devices on metallic substrates is that most of the metal foils do not form an efficient ohmic contact with CdTe and it is difficult to incorporate an additional buffer layer as ohmic contact to increase the cell efficiency. The criteria of matching thermal expansion coefficients and work function, limit the choice of available substrate materials. The progress in R&D got real impulse, in 1980s when Tyan and Perez-Albuerne reported CdTe/CdS thin film solar cells with efficiency of 10 % [20]. In 1980s the various techniques were developed, such as electro deposition (ED), screen printing, vacuum evaporation and close spaced sublimation (CSS) method. The efficiencies exceeding 10 % were achieved for CdTe/CdS heterojunction solar cells by Basol [21], by Chu [22], by Mitchell et al. [23]. The pioneering work of different groups in the 1990s pushed the efficiency to above 15 %. Ferekides et al. reported increased efficiency of 15.8 % [24]. Finally, Wu et al. reported a record efficiency of 16.5 % by modifying the conventional structure (SnO_2/CdS/CdTe/metal) with CTO/ZTO/CdS/CdTe/Cu:HgTe:Cu_xTe) structure.

5.3 Technology Development Trends by Companies in CdS/CdTe Photovoltaic Market

Early leaders in CdS/CdTe device efficiencies were General Electric in the 1960s [26] and then First Solar (USA, vapor transport) [27], British Petroleum Solar (UK, electro-deposition) [28], Matsushita (Japan, screen printing and close space sublimation) [29] and Antec (Germany, close space sublimation) [30]. In the early 2000s BP Solar finally realized that electrodeposition is too slow for large scale production and exited thin-film technology. Antec has bankrupted and was bought by a wind-turbine company, but lost its key scientific personnel. Matsushita claimed an 11 % module efficiency using CSS and then dropped out of the technology, perhaps due to internal corporate pressures over cadmium which is highly toxic and closed down their CdTe program. At present, only First Solar (USA) remains in the field [31]. The company First Solar Inc. dominates not only the production of thin film solar modules but the whole PV market in terms of large production volume and lowest cost of production. Besides First Solar, today, there are a number of start-ups in CdTe: Q-Cells' Calyxo (Germany), GE's PrimeStar Solar (Arvada, Colorado), Arendi (Italy), and Abound Solar (Fort Collins, Colorado). The progress of conversion efficiency in CdS/CdTe photovoltaic devices was reported by First Solar (FSLR) [31] and summarized in Table 5.1.

The data are reproductions from references [32–35]. Development of thin-film CdS/CdTe photovoltaic device fabrication processes was advanced by the application of a cadmium stannate transparent conductive oxide layer in superstrate design. This allowed NREL researchers [31] to increase efficiency to 16.7 %. This world record efficiency happened to be the record from 2001 through 2011. After stagnation over a long period, First Solar (FSLR) announced in 2011 an efficiency of 17.3 %. However, quickly First Solar has lost the lead in cell efficiency as the General Electric (GE) Research Firm Announced efficiency of 18.3 % in 2012 year. CdTe solar-cell efficiency has been rapidly increasing since FSLR fabricated an

Table 5.1 CdTe record cell photovoltaic parameters

Year	Team	Efficiency (%)	V_{oc} (V)	J_{sc} (mA/cm^2)	FF (%)	References
1993	USF[a]	15.8	843	25.1	74.5	[3]
1997	Matsushita[b]	16.0	840	26.1	73.1	[5]
2001	NREL[a]	16.4	848	25.9	74.5	[6]
2001	NREL[a]	16.7	845	26.1	75.5	[4]
2011	FSLR[a]	17.3	845	27.0	75.8	[7]
2012	GE[a]	18.3	857	27.0	79.0	[8]
2012	FSLR[a]	18.7	852	28.6	76.7	
	Demtsu/sites-target	19.0	900	27.0	78.5	[1]

[a]NREL certified
[b]JQA certified

18.7 % NREL certified cell at the end of 2012. Today, GE and FSLR announced a technology partnership to advance thin-film photovoltaic devices and modules. In 2013 First Solar has acquired GE's global CdTe solar intellectual property portfolio, setting a course for significant advancement of photovoltaic thin-film solar technology and announced an efficiency of 18.7 % on the cell. Through optimized processing of the CdTe thin film, the quality of the grain boundaries, doping and contacting Demtsu and Sites in their paper [36] proposed an achievable performance target for CdTe solar cells of 19 %. The Target cell is one that should be possible with current industrial processes. The current-voltage parameters were predicted to reach 900 mV open-circuit voltage, 27 mA/cm^2 short-circuit current density and 77 % fill-factor. The analysis concludes that further optimization of the cell and module design beyond the present, allows increasing cell efficiency to17–18 % without disruptive technology changes at the module level at FSLR.

5.4 Comparison of Moldova State University CdS/CdTe Photovoltaic Device with Manufacturing Target

Research in the development of CdS/CdTe photovoltaic devices fabricated by close spaced sublimation method occurs at Physics Department and Engineering of Moldova State University (MSU). Gashin and coworkers [37] fabricated the first CdS/CdTe thin film photovoltaic devices in 1984. A few years later, Potlog et al. published in the paper [38] an efficiency of about 9 %. Additional of Te layer before the metallic back contact has improved MSU CdS/CdTe solar-cell efficiency and today the MSU researchers achieved 10.5 % NREL certified cell. The NREL I-U curves of the certified 10.5 % MSU and FSLR, USA 18.7 % best devices are shown in Fig. 5.1. As one can see, the primary improvement in the MSU cell should be addressed to the fill-factor. Figure 5.2 compares the quantum efficiencies of the MSU device with the world record cell. The primary loss over this range is the reflection of the cell. Also, the loss that needs to be addressed occurs for short wavelengths, as can be seen.

5.5 Deposition Processing and Photovoltaic Device Fabrication

The close spaced sublimation (CSS) method is considered one of the most promising techniques for A_2B_6 thin films deposition. The CSS method allows growing high-quality semiconductor thin films under a controllable technological process. It should be noted that the CSS method allows one to obtain thin films under close to thermodynamically equilibrium growth conditions at high substrate

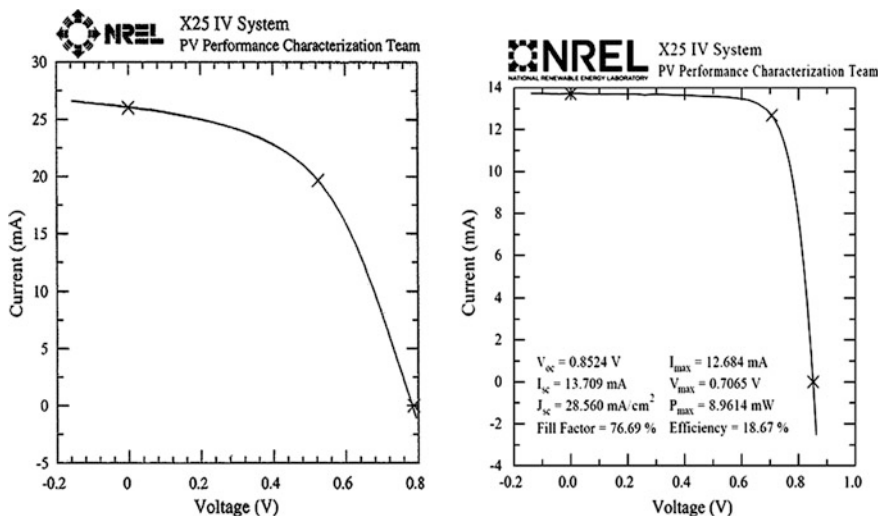

Fig. 5.1 NREL certified current-votage curves of the 10.5 % MSU and the 18.7 % FSLR photovoltaic devices

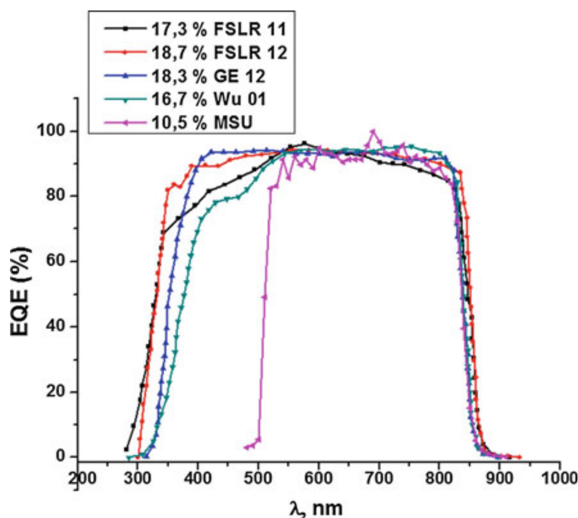

Fig. 5.2 Quantum-efficiency comparison of highest-efficiency MSU photovoltaic device with manufacturing target

temperature T_s and a small difference between substrate temperature and evaporation temperature ΔT ($\Delta T = T_e - T_s$) [39]. In our study, a source and a substrate separated by a 20 mm distance are introduced in a controlled vacuum atmosphere, and the source is maintained at a higher temperature than the substrate. The A_2B_6 source material dissociates into its A atoms and B_2 molecules which collide several times with gas molecules and then condense on the substrate surface. This process

provides direct transport of each component of the source across the space to the substrate, and in most cases, the transport mechanism is diffusion-limited. The polycrystalline CdS, ZnSe, CdTe and CdSe thin films were obtained in a short time (about 30 min) without an additional transport agent gas. The MSU CdTe heterojunction photovoltaic devices are grown in "superstrate" design. The most suitable window electrode material is the tin oxide doped by fluorine (SnO_2:F). The low-cost soda-lime glass substrates covered with SnO_2:F for a processing at temperature below 500 °C we purchased from Solaronix, Swiss. The SnO_2/glass slides with a size of 20 mm × 20 mm were washed with detergent and rinsed with deionized water followed by rinsing in methanol. SnO_2: F layer with an electron affinity below 4.5 eV forms an ohmic contact and has good band alignment with *n*-CdS and *n*-ZnSe. The ZnSe, CdS and CdTe thin films were deposited on glass substrate covered with TCO at a system pressure of $\sim 10^{-6}$ Torr. The as-deposited CdS/CdTe and ZnSe/CdTe photovoltaic devices exhibit poor PV properties and thus require a special annealing treatment that improves the device efficiency considerably. This is done by subjecting the CdS/CdTe and ZnSe/CdTe stacks to a heat treatment under $CdCl_2$ atmosphere. After this annealing treatment, a significant enlargement of grain size is observed in CdTe grown at temperatures below 500 °C. Another important issue in CdTe photovoltaic device technology is the formation of an efficient and stable ohmic contact on the *p*-CdTe layer. For forming on a *p*-type semiconductor of an ohmic contact, the work function of the metal should be higher than that of the semiconductor; otherwise, a Schottky contact is formed. For the *p*-CdTe layer, a metal with a work function higher than 5.7 eV is needed. Metals with such high work functions are not available. To overcome this problem, a heavily doped *p*-CdTe was created by deposition of Te on the surface by thermal evaporation. Ni or Cr is used as an ohmic metal contact for *p*-CdTe by thermal evaporation.

TiO_2 thin films were prepared on glass substrates by radio frequency RF magnetron sputtering of Ti target of 99.99 % purity by researchers from Al.I. Cuza University, Iasi, Romania. TiO_2 thin films doped with oxide powder Nb_2O_5 of 99.999 % purity were prepared. The sputtering was performed under a mixture of 5 sccm (standard cubic centimeters per minute) of Ar (99.99 %) and 1 sccm of O_2 (99.99 %) atmosphere supplied as working and reactive gases, respectively, through an independent mass-flow controller. The sputtering chamber was evacuated down to 1×10^{-5} mbar by the turbo molecular pump and the working pressure was kept at about 5×10^{-3} mbar. During the depositions, the RF power was 100 W and the substrates were kept at room temperature using the same deposition time of 8 h. The distance between the target and the substrate was kept constant at 6 cm. Before the deposition, the glass substrates were sequentially cleaned in an ultrasonic bath with acetone and ethanol. Finally, the substrates were rinsed with distilled water and dried. After the deposition, TiO_2 films were vacuum annealed at 420 °C for 30 min in the deposition chamber at a pressure of 4.0×10^{-5} mbar and in hydrogen atmosphere at a pressure of 2.0×10^{-3} mbar at the same temperature and duration.

The TiO_2/CdTe and TiO_2/CdSe photovoltaic devices were fabricated by CdTe and CdSe layers deposition on the Nb-doped TiO_2/glass substrates by close space sublimation method.

5.6 Analysis of Efficiency Loss Mechanism in MSU CdS/CdTe Photovoltaic Devices

5.6.1 Current-Voltage Characteristics of the CdS/CdTe Photovoltaic Devices

Two types of the CdS/CdTe photovoltaic devices fabricated by close space sublimation (CSS) [40] and high vacuum evaporation (HVE) [41] are compared here. Both types were fabricated in "superstrate" design (Fig. 5.3). In the case of devices fabricated by CSS the structures were held in either $CdCl_2$:H_2O saturated solutions and then annealed in the air at 400 °C for 25–30 min. $CdCl_2$ treatment for the cells made by HVE is applied by evaporating 400–600 nm onto the CdTe surface and then annealing them in the air at 430 °C for 30 min. Back contact in the case of CdS/CdTe fabricated by CSS was made by evaporating Te/Ni, but in the case of those fabricated by HVE–Cu/Au, followed in both cases by a short annealing at 200 °C in the air.

Photovoltaic devices are designed to work under normal sunlight and their performances are evaluated at 25 °C under an AM1.5 solar irradiation of 100 mW/cm^2 intensity through the CdS thin film. Figure 5.4 shows current-voltage characteristics of CdS/CdTe photovoltaic devices made by (HVE) and CSS methods.

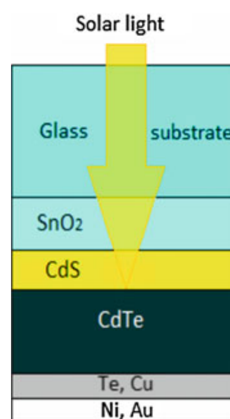

Fig. 5.3 Schematic structure of the CdS/CdTe thin film photovoltaic device

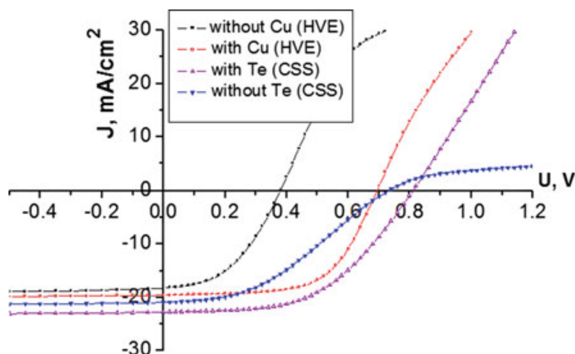

Fig. 5.4 Current-voltage characteristics of the CdS/CdTe photovoltaic devices fabricated by different methods of deposition at illumination of 100 mW/cm^2

The data can be fitted to the usual expression, which includes the effect of series and shunt resistances:

$$J = J_0 \left[\exp q \frac{(U - JR_s)}{AkT} - 1 \right] + q \frac{(U - JR_s)}{R_{sh}} \tag{5.1}$$

where J_0 is the reverse saturation current density, A is the diode ideality factor, R_s the series resistance and R_{sh} the shunt resistance, k is Boltzmann constant and T is the temperature. R_{sh}, R_s, n, J_0 are cell parameters of the device. The series resistance in the dark is appreciable for all cells but decreases to about 6–7 Ω cm^2 under 100 mW/cm^2 illuminations. This is due to the high photoconductivity of CdS and CdTe thin films. The J-U curve for the cell without the Te layer shows a stronger rollover in the light in forward bias than the cell without Cu. The addition of small amounts of Cu or Te to back contacts improves contact properties by p^+-doping the CdTe surface and creating a pseudo-ohmic contact. The cell made by close spaced sublimation method shows the highest open circuit voltage. The short circuit current is high enough for both cells. The cell deposited by CSS seriously suffers in *FF* compared to the cells fabricated by HVE. It's well known the FF is a function of the series/shunt resistance

$$FF = FF_0 \left(1 - \frac{R_s}{R_{sh}}\right). \tag{5.2}$$

FF_o—the fill factor which is not affected by the series resistance. From Table 5.2 we can observe that R_s for CdS/CdTe with Te is five times higher than for cells with

Table 5.2 Photovoltaic parameters of CdS/CdTe photovoltaic devices fabricated by HVE and CSS methods

Cell	J_{sc} (mA/cm^2)	U_{oc} (V)	FF (%)	η (%)	R_s (Ω cm^2)	R_{sh} (Ω cm^2)
Without Cu (HVE)	18.21	0.38	45.3	3.14	43.54	2003.8
With Cu (HVE)	21.42	0.65	60.8	8.47	2.01	538.6
Without Te (CSS)	20.91	0.7317	38.67	5.92	24.71	3310.5
With Te (CSS)	22.75	0.81	51.87	9.56	10.68	2917.4

Cu. This is due probably to the fact that the cell prepared by CSS used wet $CdCl_2$ treatment and may contain oxide on the surface, while cells with Cu used evaporated $CdCl_2$. There is a big difference between the value of U_{oc} in the case of cells prepared by HVE and CSS. It is well known that a cell containing a back barrier can operate in either standard: back-diode or reach-through diode regime. In order to confirm this fact the device parameters have been plotted against the intensity of illumination (*E*). The U_{oc} = f(E) dependence for devices prepared with Cu and without Cu at the back contact (Fig. 5.5) is independent of the intensity of illumination. The back barrier of these devices operates in reach-through diode regime. In the case of the cell without Te the back barrier operates as a back diode and it's considered as a good back contact. The addition of a Te layer diminishes the back barrier and the J-U curve shows a normal behavior. The U_{oc} for both cells fabricated by CSS method increases, and then tends to saturation with illumination. According to the theory, the total cell efficiency depends on the properties of the back contact only through the fill factor. The series resistance and the dark J-U characteristics determine the fill factor. The main source of the *FF* decrease is an increase in J_o. To a second approximation the diode factor *A* value can influence the *FF*, if R_s becomes high enough, even though an increase in R_s itself is much more important than enhanced *A*. Such a behaviour of the *FF* of CdS/CdTe photovoltaic devices with and without Te (Fig. 5.6) is explained by the high value of R_s, which changes with illumination (Fig. 5.7).

In contrast to our expectations, the highest value of η = 9.5 % for a CdS/CdTe (Fig. 5.8) solar cell with Te was obtained not for the highest illumination intensity of 100 mW/cm^2, but for 50 mW/cm^2. For the cells without Te the highest value of η was obtained for the lowest light intensities in the range of 30 mW/cm^2. For the cells with Cu the highest value η = 8.47 % was obtained for the highest intensity of 100 mW/cm^2, that is why the intensity R_s is smaller. As was mentioned above, the *FF* depends on both R_s and R_{sh} in a complex way. The most dramatic is the variation of R_{sh} in both cases of fabrication of the devices with a light intensity (see Fig. 5.7).

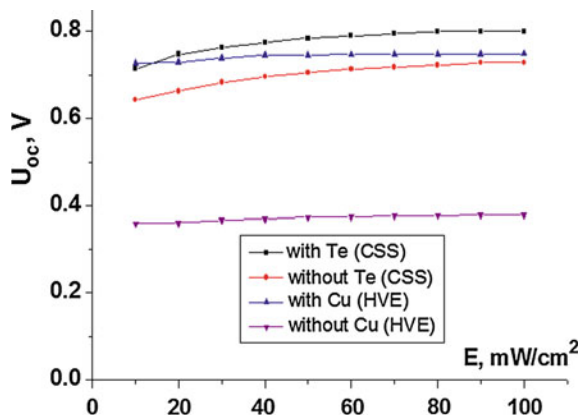

Fig. 5.5 The dependence U_{oc} = f(E) for CdS/CdTe devices fabricated by different methods of deposition

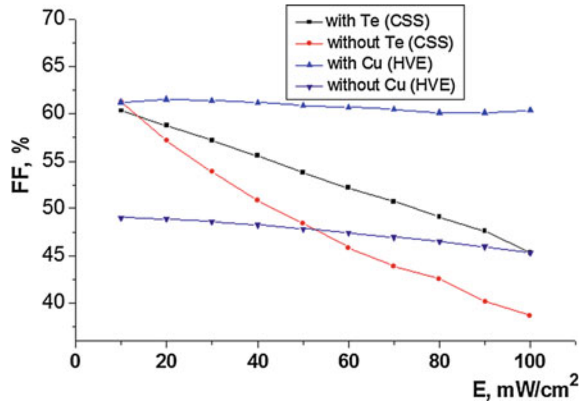

Fig. 5.6 The dependence FF = f(E) for CdS/CdTe solar cells fabricated by different methods of deposition

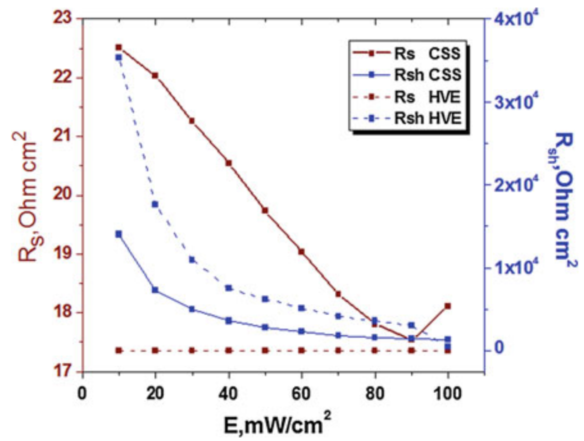

Fig. 5.7 The dependencies $R_s = f(E)$ and $R_{sh} = f(E)$ of the CdS/CdTe photovoltaic devices fabricated by CSS and HVE

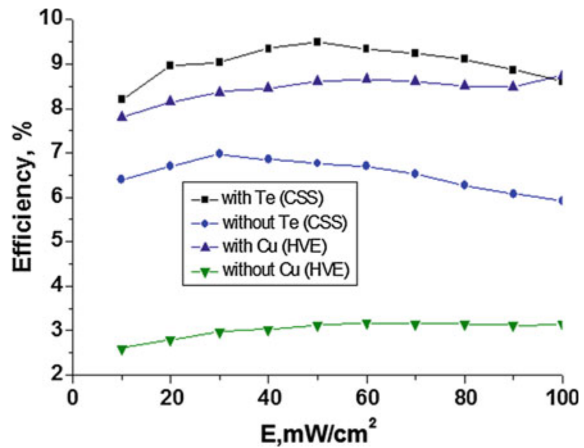

Fig. 5.8 The dependence η = f(E) for CdS/CdTe solar cells fabricated by different methods of deposition

In contrast, R_s for a cell fabricated by HVE varies very little in comparison with the cell fabricated by CSS method. We may conclude that the light-dependent R_{sh} negatively influences the efficiency of our cells.

Temperature dependent measurements often reveal additional information about solar cell operation. Figures 5.9 and 5.10 show the temperature dependence of J-V for two thin film devices. The cell shown in Fig. 9 was fabricated without additional Te layer before the metallic back contact, and the cell with the additional To is illustrated in Fig.10. In both cases, the devices open-circuit voltage increased at reduced temperatures at the expected rate of approximately 2 mV/°C. Also, the current flow becomes more limited as the temperature is reduced. The mechanism for current limitation in the two cases, however, is clearly different. For the devices with Te layer, as noted above, the curves at higher voltages are linear, while without tellurium, they show the characteristic "rollover" behavior, which becomes more pronounced as temperature is reduced. The conclusion is that the Te reduce the back-contact barrier.

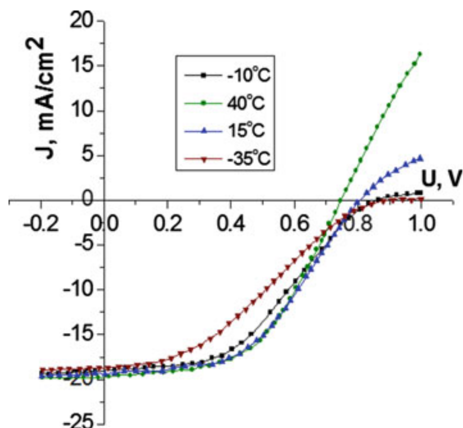

Fig. 5.9 Current-voltage characteristics of the CdS/CdTe device without Te at different measurement temperatures

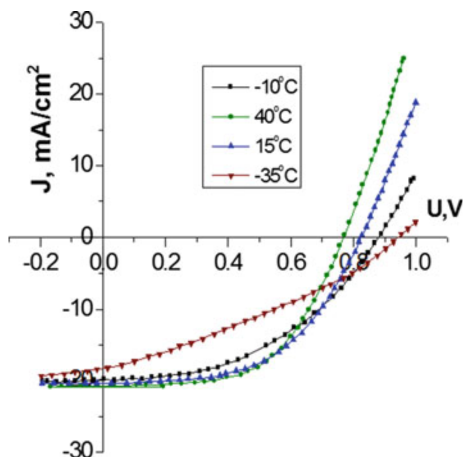

Fig. 5.10 Current-voltage characteristics of the CdS/CdTe device with Te at different measurement temperatures

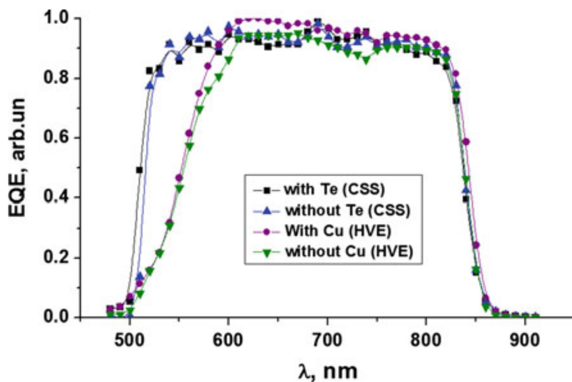

Fig. 5.11 Quantum efficiency of the CdS/CdTe photovoltaic devices fabricated by different methods of deposition

5.6.2 Quantum Efficiency

The external quantum efficiency (EQE) versus wavelength (Fig. 5.11) for the photovoltaic devices fabricated by CSS method with Te and without Te is reasonably good for wavelengths between the band gap of CdS and that of the CdTe. The cells fabricated by HVE with and without Cu have a gradual transition between 500 and 600 nm, which is characteristic for the intermixing between CdTe and CdS thin films. It is well known [42, 43] that the interface consists of $CdTe_{1-y}S_y$/ $CdS_{1-x}Te_x$, where the interfacial values of x and y correspond to the solubility limits in the CdTe-CdS system at the devices processing temperature. These alloys, formed via diffusion across the interface during CdTe deposition and post-deposition treatments, affect photocurrent and junction behavior. Formation of the $CdS_{1-x}Te_x$ alloy on the S-rich side of the junction reduces the band gap and increases absorption, reducing photocurrent in the 500–600 nm range, which we have in the case of cells fabricated by HVE. Comparisons of these cells allow concluding that the cell fabricated by CSS has a high current density because of the larger response in the short wavelengths region.

5.7 Characterization of ZnSe/CdTe Photovoltaic Devices

5.7.1 Morphological and Structural Studies of Glass/SnO_2/ ZnSe Interface

The samples with as-grown ZnSe thin films by close spaced sublimation method obtained at substrate temperatures of 500, 550, 600 and 650 K denoted as (M5.1), (M6.1), (M7.1) and (M8.1), respectively. The samples with ZnSe chloride activated films obtained at substrate temperatures of 500, 550, 600 and 650 K signed as (M5.2), (M6.2), (M7.2) and (M8.2), respectively. The surface of the ZnSe thin films

was analyzed with the SEM scanning electron microscope (SEM) and with the energy dispersive X-ray (EDX). The images were made in the secondary electron (SE) and the backscattered electron modes (BSE). In Fig. 5.12, the SEM images of the ZnSe thin films are illustrated. The SEM images of as-grown films show many round grains on the surface with an inhomogeneous grain size distribution. The films became more crystalline as the substrate temperature increased. The irregular structure of the as-deposited film transformed to a more rounded structure after the annealing. Sample M5.2 with ZnSe after $ZnCl_2$ activation at 400 °C shows many round grains on the surface, and they did not coalesce together. Also, such defects as pinholes are present in the film surfaces which are more visible after chemical activation and annealing.

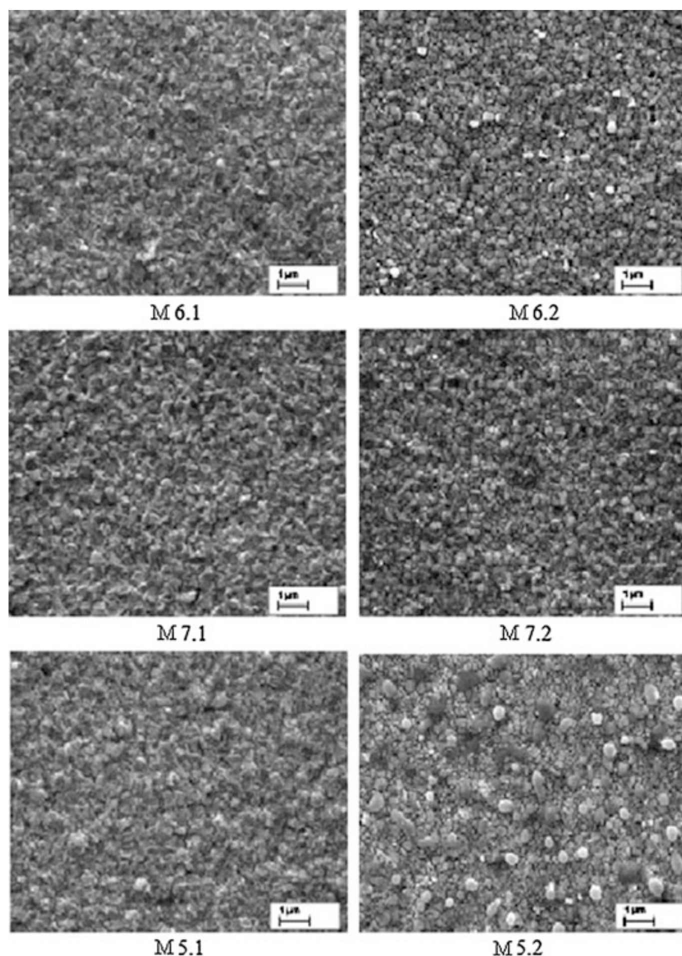

Fig. 5.12 SEM images of ZnSe thin films deposited by close spaced sublimation method: M5.1, M6.1, M7.1—as grown; M5.2, M6.2, M7.2—after $ZnCl_2$ activation and annealing

Fig. 5.13 X-ray diffraction pattern of as-grown ZnSe thin films on SnO_2/glass substrates prepared at different substrate temperatures

The structural characterization of the films was carried out by X-ray diffraction (XRD) measurements using a Rigaku diffractometer with CuKα radiation (λ = 1.5418 Å), at 30 kV, 30 mA. Figure 5.13 shows XRD 2θ scans, between 20° and 80°, for as-deposited ZnSe/SnO_2/glass samples. As seen, the XRD pattern exhibits intensive XRD peaks at 26.52°, 33.79°, 37.85°, 38.84°, 42.55°, 51.64°, 54.51°, 61.69°, 71.04°, 78.44° and 52° from polycrystalline SnO_2 with tetragonal or orthorhombic structures [44] and four peaks with a smaller intensity for the ZnSe phase. The structural parameters for the ZnSe phase are presented in Table 5.3. The X-ray diffraction (XRD) analysis was performed using Rigaku software PDXL. The crystallite size was calculated using the Scherrer's formula from the full-width at half-maximum (FWHM) [45]:

$$D = \frac{k\lambda}{\beta \cos\theta} \tag{5.3}$$

where k is a dimensionless shape factor with a value close to unity, λ is the X-ray wavelength, β—the full-width at half-maximum. The micro strain (ε) was calculated from the formula [45]:

$$\varepsilon = \beta\, \cos\theta/4 \tag{5.4}$$

where θ is Bragg angle.

The as-deposited ZnSe films are polycrystalline. The XRD patterns of the as-deposited by close spaced sublimation method ZnSe films exhibited reflections corresponding to the cubic phase i.e. 2θ, varies from 2θ = 27.22° to 27.29° with respect to the substrate temperature and corresponding to the (111) plane of the cubic phase. Pradip et al. [46] have reported similar results. Also, the other characteristic diffraction peaks of the diffraction spectra display the cubic phase of ZnSe [44]. However, in all the cases, except M61 sample, the intensity of the (400) peak was high in comparison to the (111) one (see Table 5.3). This indicates a

Table 5.3 Microstructural parameters of CSS method as-deposited ZnSe thin films on SnO_2/glass substrates at different substrate temperatures

No. M51_500 K a = 5.6707 Å	2-theta (deg)	d (ang.)	Height (cps)	β-FWHM (deg)	Size (ang.)	Plane	Strain (%)	Thickness (nm)
1	27.22	3.2728	20940	0.21	413	(111)	0.10	1159.1
2	45.19	2.0046	10239	0.225	399	(220)		
3	53.50	1.7113	15896	0.269	345	(311)		
4	65.76	1.4189	50125	0.238	415	(400)		
2	45.21	2.0036	13237	0.174	517	(220)		
3	53.58	1.7089	28674	0.135	686	(311)		
4	65.703	1.4199	59159	0.225	438	(400)		
No. M61_550 K a = 5.6572 Å	2-theta (deg)	d (ang.)	Height (cps)	β-FWHM (deg)	Size (ang.)	Plane	Strain (%)	
1	27.28	3.2656	29778	0.193	443	(111)	0.16	633.7
2	45.32	1.9991	11313	0.24	375	(220)		
3	53.66	1.7065	20446	0.228	407	(311)		
4	65.93	1.4155	26625	0.282	350	(400)		
2	45.21	2.0036	13237	0.174	517	(220)		
3	53.58	1.7089	28674	0.135	686	(311)		
4	65.703	1.4199	59159	0.225	438	(400)		
No. M71_600 K a = 5.6572 Å	2-theta (deg)	d (ang.)	Height (cps)	β-FWHM (deg)	Size (ang.)	Plane	Strain (%)	
1	27.29	3.2650	15764	0.187	456	(111)	0.23	565.1
2	45.32	1.999	8224	0.288	313	(220)		
3	53.65	1.7070	15964	0.248	375	(311)		
4	65.92	1.4158	28751	0.256	386	(400)		
4	65.703	1.4199	59159	0.225	438	(400)		
No. M81_650 K a = 5.6661 Å	2-theta (deg)	d (ang.)	Height (cps)	β-FWHM (deg)	Size (ang.)	Plane	Strain (%)	
1	27.25	3.2698	17744	0.117	731	(111)	0.13	1008.3
2	45.21	2.0036	13237	0.174	517	(220)		
3	53.58	1.7089	28674	0.135	686	(311)		
4	65.703	1.4199	59159	0.225	438	(400)		

preferential orientation of the micro-crystallites with the (400) direction in the case of the M51, M71 and M81 ZnSe films. The FWHM was found to decrease markedly with film thickness and substrate temperature to 650 K. Such a decrease reflects the increase in the concentration of the lattice imperfections due to the decrease in the internal micro-strain within the films and an increase in the crystallite size. ZnSe thin films of different thicknesses were prepared at different substrate temperatures on glass/SnO_2 substrates. It is observed that the crystallite size increases but the internal strain decreases with the increase of the film thickness and the substrate temperature. The decrease in the strain indicates the formation of higher quality films at higher substrate temperatures. The observed lattice spacing value coincided with the standard JCPDS for cubic ZnSe [44].

The adatom mobility also increases as the substrate temperature increases, which also results in the crystalline size and crystallinity of the films [47]. Good quality polycrystalline thin films of ZnSe can be prepared at a substrate temperature nearer to 650 K, at which the lattice constant 5.6661 Å is found to be closer to the value of bulk ZnSe (5.667 Å) [48].

The X-ray diffraction pattern of $ZnCl_2$ annealed ZnSe thin films at 400 °C in vacuum are shown in Fig. 5.14. The films indicated a cubic ZnSe phase, also. There is no evidence of a new phase formation after $ZnCl_2$ annealing. For all the activated samples, the ZnSe phase presents a slight lattice-parameter decrease compared to the as-grown ones. The change of the lattice constant with the substrate temperatures after $ZnCl_2$ annealing is not very prominent as in the case of films before annealing and suggests that the film grains are stressed. This can be caused by the lattice mismatch and/or differences in the thermal expansion coefficients between the SnO_2 and the glass substrate. The FWHM decreases after $ZnCl_2$ annealing of ZnSe thin films prepared at 500 and 550 K (see Table 5.4). With a further increase of the substrate temperatures, the FWHM increases. It is observed that the crystallite size increases after annealing.

The internal strain increases with the increase of the substrate temperature. The increase of the grain sizes after $ZnCl_2$ annealing indicates an improvement of the ZnSe films crystallinity at 600 and 650 K substrate temperatures in comparison to

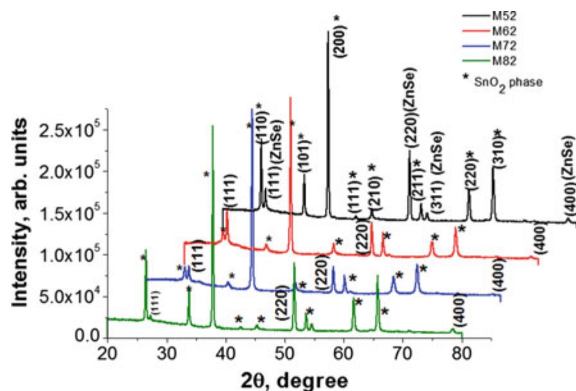

Fig. 5.14 X-ray diffraction pattern of $ZnCl_2$ annealed ZnSe thin films on SnO_2/glass substrates prepared at different substrate temperatures by close spaced sublimation method

Table 5.4 Microstructural parameters of $ZnCl_2$ annealed ZnSe thin films on SnO_2/glass substrates prepared at different substrate temperatures (D-thickness)

No. M52_500 K a = 5.6695 Å	2-theta (deg)	d (ang)	Height (cps)	FWHM (deg)	Size (ang.)	Plane	Strain (%)	D (nm)
1	27.21	3.2741	19263	0.182	470	(111)	0.000000e	1167.1
2	45.21	2.0039	10025	0.216	416	(220)		
3	53.58	1.7088	15797	0.235	396	(311)		
4	65.74	1.4192	57490	0.2351	420	(400)		
No. M62_550 K a = 5.6665 Å	2-theta (deg)	d (ang)	Height (cps)	FWHM (deg)	Size (ang.)	Plane	Strain (%)	D (nm)
1	27.23	3.2721	31484	0.182	470	(111)	0.12	948.9
2	45.24	2.0026	10560	0.236	381	(220)		
3	53.59	1.7086	24892	0.146	637	(311)		
4	65.91	1.4158	29479	0.277	357	(400)		
5	72.63	1.3006	1048	0.36	287	(331)		
No. M72_600 K a = 5.6663 Å	2-theta (deg)	d (ang)	Height (cps)	FWHM (deg)	Size (ang.)	Plane	Strain (%)	D (nm)
1	27.21	3.2735	13142	0.197	434	(111)	0.13	678.9
2	45.26	2.0016	7716	0.276	326	(220)		
3	53.59	1.7086	18775	0.172	540	(311)		
4	65.89	1.4162	29494	0.280	353	(400)		
5	72.67	1.3000	1006	0.44	235	(331)		
No. M82_650 K a = 5.6654 Å	2-theta (deg)	d (ang.)	Height (cps)	FWHM (deg)	Size (ang.)	Plane	Strain (%)	D (nm)
1	27.25	3.2689	4132	0.23	378	(111)	0	1098.2
2	45.22	2.0032	3870	0.30	296	(220)		
3	53.59	1.7084	19302	0.15	620	(311)		
4	65.71	1.4198	61355	0.215	459	(400)		

these films before annealing. The energy dispersive X-ray (EDX) analysis for all CSS method as-deposited and $ZnCl_2$ annealed ZnSe thin films shows very similar characteristics. Both as-deposited and annealed ZnSe films are Zn-deficient and are in good agreement with the results of the paper [49]. This is because the vapor pressure of Se is greater than that of Zn and their sticking coefficients are different. The incorporation of chlorine in the activated ZnSe layers at substrate temperatures is confirmed by the detection of chlorine in a standardless EDX analysis (Fig. 5.15). The chlorine spectrum is very weak because the spectra peaks are almost at the background level.

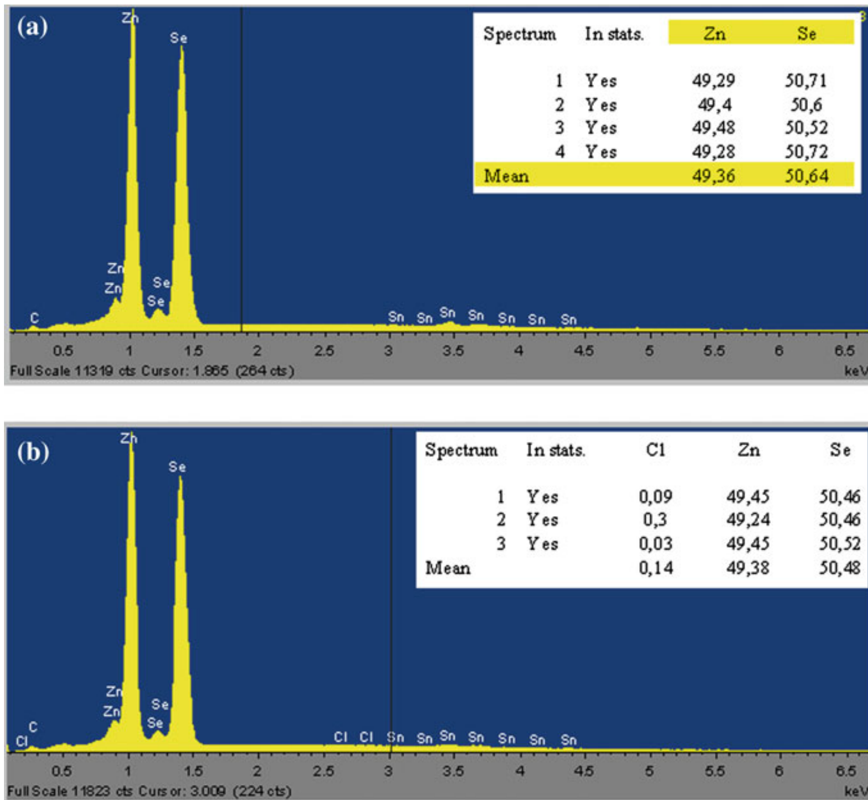

Fig. 5.15 The EDX analyses of as-deposited (**a**) and after $ZnCl_2$ activation (**b**) ZnSe films

5.7.2 Optical Properties of ZnSe Thin Films Deposited on SnO_2/Glass Substrates

The fundamental absorption, which corresponds to the transition from valence band$_2$ to conduction band, can be used to determine the band gap of the material. The relation between *a* and the incident photon energy (hν) can be written as [50]:

$$\alpha = \frac{A(hv - E_g)^n}{hv} \tag{5.5}$$

where A is a constant, E_g is the band gap of the material and the exponent *n* depends on the type of transition.

The n may have the values 1/2, 2, 3/2 and 3 corresponding to the allowed direct, allowed indirect, forbidden direct and forbidden indirect transitions, respectively. The variation of transmission with wavelength for as-deposited and $ZnCl_2$ annealed ZnSe thin films deposited on SnO_2/glass substrates at different temperatures has been shown in Fig. 5.16. There is a sharp fall of transmittance curve at the band edge, which confirms the crystalline nature of the deposited films. The transmittances in the region of 460–700 nm for $ZnCl_2$ annealed ZnSe films are smaller.

To check the transition type in films the values of n in (5.5) have been calculated by the procedure described elsewhere [50]. The $(\alpha h\nu)^2$ = f($h\nu$) dependencies (Fig. 5.17) for all CSS method ZnSe films are linear at the absorption edge, confirming the direct band gap transition in ZnSe. Extrapolating the straight-line portion of these plots to the ($h\nu$) axis allows to calculate the band gap (E_g). The optical band gap values for as-deposited ZnSe films prepared at different substrate temperatures ranged between 2.68 eV (0.63 μm) and 2.69 eV (1.16 μm). The

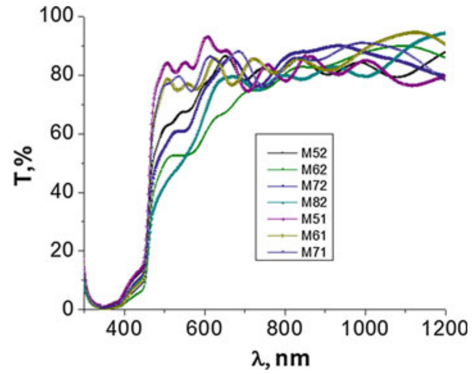

Fig. 5.16 The transmission spectra of as–grown (M5.1, M6.1, M7.1) and $ZnCl_2$ activated and annealed ZnSe thin films at different substrate temperatures

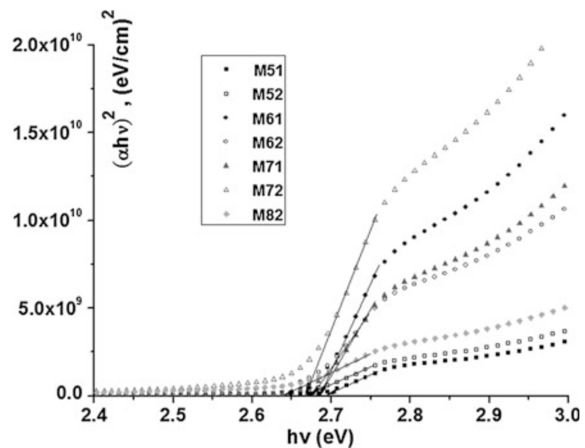

Fig. 5.17 The $(\alpha h\nu)^2$ = f(hν) spectra of as grown (M5.1, M6.1, M7.1) and $ZnCl_2$ activated ZnSe thin films at different substrate temperatures

maximum value of E_g is connected with the very small size of crystallites in films. The thick films have a lower absorption value at the forbidden gap region of the ZnSe films. Thinner films have a high absorption value in the band-band absorption region. This effect may be explained by proposing that thicker films have bigger crystallites (grains) so they are closer to the crystalline ZnSe, but bigger grain sizes give results in larger unfilled inter-granular volumes so the absorption per unit thickness is reduced. One obvious result from the $(\alpha h\nu)^2 = f(h\nu)$ dependence for $ZnCl_2$ activated at 400 °C ZnSe films grown by CSS method at different substrate temperatures is that the energy gap decreases. For example, for sample M51 E_g before annealing is 2.69 eV, after the $ZnCl_2$ activation (sample M52) E_g became 2.66 eV.

The size of crystallites increases with the increase of the substrate temperatures and with $ZnCl_2$ activation. This is confirmed by the XRD analysis (Tables 5.3 and 5.4). This is valid for all ZnSe films regardless of the substrate temperature.

5.7.3 Current-Voltage Characteristics of the ZnSe/CdTe Photovoltaic Devices

Recent effort to improve the efficiency of CdS/CdTe thin film photovoltaic devices is to use wider band gap buffer layers in order to allow more light to reach the junction, consequently improving the short wavelength response of cells and to exclude the formation of a $CdTe_{1-x}S_x$ solid solution near the CdS-CdTe interface with high resistivity and smaller band gap than that for CdS. The study of the dark current-voltage characteristics of several ZnSe/CdTe photovoltaic cells with different thicknesses of ZnSe shows that the direct curves of the I–U characteristic shift in the direction of the current abscissa (Fig. 5.18), which corresponds to an increase in the build-in voltage from 0.46 to 0.52 V. A further increase in the thickness of the ZnSe layer shows that the build-in voltage remains constant. The rectification coefficient of the heterostructure with $d_{ZnSe} = 1.4$ μm calculated at $U_d = U_{rev} = 1$ V is about 2 and increases to 60 with the increasing thickness of the ZnSe film. A further increase in the thickness of the ZnSe layer results in an increase in the series resistance of the heterojunction, which limits the direct current that leads to a decrease in the rectification coefficient. In order to see if there is any effect due to the variation of the substrate temperature of the ZnSe layer deposited by CSS method on photovoltaic parameters we investigated the current-voltage characteristic for photovoltaic devices where the substrate temperature was changed as indicated in Fig. 5.19.

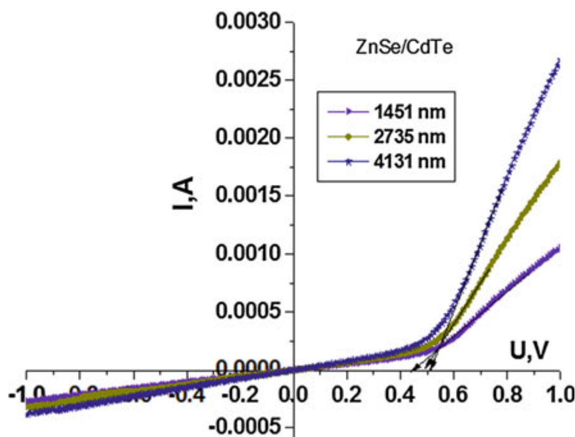

Fig. 5.18 The dark current-voltage characteristics of the ZnSe/CdTe photovoltaic cells with different thicknesses of the ZnSe layer

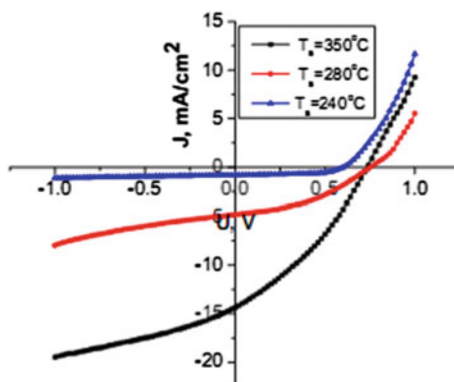

Fig. 5.19 J = f(U) characteristics of the SnO_2/ZnSe/CdTe photovoltaic cells obtained at different substrate temperatures of ZnSe (thickness 2.7 μm); 100 mW/cm^2, 300 K

The photovoltaic parameters of ZnSe/CdTe photovoltaic devices were estimated at the room temperature under the illumination of 100 mW/cm^2 through the wide band gap component ZnSe. The best efficiency of 5.2 % was achieved for the substrate temperature of 350 °C. The open circuit voltage and the current density change significantly with the substrate temperatures. The fill factor is low in general, since series resistance for ZnSe/CdTe is high enough. The photovoltaic characteristics of thin film heterojunction photovoltaic devices with different thicknesses of the ZnSe buffer thin film obtained at T_s = 350 °C are illustrated in Fig. 5.20.

It is obvious that with the ZnSe thin film thickness increase the short circuit current density increases, but the open circuit voltage decreases from 0.75 V at 1.4 and 2.7 μm of ZnSe films to 0.70 V at 4.1 μm of ZnSe thin film thickness. The ZnSe/CdTe photovoltaic cells with an efficiency of 5.5 % were obtained for ZnSe activated and annealed with a thickness of 4.1 μm. Also, the external quantum

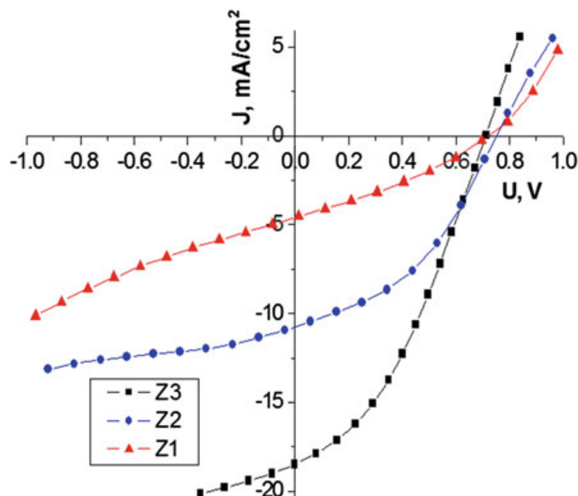

Fig. 5.20 Illuminated current-voltage characteristics of ZnSe/CdTe thin film heterojunction solar cells with different thicknesses of ZnSe: (Z1) 1.4 μm, (Z2) 2.7 μm, and (Z3) 4.1 μm

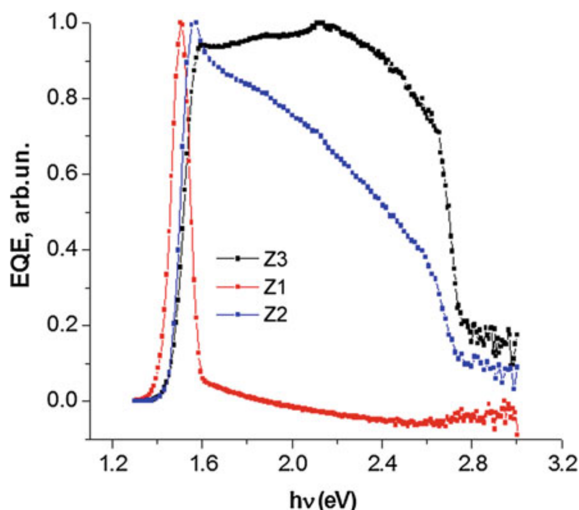

Fig. 5.21 Quantum efficiency of ZnSe/CdTe thin film heterojunction solar cells with different thicknesses of ZnSe

efficiency (Fig. 5.21) for these devices shows that the shape of these characteristics depends on the ZnSe layer thickness. In the case of samples with a thickness of 1.4 μm of ZnSe, almost the whole space charge is situated in CdTe, and the EQE is determined by the electron-hole generation in it. The redistribution of the electron-hole pair generation occurs when increasing the thickness of ZnSe. It is obvious that the contacting materials make an equal contribution to photocurrent if and only if the thickness of the epitaxial layer is on the order of the penetration depth of the contact field. If the thickness is less than the penetration depth, the

major contribution to the EQE is obtained in the sensitivity region of the narrow-band gap material; for the layer thickness higher than the penetration depth of the contact field, it is in the sensitivity region of the wide-band gap material.

5.8 Comparison of CdTe Photovoltaic Devices with Different Buffer Layers

Figure 5.22 compare J-V curves of the best efficiency CdS/CdTe cell with a ZnSe/CdTe cell made by the same technological method, in which the commonly used CdS window is replaced with wider band gap ZnSe to improve the current density.

The photovoltaic parameters for the best ZnSe/CdTe and CdS/CdTe thin film photovoltaic cells are summarized in Table 5.5.

The maximum efficiencies are η = 5.5 % for a cell with a ZnSe buffer and η = 9.6 % for a cell with a CdS buffer. It was found that the ZnSe/CdTe cells present lower values of J_{sc}, and V_{oc}, than those of the CdTe/CdS cells, despite the fact that the SnO_2/ZnSe window allows the transmission of photons in a wider spectral range than the SnO_2/CdS window (Fig. 5.23). This behavior seems to be a consequence of the formation of a better hetero-interface between the CdS and CdTe than between the ZnSe and CdTe thin films. Further studies should be carried out to give a complete explanation of the observed results.

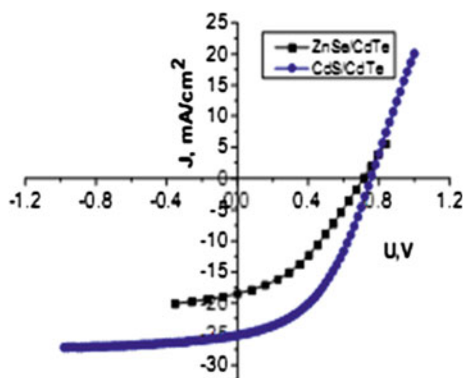

Fig. 5.22 Current-voltage characteristics for the best ZnSe/CdTe and CdS/CdTe thin film photovoltaic devices, 100 mW/cm^2, T = 300 K

Table 5.5 Photovoltaic parameters for the best ZnSe/CdTe and CdS/CdTe thin film photovoltaic devices

Photovoltaic devices	J_{sc} (mA/cm^2)	U_{CD} (V)	FF (%)	η (%)	R_s (Ω cm^2)	R_{sh} (Ω cm^2)
SnO_2/ZnSe/CdTe	20.8	0.63	42	5.5	13.7	256
SnO_2/CdS/CdTe	23.9	0.79	51	9.6	8.4	3769

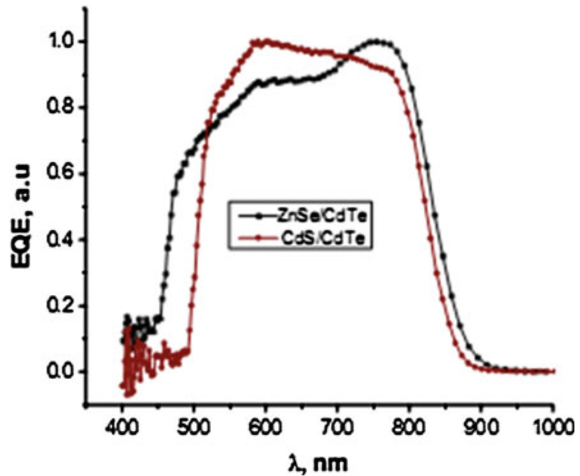

Fig. 5.23 Quantum efficiency for one of the best ZnSe/CdTe and one of the best CdS/CdTe thin film photovoltaic devices

5.9 Photovoltaic Devices Based on TiO_2/CdTe and TiO_2/CdSe Structures

Photovoltaic devices with single-crystal *p*-type CdTe, heterojunctions using stable oxides, such as In_2O_3:Sn (ITO), ZnO, SnO_2 have been investigated. First photovoltaic devices based on *p*-type CdTe single crystals with electron-beam evaporated ITO window layers with $\eta = 10.5$ % were developed by the Stanford group, 1977, with $U_{OC} = 810$ mV, $J_{SC} = 20$ mA/cm^2, and $FF = 65$ % [51]. In 1987, cells made by the reactive deposition of indium oxide, In_2O_3, on *p*-type CdTe single crystals yielded total area efficiencies 13.4 %, with $U_{OC} = 892$ mV, $J_{SC} = 20.1$ mA/cm^2, and $FF = 74.5$ % [52]. In this device, the CdTe crystal had a carrier concentration of 6×10^{15}/cm^3 and the CdTe (111) face were etched in bromine methanol prior to loading into vacuum for In_2O_3 deposition. The U_{OC} of this cell remains the highest ever reported for a CdTe device. The properties of an indium-tin-oxide ITO/CdTe solar cell fabricated by spraying an alcoholic solution of indium chloride and tin chloride on n-type single crystal CdTe were investigated Adeeb et al. [53]. The maximum sensitivity of the ITO/CdTe photovoltaic devices in the visible range attains 0.42 A/W. The efficiency of the solar cells without antireflection coating at AM1 condition is 6.2 %. Photovoltaic devices with ZnO window layers on *p*-type CdTe single crystals yielded poorer junction behavior, with an efficiency <9 % and $U_{OC} = 540$ mV [54]. Using ITO/CdTe, ZnO/CdTe as model systems, we fabricate the TiO_2/CdTe and TiO_2/CdSe photovoltaic devices.

5.9.1 Morphological and Structural Studies of TiO_2 Nanostructured Thin Films

The first set of undoped TiO_2 films was vacuum-annealed at 420 °C for 30 min in the deposition chamber at a pressure of 4.0×10^{-5} mbar and in hydrogen atmosphere at a pressure of 2.0×10^{-3} mbar. A second set of Nb-doped TiO_2 films was annealed at 420 °C for 30 min in hydrogen atmosphere at the same pressure as the first set. We denote the first set of TiO_2 films as MD_2 and the second one as $TiNbO_2$.

The diffraction pattern for the first set of undoped TiO_2 nanostructured films is shown in Fig. 5.24. The various diffraction peaks could be assigned to reflections corresponding to the anatase and rutile phases of TiO_2 (JCPDS data cards 00-021-1272 and 00-21-1276, respectively) for the unannealed and the vacuum-annealed films. For the unannealed TiO_2 film obtained by RF magnetron sputtering the weight percentage of the anatase phase (W_A) is 59.3 % as calculated with the relation [55]

$$W_A = \frac{1}{1 + 1.265^{I_R}/_{I_A}} \tag{5.6}$$

where I_A denotes the intensity of the strongest anatase reflection and I_R is the intensity of the strongest rutile reflection. For the vacuum-annealed film the weight percentage of the anatase phase (W_A) increases to 62 %.The TiO_2 films annealed in H_2 atmosphere exhibit only the anatase phase.

The diffraction spectra of the second set of Nb-doped TiO_2 films are shown in Fig. 5.25. The XRD data show, that the crystallinity is improved when the films are

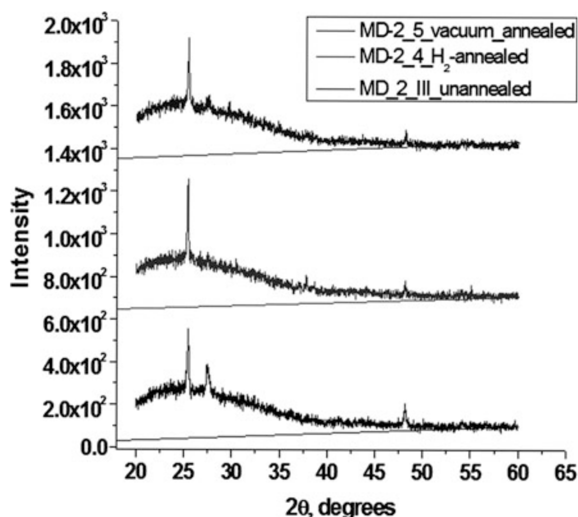

Fig. 5.24 XRD pattern of as-deposited TiO_2 film, vacuum-annealed and annealed in H_2 atmosphere at 420 °C

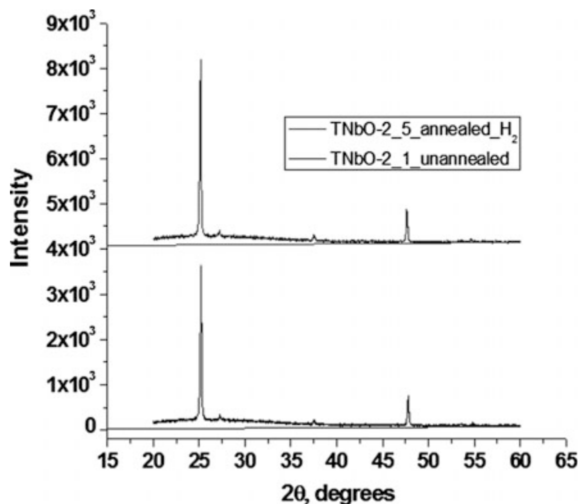

Fig. 5.25 XRD pattern of as-deposited Nb-doped TiO_2 film and annealed in H_2 atmosphere at 420 °C

doped. Annealing at 420 °C in H_2 atmosphere increases the intensity of a diffraction peak at $2\theta = 25.2^o$. No characteristic peaks of Nb_2O_5 were observed in Nb-doped TiO_2 thin films. But it is found that the peak position of (101) anatase plane shifts to a smaller diffracting angle. This may happen because of the exchange of Nb with Ti in the TiO_2 lattice [56] and the formation of the TiNbO phase with different concentrations. This fact was confirmed by the analysis with the TOPAS-Academic V5 software.

The weight percentage of the anatase phase (W_A) is 93 % for annealed Nb-doped TiO_2 film, but for the unannealed it is 96 %. The *a* and *c* lattice parameters of the TiO_2 crystalline cell decrease from (a = 3.8214 Å, c = 9.5868 Å) to (a = 3.7842 Å, c = 9.5185 Å), respectively. This is caused by the different concentration of Nb, confirmed below by the XPS analysis (Table 5.6). We suppose that the primary hydrogen annealing mechanism is the chemisorptions of the dissociated hydrogen on the surface of the films. The half width of all the peaks of the Nb-doped and annealed TiO_2 thin films increases. The crystallite size of TiO_2 nanostructured films was calculated by Scherer equation using anatase (101) and (110) rutile phases. As shown in Table 5.7, for TiO_2 samples deposited by RF magnetron sputtering and annealed in H_2 atmosphere at 420 °C the estimated crystallite size for the anatase phase increases for both sets.

Figures 5.26 and 5.27 show the AFM images of Nb-doped TiO_2 films as-deposited by RF magnetron sputtering at room temperature and annealed at 420 °C for 30 min in hydrogen atmosphere. AFM measurements reveal a net discrepancy and indicate an increase of crystallinity of the annealed films. The as-deposited TiO_2 film exhibits a smooth surface with nonuniform grains. After annealing, the surface becomes homogeneous and is composed of many nanocrystalline grains.

Table 5.6 The weight percentage for the Ti2p, Nb3d and O1s lines

Samples	Atom	%	Atom	%
MD_2_4	O1s	38.1	O1s	60.1
(H_2, 420 °C)	C1s	36.7	Ti2p	39.9
	Ti2p	25.3		
MD_2_5	O1s	42.8	O1s	74.0
(unannealed)	C1s	42.2		
	Ti2p3	15.0	Ti2p3	26.0
MD_2_I	O1s	38.1	O1s	61.5
(vacuum, 420 °C)	C1s	38.0		
	Ti2p3	23.8	Ti2p3	38.5
TiNbO_2_1	O1s	41.3	O1s	61.6
(unannealed)	C1s	32.9		
	Ti2p3	21.5	Ti2p3	32.0
	Nb3d	4.3	Nb3d	6.4
TiNbO_2_5	O1s	41.5	O1s	59.8
(H_2, 420 °C)	C1s	30.5		
	Ti2p3	22.1	Ti2p3	31.9
	Nb3d	5.8	Nb3d	8.3

Table 5.7 Structural parameters of TiO_2 nanostructured thin films

Samples	2θ	Int., arb.un	Phase name	d (ang.)	D (nm)
MD_2_5	25.508	601[a]	(101) Anatase	1.7954	51.0
(unannealed)	27.438	283	(110) Rutile	3.3228	44.1
	48.042	170	(200) Anatase	3.1042	
MD_2_1	25.503	556[a]	(101) Anatase	1.7967	51.5
(vacuum, 420 °C)	27.438	386	(110) Rutile	3.3304	
	48.043	204	(200) Anatase	3.1003	
MD_2_4	25.508	636[a]	(101) Anatase	1.7981	88.4
(H_2, 420 °C)	37.793	186	(004) Anatase	2.5118	
	48.048	162	(200) Anatase	3.1064	
TiNbO_2_1	25.192	3643[a]	(101) Anatase	1.8121	47.4
(unannealed)	27.432	246	(110) Rutile	3.3591	
	37.789	156	(004) Anatase	3.7975	
	47.783	749	(200) Anatase	4.1726	
TiNbO_2_5	25.162	4126[a]	(101) Anatase	1.8141	55.2
(H_2, 420 °C)	27.420	226	(110) Rutile	3.3738	
	37.792	207	(004) Anatase	3.7975	
	47.747	827	(200) Anatase	4.1783	

[a]Most intensive X-ray difraction peak

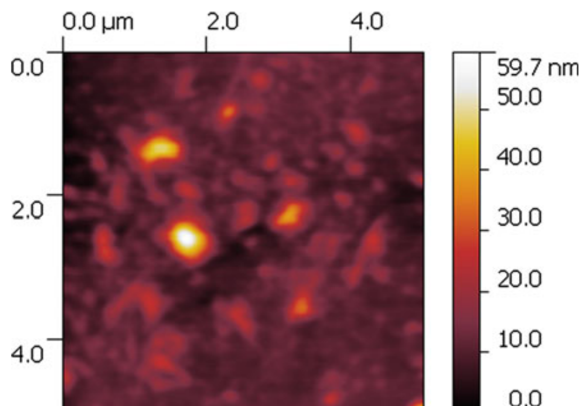

Fig. 5.26 Two-dimensional AFM image of an as-grown Nb-doped TiO_2 thin film

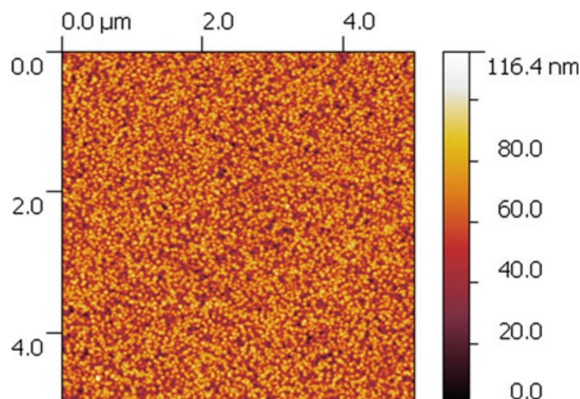

Fig. 5.27 Two-dimensional AFM images of a Nb-doped TiO_2 thin film annealed in H_2 atmosphere at 420 °C

5.9.2 XPS Analysis

Figure 5.28 shows the full range XPS spectra of the first set of TiO_2 films in the whole binding energy region. It can be seen that in the whole region of 0–1200 eV, the characteristic peaks, C1s, O1s and Ti2p are presented. During the XPS experiments for unannealed TiO_2 film the C1s peak position at 284.6 eV is set. For the vacuum and H_2 annealed TiO_2 films the C1s peak position is at 285.7 eV. For the Nb-doped TiO_2 thin films before and after annealing the C1s peak is situated at the same energy. Figure 5.29 shows the results from a fitting procedure with PHI-MATLAB of an XP spectrum of Ti2p for TiO_2 nanostructured thin films of the first set. The experimental contour fits two peaks for all samples. For the unannealed TiO_2 film the spectrum indicates binding energies at 458.5 ± 0.2 eV for Ti2*p*3/2 and 464.3 ± 0.2 eV for Ti 2*p*1/2, respectively, which are very close to the values of the Ti^{4+} valence state of stoichiometric rutile TiO_2 [57, 58]. For the vacuum and H_2 annealed films at 420 °C the binding energies of the Ti2*p* feature shifted toward higher binding energies and are situated at 459.5 ± 0.2 eV for

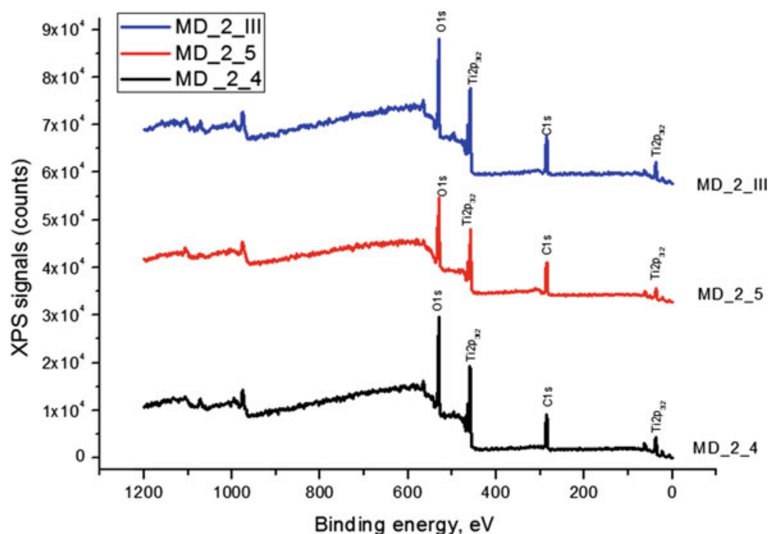

Fig. 5.28 XPS survey scan spectra of an as-deposited TiO_2 film, vacuum-annealed and annealed in H_2 atmosphere at 420 °C

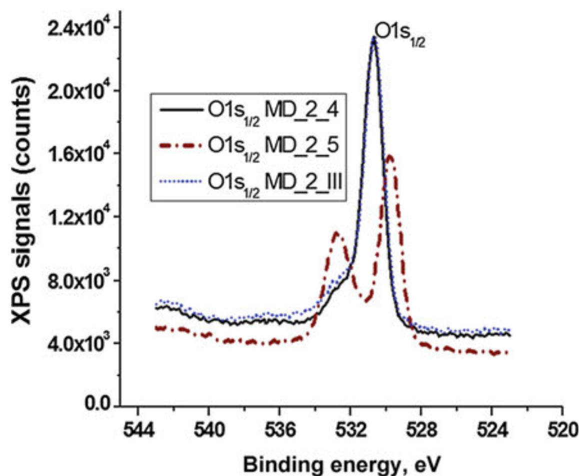

Fig. 5.29 XPS spectra of Ti2p region of an RF magnetron sputtering TiO_2 film, vacuum-annealed and annealed in H_2 atmosphere at 420 °C

Ti2p3/2 and 465.2 ± 0.2 eV for Ti2p1/2 and match well with the reported values for anatase phase [59]. We suppose that this shift may be generated by the reduction of Ti^{4+} ions to Ti^{3+} defect states, which usually are accompanied by a loss of oxygen from the surface of TiO_2.

Liu et al. [60] proposed that the interaction between H_2 and TiO_2 fell into three steps. Firstly, hydrogen interacted physically with the adsorbed oxygen on the surface of TiO_2. Secondly, electrons are transferred from the H atoms to the O atoms in the lattice of TiO_2. Then, the oxygen vacancies are formed when the O atom left

with the H atom in the form of H_2O or OH groups. Thirdly, when the temperature increased to 420 °C, the interaction between H_2 and TiO_2 proceeds more drastically, the electrons are transferred from oxygen vacancies to Ti^{4+} ions, and then Ti^{3+} defect states are formed. Zhang et al. [61] irradiated the TiO_2/Si films by electron beams and found that the number of Ti^{3+} ions increased and Ti^{4+} ions decreased after the irradiation. The weight percentage of the Ti2p and O1s elements in the above mentioned TiO_2 nanostructured thin films are shown in Table 5.7. We can conclude that the Ti^{4+} ions are reduced by both electron donators such as H_2 and lattice oxygen in TiO_2 and the binding energy of 459.5 eV may be attributed in this case to Ti^{3+} defect state of anatase TiO_2 phase according to the XRD analysis. Significant increases in the intensity of the Ti2p peaks for anatase phase are observed, also.

Figure 5.30 shows XPS spectra in O1s region. For the unannealed TiO_2 nanostructured thin film two oxygen chemical species appeared, the lower binding energy species at around 529.7 ± 0.2 eV can be attributed to the basic peak of TiO_2 lattice oxygen (O_{lat}); the other 532. 8 ± 0.2 eV represented the surface weakly bound (or adsorbed) oxygen (OH and molecular O_2 species). The O1s spectrum of the vacuum and H_2 annealed films at 420 °C consists of a main peak with high intensity at about 530.7 ± 0.2 eV and an obvious shoulder located at about 532.9 ± 0.2 eV, indicate that the detected OH group and molecular O_2 may be adsorbed from the surface of the film during annealing. The binding energies of the O1s spectrum of the vacuum and H_2 annealed films shifted toward higher binding energies with the same value 1.0 ± 0.2 eV as for Ti2*p* spectrum of these films.

Figures 5.31, 5.32 and 5.33 present the Nb3d, Ti2p and O1s regions of the RF magnetron sputeriing Nb-doped TiO_2 films and annealed in H_2 atmosphere at 420 ° C. The XPS spectra reveal the Nb3d element. From Table 5.6 we observe that the weight percentage of the Nb3d element is different in TiO_2 films unannealed and annealed in H_2. Therefore, for these samples it is hard to discuss about the influence of the H_2 atmosphere on their structural properties. The Nb3d binding energy for the

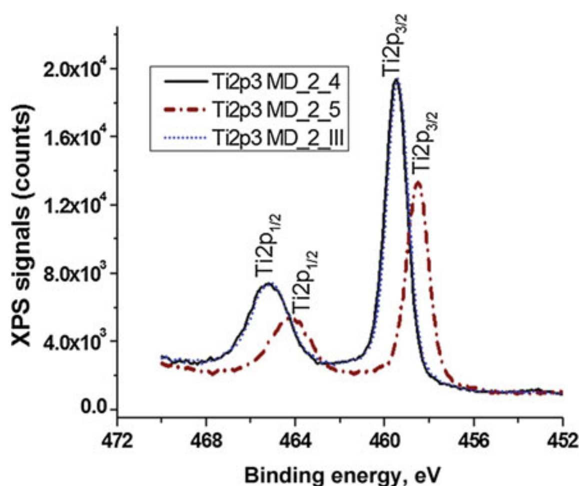

Fig. 5.30 XPS spectra of O1s region of an RF magnetron sputtering TiO_2 film, vacuum-annealed and annealed in H_2

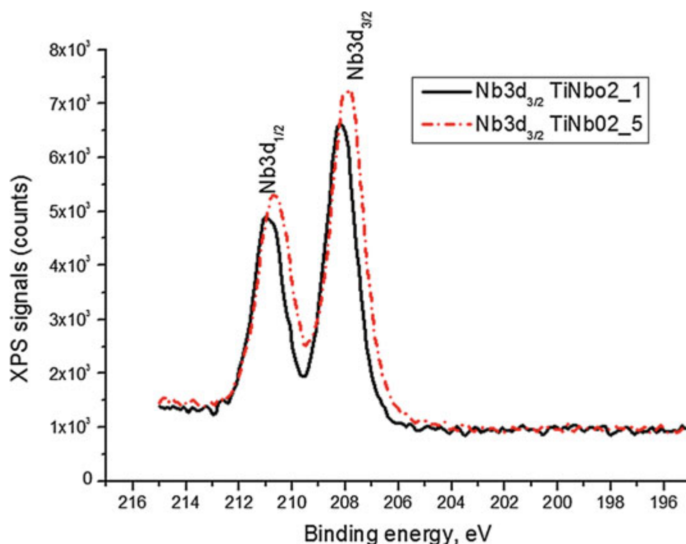

Fig. 5.31 XPS spectra of Nb3d region of an as-deposited Nb-doped TiO_2 nanostructured thin film and H_2 annealed

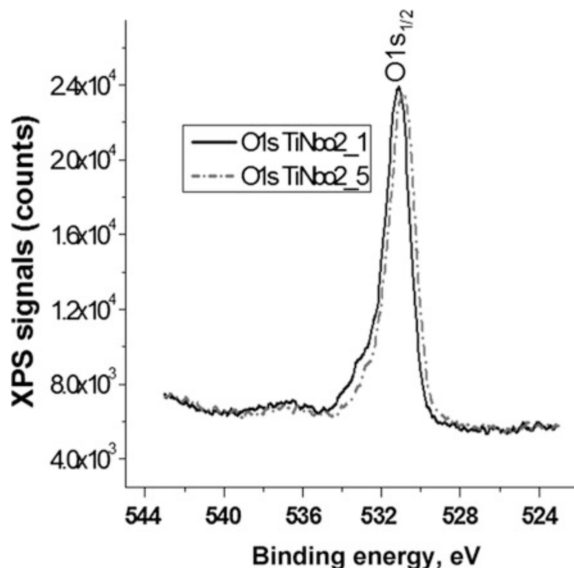

Fig. 5.32 XPS spectra of Ti 2p region of unannealed and annealed Nb-doped TiO_2 films fabricated by RF magnetron sputtering

unannealed Nb-doped TiO_2 film was determined to be 208.2 ± 0.2 eV for Nb3d5/2 and 211.0 ± 0.2 eV for Nb3d3/2, for the annealed one in H_2 atmosphere the binding energy is 207.9 ± 0.2 eV and 210.8 ± 0.2 eV, respectively. We suppose that this shift in these films is caused by the different weight percentage concentration of Nb

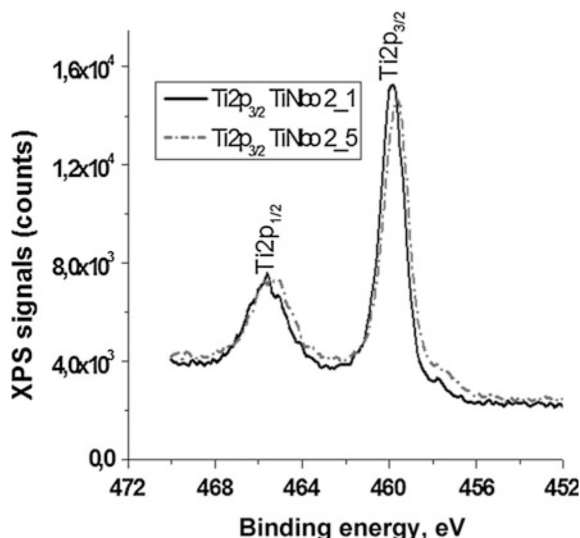

Fig. 5.33 XPS spectra of O1s region of unannealed and annealed Nb-doped TiO_2 films fabricated by RF magnetron sputtering

(Table 5.6) and by annealing in H_2 atmosphere at 420 °C. The Ti2p XPS spectra (Fig. 5.32) of unannealed Nb-doped TiO_2 films demonstrate the presence of 459.7 ± 0.2 eV for Ti2p3/2 and 464.9 ± 0.2 eV for Ti 2p1/2. For the film annealed in H_2 atmosphere a slight shift ($\sim$0.2 eV) towards higher energy is seen for Ti2p3/2 and ($\sim$0.6 eV) for Ti 2p1/2. The position of the Ti 2p3/2 peak (458.8 eV) is close to the value reported for Ti^{3+} states in the anatase phase (458.7 eV) [62].

We think that the H_2 annealing changes the Ti^{3+}/Ti^{4+} ratio in the TiO_2 thin film. Both Ti2p1/2 and Ti2p3/2 binding energies showed a change in Ti^{3+} states and the Ti^{4+} ions as a consequence of the H_2 treatment. A chemical shift of the binding energy of the peaks is known to mean changes in the structure. Since the ionic radii of Nb^{5+} (0.70 A) are larger than the ionic crystal radius of 0.68 A of the titanium we can thus conclude that the Nb is easily built into a lattice, adding electrons. The theoretical calculations of Morgan [63] predict a small-polaronic Ti^{3+}gap state within an Nb-doped TiO_2 thin film. For Nb dopant at these concentrations the defect can be characterized as Nb^{5+} and Ti^{3+}/Ti^{4+} ratio.

The center of the Nb3d3/2 peak corresponds to that of Nb^{5+} oxidation state [64, 65]. Nb^{5+} species, substituting for Ti^{4+} in the crystalline lattice, could be a reason for anatase stabilization. In order to maintain the equilibrium of charges, the extrapositive charge due to Nb^{5+} may be compensated by the creation of an equivalent amount of Ti^{3+} ions [66] or by the presence of vacancies in the cation sites [67].

The XPS spectra of the O1s region of the Nb-doped TiO_2 nanostructured thin films presented in Fig. 5.33 indicate that there is one kind of chemical state. The binding energy of 531.1 ± 0.2 eV for unannealed and 530.8 ± 0.2 eV for annealed Nb-doped TiO_2 films can be attributed to the surface species such as Ti–OH resulting from the chemisorbed water (OH) [68, 69] and to the lattice oxygen (Ti–O), respectively. The shift of the binding energy to small values for the annealed

Nb-doped TiO_2 film can be attributed to the fact that a part of the OH group is adsorbed from the surface because the weight percentage of O atoms is reduced from 61.6 to 59.8 %.

5.9.3 Optical Properties

The optical transmission spectra of the undoped TiO_2 films are shown in Fig. 5.34. The transmission decreases and the position of the interference peaks slightly changes for the annealed TiO_2 thin films. The transmittance of the layers varies between 80 and 90 %, maximum of 90 % being reached for as-deposited TiO_2 fabricated by RF magnetron sputtering. Figure 5.35 shows the variations of transmittance with the wavelength for the Nb-doped TiO_2 thin films. The nearly sharp fall of transmittance curve at the band edge confirms that the doped films have

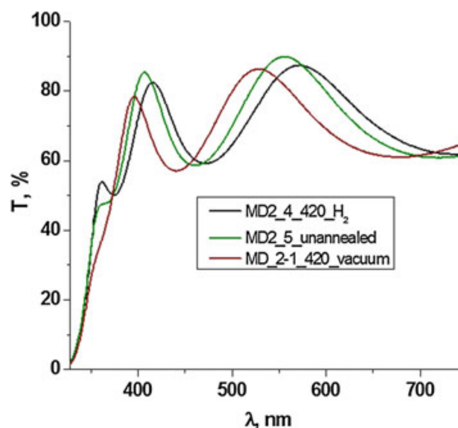

Fig. 5.34 Transmission spectra of undoped TiO_2 nanostructured thin films

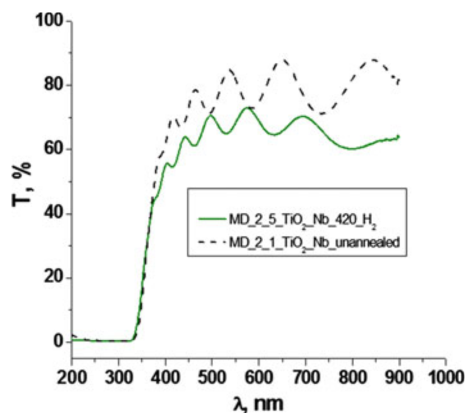

Fig. 5.35 Transmission spectra of the Nb-doped TiO_2 nanostructured thin films

a high crystallinity. The transmission decreases for annealed Nb-doped TiO_2 nastructured thin films in comparison with the undoped films. The optical band gap E_g can be determined from the absorption coefficient α, and it has been investigated by plotting the $(\alpha h\nu)^2 = f(h\nu)$ (for direct allowed transitions) $(\alpha h\nu)^{1/2}$ versus hν (for indirect allowed transitions). In the present study, the best straight line plot extended over most data points is $(\alpha h\nu)^2$ versus hν, as shown in Figs. 5.36 and 5.37. Plots of $(\alpha h\nu)^{1/2}$ versus hν show no linear relationships near the optical absorption edge for TiO_2. The estimated band gap energies of the samples from Figs. 5.36 and 5.37 are summarized in Table 5.8. The maximum band gap reduction was 0.15 eV for Nb-TiO_2 doped unannealed films. H_2 annealing increases the band gap of the Nb-TiO_2 films by 0.03 eV. All band gap values obtained for TiO_2 thin films prepared by RF magnetron sputtering are in good agreement with the reported values from the scientific literature, 3.60–3.75 eV for the direct band gap and 3.05–3.20 eV for the indirect band gap, respectively [70, 71]. Acoording to the XRD analysis TiO_2 is present in two different crystallographic phases. Due to the structural basis the band gap of anatase and rutile is different. The Ti-Ti distances in anatase structure is greater than in rutile, whereas, Ti-O distances are shorter. These

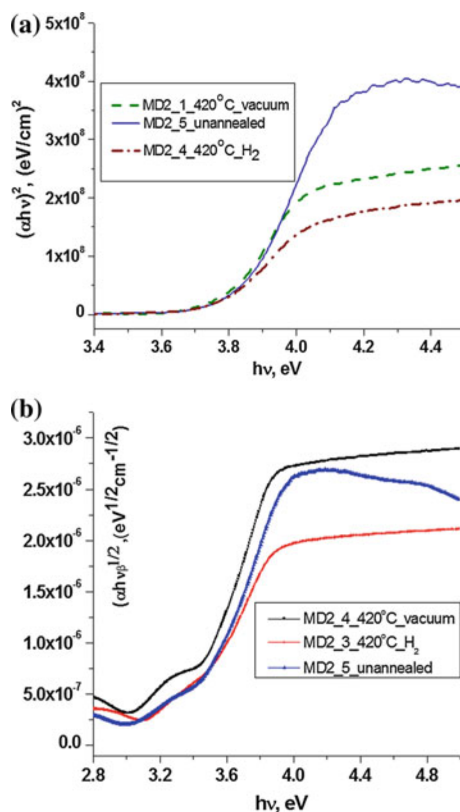

Fig. 5.36 Plots of **a** $(\alpha h\nu)^2 = f(h\nu)$ and **b** $(\alpha h\nu)^{1/2} = f(h\nu)$ of undoped and annealed TiO_2 thin films fabricated by RF magnetron sputtering

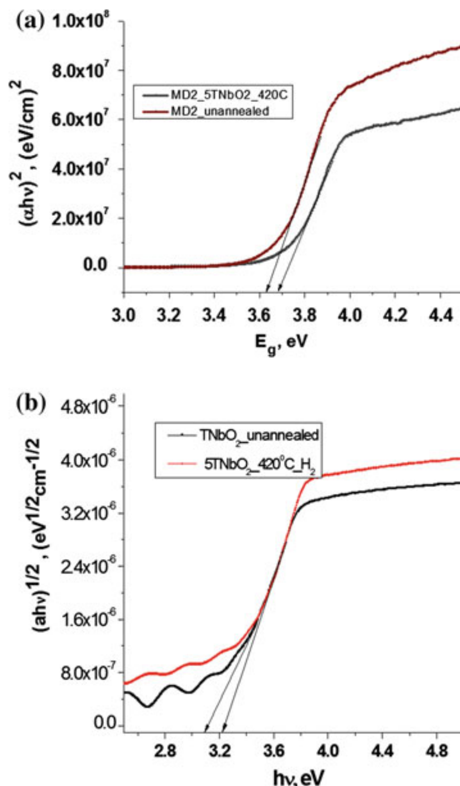

Fig. 5.37 Plots of **a** $(\alpha h\nu)^2 = f(h\nu)$ and **b** $(\alpha h\nu)^{1/2} = f(h\nu)$ of Nb-doped and annealed TiO_2 thin films fabricated by RF magnetron sputtering

Table 5.8 The band gap of the TiO_2 nanostructured thin films

Samples	*d* (nm)	E_g (eV) Direct allowed transitions	*D* (nm)	E_g (eV) Indirect allowed transitions
TNbO2_1_unannealed	321.6	3.63	47.4	3.18
TNbO2_5_ annealed_420 °C_H_2	276.4	3.66	65.2	3.26
MD2_1_vacuum _420 °C	926.7	3.74	51.5	3.26
MD2_4_annealed_420 ° C_H_2	459.6	3.72	88.4	3.27
MD2_5_unannealed	682.1	3.78	51.0	3.29

d -thickness, *D*-grain sizes

structural features change the mass density and lead to different electronic configuration. Rutile phase is 9% higher dense than the anatase presenting more pronounced localization of 3d states and therefore a narrower 3d bands. The O2p and Ti3d hybridization is different in two structure. These different features are responsible for the different band gap.

Table 5.9 Electrical parameters of Nb-TiO_2 films anealed in H_2 atmosphere

T (°C)	ρ (Ω cm)	δ $(\Omega\ cm)^{-1}$	μ (cm^2/V s)	n (cm^{-3})
420	0.74	1.34	3.4	2.4×10^{18}
460	0.4	2.5	0.13	1.7×10^{20}

5.9.4 Electrical Properties

The investigation of the I-U characteristic of the In/TiO_2 indicates that the thermally evaporated indium contact to the TiO_2 nanostructured thin film is a good ohmic contact. TiO_2 thin film possesses *n*-type of conductivity. The main measurements were performed in a constant magnetic field (0.24 T magnetic induction) and with the direct current (DC) stabilized. Each sample was measured for three different values of the current (50 μA–2 mA). For each parameter value the deviation (measurement error) was calculated. These are casual errors and do not include deviations due to the final value of the contact area, i.e. the contacts are not infinitely small points, and the contact area is comparable to the sample surface. The sheet resistance and the Hall effect were measured by the four probe method (Van der Paw method). The measured values of specific electrical conductance and the charge carriers concentration at 295 K for the TiO_2 nanostructured thin films are presented in Table 5.9.

As we can see, the TiO_2 layers treated at lowest temperatures are too resistive to measure with a 4-point probe. With the increase of the annealing temperature, the mobility decreases and the concentration of the charge carriers increases.

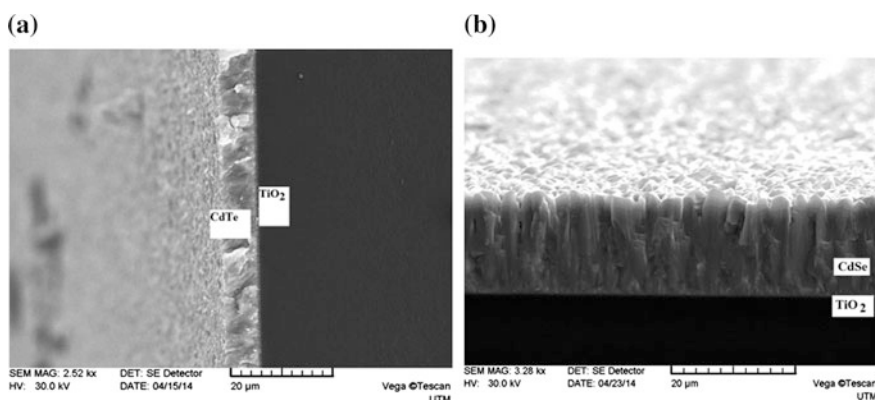

Fig. 5.38 SEM cross-section image of the *n*-TiO_2/*p*-CdTe (**a**) and *n*TiO_2/*n*-CdSe (**b**) heterojunctions

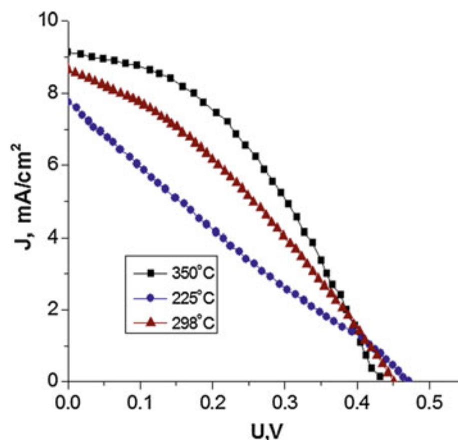

Fig. 5.39 Load J-U characteristics of the TiO_2/CdSe photovoltaic devices under 100 mW/cm^2 illumination, 300 K

5.10 TiO_2/*p*-CdTe and TiO_2/*n*-CdSe Photovoltaic Devices

The SEM cross-section images of the heterojunctions *n*-TiO_2/*p*-CdTe (a) and *n*TiO_2/*n*-CdSe (b) are shown in Fig. 5.38.

It can be seen that CdTe and CdSe thin films have a columnar morphology. The photovoltaic characteristics of the TiO_2/CdTe and TiO_2/CdSe photovoltaic devices were investigated at 300 K and under the illumination of 100 mW/cm^2 through the wide band gap of the TiO_2. The current-voltage characteristics of TiO_2/CdSe photovoltaic devices obtained at different substrate temperatures of CdSe are illustrated in Fig. 5.39. The photovoltaic parameters are presented in Table 5.10.

The best photovoltaic parameters are achieved for a photovoltaic device with CdSe deposited by CSS method at T_s = 350 °C. As one can see from Table 5.10 the value of the open circuit voltage and the current density for this device reaches 0.43 V and 9.12 mA/cm^2, respectively. The fill factor is low in general for all the devices. As one can see from the shape of the load current-voltage curves the series resistance value is high for all the devices and it is due to the fact that the resistance of Nb-doped and annealed TiO_2 thin films is high enough. The highest efficiency achieved for TiO_2/CdSe photovoltaic devices is 1.63 %.

One of the important factors determining the efficiency of a solar cell is the spectral distribution of the quantum efficiency which accounts for the formation of the drift and diffusion components of the photocurrent, and, ultimately, the short-circuit current density. The location of the long-wave edge of the spectral distribution of the external quantum yield is well correlated with the band gap energy of CdSe (Fig. 5.40).

Table 5.10 Photovoltaic parameters of TiO_2/CdSe photovoltaic devices

T_s (°C)	J_{sc} (mA/cm^2)	U_{oc} (V)	*FF*	η (%)
225	7.74	0.47	0.24	0.87
298	8.73	0.45	0.33	1.26
350	9.12	0.43	0.42	1.63

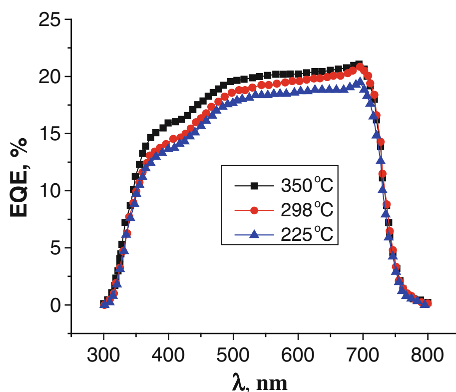

Fig. 5.40 The external quantum efficiency of the TiO_2/CdSe photovoltaic devices at different substrate temperatures of CdSe

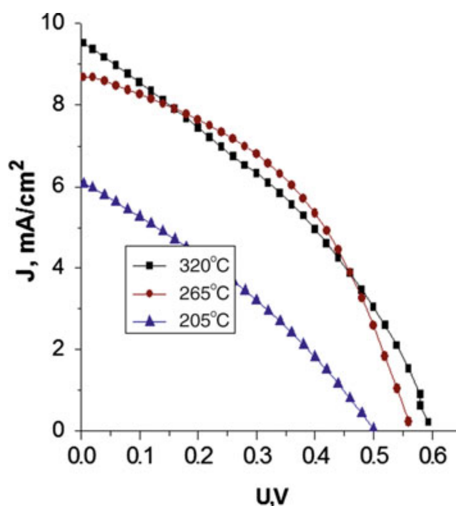

Fig. 5.41 Load current-voltage characteristics of the TiO_2/CdTe photovoltaic devices under 100 mW/cm^2 illumination, 300 K

The load current-voltage characteristics of the illuminated TiO_2/*p*CdTe photovoltaic devices are shown in Fig. 5.41. The photovoltaic parameters depend on the shape of the J-U curve, which is influenced by the substrate temperature of the CdTe thin films. An inspection of Table 5.11, where the photovoltaic parameters are presented, shows that the efficiency of the devices is low because of the low values of the open circuit voltage and the fill factor. Efforts are now in progress to improve the device photovoltaic parameters. The EQE for the TiO_2/*p*CdTe devices, when illuminated through the wide band gap semiconductor (TiO_2), is shown in Fig. 5.42.

As seen from this figure, the EQE extends from 350 to 860 nm, i.e. covers the whole visible range of the solar spectrum and consistent UV-vis region. The quantum efficiency data indicate that with the increase of the substrate temperature of the CdTe thin film fabricated by CSS method the carrier collection is improved.

Table 5.11 Photovoltaic parameters of TiO_2/CdTe photovoltaic devices

T_s (°C)	J_{sc} (mA/cm^2)	U_{oc} (V)	*FF*	η (%)
205	6.1	0.51	0.27	0.85
265	9.12	0.43	0.42	1.63
320	9.5	0.59	0.36	1.98

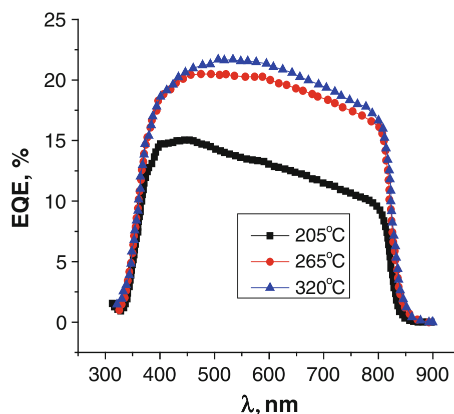

Fig. 5.42 External quantum efficiency of the TiO_2/CdTe photovoltaic devices at different substrate temperatures of CdTe

Both the blue and the red regions of the spectrum show that the charge collection in the device is affected, the red region somewhat more dramatically. This may be caused by the increase of the recombination rate of carriers. We believe that the recombination occurs primarily at the interface and then at the enlarged front and back contacts in these device structures.

5.11 Conclusions

The II–VI compounds have been and continue to be explored for electrical energy generation from solar radiation with the goal to increase efficiency at a low cost. Among A_2B_6 thin-films, CdTe based PV modules have shown remarkable progress with commercialization and become the first PV technology with the price below 1 $/Wp. The comparison of one of the best MSU CdS/CdTe photovoltaic device with a device with a world record efficiency of 18.3 % indicates optical (reflection and absorption), electrical and recombination efficiency losses. Analyses of current-voltage and EQE measurements allow us to identify the efficiency losses in the MSU device. It was shown that the efficiency loss is primarily caused by the fill factor. The *FF* losses are due to the series resistance R_s, the leakage current, and the ideality factor, the low U_{oc}, voltage dependent current collection, $J_L(U)$ and back contact. The second loss that needs to be addressed occurs for short wavelengths. The absorption losses in SnO_2 and CdS layers decrease J_{SC} to 20–24 %. The world

record efficiency device shown for comparison has partially solved that problem by using a new design at the frontal contact and much thinner CdS thin film. Analysis of J-U and EQE characteristics, of a new ZnSe/CdTe photovoltaic device, shows that the replacement of CdS with ZnSe reduces the frontal CdS absorption loss, but increases the recombination loss due to a larger mismatch (~ 12 %) between the lattice parameters of ZnSe and CdTe thin films. The grain boundary interface state density minimizes the efficiency of these devices more than in the case of CdS/CdTe thin film HJs. The losses caused by the light absorption in the ‘window’ layer of CdS/CdTe solar cells can be reduced by using a material with a wider band gap instead of CdS and ZnSe. Titanium dioxide, one of the best prospective transparent conductive oxides, is widely used in different semiconductor devices due to its high transparency for visible light, large value of the refractive index, controllable specific resistance, good adhesion and high chemical resistance. Also, TiO_2 is environment friendly. The value of the band gap energy of TiO_2 nanostructured thin film varies from 3.15 to 3.6 eV depending on the crystalline structure and deposition technology, that is, about 1 eV larger than that of CdS and ZnSe. This characteristic of TiO_2 allows broadening the spectral region of the photosensitivity of heterojunctions based on CdTe toward the short wavelengths. The photovoltaic devices based on *n*-TiO_2/*p*-CdTe and *n*-TiO_2/*n*-CdSe thin film heterojunctions were fabricated by the deposition of CdTe and CdSe onto TiO_2 thin films prepared by the DC reactive magnetron sputtering technique. Poor efficiency of these devices could be attributed first to the higher sheet resistance of TiO_2 films and, secondly, to the relatively high concentration of mismatch dislocations at the TiO_2/CdTe and TiO_2/CdSe heterojunction interfaces. Note that the TiO_2/CdTe and TiO_2/CdSe heterojunctions were fabricated without the application of additional treatments. It is evident that the controllable change of technological parameters of the TiO_2 thin films deposition, the modification of the CdTe surface, the annealing of the heterojunctions in different atmospheres, as well as the introduction of additional intermediate layers can reduce the surface states concentration at the TiO_2/CdTe and TiO_2/CdSe interfaces and enhance the efficiency of the photovoltaic conversion. Finally, for the MSU CdTe photovoltaic devices to be competitive with the world record technologies, the problems related to contact resistivity, increasing the *p*-type carrier concentration in CdTe, identification and reduction of the density of limiting intragrain defect states, defining and overcoming performance limitations related to back-contact formation on CdTe must be solved.

Acknowledgments The author would like to thank Dr. L. Ghimpu, PhD student N. Spalatu, MPs P. Dumitriu for their help in developing the photovoltaic devices fabrication technology based on A_2B_6 compounds. Also, I am thankful to all the scientists from the Department of Physics and Engineering at MSU for their support and helpful discussions. Many thanks to the team led by prof. D. Luca from Physics Department at “Al. Cuza” University, Romania, for supplying us TiO_2 thin films, for their support with XPS and XRD measurements. I am also grateful to those numerous worldwide scientists and engineers whose data have been included in this overview. This research was supported by the EU 7th Framework Program PEOPLE International Research Staff Exchange Scheme project GA-2008, no. 230861 and by the Bilateral grant no. 13.820.15.19/RoA.

References

1. A.D. Upadhyaya, V. Yelundur, A. Rohatgi, High efficiency mono-crystalline solar cells with simple manufacturable technology, in *Proceedings of 21st European Photovoltaic Solar Energy Conference and Exhibition*, Dresden, Germany, 4–8 Sept 2006
2. W. Heywang, K.H. Zaininger, Silicon: the semiconductor material, in *Silicon: Evolution and Future of a Technology*, ed. by P. Siffert, E.F. Krimmel (Springer, New York, 2004
3. M. Taguchi, *Solar Bus.* Unit (Sanyo Electr. Co., Ltd., Kobe, Japan) (A. Yano, S. Tohoda, K. Matsuyama, IEEE J. Photovolt. **4**(1), 96–99)
4. B.M. Kayes, H. Nie, R. Twist, S.G. Spruytte, F. Reinhardt, I.G. Kizilyalli, G.S. Higashi, in *Proceedings of the 37th IEEE Photovoltaic Specialists Conference*, Seattle, Washington, USA (2011)
5. M.A. Green, K. Emery, Y. Hishikawa, W. Warta, E.D. Dunlop, Progr. Photovolt. **21**, 827S (2013) (R. Wenham, M.A. Green, M.E. Watt, R. Corkish, *Applied Photovoltaics* (Earthscan, 2007), Chap. 2
6. S.R. Wenham, M.A. Green, M.E. Watt, R. Corkish, *Applied Photovoltaics* (Earthscan, 2007), Chap. 2
7. A. Morales-Vilches, C. Voz, M. Colina, G. Lopez, I. Martin, A. Orpella, J. Puigdollers, M. Garcia, R. Alcubilla, *Electron Devices (CDE), 2013 Spanish Conference* 12–14 Feb 2013, pp. 345–348
8. R.W. Collins, et al., Evolution of microstructure and phase in amorphous, protocrystalline, and microcrystalline silicon studied by real time spectroscopic ellipsometry. Solar Energy Mater. Solar Cells **78**(1–4), 143–180 (2003)
9. M. Gloeckler, I. Sankin, Z. Zhao, CdTe solar cells at the threshold to 20 %. IEEE J. Photovolt. **3**(4), 1389–1393 (2013)
10. P. Jackson, D. Hariskos, E. Lotter, S. Paetel, R. Wuerz, R. Menner, W. Wischmann, M. Powalla, New world record efficiency for Cu(In, Ga)Se2 thin-film solar cells beyond 20 %. Prog. Photovolt: Res. Appl. **19**, 894–897 (2011)
11. X. Wu, High-efficiency polycrystalline CdTe thin-film solar cells. Sol. Energy **77**(6), 803–814 (2004)
12. D.L. Baltzner, A. Romeo, H. Zogg, R. Wendt, A.N. Tiwari, Development of efficient and stable back contacts on CdTe/CdS solar cells. Thin Solid Films **387**(1–2), 151–154 (2001)
13. J. Loferski, J. Appl. Phys. **27**, 777–784 (1956)
14. E. Adirovich, Y. Yuabov, D. Yugadaev, Sov. Phys. Semicond. **3**, 61–65 (1969)
15. D. Bonnet, H. Rabenhorst, *Conference on Record on 9th IEEE Photovoltaic Specialist Conference*, pp. 129–132 (1972)
16. J.P. Enrıquez, X. Mathew, G.P. Hernández, U. Pal, D.R. Maganã, D.R. Acosta, R. Guardian, J. A. Toledo, G. Contreras Puente, J.A. Chavez Carvayar, CdTe/CdS solar cells on flexible molybdenum substrates. Solar Energy Mater. Solar Cells **82**, 307–314 (2004)
17. I. Matulionis, H. Sijin, J.A. Drayton, K.J. Price, A.D. Compaan, Cadmium telluride solar cells on molybdenum substrates, in *Proceedings of the Materials Research Society Symposium on II–VI Compound Semiconductor Photovoltaic Materials,* Warrendale, PA, USA, vol. 668, H8.23 (2001), pp. 1–6
18. P.S. Vijay, C.M. John, G.B. Lush, W. Wang, X. Wang, G.W. Thompson, E. Clark, Thin film CdTe–CdS heterojunction solar cells on lightweight metal substrates. Solar Energy Mater. Solar Cells **59**, 145–161 (1999)
19. X. Mathew, J.P. Enriquez, A. Romeo, A.N. Tiwari, CdTe/CdS solar cells on flexible substrates. Solar Energy **77**, 831–838 (2004)
20. Y.S. Tyan, E.A. Perez-Albuerne, Efficient thin-film CdS/CdTe solar cells, in *Proceedings of the 16th IEEE Photovoltaic Specialists Conference*, pp. 794–800, New York, NY, USA (1982)
21. B.M. Basol, Electrodeposited CdTe and HgCdTe solar cells. Solar Cells **23**, 69–88 (1988)

22. T.L. Chu, Thin film cadmium telluride solar cells by two chemical vapour deposition techniques. Solar Cells **23**, 31–48 (1988)
23. K.W. Mitchell, C. Eberspacher, F. Cohen, J. Avery, W. Duran, W. Bottenberg, Progress towards high efficiency thin film CdTe solar cells. Solar Cells **23**, 49–57 (1988)
24. C. Ferekides, J. Britt, Y. Ma, L. Killian, High efficiency CdTe solar cells by close spaced sublimation, in *Proceedings of the 23rd IEEE Photovoltaic Specialists Conference*, pp. 389–393, New York, NY, USA, May 1993
25. X. Wu, J.C. Keane, R.G. Dhere, C. DeHart, D.S. Albin, A. Duda, T.A. Gessert, S. Asher, D.H. Levi, P. Sheldon, 16.5 %-efficient CdS/CdTe polycrystalline thin-film solar cells, in *Proceedings of the 17th European PVSEC* (2001), pp. 995–1000
26. D.A. Cusano, CdTe solar cells and PV heterojunctions in II-VI Compounds. Solid State Electron. **6**(3), 217 (1963)
27. P. Meyers, C. Liu, T. Frey, U.S. Patent 4,710,589 (1987)
28. J.F. Nolan, P.V. Meyers, Fabrication of stable large-area thin-film CdTe photovoltaic modules. Annual subcontracting report, NREL/TP-413–5740 (1993)
29. T. Aramoto, M. Tsuji, T. Yamamoto, T. Nishio, P. Veluchamy, H. Higuchi, S. Kumazawa, J. Shibutani, S. Nakajima, Y. Nishiyama, T. Arita, A. Hanafusa, T. Hibino, K. Omura, Highly efficient large area thin film CdS/CdTe sub-module solar cells, in *Proceedings of 28th IEEE Photovoltiac Specialist Conference*, pp. 436–439
30. D. Bonnet, Manufacturing of CSS CdTe solar cells. Thin Solid Films **361–362**, 547 (2000)
31. M. Gloeckler, I. Sankin, Z. Zhao, CdTe solar cells at the threshold to 20 % efficiency, in *Proceedings of 39th IEEE Photovoltiac Specialist Conference*, 2013, pp. 436–439
32. M.A. Green, K. Emery, D.L. King, S. Igari, W. Warta, Solar cell efficiency tables (Version 18). Progr. Photovolt. Res. Appl. **9**, 287–293 (2001)
33. M.A. Green, K. Emery, Y. Hishikawa, W. Warta, E.D. Dunlop, Solar cell efficiency tables (version 40). Prog. Photovolt: Res. Appl. **20**, 606–614 (2012)
34. M.A. Green, K. Emery, Y. Hishikawa, W. Warta, E.D. Dunlop, Solar cell efficiency tables (version 41). Prog. Photovolt: Res. Appl. **21**, 1–11 (2013)
35. Press Release, First Solar, 22 April 2013, [Online]
36. A. Kanevce, D.H. Levi, D. Kuciauskas, The role of drift, diffusion, and recombination in time-resolved photoluminescence of CdTe solar cells determined through numerical simulation. Progr. Photovolt. (2013)
37. S.H. Demtsu, J.R. Sites, in *Proceedings of the 30th IEEE Photovoltaic Specialist Conference*, pp. 744–747, 2005
38. P. Gashin, T. Potlog, L. Ghimpu, T. Potlog, L. Ghimpu, P. Gashin, A. Pudov, T. Nagle, Sites. J Solar Energy Mater. Solar Cells **80**, 327–334 (2003)
39. Yu.Z. Bubnov , M.S. Lurie , F.G. Starh , G.A. Filaretov. The vacuum deposition of films in the quasi-closed volume. M. , Sov . radio,(1975)
40. T. Potlog, N. Spalatu, N. Maticiuc, J. Hiie, A. Mere, V. Valdna, V. Mikli Structural reproductibility of CdTe thin films deposited on different substrates by close space sublimation method. Phys. Status Solidi (A) **209**(2), 272–276 (2012)
41. D. Batzner, A. Romeo, H. Zogg, R. Wendt, A. Tiwari, Thin Solid Films **151**, 387 (2001)
42. E. Brian, McCandless, H. Gregory, D. Hanket, J. Garth, R.W. Birkmire, J. Vac. Sci. Technol. A **20**(4), 1462–1467 (2002)
43. S. Wei, S. Zhang, A. Zunger, J. Appl. Phys. **87**, 1304–1311 (2000)
44. JCPDS X-ray powder files data (Data file 05–0522)
45. G. Gordillo, E. Romero, C. Quinones, Study of structural properties of Zn(S,Se) thin films deposited by evaporation, in *19th European Photovoltaic Solar Energy Conference* pp. 1780–1783 (2004)
46. Pradip K. R. Kalita, B. K. Sarma and H. L. Das. Structural characterization of vacuum evaporated ZnSe thin films. Bull. Mater. Sci., Vol. 23, No. 4, August, pp. 313–317 (2000)
47. R.B. Kale, C.D. Lokhande, Influence of air annealing on the structural, morphological, optical and electrical properties of chemically deposited ZnSe thin films. Appl. Surf. Sci. **252**(4), 929–938 (2005)

48. H. Morkoç, S. Strite, G.B. Gao, M.E. Lin, B. Sverdlov, M. Burns, Large-band-gap SiC, III-V nitride, and II-VI ZnSe-based semiconductor device technologies. J. Appl. Phys. **76**, 1363–1398 (1994)
49. G. Hodes, in *Physical Electrochemistry: Principles, Methods and Applications*, ed. by I. Rubinstein (Marcel Dekker Inc., New York, 1995), pp. 515–554
50. G. Perna, M. Lastella, M. Ambrico, V. Capozzi, Temperature dependence of the optical properties of ZnSe films deposited on quartz substrate. Appl. Phys. A **83**, 127–130 (2006)
51. K. Mitchell, A. Fahrenbruch, R. Bube, J. Appl. Phys. **48**, 829–830 (1977)
52. T. Nakazawa, K. Takamizawa, K. Ito, Appl. Phys. Lett. **50**, 279–280 (1987)
53. N. Adeeb, I. Kretsu, D. Sherban, C. Sushkevich, A. Simashkevich, Spray deposited ITO/CdTe solar cells. Solar Energy Mater. **15**(1), 9–19 (1987). ISSN 0927-0248
54. J. Aranovich, D. Golmayo, A. Fahrenbruch, R. Bube, J. Appl. Phys. **51**, 4260–4265 (1980)
55. JCPDS X-ray powder file data (Data file 05–0522)
56. R. Sharma, M. Bhatnagar, Sens. Actuators B **56**(3), 215–219 (1999)
57. H.S. Kim, S.H.Kang, Effect of hydrogen treatment on anatase TiO_2 nanotube arrays for photoelectrochemical water splitting. Bull. Korean Chem. Soc. **34**(7), 2067–2072 (2013)
58. H. Bae, S.H. Park, A. Nakamura, K. Koike, K. Fujii, H.-J. Park, H.-J. Lee, T.-S. Oh, J.-S. Ha, The effect of rapid temperature annealing with N_2 and H_2 on photoelectrochemical properties of u-TiO_2. J. Electrochem. Soc. **160**(11), H800–H802. http://jes.ecsdl.org/content/160/11/H800.abstract-fn-2
59. C.D. Wagner, W.M. Riggs, L.E. Davis, J.F. Moulder, G.E. Muilenberg, *Handbook of X-ray Photoelectron Spectroscopy* (Perkin Elmer Corp. Publishers, Eden Prairie, MN, 1979), p. 68
60. J. Liu, S. Xu, L. Liu, D.D. Sun, The size and dispersion effect of modified graphene oxide sheets on the photocatalytic H_2 generation activity of TiO_2 nanorods. Carbon **60**, 445–452. doi:10.1016/j.carbon.2013.04.059
61. J. Zhang, Y. Wang, Z. Jin, Z. Wu, Z. Zhang, Visible-light photocatalytic behavior of two different N-doped TiO_2. Appl. Surf. Sci. **254**, 4462–4466 (2008)
62. M.Z. Atashbar, H.T. Sun, B. Gong, W. Wlodarski, R. Lamb, XPS study of Nb-doped oxygen sensing TiO_2 thin films prepared by sol-gel method. Thin Solid Films **326**(1–2), 238–244 (1998)
63. B.J. Morgan, D.O. Scanlon, G.W. Watson, J. Mater. Chem. 19, 5175–5178 (2009)
64. J.F. Moulder, W.F. Stickle, P.E. Sool, K.D. Bomben, *Handbook of X-Ray Photoelectron Spectroscopy* (Perkin-Elmer Corporation, Eden Prairie, Minn, USA, 1999)
65. M. Valigi, D. Cordischi, G. Minelli, P. Natale, P. Porta, A structural, thermogravimetric, magnetic, electron spin resonance, and optical reflectance study of the NbO_xTiO_2 system. J. Solid State Chem. **77**(2), 255–263 (1988)
66. M. Sacerdoti, M.C. Dalconi, M.C. Carotta et al., XAS investigation of tantalum and niobium in nanostructured TiO_2 anatase. J. Solid State Chem. **177**(6), 1781–1788 (2004)
67. M. Park, T.E. Mitchell, A.H. Heuer, J. Am. Ceram. Soc. **58**, 43–47 (1975)
68. J.C. Colmenares, M.A. Aramendıa, A. Marinas, J.M. Marinas, F.J. Urbano, Appl. Catal. A: Gen. **306**, 120–127 (2006)
69. S.P. Kowalczyk, F.R. McFeely, L. Ley, V.T. Gritsyna, D.A. Shirley, Sol. St. Commun. **23**, 161 (1977)
70. B. Liu, L. Wen, X. Zhao. The photoluminescence spectroscopic study of anatase TiO_2 prepared by magnetron sputtering. Materials Chemistry and Physics, V. 106, Iss. 2–3, pp. 350–353 (2007)
71. F.A. Jenkins, H.E. White, *Fundamentals of Optics*, 4th edn. (New York, McGraw Hill, 1976)

Part II
Magnetic Nanomaterials for Spintronic and Sensoric Applications

Chapter 6
Engineering the Magnetoelectric Response in Piezocrystal-Based Magnetoelectrics: Basic Theory, Choice of Materials, Model Calculations

João V. Vidal, Andrey A. Timopheev, Andrei L. Kholkin and Nikolai A. Sobolev

Abstract This chapter presents a theoretical basis of the anisotropic magnetoelectric (ME) effect in tri-layers of metglas and piezoelectric (PE) single crystals. The properties of various common PE and magnetostrictive substances are discussed, and arguments for the choice of the most appropriate materials are made. A linear description of the ME effects in terms of electric, magnetic and elastic material fields and material constants is presented. An averaging quasi-static method is used to illustrate the relation between the material constants, their anisotropy and the transversal direct ME voltage and charge coefficients. Subsequently, the aforementioned model is employed in the calculation of the maximum expected direct ME voltage coefficient for a series of tri-layered Metglas/Piezocrystal/Metglas composites as a function of the PE crystal orientation. The ME effects are shown to be strongly dependent on the crystal orientation, which supports the possibility of inducing large ME voltage coefficients in composites comprising lead-free PE single crystals such as $LiNbO_3$, $LiTaO_3$, α-$GaPO_4$, α-quartz, langatate and langasite through the optimization of the crystal orientation.

J.V. Vidal · A.A. Timopheev · N.A. Sobolev
Departamento de Física & I3N, Universidade de Aveiro, 3810-193 Aveiro, Portugal

A.L. Kholkin
Departamento de Física & CICECO, Universidade de Aveiro, 3810-193 Aveiro, Portugal

A.L. Kholkin
Institute of Natural Sciences, Ural Federal University, 620000 Ekaterinburg, Russia

N.A. Sobolev (✉)
National University of Science and Technology "MISiS", 119049 Moscow, Russia
e-mail: sobolev@ua.pt

© Springer International Publishing Switzerland 2016

I. Tiginyanu et al. (eds.), *Nanostructures and Thin Films for Multifunctional Applications*, NanoScience and Technology,
DOI 10.1007/978-3-319-30198-3_6

6.1 Introduction

6.1.1 The Magnetoelectric Effect

The linear magnetoelectric effect (ME), according to the original definition outlined by Debye in 1924–1926 [1], is described as the linear induction of a polarization, $\boldsymbol{P}$, in a material, in response to an applied magnetic field, $\boldsymbol{H}$. This is called the direct ME effect also designated by the acronym ME_H. In the same way, the converse ME effect (ME_E) is defined as the induction of a magnetization, $\boldsymbol{M}$, in a material as a result of an applied electric field, $\boldsymbol{E}$. These two relations can be expressed to the first order in the following way (in SI units) [2–5]:

$$P_i = \alpha_{ij} H_j; \tag{6.1}$$

$$\mu_0 M_i = \alpha_{ji} E_j, \tag{6.2}$$

where α indicates the linear ME susceptibility tensor (rank-2 tensor expressed in units of s/m), and μ_0 is the magnetic permeability of empty space. We note that the summation of the repeated index variables (i and j) over all of their integer values in tridimensional space is implicit in the above equations following the Einstein notation. Symbols in bold, on the other hand, represent vector or tensor fields.

The ME effect has given rise to a lot of interest in the scientific community over the past two decades, driven by the possibility of new and promising multifunctional device paradigms and also by the demand for a greater understanding of the fundamental physics associated with solid materials. This interest is evidenced by the large number of review articles related to developments in the field of the ME effect published in recent times [4–26].

Theoretical physical models are highly important because they allow us to draw valuable conclusions and predictions about the nature of the ME effect. Since early times, an important inequality for the ME single-phase materials has been drawn from a thermodynamic treatment. It states that [27, 28]:

$$\alpha_{ij} < \left({}^{e}\chi_{ii}\,{}^{m}\chi_{jj}\right)^{\frac{1}{2}} \tag{6.3}$$

where ${}^{e}\chi_{ii}$ and ${}^{m}\chi_{jj}$ are the electric and magnetic susceptibility tensor coefficients, respectively. The inequality (1.3) indicates the existence of a well-defined upper bound for all components of the $\boldsymbol{\alpha}$ tensor. Although this limit is much higher than the experimentally measured values for all known ME materials [29], it still represents a severe limitation on the magnitude of the linear ME response in single-phase materials (i.e., multiferroics) [30, 31]. This is due to a chemical contraindication to the simultaneous occurrence of a high permittivity and permeability in the same material and results in part from a large intrinsic difficulty in electrically polarizing magnetic ions [32]. Furthermore, by arguments from the group theory, it can also be shown that the static linear ME effect may only be

observed in media that are neither symmetrical with respect to the space inversion operation (i.e., systems without a center of symmetry) nor with respect to the time reversal (i.e. systems with a magnetic ordering) [30–33]. Therefore, the ME effect is allowed only in 58 out of the 122 magnetic point groups [34]. A more general approach to the ME coupling may include higher-order contributions (describing the so-called secondary ferroics), parameterized by tensors such as β (ME effect induced by the $\boldsymbol{H}$ field) or γ (ME effect induced by the $\boldsymbol{E}$ field), both of rank-3, as can be seen by the general electromagnetic free energy expansion of a material [5, 35]:

$$F(E,H) = F_0 - P_i^S E_i - M_i^S H_i - \frac{1}{2}\varepsilon_0 \varepsilon_{ij} E_i E_j - \frac{1}{2}\mu_0 \mu_{ij} H_i H_j - \alpha_{ij} E_i H_j - \frac{1}{2}\beta_{ijk} E_i H_j H_k - \frac{1}{2}\gamma_{ijk} H_i E_j E_k - \cdots \quad (6.4)$$

However, the linear term α_{ij} is generally the dominant contribution to the ME effect, and thus much of the current research in this area is directed towards the study of this linear effect.

Up to date, the ME effect has already been observed in several different types of materials [6, 7]. Two major classes of ME compounds can, however, be distinguished: single-phase ME materials (ME multiferroics) and ME composite materials which incorporate both piezoelectric (PE) and magnetostrictive (MS) materials in some manner. These composites may also integrate non-electric and non-magnetic compounds such as organic polymers and even multiferroic materials. Only the magnetoelectric composites will be explored in detail in this chapter, with the multiferroic compounds standing outside of its scope.

6.1.2 Magnetoelectric Composites

The bulk ME composite materials constitute a class of structures that incorporate both ferroelectric and ferri/ferromagnetic compounds [5, 6, 30]. The demand for these types of materials is essentially guided by the prospect of being able to control their internal charge distribution through the action of an applied magnetic field or, alternatively, their spin distribution by an electric field, thus allowing the development of new forms of multifunctional devices [8]. A ME coupling of large magnitude is therefore essential in order for them to be useful in efficient practical applications. Some of their most promising future applications may include [6, 7, 12, 23]: *DC* and *AC* magnetic field sensors, electric current sensors, multiple-state memories, RAM-like magnetic memories, micro-sensors in read-heads, transformers, spinners, diodes, optical devices that generate spin waves and electrically tunable microwave devices.

For the particular case of single-phase multiferroic compounds it has been known that the ME coupling constitutes a very rare phenomenon, usually being only observable at very low temperatures (low Curie and/or Néel temperatures for the electric and magnetic ordering) [6, 7, 19]. Furthermore, the single phase materials are commonly characterized by low values of the ME coupling coefficient ($\alpha_E \approx 0.4 - 20$ mV/(cm·Oe)) [16, 17], in part due to the limits imposed by inequality (1.3). On the other hand, composite materials generally exhibit ME responses orders of magnitude stronger even at room temperature and, therefore, are currently much closer to commercial applications in new devices [6, 12]. Another major advantage of this configuration is associated with its enlarged manufacture flexibility. In fact, in order to manipulate the ME behavior of a composite, several parameters may be individually tuned including [6, 7, 12, 36]: (i) the properties of the constituent phases (e.g. PE and piezomagnetic coefficients, permittivity, permeability, elastic constants, electric resistivity, loss tangents, etc.); (ii) the volume and geometrical arrangement of the various phases (e.g. particulate or laminate structures, volume fraction between phases, layer thickness, grain size, rod diameter, etc.); (iii) the quality of the coupling between interfaces (e.g., structural compatibility between materials; synthesis techniques employed such as sintering, sol-gel method, hot-pressing, tape-casting, solid-state reaction or other physical/chemical deposition techniques; binding substances used such as epoxy, polymeric matrix, cyanoacrylate glue, etc.); (iv) the modes of operation (i.e. relative orientation between the applied/measured electric and magnetic fields, static or dynamic fields, charge, i.e. short-circuit, or voltage, i.e. open-circuit, measurements, frequency of the magnetic or electric modulation fields, etc.); (v) the processing techniques (e.g., pre-poling, pre-magnetizing, heat treatments, etc.); and (vi) the use of bulk phases or nanostructures such as thin films (which can give rise to new exotic effects).

To better understand the origin of the ME effect in PE/MS composite systems, we first take a look at the concept of physical properties resulting from the combination of distinct single-phase compounds. Here, it is known that composite systems may exhibit properties similar to those of their constituent phases but also give rise to completely new ones, absent in the parent compounds. The sum and scaling properties are part of the first class, while the product properties are associated with the former [7, 17, 37]. Thus, the ME effect in composite materials is in fact an extrinsic product property resulting from the interaction between PE and MS constituent phases [13, 17, 38]. The mechanism of the direct ME (ME_H) effect is as follows: the MS material is initially deformed as a result of the application of an external magnetic field ($\boldsymbol{H}$). Part of this elongation/contraction (quadratic in the field) is then transferred to the PE phase leading to an elastic straining ($\boldsymbol{S}$) and subsequently to the induction of a macroscopic electric polarization ($\boldsymbol{P}$) due to the stress ($\boldsymbol{T}$) driven PE effect. It is obvious that the reciprocal effect may also take place (converse ME effect or ME_E effect). In this case, an external electric field ($\boldsymbol{E}$) induces a deformation of the PE component elongating or contracting it. This strain is then transmitted to the MS phase through a mechanical coupling between components. Thus, the magnetic phase experiences a magnetization ($\boldsymbol{M}$) change

induced by the electric field. In summary, we just saw how a composite material can be characterized by a new property, the ME coupling, which is manifested by the appearance of a polarization (magnetization) in response to an externally applied magnetic (electric) field. Roughly speaking, the direct and converse ME effects may then be written under the form of the products [39]:

$$\mathrm{ME_H}\ \textit{effect} = \frac{\textit{Electrical}}{\textit{Mechanical}} \times \frac{\textit{Mechanical}}{\textit{Magnetic}};\ \mathrm{ME_E}\ \textit{effect} = \frac{\textit{Magnetic}}{\textit{Mechanical}} \times \frac{\textit{Mechanical}}{\textit{Electrical}},$$

where *Electrical*/*Mechanical* and *Mechanical*/*Magnetic* represent, respectively, the generation of PE charge ($d_{ij} = \partial D_i/\partial T_j$) and the MS deformation ($q_{ij} = \partial S_j/\partial H_i$), while *Magnetic*/*Mechanical* and *Mechanical*/*Electrical* represent the piezomagnetic induction ($q_{ij} = \partial B_i/\partial T_j$) and the PE deformation ($d_{ij} = \partial S_j/\partial E_i$). With this concept of product properties in mind, the effective short-circuit ($E_i = 0$) ME coefficient can then be approximately expressed as [6, 40]:

$$\alpha_{Qij} = \partial D_i/\partial H_j = (\partial D_i/\partial T_k)(\partial T_k/\partial S_l)(\partial S_l/\partial H_j) = k_c d_{ik} s_{kl}^{-1} q_{jl} \tag{6.5}$$

where k_c is a coupling factor ($0 \leq |k_c| \leq 1$) that quantifies the efficiency of the transference of strain between phases (i.e. the ratio between the strain transferred to the PE/MS phase and the strain generated in the MS/PE phase by the external field) and depends on the fraction and connectivity between phases [41]. This expression indicates that the ME coupling should be favored by large PE coefficients (d_{ij}), piezomagnetic coefficients (q_{ij}), the inverse of averaged effective elastic compliances (s_{ij}^{-1}) and coupling factors (k_c). Consequently, the ME effect in composite materials is a coupling between electrical and magnetic fields mediated by an elastic interaction, and is therefore an extrinsic property generated from separate compounds which do not exhibit any ME behavior by themselves.

Since the ME interaction between different phases is a complex process, the ME response observed in composite materials will not simply be linear as in the case of most multiferroic compounds [7, 12]. In composites, the ME effect is actually a dynamic effect, and a large linear response can only be observed with an *AC* field (electric or magnetic) oscillating in the presence of a given *DC* field. In addition to the nonlinear response due to the quadratic effect of magnetostriction, generally the ME coupling in composites also displays a hysteretic nature [17]. Therefore, under open-circuit conditions, a dynamic direct ME voltage coefficient $\alpha_{Eij} = \partial E_i/\partial H_j$ is used as a figure of merit. For a traction-free composite the relation $\alpha_{ik} = -\varepsilon_0 \varepsilon_{rij} \alpha_{Ejk}$ can be proven [40, 42, 43], where α_{ij} represents its effective dynamic ME susceptibility, ε_{rij} the effective relative dielectric permittivity and ε_0 the permittivity of empty space. α_{Eij} is typically specified in technical units of V/(cm·Oe) which can be converted to SI units (V/m)/(A/m) through a multiplication by a factor of 4π/10.

This coefficient is usually defined for a magnetic *AC* modulated field ($\delta H_i(t) = \delta H_i \cdot \sin(\omega t)$) with small amplitude ($\delta H$ up to approximately 1 Oe) and with a frequency ($f = \omega/2\pi$) of up to about 1 MHz, superimposed on a larger (up to, say, 20 kOe) magnetic *DC* bias field ($\boldsymbol{H}$) [7]. The amplitude of the ME induced *AC* voltage (δV_i) measured between two electrodes in the sample should then be proportional to the amplitude of the *AC* magnetic field in any detection circuit, thus establishing an analogy with the linear ME response observed in single-phase compounds. Finally, in order to quantify the dynamic ME coefficients, one measures the ME voltage induced in a sample by the magnetic field and then uses the relation $\alpha_{Eij} = \delta V_i/(t \cdot \delta H_j)$, which is valid for small enough δH_j [44] and where t is the effective distance between electrodes generally equal to the thickness of the PE. In practice, two particular cases of this coefficient are commonly studied in the literature [6, 7, 12, 28]: (i) the longitudinal T-T ME voltage coefficient (α_{E33}), and (ii) the transversal L-T ME voltage coefficient (α_{E31} or α_{E32}). Additionally to α_E, another ME coefficient can be used to describe the direct ME effect in composites under distinct operation conditions. This is the so called charge ME coefficient (α_Q), usually measured under short-circuit conditions, and it quantifies the amount of charge generated as a function of the applied magnetic field i.e. $\alpha_{Qij} = \partial D_i/\partial H_j \propto -C\alpha_{Eij}$, where C is the low-frequency capacitance of the composite [45–47]. This coefficient can be measured directly by an electrometer or ammeter or indirectly as a voltage from the output of a charge amplifier and is particularly important for applications in low-noise (<5 pT/Hz$^{1/2}$) and low-frequency (<1 Hz) magnetic field sensors [46, 48, 49]. Alternatively, a less common converse ME coefficient, $\alpha_{Bij} = \partial B_i/\partial E_j$, can also be quantified by measuring the magnetic response of a sample when an electric field is applied to it (e.g., through a change in the amplitude of the magnetization induced by an applied voltage, a variation in hysteretic magnetization curves, a change in the magnetic anisotropy or a shift of ferromagnetic resonance absorption peaks) [20]. The analysis of this parameter can be important, e.g., for applications in inductances and electrically controlled microwave devices [23].

Composite materials can be manufactured with a variety of geometries and compositions. Here, a certain phase may take the shape of particles, fibers/rods, layers or three-dimensional arrays which, in the Newnham notation, can be denoted by the indices 0, 1, 2 and 3, respectively [50]. In this way, the notation 2-2, for example, indicates a two-phase composite consisting of alternating layers of different materials. As for its composition, bi-phasic composites contain a ferroelectric phase, usually $BiFeO_3$ (BFO), $BaTiO_3$ (BTO), $PbTiO_3$ (PTO), $Pb(Zr,Ti)O_3$ (PZT), (1–x)[$PbMg_{1/3}Nb_{2/3}O_3$]–x[$PbTiO_3$] (PMN-PT) or (1–x)[$PbZn_{1/3}Nb_{2/3}O_3$]–x [$PbTiO_3$] (PZN-PT), and a ferromagnetic phase, generally consisting of ferrites or magnetic alloys such as $NiFe_2O_4$ (NFO), $CoFe_2O_4$ (CFO), Fe_3O_4, $La_{1-x}Sr_xMnO_3$ (LSMO), $Y_3Fe_5O_{12}$ (YIG), $Tb_xDy_{1-x}Fe_2$ (Terfenol-D), Metglas (Fe–Ni–Co–B–Si–Mo), Permendur (Fe–Co–V) or Galfenol (Fe–Ga) [6, 14]. Table 6.1 summarizes some of the most important properties from the point of view of the ME coupling, of some of the most thoroughly investigated PE materials. PE ceramics, PZT in

Table 6.1 Main physical properties, relevant to the ME effect, of some common Z-cut piezoelectrics

	$BaTiO_3$	$LiNbO_3$	$GaPO_4$	PZT–5	PZT–4	PZN-PT	PMN-PT	PVDF	NKN
d_{31} (pC/N)	–33	–0.85	–1.58 (d_{14})	–175	–109	–1280	≈700	16.5	–
d_{33} (pC/N)	94	6	4.37 (d_{11})	400	300	2000–2500	2000	–33	158
ε^T_{r33}	132	85.2	5.38 (ε^T_{r11})	1750	1350	7200	5000	10	–
T_c (°C)	152	1210	900	360	320	163	80	129	415
ρ (g/cm^3)	6	4.63	3.57	7.7	7.6	8.2	7.8	1.78	–
Q_m	–	–	–	80	500	–	–	4	234
k^l_{33}	0.63	0.17	0.15 (k^l_{11})	0.72	0.68	0.94	≈0.9–0.94	0.19	0.46
References	[55, 56]	[57]	[58, 59]	[14]	[14]	[14, 60, 61]	[14, 62]	[14]	[24]

Here, d_{31} and d_{33} represent the PE strain coefficients,ε^T_{r33} is the dielectric relative permittivity, T_c the Curie temperature, p the mass density, Q_m the mechanical quality factor (i.e. 2π times the energy stored divided by the energy dissipated per cycle for a given fundamental resonance mode expressed as $\sqrt{L_1/C_1}/R_1$, where L_1, C_1 and R_1 are respectively the series inductance, capacitance and resistance of the equivalent electrical circuit of the PE vibrator [54]) and k^l_{33} the electromechanical coupling factor for a longitudinal oscillation (i.e. the square-root of the ratio between delivered mechanical or electrical energy and total absorbed energy in this case given by $d_{33}/\sqrt{s^E_{33}\varepsilon^T_{33}}$ [54])

particular, have been extensively studied and shown to provide a strong ME coupling thanks to their relatively large PE and electromechanical coupling coefficients [51–53]. Other compounds commonly used as the PE phase in ME composite materials are PMN-PT and PZN-PT [14, 22, 53]. These materials have PE and electromechanical characteristics superior to those of PZT but, on the other hand, are associated with low Curie temperatures and low fracture toughness, which severely limits their practical applications [14]. The polymer PVDF is another common material, less attractive from the point of view of the PE accumulation of charge (though it has a relatively large PE strain coefficient), but which has the advantages of being elastically soft and having a high electrical resistivity and resistance to solvents [14]. Some early research also has pointed out to the possibility of using single-crystalline PE materials exhibiting considerably better performances [22]. Nevertheless, the PE ceramics based on PZT, PMN-PT and PZN-PT still possess the best known dielectric and PE properties and thus are in the prime position for future applications in actuators, sensors and resonators [14, 22, 51–53]. However, lead (Pb) featured in these compounds represents a serious environmental problem, and therefore a great deal of current research is focused on identifying lead-free PE compounds which could serve as alternatives to the former [24]. In recent times, many developments have been made in this direction with the appearance of a series of new "clean" piezoelectrics. Among these, ceramics based on the compound $(Na,K)NbO_3$ (NKN) (e.g., solid solutions of NKN-$LiNbO_3$,

Table 6.2 Main physical properties, relevant to the ME effect, of some important MS materials

	$NiFe_2O_4$	Terfenol-D	Permendur	Galfenol	Metglas 2605
λ_s (ppm)	27	1400	70	200	40
q_{33} (ppm/Oe)	≈0.18	≈1–2	≈1	≈1.5	≈4.0
μ_{r33}^T	20	≈6–10	2300	20	>40 000
T_C (°C)	535	380	940	670	395
ρ (g/cm^3)	5.37	7.8	8.2	7.7	7.18
σ (S/m)	1.00×10^{-6}	1.72×10^6	2.38×10^6	1.67×10^6	7.69×10^5
References	[14, 74]	[14, 52, 72, 75]	[76–78]	[14, 79, 80]	[14, 68, 72]

Here, λ_s is the saturation magnetostriction, q_{33} the piezomagnetic coefficient, μ_{r33}^T the relative magnetic permeability, ρ the mass density, σ the electrical conductivity and T_C the Curie temperature

NKN-$LiTaO_3$, NKN-$LiSbO_3$, NKN-Li(Nb,Ta,Sb)O_3, NKN-$BaTiO_3$, NKN-$SrTiO_3$ or NKN-$CaTiO_3$) have received considerable attention for two main reasons [24]: (i) their PE properties stay unchanged over a wide temperature range and (ii) there are numerous possibilities of chemical substitution in the compounds.

Similarly, the main properties of the most attractive MS materials are summarized in Table 6.2. Here, one can identify the greatest advantage of ferrites with respect to metallic alloys when employed in particulate ME composites, viz., its high electrical resistivity. This is critical when one seeks to obtain MS phases capable of withstanding an electric displacement field on 0–3 particulate or 1–3 fiber/rod composites because, otherwise, there would be a large leakage of current through the compound thus nullifying the charge built-up. $NiFe_2O_4$, in particular, is the ferrite with the largest saturation magnetostriction (λ_s) currently known, while also possessing good mechanical properties. Despite its small magnetostriction in relation to alloys, $NiFe_2O_4$ is still widely used in ME composites and could find applications, e.g., in microwave devices [14]. However, in 2-2 laminate composites, layers of the MS phase tend to be interspersed by layers of the PE phase, commonly associated with a large electrical resistivity. In this case the leakage of current trough the thickness of the composite is minimized, so that the MS phases are no longer required to have high resistivities. Therefore, the research on ME composites in the last decade has been strongly focused on composite laminates containing the MS alloy Terfenol-D ($Tb_{0.3}Dy_{0.7}Fe_{1.92}$/$Pb(Zr_{0.52}Ti_{0.48})O_3$) [12, 63–67]. Among all known magnetic materials, Terfenol-D is still the one with the highest saturation magnetostriction [6]. On the other hand, this compound is very expensive and brittle, as well as exhibiting high losses at high frequencies (≳100 kHz) caused by eddy currents. As in all alloys, it also has a low electrical resistivity and cannot be co-sintered with ferroelectric oxides [14]. Also, its low magnetic permeability ($\mu_r \approx 3-10$) and large saturation field require high magnetic fields (typically above 1 kOe) in order to maximize the ME coupling coefficients, making it unsuitable for low-field applications [6, 23]. Consequently, the study of other lower-cost magnetic alloys such as Permendur (Fe–Co–V), Galfenol (Fe–Ga) or Metglas (Fe–Ni–Co–B) is of great interest [51, 68–70]. Currently, one of the most promising MS alloys is

Metglas, mainly because of its huge relative magnetic permeability ($\mu_r > 10\,000$), large piezomagnetic coefficient ($q_{33} \approx 4.0\,\text{ppm/Oe}$) and reasonable saturation magnetostriction ($\lambda_s = 40\,\text{ppm}$) [14]. Different types of this compound consist of soft Fe-, Co- or Fe–Ni-based amorphous alloys, also containing small quantities of B and in some cases Si and Mo, fabricated by a rapid solidification process [71]. This process provides it with unique magnetic properties such as a very high permeability and a very low coercivity and magnetic anisotropy. Despite its smaller saturation magnetostriction when compared to Terfenol-D, ME composites of Metglas can still display very large ME couplings. This is because, as will be shown later, the ME dynamic coefficients are proportional to the linear piezomagnetic constants ($q_{ij} = \partial S_j/\partial H_i = \partial \lambda_j/\partial H_i$) and not to the saturation magnetostriction (λ_s). In fact, Metglas constitutes the material with the largest known piezomagnetic coefficient, $q_{33} \approx 4$ ppm/Oe (in the case of the 2605SA1 alloy) [68, 72], being approximately twice the one observed for Terfenol-D [52]. It also has a high transversal coefficient of $q_{11} + q_{12} \approx 1.5$ ppm/Oe [73]. Additionally, its very high permeability ensures a high concentration of magnetic flux and, therefore, a saturation of the magnetization and magnetostriction at very low magnetic fields of ca. 10 Oe. Consequently, its piezomagnetic and ME coefficients, when incorporated into a ME composite, generally attain maximum values at low magnetic fields.

Since the initial research and until this day, the ME laminate composites have attracted a particularly large interest because of their large ME coefficients, due to large PE and MS coefficients and an absence of current leakage, which have paved the way to several promising applications. Thus, a wide variety of laminar geometries [66, 67, 81–83], synthesis/binding techniques [82–84] and operation modes [63–66, 85, 86] have already been studied in detail. With regard to their geometry, the most frequently employed laminate composites are based on simple structures of only two or three rectangular or disk shaped layers (i.e. sandwich structures) [6]. These structures are the most investigated primarily for their ease of manufacture and for exhibiting, in general, very intense ME effects with coefficients usually in the range from 0.05 to 45 V/(cm·Oe) in the quasi-static regime (i.e. under off-resonance conditions) [16, 18, 22, 23, 26].

When an oscillating *AC* magnetic field is applied to a ME composite, its ME response oscillates with the fundamental frequency and higher harmonics of this field. In particular, a large increase in the magnitude of the ME effect is expected whenever the frequency matches one of the natural electrical, magnetic or mechanical modes of resonance of the structure [20, 87–89]. Both phases of the composite can exhibit these phenomena. These are known as electromechanical resonance (EMR), for the case of the PE phase, and ferromagnetic resonance (FMR), for the case of the magnetic phase.

The EMR occurs when a characteristic mechanical eigenmode of the PE phase is indirectly excited by the varying magnetic field [88]. This field produces a periodic strain in the MS phase which is then transferred to the PE phase. A conventional mechanical resonance of the PE can then be observed when the elastic vibration frequency coincides with a natural frequency (or one of its harmonics) of the

system. This frequency depends on the effective material parameters and geometry of the PE. Thus, a large oscillation amplitude of the standing wave in this layer will also give rise to a large polarization/voltage through the PE effect. Theoretical models based on equivalent circuits for the composites have shown that the ME coefficient at resonance is approximately Q_m times larger than that observed off resonance, where Q_m is the effective mechanical quality factor of the composite [22]. It is also possible to show that the extensional length-resonance frequencies of a traction-free laminate composite with the shape of a long bar (i.e., with a length much larger than its width and thickness) can be given by $f_{ln} = (2n-1)/2\ell\sqrt{\rho s_{11}}$ [90], where $n \in \mathbb{N}$ is the harmonic number, ℓ the length of the PE bar, ρ its mass density and s_{11} the longitudinal elastic compliance along the length direction (here assumed to be X as in Fig. 6.1a) [14]. For laminate composites with lengths of about 1 cm and thicknesses of about 1 mm, fundamental in-plane extensional EMRs are generally observed in the range from 200–400 kHz, while fundamental thickness extensional EMRs are commonly found in the range from 2–4 MHz [91–93]. For the case of a PE with a more complex geometry, however, additional types of EM modes are expected to be found including shear and flexural modes, mainly in the case of symmetrical laminate composites, and bending modes, mainly in the case of asymmetrical laminate composites. As in the extensional case, for a traction-free long-bar shaped PE the n first bending resonant modes should be observed at $f_{bn} = \beta_n^2 t/2\pi\ell^2\sqrt{12\rho s_{11}}$ (with $\beta_1 \approx 4.730$, $\beta_2 \approx 7.853$, $\beta_3 \approx 10.996$, $\beta_4 \approx 14.137$, etc.) [90], where t is the thickness of the PE. The fundamental bending modes are typically observed in the range from 40–80 kHz in PE plates with lengths of approximately 1 cm and thicknesses of about 1 mm. Under bending EMR conditions, ME voltage coefficients as large as 737 V/(cm·Oe) have thus been detected at low frequencies in ME thin film layered composites [94] and up to 16 kV/(cm·Oe) in specially designed ME ferromagnetic-elastic-PE cantilever structured composites [95–97].

The FMR phenomenon involves the resonant absorption of a microwave by the ferromagnetic component of the composite when subjected to some magnetic bias field. An electric field (E_j) applied to the composite thus straining the ferromagnetic

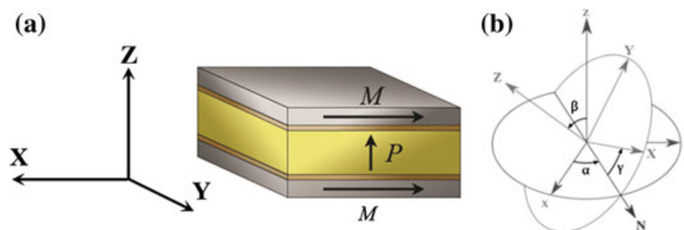

Fig. 6.1 **a** Representation of a tri-layered ME composite operating in the transversal L-T mode (i.e. longitudinal or in-plane magnetization, $\boldsymbol{M}$, of the MS layers and transversal or out-of-plane polarization, $\boldsymbol{P}$, of the PE layer). **b** Euler angles scheme used in the rotation of the crystallographic frame of a single crystal to the laminate frame of figure **a** [111]

phase may consequently shift this resonant magnetic field [88, 98]. A very large ME coupling has additionally been predicted for a superposition of EMR and FMR, in which case it is called magnetoacoustic resonance (MAR) [88]. In general, one expects to observe EMR for frequencies of the order of 100 kHz, FMR of the order of 10 GHz and antiferromagnetic resonances of the order of 100 GHz [6, 7, 12, 26]. The latter two make the ME laminates very promising from the point of view of microwave devices.

6.2 Theory of the Magnetoelectric Effect

6.2.1 Piezoelectricity and Magnetostriction

The phenomena of piezoelectricity and magnetostriction can be mathematically described by a model derived from thermodynamics, electrodynamics and continuum mechanics. The set of equations obtained including Maxwell's equations, conservation of linear momentum, angular momentum, energy and mass (in the non-relativistic approximation) thus depend on the choice of the thermodynamic potential. Starting with a PE system and considering isothermal and adiabatic conditions and ignoring higher-order effects, the system's Gibbs free energy may be described by [54, 99–101]:

$$G(\boldsymbol{E}, \boldsymbol{T}) = -\frac{1}{2}{}^{p}s^{E}_{ijkl}{}^{p}T_{ij}{}^{p}T_{kl} - d_{kij}{}^{p}E_{k}{}^{p}T_{ij} - \frac{1}{2}(\varepsilon^{T}_{kl} - \varepsilon_0\delta_{kl}){}^{p}E_{k}{}^{p}E_{l}, \tag{6.6}$$

where the Einstein summation convention is used. Here, ${}^{p}s^{E}_{ijkl}$ is an element of the elastic compliance tensor (a rank-4 tensor), d_{kij} the PE strain coefficient (a rank-3 tensor), ε^{T}_{kl} the dielectric permittivity (a rank-2 tensor), ${}^{p}T_{ij}$ the elastic stress (a rank-2 tensor), and ${}^{p}E_{k}$ the electric field (a vector). The superscripts E and T in the material constants indicate that those are defined under the conditions of a constant electric field or stress, respectively. Throughout the rest of this chapter, the subscripts i, j, k and l will range over the integers 1, 2 and 3, whereas the subscripts a, b, c and d over just 1 and 2. The superscript p on the constants and variables is meant to remind us that we are dealing with a PE medium. Through the partial differentiation of the G potential, the linear constitutive equations of piezoelectricity are obtained as [54, 99–101]:

$${}^{p}D_{k} = \varepsilon_0{}^{p}E_{k} - \frac{\partial G}{\partial{}^{p}E_{k}} = \varepsilon^{T}_{kl}{}^{p}E_{l} + d_{kij}{}^{p}T_{ij}; \tag{6.7}$$

$${}^{p}S_{ij} = -\frac{\partial G}{\partial{}^{p}T_{ij}} = {}^{p}s^{E}_{ijkl}{}^{p}T_{kl} + d_{kij}{}^{p}E_{k}, \tag{6.8}$$

where ${}^{p}D_k$ is the electric displacement (a vector) and ${}^{p}S_{ij}$ is the elastic strain (a rank-2 tensor).

All of the tensor parameters for a given property of the material mentioned so far are mathematical objects that change with the coordinate system in a predictable way and obey certain symmetry relations, which considerably reduces the number of their independent components. Those symmetry relations have three basic sources [102]: the symmetry of the partial differential equation (PDE) that defines the property, the symmetry of the tensor variables which determine the property, and the symmetry of the material that exhibits the property (i.e., its point group). The first kind of symmetry limits the number of independent elements of the tensor properties which are defined by repeated differentiation. An example of this is the PE coefficient, where $d_{kij} = d^E_{kij} = \left(\partial D_k/\partial T_{ij}\right)_E = -\partial^2 G/\partial T_{ij}\partial E_k = -\partial^2 G/\partial E_k \partial T_{ij} = \left(\partial S_{ij}/\partial E_k\right)_T = d^T_{kij}$, the dielectric permittivity $\varepsilon^T_{kl} = (\partial D_k/\partial E_l)_T = \varepsilon_0\delta_{lk} - \partial^2 G/\partial E_l \partial E_k = \varepsilon_0 \delta_{kl} - \partial^2 G/\partial E_k \partial E_l = (\partial D_l/\partial E_k)_T = \varepsilon^T_{lk}$, and the compliance $s^E_{ijkl} = \left(\partial S_{ij}/\partial T_{kl}\right)_E = -\partial^2 G/\partial T_{ij}\partial T_{kl} = -\partial^2 G/\partial T_{kl}\partial T_{ij} = s^E_{klij}$. The theory of linear elasticity yields $S_{ij} = (1/2)(\partial u_i/\partial x_j + \partial u_j/\partial x_i)$, where u_i are the displacement vectors along the x_i Cartesian directions, so that $S_{ij} = S_{ji}$, thus reducing the number of independent variables to 6. Furthermore, the conservation of angular momentum also implies that $T_{ij} = T_{ji}$. Consequently, taking into account this symmetry of the tensor variables that determine the properties $d_{kij} = \left(\partial D_k/\partial T_{ij}\right)_E$ and $s^E_{ijkl} = \left(\partial S_{ij}/\partial T_{kl}\right)_E$, one further identifies the following symmetry relations: $d_{kij} = d_{kji}$ and $s^E_{ijkl} = s^E_{jikl} = s^E_{ijlk} = s^E_{jilk}$. In summary, it follows from these two sources of intrinsic symmetry that the dielectric permittivity has a maximum of 6 independent constants, whereas the dielectric coefficient and compliance have a maximum of 18 and 21, respectively. To simplify the manipulation of these expressions, a special notation known as Voigt's notation is commonly used in literature. Here, the $\boldsymbol{\varepsilon}^{\boldsymbol{T}}$, $\boldsymbol{d}$ and $\boldsymbol{s}^{\boldsymbol{E}}$ tensors are represented as 3 × 3, 3 × 6 and 6 × 6 matrices, where the ij subscripts are reduced to a single subscript (m or n) using the substitutions $ij = 11 \to 1$, $ij = 22 \to 2$, $ij = 33 \to 3$, $ij = 23, 32 \to 4$, $ij = 13, 31 \to 5$, $ij = 12, 21 \to 6$. Other rules of conversion into this matrix notation, which must be taken into account, are [54, 103]: $S_m = S_{ij}$, when $m = 1, 2$ or 3; $S_m = 2S_{ij}$, when $m = 4, 5$ or 6; $s^E_{mn} = s^E_{ijkl}$, when both m and n are = 1, 2 or 3; $s^E_{mn} = 2s^E_{ijkl}$, when m or n are = 4, 5 or 6; $s^E_{mn} = 4s^E_{ijkl}$, when both m and n are = 4, 5 or 6; $d_{km} = d_{kij}$, when $m = 1, 2$ or 3; and $d_{km} = 2d_{kij}$, when m = 4, 5 or 6. The values of these coefficients are frequently presented in literature in this notation. Taking all these symmetry considerations into account, the constitutive equations (6.7) and (6.8) can be written in the general matrix form [54, 99]:

$$\begin{bmatrix} S_m \\ D_i \end{bmatrix} = \begin{bmatrix} {}^{p}s^E_{mn} & d^t_{mj} \\ d_{in} & \varepsilon^T_{ij} \end{bmatrix} \begin{bmatrix} T_n \\ E_j \end{bmatrix} \tag{6.9}$$

where the superscript t indicates the transpose of the $\boldsymbol{d}$ Voigt matrix. Finally, it has to be noted that the symmetry of the material is also an important source of additional constrains on its tensor properties. From the symmetry of a system we know that there are a set of symmetry operations which will not change the material in any observable way, so that the material properties will be invariant under such operations. These operations are the ones that define the point group of the system. Thus, one sees that the material properties are in part governed by the point group symmetry of the material. More precisely, the Neumann principle states that [104] *The symmetry elements of any physical property of a crystal must include all the symmetry elements of the point group of the crystal.* In other words, the components of a tensor representing a property must remain invariant under any transformation of coordinates governed by a symmetry operation valid for the point group of the crystal. This also implies that a given physical property may only possess a higher or equal symmetry than that of the crystal. Therefore, a physical property must have a symmetry at least as high as one of the 32 conventional point groups or one of the 122 magnetic points groups to which the crystal belongs. Taking, e.g., the PE $LiNbO_3$ crystal corresponding to the point group *3m*, it is possible to show that it will be associated with at most 2 independent dielectric constants (ε_{11}^T and ε_{33}^T), 4 PE constants (d_{31}, d_{33}, d_{22} and d_{15}) and 6 compliance constants (s_{11}^E, s_{12}^E, s_{13}^E, s_{14}^E, s_{33}^E and s_{44}^E) [57]. A listing of all the 32 point groups and associated tensor properties can be found, e.g., in [104–106].

Most of the discussion mentioned above for PE materials can also be applied to piezomagnetic materials. The difference resides in the fact that, because magnetic fields are pseudovectors generated by currents and change sign under time inversion, magnetic properties will necessarily have more complex symmetries [102]. In fact, there is a whole set of additional point group symmetries for the magnetic properties as a consequence of current reversal. Therefore, while the simplest magnetic properties, such as the magnetic permeability and susceptibility, have the forms that are required by the basic crystallographic point group of the material, more complex properties, such as the ferromagnetic moment and the MS coefficients, do not. Those will instead have the form required by one of the 122 magnetic point groups. Assuming the same conditions as in the case of the PE material, the elastic Gibbs function for the MS material can also be derived. From it, the linear piezomagnetic constitutive relations follow [43, 107]:

$$ {}^{m}B_k = \mu_0 {}^{m}H_k - \frac{\partial G}{\partial {}^{m}H_k} = {}^{m}B_{0k}(\boldsymbol{H}_0) + \mu_{kl}^T(\boldsymbol{H}_0)^{m}H_l + q_{kij}(\boldsymbol{H}_0)^{m}T_{ij} \tag{6.10} $$

$$ {}^{m}S_{ij} = -\frac{\partial G}{\partial {}^{m}T_{ij}} = {}^{m}S_{0ij}(\boldsymbol{H}_0) + {}^{m}s_{ijkl}^{E}\, {}^{m}T_{kl} + q_{kij}(\boldsymbol{H}_0)^{m}H_k, \tag{6.11} $$

where ${}^{m}B_k$ is the magnetic induction (a vector) and ${}^{m}H_k$ the magnetic field strength (a vector). Also, ${}^{m}B_{0k}(\boldsymbol{H}_0) = {}^{m}B_k(\boldsymbol{H}_0) - \mu_{kl}^T(\boldsymbol{H}_0)^{m}H_{0l}$ and ${}^{m}S_{0ij}(\boldsymbol{H}_0) = \lambda_{ij}(\boldsymbol{H}_0) - q_{kij}(\boldsymbol{H}_0)^{m}H_{0k}$ where $\mu_{kl}^T(\boldsymbol{H}_0)$ is the magnetic permittivity (a rank-2 tensor), $q_{kij}(\boldsymbol{H}_0)$

the piezomagnetic coefficient (a rank-3 tensor), ${}^{m}B_k(\boldsymbol{H}_0)$ the magnetic induction and $\lambda_{ij}(\boldsymbol{H}_0)$ the magnetostriction all measured at a bias $\boldsymbol{H}_0$ magnetic field. The superscript m indicates the MS nature of the material to which (6.10) and (6.11) apply. It should be noted that, when obtaining these equations, the pseudo-piezomagnetic approximation was taken. This is because magnetostriction is approximately a quadratic effect (${}^{m}S_{ij} = b_{ijkl}M_kM_l$, where $\boldsymbol{b}$ is the 6×6 magnetoelastic tensor), whereas piezomagnetism is a linear effect (${}^{m}S_{ij} = q_{kij}H_k$). However, for small variations of the applied $\boldsymbol{H}$ field close to a bias field $\boldsymbol{H}_0$, the slope $\partial S^m_{ij}/\partial H_k(\boldsymbol{H})$ of the magnetostriction curve is approximately constant in a small interval around $\boldsymbol{H}_0$. Therefore the Taylor expansion of the magnetostriction curve around $\boldsymbol{H}_0$ may be truncated to first order as follows: ${}^{m}S_{ij}(\boldsymbol{T}=0,\boldsymbol{H}) = \lambda_{ij}(\boldsymbol{H}) = \lambda_{ij}(\boldsymbol{H}_0) + \partial\lambda_{ij}/\partial H_k(\boldsymbol{H}_0) \cdot (H_k - H_{k0}) + (1/2)\partial^2\lambda_{ij}/\partial H_k\partial H_l(\boldsymbol{H}_0) \cdot (H_k - H_{k0})(H_l - H_{l0}) + \cdots \approx \lambda_{ij}(\boldsymbol{H}_0) + \partial\lambda_{ij}/\partial H_k(\boldsymbol{H}_0) \cdot (H_k - H_{k0})$, and thus the magnetostriction can be approximated in this region as a piezomagnetic effect with $q_{kij}(\boldsymbol{H}_0) = \partial\lambda_{ij}/\partial H_k(\boldsymbol{H}_0)$ [28, 108]. In practical applications, the magnetostriction is often used in this linear piezomagnetic regime with small applied AC magnetic fields. Similarly, a pseudo-paramagnetic approximation, where $\mu^T_{kl}(\boldsymbol{H}_0) = \partial B_k/\partial H_l(\boldsymbol{H}_0)$, is also assumed for the ferromagnetic material. Having taken this into consideration, one can therefore assume the validity of (6.10) and (6.11). Before advancing any further, one has to note that the assumption that the material coefficients in the constitutive equations are constants dependent only on the spatial coordinates and magnetic fields produces a very idealized model. In a more accurate description these coefficients should be complex functions of space, material fields, frequency, time and temperature thus taking into account the non-linearities, dispersion, losses, current state (e.g. remanent polarization/magnetization of the PE/MS phase, aging effects, etc.) and temperature dependence of the material's properties. A listing of all the linear dielectric, PE and elastic constants of the different piezoelectrics, measured under standard ambient conditions, can generally be easily found in literature.

6.2.2 Presentation of the Averaging Quasi-Static Method

In this Section we are going to estimate the maximum expected magnitude of the ME voltage coefficient for a series of tri-layered geometries of the type Metglas/PE/Metglas, where different single crystals are employed as the PE phase. To do this, a standard averaging low-frequency model (i.e., in the quasi-static regime), based on the constitutive equations, will be used. Being quasi-static it will naturally neglect high frequency effects such as electromechanical resonances, material dispersion and losses as well as eddy currents generated in the conductive phases.

The simultaneous resolution of the constitutive equations (6.7)–(6.8) and (6.10)–(6.11), taking into account the boundary conditions for the material interfaces,

allows one to obtain the ME voltage coefficient of the composite depending on its composition, microstructure, operating mode, etc. Currently, a number of analytical and numerical techniques are known which may be employed in solving these equations. In general, they allow estimations in terms of mean fields and are based on the formalism of Green's function [39] (multiple-scattering approach in the many-body theory) or on micromechanical methods [109]. More sophisticated models may include the quadratic effect of magnetostriction [110] and pyroelectric or pyromagnetic phenomena [109] in the constitutive equations.

In the quasi-static model, a square shaped tri-layered structure like the one shown in Fig. 6.1a is considered. Its constitutive elastostatic and electrostatic equations are solved assuming that all of the material fields are averaged constants in each layer up to the leading order. This limits the model to the study of purely extensional deformations thus excluding any kind of bending deformations which, however, are only significant for the case of asymmetrical composites such as bilayers. As we see, this composite is designed to operate in its L-T mode, i.e., with a magnetic field ($\delta H_j(t)$) applied along its longitudinal length direction (L) and with the voltage ($\delta V_3(t)$) measured across its transversal thickness direction (T). This L-T mode is generally associated with larger ME coefficients than the transversally magnetized and transversally poled (T-T) mode mainly because of the absence of the demagnetization effect (for thin enough layers) and also because the piezomagnetic coefficients tend to be larger for parallel magnetic and strain fields (q_{ii}), so that the in-plane strain component, which is transmitted to the PE phase, will be larger.

To set the boundary conditions, we start by assuming that there is no external traction applied to the system. Thus, the average tractions on the top and bottom surfaces of both phases (${}^mT_{3i}$), as well as the average tractions on the lateral surfaces (${}^pT_{ab}{}^pv + {}^mT_{ab}{}^mv$), are null. These two relations are expressed as [43, 107]:

$$ {}^mT_{3i} = {}^pT_{3i} = 0; \tag{6.12} $$

$$ {}^pT_{ab}{}^pv + {}^mT_{ab}{}^mv = 0, \tag{6.13} $$

where ${}^pv$ and ${}^mv$ are the volume fractions of the PE and MS phases, respectively. Taking into account that all layers have a square shaped surface with the same area (A), these fractions are given by ${}^pv = {}^pt/({}^pt + 2{}^mt)$ and ${}^mv = 2{}^mt/({}^pt + 2{}^mt)$, where ${}^pt$ is the thickness of the PE crystal and ${}^mt$ is the thickness of each one of the two magnetic layers. The continuity conditions at the interfaces between layers guarantee that ${}^mT_{3i} = {}^pT_{3i}$. Furthermore, a parameter known as the coupling coefficient, $k_c = \left({}^pS_{ab} - {}^pS_{0ab}\right)/\left({}^mS_{ab} - {}^pS_{0ab}\right)$, is introduced [42]. This parameter describes the coupling quality at the interface between the PE and MS materials. In the expression of k_c, ${}^pS_{0ab}$ indicates the component of the strain tensor in the PE phase that appears when the friction between layers is null (i.e. ${}^pT_{ab} = 0$, so that ${}^pS_{0ab} = d_{kab}{}^pE_k$ by (6.8)), and ${}^pS_{ab}$ and ${}^mS_{ab}$ are the strains in the PE and MS phases, respectively. The coupling parameter consequently defines the ratio between the induced strains in the PE and MS layers. For an ideal interface we then have $k_c = 1$,

whereas for an interface without any friction between layers (i.e. without mechanical coupling between them) we get $k_c = 0$. The boundary conditions for the strain components on the lateral surfaces of the composite are therefore [72]:

$$^{p}S_{ab} = k_c{}^{m}S_{ab} + (1 - k_c)^{p}S_{a0}\,. \tag{6.14}$$

It is further assumed that the interface is perfectly electromechanically bound. Consequently, the in-plane electric and magnetic fields will be continuous along the composite, the change in the normal displacement fields across the interfaces will be equal to the surface charge density (σ) and the normal magnetic induction will be continuous [43, 107]:

$$^{p}E_1 = {}^{m}E_1, {}^{p}E_2 = {}^{m}E_2, {}^{p}D_3 - {}^{m}D_3 = \sigma; \tag{6.15}$$

$$^{p}H_1 = {}^{m}H_1, {}^{p}H_2 = {}^{m}H_2, {}^{p}B_3 = {}^{m}B_3\,. \tag{6.16}$$

We now seek to find the expression for the direct ME voltage coefficient given by $\alpha_{Eij} = \partial^{p}E_i/\partial^{m}H_j$, or the electric field induced in the PE when the MS layers are subjected to an external magnetic field. By substitution of the constitutive equations (6.8) and (6.11) into (6.14) we get:

$$^{p}s^{E}_{abkl}{}^{p}T_{kl} + k_c d_{km}{}^{p}E_k = k_c{}^{m}s^{E}_{abkl}{}^{m}T_{kl} + k_c({}^{m}S_{0ab}(\boldsymbol{H}_0) + q_{kab}(\boldsymbol{H}_0)^{m}H_k) \tag{6.17}$$

Now adding the stress boundary conditions (6.12) and (6.13) to this expression and converting its parameters to the Voigt notation yields:

$$s_{mn}{}^{p}T_n + k_c d_{km}{}^{p}E_k = k_c({}^{m}S_{0m}(\boldsymbol{H}_0) + q_{km}(\boldsymbol{H}_0)^{m}H_k), \text{for}\, m, n = 1, 2\, \text{and}\, 6, \tag{6.18}$$

where $s_{mn} = {}^{p}s^{E}_{mn} + k_c f^{m}s^{E}_{mn}$ is an effective compliance and f is the ratio between the volume fractions of the PE and MS phases (${}^{p}v/{}^{m}v$). The rank-three square s_{mn} matrix in this expression can thus be inverted in order to write the PE stress ${}^{p}T_n$ explicitly as a function of the electric and magnetic fields. Subsequently, substituting this stress in the PE constitutive equation (6.7) and taking into account the elastic boundary conditions (6.12) we arrive at (in Voigt's notation):

$$\begin{aligned} ^{p}D_k = {} & (\varepsilon^{T}_{kl} - k_c d_{km} s^{-1}_{mn} d_{ln})^{p}E_l + k_c d_{km} s^{-1}_{mn}({}^{m}S_{0n}(\boldsymbol{H}_0) + q_{jn}(\boldsymbol{H}_0)^{m}H_j), \text{for}\, m, n \\ = {} & 1, 2\, \text{and}\, 6, \end{aligned} \tag{6.19}$$

where s^{-1}_{mn} is the inverse of the s_{mn} effective compliance matrix. Taking now into account that the magnetic layers consist of the electrically conductive Metglas alloy, the electric and displacement fields (${}^{m}D_i = \varepsilon_0{}^{m}E_i$) in this layer should be approximately null and its top and bottom surfaces equipotential. Therefore one has [43, 107]:

$$ {}^{m}E_1 = {}^{m}E_2 = {}^{m}D_3 = 0 \tag{6.20}$$

By a substitution of the above relations in (6.15) one gets the additional conditions:

$$ {}^{p}E_1 = {}^{p}E_2 = 0; {}^{p}D_3 = \sigma\,. \tag{6.21}$$

Replacing this conditions in (6.19) one can finally write the ${}^{p}D_3$ component of the dielectric displacement as a function of the ${}^{p}E_3$ electric field and the magnetic fields in the MS layer:

$$ {}^{p}D_3 = (\varepsilon_{33}^{T} - k_c d_{3m} s_{mn}^{-1} d_{3n})^{p}E_3 + k_c d_{3m} s_{mn}^{-1} ({}^{m}S_{0n}(\boldsymbol{H}_0) + q_{jn}(\boldsymbol{H}_0)^{m}H_j), \text{for}\, m, n = 1, 2\, \text{and}\, 6. \tag{6.22}$$

Supposing a magnetic field ${}^{m}H_k$ is applied to the composite along one of the three possible directions $k = 1, 2$ or 3, one can therefore rearrange the expression above in order to obtain the variable ${}^{p}E_3$ explicitly as a linear function of this field as well as the ${}^{p}D_3$ field. Starting by considering an open circuit situation ($I = \int_{Area} {}^{p}\dot{D}_3 dA = 0$, where I is the current in the Z direction), in which ${}^{p}D_3$ equals an initial constant surface charge σ, as shown in (6.16), which we assume to be null (${}^{p}D_3 = 0$), and differentiating ${}^{p}E_3$ with respect to ${}^{m}H_k$, one finally arrives at the desired direct ME voltage coefficient. From this it follows that for $\boldsymbol{H} \to \boldsymbol{H}_0$ the general ME voltage coefficient can be written as a function of this field by the compact expression:

$$ \alpha_{E3k}(\boldsymbol{H}) = \frac{\partial^{p}E_3}{\partial^{m}H_k}(\boldsymbol{H}) = \frac{-k_c d_{3m} s_{mn}^{-1} q_{kn}(\boldsymbol{H})}{\varepsilon_{33}^{T} - k_c d_{3m} s_{mn}^{-1} d_{3n}}\,. \tag{6.23}$$

In the special case of a uniaxial PE (such as PZT ceramic with ∞m symmetry) which has only 2, 3 and 5 independent dielectric, PE and elastic constants, respectively, and a MS material, such as Metglas, with a normal orientation (∞m symmetry), this yields the result [36, 43]:

$$ (\boldsymbol{H}) = \frac{\partial^{p}E_3}{\partial^{m}H_k}(\boldsymbol{H}) = \frac{-k_c d_{31}(q_{k1}(\boldsymbol{H}) + q_{k1}(\boldsymbol{H}))}{\varepsilon_{33}^{T}\left[({}^{p}s_{11}^{E} + {}^{p}s_{12}^{E}) + k_c f({}^{m}s_{11}^{E} + {}^{m}s_{12}^{E})\right] - 2k_c d_{31}^{2}}, \tag{6.24}$$

which shows the tendency of the direct ME effect to be larger in composites containing PE phases with a large transverse piezocoefficient (d_{31}), small out-of-plane dielectric permittivity (ε_{33}^{T}) and small longitudinal and transverse compliance or flexibility (${}^{p}s_{11}^{E} + {}^{p}s_{12}^{E}$). Additionally, the MS phase should have large longitudinal and transverse piezomagnetic coefficients ($q_{k1}(\boldsymbol{H}) + q_{k2}(\boldsymbol{H})$) and small compliances (${}^{m}s_{11}^{E} + {}^{m}s_{12}^{E}$). The curves of this ME coefficient as a function of

the external magnetic field are known to follow those of the piezomagnetic coefficients [108]. The ME coefficient is thus proportional to the first derivative of the magnetostriction curve, increasing with the H field up to a given point, where the derivative of the magnetostriction is maximum, and decreasing progressively to zero afterwards, because the strain of the magnetic phase eventually saturates. Consequently, the piezomagnetic coefficients presented in literature often correspond to their maximum values for a given magnetic field, and the ME coefficients estimated by solving (6.23) will then correspond to the maximal expected coefficients for this field. Expression (6.24) additionally shows that, in order to maximize the ME effect, it is extremely important to obtain a good mechanical coupling between phases (i.e. a large k_c), thus guarantying an efficient transference of strain between them. Also, the thickness ratio between the PE and the MS layers should be as small as possible (i.e. small f), thus maximizing the in-plane tensile stress ${}^pT_n$ applied to the PE phase by the MS phase in the direction of the applied magnetic field, as seen by (6.18), while at the same time nullifying the compressive stress ${}^mT_n$ felt by the MS phase, as seen by (6.13). However, since the voltage measured in any real detection circuit associated with some input noise is proportional to the thickness of the PE layer, the maximal signal-to-noise ratio should be observed for a finite PE thickness. On the other hand, minimizing f by infinitely increasing the thickness of the MS layers would lead to unpractically large samples, so that some compromise has to achieved for any given application.

The model shown in this part also permits the estimation of the quasi-static charge ME coefficient through a simple change in the electrical boundary conditions. For this case we consider a short-circuited composite ($V = -\int_{{}^pt} {}^pE_3 dZ = 0$, where V is the voltage developed across the PE) in such a way that we have ${}^pE_3 = 0$ instead of ${}^pD_3 = 0$ in (6.21). Subsequently (6.22) is differentiated in relation to ${}^mH_k$ thus yielding:

$$\alpha_{Q3k}(\boldsymbol{H}) = \frac{\partial^p D_3}{\partial^m H_k}(\boldsymbol{H}) = k_c d_{3m} s_{mn}^{-1} q_{kn}(\boldsymbol{H}). \tag{6.25}$$

Comparing the general (6.23) and (6.25), one notes that both the charge and voltage coefficients can be directly related by the expression $\alpha_{Q3k}(\boldsymbol{H}) = -(\varepsilon_{33}^T - k_c d_{3m} s_{mn}^{-1} d_{3n})\alpha_{E3k}(\boldsymbol{H})$, where $C = \left(\varepsilon_{33}^T - k_c d_{3m} s_{mn}^{-1} d_{3n}\right) A/{}^pt$ represents the low frequency capacitance of the composite as it will be shown later. This capacitance tends therefore to decrease with increasing k_c (better coupling between layers) and decreasing f (thicker MS layers). For the case of uniaxial PE and MS materials, expression (6.25) is simplified to:

$$\alpha_{Q3k}(\boldsymbol{H}) = \frac{\partial^p D_3}{\partial^m H_k}(\boldsymbol{H}) = \frac{k_c d_{31}(q_{k1}(\boldsymbol{H}) + q_{k2}(\boldsymbol{H}))}{({}^ps_{11}^E + {}^ps_{12}^E) + k_c f({}^ms_{11}^E + {}^ms_{12}^E)} \tag{6.26}$$

which shows that, when compared to the α_{E3k} coefficient in (6.24), the charge coefficient is generally associated with a change of sign and no longer depends on

the dielectric permittivity ε_{33}^{T} of the PE. For the rest, all of the observations made before remain valid.

As mentioned before, up to this point the demagnetization effects on the MS layers have been neglected. For the special case of uniformly magnetized ellipsoids (with magnetization M_j) subjected to an uniform external magnetic field $H_k^{'}$, the uniform field developed inside the material H_k can be given by $H_k = H_k^{'} - N_{kj}M_j$, where N_{kj} is a demagnetization factor which depends on the shape of the ellipsoid [112]. In the case of an infinite plane with a normal pointing in the Z direction this demagnetization factor is given by $N_{33} = 1$ and $N_{kj} = 0$ otherwise [112]. Therefore, for thin enough MS layers the demagnetization fields can be neglected for $H_k^{'}$ applied in the X or Y directions (i.e. $H_k^{'} = H_k$). However, in the case of thick MS phases, such that $N_{aa} \neq 0$, or the ME longitudinal effect where $H_3 \neq 0$, this effect can become quite substantial. The ME coefficients given by (6.23)–(6.26) can be corrected to take into account this effect. To do this, one starts by writing the external magnetic field $H_k^{'}$ as a function of the internal magnetic field H_k. Taking the demagnetization equation for some N_{kj} and making the substitution ${}^{m}M_j = {}^{m}B_j/\mu_0 - {}^{m}H_j$, one obtains ${}^{m}H_k^{'}$ as a function of ${}^{m}H_j$ and the magnetic induction ${}^{m}B_j$ given by (6.10). Subsequently, through a series of substitutions involving (6.12), (6.13) and (6.18) one arrives at the final result:

$$ {}^{m}H_k^{'} = \overline{H_{0k}}(\boldsymbol{H}_0) + \overline{\mu_{kl}}(\boldsymbol{H}_0)^{m}H_l + \overline{\alpha_{Qk3}}(\boldsymbol{H}_0)^{p}E_3, \tag{6.27} $$

where $\overline{H_{0k}}(\boldsymbol{H}_0) = (N_{kj}/\mu_0)({}^{m}B_{0j}(\boldsymbol{H}_0) - k_c f q_{jm}(\boldsymbol{H}_0)s_{mn}^{-1}{}^{m}S_{0n}(\boldsymbol{H}_0))$, $\overline{\alpha_{Qk3}}(\boldsymbol{H}_0) = (N_{kj}/\mu_0)k_c f q_{jm}(\boldsymbol{H})s_{mn}^{-1}d_{3n}$, $\overline{\mu_{kl}}(\boldsymbol{H}_0) = \delta_{kl} - N_{kl} + \mu_{kl}(\boldsymbol{H}_0) - k_c f q_{km}(\boldsymbol{H}_0)s_{mn}^{-1}q_{ln}(\boldsymbol{H}_0)$ and ${}^{p}E_3$ is related to ${}^{m}H_j$ and ${}^{p}D_3$ through (6.22). The corrected ME voltage coefficients written as a function of the known external magnetic fields $\boldsymbol{H}^{'} \to \boldsymbol{H}_0^{'}$ can therefore be given as $\alpha_{E3k}^{'}(\boldsymbol{H}^{'}) = \partial^{p}E_3/\partial^{m}H_k^{'}(\boldsymbol{H}^{'}) = \partial^{p}E_3/\partial^{m}H_j(\boldsymbol{H}(\boldsymbol{H}^{'}))\cdot \partial^{m}H_j/\partial^{m}H_k^{'}(\boldsymbol{H}^{'})$, which reduces to:

$$ \alpha_{E3k}^{'}\left(\boldsymbol{H}^{'}\right) = \alpha_{E3j}(\boldsymbol{H}(\boldsymbol{H}^{'}))\left[\overline{\mu_{jl}}^{-1}\left(\boldsymbol{H}(\boldsymbol{H}^{'})\right)\left[\delta_{lk} - \overline{\alpha_{Ql3}}\left(\boldsymbol{H}(\boldsymbol{H}^{'})\right)\alpha_{E3k}\left(\boldsymbol{H}(\boldsymbol{H}^{'})\right)\right]\right] \tag{6.28} $$

where $\overline{\mu_{jl}}^{-1}(\boldsymbol{H}(\boldsymbol{H}^{'}))$ is the inverse of the $\overline{\mu_{kl}}(\boldsymbol{H}_0)$ function, $\alpha_{E3j}(\boldsymbol{H}(\boldsymbol{H}^{'}))$ is given by (6.23) and $\boldsymbol{H}(\boldsymbol{H}^{'})$ is determined by solving the implicit expression (6.27). In summary, the maximum ME effects of composites subjected to demagnetization effects tend to be smaller and appear at larger applied magnetic fields [6].

The aforementioned ME coefficients were defined for ideal open-circuit or short-circuit conditions. However, in experimentation the ME composites are operated under non-ideal conditions in which case the parameters of the external measuring circuits have to be taken into account. Therefore it is useful to model the composites as equivalent electrical circuits. In this regard, assuming harmonic fields

of the type ${}^{m}H_k = {}^{m}H_{0k} + \delta H_k e^{j\omega t}$, where ${}^{m}H_{0k}$ is a bias field, δH_k a complex amplitude, j the imaginary unit, ω the angular frequency and t the time, and differentiating (6.22) with respect to time and integrating it over the volume of the composite (i.e. $\int_{{}^{p}t}\int_{Area} {}^{p}\dot{D}_3 dAdZ$) we can derive the relation:

$$\delta V_3 = (-\alpha_{E3k}({}^{m}H_{0k})^{p}t)\delta H_k - (1/j\omega C)\delta I_3, \tag{6.29}$$

where $\delta V_3 = -\int_{p_t} \delta^{p} E_3 dZ$ is the AC voltage measured between the top and bottom of the composite and $\delta I_3 = j\omega \int_{Area} \delta^{p} D_3 dA$ is the AC current flowing through it in the Z direction. This expression thus shows that the composite can be modeled as a Thévenin equivalent circuit consisting of an equivalent voltage source of $\delta V_{Th}(\boldsymbol{H}) = (-\alpha_{E3k}({}^{m}H_{0k})^{p}t)\delta H_k$ connected in series with an equivalent impedance given by $Z_{Th} = 1/j\omega C$ which represents a capacitor with capacitance $C = \left(\varepsilon_{33}^{T} - k_c d_{3m} s_{mn}^{-1} d_{3n}\right)A/{}^{p}t$. Equivalently, the composite can also be modeled as a Norton equivalent circuit composed of a current source of $\delta I_{No}(\boldsymbol{H}) = (j\omega\alpha_{Q3k}\left({}^{m}H_{0k}\right)A)\delta H_k$ connected in parallel with the same impedance. More precisely, by taking into account the important effects of dielectric dispersion ($\varepsilon_{33}^{T}(\omega)$), dielectric losses ($\varepsilon_{33}^{T''}(\omega)$) and conductivity ($\sigma$) of the PE through the introduction of the complex dielectric coefficient $\varepsilon_{33}^{T}(\omega) = \varepsilon_{33}^{T'}(\omega) - j\varepsilon_{33}^{T''}(\omega) + \sigma/j\omega = \varepsilon_{33}^{T'}(\omega) - j\varepsilon_{33}^{T'}(\omega)\tan(\delta)$, where $\omega\varepsilon_{33}^{T'}(\omega)\tan(\delta)$ is the so called dissipation factor, the equivalent impedance of the composite can be given by $Z_{Th} = 1/(1/R' + j\omega C')$ which corresponds to a capacitor with $C' = \left(\varepsilon_{33}^{T'}(\omega) - k_c d_{3m} s_{mn}^{-1} d_{3n}\right)A/{}^{p}t$ connected in parallel with a resistor with $R' = {}^{p}t/A\omega\varepsilon_{33}^{T'}(\omega)\tan(\delta)$. In conclusion, when measuring for example the ME voltage coefficient, the finite input impedance of the measuring circuit should always be taken into account. Assuming e.g. an input impedance of $Z_{in} = 1/(1/R_{in} + j\omega C_{in})$ as in the case of a lock-in amplifier, the measured voltage in such a device as a function of the magnetic fields will be given by $\delta V_{in} = (Z_{in}/(Z_{Th} + Z_{in}))\delta V_{Th}(\boldsymbol{H})$. Thus, the circuit will generally behave as a high-pass filter with a small input amplitude $|\delta V_{in}| = (R_{in}/(R' + R_{in}))|\delta V_{Th}(\boldsymbol{H})|$ being measured at zero frequency (because R' usually takes a much larger value than R_{in} in a lock-in amplifier) and a larger input amplitude $|\delta V_{in}| = (C'/(C' + C_{in}))|\delta V_{Th}(\boldsymbol{H})|$ measured at large frequencies (because C_{in} is normally much smaller than C'). Another important application of this circuit model is in the development of sensitive low-noise magnetic field sensors based on the ME effect [47, 49].

ME composites comprising PE single crystals have been the subject of a few recent studies including PMN-PT [48, 113–115], PZN-PT [116], barium titanate ($BaTiO_3$) [117], lithium niobate ($LiNbO_3$) [113, 118], gallium phosphate ($GaPO_4$) [119], quartz (SiO_2) [120], aluminum nitride (AlN) [94], zinc oxide (ZnO) [121], langatate ($La_3Ga_{5.5}Ta_{0.5}O_{14}$, LGT) [122, 123] and langasite ($La_3Ga_{5.5}SiO_{14}$, LGS)

[123]. These have promised further enhancement of the ME coupling. Since single crystals are highly anisotropic, their electric and elastic properties sensitively depend on their crystallographic orientation. Therefore, the optimization of the orientation could lead to greatly enhanced ME coefficients in composites. To study this dependency of the ME coupling on the crystal orientation, we have to subject the material tensors to a passive transformation of coordinates. Equations (6.6)–(6.29) contain the material coefficients and fields defined in the laminate *XYZ* frame of Fig. 6.1a. However, the material properties are usually described in the crystallographic *xyz* frame, and that is why we have to transform them to the laminate frame before applying the equations. To do so, the rotation matrix a_{ij} is introduced, where the Euler angles $Z_1X_2Z_3$ scheme (see Fig. 6.1b) is employed [111]:

$$\boldsymbol{a} = \begin{bmatrix} \cos(\gamma)\cos(\alpha) - \cos(\beta)\sin(\alpha)\sin(\gamma) & \cos(\gamma)\sin(\alpha) + \cos(\beta)\cos(\alpha)\sin(\gamma) & \sin(\gamma)\sin(\beta) \\ -\sin(\gamma)\cos(\alpha) - \cos(\beta)\sin(\alpha)\cos(\gamma) & -\sin(\gamma)\sin(\alpha) + \cos(\beta)\cos(\alpha)\cos(\gamma) & \cos(\gamma)\sin(\beta) \\ \sin(\beta)\sin(\alpha) & -\sin(\beta)\cos(\alpha) & \cos(\beta) \end{bmatrix} \tag{6.30}$$

This matrix describes a sequence of three elemental rotations, the first about the Z axis by an angle α, the second about the X axis by an angle β, and the third again about the Z axis by an angle γ. In this case, after applying the rotation matrix to the crystal, the angles α and β will identify the vector normal to the plane of the laminate, and the angle γ will determine the orientation of the side faces of the laminate in this plane (and consequently the direction of the applied in-plane magnetic fields). Upon changing the frame of reference, the material parameters follow the specific tensor transformation rules which also define the second-, third- and fourth-rank tensors [104]:

$$\varepsilon_{ij} = a_{im}a_{jn}\varepsilon'_{mn},\; d_{ijk} = a_{im}a_{jn}a_{ko}d'_{mno},\; s_{ijkl} = a_{im}a_{jn}a_{ko}a_{lp}s'_{mnop} \tag{6.31}$$

where the constants with an apostrophe denote the material properties in the initial crystallographic frame, and those without apostrophe—the properties in the new frame of reference described by the transformation $\boldsymbol{a}$.

6.2.3 Estimation of the Quasi-Static Transversal ME Voltage Coefficients in Magnetostrictive/Piezocrystalline/Magnetostrictive Tri-Layers

We are now in possession of all the tools we need in order to estimate and optimize the transversal ME response (α_{E3i}, with $i = 1$ or 2) in a series of tri-layered composites containing two layers of Metglas bonded to a PE single crystal of some sort. To do so, we create a fine grid of Euler angles in steps of 1° and subsequently analyze the estimations for these angles. The composites we investigated had the

shape of a square plate like the one shown in Fig. 6.1a, where we considered $10 \times 10\ mm^2$ sheets of Metglas with 29 μm of thickness bonded to opposite sides of a $10 \times 10\ mm^2$ PE crystal with a thickness of 0.5 mm. A perfect coupling between interfaces was assumed ($k_c = 1$). In a traction-free Metglas layer a maximum q_{11} value of ca. 4 ppm/Oe and q_{12} of ca. –1.7 ppm/Oe are attained at a bias field of ca. 10 Oe [124–127]. These were therefore taken as our piezomagnetic coefficients. All of the dielectric, piezoelectric, piezomagnetic (for Metglas [124–127]) and elastic material parameters needed for these calculations where obtained from the literature. The lead-free piezoelectrics studied here thus have included: $LiNbO_3$ [57, 128], α-$GaPO_4$ [58, 59], α-quartz [129, 130], langatate [131, 132], langasite [133, 134], AlN [135, 136], $LiTaO_3$ [137–139] and $BaTiO_3$ [55, 56], and also the lead-based ones, viz., PZT-2 [140], PMN-33 %PT ([111] poled) [141], PMN-30 %PT ([011] poled) [62], PMN-33 %PT ([001] poled) [142], PZN-9 %PT ([011] poled) [143] and PZN-8 %PT ([001] poled) [144].

The results obtained by solving (6.23) are summarized in Table 6.3 which shows the maximum expected direct ME coefficients for each composite and respective optimal crystallographic orientations of the PE phase. From these estimations we confirmed the possibility of generating large quasi-static ME effects in ME composites comprising lead-free PE single crystals. Here, coefficients as large as 35.6 V/(cm·Oe) are expected. These ME effects are particularly attractive for the tri-layers comprising $LiNbO_3$, $GaPO_4$, quartz, PMN–33 %PT ([111] poled) and PZN–9 %PT ([011] poled) originating from a particularly good combination of relatively large PE coefficients and low dielectric constants. Also, because the maximum expected ME effects are of the same order of magnitude in both lead-based and lead-free PEs, such exclusive features as chemical stability, linear piezoelectricity and high Curie temperature (in the range of 570–1475 °C) open up a real perspective to use these lead-free PE-based magnetoelectric tri-layers in practical applications.

The selection of crystals with an appropriate cut is a very important step in the development of ME composites. The engineering of these cuts should in principle allow one to develop materials with specific anisotropic properties desired for each type of practical application. Large ME effects are particularly important in applications requiring enhanced efficiencies and sensitivities. Figure 6.2 thus shows the maximum absolute transversal ME coefficients (in the range of all spanned γ angles) estimated as a function of the α and β angles for all considered tri-layers. In the figures we notice the great sensitivity of the ME effect to the orientation of the piezocrystal. The shape of the figures depends on the point group symmetry of the PE mainly through the term $|g_{31} - g_{32}|$ which indicates the difference between PE voltage coefficients ($g_{ij} = -\partial E_i / \partial T_j = \varepsilon_{ik}^{-1} d_{kj}$) for stresses directed along both lateral surfaces of the crystal, since the elastic term varies much less with the orientation of the crystal.

We note at this point that, alongside the dispersion and losses of the material's properties not taken into account, a much more important limitation of the model is the fact that the piezomagnetic coefficients of Metglas are also strongly dependent on the bias magnetic fields and stress tensors. A more complex model for the soft

Table 6.3 Estimation of the maximum expected transversal direct ME voltage coefficients for a series of 10 × 10 mm^2 ME tri-layered composites composed of two 29 μm thick layers of Metglas and one central 0.5 mm thick PE crystal of some kind

PE crystal	$LiNbO_3$			α–$GaPO_4$			α–Quartz			Langatate (LGT)			Langasite (LGS)			AlN			$LiTaO_3$			$BaTiO_3$		
Maximum $\lvert \alpha_{E3a} \rvert$ (V/(cm·Oe))	27.24			35.62			23.77			16.68			16.59			13.06			11.40			10.74		
Z-cut crystal α_{E3a} (V/(cm·Oe))	1.23			0			0			0			0			8.16			2.89			10.74		
Optimal orientation	α	0 120 240	60 180 300	α	90 210 330	30 150 270	α	90 210 330	30 150 270	α	30 150 270	90 210 330	α	30 150 270	90 210 330	α	0–360	0–360	α	0 120 240	60 180 300	α	0–360	0–360
	β	39	141	β	90	90	β	90	90	β	90	90	β	90	90	β	120	60	β	45	135	β	0	180
	γ	90	90	γ	12	168	γ	169	11	γ	156	24	γ	160	20	γ	90	90	γ	90	90	γ	0–360	0–360
Crystal cut	(*ZXl*) 39°			(*XYt*) 12°			(*XYt*) 11°			(*XYt*) 24°			(*XYt*) 20°			(*ZXl*) 60°			(*ZXl*) 45°			Z		

PE crystal	PZT–2			PMN–33 %PT ([111] poled)			PMN–30 %PT ([011] poled)			PMN–33 %PT ([001] poled)			PZN–9 %PT ([011] poled)			PZN–8 %PT ([001] poled)		
Maximum $\lvert \alpha_{E3a} \rvert$ (V/(cm·Oe))	7.47			27.11			12.50			10.80			23.04			8.30		
Z-cut crystal $\lvert \alpha_{E3a} \rvert$ (V/(cm·Oe))	5.41			5.78			12.50			6.29			23.04			7.66		
Optimal orientation	α	0–360	0–360	α	0 120 240	60 180 300	α	0–360	0–360	α	45 135 225 315	45 135 225 315	α	0–360	0–360	α	45 135 225 315	45 135 225 315
	β	37	143	β	42	138	β	0	180	β	116	64	β	0	180	β	38	142
	γ	90	90	γ	90	90	γ	90– α	90– α	γ	90	90	γ	90– α	90– α	γ	0	0
Crystal cut	(*ZXl*) 37°			(*ZXl*) 42°			Z			(*ZXtl*) 45°/64°			Z			(*ZXtl*) 45°/38°		

The optimal crystallographic orientations and corresponding crystal cuts according to the IEEE standard [54] are also presented. Here, the optimal orientations are given as a set of Euler angles (α, β and γ in deg.), where the first column indicates the possible combinations of angles (equivalent by symmetry) corresponding to the same absolute maximum positive ME effect, whereas the second column gives the combination of angles for the same absolute maximum but negative ME effect (i.e., with an inversion in the sign of the ME coupling coefficient). The frame of reference in each case corresponds to the crystallographic frame except in PZT, PMN-PT and PZN-PT, where it corresponds to their respective poled multidomain frames with the Z axis directed along their poling directions

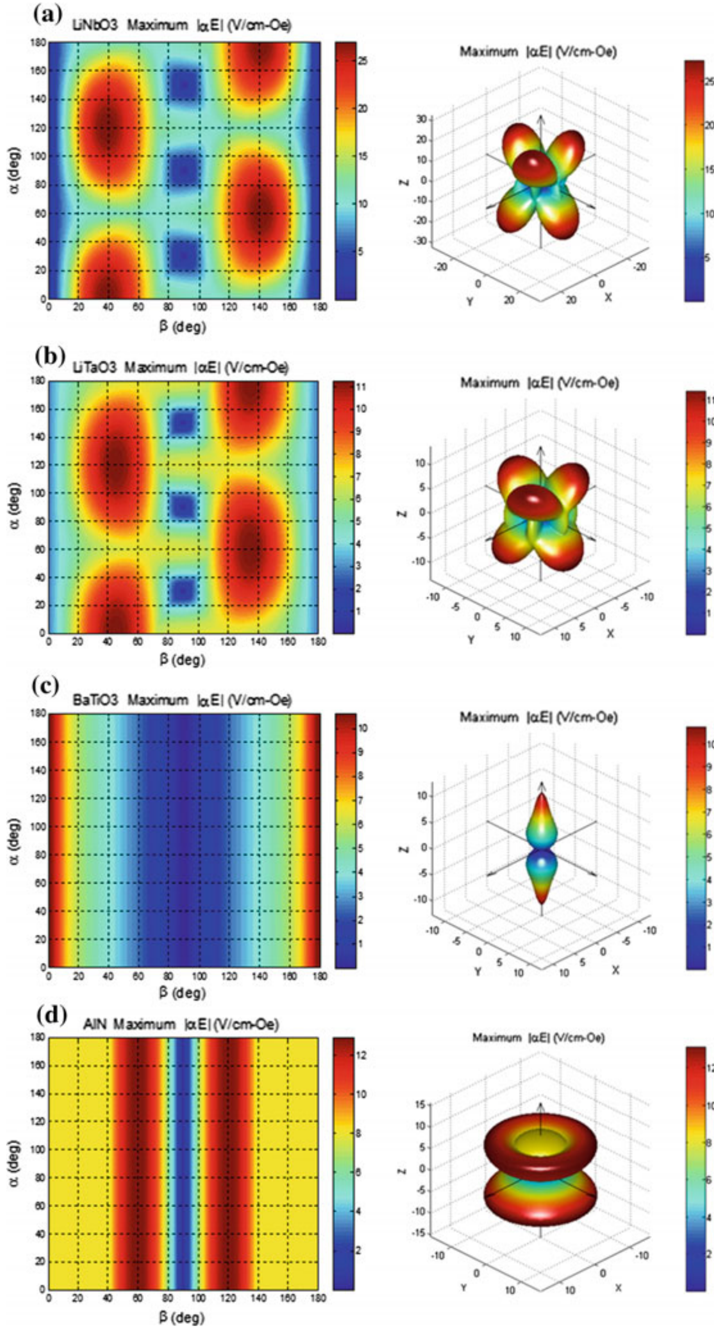

Fig. 6.2 Contour plots and $|\alpha_{E3i}|$ representation surfaces depicting the maximum estimated absolute values of the transversal ME voltage coefficient α_{E3i} (across $0 < \gamma < 180°$) as a function of the crystal orientation (α and β angles) for the tri-layered ME composites of Metglas/PE/Metglas, where the PE phase is a single crystal of: **a** $LiNbO_3$; **b** $LiTaO_3$; **c** $BaTiO_3$; **d** AlN; **e** α-quartz; **f** α-$GaPO_4$; **g** langatate; **h** langasite; **i** PZT-2; **j** PMN-33 %PT ([111] poled); **k** PMN-30 %PT ([011] poled); **l** PMN-33 %PT ([001] poled); **m** PZN-9 %PT ([011] poled) and **n** PZN-8 %PT ([001] poled)

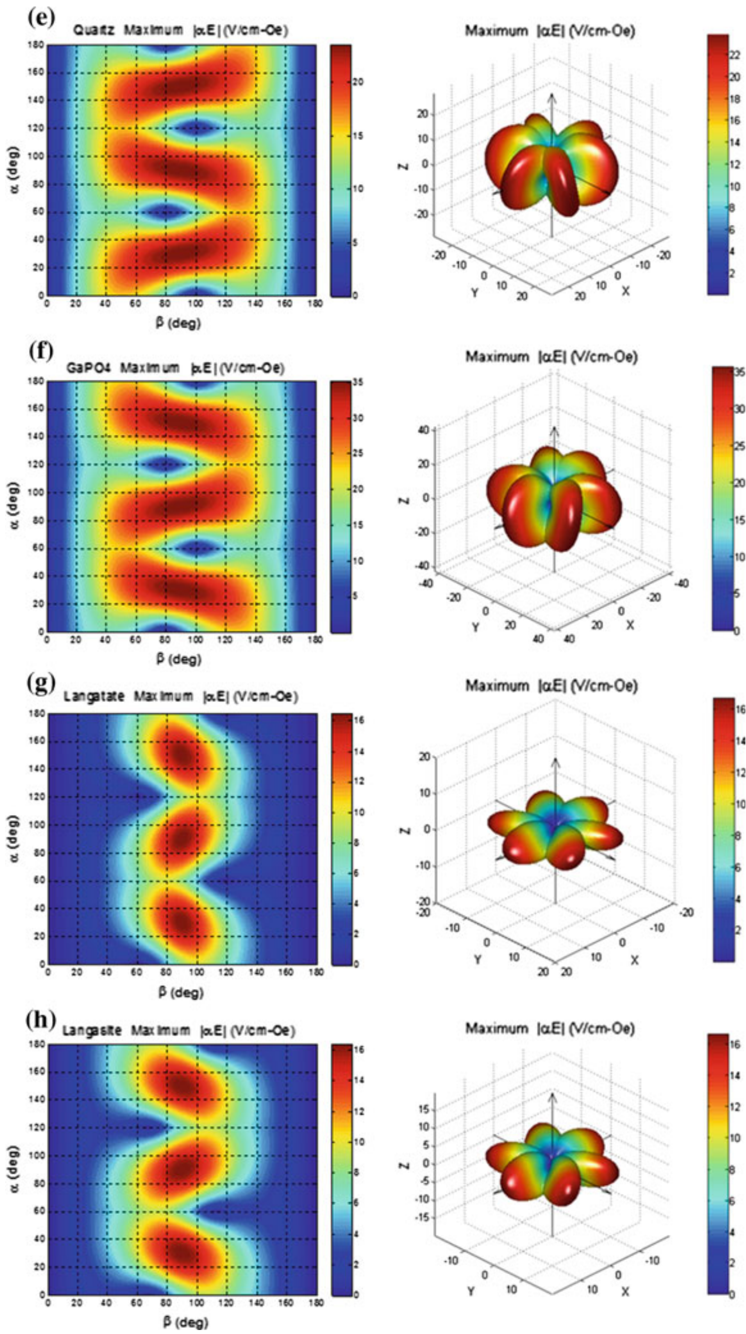

Fig. 6.2 (continued)

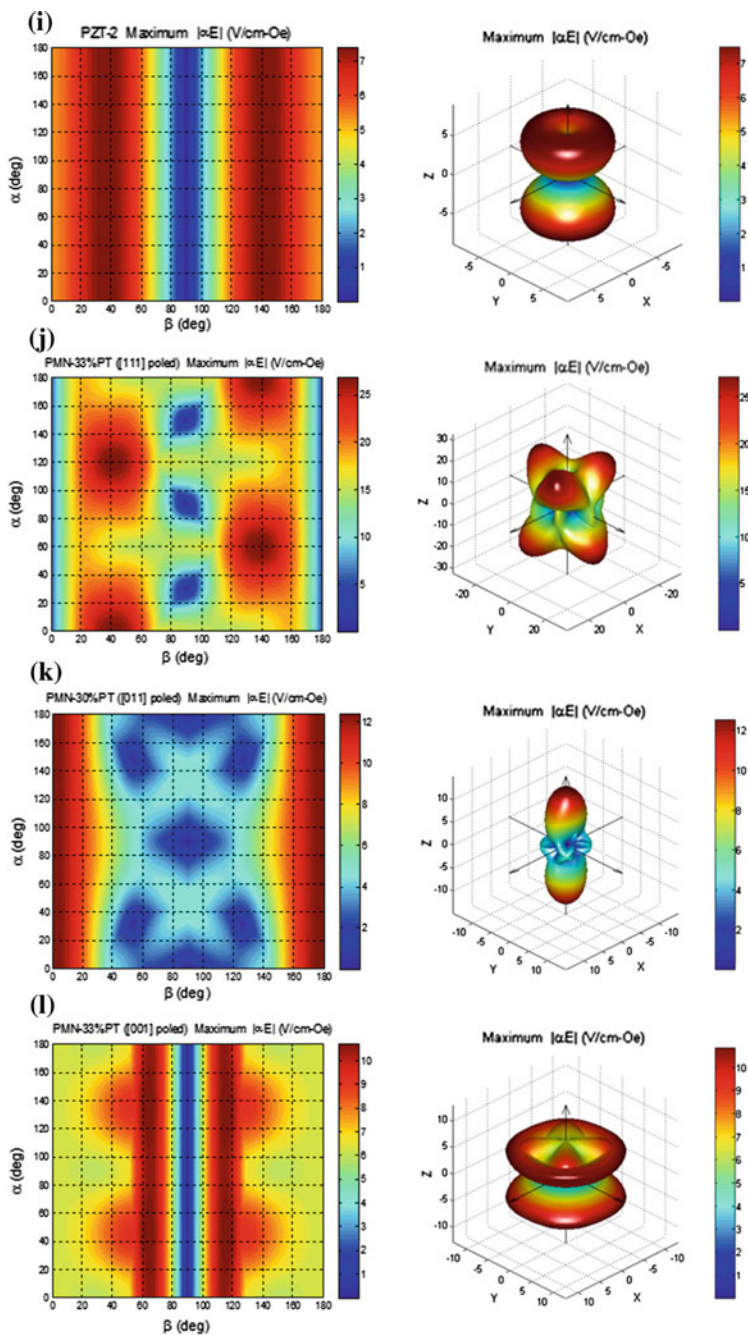

Fig. 6.2 (continued)

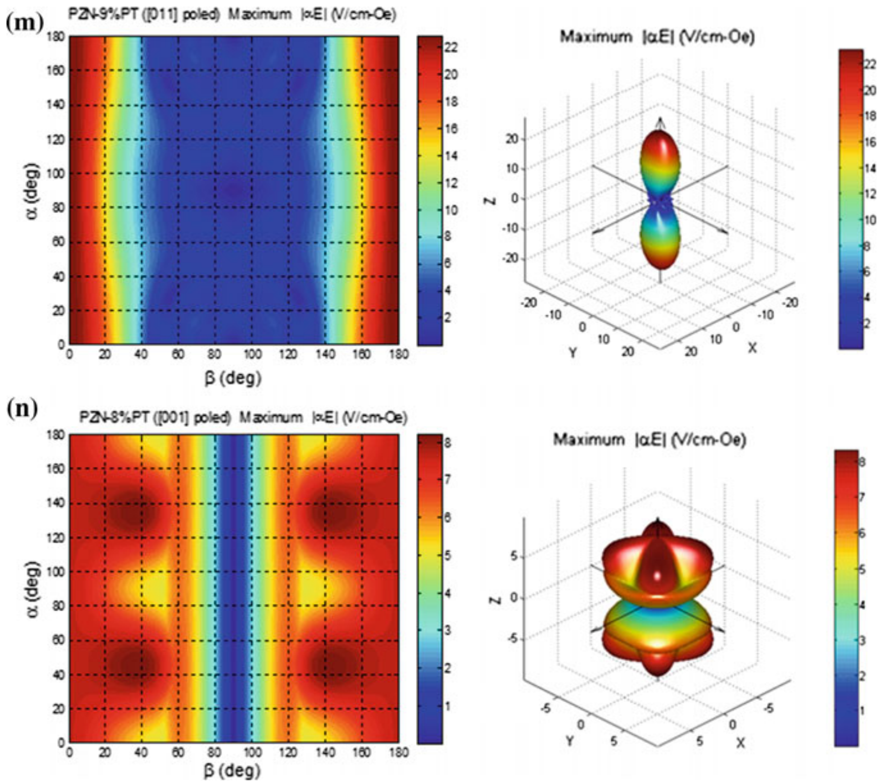

Fig. 6.2 (continued)

MS phase shows for example that the large compressive pre-stress produced by the PE substrate in the MS sheets tends to decrease the maximum value of q_{kn} and at the same time increase the bias field at which it is attained [145]. Therefore, the maximum ME coefficients predicted in this part should be somewhat overestimated. Nonetheless, the relation between ME coefficients obtained for the composites with different PE crystals still remains valid. Furthermore, we point out that the thickness ratio between the MS and PE layers in the composites was not optimized for a maximum ME response. Thicker MS layers are expected to produce a larger effective strain on the PE crystal and thus increase the amplitude of the ME effect by up to one order of magnitude. In this calculations, 29 μm thick layers of Metglas were used because, in practice, some peculiarities associated with the fabrication of these alloys (i.e. a melt spinning rapid solidification process) restricts their thickness to just a few of tens of μm. Also, commercial PE crystals are generally found with thicknesses no smaller than 0.2 mm.

In the next paragraphs we are going to discuss the results of the calculations in greater detail. Starting with the case of the $LiNbO_3$ crystal, which belongs to the trigonal *3m* symmetry point group, we see that the estimated ME coefficient could

be as large as 27.24 V/(cm·Oe) for a crystal with a (*ZXl*) 39°-cut ($\alpha = 0°$, $\beta = 39°$ and $\gamma = 90°$), commercially commonly referred to as 129ºY-cut, and five other cuts equivalent by symmetry. We also see that this effect stays within 90 % of its maximum value for cut deviations, in relation to its optimal orientation, of approximately $\Delta\alpha = \pm 20°$ and $\Delta\beta = \pm 10°$. $LiTaO_3$ has the same symmetry as $LiNbO_3$, but we calculated in this case an expected coefficient of 11.40 V/(cm·Oe), being about 3 times smaller than that in the former material. This is mainly because of its characteristically smaller PE coefficients (especially its d_{15} and d_{22} components), as well as comparable dielectric constants. The maximum effect should be observed in a (*ZXl*) 45°-cut crystal ($\alpha = 0°$, $\beta = 45°$ and $\gamma = 90°$) and also other five equivalent cuts. This coefficient decreases by less than 10 % for cut deviations of about $\Delta\alpha = \pm 25°$ and $\Delta\beta = \pm 10°$. $BaTiO_3$ single crystals belong to the tetragonal *4mm* point group and have much larger PE and dielectric coefficients than $LiNbO_3$. The largest expected ME coefficient here is just of 10.74 V/(cm·Oe) and is only observed in the Z-cut crystal, decaying very rapidly as we move away from this optimal orientation. AlN piezocrystals exhibit a hexagonal *6mm* symmetry and relatively small dielectric and PE coefficients. The maximum coefficient for a composite containing this phase was calculated as 13.06 V/(cm·Oe) for the (*ZXl*) 60°-cut ($0° \leq \alpha < 360°$, $\beta = 60°$ and $\gamma = 90°$) and (*ZXl*) 120°-cut crystals. As in $BaTiO_3$, this effect is axially symmetric and stays within 90 % of its maximum value for cut deviations of approximately $\Delta\beta = \pm 10°$.

The α-quartz and α-$GaPO_4$ PE crystals are another class of lead-free piezoelectrics which, like $LiNbO_3$, exhibit relatively large ratios between PE and dielectric constants. They both belong to the trigonal 32 point group. The most noticeable differences between them are related to the PE coefficients, which are approximately twice as large for the case of $GaPO_4$, as well as the dielectric coefficients which are about 20 % larger in $GaPO_4$ as compared to quartz. Even though they have some of the smallest piezoconstants among the piezocrystals studied in this chapter, their dielectric permittivities are also comparatively small, which therefore gives rise to large PE/dielectric ratios and consequently opens the possibility for large ME responses in the composites. Indeed, following the model described above we calculated maximum ME coefficients of 35.62 and 23.77 V/(cm·Oe) for the $GaPO_4$ and quartz crystals, respectively. These values are quite high and may be observed in (*XYt*) 12°-cut ($\alpha = 90°$, $\beta = 90°$ and $\gamma = 12°$) crystals of $GaPO_4$ and in (*XYt*) 11°-cut ($\alpha = 90°$, $\beta = 90°$ and $\gamma = 11°$) crystals of quartz, as well as in other five cut directions equivalent by symmetry. We also note that these cuts are quite near the X-cut direction. In this case, the ME coefficient decreases by less than 10 % for cut deviations from the maximum direction of about $\Delta\alpha = \pm 10°$ and $\Delta\beta = \pm 25°$.

Langatate and langasite are other two piezoelectrics belonging to the trigonal 32 point group. They are characterized by PE coefficients comparable to the ones of $GaPO_4$, but also exhibit considerably larger dielectric coefficients. Their maximum expected ME coefficients where calculated as 16.68 V/(cm·Oe) for an (*XYt*) 24°-cut crystal ($\alpha = 90°$, $\beta = 90°$ and $\gamma = 24°$), in the case of langatate, and 16.59 V/(cm·Oe) for an (*XYt*) 20°-cut crystal ($\alpha = 90°$, $\beta = 90°$ and $\gamma = 20°$), in the case of langasite.

Furthermore, the maximum ME effect is more sensitive to the cut angle in these two crystals. We observe that the effect stays within 90 % of its maximum value for cut deviations of just about $\Delta\alpha = \pm 10°$ and $\Delta\beta = \pm 10°$.

In the class of the lead-based piezoelectrics we start by looking at the PZT-2 uniaxial ceramic having an ∞mm symmetry. As we know, its PE and dielectric properties are quite distinguished. Still, the maximum direct ME coefficient of just about 7.47 V/(cm·Oe) was calculated for the (*ZXl*) 37°-cut direction ($0° \leq \alpha < 360°$, $\beta = 37°$ and $\gamma = 90°$) and another equivalent direction. Even though this compound constitutes one of the piezoelectrics most commonly employed in practice, we note that its maximum expected ME response is the smallest among all piezo-crystals studied in this chapter. This fact underlines the importance of the dielectric properties of the materials employed in ME composites. Thus, we see that compounds with merely large PE coefficients do not necessarily yield large direct ME effects. We also observe that for this PZT-2 ceramic the maximum ME coefficient changes little for cut angles in the range $0° \leq \beta < 60°$ and $120° \leq \beta < 180°$. Therefore, common commercially available Z-cut ceramics still could exhibit a maximum 5.41 V/(cm·Oe) ME response.

PMN-PT crystals are a family of lead-based macrosymmetric multidomain engineered piezoelectrics. Here we studied the ME effect in composites featuring the following compositions: [111] poled PMN-33 %PT, [011] poled PMN-30 %PT and [001] poled PMN-33 %PT. The first compound has a trigonal *3m* symmetry, while the second and third have an orthorhombic *mm2* and tetragonal *4mm* macrosymmetry, respectively. From a general point of view, the [011] poled crystal exhibits the largest dielectric coefficients, followed by the [001] poled and the [111] poled ones. The largest piezocoefficients in each crystal are d_{15} = 4100 pC/N, d_{15} = 3262 pC/N and d_{33} = 2820 pC/N in the [111], [011] and [001] poled compounds, respectively. In the calculations we identified a relatively large maximum direct ME coefficient of 27.11 V/(cm·Oe) in the [111] poled and (*ZXl*) 42°-cut PMN-PT crystal ($\alpha = 0°$, $\beta = 42°$ and $\gamma = 90°$), and five other equivalent directions, although this is just of 5.78 V/(cm·Oe) in the Z-cut crystal. The maximum coefficient decays by more than 10 % of its highest value for angle deviations larger than $\Delta\alpha = \pm 10°$ and $\Delta\beta = \pm 10°$ from the optimal orientation. In the [011] poled crystal, the largest expected value is of 12.50 V/(cm·Oe), and it is observed in the Z-cut crystal. This coefficient changes only slightly for $\Delta\beta = \pm 10°$. In the [001] poled PMN-PT crystal the maximum is of 10.80 V/(cm·Oe) and should be attained in the crystal with a (*ZXtl*) 45°/64° complex cut ($\alpha = 45°$, $\beta = 64°$ and $\gamma = 90°$), and seven other directions. The most common Z-cut could exhibit a ME response of up to 6.29 V/(cm·Oe). By symmetry considerations, an almost maximized ME effect could, nonetheless, be observed in the range of $60° \leq \beta < 70°$ and $110° \leq \beta < 120°$, for any α angle.

Finally, we also studied PZN-PT piezocrystals with engineered domain structures. Those where the [011] poled PZN-9 %PT, with an orthorhombic *mm2* macrosymmetry, and the [001] poled PZN-8 %PT, with a tetragonal *4mm* macrosymmetry. The first crystal has a large difference between transversal PE coefficients $|d_{31} - d_{32}|$ = 2181 pC/N, which therefore explains its large calculated

maximum direct ME coefficient of 23.04 V/(cm·Oe) in the Z-cut crystal. As in the [011] poled PMN-PT, this coefficient changes only slightly for $\beta = \pm 10°$. In the [001] poled PZN-8 %PT, the maximum effect was estimated as 8.30 V/(cm·Oe) for the (*ZXtl*) 45°/38°-cut ($\alpha = 45°$, $\beta = 38°$ and $\gamma = 0°$), and seven other directions. In the Z-cut crystal, this decays just to 7.66 V/(cm·Oe). Mainly, the maximum coefficient decreases by less than 10 % of its largest value for cut deviations of approximately $\Delta\alpha = \pm 10°$ and $\Delta\beta = \pm 10°$.

In summary, using an averaging model based on the constitutive equations, we have predicted the possibility of producing large ME responses in tri-layered composites employing suitably cut PE crystals. Especially strong ME effects are expected for single crystals of $LiNbO_3$, α-$GaPO_4$, α-quartz, [111] poled PMN-33 % PT and [011] poled PZN-9 %PT. Even so, in practice the use of the first three in ME composites still remains largely unexplored.

6.3 Conclusions

A theoretical model of the anisotropic quasi-static direct ME effect in tri-layered composites of metglas and PE single crystals has been used in the quantitative estimation of the ME coupling as a function of the crystallographic orientation (i.e. PE cut plane). First, a description of the PE and linear MS (in the pseudo-piezomagnetic approximation) effects in terms of electric, magnetic and elastic material fields and constants has been given. An averaging quasi-static method was subsequently used together with specific boundary conditions in order to derivate the relation between the material constants and the transversal (T-L) direct ME voltage (α_{E3a}) and charge coefficients (α_{Q3a}). The method consisted of the solution of the elastostatic and electrostatic equations taking into account the linear constitutive relations of the two phases. The properties of some common PE and MS materials (the latter with emphasis on the metglas alloy exhibiting giant MS) have been discussed, and their influence on the ME coupling has been explored. It has been demonstrated that large ME voltage coefficients tend to be favored by large transversal PE coefficients, transversal and longitudinal piezomagnetic coefficients and coupling constants as well as small out-of-plane dielectric and compliance constants and the volume ratio between the PE and MS phases. On the other hand, it has also been shown that the ME charge coefficients do not depend on the dielectric constants of the PEs and thus tend to be much larger in lead-based crystals with very large piezoelectric constants such as PMN-PT and PZN-PT. The effects of the demagnetization fields on the attenuation of the ME coefficients were briefly explored. A description of the ME composites as equivalent Thévenin/Norton circuits composed of a magnetically driven voltage/current source in series/parallel with a characteristic impedance of the composite has also been exposed.

After that, we used the quasi-static model for the calculation of the maximum expected direct transversal ME voltage coefficients in a series of tri-layered composites of the type Metglas/Piezocrystal/Metglas, as a function of the PE crystal

orientation. The PE single crystals studied in this chapter included lead-free lithium niobate, α-galium phosphate, α-quartz, langatate, langasite, aluminum nitride, lithium tantalate and barium titanate, as well as the lead-based PZT-2, PMN-33 % PT ([111] poled), PMN-30 %PT ([011] poled), PMN-33 %PT ([001] poled), PZN-9 %PT ([011] poled) and PZN-8 %PT ([001] poled). The estimations revealed a strong dependence of the ME effects on the crystal orientation. They also supported the possibility of generating large quasi-static ME voltage coefficients in composites comprising lead-free PE single crystals through the optimization of the crystal orientation. These ME effects were found to be particularly attractive for the case of lithium niobate, α-galium phosphate, quartz, [111]-poled PMN-33 %PT and [011]-poled PZN-9 %PT. The enhanced effects were found to originate from a particularly good combination of relatively large PE coefficients and low dielectric constants. We thus have revealed that the choice of crystals with an appropriate cut is a vital step in the development of ME composites valuable for practical applications.

Acknowledgments This work was developed in the scope of the projects I3N/FSCOSD (Ref. FCT UID/CTM/50025/2013), CICECO – Aveiro Institute of Materials – POCI-01-0145-FEDER-007679 (FCT Ref. UID/CTM/50011/2013), and RECI/FIS-NAN/0183/2012 (FCOMP-01-0124-FEDER-027494) financed by national funds through the FCT/MEC and when applicable cofinanced by FEDER under the PT2020 Partnership Agreement. J.V.V. and A.A.T. thank for the FCT grants SFRH/BD/89097/2012 and SFRH/BPD/74086/2010, respectively. N.A.S. acknowledges support by NUST "MISiS" through grant no. K3-2015-003.

References

1. P. Debye, Bemerkung zu einigen neuen Versuchen über einen magneto-elektrischen Richteffekt. Z. Phys. **36**(4), 300–301 (1926)
2. T.H. O'Dell, *The Electrodynamics of Continuous Media* (North-Holland, Amsterdan, 1970)
3. L.D. Landau, L.P. Pitaevskii, E. M. Lifshitz, *Electrodynamics of Continuous Media.* 2nd edn. vol. 8 (Course of Theoretical Physics), Butterworth-Heinemann (1984)
4. M. Fiebig, N.A. Spaldin, Current trends of the magnetoelectric effect. Eur. Phys. J. B **71**(3), 293–297 (2009)
5. W. Eerenstein, N.D. Mathur, J.F. Scott, Multiferroic and magnetoelectric materials. Nature **442**(7104), 759–765 (2006)
6. C.-W. Nan, M.I. Bichurin, S. Dong, D. Viehland, G. Srinivasan, Multiferroic magnetoelectric composites: historical perspective, status, and future directions. J. Appl. Phys. **103**(3), 031101–031135 (2008)
7. M. Fiebig, Revival of the magnetoelectric effect. J. Phys. D Appl. Phys. **38**(8), R123–R152 (2005)
8. S.-W. Cheong, M. Mostovoy, Multiferroics: a magnetic twist for ferroelectricity. Nat. Mater. **6**(1), 13–20 (2007)
9. R. Ramesh, N.A. Spaldin, Multiferroics: progress and prospects in thin films. Nat. Mater **6**(1), 21–29 (2007).\
10. R. Ramesh, Materials science: Emerging routes to multiferroics. Nature **461**(7268), 1218–1219 (2009)

11. N.A. Spaldin, M. Fiebig, The renaissance of magnetoelectric multiferroics. Science **309**(5733), 391–392 (2005)
12. M. Bichurin, D. Viehland, G. Srinivasan, Magnetoelectric interactions in ferromagnetic-piezoelectric layered structures: phenomena and devices. J. Electroceram. **19**(4), 243–250 (2007)
13. Y. Wang, J. Hu, Y. Lin, C.-W. Nan, Multiferroic magnetoelectric composite nanostructures. NPG Asia Mater. **2**(2), 61–68 (2010)
14. J. Zhai, Z. Xing, S. Dong, J. Li, D. Viehland, Magnetoelectric laminate composites: an overview. J. Am. Ceram. Soc. **91**(2), 351–358 (2008)
15. S. Picozzi, C. Ederer, First principles studies of multiferroic materials. J. Phys.: Condens. Matter **21**(30), 303201–303237 (2009)
16. M. Vopsaroiu, J. Blackburn, M.G. Cain, Emerging technologies and opportunities based on the magneto-electric effect in multiferroic composites. MRS Proc. **1161**, 1161-I05-04 (2009)
17. J. Ryu, S. Priya, K. Uchino, H.-E. Kim, Magnetoelectric effect in composites of magnetostrictive and piezoelectric materials. J. Electroceram. **8**(2), 107–119 (2002)
18. R.C. Kambale, D.-Y. Jeong, J. Ryu, Current status of magnetoelectric composite thin/thick films. Adv. Cond. Matter Physics **2012**, 824643 (2012)
19. G. Lawes, G. Srinivasan, Introduction to magnetoelectric coupling and multiferroic films. J. Phys. D Appl. Phys. **44**(24), 243001 (2011)
20. G. Srinivasan, Magnetoelectric composites. Annu. Rev. Mater. Res. **40**, 153–178 (2010)
21. L.W. Martin, R. Ramesh, Multiferroic and magnetoelectric heterostructures. Acta Mater. **60** (6–7), 2449–2470 (2012)
22. S. Priya, R. Islam, S. Dong, D. Viehland, Recent advancements in magnetoelectric particulate and laminate composites. J. Electroceram. **19**(1), 149–166 (2007)
23. J. Ma, J. Hu, Z. Li, C.-W. Nan, Recent progress in multiferroic magnetoelectric composites: from bulk to thin films. Adv. Mater. **23**(9), 1062–1087 (2011)
24. M. Bichurin, V. Petrov, A. Zakharov, D. Kovalenko, S.C. Yang, D. Maurya, V. Bedekar, S. Priya, Magnetoelectric interactions in lead-based and lead-free composites. Materials **4**(4), 651–702 (2011)
25. R. Grössinger, G.V. Duong, R. Sato-Turtelli, The physics of magnetoelectric composites. J. Mag. Mag. Mat. **320**(14), 1972–1977 (2008)
26. Ü. Özgür, Y. Alivov, H. Morkoç, Microwave ferrites, part 2: passive components and electrical tuning. J. Mater. Sci.: Mater. Electron. **20**(10), 911–951 (2009)
27. T.H. O'Dell, The field invariants in a magneto-electric medium. Phil. Mag. **8**(87), 411–418 (1963)
28. M.I. Bichurin, V.M. Petrov, D.A. Filippov, G. Srinivasan, *Magnetoelectric Effect in Composite Materials (em russo).* Veliki Noogorod (2005)
29. W.F. Brown, Jr., R.M. Hornreich, S. Shtrikman, Upper bound on the magnetoelectric susceptibility. Phys. Rev. **168**(2), 574–577 (1968)
30. N.A. Spaldin, R. Ramesh, Electric-field control of magnetism in complex oxide thin films. MRS Bull. **33**, 1047–1050 (2008)
31. G.A. Gehring, On the microscopic theory of the magnetoelectric effect. Ferroelectrics **161**(1), 275–285 (1994)
32. N.A. Hill, Why are there so few magnetic ferroelectrics? J. Phys. Chem. B **104**(29), 6694–6709 (2000)
33. J.-P. Rivera, A short review of the magnetoelectric effect and related experimental techniques on single phase (multi-) ferroics. Eur. Phys. J. B **71**(3), 299–313 (2009)
34. J.P. Rivera, On definitions, units, measurements, tensor forms of the linear magnetoelectric effect and on a new dynamic method applied to Cr-Cl boracite. Ferroelectrics **161**(1), 165–180 (1994)
35. H. Grimmer, The forms of tensors describing magnetic, electric and toroidal properties. Ferroelectrics **161**(1), 181–189 (1994)
36. R.A. Islam, S. Priya, Progress in dual (Piezoelectric-Magnetostrictive) phase magnetoelectric sintered composites. Adv. Cond. Matter Phys. **2012**, 1–29 (2012)

37. J.V. Suchtelen, Product properties: a new application of composite materials. Philips Res. Rep. **27**(1), 28–37 (1972)
38. J.V.D. Boomgard, A.M.J.G.V. Run, J.V. Suchtelen, Piezoelectric-piezomagnetic composites with magnetoelectric effect. Ferroelectrics **14**(1), 727–728 (1976)
39. C.-W. Nan, Magnetoelectric effect in composites of piezoelectric and piezomagnetic phases. Phys. Rev. B **50**(9), 6082–6088 (1994)
40. D.C. Lupascu, H. Wende, M. Etier, A. Nazrabi, I. Anusca, H. Trivedi, V.V. Shvartsman, J. Landers, S. Salamon, C. Schmitz-Antoniak, Measuring the magnetoelectric effect across scales. GAMM-Mitteilungen **38**(1), 25–74 (2015)
41. C.-W. Nan, Physics of inhomogeneous inorganic materials. Prog. Mater Sci. **37**(1), 1–116 (1993)
42. M.I. Bichurin, V.M. Petrov, G. Srinivasan, Theory of low-frequency magnetoelectric effects in ferromagnetic-ferroelectric layered composites. J. Appl. Phys. **92**(12), 7681–7683 (2002)
43. M.I. Bichurin, V.M. Petrov, G. Srinivasan, Theory of low-frequency magnetoelectric coupling in magnetostrictive-piezoelectric bilayers. Phys. Rev. B **68**(5), 054402–054414 (2003)
44. G.V. Duong, R. Groessinger, M. Schoenhart, D. Bueno-Basques, The lock-in technique for studying magnetoelectric effect. J. Mag. Mag. Mat. **316**(2), 390–393 (2007)
45. X. Zhuang, M.L.C. Sing, C. Cordier, S. Saez, C. Dolabdjian, J. Das, J. Gao, J. Li, D. Viehland, Analysis of noise in magnetoelectric thin-layer composites used as magnetic sensors. IEEE Sens. J. **11**(10), 2183–2188 (2011)
46. Y.J. Wang, J.Q. Gao, M.H. Li, Y. Shen, D. Hasanyan, J.F. Li, D. Viehland, A review on equivalent magnetic noise of magnetoelectric laminate sensors. Phil. Trans. R. Soc. A **372**(2009), 20120455 (2014)
47. Z.P. Xing, J.Y. Zhai, S.X. Dong, J.F. Li, D. Viehland, W.G. Odendaal, Modeling and detection of quasi-static nanotesla magnetic field variations using magnetoelectric laminate sensors. Meas. Sci. Technol. **19**(1), 015206–015214 (2008)
48. Y. Wang, D. Gray, D. Berry, J. Gao, M. Li, J. Li, D. Viehland, An extremely low equivalent magnetic noise magnetoelectric sensor. Adv. Mater. **23**(35), 4111–4114 (2011)
49. R. Jahns, H. Greve, E. Woltermann, E. Quandt, R.H. Knochel, Noise performance of magnetometers with resonant thin-film magnetoelectric sensors. IEEE T. Instrum. Meas. **60**(8), 2995–3001 (2011)
50. R.E. Newnham, D.P. Skinner, L.E. Cross, Connectivity and piezoelectric-pyroelectric composites. Mater. Res. Bull. **13**(5), 525–536 (1978)
51. S.N. Babu, T. Bhimasankaram, S.V. Suryanarayana, Magnetoelectric effect in metal-PZT laminates. Bull. Mater. Sci. **28**(5), 419–422 (2004)
52. C.P. Zhao, F. Fang, W. Yang, A dual-peak phenomenon of magnetoelectric coupling in laminated Terfenol-D/PZT/Terfenol-D composites. Smart Mater. Struct. **19**(12), 125004–125010 (2010)
53. J. Ryu, A.V. Carazo, K. Uchino, H.-E. Kim, Magnetoelectric properties in piezoelectric and magnetostrictive laminate composites. Jpn. J. Appl. Phys. **40**(8), 4948–4951 (2001)
54. IEEE Standard on Piezoelectricity. *ANSI/IEEE Std 176-1987*, pp. 1–74 (1988)
55. M. Zgonik, P. Bernasconi, M. Duelli, R. Schlesser, P. Günter, M.H. Garrett, D. Rytz, Y. Zhu, X. Wu, Dielectric, elastic, piezoelectric, electro-optic, and elasto-optic tensors of BaTiO_{3} crystals. Phys. Rev. B **50**(9), 5941–5949 (1994)
56. H. Xiao-Kang, Z. Li-Bo, W. Qiong-Shui, Z. Li-Yan, Z. Ke, L. Yu-Long, Determination of elastic, piezoelectric, and dielectric constants of an R:BaTiO3 single crystal by Brillouin scattering. Chin. Phys. B **21**(6), 067801 (2012)
57. R.S. Weis, T.K. Gaylord, Lithium niobate: summary of physical properties and crystal structure. Appl. Phys. A Mater. Sci. Process. **37**(4), 191–203 (1985)
58. P. Davulis, J.A. Kosinski, M.P. da Cunha, GaPO4 stiffness and piezoelectric constants measurements using the combined thickness excitation and lateral field technique. in *International Frequency Control Symposium and Exposition, 2006 IEEE*, 664–669 (2006)

59. W. Wallnöfer, P.W. Krempl, A. Asenbaum, Determination of the elastic and photoelastic constants of quartz-type GaPO4 by Brillouin scattering. Phys. Rev. B **49**(15), 10075–10080 (1994)
60. M. Šulca, J. Erharta, J. Noseka, Interferometric measurement of the temperature dependence of piezoelectric coefficients for PZN-8 %PT single crystals. Ferroelectrics **293**(1), 283–290 (2003)
61. D.-S. Paik, S.-E. Park, T.R. Shrout, W. Hackenberger, Dielectric and piezoelectric properties of perovskite materials at cryogenic temperatures. J. Mater. Sci. **34**(3), 469–473 (1999)
62. M. Shanthi, L.C. Lim, K.K. Rajan, J. Jin, Complete sets of elastic, dielectric, and piezoelectric properties of flux-grown [011]-poled Pb(Mg1/3Nb2/3)O3-(28–32)%PbTiO3 single crystals. Appl. Phys. Lett. **92**(14), 142906 (2008)
63. S.S. Guo, S.G. Lu, Z. Xu, X.Z. Zhao, S.W. Or, Enhanced magnetoelectric effect in Terfenol-D and flextensional cymbal laminates. Appl. Phys. Lett. **88**(18), 182906–182908 (2006)
64. J.G. Wan, Z.Y. Li, Y. Wang, M. Zeng, G.H. Wang, J.-M. Liu, Strong flexural resonant magnetoelectric effect in Terfenol-D/epoxy-Pb(Zr, Ti)O3 bilayer. Appl. Phys. Lett. **86**(20), 202504–202506 (2005)
65. S. Dong, J.-F. Li, D. Viehland, Longitudinal and transverse magnetoelectric voltage coefficients of magnetostrictive/piezoelectric laminate composite: theory. IEEE Trans. Ultrason. Ferroelectr. Freq. Control **50**(10), 1253–1261 (2003)
66. S. Dong, J.-F. Li, D. Viehland, Ultrahigh magnetic field sensitivity in laminates of TERFENOL-D and Pb(Mg1/3Nb2/3)O3–PbTiO3 crystals. Appl. Phys. Lett. **83**(11), 2265–2267 (2003)
67. S. Dong, J. Cheng, J.F. Li, D. Viehland, Enhanced magnetoelectric effects in laminate composites of Terfenol-D/Pb(Zr, Ti)O3 under resonant drive. Appl. Phys. Lett. **83**(23), 4812–4814 (2003)
68. J. Zhai, S. Dong, Z. Xing, J. Li, D. Viehland, Giant magnetoelectric effect in Metglas/polyvinylidene-fluoride laminates. Appl. Phys. Lett. **89**(8), 083507–083509 (2006)
69. Y. Yang, J. Gao, Z. Wang, M. Li, J.-F. Li, J. Das, D. Viehland, Effect of heat treatment on the properties of Metglas foils, and laminated magnetoelectric composites made thereof. Mater. Res. Bull. **46**(2), 266–270 (2011)
70. U. Laletsin, N. Padubnaya, G. Srinivasan, C.P. DeVreugd, Frequency dependence of magnetoelectric interactions in layered structures of ferromagnetic alloys and piezoelectric oxides. Appl. Phys. A **78**(1), 33–36 (2004)
71. http://www.metglas.com/products/magnetic_materials/
72. S. Dong, J. Zhai, J. Li, D. Viehland, Near-ideal magnetoelectricity in high-permeability magnetostrictive/piezofiber laminates with a (2-1) connectivity. Appl. Phys. Lett. **89**(25), 252904–252906 (2006)
73. G. Sreenivasulu, S.K. Mandal, S. Bandekar, V.M. Petrov, G. Srinivasan, Low-frequency and resonance magnetoelectric effects in piezoelectric and functionally stepped ferromagnetic layered composites. Phys. Rev. B **84**(14), 144426–144431 (2011)
74. J. Wang, Y. Zhang, J. Ma, Y. Lin, C.W. Nan, Magnetoelectric behavior of $BaTiO_3$ films directly grown on $CoFe2O_4$ ceramics. J. Appl. Phys. **104**(1), 014101–014105 (2008)
75. T. Kiyomiya, Y. Yamada, Y. Matsuo, H. Wakiwaka, Y. Torii, M. Makimura, Magnetostrictive properties of Tb-Fe and Tb-Fe-Co films. Electron. Comm. Jpn. **91**(5), 49–55 (2008)
76. G. Sreenivasulu, U. Laletin, V.M. Petrov, V.V. Petrov, G. Srinivasan, A permendur-piezoelectric multiferroic composite for low-noise ultrasensitive magnetic field sensors. Appl. Phys. Lett. **100**(17), 173506–173510 (2012)
77. M. Matsumoto, T. Kubota, M. Yokoyama, T. Okazaki, Y. Furuya, A. Makino, M. Shimada, Magnetic properties of rapidly solidified ribbon of Fe49Co49V2 and spark-plasma-sintered pellet of its powder. Mater. Trans. **51**(10), 1883–1886 (2010)

78. D.A. Burdin, D.V. Chashin, N.A. Ekonomov, L.Y. Fetisov, Y.K. Fetisov, G. Sreenivasulu, G. Srinivasan, Nonlinear magneto-electric effects in ferromagnetic-piezoelectric composites. J. Mag. Mag. Mat. **358–359**, 98–104 (2014)
79. A.E. Clark, M. Wun-Fogle, J.B. Restorff, T.A. Lograsso, J.R. Cullen, Effect of quenching on the magnetostriction on Fe < sub > 1-x </sub > Ga < sub > x</sub > (0.13x < 0.21). IEEE Trans. Magn. **37**(4), 2678–2680 (2001)
80. A.E. Clark, M. Wun-Fogle, J.B. Restorff, T.A. Lograsso, Magnetostrictive properties of galfenol alloys under compressive stress. Mater. Trans. **43**(5), 881–886 (2002)
81. S. Dong, J.-F. Li, D. Viehland, Magnetoelectric coupling, efficiency, and voltage gain effect in piezoelectric-piezomagnetic laminate composites. J. Mater. Sci. **41**(1), 97–106 (2006)
82. G. Srinivasan, I.V. Zavislyak, A.S. Tatarenko, Millimeter-wave magnetoelectric effects in bilayers of barium hexaferrite and lead zirconate titanate. Appl. Phys. Lett. **89**(15), 152508–152510 (2006)
83. G. Srinivasan, E.T. Rasmussen, J. Gallegos, R. Srinivasan, Y.I. Bokhan, V.M. Laletin, Magnetoelectric bilayer and multilayer structures of magnetostrictive and piezoelectric oxides. Phys. Rev. B **64**(21), 214408–214413 (2001)
84. G. Srinivasan, C.P. DeVreugd, C.S. Flattery, V.M. Laletsin, N. Paddubnaya, Magnetoelectric interactions in hot-pressed nickel zinc ferrite and lead zirconante titanate composites. Appl. Phys. Lett. **85**(13), 2550–2552 (2004)
85. G. Liu, C.-W. Nan, N. Cai, Y. Lin, Calculations of giant magnetoelectric effect in multiferroic composites of rare-earth-iron alloys and PZT by finite element method. Int. J. Solids Struct. **41**(16–17), 4423–4434 (2004)
86. S. Dong, J. Zhai, F. Bai, J.-F. Li, D. Viehland, Push-pull mode magnetostrictive/piezoelectric laminate composite with an enhanced magnetoelectric voltage coefficient. Appl. Phys. Lett. **87**(6), 062502–062504 (2005)
87. D.R. Tilley, J.F. Scott, Frequency dependence of magnetoelectric phenomena in $BaMnF_4$. Phys. Rev. B **25**(5), 3251–3260 (1982)
88. M.I. Bichurin, V.M. Petrov, O.V. Ryabkov, S.V. Averkin, G. Srinivasan, Theory of magnetoelectric effects at magnetoacoustic resonance in single-crystal ferromagnetic-ferroelectric heterostructures. Phys. Rev. B **72**(6), 060408–060411 (2005)
89. M.I. Bichurin, V.M. Petrov, Y.V. Kiliba, G. Srinivasan, Magnetic and magnetoelectric susceptibilities of a ferroelectric/ferromagnetic composite at microwave frequencies. Phys. Rev. B **66**(13), 134404–134413 (2002)
90. S. Timoshenko, *Vibration Problems in Engineering* (D. Van Nostrand, New York, 1961)
91. U. Laletsin, N. Padubnaya, G. Srinivasan, C.P. DeVreugd, Frequency dependence of magnetoelectric interactions in layered structures of ferromagnetic alloys and piezoelectric oxides. Appl. Phys. A **78**(1), 33–36 (2004)
92. Y.K. Fetisov, K.E. Kamentsev, A.Y. Ostashchenko, G. Srinivasan, Wide-band magnetoelectric characterization of a ferrite-piezoelectric multilayer using a pulsed magnetic field. Solid State Commun. **132**(1), 13–17 (2004)
93. N. Cai, C.-W. Nan, J. Zhai, Y. Lin, Large high-frequency magnetoelectric response in laminated composites of piezoelectric ceramics, rare-earth iron alloys and polymer. Appl. Phys. Lett. **84**(18), 3516–3518 (2004)
94. H. Greve, E. Woltermann, H.-J. Quenzer, B. Wagner, E. Quandt, Giant magnetoelectric coefficients in (Fe90Co10)78Si12B10-AlN thin film composites. Appl. Phys. Lett. **96**(18), 182501–182503 (2010)
95. G. Liu, X. Li, J. Chen, H. Shi, W. Xiao, S. Dong, Colossal low-frequency resonant magnetomechanical and magnetoelectric effects in a three-phase ferromagnetic/elastic/piezoelectric composite. Appl. Phys. Lett. **101**(14), 142904–142907 (2012)
96. H. Greve, E. Woltermann, R. Jahns, S. Marauska, B. Wagner, R. Knöchel, M. Wuttig, E. Quandt, Low damping resonant magnetoelectric sensors. Appl. Phys. Lett. **97**(15), 152503–152505 (2010)

97. Y. Zhang, G. Liu, H. Shi, W. Xiao, Y. Zhu, M. Li, M. Li, J. Liu, Enhanced magnetoelectric effect in ferromagnetic–elastic–piezoelectric composites. J. Alloy. Compd. **613**, 93–95 (2014)
98. M. Liu, O. Obi, J. Lou, Y. Chen, Z. Cai, S. Stoute, M. Espanol, M. Lew, X. Situ, K.S. Ziemer, V.G. Harris, N.X. Sun, Giant electric field tuning of magnetic properties in multiferroic ferrite/ferroelectric heterostructures. Adv. Funct. Mater. **19**(11), 1826–1831 (2009)
99. S. Sherrit, B.K. Mukherjee, Characterization of Piezoelectric Materials for Transducers, arXiv (2007)
100. W.P. Mason, *Physical Acoustics and the Properties of Solids (The Bell Telephone Laboratories Series)* (Van Nostrand, 1958)
101. T. Ikeda, *Fundamentals of Piezoelectricity* (Oxford Science Publications, 1990)
102. J.W. Morris, *Notes on the Thermodynamics of Solids (Chapter 15: Tensors and Tensor Properties)* (Department of Materials Science and Engineering, University of Califormia, Berkeley, 2008)
103. D. Damjanovic, Ferroelectric, dielectric and piezoelectric properties of ferroelectric thin films and ceramics. Rep. Prog. Phys. **61**(9), 1267 (1998)
104. R.F. Tinder, *Tensor Properties of Solids: Phenomenological Development of the Tensor Properties of Crystals* (Morgan & Claypool Publishers, 2008)
105. J.F. Nye, *Physical Properties of Crystals: Their Representation by Tensors and Matrices* (Oxford University Press, 1985)
106. IRE Standards on Piezoelectric Crystals: Determination of the Elastic, Piezoelectric, and Dielectric Constants-The Electromechanical Coupling Factor, 1958. Proc. IRE **46**(4), 764–778 (1958)
107. H.-Y. Kuo, A. Slinger, K. Bhattacharya, Optimization of magnetoelectricity in piezoelectric–magnetostrictive bilayers. Smart Mater. Struct. **19**(12), 125010–125022 (2010)
108. D.A. Burdin, D.V. Chashin, N.A. Ekonomov, L.Y. Fetisov, Y.K. Fetisov, G. Sreenivasulu, G. Srinivasan, Nonlinear magneto-electric effects in ferromagnetic-piezoelectric composites. J. Mag. Mag. Mat. **358–359**, 98–104 (2014)
109. Y. Benveniste, Magnetoelectric effect in fibrous composites with piezoelectric and piezomagnetic phases. Phys. Rev. B **51**(22), 16424–16427 (1995)
110. C.W. Nan, M. Li, J.H. Huang, Calculations of giant magnetoelectric effects in ferroic composites of rare-earth–iron alloys and ferroelectric polymers. Phys. Rev. B **63**(14), 144415 (2001)
111. R. Tinder, *Tensor Properties of Solids* (Morgan & Claypool, 2007)
112. J.A. Osborn, Demagnetizing factors of the general ellipsoid. Phys. Rev. **67**(11–12), 351–357 (1945)
113. A.A. Timopheev, J.V. Vidal, A.L. Kholkin, N.A. Sobolev, Direct and converse magnetoelectric effects in Metglas/LiNbO3/Metglas trilayers. J. Appl. Phys. **114**(4), 044102–044108 (2013)
114. Y. Wang, S.W. Or, H.L.W. Chan, X. Zhao, H. Luo, Enhanced magnetoelectric effect in longitudinal-transverse mode Terfenol-D/$Pb(Mg_{1/3}Nb_{2/3})O_3$–$PbTiO_3$ laminate composites with optimal crystal cut. J. Appl. Phys. **103**(12), 124511 (2008)
115. C.-S. Park, K.-H. Cho, M.A. Arat, J. Evey, S. Priya, High magnetic field sensitivity in $Pb(Zr,Ti)O_3$–$Pb(Mg_{1/3}Nb_{2/3})O_3$ single crystal/Terfenol-D/Metglas magnetoelectric laminate composites. J. Appl. Phys. **107**(9), 094109 (2010)
116. J. Lou, M. Liu, D. Reed, Y. Ren, N.X. Sun, Giant Electric Field Tuning of Magnetism in Novel Multiferroic FeGaB/Lead Zinc Niobate-Lead Titanate (PZN-PT) Heterostructures. Adv. Mater. **21**(46), 4711–4715 (2009)
117. H.F. Tian, T.L. Qu, L.B. Luo, J.J. Yang, S.M. Guo, H.Y. Zhang, Y.G. Zhao, J.Q. Li, Strain induced magnetoelectric coupling between magnetite and BaTiO3. Appl. Phys. Lett. **92**(6), 063507–063509 (2008)

118. P. Yang, K. Zhao, Y. Yin, J.G. Wan, J.S. Zhu, Magnetoelectric effect in magnetostrictive/piezoelectric laminate composite Terfenol-D/LiNbO3 [(zxtw) − 129°/30°]. Appl. Phys. Lett. **88**(17), 172903–172905 (2006)
119. J.V. Vidal, A.A. Timopheev, A.L. Kholkin, N.A. Sobolev, Anisotropy of the magnetoelectric effect in tri-layered composites based on single-crystalline piezoelectrics. Vacuum, 1–7
120. G. Sreenivasulu, V.M. Petrov, L.Y. Fetisov, Y.K. Fetisov, G. Srinivasan, Magnetoelectric interactions in layered composites of piezoelectric quartz and magnetostrictive alloys. Phys. Rev. B **86**(21), 214405–214411 (2012)
121. R. Viswan, D. Gray, Y. Wang, Y. Li, D. Berry, J. Li, D. Viehland, Strong magnetoelectric coupling in highly oriented ZnO films deposited on Metglas substrates. Phys. Status Solidi-R **5**(10–11), 391–393 (2011)
122. G. Sreenivasulu, L.Y. Fetisov, Y.K. Fetisov, G. Srinivasan, Piezoelectric single crystal langatate and ferromagnetic composites: Studies on low-frequency and resonance magnetoelectric effects. Appl. Phys. Lett. **100**(5), 052901–052904 (2012)
123. G. Sreenivasulu, P. Qu, E. Piskulich, V.M. Petrov, Y.K. Fetisov, A.P. Nosov, H. Qu, G. Srinivasan, Shear strain mediated magneto-electric effects in composites of piezoelectric lanthanum gallium silicate or tantalate and ferromagnetic alloys. App. Phys. Lett. **105**(3), 032409–032412 (2014)
124. F. Fang, C. Zhao, W. Yang, Thickness effects on magnetoelectric coupling for Metglas/PZT/Metglas laminates. Sci. China Phys. Mech. Astron. **54**(4), 581–585 (2011)
125. D. Hasanyan, J. Gao, Y. Wang, R. Viswan, Y.S.M. Li, J. Li, D. Viehland, Theoretical and experimental investigation of magnetoelectric effect for bending-tension coupled modes in magnetostrictive-piezoelectric layered composites. J. Appl. Phys. **112**(1), 013908–013918 (2012)
126. Y. Wang, D. Hasanyan, M. Li, J. Gao, J. Li, D. Viehland, H. Luo, Theoretical model for geometry-dependent magnetoelectric effect in magnetostrictive/piezoelectric composites. J. Appl. Phys. **111**(12), 124513–124518 (2012)
127. http://bostonpiezooptics.com/crystal-quartz
128. R.T. Smith, F.S. Welsh, Temperature dependence of the elastic, piezoelectric, and dielectric constants of lithium tantalate and lithium niobate. J. Appl. Phys. **42**(6), 2219–2230 (1971)
129. A. Balatto, Basic Material Quartz and Related Innovations. *Springer Series in Materials Science,* **114**, 9–35 (2008)
130. J. Kushibiki, I. Takanaga, S. Nishiyama, Accurate measurements of the acoustical physical constants of synthetic/spl alpha/-quartz for SAW devices. IEEE Trans. Ultrason. Ferroelectr. Freq. Control **49**(1), 125–135 (2002)
131. P.M. Davulis, M.P.D. Cunha, A full set of langatate high-temperature acoustic wave constants: elastic, piezoelectric, dielectric constants up to 900 °C. IEEE Trans. Ultrason., Ferroelectr., Freq. Control. **60**(4), 824–33 (2013)
132. Y.K. Fetisov, D.A. Burdin, D.V. Chashin, N.A. Ekonomov, High-Sensitivity Wideband Magnetic Field Sensor Using Nonlinear Resonance Magnetoelectric Effect. Sens. J., IEEE **14** (7), 2252–2256 (2014)
133. M. Adachi, T. Kimura, W. Miyamoto, Z. Chen, A. Kawabata, Dielectric, elastic and piezoelectric properties of La3Ga5SiO14 (LANGASITE) single crystals. J. Korean Phys. Soc. **32**, S1274–S1277 (1998)
134. R. Tarumi, H. Nitta, H. Ogi, M. Hirao, Low-temperature elastic constants and piezoelectric coefficients of langasite ($La3Ga_5SiO_{14}$). Philos. Mag. **91**(16), 2140–2153 (2011)
135. A. Sotnikov, H. Schmidt, M. Weihnacht, E. Smirnova, T. Chemekova, Y. Makarov, Elastic and piezoelectric properties of AlN and $LiAlO_2$ single crystals. IEEE Trans. Ultrason. Ferroelectr. Freq. Control **57**(4), 808–811 (2010)
136. G. Bu, D. Ciplys, M. Shur, L.J. Schowalter, S. Schujman, R. Gaska, Electromechanical coupling coefficient for surface acoustic waves in single-crystal bulk aluminum nitride. Appl. Phys. Lett. **84**(23), 4611–4613 (2004)
137. http://www.roditi.com/SingleCrystal/Lithium-Tantalate/LiTaO3-Properties.html

138. R.T. Smith, F.S. Welsh, Temperature dependence of the elastic, piezoelectric, and dielectric constants of lithium tantalate and lithium niobate. J. Appl. Phys. **42**(6), 2219–2230 (1971)
139. A.W. Warner, M. Onoe, G.A. Coquin, Determination of elastic and piezoelectric constants for crystals in class (3 m). J. Acoust. Soc. America **42**(6), 1223–1231 (1967)
140. Technical Publication TP-226 - Properties of Piezoelectricity Ceramics, Morgan Electro Ceramics
141. R. Zhang, B. Jiang, W. Cao, Single-domain properties of $0.67Pb(Mg_{1/3}Nb_{2/3})O_3$–$0.33PbTiO_3$ single crystals under electric field bias. Appl. Phys. Lett. **82**(5), 787–789 (2003)
142. R. Zhang, B. Jiang, W. Cao, Elastic, piezoelectric, and dielectric properties of multidomain $0.67Pb(Mg_{1/3}Nb_{2/3})O_3$–$0.33PbTiO_3$ single crystals. J. Appl. Phys. **90**(7), 3471–3475 (2001)
143. C. He, J. Weiping, W. Feifei, K. Zhu, Q. Jinhao, Full tensorial elastic, piezoelectric, and dielectric properties characterization of [011]-poled PZN-9 %PT single crystal. IEEE Trans. Ultrason. Ferroelectr. Freq. Control **58**(6), 1127–1130 (2011)
144. R. Zhang, B. Jiang, W. Jiang, W. Cao, Complete set of properties of $0.92Pb(Zn_{1/3}Nb_{2/3})O_3$–$0.08PbTiO_3$ single crystal with engineered domains. Mater. Lett. **57**(7), 1305–1308 (2003)
145. H.-M. Zhou, Y.-H. Zhou, X.-J. Zheng, Q. Ye, J. Wei, A general 3-D nonlinear magnetostrictive constitutive model for soft ferromagnetic materials. J. Mag. Mag. Mat. **321**(4), 281–290 (2009)

Chapter 7
Dynamic Measurements of Magnetoelectricity in Metglas-Piezocrystal Laminates

João V. Vidal, Andrey A. Timopheev, Andrei L. Kholkin and Nikolai A. Sobolev

Abstract This chapter describes an experimental technique, developed experimental setup and respective experimental study of the dynamic properties of direct magnetolelectric (ME) effect measured in metglas-piezocrystal laminates. We have prepared a variety of different magnetoelectric laminates by bonding magnetostrictive metglas foils onto single-crystalline substrates of $LiNbO_3$ (LNO), $GaPO_4$ (GPO) and PMN-PT. The measurements have been performed as a function of the crystal cut, magnitude and orientation of the magnetic bias field and the frequency of the modulation field. Despite much weaker PE coefficients of LNO and GPO, direct ME effects have been found to have comparative magnitudes in the samples based on them and on PMN-PT. Greatly enhanced ME coefficients in certain resonance modes are explored and their relations to the material properties of the crystals and the geometry of the composites are investigated. We demonstrate that control of the PE crystal's orientation can be successfully used in order to obtain almost any desired quasi-static and resonant anisotropic ME properties for some given application. Such unique features as chemical stability, linear piezoelectricity, thermal robustness open up a real perspective to use lead-free LNO and α-GPO based ME tri-layers, e.g., as vector magnetic field sensors working in a wide range of temperatures.

J.V. Vidal · A.A. Timopheev · N.A. Sobolev
Departamento de Física and I3N, Universidade de Aveiro, 3810-193 Aveiro, Portugal

A.L. Kholkin
Departamento de Física and CICECO, Universidade de Aveiro, 3810-193 Aveiro, Portugal

A.L. Kholkin
Institute of Natural Sciences, Ural Federal University, 620000 Ekaterinburg, Russia

N.A. Sobolev (✉)
National University of Science and Technology "MISiS", 119049 Moscow, Russia
e-mail: sobolev@ua.pt

© Springer International Publishing Switzerland 2016

I. Tiginyanu et al. (eds.), *Nanostructures and Thin Films for Multifunctional Applications*, NanoScience and Technology,
DOI 10.1007/978-3-319-30198-3_7

7.1 Introduction

The magnetoelectric (ME) effect, in its most general definition, describes any type of coupling between polarization and magnetic fields (direct effect) and conversely between magnetization and electric fields (converse effect) in matter. This effect has given rise to a lot of interest in the scientific community over the past few years [1–8]. Unlike the ME single-phase multiferroics, several ME composites, combining elastically coupled piezoelectric (PE) and magnetostrictive (MS) phases, have been shown to yield very strong ME effects even at room temperature [1–3]. These structures also offer a great flexibility in the sense that a large number of parameters may be adjusted independently including the material properties of the constituent phases as well as the connectivity arrangement between them. Consequently, nowadays these materials are already very close to some promising applications which include [1, 2, 5]: *DC* and *AC* magnetic vector field sensors and electric current sensors, magneto-electro-elastic energy harvesters, multiple-state memory devices, micro-sensors in read heads, transformers, spinners, diodes, spin-wave generators and electrically tunable microwave devices. The 2-2 type tri-laminated structures, among other the types of connectivity, comprising a layer of a PE material sandwiched between two layers of a MS phase, are characterized by a particularly rich anisotropy as well as an enhanced ME coupling due to both the absence of leakage currents and a strong mechanical coupling between phases [1–3]. Also, the transversal "L-T" operation mode, in which the MS phase is longitudinally magnetized while the PE layer is perpendicularly polarized (see Fig. 7.1), tends to maximize the exchange of strain between phases and also minimize the

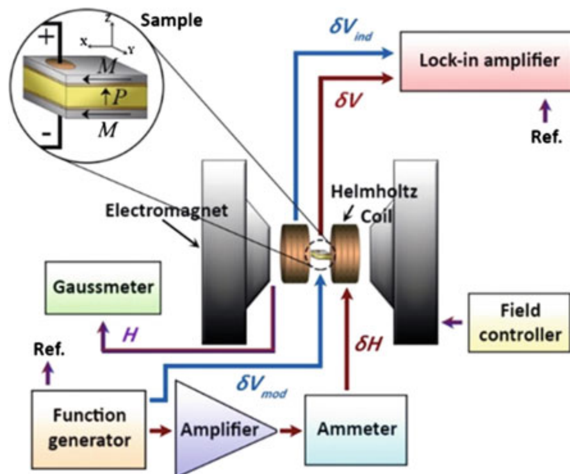

Fig. 7.1 Schematic presentation of the experimental setup used to perform the ME measurements. *Red* and *blue arrows* are associated with the measurements of the direct and converse ME effects, respectively [30] (Color in online)

demagnetizing fields in the MS layer and is therefore the most commonly employed operation mode [1–3].

In the experimental quantification of the direct ME effect a dynamic direct ME voltage coefficient $\alpha_{Eij} = \partial E_i / \partial H_j$ (where E_i is the component of the electric field in the i direction and H_j is the component of the magnetic field in the j direction) is generally used as a figure of merit under open-circuit conditions (i.e. with a displacement field $D_i = 0$). Also, a large enhancement in the magnitude of the ME effect is expected whenever the frequency of an applied modulation magnetic field with amplitude (δH) matches one of the natural electrical, magnetic or mechanical modes of resonance of the composite [9–12]. For the case of the PE phase this is known as electromechanical (EM) resonance and it occurs whenever a characteristic elastic eigenmode of the PE phase is indirectly excited by the time varying magnetic field [10]. Thus, a large oscillation amplitude of the standing wave in this phase gives rise to a large polarization/voltage through the PE effect. The frequency of these important EM resonances then depends on the effective material parameters and geometry of the PEs.

From the point of view of the constituent phases, large transversal direct voltage ME effects (α_{E3a}, where a and b are the direction indexes equal to 1 or 2) tend to be favored by MS phases with large longitudinal pseudo-piezomagnetic coefficients ($q_{ab} = \partial \lambda_b / \partial H_a$, where λ_b is the H dependent MS strain) and PE phases with a large ratio between transversal piezoelectric (d_{3a}) and longitudinal dielectric constants (ε_{33}), as well as an efficient stress transfer between layers [1, 2]. A very promising class of MS materials are the Metglas® (Ni-Fe-Mo-B, Fe–Si-B, Co-Fe–Si-Ni-B, etc.) amorphous alloys. This is mainly because of their large piezomagnetic coefficients of $q_{11} \approx 4.0$ ppm/Oe and $q_{12} \approx -2.5$ ppm/Oe [13], very low coercivity and low saturation fields which results in a huge relative magnetic permeability ($\mu_{33} > 10^4$) [7]. As for the PE phase, ferroelectric ceramics of PZT ($Pb(Zr,Ti)O_3$) have been extensively studied and tend to provide a strong ME coupling due to their relatively large piezoelectric and electromechanical (EM) coupling coefficients [14–16]. Nonetheless, the use of highly anisotropic single-crystalline ferroelectrics, poled and cut along desirable crystallographic directions, constitutes an alternative way to achieve large but also anisotropic ME effects [17, 18]. The current research on ME composites has therefore been remarkably focused on lead-based compounds such as PMN-PT or PZN-PT [1, 3, 19, 20]. Nevertheless, some lead-free PE single-crystals have been recently explored and shown to potentially yield a comparably large direct ME effect in composites. Such systems have included quartz [18], aluminum nitride [17], zinc oxide [21], langatate ($La_3Ga_{5.5}Ta_{0.5}O_{14}$, LGT) [22, 23] and langasite ($La_3Ga_{5.5}SiO_{14}$, LGS) [23].

In the present chapter, we report a study of the anisotropic direct ME properties of bulk tri-layered structures of Metglas/LNO/Metglas, Metglas/GPO/Metglas and Metglas/PMN-PT/Metglas using different cuts of the crystalline PEs and under quasi-static and EM resonance conditions.

7.2 Magnetoelectric Measurement Techniques

7.2.1 Dynamic Magnetoelectric Technique

In general, the experimental measurement of the direct ME effect has proven to be a simpler and more accurate method for the quantification of the ME effect when compared to the measurement of the converse ME effect. The advantages of the first technique include the relative easiness of producing large magnetic fields used to excite the samples and the fact that magnetic fields can generate higher energy densities than electric fields [24]. Also, the possibility of destructive dielectric breakdown, which could be caused by excessively high voltages applied during the measurement of the reverse effect, is avoided. The direct voltage and charge ME effects, quantified by the respective coefficients $\alpha_{Eij} = \partial E_i / \partial H_j$ and $\alpha_{Qij} = \partial D_i / \partial H_j$, with indexes i and j equal to 1, 2 or 3, can be experimentally measured via three fundamental methods [24, 25]:

(i) The static method, where the sample is subjected to a uniform magnetic bias field (H), and the voltage ($V = E_i \cdot t$, where t is the thickness of the PE phase) or charge ($Q = D_i \cdot A$, where A is the area of the electrodes placed on the PE) developed across its electrodes is measured with an electrometer in voltage (high-input-impedance) or charge (low-input-impedance) mode, respectively. In the charge mode, the input of the electrometer is a virtual ground, and therefore the measurement of charge instead of voltage should be less affected by the problem of leakage currents flowing through the sample due to an eventually small PE conductivity. By applying different magnetic fields, the induced ME voltage can therefore be quantified as a function of H;

(ii) The quasi-static method, where a voltage or charge generated across the sample's electrodes is measured using an electrometer as a function of time simultaneously with a slow variation of the applied DC magnetic field (with a rate of ca. 0.05–0.5 T/min). Here, the magnetic field is generally increased from zero up to a maximum value, stabilized at this value and subsequently decreased back to zero. A baseline can be subsequently used to correct for an eventual time drift of the voltage/charge due, e.g., to the pyroelectric effect;

(iii) The dynamic method, where a modulation magnetic field with a frequency f and a small amplitude δH is superimposed on a comparatively large magnetic DC bias field H. Using a lock-in amplifier, the AC ME voltage generated across the sample or the current flowing through it is then measured as a function of H or f. This dynamic method presents a series of advantages in comparison to the static and quasi-static methods [26, 27]. The first one is a very efficient reduction of the electronic noise thanks to the phase-sensitive detection using a lock-in amplifier. Here, signals with a frequency distinct from the frequency of a reference signal are rejected and filtered by the unit. This method also allows one to eliminate the problem of charge accumulation, observed for certain ceramics, where the charge generated during polarization

of the sample accumulates at its grain boundaries. These charges can move toward the electrodes during the measurements, thus disturbing the experimental results. The relatively high speed of measurement in this method thus allows a minimization of the accumulation of charge. Another advantage is that the ME response may be studied in different modes of operation, e.g., with different values of the magnetic bias field or at different time scales by changing the frequency of the modulation field. However, some negative aspects and special cautions should also be noted. These include [3, 6, 26, 28]: the leakage of charge under periodic conditions, which may occur through the Ohmic resistance of the samples at low frequencies of the *AC* field, or through the capacitance formed between the two surfaces at higher frequencies. Some parasitic mutual inductance will also exist between the source of the magnetic field and the system composed of the sample and cables connected to its electrodes. A frequency-proportional voltage will therefore always be induced across the electrodes by the applied time-changing magnetic field due to the effect of electromagnetic Faraday induction. Furthermore, we may also have the induction of eddy currents in the system, thus decreasing the effective modulated magnetic field felt by the sample. For high enough frequencies, these effects might even be more significant than the voltage generated by the ME effect in the samples. Some external sources of synchronized noise can also be especially harmful to this technique, including, e.g., the thermal noise, introduced by pyroelectric currents, and, more importantly, external vibrational or acoustic noises (microphony) which can be coupled to the sample via the piezoelectric effect.

In addition to the aforementioned techniques that can be used to measure the direct ME effect, several others have also been tested [25]. Some of those include: (i) active modes of analysis, where a test current is passed through the sample, and subsequently dielectric and polarization measurements are performed in various applied magnetic fields [3]; (ii) techniques using a pulsed magnetic field, which are ideal for the study of EM resonance phenomena [29], and (iii) ME measurements based on the PE effect making use of a microwave microscope or a magnetic cantilever [12].

From this point onwards we will mainly focus on the dynamic lock-in technique since this is the method in which we are most experienced. Thus we begin by presenting a formalism describing this technique and consequently show how the different order ME coefficients can be extracted from the measurements of the voltages synchronized with the fundamental and harmonic frequencies of the magnetic exciting signal. Assuming that the non-linear ME voltage ($V = E \cdot t$) induced across a ME composite as a function of an applied magnetic field (H) can be expanded in a Taylor series centered at a bias field H_0, it follows that [26]:

$$V(H) = \sum_{n=0}^{\infty} \alpha_n (H - H_0)^n, \text{ with } \alpha_n = \frac{1}{n!} \frac{\partial^n V}{\partial H^n}(H_0). \tag{7.1}$$

When a bias and a modulated AC magnetic field with frequency $f = \omega/2\pi$, given by $H = H_0 + \delta Hcos(\omega t)$ where t stands for time, are applied to this composite, the output voltage thus becomes:

$$V = \sum_{n=0}^{\infty} \alpha_n \cdot \delta H^n \cos(\omega t)^n. \tag{7.2}$$

Next, taking into account that:

$$\cos(\omega t)^n = \begin{cases} \frac{1}{2^{n-1}} \sum_{j=0}^{\frac{n-1}{2}} \binom{n}{j} \cos((n-2j)\omega t), \text{ if } n \subset \mathbb{N} \text{ is odd} \\ \frac{1}{2^n} \binom{n}{\frac{n}{2}} + \frac{1}{2^{n-1}} \sum_{j=0}^{\frac{n}{2}-1} \binom{n}{j} \cos((n-2j)\omega t), \text{ if } n \subset \mathbb{N} \text{ is even} \end{cases} \tag{7.3}$$

where $\binom{n}{j}$ are the binomial coefficients and substituting this expression in (7.2), one gets:

$$V = \sum_{l=0}^{\infty} \frac{1}{2^{2l}} \binom{2l}{l} \cdot \alpha_{2l} \cdot \delta H^{2l} + \sum_{n=1}^{\infty} \frac{1}{2^{n-1}} \cdot \alpha_n \cdot \delta H^n \sum_{j=0}^{\lfloor \frac{n-1}{2} \rfloor} \binom{n}{j} \cos((n-2j)\omega t), \tag{7.4}$$

where $\lfloor \ldots \rfloor$ indicates the nearest lower integer. Introducing the new variable $k = n - 2j$ and changing the order of summation allows us to collect the cosine terms in the last part of the equation:

$$V = \sum_{l=0}^{\infty} \frac{1}{2^{2l}} \binom{2l}{l} \cdot \alpha_{2l} \cdot \delta H^{2l} + \sum_{k=1}^{\infty} \left[\sum_{j=0}^{\infty} \frac{1}{2^{k+2j-1}} \binom{k+2j}{j} \cdot \alpha_{k+2j} \cdot \delta H^{k+2j} \right] \cos(k\omega t), \tag{7.5}$$

which shows that this voltage will be a combination of sinusoidal functions of time with frequencies equal to the frequency of the applied modulation field and its harmonics. The amplitudes associated with each of these harmonic signals will therefore be given by the parameter in brackets:

$$\delta^k V = \sum_{j=0}^{\infty} \frac{1}{2^{k+2j-1}} \binom{k+2j}{j} \cdot \alpha_{k+2j} \cdot \delta H^{k+2j}. \tag{7.6}$$

For example, the amplitudes of the fundamental signal and its first two harmonics are then:

$$\begin{aligned} \delta^1 V &= \alpha_1 \delta H + \frac{3}{4}\alpha_3 \delta H^3 + \frac{10}{16}\alpha_5 \delta H^5 + \cdots; \\ \delta^2 V &= \frac{1}{2}\alpha_2 \delta H^2 + \frac{1}{2}\alpha_4 \delta H^4 + \frac{15}{32}\alpha_6 \delta H^6 + \cdots; \\ \delta^3 V &= \frac{1}{4}\alpha_3 \delta H^3 + \frac{5}{16}\alpha_5 \delta H^5 + \frac{21}{64}\alpha_7 \delta H^7 + \cdots. \end{aligned} \tag{7.7}$$

Assuming that the partial derivatives in expansion (7.1) decrease fast enough and δH is sufficiently small, so that $\sum_{j=1}^{\infty} \frac{1}{2^{2j}} \binom{k+2j}{j} \cdot \frac{\alpha_{k+2j}}{\alpha_k} \cdot \delta H^{2j} \ll 1$ for all $k \in \mathbb{N}$, then all higher-order terms in the expansion (7.6) may be neglected, and one can arrive at the commonly made approximation:

$$^{k}\alpha_E = \frac{1}{t} \cdot \frac{\partial^k V}{\partial H^k} \simeq 2^{k-1} k! \frac{\delta^k V}{t \cdot \delta H^k}, \tag{7.8}$$

where $^{k}\alpha_E$ is the k-th order H_0 dependent voltage ME coefficient and t is the effective thickness of the PE phase. This expression shows that the amplitude of the k-th harmonic of the voltage ($\delta^k V$) as measured in the lock-in should be approximately proportional to the k-th power of the amplitude of the applied modulation field (δH^k) and to the k-th derivative of the V versus H curve at some bias H_0 field. Therefore we see that in the first order this ratio will be related to the direct voltage ME coefficient through: $\alpha_E = \delta^1 V/(t \cdot \delta H)$.

More generally, to take into account the dispersion and energy losses in the response of the ME coefficients α_n in expansion (7.1) we assume that the output voltage in (7.4) can be described by the convolution relation:

$$V(t) = V_0 + \sum_{k=1}^{\infty} \int_{-\infty}^{t} \delta^k V(t - t') \cdot \cos(k 2\pi f t') dt', \tag{7.9}$$

where t and t' represent the time. Making use of the convolution theorem, the Fourier transform of the above expression will then be:

$$V'(f') = V_0 \delta(f') + \sum_{k=1}^{\infty} \delta^k V'(f') \cdot \frac{1}{2}[\delta(f' - kf) + \delta(f' + kf)], \tag{7.10}$$

where $V'(f')$ and $\delta^k V'(f')$ represent the Fourier transforms of $V(t)$ and $\delta^k V(t)$, respectively, f' the frequency of the output voltage signal, f the frequency of the modulated H field and $\delta(x)$ the Dirac delta function. Therefore, all complex coefficients $\delta^k V'(f')$ in the expansion are now described as functions of the frequency f'. As before, this expression shows that the amplitude of the output voltage signal measured in a lock-in amplifier should only be nonzero at integer multiple frequencies of f. As an example, supposing that all the factors $\delta^k V'(f')$ in this

expression, which depend on the complex ME coefficients ${}^{n}\alpha'_{E}(f') = \alpha'_{n}(f') \cdot n!/t$ corresponding to the Fourier transforms of the ME coefficients ${}^{n}\alpha_{E}$ in expression (7.6), given by:

$$\delta^{k} V'(f', H_0) = \sum_{j=0}^{\infty} \frac{1}{2^{k+2j-1} j!(k+j)!} \cdot t \cdot {}^{k+2j}\alpha'_{E}(f', H_0) \cdot \delta H^{k+2j}, \tag{7.11}$$

are associated with a ME resonance peak at an arbitrary frequency $f' = f_R$. Then, in the ME measurements (with some constant applied bias H_0) this peak will be observed at $f = f_R$ in the fundamental frequency mode having an amplitude given by $\left|\delta^{1} V'(f_R)\right| = \sqrt{\delta^{1} V'(f_R)^{*} \cdot \delta^{1} V'(f_R)}$. Furthermore, for the 1st and 2nd harmonic frequency detection with $f' = 2f$ and $f' = 3f$, this peak should appear at lower frequencies, $f = f_R/2$ and $f = f_R/3$, with amplitudes $\left|\delta^{2} V'(f_R)\right|$ and $\left|\delta^{3} V'(f_R)\right|$, respectively. This last general expression thus allows us to relate the output voltage measured in any detection circuit with the magnetic bias and modulated fields, frequency and characteristic ME voltage coefficient of a particular composite.

7.2.2 Experimental Dynamic Magnetoelectric Measurement Setup

As implied in the previous Section, the basic blocks needed to perform dynamic measurements of the direct ME effect are a magnetic field source (usually one or two electromagnets), capable of producing constant and *AC* magnetic fields which are applied to the sample, and a lock-in amplifier, whose purpose is to measure the *AC* voltage generated on the sample through the ME effect. Since commercial systems are still unavailable at this point, as an example Fig. 7.1 shows schematically an experimental setup built by our group in order to measure the dynamic direct and converse ME effects [30]. Here, the samples are placed in the center of a plastic box containing a Helmholtz coil capable of generating *AC* magnetic fields with amplitudes δH of up to 100 Oe as well as constant bias fields H of up to the same value. A *DC* bias field, in the range of 0–15 kOe, can also be produced by an external electromagnet (Bruker® ESP 300E) collinear with the Helmholtz coil and directed along the X direction. This bias field is stabilized by a Hall-sensor-based regulating feedback loop. The Helmholtz coil is driven by a power amplifier (*AE Techron*®, model 7224) with a gain between 1 and 20 and low output impedance (28 mOhm in Series with 1 μH). The current flowing through the coil is stabilized by a current control loop or by taking into account the complex impedance of the whole circuit. The amplitude and frequency of the *AC* current are set either by an external function generator (SRS®, model DS345) or by the internal generator of the lock-in amplifier (Zurich Insruments®, model HF2LI). The *AC* current passing through the Helmholtz coil is continuously measured by a multimeter (Agilent®,

model 34401A). The measured current is then used to calculate the previously calibrated magnetic *AC* field amplitude δH, where a gaussmeter was used, throughout a large frequency range of up to about 600 kHz (for $\delta H = 0.1$ Oe). This current is measured directly, with the multimeter in its ammeter mode, up to a frequency of ca. 10 kHz due to accuracy limitations of the device, and indirectly, with the multimeter in its voltmeter mode, for frequencies larger than 10 kHz by making use of the known complex impedance of the Helmholtz coil or a known reference resistor. A gaussmeter (DSP®, model 475) is used to measure the exact value of the bias field produced by the external electromagnet. The amplitude and phase of the transverse voltage δV induced across the sample by the applied in-plane *AC* magnetic field δH is measured with the lock-in. Higher harmonics of the ME signal can also be measured simultaneously in this way by using multiple independent demodulators. The measuring system as a whole can be synchronized by a TTL output signal from the function generator or alternatively by the internal oscillator of the lock-in, depending on the source of the *AC* signal. The entire setup is autonomously driven by a home-made data acquisition software based on LABview®. The direct ME measurements are consequently presented as the direct ME coefficient given by equation $\alpha_E = \partial E/\partial H = \delta V/(t \cdot \delta H)$ as a function of the magnetic bias field H, with an applied constant-frequency modulation field, or as a function of the frequency f of the *AC* field, with an applied constant bias field. We also point out that, since most lock-in amplifiers have an input impedance of just about between 1 and 10 MΩ, the use of a high input impedance voltage pre-amplifier is usually required in this system, at least at low frequencies (ca. < 10 kHz), in order to achieve the open-circuit condition specified by the definition of the ME voltage coefficient (α_E). Otherwise, the circuit parameters of the sample and measuring device should be taken into account in the calculation of α_E.

Although not optimized for this purpose, we note that this system may also be used to measure the converse ME effect. This measurements are performed by applying an *AC* voltage (δV_{mod}), produced by a function generator, to the sample and using the Helmholtz coil to pick up the magnetic flux variation due to the changing magnetic permeability of the sample. The amplitude and phase of the voltage induced on the coil (δV_{ind}) as a function of either the driving frequency, at a constant *DC* magnetic bias field, or of the swept magnetic field, at a constant excitation frequency, are then detected by the lock-in. The resulting ME effect can then be represented as a ratio between the *AC* voltage detected on the Helmoltz coil and the voltage applied to the sample ($\delta V_{ind}/\delta V_{mod}$) or as the traditionally used converse ME coefficient $\alpha_B = \partial B/\partial E$, in units of G·cm/kV, after properly calibrating the pickup coil. The accessible frequency range for this type of measurements goes from several Hz up to several tens of MHz.

Figure 7.2 displays a picture of the whole setup with its components labeled. A plastic box is used to house the sample and contains the Helmholtz coil which produces the *AC* magnetic field. It consists of a $60 \times 55 \times 68$ mm^3 container built with non-conductive and non-ferromagnetic materials (mostly PVC) close to the coils in order to avoid losses at large frequencies due to eddy currents and a

Fig. 7.2 Photo of the setup used in the ME measurements. The labeled components are: *1* electromagnet; *2* box containing the Helmholtz coil; *3* sample support and goniometer; *4* PC; *5* lock-in amplifier; *6* function generator; *7* multimeter (ammeter/voltmeter); *8* power amplifier; *9* gaussmeter

concentration of the field lines away from the center of the coil. The two modulation coils are fixed on opposed interior side walls. This box can then be connected to a goniometer and used in sync with a helium flow or a nitrogen flow cryostat, thus allowing measurements from cryogenic temperatures up to about 600 K. The Helmholtz coil scheme was adopted for the modulation because of its simplicity and high uniformity of the generated field in the center of the coils with variations of less than 1 % of its central value inside a central cube with a side length of about ½ the radius of the coil. Both coils were electrically connected in parallel between themselves and into the output of the power amplifier. This type of connection minimizes the equivalent inductance of the coil circuit and thus allows one to produce higher currents with the same voltage for higher frequencies of operation. In order to magnetically calibrate the Helmholtz coil, we calculated and experimentally measured the magnetic field generated in the center of the coil using a gaussmeter, as a linear function of the *DC* driven current, as measured by the ammeter. In order to generate a constant *AC* field over a wide range of frequencies, the complex impedance of the circuit of the Helmholtz coil has to be known. This impedance was measured with the help of the lock-in amplifier. With this information we are thus able to calculate the amplitude of the voltage signal (δv) that has to be applied to the coil at any given frequency (f) in order to generate a desired current amplitude ($\delta i \propto \delta H$) through the simple relation $\delta v/\delta i = \sqrt{R^2 + (2\pi f L)^2}$. All of the aforementioned steps were integrated into the measurement program

written in LabVIEW. We note that, beside the *AC* field, the Helmholtz coil may also simultaneously be used to produce a bias field of up to 100 Oe, thus allowing direct ME measurements to be performed independently without any external electromagnet.

An important component in this kind of systems is the electrical contact and support for the samples. This support must be able to fix the samples in place while taking into account that a large enough stress applied by the support may negatively affect the sensitive ME effects under resonant conditions. The support must also ensure a good electrical contact to the sample's top and bottom electrode surfaces. The ME voltage signal produced between the electrodes must then be carried by a cable to the input of the lock-in. A very short low-noise coaxial cable or twisted pair cable are ideal in this case. These cables can also be enclosed by a conductive shield thus functioning as triaxial cables where the external conductor provides an electromagnetic shielding of the inner conductors mainly from the *AC* magnetic field. The voltage difference between the inner conductors of the signal cable can subsequently by measured by the lock-in amplifier operating in differential mode.

There are several issues that should be taken into account in the measurements of the dynamic direct ME effect. One of the most important is the generation of an electromotive force between the electrodes of the sample induced by the time changing *AC* magnetic flux due to the effect of Faraday induction [3]. This magnetically generated signal, having the same frequency as the modulation field, will thus be detected by the lock-in and can easily pass as a ME signal. From the Faraday law of induction we known that the amplitude of the induced signal is proportional to the amplitude of the modulation field (δB), the area of the "loop" formed by the electrodes and the frequency of the field. It should also be shifted by 90° with respect to the modulated field. Since the phase of an eventual ME signal obtained in the lock-in is generally measured relatively to the phase of the voltage applied to the power amplifier that drives the coil, this fact can be used to our advantage in order to obtain the phase of this ME signal relatively to the modulated field. The expression of the induced electromotive force shows that this effect in principle can be minimized by using relatively small frequencies of operation and reducing the surface area normal to the magnetic field formed between the electric wires (decreasing the amplitude of the modulation field does not help because, as we have seen in (7.8), the amplitude of the ME voltage also tends to be proportional to this value). The effective surface area between wires can be minimized by using coaxial cables or twisted pairs of thin wires or/and by carefully orienting these wires in relation to the applied time-varying magnetic field. Even so, test measurements using a non-ME reference sample with dimensions of approximately $10 \times 10 \times 0.5\ \text{mm}^3$ in our support in the frequency range of up to 600 kHz have shown linear output voltages with slopes of up to ca. 873 mV/(Oe·MHz) (see Fig. 7.3a). This value of the induced voltage was obtained for the case of the single-mode detection of the lock-in (i.e. using a simple coaxial cable). On the other hand, in the differential detection mode of the lock-in with the signal being measured between the inner conductors in a triaxial cable, the induced voltage was found to be 467 mV/(Oe·MHz). Finally, the use of the lock-in in the differential

detection mode together with a grounded outer thick conductive shield was shown to reduce the Faraday induced voltage in the support by up to ten times down to ca. 81 mV/(Oe·MHz). This is the case because of the ability of the conductive outer tube to effectively shield the interior signal-carrying conductors from the external modulated field. Nonetheless, in most bulk laminate and particulate ME composites this effect is not an issue at low frequencies (up to ca. 1 kHz) because they usually yield ME responses of the order of some tens or hundreds of mV/(cm·Oe) [1, 2, 7, 31, 32]. However, for the case of single-phase multiferroics and thin-film composites this induction can become noteworthy because of the weak nature of the ME coupling. Indeed, in the first case maximum direct ME coefficients of the order of only some mV/(cm·Oe) [32, 33] tend to be observed, while in the second even smaller signals of the order of tens or hundreds of μV/Oe [3, 33] can be detected due to the small thickness of the thin films (even though the direct coefficients can still be comparable to the ones observed in bulk composites). Also, the eventual generation of eddy currents in the wires may also take an important part in this last case [34]. For samples associated with a weak ME effect a simple method can be used to correct the data from the induction effects. Here, a preceding reference measurement is carried out with a non-ME reference sample with about the same dimensions as the ME sample (e.g. a tri-layered composite of Metglas and Teflon) and using the same parameters as in the subsequent ME measurement. The complex in-phase (X) and out-of-phase (Y) components of the parasitic signal can posteriorly be subtracted from the second ME measurement. An example of this procedure is illustrated in Fig. 7.3b.

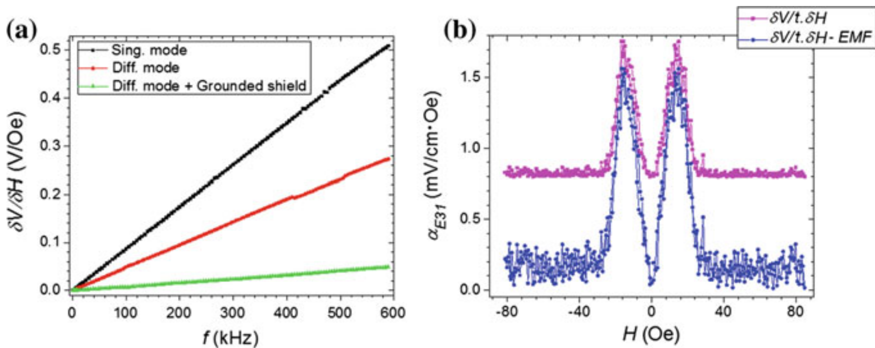

Fig. 7.3 **a** Test dynamic ME measurements performed in a reference non-ME sample while operating the lock-in in its single or differential mode whit a grounded or not grounded exterior conductive shield. The observed voltages increase linearly with the frequency of the modulated field (δH = 0.1 Oe) and are induced between the electrodes by the Faraday effect. **b** Small transversal direct ME effect (α_{E31}) measured in a bi-layered composite of Metglas/Z-cut $LiNbO_3$ (1 mm thick) with f = 10 kHz and δH = 1 Oe. The originally measured signal $\delta V/t.\delta H$ represents the amplitude of the voltage due to the ME effect superimposed on that generated by the Faraday induction (*EMF*), of about 0.81 mV/(cm·Oe), which is independent of the bias field. The second curve shows the corrected ME effect obtained by subtracting this second known component

In addition to the electromagnetic induction and intrinsic noise sources such as Johnson, shot and 1/*f* noise, various other extrinsic sources of synchronous noise may negatively influence the results of the experiment. They can be originated, e.g., by capacitive, inductive or resistive coupling between components of the system. The capacitive coupling can be reduced by the use of short cables connected to the samples and by placing such cables far away from eventual sources of stray electric fields (e.g., power amplifiers). Coaxial or twisted cables can be used to minimize the inductive coupling. An electromagnetic shield may also be used to enclose the system containing the sample and Helmholtz coil in order to shield it from stray external *DC* and time changing electric and magnetic fields. Ground loops can also give rise to a synchronous voltage and are avoided by grounding all of the instruments to the same physical point. Microphonic noise can be minimized by properly fixing the cables and sample support. In our case we also noted the existence of a 50 Hz harmonic noise from the power line, and so measurements at multiple frequencies of 50 Hz were avoided at least up to about 800 Hz, after which this effect is no longer noticeable. The value of the spectral noise density at 1 kHz was estimated as 31 $\mu V_{rms}/Oe\cdot\sqrt{Hz}$, and therefore, in order to obtain a single-to-noise ratio of 100 at 1 kHz with a bandwidth of 1 Hz, a signal of only about 0.44 mV/Oe should be required.

In order to demonstrate the capabilities of this system and the applicability of (7.6) and (7.8), in this part we now present an example of a direct ME measurement performed on a tri-layered composite. In this case, two sheets of the magnetostrictive alloy Metglas were bonded with epoxy to both surfaces of square shaped piezoelectric single crystals of $LiNbO_3$. Y- and 41°Y-cut crystals were employed here. Using the setup described above, we first measured the direct ME response of the Y-cut sample as a function of the in-plane magnetic bias field using a modulation field with an amplitude of 1 Oe and a frequency of 1 kHz. The fundamental-frequency voltage signal ($\alpha_{ME1} = \delta V/t \cdot \delta H$), as well as its 1st ($\alpha_{ME2} = \delta^2 V/t \cdot \delta H^2$) and 2nd ($\alpha_{ME3} = \delta^3 V/t \cdot \delta H^3$) harmonics, for $k = 2$ and $k = 3$, respectively, as in (7.8), were measured simultaneously relative to the applied modulated field. These correspond to the component of the generated voltage in phase with the applied modulated field (i.e. the real part of $\delta^k V'(f', H_0)$ as in (7.11)). Figure 7.4 shows the results obtained in this way. The uppermost graph depicts the real part (i.e. in-phase with the modulated field) of the direct ME coefficient (α_{E31}) in units of mV/(cm·Oe) as a function of the bias field. Here we can observe that a coefficient as large as 946 mV/(cm·Oe) was generated for a field of just about 24 Oe. In general, the shape of the ME curves tend to follow the first derivative of a typical magnetostrictive curve for the Metglas alloy (i.e. $\alpha_{ME1} \simeq \alpha_E = (1/t) \cdot \partial V/\partial H \propto q = \partial\lambda/\partial H$) since the corresponding piezoelectric curve of the PE crystal is highly linear in this range of coupled strains. The second graph, on the other hand, depicts the measured 1st harmonic (at 2 kHz) of the ME output signal in units of mV/(cm·Oe^2). In particular, this signal is shown to be relatively large even for a null bias field. The superimposed red line in this graph

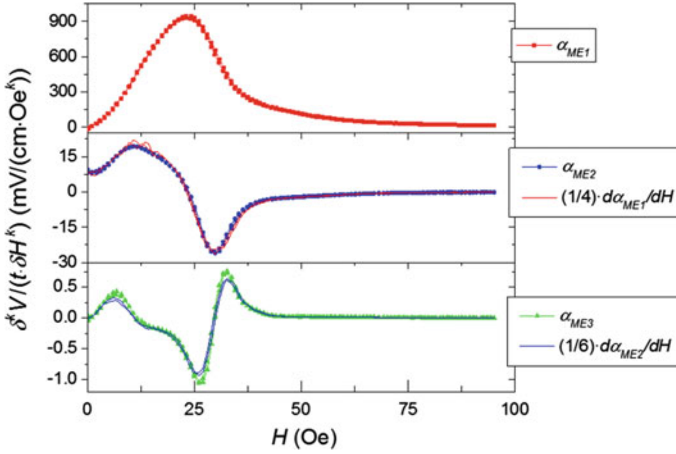

Fig. 7.4 Direct ME effect measurements of a Metglas/Y-cut $LiNbO_3$/Metglas sample as a function of the bias field at 1 kHz and with δH = 1 Oe. The uppermost graph shows the ME response detected at its fundamental frequency (α_{ME1}) equal to the frequency of the applied modulated field. The second and third graphs show the 1st (α_{ME2}) and 2nd (α_{ME3}) harmonic response functions, respectively. Superimposed on them are lines representing the numerical derivatives of the previous lower-order harmonic responses

represents 1/4 times the numerical field derivative of the fundamental response in the above graph. This derivative perfectly fits the measured data as predicted by (7.8), where we have: $\alpha_{ME2} = \delta^2 V/t \cdot \delta H^2 \simeq (1/(4 \cdot t)) \cdot \partial^2 V/\partial H^2 \simeq (1/4) \cdot \partial(\delta V/t \cdot \delta H)/\partial\, H = (1/4) \cdot \partial\alpha_{ME1}/\partial H$. The third graph shows the measured 2nd harmonic (at 3 kHz) of the ME response in units of mV/(cm·Oe^3) as a function of the bias field. Superimposed on this response is a line which represents 1/6 times the numerical derivative of the 1st harmonic response. Yet again we see that this derivative fits well the measured signal as predicted by (7.8): $\alpha_{ME3} = \delta^3 V/t \cdot \delta H^3 \simeq (1/(24 \cdot t)) \cdot \partial^3 V/\partial H^3 \simeq (1/6) \cdot \partial(\delta^2 V/t.\delta\, H^2)/\partial H = (1/6) \cdot \partial\alpha_{ME2}/\partial H$. In conclusion, in this measurement we have proven experimentally the validity of (7.8). In practice these ME curves are generally closely related to the non-linear magnetostrictive curves of the MS phase as shown by: $\alpha_{MEk} \simeq (1/2^{k-1}k!) \cdot {}^k\alpha_E \propto {}^k q = \partial^k \lambda/\partial H^k$, where ${}^k q$ are the k-th order piezomagnetic coefficients.

The aforementioned setup also allows the measurement of the ME response as a function of the frequency of the modulated field (f) for a fixed bias field. Figure 7.5 shows an example of this measurement for the case of a Metglas/41°Y-cut $LiNbO_3$/ Metglas composite. This measurement was made in the T-L mode (in-plane magnetic field and out-of-plane voltage detection), using a bias field of 25 Oe and a modulated field with an amplitude of 0.1 Oe. The fundamental response (α_{ME1}) as well as its 1st (α_{ME2}) and 2nd (α_{ME3}) harmonics were recorded. In the fundamental mode we note the existence of a single in-plane contour EM resonance mode at a

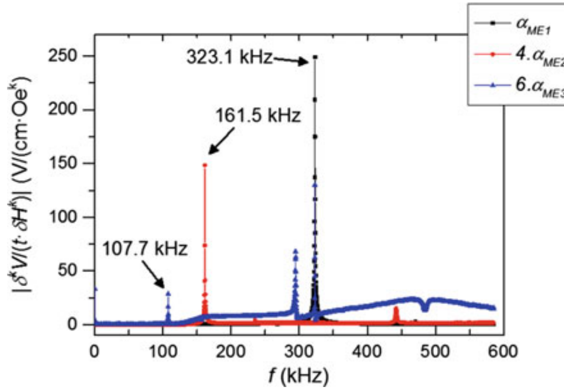

Fig. 7.5 Direct ME effect measurements of a Metglas/41°Y-cut $LiNbO_3$/Metglas sample as a function of the modulated field frequency with δH = 0.1 Oe and H = 25 Oe. Here, the fundamental frequency detection (α_{ME1}) is plotted in *black*, whereas the 1st ($4\cdot\alpha_{ME2}$) and 2nd ($6\ \alpha_{ME3}$) harmonic detections are plotted in *red* and *blue*, respectively. The single peak observed in the fundamental mode corresponds to an electromechanical resonance of the composite

frequency of ca. f_R = 323.1 kHz. At this frequency, a coefficient as large as 250 V/(cm·Oe) has therefore been measured. As predicted by (7.10), we also see that this same resonance mode is also excited by modulated fields with frequencies of 161.5 kHz ($\simeq f_R/2$) and 107.7 kHz ($\simeq f_R/3$) in the 1st and 2nd harmonic measurements, respectively, through the non-linear MS effect (i.e. $\alpha_{MEk} \propto {}^k q = \partial^k \lambda / \partial H^k$). The amplitudes of these peaks are of approximately 37.1 V/(cm·Oe^2) and 4.7 V/(cm·Oe^3), respectively. Furthermore, we can also observe the existence of another resonance peak at 323.1 kHz in the 2nd harmonic detection. This resonance peak should correspond obviously to the first harmonic mode of the fundamental contour mode observed at 323.1 kHz, since it is observed at an odd integer multiple of this frequency, and therefore should be strongly excited by a modulated field frequency of 969.3 kHz. This frequency is larger than the maximum modulated field frequency of 600 kHz which can be attained with the equipment due to technical limitations. Thus, we note that higher-harmonic detection can be useful, e.g., in the study of resonance modes of vibration at frequencies larger than the ones which can be achieved in a given Helmholtz coil. The resonance peak observed at 442.3 and 294.7 kHz in the 1st and 2nd harmonic detection, respectively, corresponds to another contour mode of resonance which in the fundamental frequency detection should be observed at ca. 884.4 kHz. In summary, three distinct contour modes of EM resonance of the composite were identified using the aforementioned technique as seen in the 2nd harmonic detection. We finally note that these non-linear resonant ME effects may be found to be very useful in future e.g. for the development of highly sensitive and low-power wideband *AC* magnetic field sensors [35, 36].

7.3 Experimental Results

7.3.1 Comparative Study of the Direct and Converse Magnetoelectric Effects in Tri-Layered Composites of Metglas with $LiNbO_3$ and PMN-PT Single Crystals

As we noted in the introduction, since the estimated magnitude of the direct ME effect is approximately proportional to the product of the magnetostrictive and piezoelectric properties of the MS and PE phases, carefully engineered composites can in principle exhibit a remarkable ME coupling, orders of magnitude larger than the ones observed in single-phase multiferroics [1, 2]. The same behavior is expected in the case of the converse ME effect. While the former can find applications in the electric detection of magnetic fields [37–39], the latter could be useful in the electrical control of magnetism [40, 41].

For laminated composites operating in the L-T mode, necessary requirements for a large voltage ME effect (α_{E3a}) include a PE phase with large transversal PE coefficients (d_{3a}), small thickness dielectric permittivity (ε_{33}^{T}) and small longitudinal and transversal compliance (s_{ab}^{E}). Although $Pb(Zr,Ti)O_3$ (PZT) ceramics do not satisfy these requirements from a general point of view, the fabrication of PZT-based ME composites is still commonplace [42, 43]. The use of single-crystalline PEs, poled and cut along desirable crystallographic directions, is another possible approach to achieve large ME effects [17, 18, 30]. Among the commercially available single crystals, lead magnesium niobate–lead titanate (PMN-PT) [44] and lead zinc niobate–lead niobate (PZN-PT) exhibit the largest known piezocoefficients and are thus frequently employed in laminate ME structures [19, 20, 39, 45–47]. Nonetheless, both of them are characterized by some notorious drawbacks which include their low Curie and depolarization temperatures (ca. 100 °C), large chemical and electrical instabilities, non-linear hysteretic behavior, uneasy growth of high-quality crystals and consequently a very high price.

Due to these factors, other single crystalline piezoelectrics are being tested at present [17, 18, 21, 22, 30, 48]. Those have included so far lead-free crystals such as barium titanate ($BaTiO_3$) [49], lithium niobate ($LiNbO_3$) [30, 50], gallium phosphate ($GaPO_4$) [51], quartz (SiO_2) [18], aluminum nitride (AlN) [17], zinc oxide (ZnO) [21], langatate ($La_3Ga_{5.5}Ta_{0.5}O_{14}$, LGT) [22, 23] and langasite ($La_3Ga_{5.5}SiO_{14}$, LGS) [23]. $LiNbO_3$ (LNO), a uniaxial PE with a very high Curie temperature ($\sim$1210 °C), in particular could be proven to be a very promising choice. Although the PE coefficients of LNO are up to three orders of magnitude smaller than those of PMN-PT and PZN-PT, its dielectric coefficients also are, and therefore a comparable ME voltage coefficient can be anticipated in composites featuring this compound. Even in the weakly PE quartz [18], the induced ME coefficient has been found to be very large (ca. 175 V/(Oe·cm)) under EM resonance conditions. Optimization of the LNO-based structures is therefore believed to yield comparable or even larger ME coefficients. Among other attractive features of

LNO, one can highlight its relatively low price, high chemical, thermal and mechanical stability, availability of large crystals of high quality and its lead-free nature [30]. Its multifunctionality could also bring new opportunities for devices based on a coupling between optical, magnetic and electric properties. LNO and a closely related PE $LiTaO_3$ have already been widely used in surface and bulk acoustic wave devices, optical modulators, waveguides, filters, transducers, acoustic microscopes, etc. [52–56]. Experimentally, magnetically tunable surface wave devices were already tested in doped LNO [57, 58]. However, as a PE layer in ME laminate structures, LNO has been considered only in a few studies [50, 59, 60]. A theoretical estimation of the ME effect in a structure of Terfenol/LNO/Terfenol was made in [59] and an experimental study, in [50]. A very significant tunability of the magnetic properties of a polycrystalline nickel film deposited over a LNO single crystal has also been shown [60].

In this section we present a study of the direct and converse ME effects in tri-layered structures of Metglas/LNO/Metglas and Metglas/PMN-PT/Metglas [30]. As the thickness of the MS layer and bonding method were not optimized, those two types of PE crystals were employed in order to perform a comparative study.

In greater experimental detail, several tri-layered ME composites of the 2-2 connectivity type were fabricated by bonding thin foils of the amorphous Metglas (Ni-Fe-Mo-B) MS alloy to opposite sides of square shaped 10 × 10 × 0.5 mm^3 PE single crystals of LNO and PMN-31 %PT poled in the [011] direction. Commercially available 29 μm thick sheets of 2826 MB type Metglas® (Hitachi Metals Europe GmbH) were cemented to opposite surfaces of LNO single-crystals (Roditi International Corporation Ltd.) and PMN-PT (H.C. Materials Corp.) using a commercial cyanoacrylate-based glue. Both PE crystals were poled by the suppliers after growth. In this study we used Y-cut and 41°Y-cut crystals of LNO. The LNO crystal has a trigonal symmetry (belonging to the point group *3 m*), and its polarization vector lies along the c-axis. The corresponding anisotropic PE, dielectric and elastic constants of the substrates can be calculated by rotating the crystallographic frame of the system, for which the coefficients can be obtained from the literature [61], with respect to their respective laminate frames [59]. The in-plane PE coefficients of the Y-cut LNO substrate were therefore calculated as d_{31} = –20.8 pC/N and d_{32} = 0, while an out-of-plane dielectric constant of ε_{r33}^{T} = 85.2 was obtained. On the other hand, the 41°Y-cut crystal has PE constants d_{31} = –16.3 pC/N and d_{32} = –17.5 pC/N and a relative permeability of ε_{r33}^{T} = 60.9. The PMN-PT crystals used were poled along their thickness direction (i.e. along [011]), so that a *mm*2 multidomain symmetry was engineered [44, 62] with effective in-plane extensional PE constants $d_{31} \approx -1750$ pC/N and $d_{32} \approx 564$ pC/N and relative dielectric out-of-plane constant of $\varepsilon_{r33}^{T} \approx 4600$ [44, 62].

In order to study the EM and ME properties of the samples, impedance spectroscopy, as well as direct and converse ME effect measurements were carried out. The impedance measurements were performed in the frequency range of 10 Hz–10 MHz. In this case a simple I-V circuit was used with a reference resistor connected in series with the piezocrystal, with gold electrodes deposited on each

surface, and the frequency of a constant voltage signal generated by and internal source of the lock-in was swept. The amplitudes and phases of the voltage developed across the reference resistor were then detected by the lock-in amplifier, and, using a simple equivalent circuit model, the active and reactive parts of the sample impedance were subsequently obtained. The whole measuring procedure was controlled by a home-made LabVIEW® based program. This technique was used mainly in order to determine the quasi-static dielectric constant of the tri-layers and observe their characteristic EM resonances.

The results of the impedance measurements are shown in Fig. 7.6 in the form of the absolute admittance, $|Y|$, as a function of the frequency. Here we can distinguish a series of characteristic EM resonance and anti-resonance peaks. The sound velocity for longitudinal waves in $LiNbO_3$ propagating along the principal axes is: for the Z direction, 7.271×10^5 cm/s; for the Y direction, 6.549×10^5 cm/s; and for the X direction, 6.580×10^5 cm/s [61, 63, 64]. Applying these values to the case of

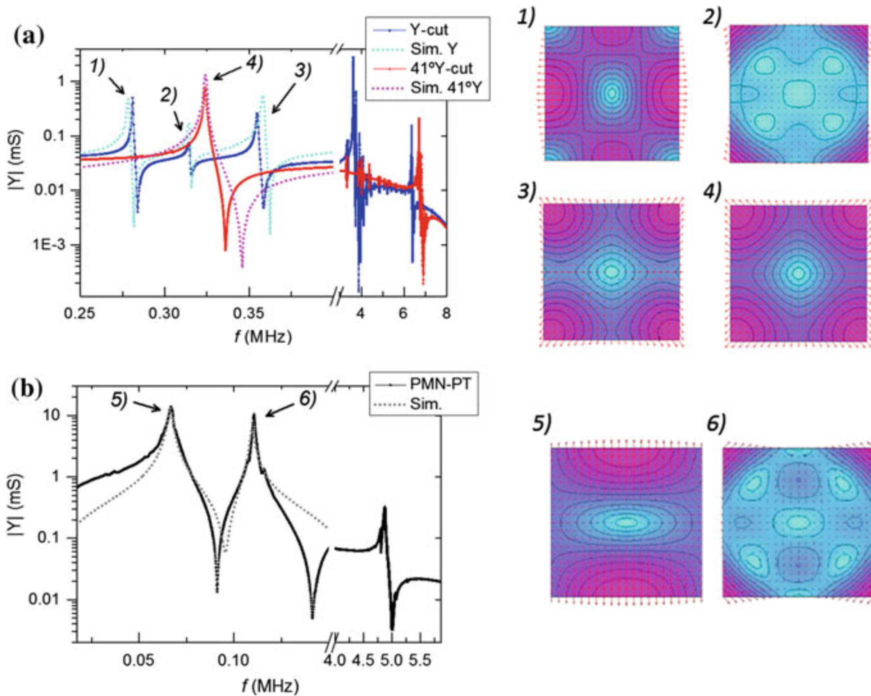

Fig. 7.6 *On the left* experimental and simulated impedance spectra of **a** LNO and **b** [011]-poled PMN-PT PE single crystals depicting its various characteristic EM resonance ($|Y| \to \infty$) and anti-resonance ($|Y| \to 0$) modes. *On the right* spatial distribution of the in-plane relative displacement fields associated with each type of observed contour EM resonance mode labeled as (1)–(6). Here, more purple regions correspond to larger relative displacement amplitudes while more cyan regions are associated with small displacements. The superimposed small *red arrows* depict the direction of such displacements [30]

a $10 \times 10 \times 0.5$ mm^3 Y-cut LNO crystal, we see that the thickness extensional mode should roughly appear at ca. 6.58 MHz. The closest observed peak is centered at a slightly lower frequency of 6.34 MHz. The calculated length extensional resonances along the X and Z directions (327.5 and 363.5 kHz, respectively) can be associated with the peaks observed at 281, 314 and 355 kHz. The remaining peak centered at 3.65 MHz should be attributed to a shear thickness mode. This mode could be mediated by the relatively large d_{34} coefficient (–69.2 pC/N). In the case of the 41°Y-cut LNO crystal, the thickness shear mode is much less intense because of a much smaller d_{34} = 3.83 pC/N [63, 64]. Also, in this case the two largest peaks observed at 323.9 kHz and 6.71 MHz must correspond to contour and thickness modes of vibration, respectively.

In order to exactly identify the in-plane contour acoustic vibrational modes of the LNO crystals observed in the impedance measurements, we implemented a simple model capable of predicting the dynamic electrical behavior of the crystals. More precisely, we numerically solved the thickness-averaged linear elastic and quasi-electrostatic equations of the crystals using a two-dimensional finite element-method (FEM). In the two-dimensional approximation [65, 66], where the thickness of the crystal is assumed to be much smaller than its length, we end up with a system of partial differential equations (PDEs) that can be solved numerically after prescribing the elastic displacements or stresses and electric potentials or electric displacements on the boundary surfaces of the media (i.e. the boundary conditions). Setting the appropriate material constants for each orientation of the crystal and assuming a grounded bottom electrode and a harmonic homogenous potential on the upper electrode ($\delta V_3 e^{j\omega t}$), as well as a null electric displacement field normal to the side surfaces and a null traction over all boundaries, the admittance at each frequency was calculated. To do this, the current flowing through a transverse section of the crystal was obtained by integrating the time derivative of the harmonic displacement field over this surface (i.e. $\delta I_3 = j\omega \int_{Area} \delta D_3 dA$).

The results of these simulations for the Y-cut and 41°Y-cut crystals are plotted in Fig. 7.6a along with the experimental data. Here we observe a good agreement between the simulated and experimental results and can perfectly identify a correspondence between the resonance and anti-resonance peaks in each type of Y-cut crystal. Therefore, we confirm the existence of three contour modes of resonance in the Y-cut crystal, situated at approximately 278, 314 and 358 kHz, and a single mode for the 41$^{\text{o}}$Y-cut crystals at ca. 324 kHz. By setting the frequency of the applied voltage in the model to a value corresponding to some characteristic resonance mode and plotting the amplitude of the spatial distribution of the in-plane displacement fields, we can analyze and identify the contour resonance modes associated with each peak. The modes thus found are labeled and represented in Fig. 7.6a which shows the absolute value of the displacements along the plane of the PE in a color scale (from blue for a null displacement to pink for large displacements) and the directions of these displacements as red arrows. Thus, the three resonance modes observed in the Y-cut crystal correspond to the three contour

acoustic modes labeled as: (1), (2) and (3). All of those are non-trivial modes because of the relatively complex geometry of the system. The mode (1) is comparable to an extensional mode of type I, as labeled by the IRE standard [67], just like the mode (3). In summary, the mode (1) is characterized by oscillatory displacements mainly along the central region of each face, while the central and vertex regions stay almost still. In mode (2) there is a periodic bending of the vertexes to the sides. The (3) mode is associated with a periodic displacement of the vertex regions of the plane along the radial direction. Since the (1) and (3) modes are associated with larger displacements over larger areas, they naturally produce larger variations of the current flowing through the crystals and consequently larger resonant peaks. The single large resonant mode observed in the 41°Y-cut crystal labeled (4), on the other hand, corresponds to a symmetric contour mode of the type III [67] where the crystal periodically expands and contracts almost isotopically in both in-plane directions and is generated due to the almost in-plane isotropic nature of the material constants in this case.

For the case of the PMN-PT based tri-layer, two low-frequency modes (67 and 111 kHz) and one high-frequency mode (4.87 MHz) are observed, as shown in Fig. 7.6b. According to [68], the sound velocity for the longitudinal mode propagating along the Z direction is 4.727 cm/s, which yields for a thickness extensional resonance a frequency of about 4.73 MHz that is close to the experimentally observed value. Using the same model as in the aforementioned case, we identified the contour resonance modes responsible for the two observed low-frequency peaks. Those are labeled (5) and (6) and are shown in Fig. 7.6b. The first of these modes therefore corresponds to a simple extensional mode, while the second exhibits a behavior similar to the one observed in the mode (2). When compared to the electrically excited contour resonant modes of the LNO crystals, the resonant admittance peaks measured in the PMN-PT crystal are shown to be one order of magnitude larger, which should be a result of a much stronger PE effect in this crystal.

Measurements of the direct ME effect were carried out at room temperature and at a frequency of 5 kHz in the quasi-static regime, i.e. far enough from any observed EM resonances. The modulation amplitude of the AC field was fixed at $\delta H = 1$ Oe, while the transversal ME voltage coefficients α_{E31} and α_{E32} (given by (7.8) for $k = 1$) were measured in two orthogonal in-plane orientations. Thus, α_{E31} was measured with the bias field H oriented along the X direction in the laminate frame, while α_{E32} was measured with H oriented along the Y direction. Figure 7.7 shows the experimental results obtained. In the general case we start by noting that the soft magnetic properties of the Metglas alloy are responsible for the appearance of the maximum ME effect in magnetic fields as low as 25 Oe. The region where the ME effect is not null corresponds to the field range where the magnetization vector of the MS phase increases by the rotation of magnetic domains and by domain wall motion. The saturation of the ferromagnetic foil occurs at $H \approx 50$ Oe, after which any further increase of the external bias field does not lead to any substantial increase of the strain in the thin foil (i.e. the magnetostriction attains its saturation value λ_S), and consequently the ME effect vanishes. Furthermore, as it was

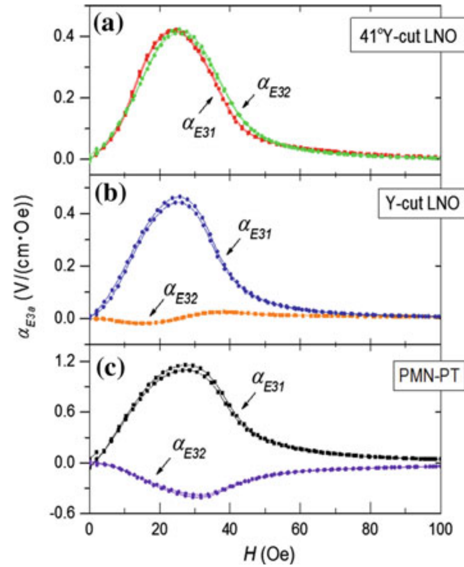

Fig. 7.7 Direct voltage ME effects measured in the tri-layered composites of Metglas/PE/Metglas with PE single-crystals of **a** 41°Y-cut LNO; **b** Y-cut LNO and **c** [011]-poled PMN-PT (with $f = 5$ kHz and $\delta H = 1$ Oe) [30]

expected, we see that the samples demonstrate an anisotropy of their in-plane ME properties due to the anisotropy of the PE properties. The sample containing the Y-cut LNO crystal exhibits a difference between α_{E31} and α_{E32} of more than an order of magnitude. The respective measured values were α_{E31} = 0.46 V/(cm·Oe) and α_{E32} = 0.024 V/(cm·Oe). In this crystal we have d_{31} = –20.8 pC/N and d_{32} = 0 and, consequently, the small observed α_{E32} coefficient is exclusively generated by the transversal Poisson stress of the magnetostriction acting on the d_{31} component. In the latter case, the magnitude of the ME induced voltage was comparable to the parasitic electromagnetic induction voltage, so that the corresponding correction has been applied. On the other hand, in the 41°Y-cut LNO crystal sample an almost isotropic in-plane behavior has been observed with $\alpha_{E31} \approx \alpha_{E32} \approx 0.42$ V/(cm·Oe), which is due to almost equivalent values of the d_{31} and d_{32} piezocoefficients (–16.3 pC/N and –17.5 pC/N, respectively). For the case of the PMN-PT composite, the d_{31} piezoconstant is twice as large as d_{32} and has a different sign. As a result, the maximum of α_{E31} corresponds to 1.15 V/(cm·Oe), while the maximal amplitude of α_{E32} equals –0.41 V/(cm·Oe). Following the procedure described in [59] and using the Metglas and PMN-PT material parameters measured by the suppliers and by independent sources [44, 62], we calculated the maximum expected quasi-static values of α_{E31} and α_{E32} for our specific sample to be α_{E31} = 23.2 V/(cm·Oe) and α_{E32} = –7.2 V/(cm·Oe). These values are more than one order of magnitude larger than the experimental ones. This may be mainly due to a weak coupling between interfaces, where the intermediate glue layers absorb part of the tensile stress being transferred from the MS to the PE phase, and a non-optimized PE/MS thickness ratio between phases, where composites with much thicker MS phases are expected to generate considerably larger effects due to a minimal compressive stress

produced by the thin PE substrate on the MS phases [69]. Nevertheless, as both of these factors should result in an identical reduction of the ME effect in the PMN-PT and LNO based composites, further discussion shall be more focused on the relation between the measured coefficients rather their absolute values.

A very important point can be drawn from the quasi-static direct ME measurements. The maximum amplitudes of the observed ME voltage coefficients for the LNO tri-layers are only about three times lower than those for the PMN-PT composite. The maximal ME voltage coefficient for the PMN-PT tri-layer is 1.16 V/(cm·Oe), while for the LNO tri-layers employing Y-cut and 41°Y-cut crystals it is 0.47 and 0.42 V/(cm·Oe), respectively. Comparable magnitudes are mainly explained by the fact that the dielectric constant of PMN-PT is more than 60 times larger than that of LNO. Consequently, the same amount of charge generated by piezoelectricity gives rise to a 60 times lower voltage in PMN-PT. Therefore, the huge piezoelectric coefficients of PMN-PT are effectively nullified by its also huge dielectric coefficients in terms of the open-circuit ME effect.

As we have seen, the magnitude of the direct ME voltage coefficient can be comparable in LNO- and PMN-PT-based composites because this response is approximately proportional to the ratio between the PE coefficients and dielectric constants. However, this concurrent influence on the composite's performance is no longer favorable for the case of the converse ME effect because this effect is independent of the dielectric constants [70–73]. Thus, in this regime, the huge difference in piezoelectric coefficients between PMN-PT and LNO becomes crucial, and the PMN-PT composites should exhibit much stronger converse ME responses. To show this, we performed converse ME measurements on the three composites. Figure 7.8 shows the converse magnetoelectric response represented as the ratio between the electromotive force induced on the sensing Helmholtz coil, δV_{ind}, and the voltage applied to the tri-layered composite, $\delta V_{mod} = 10$ V. This effect is associated with a change in the effective permeability of Metglas when under a stress, which is transferred from the PE substrate. As expected, the dependences of the converse ME effect as a function of the external magnetic bias field are shown to be qualitatively similar to those observed in the direct ME effect measurements, diverging between the different composites only in terms of amplitude. In fact, the composite with the 41°Y-cut LNO exhibits a two orders of magnitude lower response than the one with PMN-PT. Beyond any doubt, the large difference between PE coefficients becomes crucial in this mode. In conclusion, even though the direct ME voltage response is comparable in both composites, the benefits of using PMN-PT crystal for the converse ME effect as well as the direct short-circuit ME charge response in such laminate structures remains indisputable.

Returning to the direct ME effect measurements, the benefits of PMN-PT already do not look so convincing. The three times greater ME voltage coefficient hardly seems to justify an order of magnitude higher price and lower Curie temperature of the PMN-PT crystal. When measured as a function of the *AC* magnetic field frequency, f, the EM resonance modes observed in the impedance measurements can also be detected in the direct ME effect. These measurements were performed in the range of 20 Hz–600 kHz (with a fixed bias field $H = 25 - 30$ Oe and an *AC* field

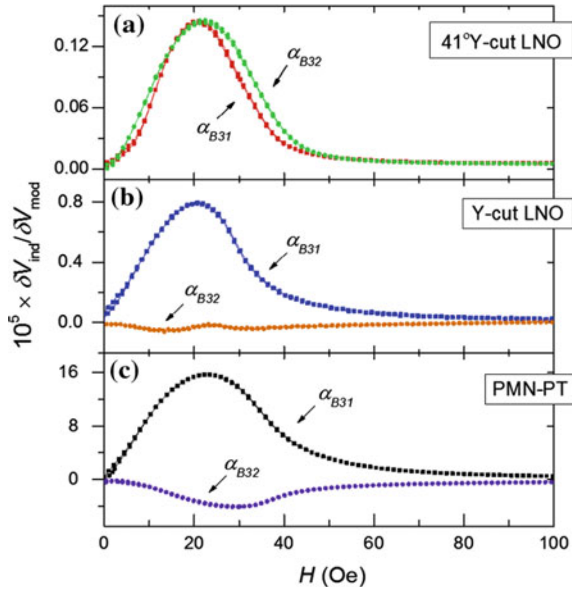

Fig. 7.8 Converse ME effects measured (given by the ratio between the voltage induced in the sensing coil, δV_{ind}, and the voltage applied to the composites, δV_{mod} = 10 V) in the tri-layered composites of Metglas/PE/Metglas with PE single-crystals of **a** 41°Y-cut LNO; **b** Y-cut LNO and **c** [011]-poled PMN-PT [30]

amplitude δH = 0.5 Oe). The results depicted in Fig. 7.9 show the characteristic large increase in the direct response of the composites under such resonance conditions (more precisely the impedance anti-resonance conditions). Surprisingly, the system with the 41°Y-cut LNO crystal yielded the largest effect of ca. 88 V/(cm·Oe) at the largely symmetric resonant mode (4) shown in Fig. 7.6, while in the PMN-PT system the maximum was only of 66 V/(cm·Oe). We also note that the EM resonance is situated in a very suitable frequency range. From the point of view of possible sensor applications, a full implementation could be done using standard low-cost electronic components.

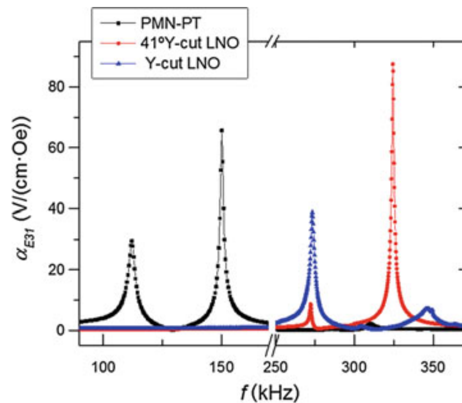

Fig. 7.9 Direct transversal ME effects (α_{E31}) measured in the tri-layered Metglas/PE/Metglas composites as a function of the modulated field frequency f with H = 25 Oe and δH = 0.5 Oe [30]

In summary, in this part we presented a study of the ME and EM properties of 2-2 type Metglass/$LiNbO_3$/Metglas and Metglas/PMN-PT/Metglas tri-layers using single-crystalline substrates with different cuts. Due to the simplified preparation method, the amplitude of the observed ME effect was rather modest. In qualitative terms, although the highly piezoelectric PMN-PT-based composite has exhibited an orders of magnitude stronger converse ME effect, the measurements of the direct ME effect have shown comparable magnitudes for both types of systems, mainly due to the much higher dielectric constant of PMN-PT. At EM resonance, the largest direct ME voltage coefficient of about 88 V/(cm·Oe) has been obtained for the 41°Y-cut LNO composite, while the second largest coefficient of 66 V/(cm·Oe) was observed for the PMN-PT-based structure. Therefore, in this study we identified crystalline LNO as a valuable alternative to lead-based PEs in ME applications with the potential to form its own field of ME-based low-cost high-temperature magnetic-field sensors.

7.3.2 Comparison of the Anisotropic Magnetoelectric Effects in Tri-Layered Composites of Metglas with LiNbO3 and GaPO4 Single Crystals

In the previous section we showed how the use of highly anisotropic single crystalline LNO in ME tri-layered composites can yield very remarkable quasi-static and resonant ME effects. Besides LNO, a noteworthy piezocrystal for ME applications is gallium orthophosphate ($GaPO_4$, GPO) a commercially available piezoelectric crystal with a trigonal structure (point group 32) and excellent high-temperature properties [74]. As a crystal homeotypic to quartz, it possesses many properties similar to the latter. Characteristic of this material are its larger piezoelectric coefficients when compared to quartz (ca. 1.2 times larger e_{11} and 2.5 times larger e_{14}) [74]. Other desirable properties of the compound are its high thermal stability, with its piezoelectric coefficients and most of its properties barely changing up to a cristobalite transition at 933 °C, large ratio between PE and dielectric constants (d_{3a}/ε_{33}), the absence of ferroelectricity and pyroelectricity, a higher EM coupling as compared to quartz, and a high purity of the as-grown crystals [74, 75]. In the present part, we report a study of the anisotropic direct ME properties of enhanced bulk tri-layered composites of Metglas/LNO/Metglas and Metglas/GPO/Metglas, making use of differently oriented crystalline PEs and under quasi-static and EM resonance conditions [76]. The maximum expected quasi-static ME coefficients in each case were numerically estimated as a function of the crystal orientation and compared with the experimental results. The physical origin of the in-plane directional ME response was therefore uncovered.

In order to numerically investigate the nature of the anisotropic ME coupling in tri-layered composites of amorphous Metglas and piezocrystals of LNO and GPO, the maximum direct transversal ME voltage coefficients, $\alpha_{E3a} = \partial E_3/\partial H_a$, were

numerically estimated for a series of such structures. A standard averaging linear quasi-static micromechanical method based on coupled constitutive equations for each layer was used for this purpose [59, 69]. Here, a square shaped 10 × 10 mm^2 ME tri-layered structure composed of two 29 μm thick foils of Metglas and one central 0.5 mm thick piezoelectric crystal, operating in the L-T mode, like the one shown in Fig. 7.1, was considered. Its constitutive elastostatic, electrostatic and magnetostatic equations were then solved assuming averaged homogeneous tensor fields in each perfectly elastically coupled layer ($k_C = 1$) and under unclamped and open circuit boundary conditions. The required linear anisotropic electric, magnetic and elastic material constants were obtained from the literature (Metglas [77–79], LNO [61], and α-GPO [74, 75]). We note at this point that a pseudo-piezomagnetic approximation was assumed for the MS layer which is valid in the small region of the magnetostriction curve where the elastic strain (S_i) changes linearly with the applied bias field (H_k), and the slope $\partial S_i/\partial H_k$ is maximized so that $S_i = q_{ki}H_k$ where q_{ki} describes the piezomagnetic coefficient. In the case of a traction-free Metglas layer the $\partial S_i/\partial H_k$ slope takes a maximum value of ca. 4 ppm/Oe for a bias field of ca. 10 Oe, which was therefore used as our q_{11} coefficient [80].

Since the material properties of single crystals are highly anisotropic, the optimization of the piezocrystal orientation (crystal-cut) can in principle lead to significantly enhanced ME coefficients in composites. To investigate the dependence of the maximum ME coupling coefficient with the crystal orientation, the material tensors were transformed from the crystalline frame to the frame of the laminate using the classic Euler angles $Z_1X_2Z_3$ corresponding to a sequence of three rotations each denoted by the angles α, β and γ [59, 62, 81]. The results obtained in this way are shown in Fig. 7.10 as representation surfaces of $|\alpha_{E3a}|$ maximized in the range of all γ angles between 0° and 180° and as a function of the α and β angles for the

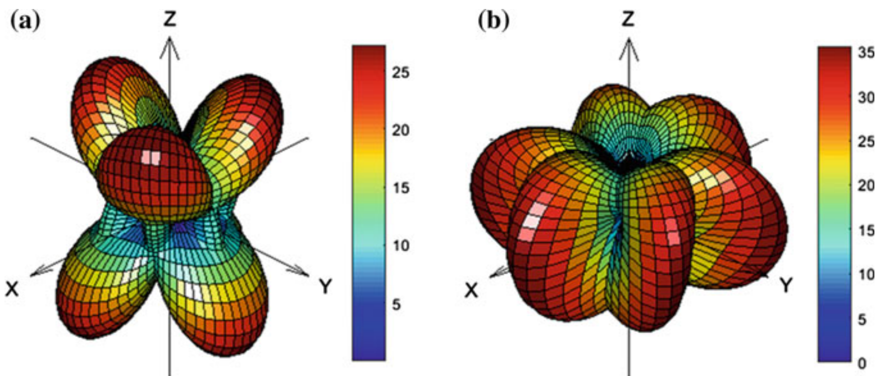

Fig. 7.10 Representation surfaces depicting the maximum estimated absolute values of the transversal ME voltage coefficient $|\alpha_{E3a}|$ (across $0 < \gamma < 180°$) as a function of the crystal orientation (normal to the plane of the laminate associated with the rotation angles α and β) for the tri-layered ME composites of Metglas/Piezocrystal/Metglas, whit piezocrystals of: **a** $LiNbO_3$; and **b** α-$GaPO_4$

composites containing LNO and GPO. A very large variation of the magnitude of the transversal ME effect with the orientation of the piezocrystal, whose symmetry coincides with the symmetry of the corresponding crystal's point group, can be observed. As strong ME effects are particularly important in applications requiring high efficiencies and sensitivities, we conclude that the selection of a crystal with an appropriate cut is a very important step in the development of ME sensors. For the case of the LNO crystal, we see that the calculated ME coefficient could potentially be as large as 27.24 V/(cm·Oe) for a crystal with a (*ZXl*) 39°-cut (α = 0°, β = 39° and γ = 90°) and five other cuts equivalent by symmetry. In commercially available crystals this orientation is commonly denoted as 129°Y-cut. An even larger maximum coefficient of 35.62 V/(cm·Oe) was predicted for the GPO crystal with a (*XYt*) 12°-cut (α = 90°, β = 90° and γ = 12°) and five other equivalent orientations. This cut is very close to the commonly available X-cut crystals (α = 90°, β = 90° and γ = 0°).

For comparison we also used the model described above in order to calculate the transversal ME coefficients for the particular case of the piezocrystals employed in the experimental part. Those consisted of Y-cut (α = 0°, β = –90° and γ = 0°) and 41°Y-cut (α = 0°, β = –49° and γ = 0°) LNO as well as X-cut (α = 90°, β = 90° and γ = 0°) GPO. The results thus obtained indicate, for the 41°Y-cut crystal, maximum values of α_{E31} and α_{E32} in-phase and with approximately the same magnitude (α_{E31} = 11.2 V/(cm·Oe) and α_{E32} = 11.9 V/(cm·Oe)), which is due to almost equivalent d_{31} and d_{32} PE coefficients (–16.5 pC/N and –17.5 pC/N, respectively). In the composite containing the Y-cut crystal, on the other hand, there should be a very large anisotropy in its transversal ME effect (α_{E31} = 11.6 V/(cm·Oe) and α_{E32} = −1.3 V/(cm·Oe)). This is the case because the transversal piezoelectric coefficients are very different: d_{31} = –20.8 pC/N and d_{32} = 0. Consequently, the small α_{E32} coefficient is generated only by the traction component perpendicular to the magnetic field, which originates from the Poisson effect, acting on the d_{31} PE component. In the system with X-cut GPO a behavior similar to the aforementioned one was also predicted (α_{E31} = 34.0 V/(cm·Oe) and α_{E32} = –3.8 V/(cm·Oe)), since the PE constants are similarly given by d_{31} = –4.37 pC/N and d_{32} = 0.

Subsequently, to experimentally investigate the direct ME effect we prepared tri-layered structure containing two 29 μm layers of 2826 MB Metglas (Hitachi Metals Europe GmbH) bonded on both faces of 10 × 10 × 0.5 mm^3 square-shaped commercial PE single crystals of congruent LNO and GPO (Roditi International Corporation Ltd.) cut along desirable crystallographic directions. These consisted of substrates of Y-cut, 41°Y-cut LNO and X-cut GPO (Roditi International Corporation Ltd.) bounded to Metglas using a commercial epoxy resin which was cured for 24 h. This type of adhesive is commonly used in the preparation of ME layered composites [1–5, 7, 12, 31, 33, 82] and is well known for its good mechanical, thermal and chemical properties. Their anisotropic ME and EM properties were subsequently studied.

Using the setup described in Sect. 2.2, we measured the direct ME effect in the quasi-static regime in each of the three composites. The tri-layered structures were subjected to a fixed *AC* magnetic field with amplitude δH = 1 Oe and a frequency of

1 kHz. The magnetic bias field H was then applied in the X and Y directions in relation to the samples and swept in such a way so as to measure the hysteretic in-plane α_{E31} and α_{E32} ME coefficients (i.e., with the field increasing from zero up to its maximum value followed by a decrease down to a minimum value and an increase back to zero). The results of these measurements are plotted in Fig. 7.11. As in the previous comparative study, we see that the maxima of the ME effects are attained at magnetic fields as low as 25 Oe, which is due to the soft magnetic properties of Metglas. We also note an almost complete absence of a hysteretic response, which confirms the linear nature of the piezoelectric properties of both LNO and GPO. An imperative observation is that, as expected, all of the samples exhibit a significant anisotropy of their in-plane ME properties ($\alpha_{E31} \neq \alpha_{E32}$). Such noticeable differences are mostly related to the anisotropic nature of the material constants of the piezocrystals, mainly their piezoelectric d_{3a} coefficients. In the case of the tri-layered composite with the 41°Y-cut LNO crystal, maximum effects of α_{E31} = 0.83 V/(cm·Oe) and α_{E32} = 0.92 V/(cm·Oe) were obtained. This response corresponds to an almost isotropic in-plane ME behavior with $\alpha_{E32} \approx \alpha_{E31}$ in agreement with the predictions made in the preliminary calculations. This behavior

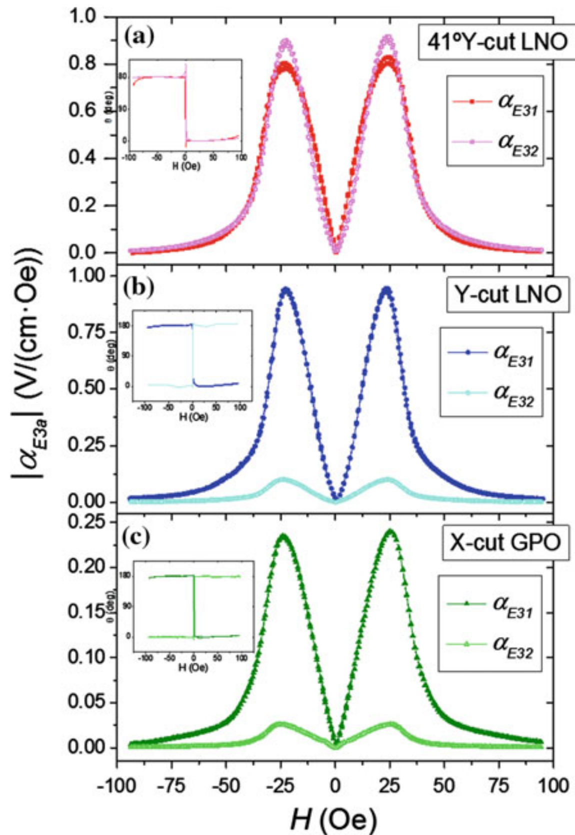

Fig. 7.11 Direct quasi-static transversal ME effect measurements ($|\alpha_{E31}|$ and $|\alpha_{E32}|$) of the tri-layered composites of Metglas and a 41°Y-cut LNO, **b** Y-cut LNO, or **c** X-cut GPO, with f = 1 kHz and δH = 1 Oe [76]. The insets depict the phase (in degrees) corresponding to each ME coefficient

contrasts with the structure containing the Y-cut LNO crystal which exhibits a difference between maximum absolute values of α_{E31} and α_{E32} by almost an order of magnitude. This is the case because the d_{32} PE coefficient happens to be null in this orientation. The obtained values here were α_{E31} = 0.95 V/(cm·Oe) and α_{E32} = –0.10 V/(cm·Oe). We also note that both maximum coefficients have a different sign. The positive value defines an in-phase dependence between the applied *AC* magnetic field and the induced *AC* voltage and the negative value indicates an out-of-phase relation between these fields. Finally, we see that the sample with the X-cut GPO piezocrystal equivalently yields an almost anisotropic unipolar response with maximum ME coefficients of α_{E31} = 0.24 V/(cm·Oe) and α_{E32} = –0.03 V/(cm·Oe), as was already predicted by our calculations.

Considering again the preliminary calculations, we conclude that all of the experimental results are in a good qualitative agreement with the theoretically estimated effects. However, in quantitative terms, the obtained coefficients were still one order of magnitude smaller than the maximum calculated ones. The main reasons for this should be attributed to a far from optimal thickness ratio between the PE and MS phases and elastic coupling between phases. Additionally, because the magnetostrictive response of the MS alloy is highly non-linear, its pseudo-piezomagnetic q_{ki} coefficients change abruptly with the bias field and stress tensor. In fact, a more sophisticated model for the MS phase [83] shows that the large compressive pre-stress produced by the thick PE in the direction of the applied bias field tends to decrease the maximum value of q_{ki} and increase the bias field at which it is attained. Also, our calculations predicted a three times larger effect in the system with GPO in relation to the one with Y-cut LNO. Since all samples were prepared in the same manner, this seems to be in disagreement with the experiment. A likely explanation is the existence of a large discrepancy between piezoelectric and dielectric coefficients of GPO as the ones found in the literature due to variations in the growth and poling techniques [74, 75, 84]. It may also be related to limitations of the model which, e.g., does not take into account possible stress relaxation occurring along the thickness of the piezoelectric layer nor the properties of the interfaces between the piezoelectric crystals and the layers of epoxy with a finite thickness.

To investigate the dynamic properties of the composites we again started by performing impedance measurements of the PE crystals alone. Figure 7.12 shows the results thus obtained in the form of a) the absolute impedance $|Z|$.as a function of the frequency and (b) the corresponding Nyquist plots of the impedance ($-Z''$ *vs* Z', where Z' is the real and Z'' the imaginary parts of Z, respectively). These figures clearly illustrate a multitude of EM resonances (where $|Z|$ attains a minimum value) and anti-resonances (where $|Z|$ attains a maximum value) in the frequency range between 150 and 390 kHz. The amplitude and frequency of the anti-resonance modes is particularly interesting because, as we shall see later, these modes are strongly linked with the resonant peaks observed in the dynamic ME measurements. Of notice is the fact that the X-cut GPO crystal was shown to produce four different resonant modes which are nonetheless much weaker than those found in the LNO substrates and appear at smaller frequencies, due to ca. 3 times larger compliance coefficients in the former [61, 74, 75].

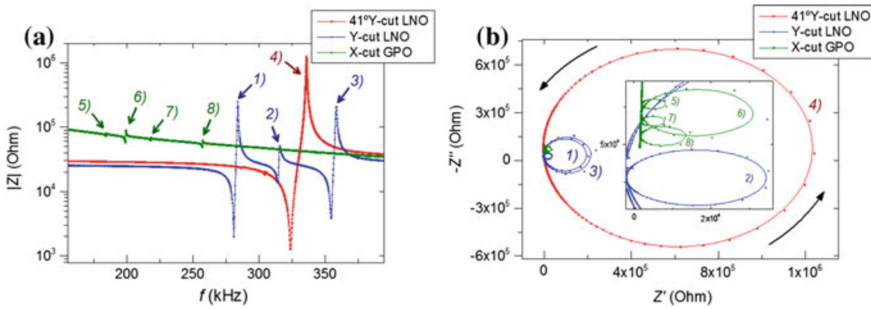

Fig. 7.12 Impedance spectra of the 41°Y-cut LNO, Y-cut LNO and X-cut GPO single-crystals showing its characteristic EM resonance ($|Z| \rightarrow 0$) and anti-resonance ($|Z| \rightarrow \infty$) modes labeled as (1)–(8) and depicted as: **a** the absolute value of the impedance $|Z|$ *versus* f and; **b** Nyquist plots of the impedance ($-Z''$ *vs.* Z'). In the last case, the *arrows* indicate the direction of the increasing frequency and the *inset* shows in detail the small loops associated with the weak resonance modes of the Y-cut LNO and X-cut GPO crystals

Another important observation is that the difference between the anti-resonant and resonant frequencies of the 41°Y-cut LNO is much larger than in the other crystals which indicate an enhanced effective EM coupling factor (k_{eff}) and consequently a more efficient conversion of energy [85]. The Nyquist plots show us how the real and imaginary parts of the impedance of the PEs change with the frequency close to a certain resonance mode. Thus we see that, as the frequency increases, the imaginary part of Z starts to increase up to a maximum value where the resonance frequency is ca. attained. After this, the imaginary part starts to drop to zero while the real part of Z starts to increase from a very low positive value up to a maximum close to the anti-resonance frequency. After this frequency, the real part returns to its initial positive value while the imaginary part decreases down to a negative minimum and subsequently returns to its initial value. Each of these resonance modes therefore form a closed loop in the Nyquist plot. More intense resonances in general thus give rise to wider loops and larger resonance peaks. To identify each acoustic resonant mode we again implemented in Matlab® a two-dimensional finite element-method in order to simulate the results [65, 66]. These calculations clearly proved that the resonant peaks observed correspond to different types of in-plane contour resonance modes. The obtained modes are thus labeled in Fig. 7.12 as (1)–(8) and depicted in Fig. 7.13c. To summarize this part, the frequency and $|Z|$ amplitude associated with each anti-resonant mode is listed next: (1) f = 284.0 kHz; $|Z|$ = 246 kOhm; (2) f = 315.8 kHz; $|Z|$ = 51 kOhm; (3) f = 358.6 kHz; $|Z|$ = 205 kOhm; (4) f = 336.1 kHz; $|Z|$ = 1.25 MOhm; (5) f = 184.8 kHz; $|Z|$ = 80 kOhm; (6) f = 199.3 kHz; $|Z|$ = 90 kOhm; (7) f = 218.4 kHz; $|Z|$ = 69 kOhm; (8) f = 257.5 kHz; $|Z|$ = 63 kOhm.

The dynamic ME effects (α_{E31} and α_{E32} components) were subsequently measured for the three composites as a function of the frequency of the *AC* magnetic field. The measurements were performed in the range from 20 Hz–600 kHz, with a fixed bias field of H = 25 Oe and a modulation field amplitude of δH = 0.1 Oe. The

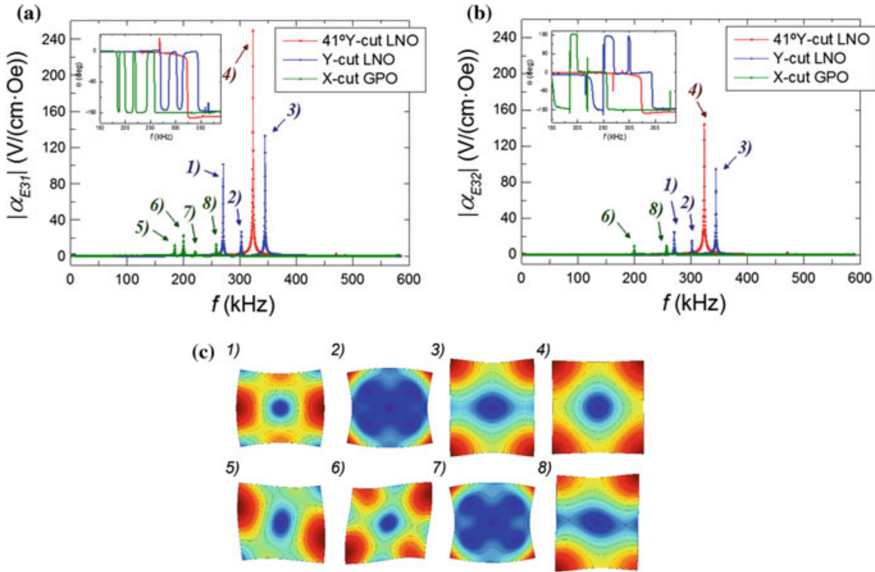

Fig. 7.13 **a** α_{E31} and **b** α_{E32} direct dynamic ME effect measured in tri-layered composites consisting of Metglas and LNO and GPO as a function of the modulation frequency with $H = 25$ Oe and $\delta H = 0.1$ Oe [76]. The various resonant peaks seen here are labeled (1)–(8). The *insets* in each graph shows the variation of the phase of the ME voltage coefficients (in degrees) as a function of the frequency. **c** Spatial distribution of the in-plane relative displacement field and deformation associated with each type of contour EM resonance mode. Here, redder regions correspond to larger relative displacement amplitudes. The deformation of the crystals are largely exaggerated for the sake of clarity

obtained results are depicted in Fig. 7.13a, b. Here, we can again identify the existence of multiple high-amplitude peaks in the ME response of the samples. By taking into account the sound velocity for the propagation of longitudinal waves in these crystals, of the order of 6.5×10^5 cm/s [61], and their dimensions we conclude that the observed peaks in the kHz range can be attributed to different types of in-plane contour acoustic modes.

With a bias field applied in the X direction (α_{E31} mode), for the case of the composite with the 41°Y-cut LNO crystal a single and very intense ME peak of up to 249.0 V/(cm·Oe) was observed at a frequency of 323.1 kHz. For the sample with the Y-cut LNO crystal, on the other hand, three different smaller peaks were observed in this range. This clearly illustrates how the anisotropic nature of the material constants takes an important part in the determination of which kinds of EM modes may or may not be excited under certain conditions. Consequently we conclude that the anisotropic nature of the PE crystals is even more noticeable in the resonant regime in relation to the quasi-static. In the structure with the Y-cut LNO crystal, the largest peak occurs at approximately 344.3 kHz and takes the value of 132.9 V/(cm·Oe). The other two peaks appear at 270.1 and 302.3 kHz and reach heights of 101.1 and 26.8 V/(cm·Oe), respectively. In the GPO sample we

observed four different resonance modes associated with comparatively smaller ME coefficients. The largest resonant effect here is of 23.2 V/(cm·Oe), occurring at 199.7 kHz. The other three peaks take values of 12.0, 5.0 and 13.0 V/(cm·Oe) and are excited at frequencies of 184.3, 220.5 and 257.9 kHz, respectively. Furthermore we note that all of the aforementioned peaks are associated with a characteristic sudden decrease in phase by ca. 180° as it can been seen in the inset of Fig. 7.13a. In this case the ME resonance peaks are all followed by a change of phase from 0° down to –180° and therefore the imaginary part of the ME coefficients have peaks with negative values in resonance. A comparison with the impedance of the crystals in Fig. 7.12 demonstrates that the same number of resonant modes can be identified in both experiments and that the frequencies and amplitudes of the resonant ME effects in the composites are closely related to the frequencies and amplitudes of the anti-resonant EM modes in the PEs. Thus we conclude that they must correspond to the same type of resonance patterns. This is the case because, as the impedance of the PE crystals is maximized in the anti-resonant mode, its capacitance and longitudinal effective dielectric constant (ε) is consequently minimized which results in a large enhancement of the direct voltage ME effect (increase in the d/ε ratio) [86].

Having obtained a good agreement between the simulated and experimental values of the anti-resonance frequencies, with relative errors inferior to 4 %, the spatial distribution of the relative displacement fields for each mode can then be plotted as shown in Fig. 7.13c. Thus, we see that the three resonance modes observed in the Y-cut LNO crystal correspond to the three contour acoustic modes (where the in-plane components of the displacement fields do not change significantly in the Z direction and the out-of-plane displacement u_3 is null) dubbed as (1), (2) and (3). We can identify mode (1) as an extensional mode closely related to type I, as labeled by the IRE standard [67], and mode (3) as an extensional mode of type I. In the 41°Y-cut LNO crystal, the observed single resonance (4) corresponds to an extensional mode of type III which is a very symmetric almost isotropic mode. This seems to suggest that remarkably strong resonance modes can be excited in PE crystals, whose geometric symmetry coincides in some way with the symmetry of its anisotropic material constants. This is the case for the 41°Y-cut square-shaped crystal, which is associated with almost equal in-plane d_{31} and d_{32} PE coefficients as well as c_{11}^E and c_{22}^E elastic stiffness constants. By comparison with the properties of some bulk tri-layered composites found in the literature with equivalent structures but employing different compounds, we conclude that the 249 V/(cm·Oe) coefficient observed in the 41°Y-cut LNO sample is one of the largest ever found in ME 2-2 bulk tri-layered structures, being even larger than the 175 V/(cm·Oe) value measured in a Permendur/Quartz/Permendur system [18]. It is also remarkably larger than those found in lead-based PMN-PT (70 V/(cm·Oe)) and PZT (110 V/(cm·Oe)) composites with Permendur [22]. In the X-cut GPO piezocrystal, the first two modes at 184.3 and 199.7 kHz and the fourth one at 257.9 kHz were identified as different kinds of contour shear modes. The first two modes, (5) and (6), and the (8) respectively resemble variations of the modes (1) and (3) in the Y-cut crystal with the addition of an in-plane shear component. The third smallest mode at

220.5 kHz, labeled (7), is characterized by an oscillatory displacement of the vertexes of the crystal in a way similar to mode (2) in the Y-cut LNO piezocrystal.

When a bias field of $H = 25$ Oe was applied in the Y direction instead of X (α_{E32} mode) we obtained the results indicated in Fig. 7.13b. The observed peaks are in general associated with a drop in amplitude in relation to α_{E31} which proves that the ME effects under resonance conditions are also strongly affected by the direction of the applied bias field. The most noticeable change here is the large decrease in amplitude or even disappearance of some of the resonant modes observed in the previous measurement. This is the case of the modes labelled as (5), (7) and (1). In order to explain this we note that these modes are mainly characterized by large elastic displacements in the X direction of the crystals as shown in Fig. 7.13c. Since the Metglas layer tends to expand mainly in the direction of the applied bias field we thus conclude that a magnetic field applied in the Y direction will induce only a small straining of this layer in the X direction. This will thus constrain the capacity of the thin Metglas foil to excite the corresponding EM modes of the PE phases. Additionally we note that the modes labelled as (3), (6) and (8), which are characterized by large displacements in the Y direction tend to be less affected by the change in the direction of the applied bias. Nevertheless the reason for the decrease observed in the amplitude of the mode (4) is not very clear. Furthermore we see that the phase of all of the ME signals still drops by ca. 180° during resonance but now we notice that outside of resonance conditions the phase of the ME effects for the GPO and Y-cut LNO samples is reversed just like in the quasi-static case. Therefore the imaginary part of the ME coefficients will have peaks with positive values in resonance. This kind of behavior has also been observed e.g. in [87].

From a theoretical point of view, considering only the linear elastic properties of the PE crystals and solving their eigenvalue equations of motion under traction-free boundary conditions, several resonance modes in addition to the ones observed in the measurements can be predicted. We therefore conclude that the pattern and natural frequency of these normal modes are mainly determined by the elastic coefficients of the crystals as well as their mass density and geometry. The excitation or not of some of these modes in the ME measurements, under specific mechanical and electrical boundary conditions, is then driven by the PE effect and thus depends on its anisotropic coefficients. While strong ME effects were observed for the extensional EM resonance modes in the samples with LNO, much weaker effects were seen for the asymmetrical shear modes in the one with GPO. These shear modes arise primarily because of non-null stiffness coefficients c_{16}^{E} in the X-cut crystal which couple in-plane normal and shear type stresses and strains. Having seen this, we note that extensional normal modes, similar to the ones identified in the LNO crystals, as well as more symmetrical shear modes can also be solutions of the equations of motion in crystals of GPO e.g. with a Z- or Y-cut, since here we have $c_{16}^{E} = c_{26}^{E} = 0$. Nevertheless, the form of its corresponding PE tensors in principle doesn't permit the ME excitation of the extensional modes in L-T tri-layered composites, since in these cases we have both null d_{31} and d_{32} components. In conclusion, we see that even though a large ME effect may be predicted for a given

anisotropic composite under quasi-static conditions, under resonant conditions the picture changes radically. Thus, in this case, a more sophisticated investigation must be carried out taking into account further parameters such as the relation between the crystal orientation and the geometry of the composite.

In summary, in this experimental part we investigated the relation between the cut orientation of the piezocrystals and respective in-plane anisotropic ME response of the corresponding tri-layered composites. By precisely selecting this cut direction, systems with different relations between perpendicular α_{E31} and α_{E32} ME coefficients could be designed, thus finding applications in specific orientation-sensitive devices. A composite with a Y-cut LNO crystal, for example, was shown to operate closely to the anisotropic unipolar regime ($\alpha_{E31} > 0$ and $\alpha_{E32} = 0$), and one with a 41°Y-cut LNO crystal closely to the in-plane isotropic regime ($\alpha_{E31} = \alpha_{E32}$). Figure 7.14a further illustrates the results of calculated quasi-static α_{E31} and α_{E32} coefficients as a function of the LNO crystal cut angle in the *YZ* plane in relation to the *Y* axis, i.e. the θ angle in the standard notation (*YXl*) θ or $\theta = 90° + \beta$ in the Euler angles scheme. According to the calculations, the anisotropic unipolar regime and the in-plane isotropic regime should be observed for LNO crystals with cut angles of 2°Y and 45°Y, respectively. From this point of view, other cuts could also be interesting, such as the 162.1°Y-cut LNO, corresponding to an anisotropic bipolar regime ($\alpha_{E31} = -\alpha_{E32}$), and the 129°Y-cut LNO, corresponding to the maximum expected ME voltage coefficient as seen in Fig. 7.10a. Also, Fig. 7.14b depicts the calculated ME voltage coefficients as a function of the relative thickness ratio between the PE and MS phases using the same formalism. This calculation was made for some of the most interesting LNO crystal cuts. From this we see that a decrease in the thickness of the PE layer results in more stress being transferred to it from the MS and, consequently, in an increase of the ME effect. However, since the detected voltage is proportional to the PE layer thickness, the thinner the layer is, the lower the output signal will be. Therefore, taking into account that any measuring circuit has its own input noise, the maximal signal-to-noise ratio should be observed for a finite ferroelectric film thickness.

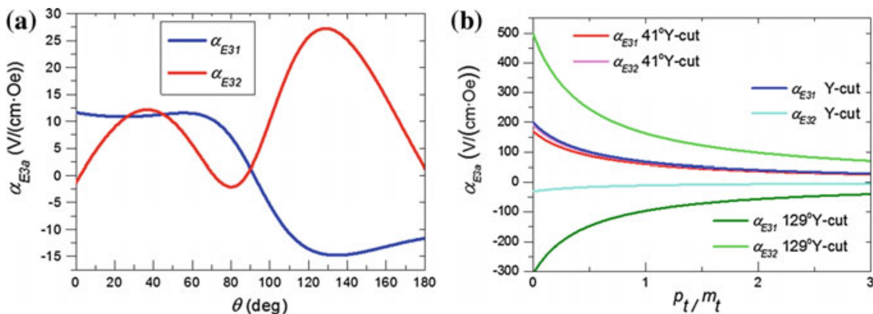

Fig. 7.14 **a** Calculated in-plane quasi-static ME voltage coefficients as a function of the θ piezocrystal cut angle (measured from the Y axis). **b** ME coefficients for different crystal cuts as a function of the PE/MS relative thickness ratio ($^{p}t/^{m}t$) [30]

7.4 Conclusions

In this chapter we have presented an experimental study of the direct and converse magnetoelectric (ME) effects in tri-layered composites based on Metglas and piezoelectric (PE) single-crystals of lithium niobate and gallium phosphate in comparison with laminates based on the popular piezoelectric PMN-PT. In the first part, various techniques used in the measurement of the ME effect were explored, with special emphasis on the dynamic lock-in technique employed in our experiments. In this technique the sample is subjected to two magnetic fields, a DC bias and an AC modulation field. The AC voltage generated across the sample is subsequently measured in a lock-in amplifier. This measurements can then be performed as a function of the magnetic bias field or the frequency of the modulation field. The formalism describing this technique was presented, and we showed how the different order ME coefficients can be extracted from the measurements of the voltages synchronized with the fundamental and harmonic frequencies of the exciting signal. Subsequently we presented a custom-made setup used by us to measure the dynamic ME effect. Its scheme and characteristics as well as ways to reduce the noise and the parasitic induction voltage were explored.

In the second part we introduced a comparative study between the direct and converse ME effects in tri-layered composites of the type Metglas/PE/Metglas based on single crystals of $LiNbO_3$ (LNO) and [011]-poled PMN-PT bonded with a cyanoacrylate glue. In the quasi-static regime we showed that the transversal direct ME effects had comparable magnitudes in both LNO and PMN-PT samples, which was due to comparable ratios between piezoelectric and dielectric coefficients of both crystals. The converse ME effects, on the other hand, were shown to be much stronger in the sample with the PMN-PT crystal since, according to the theory, this effect depends only on the piezoelectric constants which are much larger in this case. We also presented the results of the direct ME measurements in the resonant regime. Here we found an even larger ME effect peak in the composite with the 41° Y-cut LNO than in the one with PMN-PT. We therefore conclude that lead-free single-crystals like LNO might constitute a good alternative to PMN-PT in terms of practical ME applications.

Subsequently we describe a study of the anisotropic direct ME and electromechanical (EM) properties in tri-layered composites featuring Metglas and differently cut PE single crystals of LNO and $GaPO_4$ (GPO) bonded with epoxy. Results of the quasi-static measurements were shown to vary strongly with the direction of the applied transverse magnetic fields and the crystallographic orientation of the PE. In greater detail, the 41°Y-cut LNO crystal was shown to produce an in-plane isotropic ME response while the Y-cut LNO and X-cut GPO generated an in-plane unipolar effect.

In the resonant regime, several in-plane contour EM resonant peaks were observed in the ME spectrum. Here we saw how strongly the anisotropic nature of the PE crystals influences the excitation of certain contour acoustic resonance modes. So, e.g., three distinct resonance modes were observed in the system

featuring the Y-cut LNO crystal, whereas a single one was observed in the composite with the 41°Y-cut LNO one. A very intense single peak exhibiting a ME coefficient of up to 249 V/(cm·Oe) was detected in the sample with the 41°Y-cut LNO crystal. In order to predict, which kinds of modes could be excited under given conditions and to identify such modes by comparison with simulated results, we employed impedance measurements, thus clarifying the relation between the anisotropic constants and the excitation of such peaks. The aforementioned large symmetric peak was therefore shown to be related to the in-plane isotropic properties of the crystal, so that a very symmetric and high-amplitude resonance mode was generated. In the GPO sample, four weak contour asymmetrical shear modes of resonance were identified, with the largest having a response of up to 23.2 V/(cm·Oe) and appearing at a frequency of 199.7 kHz.

In conclusion, we were able to identify relatively large anisotropic ME effects in composites based on PE single-crystals which were in good agreement with the theory. In principle, such ME responses can be further enhanced through the optimization of the volume ratio and the coupling between layers. Finally we showed how the control of the crystal orientation can be used to greatly enhance the anisotropic ME effects in composites. The selection of the crystal orientation should therefore allow one to engineer almost any desired anisotropic properties for some given application.

Acknowledgments This work was developed in the scope of the projects I3N/FSCOSD (Ref. FCT UID/CTM/50025/2013),CICECO—Aveiro Institute of Materials—POCI-01-0145-FEDER-007679 (FCT Ref. UID /CTM /50011/2013),and RECI/FIS-NAN/0183/2012 (FCOMP-01-0124-FEDER-027494), financed by national funds through theFCT/MEC and when applicable cofinanced by FEDER under the PT2020 Partnership Agreement. J.V.V. andA.A.T. thank for the FCT grants SFRH/BD/89097/2012 and SFRH/BPD/74086/2010, respectively. N.A.S.acknowledges support by NUST "MISiS" through grant no. K3-2015-003.

References

1. C.-W. Nan, M.I. Bichurin, S. Dong, D. Viehland, G. Srinivasan, Multiferroic magnetoelectric composites: historical perspective, status, and future directions. J. Appl. Phys. **103**(3), 031101–031135 (2008)
2. M. Fiebig, Revival of the magnetoelectric effect. J. Phys. D Appl. Phys. **38**(8), R123–R152 (2005)
3. J. Ma, J. Hu, Z. Li, C.-W. Nan, Recent progress in multiferroic magnetoelectric composites: from bulk to thin films. Adv. Mater. **23**(9), 1062–1087 (2011)
4. J. Ryu, S. Priya, K. Uchino, H.-E. Kim, Magnetoelectric effect in composites of magnetostrictive and piezoelectric materials. J. Electroceram. **8**(2), 107–119 (2002)
5. M. Bichurin, D. Viehland, G. Srinivasan, Magnetoelectric interactions in ferromagnetic-piezoelectric layered structures: phenomena and devices. J. Electroceram. **19**(4), 243–250 (2007)
6. Y. Wang, J. Hu, Y. Lin, C.-W. Nan, Multiferroic magnetoelectric composite nanostructures. NPG Asia Mater. **2**(2), 61–68 (2010)
7. J. Zhai, Z. Xing, S. Dong, J. Li, D. Viehland, Magnetoelectric laminate composites: an overview. J. Am. Ceram. Soc. **91**(2), 351–358 (2008)

8. W. Eerenstein, N.D. Mathur, J.F. Scott, Multiferroic and magnetoelectric materials. Nature **442**(7104), 759–765 (2006)
9. D.R. Tilley, J.F. Scott, Frequency dependence of magnetoelectric phenomena in BaMnF4. Phys. Rev. B **25**(5), 3251–3260 (1982)
10. M.I. Bichurin, V.M. Petrov, O.V. Ryabkov, S.V. Averkin, G. Srinivasan, Theory of magnetoelectric effects at magnetoacoustic resonance in single-crystal ferromagnetic-ferroelectric heterostructures. Phys. Rev. B **72**(6), 060408–060411 (2005)
11. M.I. Bichurin, V.M. Petrov, Y.V. Kiliba, G. Srinivasan, Magnetic and magnetoelectric susceptibilities of a ferroelectric/ferromagnetic composite at microwave frequencies. Phys. Rev. B **66**(13), 134404–134413 (2002)
12. G. Srinivasan, Magnetoelectric comosites. Annu. Rev. Matrer. Res. **40**, 153–178 (2010)
13. G. Sreenivasulu, S.K. Mandal, S. Bandekar, V.M. Petrov, G. Srinivasan, Low-frequency and resonance magnetoelectric effects in piezoelectric and functionally stepped ferromagnetic layered composites. Phys. Rev. B **84**(14), 144426–144431 (2011)
14. S.N. Babu, T. Bhimasankaram, S.V. Suryanarayana, Magnetoelectric effect in metal-PZT laminates. Bull. Mater. Sci. **28**(5), 419–422 (2004)
15. C.P. Zhao, F. Fang, W. Yang, A dual-peak phenomenon of magnetoelectric coupling in laminated Terfenol-D/PZT/Terfenol-D composites. Smart Mater. Struct. **19**(12), 125004–125010 (2010)
16. J. Ryu, A.V. Carazo, K. Uchino, H.-E. Kim, Magnetoelectric properties in piezoelectric and magnetostrictive laminate composites. Jpn. J. Appl. Phys. **40**(8), 4948–4951 (2001)
17. H. Greve, E. Woltermann, H.-J. Quenzer, B. Wagner, E. Quandt, Giant magnetoelectric coefficients in (Fe90Co10)78Si12B10-AlN thin film composites. Appl. Phys. Lett. **96**(18), 182501–182503 (2010)
18. G. Sreenivasulu, V.M. Petrov, L.Y. Fetisov, Y.K. Fetisov, G. Srinivasan, Magnetoelectric interactions in layered composites of piezoelectric quartz and magnetostrictive alloys. Phys. Rev. B **86**(21), 214405–214411 (2012)
19. Y. Shen, K.L. McLaughlin, J. Gao, M. Li, J. Li, D. Viehland, Effective optimization of magnetic noise for a Metglas/Pb(Zr, Ti)O3 magnetoelectric sensor array in an open environment. Mater. Lett. **91**, 307–310 (2013)
20. Y. Wang, D. Gray, J. Gao, D. Berry, M. Li, J. Li, D. Viehland, H. Luo, Improvement of magnetoelectric properties in Metglas/$Pb(Mg_{1/3}Nb_{2/3})O_3$–$PbTiO_3$ laminates by poling optimization. J. Alloys Compd. **519**, 1–3 (2012)
21. R. Viswan, D. Gray, Y. Wang, Y. Li, D. Berry, J. Li, D. Viehland, Strong magnetoelectric coupling in highly oriented ZnO films deposited on Metglas substrates. Phys. Status Solidi-R **5** (10–11), 391–393 (2011)
22. G. Sreenivasulu, L.Y. Fetisov, Y.K. Fetisov, G. Srinivasan, Piezoelectric single crystal langatate and ferromagnetic composites: Studies on low-frequency and resonance magnetoelectric effects. Appl. Phys. Lett. **100**(5), 052901–052904 (2012)
23. G. Sreenivasulu, P. Qu, E. Piskulich, V.M. Petrov, Y.K. Fetisov, A.P. Nosov, H. Qu, G. Srinivasan, Shear strain mediated magneto-electric effects in composites of piezoelectric lanthanum gallium silicate or tantalate and ferromagnetic alloys. App. Phys. Lett. **105**(3), 032409–032412 (2014)
24. J.-P. Rivera, A short review of the magnetoelectric effect and related experimental techniques on single phase (multi-) ferroics. Eur. Phys. J. B **71**(3), 299–313 (2009)
25. D.C. Lupascu, H. Wende, M. Etier, A. Nazrabi, I. Anusca, H. Trivedi, V.V. Shvartsman, J. Landers, S. Salamon, C. Schmitz-Antoniak, Measuring the magnetoelectric effect across scales. GAMM-Mitteilungen **38**(1), 25–74 (2015)
26. G.V. Duong, R. Groessinger, M. Schoenhart, D. Bueno-Basques, The lock-in technique for studying magnetoelectric effect. J. Mag. Mag. Mat. **316**(2), 390–393 (2007)
27. M.M. Kumar, A. Srinivas, S.V. Suryanarayana, G.S. Kumar, T. Bhimasankaram, An experimental setup for dynamic measurement of magnetoelectric effect. Bull. Mater. Sci. **21** (3), 251–255 (1998)

28. Y.J. Wang, J.Q. Gao, M.H. Li, Y. Shen, D. Hasanyan, J.F. Li, D. Viehland, A review on equivalent magnetic noise of magnetoelectric laminate sensors. Phil. Trans. R. Soc. A **372** (2009), 20120455 (2014)
29. Y.K. Fetisov, K.E. Kamentsev, A.Y. Ostashchenko, G. Srinivasan, Wide-band magnetoelectric characterization of a ferrite-piezoelectric multilayer using a pulsed magnetic field. Solid State Commun. **132**(1), 13–17 (2004)
30. A.A. Timopheev, J.V. Vidal, A.L. Kholkin, N.A. Sobolev, Direct and converse magnetoelectric effects in Metglas/LiNbO3/Metglas trilayers. J. Appl. Phys. **114**(4), 044102–044108 (2013)
31. S. Priya, R. Islam, S. Dong, D. Viehland, Recent advancements in magnetoelectric particulate and laminate composites. J. Electroceram. **19**(1), 149–166 (2007)
32. M. Vopsaroiu, J. Blackburn, M.G. Cain, Emerging technologies and opportunities based on the magneto-electric effect in multiferroic composites. MRS Proc. **1161**, 1161-I05-04 (2009)
33. R.C. Kambale, D.-Y. Jeong, J. Ryu, Current status of magnetoelectric composite thin/thick films. Adv. Cond. Matter Phys. **2012**, 824643 (2012)
34. J. More-Chevalier, C. Cibert, R. Bouregba, G. Poullain, Eddy currents: a misleading contribution when measuring magnetoelectric voltage coefficients of thin film devices. J. Appl. Phys. **117**(15), 154104–154110 (2015)
35. D.A. Burdin, D.V. Chashin, N.A. Ekonomov, L.Y. Fetisov, Y.K. Fetisov, G. Sreenivasulu, G. Srinivasan, Nonlinear magneto-electric effects in ferromagnetic-piezoelectric composites. J. Mag. Mag. Mat. **358–359**, 98–104 (2014)
36. Y.K. Fetisov, D.A. Burdin, D.V. Chashin, N.A. Ekonomov, High-Sensitivity Wideband Magnetic Field Sensor Using Nonlinear Resonance Magnetoelectric Effect. Sens. J. IEEE, **14** (7), 2252–2256 (2014)
37. Y. Chen, S.M. Gillette, T. Fitchorov, L. Jiang, H. Hao, J. Li, X. Gao, A. Geiler, C. Vittoria, V. G. Harris, Quasi-one-dimensional miniature multiferroic magnetic field sensor with high sensitivity at zero bias field. Appl. Phys. Lett. **99**(4), 042505 (2011)
38. J. Gao, Z. Wang, Y. Shen, M. Li, Y. Wang, P. Finkel, J. Li, D. Viehland, Self-powered low noise magnetic sensor. Mater. Lett. **82**, 178–180 (2012)
39. J. Gao, Y. Shen, P. Finkel, J. Blottman, J. Li, D. Viehland, Geomagnetic field tuned frequency multiplication in Metglas/Pb(Zr, Ti)O_3 heterostructure. Mater. Lett. **88**, 47–50 (2012)
40. N.X. Sun, G. Srinivasan, Voltage control of magnetism in multiferroic heterostructures and devices. Spin **02**(03), 12240004 (2012)
41. C.A. Vaz, Electric field control of magnetism in multiferroic heterostructures. J. Phys.: Cond. Matt. **24**(33), 333201 (2012)
42. M. Li, Y. Wang, D. Hasanyan, J. Li, D. Viehland, Giant converse magnetoelectric effect in multi-push-pull mode Metglas/Pb(Zr, Ti)O_3/Metglas laminates. Appl. Phys. Lett. **100**(13), 132904–132906 (2012)
43. S. Dong, J. Zhai, F. Bai, J.-F. Li, D. Viehland, Push-pull mode magnetostrictive/piezoelectric laminate composite with an enhanced magnetoelectric voltage coefficient. Appl. Phys. Lett. **87** (6), 062502–062504 (2005)
44. S.-E. Park, T.R. Shrout, Ultrahigh strain and piezoelectric behavior in relaxor based ferroelectric single crystals. J. Appl. Phys. **82**(4), 1804 (1997)
45. C.-S. Park, K.-H. Cho, M.A. Arat, J. Evey, S. Priya, High magnetic field sensitivity in Pb(Zr, Ti)O_3–Pb($Mg_{1/3}Nb_{2/3}$)O_3 single crystal/Terfenol-D/Metglas magnetoelectric laminate composites. J. Appl. Phys. **107**(9), 094109 (2010)
46. S. Dong, J. Cheng, J.F. Li, D. Viehland, Enhanced magnetoelectric effects in laminate composites of Terfenol-D/Pb(Zr, Ti)O_3 under resonant drive. Appl. Phys. Lett. **83**(23), 4812–4814 (2003)
47. S. Dong, J.-F. Li, D. Viehland, Ultrahigh magnetic field sensitivity in laminates of TERFENOL-D and Pb($Mg_{1/3}Nb_{2/3}$)O_3–$PbTiO_3$ crystals. Appl. Phys. Lett. **83**(11), 2265–2267 (2003)

48. M. Bichurin, V. Petrov, A. Zakharov, D. Kovalenko, S.C. Yang, D. Maurya, V. Bedekar, S. Priya, Magnetoelectric interactions in lead-based and lead-free composites. Materials **4**(4), 651–702 (2011)
49. H.F. Tian, T.L. Qu, L.B. Luo, J.J. Yang, S.M. Guo, H.Y. Zhang, Y.G. Zhao, J.Q. Li, Strain induced magnetoelectric coupling between magnetite and BaTiO3. Appl. Phys. Lett. **92**(6), 063507–063509 (2008)
50. P. Yang, K. Zhao, Y. Yin, J.G. Wan, J.S. Zhu, Magnetoelectric effect in magnetostrictive/piezoelectric laminate composite Terfenol-D/$LiNbO_3$ [(zxtw) − 129°/30°]. Appl. Phys. Lett. **88** (17), 172903–172905 (2006)
51. J.V. Vidal, A.A. Timopheev, A.L. Kholkin, N.A. Sobolev, Anisotropy of the magnetoelectric effect in tri-layered composites based on single-crystalline piezoelectrics. Vacuum 1–7
52. M. Yachi, M. Ono, The third overtone resonator using 36° rotated Y cut LiNbO3 crystal, in*Ultrasonics Symposium, 1995. Proceedings. 1995 IEEE,* vol 2, p. 1003 (1995)
53. L.E. Myers, R.C. Eckardt, M.M. Fejer, R.L. Byer, W.R. Bosenberg, J.W. Pierce, Quasi-phase-matched optical parametric oscillators in bulk periodically poled $LiNbO_3$. J. Opt. Soc. Am. B **12**(11), 2102–2116 (1995)
54. A. Heinrich, A.L. Hörner, A. Wixforth, B. Stritzker, Pulsed laser deposition of La0.67Ca0.33MnO_3 thin films on $LiNbO_3$ and surface acoustic wave studies. Thin Solid Films **510**(1–2), 77–81 (2006)
55. A. Kawamata, H. Hosaka, T. Morita, Non-hysteresis and perfect linear piezoelectric performance of a multilayered lithium niobate actuator. Sens. Actuators A Phys. **135**(2), 782–786 (2007)
56. G. Matsunami, A. Kawamata, H. Hosaka, T. Morita, Multilayered LiNbO3 actuator for XY-stage using a shear piezoelectric effect. Sens. Actuators A Phys. **144**(2), 337–340 (2008)
57. L. Dreher, M. Weiler, M. Pernpeintner, H. Huebl, R. Gross, M.S. Brandt, S.T.B. Goennenwein, Surface acoustic wave driven ferromagnetic resonance in nickel thin films: theory and experiment. Phys. Rev. B **86**(13), 134415 (2012)
58. N. Obata, T. Kawahata, R. Suzuki, K. Nishimura, H. Uchida, M. Inoue, Fabrication and properties of InSb films with ion-beam sputtering for use in the amplification of magneto-surface-acoustic waves. Phys. Stat. Sol. (a) **201**(8), 1973–1975 (2004)
59. H.-Y. Kuo, A. Slinger, K. Bhattacharya, Optimization of magnetoelectricity in piezoelectric–magnetostrictive bilayers. Smart Mater. Struct. **19**(12), 125010–125022 (2010)
60. T. Wu, A. Bur, J.L. Hockel, K. Wong, T.-K. Chung, G.P. Carman, Electrical and mechanical manipulation of ferromagnetic properties in polycrystalline nickel thin film. IEEE Magn. Lett. **2**, 6000104–6000104 (2011)
61. R.S. Weis, T.K. Gaylord, Lithium niobate: Summary of physical properties and crystal structure. Appl. Phys. A Mater. Sci. Process. **37**(4), 191–203 (1985)
62. P. Han, W. Yan, J. Tian, X. Huang, H. Pan, Cut directions for the optimization of piezoelectric coefficients of lead magnesium niobate–lead titanate ferroelectric crystals. Appl. Phys. Lett. **86** (5), 052902–052904 (2005)
63. A.W. Warner, M. Onoe, G.A. Coquin, Determination of elastic and piezoelectric constants for crystals in class (3 m). J. Acoust. Soc. Am. **42**(6), 1223–1231 (1967)
64. W. Yue, J. Yi-jian, Crystal orientation dependence of piezoelectric properties in $LiNbO_3$ and $LiTaO_3$. Opt. Mater. **23**(1–2), 403–408 (2003)
65. C. Zhang, W. Chen, J. Li, J. Yang, Two-dimensional analysis of magnetoelectric effects in multiferroic laminated plates. IEEE Trans. Ultrason. Ferroelectr. Freq. Control **56**(5), 1046–1053 (2009)
66. C. Zhang, W. Chen, C. Zhang, Two-dimensional theory of piezoelectric plates considering surface effect. Eur. J. Mech.—A/Solid. **41**, 50–57 (2013)
67. IRE Standards on Piezoelectric Crystals: Determination of the Elastic, Piezoelectric, and Dielectric Constants-The Electromechanical Coupling Factor, 1958. Proc. IRE **46**(4), 764–778 (1958)
68. R. Zhang, B. Jiang, W. Cao, Elastic, piezoelectric, and dielectric properties of multidomain 0.67Pb(Mg[sub 1/3]Nb[sub 2/3])O[sub 3]–0.33PbTiO[sub 3] single crystals. J. Appl. Phys. **90** (7), 3471–3475 (2001)

69. M.I. Bichurin, V.M. Petrov, G. Srinivasan, Theory of low-frequency magnetoelectric coupling in magnetostrictive-piezoelectric bilayers. Phys. Rev. B **68**(5), 054402–054414 (2003)
70. Z. Huang, Theoretical modeling on the magnetization by electric field through product property. J. Appl. Phys. **100**(11), 114104–114108 (2006)
71. M. Bichurin, V. Petrov, *Modeling of Magnetoelectric Effects in Composites*, Springer (2014), 9401791562, 9789401791564
72. G. Wu, T. Nan, R. Zhang, N. Zhang, S. Li, N.X. Sun, Inequivalence of direct and converse magnetoelectric coupling at electromechanical resonance. Appl. Phys. Lett. **103**(18), 182905–182909 (2013)
73. J.-P. Zhou, Y.-J. Ma, G.-B. Zhang, X.-M. Chen, A uniform model for direct and converse magnetoelectric effect in laminated composite. Appl. Phys. Lett. **104**(20), 202904–202908 (2014)
74. P. Davulis, J.A. Kosinski, M.P. da Cunha, GaPO4 Stiffness and Piezoelectric Constants Measurements using the Combined Thickness Excitation and Lateral Field Technique, in *International Frequency Control Symposium and Exposition*, pp. 664–669 (2006)
75. W. Wallnöfer, P.W. Krempl, A. Asenbaum, Determination of the elastic and photoelastic constants of quartz-type GaPO4 by Brillouin scattering. Phys. Rev. B **49**(15), 10075–10080 (1994)
76. J.V. Vidal, A.A. Timopheev, A.L. Kholkin, N.A. Sobolev, Anisotropy of the magnetoelectric effect in tri-layered composites based on single-crystalline piezoelectrics. Vacuum **122**, Part B, 286–292 (2015)
77. F. Fang, C. Zhao, W. Yang, Thickness effects on magnetoelectric coupling for Metglas/PZT/Metglas laminates. Sci. China Phys. Mech. Astron. **54**(4), 581–585 (2011)
78. D. Hasanyan, J. Gao, Y. Wang, R. Viswan, Y.S.M. Li, J. Li, D. Viehland, Theoretical and experimental investigation of magnetoelectric effect for bending-tension coupled modes in magnetostrictive-piezoelectric layered composites. J. Appl. Phys. **112**(1), 013908–013918 (2012)
79. Y. Wang, D. Hasanyan, M. Li, J. Gao, J. Li, D. Viehland, H. Luo, Theoretical model for geometry-dependent magnetoelectric effect in magnetostrictive/piezoelectric composites. J. Appl. Phys. **111**(12), 124513–124518 (2012)
80. S. Dong, J. Zhai, J. Li, D. Viehland, Near-ideal magnetoelectricity in high-permeability magnetostrictive/piezofiber laminates with a (2-1) connectivity. Appl. Phys. Lett. **89**(25), 252904–252906 (2006)
81. R. Tinder, *Tensor Properties of Solids* (Morgan & Claypool, 2007), 9781598293494
82. L.W. Martin, R. Ramesh, Multiferroic and magnetoelectric heterostructures. Acta Mater. **60** (6–7), 2449–2470 (2012)
83. H.-M. Zhou, Y.-H. Zhou, X.-J. Zheng, Q. Ye, J. Wei, A general 3-D nonlinear magnetostrictive constitutive model for soft ferromagnetic materials. J. Mag. Mag. Mat. **321** (4), 281–290 (2009)
84. M. Cochez, J.D. Foulon, A. Ibanez, A. Goiffon, E. Philippot, B. Capelle, A. Zarka, J. Schwartzel, J. Detaint, Crystal growth and characterizations of a quartz-like material: GaPO4. J. Phys. IV France, **04**, C2-183–C2-188 (1994)
85. IEEE Standard on Piezoelectricity, *ANSI/IEEE Std 176–1987*, pp. 1–74 (1988)
86. K.-H. Cho, S. Priya, Direct and converse effect in magnetoelectric laminate composites. Appl. Phys. Lett. **98**(23), 232904 (2011)
87. D. Rajaram Patil, Y. Chai, R.C. Kambale, B.-G. Jeon, K. Yoo, J. Ryu, W.-H. Yoon, D.-S. Park, D.-Y. Jeong, S.-G. Lee, J. Lee, J.-H. Nam, J.-H. Cho, B.-I. Kim, K. Hoon Kim, Enhancement of resonant and non-resonant magnetoelectric coupling in multiferroic laminates with anisotropic piezoelectric properties. Appl. Phys. Lett. **102**(6), 062909 (2013)

Chapter 8
Peculiarities of Physical Properties of Semimagnetic Semiconductors and Their Practical Application

E.I. Gheorghitza, V.I. Ivanov-Omskii and I.T. Postolaki

Abstract This chapter presents a review on studies of fundamental properties of narrow-bandgap solid solutions $Hg_{1-x}Mn_xTe$ and $Hg_{1-x-y}Cd_xMn_yTe$. The structure and parameters of energy bands, electrical, photoelectrical and photoluminescence properties of bulk monocrystals and epitaxial layers are also reviewed. The impact of manganese on the restructuring of energy spectrum of free carriers and localized states are discussed. The basic properties of semimagnetic materials $Hg_{1-x}Mn_xTe$ and $Hg_{1-x-y}Cd_xMn_yTe$ are compared with the properties of more intensively studied $Hg_{1-x}Cd_xTe$ solid solutions. It is shown that semimagnetic solid solutions $Hg_{1-x-y}Cd_xMn_yTe$ and $Hg_{1-x}Mn_xTe$ are prospective alternatives to $Hg_{1-x}Cd_xTe$ materials for the creation of infrared detector structures.

8.1 Introduction

Mercury telluride and cadmium telluride form a continuous series of solid solutions over the entire range of substitution compositions, whereas in the *Hg–Mn–Te* solid solution with zinc blend structure they are formed in a limited range of compositions. Although *HgTe* crystallizes in the zinc blende structure with a lattice constant a = 6.46 Å, and manganese telluride has a hexagonal structure of the *NiAs* type with lattice constant a = 4.05 Å and c = 6.71 Å, it was stated that in the *HgTe–MnTe* system a very large number of mercury atoms (over 80 %) can be substituted by manganese atoms retaining the zinc blende structure [1]. The most thoroughly studied in the group of quaternary semimagnetic alloys are $Hg_{1-x-y}Cd_xMn_yTe$.

The first studies of such a system were conducted by Delwes and Lewis [1]. Becla have shown on the basis of X-ray studies and differential thermal analysis of the phase diagram that α-phase with sphalerite structure exists within $0 \leq y \leq 0.35$ while other

E.I. Gheorghitza · I.T. Postolaki (✉)
Tiraspol State University, Chisinau, Moldova
e-mail: postolachi@list.ru

V.I. Ivanov-Omskii
Physical-Technical Institute A. F. Ioffe RAN, 94021 St. Petersburg, Russia

© Springer International Publishing Switzerland 2016

I. Tiginyanu et al. (eds.), *Nanostructures and Thin Films for Multifunctional Applications*, NanoScience and Technology,
DOI 10.1007/978-3-319-30198-3_8

phases are formed in $Hg_{1-x-y}Cd_xMn_yTe$ with $y > 0.35$, that makes the material unsuitable for device structures [2]. The epitaxial growth of high-quality layers of $Hg_{1-x-y}Cd_xMn_yTe$ with $0 \le x \le 0.20$, $0 \le y \le 0.15$ has been reported [3, 4].

Peculiarities of the crystal structure and the energy spectrum of $Hg_{1-x}Mn_xTe$ as compared with non-magnetic materials have been described [5–11]. However, one significant difference between these materials and the well-known $Hg_{1-x}Cd_xTe$ was distinguished [12], namely the degree of bond ionicity and the stability of properties. The ionicity of *Hg-Te* bonds is slightly modified in ternary compounds as compared to binary compound of tellurium mercury, whereas in $Hg_{1-x}Cd_xTe$ a strong loosening of bonds takes place, leading to instability of the material properties. Therefore, $Hg_{1-x}Mn_xTe$, similarly to *HgTe*, should be much stable as compared to $Hg_{1-x}Cd_xTe$. This suggests that semimagnetic semiconductors like $Hg_{1-x}Mn_xTe$ and $Hg_{1-x-y}Cd_xMn_yTe$ are more favorable materials for the creation of infrared (IR) detectors than their non-magnetic $Hg_{1-x}Cd_xTe$ counterparts. The main parameters of $Hg_{1-x-y}Cd_xMn_yTe$, $Hg_{1-x}Mn_xTe$, and $Hg_{1-x}Cd_xTe$ solid solutions as a function of their composition have been previously reported [9, 13–15].

8.2 Structure and Parameters of the Energy Bands

The basic physical properties of narrow-gap semiconductor materials like $Hg_{1-x}Mn_xTe$ as well as $Hg_{1-x}Cd_xTe$ are defined by their energy structure near the point of symmetry T (center of the Brillouin zone), and in the $\vec{k} \cdot \vec{p}$ calculation of this structure it is necessary to take into consideration at least three closely spaced zones—Γ_6, Γ_7 and Γ_8. [16].

Taking into account the presence of manganese ions in the crystal lattice of $Hg_{1-x}Mn_xTe$, the so-called "modified" model of Pigeon Brown has been used for the description of the band structure of semimagnetic alloy $Hg_{1-x}Mn_xTe$ or $Hg_{1-x-y}Cd_xMn_yTe$ in a magnetic field [17–23]. This model is different from the usual one [24] by the fact that it even takes into account the exchange interaction between electrons and holes with manganese ions.

In this model the Hamiltonian is as follows:

$$\hat{H} = \hat{H}_0 + \hat{H}_{ex} = \hat{H}_0 + \vec{S}_i \sum_{\vec{R}_i} \vec{I}(\vec{r} - \vec{R}_i)\vec{\sigma}, \tag{8.1}$$

where $\vec{S}_i, \vec{\sigma}$ are spin operators of manganese ions and electrons of the conduction band; $\vec{I}$ is a constant of the electron-ion exchange splitting; $\vec{r}, \vec{R}_i$ are coordinates of the electrons and manganese ions. Since the manganese ions are located at the crystal lattice sites, and the wave function of the electron is extended, it is possible to make two simplifications.

The energy levels at the point of symmetry Γ can be obtained by calculating the Hamiltonian in the form of a matrix (8 × 8) (D). When the asymmetrical inversion zone Γ_8 is insignificant the Hamiltonian becomes two separate matrixes (4 × 4) D_a and D_b:

$$D = \begin{vmatrix} \overline{D_a} & 0 \\ 0 & \overline{D_b} \end{vmatrix} \begin{matrix} \overline{D_a} = D_a + M_a \\ \overline{D_b} = D_b + M_b \end{matrix}, \tag{8.2}$$

where a and b correspond to the two orientations of the electron spin:

$\vec{a}(\uparrow), \vec{b}(\downarrow)$, D_a, D_b are Hamiltonian Matrix of the not modified model of Pigeon Brown, M_a, M_b are matrix of the exchange interaction.

The contribution of the exchange interaction is taken into account by adding additional members representing the exchange integrals of electrons interaction and holes with Mn^{+2} ions to the matrix of Pigeon Brown. According to calculations, the eigenvalues describing the lower levels of spin zones reducibility (Γ_6), and the upper levels of heavy holes of the valence band (Γ_8) at the point of symmetry Γ in the parabolic approximation, have the form:

$$E_a(0) = \frac{1}{2}\hbar\omega_c + \frac{1}{2}g^*\mu_B H + 3A, \tag{8.3}$$

$$E_b(0) = \frac{1}{2}\hbar\omega_c - \frac{1}{2}g^*\mu_B H - 3A, \tag{8.4}$$

$$E_a(-1) = \hbar\omega_0\left[\frac{(\tilde{\gamma} - \gamma_1)}{2} + \frac{k}{2}\right] - B, \tag{8.5}$$

$$E_b(-1) = \hbar\omega_0\left[-\frac{(\tilde{\gamma} + \gamma_1)}{2} + \frac{3k}{2}\right] - 3B, \tag{8.6}$$

where $a(\uparrow), b(\downarrow)$ indicate the direction of the spin relative to the magnetic field;

ω_c is the cyclotron frequency of an electron in a semiconductor;
ω_o is the free electron cyclotron frequency;
$\tilde{\gamma}, \gamma_1, k$ are the modified parameters Latinzhera;
μ_B is the Bohr magneton;
g^*—g is the factor of an electron without the exchange interaction;
A and B are the contributions of the exchange interaction to the spin splitting;

$$\begin{aligned} A &= \frac{1}{6}N_0\alpha x\langle S_z\rangle \\ B &= \frac{1}{6}N_0\beta x\langle S_z\rangle \\ \langle S_z\rangle &= -S_0 B_{5/2}\left[\frac{\frac{5}{2}g_{Mn}\mu_B H}{k_B(T + T_o)}\right] \end{aligned} \tag{8.7}$$

S_0 is the effective spin of magnetic moment; $B_{5/2}$ is the Brillouin function; k_B is the Boltzmann constant; T_0 is the effective temperature. S_0 and T_0 are tabulated depending on composition and temperature of the crystal.

From the (8.3)–(8.6) it is clear that the account of the exchange interaction significantly affects the spin splitting of the electron and hole states in a magnetic field. Since $g^* < 0$, and $A > 0$, the contributions from interband exchange interaction in the spin splitting are opposite, so the relative positioning of the energy sublevels $E_a(n)$ and $E_b(n)$ depend on the values of the last two terms in the (8.3)–(8.6). For samples of $Hg_{1-x}Mn_xTe$ with $x > 0.12$ there is an inequality:

$$3A > \left|\frac{1}{2}\mu_B g^* H\right| \tag{8.8}$$

It means the splitting of sublevels with different spin projections on H due to the exchange interaction is so great that the levels of the series $a(n)$ and $b(n)$ are reversed, unlike conventional narrow-gap semiconductors where $E_b(n) > E_a(n)$.

The valence band in semimagnetic semiconductors is fourfold degenerated at symmetry point Γ. As a result of the exchange interaction of holes with manganese ions, the levels of $E_a(-1)$ and $E_b(-1)$ move the energy up, unlike the non-magnetic semiconductors, where the splitting of the heavy holes is very weak.

Figure 8.1 shows the theoretical dependence of the Landau levels on the magnetic field for $H_{0.872}Mn_{0.128}Te$ when $T = 2$ K, calculated by using the modified Pigeon Brown model [23, 25].

The dependence of the band-gap width on the composition of $Hg_{1-x}Mn_xTe$ and temperature has the form [26].

$$E_g(x, T) = (-0.253 + 3.446x + 4.9 \times 10^{-4}T - 2.55 \times 10^{-3}xT)\,\mathrm{eV} \tag{8.9}$$

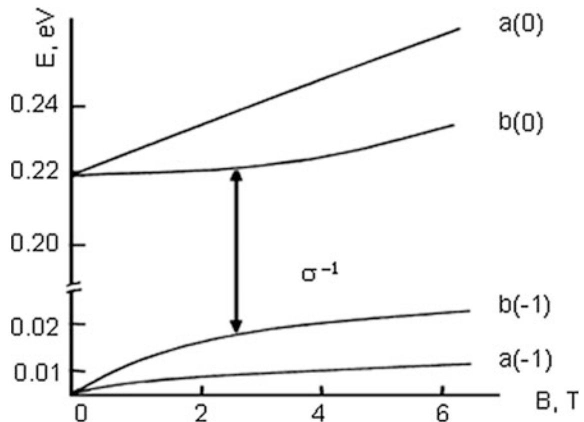

Fig. 8.1 Theoretical dependence of the Landau levels on the induction of the magnetic field for $Hg_{1-x}Mn_xTe$ (x = 0.128) at $T = 2$ K [23, 25]

A little different from (8.9) expression for $E_g(x, T)$ is given by Gavaleshko et al. [27] and Rogalski [9]. According to the three-band model, the effective masses of electrons and light holes in extrema are defined by:

$$\begin{aligned} m_0/m_{n0} &= 1 + (2m_0P^2/3\hbar^2)[2\varepsilon_g^{-1} + (\varepsilon_g + \Delta)^{-1}], \\ m_0/m_{l0} &= 1 - 4m_0P^2/3\hbar^2\varepsilon_g, \end{aligned} \tag{8.10}$$

where P is the interband matrix element of the momentum operator, that is linearly dependent on the composition of the solid solution [28].

$$P(x) = (8.35 - 7.94x) \times 10^{-8}\,\text{eV} \cdot \text{cm}^{-3} \tag{8.11}$$

Due to non parabolic conduction band, the electron effective mass m_n increases with density n.

$$\left(\frac{m_n}{1 - m_n}\right)^2 = 32.6 \times 10^{-32}\frac{E_g^2}{p^4} + 8.32 \times 10^{-30}\frac{n^{2/3}}{p^2} \tag{8.12}$$

where E_g is in eV, p is in eV*cm^{-3}, m_n is in units $m_{0.}$

The parameters of the valence band of $Hg_{1-x}Mn_xTe$ are not yet determined with sufficient accuracy: values of ~0.5 m$_0$ [9, 26] and 0.55 m$_0$ [29] have been reported for the effective mass of heavy holes, while values of 1 eV [13] and 1.08 eV [9] have been reported for Δ.

The structure and parameters of the energy bands of $Hg_{1-x}Cd_xTe$ solid solutions have been studied in many papers (see. e.g. [14, 15, 30]. It should be noted that the width of the bandgap in $Hg_{1-x}Mn_xTe$ [1, 9] changes with the composition x about twice as fast as $E_g(x)$ in $Hg_{1-x}Cd_xTe$. The reason for this quantitative difference is as follows. The Γ_6 band (the conduction band in the semiconductor $Hg_{1-x}Mn_xTe$ with $E_g > 0$) is formed from $6S^2$ and $4S^2$ states of mercury and manganese. Electronic P—state of the tellurium forms the valence band of Γ_8 and the spin—orbit splitting of the Γ_7 band.

Since the change of the band gap width $E_g = E(\Gamma_6) - E(\Gamma_8)$ with $MnTe$ content in solid solution is related to the displacement of the S—zone Γ_6, a stronger dependence of $E_g(x)$ in $Hg_{1-x}Mn_xTe$ is related to greater energy difference between the S-levels of mercury and manganese atoms in comparison with the existing difference in the atomic levels of mercury and cadmium [5]. In particular, the semimetal-semiconductor transition, ($E_g = 0$), in $Hg_{1-x}Mn_xTe$ corresponds to the compositions $x = 0.075$ at $T = 4.2$ K; $x = 0.066$ at $T = 77$ K; and $x = 0.04$ at $T = 300$ K. For comparison, the corresponding values of x in $Hg_{1-x}Cd_xTe$ equal to 0.156, 0.143 and 0.093 [31].

Partially filled and highly localized $3d^5$ ions' shell of Mn^{2+} corresponds to the level (a narrow d-band) located in the valence band at about 3 eV below its top,

which has almost no effect on the structure of bands in the vicinity of Γ point and, consequently, on the electrical properties of narrow-gap solid solutions [9].

However, 3*d* electrons of the manganese ions fundamentally determine the properties of $Hg_{1-x}Mn_xTe$ solid solutions. The presence of manganese ions, as described above, leads to the exchange interaction between localized magnetic moments and itinerant electrons (spin-spin e-$3d^5e$ Mn^2), which changes the zone parameters and has interesting effects on transport phenomena and optical properties in the presence of a magnetic field.

In a number of studies [5, 10, 32], devoted to the study of the energy spectrum of solid solutions $Hg_{1-x}Mn_xTe$ it is shown that in the absence of a magnetic field the energy spectrum of free and localized carriers is the same as the corresponding spectrum for $Hg_{1-x}Cd_xTe$ at the same width of the band gap. It is known that the exchange interaction in $Hg_{1-x}Mn_xTe$ is determined by the content of manganese in the solution. In order to investigate the influence of the exchange interaction it is necessary to have materials with the same band parameters but with different contents of manganese.

These requirements are satisfied by $Hg_{1-x-y}Cd_xMn_yTe$ solid solutions. It is in these semimagnetic words, that by changing the relative content of cadmium and manganese it is possible to obtain materials with the same band parameters but with different contents of manganese. Alloys of the quaternary system $Hg_{1-x-y}Cd_xMn_yTe$ in addition to purely scientific interest, which was described above, also have a special practical interest.

Previously carried our research [33, 34] confirms the possibility of creating by ion implantation photodiodes based on epitaxial layers of $Hg_{1-x-y}Cd_xMn_yTe$ ($y = 0.14$; $0.05 \leq x \leq 0.08$). It was found that the current in a range of temperatures (77–254 K) is determined by the thermal activation mechanisms, it being a diffusion mechanism at $T > 110$ K, and a generation-recombination mechanism at $T < 110$ K. The reverse currents do not exceed 1 nA at 1 V, and the value R_0A at $T = 85$ K is $1.7 \times 10^7\ \Omega\cdot\text{cm}^2$. It was shown that these values are record ones for diodes on $Hg_{1-x}Mn_xTe$ and $Hg_{1-x-y}Cd_xMn_yTe$ of similar composition. The specific detectivity at $T = 77$ K and the aperture backlight $2\pi{*}sr$ is 5×10^{11} cm * $\text{Hz}^{1/2}\text{W}^{-1}$. The given parameters are at the level corresponding to the best photodiodes on $Hg_{1-x}Cd_xTe$ of the given diapason. This suggests that the technology of the $Hg_{1-x-y}Cd_xMn_yTe$ material came to the same level with $Hg_{1-x}Cd_xTe$ and now it is possible to attain a better stability of photodiodes due to higher structural perfection of $Hg_{1-x-y}Cd_xMn_yTe$ solid solutions. This conclusion is supported by studies conducted in recent years [35].

The dependence of the main band parameters of $Hg_{1-x-y}Cd_xMn_yTe$ on the composition of (x, y) and the temperature is more complex than for $Hg_{1-x}Mn_xTe$. The following expression was obtained in the framework of the virtual crystal model for $E_g(x, y, z)$ [32]:

$$\varepsilon_g = \frac{(1-x-y)x \cdot \varepsilon_{12}(u) + xy \cdot \varepsilon_{23}(\upsilon) + (1-x-y)y \cdot \varepsilon_{13}(\omega)}{(1-x-y)x + xy + (1-x-y)y} \tag{8.13}$$

$$\begin{aligned} &u = 0.5(2x+y) \quad \upsilon = 0.5(1-x+y \quad \omega = 0.5(2y+x) \\ &\varepsilon_{12} = \varepsilon_g(Hg_{1-u}Cd_uTe) \\ &\varepsilon_{23} = \varepsilon_g(Cd_{1-\upsilon}Mn_\upsilon Te) \\ &\varepsilon_{13} = \varepsilon_g(Hg_{1-\omega}Mn_\omega Te) \end{aligned}$$

Experimental studies of the energy spectrum of $Hg_{1-x-y}Cd_xMn_yTe$ confirmed the validity of the chosen model and the obtained analytical expression for $E_g(x, y, T)$ in the framework of this model [36, 37].

It follows from the above performed analysis of literature data that the spin-independent properties of narrow-gap $Hg_{1-x-y}Cd_xMn_yTe$ and $Hg_{1-x}Mn_xTe$ solid solutions are largely similar to those of $Hg_{1-x}Cd_xTe$ solid solutions.

8.3 Electrical Properties of $Hg_{1-x}Mn_xTe$ and $Hg_{1-x-y}Cd_xMn_yTe$ Semimagnetic Semiconductors

The electrical properties of $Hg_{1-x}Mn_xTe$ solid semimagnetic solutions as a function of composition, in a magnetic field and in the absence of the magnetic field, are discussed in a number of studies [8, 38–43]. This review will focus on more recent works performed on more qualitative materials.

The dependence of the intrinsic carrier concentration on the composition and temperature obtained using the Kane dispersion law and the effective mass of the heavy holes $m_p = 0.5m_0$ is [9]

$$\begin{aligned} n_i(x,T) &= (4.65 - 1.59x + 0.00264T - 0.017xT + 34.15x^2) \\ &\times 10^{14}\varepsilon^{3/4}T^{3/2} \cdot \exp\left(-5802^{\varepsilon_y}/T\right) \text{cm}^{-3} \end{aligned} \tag{8.14}$$

where $\varepsilon_{\mathcal{H}}$ is expressed in electron volts. This expression is valid in the temperature range $17 \le T \le 350$ K and composition range $0.07 \le x \le 0.20$. The dependence is somewhat different from (8.11), and is also given in [13].

Various methods were used to obtain a sufficiently homogeneous composition of crystals and epitaxial layers of $Hg_{1-x}Mn_xTe$ solid solutions. Mani et al. [44] investigated the degree of uniformity of $Hg_{1-x}Mn_xTe$ crystals with $x = 0.125$ and $Hg_{1-x}Cd_xTe$ with $x = 0.21$ grown by solid-state crystallization, and have found that the composition distribution along the length of the ingot of these solid solutions is approximately the same. Highly homogeneous in composition (Δx no more than 0.003) monocrystalline $Hg_{1-x}Mn_xTe$ ingots with dislocation density up to 3×10^5 cm^{-2} without low-angle boundaries were obtained by zone melting in of a solution of tellurium melt [47]. Similar results were obtained when growing $Hg_{1-x}Mn_xTe$ crystals with x $\sim$ 0.1, by a modified zone melting method [45]. It should be

noted that the grown bulk crystals have p-type conductivity and typically a high concentration of charge carriers 10^{17}–10^{18} cm^3, caused by mercury vacancies, similarly to $Hg_{1-x}Cd_xTe$ solid solutions. However, $Hg_{1-x}Mn_xTe$ single crystals obtained by a modified vertical Bridgeman method at a rate of growing of 0.4 mm/h and temperature gradient 50 K/cm, were found to have the hole concentration $p = (1–4) \times 10^{16}$ cm^{-3} and mobility μ_h =s (400–500) cm^2/(Vs) at the temperature of liquid nitrogen [46].

To reduce the concentration of holes and to produce electronically conductive material, the prolonged annealing of the grown crystals or of epitaxial layers of *p*-type conductivity in mercury vapor is used [45, 47–50]. Annealing leads to a drastic reduction in the mercury vacancy concentration, resulting in a material with a reduced concentration of holes or n-type material, with the free electron density of the order of 10^{15} cm^{-3}, and the mobility $\mu_n = (10^4–10^5)$ cm^2/(Vs) depending on the composition. The studies of galvanomagnetic properties confirm that, similarly to $Hg_{1-x}Cd_xTe$, the electron mobility is twice higher than the mobility of holes. Therefore, one can suggest that the *p*-type $Hg_{1-x}Mn_xTe$ crystals have mixed-type conductivity in a fairly wide range of temperatures. The investigations of crystals of quaternary $Hg_{1-x-y}Cd_xMn_yTe$ solid solutions by electron paramagnetic resonance method have shown that annealing in mercury vapor also leads to some redistribution of atoms and to a more ordered state [51].

Anomalies in the temperature dependence of the Hall coefficient in *p*-type $Hg_{1-x-y}Cd_xMn_yTe$ quaternary solid solutions, similar to those observed in $Hg_{1-x}Cd_xTe$, were studied by Gheorghita et al. [42]. A hopping conductivity mechanism related to the restructuring of the acceptor states due to ion exchange interaction was observed in the p-type $Hg_{1-x}Cd_xTe$ material [52–54]. These authors also explained the formation of the S-shaped current-voltage characteristic in the given material, and the occurrence of non-equilibrium distribution of charge carriers in the impurity zone at the impact ionization [53].

In contrast to $Hg_{1-x}Cd_xTe$ solid solutions, for which the behavior of impurities was studied in a large number of works (see. [55–57]), this issue is still in the early stages of research in the semimagnetic semiconductors, particularly in $Hg_{1-x}Mn_xTe$ and $Hg_{1-x-y}Cd_xMn_yTe$.

The production of high-quality epitaxial layers of $Hg_{1-x}Mn_xTe$ and $Hg_{1-x-y}Cd_xMn_yTe$ from tellurium solution-melts on substrates of cadmium telluride was reported for the first time by Bazhenov et al. [38] and Mironov et al. [58].

The electrical properties and the mechanisms of scattering of electrons and holes have been researched recently in details in a wide range from room temperature to the temperature of liquid helium in epitaxial layers of $Hg_{1-x}Mn_xTe$ with *n*- and *p*-type conductivity and with different composition [59–63]. In these studies, single-crystal layers were grown by liquid-phase method on substrates of cadmium telluride, sapphire or polished quartz from tellurium solution melts. The samples were of *p*-type conductivity with the concentration and mobility of holes about 10^{17} cm^{-3} and 77 K. The concentration of holes was reduced and layers of n-type

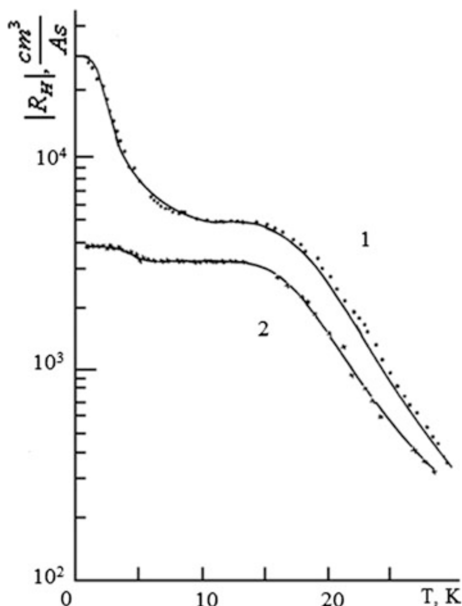

Fig. 8.2 Dependence of Hall coefficient R_H on temperature for $Hg_{1-x}Mn_xTe$; *1*—$x = 0.105$; *2*—$x = 0.095$

conductivity were obtained by annealing of samples in mercury vapor. In most of the layers of n-type conductivity, the Hall coefficient is practically constant in the region of impurity conductivity up to 4.2 K. However, in some cases there was an increase in value of $|R_H|$ at low temperatures, indicating the presence of local levels in the bandgap.

The dependence of $R_H(T)$ for two layers with $x = 0.105$ and $x = 0.095(\varepsilon_g > 0)$ is shown in Fig. 8.2.

These relationships have been explained by the presence of an energy level at about 5 meV below the conduction band along with very shallow donors and acceptors, the deep acceptor concentration being equal to $1 \times 10^{15}\,\text{cm}^{-3}$ and $2.4 \times 10^{14}\,\text{cm}^{-3}$ in the layers 1 and 2, respectively. The curves in Fig. 8.2 represent the solution of the equation of electrical neutrality for these two samples.

A model with two independent acceptor levels in the bandgap was adopted in order to explain the dependence *R*(*T*) in the region of impurity conduction. The dashed curves in Fig. 8.3 provide solutions to the equation of electrical neutrality for these layers for the model with the following parameters:

$$\begin{aligned} &\varepsilon_{a1} = 1.6\,\text{meV}, \qquad N_{a1} = 6 \times 10^{15}\,\text{cm}^{-3} \qquad (x = 0.08) \\ &N_{a2} = 3 \times 10^{15}\,\text{meV}, \quad N_d = 5.8 \times 10^{15}\,\text{cm}^{-3} \qquad \varepsilon_{a2} = 21\,\text{meV} \end{aligned}$$

Figure 8.3 shows the temperature dependence of the Hall coefficient and electrical conductivity for two $p - Hg_{1-x}Mn_xTe$ layers with $x = 0.08$ and $x = 0.127$, (curves 1, 1′ and 2, 2′, respectively).

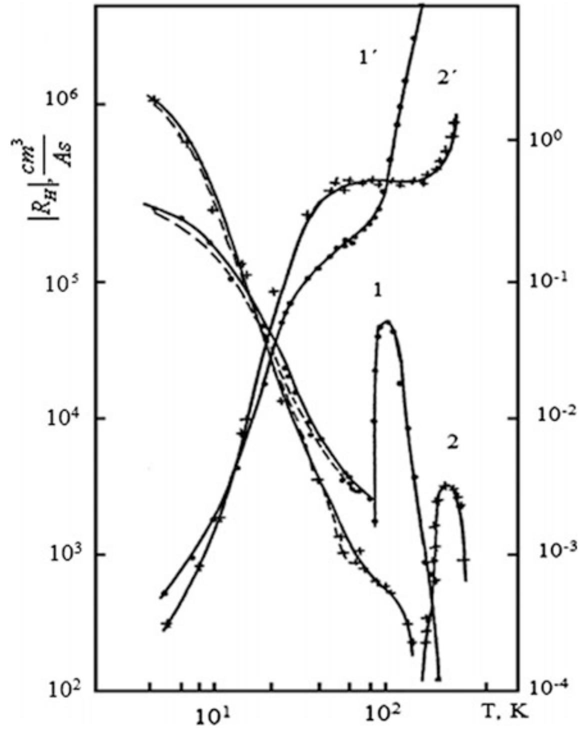

Fig. 8.3 Dependence of R_H and electrical conductivity (σ) on temperature for epitaxial layers of *p-*$Hg_{1-x}Mn_xTe$
1, *1′*—$x = 0.08$;
2, *2′*—$x = 0.127$

$$\varepsilon_{a1} = 2\,\text{meV}, \quad N_{a1} = 1.4 \times 10^{15}\,\text{cm}^{-3} \quad (x = 0.127)$$
$$N_{a2} = 1.2 \times 10^{16}\,\text{meV}, \quad N_d = 1.38 \times 10^{15}\,\text{cm}^{-3} \quad \varepsilon_{a2} = 19\,\text{meV}$$

Here ε_a is the value of the acceptor levels energy above the valence band, N_a, N_d are concentrations of acceptor and donor centers.

The temperature dependence on the mobility of electrons and holes in the researched layers of *n*- and *p*-type conductivity for these compositions are shown in Figs. 8.4 and 8.5.

The analysis showed that at high temperatures the main mechanism of scattering is the scattering by polar optical phonons (similarly to $Hg_{1-x}Cd_xTe$ solid solutions). In addition, Trifonova et al. suggested that one must take into account the scattering of electrons on heavy holes [60], the concentration of which is high enough and which can be regarded as fixed ions with respect to the electrons due to the large differences in their effective masses.

At low temperatures, both the electrons and holes are scattered on charged donor and acceptor centers with a total concentration in the studied layers of about (0.5–2.0) × 10^{16} cm^{-3}. The solid curves in Fig. 8.4, and the dashed curves in Fig. 8.5 present the results of theoretical calculations of μ_n and μ_p, which explain satisfactorily the observed temperature dependence.

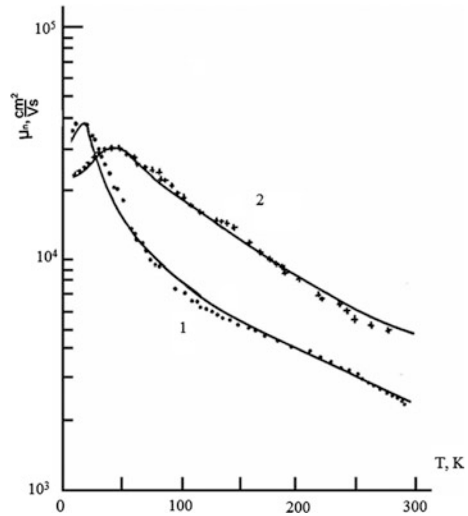

Fig. 8.4 The temperature dependence of the electron mobility for epitaxial layers *n-*$Hg_{1-x}Mn_xTe$; *1*—x = 0.08; *2*—x = 0.127

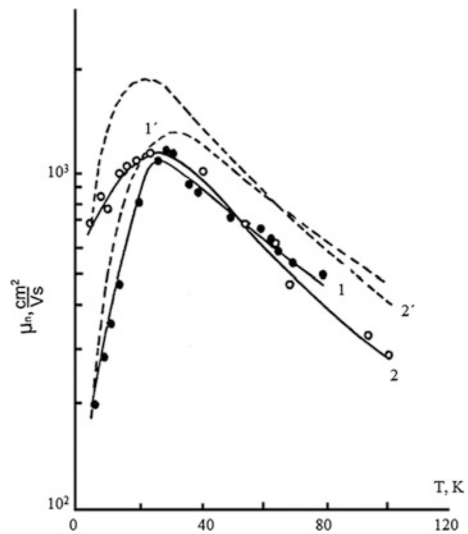

Fig. 8.5 The temperature dependence of the mobility of holes in semimagnetic semiconductors in *p-* $Hg_{1-x}Mn_xTe$ (experiment and theory) *1,1′*—*x* = 0.08*; 2,2′*—*x* = 0.127

Extra channels of scattering due to the presence of manganese in the lattice of $Hg_{1-x}Mn_xTe$ solid solution were not revealed in the above mentioned works. In our opinion, this suggests that in the absence of a magnetic field the energy structure of semimagnetic $Hg_{1-x}Mn_xTe$ and nonmagnetic $Hg_{1-x}Cd_xTe$ alloys is, in fact, the same.

We studied in details the electrical properties of $Hg_{1-x-y}Cd_xMn_yTe$ epitaxial layers and the mechanism of electrons and holes scattering in a wide range of temperatures and compositions [38, 41, 42].

Brandt et al. reported the results of investigation of electrical properties of $p - Hg_{1-x-y}Cd_xMn_yTe$ epitaxial layers with the width of the bandgap of 250–350 meV obtained by liquid-phase epitaxy from solutions-melts enriched with tellurium [38]. Measurements of the Hall coefficient and conductivity were carried out according to standard procedures on direct current in magnetic fields 0.6–1.5 kOe in the range of temperatures of 4.2–300 K. A number of features of the temperature dependence on the Hall coefficient was identified [38]. The Hall coefficient was found to change the sign from negative to positive as the temperature decreases, this change being associated with the transition of the intrinsic conductivity to the impurity conductivity. It was also found that the Hall coefficient further increases exponentially due to the freezing of holes on a localized acceptor level.

The increase of the Hall coefficient with decreasing the temperature slows down abnormally at $T < 30$ K. This behavior of R at low temperatures is typical for $Hg_{1-x}Cd_xTe$ crystals [64]. The analysis of numerous studies (see, e.g. [64]) shows that the $Hg_{1-x}Cd_xTe$ epitaxial layers obtained during the epitaxy process from solutions enriched with tellurium as well as monocrystals have p-type conductivity with concentration of uncompensated acceptors due to intrinsic defects $N_A - N_D = (0.5–5) \times 10^{17}$ cm^{-3}. The concentration of compensating donors N_D is on the level of 10^{17} cm^{-3}. In order to reduce $N_A - N_D$ to the value of (0.1–1) $\times$ 10^{16} cm^{-3}, which is required for the creation of diode structures in narrow-gap semiconductors, annealing in mercury vapor is carried out. Brandt et al. suggested that the value $N_A - N_D$ in $Hg_{1-x-y}Cd_xMn_yTe$ layers is by 1–2 orders of magnitude lower as computed to epitaxial $Hg_{1-x}Cd_xTe$ layers, while the concentration of donors is at the same level [38]. It was also suggested that the proximity of values of ε_A in $Hg_{1-x}Cd_xTe$ and $Hg_{1-x-y}Cd_xMn_yTe$ reflects the similar nature of the acceptors, which are associated, most probably, with intrinsic defects of a similar nature. Their lower concentration determines a narrower region of homogeneity in this system with respect to the defects acting as acceptors, which are associated with the introduction of the manganese in the composition of solid solution.

8.4 Photoelectrical Properties

The processes of generation and recombination of carriers basically determine the operation of the most important types of semiconductor devices such as radiation detectors, lasers, transistors, photodiodes, phototransistors, etc. The processes determine the lifetime of nonequilibrium charge carriers—a basic photoelectric parameter of semiconductor materials.

The investigation of photoelectrical properties of bulk single crystals and epitaxial layers of $Hg_{1-x}Mn_xTe$, $Hg_{1-x-y}Cd_xMn_yTe$ as well as investigation of non-equilibrium processes has been started quite recently. Let us review the results of this study carried out in a magnetic field as well as in the absence of a magnetic field.

8.4.1 Photoelectrical Properties of $Hg_{1-x}Mn_xTe$ and $Hg_{1-x-y}Cd_xMn_yTe$ in the Absence of Magnetic Field

A first study of photoconductivity of semimagnetic $Hg_{1-x}Mn_xTe$ alloys at low temperatures was reported by Gelmont et al. [65]. The authors measured the photoconductivity spectra of $Hg_{1-x}Mn_xTe$ single crystals with $0.13 \leq x \leq 0.15$ and $0.2 \leq x \leq 0.30$, grown by the Bridgeman method (p $\sim$ 10^{18} cm^{-3}) and annealed in mercury vapour ($p = 3 \times 10^{15}$–2×10^{16} cm^{-3} at 77 K). Two peaks identified as "band-to-band" and "acceptor-to-conduction band" transitions have been found in the photoconductivity spectra of samples with any composition. The lifetime of carriers was measured to be around (6–9) μs.

The recombination of nonequilibrium charge carriers in $Hg_{1-x}Mn_xTe$, $Hg_{1-x-y}Cd_xMn_yTe$ bulk crystals was studied in a series of papers [45, 65–72]. Recombination centers with energy level around 110 meV above the valence band have been detected by means of deep level transient spectroscopy in $Hg_{1-x}Mn_xTe$ of p-type conductivity with $x = 0.18$ and $x = 0.20$ [69]. The concentration of these centres and their effective capture cross section of holes and electrons were found to be 5×10^{15} cm^{-3} and 10^{-17} cm^{-2}, respectively. The recombination of carriers was also analysed in single crystals grown by a modified method of zone melting and annealed in mercury vapour in order to homogenize the solid solution and to reduce the concentration of charge carriers [45, 70, 71]. It was found that the lifetime of no equilibrium charge carriers in the temperature range from room temperature to liquid nitrogen in the $p - Hg_{1-x}Mn_xTe$ material with the composition $x \sim 0.1$ with uncompensated acceptor concentration 10^{15}–10^{16} cm^{-3} is determined by the impact recombination processes, namely, by the impact recombination in collisions of heavy holes with transmission of the released energy to the light holes and by the impact recombination in electron-electron collisions [70]. In contrast to this, in $n - Hg_{1-x}Mn_xTe$ obtained by $p \rightarrow n$ conversion of conductivity as a result of crystal annealing, the lifetime in the region of impurity conduction (at low temperature) was found to be determined by carrier recombination on Shockley-Reed centres with an energy level located at 65–67 meV above the top of the valence band [45]. According to estimations, the concentrations of recombination centres in the investigated crystals are in the range from 4.7×10^{14} to 1.7×10^{15} cm^{-3}.

Two recombination levels situated about 125 meV and 70 meV above the valence band top were found in wider bandgap $n - Hg_{1-x-y}Cd_xMn_yTe$ $x = 0.28$–0.35; $y = 0.01$–0.02 quaternaly compounds [71]. The position of these levels is close to the energy levels of recombination centres found in $Hg_{1-x}Mn_xTe$ crystals [45, 69]. The photoconductivity spectra of epitaxial $Hg_{1-x}Mn_xTe$ layers grown by a combined procedure using vapour-phase and liquid-phase epitaxy as well as the photoconductivity spectra of bulk single crystals consist of two bands associated with band-to-band and level-to-band transitions [73, 74]. The distance between the peaks in the photoconductivity spectra increases from 15 to 55 meV when the content of manganese telluride in layers is increased from 12 to 15 %. The lifetime changes slightly at low temperatures (77–110) K in layers with local inhomogeneity

of the electron density at the surface, and this lifetime is always longer than the one in electrically homogeneous samples.

The recombination and trapping processes of nonequilibrium charge carriers in compensated $Hg_{1-x}Mn_xTe$ layers with $x \sim 0.1$ $n, p < 10^{15}$ cm^{-3} at 77 K, grown by liquid phase epitaxy and subjected to prolonged annealing in mercury vapour, have been studied in details in a series of papers [75–77]. The results of these studies demonstrated that the lifetime in the region of intrinsic conductivity is limited by the impact recombination processes, while it is determined by the recombination on Shockley-Reed centres in the extrinsic region. The energy levels of recombination centers in p-type layers are situated at (26–30) meV below the conduction band bottom, while they are located at about 50 meV above the valence band top in n-type layers [73] (Fig. 8.6).

At low temperatures ($T \leq 70$ K for the n-layers and $T \leq 25$ K for p-layers) the lifetime is determined by recombination through these levels and by trapping of minority non-equilibrium carrier on shallow levels (8–10) meV (Fig. 8.7). The recombination of carriers has been also investigated in $Hg_{1-x}Mn_xTe$ and $Hg_{1-x-y}Cd_xMn_yTe$ grown by liquid phase epitaxy [78–80]. It should be noted that there are many similarities in the photoelectric properties of $Hg_{1-x}Mn_xTe$ solid solutions with x = 0.1–0.5 and the more intensively studied $Hg_{1-x}Cd_xTe$ solid solutions with x = 0.2–0.3 (for comparison, see, e.g. [81–84]).

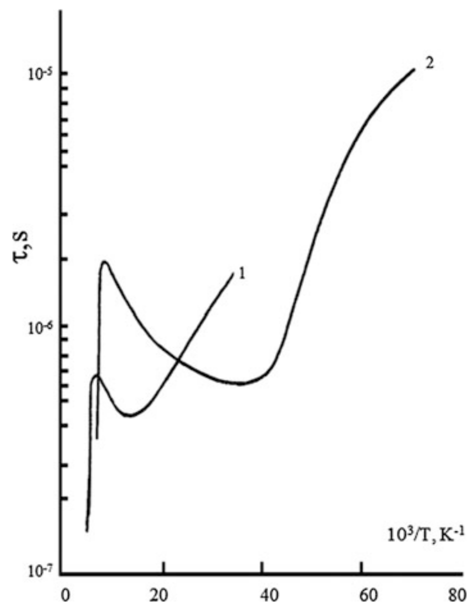

Fig. 8.6 Dependence of the lifetime (τ) on *1/T* for $Hg_{1-x}Mn_xTe$; *1*—*n*-type; *2*—*p*-type

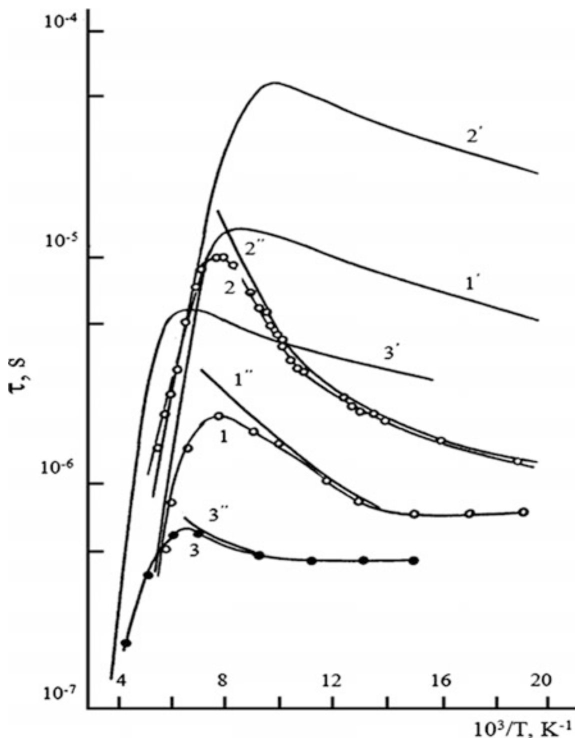

Fig. 8.7 The temperature dependence of the lifetime of nonequilibrium charge carriers in $Hg_{1-x}Mn_xTe$ epitaxial layers. (*1*: $x = 0.097$ and $N_a - N_d = 4 \times 10^{14}\ cm^{-3}$; *2*: $x = 0{,}10$ and $N_a - N_d = 1 \times 10^{14}\ cm^{-3}$; *3*: $x = 0.11$ and $N_d - N_a = 5.5 \times 10^{14}\ cm^{-3}$; *1′, 2′, 3′*—lifetimes due to the inter-band recombination processes *r, 1, 7; 1″, 2″, 3″*—lifetimes due to recombination on Shockley—Reed centers)

8.4.2 Photoelectrical Properties in a Magnetic Field

As shown above, in the absence of the magnetic field the properties of $Hg_{1-x}Mn_xTe$, $Hg_{1-x-y}Cd_xMn_yTe$ semimagnetic semiconductors are similar to those of conventional non-magnetic semiconductors of the $Hg_{1-x}Cd_xTe$ type, having similar band parameters. The exchange interaction caused by the presence of manganese ions in the lattice results in a substantial rearrangement of the energy spectrum of free and localized carriers when a semimagnetic semiconductor is placed in an external magnetic field. The corresponding photoelectric properties of semimagnetic semiconductors will also change significantly under the influence of the exchange interaction.

The photoconductivity spectra of $p - Hg_{1-x}Mn_xTe, (0.2 \leq x \leq 0.25)$, $(0.12 \leq x \leq 0.15)$; single crystals and $p - Hg_{1-x-y}Cd_xMn_yTe$ epitaxial layers in a magnetic field at helium temperatures have been measured in a series of papers [65–68, 72, 73, 82]. The photoconductivity was measured in the Faraday geometry $\vec{q}\,\|\,\vec{B} \perp \vec{E}$, where $\vec{q}$ is the electromagnetic wave vector. It was experimentally found that the photoconductivity signal for $Hg_{1-x}Mn_xTe$ sharply decreases with increasing magnetic field intensity [65, 66], when the magnetic field is turned on, in

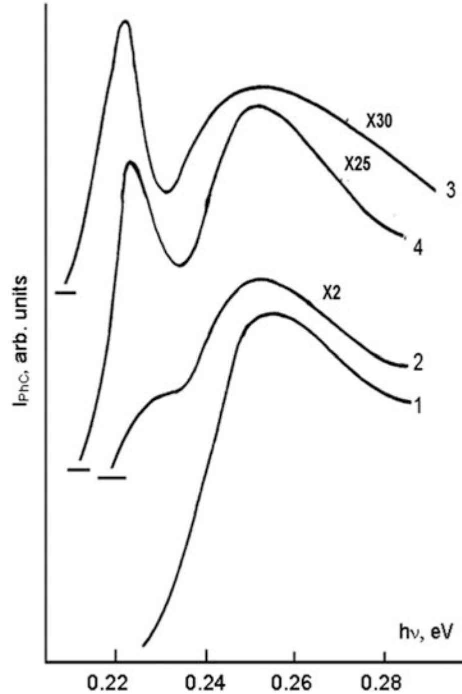

Fig. 8.8 Photoconductivity spectra in a magnetic field for the sample $Hg_{0.86}Mn_{0.14}Te$ at T = 4.2 K

contrast to $Hg_{1-x}Cd_xTe$, while the spectrum of photoconductivity shifts abnormally to longer wavelengths.

The study of photoconductivity in a magnetic field has shown that the photoconductivity signal has a non-monotonic dependence on the magnetic field strength. Figure 8.8 shows the spectra of photoconductivity for $Hg_{0.86}Mn_{0.14}Te$ measured in an external magnetic field. A long-wavelength peak appears as the magnetic field gets stronger. This peak increases in intensity and shifts to longer wavelengths with increasing the magnetic field strength.

Georgitse et al. measured the photoconductivity in a magnetic field under the excitation by circularly polarized light σ^+, σ^- [66], and found that photoconductivity spectra have a complex structure. For instance, Fig. 8.9 shows the photoconductivity spectra of the $p - Hg_{0,78}Mn_{0,22}Te(\sigma^+, \sigma^-)$ alloy in a magnetic field of B = 6T at 4.2 K and the photoluminescence spectrum of the same alloy in the same field. These investigations confirmed that the fine structure observed in the photoconductivity spectra measured in both σ^+ and in σ^- polarizations can be associated with the paramagnetic band splitting. The identification of the observed structure is performed taking into account the selection rules and by comparing the experimental spectra with the results of calculations with the following parameters: the width of the bandgap and the manganese content $\varepsilon_H = 0.533\,\text{eV}; x = 0.22$; the exchange interaction integral for the conduction band $N_0\alpha = -0.45\,\text{eV}$; the effective temperature $T_0 = 54\,\text{K}$; the effective spin $S_0^{(n)} \sim 1$. The following transitions

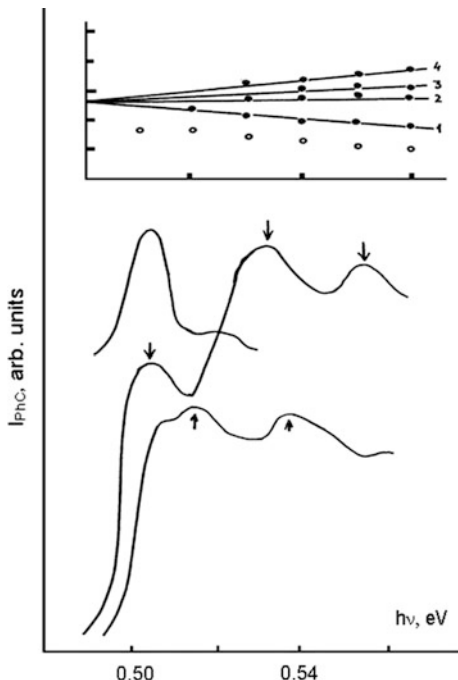

Fig. 8.9 Photoconductivity spectra of the alloy $Hg_{1-x}Mn_xTe$ at $\sigma^+(1)$ and $\sigma^-(1)$ polarization in a magnetic field $B = 6T$

are identified in σ^- polarization $b_n(-1) \to b_c(0); a_n(-1) \to a_c(0)$, and in σ^+ polarization $b_n(1) \to b_c(0); a_n(1) \to a_c(0)$, as well as the impurity transition in σ^+ polarization $|-3/2 > \ \to b_c(0)|$.

As one can see from the results shown in Fig. 8.9, the authors supposed that the low-energy shoulder at the edge of photoconductivity (Peak 1) in σ^- polarization corresponds to the transition $|+3/2 > \ \to a_c(0)|$. The estimated paramagnetic splitting of the ground state of the acceptor, defined as the difference between the energies of $|-3/2 > \ \to b_c(0)|$ and $|+3/2 > \ \to a_c(0)|$ transitions proved to be around 3 meV in a field of 6*T*.

Further, by using the experimentally determined value of the paramagnetic spin splitting, a value of ~ 10 was obtained for the g factor of a hole on the acceptor (g^h_{eH}). By using this estimate for g^h_{eff}, the value of $S_0^{(h)}$ was calculated with the following fitting parameters of the valence band: the exchange integral $N_0\beta = 0.80\,\text{eV}$, the effective mass of the heavy holes $m^*_{hh} = 0.4m_0$. The effective spin $S_0^{(h)}$ of the manganese ions Mn^{++} in the acceptor proved to be of the order of ~ 0.1. These results are consistent with data obtained from optically detected magnetic resonance (ODMR) studies for this alloy [85].

8.5 Photoluminescence Properties

8.5.1 Photoluminescence Properties in the Absence of Magnetic Field

The first results concerning the research of photoluminescent properties of $Hg_{1-x}Mn_xTe$ single crystals with $(0.13 \leq x \leq 0.3)$ and $Hg_{1-x-y}Cd_xMn_yTe$ epitaxial layers have been published at the very beginning of 90th [66–68, 72]. A combined research of photoconductivity and photoluminescence in the reflection and transmission geometries allowed one to identify the observed structure of the photoluminescence spectra. Typical photoluminescence spectra in the absence of a magnetic field for $p - Hg_{1-x}Mn_xTe$ measured at 4.2 K are shown in Fig. 8.10.

The short-wavelength band B in the photoluminescence spectrum corresponds to the interband radiative transitions. The long-wavelength band A in the spectrum is related to "conduction band—acceptor" transitions according to its energy position and behaviour. The intensity of the band A decreases with decreasing the concentration of the acceptor. A similar structure was revealed in the photoluminescence spectra of alloys in the absence of a magnetic field.

Georgitse et al. reported the results of a photoluminescence study of $Hg_{1-x}Mn_xTe(0,19 \leq x \leq 0,30)$ solid solutions in a temperature range of 2–200 K in the absence of a magnetic field [68]. It was shown that in alloys enriched with manganese there are optical transitions between states strictly connected to the valence band. These states, along with shallow acceptors, are related to anti-bonding states with an incomplete d-shell $Mn^+(3d^6)$ in the bandgap on the shallow acceptor level, usually attributed to intrinsic defects. An energy model was proposed in this paper which explains the observed features of the photoluminescence spectra. According to this model, the level related to manganese Mn^+ in $Hg_{1-x}Mn_xTe(x < 0,20)$ diluted semimagnetic alloys is located in the conduction band and it is not revealed in radiative processes. However, this level goes into the

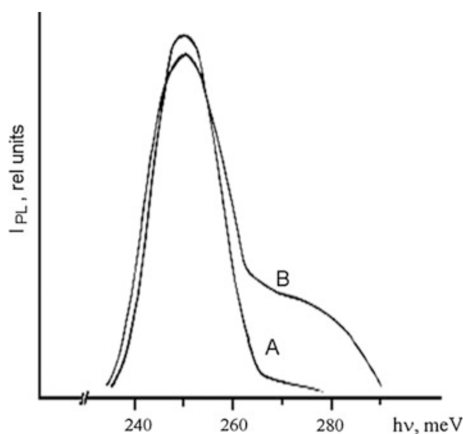

Fig. 8.10 Photoluminescence spectrum $p\text{-}Hg_{1-x}Mn_xTe$ (x = 0.14) at T = 4.2 K

bandgap in samples with $x > 0.20$ and it participates in recombination processes. The degeneration of the Mn^{+} level with the conduction band is lifted in samples with $x = 0.24$, while the depth of the $3d^5(Mn^{++})$ level in the valence band is estimated to be around 4.9 eV.

The analysis of $Hg_{1-x}Mn_xTe$ and $Hg_{1-x-y}Cd_xMn_yTe$ photoluminescence spectra for a wide range of temperatures in the absence of a magnetic field allowed to defined the dependence on the bandgap width upon temperature and composition of alloys [65, 67]. The depth of the acceptor level participating in radiative transitions was found to be around 18–20 meV, and it was attributed to intrinsic defects (mercury vacancies).

New papers have been published in recent years concerning the study of optical of narrow-gap semimagnetic semiconductors [86–99].

Mazur [91] investigated the photoluminescence spectra of $Hg_{0.651}Cd_{0.335}Mn_{0.014}Te$ at low temperatures (Figs. 8.11 and 8.12) by means of photoluminescence excitation spectroscopy technique described by Fuchs et al. [9, 100]. The results led to the conclusion about the observation of exciton states in narrow-gap semimagnetic semiconductors [91].

8.5.2 Photoluminescence Properties in a Magnetic Field

The first results concerning the research of photoluminescent properties of $Hg_{1-x}Mn_xTe$ and $Hg_{1-x-y}Cd_xMn_yTe$ alloys in a magnetic field at low temperatures have also been published at the very beginning of 90th [66–68, 72]. It was found in these works that the intensity both A and B bands increases significantly when the magnetic field is turned on at low temperatures, and their maximum shifts to the

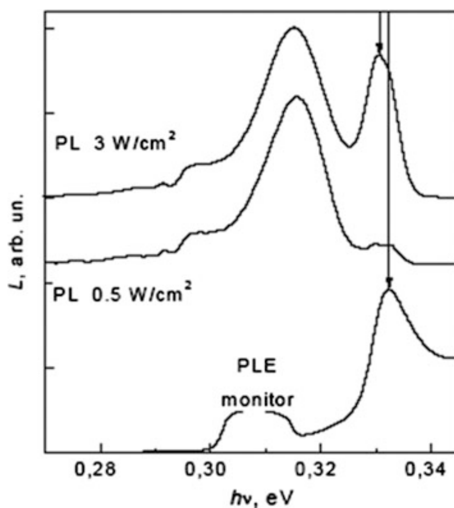

Fig. 8.11 The photoluminescence spectra (at the *top*) $Hg_{0.651}Cd_{0.335}Mn_{0.014}Te$ measured at temperature T = 12 K, at two levels of excitation [114]

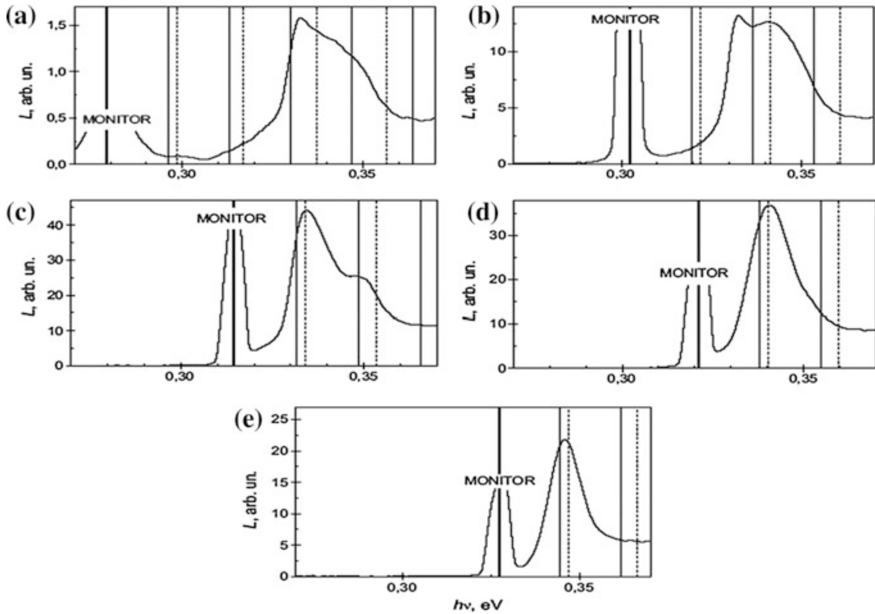

Fig. 8.12 The Photoluminescence excitation spectra at different positions of the monitor: **a** 279.0 meV; **b** 302,5 meV; **c** 314.5 meV; **d** 321.0 meV; **e** 327.5 meV. *Direct* and *dashed vertical lines* indicate the position of the phonon replicas and monitor lines ($E_m + nE_{LO}$, where n is an integer)

long wavelength region of the spectrum with increasing the magnetic field strength (Fig. 8.13), in contrast to conventional semiconductors $Hg_{1-x}Cd_xTe$, $InSb$, in which the photoluminescence bands shift to short wavelengths, and their intensity remains practically unchanged. Besides the shift of the maxima of photoluminescence bands to the long wavelengths region of the spectrum in a magnetic field, the decrease of the distance between them was also observed in the experiment. It was shown that the dependence of the radiation intensity non-monotonically varies with changing the magnetic field strength (Fig. 8.14) [67].

In weak magnetic fields the photoluminescence intensity increases rapidly with increasing magnetic field strength and it reaches a maximum at a certain value of $B = B_{\max}$. The value B_{max} depends on the composition, on the content of manganese, it being shifted toward large fields with increasing the manganese content in the crystal lattice of the semimagnetic alloy. A significant increase in photoluminescence intensity was observed in a magnetic field. For instance, for the band A in a $Hg_{1-x}Mn_xTe$ (x = 0.13) sample the photoluminescence intensity at $B = B_{\max}$ increases by about 50 times as compared to the photoluminescence intensity at B = 0. At the same time, a further increase of the strength of the magnetic field $B > B_{\max}$ leads to a decrease in the photoluminescence intensity. In a magnetic field the radiation is polarized [89].

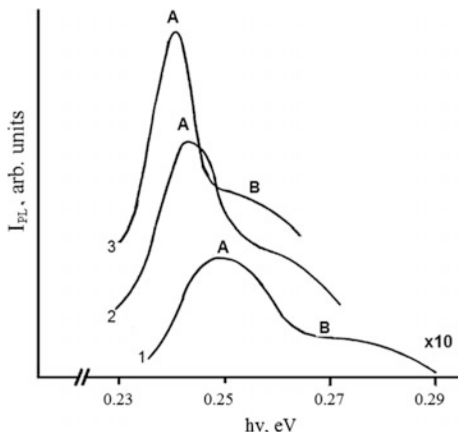

Fig. 8.13 The photoluminescence spectra in a magnetic field of the alloy $Hg_{1-x}Mn_xTe$ (x = 0.14) at 4.2 K. (*1*) $B = 0$; (*2*) $B = 0.5T$; (*3*) $B = 1.0T$

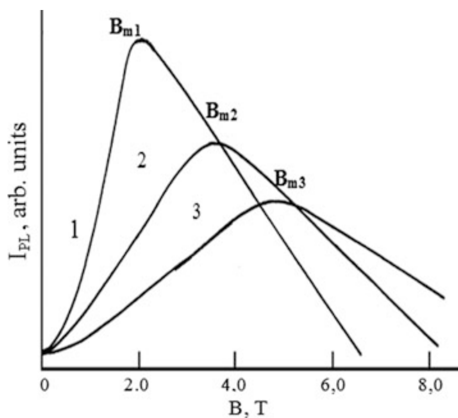

Fig. 8.14 The experimental dependence of the photoluminescence intensity $Hg_{1-x}Mn_xTe$ on the magnetic field induction for the three compositions: *1*—x = 0.13; *2*—x = 0.14; *3*—x = 0.15

A similar situation was observed in $Hg_{1-x-y}Cd_xMn_yTe$ quaternary alloys [72]. The observed peculiarities of photoluminescence of $Hg_{1-x}Mn_xTe$ and $Hg_{1-x-y}Cd_xMn_yTe$ semimagnetic alloys are explained on the basis of the Pigeon Brown model taking into account the exchange interaction. The energy of other transitions allowed by the selection rules in the Faraday or Voigt geometry increases with increasing the magnetic field strength. Taking into account the population of the sublevels at low temperatures and the large value of the spin splitting, Galazka et al. suggested in their experiments that the short-wavelength band B corresponds to the interband radiative transition $b_{\Gamma_8}(0) \to b_{\Gamma_6}(-1)$, which actually determines the width of the bandgap in the magnetic field [67]. Therefore, the displacement of the *B*-band maximum in the long-wavelength region of the spectrum with increasing the magnetic field strength is a direct consequence of the restructuring of the semimagnetic semiconductor energy spectrum as a result of the exchange interaction.

It was show that, in the frame of the proposed model, the energy decreases only for the transition $b_{\Gamma_8}(-1) \rightarrow b_{\Gamma_6}(0)$ with increasing the magnetic field strength in the Faraday configuration in σ^- polarization.

The unusual behavior of the dependence of photoluminescence intensity upon the magnetic field strength was explained taking into account the behavior of the energy acceptor energy in semimagnetic semiconductors placed in a magnetic field [101]. In was shown that the exchange interaction of holes with manganese ions leads to a sharp decrease of the acceptor ionization energy in relatively weak magnetic fields, when the exchange interaction energy is larger than the acceptor ionization energy ε_A at $B = 0$, in semi-magnetic $Hg_{1-x}Mn_xTe$ alloys with fourfold degenerated valence band in the Γ-symmetry point.

Therefore, if in the absence of the magnetic field the energy of the acceptor ground state is of the order of Bohr energy of a the heavy hole

$$\varepsilon_A = \frac{4}{9}\varepsilon_{hh} = \frac{2m_{hh}^* e^4}{9\chi^2\hbar^2} \tag{8.15}$$

where m_{hh} is the mass of the heavy hole, χ is the dielectric permeability, $\hbar$ is Planck's constant, then in the magnetic field the acceptor ionization energy is of the order of Bohr energy of the light hole. This dependence of the acceptor ionization energy on the magnetic field strength occurs in magnetic fields, when the light hole becomes quantized. In even stronger fields, when heavy holes become quantized, the ionization energy of the acceptor will again be of the order of heavy hole energy.

The probability of radiative recombination is proportional to the effective volume of the hole wave function. The nonmonotonous dependence of the ionization energy of the acceptor leads to a change in the effective volume of the hole wave function, which according to Galazka et al. should be reflected in the luminescence intensity in the magnetic field [67]. If $B = 0$, the effective volume of the hole wave function is $V_{eff} \sim a_{hh}^3$, where $a_{hh} = \hbar^2\chi/m_{hh}^* e^2$ is the Bohr radius of a heavy hole. It was shown that in semimagnetic semiconductors the hole wave function in a magnetic field is anisotropic [102]. Its transverse size is of the order of $a_\perp = \hbar^2\chi/m_\perp^* e^2$, where $m_\perp = m_0(\tilde{\gamma} + \gamma_1)$, m_0 is the free electron mass, $\tilde{\gamma}, \gamma_1$ are the modified Luttinger parameters. The value of $m_\perp^*$ is of the order of light hole mass. The longitudinal size of the wave function is of the order of $a_\perp(m_\perp/m_{hh})^{1/3}$. Thus, V_{eff} increases with increasing the magnetic field strength and reaches values of the order $a_{hh}^{1/3} a_\perp^{8/3}$. In magnetic fields, when the heavy hole becomes quantized, the V_{eff} value will decrease with increasing the magnetic field strength. In the ultra-quantum limit the transverse size of the hole wave function is of the order of the magnetic length $\lambda = (\hbar c/eB)^{1/2}$, and the longitudinal size is $\lambda^{2/3} a_{hh}^{1/3}$, i.e. $\lambda^{8/3} a_{hh}^{1/3}$. Thus, a maximum should be observed on the curve representing the dependence of the photoluminescence intensity upon the magnetic field for the transitions "conduction band-to-acceptor".

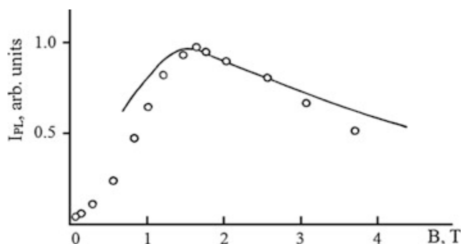

Fig. 8.15 The dependence of photoluminescence intensity in $Hg_{0.868}Mn_{0.132}Te$ upon the magnetic field, *circles*—experiment, *curve*—theory

The theoretical curve of the dependence of photoluminescence intensity upon the magnetic field strength calculated by Bykhovckiy et al. by using the wave functions of the hole on the acceptor is shown in Fig. 8.15 [102].

The experimental dependence of the photoluminescence intensity upon the magnetic field strength for the transitions "conduction band-to-acceptor" measured at 1.8 K for the $Hg_{0.868}Mn_{0.132}Te$ alloy is shown in the figure for comparison. The presented results demonstrate a good agreement between theory and experiment.

Thus, as a result of the performed research [67, 102], it was conclusively demonstrated that the non-monotonic dependence of the photoluminescence intensity for transitions "conduction band-to-acceptor" upon the magnetic field strength is connected with the behaviour of the ionization energy of the acceptor in a magnetic field. As mentioned above, the magnetic field value at which there is a maximum in the photoluminescence intensity depends on the content of manganese in $Hg_{1-x}Mn_xTe$, $Hg_{1-x-y}Cd_xMn_yTe$.

The experiments confirm also that the increase in the photoluminescence intensity in the magnetic field $B = B_{max}$ decreases with increasing the content of manganese. This behavior of the values B_{max} and $I_{FL}(B = B_{max})$ was explained taking into account the dependence of the ionization energy of the acceptor on the manganese content [65, 67]. It was also shown that the acceptor ionization energy increases with increasing the manganese content in the crystal lattice of the semiconductor [103]. Therefore, the change in the effective volume of the hole wave function at a deep acceptor is less sharp as compared to the change in the effective volume of the wave function of a hole at a shallow acceptor. Since the probability of radiative recombination is proportional to the effective volume of the wave function of the hole on an acceptor, the increase of the photoluminescence intensity in the magnetic field must decrease with increasing the manganese content.

Some oscillations have been observed on the non-monotonic dependence of the photoluminescence intensity as a function of the magnetic field strength for "conduction band-to-acceptor" transitions at high levels of excitation [67]. A certain concentration of nonequilibrium charge carriers is created in the conduction band when the photoluminescence is excited by laser radiation. A definite Fermi level corresponds to the given concentration of non-equilibrium carriers, determined by the excitation level. It was supposed that the oscillation on the dependence $I_{FL} = f(B)$ are connected with the intersection of the Fermi level with the Landau levels in a magnetic field. A method has been developed for the determination of the

concentration of the nonequilibrium carriers and the exchange parameters based on the analysis of the oscillatory structure of photoluminescence spectra in a magnetic field [67]. It was obtained for the integrals of the exchange interaction that $N_0\alpha = -0.45\,\text{eV}, N_0\beta = 0.80\,\text{eV}$. In our opinion, these data obtained directly from the experiment are the most reliable as compared to the large spread of data in the literature for these parameters.

The peculiarities of the photoluminescence spectra of $Hg_{1-x}Mn_xTe$ in a magnetic field for the composition ($0.09 < x < 0.11$) have been discussed by Fuchs et al. [97]. The strong increase of the recombination radiation and the narrowing of the line width to less than 2.5 meV in an external magnetic field was associated with the formation of a magnetic exciton polaron [97].

8.6 Magneto-Optical Properties

It is known that in semimagnetic semiconductors the spectrum of charge carriers is greatly modified as a result of the exchange interaction of their spins with the spins of the magnetic impurities. The parameters of the electronic states in such semiconductors are changed when the concentration of magnetic impurities, the temperature or the applied magnetic field is changed. The measurement of the resonant absorption of light in an external magnetic field is a powerful method for studying such states. The magneto-optical properties of $Hg_{1-x}Mn_xTe$ and $Hg_{1-x-y}Cd_xMn_yTe$ semimagnetic alloys were studied in a series of works [104–106]. The combined and cyclotron resonances have been studied in the narrow bandgap $Hg_{1-x-y}Cd_xMn_yTe$ semimagnetic alloys. This study opens up new possibilities for the elucidation of the effect of exchange interaction on the energy spectrum of these materials. The studies of the cyclotron resonance allow to determine The parameters of the energy spectrum are determined from the cyclotron resonance investigations, while the effect of the exchange interaction is assessed from the combined resonance study.

Georgitse et al. measured the optical transmission in a spectral range of 96.52–294.8 μm and a temperature range of 2–12 K in magnetic fields up to $6.5T$ in $n - Hg_{1-x-y}Cd_xMn_yTe(x = 0.03; x = 0.08; y = 0.11; y = 0.12)$ epitaxial solid solutions obtained by liquid-phase epitaxy method in a closed system on substrates of cadmium telluride. The studies were conducted on a laser magnetic spectrometer with $CH_3OH(\lambda = 96.52;\ 118.83;\ 133.2;\ 170.58)$ μm and $CH_3OD(\lambda = 145.66;\ 294.8)$ μm lasers pumped by a tunable CO_2 laser in Voigt and Faraday geometry as radiation source. The value of $N_D - N_A$ at 77 K in the investigated samples vary in a range of (4×10^{14}–1×10^{15}) cm^{-3}, the compensation degree being $\sim$0.9. The samples were illuminated during the measurements by radiation from the region of fundamental absorption in order to reduce the influence of nonuniformity in the distribution of impurities. Some lines with a complex structure have been observed in the magneto-absorption spectra [104, 105]. The form of the lines is changed with

changing the temperature. The splitting of the Landau levels in a magnetic field has been calculated using the modified model of Pigeon Brown in order to identify the observed magneto-absorption lines in the spectrum [104, 105]. The following values of the energy spectrum parameters have been used in calculations: $\varepsilon_p = 18.3\,\text{eV}$; $\Delta = 1.0\,\text{eV}$; $\gamma_1 = 3.3$; $\tilde{\gamma} = 0.3$; $k = 0.09$. Assuming that the center of the line corresponds to the cyclotron resonance, it was found that $\varepsilon_g = 0.245\,\text{eV}$ and the effective mass of the electron is $m_e^* = 2.1 \times 10^{-2} m_0$. The following parameters were used for fitting: $N_0\alpha, S_0, T_0$, and the following values were obtained for the best fitting: the efficient spin $S_0 \approx 0.95$; the effective temperature $T_0 = 10.7$ K; and the integral $N_0\alpha = -(0.38 \pm 0.02)$ eV. The energy levels of electrons of the off-diagonal matrix elements of the Hamiltonian have been theoretically calculated taking into account the antiferromagnetic interaction between the manganese ions Mn^{+2}. It was shown that this contribution can be neglected for the concentration of manganese ions Mn^{+2}(11–12) % in a magnetic field of above $0.8T$. Three conduction band electronic resonances have been identified as a result of spectrum analysis and theoretical calculations [85]: the combined resonance (CR1) $b(1) \rightarrow a(2)$; the cyclotron resonance $a(0) \rightarrow a(1)$; and the combined resonance (CR3) ($a(0) \rightarrow b(1)$). Note that two combined resonances have been observed in the $Hg_{1-x-y}Cd_xMn_yTe$ narrow-gap semimagnetic semiconductor [104, 105]. It was found that the combined resonance CR1 shifts to higher magnetic fields with increasing temperature, while the CR3 shifts to lower magnetic fields. It was observed that the line shape and the position of resonances are identical for the Faraday and the Vogt geometry, which is in contrast with the behaviour of usual semiconductors, wherein the combined resonance can be observed only in the Vogt geometry. It was previously predicted that combined resonances can be observed in semimagnetic semiconductors regardless of the used geometry [107, 108].

The problem of a reliable determination of exchange interaction parameters in semimagnetic semiconductors has still not lost its relevance. The electric dipole spin resonance (EDSR) can be considered as a most direct and therefore a most accurate method of assessing the value of the exchange integral for electrons in the conduction band. The observation of EDSR in the $Hg_{1-x}Mn_xTe$, $Hg_{1-x-y}Cd_xMn_yTe$ systems has been reported by Stepnewski et al. [109] and Georgitse et al. [77]. The observed EDSR line in the system $Hg_{1-x}Mn_xTe$ system proved to be so wide that it was not possible to estimate the value of the exchange integral of conduction band electrons $N_0\alpha$ [109]. At the same time, it was possible to observe quite narrow EDSR lines by a careful selection of $Hg_{1-x-y}Cd_xMn_yTe$ samples [77], and to assess the values of band parameters and the exchange integral $N_0\alpha$ of the conduction band on the basis of the position of magnetic resonances. Georgitse et al. demonstrated the possibility to determine the concentration of free carriers, and the dielectric permittivity from the position of plasma-shifted cyclotron resonance in Vogt geometry in the magnetic field [77].

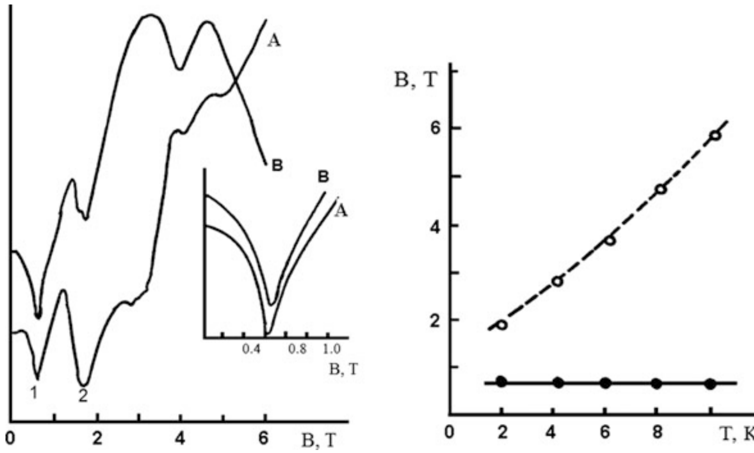

Fig. 8.16 The spectra of the magneto-transmission for the $Hg_{1-x-y}Cd_xMn_yTe$ alloy in the Farday and Vogt geometries for λ = 294.8 μm at T = 2 K [77]

Figure 8.16 shows the typical spectra of magneto-transmission measured by Georgitse et al. [77] for the $Hg_{0.85}Cd_{0.03}Mn_{0.12}Te$ alloy in Vogt and Faraday geometries for $\lambda = 294.8$ μm at 2 K. The choice of this radiation frequency is conditioned by the fact that it allows to observe various types of spectrally separated resonances, which improves the accuracy of determining the position of resonance lines in a magnetic field. Several resonance lines are observed in this figure, which have been identified by Georgitse et al. [77]. The positions of the line 1 in the Faraday and Voigt geometries are shown in the inset to this figure. One can see that in the Vogt geometry the line are shifted towards lower magnetic fields as compared to the Faraday geometry. This fact was explained as follows [77]: in the Faraday geometry the contribution to the line 1 comes from the cyclotron resonance and from the combined resonance, while in the Vogt geometry it comes from the combined resonance as well as from a resonance with a frequency given by the expression:

$$\omega = \sqrt{\omega_c^2 + \omega_p^2} \tag{8.16}$$

where ω_c is the cyclotron frequency, $\omega_p^2 = 4\pi Ne^2/m_c^*\chi$ is the electron plasma frequency, N is the concentration of electrons, m_c^* is the electron effective mass, χ is the dielectric permittivity.

The expression (8.16) is the condition for observing the so-called plasma-shifted cyclotron resonance (PSSR). Georgitse et al. determined the concentration of electrons in the investigated samples by comparing the frequency of CR with that of PSSR making use of the expression (8.16) [77]. For instance, for the $Hg_{0.85}Cd_{0.03}Mn_{0.12}Te$ alloy the plasma frequency is $\omega_p = 3.42 \times 10^{12}\,\mathrm{c}^{-1}$, and for

the given χ = 16 the electron density is $N = 1.09 \times 10^{15}\,\text{cm}^{-3}$, which is in agreement with the results of Hall effect measurements. The Fermi level in this case is $\varepsilon_F = 2.1\,\text{meV}$. Georgitse et al. suggested that the line 2 corresponds to EDSR for the transition *b(0)* → *a(0)*, it being observed in both geometries. The observation of resonances with spin flipping regardless of the selected geometry is possible due to the relaxation of the selection rules in semimagnetic materials [107]. One of the reasons for this relaxation is the giant splitting of the Landau spin sublevels. The energy of the EDSR transition is given by the expression:

$$\Delta\varepsilon = \varepsilon_{a(0)} - \varepsilon_{b(0)} = g_{eff}\,\mu_B B \tag{8.17}$$

where μ_B is the Bohr magneton, B is the magnetic field, g_{eff} is the effective g-factor given by the expression:

$$g_{eff} = g^* - \frac{xN_0\alpha\langle S_z\rangle}{\mu_B} \tag{8.18}$$

where g^* is the g-factor of electrons without taking into account the exchange interaction, $\langle S_z\rangle$ is the mean spin.

$$\langle S_z\rangle = -S_0 B_{5/2}\left(g_{Mn}\mu_B B/k(T+T_0)\right) \tag{8.19}$$

In this expression, $B_{5/2}$ is the Brillouin function, g_{Mn} is the g-factor of the manganese ions, which value is 2, k is the Boltzmann constant, T is the temperature at which the experiment is conducted.

By using the EDSR position in the magnetic field, the value of g_{eff} has been determined from the expression (8.17), and the value of the exchange integral of the conduction band electrons $N_0\alpha$ has been determined from the expression (8.17). The spin relaxation time $\tau_S = \alpha B/\Delta B\omega_S$ was determined from the half-width of the EDSR line (ΔB) [77]. It was found that the spin relaxation time in the investigate alloys ranges in the limits of (7–8) $\times$ 10^{-13} s and the resonance figure of merit is $\omega_S\tau_S = 4$–5.

The temperature shift of resonances has also been investigated. It was found that the resonances can be classified in two groups according to the temperature dependence. A strong dependence of the line upon temperature is characteristic for the spin resonance. The EDSR line moves to high magnetic fields due to the decrease of magnetization $M = -xN_0 g_{Mn}\mu_B\langle S_z\rangle$ with increasing temperature. A weak temperature dependence is characteristic for the diamagnetic resonance and it is well described by the theory with $d\varepsilon_g/dT = 0.35\,\text{meV/K}$ which is in agreement with the restructuring of the energy spectrum under the influence of temperature.

The values of energy spectrum parameters and of the exchange interaction, calculated from the analysis of magnetic resonances in $Hg_{1-x-y}Cd_xMn_yTe$ semimagnetic alloys are shown in Table 8.1.

The data, obtained for the exchange parameters from the magnetic resonance analysis agree well with the previously obtained results [65–68, 85].

Table 8.1 The values of energy spectrum parameters and of the exchange interaction in the $Hg_{1-x-y}Cd_xMn_yTe$ semimagnetic alloys

Samples	T, K	g_{eff}	g^*	$N_0\alpha$, eV	S_0	T_0	m_c^*/m_0	ε_g, V g
$Hg_{0.81}Cd_{0.08}Mn_{0.11}Te$	2	19.1	−37.6	−(0.35 ± 0.02)	0.95	10.7	2.1×10^{-2}	0.245
	4.2	14.7						
$Hg_{0.85}Cd_{0.03}Mn_{0.12}Te$	2	40.4	−44.2	−(0.41 ± 0.02)	0.87	11.6	1.85×10^{-2}	0.215
	4.2	25.1			0.89	11.2		
	6	19			0.9	10.7		
	8	15.1			0.92	10.3		
	10	12.2			0.93	9.7		

8.7 ODMR in Semimagnetic Semiconductors. Optical Orientation

ODMR is based on the phenomenon of resonance effects of microwave fields on the optical characteristics of a system. Such effects may be due to both the individual properties of charge carriers, and the spin-dependent phenomena related to the interaction of carriers with external electric and magnetic fields. The first information about the research of ODMR in semimagnetic structures was reported by Georgitse et al. [85], with a $Hg_{1-x}Mn_xTe$ solid solution with a high manganese content $x > 0.2$ and p-type conductivity with impurity concentration of $\sim 10^{15}$ cm^{-3} as the object of the research. Two resonances were observed in the ODMR spectra measured at 2 K. The first resonance observed in a field of 0.2T was assumed to be due to the electron spin resonance (ESR) of holes bound to an acceptor ($g = 12 \pm 1$), while the second resonance, the so-called magnetic dipole resonance, observed in a field of 1.15T is due to the magnetic dipole interaction between the manganese ions Mn^{+2} ($g \approx 2.0$). The analysis of experimental results enabled to determine the spin relaxation time, as well as the internal magnetic field in $Hg_{1-x}Mn_xTe$ ($x > 0.2$) alloys [85].

The spin orientation of electrons has been inevestigated at a temperature of 4.2 K under excitation by circularly polarized light with the energy close to the bandgap of non-magnetic alloys $Hg_{0.69}Cd_{0.31}Te$ and $Hg_{0.39}Cd_{0.61}Te$, as well as close to the parameters of the energy spectrum of the $Hg_{0.77}Mn_{0.23}Te$ semimagnetic alloy [110]. The mechanisms of spin relaxation of electrons in $Hg_{1-x}Cd_xTe$ and $Hg_{1-x}Mn_xTe$ have been analysed. A careful analysis of the experimental results proved that the Beer-Aronov Picus spin relaxation mechanism plays a significant role in $Hg_{1-x}Cd_xTe$ alloys at low temperatures, while in $Hg_{1-x}Mn_xTe$ semimagnetic alloys the spin relaxation is due to the exchange interaction of nonequilibrium electrons with the manganese ions [110]. The spin relaxation time was determined in $Hg_{1-x}Mn_xTe$ alloys, and the concentration of deep recombination centres was estimated.

8.8 Photoreceivers Based on $Hg_{1-x}Mn_xTe$, $Hg_{1-x-y}Cd_xMn_yTe$

The first reports about the photovoltaic receivers based on $Hg_{1-x}Mn_xTe$ and $Hg_{1-x-y}Cd_xMn_yTe$ solid solutions have been published in 1986 [111, 112]. The carrier transporter mechanisms in photodiodes have been investigated in the next years, and the parameters of devices have been improved [113, 114]. It was demonstrated that the current flow in the temperature range from liquid nitrogen to 250 K is determined by the thermal activation mechanisms [115], it being governed by a diffusion mechanism at $T > 110$ K, and by a generation-recombination mechanism at T < 110 K. The reverse currents at a bias of 1 V do not exceed 1 nA, and the value of R_oA at 85 K was found to be of $1.7 \times 10^7\ \Omega \cdot cm^2$. These values, in our opinion, are record ones for $Hg_{1-x}Mn_xTe$, $Hg_{1-x-y}Cd_xMn_yTe$ diodes of similar composition. The specific detectivity at 77 K and at a backlight aperture of $2\pi sr$ was found to be $\sim 5 \times 10^{11}$ $Hz^{1/2}Вм^{-1}$, which corresponds to the BLIP regime. These parameters are at a level corresponding to the best diodes on $Hg_{1-x}Cd_xTe$, and the photodiodes are sensitive for $\lambda_{1/2} = 3.8$ µm at the temperature of 77 K [115]. The obtained results demonstrate that the technology for producing epitaxial layers $Hg_{1-x-y}Cd_xMn_yTe$ layers is at the same level as the previously developed technology for $Hg_{1-x}Cd_xTe$ laters. On the other hand, one can expect that the photodiodes on $Hg_{1-x-y}Cd_xMn_yTe$ solid solutions will demonstrate better stability due to the higher structural perfection of these solid solutions. Note that only a few publications are available on photodetectors based on $Hg_{1-x}Mn_xTe$ and $Hg_{1-x-y}Cd_xMn_yTe$, (a review of early work is given by Pawlikowski [11]), whereas there are many studies on $Hg_{1-x}Cd_xTe$ with various types of photodetectors (photoconductive, photovoltaic, SPRITE-type, etc.), (see, e.g. [116–121]).

8.9 Conclusions

The semimagnetic $Hg_{1-x}Mn_xTe$ semiconductors are attractive primarily due to higher mechanical strength and thermal stability as computed to $Hg_{1-x}Cd_xTe$. The possibility of obtaining materials with the same bandgap parameters but with different contents of manganese in the quaternary $Hg_{1-x-y}Cd_xMn_yTe$ alloys system by changing the relative content of cadmium and manganese, apart from a purely scientific interest, has also a special practical interest. Therefore, the semimagnetic semiconductors $Hg_{1-x}Mn_xTe$, $Hg_{1-x-y}Cd_xMn_yTe$ have a series of advantages as materials for the creation of infrared detectors and infrared lasers as compared to their non-magnetic $Hg_{1-x}Cd_xTe$ counterparts.

References

1. R.T. Delvis, B. Lewis, J. Phys Solids **24**, 549 (1968)
2. P. Becla, P.A. Wolff, R.L. Aggarwal, S.Y. Tuen, R.R. Galazka, J. Vac. Sci. Technol. A **3**(1), 119 (1985)
3. N.L. Bazhenov, V.I. Ivanov- Omskii, K.E. Mironov, V.R. Movila, FTP **22**, 1258 (1988)
4. N.L. Bazhenov, S.I. Gasanov, V.I. Ivanov-Omskii, V.R. Movila, Lett. JETF **17**, 48 (1990)
5. J.K. Furdyna, Appl. Phys. **64**, R29 (1988)
6. B.A. Bunker, W.F. Pong, V. Debska, D.R. Yorder-Shortand, J.K. Furdyna, in *Diluted Magnetic (Semimagnetic) Semiconductors*, vol. 89, ed. by R.L. Aggarwal, J.K. Furdyna, S. Molnar (Materials Research Society, Pittsburg, 1987), p. 231
7. W. Girrat, J.K. Furdyna, in *Semiconductors and Semimetals*, vol. 25, ed. by R.K. Willardson, A.C. Becr, J.K. Furdyna, I. Kossut (Academic, Boston, 1988), p. 1
8. J.K.J. Furdyna, Vac. Sci Technol. **21**, 220 (1982)
9. A. Rogalski, Infrared Phys. **31**, 117 (1991)
10. I.I. Lyapilin, I.M. Tsidilkovskii, UFN **146**, 35 (1985)
11. I.M. Pawlikowski, Infrared Phys. **3**, 295 (1990)
12. A. Wall, C. Caprile, A. Franciosi, R. Reifenberger, U. Debska, J. Vac. Sci. Technol. **A4**, 818 (1986)
13. I. Piotrowski, W. Galus, M. Grudrien, Infrared Phys. **31**, 1 (1991)
14. W.M. Higgins, G.N. Pultz, R.G. Roy, R.A. Lancaster, I.L. Schmit, J. Vac. Sci. Technol. **A7**, 271 (1989)
15. A. Schenk, Phys. Stat. Solidi (a) **122**, 413 (1991)
16. E.O. Kane, J. Phys. Chem. Solids **1**, 249 (1957)
17. S. Datta, J.K. Furdyna R.L. Gunshor, Superlattices Microstruct. **1**, 327 (1985)
18. R.L. Gunshor, M. Otsuka, M. Yamanishi, L.A. Kolodzeijski, T.C. Bonsett, R.B. Bylsma, S. Datta, J.K. Furdyna, J. Cryst. Growth **72**, 294 (1985)
19. R.B. Galzka, I. Kossut, *Lecture Notes in Physics,* vol 132 (Springer, Berlin, 1980), p. 245
20. I. Mycielski, in *Recent Developments Metter Physics*, ed. by I.T. Devreese (Plenum, New York, 1981), p. 257
21. I. Kossut, in *Semiconductors and Semimetals*, vol. 25, ed. by R.K. Willardson, A.C. Beer, J. K. Furdyna, I. Kossut (Academic, Boston, 1988), p. 183
22. I. Mycielski, in *Semiconductors and Semimetals*, vol. 25, ed. by R.K. Willardson, A.C. Beer, I. K. Furdyna, I. Kossut (Academic, Boston, 1988), p. 311
23. G. Bastard, C. Rigaux, Y. Guldner, A. Mycielski, J.K. Furdyna, D. Mullin, Phys. Rev. **24**, 1961 (1981)
24. C.R. Pidgenon, R.N. Brown, Phys. Rew. **146**, 575 (1966)
25. M. Jaczinski, I. Kossut, R. Galazka, Phys. Stat. Solidi (b) **88**, 73 (1978)
26. A. Rogalski, K. Iozwikowski, Phys. Stat. Solidi (a) **122**, K39 (1991)
27. N.P. Gavaleshko, P.N. Gorley, V.A. Shenderovsky, Narrow-Gap Semiconductors. Preparation and Physical Properties. (Kiev, 288, 1984)
28. R.B. Galazka, I. Kossut, L. Bornstein, *New Series 17b* (Springer, Berlin, 1982), p. 302
29. I. Kaniewski, A. Mycielski, Solid Stat. Commun. **41**, 959 (1982)
30. A. Jozwikowska, K. Jozwikowski, A. Rogalski, Infrared Phys. **31**, 543 (1991)
31. I.D. Wiley, R.N. Dexter, Phys. Rev. **181**, 1181 (1969)
32. U. Debesk, T. Dietl, G. Grabeski, E. Ianck, Phys. Stat. Solidi (a) **64**, 707 (1981)
33. N.L. Bazhenov, S.I. Hasanov, V.I. Ivanov-Omskii, K.E. Mironov, K.D. Mynbayev, FTP **25**, 2345 (1991)
34. N.L. Bazhenov, S.I. Hasanov, Ivanov- Omskii V.I. Tech. Phys. Lett. **17**, 9 (1991)
35. L.A. Kosyachenko, A.V. Markov, S.E. Ostapov, I.M. Rarenko, V.M. Sklyarchuk, E.F. Sklyarchuk, FTP **36**, 1217 (2002)
36. N.P. Gavaleshko, V.V. Teterin, F.F. Sizov, S.J. Paranchich, FTP **27**, 459 (1943)

37. E.I. Gheorghita, A.E. Gheorghita, P.G. Untila, in *Materials of the IVth Conference on Physics of Crystalline and Amorphous States in Semiconductors* (Iasi, 1996)
38. N.L. Bazhenov, V.I. Ivanov-Omskii, K.E. Mironov, V.F. Movila, FTP **22**, 1258 (1988)
39. N.B. Brandt, V.V. Moshchalkov, L.O. Orlov, JETF **84**, 1059 (1983)
40. I. Newodniczanska-Zawadzka, R. Protrowski, J. Kossut, J. Cryst Growth **72**, 384 (1985)
41. E.I. Gheorghita, V.I. Ivanov-Omskii, K.E. Mironov, P.G. Untila, Proceedings of the universities of the USSR. Physics **3**, 96 (1990)
42. E.I. Gheorghita, V.I. Ivanov-Omskii, K.E. Mironov, P.G. Untila, Proceedings of the universities of the USSR. Physics **4**, 114 (1990)
43. L.P. Zverev, V.V. Kruzhayev, G.M. Minkov, O.E. Rut, N.P. Gavaleshko, V.M. Frasunyak, JETF **86**, 1073 (1984)
44. R.G. Mani, T. McNair, C.R. Lu, R. Crober, J. Cryst. Growth **97**, 617 (1989)
45. P.I. Baranskiy, A.Ye. Belyayev, O.A. Bodnaruk, I.N. Gorbatyuk, S.M. Komirenko, I.M. Rarenko, N.V. Shevchenko, FTP **24**, 1490 (1990)
46. T. Piotrowski, J.W. Tomm, N. Puhlmann, Phys. Stat. Solidi (a) **117**, K181 (1990)
47. N.G. Garbuz, S.V. Kondrakov, S.A. Popov, E.V. Susov, A.V. Filatov, R.A. Khaziyeva, E.N. Holina, Izv. AN SSSR. Inorg. Mater. **26**, 536 (1990)
48. R.E. Kremer, J. Tang, F.G. Moore, J. Cryst. Growth **86**, 797 (1988)
49. Chen Chenjia, Liu Jirhou, Zhang Bei, Rong Zuxii, Rare Met. **9**, 272 (1990)
50. P. Brogowski, T. Piotrowski, Semicond. Sci Technol. **6**, 530 (1990)
51. V.D. Prozorovskiy, IYu. Zreshidova, SYu. Paranchich, L.D. Paranchich, FTT **31**, 326 (1989)
52. A.E. Belyayev, YuG Semenov, N.V. Shevchenko, Tech. Phys. Lett. **51**, 164 (1990)
53. A.E. Belyayev, YuG Semenov, N.V. Shevchenko, Tech. Phys. Lett. **53**, 519 (1991)
54. R.I. Bashirov, V.A. Yelizarov, N.Yu. Matveyeva, FTP **28**, 519 (1994)
55. F. Capper, J. Vac. Sci. Technol. B **9**, 1666 (1961)
56. A.V. Gorshkov, Highly-pure materials. **207**, (1989)
57. M.I. Ibragimova, N.S. Baryshev, I.B. Khaybullin, F.I. Akhmedova, A.P. Fadeyeva, FTP **23**, 1249 (1989)
58. K.E. Mironov, P.G. Untila, O.V. Zelenova, in *Proceedings of the VIIth All-Union Symposium `Semiconductors with a Narrow Band Gap and Semimaterials*, vol. 148 (Lvov, 1986)
59. M.M. Trifonova, N.S. Baryshev, M.P. Mezentseva, FTP **25**, 1014 (1991)
60. M.M. Trifonova, N.S. Baryshev, M.P. Mezentseva, FTP **26**, (1992)
61. M.M. Trifonova, N.S. Baryshev, I.S. Averyanov, in *Proceedings of Rep. III All-Union. Sci-tech. Conference Materials of Chalcogenide Semiconductors,* vol. 1 (Chernovtsy, 1991), p. 69
62. N.S. Baryshev, M.M. Trifonova, M.P. Mezentseva, I.S. Averyanov, in *Proceedings of Report XXIX of the Conference. In low-temperature physics, Tez. dokl. XXIX Conference in Low-Temperature Physics*, vol. 342 (Kazan, 1992)
63. M. Ortenberg, Semicond. Sci. Technol. **8**, 566 (1993)
64. V.I. Ivanov-Omskii, N.N. Berchenko, A.I. Elizarov, Phys. Stat. Solidi (a) **163**, 11 (1987)
65. B.L. Gelmont, R.R. Golonska, V.I. Ivanov-Omskii, I.T. Postolaki, V.A. Smirnov, FTP **20**, 73 (1986)
66. Ye.I. Georgitse, V.I. Ivanov-Omskii, V.M. Pogorletski, T. Piotrovskiy, V.A. Smirnov, FTP **24**, 1732 (1990)
67. R.R. Galazka, B.L. Gelmont, V.I. Ivanov-Omskii, I.T. Postolaki, V.A. Smirnov, Solid Stat. Commun. **58**, 311 (1986)
68. Ye.I. Georgitse, V.I. Ivanov-Omskii, V.R. Masterov, V.M. Pogorletski, V.A. Smirnov, FTP **24**, 2160 (1990)
69. L. Dobacrewski, E. Jenik, G. Karcrewski, Acta Phys. Pol. A **75**, 63 (1989)
70. V.Ye. Begovatov, N.S. Baryshev, N.N. Belyy, M.N. Bryazkiy, I.N. Gorbatyuk, FTP **23**, 2074 (1989)
71. P.I. Baranskiy, A.E. Belyayev, I.N. Gorbatyuk, S.M. Komirenko, N.M. Rarenko, N.V. Shevchenko, FTP **25**, 1183 (1991)

72. E.I. Georgitse, I.T. Postolaki, V.M. Pogorletski, P.G. Untila, V.A. Smirnov, V.A. Maltseva, Izv. AN MSSR. Phys. Mech. **14** (1990)
73. T.I. Nazarenkova, E.I. Salkov, N.V. Sochinskiy, FTP **23**, 1309 (1989)
74. N.V. Sochinskiy, T.I. Nazarenkova, I.S. Bakim, B.I. Khizhnyak, in *Materials of All-Union Seminar of Impurities and Defects in Narrow-Gap Semiconductors*, vol. 72 (Pavlodar, 1989)
75. N.S. Baryshev, V.E. Begovatov, M.P. Mezentseva, Trifanova, Averyanov I.S. Inorg. Mater. **27**, 2536 (1991)
76. N.S. Baryshev, V.E. Begovatov, I.S. Averyanov, Thez. in *Report of the II-nd scientific. Conference. The Photoelectric Phenomena in Semiconductors* (Ashkhabad, 1991), p. 72
77. E.I. Georgitse, V.I. Ivanov-Omskii, V.F. Movila, D.I. Tsypishka, FTP **25**, 41 (1991)
78. K. Takita, T. Uchinc, T. Ipposhe, K. Masuda, Solid. Stat Commun. **56**, 603 (1985)
79. T. Uchinc, K. Takita, K. Masuda, J. Phys. Soc. Jpn. **58**, 627 (1989)
80. K. Takita, T. Uchnco, K. Masuda, Semicond. Sci. Technol. **5**, 5277 (1990)
81. N.S. Baryshev, in *Materials of All-Union Seminar of Impurities and Defects in Narrow-Gap Semiconductors* (Pavlodar, 1989), p. 135
82. N.S. Baryshev, B.L. Gelmont, M.I. Ibragimova, FTP **24**, 209 (1990)
83. O.A. Bonaruk, A.A. Vertiy, I.N. Gorbatyuk, I.V. Ivanchenko, N.A. Popenko, I.M. Rarenko, S.I. Tiratov, FTP **30**, 1236 (1996)
84. S.G. Gasan-Zade, V.I. Kalenik, G.A. Shepelskiy, FTP **30**, 63 (1996)
85. E.I. Georgitse, V.V. Dyakonov, V.I. Ivanov-Omskii, V.M. Pogorletski, N.G. Romanov, V.A. Smirnov, Tech. Phys. Lett. **16**, 74 (1990)
86. I. Postolaki, University education from Moldova to 75 years, in *The Conference Scientific-Methodological Materials*, vol. III (Chisinau, 2005), p. 85
87. V. Kantser, E. Georgitse, L. Gutsuleak, I. Postolaki, in *VIIth Russian Conference on Semiconductor Physics* (Moscow, 2005), p. 145
88. I. Postolaki, New resercarch trends in materials science. ARM-4 Proc. **I**, 383, (2005). Constanta
89. I.T. Postolaki, in *VIIth Russian Conference on Semiconductor Physics* (Moscow, 2005), p. 143
90. I. Postolaki, in *Conference of Physicists from Moldova* (*CFM-2005*) (Chisinau, 2005), p. 53
91. Yu.I. Mazur, Semicond. Phys. Quant. Electron. Optoelectron. **1**, 33 (1999)
92. Yu.I. Mazur, S.I. Kriven, G.G. Tarasov, N.V. Shevchenko, Semicond. Sci. Technol. **8**, 1187 (1993)
93. G.G. Tarasov, YuI Mazur, J.W. Tomm, V. Jahnke, Phys. Rev. B **52**, R11565 (1995)
94. Yu.I. Mazur, G.G. Tarasov, V. Jahnke, J.W. Tomm, W. Hoerstel, Semicond. Sci. Technol. **11**, 1291 (1996)
95. G.G. Tarasov, Yu.I. Mazur, S.R. Lavoric, J.W. Tomm, J. Cryst. Growth, **184**(185), 1214 (1998)
96. S.E. Ostapov, I.M. Rarenko, M.D. Timochenko, Semicond. Phys. Quant. Electron. Optoelectron. **7**, 339 (2004)
97. Yu.I. Mazur, Semicond. Phys. Quant. Electron. Optoelectron. **1**, 33 (1998)
98. G.G. Tarasov, Yu.I. Mazur, M.P. Lisitsat et al., Semicond. Sci. Technol. **14**, 187 (1999)
99. V.F. Radantsev, A.M. Yafyasov, V.B. Bogevolnov, Semicond. Sci. Technol. **16**, 320 (2001)
100. F. Fuchs, K. Kheng, K. Schwarz, P. Koidl, Semicond. Sci. Technol. **8**, S75 (1993)
101. A. Mycielski, J. Mysielski, J. Phys. Soc. Jpn. **49**, 807 (1980)
102. A.D. Bykhovckiy, E.M. Vakhabova, B.L. Gelmont, A.A. Efros, FTP **18**, 2094 (1984)
103. T. Woitowica, A. Mysielski, Acta Phys. Pol. **67**, 363 (1985)
104. E.I. Georgitse, V.I. Ivanov-Omskii, V.F. Movila, D.I. Tsypishka, FTP **24**, 1823 (1990)
105. E.I. Georgitse, V.I. Ivanov-Omskii, V.F. Movila, D.I. Tsypishka, in *Proceedings of the VIIIth All-Union Symposium Semiconductors with a Narrow Band Gap, and Semimetals*. Lvov **124** (1991)
106. M. Dobrovolska, Semicond. Sci. Technol. 5159 (1990)
107. Yu.G. Rubo, L.S. Khazan, V.I. Sheka, A.S. Ioselevich, Tech. Phys. Lett. **48**, 30 (1988)
108. Yu.G. Rubo, L.S. Khazan, V.I. Sheka, E.V. Mozdor, Tech. Phys. Lett. **95**, 1880 (1989)

109. R. Stepnewski, M. Grinberg, Acta Phys. Pol. A **67**, 373 (1985)
110. E.I. Georgitse, V.I. Ivanov-Omskii, V.M. Pogorletskii, V.A. Smirnov, Semicond. Sci. Technol. **6**, 924 (1991)
111. P. Becla, J. Vac. Sci Technol. **A4**, 2014 (1986)
112. S. Wong, P. Becla, J. Vac. Sci. Technol. **A4**, 2019 (1986)
113. E. Janik, G. Karczewski, Acta Phys. Pol. **A 73**, 439 (1988)
114. E. Placzek-Popko, L. Jedral, Infrared Phys **26**, 249 (1988)
115. N.L. Bazhenov, S.I. Gasanov, V.I. Ivanov-Omskii, K.E. Mironov, V.F. Movila, Tech. Phys. Lett. **17**, 48 (1991)
116. N.R. Aigina, P.A. Bogomolov, V.I. Sidorov, Foreign electronic appliances. **3** (1982)
117. N.R. Aigina, P.A. Bogomolov, V.I. Sidorov, Foreign electronic appliances. **3** (1984)
118. C.T. Elliot, J. Cryst. Growth **72**, 453 (1985)
119. A. Rogalski, J. Piotrowski, Progr. Quant. Electron. **12**, 87 (1988)
120. N.L. Bazhenov, S.I. Gasanov, V.K. Ogorodnikov, V.I. Protsyk, Foreign electronic appliances. **3** (1986)
121. A.V. Voytsekhovskiy, I.I. Ijnin, V.A. Kemarskiy, N.A. Kulchitskiy, Foreign electronic appliances. **3** (1991)

Chapter 9
Cobalt/Cobaltoxide Exchange Bias System for Diluted Ferromagnetic Alloy Films in Superconducting Spin-Valves

A.S. Sidorenko, D. Lenk, V.I. Zdravkov, R. Morari, A. Ullrich, C. Müller, H.-A. Krug von Nidda, S. Horn, L.R. Tagirov and R. Tidecks

Abstract The present work reports on the influence of a Cobalt sublayer on a conventional exchange bias $CoO_x/Cu_{41}Ni_{59}$ interface. For superconducting spintronics the ability to exchange bias diluted ferromagnetic alloys is an essential building block, as they have advantages for the application in superconductor-ferromagnet spin-valve heterostructures. The magnetic properties are investigated by SQUID magnetometry and two separate strongly exchange biased signals are observed. The obtained results are compared with predictions of the domain state and spin-glass model of exchange bias.

9.1 Introduction

Superconductor-ferromagnet (S-F) heterostructures with nanoscale thickness of the layers provide rich physics arising from the mutual penetration of the two long-range orders via interfaces between the layers [1–5]. Moreover, device physics may follow, and superconducting spintronics can be developed based on unusual intrinsic physical properties of S-F hybrids [6–13]. Investigations concerning S-F heterostructures [14–29] have shown that weak ferromagnets with low Curie temperature (i.e. $T_C \approx 15-120$ K, in our actual copper-nickel samples T_C is between

A.S. Sidorenko (✉) · V.I. Zdravkov · R. Morari
Institute of Electronic Engineering and Nanotechnologies "D. Ghitu", Academy of Sciences of Moldova, Chisinau, Moldova
e-mail: anatoli.sidorenko@kit.edu

D. Lenk · V.I. Zdravkov · R. Morari · A. Ullrich · C. Müller · H.-A. Krug von Nidda · S. Horn · L.R. Tagirov · R. Tidecks
Institut für Physik, Universität Augsburg, D-86159 Augsburg, Germany

R. Morari · L.R. Tagirov
Solid State Physics Department, Kazan Federal University, 420008 Kazan, Russia

© Springer International Publishing Switzerland 2016

I. Tiginyanu et al. (eds.), *Nanostructures and Thin Films for Multifunctional Applications*, NanoScience and Technology,
DOI 10.1007/978-3-319-30198-3_9

110 and 120 K [27]) are most suitable for application in functional S-F heterostructures. Inspired by impressive developments of room-temperature spintronics ([30–32] and references therein), several types of superconducting spin-valves have been proposed or even realized, e.g. spin-valves for superconducting transport current [9–11, 20, 33–47] and for Josephson supercurrent [48–50]), which are switched by magnetic field or possibly by spin-torque (i.e. reversal of magnetization by spin-polarized current, for details see recent reviews [31, 32] and references therein). Superconducting memory functions for superconducting computing systems [51–53] could be realized by such superconducting spin-valves. Spin-valves for transport current, in which the different switching states are realized by different mutual orientation of two ferromagnetic layers adjacent to a superconducting film, usually need the pinning of the magnetization direction of one of the ferromagnetic layers by exchange bias [54–57], which is not trivial for diluted ferromagnetic alloys.

Since the discovery of the exchange bias effect (EB) by Meiklejohn and Bean in ferromagnet (F)-antiferromagnet (AF) Co/CoO core-shell nanoparticles [58], it was realized that the EB is an interface effect. When an F/AF system is exposed to an external static magnetic field at a temperature higher than the Néel temperature (T_N) of the AF, and then cooled down to low temperatures (i.e. $T \ll T_N$), the AF layer pins the magnetization of the F layer at the F/AF interface, resulting in a unidirectional magnetic anisotropy in the direction of the cooling field, i.e. the field applied during cooling below T_N.

A common situation in the conventional spintronics is that the magnetic ordering temperature T_C of the F layer is much higher than the Néel temperature of the AF layer, i.e. $T_C \gg T_N$ [30, 54–57]. In superconducting spintronics, utilizing ferromagnetic alloys with low-T_C the inverse case is present, i.e. T_C(alloy) $\ll T_N$. The EB (a negative shift H_{EB} of the magnetic hysteresis loop with respect to the cooling field) appeared to be small, e.g. $H_{EB} \approx 100$ Oe for a $Cu_{47}Ni_{53}/Fe_{50}Mn_{50}$ system, with $T_N(Fe_{50}Mn_{50}) \sim 425$ K, studied in [33]. An EB of similar small order of magnitude was obtained in a $Cu_{41}Ni_{59}$ alloy layer exchanged biased by a CoO_x antiferromagnet ($T_N(CoO) \sim 291$ K; $T_N(Co_3O_4) \sim 40$ K) [59]. We attributed this small magnitude of the EB mainly to the mismatch of the magnetic easy axes of the $Cu_{41}Ni_{59}$ and CoO_x film, which are perpendicular to the film plane for $Cu_{41}Ni_{59}$ and in-plane for CoO_x [57, 60–62], respectively. Furthermore, it was unclear if the EB is limited due to an intrinsic atomic disorder of $Cu_{41}Ni_{59}$ alloy, or if there is a unknown common reason for any ferromagnet with T_C(alloy) $\ll T_N$(AF). To increase the EB of an diluted ferromagnet, the authors of [33] put a thin permalloy (Py, $T_C \sim 850$ K) interlayer between the F- and AF-layer (i.e. deposited a stack of $Cu_{47}Ni_{53}/Py/Fe_{50}Mn_{50}$) and obtained an EB of the hysteresis loop $H_{EB} \approx 800$ Oe. This means that the intrinsic atomic disorder in the case of Py is not an obstacle to get and transmit the EB to the $Cu_{47}Ni_{53}$ alloy. In this case $T_C(Py) > T_N(Fe_{50}Mn_{50})$ and the Py layer thickness is below the exchange stiffness length $l_{Ex} \approx 18$ nm [63] (see also [64] on the exchange bias in $Cu_{99}Mn_1$-alloy/Py/α-Fe_2O_3 system).

The problem of the exchange biasing of low-T_C alloy layers was studied in [65]. A layer of $Cu_{45}Ni_{55}$ alloy was deposited on a $Co/Fe_{50}Mn_{50}$ bilayer, and the

dependence of the EB on the thickness of the antiferromagnetic $Fe_{50}Mn_{50}$ layer was studied. A notable exchange bias of the $Cu_{45}Ni_{55}$ alloy was observed only in the absence of the Co sublayer. However, both in the presence and the absence of the Co sublayer they observed a substantial increase of the coercitivity of $Cu_{45}Ni_{55}$ for all thicknesses of the antiferromagnetic giving evidence for an exchange interaction with the antiferromagnet. The experimental results were qualitatively explained in the framework of a model by Nowak et al. [66], in which upon field cooling below the irreversibility line in an external field and in the presence of the interfacial exchange field of a ferromagnet, the antiferromagnet develops a frozen domain state with an irreversible surplus of magnetization at the interface between the layers in direction of the cooling field.

While there has been progress in the efforts to exchange bias diluted ferromagnetic alloys, it is unquestionable that more investigations and systematic studies are needed for an extensive and deep understanding of the EB in the case of T_C(alloy) $\ll$ T_N(AF).

In the present study we investigate the influence of an adjacent non-conducting AF-layer of CoO_x with a ferromagnetic sublayer of metallic Co on the EB of a $Cu_{41}Ni_{59}$ alloy layer. This design prevents leakage of superconducting Cooper pairs from the F/S/F core of a spin-valve.

The F_1/AF/F_2/S/F_2 design of the samples, where F_2/S/F_2 represents the core of a superconducting spin-valve (SSV-core) [59], was realized as a stack of Si (substrate)/Si (buffer)/Co/CoO_x/$Cu_{41}Ni_{59}$/Nb/$Cu_{41}Ni_{59}$/Si (cap). The magnetic properties of the structure were studied using a Superconducting Quantum Interference Device (SQUID) magnetometer. The experimental findings are interpreted in the framework of the domain-state model [65, 66] and spin-glass model [57] of EB. The superconducting properties of the structure were reported earlier in [53].

9.2 Sample Preparation and Characterization

The samples were grown by magnetron sputtering, using a Leybold Z-400 sputtering machine, if not mentioned otherwise, at room temperature and argon atmosphere (99.999 % purity, operating pressure 8×10^{-3} mbar). The residual pressure in the sputtering chamber before the deposition was about 2×10^{-6} mbar. Substrates for the film deposition (with dimensions about 80×7 mm^2) were cut from a commercial silicon {111}-oriented wafer. For deposition of the films, four sputtering targets were used: niobium, silicon, and cobalt with a purity of 99.99 %, 99.999 %, and 99.95 %, respectively, and a copper (40 at.%)–nickel (60 at.%) alloy.

The set of samples investigated in the present work was fabricated in a single run. First, we deposited a flat silicon buffer layer to prepare a clean surface for the subsequent layers. After a flat metallic Co layer was deposited, reactive oxygen gas was mixed to argon (Ar:O_2 = 6:1) for the CoO_x deposition. Subsequently, the $Cu_{41}Ni_{59}$ film was grown at a temperature of 200 °C. To obtain a layer with variable thicknesses we used the technology of growing films with wedge-like

profile [26–29]. The substrate was positioned off-axis below the target of $Cu_{40}Ni_{60}$ alloy, yielding a wedge-like profile due to the natural gradient of sputtering (see Fig. 9.1a). RF-magnetron sputtering yields a composition of $Cu_{41}Ni_{59}$, as discussed in detail in our previous papers [26–29].

A flat superconducting niobium layer is then obtained by monotonous movement of the sputtering target along the substrate during deposition [26–29] (see Fig. 9.1b). Subsequently, a second wedge-like $Cu_{41}Ni_{59}$ layer was deposited. Finally, the stack was capped with a thin silicon cap to protect it against oxidation at ambient conditions.

To obtain separate samples with different thicknesses of the $Cu_{41}Ni_{59}$ films, the substrate was cut perpendicular to the thickness gradient, yielding 2.5 mm wide stripes. Four of them (shown in Fig. 9.2a) were used for the measurements described below.

Cross-sectional Transmission Electron Microscopy (TEM) of Samples I and II was used, as well as our experience in evaluating the wedge profile by Rutherford Backscattering Spectrometry (RBS) [26–29] to evaluate thicknesses of the layers of samples III and IV. The values obtained are given in Table 9.1.

The TEM image presented in Fig. 9.2b shows polycrystalline structure of all layers.

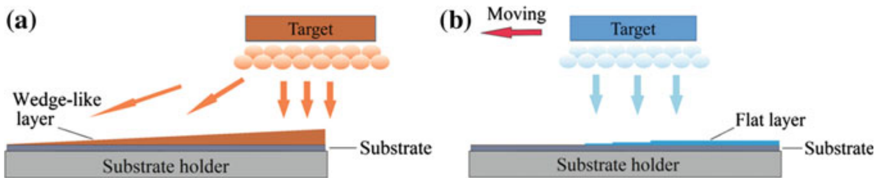

Fig. 9.1 Fabrication steps of the heterostructures. **a** Application of the wedge technology to deposit a film with a wedge-like profile. **b** Deposition of a Nb-layer of constant thickness. The target moves monotonously over the substrate during the deposition

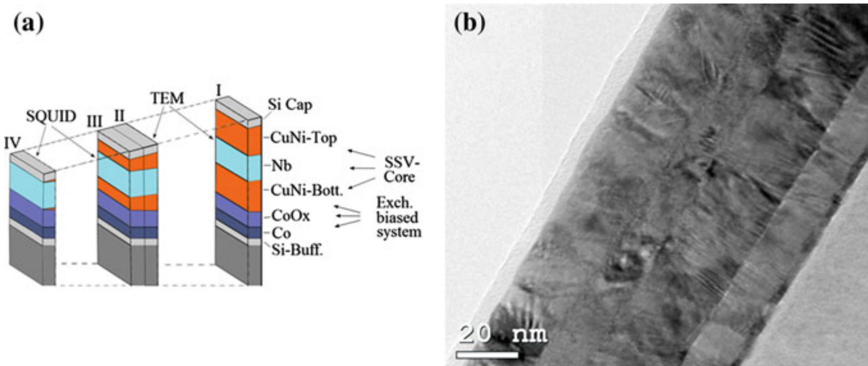

Fig. 9.2 **a** Sketch of the samples. **b** Cross-sectional TEM image of the sample I

Table 9.1 The layers thickness of samples I–IV

Sample number	Co (nm)	CoO_X (nm)	CuNi-Bottom (nm)	Nb (nm)	CuNi-Top (nm)
I	4	14	25	13	22
II	5	19	9	12	10
III	5	19	8	12	9
IV	4	14	≤1	11.5	≤1

A high resolution TEM image of the exchange bias system has been taken to analyze the present phase of cobalt oxide. Figure 9.3 shows the obtained image with white lines indicating interfaces between the layers.

The Si substrate has a {111} surface. The lattice spacings obtained for the two visible {111} planes were normalized to the theoretical value of 3.134 Å, resulting in a correction of about 0.8 % of the scale of the image, both in horizontal and vertical direction.

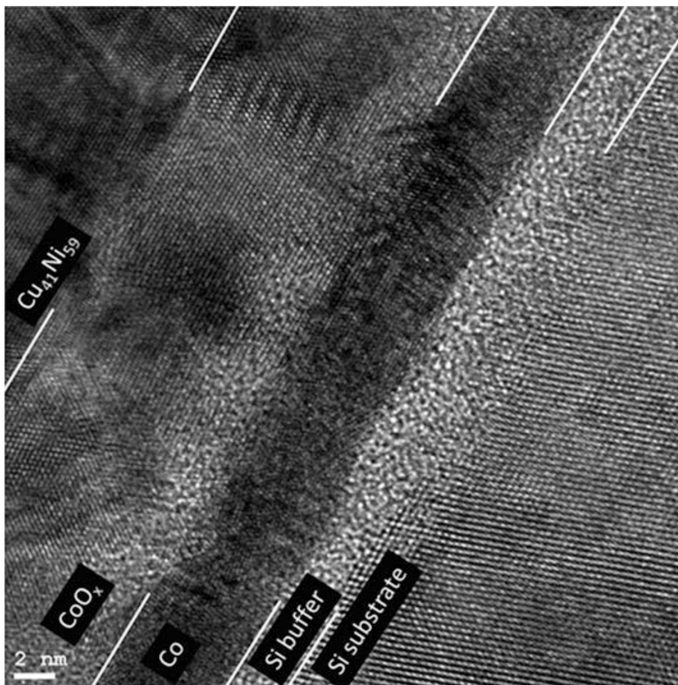

Fig. 9.3 Cross-sectional high-resolution TEM image of sample I at the exchange bias region of the system. *White lines* depict interfaces between layers, however being only a guide to the eyes. The actual layer thicknesses in Table 9.1 are extracted as the distance between the changes in the spatial distribution of intensity integrated parallel to the layers

There are basically two different cobalt oxides stable at low temperatures, CoO and Co_3O_4. Although both are antiferromagnetic, the exchange bias effect between Co_3O_4 and a ferromagnet is believed to be not intrinsic to the Co_3O_4, but arises from formation of a CoO layer at the interface due to oxygen diffusion to the ferromagnet [67]. Kehrle [68] (see also [59]) investigated a wedge of cobalt oxide grown on silicon (prepared in a similar way as the samples in this work) by cross-sectional electron diffraction and found the cobalt oxide to be Co_3O_4, however, the presence of CoO could not be entirely ruled out. From an investigation of lattice spacings and angles we conclude that the cobalt oxide layer obtained in this work is CoO. We found no evidence for Co_3O_4. This could be a result of lowering the partial oxygen pressure while sputtering the CoO_x layer to yield a ratio of argon to oxygen of 6:1 instead of 5:1 in our previous work [59]. Furthermore, this could also possibly be explained by the fact that our cobalt oxide layer is quite thin and, in addition, is sandwiched between two ferromagnetic layers, which both can extract oxygen from the cobalt oxide layer.

Moreover, we found the $Cu_{41}Ni_{59}$ to grow with the {111} direction parallel to the plane, as we reported in the earlier works [59, 68].

9.3 Results of Magnetic Measurements and Discussion

To study the exchange bias in the deposited system we performed magnetic moment (m) measurements by a Quantum Design MPMS-5 SQUID magnetometer with a magnetic field applied (H) parallel to the sample plane and perpendicular to the thickness gradient of the Cu_4, Ni_{59} layers. The samples were cooled down from above the Néel temperature of CoO (291 K) to a measurement temperature at the field of 10 kOe and 15 kOe for Sample III and IV, respectively. Then, the first and the second magnetic moment hysteresis loops were subsequently recorded in the DC "no-overshoot" mode (i.e. no internal data processing) of the SQUID magnetometer.

To identify the coercive fields of the constituent ferromagnetic layers, we have numerically taken field-derivatives of the $m(H)$ dependence (red and blue curves in figures, the derivatives scales are arbitrary).

Figure 9.4 displays the magnetic moment hysteresis loops of Sample III measured at 10 K after field cooling. The left panel shows the first loop, the right panel the second loop. First, the applied field was swept from the cooling field (i.e. positive field), towards negative fields. Then, the loop was completed by the field sweep in the opposite direction, i.e. from negative to positive field.

The exchange bias fields, i.e. $H_{EB} = \frac{1}{2}\left(H_c^+ + H_c^-\right)$, with H_c^+ and H_c^- the coercive fields of the respective constituent loops, as obtained from the peaks in the derivative in Fig. 9.4 for sweeps from negative to positive fields and vice versa, respectively, are found as follows: $H_{EB,Co} \approx -1950$ Oe and $H_{EB,CuNi-hard} \approx -1750$ Oe for the first and $H_{EB,Co} \approx -1300$ Oe and $H_{EB,CuNi-hard} \approx -1450$ Oe for the second loop, respectively. We decided against evaluation of an exchange bias

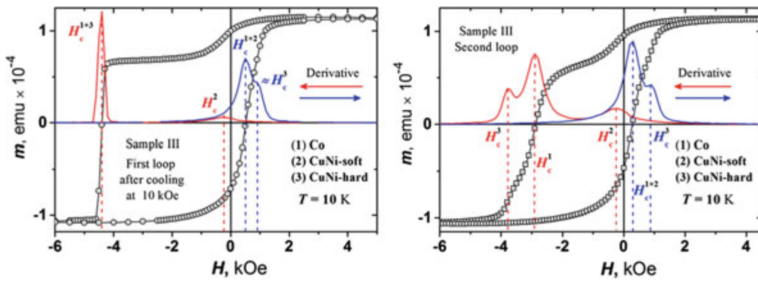

Fig. 9.4 Magnetic hysteresis loops of sample III: first loop—*left panel*, second loop—*right panel*. The magnetically soft signal can possibly be ascribed to the $Cu_{41}Ni_{59}$ material which is probably consisting of the top $Cu_{41}Ni_{59}$ layer and a certain part of the bottom $Cu_{41}Ni_{59}$ layer, while the rest of the bottom $Cu_{41}Ni_{59}$ layer forms the magnetically hard signal [53]. The *red* and *blue solid lines* represent numerical derivatives of the hysteresis loops for the sweep with decreasing and increasing field, respectively. Peaks in the derivative indicate coercive fields of the constituent layers, which are noted as superscript indices according to the legend

field for the CuNi-soft signal, because it cannot be evaluated with a reasonable precision, as the peaks for the scan from negative to positive fields is unresolved.

Figure 9.5 displays the magnetic moment hysteresis loops of Sample IV (very thin $Cu_{41}Ni_{59}$-alloy layer, see Fig. 9.2a and Table 9.1) measured at 10 K. The left panel shows the first loop, the right panel the second loop, after field cooling. An evaluation of the exchange bias fields, as described above, yield: $H_{EB,Co} \approx -2550$ Oe and $H_{EB,CuNi-hard} \approx -1950$ Oe for the first and $H_{EB,Co} \approx -1125$ Oe and $H_{EB,CuNi-hard} \approx -1300$ Oe for the second loop, respectively. Again, we decided against evaluation of an exchange bias field for the CuNi-soft signal, as the corresponding peaks are broad and faint.

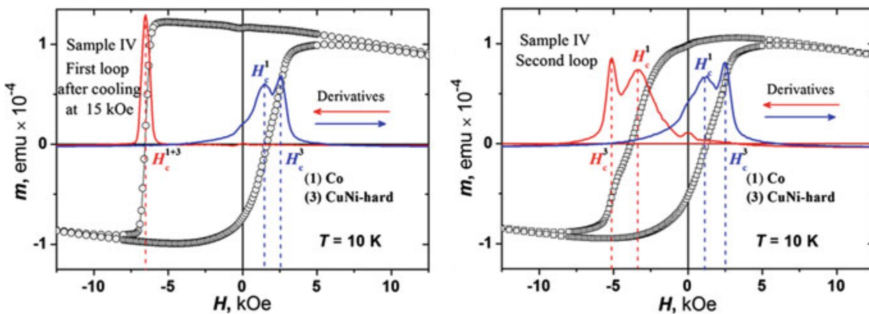

Fig. 9.5 Magnetic hysteresis loops of sample IV: first loop—*left panel*, second loop—*right panel*. The magnetically soft signal can possibly be ascribed to the $Cu_{41}Ni_{59}$ material which is probably consisting of the top $Cu_{41}Ni_{59}$ layer and a certain part of the bottom $Cu_{41}Ni_{59}$ layer, while the rest of the bottom $Cu_{41}Ni_{59}$ layer forms the magnetically hard signal [53]. The *red* and *blue solid lines* represent numerical derivatives of the hysteresis loops for the sweep with decreasing and increasing field, respectively. Peaks in the derivative indicate coercive fields of the constituent layers, which are noted as superscript indices according to the legend

Figure 9.6 displays the second magnetic moment hysteresis loops of Sample III (left panel) and Sample IV (right panel) measured at 120 K close to the Curie temperature of our $Cu_{41}Ni_{59}$ alloy [27].

An evaluation of the exchange bias fields, as described above, yield: $H_{EB,Co} \approx -100$ Oe and $H_{EB,CuNi-hard} \approx -100$ Oe for sample III and $H_{EB,Co} \approx -275$ Oe and $H_{EB,CuNi-hard} \approx -150$ Oe for sample IV respectively. While there are small features visible around zero field in Sample IV and a slight asymmetric broadening of the peaks of H_c^1 towards zero field in sample III, which both possibly indicate an additional contribution of a weak CuNi-soft signal with vanishing exchange bias, we decided against an evaluation of a numeric value for the exchange bias field, as we cannot determine reliable values for the coercive fields.

There are several trends observable from the exchange bias fields evaluated from Figs. 9.4 to 9.6. First, the exchange bias fields in the second loops is smaller than in the first loops for both samples, which is expected due to the training effect, discussed below. Furthermore, the training effect is stronger in Sample IV compared to Sample III. Second, the exchange bias fields are higher in Sample IV compared to Sample III, as the exchange bias is predicted and observed to increase for decreasing thickness [57]. Moreover, the exchange bias decreases for increasing temperature, in accordance with the domain state model [65].

According to the domain state model, the domain structure of the antiferromagnet has to be altered to align with the local direction of the adjacent ferromagnet in order to yield an exchange bias. However, we do not expect that the ferromagnet is able to align the complete antiferromagnetic domain in our samples, as our antiferromagnetic layer is much thicker than the one investigated in [65]. Furthermore, the anisotropy constant of $K_{\text{coO}} = 2.5 \cdot 10^8 \text{erg/cm}^3$ for CoO [57], is orders of magnitude larger than $K_{\text{FeMn}} = 1.3 \cdot 10^5 \text{erg}/\text{cm}^3$ of $Fe_{50}Mn_{50}$ [69], and is even more increased by an additional anisotropy induced to the antiferromagnet by the Co sublayer [65]. This further increases the strength of the exchange interaction between CoO and

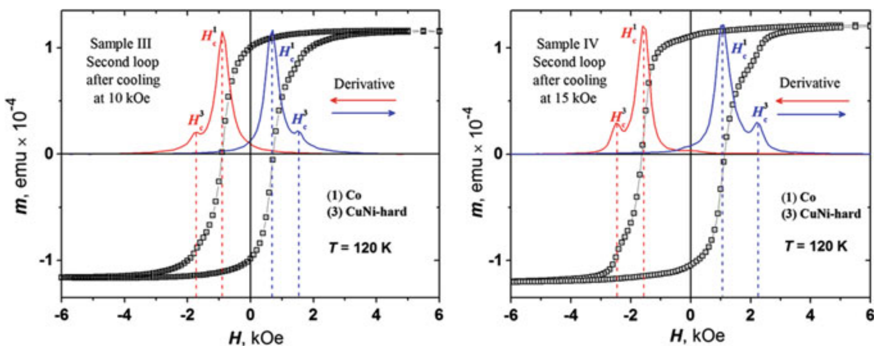

Fig. 9.6 Sweep magnetic hysteresis loops of sample III (*left panel*) and sample IV (*right panel*) measured at 120 K. *Red* (*blue*) lines represent field derivatives of the *leftward* (*rightward*) scans of the magnetic field (the derivatives scale is arbitrary). Peaks in the derivative indicate coercive fields of the constituent layers, which are noted as high indices according to the legend

$Cu_{41}Ni_{59}$ necessary to influence the domain state of the antiferromagnet and, thus decreases the maximal antiferromagnetic thickness, up to which an EB is possible [65]. Blamire et al. [65] also discuss the special case of $T_C < T_N$ in the framework of the domain state model, showing that the EB field, as well as the maximal antiferromagnetic thickness is smaller in this case than for $T_C > T_N$.

Thus, the domain state model is probably not able to explain our experimental findings, while basically including the possibility to mediate exchange coupling between two ferromagnetic layers by the domains of the antiferromagnet.

In contrast, the spin-glass model [57] explains the exchange bias by a magnetically frustrated surface of the antiferromagnet adjacent to the ferromagnet, which consists of a layer of rigidly frozen spins, which has a magnetization surplus in field cooling direction, generating exchange bias, and a layer of weakly coupled spins, contributing to the coercive field enhancement.

This explanation yields the possibility of an EB even for arbitrary thick antiferromagnets with arbitrary high anisotropy, as it is a pure surface effect, however, it is unable to explain a coupling of two ferromagnetic layers across a thick antiferromagnetic layer.

The easy axis of thin $Cu_{1\text{-}x}Ni_x$ films, with x from 53 to 60, is preferably out of plane [60–62]. In contrast CoO_x has an in-plane easy axis [57]. The influence of this easy axis mismatch is unclear and possibly weakens the exchange coupling.

Recently, there were several efforts undertaken, both experimentally and theoretically, in investigating interlayer coupling [57, 70, 71]. While, basically being able to explain a coupling of ferromagnetic states across antiferromagnetic layers of up to 25 nm thickness, it shows no exchange bias, independent of the thickness.

Thus, so far none of the discussed models is able to explain our experimental findings. However, we can see evidence for a strong, exchange biased interlayer coupling in our samples in the second loop of sample IV (see Fig. 9.5 right panel). The contribution corresponding to H_c^3 seems to be much too high to be generated by the very thin $Cu_{41}Ni_{59}$ alone and is strongly exchange biased. A possible explanation could be that a certain part of the Co layer being exchange coupled to the lower $Cu_{41}Ni_{59}$ layer, rotates simultaneously in the field. The mechanism responsible for this coupling is so far not clear.

By comparison of the first and second loops in Figs. 9.4 and 9.5, we can observe a decrease of the exchange bias by the training effect. In the domain state model, this is explained by a relaxation of the domain structure of the AF, which is unfavorable, once the field is below the cooling field or even antiparallel to it [66]. In the spin glass model, the training effect is ascribed to an increase of the fraction of almost freely rotating spins at the cost of the frozen spins [57]. Both explanations yield a decrease of the surface surplus of magnetization in the direction of the cooling field, thus decreasing exchange bias. The effect of this decrease on the Co and CuNi-hard signal seems to be different, yielding a splitting of the coercive fields, which can be seen from a splitting of the maxima in the magnetization derivatives in Figs. 9.4 right panel and Fig. 9.5 right panel in the sweep from positive to negative fields. This indicates a different strength of the training effect for the different components.

9.4 Conclusion

To conclude, evidence for a drastic enhancement of exchange bias has been observed in a diluted ferromagnetic $Cu_{41}Ni_{59}$-alloy layer by addition of a cobalt sublayer below the antiferromagnetic layer, yielding a composite F/AF (Co/CoO) exchange bias system. We compared our finding with the domain state and spin-glass model. However, the phenomenon remains so far unexplained. The results of the present work, especially the possibility to strongly exchange bias diluted ferromagnets, could possibly be an important building block in the development of superconducting spintronics.

Acknowledgments The authors are grateful to S. Heidemeyer, B. Knoblich, and W. Reiber for assistance in the TEM-sample preparation, additionally to W. Reiber for assistance in RBS-Measurements, and to D. Vieweg for assistance in magnetic measurements.

This work was supported by the Deutsche Forschungsgemeinschaft (DFG) under the Grant No. HO 955/9-1. L.R.T. was supported in part by the Russian Fund for Basic Research (RFBR) under the Grant No. 16-02-01171-a and by the Program of Competitive Growth of Kazan Federal University funded by Russian Government. R.M. was partially supported by the Program of Competitive Growth of Kazan Federal University funded by Russian Government. The magnetic investigations (H.-A. K.v.N.) were partially supported by the Deutsche Forschungsgemeinschaft (DFG) within the Transregional Collaborative Research Center TRR 80 "From Electronics Correlations to Functionality" (Augsburg, Munich).

Appendix

From the magnetic moment per atom, m_{at}, the saturation magnetic moment, m_s, of samples III and IV can be calculated, summing up the saturation magnetic moments m_L of the Co and $Cu_{41}Ni_{59}$ layers of the thin-film heterostructure, according to $m_L = m_{at}\ (V_L\ /V_{mol,\ L})\ N_A$. Here V_L is the volume of the respective layer, $V_{mol,\ L}$ is the molar volume of the material of the layer, and N_A is the Avogadro constant. With $m_{at,Cu41Ni59} = 0.14\ \mu_B$ [72] and$m_{at,Co} = 1.7\ \mu_B$ [73], $V_{mol,Cu41Ni59} = 6.8\ cm^3$ [27], $V_{mol,Co} = 6.62\ cm^3$, $\mu_B = 0.9274 \cdot 10^{-20}$ emu [27], and considering that the area of sample III and IV is $A = 19.75\ mm^2$ and $A = 27.0\ mm^2$, respectively, we obtain $1.80 \cdot 10^{-4}$ emu and $1.61 \cdot 10^{-4}$ emu for m_s of sample III and IV, respectively. This is considerably larger than the magnetic moment observed for a magnetic field of 5 kOe in Figs. 9.4 and 9.5, respectively. One has, however, to consider that a large diamagnetic background of the 0.5 mm thick Si substrate is present in such measurements. Therefore, the measured total magnetic moment is lower than that one of the ferromagnetic material. For high magnetic fields, as soon as the ferromagnetic material has reached its saturation magnetization, the $m(H)$ curve becomes a straight line (see, e.g., [27] for a measurement of a single $Cu_{41}Ni_{59}$ film on a Si substrate). However, in the field range of Figs. 9.4, 9.5 and 9.6 this linear behavior is almost not visible. The reason may be a linear paramagnetic contribution from the CoO_x antiferromagnet [74] superimposed to the diamagnetic contribution. Moreover, one has to

consider that there are several sources of experimental errors possible in SQUID measurements of small magnetic moments, as discussed in detail by Garcia et al. [75] and Hautot et al. [76].

References

1. J.J. Hauser, H.C. Theuerer, N.R. Werthamer, Phys. Rev. **142**, 118 (1966)
2. A.I. Buzdin, Rev. Mod. Phys. **77**, 935 (2005)
3. F.S. Bergeret, A.F. Volkov, K.B. Efetov, Rev. Mod. Phys. **77**, 1321 (2005)
4. K.B. Efetov, I.A. Garifullin, A.F. Volkov, K. Westerholt, Proximity effects in ferromagnet/superconductor heterostructures, in *Magnetic Heterostructures*, ed. by H. Zabel, S.D. Bader. Springer Tracts in Modern Physics, vol. 227 (Springer, Berlin, 2008), Ch. 5, pp. 251−290
5. M. Eschrig, Phys. Today **64**, 43 (2011)
6. A.I. Buzdin, M.Yu. Kupriyanov, Pis'ma v ZhETF **53**, 308 [JETP Lett. **25**, 290 (1991)]
7. V.V. Ryazanov, Physics—Uspekhi **42**, 825 (1999)
8. V.V. Ryazanov, V.A. Oboznov, AYu. Rusanov, A.V. Veretennikov, A.A. Golubov, J. Aarts, Phys. Rev. Lett. **86**, 2427 (2001)
9. S. Oh, D. Youm, M. Beasley, Appl. Phys. Lett. **71**, 2376 (1997)
10. L.R. Tagirov, Phys. Rev. Lett. **83**, 2058 (1999)
11. A.I. Buzdin, A.V. Vedyayev, N.V. Ryzhanova, Europhys. Lett. **48**, 686 (1999)
12. Y.V. Fominov, A.A. Golubov, T.Yu. Karminskaya, M.Y. Kupriyanov, R.G. Deminov, L.R. Tagirov, Pis'ma v ZhETF **91**, 329 (2010) [JETP Lett. **91**, 308 (2010)]
13. A.V. Ustinov, V.K. Kaplunenko, J. Appl. Phys. **94**, 5405 (2003)
14. L.V. Mercaldo, C. Attanasio, C. Coccorese, L. Maritato, S.L. Prischepa, M. Salvato, Phys. Rev. B **53**, 14040 (1996)
15. A. Rusanov, R. Boogaard, M. Hesselberth, H. Sellier, J. Aarts, Physica C **369**, 300 (2002)
16. V.V. Ryazanov, V.A. Oboznov, A.S. Prokofiev, S.V. Dubonos Pis'ma v ZhETF **77**, 43 (2003) [JETP Lett. **77**, 39 (2003)]
17. C. Baraduc, F. Lefloch, R. Calemczuk, Phys. Rev. B **68**, 054531 (2003)
18. L. Crétinon, A.K. Gupta, H. Sellier, F. Lefloch, M. Fauré, A. Buzdin, H. Courtois, Phys. Rev. B **72**, 024511 (2005)
19. C. Cirillo, S.L. Prischepa, M. Salvato, C. Attanasio, M. Hesselberth, J. Aarts, Phys. Rev. B **72**, 144511 (2005)
20. A. Potenza, C.H. Marrows, Phys. Rev. B **71**, 180503 (2005)
21. J. Kim, J.H. Kwon, K. Char, H. Doh, H.-Y. Choi, Phys. Rev. B **72**, 014518 (2005)
22. G.P. Pepe, R. Latempa, L. Parlato, A. Ruotolo, G. Ausanio, G. Peluso, A. Barone, A.A. Golubov, Y.V. Fominov, Y.V. Kupriyanov, Phys. Rev. B **73**, 054506 (2006)
23. M.I. Khabipov, D.V. Balashov, F. Maibaum, A.B. Zorin, V.A. Oboznov, V.V. Bol'ginov, A. N. Rossolenko, V.V. Ryazanov, Supercond. Sci. Techol. **23** 045032 (2010)
24. A.K. Feofanov, V.A. Oboznov, V.V. Bol'ginov, J. Lisenfeld, S. Poletto, V.V. Ryazanov, A.N. Rossolenko, M. Khabipov, D. Balashov, A.B. Zorin, P.N. Dmitriev, V.P. Koshelets, A.V. Ustinov, Nat. Phy. **6**, 593 (2010)
25. V.V. Ryazonov, V.V. Bol'ginov, D.S. Sobanin, I.V. Vernik, S.K. Tolpygo, A.M. Kadin, O.A. Mukhanov, Physics Procedia **36**, 35 (2012)
26. V.I. Zdravkov, A.S. Sidorenko, G. Obermeier, S. Gsell,M. Schreck, C. Müller, S. Horn, R. Tidecks, L.R. Tagirov, Phys. Rev. Lett. **97**, 057004 (2006)
27. V.I. Zdravkov, J. Kehrle, G. Obermeier, S. Gsell, M. Schreck, C. Müller, H.-A. Krug von Nidda, J. Lindner, J. Moosburger-Will, E. Nold, R. Morari, V.V. Ryazanov, S.A. Sidorenko, S. Horn, R. Tidecks, L.R. Tagirov, Phys. Rev. B **82**, 054517 (2010)

28. V.I. Zdravkov, J. Kehrle, G. Obermeier, A. Ulrich, S. Gsell, M. Schreck, C. Müller, R. Morari, A.S. Sidorenko, L.R. Tagirov, R. Tidecks, S. Horn, Supercond. Sci. Technol. **24**, 095004 (2011)
29. J. Kehrle, V.I. Zdravkov, G. Obermeier, J. Garcia-Garcia, A. Ullrich, C. Müller, R. Morari, A. S. Sidorenko, S. Horn, L.R. Tagirov, R. Tidecks, Ann. Phys. **524**, 37 (2012)
30. I. Žutić, J. Fabian, Das Sarma. S. Rev. Mod. Phys. **76**, 323 (2004)
31. D.C. Ralph, M.D. Stiles, J. Magn. Magn. Mater. **320**, 1190 (2008)
32. N. Locatelli, V. Cros, J. Grollier, Nat. Mater. **13**, 11 (2014)
33. J.Y. Gu, C.-Y. You, J.S. Jiang, J. Pearson, Y.B. Bazaliy, S.D. Bader, Phys. Rev. Lett. **89**, 267001 (2002)
34. R. Steiner, P. Ziemann, Phys. Rev. B **74**, 094504 (2006)
35. I.C. Moraru, W.P. Pratt Jr., N.O. Birge, Phys. Rev. Lett. **96**, 037004 (2006)
36. I.C. Moraru, W.P. Pratt Jr., N.O. Birge. Phys. Rev. B **74**, 220507 (2006)
37. J. Aarts, A.Y. Rusanov, C.R. Physique **7**, 99 (2006)
38. A.Y. Rusanov, S. Habraken, J. Aarts, Phys. Rev. B **73**, 060505 (2006)
39. A. Singh, C. Surgers, H.V. Löhneysen Phys. Rev. B **75**, 024513 (2007)
40. A. Singh, C. Sürgers, H.V. Löhneysen, R.T. Hoffmann, V. Ashworth, N. Pilet, H.J. Hug, Appl. Phys. Lett. **91**, 152504 (2007)
41. D.H. Kim, T.J. Hwang, Physica C **455**, 58 (2007)
42. G. Nowak, H. Zabel, K. Westerholt, I. Garifullin, M. Marcellini, A. Liebig, B. Hjörvarsson, Phys. Rev. B **78**, 134520 (2008)
43. P.V. Leksin, R.I. Salikhov, I.A. Garifullin, H. Vinzelberg, V. Kataev, R. Klingeler, L.R. Tagirov, B.Büchner, Pis'ma v ZhETF **90**, 64 (2009) [JETPL **90**, 59 (2009)]
44. J. Zhu, X. Cheng, C. Boone, I.N. Krivorotov, Phys. Rev. Lett. **103**, 027004 (2009)
45. Y. Luo, K. Samwer, Europhys. Lett. **91**, 37003 (2010)
46. P.V. Leksin, N.N. Garif'yanov, I.A. Garifullin, J. Schumann, H. Vinzelberg, V.E. Kataev, R. Klingeler, O.G. Schmidt, B. Büchner, Appl. Phys. Lett. **97**, 102505 (2010)
47. P.V. Leksin, N.N. Garif'yanov, I.A. Garifullin, J. Schumann, H. Vinzelberg, V.E. Kataev, R. Klingeler, O.G. Schmidt, B. Büchner, Appl. Phys. Lett. **106**, 067005 (2011)
48. T.Y. Karminskaya, M.Y. Kupriyanov, Pis'ma v ZhETF **86**, 65 (2007) [JETP Lett. 86, 61 (2007)]
49. M. Houzet, A.I. Buzdin, Phys. Rev. B **76**, 060504(R) (2007)
50. T.Y. Karminskaya, M.Y. Kupriyanov, Pis'ma v ZhETF **87**, 657 (2008) [JETP Lett. **87**, 570 (2008)]
51. T.I. Larkin, V.V. Bol'ginov, V.S. Stolyarov, V.V. Ryazanov, I.V. Vernik, S.K. Tolpygo, O.A. Mukhanov, Appl. Phys. Lett. **100**, 222601 (2012)
52. I.V. Vernik., V.V. Bol'ginov, S.V. Bakurskiy, A.A. Golubov, M.Y. Kupriyanov, V.V. Ryazanov, O.A. Mukhanov IEEE Trans. Appl. Supercond. **23**, 1701208 (2013)
53. V.I. Zdravkov, D. Lenk, R. Morari, A. Ullrich, G. Obermeier, C. Müller, H.-A. Krug von Nidda, A.S. Sidorenko, S. Horn, R. Tidecks, L.R. Tagirov, Appl. Phys. Lett. **103**, 062604 (2013)
54. J. Nogués, I.K. Schuller, J. Magn. Magn. Mater. **192**, 203 (1999)
55. E.E. Fullerton, J.S. Jiang, S.D. Bader, J. Magn. Magn. Mater. **200**, 392 (1999)
56. J. Nogués, J. Sort, V. Langlais, V. Skumryev, S. Suriñach, J.S. Muñoz, M.D. Baró, Phys. Rep. **422**, 65 (2005)
57. F. Radu, H. Zabel, Exchange bias effect of ferro-/antiferromagnetic heterostructures, in *Magnetic Heterostructures*, ed. by H. Zabel, S.D. Bader. Springer Tracts in Modern Physics, vol. 227, (Springer, Berlin 2008), Ch. 3, pp 97–184
58. W.H. Meiklejohn, C.P. Bean, Phys. Rev. **102**, 1413 (1956)
59. V.I. Zdravkov, J. Kehrle, D. Lenk, G. Obermeier, A. Ullrich, C. Müller, H.-A. Krug von Nidda, A.S. Sidorenko, L.R. Tagirov, L.R. Horn, R. Tidecks, J. Appl. Phys. **114**, 033903 (2013)
60. A. Ruotolo, C. Bell, C.W. Leung, M.G. Blamire, J. Appl. Phys. **96**, 512 (2004)

61. I.S. Veshchunov, V.A. Oboznov, A.N. Rossolenko, A.S. Prokofiev, L.Y. Vinnikov, A.Y. Rusanov, D.V. Matveev, Pis'ma v ZhETF **88**, 873 (2008) [JETP Lett. **88**, 758 (2008)]
62. V.I. Zdravkov, J. Kehrle, G. Obermeier, D. Lenk, H.-A. Krug von Nidda, C. Muller, M.Y. Kupriyanov, A.S. Sidorenko, S. Horn, R. Tidecks, L.R. Tagirov, Phys. Rev. B **87**, 004500 (2013)
63. M.-F. Lai, C.-R.Chang, J.C. Wu, Z.-H. Wei, J.H. Kuo, J.-Y. Lai, IEEE Trans. Magn. **38**, 2550 (2002)
64. C. Cirillo, C. A. García-Santiago , J.M. Hernandez, C. Attanasio, J. Tejada, J. Phys.: Condens. Matter **25**, 176001 (2013)
65. M.G. Blamire, M. Ali, C.-W. Leung, C.H. Marrows, B.J. Hickey, Phys. Rev. Lett. **98**, 217202 (2007)
66. U. Nowak, K.D. Usadel, J. Keller, P. Miltényi, B. Beschoten, G. Güntherodt, Phys. Rev. B **66**, 014430 (2002)
67. C.A.F. Vaz, E.I. Altman, V.E. Henrich, Phys. Rev. B **81**, 104428 (2010)
68. J. Kehrle, The Fulde-Ferrell Larkin-Ovchinnikov like state in bilayers and trilayers of superconducting and ferromagnetic thin films. Ph.D. thesis, University of Augsburg, Germany, 2012
69. J. Wang, W.N. Wang, X. Chen, H.W. Zhao, J.G. Zhao, WSh Zhan, Appl. Phys. Lett. **77**, 2731 (2000)
70. S.O. Demokritov, J. Phys. D Appl. Phys. **31**, 925 (1998)
71. J. Camarero, Y. Pennec, J. Vogel, M. Bonfim, S. Pizzini, F. Ernult, F. Fettar, F. Garcia, F. Lançon, L. Billard, B. Dieny, A. Tagliaferri, N.B. Brookes, Phys. Rev. Lett. **91**, 027201 (2003)
72. S.A. Ahern, M.J.C. Martin, W. Sucksmith, Proc. Roy. Soc. London, A248, **145** (1958)
73. V.S.R Murthy, A.K. Jena, K.P. Gupta, G.S. Murty, Structure and Properties of Engineering Materials; Tata McGraw Hill: New Delhi Ch. 12, p. 381 (2003)
74. S. Chikazumi, Physics of Ferromagnetism, 2nd Edition, Oxford University Press: Oxford, New York §19.1. (1997)
75. M.A. Garcia, E. Fernandez Pinel, J. de la Venta, A. Quesada, V. Bouzas, F. Fernández, J.J. Romero, M.S. Martín González, J.L. Costa-Krämer, J. Appl. Phys. **105**, 013925 (2009)
76. D. Hautot, Q.A. Pankhurst, J. Dobson, Rev. Sci. Instrum. **76**, 045101 (2005)

Part III
Nanostructured and Composite Materials

Chapter 10
Local Ordering at the Interface of the TiO_2-WO_3 Bi-Layers

Dan Macovei, Vasile Dăscăleanu, Cristian M. Teodorescu and Dumitru Luca

Abstract Reducing the recombination rate of photo-generated electron-hole pairs in the surface of pristine TiO_2 materials can be done, among others, via local spatial charge separation in the photocatalytically active surface region. A local electric field acting for this purpose can be ensured, for instance, in hetero-junction regions formed at the interface between a TiO_2 film and a WO_3 ultra-thin layer. The option for the WO_3–TiO_2 semiconductor pair is related to the suitable fit of their band structures. To model the interface, a more in-depth knowledge of local atomic environment is required. Here, we discuss the local atomic ordering and the related effects in the interface region of TiO_2/WO_3 and WO_3/TiO_2 structures grown on Si (100) substrates. Materials characterization was done by using XRD, XPS and XAS techniques. We demonstrate that tungsten atoms enter as W^{6+} or W^{4+} cations into the rutile-type TiO_2 lattice, by substituting the Ti^{4+} cations. While W^{6+}-Ti^{4+} substitution leaves the surrounding rutile matrix unchanged, the W^{4+}-Ti^{4+} substitution induces a local rutile-to-anatase transition. The current results are relevant in designing new applications structures with enhanced photocatalytic performances.

10.1 Introduction

TiO_2 is known as one of the most stable and highly reactive photocatalysts in a wide range of applications, recommended by low cost, non-toxicity, and long-life operation. It is extensively applied to degrade organic pollutants and for air purification, photocatalytic sterilization, reduction of nitrogen to ammonia, water splitting, electrochemical conversion of solar energy [1]. Under UV light irradiation, titania films feature super-hydrophilicity, therefore being used in surface self-cleaning and antifogging applications [1]. Yet, pristine TiO_2 materials'

D. Macovei · C.M. Teodorescu
National Institute of Materials Physics, 077125 Măgurele-Ilfov, Romania

V. Dăscăleanu · D. Luca (✉)
Alexandru Ioan Cuza University, Iasi, Romania
e-mail: dumitru.luca@uaic.ro

© Springer International Publishing Switzerland 2016

I. Tiginyanu et al. (eds.), *Nanostructures and Thin Films for Multifunctional Applications*, NanoScience and Technology,
DOI 10.1007/978-3-319-30198-3_10

applications are associated with two shortcomings: (i) limited photo-activation to only UV range (i.e. less than about 5 % of the sunlight energy), and (ii) limited catalytic activity lifetime, due to due to the recombination of the photo-generated electron-hole pairs on defect centers [2].

TiO_2 photo-activity has been improved by doping with transition metals [3–6], rare earths [7–10] or non-metals [11–16], resulting in extension of the optical response from UV towards the blue region of the visible light. Non-metal dopants are generally considered as more effective, since they lead to both band-gap narrowing and charge-carrier separation, whereas the metal doping often enhances carrier trapping on the localized metal states in the band gap of TiO_2. However, W-doped TiO_2 materials received much attention, due to associated significant improvement of the photocatalytic activity in comparison with pristine TiO_2. The Ti substitution by W^{6+} ions modifies the electronic structure of the TiO_2 host, resulting in a better charge separation and higher photocatalytic efficiency [17]. Besides, the Ti^{4+} substitution by higher-valence cations (like W^{6+}) generates Ti^{3+} ions, in order to maintain the electrical neutrality of the lattice. These ions reduce the carrier recombination rate, thus enhancing the photocatalytic activity. Such a mechanism is similar to that proposed by Yu et al. for F-doped TiO_2 [14] to explain the improved lifetime of the photo-generated carriers and enhanced quantum efficiency.

An alternate way to overcome the TiO_2 shortcomings consists in its coupling with other semiconductors such as CdS, ZnO, SnO_2, SiO_2 or WO_3, featuring different energy levels [18]. In such heterogeneous semiconductor systems, the transfer of the photo-generated carriers between the two semiconductors considerably lowers the recombination rate, thus improving the efficiency of the photocatalytic reactions. Among these hetero-junctions, that between WO_3 (E_g = 2.8 eV) and TiO_2 (E_g = 3.2 eV for anatase and 3.0 eV for rutile) is of particular interest, due to the suitable distribution of the valence and conduction bands. This facilitates charge separation, by transferring the photo-generated electrons from the conduction band of TiO_2 towards WO_3 (with a lower bottom of the conduction band), while the holes move from WO_3 into the valence band of TiO_2 [17].

While the photocatalytic properties of the TiO_2-WO_3 hetero-junctions, as well as their connection with the electronic structure, were widely studied, little attention has been paid to their interface interaction from a structural point of view. We report here on the interface structural interactions in rutile TiO_2-WO_3 photocatalytic bilayer films, prepared by plasma vapor deposition (PVD). The structure and chemical composition of the films were investigated by X-ray diffraction (XRD), X-ray absorption near-edge structure (XANES) spectroscopy, extended X-ray absorption fine-structure (EXAFS) spectroscopy, and X-ray photoelectron spectroscopy (XPS). We show that the oxide layers interact at their interface, with the W diffusion into the TiO_2 lattice, on Ti sites, as W^{6+} and W^{4+} ions. The Ti^{4+} substitution by W^{6+} leaves the surrounding rutile host unchanged, while the substitution by W^{4+} (of larger radius than Ti^{4+}) changes the local environment towards a dilated anatase-like structure.

10.2 Materials and Methods

Bilayer TiO_2/WO_3 (TWS) and WO_3/TiO_2 (WTS) thin films were sequentially deposited on Si(100) substrates, by using an RF magnetron sputtering facility (Hüttinger, PFG 300 RF; 13.56 MHz, 2×10^{-5} mbar base pressure). The details of the preparation were given elsewhere [19]. The deposition setup was equipped with two ceramic disk targets (K. J. Lesker, 99.9 % purity), with a diameter of 76.2 mm. The RF power injected in the discharge (in Ar gas), via an automatic matching box, was adjusted to 70 W to deposit the TiO_2 layers and to 50 W for the WO_3 layers. The deposition pressure (4×10^{-3} mbar) and the target-substrate distance (5 cm) were maintained constant during deposition in all experiments. The film thickness was determined by an in situ quartz microbalance (Sigma Instruments, SQM-160), calibrated against a surface profilometer, prior to deposition experiments. The top-layer thickness was 50 nm for both TWS and WTS samples, whereas the thickness of the bottom layer was $\sim$150 nm for sample TWS (WO_3 layer) and $\sim$200 nm for WTS (TiO_2 layer).

The film structure was determined by XRD, performed on a Shimadzu XRD–6000 diffractometer using Cu Kα radiation (λ = 1.5406 Å). Elemental composition and atomic concentration depth profile of the bilayer films were determined by the XPS technique, carried out on a Physical Electronics PHI-5000 VersaProbe spectrometer equipped with a monochromatic Al Kα radiation source (1486.6 eV). The energies in the XPS spectra were calibrated by using the C 1*s* level (284.6 eV) of the adventitious carbon as an internal reference. The concentration depth profiles were acquired by etching the sample surface with Ar^+ ions (1 keV, 500 nA beam current). XPS data processing was done using the PHI-MultiPak software.

Local structure around the metallic atoms was investigated by EXAFS spectroscopy at the Ti K (4966 eV) and W L_3 (10207 eV) edges. The primary absorption spectra (including the XANES and EXAFS ranges) were performed at the beamlines A1 (Ti K) and CEMO (W L_3) of the HASYLAB synchrotron-radiation facility (Hamburg, Germany). The incident radiation was analyzed by a Si(111) double-crystal monochromator and the absorption was measured in fluorescence mode. Powdered TiO_2 (anatase) and a WO_3 thin film were also measured, with a transmission setup for the former compound.

The EXAFS data were analyzed by a standard procedure, using the REX2000 package [20]. The pre-edge background was subtracted from the spectra, after its fit with a Victoreen formula. The EXAFS function $\chi(k)$ (where k is photoelectron wave number) was subsequently calculated from the absorption oscillations normalized through the atomic absorption (approximated by the smooth post-edge background). The $k^3\chi(k)$ spectra were Fourier transformed into physical r space resulting in radial atomic quasi-distributions with maxima corresponding, up to systematic shifts, to the neighboring shells of the absorbing atoms (Ti, W). The Fourier inversion of EXAFS was performed over the k-ranges 3.2–12.2 Å^{-1} and

2.8–12.6 $Å^{-1}$ for the Ti K and W L_3 edges, respectively. The first three maxima of the Fourier transforms (FT) of the TiO_2-WO_3 films, corresponding to the O and Ti neighbors of the absorbing atoms, were isolated by Hanning windows and back-transformed into the k space. The so-filtered spectra, describing the EXAFS contribution of the selected neighboring shells, were non-linearly fitted with structural models, by a least-square method. The fit provided the structural parameters of the close surrounding of the absorbing atoms, i.e. the number (N) of the neighboring atoms, the absorbing atom−neighbor mean distances (R), and their mean square fluctuation (σ^2) around average values.

The EXAFS standards (electron backscattering amplitudes, phase-shifts, and mean free path between inelastic scatterings) characteristic of the Ti-O and Ti–Ti atomic pairs were derived from the spectrum of the anatase TiO_2, of known structure [21]. During the fit of the TiO_2 EXAFS, we have neglected the contribution of the higher oxygen neighbors (beyond 3.5 Å), superposed to the contribution of the titanium neighbors. This approximation is reasonable, taking into account that the oxygen contribution to EXAFS in the fitted k range is smaller than that of titanium by a factor of two to three. The EXAFS standards of the W-O and W-Ti pairs were calculated by the FEFF6 code [22]. The WO_3 film, of monoclinic structure [23], could not be used as a reference compound for the W-O distance, due to the split of the nearest oxygen shell around the W atoms. The R-factor of the fit of k^3-weighted EXAFS varied between 0.04 and 0.08.

10.3 Results and Discussion

10.3.1 XRD Analysis

The XRD patterns of the TWS and WTS bilayers (Fig. 10.1) show the (002), (020), and (200) maxima of the monoclinic WO_3 (JCPDS card no. 43-1035, space group $P2_1/n$), known to be the most stable phase of the bulk WO_3 at temperatures up to 330 °C [24]. However, the coexistence of this phase with a triclinic one (JCPDS card no. 32-1395) cannot be definitely ruled out, taking into account the close similarity of their diffraction patterns. The (002) and (020) maxima (at $2\theta = 23.1°$ and 23.6°, respectively) of these phases are superposed in the XRD patterns, due to their broadening by crystallite-size effects and instrumental resolution.

The TiO_2 layer is manifest by the (110) peak of the rutile structure (JCPDS card no. 21-1276), of a high intensity in the pattern of the sample WTS. This peak markedly diminishes in the TWS pattern, while the (101) peak of anatase (JCPDS card no. 21-1272) becomes visible, pointing out the presence of the both phases in this film. The Si substrate contributes to XRD plots by the Si (111) maximum, at $2\theta = 28.4°$.

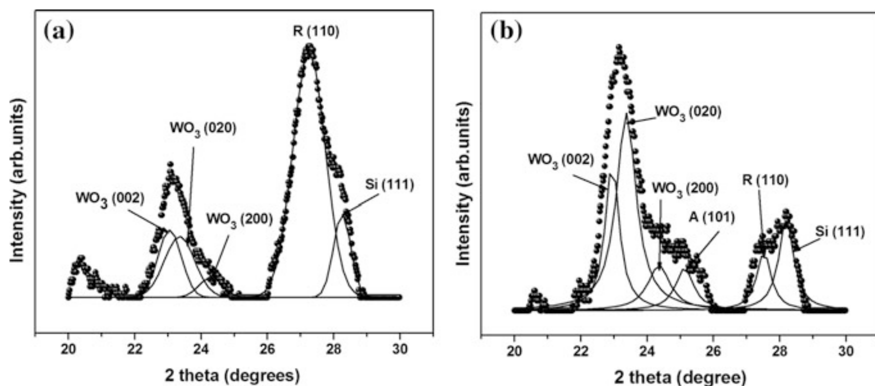

Fig. 10.1 Details of the diffraction patterns of the samples WTS (**a**) and TWS (**b**), including the most intense maxima of WO_3, rutile TiO_2 (R), and anatase TiO_2 (A)

10.3.2 XPS Analysis

The XPS survey spectrum of the WTS film (Fig. 10.2) displays the W core-level peaks of the WO_3 overlayer. A detail of the TWS spectrum was also shown on top of the figure, with the most intense Ti $2p_{3/2,1/2}$ peaks of the TiO_2 top layer. Both spectra show the XPS signals of the top layer exclusively, without a visible contribution from the bottom layer. This is due to the mean-free path λ of the photoelectrons, which is limited to about 15 Å for the measured kinetic energies of the photoelectrons. The corresponding escape depth, estimated as ∼3 λ, is smaller

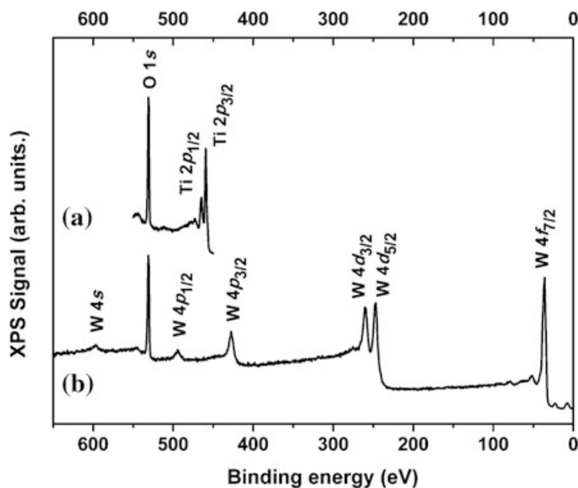

Fig. 10.2 XPS survey spectra of the TWS (**a**) and WTS (**b**) samples

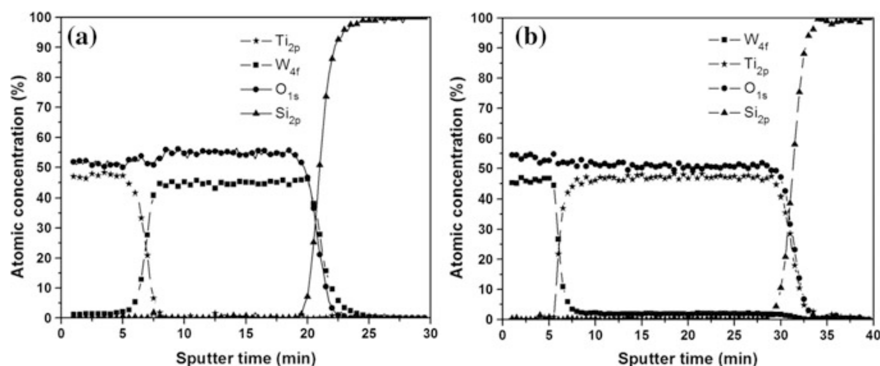

Fig. 10.3 The chemical depth profiles of samples TWS (**a**) and WTS (**b**)

than ∼45 Å, thus slightly inferior to the overlayer thickness. The elemental analysis of the film surface, carried out on narrow-scan spectra (not shown here), confirmed the WO_3 stoichiometry of the upper layer in the WTS sample.

The XPS depth profiles of the elemental composition of the TWS and WTS films are shown in Fig. 10.3. The quantitative analysis of the elemental concentration around the bilayer interface has been done taking into account the sensitivity factors of titanium and tungsten [25]. A sharp TiO_2-WO_3 interface is evidenced after etching the 50 nm thickness WO_3 (WTS) or TiO_2 (TWS) top layer by Ar^+ ion bombardment. After further removal of the bottom layer (TiO_2 in WTS and WO_3 in TWS), the next interface, with the Si substrate, became also clearly visible.

The XPS depth profiles of the two samples explain the intensity ratios between the XRD maxima of the TiO_2 and WO_3 layers. In WTS, the thin WO_3 overlayer contributes by weaker peaks with respect to the TiO_2 bottom layer, of a thickness about four times larger. By contrast, the WO_3 sublayer in TWS is thicker than the TiO_2 overlayer and its diffraction maxima are correspondingly stronger. As will be further discussed, a partial rutile-to-anatase transition takes place at the TiO_2-WO_3 interface, caused by the W inclusion into the TiO_2 lattice. The A(101) peak in the diffraction pattern of the sample TWS corresponds to the interface anatase. As shown by the XPS depth profile, the interface region in this sample is rather broad, of a thickness relatively comparable with that of the rutile TiO_2 overlayer. Consequently, both R(110) and A(101) peaks are visible in the XRD pattern, with comparable intensities. The interface is much narrower than the rutile sublayer in the sample WTS, which makes the A(101) peak hardly visible on the XRD pattern. The strongest peak of the WTS pattern is R(110), contributed by the dominating rutile sublayer.

10.3.3 Ti K-Edge XANES

The Ti K-edge XANES spectra (normalized to the absorption at ~280 eV above the edge) of the TiO_2-WO_3 films and anatase TiO_2 are shown in Fig. 10.4. The pre-edge (A_1–A_3) and edge (C_1–C_3) spectral features of the samples TWS and WTS are specific to the rutile structure [26–28]. The both pre-edge and edge features of the experimental XANES spectra of rutile and anatase were theoretically reproduced by band-structure and multiple-scattering calculations on atomic clusters sufficiently large around the absorbing Ti atom, connecting the atomic arrangements and electronic structures of the two titanium oxides with the positions and intensities of the spectral features [26, 27, 29]. Although the origin of the rutile XANES features was rather controversial in literature, the pre-edge peaks were generally explained by the mixture of the 3*d* and 4*p* orbitals of Ti atoms on the same or neighboring sites of the structure [26, 29–33]. Wu et al. [29] attributed the first and second pre-edge peaks (A_1, A_2) to dipolar transitions of the photoelectrons from Ti 1*s* to the 4*p* orbital of the absorbing Ti atom hybridized with 3*d* orbitals of the neighboring Ti atoms, split by the octahedral crystal field into t_{2g} and e_g band-like states. The A_3 peak was assigned by the same authors to the transitions on Ti 4*p* hybridized with the 4*s* orbitals of the neighboring Ti atoms and/or 2*p* orbitals of the O atoms. The C_1–C_3 crests were assigned to the transitions on Ti 4*p* states hybridized with O 2*p* states.

As shown by Fig. 10.4, the edge features C_1–C_3 are more sensitive to the changes of the local structure around Ti by going from anatase to rutile, resulting in more marked differences in this range with respect to the pre-edge peaks. The C_1–

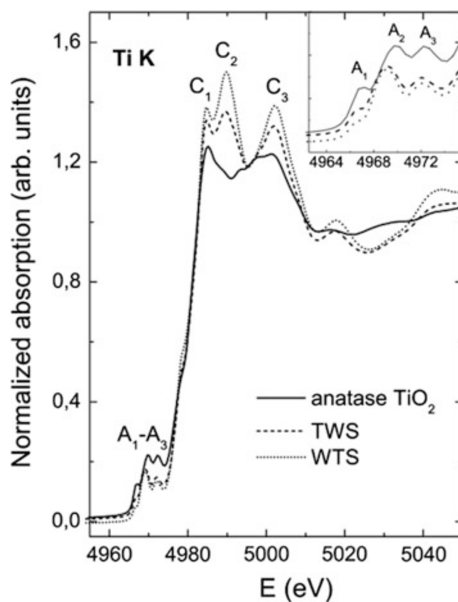

Fig. 10.4 Ti K-edge XANES normalized spectra of the TiO_2-WO_3 films and anatase TiO_2. The spectra were vertically translated for the sake of clarity. A detail with the pre-edge peaks of the spectra is shown in the inset

C_3 peaks undoubtedly point out the rutile structure of TiO_2 in the TiO_2-WO_3 films, in agreement with the XRD results. However, the reduced intensities of the C_2 and C_3 peaks of the sample TWS, somehow closer to the anatase XANES, could indicate a small TiO_2 fraction of anatase-like structure in this sample. This is also in line with the XRD pattern of the sample TWS, containing a faint anatase contribution (A(101) maximum in Fig. 10.1b).

10.3.4 EXAFS Measurements

10.3.4.1 Ti Environment

The k^3-weighted EXAFS of the Ti K and W L_3 edges, as well as the magnitude of the corresponding Fourier transforms (FT) are shown in Fig. 10.5, for the TiO_2-WO_3 bilayers and the anatase TiO_2 and WO_3 oxides. In the tetragonal structure of anatase TiO_2 [21], Ti is surrounded by six oxygen neighbors at a mean distance of 1.95 Å and by farther Ti neighbors at 3.04 Å (4 Ti1) and 3.78 Å (4 Ti2). The three main maxima of the anatase FT (Fig. 10.5b) correspond to this environment.

The rutile structure [34], despite the same tetragonal symmetry, shows several changes of the Ti environment. The oxygen surrounding is practically the same as in anatase, but the Ti neighbors arrange differently (see Table 10.1). The number of the Ti1 neighbors (N_{Ti1}) is reduced to a half (2 instead of 4 in anatase), whereas

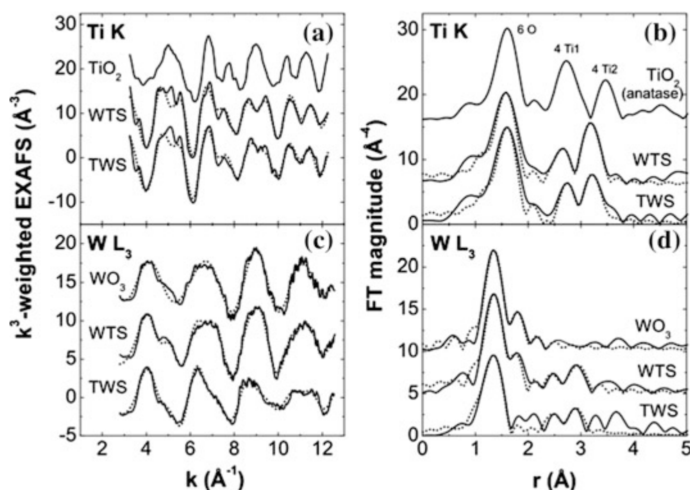

Fig. 10.5 **a**, **c** k^3-weighted EXAFS of the Ti K and W L_3 edges of the TiO_2-WO_3 bilayers, anatase TiO_2 and WO_3. **b**, **d** Magnitude of the corresponding Fourier transforms. The raw data and their fit with the O and Ti neighbors of the absorbing atoms were shown by continuous lines and dots, respectively. The EXAFS spectra and their transforms were vertically shifted for clarity

N_{Ti2} doubles to 8. The distances to the Ti1 and Ti2 neighbors also shorten with respect to the anatase structure, by about 0.10 and 0.20 Å, respectively. The shift towards smaller distances of the maxima corresponding to the Ti shells in the FTs of the samples TWS and WTS, more visible for the Ti2 neighbors, indicates the rutile structure of the TiO_2 layers in the TiO_2-WO_3 films. This result is in accord with the presence of the rutile (110) peak in the diffraction patterns of the samples. However, the weak anatase (101) peak in the XRD pattern of the sample TWS suggests a partial rutile-to-anatase transition of TiO_2 in this sample. A more detailed description of the Ti environment was possible by the fit of EXAFS. The results of the fit, i.e. coordination numbers (N) and interatomic distances (R), were given in Table 10.1. For simplification, the mean-square fluctuations (σ^2) of the interatomic distances, less relevant in the further analysis, were not indicated in the table.

The nearest surrounding of Ti in the TiO_2-WO_3 bilayers, consisting of six oxygen ions at 1.95 Å, closely resembles the rutile structure. However this is not very conclusive, since the Ti-O distance differs by only 0.01 Å in anatase and rutile, within the fit uncertainties. The next-nearest neighboring of Ti (Ti1 and Ti2 cations) in the sample WTS is characteristic of the rutile structure, although the depletion of the Ti2 neighbors, from $N_{Ti2} = 8$ in rutile to $N_{Ti2} = 4$ in WTS, suggests a defective structure, with Ti vacancies at larger distances.

A partial rutile-to-anatase transition is manifest for the sample TWS, with Ti2 neighbors at 3.56 Å, close to the rutile structure, but with 3 Ti1 at 3.04 Å, almost identical with the anatase structure. This environment points out a mixture of the initial rutile matrix and a developing anatase phase. The long-distance Ti2 neighbors in the anatase phase are probably strongly disordered, so that their contribution at around 3.78 Å wipes out of EXAFS.

10.3.4.2 W Environment

At the growth temperature (200 °C) of the WO_3 and TiO_2-WO_3 films, the WO_3 structure is expectedly monoclinic [24]. However, as previously observed for WO_3 thin films deposited under 300 °C, the presence of the both monoclinic and triclinic polymorphs in the WO_3 structure cannot be entirely precluded [35]. Despite their different symmetries, these varieties have closely related structures [23, 36], resulting in similar long-range order and diffraction patterns. The short-range order (W environment) is also almost identical in the two phases, as shown in Table 10.1. This makes quite difficult to distinguish between them by XRD or EXAFS. However, the possible presence of a triclinic phase in the WO_3 layers, besides the stable monoclinic form, does not change the further analysis focused on the TiO_2-WO_3 interface interaction.

The WO_3 structure generally consists of an arrangement of distorted corner-sharing WO_6 octahedra. The shape of these octahedra and the W-O distances depend on the particular symmetry of the WO_3 structure (triclinic, monoclinic, orthorhombic, tetragonal, or hexagonal). In the monoclinic structure, the W atoms are surrounded by four and two oxygen nearest-neighbors at 1.82 and 2.14 Å,

Table 10.1 Ti and W environments in the investigated samples compared to the reference titanium and tungsten oxides. The fit uncertainties on the last significant digit of the EXAFS-derived parameters are shown between parantheses

Sample	Ti environment		
TiO_2 rutile	6 O / 1.96 Å	2 Ti1 / 2.96 Å	8 O / 3.52 Å 8 Ti2 / 3.57 Å
TiO_2 anatase	6 O / 1.95 Å	4 Ti1 / 3.04 Å	4 Ti2 / 3.78 Å 8 O / 3.86 Å
WTS	6 (1) O / 1.95 (1) Å	2 (1) Ti1 / 2.96 (1) Å	4 (1) Ti2 / 3.543 (5) Å
TWS	6 (1) O / 1.95 (1) Å	3.0 (6) Ti1 / 3.04 (1) Å	1.9 (4) Ti2 / 3.562 (5) Å
Sample	**W environment**		
WO_3 monoclinic	4 O / 1.82 Å 2 O / 2.14 Å		4 W / 3.79 Å 6 O / 3.81 Å
WO_3 triclinic	4 O / 1.83 Å 2 O / 2.12 Å		3 W / 3.79 Å 6 O / 3.81 Å
WO_3 film	4 (1) O / 1.82 (1) Å 2 (2) O / 2.14 (3) Å		
WTS	4 (1) O / 1.81 (1) Å 2 (2) O / 2.13 (3) Å	1.4 (6) Ti1 / 2.96 (3) Å 1.6 (5) Ti1 / 3.14 (2) Å	
TWS	3.8 (5) O / 1.814 (6) Å	0.7 (4) Ti1 / 2.93 (3) Å 1.4 (4) Ti1 / 3.10 (2) Å	

respectively (see Table 10.1). The split main maximum of the EXAFS FT of the WO_3 film (Fig. 10.5d) describes this surrounding. A similar split is observed for the sample WTS, but it is absent for the sample TWS. This indicates a defective or disordered WO_3–like structure in the latter sample, with vacant or strongly disordered oxygen sites around W. The next-nearest neighbors (4 W and 6 O ions at the average distances 3.79 and 3.81 Å, respectively) do not significantly contribute to the FTs of EXAFS, also related to disordering effects.

The most interesting details in the Fourier transforms of the W L_3-edge EXAFS are the two faint maxima in the range 2.2–3.2 Å, susceptible to be attributed to Ti neighbors, similarly with the FTs of the Ti K-edge EXAFS. Such a neighborhood demonstrates the W incorporation into the TiO_2 lattice, on Ti sites, at the TiO_2-WO_3 interface. The first FT main maximum describes the W atoms in the WO_3 structure, while the next two maxima correspond to the fraction of W substituting for Ti in the TiO_2 lattice. The fit of the W-L_3 EXAFS (Table 10.1) points out the same nearest oxygen neighboring in the sample WTS as in the WO_3 film. The absence of the longer-distance O neighbors in TWS could suggest rather severe oxygen depletion around W. However, this result is intriguing, since it would imply the lack of the oxygen planes in the alternating O and WO_2 planes in the normal structure of WO_3. Such a change should have significant effects on the XRD pattern, which were not actually observed. More plausibly, the O neighbors at 2.14 Å still exist, but in a highly disordered arrangement. This weakens their contribution to EXAFS, under the level of statistical noise in the spectrum.

The W-Ti distances range in two narrow intervals: 2.93–2.96 Å, specific to the rutile TiO_2, and 3.10–3.14 Å, close to the anatase structure. This corresponds to two kinds of substitutional W insertion into the TiO_2 host: one with preserving the rutile structure of the host and the other with a change of the local surrounding towards the anatase symmetry. Therefore at interface, a fraction of the substitutional W brings about a transition of the rutile host towards anatase. The other W ions are accommodated on the Ti sites without altering the rutile symmetry of the host lattice.

It is worthwhile mentioning that the second and third maxima in the FTs of the Ti-K EXAFS describe the Ti1 and Ti2 neighboring shells, respectively, in the rutile or anatase structure, while these maxima in the FTs of the W-L_3 EXAFS corresponds to Ti1 shells only in the rutile and anatase-like environments. The Ti2 contribution is not seen in the latter FTs, probably due to their disordered arrangement. This contribution is clearly visible in the transforms of the Ti-K EXAFS since all Ti ions belong to the TiO_2 lattice, enhancing the Ti1,2 signals. In the case of the W-L_3 EXAFS, only a W fraction lies on Ti sites, which strongly diminishes the contribution of the Ti neighbors to EXAFS. An additional reduction of the Ti2 signal by disorder effects can thus easily eliminate it from FTs.

For the substitutional W in the rutile structure, the W-Ti1 distances are almost the same as the Ti-Ti1 distances in the rutile-TiO_2 host. This indicates the W incorporation in the rutile lattice as W^{6+} ions, of a similar radius with that of Ti^{4+} (W^{6+}: 0.60 Å; Ti^{4+}: 0.605 Å, for sixfold coordination [37]). This leaves the local rutile structure almost unmodified around W, but generates defects such as Ti^{4+} vacancies [38, 39] or Ti^{3+} ions [40, 41] to compensate the extra charge of the W^{6+} ions. On the contrary, for the W fraction with anatase-like environment, the W-Ti1 distance elongates by 0.06–0.10 Å with respect to the Ti-Ti1 distance in anatase. This suggests substitutional W^{4+} ions, of a larger radius (0.66 Å) than that of Ti^{4+}. In this case there is no charge imbalance between the dopant and host cations, but the more voluminous W^{4+} ions force the change of the local rutile surrounding towards an anatase structure and move away the Ti neighbors. Obviously, such an elongation effect should be manifest for the W-O distances too. However, it cannot be observed because the EXAFS signal of the W-O distances around substitutional W is dominated by that contributed by the W-O distances in the WO_3 majority phase

As shown by the above analysis, the TiO_2-WO_3 interface contributes to EXAFS in different ways for the Ti K and W L_3 edges, describing the Ti and W environments, respectively. The interface signature in the Ti environment consists of the partial rutile-to-anatase transition, induced by the substitutional W^{4+} ions. This is shown by the Ti-Ti1 distance of 3.04 Å, specific to anatase, in the TWS structure. In this sample, the TiO_2 overlayer has the thickness relatively comparable with that of the interface (see Fig. 10.3a), and both 'bulk' rutile and interface anatase contribute to EXAFS. This is similar with the superposed contributions of the two phases to the XRD pattern of the sample TWS (see Fig. 10.1b). In the case of the sample WTS, the EXAFS signal of the bulky rutile sublayer (see Fig. 10.3b) dominates the interface signal, i.e. the anatase contribution, and both Ti-Ti1 and Ti-Ti2 distances are specific to the rutile structure.

The interface contribution to the W environment consists of the Ti neighboring of the W ions incorporated in the TiO_2 lattice. The W-Ti distances are specific to the rutile and anatase lattices, corresponding to the substitutional W^{6+} and W^{4+} ions, respectively. The W L_3-edge EXAFS 'feels' the interface regardless of its relative thickness with respect to that of the WO_3 layer. This is so because the contributions of the interface (W-Ti distances) and WO_3 layer (W-O distances) are well separated in the Fourier transforms of EXAFS.

10.3.5 XPS Analysis of the Interface

While the +6 oxidation state of substitutional W in W-doped TiO_2 is currently accepted, the presence of substitutional W^{4+} ions was seldom reported [42]. In order to verify the formation of these ions at the TiO_2-WO_3 interface, we measured the W 4*f* XPS spectrum of the WTS and TWS samples, after their Ar etching, with sputtering times corresponding to the interface (see Fig. 10.3).

Unfortunately, the Ar^+ bombardment has a reducing effect on the W and Ti ions, preventing a correct determination of the W oxidation states. This is clearly seen in Fig. 10.6, illustrating the W 4*f* spectrum of the sample WTS at increasing sputtering times. For the uppermost WO_3 layers, with no Ar sputtering, the $4f_{7/2,5/2}$ doublet is well resolved, with peaks at 35.7 and 37.9 eV, specific to the W^{6+} ions in WO_3 [43]. After a sputtering of 15 s, exposing the subsurface WO_3 layers, the doublet displays a marked broadening due to additional contributions at 33.2 and 35.4 eV, characteristic of the W^{4+} state [44]. Obviously, the partial reduction of W^{6+} to W^{4+} in this region, much closer to the surface than to the WO_3-TiO_2 interface, is an effect of the Ar sputtering. Moreover, similar reduction effects of the ion bombardment were earlier reported for TiO_2 thin films, with changes of TiO_2 to Ti_2O_3 or TiO, depending on the sputtering time [45, 46].

In the WO_3-TiO_2 films, W can even reach the metallic state, for long enough sputtering times. This is the case of the WO_3-TiO_2 interface, accessed by XPS after 6.5 min of Ar sputtering (Fig. 10.6c). The W 4*f* spectrum of the interface exhibits, besides the W^{6+} and W^{4+} contributions, two sharp peaks at 31.3 and 33.5 eV, corresponding to the $4f_{7/2,5/2}$ doublet of metallic W [47]. The W^0 $5p_{3/2}$ and W^{4+} $5p_{3/2}$ peaks are visible as well at 37.2 and 39.3 eV, respectively. Ti is also partially reduced to the metallic state, as pointed out by the faint Ti^0 $3p_{3/2}$ peak at 32.2 eV [48]. Other contributions of the Ti states (3+, 4+) to the spectrum are difficult to be unambiguously established, since they superpose over the W peaks: the Ti^{3+} $3p_{3/2}$ peak at 36.0 eV [49] superposes over W^{6+} $4f_{7/2}$, while Ti^{4+} $3p_{3/2}$ at 37.3 eV [50] has practically same binding energy as W^0 $5p_{3/2}$.

Due to the large number of components contributing to the interface spectrum, its fitting analysis is not beyond any doubt, making rather uncertain the relative weights of the different W and Ti states. However, the presence of intense W^0 $4f_{7/2,5/2}$ peaks clearly demonstrates the W reduction to the metallic state after a long sputtering time, corresponding to the WO_3-TiO_2 interface. These results show that

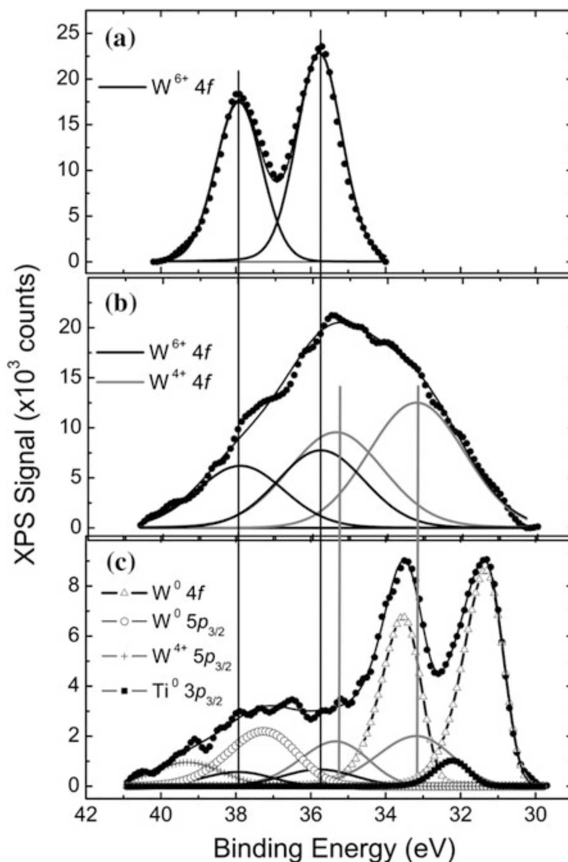

Fig. 10.6 W 4*f* core-level XPS spectra of: **a** uppermost WO_3 layer of the sample WTS, without Ar sputtering; **b** subsurface WO_3 layer, after Ar sputtering of 15 s; **c** WO_3-TiO_2 interface, after Ar sputtering of 6.5 min. The positions of the W^{6+} and W^{4+} $4f_{7/2,5/2}$ peaks are indicated by vertical guidelines

the XPS determination of the W states (and implicitly the confirmation of the W^{4+} species) at the interface cannot give reliable results, due to the chemical changes caused by the Ar^+ bombardment.

10.4 Conclusions

TiO_2/WO_3 and WO_3/TiO_2 bilayer structures have been grown on Si single-crystal substrates by PVD. Combined XRD, XPS, XANES, and EXAFS analyses evidenced the W substitution for Ti in the TiO_2 lattice at the TiO_2-WO_3 interface. A fraction of the substitutional W enters the TiO_2 lattice as W^{6+} ions, leaving almost unchanged the rutile structure of the host matrix. The other fraction, consisting of W^{4+} ions, changes the local surrounding towards the anatase symmetry. The substituting W^{4+} ions also cause a local expansion of the anatase lattice, due to the difference between the ionic radii of W^{4+} (0.66 Å) and Ti^{4+} (0.60). These results

highlight specific interface phenomena in TiO_2-based composite semiconductors, with expected effects on their photocatalytic properties and of relevance for further implementation in environmental and energy-related applications.

Acknowledgements Two of the authors (DM and CMT) have contributed to this work within the "Kernel" Project PN09-450101, funded by the Romanian Ministry of Education and the National Authority for Scientific Research. Part of the investigations have been done in the frame the COFOBIST project financed by the Romanian Ministry of Education (proj. 697/2013).

References

1. M.R. Hoffmann, S.T. Martin, W. Choi, D.W. Bahnemann, Chem. Rev. **95**, 69 (1995)
2. Y. Cui, H. Du, L. Wen, J. Mater. Sci. Technol. **24**, 675 (2008)
3. M.I. Litter, J.A. Navío, J. Photochem. Photobiol., A **98**, 171 (1996)
4. J. Zhu, F. Chen, J. Zhang, H. Chen, M. Anpo, J. Photochem. Photobiol., A **180**, 196 (2006)
5. M.M. Mohamed, M.M. Al-Esaimi, J. Mol, Catal. A **255**, 53 (2006)
6. M. Takeuchi, H. Yamashita, M. Matsuoka, M. Anpo, T. Hirao, N. Itoh, N. Iwamoto, Catal. Lett. **67**, 135 (2000)
7. W. Li, A.I. Frenkel, J.C. Woicik, C.Ni, S. Ismat Shah, Phys. Rev. B **72**(155315), 1–6 (2005)
8. L. Diamandescu, F. Vasiliu, D. Tarabasanu-Mihaila, M. Feder, A.M. Vlaicu, C.M. Teodorescu, D. Macovei, I. Enculescu, V. Parvulescu, E. Mater, Chem. Phys. **112**, 146 (2008)
9. S. Matsuo, N. Sakaguchi, K. Yamada, T. Matsuo, H. Wakita, Appl. Surf. Sci. **228**, 233 (2004)
10. F.B. Li, X.Z. Li, M.F. Hou, Appl. Catal. B **48**, 185 (2004)
11. R. Asahi, T. Morikawa, T. Ohwaki, T. Aoki, I. Taga, Science **293**, 269 (2001)
12. A.V. Emeline, V.N. Kuznetsov, V.K. Rybchuk, N. Serpone, Int. J. Photoenergy **258394**, 1–19 (2008)
13. S.U.M. Khan, M. Al-Shahry, M.W.B. Ingler Jr, Science **297**, 2243 (2002)
14. J.C. Yu, J. Yu, W. Ho, Z. Jiang, L. Zhang, Chem. Mater. **14**,3808 (2002)
15. T. Ohno, M. Akiyoshi, T. Umebayashi, K. Asai, T. Mitsui, M. Matsumura, Appl. Catal. A **265**, 115 (2004)
16. L. Lin, W. Lin, Y. Zhu, B. Zhao, Y. Xie, Chem. Lett. **34**, 284 (2005)
17. O. Lorret, D. Francová, G. Waldner, N. Stelzer, Appl. Catal. B **91**, 39 (2009)
18. M. Miyauchi, A. Nakajima, K. Hashimoto, T. Watanabe, Adv. Mater. **12**, 1923 (2000)
19. D. Luca, D. Mardare, F. Iacomi, C.M. Teodorescu, Appl. Surf. Sci. **252**, 6122 (2006)
20. T. Taguchi, T. Ozawa, H. Yashiro, Phys. Scripta T **115**, 205 (2005)
21. C.J. Howard, T.M. Sabine, F. Dickson, Acta Crystallogr. B **47**, 462 (1991)
22. J.J. Rehr, J. Mustre de Leon, S.I. Zabinsky, R.C. Albers, J. Am. Chem. Soc. **113**, 5135 (1991); J. Mustre de Leon, J.J. Rehr, S.I. Zabinsky, R.C. Albers, Phys. Rev. B **44**, 4146 (1991)
23. P.M. Woodward, A.W. Sleight, T. Vogt, J. Phys. Chem. Solids **56**, 1305 (1995)
24. T. Vogt, P.M. Woodward, P.A. Hunter, J. Solid State Chem. **144**, 209 (1999); E. Cazzanelli, C. Vinegoni, G. Mariotto, A. Kuzmin, J. Purans, J. Solid State Chem. **143**, 24 (1999)
25. J.F. Moulder, W.F. Stickle, P.E. Sobol, K.D. Bomben, *Handbook of X-ray Photoelectron Spectrosopy* (Physical Electronics, USA, ULVAC-PHI Japan, 1995), p. 184
26. M.F. Ruiz-López, A. Muñoz-Pàez, J. Phys.: Condens. Matter **3**, 8981 (1991)
27. F. Farges, G.E. Brown Jr, J.J. Rehr, Phys. Rev. B **56**, 1809 (1997)
28. A. Niltharach, S. Kityakarn, A. Worayingyong, J.T- Thienprasert, W. Klysubun, P. Songsiriritthigul, S. Limpijumnong. Phys. B **407**, 2915 (2012)
29. Z.I. Wu, G. Ouvrard, P. Gressier, C.R. Natoli, Phys. Rev. B **55**, 10382 (1997)
30. B. Poumellec, J.F. Marucco, B. Touzelin, Phys. Rev. B **35**, 2284 (1987)
31. B. Poumellec, P.J. Durham, G.Y. Guo, J. Phys.: Condens. Matter **3**, 8195 (1991)

32. M.A. Khan, A. Kotani, J.-C. Parlebas, J. Phys.: Condens. Matter **3**, 1763 (1991)
33. T. Uozumi, K. Okada, A. Kotani, O. Durmeyer, J.P. Kappler, E. Beaurepaire, J.C. Parlebas, Europhys. Lett. **18**, 85 (1992)
34. K. Sugiyama, Y. Takeuchi, Z. Kristallogr. **194**, 305 (1991)
35. C.V. Ramana, S. Utsunomiya, R.C. Ewing, C.M. Julien, U. Becker, J. Phys. Chem. B **110**, 10430 (2006)
36. B.O. Loopstra, H.M. Rietveld, Acta Crystallogr. B **25**, 1420 (1969)
37. R.D. Shannon, Acta Crystallogr. **32**, 751 (1976)
38. A. Kubacka, G. Colon, M. Fernandez-Garcia, Catal. Today **143**, 286 (2009)
39. A.M. Márquez, J.J. Plata, Y. Ortega, J.F. Sanz, J. Phys. Chem. C **115**, 16970 (2011)
40. Y.C. Lee, Y.P. Hong, H.Y. Lee, H. Kim, Y.J. Jung, K.H. Ko, H.S. Jung, K.S. Hong, J. Colloid Interf. Sci. **267**, 127 (2003); K.H. Ko, Y.C. Lee, Y.J. Jung, J. Colloid Interf. Sci. **283**, 482 (2005)
41. E.S. Lee, Trans. Electr. Electron. Mater. **12**, 68 (2011)
42. D.M. Chen, G. Xu, L. Miao, L.H. Chen, S. Nakao, P. Jin, J. Appl. Phys. **107**, 063707–4 (2010)
43. A. Katrib, F. Hemming, P. Wehrer, L. Hilaire, G. Maire, J. Electron Spectrosc. Relat. Phenom. **76**, 195 (1995)
44. P.G. Gassman, D.W. Macomber, S.M. Willging, J. Am. Chem. Soc. **107**, 2380 (1985)
45. S. Hashimoto, A. Tanaka, A. Murata, T. Sakurada, Surf. Sci. **556**, 22 (2004)
46. D. Luca, D. Macovei, C.M. Teodorescu, Surf. Sci. **600**, 4342 (2006)
47. C.J. Powell, J. Electron Spectrosc. Relat. Phenom. **185**, 1–3 (2012)
48. A. Lebugle, U. Axelsson, R. Nyholm, N. Martensson, Phys. Scr. **23**, 825 (1981)
49. F. Werfel, O. Brummer, Phys. Scr. **28**, 92 (1983)
50. F. Lange, H. Schmelz, H. Knozinger, J. Electron Spectrosc. Relat. Phenom. **57**, 307 (1991)

Chapter 11
Crystalline Structure and Surface Morphology of $A^{III}B^{VI}$ Type Lamellar Semiconductor Nanocomposites Obtained by Heat Treatment in *Cd* and *Zn* Vapor

Igor Evtodiev, Iuliana Caraman, Valeriu Kantser, Dumitru Untila, Irina Rotaru, Liliana Dmitroglo, Silvia Evtodiev and Mihail Caraman

Abstract The semiconductors like *GaS*, *GaSe* and *InSe* crystallize in lamellar structures with crystal lattice composed of B–A–A–B type packings bound by Van der Waals forces. Materials composed of *Ga*, *In*, *Cd* and *Zn* chalcogenide crystallites with sizes of 10–30 nm are obtained by heat treatment of *GaS*, *GaSe*, *GaTe* and *InSe* single crystalline plates in *Zn* and *Cd* vapor at temperatures from 653 to 853 K. Phase transformations of *GaSe* and *GaTe* compounds with formation of Ga_2Se_3, $CdGa_2Se_4$ and Ga_2Te_3 compounds occur, as well as the formation of *Ga-Cd* and *Cd-Te* clusters on the surface, during the process of producing *CdTe-GaTe* and *CdSe-GaSe* nanocomposites.

11.1 Introduction

The single crystals of layered $A^{III}B^{VI}$ semiconductors are materials with high anisotropy of mechanical, optical and photoelectrical properties that are determined by the lamellar crystalline structure and the presence of two types of atomic bonds in the crystal [1–3]. The single crystals of these compounds consist of elementary packings that contain four atomic planes of the B–A–A–B type. The packings are

I. Evtodiev · V. Kantser · D. Untila · I. Rotaru · L. Dmitroglo · S. Evtodiev · M. Caraman
Photonics and Physical Metrology Laboratory, Department of Physics and Engineering, Moldova State University, Chisinau, Moldova

I. Caraman
“Vasile Alecsandri” University of Bacau, Bacau, Romania

I. Evtodiev (✉) · V. Kantser · D. Untila
Institute of Electronic Engineering and Nanotechnologies “D. Ghitu”, Academy of Sciences of Moldova, Chisinau, Moldova
e-mail: ievtodiev@yahoo.com

S. Evtodiev
University of European Political and Economical Studies “Constantin Stere”, Stefan cel Mare si Sfint bd 200, MD-2004 Chisinau, Moldova

© Springer International Publishing Switzerland 2016

I. Tiginyanu et al. (eds.), *Nanostructures and Thin Films for Multifunctional Applications*, NanoScience and Technology,
DOI 10.1007/978-3-319-30198-3_11

oriented perpendiculary to the C_6 symmetry axis in crystals with a hexagonal unit cell (*GaS*, *GaSe*, *InSe*) [4, 5]. The anisotropy of optical, electrical and mechanical properties with specific valence bonds between atoms of elementary packings determines the technical application of these materials [6, 7].

Inside the elementary packing the atoms are bound by strong forces of ionic–covalent nature while Van der Waals forces act between the layers. The low density of free valence bonds on the surface of the *GaS*, *GaSe*, *InSe* and *GaTe* semiconductor layers (10^{10} cm^{-2}) [8] is the determinant factor for obtaining nanoscale lamellar structures and heterojunctions from materials with different crystal structures such as intrinsic oxides [9–11] and carbides [12] etc.

The cracks that width is comparable to dimensions of atoms and molecules are called Van der Waals crack and they are formed because of the weak links between atomic planes of neighboring packages. The Van der Waals crack may be filled with the atoms, ions and molecules in amounts comparable to the concentration of the basic substance molecules [9, 13–18] through various methods (heat treatment in solutions and vapor, laser pulses, electrolysis etc.). The various methods of intercalation of a heterogeneous substance in the base material are applied. However, the most commonly used techniques are the vapor phase, electrolyte, liquid–state or melt diffusion [13]. If the insertion of the material in the Van der Waals space occurs without chemical changes and deformation of the base material and the intercalant material, then this method can be used to obtain 2D nanolamellar structures. The elementary 4-plane packings of the layered crystal will be arranged periodically between the nanometer-thick layers of the intercalant in these structures. The electronic properties of these crystals can be properly described in terms of the model of an ensemble of independent 2D layers [19, 20].

The *InSe* and *GaSe* layered semiconductors intercalated with atoms and molecules acquire fundamentally new properties. Thus *GaSe* intercalated with Na^+ and Li^+ ions becomes a good solid electrolyte [21]. In addition the *InSe* and *GaSe* can be easily intercalated with hydrogen and transformed into hydrogen accumulators [22]. The material obtained by intercalation with *Co* [23] and *Ni* [24] shows the ferromagnetic properties.

Periodic nanostructures can be obtained by heat treatment of layered semiconductors such as *GaSe*, *GaTe*, and *InSe* in vapors of highly volatile chemical elements such as *Cd*, *Zn*, *S*, *Hg* etc. The lamellar composites are formed at temperatures sufficient to provide a chemical reaction between the atoms of the intercalated metal and the chalcogenide (*S*, *Se*, *Te*) [15–17]. The resulting structures have the electronic properties typical to both materials $A^{II}B^{VI}$ and $A^{III}B^{VI}$ chalcogenides. Nanostructures based on different materials are prepared by different technologies like the oxidation of the Van der Waals surface with defects [24, 25], the treatment in a vapor atmosphere, intercalation at the temperature gradient, thin layer intercalation by laser pulses, etc.

The estimated studies by XRD, Raman and photoluminescence measurements of *GaSe*, *GaTe*, *InSe* and *GaS* single crystal plates that were treated in *Zn* and *Cd* vapors have shown the possibility of obtaining the micro- and nanolamellar structures of $A^{III}B^{VI}$ and $A^{II}B^{VI}$ semiconductors that have structural properties characteristic of both materials and exhibit properties characteristic to low dimensional structures.

11.2 Growth of Single Crystals of $A^{III}B^{VI}$ Lamellar Compounds

The physical properties of $A^{III}B^{VI}$ lamellar semiconductors have been studied for many years [26, 27]. However the intense studies that have the aim to determine the priority directions for application in optoelectronic devices have been conducted in the last 10–15 years [28–30]. A few of specific features of *Ga* and *In* compounds with chalcogenides (*S*, *Se*, *Te*) that determine the applied properties of these compounds are as follows:

- the bandgap that covers the energy range from 3.5 to 1.1 eV;
- the lamellar structure of the crystals are composed of planar atomic packings of the B–A–A–B type with ionic-covalent bonds between the metal atoms and weak polarization bonds between the lamellas;
- the radiative absorption and emission of excitons;
- the low density of surface states;
- the structural polymorphism and strong anisotropy that affects electrical, optical and photoelectric measurements.

In terms of crystallography, the chemical compound of III and VI group elements forms two classes of crystals that are referred to as crystals with lattice defects $\left(\mathbf{A}_2^{\mathbf{III}}\mathbf{B}_3^{\mathbf{VI}}\right)$ and film-pack crystals ($A^{III}B^{VI}$). The film pack is composed of monatomic films arranged in the order of Cal–M–M–Cal bounded by strong ionic-covalent interactions. The anions (chalcogens) and the cations (metals) form an atomic plane perpendicular to the C_6 six order axis (Fig. 11.1).

The *GaS*, *GaSe*, *GaTe* and *InSe* single crystals were grown by the Bridgman–Stockbarger method from the spectrally pure *Ga* (5 N), *In* (5 N), *Te* (5 N) and *Se* (4 N) elementary components taken in stoichiometric amounts.

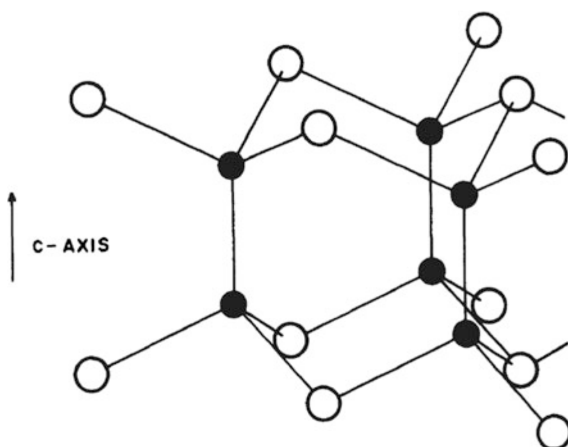

Fig. 11.1 The atoms in a *GaSe* layer. The black circles represent *Ga* atoms and the white are *Se* [31]

Because of the anisotropy of the chemical bonds between the layers and within them, the surface of the $A^{III}B^{VI}$ compound obtained by splitting is perfect in terms of both the geometry and the adsorption of atoms from the atmosphere [32]. The density of surface states on the surface of freshly split *GaSe* plates according to estimates [8] is less than 10^{10} cm^{-2}.

The percentage composition of the *Ga* and *Se* components measured in two points on the surface (0 0 0 1) of the *GaSe* plates was determined by the EDXS method. The Table 11.1 shows that the change in the concentration of the *Ga* and *Se* elements in the direction of the C_6 crystallographic axis does not exceed 0.01 %.

11.3 Crystal Structure of *GaS*, *GaSe*, *GaTe* and *InSe* Single Crystals

The crystallographic characteristics of the *GaS*, *GaSe*, *GaTe* and *InSe* compounds are listed in Table 11.2.

Table 11.1 The distribution of chemical elements on the surface of *GaSe* lamella

Spectrum	Element	Series	Atom. C (at.%)	Error (%)
1	Gallium	K-series	46.82	1.0
	Selenium	K-series	53.18	1.5
		Total	100.00	
2	Gallium	K-series	46.83	1.1
	Selenium	K-series	53.17	1.5
		Total	100.00	

Table 11.2 The crystallographic characteristics of gallium and indium monochalcogenides [33]

Semiconductor compound	Polytype	Singony	Group of symmetry	Solidification temperature, °C	Parameters of the crystal lattice, Å		
					a	b	c
InSe	*α*	Rhombohedral	P3 m-C_{3V}^5	615	4.023	–	25.05
	β	Hexagonal	$P6_3$/ mmc-D_{6h}^4		4.04	–	16.92
GaSe	*ε*	Hexagonal	($P6_3$/ mmc-D_{6h}^4)	960 ± 10	3.742	–	15.918
	β	Hexagonal			3.755	–	15.94
	γ	Rhombohedral			3.755	–	23.92
	δ	Hexagonal				–	
GaS		Hexagonal	$P6_3$/ mmc-D_{6h}^4	1015 962		–	
GaTe	*α*	Hexagonal (metastable)	$P6_3$/ mmc-D_{6h}^4	840	4.06	–	16.96
	β	Monoclinic	$C2_3$/-C_{2h}^3		17.37	4.074	10.44

In Figs. 11.2 and 11.3 are shown the XRD patterns of *GaSe* crystals obtained by the Bridgman–Stockbarger method and, respectively, thin films deposited on glass substrate at temperature 473 and 573 K. The diffraction lines were identified by ICDD–JCPDS card (Table 11.3). The non-crystalline *GaSe* layers are obtained at the temperature of the substrate (glass K8) of 473 K by vacuum thermal evaporation. The crystallization of *GaSe* layers takes place at 573 K as it is shown in Fig. 11.3 (curve 2).

The hexagonal unit cell constants of *GaS* and *GaSe* crystals and rhombohedral unit cell constants for *InSe* were calculated from X–ray diffraction angles 2θ at $\lambda_{CuK\alpha}$ = 1.54178 Å from atomic plane ansambles with Miller indices (h k l) are shown in Table 11.3.

It is evident from the arrangement of *Ga* and *Se* atoms in the ε–*GaSe* and β–*GaSe* unit cell (Fig. 11.4) that these two structures differ one from another only by the symmetry properties.

The arrangement β of *Ga* and *Se* (*S*) atoms has an ion center while ε and γ crystalline lattices do not have this property. Thus, in accordance with the principle

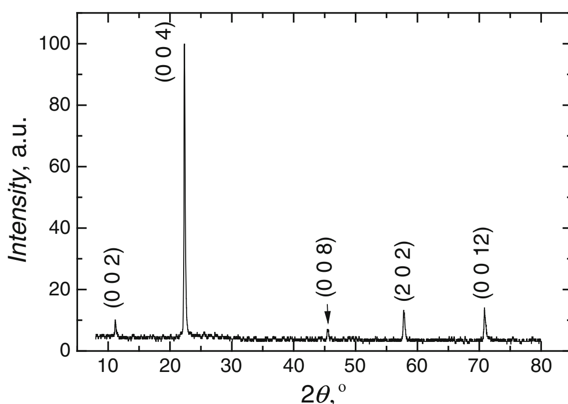

Fig. 11.2 The XRD pattern of primary *GaSe* single crystal

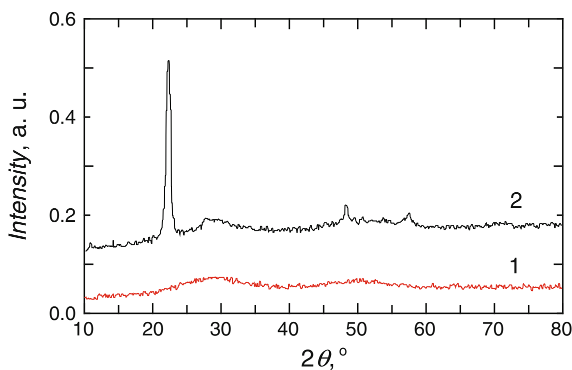

Fig. 11.3 The XRD pattern of *GaSe* thin films grown on glass substrate at T_s = 473 K (1) and T_s = 573 K (2) [34]

Table 11.3 The identification of XRD lines for *GaSe* and *β-GaS* crystals

GaSe (stoichiometrical)					*GaSe* (0.5 at.% *Se* surplus)					*β-GaS*				
2θ (°)	Intensity	*h*	*k*	*l*	2θ (°)	Intensity	*h*	*k*	*l*	2θ (°)	Intensity	*h*	*k*	*l*
11.13	10.1	0	0	2	11.12	24.4	0	0	2	–				
22.33	100	0	0	4	22.34	100				23.08	100	0	0	4
					31.47	88	0	0	6					
45.62	7	0	0	8	45.59	1.8	0	0	12	45.59	10	0	0	8
57.90	12.4	2	0	2	57.93	4.5	0	0	15	–				
70.98	10.9	0	0	12	70.33	14.2	0	2	10	73.40		0	0	12

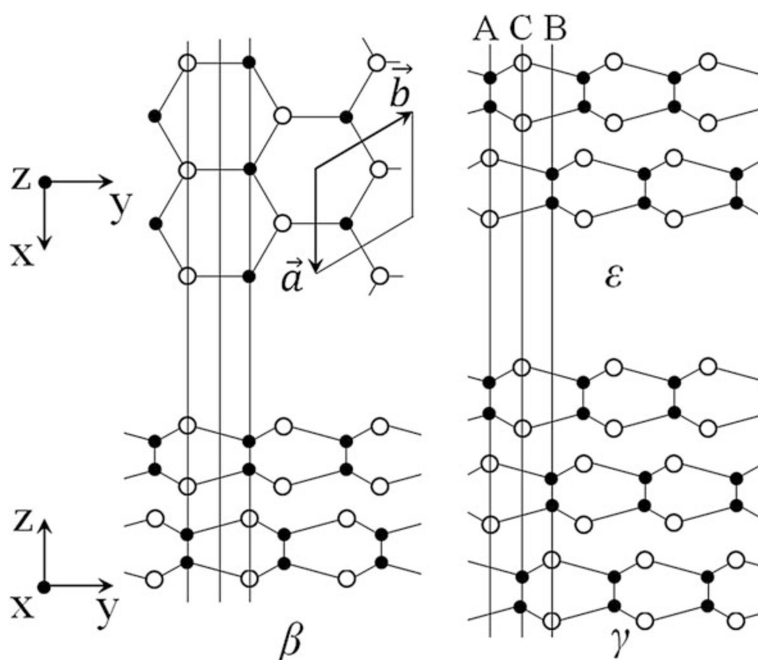

Fig. 11.4 Structural modifications of *GaSe* single crystals

of alternative prohibition, the IR and Raman vibrational modes of β lattice do not coincide while the vibration modes of crystal lattice are allowed in both absorption/reflection spectra and Raman spectra for ε and γ arrangements of *Ga* and *Se* atoms.

In Fig. 11.5 is shown the transmission spectra of *GaS* monocrystalline layer in the region of transverse monophononic vibrations. The energy E_{1u} of transverse optical phonon is equal to 296 cm^{-1} as it is shown in this presentation. The vibration modes with E_{1g} and E_{2g} symmetry are active in the Raman spectrum of the *GaS* crystals around the wave number of 300 cm $^{-1}$ [35]. The energies of these vibrations differ from the E_{1u} vibration by more than 1 cm^{-1}.

The Raman spectrum of *GaSe* single crystal plates was excited with *He–Ne* laser radiation at λ = 6328.3 Å. The density of the beam on the (0 0 0 1) surface of the

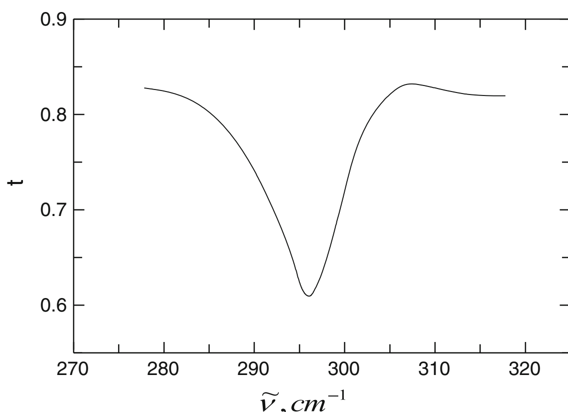

Fig. 11.5 The transmission spectra in monophononic absorption region of *GaS* plate of 250 μm thickness in $\vec{E}\perp\vec{C}$ polarization

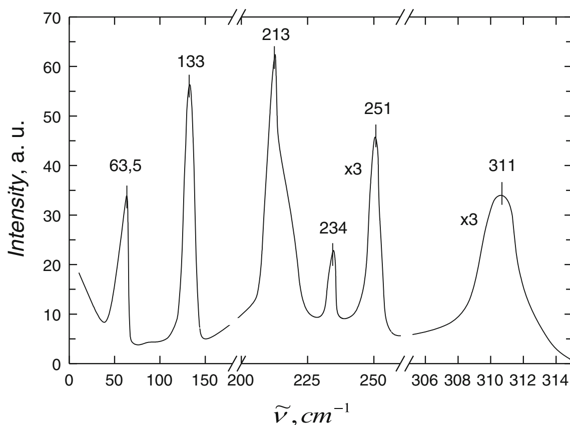

Fig. 11.6 The Raman spectrum of *GaSe* single crystalline plate

crystal can be varied in a range of (1–15) × 10^3 W/cm^2. Diffuse radiation was registered under reverse diffusion. The Fig. 11.6 shows that the combined diffusion spectrum (Raman) of light consists of six bands with wavenumbers in a range of 60–320 cm^{-1}. The wave numbers, the symmetry of the Raman bands and IR region absorption bands are listed in Table 11.4.

The combined diffusion spectra (Fig. 11.6) and the vibrational particularities of IR/FTIR reflection spectra on the (0 0 0 1) freshly cleaved surface from the *GaSe* block in a wave number range of 1000–80 cm^{-1} are compared in Fig. 11.7. The indexation of wave numbers is shown in Table 11.5.

The combined diffusion band with maximum intensity at 251 cm^{-1} is obtained as a result of the superposition of two vibration modes: A_2''(LO) (247 cm^{-1}) and E'(LO) (254 cm^{-1}). These two vibration modes and Raman spectra can be identified as the movement of phonons in the direction of the C_6 axis. These two modes are combined to form a mixed band with a maximum at 251 cm^{-1} for other directions of propagation of phonons with respect to the C_6 axis. The maximum of this band shifts as a function of θ angle between the direction of propagation of phonons and

Table 11.4 The identification of Raman bands for *GaSe*

Nr.	Raman		$\tilde{\nu}_1$, cm^{-1}	$\tilde{\nu}_2$, cm^{-1}	References	ATR, FTIR
	$\tilde{\nu}$, cm^{-1}	Simetry				$\tilde{\nu}$, cm^{-1}
1.	63.5	E'				360
2.	133	A''				254, 244, 226
3.	213	E'(TO)		211	[36]	210
4.	234	A_2 (TO)	235	215	[36]	200, 190
5.	251	A_2''(LO) E'(LO)	247	254	[37]	131
6.	311	$A_1^{'(4)}(A_{1g}^2)$				113
7.						100

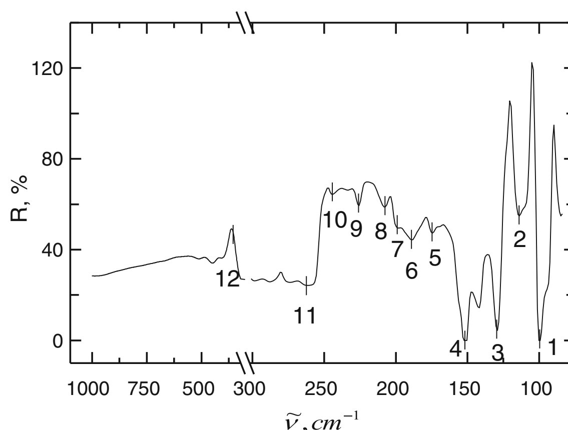

Fig. 11.7 The FTIR reflectance spectra of *GaSe* crystal plate

the C_6 crystallographic axis. In addition, the vibration modes A_2'' (TO) (235 cm^{-1}) and E′(TO) (215 cm^{-1}) can also be shifted in small limits because they are affected by the degree of intercombination of phonons (235 and 215 cm^{-1}) [38].

The Fig. 11.8 shows the ATR FTIR spectrum of the *GaSe* single-crystal plate from the (0 0 0 1) surface. The wave numbers of the absorption bands are listed in Table 11.6. The Raman scattering and ATR FTIR spectra shows that the fundamental vibration modes A_2''(LO), E′(TO) and A″ are active both in the combined light scattering spectra and in the ATR FTIR spectra. This fact confirms that the studied *GaSe* single crystals that were used to prepare *GaSe–CdSe* and *GaSe-ZnSe* composites belong to D_{6h}^4 symmetry group without inversion center which is known as ε–*GaSe*.

The *GaS* compound was synthesized from spectrally pure elementary components *Ga* (5 N) and *S* taken in stoichiometric amounts. The synthesis and growth of

Table 11.5 The index of absorbance bands from FTIR reflectance spectra of *GaSe* crystal plate (Fig. 11.7)

Nr.	ν, cm^{-1}	Nr.	ν, cm^{-1}	Nr.	ν, cm^{-1}	Nr.	ν, cm^{-1}
1	100	4	151	7	200	10	244
2	113	5	174	8	210	11	254
3	131	6	190	9	226	12	360

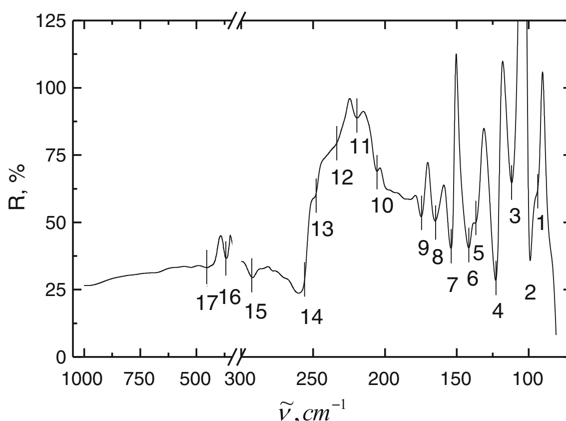

Fig. 11.8 The FTIR reflectance spectra of *GaSe* crystal plate heat treated at 470 °C for 90 min

Table 11.6 The index of absorbance bands from FTIR reflectance spectra of *GaSe* crystal plate that was heat treated at 470 °C for 90 min (Fig. 11.8)

Nr.	ν, cm^{-1}	Nr.	ν, cm^{-1}	Nr.	ν, cm^{-1}	Nr.	ν, cm^{-1}
1	93.5	6	142	11	220	16	367
2	100	7	154	12	233	17	454
3	112	8	165	13	247		
4	122	9	174	14	260		
5	137	10	205	15	292		

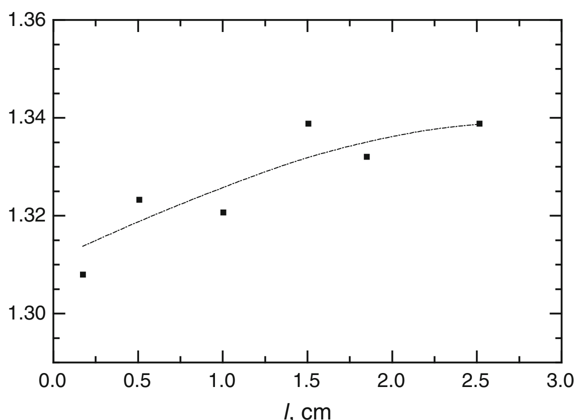

Fig. 11.9 The ratio of relative intensities of 2560.22 Å (*In*) and 2413.00 Å (*Se*) spectral lines

the single crystals was done in an oven with two heating sections. The synthesis took place at the temperature of 1250 °C for 6 h. The melt was passed through a temperature gradient of 35°/cm at a rate of 2.5 mm/h.

The crystallization temperature of the *GaTe* compound with a stoichiometric composition of components *Ga* and *Te* (5 N) was 1097 K. The prism shape single crystals of *GaTe* were grown by the Bridgman method on the entire length of the ingot. The single crystals of *GaTe* that are similar to *GaSe* and *GaS* single crystals can be easily split into submicron-thick lamellas.

The *InSe* single crystals of stoichiometric composition were grown by Bridgman–Stockbarger method. The resulting single-crystal ingots had a weight of 15–20 g and a shape of cylinders with a conical tip with a diameter of 12 mm and a length of 2.5–3.0 cm. The atomic emission analysis was used to study the elemental composition of the crystals on the length of the ingot. As analytical lines were used the spectral lines with wavelengths of 2560.22 Å (*In*) and 2413.00 Å (*Se*). These two lines satisfy the requirement of a pair of homogeneous lines ($\lambda_1 - \lambda_2 \leq 150$ Å) [39]. The ratio of the relative intensities of these two lines function of length of the ingot is shown in Fig. 11.9.

11.4 Electrical Properties of the $A^{III}B^{VI}$ Compounds (*GaS*, *GaSe*, *InSe*, and *GaTe*) Undoped and Doped with Group I, II and IV Elements

11.4.1 Electrical Properties of $A^{III}B^{VI}$ Compounds

It is well known that Group II metals like *Cd* and *Zn* increase the concentration of holes in *GaSe*. However, they are compensatory elements in n–*InSe* and n–*GaS* compounds [40, 41]. The amount of 0.01–0.10 at.% of *Cd* and *Zn* changes the ratio

of concentration of electrons and holes and transforms the *InSe* compound into a semiconductor with hole conductivity [42]. The doping of *GaS* crystals with *Cu* atoms and the *GaTe* crystals with *Cd* and *Cu* in an amount of 0.01, 0.05 and 0.1 at.% was done during synthesis. The single crystals of *InSe* were doped with *Cd*.

The optically homogeneous single-crystal plates of *GaS*, *GaSe*, *GaTe* and *InSe* were cut in parallelograms with a medium size of 0.2 × 4.0 × 8.0 mm^3 perpendicularly to the C_6 crystallographic axis by evaporation from five electrodes for the Hall effect measurements. The electrode material was In and a *Cu–Ag* alloy. The characteristics of the electrodes are shown in Table 11.7.

The samples were annealed at a temperature of 673 K in *Ar* atmosphere for 4 h. The relatively high chemical resistance of the samples and the noise (whose intensity increases at temperatures below the room temperature) made it possible to do measurements in temperatures range from 270 to 500 K (function of the sample).

Figure 11.10 shows the typical temperature dependences of the concentration of majority charge carrier.

Table 11.7 The characteristics of electrodes used for Hall effect measurements

Chemical compound	Electrode	Generated voltage, mV, E = 500 l×	Metal adhesion
GaTe	*In*	17	Unstable
GaTe:0.1 *Cu*	*In*	20–24	Good
GaTe:0.1 *Cu*	*Cu–Ag*	6–8	Satisfactory
GaTe:0.05 *Cd*	*In*	15–17	Good
GaTe:0.05 *Cd*	*Cu–Ag*	0–2	Weak
GaS	*In*	48	Satisfactory
GaS	*Cu–Ag*	16–20	Satisfactory
GaS:0.05 *Cu*	*Cu–Ag*	12	Satisfactory
GaTe:Sn	*In*	3–5	Good
GaS:Sn	*Al*	10–12	Easy fails, resistivity increases in time
InSe:Sn	*Cu-Ag*	0–5	Good

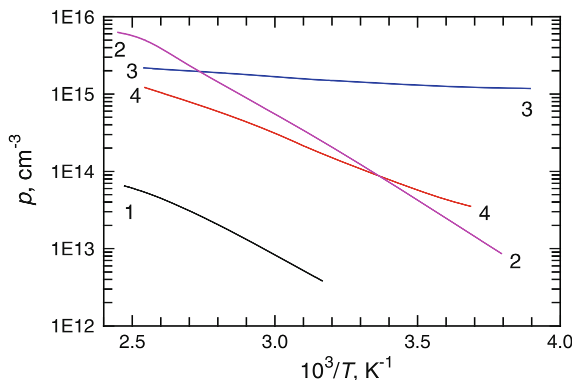

Fig. 11.10 The majority charge carriers concentration dependences of inverse temperature: undoped *GaSe* (*curve 1*), *GaSe* < 0.2 at.% *Cd* > (*curve 2*), undoped *InSe* (*curve 3*) and *InSe* < 0.1 at.% *Cd* > (*curve 4*)

It is obvious that *Cd* in a concentration of 0.1 at.% in *InSe* changes the type of the majority charge carriers from *n* to *p*. The holes concentration in the *p–InSe* crystals (0.1 at.% *Cd*) at room temperature is ~(1.8–2.0) × 10^{14} cm^{-3}. Cadmium atoms in a concentration of 0.1 at.% in *GaSe* at the temperature of 310 K increase the holes concentration from ~5.0 × 10^{12} cm^{-3} in undoped crystals to 2.3 × 10^{14} cm^{-3}.

The Fig. 11.11 (curve 1) shows that in a temperature range of 295–500 K the holes concentration increases by ~1.6 orders of magnitude.

The introduction of 0.05 at.% of *Cd* in the *GaSe* melt leads to an increase of holes concentration by 3 orders of magnitude (Fig. 11.11, curve 1). A further increase of the concentration of *Cd* atoms to 0.50 at.% (Fig. 11.11, curve 3) in stoichiometric *GaSe* points the monotonic increase in the holes concentration throughout the entire temperature range. The temperature dependence of holes concentration in the *GaSe* crystals doped with *Cd* show the same behavior as the undoped crystals.

The uncontrollable impurities and the intrinsic defects of both *Cd* and the dopant along with the acceptor energy states form donor levels in *GaSe* that partially compensates the majority charge carriers (holes).

The temperature dependence of holes (p) concentration in partially compensated semiconductor materials is an exponential function of the energy of acceptors and depends not only on the concentration of acceptors N_A and donors N_D, but also on the degree of degeneration of the acceptor level $\gamma = 2$.

The dependence $p(T)$ is given by the expression:

$$p = \frac{2(N_A - N_D)}{\left[1 + \frac{\gamma \cdot N_D}{N_V}\exp\left(-\frac{E_A}{kT}\right)\right] + \left\{\left[1 + \frac{\gamma \cdot N_D}{N_V}\cdot\exp\left(-\frac{E_A}{kT}\right)\right]^2 + \frac{4\gamma\cdot(N_A - N_D)}{N_V}\cdot\exp\left(-\frac{E_A}{kT}\right)\right\}^{1/2}} \quad (11.1)$$

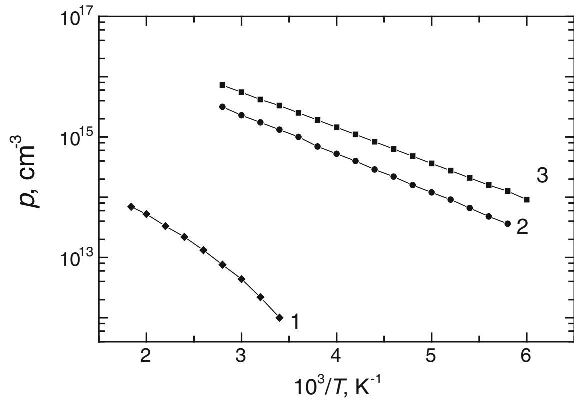

Fig. 11.11 The dependences of inverse temperature for holes concentration in *GaSe* stoichiometric crystals (1), *GaSe*: 0.05 at.% *Cd* (2) and *GaSe*: 0.50 at.% *Cd* (curve 3)

where E_A is the activation energy of acceptors and N_V is the density of states in the valence band.

The average values of the N_A, N_D, and E_A that satisfy the experimental measurements are shown in Fig. 11.11 (curves 1–3) and Table 11.8.

The Fig. 11.12 shows the inverse temperature dependence of electrical conductivity for undoped *GaSe* crystals (a) and the crystals doped with 0.05 and 0.50 at.% *Cd* (b). It is obvious that the $\ln(\sigma \cdot T^{1/2}) = f(10^3/T)$ curve has a few distinct linear portions. The thermal activation energy of electric photoconductivity E_a for these linear segments were determined from the slope of the $\ln(\sigma \cdot T^{1/2}) = f(10^3/T)$ curve. The values of the activation energy of electric conductivity are listed in Table 11.8.

Table 11.9 lists the average concentrations of majority charge carriers in the *GaS*, *GaTe*, *GaSe* and *InSe* ingots. Samples for measurements of Hall tension and electric conductivity were selected from the middle and at the edge of the ingot.

Table 11.8 The average values of parameters N_A, N_D and E_A for gallium monoselenide with different concentrations of *Cd* atoms

Cd concentration, at.%	N_A ($\times 10^{16}$ cm^{-3})	N_D ($\times 10^{12}$ cm^{-3})	E_A, eV	E_A thermal, meV
0.00	3.8×10^{-2}	3	0.56	22.45
0.05	5.4	3	0.24	27
0.50	6.3	4.2	0.22	42

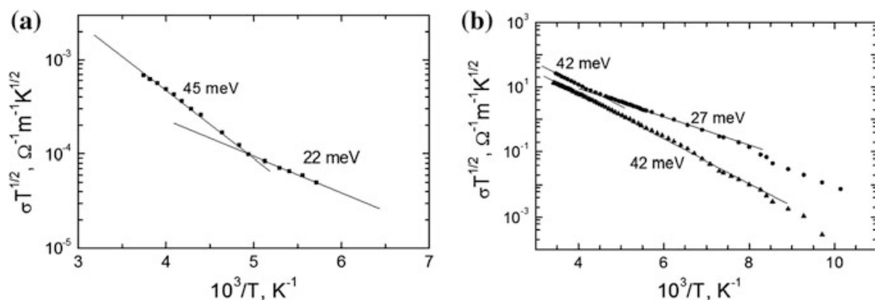

Fig. 11.12 The dark electrical conductivity dependences of inverse temperature for undoped *GaSe* crystals (**a**) and *GaSe*: *Cd* – 0.05 at.% and 0.50 at.% (**b**) (activation energies are shown in meV)

Table 11.9 The average concentrations of majority charge carriers in *GaS*, *GaTe*, *GaSe* and *InSe* ingots

Compound	Region 1		Region 2		Region 3	
	Edge	Center	Edge	Center	Edge	Center
GaS	7.2×10^{12}	1×10^{13}	8×10^{12}	1.2×10^{13}	4×10^{12}	8×10^{12}
GaTe	–	6×10^{14}	–	2×10^{15}	–	1.2×10^{15}
GaSe	1.5×10^{13}	4×10^{13}	2×10^{13}	5×10^{13}	2×10^{13}	4.5×10^{13}
InSe	3.4×10^{15}	2×10^{15}	1.2×10^{16}	8×10^{15}	1.2×10^{15}	3×10^{15}

11.4.2 *Structure and Some Physical Properties of* Cd *and* Zn *Chalcogenides Thin Films*

The $A^{II}B^{VI}$ compounds crystallize in the zinc-blende type cubic or hexagonal structure that symmetry group respectively are T_d^2 and C_{6v}^4. The elemental cell of cubic structure contains two atoms, while the unit cell of hexagonal structures contain 4 atoms that are bound by the ionic-covalent forces. The *Cd* and *Zn* chalcogenides decompose at high temperatures and form vapor in atomic state. The bandgap width of these materials covers a wide range of energies from 3.66 eV for *ZnS* to 1.50 eV for *CdTe* [33] which determine the increased interest for technical applications of these materials in devices for photo- and optoelectronics.

The basic characteristics of these compounds are listed in Table 11.10.

11.5 Crystal Structure and Composition of the Material Obtained by Treatment in *Zn* Vapors of *GaS*, *GaSe*, *GaTe* and *InSe* Lamellar Single Crystals

The pressure of intrinsic vapors accross the inorganic materials, particularly for *In* and *Ga* chalcogenides, increases with temperature. The pressure of vapors formed at temperatures under melting point increases with temperature. The semiconductor materials widely used in optoelectronics and photonics include *Zn* and *Cd* compounds with chalcogenides (*S*, *Se*, *Te*) [43–46]. At the same time, these materials sublime at temperatures much lower than the solidification temperature and form free atoms or molecules. The materials that can be easily intercalated with molecules and atoms from the vapor phase include layered inorganic materials. The weak polarization forces form the bonds between the layers. Among the materials intercalated with atoms and molecules the most common is graphite [47], transition metal chalcogenides [48] and semiconductors from III^B group of halcogenides elements [49].

Table 11.10 Electrical and optical parameters at T = 300 K of *GaSe*, *InSe* and *GaTe* single crystals

Semiconductor compound	Type	Concentration of charge carriers, cm^{-3}	Mobility μ_p/μ_n, $cm^2/V \cdot s$	$\rho_{\perp C}$, $\Omega \cdot cm$	E^{ex}, eV	$\alpha_{\perp}$, cm^{-1} n = 1	E_g, eV
GaSe	p	5.6×10^{14}	25–40	30–50	2.020	8×10^3	1.995
InSe	n	2.3×10^{16}	520	3–5	1.320	1.4×10^3	1.300
GaTe	p	4×10^{15}	30–40	8–10	1.667	7.8×10^3	1.650
GaS	n	5×10^{13}	–	–	–	–	2.44

The specific features of chemical bonds between atoms and multiple types of arrangements in the *Se–Ga–Ga–Se* elementary packings with respect to each other lead to the formation of spaces between the packings with widths commensurable with those of atoms and molecules (Fig. 11.13). The *Zn* and *Cd* were used for intercalation purposes.

The Fig. 11.14 shows the temperature dependence of pressure of *Cd* and *Zn* vapors [50].

It is obvious from Fig. 11.14 that at the temperature of ~673 K the pressure of *Cd* and *Zn* vapor in containers that contain *GaS*, *GaSe*, *GaTe* and *InSe* single-crystal plates is respectively ~1 and ~0.2 mm *Hg*. The metal atoms (*Zn* and *Cd*) are easily incorporated into spaces between the layered packages. The strong covalent bonds between the metal atoms (*Ga* and *In*) inside the elementary package and the dense arrangement of the metal atoms in the package are two factors that

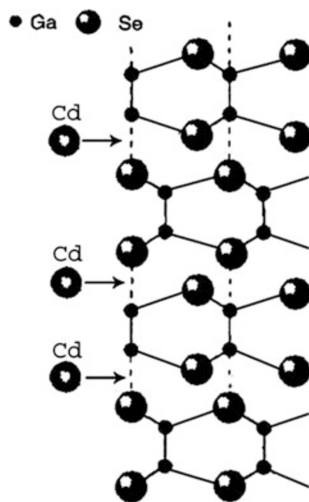

Fig. 11.13 The arrangement of atomic planes in *GaSe* lattice

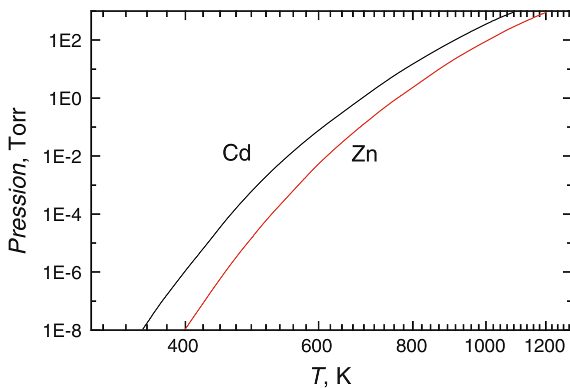

Fig. 11.14 The dependence of *Cd* and *Zn* vapor pressure of temperature

limit the incorporation of heterogeneous atoms (*Cd* and *Zn*) into elementary packings.

According to the estimates made in work [51], the width of the space between the planes of *Se* atoms in ε–*GaSe* crystals is ~0.3 nm which is sufficient to initiate the intercalation not only of atoms of chemical elements with a small diameter but also of macromolecules such as molecules of fullerene C_{60} [14, 18], the ferroelectric and organic molecules [23, 52].

The valence bonds on the surface of the planar *Se–Ga–Ga–Se* elementary packages are closed. This feature causes a low concentration ($c < 10^{10}$ cm^{-2}) of surface states. Thus, it is possible to obtain lamellas with plane-parallel and smooth surfaces at atomic level by splitting of single crystal blocks. A long-term holding of crystals in normal atmosphere leads to the formation of oxidation centers on the outer surface of the *GaSe* plate and at the interface between the packings. This is the result of the presence of spaces between the packages of molecular sizes of (0.3–1 nm). The density of the centers on the surface is 10^9–5×10^{10} cm^{-2}.

The lamellar structure of the single crystals and the presence of spaces between the packages along with mechanical properties stimulate the intercalation of atoms between the packages. The intercalation of *GaSe* plates with *Cd* was provided in sealed quartz ampoules. The amount of 2 mg/cm^2 of *Cd* was introduced in ampoules that contain *GaSe* plates. The samples were treated at the temperatures from 723 to 863 K.

The lamellar structures of micro- and nanocrystalline semiconductors of $A^{III}B^{VI}$ (*GaS*, *GaSe*, *GaTe*, and *InSe*) and $A^{II}B^{VI}$ (*CdS*, *CdSe*, *CdTe*, *ZnSe*, and *ZnTe*) were obtained using the plates of single-crystal optically transparent *GaS*, *GaSe*, *GaTe* and *InSe* without microscopic defects grown by the Bridgman–Stockbarger method. The physical characteristics of $A^{III}B^{VI}$ and $A^{II}B^{VI}$ compounds are shown in Tables 11.10 and 11.11, respectively.

Table 11.11 Crystallographic and physical characteristics of *Cd* and *Zn* chalcogenides

Compound	Solidification temperature *T*, K	Lattice constants, nm [33]		Band gap width at 300 K, eV [53]	
		Cubic	Hexagonal (a/c)	Cubic	Hexagonal
ZnS	–	0.541	0.382/0.6260	3.66	3.74
CdS	1748	0.583	0.413/0.6715	–	2.53
ZnSe	1793	0.569	0.4001/0.684	2.58	–
ZnTe	1512	0.608	0.431/0.702	–	1.74
CdSe	1568	0.609	0.431/0.710	2.28	–
CdTe	1356	0.648	0.457/0.747	1.50	–

11.5.1 *Crystal Structure and the Morphology of the Surface and Interface of the Composite Obtained by Heat Treatment of Single Crystal* GaS *Lamellas in* Cd *and* Zn *Vapors*

Primary *GaS* single crystals were obtained from spectrally pure *Ga* and *S* elementary components (5 N) taken in stoichiometric amounts. The electron concentration at the temperature of 420 K was in a range of (2–6) × 10^{13} cm^{-3}. The perfectly smooth plates with a thickness of 0.1–0.5 mm and a surface area of 3–5 cm^2 were cleaved from the bulk single crystals. The *GaS* plates with respectively *Zn* and *Cd* that were taken in an amount of 5 % of the weight of the *GaS* plates and placed in SiO_2 ampoules. Than they were welded after air evacuation to a residual pressure of 0.5 × 10^{-6} Torr. The diffusion of *Cd* (*Zn*) atoms occurred at the temperature of 753 K for 6 h. The pressure of *Cd* vapour at this temperature was 10 mm *Hg*.

GaS intercalated with *Cd*. The XRD pattern of the *GaS* plates intercalated with *Cd* is shown in Fig. 11.15. The identification of the diffraction planes according to the Miller indices and the respective chemical compound was conducted using the ICSD–POWD–12 card PDF of corresponding diffraction lines.

The results from Table 11.12 show that along with peaks characteristic to *GaS* there are reflections of (0 4 0) and (2 1 4) planes that are characteristic to *CdS* crystals (hexagonal modification) and less intense reflections of (2 2 0) and (1 1 2) planes of $CdGa_2S_4$ compound.

The morphology of the outer surface of the *GaS* plates subjected to heat treatment in *Cd* vapor and at the interface of the planar *S–Ga–Ga–S* packages is clearly evident in SEM images from Fig. 11.16a, b. According to Fig. 11.16a the outer surface of the plate is smooth on a micrometer scale while at the interface of the packings there are two types of new entities that have a drop shape. Some of the entities have large sizes (3–8 μm) and a smooth surface while the other entities with submicron sizes are light scattering centers.

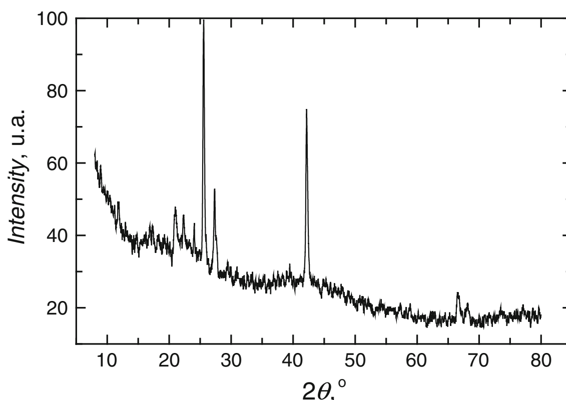

Fig. 11.15 The XRD pattern of *GaS* intercalated with *Cd*

Table 11.12 XRD lines identification for *GaS* intercalated with *Cd*

N	Experimental values			ICDD-JCPDS cards			
	2θ (°)	Iht-f	Compound	PDF	2θ (°)	Int-f	*h k l*
1	23.22	1000	*GaS*	08-0417	23.082	700	0 0 4
2	25.14	17.261	*CdS*	89-0440	25.281	700	0 4 0
3	26.8	22.62	β-$CdGa_2S_4$	37-1131	26.897	340	2 2 0
			CdS	89-0440	26.456	999	1 1 1
4	29	49.91	*CdS*	47-1179	28.530	900	2 1 4
			$CdGa_2S_4$	75-1780	28.723	999	1 1 2
			β-$CdGa_2S_4$	37-1131	28.899	100	0 0 2
			GaS	84-0499	29.261	820	1 0 1
5	29.58	25.425	β-*GaS*	48-1435	29.300	810	1 0 1
			GaS	08-0417	29.355	800	1 0 1
			β-Ga_2S_3	48-1434	29.600	600	0 0 2
			GaS	49-1362	29.840	1000	1 0 1
6	29.92	25.892	Ga_2S_3	15-0104	29.679	600	1 1 2
			γ-Ga_2S_3	49-1361	29.900	1000	1 1 1
7	33.92	21.460	*GaS*	84-0499	33.622	479	1 0 3
8	34.96	295.311	*GaS*	08-0417	34.826	300	0 0 6
9	37.3	14.229	*GaS*	08-0417	37.072	400	1 0 4
10	41.36	30.09	*GaS*	08-0417	41.166	600	1 0 5
11	44.00	10.497	*CdS*	77-2306	43.737	4190	1 1 0
			CdS	89-0440	43.885	4140	2 2 0
12	45.88	12.129	*GaS*	08-0417	45.594	500	1 0 6
13	47.12	88.1735	*CdS*	77-2306	47.893	3940	1 0 3
14	48.12	12.596	*CdS*	47-1179	47.941	850	7 2 2
15	50.84	77.21	*GaS*	49-1362	50.700	500	1 1 0
			GaS	08-0417	50.946	800	1 1 0
			CdS	77-2306	50.948	600	2 0 0
16	52.14	12.363	*CdS*	77-2306	51.889	2960	1 1 2
			CdS	89-0440	51.975	2760	3 1 1
			GaS	49-1362	52.08	370	1 1 3
17	56.72	12.1296	*GaS*	49-1362	56.240	400	1 1 6
			GaS	08-0417	56.553	400	1 1 4
18	59.86	12.596	*GaS*	08-0417	59.767	100	2 0 1
19	73.46	89.80	*GaS*	08-0417	73.327	60	0 0 12
20	73.68	48.518	*GaS*	84-0499	73.412	240	0 0 12
21	74.00	29.624	*GaS*	84-0499	73.921	1000	1 0 11
22	74.76	10.963	*GaS*	08-0417	74.608	400	2 0 7

The distribution of chemical elements in the entities formed as a result of treatment of *GaS* plates in *Cd* vapors was determined from the intensity of the characteristic X–ray emission of the *Ga*, *Cd*, and *S* atoms and it is shown in Table 11.13.

Table 11.13 clearly shows that the micrometric droplets are the mixture of *Cd* and *Ga* with small concentrations of *S* while the submicrometer entities are a mixture of *GaS* and *CdS* microcrystals.

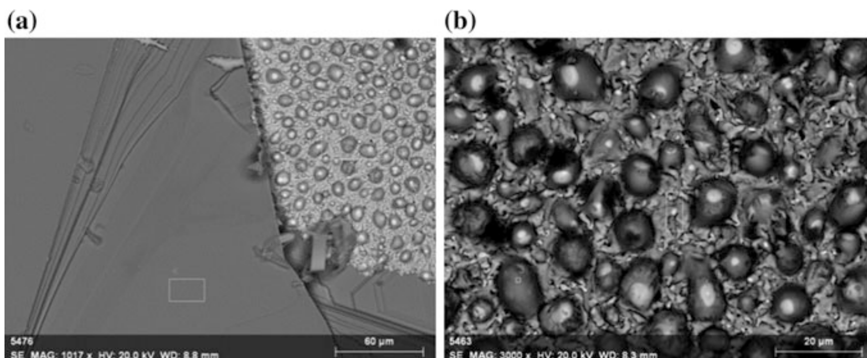

Fig. 11.16 The SEM images of *GaS* plates intercalated with *Cd*: cross-sectional view (**a**) and top view (**b**)

Table 11.13 The distribution of elements on different surface regions of *GaS* lamella intercalated with *Cd*

View	Spectrum	Element	Series	Atom. C (at.%)	Error (%)
Cross section	1	Gallium	K-series	31.55	0.8
		Sulfur	K-series	27.82	0.4
		Cadmium	L-series	40.63	1.7
			Total	100.00	
	2	Gallium	K-series	52.77	1.6
		Sulfur	K-series	46.94	0.9
		Cadmium	L-series	0.29	0.0
			Total	100.00	
Top view	1	Gallium	K-series	14.02	0.3
		Cadmium	L-series	84.15	2.3
		Sulfur	K-series	1.83	0.0
			Total	100.00	
	2	Gallium	K-series	25.19	0.5
		Cadmium	L-series	44.89	1.6
		Sulfur	K-series	29.91	0.4
			Total	100.00	

GaS intercalated with Zn

As it can be seen from Fig. 11.13, the pressure of *Zn* vapors in the temperature range from 700 to 1000 K in the ampoule with *β–GaS* plates is from 6×10^{-2} Torr to $\sim 10^2$ Torr.

Since the *S* atoms from the surface of *S–Ga–Ga–S* layered packings at these temperatures are bound inside the packing by much weaker forces than those of the metal atoms (*Ga*), the *S–Ga* bonds are broken and form *ZnS* crystals and *Ga* in a free state.

Figure 11.17 shows the AFM image of the (0 0 0 1) surface of the *GaS* lamella treated in *Zn* vapors at the temperature of ~480 °C for 30 min (a) and 6 h (b). The amount of 2 mg/cm^3 of *Zn* was introduced in an ampoule in addition to 5 g of *GaS*.

It can be seen the nanoclusters with a hexagonal deformed shape and well-defined nanometer nodes that are liquid at room temperature are presented on the surface. Since *Zn* and its solutions with *S* and *Ga* have a much higher solidification temperature, these points are attributed to liquid gallium. The surfaces of hexagonal clusters with well pronounced nodes of metallic color were obtained by treatment of *GaSe* crystals in normal atmosphere at the temperature of 933 K [54, 55]. Analysis of XRD patterns of these materials has revealed that on the (0 0 0 1) surface of the *GaSe* crystals heat treated in normal atmosphere a polycrystalline structure of gallium oxide (Ga_2O_3) is formed.

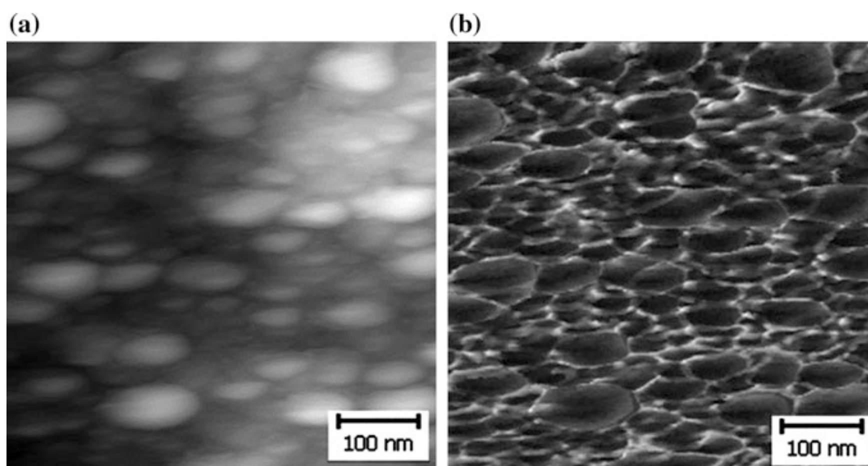

Fig. 11.17 The AFM images of the surface (0 0 0 1) of *GaS* plates heat treated at ~480 °C in *Zn* vapor for 30 min (**a**) and 6 h (**b**)

11.5.2 *The Crystal Structure and the Surface Morphology of Nanolamellar* GaSe*–Intrinsic Oxide Composites and Composites Prepared by Heat Treatment of ε–*GaSe *Single Crystal Plates in* Cd *and* Zn *Vapors*

The SEM image of the *GaSe* plate surface kept in atmosphere for 1 year (a) and the surface of the *GaSe* lamella cleaved from a single crystal (b) as well as the morphology and surface of the composite prepared by heat treatment of *GaSe* plates in *Cd* vapors (c) are shown in Fig. 11.18. It is clearly seen from comparison of Fig. 11.18a, b that under the action of the environment the surface of the *GaSe* lamella granulates and it is covered with the nanosized formations in spite of the fact that the free valence bonds are absent on the surface.

The surface of *GaSe* plates freshly cleaved from perfect single crystals is smooth at the nanometer level. The heat treatment at the temperature of $T \geq 593$ K (at 593 K, the *Cd* vapor pressure is 0.1 mm *Hg*) in the atmosphere of *Cd* vapors leads to the formation of nano- and microstructures of various shapes on the surface of the plates. The presence structures with a shape of circular points and unordered areas is clearly evident in reflected light and much more pronounced in a polar field of monochrome light in reflection and luminescence spectra (Fig. 11.19).

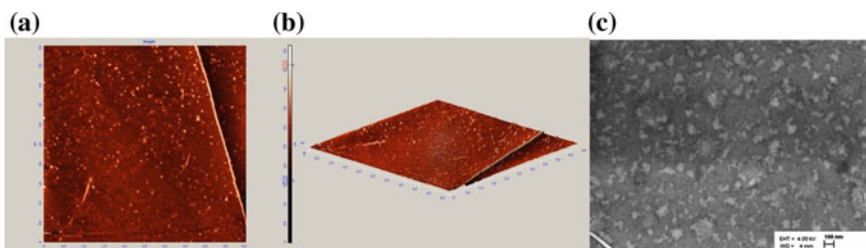

Fig. 11.18 The SEM images of surface of *GaSe* plate kept in the atmosphere for 1 year (**a**), the surface of splitted plate from the *GaSe* single crystal (**b**) and nanolamellar composites obtained by heat treatment of the *GaSe* plates in *Cd* vapor (**c**)

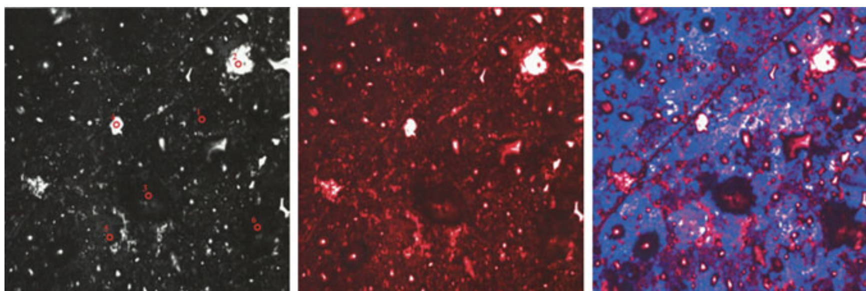

Fig. 11.19 The microscopic image in reflected light and the surface luminescence of the *GaSe* blade heat treated at 823 K in *Cd* vapor for 24 h. Printed aria: (191.3 × 191.3) μm^2

The atomic emission spectroscopy analysis of the points that are easily separated from the surface of the *GaSe* plates shows that they are clusters of metallic *Ga* and at the temperature of 303 K is in a liquid state.

The probability of breaking of the *Se–Ga* bonds on the Van der Waals surface and replacement of them by much stronger *Se–Cd* bonds increases at the fairly high temperatures and low pressures. The *GaSe* compound evaporates congruently at high temperatures where the compound is in a liquid state. Mostly, the vapors are composed of Ga_2Se and Se_2 molecules [56].

Low gallium vapor pressure contributes to the formation of *Ga* nanodrops on the Van der Waals surface of the *GaSe* plate. The gallium of droplets shape is present in *GaSe–CdSe* composite obtained in a temperature range of 653–873 K. It was found that the *Ga* nanodrops on the (0 0 0 1) surface of *GaSe* plates are formed at the temperatures above 570 K as it is shown by Bakhtinov [56]. The Ga_2Se_3 crystals are present on the Van der Waals surface of the *GaSe* compound in addition to droplets of *Ga* and *CdSe* crystallites. Thus, there are two possible ways of formation of the material that contains *CdSe* and *GaSe* crystals:

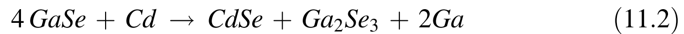

$$4\,GaSe + Cd \rightarrow CdSe + Ga_2Se_3 + 2Ga \qquad (11.2)$$

$$Ga\,Se + Cd \rightarrow CdSe + Ga \qquad (11.3)$$

The reaction (3) is energetically more favorable. Since the XRD pattern along with the diffraction lines of the crystalline lattice of *GaSe* and *CdSe* crystals contains diffraction lines of planes with Miller indices (1 0 3) of Ga_2Se_3 crystals, it can be assumed that the formation of the *GaSe–CdSe* composite occurs through reactions (2) and (3). The Ga_2Se_3 crystals are formed at the temperatures higher than $T \geq 600$ K because the pressure of Se vapor is higher than the *Cd* vapor and in addition the formation of the *CdS* crystals took place. The defects on the (0 0 0 1) surface of *GaSe* act as the nanostructures formation centers. The surface density of these defects as can be approximated from the SEM image (Fig. 11.18c), is about 10^{10} cm^{-2}.

The dynamics of intercalation of *GaSe* single crystal plates is clearly evident from the images shown in Figs. 11.20, 11.21, 11.22, 11.23, 11.24, 11.25 and 11.26. Initially, the atoms (molecules) of the intercalant penetrate between the elementary packings from the surface and deform it so that the space increases in a given direction (Fig. 11.20).

The intercalant penetrates into this space and initiates deformation of the surface layer in other directions (Fig. 11.21). The longer the duration of the process, the higher is the process rate. The area of intercalated surface as shown in Figs. 11.22 and 11.23 increase when the process temperature also increase.

The small radius atoms intercalated between the *Se* planes of two Van der Waals surfaces of *GaSe* crystals can form structures with tetrahedral (T_1 and T_2) and octahedral (O) symmetry [57]. Both arrangements of atoms of the intercalant can contribute to the formation of the *GaSe–CdSe* or *GaSe–*Ga_2Se_3*–CdSe* composite. The atoms with a covalent radius commensurate with or greater than the width of the space between the packings are predominantly octahedrally arranged between

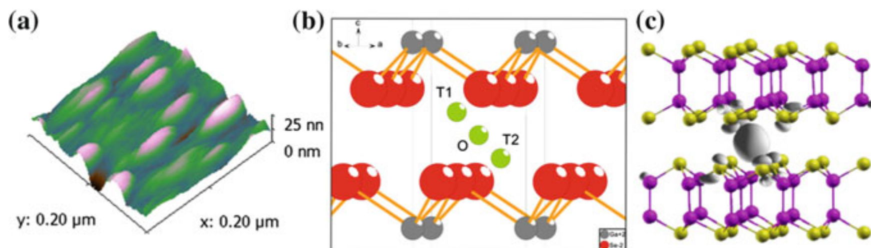

Fig. 11.20 The AFM image of the deformation of surface layer of *GaSe* blade heat treated at 723 K in *Cd* vapor for 6 h (**a**). Intercalation models of the layered semiconductors: atoms with diameter much smaller than the width of the crack (**b**) [57] and commensurable diameter or greater than the width of the crack (**c**) [58]

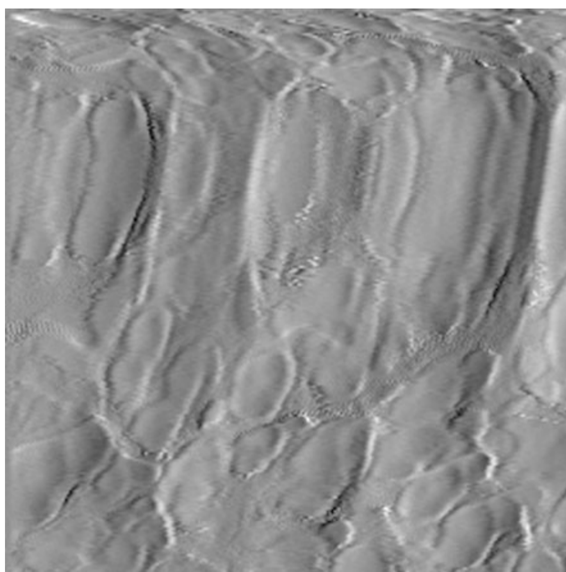

Fig. 11.21 The image of surface of *GaSe* plate heat treated at 480 °C in *Cd* vapor for 30 min

the selenium planes. The covalent radius of the *Cd* atoms is 0.97 [59]. It is three times less than the width of the space between the selenium planes of ~0.3 nm [51]. Thus, the *Cd* atoms intercalated in *GaSe* have an octahedral symmetry [58]. At high temperatures, these atoms form bridges between *Cd–Se* layered packings and strengthens the bonds between the Van der Waals surfaces of the *CdSe–GaSe* nanolamellar composites. This mechanism of formation of a semiconductor *CdS* and *GaSe* composite is confirmed by the fact that the formation of the *CdSe* molecule is energetically more favorable with respect to bonds of the *Ga* atoms with the *Se* atoms. The caloric of the *Cd–Se* molecule formation is 143 kJ/mol while the formation of bonds between *Ga* and *Se* requires energy of 163 kJ/mol.

The Fig. 11.22 shows the AFM image of the surface of a single crystal plate of *GaSe* treated at the temperature of 520 °C for 20 min in *Cd* vapors. When the duration of treatment is increased the deformation of layers inside the crystal plate take place (the plate thickness increases) and the nanostructures form on the surfaces of the plates. Thus, during the treatment of surface at the temperature of 520 °C for 6 h (Fig. 11.23) the irregularly shaped micrometer structures are formed on the surface. The surface of the *GaSe* plates is almost homogeneously covered with new structures with submicrometer sizes (Fig. 11.24). The Figs. 11.23 and 11.24 clearly show that the nanostructures mostly grow throughout the direction of the C_6 crystallographic axis of the *GaSe* crystals.

The Fig. 11.25 shows an AFM image of the *GaSe* plate surface treated at the temperature of 833 K for 24 h. Under these conditions of formation of the composite on the (0 0 0 1) surface of the *GaSe* plates emerge the pyramidal and conical

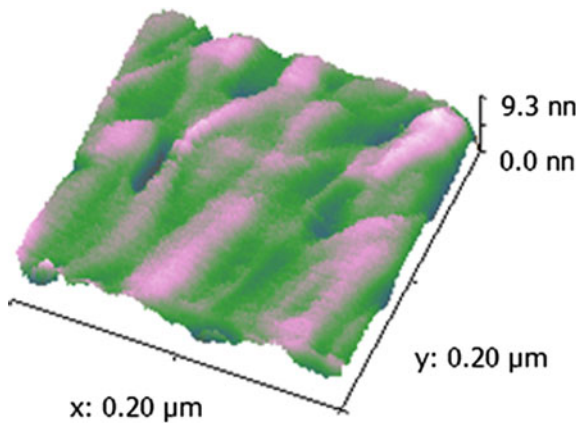

Fig. 11.22 The AFM image of the surface of *GaSe* plate heat treated at 480 °C in *Cd* vapor for 6 h

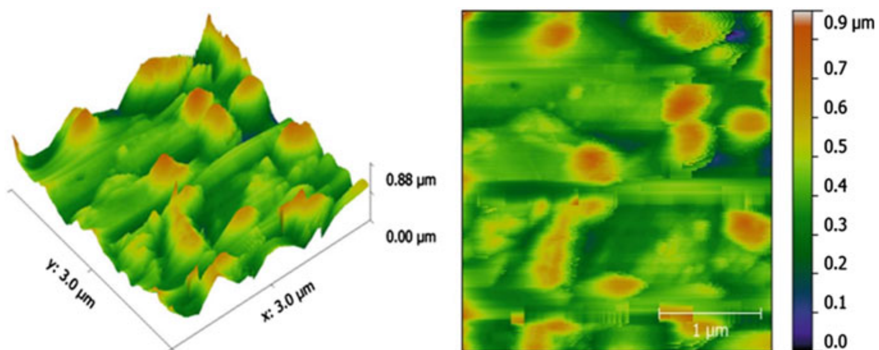

Fig. 11.23 The image of *GaSe* plate surface heat treated at 520 °C in *Cd* vapor for 6 h

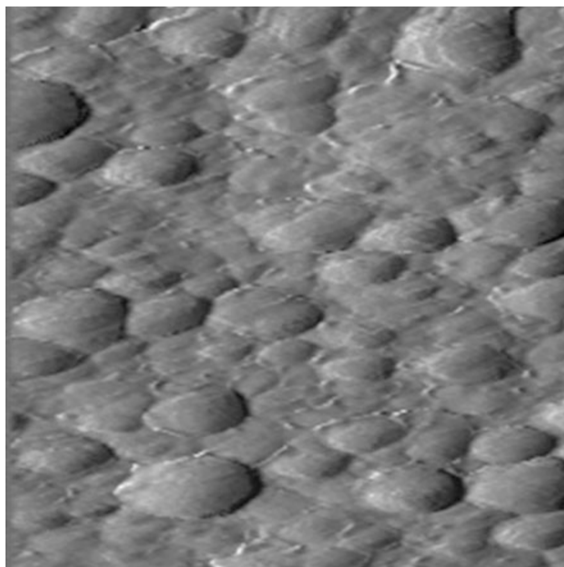

Fig. 11.24 The surface nano-structuration of *GaSe* plate as result of heat treatment at 520 °C in *Cd* vapor for 6 h

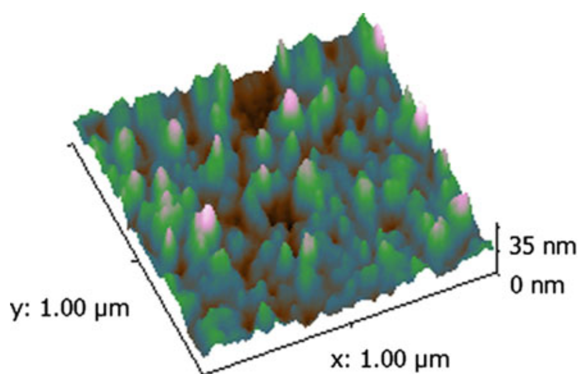

Fig. 11.25 The AFM image of *GaSe* plate surface heat treated at 833 K in *Cd* vapor for 24 h

structures with area of a few hundreds of nanometers. The height of these structures achieves 15–20 nm which corresponds to more than ten *Se–Ga–Ga–Se* layered packings.

The presence of clusters of conical and pyramidal shapes with medium submicron sizes is clearly seen in the reflection images in the red field (reflection from the surface of *GaSe* crystals) (Fig. 11.26) and black-white field (diffuse reflection of nano- and microformaţiuni) (Fig. 11.26b). The compositional structure of the samples was studied by X–ray diffraction ($\lambda_{Cu\mathrm{K}\alpha}$ = 1.54056 Å). The Fig. 11.27 shows XRD patters of the undoped *GaSe* crystals (a) and the crystals doped with 0.5 at.% of *Cd* (b).

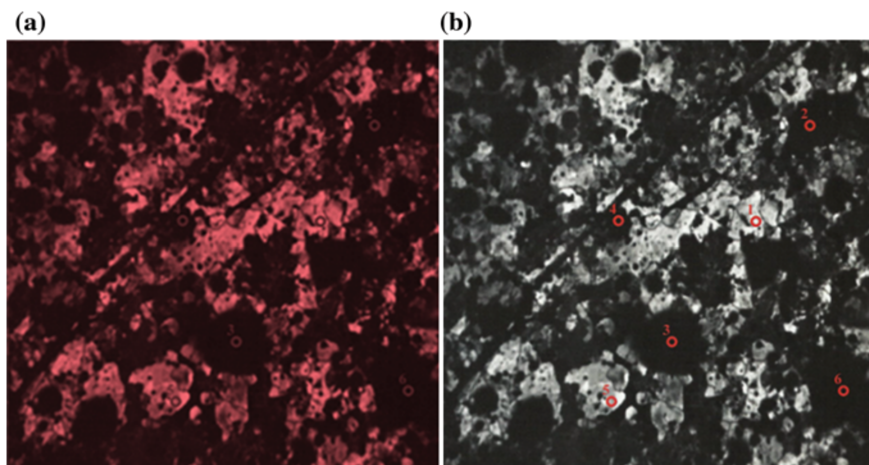

Fig. 11.26 The optical image in red field reflection (**a**) and white-black (**b**) of *GaSe* plate heat treated at 833 K in *Cd* vapor for 24 h

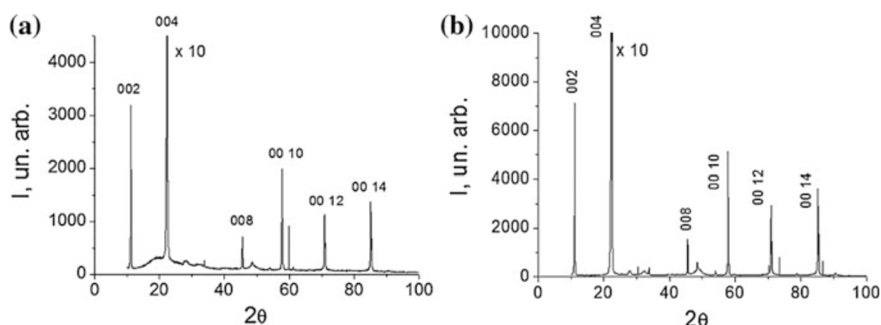

Fig. 11.27 The XRD patterns of single crystals of *ε-GaSe* (**a**) and *ε-GaSe* (0.50 at.% *Cd*) (**b**)

As it can be seen from Fig. 11.27, along with the diffraction line of a high intensity of $2\theta = 22.34°$ and an average intensity of $2\theta = 45.56°$ which are univocally identified by several authors [60] it is a reflection of the plane system with Miller indices (0 0 4) and (0 0 8) in the hexagonal cell of the *GaSe* crystals a line with low a low intensity of $2\theta = 27.50°$ is observed. This line is a reflection from the systems of the crystallographic plane with Miller indices (0 0 8) of β–$CdGa_2Se_4$ clusters. The heat treatment of the ingot at the temperature of 860–880 °C for 24 h leads to the disappearance of $CdGa_2Se_4$ clusters. Thus, the long-term hardening provides the formation of single crystals that are homogeneously doped with this chemical element.

The analysis of the XRD patterns shows that during the synthesis of the compound and the growth of single crystal the cadmium in amounts of up to 0.50 at.% is homogeneously dissolved in the *GaSe* crystals by further annealing. The structure

of the composite obtained by intercalation of *GaSe* crystal plates in *Cd* vapors was studied in sample that was heat treated at the temperatures from 723 to 873 K for 10 min to 24 h. The XRD patterns of the primary crystals of *GaSe* (sample no. 1) and *GaSe* intercalated at the temperature of 833 K with *Cd* from the vapor phase for respectively 10 min (sample no. 2), 20 min (sample no. 3) and 60 min (sample no. 4) contain lines of the basic *GaSe* chemical compound and diffraction lines of *CdSe* crystallites. Taking as a basis the reflections of the ensemble of planes with Miller indices (0 0 4), (2 0 2) and (0 0 12), the parameters *a* and *c* of the hexagonal lattice were calculated for the primary *GaSe* crystal (sample no. 1) and samples intercalated with *Cd* (sample 2, 3, and 4) (Table 11.14). The treatment at the temperature of 833 K for 10 min of the samples leads to a ~0.7 % decrease in *c* parameter. This result can be attributed to the fact that the initial *Cd* atoms eliminate structural defects in the metal sublattice and thus contribute to an increase in the force of cohesion between the elementary packets. When the intercalation process in the space between the packets increases, the germs of *CdS and* $CdGa_2S_4$ crystals are

Table 11.14 Crystallographic characteristic of *GaSe* crystals (sample 1) and *GaSe*-*Cd*Se composite obtained by intercalation with *Cd* during 10 min (sample 2), 20 min (sample 3), and 60 min (sample 4)

Sample	Treatment duration, min	2θ, (grad)	*d*, (Å)	*h k l*	*a*, (Å)	a_M, (Å)	*c*, (Å)	c_M, (Å)	*D*, (Å)
1	0	22.37	3.9742	0 0 4	3.62	3.68	15.89	15.9	378.75
		57.84	1.5941	2 0 2					
		71.08	1.3262	0 0 12	3.75		15.91		
2	10	22.37	3.9742	0 0 4	3.76	3.75	15.89	15.84	326.36
		57.81	1.5949	2 0 2					
		71.68	1.3166	0 0 12	3.75		15.79		
3	20	22.4	3.9689	0 0 4	3.75	3.75	15.87	15.88	322.29
		57.93	1.5918	2 0 2					
		71.11	1.3257	0 0 12	3.75		15.9		
4	60	22.33	3.9812	0 0 4	3.75	3.75	15.92	15.93	345.25
		57.9	1.5926	2 0 2					
		70.98	1.3278	0 0 12	3.75		15.93		

formed. This contributes to increase of the space between the packets and the *c* parameter when the time of intercalation increases.

In the Table 11.15 is shown the X–ray diffraction lines ($\lambda_{CuK\alpha} = 1.54186$ Å) for *Cd*, *CdSe*, $CdGa_2Se_4$ and *GaSe* compounds that are most likely formed as a result of intercalation of *GaSe* single crystals with *Cd* from the vapor phase. The XRD pattern of the *GaSe* sample treated in *Cd* vapors at 530 °C for 10 min contains only the diffraction lines of the system of planes of the *GaSe* single crystal. In addition, two low-intensity reflections at $2\theta = 25.4°$ and $2\theta = 42.2°$ respectively with an intensity of 5.3 and 1.8 are observed. They may be associated with *CdSe* crystallites. The diffraction line at $2\theta = 45.66°$ is best correlated with the diffraction of the system of planes (2 2 0) or (2 0 4) in the $CdGa_2Se_4$ crystals. The Figs. 11.28 and 11.29 show XRD patterns of two samples of *GaSe* plates with a thickness of 0.3 mm and 1.2 mm obtained by treatment in *Cd* vapors at temperature of 753 K (Fig. 11.28) and 833 K (Fig. 11.29) for 24 h. The 2θ diffraction angles that cor-

Table 11.15 Diffraction angle (2θ) and diffraction lines intensity for *Cd*, *CdSe*, $CdGaSe_4$ and *GaSe*, formed as result intercalation of *GaSe* single crystals with *Cd* from vapor phase

Nr.	*Cd*			*CdSe*			*GaSe*			$CdGa_2Se_4$		
	2θ	*I*	*h k l*	2θ	*I*	*h k l*	2θ	*I*	*h k l*	2θ	*I*	*h k l*
1	31.830	394	0 0 2	25.375	999	1 1 1	27.533	999	1 1 2	22.213	758	0 0 4
2	34.740	227	1 0 0	42.215	626	2 2 0	44.631	228	2 2 0	27.442	881	1 0 0
3	38.358	999	1 0 1	49.957	375	3 1 1	46.279	323	2 0 4	32.249	999	1 0 3
4							53.245	226	1 3 2	48.514	813	1 1 0
5										48.695	932	1 0 7
6										70.960		1 0 1

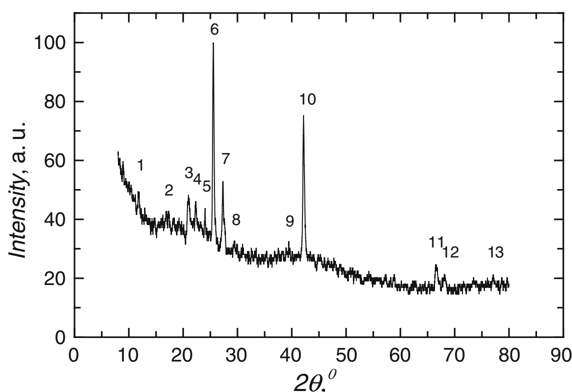

Fig. 11.28 The XRD pattern of *GaSe* heat treated at 753 K in *Cd* vapor for 24 h

responds to the diffraction lines, the intensity of the lines, and the identification of the ensembles of planes from which the X–ray diffraction occurs are shown in Table 11.16. It is evident that the diffraction lines of the ensemble of planes both of the parent *GaSe* compound and the *CdS* crystallites are observed as it can be observed from Figs. 11.28 and 11.29 and the Table 11.16. The XRD reflections of crystalline *CdS* clusters in *GaSe* at the temperatures of 753 and 833 K and the reflections of the ensemble of planes [1 0 1] of the $CdGa_2Se_4$ compound are present. A change in the ratio of intensities of the XRD reflections with an increase in the treatment temperature from 753 to 833 K (the vapor pressure of *Cd* increases) can indicate an increase of *CdSe* crystallites concentration in the composite.

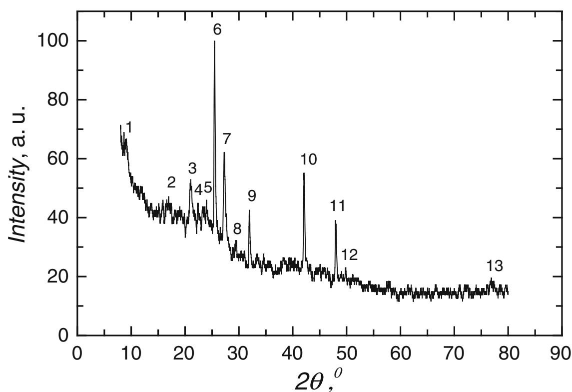

Fig. 11.29 The XRD pattern of *GaSe* heat treated at 833 K in *Cd* vapor for 24 h

Table 11.16 The identification of XRD lines for *GaSe*–*Cd*Se composite

Nr.	753 K		Identification	833 K		Identification
	2θ	*I* (u.a)		2θ	*I* (u.a)	
1						[101] *CdSe*
2	11.85	49.05	[001] *CdSe*	20.96	51.7	[002] *GaSe*
3	20.99	47.44	[103] *CdSe*	22.46	44.23	[103] *GaSe*
4	22.32	45.43	[004] *GaSe*	25.49	100	[002] $CdGa_2Se_4$
5	22.35	46.1	[002] *GaSe*	27.27	62.1	[100] *GaSe*
6	25.56	100	[101] $CdGa_2Se_4$	31.93	42.5	[004] *GaSe*
7	27.33	52.8		42.08	55.2	[004] *GaSe*
8	29.53	32.24	[200] *CdSe*	47.93	39.1	[002] *CdSe*
9	39.39	31.22	[210] *GaSe*	57.91	17.80	[110] *CdSe*
10	42.17	75.3	[004] *GaSe*	76.93	19.19	[222] $CdGa_2Se_4$
11	68.14	20.40	[1118] *GaSe*			
12	73.5	20.00	[414] Ga_2Se_3			
13	76.93	20.00	[222] $CdGa_2Se_4$			

The composition of the material generated in *GaSe* obtained by intercalation of hexagonal *GaSe* crystals with *Cd* was analyzed by Raman scattering. The *ε–GaSe* modification crystallizes in a hexagonal lattice. The unit cell without an inversion center is composed of two packets of the *Se–Ga–Ga–Se* type shifted to a quarter of the *Se–Se* interval with respect to one another. The modes of vibration of the crystal lattice are active both in the absorption (reflection) spectra in the IR region and in Raman scattering spectra according to autoexclusion principle.

The Raman scattering spectra under excitation by laser radiation with a wavelength of 633 nm (photons energy of 1.959 eV) are shown in Fig. 11.30a, b. The wave numbers and the intensity of the bands of Raman scattering in the *GaSe–CdSe* composite are listed in Table 11.17.

The data from Table 11.17 shows that along with monophonic vibration patterns in *GaSe* crystals the vibrational bands of the *CdSe* crystal lattice are well defined. The lower intensity of the diffusion bands of *CdSe* crystallites compared to *GaSe* corresponds to the composition percentage of the composite obtained at 733 K. These results correlate well with the intensity of the XRD reflections of planar systems in *GaSe* and *CdSe* crystals shown in Table 11.17.

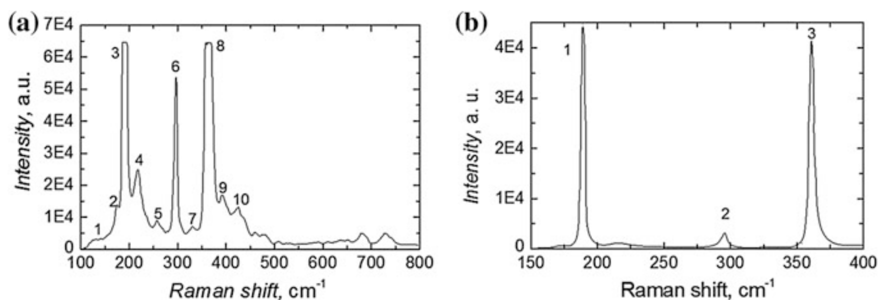

Fig. 11.30 The spectra of Vibration modes (**a**) and Raman spectrum (**b**) in *GaSe* plates heat treated at 753 K in *Cd* vapor for 6 h

Table 11.17 Crystalline lattice vibration modes of *GaSe-CdSe* composite obtained from Raman spectrum

Nr.	$\widetilde{\nu}$, cm^{-1}	Intensity (u.a)	Compound	Vibration simetry
1	135	3000	*GaSe*	A_1
2	174.4	14000	*Cd*Se	E(TO)
3	188.9	>60000	*GaSe*	
4	217.5	25000	*GaSe*	E(TO)
5	256.8	8000	*GaSe*	E′(LO)
6	295.4	52000	*GaSe*	
7	329.9	6000	*GaSe*	
8	361.6	>60000		
9	393.9	16000	*Cd*Se	
10	426.8	12000	*Cd*Se	

There is a well known classification of vibration modes according to the type of symmetry and energy shifts of Raman bands related to intercombination of different vibration modes for *GaSe* single crystals [61, 62]. The low intensity of resonant vibration modes E(TO) (267.5 cm^{-1}) and E′(LO) (256.8 cm^{-1}) with respect to the bands (188.9 cm^{-1}) and (361.6 cm^{-1}) can be attributed to the fact that the formation of the composite is accompanied by the degradation of the crystal lattice of the primary *GaSe* compound.

The composition of the material obtained by heat treatment of the *GaSe* plates in *Zn* vapors at the temperature of 833 K for 24 h was established in XRD measurements in a range of $20° \leq 2\theta \leq 80°$.

The Fig. 11.31 shows the XRD pattern of the composite obtained by treatment at 833 K of the *GaSe* plates in *Zn* vapors for 24 h.

The XRD pattern of the composite obtained by treatment of the *GaSe* plates in *Zn* vapors at 833 K for 24 h contains the diffraction lines of the ensemble of planes characteristic for hexagonal *GaSe* and crystals a set of additional reflections. The diffraction angles 2θ of the XRD lines, their relative intensity, the identification of the compound and diffraction planes from their Miller indices are listed in Table 11.18.

As a result of the heat treatment of the *GaSe* plates in *Zn* vapors, the material composed of *GaSe*, *ZnSe* and $ZnGa_2Se_4$ crystallites is obtained. The low intensity of the XRD lines from the planes with Miller indices of (2 0 0), (3 2 3) and (1 1 4) is a criterion for the low concentration of the $ZnGa_2Se_4$ compound in the composite. At the same time, the width of the contour of the XRD line of the atomic planes of this compound it is the result of X–ray diffraction from nanometer-sized crystallites.

The Fig. 11.32 shows the XRD line contour of planes with Miller indices (2 2 0) in the *ZnSe* crystallites of the *GaSe–ZnSe* composite. The average size *d* of the *ZnSe* crystals from the composite was determined from analysis of the contour of diffraction lines using the Scherrer formula [63–65]:

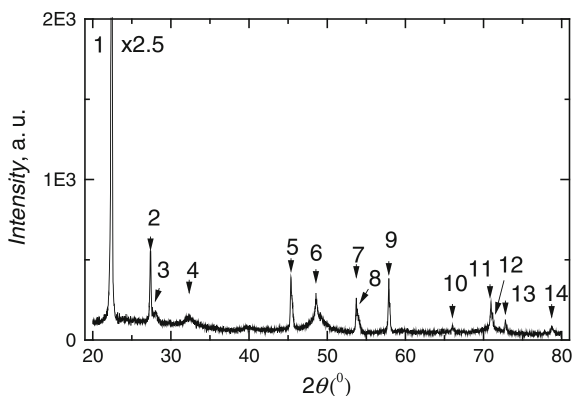

Fig. 11.31 The XRD pattern of composite obtained by *GaSe* heat treatment at 833 K in *Zn* vapor for 24 h

Table 11.18 The identification of XRD lines for *GaSe* heat treated in *Zn* vapor at 833 K, for 24 h

Experimental values			ICDD-JCPDS cards				
Nr.	2θ (°)	I (a. u.)	PDF	2θ (°)	I	$h\ k\ l$	Compound
1	22.44	4558	81-1971	22.338	99.9	0 0 6	*GaSe*
2	27.38	556	70-0777	27.402	99.9	1 1 1	*ZnSe*
3	28.02	182	78-1927	28.013	6.5	1 0 1	*GaSe*
4	32.34	160	47-1590	32.339	5	2 0 0	$ZnGa_2Se_4$
5	45.36	392	15-0105	45.378	100	1 1 0	*ZnSe*
6	48.56	292	78-1927	48.514	17	1 1 0	*GaSe*
7	53.72	262	05-0522	53.645	44	3 1 1	*ZnSe*
8	53.86	194	78-1927	53.969	28.0	1 1 4	*GaSe*
9	57.88	384	78-1927	57.902	3	2 0 2	*GaSe*
10	66.02	94	47-1590	66.016	2	3 2 3	$ZnGa_2Se_4$
11	70.96	238	78-1927	70.961	7.4	1 0 11	*GaSe*
12	71.18	170	78-1927	71.178	21.9	2 0 7	*GaSe*
13	72.80	128	05-0522	72.731	13	3 3 1	*ZnSe*
14	78.72	90	81-1971	78.722	3.2	1 2 2	*GaSe*

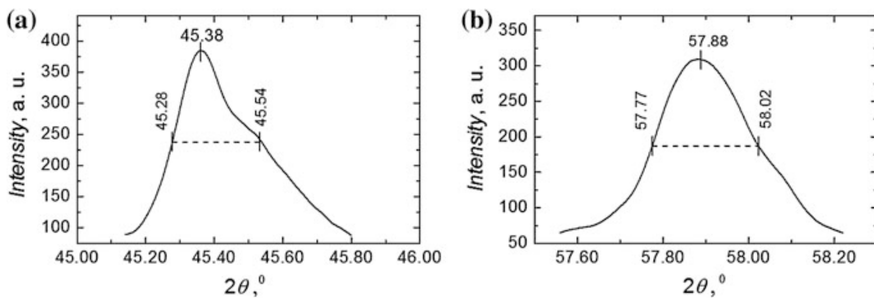

Fig. 11.32 The contour of diffraction line from (2 2 0) planes assembly of *ZnSe* compound (**a**) and (2 0 2) planes assembly of *GaSe* compound (**b**)

$$d_m = \frac{k\lambda}{\beta cos\theta_{hkl}}, \quad (11.4)$$

where k is the Scherrer constant of 0.94; λ is the X–ray wavelength; $\theta_{h\ k\ l}$ is Bragg diffraction angle and β is the full width at half maximum of the diffraction intensity of the XRD line from the planes with Miller indices ($h\ k\ l$). The average size of the *ZnSe* crystallites is approximately 30 nm for $\lambda_{CuK\alpha}$ = 1.54060 Å, 2θ = 45.38° and $\beta = 5.4 \times 10^{-3}$ rad (Fig. 11.32a). The average size of the *GaSe* crystallites from the

composite determined from the analysis of the recorded line contour at $2\theta = 57.88°$ (Fig. 11.32b) is ~63 nm and the size of the $ZnGa_2Se_4$ crystallite calculated from the width of diffraction line of the planes with Miller indices (2 0 0) and $2\theta = 32.339°$ is ~18 nm.

11.5.3 Crystal Structure and the Surface Morphology of the Interface Between the Packets of the Composite Obtained by Heat Treatment of GaTe Single–Crystal Lamellas in Cd and Zn Vapors

The *GaTe* single crystals were used as a primary material was grown by the Bridgman–Stockbarger method. The crystal structure and composition of the material obtained by the treatment at 653 and 723 K of the *GaTe* single-crystal plate in *Cd* vapors was analyzed by X–ray diffraction ($\lambda = 0.154060$ nm).

The Fig. 11.33 shows the XRD pattern of the composite obtained by treatment at the temperature of 653 K for 60 h of *GaTe* plates in *Cd* vapors. The pressure of *Cd* vapor at this temperature is ~1 mm *Hg* [50]. Along with the characteristic diffraction lines of the *GaTe* compound the intense lines from atomic planes of *CdTe* crystallites are present. The presence of diffraction lines of the Te crystallites confirms that the treatment at the temperature of 653 K of *GaTe* plates in *Cd* vapors leads to the breaking of *Ga–Te* bonds resulting in the formation of *Ga* clusters in a liquid state while the characteristic diffraction lines of *Ga* and *Te* crystallites are absent. These compositional transformations are facilitated by the fact that at 653 K the pressure of *Cd* vapor is an order of magnitude higher than the pressure of *Te* vapors [50]. Therefore, the treatment at ~653 K of *GaTe* single crystal lamellas in *Cd* vapors leads to the formation of a material composed of *GaTe*, *CdTe* and *Te* crystals. The presence of Ga_7Te_{10} crystallites in the composite suggests that the

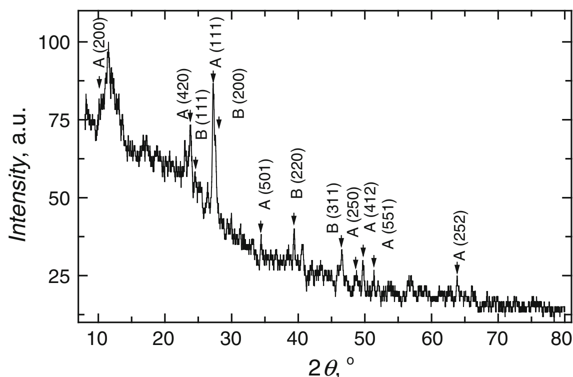

Fig. 11.33 The XRD pattern of composite obtained by *GaTe* heat treatment at 653 K in *Cd* vapor for 60 h: A—*GaTe*; B—*CdTe*

GaTe ↔ *CdTe* transformation takes place through the Ga_7Te_{10} phase, similar to the case of the *GaSe–CdSe* transition involving the Ga_2Se_3 phase. The solidification temperature of tellurium at normal pressure is 725 K. Since the temperature of heat treatment is much lower than the crystallization temperature of the metallic tellurium, the Te crystallites are formed via restructuring the crystal lattice of the *GaTe* compound. This restructuring takes place with the formation of intermediate phases of Ga_2Te_3, Ga_7Te_{10}. These transformations result in the formation of a *CdTe* compound on the outer surface of the *GaTe* plate and also at the interface between elementary packets *Te–Ga–Ga–Te*.

The pressure of *Cd* vapor increases more than 50 times when the treatment temperature increases from 650 to 833 K. The *Te–Ga* bond-breaking process enhances at this temperature and it contributes to the formation of the *CdTe* compound. The reaction of formation of a *CdTe* compound via the decomposition of *GaTe* crystals at lower temperatures than the melting points is energetically provided while the energy of formation of the *CdTe* compound (ΔH = –24 kcal/mol) [66] is lower than that of the *GaTe* compound (ΔH = –28.6 kcal/mol) [67]. The XRD pattern of the composite obtained by heat treatment at 833 K for 3 h of the single crystal of *GaTe* plates in *Cd* vapors (Fig. 11.34) contains the diffraction lines ($\lambda_{Cu\mathrm{k}\alpha}$ = 1.54060 Å) of the atomic planes of *GaTe* and *CdTe* crystallites from the composite. The 2θ angles, the intensity of X–ray diffraction lines and identification them of according to the PDF card file is shown in Table 11.19. As it can be seen from Table 11.19, the XRD pattern of the sample that was heat-treated for 3 h mostly contains diffraction lines of the atomic planes of the *GaTe* crystals. When the heat treatment duration increase from 3 to 24 h (Fig. 11.35) the fraction of *CdTe* crystals in the composite increases. This fact is confirmed by the atomic planes with Miller indices (4 1 0) and (4 0 0) and indirectly by an increase in the intensity of the XRD reflections of the *CdTe* crystals.

Further will be analyzed the morphology of the *GaTe* lamella interface that is intercalated at 623 K for 60 h with *Cd* obtained by splitting the surface layer. The Fig. 11.36a shows the SEM image of this surface. Along with the areas from the

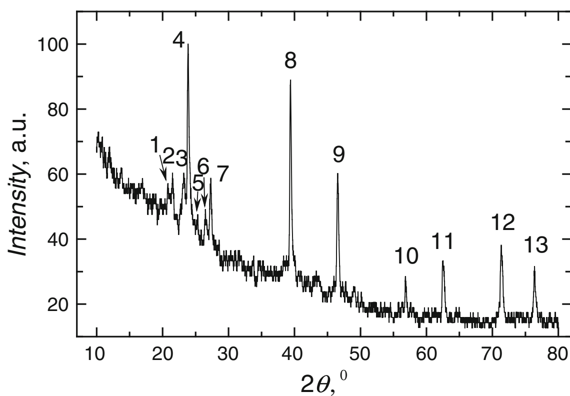

Fig. 11.34 The XRD pattern of composite obtained by *GaTe* heat treatment at 833 K in *Cd* vapor for 3 h

Table 11.19 The identification of XRD lines for heat treated at 833 K of *GaTe* in *Cd* vapor for 3 h

Experimental values			ICDD-JCPDS cards				
Nr.	2θ (°)	*I* (u.a.)	Compound	PDF	2θ (°)	*I*	*h k l*
1	20.79	57.1	*GaTe*	44-1127	20.673	10	2 0 1
2	21.50	60.3	*GaTe*	44-1127	21.045	10	4 0 0
3	23.22	60.3	*CdTe*	19-0193	23.707	100	0 0 2
4	23.82	100	*GaTe*	44-1127	23.849	20	0 0 2
5	25.31	47.6	*CdTe*	19-0193	25.281	80	1 0 1
6	26.51	49.2	*GaTe*	33-0571	26.425	40	0 3 0
7	27.31	58.7	*GaTe*	44-1127	27.14	10	1 1
8	39.39	58.9	*CdTe*	19-0193	39.222	100	1 1 0
9	46.55	60.3	*GaTe*	33-0571	46.551	8	7 1 1
10	56.83	28.6	*GaTe*	71-0620	56.845	4	7 3 1
11	62.49	33.3	*GaTe*	71-0620	62.479	18	–6 4 2
12	71.35	38.1	*GaTe*	71-0620	71.347	56	3 0 3
13	76.39	31.7	*CdTe*	19-0193	76.154	20	0 0 6

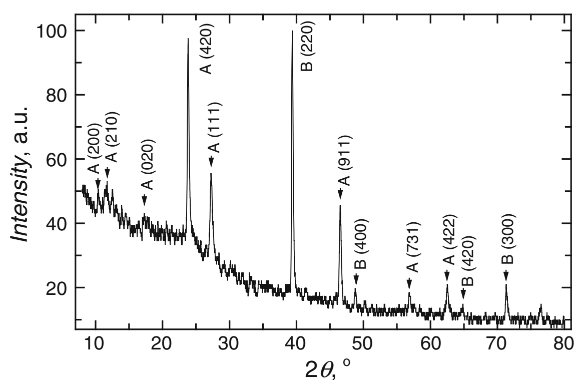

Fig. 11.35 The XRD pattern of composite obtained by *GaTe* heat treatment at 833 K in *Cd* vapor for 24 h temperature: A—*GaTe*; B—*CdTe*

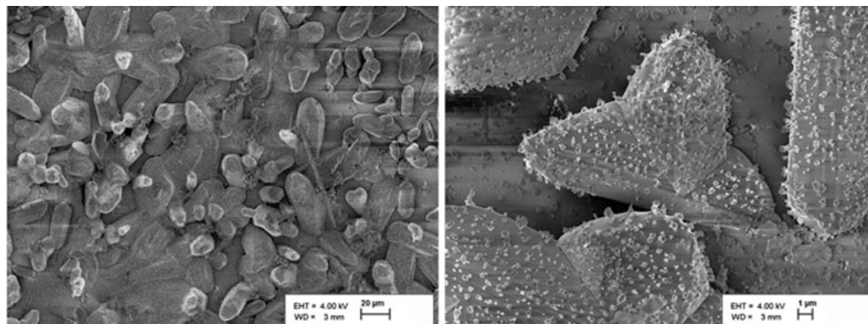

Fig. 11.36 The SEM images of *GaTe* plates surface heat treated at 623 K in *Cd* vapor for 60 h that was obtained by surface layer splitting

surface of the *GaTe* plates (blackened and smooth areas), there are two types of microstates: some have a lamellar shape with dimensions of a few tens of square micrometers and the others (bright) with much smaller sizes and the homogeneous form. The growth points of the crystallites with a needle shape of a submicron size are observed on the surface of these lamellas (Fig. 11.36).

The elemental composition of the sectors of the *GaTe* lamella surface that is intercalated with *Cd* at $T = 623$ K was analyzed from characteristic X–ray emission excited by electron beam with the energy of 20.0 keV. The Fig. 11.37 shows the SEM image (magnification of 1000) of the surface of this lamella with indication of the dark sectors (sector 1) and the one known from intercalation (sector 2, bright formations). The concentration percentage of constituent elements like *Ga*, *Cd* and *Te* are shown in Table 11.20.

The analysis of the concentrations of elements suggests that at the temperature of 623 K, the *CdTe* microplates are formed at the interface between the packets while the released *Ga* atoms are localized in sectors of type 1. However, microcrystals of *CdTe* and *GaTe* can be probably found here. The Te is localized mostly in microcrystals with small amounts of *Ga* and *Cd* (sector 2).

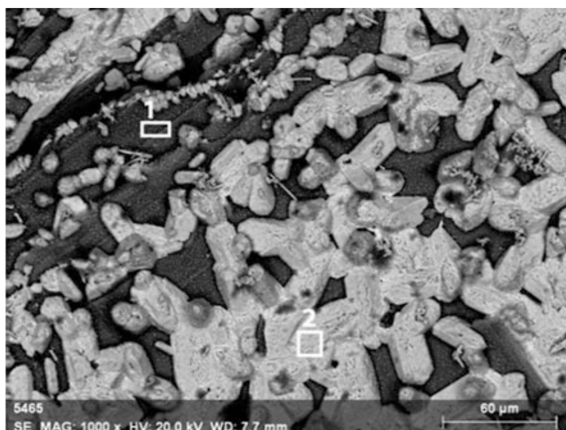

Fig. 11.37 The SEM images of the interface of *GaTe* plates heat treated at 623 K in *Cd* vapor

Table 11.20 The distribution of elements of *GaTe-Cd*Te composite that was obtained at 623 K

Spectrum	Element	Series	Atom. C (at.%)	Error (%)
1	Gallium	K-series	89.27	2.0
	Tellurium	L-series	5.55	0.3
	Cadmium	L-series	5.18	0.2
2	Gallium	K-series	3.41	0.1
	Tellurium	L-series	92.51	2.8
	Cadmium	L-series	4.08	0.2

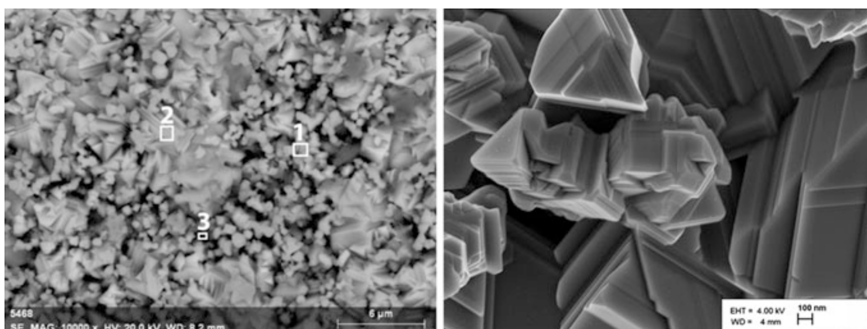

Fig. 11.38 The SEM images of the surface of *GaTe* plates heat treated at 723 K in *Cd* vapor

Table 11.21 The distribution of elements of *GaTe*-*Cd*Te composite obtained at 723 K

Spectrum	Element	Series	Atom. C (at.%)	Error (%)
1	Gallium	K-series	2.985	0.1
	Cadmium	L-series	41.950	1.5
	Tellurium	L-series	55.07	1.7
2	Gallium	K-series	1.61	0.1
	Cadmium	L-series	49.29	1.4
	Tellurium	L-series	49.10	1.7
3	Gallium	K-series	1.91	0.0
	Cadmium	L-series	52.86	1.5
	Tellurium	L-series	45.23	0.9

The Fig. 11.38 shows the SEM image of the *GaTe* plates interface intercalated with *Cd* at 723 K. At the interface of packets *Te–Ga–Ga–Te*/*Te–Ga–Ga–Te*, there are structures with areas of a few μm^2 to a few tens of μm^2. However, the composition of the clusters also changes. The elemental compositions of the three points are shown in Fig. 11.38 and Table 11.21. Thus, by treatment at 723 K of the *GaTe* plates in *Cd* vapors, the *CdTe* crystallites are formed. The crystallites are arranged in the form of single-crystal layers oriented parallel to the surface of the *GaTe* lamella at the interface of the *GaTe* elementary packets. The SEM image of the of the composite plate surface obtained at $T = 723$ K in which is observed the characteristic growth Figures of *CdTe* single crystals is shown in Fig. 11.38b.

The composition of the material obtained by heat treatment at the temperature of 833 and 873 K of *GaTe* single-crystal plates in *Zn* vapors was studied using X–ray diffraction with $\lambda_{Cuk\alpha} = 0.154182$ nm in the range of angles of $10° < 2\theta < 80°$. The pressure of *Zn* vapor at these temperatures is respectively 8 and 20 mm *Hg*. The XRD pattern of the material that was heat treated at 833 K for 3 h is presented in Fig. 11.39. The 2θ angles, the intensity of the diffraction lines, the Miller indices $(h\ k\ l)$ for these compounds are listed in Table 11.22.

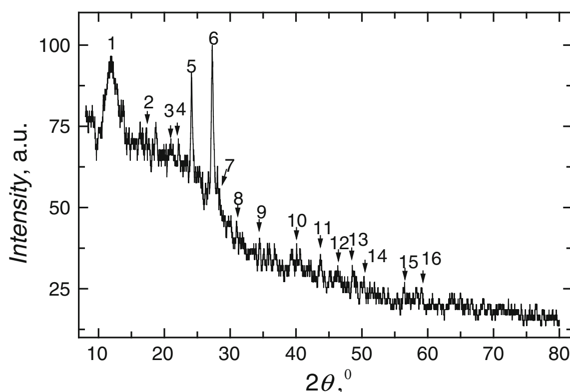

Fig. 11.39 The XRD pattern of composite obtained by *GaTe* heat treatment at 833 K in *Zn* vapor for 3 h

Table 11.22 The identification of XRD lines for heat treated at 833 K of *GaTe* in *Zn* vapor for 3 h

Nr.	Experimental values		Cards ICDD-JCPDS				
	2θ (°)	*I* (a. u.)	Compus	PDF	2θ (°)	*I*	*h k l*
1	11.89	96.6	*GaTe*	65-2208	11.86	7.4	2 1 0
2	17.24	74.6	Ga_7Te_{10}	85-0007	17.397	9	2 0 2
3	21.00	71.2	*GaTe*	44-1127	21.04	10	4 0 0
4	22.12	71.2	Ga_2Te_5	31-0549	22.418	1	2 0 0
5	24.11	91.5	*ZnTe*	80-0022	24.028	999	100
6	27.27	100.0	*ZnTe*	80-0022	27.246	932	1 0 1
7	28.40	62.7	Ga_2Te_5	31-0549	28.407	100	2 1 1
8	30.95	45.8	*GaTe*	44-1127	30.86	80	−8 0 3
9	34.46	40.7	*GaTe*	44-1127	34.48	10	5 1 0
10	40.11	37.3	Ga_7Te_{10}	85-0007	40.217	3.6	2 1 7
11	43.71	35.6	Ga_7Te_{10}	85-0007	43.752	3.0	6 0 0
12	46.28	32.2	Ga_7Te_{10}	85-0007	46.293	3.9	4 2 5
13	48.54	32.2	Ga_7Te_{10}	85-0007	48.586	16.7	3 1 8
14	50.29	28.8	*ZnTe*	80-0022	50.000	35.9	3 1 1
15	56.49	27.1	*ZnTe*	80-0022	56.206	7.1	2 0 2
16	59.12	25.4	*GaTe*	65-3511	59.144	2	2 0 5

It is evident from Table 11.22 that the material obtained by heat treatment at the temperature of 833 K is a composite from *GaTe* (starting material), *ZnTe*, Ga_7Te_{10} and small amounts of Ga_2Te_5. The increase of treatment temperature from 833 to 873 K leads to a decrease in the intensity of the diffraction lines of the Ga_7Te_{10}

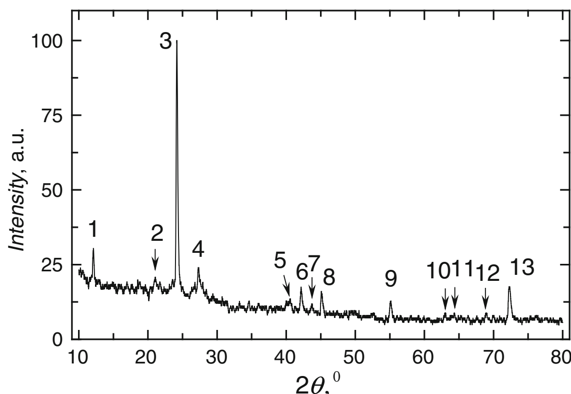

Fig. 11.40 The XRD pattern of composite obtained by *GaTe* heat treatment at 873 K in *Zn* vapor for 6 h

Table 11.23 XRD lines identification for *GaTe* heat treated in *Zn* vapor at 873 K, for 6 h

Nr.	Experimental values		ICDD-JCPDS cards				
	2θ (°)	I (a. u.)	Compound	PDF	2θ (°)	I	$h\ k\ l$
1	12.11	30.4	Ga_7Te_{10}	85-0007	12.205	8.8	0 1 2
2	21.09	20.80	*GaTe*	44-1127	21.04	10	4 0 0
3	24.18	100.00	*ZnTe*	80-0022	24.028	99.9	1 0 0
4	27.31	24.00	*ZnTe*	80-0022	27.246	93.2	1 0 1
5	40.53	13.6	*GaTe*	44-1127	40.32	10	–10 0 2
6	42.16	17.6	*ZnTe*	80-0022	42.266	71.6	1 1 0
7	43.74	12.00	Ga_7Te_{10}	85-0007	43.752	20.9	6 0 0
8	45.09	16.00	Ga_7Te_{10}	85-0007	45.250	17.0	1 4 6
9	55.11	12.80	*GaTe*	44-1127	55.01	50.0	4 2 1
10	62.95	8.80	*GaTe*	44-1127	62.87	10.0	4 2 2
11	64.37	8.80	*ZnTe*	80-0022	64.232	20.1	2 0 3
12	68.98	8.80	*ZnTe*	80-0022	68.339	8.8	2 1 1
13	72.28	17.60	*ZnTe*	80-0022	72.182	12.7	1 0 5

crystallites and does appear in the Ga_2Te_5 crystals composite (Fig. 11.40, Table 11.23).

However, there is a intense decrease of the diffraction intensity of the planes with Miller indices (1 0 1) and an amplification of the intensity of the line with $2\theta = 24.18°$ that corresponds to the diffraction of planes (1 0 0). XRD pattern restructuring at the treatment temperature increase from 833 to 873 K can be determined by the orientation of the *ZnTe* crystals growth direction on the surface of the *Te–Ga–Ga–Te* packages. According to the above, it can be assumed that the

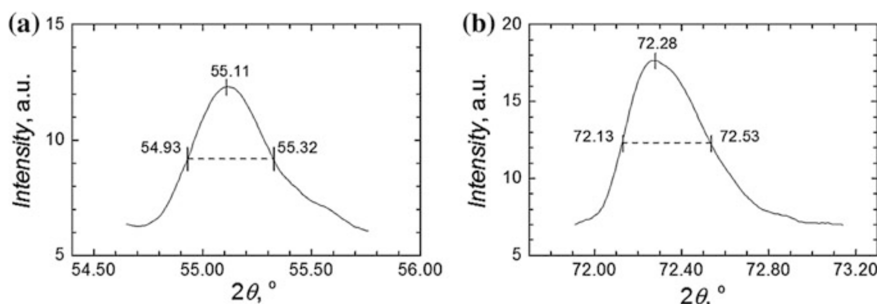

Fig. 11.41 The contour of diffraction line from (4 2 1) planes assembly of *GaTe* compound (**a**) and (1 0 5) planes assembly of *ZnTe* compound (**b**)

treatment at the temperature of ~873 K of *GaTe* single-crystal plates in zinc vapors leads to the formation of a composite of *ZnTe* and *GaTe* lamellas.

The broad contour of the diffraction lines from *GaTe* ($2\theta = 55.11°$) and *CdTe* ($2\theta = 72.28°$) crystallites indicates the nanoscale dimensions of the composite components. The contours of XRD lines of the system of planes with Miller indices (4 2 1) and $2_\theta = 55.11°$ that correspond to *GaTe* and *ZnTe* crystallites ($2\theta = 72.28°$) are shown in Fig. 11.41. The average size of the *GaTe* and *ZnTe* crystals from the composite was determined from Scherrer formula (4) and it is respectively about 37 and 68 nm.

11.5.4 Crystal Structure and the Morphology of the Surface and Interfaces Between the Packets of the Composite Prepared by Heat Treatment of InSe Single-Crystal Lamellas in Cd and Zn Vapors

The *InSe–CdSe* and *InSe–ZnSe* composites were prepared by heat treatment in the temperature range from 673 to 853 K of *InSe* plates in *Cd* and *Zn* vapors. The *InSe* single crystals plates doped with 0.01 at.% Sn with the electron concentration at room temperature of 2.3×10^{14} cm^{-3} and a mobility of 500–530 cm^2/V·s were heat treated in *Cd* and *Zn* vapors. The *InSe* single crystal plates were subjected to heat treatment at 753 K for 100 min to 60 h. The pressure of *Cd* vapor at 753 K was ~80 mm *Hg*. After treatment, the outer surface of the *InSe* plates becomes dark–red. The island structure of the surface is clearly seen in reflection.

The formation of the *InSe–CdSe* composite by intercalation in the Van de Waals space of *Cd* atoms from vapour phase takes place in several stages: (1) breaking of *Se–In* bonds and forming of the In_2Se intermediate phase; (2) the formation of molecules and crystals of *CdSe* and the free state *In*; and (3) a long–term heat treatment at $T = 673$ K from 3 to 24 h which contributes to the formation of *CdS*

crystals and, at the same time, dissociation of the In_2Se molecules and enrichment of eutectics with *In* and $In_2Se + In$. Cadmium which has an atomic beam radius (1.49 Å) smaller than that of the indium atoms (1.57 Å) easily replaces them in *InSe* molecules. Thus, as a result of diffusion of *Cd* atoms in the Van der Waals space of the *InSe* crystals, the contracting deformation occurs in the crystal lattice. This process is similar to the formation of indium oxide (In_2O_3). As a consequence the structural defects are generated that serve as nucleation centers of *CdSe* crystallites.

The crystal structure of the composites obtained by the intercalation of *InSe* single crystal plates with *Cd* and *Zn* in the vapor phase was studied by X–ray diffraction with a wavelength of $\lambda_{Cuk\alpha} = 1.54182$ Å. The elemental composition and morphology of the outer surface of the plates and the interfaces between packings were studied by scanning electron microscopy (SEM) and energy-dispersive X–ray spectroscopy (EDX).

The XRD pattern of the composite material obtained by heat treatment at 753 K of *InSe* single crystal plates in *Cd* vapors contains the diffraction lines of atomic planes of the *InSe* and *CdSe* crystallites (Fig. 11.42). The identification of the composition of the crystallites components of the obtained composite and Miller indices (*h k l*) of the planes at which the X–ray diffraction occurs is shown in Table 11.24.

The sizes of the *InSe* and *CdSe* crystallites from the composite were determined using Debye–Scherrer formula from the analysis of the diffraction lines profile of the planes with Miller indices (1 1 1) in *CdSe* (Fig. 11.43a) with $2\theta = 27.31°$ and (8 0 0) in *InSe* with $2\theta = 68.21°$ (Fig. 11.43b).

The dislocation density (δ) which is defined as the number of dislocations lines per unit volume of the crystal was calculated using the relation $\delta = D^{-2}$ [68]. The crystallite sizes and the dislocation density calculated from the XRD lines are 52 nm and 3.7×10^{14} lin/m^2 respectively for *InSe* and 23 nm and 18.3×10^{14} lin/m^2 for *CdSe*.

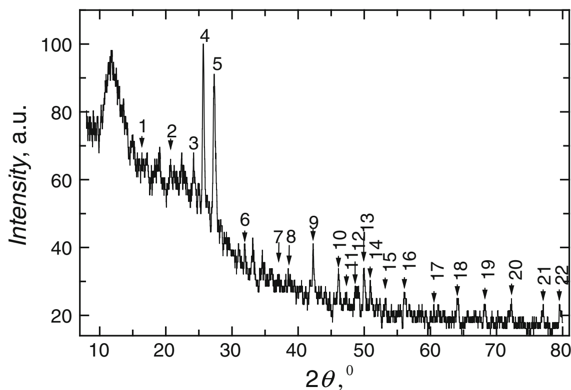

Fig. 11.42 The XRD pattern of composite obtained by *InSe* heat treatment at 753 K in *Cd* vapor

Table 11.24 XRD lines identification for *InSe* heat treated in *Cd* vapor at 753 K

Nr.	Experimental values		ICDD–JCPDS cards				
	2*θ*, °	*I*, a.u.	Compound	PDF	2*θ*, °	*I*, a.u.	*h k l*
1	16.37	67.9	*InSe*	44-1007	16.102	6	0 0 2
2	20.72	66.1	*InSe*	44-1007	20.523	6	0 1 1
3	24.19	67.9	*CdSe*	08-0459	23.901	100	1 0 0
4	25.69	100.0	*CdSe*	19-0191	25.375	100	1 1 1
5	27.31	91.1	*CdSe*	08-0459	27.080	75	1 1 1
6	31.88	41.1	*InSe*	80-2272	31.886	25	–4 0 1
7	36.88	32.1	*InSe*	75-1008	36.867	243	1 0 5
8	38.50	33.9	*InSe*	71-0354	38.496	621	0 1 8
9	42.26	41.1	*CdSe*	77-2307	41.999	712	1 1 0
10	46.10	33.9	*InSe*	34-1431	46.034	28	1 0 7
11	47.30	26.8	*InSe*	71-0354	47.379	211	0 1 11
12	48.61	28.6	*CdSe*	65-3415	48.767	111	2 0 0
13	49.92	33.9	*CdSe*	19-0191	49.740	25	3 1 1
14	50.88	30.4	*InSe*	80-2272	50.842	166	1 1 2
15	53.16	25.0	*InSe*	71-0447	53.292	78	2 0 2
16	56.08	26.8	*InSe*	71-0354	56.071	39	2 0 5
17	60.55	23.2	*InSe*	80-2272	60.441	14	–2 0 3
18	64.08	25.0	*InSe*	71-0354	64.101	47	1 1 12
19	68.21	23.2	*InSe*	80-2272	68.088	54	8 0 0
20	72.26	25.0	*CdSe*	08-0459	72.292	6	2 1 2
21	77.04	23.2	*CdSe*	65-2891	77.181	151	4 2 2
22	79.49	23.2	*CdSe*	08-0459	79.430	18	2 1 3

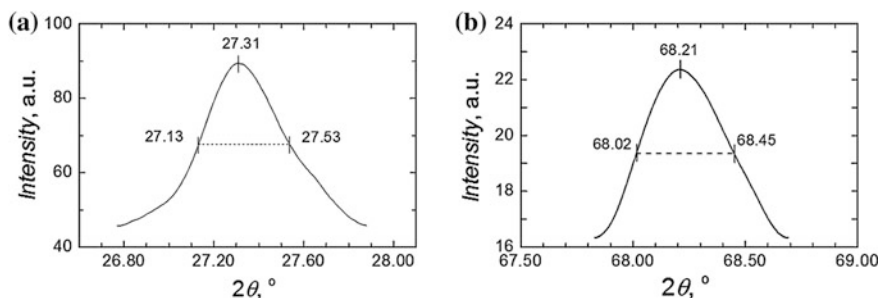

Fig. 11.43 The contour of diffraction line from (1 1 1) planes assembly of *CdSe* compound (**a**) and (8 0 0) planes assembly of *InSe* compound (**b**)

The AFM image of the fragment of the (0 0 0 1) surface of the *InSe* plates kept in a normal atmosphere for 60 days is presented in Fig. 11.44. The degree of granulation of the freshly cleaved surface (arithmetic mean of inhomogenities)

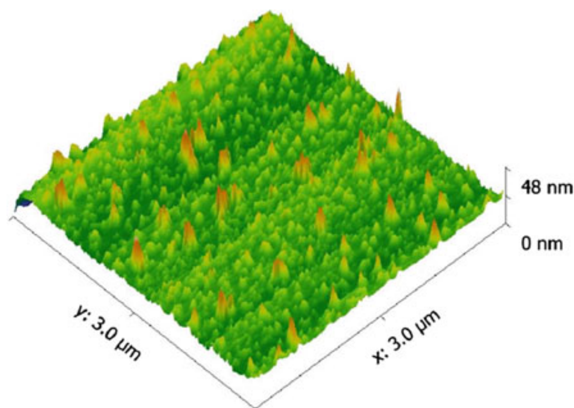

Fig. 11.44 The AFM image of (0 0 0 1) surface of *InSe* kept in normal atmosphere for 60 days

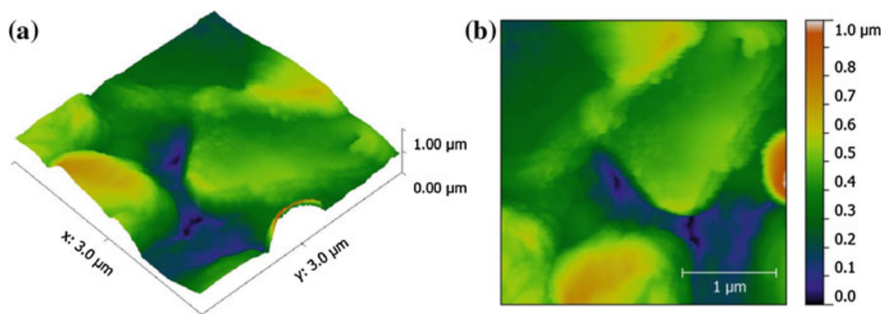

Fig. 11.45 The AFM images of surface (0 0 0 1) of *InSe* plate heat treated at 753 K in *Cd* vapor for 3 h

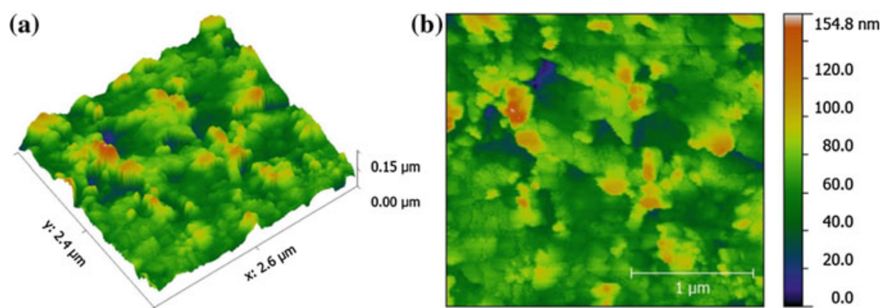

Fig. 11.46 The AFM images of (0 0 0 1) surface of *InSe* plate heat treated at 753 K in *Zn* vapor for 3 h

was $\sim 0.08\ nm^{-2}$ while after 60 days this parameter increased by more than 100 times ($\sim 14\ nm^{-2}$). The freshly cleaved *InSe* lamellas were used for intercalation because of the high degree of formation of nanostructures on the surface.

Figure 11.45 shows the AFM image of the (0 0 0 1) surface of the *InSe* lamella treated at 753 K in *Cd* vapors for 3 h. The AFM image of the (0 0 0 1) surface of the *InSe* lamella subjected to treatment at 753 K in *Zn* vapors for 3 h is presented in Fig. 11.46. The formation of *CdSe* crystallites as well as the *ZnSe* results in the contraction to the micrometer size on the (0 0 0 1) surface of the *InSe* plates. The microsystems formed on the surface of the *InSe* plates that were treated *Cd* and *Zn* vapors are distinguished by shape and size (Figs. 11.45 and 11.46). The *CdSe* microsystems on the surface of plate have sizes of 1–2 μm^2 and heights of $\sim 1.0\ \mu m$ while *ZnSe* have submicrometer dimensions and heights of tenths of micrometers. This morphology is characteristic to deformed surfaces of layered crystals with a hexagonal crystal structure. Similar deformations are obtained after oxidation of single crystal plates of *GaSe* [10] and *InSe* [56], layered VSe_2 crystals after deposition of a *Cu* layer on the surface by thermal evaporation [69] and *GaSe* crystals heat-treated in sulfur vapors [9].

11.6 Conclusions and Generalities

- The *GaS* and *GaSe* semiconductors belong to the class of layered semiconductors and form the single crystals with hexagonal primitive cell. The *InSe* and *GaTe* single crystals have respectively rhombohedral and monoclinic primitive cell. The single crystals are composed of planar packages of B–A–A–B type (A: *Ga*, *In*; B: *S*, *Se*, *Te*) with closed valence bonds at the packages surface. The structural anisotropy determines a strong anisotropy of electrical, photoelectrical and optical properties.
- Uncontrolled impurities and dopants localized at the interface between the packages serves as condensation centers for ions from the environment, of own oxides formation, and, by intercalation, of new chemical compounds. The density of own oxides formation centers on the surface of *GaS*, *GaSe*, *GaTe* and *InSe* single crystals is of the order of $10^{10}\ cm^{-2}$ and smaller.
- The treatment at the temperatures from 703–1173 K *GaSe* single crystals in normal atmosphere initially leads to nanostructuration of outer surface and the complete oxidation of micrometer thick plates. The forming process of the Ga_2O_3 oxide occurs by phase transformation of the type 3: $GaSe \rightarrow Ga_2Se_3 + Ga$; $Ga_2Se_3 + 6O_2 \rightarrow Ga_2O_3 + 3SeO_3$. The defects in the atomic layers of *Se–Ga–Ga–Se* elementary packages serve as centers of own oxide formation.
- The heat treatment at the temperatures of 623–873 K in the normal atmosphere of *GaTe* single crystals leads to the formation of Ga_2O_3 stable oxide and TeO_2 oxide, which easy sublime at these temperatures.

- The composite materials composed of basic material crystallites and crystals of sulphide, selenide and telluride of *Cd* with dimensions from nanometers to micrometers obtained by thermal treatment at 673–903 K of *GaSe*, *GaS*, *GaTe* and *InSe* single crystals in *Cd* was identified by XRD, EDXS and Raman measurements. *GaS–ZnS*, *GaSe–ZnSe*, *GaTe–ZnTe* and *InSe–ZnSe* nano- and microcompozite are obtained by heat treatment of *GaS*, *GaSe*, *GaTe* and *InSe* single crystals in *Zn* vapor at temperatures of 623–873 K, with duration up to 60 h.
- The formation process of *CdSe-GaSe* nanocomposite occurs by intercalation of *Cd* atoms into Van der Waals crack with formation of links between *Cd* atoms and *Se* atoms from neighboring elementary packs. This process is followed by phase transformations of *GaSe* single crystals with the formation of Ga_2Se_3 and $CdGa_2Se_4$ compounds. The formation of *GaTe-CdTe* nanocomposite is accompanied by the breaking of *Ga-Te* bonds and the formation of *Te* clusters enriched with *Cd* and *Ga* condensate.

References

1. F. Hulliger, *Structural Chemistry of Layer-type Phases* (D. Reidel Publishing Company, Dordrecht, 1976), p. 400
2. J.C.J.M. Terhell, Prog. Cryst. Growth Charact. **7**, 55 (1983)
3. D. Olguin, A. Rubio-Ponce, A. Cantarero, Eur. Phys. J. B **86**, 350 (2013)
4. K. Uosaki, M. Koinuma, J. Appl. Phys. **74**, 1675 (1993)
5. O.A. Balitskii, B. Jaeckel, W. Jaegermann, Phys. Lett. A **372**, 3303 (2008)
6. I. Evtodiev, J. Nanoelectronics Optoelectron. **4**, 76 (2009)
7. P.M. Reshmi, A.G. Kunjomana, K.A. Chandrasekharan, M. Meena, C.K. Mahadevan, Int. J. Soft Comput. Eng. **1**, 228 (2011)
8. R.H. Williams, A.J. McEvoy, J. Vac. Sci. Technol. **9**, 867 (1972)
9. A.P. Bakhtinov, Z.R. Kudrynskyi, O.S. Litvin, Phys. Solid State **53**, 2154 (2011)
10. S.I. Drapak, S.V. Gavrylyuk, Z.D. Kovalyuk, O.S. Lytvyn, Semiconductors **42**, 414 (2008)
11. C. Coskun, H. Efeoglu, Semicond. Sci. Technol. **18**, 23 (2003)
12. F. Claeyssens, G.M. Fuge, N.L. Allan, P.W. May, S.R.J. Pearce, M.N.R. Ashfold, Appl. Phys. A **79**, 1237 (2004)
13. J.V. Acrivos, in *On the Intercalation Reaction*, ed by F. Levy. Intercalated layered materials (D. Reidel Publishing Company, Dordrecht–Holland/Boston–U.S.A/London–England, 1979), pp. 33–99
14. A. Herold, in *Crystallo-chemistry of Carbon Intercalation Compounds*, ed by F. Levy. Intercalated layered materials. (D. Reidel Publishing Company, Dordrecht–Holland/Boston–U.S.A/London–England, 1979), pp. 323–421
15. I. Caraman, E. Vatavu, L. Leontie, M. Stamate, D. Untila, Phys. Status Solidi C **12**, 70 (2015)
16. L. Leontie, I. Evtodiev, N. Spalatu, M. Caraman, S. Evtodiev, O. Racovet, M. Girtan, C. Focsa, J. Alloy. Compd. **584**, 542 (2014)
17. D. Untila, V. Cantser, M. Caraman, I. Evtodiev, L. Leontie, L. Dmitroglo, Phys. Status Solidi C **12**, 65 (2015)
18. I. Evtodiev, P. Lozovanu, E. Cuculescu, Moldavian J. Phys. Sci. **6**, 180 (2007)
19. I.D. Koz'mik, V.V. Netyaga, B.P. Bakhmatyuk, I.I. Grigorchak, Z.D. Kovalyuk, Soviet physics. Semiconductors **26**, 1120 (1992)

20. A.P. Bakhtinov, V.N. Vodopyanov, Z.D. Kovalyuk, V.V. Netyaga, DYu. Konoplyanko, Semiconductors **45**, 338 (2011)
21. D. Fargues, G. Tyuliev, G. Brojerdi, M. Eddrief, M. Balkanski, Surf. Sci. **370**, 201 (1997)
22. YuI Zhirko, I.P. Zharkov, Z.D. Kovalyuk, M.M. Pyrlja, Semiconductor physics. Quantum Electron. Optoelectron. **7**, 404 (2004)
23. Z.D. Kovalyuk, V.B. Boledzyuk, V.V. Shevchyk, V.M. Kaminskii, A.D. Shevchenko, Semiconductors **46**, 971 (2012)
24. I.M. Stakhira, N.K. Tovstyuk, V.L. Fomenko, V.M. Tsmots, A.N. Shchupliak, Semiconductors **45**, 1258 (2011)
25. H. Peng, S. Meister, C.K. Chan, X.F. Zhang, Y. Cui, Nano Lett. **7**, 199 (2007)
26. V.P. Mushinsky, M.I. Caraman, *The Optical Properties of Gallium and Indium Chalcogenides* (Shtiintsa, Chisinau, 1972). (in Russian)
27. R.M.A. Lieth, *Preparation and Crystal Growth of Materials with Layered Structures* (D. Reidel Publishing Company, Dordrecht, 1977)
28. A. Seyhan, O. Karabulut, B.G. Akįnoğlu, B. Aslan, R. Turan, Cryst. Res. Technol. **40**, 893 (2005)
29. C.M. Julien, M. Balkanski, Mater. Sci. Eng., B **100**, 263 (2003)
30. M.M. Nassary, Turkish J. Phys. **30**, 95 (2006)
31. T.I. Wieting, M. Schluter (eds.), *Electrons and Phonons in Layered Crystal Structures*, vol. 3 (D. Reidel Publishing Company Dordrecht/Holland; Boston/U.S.A.; London/England, 1979), p. 482
32. J.P. Guesdon, D. Kobbi, C. Julien, M. Balkanski, A. Chery, Phys. Status Solidi (a) **102**, 327 (1987)
33. Z.S. Medvedeva (ed.), *Physico-Chemical Properties of Semiconductor Materials* (Moscow, Nauka, 1979) (in russian)
34. M. Parlak, A.F. Qasrawi, C. Ercelebi, J. Mater. Sci. **38**, 1507 (2003)
35. M.J. Taylor, J. Raman Spectrosc. **1**, 355 (1973)
36. R.M. Hoff, J.C. Irwin, Phys. Rev. B **10**, 3464 (1974)
37. A. Baidullaeva, Z.K. Vlasenko, B.K. Dauletmuratov, L.F. Kuzan, P.E. Mozol', Semiconductors **39**, 381 (2005)
38. R.M. Hoff, J.C. Irwin, R.M.A. Lieth, Can. J. Phys. **53**, 1606 (1975)
39. A.N. Zaidel', N. Kaliteevskii, L. Lipis, M. Cheayka, *Emission Spectral Analysis of Nuclear Materials*. Phys. Mat. Lit., Leningrad/Moscow, 1960 (in Russian)
40. A. Segura, J.P. Guesdon, J.M. Besson, A. Chevy, J. Appl. Phys. **54**, 876 (1983)
41. A. Chevy, J. Appl. Phys. **56**, 978 (1984)
42. S. Shigetomi, H. Ohkubo, T. Ikari, H. Nakashyma, J. Appl. Phys. **66**, 3647 (1989)
43. N. Okamoto, N. Hara, H. Tanaka, IEEE Trans. Electron Dev. **47**, 2284 (2000)
44. M. Ishikawa, T. Nakayama, Phys. Stat. Sol. b **242**, 1179 (2005)
45. I.M. Dharmadasa, A.P. Samantilleke, N.B. Chaure, J. Young, Semicond. Sci. Technol. **17**, 1238 (2002)
46. A. Burger, K. Chattopadhyay, J.O. Ndap, X. Ma, S.H. Morgan, C.I. Rablau, C.H. Su, S. Feth, R.H. Page, K.I. Schaffers, S.A. Payne, J. Cryst. Growth **225**, 249 (2001)
47. J.E. Fischer, in *Electronic Properties of Graphite Intercalation Compounds*, ed. by F. Levy. Intercalated Layered Materials (D. Reidel Publishing company, Dodrecht, Holland/Boston, USA/London, England, 1979), pp. 481–533
48. W.B. Clark, P.M. Williams, Phil. Mag. **35**, 883 (1977)
49. Z.R. Kudrynskyi, Z.D. Kovalyuk, Tech. Phys. **58**, 1840 (2013)
50. S. Kasap, P. Capper (ed.), *Springer Handbook of Electronic and Photonic Materials* (Springer Science + Busines Media Inc., New York, 2006)
51. M. Jouanne, C. Julien, M. Balkanski, Phys. Stat. Sol. (b) **144**, K147 (1987)
52. F.O. Ivashchishin, I.I. Grygorchak, Phys. Solid State **52**, 2026 (2010)
53. M. Cardona, G. Harbeke, Phys. Rev. **137**, A1467 (1965)
54. B. Cheng, E.T. Samulski, J. Mater. Chem. **11**, 2901 (2001)
55. O.A. Balitskii, Mater. Lett. **60**, 594 (2006)

56. A.P. Bakhtinov, Z.D. Kovalyuk, O.N. Sydor, V.N. Katerinchuk, O.S. Lytvyn, Phys. Solid State **49**, 1572 (2007)
57. I. Grygorchak, S. Voitovych, I. Stasyuk, O. Velychko, O. Menchyshyn, Condens. Matter Phys. **10**, 51 (2007)
58. Zs. Rak, S.D. Mahanti, Krishna C. Mandal, N.C. Fernelius. *Phys. Rev. B* **82**, 155203 (2010)
59. I.T. Goronovskii, YuP Nazarenko, E.F. Nekryach, *A Short Handbook to Chemistry* (Naukova Dumka, Kiev, 1964). (in Russian)
60. N.E. Lushchyk (ed.), *Proceedings of the IFA* (USSR Academy of Sciences, Moscow, 1958) (in Russian)
61. S. Benazeth, N.-H. Dung, M. Guittard, P. Laruelle, Acta Crystallogr C **44**, 234 (1988)
62. I. Evtodiev, Moldavian J. Phys. Sci. **1**, 52 (2002)
63. S.T. Tan, B.J. Chen, X.W. Sun, W.J. Fan, H.S. Kwok, X.H. Zhang, S.J. Chua, J. Appl. Phys. **98**, 013505 (2005)
64. B.D. Cullity, *Elements of X-ray Diffraction* (Addison-Wesley Publishing Company INC, Reading, Massachusetts–Menlo Park, California, London–Amsterdam–Don Mills, Ontario–Sydney, 1972), p. 555
65. S. Gopal, C. Viswanathan, B. Karunagaran, S.K. Narayandass, D. Mangalaraj, J. Yi. Cryst. Res. Technol. **40**, 557 (2005)
66. A.S. Abbasov, A.V. Nikolaev, Y.I. Gerasimov, Reports the Academy of Sciences of the USSR **156**, 1140 (1964). (in Russian)
67. Glushko P. (ed.), *Thermal Constants of Substances*. vol. 6 (Viniti, Moscow, 1972) (in Russian)
68. G.K. Williamson, R.E. Smallman, III. Phil. Mag. **1**, 34 (1956)
69. R. Adelung, F. Ernst, A. Scott, M. Tabib-Azar, L. Kipp, M. Skibowski, S. Hollensteiner, E. Spiecker, W. Jäger, S. Gunst, A. Klein, W. Jägermann, V. Zaporojtchenko, F. Faupel, Adv. Mater. **14**, 1056 (2002)

Chapter 12
Optical and Photoelectric Properties of *GaS*, *GaSe*, *GaTe* and *InSe* Semiconductors and Nanocomposites Obtained by Heat Treatment in *Cd* and *Zn* Vapor

Igor Evtodiev, Iuliana Caraman, Valeriu Kantser, Dumitru Untila, Irina Rotaru, Liliana Dmitroglo, Silvia Evtodiev and Mihail Caraman

Abstract *GaS* is an n-type semiconductor with indirect bandgap at 293 K equal to 2.5 eV. The average energy of phonons active in the formation of the edge of indirect absorption band is equal to 44.5 meV. The energy of transverse optical phonon of 23.9 meV was determined from the absorption spectra in the vibrations region of monophononic and crystal lattice. The phonons with average energy equal to 17 meV participate in the formation of the edge of indirect bandgap of *GaSe* crystals in absorption spectra. Direct bandgap width at 293 K is equal to 2.020 eV and 1.320 eV in *GaSe* and *InSe,* respectively. *GaTe* is a p-type semiconductor with direct bandgap width at 293 K equal to 1.6 eV. The edge of direct absorption in *GaSe*, *GaTe* and *InSe* lamellar crystals is formed by excitons with binding energy of 22 meV, 17 meV and 16 meV, respectively. Heterojonctions consisting of *Cd* and *Zn* chalcogenides and lamellar $A^{III}B^{VI}$ semiconductors that are photosensitive in UV-VIS and NIR regions of spectrum were obtained by heat treatment of *GaS*, *GaSe*, *GaTe* and *InSe* single crystals in *Cd* and *Zn* vapor.

I. Evtodiev · V. Kantser · D. Untila · I. Rotaru · L. Dmitroglo · S. Evtodiev · M. Caraman
Laboratory of Photonics and Physical Metrology,
Department of Physics and Engineering, Moldova State University,
Chisinau, Moldova

I. Caraman
"Vasile Alecsandri" University of Bacau, Bacau, Romania

I. Evtodiev (✉) · V. Kantser · D. Untila
Institute of Electronic Engineering and Nanotechnologies "D. Ghitu",
Academy of Sciences of Moldova, Chisinau, Moldova
e-mail: ievtodiev@yahoo.com

S. Evtodiev
University of European Political and Economical Studies "Constantin Stere",
Stefan cel Mare si Sfint bd 200, MD-2004 Chisinau, Moldova

© Springer International Publishing Switzerland 2016

I. Tiginyanu et al. (eds.), *Nanostructures and Thin Films for Multifunctional Applications*, NanoScience and Technology,
DOI 10.1007/978-3-319-30198-3_12

12.1 Introduction

The *GaS*, *GaSe*, *GaTe* and *InSe* layered semiconductors have a high potential for applications in various optoelectronic and electronic devices such as: receptors for X-rays, γ radiation, energetic particles; optical bistable elements; photovoltaic cells; generators in the THz range and elements of quantum electronics [1–10].

This wide range of technical applications is determined by a number of properties that are characteristic for $A^{III}B^{VI}$ lamellar semiconductors like anisotropy of structural, optical, electrical and photoelectrical properties, specific self-purification from impurities and binding forces between the atoms, wide bandgap width from blue (*GaS*) to NIR (*InSe*) region of spectrum and low density of surface states [11–14].

The physical properties and applicative possibilities are multiply if they are dopped and intercalated with atoms and molecules [15]. The *GaSe* single crystals intercalated with hydrogen and ions of metals from group I are effective solid electrolyte and hydrogen accumulators [16, 17]. The interlation of *GaSe* single crystals with *Co* by electrochemical method transforms them in materials with well-pronounced ferromagnetic properties [18]. The planar nanolamellar structures with properties characteristic to ferroelectrics were obtained by intercalation of *InSe* and *GaSe* single crystals in Van der Waals crack with $NaNO_2$ and KNO_2 macromolecules that have segnetoelectrical properties [19].

Nanocomposites made of lamellar $A^{III}B^{VI}$ semiconductor crystallites (*GaS*, *GaSe*, *GaTe* and *InSe*) and *Cd/Zn* calcogenides were obtained by heat treatment of $A^{III}B^{VI}$ single crystals in *Zn* and *Cd* vapor. The size of the obtained composites varies from units to tens of nanometers. The composite materials keep structural, optical and luminescent characteristics of component materials.

The optical and photoluminescent properties of $A^{III}B^{VI}$ crystals used as basic materials for the composites and nanocomposites will be analyzed.

12.2 Optical and Photoluminescence Properties of Oxide—$A^{III}B^{VI}$ Structures

The crystalline structure of *GaS*, *GaSe*, *InSe* and *GaTe* lamellar semiconductors allows the obtaining by cleavage of plan parallels blades with thickness and areas sufficient for reflection and transmission measurements not only in the region of the edge of intrinsic absorption band, but also in its depth. The absorption and reflectance spectra in the deep of fundamental band contain information regarding the structure of electronic band in high symmetry points of Brillouin zone. Since the valence bonds at the surface of layered packages in *Ga* and In monocalcogenides are mostly closed (the density of surface states being less than 10^{10} cm^{-2}), the surface layer that disturb specific measurements in layered semiconductors ($A^{II}B^{VI}$, A^{IV}, $A^{III}B^{V}$ etc.) is practically missing in plates prepared for optical measurements [20].

The high precision measurements can be performed (2–3 % relative error) at the absorption coefficients of $\sim 10^5$–10^6 cm^{-1} for samples with submicron thicknesses.

The absorption coefficient at light propagation along C_6 axis on direction ($\alpha_\perp$) of *GaSe*, *GaS*, and *InSe* single crystals and C_2 axis of *GaTe* samples was determined from transmittance ($t_\perp$) and reflectance (R) measurements without taking into account the interferential effects given in the next expression [21]:

$$t_\perp = \frac{(1 - R_\perp)^2 exp(-\alpha_\perp d)}{1 - R_\perp^2 exp(-2\alpha_\perp d)} \qquad , R_\perp = \left(\frac{n_\perp - 1}{n_\perp + 1}\right)^2 \tag{12.1}$$

The absorption coefficient in $E \| \mathbf{C}$ ($\alpha_\|$) polarization was determined from transmittance at oblique incidence (the angle of φ to the normal of (0 0 1) plane) using equation:

$$\alpha_\| = \frac{n_\|}{n_\perp}\left[\alpha_\perp + (\alpha^* - \alpha_\perp)\frac{n_\|^2}{sin^2 2\varphi}\right], \tag{12.2}$$

where α^* is determined from transmittance at light polarization parallel to C_6 (C_2):

$$T_\| = \frac{\left(1 - R_\|\right)^2 exp(-\alpha^* d^*)}{1 - R_\|^2 exp(-2\alpha^* d^*)}, \tag{12.3}$$

here

$$R_\| = \frac{a - n_\perp cos\varphi}{a + n_\perp cos\varphi}, \tag{12.4}$$

$$d^* = \frac{d}{a}, \tag{12.5}$$

$$a = \left(1 - \frac{sin^2\varphi}{n^2}\right)^{1/2}. \tag{12.6}$$

The equation's application field is determined by the inequalities $\alpha_\| < \frac{1}{\pi}\frac{n_\|}{\lambda}$ and $\alpha_\perp < 4\pi\frac{n_\perp}{\lambda}$.

The $n_\perp$ and $n_\|$ refractive indices in the light absorption region ($\alpha d \le 7$, $t \ge 10^{-3}$) were determined from the interferential structure of transmission spectra. The $n_\perp$ refractive index was determined from the interferential structure of transmission/reflection spectra at normal incidence and $n_\|$ was determined at oblique incidence using formula [22]:

$$m\lambda = n_{\perp} d\left[\left(1 - \frac{\sin^2 \varphi}{n_{\perp}^2}\right)^{1/2} - \left(1 - \frac{\sin^2 \varphi}{n_{II}^2}\right)\right] \tag{12.7}$$

where m is the order of interference maximum/minimum, φ is the light incidence angle on the blade surface.

The absorption coefficient of incident light which is normal to the surface in oxide-semiconductor nano lamellar structures with optically transparent oxide film was determined from the equation:

$$\alpha = \frac{1}{d}\ln\left[\frac{-(1-R)(1-R_0) + \sqrt{(1-R)^2(1-R_0)^2 + 4R_0t^2}}{2R_0t}\right] \tag{12.8}$$

where d is the semiconductor blade's thickness, t—the optical transmittance, R—the surface reflectivity, and

$$R_0 = \left(\frac{n_0 - 1}{n_0 + 1}\right)^2 \tag{12.9}$$

where n_o is the refractive index of the oxide film that was measured independently.

The refractive index n_o of the oxide layer on semiconductor support was determined from the interference picture of the fascicles reflected from the outer surface and from the oxide–semiconductor interface.

12.3 Dispersion of the n$_{\perp}$ and n$_{||}$ Refractive Indices

(a) *GaSe*

The $n_{\perp}$ (at normal incidence) and $n_{||}$ (incidence under angle φ = 45°) refractive indices were determined from the interferential structure of transmission spectra of plan-parallel plates (with thicknesses in the range of 0.6–120 μm).

The dependence of the $n_{||}$ and $n_{\perp}$ refractive indices function of wavelength in the range from 0.36 μm to 22 μm for undoped *GaSe* and doped *GaSe* samples with the concentration of respectively 0.1 at% and 0.5 at% of *Cu* and *Cd* are presented in Fig. 12.1. The $n_{\perp}(\lambda)$ and $n_{||}(\lambda)$ dependencies presented in works [22–24] are shown for comparison.

The $n_{\perp}(\lambda)$ and $n_{||}(\lambda)$ spectral dependencies obey to normal dispersion in the region of $\lambda > 600$ nm as it is shown in Fig. 12.1. The $n_{\perp}$ index is increasing with the wavelength decrease in the fundamental absorption band while $n_{||}$ in the deep of intrinsic absorption band tends to decrease with wavelength.

The *GaSe* compounds doped with low concentrations (c ≤ 1.0 %) of *Cd* and *Cu* does not change the dispersion law for $n_{\perp}$ and $n_{||}$ (Fig. 12.1). The moderate

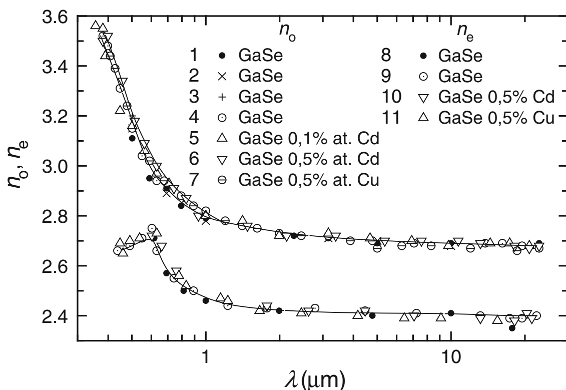

Fig. 12.1 The dispersion of refractive indexes $n_{\perp}$ and $n_{\|}$ for *GaSe* crystals (1 [24], 2 [23], 3 [22], 8 [24], 9) and *GaSe* doped with *Cd* in concentrations of: 0.1 at% (5); 0.5 at% (6, 10) and doped with *Cu*: 0.5 at% (7, 11)

increase in the values of $n_{\perp}$ and $n_{\|}$ in the region of the edge of absorption band can be caused by the interaction mechanisms of excitons with impurity atoms.

(b) *GaS*

The transmission spectra of *GaS* lamella with the thicknesses $d \leq 70$ µm consists of interferential bands neatly arranged till the wavelength of $\lambda \approx 20$ µm. The interferential bands overlap with phonon absorption and impurity bands occurs at the wavelength $\lambda > 20$ µm.

In Fig. 12.2 is presented the spectral dependence $n_{\perp}(\lambda)$ of undoped *GaS* lamella (curve 1) and doped with *Cd* (curve 2) and *Cu* (curve 3) in small amounts (c = 0.1 % at.). The measurements of refractive index of dispersion $n_o(\lambda)$from the work of McMath and Irwin [23] are presented for comparison.

The $n(\lambda_o)$ characteristic in the wavelength range from 330 nm to 20 µm for both undoped and doped *GaS* blades is well described by a polynomial:

$$n(\lambda) = A + \frac{B}{\lambda^2} + \frac{C}{\lambda^4} + \frac{D}{\lambda^6} \tag{12.10}$$

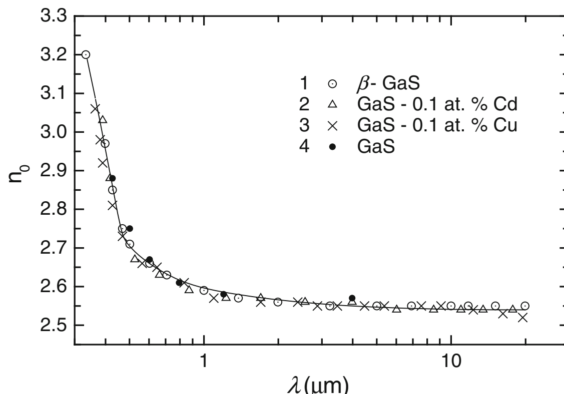

Fig. 12.2 The dispersion of refractive indexes $n_{\perp}$ for undoped *GaS* crystals *1* and *GaS* doped with 0.1 at% *Cd* *2*, 0.1 at% de *Cu* *3* and *4* from work [23]

where $A = 2.548$; $B = 0.0279$; $C = 3.321 \times 10^{-3}$ and $D = 4.213 \times 10^{-4}$ for λ in μm. A small deviation from the function (12.8) at $\lambda < 0.390$ μm may be caused by the influence of optical transitions near the M point of Brillouin zone [25].

12.4 Light Absorption in Undoped *GaSe*, *GaS*, *GaTe* and *InSe* Single Crystals, Doped and Intercalated with *Cd* and *Zn*

12.4.1 Absorption at the Edge and Depth of Fundamental Band ($h\nu \geq E_g$)

(a) *GaSe*

The absorption spectra α ($h\nu$) of *GaSe* crystals at 293 and 78 K are shown in Fig. 12.3. A narrow band of excitonic absorption at 293 K (curve 1) with the peak at 2.00 eV is highlighted at the edge of fundamental absorption band. The absorption coefficient in the maximum of this band is ~ 1700 cm^{-1}. The absorption coefficient in the center of the band increases to ~ 2900 cm^{-1} and the exciton band width at half of the maximum decreases when the sample's temperature decrease to 78 K (curve 2) and it is in accordance with the following formula [26]:

$$G(T) = G(0) + \frac{W}{e^{h\nu_f/kT} - 1} \tag{12.11}$$

where $G(T)$ and $G(0)$ is the FWHM of the exciton band n = 1, at the temperature T and 0 K, W is a calibration constant, $h\nu_f$—phonon energy equal to 20 meV, k—Boltzmann constant.

At the same time the band shifts to higher energy. The temperature dependence of energy of the exciton maximum is well described by the polynom [27]:

$$E_{exc}(T) = E_{exc}(0) - \frac{\alpha T^2}{T + \beta} \tag{12.12}$$

where $E_{ex}(0) = 2.134$ eV, $\alpha = 2.33 \times 10^{-4}$ eV/K and $\beta = -38.5$ K.

The exciton line in state n = 1 ($E_{n=1} = 2.098$ eV) and the n = 2 band with the maximum at the energy of $E_{n=2} = 2.115$ eV at the temperature of 78 K is clearly higlited. We admit that the excitons in *GaSe* satisfy the large radius exciton model (Wannier–Mott excitons) for which the energy of absorption lines is given by the formula:

$$E_n = E_{go} - \frac{R_{ex}}{n^2} = E_{go} - \frac{\mu e^4}{2\varepsilon_0^2 \hbar^2 n^2 \varepsilon^2}, \quad \text{n = 1, 2, 3} \tag{12.13}$$

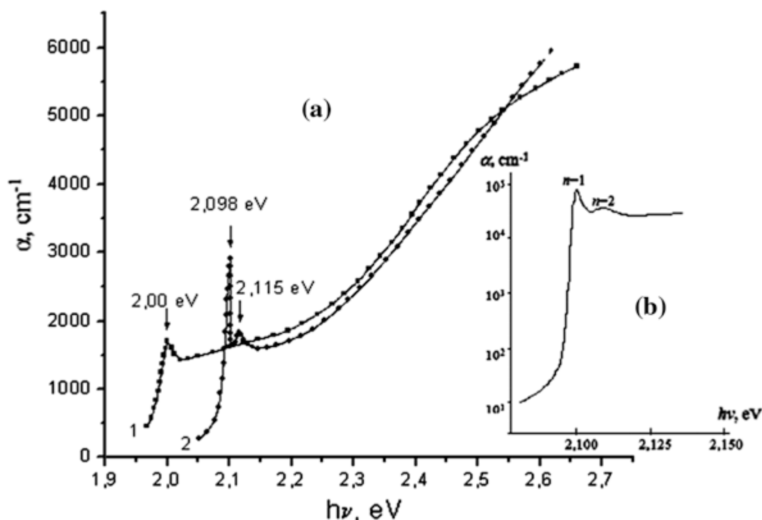

Fig. 12.3 The absorption spectra $\alpha(h\nu)$ in $\vec{E}_{\perp}\vec{C}$ polarization (*a*) at 293 K (*curve 1*) and 78 K (*curve 2*), and $\vec{E} \parallel \vec{C}$ polarization (*b*) at 78 K of *GaSe* crystals

where E_n is the energy of the excitons in the state n = 1, 2, 3, μ is the effective mass of the electron–hole pair (exciton), ε_0 is the static dielectric constant, E_{go}—bandgap width at given temperature, n–quantum number of the absorption band, R_{ex}—the binding energy of the electron–hole pair (exciton). The bandgap width and exciton binding energy at 78 K were determined knowing the energies of n = 1 and n = 2 exciton bands and are equal respectively to 2.121 eV and 22.6 meV.

The absorption spectrum of $\vec{E} \parallel \vec{C}$ polarization is shown in Fig. 12.3b. As can be seen from the comparision of spectra shown in Fig. 12.3, a, curve (2) and b, the optical absorption anisotropy manifests more pronounced in the region of direct transitions and direct exciton at the energy of $h\nu$ = 2.15 eV. The relatin of absorption coefficients in $E \parallel C$ ($\alpha_{\parallel}$) polarization and $E \perp C$ ($\alpha_{\perp}$) polarization is $\alpha_{\text{II}}/\alpha_{\perp} = 10$. This parameter is 17 for the maximum of exciton band in n = 1. This value is in a good agreement with the anisotropy coefficient of effective mass which is equal to $m^*_{\parallel}/m^*_{\perp} = 16$ [28].

(b) *GaSe intercalated with Cd*

The width of direct bandgap at T = 293 K in the center of Brillouin zone is equal to E_{gd} = 2.020 eV. The absolute minimum of the conduction band is in the M point of Brillouin zone and is shifted by 25 meV from the absolute minimum of the conduction band in the center of Brillouin zone [29]. Since the energy of direct exciton (Brillouin zone center) coincides with the absolute minimum of the conduction band in M point, a number of uncertainties appear regarding the character of optical transitions at the edge of absorption band in *ε–GaSe* semiconductor. Among them are the problems linked to the calculas of the structure of electronic bands that use

the states density model carried out in recent years. The minimum of conduction band in the center of Brillouin zone according to these calculas is at 0.89 eV from the valence band [30] and the width of the indirect band gaps in M, H and K points of Brillouin zone are equal to $E_M = 1.22$ eV, $E_H = 1.54$ eV and $E_K = 1.66$ eV [30]. A value much lower than the width of experimental bandgap was obtained in work of Zhang [31], from which results that the width of direct bandgap in the center of Brillouin zone is equal to 0.816 eV. These results are confirmed with small corrections in a few works [31–33]. The quite large difference in the appreciation of bandgap width and nature of electronic transitions according to theoretical calculation of 0.816 eV and experimental measurement (excitonic absorption and photoluminescence) [34] may be due to the fact that in theoretical calculations is not taken into account the contribution of the local density of states [35] and the experimental measurements are influenced by uncontrollable errors [36]. The values for direct and indirect width of bandgap obtained in the last years for ε–*GaSe* are presented in Table 12.1. Although at the high concentration of own defects ($\sim 10^{14}\text{cm}^{-3}$ [37]) the *GaSe* single crystals are materials with low optical absorption in the energy region lowest than the width of indirect bandgap.

As shown in Fig. 12.3 at energies $hv < 1.93$ eV, the absorption coefficient is less than 10 cm^{-1} (in $\vec{E} \parallel \vec{C}$ polarization, at $T = 78$ K) and reach the subunitar values (cm^{-1}) at $hv < 1.8$ eV. Thus, at the energy of $hv < E_{ex1}$ (n = 1) the absorption coefficient is reduced by more than three orders of magnitude from $\sim 10^4$ cm^{-1} to the units of cm^{-1}.

To measure the absorption coefficients in the region of indirect optical transitions were prepared plan-parallel samples with thicknesses satisfying minimum error condition $0.8 \leq \alpha d \leq 2.0$ with a sufficient surface area ($S \leq 25$ mm^2) for the measurements of transmittance $t(hv)$ and reflectivity R (hv). The absorption coefficient α was calculated at three temperatures 77, 293 and 380 K in the region of 1.80–2.05 eV. The spectral dependence of absorption coefficient at the energies below the n = 1 excitons band in lamellar $A^{III}B^{VI}$ type semiconductors is well described with an exponential function [42].

The $\alpha(hv)$ dependence differs from the exponential function at the absorption coefficient of $\alpha \leq 50$ cm^{-1} as it is shown in Fig. 12.4. This indicates about the

Table 12.1 Values of direct and indirect band gap width of ε–*GaSe*

Nr.	E_g direct, eV		E_g indirect, eV		References
	Experimental	Theoretical	Experimental	Theoretical	
1	2.1	1.34	–		[32]
2	–	1.20	–		[38]
3	1.0		–		[39]
4	0.89		–		[30]
5	2.12 (T = 77 K), 2.0 (300 K)		2.10 (T = 77 K), 1.985 (300 K)		[40]
6	1.966		–		[41]

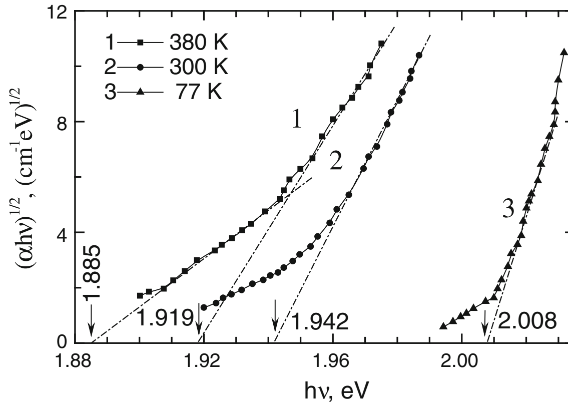

Fig. 12.4 The dependence $(\alpha h\nu)^{1/2} = f(h\nu)$ at 380 K (*curve 1*), 293 K (*curve 2*), 77 K (*curve 3*) for *GaSe* compound

inclusion of a new absorption mechanism. The absorption coefficient at direct optical transitions depends on energy by a function of the next type [43]:

$$\alpha(h\nu) \sim \left(h\nu - E_g^d\right)^{1/2} \tag{12.14}$$

The indirect optical transitions occur with absorption and emission of phonons with energy E_f. The spectral dependence α(hν) of absorption coefficient satisfies the relation [44]:

$$\alpha(h\nu) = C\left\{\frac{\left(h\nu - E_g^i - E_f\right)^2}{exp\left(E_f/kT\right)^{-1}} - \frac{\left(h\nu - E_g^i + E_f\right)^2}{1 - exp\left(-E_f/kT\right)}\right\}, \tag{12.15}$$

where C is a proportionality coefficient, E_g^i is the width of indirect bandgap, E_f—phonon energy, k—Boltzmann constant and T—absolute temperature.

At low temperatures the probability of indirect electronic transitions with phonon absorption is low and the spectral dependence of absorption coefficient can be written:

$$\alpha(h\nu) \sim \left(h\nu - E_g^i - E_f\right)^2 \tag{12.16}$$

The spectral dependence α(hν) for temperatures $T > 290$ K as shown in Fig. 12.4a (curves 1 and 2), satisfies the relation (15). The width of indirect bandgap of 1.902 eV and the average phonon energy at 380 K of 17 meV were determined by extrapolating the linear segments to α(hν) = 0. The phonons with energy of

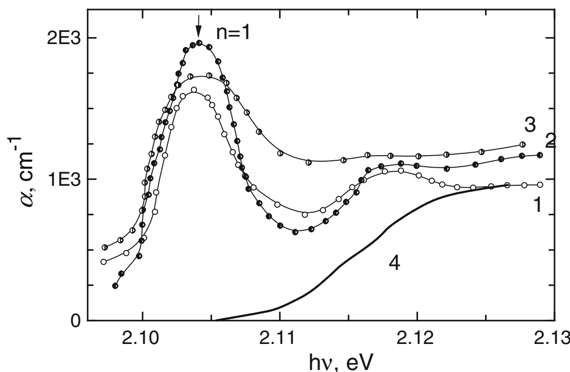

Fig. 12.5 The excitonic absorption in *GaSe* (*curve 1*) and *GaSe* plates heat treated at 853 K in *Cd* vapor for 10 min (*curve 2*), 20 min (*curve 3*) and 60 min (*curve 4*)

17 meV (134 cm^{-1}) are active in the Raman spectra [45], IR absorption spectra [46] and in the formation of excitonic photoluminescence bands [47].

Among the specific properties of layered crystals of $A^{III}B^{VI}$ semiconductors, especially the *GaSe* are the accumulation of impurities at the interface of *Se–Ga–Ga–Se* elementary packages. The *Cd* surplus accumulates in the space between the packages of *GaSe* crystals doped or intercalated with *Cd*. The *Cd* atoms can form at high temperatures ($T > 673$ K) the chemical bonds with the Se atoms from atomic layers of neighboring elementary packages. The presence of atomic *Cd* layer and *CdSe* compound formed by chemical bonds between the intercalated *Cd* and the selenium from the two planes directly influences the exciton bonds and leads to the widening of exciton band contours and shielding.

As shown in Fig. 12.5, when the duration of intercalation increase, the asymmetry of n = 1 exciton band increases more pronounced in the high energy region. At the same time the structural defects generated by layers from mixture of *Cd* and *CdSe* crystallites localized in the Van der Waals spectrum of the *GaSe* crystals influences the first excited state (n = 2) of exciton.

The crystal lattice defects caused by the intercalation of *GaSe* crystal through heat treatment at temperatures of 693–703 K for 20 min in *Cd* vapor attenuates to the background absorption of ionized exciton band (n = 2) at 80 K. The presence of this inhomogeneity requires exciton band contour analysis n = 1 as the sum of several contours normally distributed under the central line. The result of overlapping bands described by Lorentz and Gauss elementary functions for direct excitons is well known as Voigt contour:

$$\alpha(E) = \left(\frac{4ln2}{\pi G}\right)^{1/2} \int_{-\infty}^{\infty} exp\left[(-4ln2)^2\left(\frac{E_v - E_c}{G}\right)^2\right] \alpha_H \cdot g_H(E, E_v) dE_v \qquad (12.17)$$

where $g_H(E, E_v) = \frac{G_H}{4(E-E_v)^2 + G_H^2}$, G—inhomogeneous width of excitonic band, G_H—homogeneous width of excitonic band, α_H—absorption coefficient, E_c—the energy of exciton line center.

It is necessary to select the component functions for a quantitative calculation of the absorption spectrum at the edge of fundamental band region. One of the approximations of absorbance dispersion in the region of the edge of absorption band at medium and high temperatures corresponds to Urbach rule for many materials [48, 49]:

$$\alpha(h\nu) = A_0 exp[-\sigma(h\nu - E_0)/kT]. \tag{12.18}$$

where A_0, σ and E_0 are the energy parameters that are characteristic for material.

The excitonic continuum α(hν) which represents the spectral dependence of absorption coefficient at energy $E_{n=2} < h\nu \le E_g$ is decribed with formula [50]:

$$\alpha(h\nu) = 2\pi G_{ex}\frac{1}{\left[(1 - \frac{\exp(-2\pi G_{ex})}{(h\nu - E_g)}^{1/2}\right]}\cdot\frac{1}{1 - exp(-2\pi\frac{G_{ex}}{(h\nu - E_g)})}. \tag{12.19}$$

The absorption spectrum in the region of the edge of fundamental band from (12.16) and (12.17) can be described by the equation:

$$\alpha(h\nu) = \sum A_i g_i[(h\nu - E_i)/G_i] + A_0\frac{1}{1 + exp\left[\frac{E_0 - h\nu}{G_g(T)}\right]}\cdot\frac{1}{1 - exp\left[-2\pi\sqrt{\frac{G_{ex}}{h\nu - E_g}}\right]}, \tag{12.20}$$

where A and g are characteristics (amplitude and the function that describe the spectrum of discrete lines), E_i and G_i—spectral position of exciton band and width at half of the maximum of the excitonic line, A_0 and G_0—the absorption coefficient in the region of excitonic continuum and its width, G_{ex} is the characteristic energy obtained by Urbach edge extrapolation to $\alpha = 0$.

The absorption spectrum at 78 K of the *GaSe* blade with the thickness of 10.2 μm is shown in Fig. 12.5 (curve 1). The curve 4 is the absorption spectrum at the edge of fundamental band that is calculated using the second term from formula (12.20) and represents the differentiation of discrete absorption spectrum (exciton bands n = 1 and n = 2).

When the duration of heat treatment increase from 20 min (curve 2) to 60 min (curve 3), the n = 2 exciton line is missing and the line n = 1 is highly attenuated in the absorption spectrum as can be observed from Fig. 12.5.

The absorption spectrum of this sample contains only a weak pronounced background at the energy of 2.104 eV. The *Cd* atoms that are intercalated between elementary *Se–Ga–Ga–Se* packages toghether with the formation of *CdSe* bond shield the exciton bonds. The experimental absorption spectrum of the *GaSe* blade with the thickness of ~ 15 μm that was heat treated at 713 K for 60 min in *Cd* vapor (curve 1) is shown in Fig. 12.6.

The spectrum of excitonic continuum calculated from the second term of formula (12.20) it is shown in Fig. 12.6, curve 2. The contour of excitonic band from

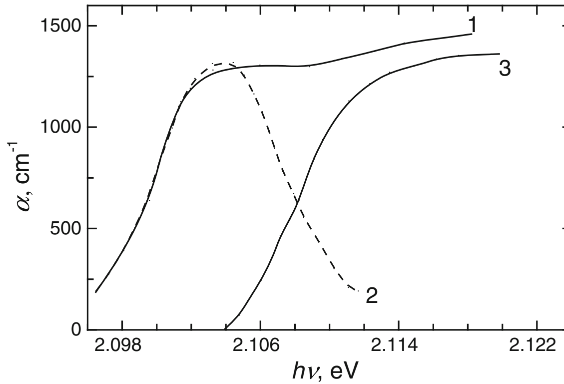

Fig. 12.6 The experimental absorption spectrum of the *GaSe* blade with the thickness of ~15 μm that was heat treated at 713 K for 60 min in *Cd* vapor for excited state n = 1 (*curve 1*); Discrete spectrum of exciton in n = 1 state obtained by subtraction from experimental spectrum (*curve 2*) and the approximation of excitonic continuum (*curve 3*)

experimental absorption spectrum is also presented (Fig. 12.6, curve 3). The value obtained from relation $G_d = \left(\frac{k}{\sigma}\right)T$ was used for excitonic continuum broadening G_d, where the parameter σ for *GaSe* was taken as the slope of lgα = f (hν) characteristic. Because the exponential dependence of the absorption band edge in semi-logarithmic coordinates should not depend on temperature within a wide range, in paper of Gnatenco and Kurik [51] was introduced the correction of type:

$$\sigma = \sigma_0 \frac{2kT}{\hbar\omega_f} th \cdot \frac{\hbar\omega_f}{2kT}. \tag{12.21}$$

where $\hbar\omega_f$ is the transverse optical phonon energy that is equal to 27 meV; *k*–Boltzmann constant, $T = 78$ K.

The parameter that determines the characteristic slope for the edge of absorption band in the sample is shown in Fig. 12.6 and it is equal to 2.1. A satisfactory approximation for Urbach energy (E_0) from formula (12.18) was obtained for $E_0 \approx E_g - \frac{G_{ex}}{4}$ and it is equal to 2.119 eV. It is known from Mahr [52] that the parameter σ_0 and the exciton–phonon interaction constant *g* are linked by relation $G_0 = 2/3g^{-1}$ where the value of exciton–phonon interaction is equal to 0.31 and it is indicate the weak character of exciton–phonon interaction in *GaSe* lamella intercalated with *Cd*. So, the *Cd* atoms intercalated between the layered packages toghether with the electron–hole bonds influences the interaction mechanism of excitons with lattice vibrations. The second term in formula (12.20) represents the continuum of the excitonic spectrum at energies $E \leq E_g$.

The edge of excitonic absorption band is well described by empirical formula for excitonic band complex contours it is shown in Fig. 12.6 (curve 3). As shown in Fig. 12.5, the spectrum α(hν) for both nonintercalated *GaSe* blade of ~10.2 μm

thickness and heat treated in *Cd* vapor at 853 K temperature for 10 min, contains both the line for n = 1 and the line which represents the direct exciton first excited state. Exciton energy levels of three–dimensional excitons with large radius (Wannier–Mott excitons) describe by formula (12.13).

The energy of exciton binding R_{ex} = 20 meV was determined from the values energy of excitonic absorption lines $E_{n=1}$ = 2.104 eV and $E_{n=2}$ = 2119 eV. The reduced mass μ_{ex} of electron–hole pair is determined from the formula:

$$\mu = \frac{2\text{h}^2(4\pi\varepsilon\varepsilon_0)^2}{e^4} R_{ex}. \tag{12.22}$$

The dielectric permittivity of *GaSe* semiconductor is equal to 7.95. Thus, the reduced mass is μ_{ex} = 8.3 × 10^{-2} m_0. The average radius a_{ex} of the exciton calculated from equality $a_{ex} = \varepsilon_r \frac{m_0}{\mu} a_H$ is equal to 50.4 Å. The radius of n = 1 exciton in the *GaSe* plates intercalated with *Cd* at 853 K for 10 min is equal to 53.3 Å. Comparing the basic parameters of excitons in *GaSe* crystals before and after short time *Cd* intercalation, it appears that as a result of intercalation decreases both the Rydberg constant and direct exciton Bohr radius.

The exciton radius from formula (12.13) is directly proportional to the relative dielectric permittivity ε_r. The increase of average radius of the exciton n = 1 in *GaSe* intercalated with *Cd* prove that dielectric permittivity of the layered composite is less than that of *GaSe* crystal at the energy of 2.104 eV. The dielectric permittivity of *CdSe* compound is ~8.7 whereas dielectric permittivity of *GaSe* determined as n_0^2 in the center of excitons band n = 1 is ~13.

The trend of decrease of absorption coefficient of *GaSe–CdSe* nanolamelar composite at energies $h\nu < 1.95$ eV can be explained by the fact that in this spectral region prevails the electronic transitions in fundamental absorption band of *CdSe* compound from composite.

(c) *GaSe intercalated with Zn*

Microcrystals from the outer surface of *ZnSe–GaSe* composite serve as light diffusion centers. This fact does not allow the direct measurements of linear reflection and optical transmittance of composite plates. The spectral dependence of *ZnSe–GaSe* composite absorption was determined from measurements of diffuse reflectance using the Kubelka—Munk function $F(R_\infty)$[53]:

$$F(R_\infty) = \frac{\alpha}{S} = \frac{(1 - R_\infty)^2}{2R_\infty}, \tag{12.23}$$

where α is the absorption coefficient, *S*—light diffusion factor (dependent on the wavelength and on the grain size at which the light scatter), R_∞—the diffuse reflection coefficient.

The type of optical transitions and the width of bandgap of semiconductor can be determined from the analysis of the next function [54]:

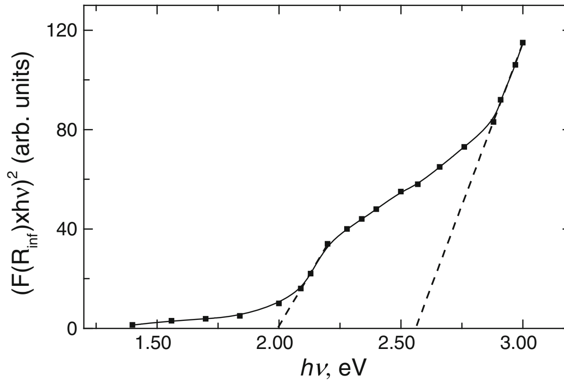

Fig. 12.7 The $(F(R_\infty)\cdot h\nu)^2$ dependence by energy $h\nu$ for composite obtained by heat treatment at 833 K of *GaSe* plates in *Zn* vapor for 24 h

$$(F(R_\infty)\cdot h\nu) = (h\nu - E_g)^n. \tag{12.24}$$

where n is equal to 2 for indirect optical transitions and ½ for allowed direct optical transitions.

In Fig. 12.7 it is shown the dependence $(F(R_\infty)\cdot h\nu)^2$ of energy hν for the composite obtained by heat treatment at the temperature of 833 K for 24 h of *GaSe* lamella in *Zn* vapor.

Two line segments clearly is evidenced in this graph, one in the region of 1.9–2.2 eV and another in the region of 2.5–3.0 eV. The extrapolation of these line segments to $(F(R_\infty)\cdot h\nu) = 0$ allows us to determine the width of bandgap that is equal to 1.99 eV and corresponds to *GaSe* crystals and 2.56 eV. The last value correlates well with the width of bandgap of the *ZnSe* compound in thin layers [22, 55].

(d) *GaS*

The transmission (t) and reflectance (R`) spectra from the surface perpendicular to the C_6 axis of *GaS* and *GaS*:*Mn* plates were recorded using the spectrophotometer Specord M–40 dapted for measurements at low temperatures. The PL spectra were analyzed using a monochromator of high optical power (MDR–2) and a photomultiplier with $(Na_2K)Sb{:}Cs$ photocathode.

The absorption coefficient α was determined from the formula [23]:

$$\alpha = \frac{1}{d} ln \frac{(1-R)^2}{t}, \tag{12.25}$$

where d is the sample thickness.

It is well known [56] that *GaS* is a semiconductor with indirect electronic bands in which the maximum of valence band is in the center of Brillouin zone (Γ point) and conduction band minimum at the M point. The edge of absorption band in

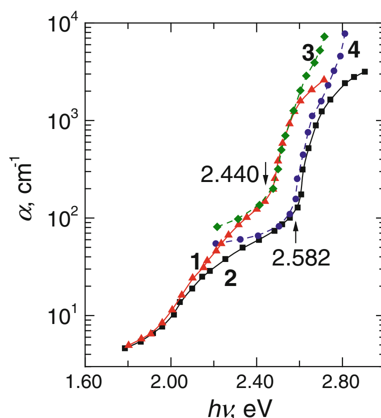

Fig. 12.8 The absorption spectra of *GaS* plates at 293 K (*curve 1*) and 78 K (*curve 2*), and *GaS* intercalated at 293 K with *Cd* (*curve 3*) and 78 K (*curve 4*)

indirect semiconductors and particularly in *GaSe* and *GaS* consists of electronic transitions with emission and absorption of phonons. Interaction of three particles: electron, photon and phonon it is achieved with a low probability, which determines relatively low values of absorption coefficient in the region of the edge of indirect absorption band in semiconductors [57]. The energy range in that electronic transitions involving phonons occurs is quite wide in the *GaS* crystals absorption spectra and as it is shown in Fig. 12.8 covers the range from 2.0 to 2.4–2.5 eV. In this energy interval the absorption coefficient does not exceed 300 cm^{-1} at temperatures in the range of 80–293 K.

As it can be seen in Fig. 12.8, spectral dependence of absorption coefficient in the range of 10^2–10^3 cm^{-1} almost coincide for *GaS* plates and *Cd* intercalated *GaS* plates at 293 K (curves 1 and 3) and at 78 K (curves 2 and 4). A steeper increase of the absorption coefficient is seen for *GaS* lamella *Cd* intercalated for $\alpha > 10^3$ cm^{-1} (curves 3 and 4). A behavior of the absorption coefficient similar to the one above in the fundamental absorption spectral region can be explained if one considers that as a result of *Cd* intercalation process in *GaS* plates, a composite is formed consisting predominantly of *GaS* and *CdS*. The band gap of *CdS* single crystals at 293 K determined form ellipsometrical measurements is 2.55 eV [58]. This value correlates with the edge of the absorption band due to direct transitions of *GaS* single crystals (curve 1 and 3). As one can see from Fig. 12.8, for energies $h\nu > 2.55$ eV at 293 K and $h\nu > 2.65$ eV at 78 K one can notice a steeper increase of the absorption coefficient along with energy increase for *Cd* intercalated *GaS* rather than as cleaved ones. A steep increase of the absorption coefficient in the fundamental absorption spectral region is typical for $A^{II}B^{VI}$ compounds and in particular in *CdS* single crystals. It can be admitted that the spectral characteristics of the absorption coefficient at the energies bigger than 2.5 eV ($T = 293$ K) and 2.58 eV ($T = 78$ K) are determined by indirect optical transitions in *GaS* crystals and direct optical transitions in *CdS* crystallites from composite. Relatively high values of the absorption mechanisms (70–90 cm^{-1}) for $h\nu < 2.40$ eV (293 K) and $h\nu < 2.50$ eV

(78 K) are caused mostly by difference in lattice constants of *CdS* and *GaS* as well as by metallic inclusions detected in the intercalated samples.

The absorption spectra of *GaS* single crystalline plates (curve 1) and *GaS* doped with 1.5 at% *Mn* (curve 2) are shown in Fig. 12.9. The presence of threshold in α(hν) dependencies at the temperature of 293 and 78 K is characteristic for these samples and it corresponds to indirect electrons transitions from the maximum of valence band (point Γ) to the absolute minimum of conduction band in point M of the Brillouin zone [59]. The indirect optical transitions occur with absorption and emission of phonons with the energy $\hbar\omega_f$. As can be observed from formula (12.15) the absorption coefficient at indirect transitions is proportional with $\left(h\nu - E_{gi} \pm \hbar\omega_f\right)^2$. In Fig. 12.10 are presented the spectra $(\alpha h\nu)^{1/2} = f(h\nu)$ in *GaS* single crystals at 80 K (curve 1) and 293 K (curve 2).

The average phonon energy and the indirect band gap width were determined by extrapolating the linear segments of the dependence $(\alpha h\nu)^{1/2} = f(h\nu)$ at α = 0 and it is equal respectively to 44.5 meV and 2.508 eV at T = 80 K. A single linear segment is obtained at T = 293 K (curve 2) in the region of indirect transitions and it

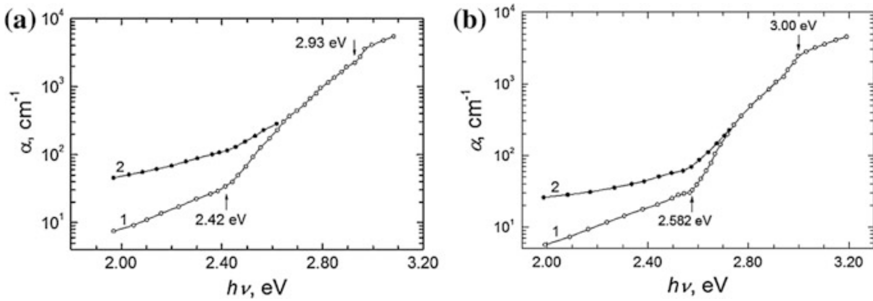

Fig. 12.9 The absorption spectra of *GaS* single crystalline plates (*curve 1*) and thin films of *GaS*: *Mn* (1.5 at%) obtained by evaporation in cvasi-closed volume (*curve 2*) at 293 K (**a**) and 78 K (**b**)

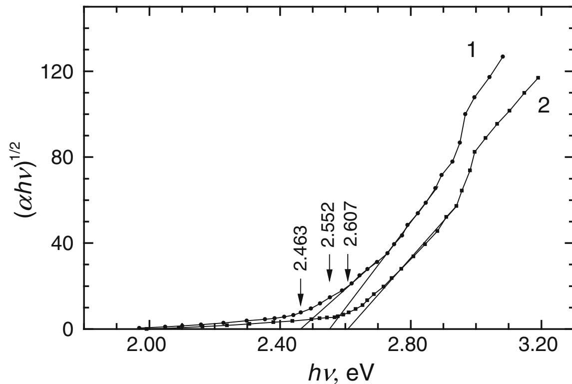

Fig. 12.10 The $(\alpha h\nu)^{1/2} = f$ ($h\nu$) dependence for *GaS single crystals at* 80 K (*curve 1*) and 293 K (*curve 2*)

corresponds to the absorption process with phonon emission with the energy of 44.5 meV. Note that the energy of optical phonon is determined from the measurement of the Raman spectra [60] and absorption in thin *GaS* films. The energy of optical phonon is equal to 37 meV for the transverse optical phonons [61] and 44.6 meV for longitudinal optical phonons. In the absorption spectra of *GaS* single crystalline plates (Fig. 12.9, curve 1) second absorption threshold is present at the energy of 2.93 eV (293 K) and 3.00 eV (78 K) which is associated with the direct optical transition between the valence and conduction bands in the point M of Brillouin zone. The width of indirect bandgap of *GaS* is equal to 2.595 eV at 77 K [62] and therefore the absorption threshold with the edge at 2.582 eV (78 K) can be considered photon absorption as the result of which the indirect excitons with binding energy of 13 meV are formed (n = 1). The presence of *Mn* in *GaS* monocrystalline layers results in increase of absorption coefficient in the region of optical transmittance band ($h\nu < E_{gi}$) of undoped *CdS* semiconductor can be observed from Fig. 12.9. At the same time the *Mn* impurity atoms form structural defects that shield the indirect excitons at both temperatures of 293 and 78 K.

The absorption coefficient at the edge of indirect absorption band at room temperature is $\sim$300 cm^{-1} and is reduced up to $\sim$220 cm^{-1} at the temperature of 80 K. In the direct absorption band edge region the absorption coefficient is 2000–3500 cm^{-1}. Note that the absorption coefficient at the edge of direct absorption band in the center of Brillouin zone for *GaSe* and *InSe* crystals is 1000–2000 cm^{-1} and in the point M of the Brillouin zone the absorption coefficient is $\sim$(1–3) × 10^4 cm^{-1}. The reflection spectra from the surface of *GaS* plate with the thickness of 35 μm in the wavelength number 400–100 cm^{-1} are shown in Fig. 12.11.

The wavelength number of the reflection minima and the identification of the corresponding vibration modes are given in Table 12.2.

The characteristic vibration modes of *β–GaS* and the vibration bands of crystal lattice of β–Ga_2O_3 oxide are present in *GaS* samples as it is shown in Table 12.2. Due to the cracks between elementary packagess of *GaS* and *GaSe* crystals kept in normal atmosphere the oxygen intercalates and forms β–Ga_2O_3 oxide crystallites.

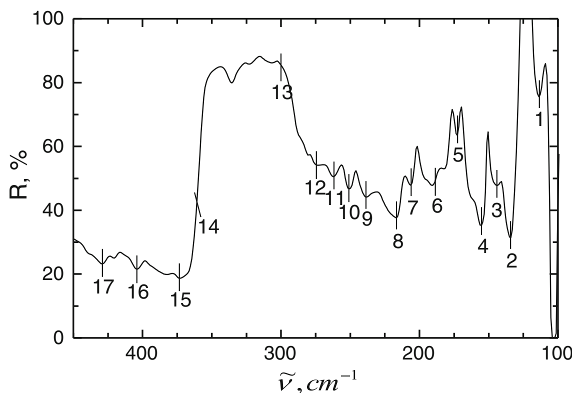

Fig. 12.11 The reflection spectrum from (0 0 1) surface of *GaS* monocrystalline films with thickness of 35 μm at light incidence of 30° to C_6 axis

Table 12.2 Mono-phononic optical vibrations energies of the crystal lattice vibration plane assemblies and atomic vibrations combinations determined from the transmission spectra of *GaS* plate with thickness of ∼3.5 μm

	Nr.	$\tilde{\nu}$, cm^{-1}	Interpretation	Vibration mode	References
A	1	113.5	β–Ga_2O_3	A_g	[63]
	2	133.8	β–GaS	A'_1 (analogical with *GaSe*)	[64]
	3	143.0	β–Ga_2O_3		[65]
	4	154.0	Ga_2S_3	E′ (LO)	
	5	173.0	β–Ga_2O_3		[65]
	6	188.5	β–GaS	A'_{1g}	[66, 67]
	7	206.5	*GaS*	E''_g	
	8	216.5	*GaS*	E'_g	
	9	250.0	–		
	10	297.0	*GaS*	E'_{2g} (IR active)	[66]
	11	367.0	*GaS*	A^2_{1g}	[66]
	12	406.0	*GaS*	$2E''_g$	
B	1	640	H_2O		
	2	637	H_2O		
	3	595	*GaS*	$2E'_{2g}$	
	4	480	–		
	5	422	–		
	6	400	Raman active		
	7	377	β–GaS	$2A'_{1g}$	

(e) *InSe*

The weak links between *Se–In–In–Se* atomic packages allows obtaining of *InSe* monocrystalline blades by splitting with required thicknesses for measurements of the absorption coefficients of order 10^5 cm^{-2}. The valence bonds that are closed at the layer surface determine the low density of surface states that does not influence the generation—recombination mechanisms of the non-equilibrium charge carriers. Transmission spectrum at T = 80 K in the fundamental band edge region for an 11.2 μm thickness of *InSe* lamella is shown in Fig. 12.12. At the same time with the structure of interferential bands there is present the direct unionized exciton absorption band with the transmission minimum at energy 1.328 eV.

The absorption spectrum of the *InSe* crystals at 80 and 293 K is shown in Fig. 12.13. The spectrum of the edge of absorption band is determined by electronic transitions with excitons formation as can be seen from the figure. The absorption edge band at the temperature of 293 K located at 1.250 eV has a large contour and a relatively small intensity which indicates that the binding energy of electron–hole pair (exciton) is smaller than the thermal energy at T = 293 K. The absorption band edge at the temperature of 80 K shifts to higher energies. This shift is well described by the formula that links the bandgap width E_g and the temperature T (K) [68]:

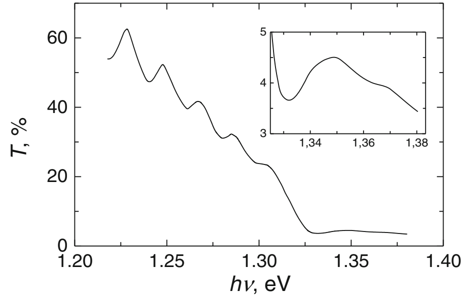

Fig. 12.12 The transmission spectrum in fundamental band edge region of a *InSe* with thicknes of 11.2 μm at $T = 80$ K

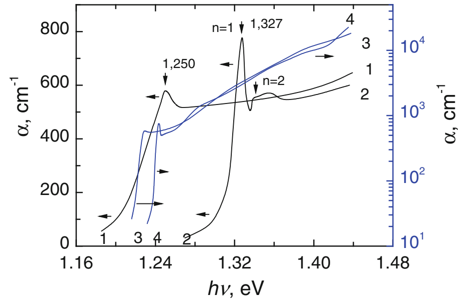

Fig. 12.13 The absorption spectra of *InSe* single crystalline layers at $T = 293$ K (*curves 1* and *3*) and T = 80 K (*curves 2* and *4*)

$$E_g = 1352{,}5 - [65/\{\exp(165/T) - 1\}]. \tag{12.26}$$

The n = 1exciton line with maximum at 1.327 eV and a low intensity line at 1.339 eV are clearly presented at the temperature of 80 K in the absorption band edge region. Also in this region is present an absorption band at the energy of 1.80–1.95 eV. Such bands are present in the absorption spectra of *CdTe* polycrystalline layers and in *GaSe* and *GaTe* single crystalline lamella. The intensity of absorption bands decrease when the lamella is heat-treated in an inert atmosphere which indicates the presence of a high structural defects density. In the case of layered semiconductors such defects may be the relative movement of the packages to one to one another. Note that these two excitonic features are well highlighted by the maximum of quantum effectiveness of *InSe*–own oxide heterojunctions at the temperature of 100 K [69].

The binding energy of the electron–hole pair (excitonic Rydberg) determined from (12.13) taking the n = 1 and n = 2 bands peaks energy is equal to 16 meV and respectively the bandgap width at $T = 80$ K is 1.343 eV for *InSe* plates. In the depth of intrinsic band the absorption coefficient rapidly increases with energy and reach the size of $\sim 2 \times 10^4$ cm^{-1} at the energy of 1.42 eV.

Absorption coefficient in the fundamental absorption band increases from (9–10) × 10^2 cm^{-1} (in the close proximity of the n = 1 excitonic line, $h\nu = 1.345$ eV at $T = 80$ K) to $\sim 2 \times 10^4$ cm^{-1} at the phonon energy of 2.25 eV (Fig. 12.14). The

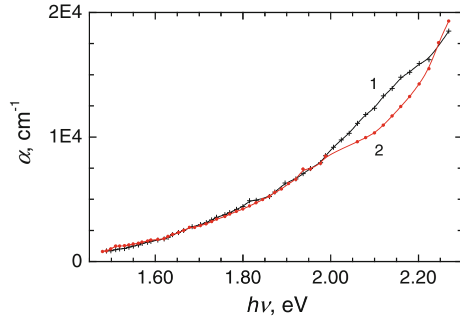

Fig. 12.14 The absorption spectra of *InSe* plates at $T = 293$ K (*curve 1*) and 80 K (*curve 2*)

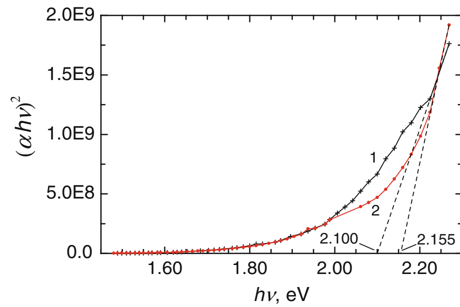

Fig. 12.15 The absorption spectra of *InSe* single crystalline lamella with submicrometric thicknesses at $T = 293$ K (*curve 1*) and 80 K (*curve 2*)

sharp increase of absorption coefficient at phonon energy of $h\nu \gtrsim 2.2$ eV is determined by optical transitions of electrons from the valence band (BV) in the conduction band (CB) in the point M of Brillouin zone [59].

The $(\alpha h\nu)^2 = f(h\nu)$ spectra of *InSe* monocrystalline blades at $T = 293$ K (curve 1) and 80 K (curve 2) are shown in Fig. 12.15. The experimental data points of $(\alpha h\nu)^2 = f(h\nu)$ function are arranged on a line which extrapolation to $\alpha = 0$ indicates the energy range between the extremities of valence band and conduction band in *M* point of Brillouin zone, which is equal to 2.100 eV at $T = 293$ K and 2.155 eV at 80 K.

The coefficient of thermal displacement of bandgap in the M point is equal to 2.6×10^{-4} eV. Note that in this spectral region there is a marked increase for both the absorption and reflection coefficients [14].

(f) *GaTe and GaTe intercalated with Cd*

The *GaTe* having a band gap of ~1.65 eV with direct electronic bands is ranked in the top 10 semiconductor materials for photovoltaic energy [9]. Specific for $A^{III}B^{VI}$ lamellar semiconductors is the presence of closed valence bonds at the surface of B-A-A-B packages that determines a low surface states density (~10^{10} cm^{-2}), high photosensitivity and stability of receptor characteristics at ionizant radiations [70–72].

The plan–parallel blade with thickness of 5.2, 28, 136 and 210 μm were used for the determination of absorption coefficient in a wide range of values 10–10^5 cm^{-1}.

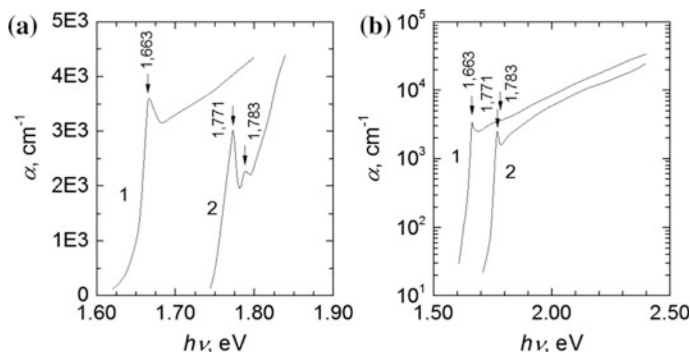

Fig. 12.16 The absorption spectra of *GaTe* single crystalline layers: in intrinsic edge region (**a**) and deep fundamental absorption band (**b**), at T = 293 K (*curve 1*) and T = 80 K (*curve 2*)

In Fig. 12.16 are shown the absorption spectra at normal incidence on the plate surface at 293 K (curve 1) and 80 K (curve 2).

The absorption coefficient increases by more than two orders of magnitude in a narrow range of energies ($\sim$0.05 eV). This property is characteristic for semiconductors with direct optical transitions. The absorption coefficient at both temperatures of 80 and 293 K is growing at the same time with the photon energy and achieve a value of $\sim 3 \times 10^4$ cm^{-1} at the energy of 2.4 eV in the depth of intrinsic absorption band.

The edge of the absorption band is formed by bands of free excitons with the maximum at the energy of 1.663 eV (T = 293 K). The maximum of direct exciton band in the state n = 1 at the temperature of 80 K is at energy of 1.771 eV and at the energy of 1.783 eV is located the maximum of absorption band of excited exciton (n = 2). The binding energy of the electron–hole pair based on excitons with large radius model (Wannier–Mott excitons) is $\sim$12 meV. Thus, the energy between the maximum of valence band and the minimum of conduction band in the center of the Brillouin zone of the *GaTe* semiconductor at the temperature of 80 K is 1.783 eV. If we assume that the exciton binding energy (excitonic Rydberg) does not change in the temperature range of 80–293 K, then the width of direct bandgap at 293 K will be equal to 1.675 eV. The width of bandgap that is calculated in the paper of Yamamoto [73] is 1.13 eV and corresponds to direct transitions between the maximum of valence band and the minimum of conduction band in the point M of Brillouin zone. The difference of $\sim$40 % between the theoretical calculations of the structure of electronic bands and experimental results are considered a result of the omission in calculations of volume and localized states density variations.

The absorption band with threshold at 1.50 eV (Fig. 12.17, curves 2 and 3) is formed in the region of optical transparency of *GaTe* compound at the energies $h\nu < 1.62$ eV in the absorption spectra of the samples obtained by heat treatment of this material in *Cd* vapor.

Fig. 12.17 The absorption spectra of *GaTe* single crystals (*curve 1*), *GaTe* heat treated at 623 K in *Cd* vapor (*curve 2*), 653 K (*curve 3*), for 60 h

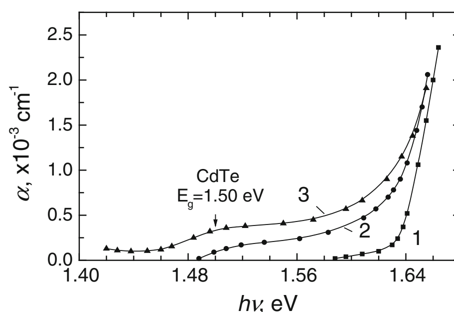

This feature of absorption spectrum is amplified when the temperature of treatment increase from 623 to 653 K (Fig. 12.17, curves 2 and 3). It is known that the edge of absorption band of *CdTe* thin layers in polycrystalline state is in the region of 1.50–1.54 eV [58]. The presence of absorption threshold at 1.5 eV serves as a criterion for admission that as a result of *GaTe* crystals treatment in *Cd* vapor at 350–653 K the Te atoms from the elementary packages surface combines with *Cd* and form *CdTe–GaTe* composite and free *Ga*. From Fig. 12.17, it can be concluded that at the increasing of treating temperature from 623 to 653 K, results an increase of absorption coefficient in the range of energies 1.46 eV $\leq h\nu \leq$ 1.52 eV (Fig. 12.17, curves 2 and 3), which indicates the obtaining of similar *CdTe* layers at the interface of *Te–Ga–Ga–Te* elementary packages.

As can be seen from Figs. 12.18 and 12.19 as a result of heat treatment at 723 K of *GaTe* plates in *Cd* vapor its surface is covered with a layer of *CdTe* crystallites with micrometrical dimensions. Both the presence of microcrystals and insular substrate enriched with *Ga* lead to intense light scattering.

Fig. 12.18 The SEM image of *GaTe* plate surface heat treated at 723 K in *Cd* vapor for 12 h

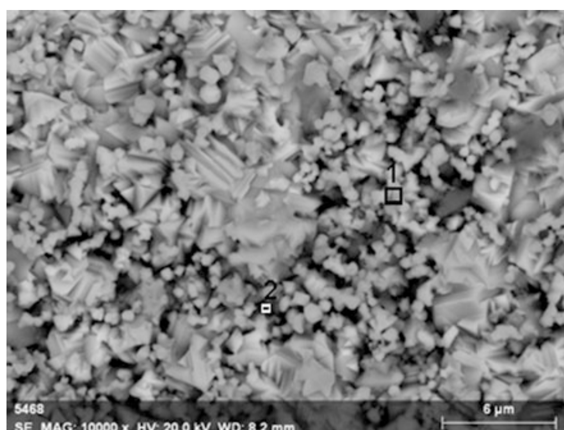

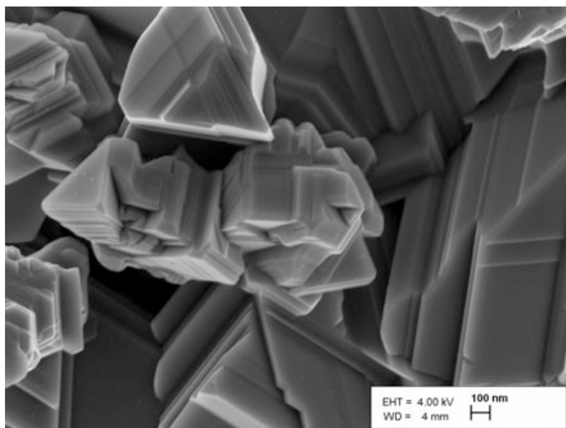

Fig. 12.19 The orientation of *CdTe* crystallites onto the surface of *GaTe* plate

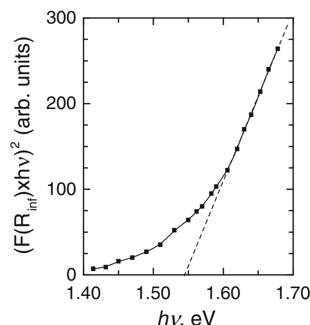

Fig. 12.20 The determination of bandgap energy for composite obtained by heat treatment at 633 K of *GaTe* plates in *Cd* vapor for 24 h

The edge of absorption band of the samples obtained by treatment at 723 K for 12 h was analyzed using the Kubelka–Munk function [74]. The type of optical transitions and the width of bandgap of the composite obtained on the outer surface of *GaTe* lamella was determined using the following equation:

$$h\nu \times F(R_\infty) = B(h\nu - E_g)^n \quad (12.27)$$

where B is a constant that does not depend on the energy; E_g—the width of bandgap; n—the factor that determines the type of optical transitions (n = 2 for indirect optical transitions and n = 1/2 for allowed direct optical transitions).

The $(F(R_\infty) \times h\nu)^2$ dependence of energy hν it is shown in Fig. 12.20. The width of direct bandgap for *CdTe–GaTe* composite was determined by extrapolation of the linear segment of function $(F(R_\infty) \times h\nu)^2 = f(h\nu)$ to zero and it is equal to 1.546 eV.

Therefore, we can conclude that outer surface was covered with a *CdTe* polycrystalline layer which edge of absorption band is determined by direct optical transitions with bandgap at $T = 293$ K equal to 1.546 eV for *GaTe* plates that were

heat treated at 653 K in *Cd* vapor for 24 h. This value of width of bandgap well correlates with the energy of the edge of absorption band for direct optical transitions in *CdTe* thin layers obtained by vapor condensing on a quartz substrate [75].

12.4.2 Light Absorption of GaSe *and* GaSe *Doped with* Cd *in the Region of* hν < E_g

Impurity atoms and structural defects form a broad spectrum of energy levels in the compound's bandgap. Through these electronic levels occurrs transitions determining the optical, electrical and photoelectrical properties of material. The structure of optical spectra in the region of $h\nu < E_g$ in perfect crystals is determined by lattice vibration, the concentration and type of own and induced by doping of structural defects.

In Fig. 12.21 is shown the transmission spectrum of the *GaSe* plate with the thickness of 2.5 μm in the wavelength number range from 100 to 600 cm^{-1}. The intense absorption band with maximum at 214 cm^{-1} corresponds to transverse optical monofononic vibrations of ε–*GaSe* semiconductor hexagonal lattice. The first harmonic of the fundamental vibration $2\tilde{\nu}_{LO}$ and $2\tilde{\nu}_{TO}$ manifests by low-intensity absorption bands respectively at 510 cm^{-1} and 428.12 cm^{-1}. Vibrational absorption bands of hexagonal crystal lattice of the semiconductor ε–*GaSe* with low intensity, at the same time with the monofononic vibrations band from 250–170 cm^{-1} region, are present in the region of 100–200 cm^{-1} (Fig. 12.21). The lattice vibration mode of ε–*GaSe* with ν = 117 cm^{-1} which is identified as transverse vibration of atoms within layered packages are active in this spectral region. The vibration with wavelength number 134–137 cm^{-1} is identified as A_1' vibration and it is active in the the Raman and IR absorption spectra. The vibrational bands at 163.92 and 146.56cm^{-1} are probably vibrational modes of impurity atoms in the hexagonal lattice of ε–*GaSe* compound. As shown in Fig. 12.21, the

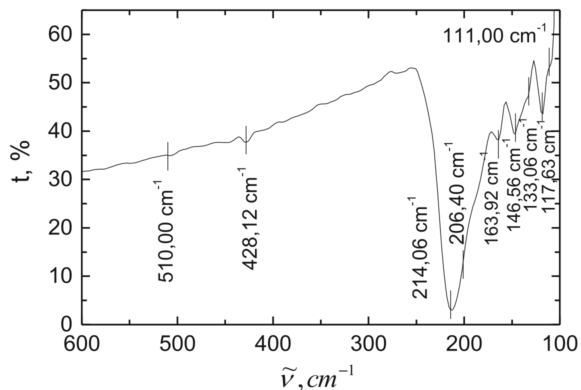

Fig. 12.21 Transparency $t(\tilde{\nu})$ of *GaSe* lamella with thickness of 2.5 μm

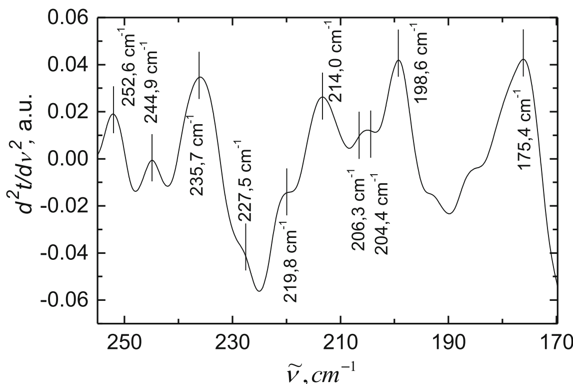

Fig. 12.22 Second derivative of optical transmittance by wavenumber in monophononic vibrations region of *ε–GaSe* single crystalline plate with thickness of 2.5 μm

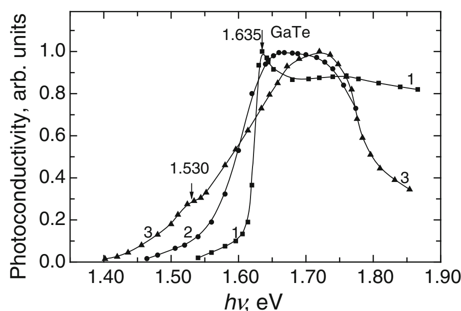

Fig. 12.23 The spectra of photoconductivity of *GaTe* crystals (*curve 1*) and *GaTe* crystals that were heat treated in *Cd* vapor for 60 h at temperature of: 623 K (*curve 2*) and 653 K (*curve 3*)

absorption band with minimum at 214.06 cm^{-1} has a complex structure. These peculiarities of band structure are better outlined in the second derivative spectrum ($d^2t/d\tilde{v}^2$) shown in Fig. 12.22.

The layered crystalline structure of *GaSe* compound leads to anisotropy of excitonic absorption (Fig. 12.3) and vibrational modes in the IR region. The peaks in the ($d^2t/d\tilde{v}^2$) ($\tilde{v}$) spectrum correspond to the wavenumbers of elementary phonons. In this spectrum are clearly highlighted optical longitudinal and transverse phonons in polarization $\tilde{E}\perp\tilde{C}$ $\tilde{v}_{\perp}(LO) = 252.63\text{cm}^{-1}$ and $\tilde{v}_{\perp}(TO) = 214.60\,\text{cm}^{-1}$ and a several bands 244.92, 235.7, 219.84, 206.35,198.63, and 175.49 cm^{-1}.

The fact that the absorption spectra of layered crystals, especially for *GaS*, consist of vibration bands in $\tilde{E}\perp\tilde{C}$ polarization the vibration and subbands in $\tilde{E} \parallel \tilde{C}$ polarization was proved in Mustafaev work [61]. Moreover in the work of Jandl [76] the absorption bands in this spectral region are identified as phonons in the modification *γ–GaSe* ($\tilde{v}_2 = 235.7\,\text{cm}^{-1}$ and $\tilde{v}_1 = 245\,\text{cm}^{-1}$). At the same time with a low intensity minimum a di-phononic band is highlighted at $2\tilde{v}_{(TO)} = 428.12\,\text{cm}^{-1}$ and impurity monofononic absorption bands at $\tilde{v} < 200\,\text{cm}^{-1}$ in this spectral region. The symmetrical vibration A_1' type in *ε–GaSe* with $\tilde{v} = 133\,\text{cm}^{-1}$,

symmetrical vibration A_1' type (A_g) with $\tilde{\nu} = 111\,\text{cm}^{-1}$ and (B_g) with $\tilde{\nu} = 147\text{cm}^{-1}$ in β–Ga_2O_3 oxide are active in this region. Note that the β–Ga_2O_3 oxide is formed on the surface of *GaSe* lamella that was kept in the atmosphere. The lattice vibrations of this oxide can be assigned to the band with ν = 198.6 cm^{-1} in the Raman spectra of β–Ga_2O_3 crystals obtained by heat treatment of *GaSe* plates in normal atmosphere [63].

The phonon absorption bands intensity ratio $I_{\tilde{\nu}(TO)}/I_{2\tilde{\nu}(TO)}$ is equal to 36. The alternative interdiction rule allows the presence of lattice vibrations in IR absorption and combined diffusion (Raman) because the unit cell of *ε–GaSe* politype has not the inversion center. For this reason the threshold at $\tilde{\nu}$ ≈131.1 cm^{-1} can be identified as symmetric vibration within layerd package toward the active vertical plane in the Raman spectra [76].

12.5 Photoelectrical Properties of Nanolamellar Structures with *GaS*, *GaSe*, *GaTe* and *InSe* Semiconductors

12.5.1 Photosensitive Elements on GaTe Semiconductor

The distributions of spectral photoconductivity for primary *GaTe* crystals (curve 1) and composite obtained by heat treatment at 623 K (curve 2) and 653 K (curve 3) of *GaTe* lamella in *Cd* vapor for 60 h are presented in Fig. 12.23. The sharply decrease of photosensitivity (curves 2 and 3) at energies hν > 1.75 eV indicates the presence of a high surface states concentration. Thus, the nanoformations from the surface of *GaTe* plates generate fast recombination centers for nonequilibrium charge carriers. The plateau at the energy of 1.55 eV is probably caused by the generation of nonequilibrium charge carriers in *CdTe* crystallites from composite.

12.5.2 GaSe–CdSe *Heterojunctions*

The XRD patterns show that by intercalation of *GaSe* plates with *Cd* in the temperature range of 633–833 K (Figs. 12.24 and 12.25) it is obtained a material that composed of both *GaSe* and *CdSe* crystallites. The *CdSe* formations can be well seen from the SEM images of the outer surface of lamella that are shown in Figs. 12.26 and 12.27. It is easy to see that by intercalation at high temperatures (633, 753, 833 K) *GaSe* blade surface is covered with a *CdSe* submicron thick layer. The *CdSe* polycrystalline layer is a good electrical conductor with σ ∼ (1–2) × 10^2 $\Omega^{-1}\text{cm}^{-1}$ and the concentration of major electrical charge carriers (electrons) of (3–5) × 10^{18} cm^{-3}.

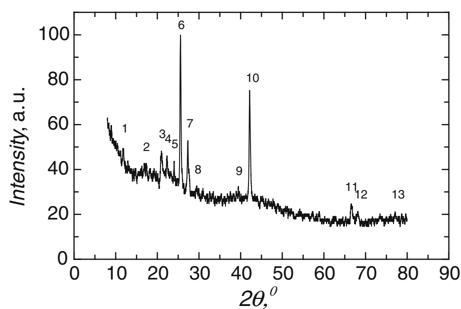

Fig. 12.24 The XRD pattern of *GaSe* heat treated at 753 K in *Cd* vapor for 24 h

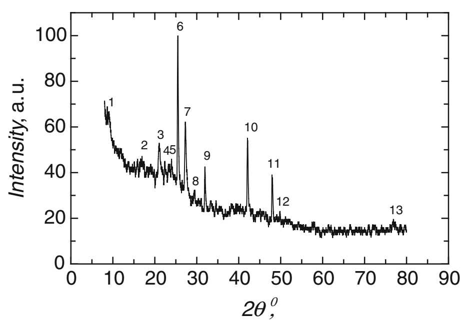

Fig. 12.25 The XRD pattern of *GaSe* heat treated at 833 K in *Cd* vapor for 24 h

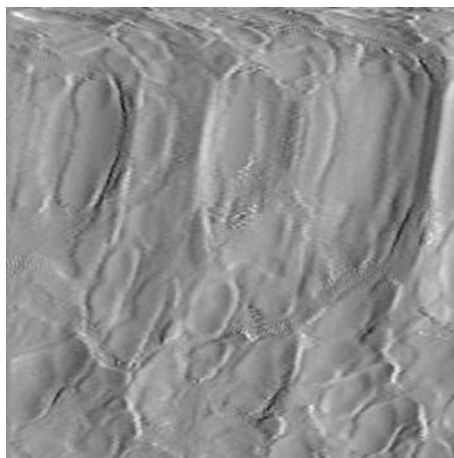

Fig. 12.26 The image of surface of *GaSe* plate heat treated at 480 °C in *Cd* vapor for 30 min

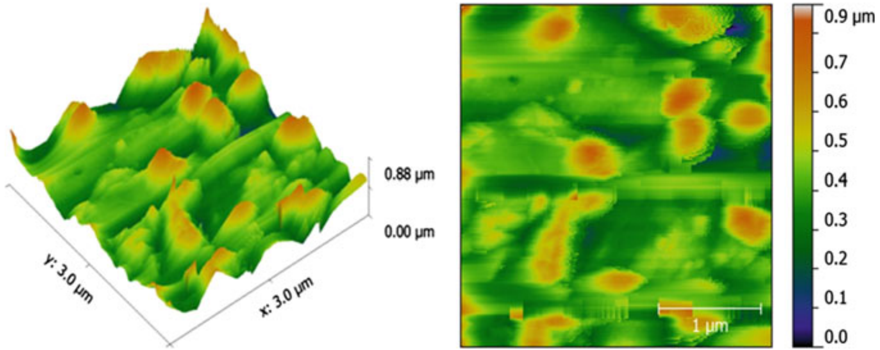

Fig. 12.27 The image of *GaSe* plate surface heat treated at 793 K in *Cd* vapor for 6 h

The current density of nonequilibrium charge carriers (holes) in the *CdSe* layer from heterojonction interface j_p is given by expression [77]:

$$j_p = q\Phi_0 \frac{\alpha L_p}{\alpha L_p + 1}\left[\exp\left(-\frac{d}{L_p}\right) - \exp(-\alpha d)\right], \tag{12.28}$$

where q is the electric charge of the electron, Φ_0—the density of photon flux, α—absorption coefficient, L_p—holes free path in the *CdSe* layer, d—the depthof radiation penetration.

For $\alpha d \gg 1$ and $L_p \gg d$ from (12.28) we get:

$$j_p = q\phi_0 \frac{1}{1 + \frac{1}{j} \cdot \frac{1}{L_p}}. \tag{12.29}$$

The holes free path in the *CdSe* layer L_p at the interface of *GaSe–CdSe* junction was estimated from (12.28) being measured the J_p, Φ_0 and α at wavelength that is emitted by *He–Ne* laser. For $\lambda = 632.8$ nm, $\Phi_0 = 4$ mW·cm^{-2}, $j = 2 \times 10^4$ cm^{-1} and $J_p = 1.5$ mA, we obtain $L_p = 1.5 \times 10^{-6}$ m. Since the thickness of *CdSe* layer on the (001) surface of *GaSe* plate did not exceed 0.3 µm, we can conclude that nonequilibrium charge carriers generated in *CdSe* layer of *GaSe–CdSe* heterojonction reach the junction.

In Fig. 12.28 are presented the photovoltaic spectra for two heterojunctions at the lighting throw a *GaSe* layer with thicknesses of 7.6 and 28.1 µm. As shown in Fig. 12.28, the non-equilibrium charge carriers are generated in both *CdSe* polycrystalline layer and in the *GaSe*. The jump in photovoltage spectra at energies higher than 1.9 eV is caused by the *GaSe* layer absorption band edge.

The absorption coefficient of photons with energy $h\nu \approx 2.0$ eV is $\alpha \approx 10^3$ cm^{-1} and tends to increase monotonous with the increasing of photon energy. Thus, the presence of photovoltaic voltage at energy $h\nu > 2.0$ eV in heterojunction with a *GaSe* layer, which thickness is 7.6 and 28.1 µm, is determined by the spectral

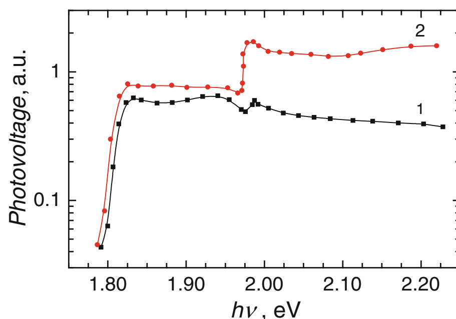

Fig. 12.28 The photovoltaic spectra of *GaSe–CdSe* heterojunction obtained by intercalation at 633 K with *Cd* for 60 h of *GaSe* lamella with thicknesses of: 28.1 μm (*curve 1*) and 7.6 μm (*curve 2*)

dependence of the absorption coefficient in this spectral region. From Fig. 12.28 it can be observed that the *GaSe–CdSe* heterojunctions obtained by heat treatment of *GaSe* plates in *Cd* vapor can serve as nonselective spectral photoreceptors with broadband sensitivity and as solar photovoltaic energy elements.

12.5.3 InSe–CdSe *Heterojunctions*

The surface of *InSe* plate covers with a monocrystalline *CdSe* layer of ~1.0 μm thick as a result of heat treatment of plates in *Cd* vapor at 633 K for 60 h. Also, the micro–zones in which metallic *Ga* is concentrated with small amount of *Cd* (<10 %) are formed on the surface.

The photovoltage spectra for two heterojunctions with *InSe* layer that thickness is 5.1 μm (curve 1) and 12.4 μm (curve 2) are presented in Fig. 12.29. The red edge of these spectra coincides with the edge of absorption band of the *InSe* basic material. The jump present in photovoltage spectra at energy 1.76 eV indicates the charge carriers' generation in both semiconductor layers of heterojonction (*InSe* and *CdSe*). The decrease of photovoltaic voltage (PV) at energies *hν* > 1.9 eV can be conditioned by the presence of surface states in both *CdSe* layer and *InSe* generated by long duration treatment at 633 K.

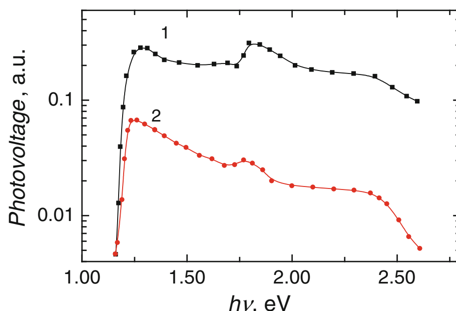

Fig. 12.29 The photovoltaic spectra of *InSe-CdSe* heterojunction

The spectral characteristics shown in Fig. 12.29 indicates that *InSe–CdSe* heterojunctions can serve as photosensitive elements in solar energy converters with higher efficiency than those with photosensitive elements based on *Si* and *GaAs*.

12.6 Conclusions and Generalities

- The *GaSe* is a p-type semiconductor in which the maximum of valence band is in the Γ point and the minimum of conduction band is shifted to the edge of the first Brillouin zone. The edge of indirect bandgap is formed with the emission of A_1' phonons that energy is equal to 17 meV at the temperatures $T < 300$ K and at $T = 380$ K it is equal to 1.902 eV. The dispersion of ordinary refractive index is described by a power function of the inverse wavelength in the wavelength range from 0.330 to 20 μm. The edge of the absorption band of the *GaSe* compound is formed by the direct excitons with binding energy of electron-hole pair equal to ∼20 meV. The direct bandgap width at $T = 293$ K is equal to 2.002 eV.
- The Gallium monosulfide is an indirect semiconductor. The edge of absorption band is formed by photon absorption with absorption and emission of phonons with the energy of 44.5 meV. The width of indirect bandgap at $T = 80$ K is equal to 2.508 eV.
- The *InSe* is an n-type semiconductor with indirect optical transitions. The minimum interval between the valence and conduction bands in the center of the Brillouin zone at $T = 80$ K is equal to 1.343 eV.
- The *GaTe* is a p-type semiconductor in which the maximum of valence band and the absolute minimum of the conduction band are at the edge of the first Brillouin zone in the Z point. The edge of absorption band is formed by direct excitons with binding energy of 12 meV. The width of bandgap at $T = 80$ K is equal to 1.783 eV and at $T = 300$ K is 1.675 eV.
- The nanocomposite materials with *Ga* and *Cd* chalcogenids are materials in that the light scattering occurs at the frontier of separating the crystallites. The edge of absorption band was analyzed using the Kubelka-Munk function in order to minimize the intensity of scattered light. The absorption spectra of *CdS–GaS*, *CdSe–GaSe* and *CdTe–GaTe* nanocomposites calculated from the spectra of diffuse reflectance using this function contain the edges of absorption bands that are characteristic for crystallites from composite. This coincidence find explanation if we admit that the absorption processes occur in the semiconductors macrocristalites of composite compounds.
- Based on obtaining technologies of micro–and nanostructures with own oxides and $A^{II}B^{VI}$ nanolamellar compounds (*CdSe*, *CdTe*, *ZnSe*) were obtained broadband and narrowband sensitivity photoreceptors that cover the UV (5.8 eV)–NIR (1.0 eV) spectral range of optical filters for spectral region of 500–1600 nm.

- Structural defects generated by movements of atomic planes of the elementary packages influence weakly on the processes of light absorption in the photon energy region of $hv < E_g$. At the same time they contribute to the stability of generation–recombination processes of nonequilibrium charge carriers and respectively to stability of the characteristics of photoelectron device (photorezistors, heterojunctions) at ionizing radiation.
- Low density of surface states is the dominant factor by which the violet edge of photosensitivity bands of structures formed by *GaS*, *GaSe* and *InSe* compounds with own oxides is located in the UV region of the spectrum. The own oxides of Ga_2O_3 and In_2O_3 form states with low lifetime in the contact region of the respective heterojunctions, which allows the selection of photosensitivity bandwidth in photoelectronic devices with *GaS*, *GaSe*, *InSe*, and *GaTe* semiconductors.
- Micro- and nanocrystalline composites obtained by heat treatment of monocrystalline *GaS*, *GaSe*, *InSe*, and *GaTe* plates in *Zn* and *Cd* vapor exhibit optical properties in intrinsic edge region and in the region characteristic for lattice vibration of crystalline compounds components.

References

1. K.C. Mandal, S.H. Kang, M. Choi, J. Chen, X.C. Zhang, J.M. Schleicher, C.A. Schmuttenmaer, N.C. Fernelius, IEEE J. Sel. Top. Quantum Electron. **14**, 284 (2008)
2. Y. Cui, D.D. Caudel, P. Bhattacharya, A. Burger, K.C. Mandal, D. Johnstone, S.A. Payne, J. Appl. Phys. **105**, 053709 (2009)
3. C. Kubler, R. Huber, S. Tubel, A. Leitenstorfer, Appl. Phys. Lett. **85**, 3360 (2004)
4. C. Ferrer-Roca, J. Bouvier, A. Segura, M.V. Andres, V. Munoz, J. Appl. Phys. **85**, 3785 (1999)
5. R. Zallen, M. Slade, Phys. Rev. B **9**, 1637 (1974)
6. W.C. Eckhoff, R.S. Putnam, S. Wang, R.F. Curl, F.K. Tittel, Appl. Phys. B **63**, 437 (1996)
7. Y.-Z. Lu, X.-B. Wang, L. Miao, D.-L. Zuo, Z.-H. Cheng, Chin. Phys. Lett. **28**, 034201 (2011)
8. A.J. Nelson, A.M. Conway, B.W. Sturm, E.M. Behymer, C.E. Reinhardt, R.J. Nikolic, S.A. Payne, G. Pabst, K.C. Mandal, J. Appl. Phys. **106**, 023717 (2009)
9. E. Bucher, photoelectrochemistry and photovoltaics of layered semiconductors, in *Physics and Chemistry of Materials with Low-Dimensional Structures*, ed. by A. Aruchamy (Kluwer Academic Publishers, Dordrecht, 1992), pp. 1–81
10. D.J. Late, B. Liu, J. Luo, A. Yan, H.S.S. Ramakrishna Matte, M. Grayson, C.N.R. Rao, V. P. Dravid, Adv. Mater. **24**, 3549 (2012)
11. J.P. Voitchovsky, A. Mercier, Il Nuovo Cimento B **22**, 273 (1974)
12. A. Seyhan, O. Karabulut, B.G. Akįnoğlu, B. Aslan, R. Turan, Cryst. Res. Technol. **40**, 893 (2005)
13. A. Mercier, J.P. Voitchovsky, J. Phys. Chem. Solids **36**, 1411 (1975)
14. V. Grasso, P. Perillo, Solid State Commun. **21**, 323 (1977)
15. J.V Acrivos, Intercalated layered materials, *On The Intercalation Reaction*, ed. by F. Levy (D. Reidel Publishing Company, Dordrecht, 1979), pp. 33–99
16. Z.D. Kovalyuk, M.M. Pyrlya, V.B. Boledzyuk, J. Optoelectron. Adv. Mater. **5**, 869 (2003)
17. C.M. Julien, M. Balkanski, Mater. Sci. Eng., B **100**, 263 (2003)

18. Z.D. Kovalyuk, V.B. Boledzyuk, V.V. Shevchyk, V.M. Kaminskii, A.D. Shevchenko, Semiconductors **46**, 971 (2012)
19. I.I. Grigorchak, V.V. Netyaga, Z.D. Kovalyuk, J. Phys.: Condens. Matter **9**, L191 (1997)
20. B.A. Orlowski, I.A. Kowalik, B.J. Kowalski, M. Suffczynski, A. Mycielski, S. Colonna, C. Ottaviani, F. Ronci, A. Cricenti, J. Alloy. Compd. **382**, 224 (2004)
21. E.J. Johnson, Semiconductors and semimetals, in *Optical Properties of III–V Compounds*, ed. by A.C. Beers, R.K. Willardson. (Academic Press, New York, 1967), p. 169
22. R. Le Toullec, N. Piccioli, M. Mejatty, M. Balkanski, Nuovo Cimento B **38**, 159 (1977)
23. T.A. McMath, J.C. Irwin, Phys. Stat. Sol. (a) **38**, 731 (1976)
24. K.L. Vodopyanov, L.A. Kulevskii, Optics Commun. **118**, 375 (1995)
25. M. Schlüter, J. Camassel, S. Kohn, J.P. Voitchovsky, Y.R. Shen, M.L. Cohen, Phys. Rev. B **13**, 3534 (1976)
26. G.M. Mamedov, M. Karabulut, A.O. Kodolbaş, O. Oktu, Phys. Stat. Sol. (b) **242**, 2885 (2005)
27. Y.P. Varshni, Physica **34**, 149 (1967)
28. G.L. Belen'kii, V.B. Stopachinskii, Sov. Phys. Usp. **26**, 497 (1983)
29. J.J. Forney, K. Maschke, E. Mooser, J. Phys. C: Solid State Phys. **10**, 1887 (1977)
30. U. Schwarz, D. Olguin, A. Cantarero, M. Hanfland, K. Syassen, Phys. Stat. Sol. (b) **244**, 244 (2007)
31. S.-R. Zhang, S.-F. Zhu, B.-J. Zhao, L.-H. Xie, K.-H. Song, Phys. B **436**, 188 (2014)
32. L. Ghalouci, B. Benbahi, S. Hiadsi, B. Abidri, G. Vergoten, F. Ghalouci, Comput. Mater. Sci. **67**, 73 (2013)
33. L. Plucinski, R.L. Johnson, B.J. Kowalski, K. Kopalko, B.A. Orlowski, Z.D. Kovalyuk, G.V. Lashkarev, Phys. Rev. B **68**, 125304 (2003)
34. R. Le Toullec, N. Piccioli, J.C. Chervin, Physical Review B **22**, 6162 (1980)
35. N.E. Christensen, High pressure in semiconductors physics, in *Semiconductors and Semimetals,* vol. 54, ed. by E.R. Webber R.K. Willardson (Academic Press, New York, 1998), p. 40
36. K.J. Chang, S. Froyen, M.L. Cohen, Solid State Commun. **50**, 105 (1984)
37. M. Kizilyalli, M. Bilgin, A. Usanmaz, J. Solid State Chem. **80**, 75 (1989)
38. D. Errandonea, A. Segura, F.J. Manjyn, A. Chevy, E. Machado, G. Tobias, P. Ordejyn, E. Canadell, Phys. Rev. B **71**, 125206 (2005)
39. Z. Dong-Wen, J. Feng-Tao, Y. Jian-Min, Chin. Phys. Lett. **23**, 1876 (2006)
40. S. Nagell, A. Baldereschi, K. Maschke, J. Phys. C: Solid State Phys. **12**, 1625 (1979)
41. Y. Fan, T. Schittkowski, M. Bauer, L. Kador, K.R. Allakhverdiev, EYu. Salaev, J. Lumin. **98**, 7 (2002)
42. A. Ates, M. Yildirim, B. Gurbulak, Opt. Mater. **28**, 488 (2006)
43. T.S. Moss, G.J. Burrell, B. Ellis, in *Semiconductor Opto-electronics*, vol. 67 (Butterworths, London, 1973)
44. N. Kuroda, O. Ueno, Y. Nishina, J. Phys. Soc. Jpn. **55**, 581 (1986)
45. M. Gauthier, A. Polian, J.M. Besson, A. Chevy, Phys. Rev. B **40**, 3837 (1989)
46. J.F. Sanchez-Royo, A. Segura, A. Chevy, L. Roa, J. Appl. Phys. **79**, 204 (1996)
47. V. Capozzi, Phys. Rev. B **23**, 836 (1981)
48. F. Urbach, Phys. Rev. **92**, 1324 (1953)
49. M. Schreiber, Phys. Rev. B **34**, 2914 (1986)
50. V.P. Gribkovskii, *Theory of Absorption and Emission of Light in Semiconductors* (Science and Technology, Minsk, 1975)
51. I. Gnatenko, M. Kurik, Fizika I tekhnika poluprovodnikov **5**, 1347 (1971)
52. H. Mahr, Ultraviolet. Phys. Rev. **125**, 1510 (1962)
53. S.I. Boldish, W.B. White, Am. Mineral. **83**, 865 (1998)
54. J. Tauc (ed.), *Amorphous and Liquid Semiconductors* (Plenum Press, New York, 1974), p. 444
55. R.K. Swank, Phys. Rev. **153**, 844 (1967)
56. T. Aono, K. Kase, Solid State Commun. **81**, 303 (1992)
57. Zh. Pankove, in *Optical Processes in Semiconductors* (Mir, Moscow, 1973)
58. K. Wei, H.F. Pollak, J.L. Freeouf, D. Shvydka, A.D. Compaan, J. Appl. Phys. **85**, 7418 (1999)

59. E. Doni, R. Girlanda, V. Grasso, A. Balzarotti, M. Piacentini, Il Nuovo Cimento B **51**, 154 (1979)
60. V. Riede, H. Neumann, H.X. Nguyen, H. Sobotta, F. Levy, Physica **100B**, 355 (1980)
61. N.B. Mustafaev, N.B. Mustafaev, Thin Solid Films **324**, 159 (1998)
62. S. Shigetomi, K. Sakai, T. Ikari, Phys. Stat. Sol. (b) **241**, 2607 (2004)
63. T. Siciliano, M. Tepore, A. Genga, G. Micocci, M. Siciliano, A. Tepore, Vacuum **92**, 65 (2013)
64. A.M. Kulibekov, H.P. Olijnyk, A.P. Jephcoat, Z.Y. Salaeva, S. Onari, K.R. Allakhverdiev, Phys. Stat. Sol. (b) **235**, 517 (2003)
65. E. Filippo, M. Siciliano, A. Genga, G. Micocci, A. Tepore, T. Siciliano, Mater. Res. Bull. **48**, 1741 (2013)
66. A. Mercier, J.P. Voitchovsky, Solid State Commun. **14**, 757 (1974)
67. N.M. Gasanly, A. Aydinli, H. Ozkan, C. Kocabas, Solid State Commun. **116**, 147 (2000)
68. J. Camassel, P. Merle, H. Mathieu, A. Chevy, Phys. Rev. B **17**, 4718 (1978)
69. S. Shigetomi, T. Ikari, Jpn. J. Appl. Phys. **41**, 5565 (2002)
70. V.N. Katerinchuk, M.Z. Kovalyuk, Tech. Phys. Lett. **25**, 54 (1999)
71. C. Rocha Leao, V. Lordi, Physical review b **84**, 165206 (2011)
72. P.M. Reshmi, A.G. Kunjomana, K.A. Chandrasekharan, M. Meena, C.K. Mahadevan, Int. J. Soft Comput. Eng. **1**, 228 (2011)
73. A. Yamamoto, A. Syouji, T. Goto, E. Kulatov, K. Ohno, Y. Kawazoe, K. Uchida, N. Miura, Phys. Rev. B **64**, 035210 (2001)
74. W.W. Wendlandt, H.G. Hecht (ed.), Reflectance Spectroscopy (Wiley Interscience, New York, 1966), p. 298
75. B.J. Feldman, J.L. Boone, T. Van Doren, Appl. Phys. Lett. **38**, 703 (1981)
76. S. Jandl, J.L. Brebner, B.M. Powell, Phys. Rev. B **13**, 686 (1976)
77. J.C.J.M. Terhell, Prog. Cryst. Growth Charact. **7**, 55 (1983)

Chapter 13
Photoluminescence of Nanocomposites Obtained by Heat Treatment of *GaS*, *GaSe*, *GaTe* and *InSe* Single Crystals in *Cd* and *Zn* Vapor

Igor Evtodiev, Iuliana Caraman, Valeriu Kantser, Dumitru Untila, Irina Rotaru, Liliana Dmitroglo, Silvia Evtodiev and Mihail Caraman

Abstract The photoluminescence (PL) spectra of *GaS*, *GaSe*, *GaTe* and *InSe* semiconductors used as the basis materials to obtain nanocomposite by heat treatment in *Zn* and *Cd* vapor were studied. The PL spectra of *ZnS–GaS*, *CdSe–GaSe*, *CdSe–InSe*, *ZnSe–InSe* composites consist of wide bands covering a wide range of wavelengths in the antistokes region for *CdSe*, *ZnSe* and *GaS* crystallites from composites. The antistokes branches of spectra are interpreted as the shift of PL bands to high energies for nanosized crystallites.

13.1 Introduction

The material composed of semiconductor nanocrystallites of $A^{III}B^{VI}$ and $A^{II}B^{VI}$ type is obtained by heat treatment in the range temperatures of 623–1073 K of *GaS*, *GaSe*, *GaTe* and *InSe* single crystals in *Cd* and *Zn* vapor [1–3]. The *Ga*, *In*, *Zn* and *Cd* chalcogenides are luminescent materials in the wavelength range from UV to NIR. The photoluminescence spectrum of undoped *GaS* crystals at low temperatures ($T < 100$ K) contains a low intensity band localized in the region of indirect optical transitions. The structure of these bands is determined by the radiative

I. Evtodiev · V. Kantser · D. Untila · I. Rotaru · L. Dmitroglo · S. Evtodiev · M. Caraman
Laboratory of Photonics and Physical Metrology, Department of Physics and Engineering, Moldova State University, Chisinau, Moldova

I. Caraman
"Vasile Alecsandri" University of Bacau, Bacau, Romania

I. Evtodiev (✉) · V. Kantser · D. Untila
Institute of Electronic Engineering and Nanotechnologies "D. Ghitu", Academy of Sciences of Moldova, Chisinau, Moldova
e-mail: ievtodiev@yahoo.com

S. Evtodiev
University of European Political and Economical Studies "Constantin Stere", Stefan cel Mare si Sfint bd 200, MD-2004 Chisinau, Moldova

© Springer International Publishing Switzerland 2016

I. Tiginyanu et al. (eds.), *Nanostructures and Thin Films for Multifunctional Applications*, NanoScience and Technology,
DOI 10.1007/978-3-319-30198-3_13

annihilation of indirect exciton through phonons with the energy of 10 meV [4–6]. The intensity of impurity band with maximum at energy 1.24 eV prevails in the PL spectrum of *GaS* single crystals. The energy of the impurity PL band depends on the growth technology of the single crystal and the nature of structural defects and uncontrollable impurities. The *Mn*, *Zn* and *P* dopants form levels of self recombination in the bandgap that lead to the formation of intense PL bands with maximum at energies respectively of 2.00, 2.20 and 2.12 eV [6–8].

The PL spectra of *GaSe*, *GaTe* and *InSe* single crystals have a structure with one or two bands [9–12]. One of these bands corresponds to radiative annihilation of free or bound excitons with phonon repetitions and the other band is determined by the structural defects of crystal and impurities and the nature of uncontrollable dopants.

The copper as the dopant in concentrations from 0.1 to 1.0 mol% forms two donor levels with energies of ~195 and 445 meV in the bandgap of the *GaSe* from the minimum of the conduction band in the center of Brillouin zone and four acceptor levels that energies are respectively 31, 51, 93 and 152 meV. The PL band is formed in the energy range of 1.6–2.0 eV with maximum at about 1.9 eV as the result of donor-acceptor recombination [13, 14]. The large PL bands are contained in the spectra of *GaSe* crystals doped with *Zn* [15].

The elements of group III (*Ga*) and VI (*Te*) form deep acceptor levels (175 meV) and donor levels with low energies respectively of 20 and 80 meV [16]. Acceptor levels that energy is in the range of 18–173 meV are formed in the bandgap of the *GaSe* compound by the elements from transition metal group like *Mn* and *Cr* [17–19].

The amount of *Cd* up to 1.0 mol% forms an impurity band with maximum at 1.21 eV with thermal activation energy of 0.17 eV in the PL spectrum of *InSe* crystals. The *Se* vacancies form a complex PL band with maximum at 1.31 eV. The intensity of this band depends on the granulation degree of *InSe* plate surface [19].

The $A^{II}B^{VI}$ semiconductors (*ZnS*, *ZnSe*, *CdS*, *CdSe*, *CdTe*) are luminescent materials in a wide range of wavelengths [20–22]. The PL and absorption bands of these materials as nanoparticules are shifted to higher energies when the size of crystallites decrease. It is experimentally established that the efficiency of PL increase when the size of these materials is reduced to nanometric dimensions. That's why these materials are widely used in the VIS region of the spectrum for PL devices [23].

The photoluminescence (PL) of nanocomposites obtained by heat treatment of *GaS*, *GaSe*, *GaTe* and *InSe* single crystals in *Zn* and *Cd* vapor is studied in this work.

13.2 Photoluminescence of Nanocomposites with *GaS* Lamellar Semiconductors

13.2.1 Undoped GaS *and* GaS *Doped with* Mn

The *GaS* is a lamellar semiconductor with indirect bandgap of 2.55 eV ($T = 293$ K) is considered a promising material for optoelectronic devices in visible and UV region of the spectrum [7, 24, 25]. The direct electronic transitions and indirect electronic

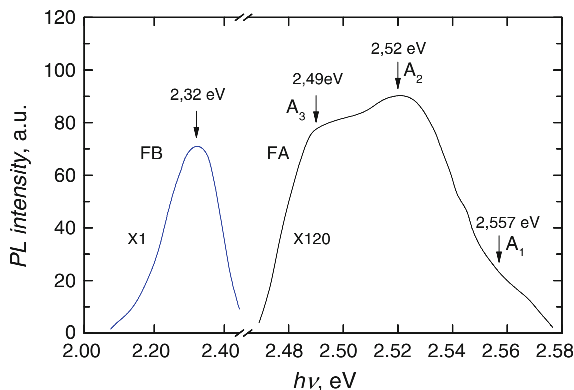

Fig. 13.1 The PL spectrum of *GaS* lamella at $T = 80$ K

transitions (in the photoluminescence, photoconductibility and absorption spectra) at $T = 293$ K are allowed at energies higher than 3.0 eV. The photoluminescence (PL) spectrum of the *GaS* blades at $T = 80$ K consists of two bands A and B in the visible region (Fig. 13.1). It is known theat band A is formed by overlay of at least three bands with peaks at 2.557 eV (A_1), 2.520 eV (A_2) and 2.490 eV (A_3). The indirect free exciton emission band with maximum at energy of 2.571 eV is located near the fundamental absorption band edge [4, 26].

The process of luminescent emission at low temperatures as the result of indirect exciton annihilation is performed simultaneously with emission of phonons with the energy $\hbar\omega_f = 10$ meV [4]. The width of indirect bandgap at the temperature of 80 K for *GaS* crystals is equal to the sum of:

$$E_{gi} = E_{ex\,i} + R_{ex} + \hbar\omega_f, \tag{13.1}$$

where R_{ex}—is the energy of indirect free exciton binding.

It is obtained the value of $E_{gi} = 2.595$ eV for $E_{ex\,i} = 2.571$ eV and $R_{ex} = 14$ meV. The band A_1 (Fig. 13.1) can be interpreted as luminescencent recombination of localized indirect exciton with the binding energy of 14 meV.

The bands A_2 and A_3 with broad contour prevail as intence in blue region of the spectrum and it can be associated with donor–acceptor type recombination. These bands are shifted to lower energies from the emission band of indirect free excitons with the energy of 71 and 64 meV. The energies of these bands do not depend on the dopant presence, such as *Mn* [6], *Zn* [27], *Cu* [5] and are shifted from the line of indirect excitons to highest energies than fundamental optical phonons energy in the *β–GaS* crystals whose energies are equal to 36.6 meV (transverse optical phonon) and 44 meV (longitudinal optical vibrational mode) [28]. It is known that longitudinal optical phonons may not participate in the luminescence generation–recombination processes.

The pronounced thermal attenuation of A_1 and A_2 bands whose intensities at 120 K are at the measurements background level serve as indicator of their excitonic nature. Since the free indirect exciton emission band is located at 2.571 eV

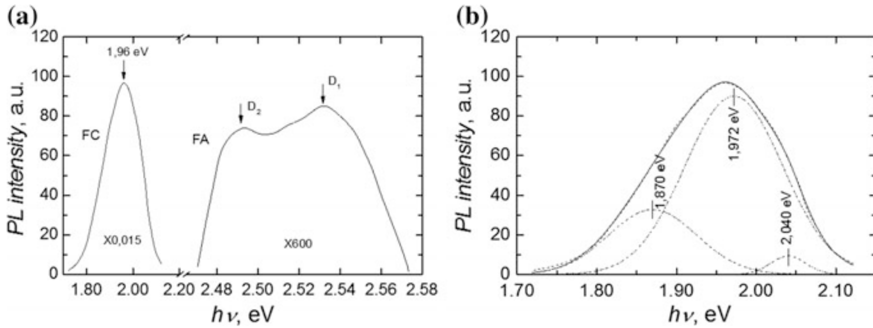

Fig. 13.2 The PL spectra at T = 80 K, of *GaS* lamella doped with 1.0 at.% *Mn* (**a**) and the deconvolution of C band in elementary bands (**b**)

and occurs with phonon emission of 7–10 meV result that the emission bands A_1 (2.557 eV), A_2 (2.520 eV) and A_3 (2.49 eV) may be considered as indirect exciton luminescence annihilation with phonons emission of energies respectively 21, 58 and 88 meV. Such phonon energies were obtained from absorption measurements of modulated light in electric field [29]. Since the binding energy of the indirect electron–hole exciton is ~14 meV, results that the cumulative donor and acceptor levels energy due to which photoluminescence emission bands in the blue region of the spectrum are formed is equal respectively to 65 meV (A_2) and 95 meV (A_3).

The band B with maximum at the energy of 2.32 eV (λ = 534 nm) is dominant in PL spectrum and as shown in Fig. 13.1 has a contour without fine structure which is characteristic for impurity bands [7, 27]. The energy of the band from the green spectrum region depends on the nature and concentration of impurities introduced by doping in the material. In the work of Belenkii and Godzhaev [4] from the analyses of the intensity dependence of the temperature and of the excitation intensity is concluded that this band is formed as donor–acceptor recombination. Further it will be analyzed the PL spectra of *GaS* single crystals doped with *Mn* in order to have additional information about the influence of impurities on the structure of PL spectrum.

The PL spectrum at T = 80 K of *GaS* single crystalline blade doped with 1.0 at. %. *Mn* is shown in Fig. 13.2. The luminescence was recorded from the surface (0 0 0 1). The presence of 1.0 at.% *Mn* leads to an attenuation of ~2 times of edge luminescence comparing to undoped *GaS* single crystals PL. The dopant (*Mn*) does not modify the structure of edge PL bands, but leads to attenuation to the background level of PL band from the green spectral region (band with maximum at 2.32 eV) as shown in Figs. 13.1 and 13.2. Instead of band B (Fig. 13.1) there is present a new intense PL band in the orange–red spectral region (band C). As shown in Figs. 13.1 and 13.2 the intensity of the band C is at least 90 times greater than the impurity band B. The contour of C band at T = 80 K can be decomposed into three elementary Gaussian bands with the maximum energies respectively at 1.870, 1.972 and 2.040 eV.

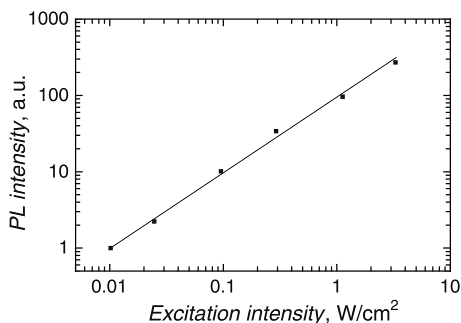

Fig. 13.3 The PL intensity dependence on excitation with radiation of λ = 337.1 nm at T = 80 K

In Fig. 13.3 is presented the PL intensity variation at the temperature 80 K as function of the excitation intensity with the radiation of λ = 337.1 nm. PL intensity increases linearly with the excitation intensity and satisfy the requirement of monomolecular kinetics [30] characteristic for luminescence centers. It is believed that this band is obtained as a result of electronic transitions in centers of acceptor–vacancy type complexes [5] from analysis of C band contour and PL intensity of temperature.

13.2.2 GaS *Intercalated with* Zn *from Vapor Phase*

The *GaS* single crystal blades intercalated with *Zn* at 753 K leads to changes in the structure of PL spectrum at 80 K. A narrow PL band with maximum at 2.84 eV, a band of low intensity with maximum at 2.48 eV and a intense dominant band with maximum at 2.12 eV is present in the region of the edge of fundamental absorption band of *GaS* crystals as shown in Fig. 13.4. The intercalation of *Zn* atoms between *S–Ga–Ga–S* packages leads to attenuation of the band with maximum of intensity at 2.32 eV.

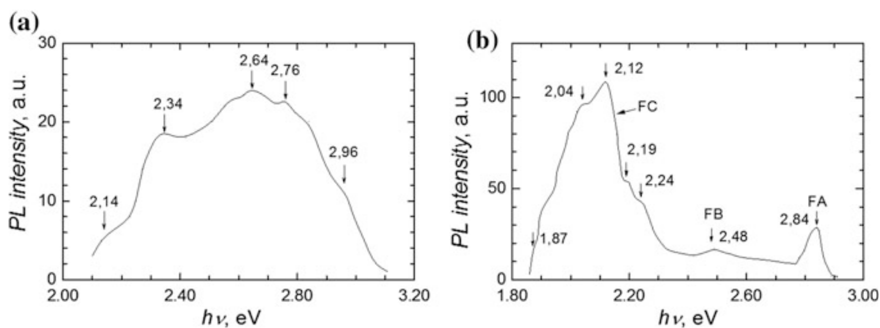

Fig. 13.4 The PL spectra of *GaS* plates heat treated in *Zn* vapor at 753 K for 6 h at: 293 K (**a**) and 80 K (**b**)

The indirect width of bandgap in the undoped *GaS* semiconductor at the temperature of 77 K is equal to 2.591 eV [29]. Four indirect excitons emission bands with phonon emission with maximum intensity at 2570, 2.555, 2.534, 2.521 and 2.480 eV [27] are active in *GaS* doped with *Zn* at T = 77 K. As was discussed above, the PL bands at 2.521 and 2.555 eV are also active in the PL spectra of undoped *GaS* single crystals. At the same time, in the crystals doped with *Zn* in an amount of ~1.0 at.% there is formed a band with dominant intensity in the region of 1.6–2.2 eV and the maximum at 1.85 eV [27].

As is shown in Fig. 13.4 in the PL spectrum at T = 293 K of *GaS* blades intercalated with *Zn* is present a complex emission band located in the spectral region of 1.86–2.30 eV and maximum at ~2.12 eV. This band is composed of at least five sub-bands with peaks at ~2.24, 2.19, 2.12, 2.04 and 1.87 eV. Regarding the nature of the particularity at 1.87 eV [27] by measurements of PL intensity variation with temperature and excitation intensity demonstrates the emission mechanism of the center that consists of acceptor–vacancies complexes. The material composed of *ZnS* and *GaS* crystallites are formed as the result of intercalation of *Zn* atoms as was demonstrated by XRD measurements. Thus, the PL band with maximum at 2.84 eV is connected with the presence of *ZnS* crystallites. The structure of PL spectrum for *ZnS* crystals depends on the dopant nature and contains several emission bands that maxima depend on the dopant type.

The width of the direct band gap in *ZnS* crystals at T = 80 K is equal to 3.82 eV [31]. The PL spectrum of *ZnS* polycrystals contains a broad band that cover the energy range 2.2–3.0 eV which maximum varies function of the dopant. The maximum of PL band in *Ga*–doped *ZnS* crystals is located at 2.64 eV [32]. Thus, the PL band with maximum at 2.84 eV may be interpreted as a radiative recombination in *ZnS* crystallites from composite. The nature of 2.48 and 2.12 eV bands is related to the recombination processes in *GaS* crystals doped with *Zn*. The PL spectrum of *GaS* crystals doped with *Zn* at 80–100 K is composed of two bands wit peaks at 2.47 and 2.17 eV. The *Ga* vacancies forme three acceptor levels in *GaS* crystals. These vacancies electricaly are in three ionization states V_{Ga}^{+2}, V_{Ga}^{+1} and V_{Ga}^{0}. The *Zn* atoms substitute the *Ga* vacancies in the Zn^{-1} and Zn^{0} states to keep electrical neutrality. The emission band with maximum at energy of 2.47 eV in the work of Aono [8] is considered as electronic transition in the complex of *Zn* located in vacancy V_{Ga}^{+2}–donor.

The PL emission band with maximum at the energy of 2.12 eV can be considered as radiative emission of the V_{Ga}^{+2} donor complex—*Zn* acceptor in *GaS* crystals. The substitution of *Ga* vacancy with *Zn* leads to the formation of *Zn–S* chemical bond within layered package. At the same time, zinc intercalated between the chalcogenide planes (*S*) of two layered packages at sufficient temperatures forms the valence bond with *S* atoms. Thus, by intercalation of *GaS* with *Zn* from vapor phase are obtained two kinds of luminescent centers one within *S–Ga–Ga–S* elementary packages and other between them.

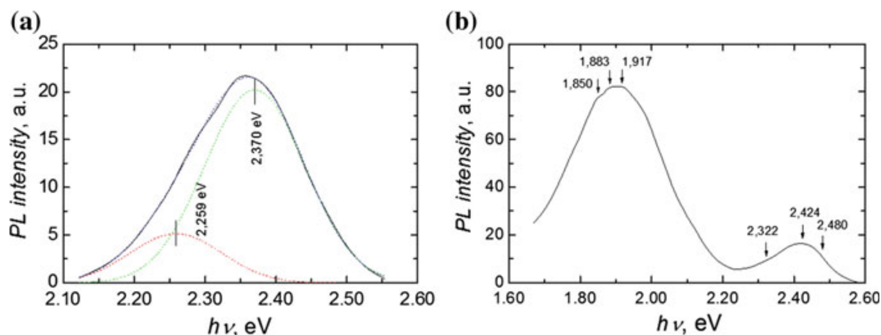

Fig. 13.5 The PL specterum of *GaS* plates heat treated at 753 K in *Cd* vapor for 6 h at: 293 K (**a**) and 80 K (**b**)

13.2.3 GaS *Intercalated with* Cd *from Vapor Phase*

The PL spectra at the temperature of 293 K (a) and 80 K (b) of *GaS* single crystalline plates intercalated with *Cd* from the vapor phase at 753 K for 6 h are shown in Fig. 13.5. The PL spectrum at $T = 293$ K is formed by overlapping of two bands with peaks at 2.590 and 2.370 eV. The dominant PL maximum is localized at energy ~50 meV lower than the width of direct bandgap of *CdS* compound that is equal to 2.42 eV [33] and it is much smaller than the width of direct bandgap in *GaS*. The resulting PL emission band has no analogue in the PL spectrum of the *GaS* semiconductor. So, we can regard that complex PL band with maximum at the energy of 2.37 eV of *GaS–CdS* micro- and nano-crystalline composite is determined by luminescencent transitions through recombination levels of *CdS* crystallites from composite.

13.3 Photoluminescence of Nanocomposites with *GaSe* Lamellar Semiconductors

The *GaSe* in single crystalline state is among the first materials of chalcogenides class in which has been demonstrated the stimulated emission effect at excitation with accelerated electrons beam [34]. The photoluminescencent emission spectrum from the (0 0 0 1) surface of the *GaSe* single crystalline lamella at the room temperature shown in Fig. 13.6 is obtained by two bands overlaying “A” and “B” with maximum respectively at 2.000 and 1.930 eV.

The binding energy of the electron–hole pair (excitonic Rydberg) is 22 meV. This size is smaller than the thermal energy at room temperature (25 meV). The excitons are strongly ionised at room temperature. During the formation of the edge of the absorption band in *GaSe* crystals at T = 293 K together with the direct

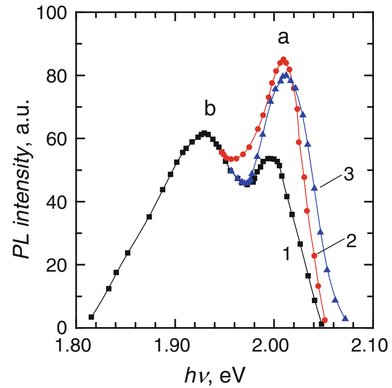

Fig. 13.6 The PL spectra at T = 293 K of *GaSe* lamella: experimental curve (*curve 1*), experimental curve with absorption correction (*curve 2*) and curve calculated from absorption and Van Roosbroeck-Shockley theory (*curve 3*)

transitions (band–band) the transitions with excitons formation take place. The last mechanism is even less probable as the sample temperature is higher. Since the maximum of band "a" (Fig. 13.6) at T = 293 K well correlates with the peak of edge absorption coefficient as well as the broad contour of the band leads to the conclusion that the basic mechanism of its formation is band to band recombination in the center of Brillouin zone.

The growth rate of the absorption coefficient in the edge region of the fundamental absorption band of *GaSe* single crystals at T = 300 and 80 K is $\sim 3 \times 10^4$ cm^{-1} eV^{-1}. It was calculated the luminescence spectral dependence of the band "a" (Fig. 13.6) considering this variation of the edge absorption coefficient in the edge absorption band region.

The intensity of PL band—I_{PL} band is proportional to radiative recombination velocity R which according to Van Roosbroeck–Shockley theory is expressed by the next equality [35]:

$$R = 1.785 \times 10^{22} \left(\frac{T}{300}\right)^4 \int_{u_0}^{\infty} \frac{n^3 \chi u^3 du}{e^u - 1}, \tag{13.2}$$

where n is the refractive index of the luminescent environment; χ–extinction coefficient; $u = \frac{h\nu}{kT}$; ν–radiation frequency with $u_0 = \frac{E_g}{kT}$.

The PL maximum of "a" band is shifted with $\sim$2–10 meV to higher energies from the maximum of experimental band as it is shown in Fig. 13.6. The difference between the wing of PL band (Fig. 13.6, curve 2) and those calculated using Van Roosbroeck–Shockley theory (Fig. 13.6, curve 3) [36] is determined by the presence of excitonic continuum in this spectral region. The good correlation between curves 2 and 3 at energies $h\nu < 2.05$ eV (Fig. 13.6) indicates that the PL emission band "a" with maximum at the energy of 2.00 eV is obtained as a result of nonequilibrium thermalized charge carrier recombination from the conduction band (CB) with holes from the valence band (VB) in the center of the Brillouin zone.

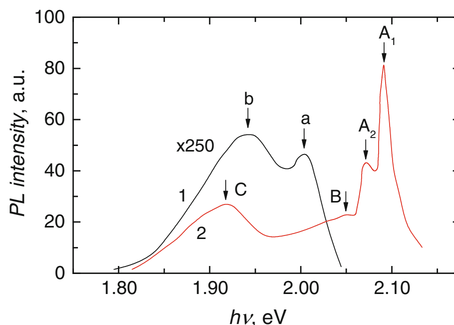

Fig. 13.7 The PL spectra of *GaSe* crystals at $T = 293$ K (*curve 1*) and 80 K (*curve 2*)

The PL band with maximum at the energy of 1.930 eV is determined by the presence of structural defects and uncontrollable impurities in *GaSe* crystals.

The edge of PL band of *GaSe* lamella shifts to higher energies and the complete restructuration taking place in PL spectrum (Fig. 13.7) when the temperature of sample decrease from 293 to 80 K.

Two narrow bands (A_1 and A_2) with maximum at the energy respectively of 2.092, 2.072 eV and a plateau C with maximum at energy 1.920 eV are present in the edge region of absorption band. The band A_1 at the temperature of 80 K is shifted by $\sim$6 meV toward low energies from the absorption line of free excitons in state n = 1. This shift is much smaller than the energy of phonons that are active in photoluminescence emission (15 meV) [12]. It can be considered that the band A_1 is obtained as a result of luminescent annihilation of direct exciton in n = 1 state localized at the acceptor with binding energy of 6 meV. The band B that is shifted by 20 meV from the band A can be considered as phononic repetition of line A of localized direct excitons.

The phonon with the energy of $\sim$20 meV is emitted in the emission process of B band. Note that the phonon with energy of $\sim$18.8 meV corresponds to the vibration of *Se–Ga–Ga–Se* packages one to another [37]. The elemental cell of ε-*GaSe* modification consists of three elementary packings that are displaced one from each other by 1/3 *a* [38]. The plateau C (2.050 eV) in Capozzi and Minafra [12] is interpreted as luminescent emission of indirect exciton in the M point of Brillouin zone with the emission of phonon with the energy of 13 meV.

The band B with maximum at the energy of 1.920 eV is highlighted in the PL spectra at low excitation intensities of undoped *GaSe* crystals. The relative intensity of this PL band depends on the temperature as an exponential function of the $I_{FL} \sim exp\frac{\Delta E}{kT}$ type. At the same time, the intensity of B band depends on the dopants and increases with the *Cu* concentration and it is interpreted as radiative electron transition in the VB from the deep donor level with energy 1.92 meV from the CB.

The PL spectrum of the *CdSe* polycrystalline compound at 300 and 78 K consists of the intense band with maximum in the edge region of absorption band (Fig. 13.8). As shown in Fig. 13.8, curve a, the maximum of PL band of *CdSe* compound at $T = 293$ K is situated at the energy of 1.72 eV. This result well

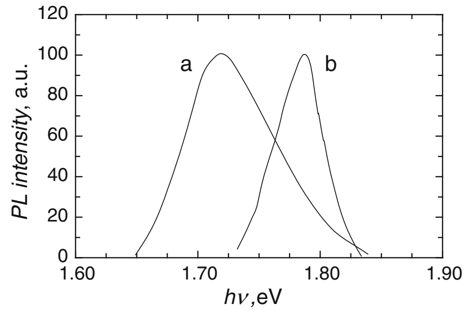

Fig. 13.8 The PL spectra of *CdSe* compound at 293 K (*curve a*) and 80 K (*curve b*)

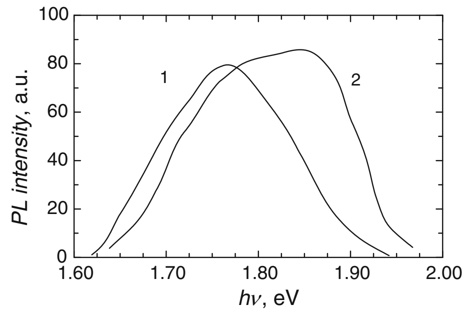

Fig. 13.9 The PL spectra of *GaSe–CdSe* composite obtained by *GaSe* plates heat treated at 833 K in *Cd* vapor for 20 h at: 293 K (*curve 1*) and 80 K (*curve 2*)

correlates with PL spectrum from the surface of the *GaSe* that was heat treated in *Cd* vapor (Fig. 13.9, curve a). Additional information on the composition of the formations on the *GaSe* plates surface that was heat treated in *Cd* vapor (*GaSe–CdSe* composite) can be obtained from the analysis of PL spectra at the temperature of 293 and 80 K (Fig. 13.9). The photoluminescence was excited by radiation of N_2 laser (λ = 337.4 nm) with energy of 3.67 eV.

As can be seen from the comparison of Figs. 13.8 and 13.9, the PL spectrum of composite at room temperature contains the PL spectrum of the *CdSe* compound and two bands, one at $\sim$1.65 eV with low intensity and the second more intense with a maximum in the region of 1.80 eV. The decreasing of the intensities of component bands occurs when the intensity of the emission band of *CdSe* crystallites from composite increasing. The nature of bands at 1.65 and 1.80 eV is probably determined by restructuration of diagram of recombination levels in the *GaSe* crystallites as result of crystal micro-structuration and the formation of new luminescencent recombination levels. The PL spectrum of *CdSe–GaSe* composite obtained at 853 K (Fig. 13.10) can be decomposed into four Gaussian curves with maxima at energies 1.78 eV (A), 1.73 eV (B), 1.71 eV (C) and 1.68 eV (D).

The probability of excitons formation is small and respectively their contribution to the formation of PL emission band at room temperature is small. Thus, the curves B and C can be caused respectively by band to band recombination and recombination that involve low energy acceptors ($\sim$20 meV) from VB in *CdSe*. The A

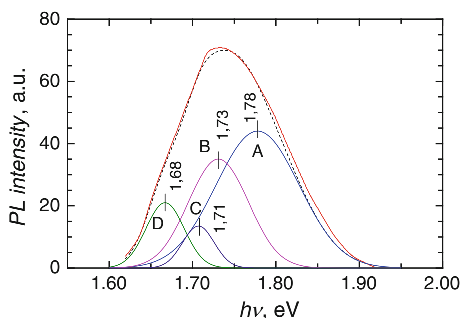

Fig. 13.10 The PL spectrum at 293 K of *GaSe–CdSe* composite obtained by heat treatment at 853 K of *GaSe* plates in *Cd* vapor

band having lower energy than the width of bandgap in *CdSe* semiconductor allows to admit that it is donor–acceptor type recombination in *GaSe* crystallites. It is known that as a result of the heat treatment at the temperature of ~800 K and higher in *GaSe* crystals are formed structural defects by the accumulation of *Se* atoms between elementary *Se–Ga–Ga–Se* packages and creates *Se* vacancies in their atomic planes. These defects form deep acceptor levels that are located at 0.45 eV from VB. The CB–deep acceptor recombination in the *GaSe* crystallites of the composite may cause the luminescence in the region of D curve. The forming process of the *CdSe–GaSe* composite occurs with *Ga–Se* bonds breaking. The *Ga* atoms at heat treatment temperature of ~853 K are doping the new formed *CdSe* crystallites and *GaSe* crystallites. The *Ga* atoms interstitially arranged form deep donor levels [16] and PL band A is obtained as a result of transition from this donor level on the acceptor level in *GaSe*.

The PL edge band at T = 80 K of *CdSe–GaSe* composite obtained by *GaSe* plates that was heat treated at 853 K in *Cd* vapor is formed by the band "a" (Fig. 13.11) with maximum at the evergy of 1.880 eV. The PL band with maximum at the energy of 1.870 eV were found in the PL spectra of undoped *GaSe* crystals and in PL spectrum of *GaSe* crystals doped with ~10^{18} cm^{-3} of copper there are highlighted lines with maximum at 1.870 and 1.890 eV [12]. The *Cd* as a dopant in small amounts forms in the bandgap of *GaSe* crystals acceptor levels with energy from 0.26 to 0.30 eV from VB. Since the band "a" from Fig. 13.11 is found at the

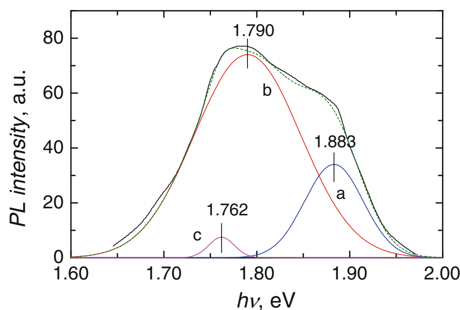

Fig. 13.11 The PL spectrum at T = 80 K of *GaSe–CdSe* composite obtained by *GaSe* plates heat treatment at 853 K in *Cd* vapor

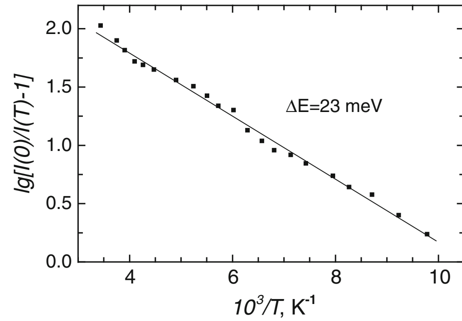

Fig. 13.12 The energy of PL thermal activation for *GaSe* lamella intercalated with *Cd*

energy greater than the width of bandgap in *CdSe* at $T = 80$ K, it can be obtained as a result of nonequilibrium radiative transition of electrons from CB to the acceptor level with the energy of 0.24 eV from VB of *GaSe* crystallites from composite.

The intensity of PL band with the maximum at 1.790 eV decreases monotonous when the temperature of intercalation process of *GaSe* with *Cd* from 80 to 293 K. The dependence of PL intensity (I_{PL}) on temperature in the temperatures range of 78–293 K as shown in Fig. 13.12 is well described by the expression [39]:

$$I_L = \frac{I_0}{1 + A\exp\left[-\frac{E_T}{kT}\right]}, \tag{13.3}$$

where I_0 is the PL intensity extrapolated to 0 K, E_T–PL thermal activation energy, A–the ratio of the probabilities of emisional and non–emisional transitions, k–Boltzmann constant.

There is observed a good coincidence of the respective bands maxima at 78 and 293 K by comparing the PL spectra of *GaSe* crystals intercalated with *Cd* at 823 K for 6 and 24 h. At the same time, the PL bands of both primary *GaSe* crystals and *Cd* intercalated *GaSe* crystals are identical at high energies. So we can admit that *Cd* atoms in vapor phase at 823–853 K probably intercalate between *Se* atoms planes within *Se–Ga–Ga–Se* layered packages and forming *CdSe* layers. This conclusion is argued and by the fact that at doping with *Cd* (concentration of 0.01–0.10 at.%) in the synthesis process of *GaSe*, the *Cd* atoms form deep acceptor levels at 0.26–0.28 eV [40]. Thermal activation energy of impurity bands present in luminescent emission spectra of *GaSe* crystals doped with *Cd* also has a magnitude of hundreds meV (130–370 meV) [41]. At thermal quenching of photoluminescence of *GaSe* intercalated with *Cd* is obtained the activation energy of 23 meV.

Much more pronounced highlights the complex structure of PL spectrum at 80 K (Fig. 13.9). The spectrum of *CdSe–GaSe* micro-composite at this temperature contains edge emission band of *CdSe* crystallites with the maximum at the energy of 1.79 eV, a medium intensity band in the energy range of 1.65–1.75 eV and a band localized at higher energy with maximum in the range of 1.85–1.95 eV. The intensity of PL band localized at higher energies increase and the intensity of the band localized at lower energies than PL band of *CdSe* crystallites decreases when

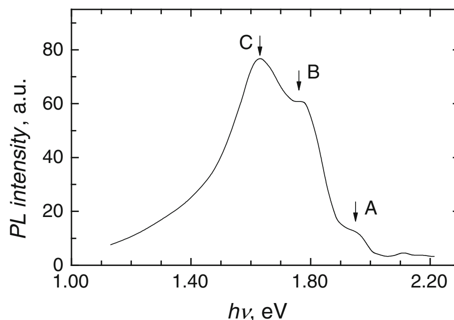

Fig. 13.13 The PL spectrum at T = 78 K of *GaSe* crystals doped with 0.05 at.% *Cd*

the temperature of heat treatment decrease from 883 to 853 K. This dynamic of the structure of PL spectra can be explained if we admit that the PL band from high energy region is determined by radiative processes in *GaSe* crystallites probably doped with *Cd* and *Ga* from composite.

It is known [41] that by *Cd* doping of *GaSe* crystal in the concentrations range of 0.05–0.10 at.% the PL spectrum suffers cardinal changes. If in undoped *GaSe* crystals the PL spectrum contains direct exciton annihilation line in the state n = 1 by 2.10 eV energy band emission and LO phonon repetition of indirect luminescent recombination from CB in point M of Brillouin zone, then 0.01 at.% concentrations of *Cd* atoms in *GaSe* occurs the attenuation of edge line intensity and formation of two other bands. In the PL spectrum of the *GaSe*: 0.01 at.% *Cd* compound is present a dominant band with maximum at energy 1.95 eV and a much smaller intensity band with maximum at 1.60–1.65 eV. The intensity of this band increases when the concentration of the dopant increase and at 0.10 at.% concentration it becomes the dominant band. The PL spectrum contains three bands: a low intensity band (A) with peak at the energy of 1.95 eV and two intense bands with maxima at 1.75 eV (B) and 1.62 eV (C) for *Cd* atoms concentration of 0.05 at.% in *GaSe*. The wing of C band covers the range of energies up to ~1.1 eV (Fig. 13.13) [41].

Note that the PL emission bands at T = 80 K are also obtained in *GaSe* crystals doped with 0.05 at.% *Ag* [42]. The excess of *Ga* atoms form deep donor and acceptor levels in the *GaSe* semiconductor band gap. Through 0.152 eV acceptor level and 0.175 eV donor level occurs the donor–acceptor band PL emission with maximum at 1.77 eV [16]. As shown in Fig. 13.11, the PL spectrum of the *GaSe*–*CdSe* composite obtained by *GaSe* plates treatment in *Cd* vapor at 853 K, well decompose in three Gaussian curves (a, b, and c) with maxima at energies respectively 1.883, 1.790 and 1.762 eV.

Good coincidence of the PL spectrum at 80 K of *CdSe* compound (Fig. 13.8a) with the curve *b* with the maximum at the energy of 1.790 eV from Fig. 13.11 it is an additional confirmation of the presence of *CdSe* crystallites in the composite. The *c* curve from Fig. 13.11 correlates well energetically with the luminescent emission band present in *GaSe* crystals doped with 0.05 at.% *Cd* (Fig. 13.13). The presence of band in the PL spectrum is determined by a certain concentration of *Cd* atoms in the sample because at *Cd* concentrations of 0.01 and 0.10 at.% this band is

missing [41]. The nature of C band finds interpretation if we admit that in *Cd* doped *GaSe* crystals at the same time with two acceptor levels localized at 0.10–0.13 eV from VB there is formed a donor level at 0.36 eV from CB. The luminescence emission band with maximum at 1.762 eV is obtained as a result of electrons transition in VB from the donor level with energy of 0.36 eV from CB.

The treatment temperature and its duration are the factors that determine the size of the *CdSe* crystallites, both on the outer surface and at the interface between the *Se–Ga–Ga–Se* elementary packages. The modification of PL spectra function of these two technological parameters will be analysed. In Fig. 13.14a, b are presented PL spectra at the temperature of respectively 293 and 80 K for the *GaSe–CdSe* composite obtained by heat treatment of *GaSe* plates in *Cd* vapor at 793 K for 6 h. The PL spectra at 293 K of the composites obtained respectively at the temperature of 853 and 793 K have identical form as it was shown in Figs. 13.14a and 13.9. Thus the material composition and the diagram of energy levels through which the radiative electronic transitions occur does not substantially changes at the reduction of heat treatment temperature of $\sim$60 K and the length of the process from 24 to 6 h.

More pronounced differencies are present between PL spectra measured at 80 K (Fig. 13.14b). As shown in Fig. 13.14b the PL spectrum at T = 80 K is composed of an intense band (A) with the maximum at $\sim$1.837 eV and a low intensity structured band (B) in the region of 2.1–2.8 eV with the maximum of intensity at the energy of 2.478 eV. The band A can be decomposed into two Gaussian curves with a maxima at 1.76 and 1.85 eV. The band with maximum at the energy of 1.76 eV is present in the PL spectrum of *GaSe–CdSe* composite obtained at the temperature of 853 K (Fig. 13.11, curve c).

The PL band (Fig. 13.14b, the curve B) covers a wide range of energies and it can be decomposed into four elementary curves (Gaussian) with the peaks at the energies of 2.300, 2.478, 2.660 and 2.776 eV. This PL band lies at higher energies than the width of bandgap of *GaSe* (2.120 eV) and *CdSe* (1.792 eV) crystallites. A qualitative interpretation of the nature of this band (Fig. 13.14b, the curve B) can be found if we admit that the composite contains both *GaSe* and *CdSe* crystallites with micro and nano dimensions. The presence of nanoparticles with sizes of

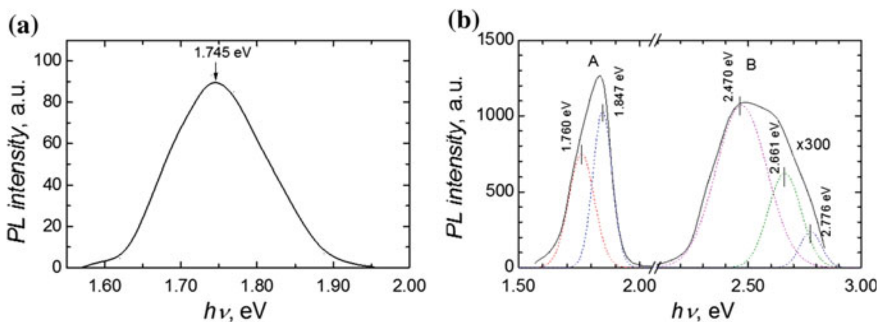

Fig. 13.14 The PL spectra of *GaSe–CdSe* composite obtained by *GaSe* plates heat treatment at 793 K in *Cd* vapor for 6 h at: 293 K (**a**) and 80 K (**b**)

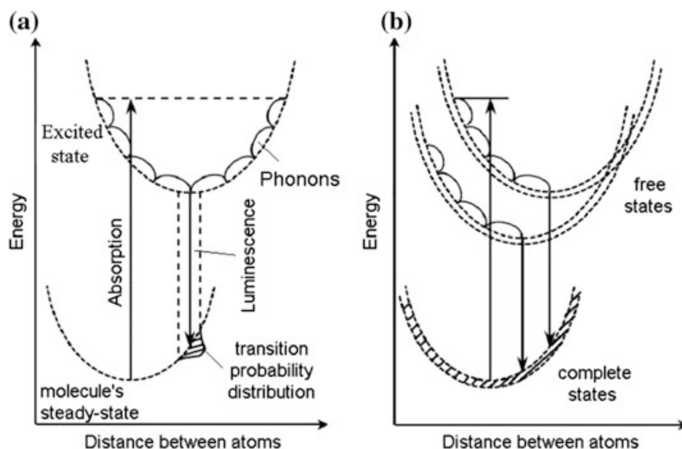

Fig. 13.15 The energetic diagram of diatomic molecule (**a**) and nanocrystal (**b**)

10–20 nm in researched *GaSe–CdSe* composites was demonstrated by XRD diffraction line contour analysis.

The PL spectrum of *CdSe* composites consisting of nanoparticles in various inorganic and organic solutions is shifted to the green region of the spectrum [43]. The PL spectrum of *CdSe* quantum dots with diameters in the range of 1.40–1.82 nm covers the energy range of 1.7–3.0 eV with broad peak at ~2.3 eV. The PL band maximum at $T = 293$ K for *CdSe* quantum dots varies in a wide range of energies 2.14–2.60 eV and it depends on the size of the nanoparticles (3.0–10.0 nm) [44]. However in Boatman [44] is mentioned that the PL intensity depends on obtaining technology of *CdSe* structures.

The *CdSe* nanoparticles into semiconductor matrix are promising materials for light sources in blue–green region of the spectrum with low excitation energy loss [45]. The *CdSe* quantum dots at excitation with photon energy of $h\nu \geq 3.0$ eV emit radiation in the green region of the spectrum. The emission band at $T = 80$ K PL shifts in the blue region of the spectrum (2.5–2.6 eV). The PL maxima of nanostructures based on nanoscale *CdSe* layers are effective violet radiation sources. The maximum of luminescence band of nano-structure with *CdSe* films on the *ZnSe* layer is at 2.57 eV [45].

The PL spectrum of *GaSe–CdSe* composite at both room and low temperature ($T = 80$ K) was excited with the radiation of N_2 laser ($\lambda = 337.4$ nm) with the energy of 3.67 eV and it is much higher than the energy of PL bands. The absorption spectra and simple contour of PL bands of nanometric composites are interpreted using the approximation of configurational diagrams [46] analogically with absorption and emission processes in molecules (luminescence centers in crystals) (Fig. 13.15a) and semiconductor nanocomposites (Fig. 13.15b).

The composite's PL bands contour shape finds explanation based on the Frank–Condon principle. The probability of electronic transitions $W_{v'v''}$ of *CdSe* molecule/quantum point from the excited state (n′v′) in the basic state (n″v″) is equal to the square of the overlap integral [47]:

$$W_{v'v''} = C\left|\int \psi'_{v'}(\rho)\psi''_{v''}(\rho)d\rho\right|^2, \tag{13.4}$$

where C is a constant, v' and v'' are the vibrational quantum numbers respectively of excited electronic state and the basic state, $\psi'_{v'}(\rho)$ and $\psi''_{v''}(\rho)$ are the vibrational wave functions of respectively the excited electronic state and the basic state of nanoparticles. Therefore, the PL subbands of the *GaSe–CdSe* composite with peaks at 2.32, 2.48 and 2.62 eV, can be obtained if we admit that as a result of the *GaSe* plates treatment in *Cd* vapor at 793 K temperature for 6 h are obtained the *CdSe* microcrystalline with PL spectrum of in the range of 1.79 eV and three types of *CdSe* nanocrystallites with sizes from units to tens of nm. We'll analyze the PL of *GaSe* plates that were heat treated in *Cd* vapor for 10–100 min. In Fig. 13.16 is shown the PL spectrum at T = 293 K (a) and 80 K (b) of the composite obtained by treatment at 823 K for 10 min. The PL spectrum at T = 293 K (Fig. 13.16a) is located at energies $h\nu \leq E_g$ (*GaSe*) and is composed of at least three bands with peaks at 1.99, 1.97 and ~1.95 eV. The PL band with maximum at 1.99 eV is obtained by overlay of PL spectra of electronic transitions from CB in the maximum of VB in the center of Brillouin and the emission band of direct excitons annihilation in *GaSe*. The particularity "a" finds interpretation as phonon repetition of the band of direct excitons with phonon emission that have the energy of ~20 meV. The particularity "b" may be associated to radiative emission at indirect electronic transitions (M–Γ) with phonon emission that has the energy of 15 meV. The contribution of phonon with the energy of 15 meV in the PL spectrum of *GaSe* compound it is demonstrated in several works including Abdullaev [48]. Two new particularities apears in the PL spectrum at T = 80 K (Fig. 13.16b)—one impurity

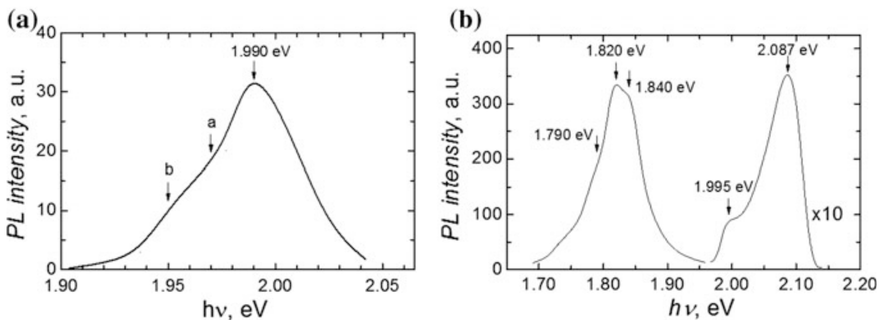

Fig. 13.16 The PL spectra of *GaSe* plates heat treated at 823 K in *Cd* vapor for 10 min at: T = 293 K (**a**) and 80 K (**b**)

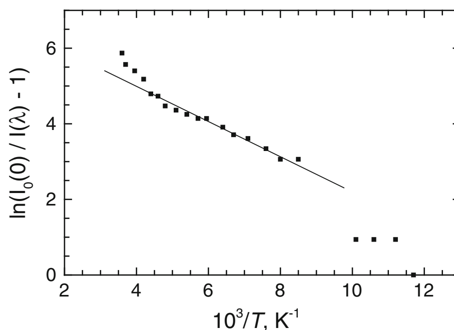

Fig. 13.17 Thermal quenching of PL band with maximum at the energy of 2.087 eV

band with absolute maximum at the energy of 1.820 eV and the edge band with maximum at 2.087 eV. The band with maximum at 2.087 eV can be interpreted as radiative emission of direct excitons located at ionized acceptor. The energy of acceptors that was formed by own structural defects in *GaSe* has values of ~0.11 and 0.13 eV while the energy range between the width of direct bandgap of *GaSe* at *T* = 80 K (2.120 eV) and the energy of the edge band (Fig. 13.16b) is only 33 meV. In order to interpret this band was studied the inverse temperature dependence of its intensity (Fig. 13.17).

From this graph can be well seen that thermal quenching of the band 2.087 eV is well described by function (13.3). Thermal activation energy at low temperatures (for 10^3/T in the range of 8–11) is equal to 55 meV, and in the average temperatures range of 125–250 K) the photoluminescence thermal activation energy is equal to 33 meV. It follows that the PL emission band with maximum at 2.087 eV is obtained as a result of electron transitions from CB on an acceptor level located at 33 meV from the CB in the center of Brillouin zone. The band at 1.955 eV [14] is associated to electronic transition CB–acceptor level with the energy of 0.093 eV and it is formed by *Cd* as dopant in *GaSe*. The structural defects and respectively acceptor and donor deep energy levels are formed by the heat treatment at high temperatures due to movements of elementary packages. Simultaneously with the formation of *CdSe* compound, the *Ga* atoms surplus is formed. A part of them forms metallic clusters and defects in *GaSe* crystallites lattice and probably *CdSe*. The *Ga* surplus in the work of Shigetomi [16] is assigned to the formation of donor level 0.175 eV and acceptor level 0.152 eV that are active in the process of luminescent recombination. Thus, the PL band from energies region of 1.840 eV is obtained as the result of donor–acceptor electronic transitions with the participation of donor level formed by the surplus of *Ga* atoms in *GaSe* crystallites with the energy of 0.175 eV and acceptor level with the energy of 0.100 eV.

The band at 1.820 eV can be considered as a result of overlapping of the band 1.840 eV and the edge luminescence band in *CdSe* crystallites with the maximum at the energy of 1.790 eV. A pronounced change in the PL structure at *T* = 293 K is observed when the duration of heat treatment increases from 10 to 40 min (Fig. 13.18a).

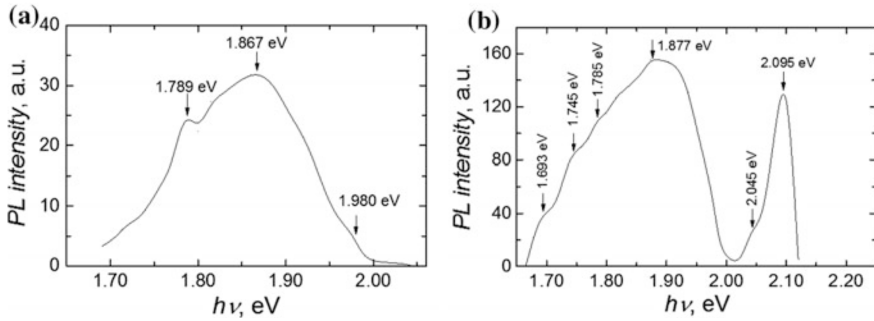

Fig. 13.18 The PL spectra of *GaSe* plates heat treated at 823 K in *Cd* vapor for 40 min at: *T* = 293 K (**a**) and 80 K (**b**)

The PL intensity decreases substantially for CB–VB recombination band (maximum 1.99 eV). The band at energy of 1.867 eV increases and a band at the energy of 1.789 eV is clearly highlighted. These two bands are obtained as a result of luminescent emission overlay in *GaSe* and *CdSe* crystallites from composite. The PL spectrum at *T* = 80 K (Fig. 13.18b) of the composite obtained by heat treatment at 823 K for 40 min is composed of direct exciton emission band with maximum at 2.095 eV. The PL band with maximum at 2.045 eV is attributed to luminescent recombination through indirect excitons. The PL band with maximum at 1.877 eV is associated to donor–acceptor type transitions in *GaSe* crystals with *Ga* surplus also with the participation of deep donor levels with the energy of 0.175 eV and an acceptor level with the energy of ~50–60 meV. The structure with three thresholds at the energies of 1.693, 1.745 and 1.785 eV probably is obtained as the result of impurity bands overlapping in *GaSe* crystallites with edge emission band of *CdSe* crystallites (1.790 eV) from composite.

The *GaSe–CdSe* composite was subjected to short heat treatment for ~20 min in oxygen atmosphere in order to determine the nature of the 1.877 eV band. As it can be seen from the comparison of Figs. 13.18a, 13.19a the treatment in oxygen leads to the extinction of 1.98 eV band. Also, the dominant bands remain at the energies of 1.87 and 1.79 eV and two additional bands at 1.742 and 1.69 eV appear. As can be seen from the comparison of Figs. 13.18b, 13.19b the oxygen presence in the composite influences on energy levels diagram located in the bandgap of *GaSe* compound. Thus, the attenuation of impurity band with maximum at 1.877 eV and shaping of edge emission band in *CdSe* crystallites from composite take place (1.790 eV band amplifies). At the same time, the oxygen creates donor energy levels at 0.256, 0.330 and 0.41 eV from the CB minimum. The emission bands with maxima at 1.734, 1.664 and 1.575 eV are considered the PL emission of donor–acceptor type with participation of acceptor level of 0.13 eV.

The increasing of heat treatment duration up to 100 min changes the structure of PL spectrum in temperature range from 80 to 290 K. Thus, as the result of *Cd* intercalation in *GaSe* crystals occurs shielding of the electron–hole (excitons) bonds

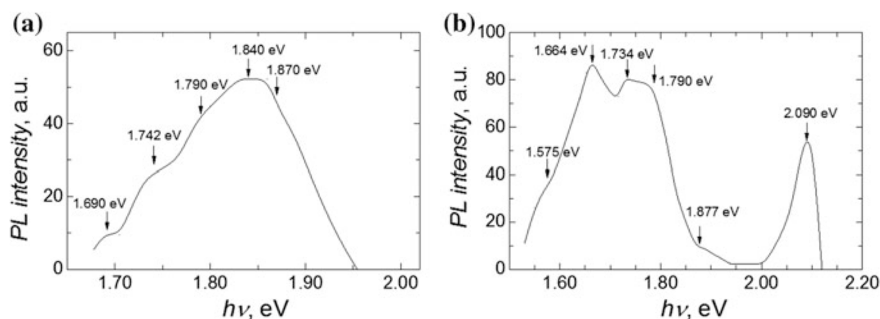

Fig. 13.19 The PL spectra of *GaSe–CdSe* composite obtained by heat treatment at 823 K of *GaSe* plates in *Cd* vapor for 40 min and heat treated for 20 min. in oxygen atmosphere at: T = 293 K (**a**) and 80 K (**b**)

in the whole temperature range. At the same time, in the plates intercalated for 40 min the donor–acceptor band with maximum at 1.88 eV shifts toward to low energies.

The plateau at the energy of 1.79 eV together with PL band with maximum at the energy of 1.848 eV clearly highlights in Fig. 13.20a. This peculiarity's energy coincides with the energy of maximum PL band in polycrystalline *CdSe* layers and it is considered as donor–acceptor luminescence in *CdSe* crystals.

In Fig. 13.21 are shown the temperature dependences of the n = 1 exciton energy (a) and the maximum of PL band of the *GaSe* semiconductor (b). The linear decrease of occurs the band with the energy of 1.848 eV and it's shift toward low energies (Fig. 13.21b) occurs when the temperature increase from 80 to 293 K. The good coincidence of the dependency $E_{n=1}(T)$ and the maximum at the energy of 1.848 eV (T = 80 K) indicates that this band can be considered as luminescent recombination from CB on acceptor level.

To establish the minimum temperature of composite *CdSe–GaSe* obtaining were prepared samples at the temperature of 753 and 773 K. In Fig. 13.20 is shown the

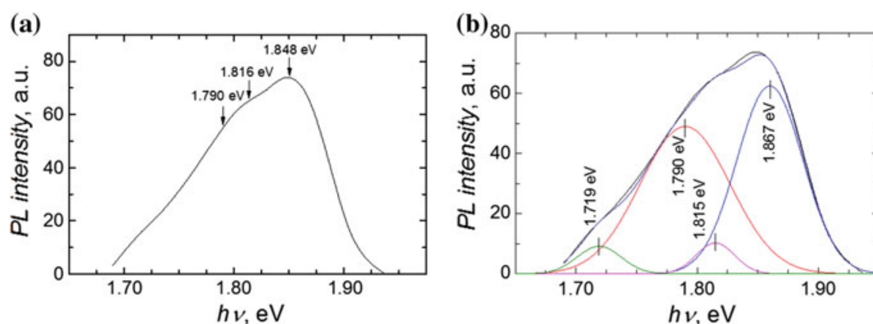

Fig. 13.20 The PL spectrum at T = 80 K of *GaSe* plates heat treated at 773 K in *Cd* vapor for 100 min

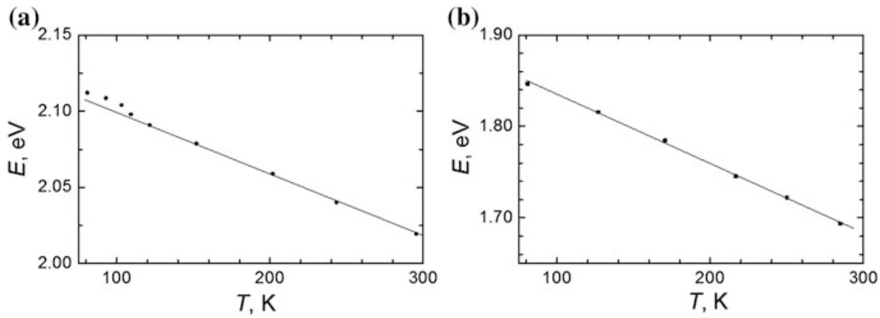

Fig. 13.21 The temperature dependence of n = 1 exciton energy (**a**) and PL band with maximum at 1.848 eV of *GaSe* plates heat treated at 773 K in *Cd* vapor for 100 min

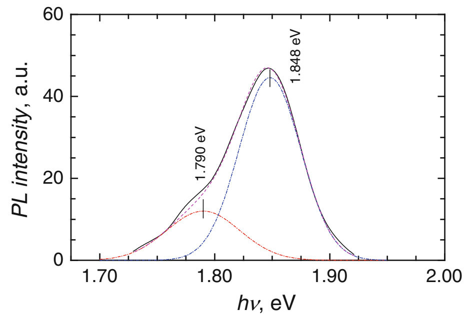

Fig. 13.22 The PL spectrum at T = 80 K of *GaSe* plates heat treated at 753 K in *Cd* vapor for 6 h

PL spectrum at T = 80 K of this sample (773 K). The PL spectrum consists of four bands with peaks at energies 1.867, 1.815, 1.790 and 1.720 eV. These PL bands are obtained as a result of PL overlapping of the impurity luminescence band of *GaSe* crystallite and the edge band with maximum at 1.79 eV of *CdSe* crystallites from composite. The PL spectrum of the composite obtained at 753 K and treated in *Cd* vapors for 6 h is presented in Fig. 13.22. The emission band of this sample at T = 80 K covers the energy range of ~1.70–1.92 eV and has the maximum at 1.847 eV. The impurity emission band in *GaSe* crystallites (1.847 eV) and the plateau is highlighted. It is energy well correlates with the maximum of PL emission band at this temperature of *CdSe* policrystals.

The structure of *GaSe* layered crystalline compound determines the anisotropy density of surface states in perpendicular and parallel planes to the C_6 crystallographic axis. If the density of free valence bonds on the surface (0 0 0 1) of *GaSe* single crystalline plates is $\sim 10^{10}$ cm^{-2}, then the density of free bonds exceeds 10^{20} cm^{-2} on the surface (0 1 0 0). The possibility to obtain *CdSe* crystallites by heat treatment of *GaSe* crystals in *Cd* vapor was analyzed through PL spectra of *CdSe*–*GaSe* composite (Fig. 13.23). The *GaSe* poweder with mean particle size

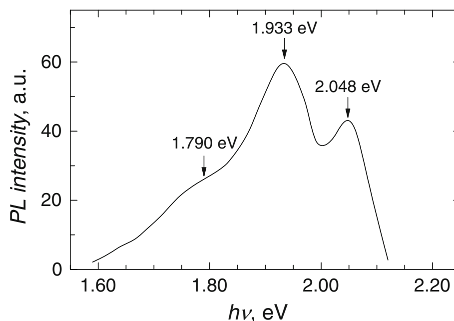

Fig. 13.23 The PL spectrum at T = 80 K of compound obtained by the mixture of *GaSe* and *Cd* powders that was heat treated at 573 K in vacuum for 3 h

of ~ 1–10 μm that was mixed with *Cd* powder (Ø = 1–5 μm) was used to obtain the samples. The mixture was subjected to heat treatment at ~ 573 K in vacuum for 3 h.

There are various methods of metal intercalation in layered materials including most commonly the electrochemical intercalation from solutions. In Fig. 13.24 is shown the PL spectrum at T = 80 K of *GaSe* plate intercalated with *Cd* ions from the $CdCl_2$ aqueous solution of 10 % concentration.

The *Cd* ions intercalation occurred at the current density of 30 mA/cm^2 for 45 min. After electrolytical intercalation the sample was subjected to heat treatment in vacuum at 753 K for 40 min. The PL spectrum at T = 80 K presents a wide emission band with strongly asymmetrical contour and maximum at the energy of 2.047 eV. The *Cd* dopant in *GaSe* forms two acceptor levels, with energies of 0.28 and 0.13 eV from the valence band [15]. The accumulation of $CdCl_2$ molecules and *Cd* ions occurs between the layers because of the weak bonds between the elementary packages in electric field. Thus, the doping of *GaSe* semiconductor with *Cd* and Cl occurs at the heat treatment at 753 K of *GaSe* samples intercalated with *Cd* and $CdCl_2$. The heat treatment was performed in ~ 5×10^{-5} mm *Hg* vacuum or the evacuation of $CdCl_2$ molecules from *GaSe* plates. The *Cl* atoms formes donor levels in the *GaSe* bandgap at the energies of 0.38, 0.56, 0.57 and 0.62 eV [49, 50] and acceptor levels at 0.2 eV from the VB. As it was mentioned above, the *Cd* as dopant formes in the *GaSe* bandgap an acceptor level at 0.13 eV from VB and a deep donor level at 0.37 eV from CB. The particularity of PL spectrum at the

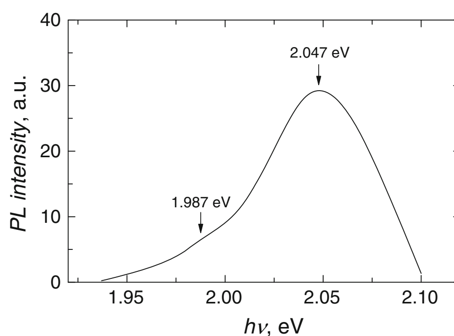

Fig. 13.24 The PL spectrum at T = 78 K, of *GaSe* plate intercalated with *Cd* ions from $CdCl_2$ aqueous solutions and heat treated at 753 K in *Cd* vapor for 40 min

energy of 1.987 eV can be interpreted as electronic transition from CB minimum in the center of the Brillouin zone onto acceptor level (0.13 eV). This conclusion was done taking into account the diagram of the energy levels formed by *Cd* and *Cl* as a dopant in *GaSe*. The wide PL band with the maximum at the energy of 2.047 eV is obtained as a result of overlapping of unionized indirect exciton emission bands and low energy phonons emission (10–15 meV).

The intercalation of *Cd* ions and $CdCl_2$ molecules leads to the deformation of crystal lattice, particularly on the C_6 axis direction which is manifested by shielding of exciton links in the center of Brillouin zone and complete attenuation of the radiative annihilation of PL band of these excitons. This band is well pronounced in the PL spectra of *CdSe–GaSe* composites obtained from the vapor phase.

13.4 Photoluminescence of Nanocomposites with *GaTe* Lamellar Semiconductors

The physical and chemical properties of materials are determined by their electronic states. The materials with cardinally new properties are obtained by doping and intercalation of semiconductors. As the result the filling of energy levels occurs [51]. The characteristics of materials, and especially the electronic states, are well evidenced by absorption and emission measurements of radiation close to bandgap of materials.

The PL spectrum at $T = 78$ K of *GaTe* plate excited with the radiation of *He–Ne* laser ($\lambda = 632.8$ nm, $P = 5$ mW) contains a narrow peak at 1.770 eV and a low intensity band with poor shaped maximum at ~ 1.68 eV (Fig. 13.25a). The maximum of dominant band coincides with the state n = 1 of direct excitons absorption line [52] and can be considered as radiative annihilation of excitons. The PL band from 1.63 to 1.75 eV has an impurity nature, including structural defects that can be caused by the movements of *Te–Ga–Ga–Te* elementary packages. The intensity of this band decreases down to the fund level as the result of long-term treatment (60–80 h) in an inert atmosphere (*Ar*) at 673–693 K.

The PL spectra at $T = 80$ K of the composites obtained by heat treatment of *GaTe* plates in *Cd* vapor at 653 K for 60 h and 833 K for 24 h are shown in Fig. 13.25b, c. The PL spectrum of composite obtained *GaTe* plates that were splitted from single crystals and kept in normal atmosphere for 3 years then treated in *Cd* vapor at the temperature of 653 K for 60 h (Fig. 13.25d).

The contour of PL spectrum at 78 K of the composites obtained from *GaTe* plates that was heat treated in *Cd* vapor at the temperature of 653 K for 60 h well decomposes into three Gaussian curves with maxima at 1.460, 1.402 and 1.372 eV (Fig. 13.25b). The band with maximum at 1.460 eV is interpreted as luminescent recombination through states formed by structural defects and particulary by *Cd* vacancies in *CdTe* [53, 54]. The band at 1.372 eV is well studied in the work of

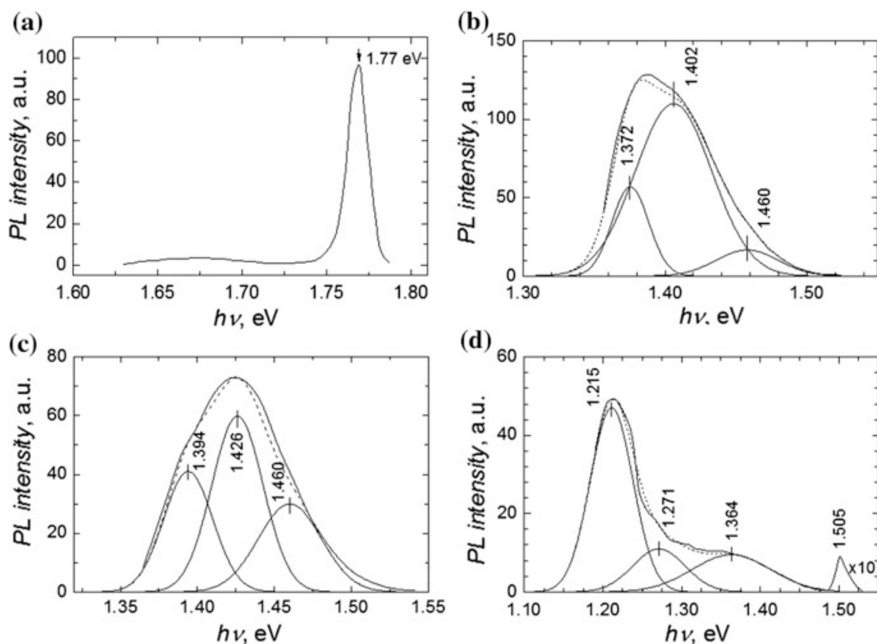

Fig. 13.25 The PL spectra at T = 80 K of *GaTe* plate (**a**) and composites obtained by heat treatment at: 653 K of *GaTe* plates in *Cd* vapor for 60 h (**b**), 833 K for 24 h and (**c**) 653 K temperature for 60 h in *Cd* vapor and kept in atmosphere for 3 years

Vatavu [55] and is interpreted as donor–acceptor radiative emission. The band with the maximum at 1.402 eV probably also has a donor–acceptor nature.

The increase of the temperature of heat treatment from 653 to 833 K leads to the shift of the maximum of PL band from 1.387 to 1.427 eV (Fig. 13.25c). This band is well decomposed into three Gaussian curves with peaks at 1.460, 1.426 and 1.394 eV. As shown in Fig. 13.25b, c the relative intensity of the band with the maximum at 1.460 eV increase compared to component sub–bands from 1.426 and 1.394 eV. This fact indicates an increase in structural defects in metal sublattice of the *CdTe* crystallites from composite. More pronounced changes occurs in the structure of PL spectrum of the composite obtained from *GaTe* plates splitted from *GaTe* single crystals that was kept for 3 years in normal atmosphere (Fig. 13.25d). This composite PL spectrum covers the range of energies from 1.12 to 1.52 eV with absolute maximum at 1215 eV. In this spectrum a low intensity band highlights at 1.505 eV. Note that the presence of this band and the shift of dominant PL band toward low energy region are characteristic of *CdTe* films obtained in oxygen enriched atmosphere [56]. We can admit that as a result of keeping the *GaTe* crystals in the normal atmosphere it took place an oxygen intercalation between *Te–Ga–Ga–Te* layered packages. The oxygen presence contributes to valence bonds formation with its closest *Te* atoms and forms TeO_2 oxide. The TeO_2 impurities in

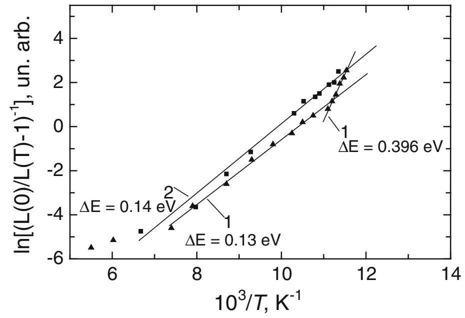

Fig. 13.26 The dependence of PL peak intensity on the reciprocal temperature for *GaTe* single

CdTe form an emission band in the range of 1.20–1.30 eV and also attenuates the PL band with peak at 1.42 eV as shown in Augelli [57]. As a result of heat treatment at 653 K for 6 h of *GaTe–CdTe* composite the low energy donor levels are formed in *CdTe* crystallites. The temperature and excitation intensity dependences for PL band in the region of 1.2 eV are analized in the work of Vatavu and Gasin [58]. It can be concluded that the PL is determined by donor–acceptor recombination with the participation of acceptor level of 9 meV. So we can admit that interstitial oxygen in *GaTe* plates contribute to the formation of donor levels in *CdTe* crystallites from composite. These levels form donor–acceptor complexes responsible for PL in the range of 1.4–1.2 eV.

The composite consisting of *CdTe* and *GaTe* microcrystals was obtained by heat treatment at temperatures from 623 to 833 K of *GaTe* single crystalline blades in *Cd* vapor. The edge of absorption band of the composite that was obtained at the temperature of 653 K is determined by direct optical transitions with the bandgap width equal to 1.56 eV.

The PL spectra at the temperature of 78 K of *GaTe–CdTe* microcrystalline composite obtained at the temperatures of 623–833 K is composed of PL bands of both *CdTe* and *GaTe* crystallites. The PL spectra of studied samples are strongly influenced by sample's temperature and are practical quenched at $T \geq 200$ K. The PL intensity dependence on temperature is described by a formula of type (3) in the temperature range of 78–200 K. As shown in Fig. 13.26 PL thermal activation energy of PL band with maximum at 1.4 eV is 0.14 eV.

The own structural defects and uncontrollable impurities form in the intrinsic band of *GaTe* semiconductor deep acceptor energy levels. Two acceptor levels with the energies of 0.13 and 0.396 eV are formed in the intrinsic bandgap by intercalation of *Cd* into *GaTe*. The nonequilibrium charge carriers from CB recombine with holes from the acceptor level with energy 0.13 eV in the temperature range of 80–140 K. The PL extinction process is determined by the acceptor level with energy of 0.396 eV in the temperature range of 80–90 K. The process of photoluminescence extinction is dictated by the level with the energy of 0.396 eV.

13.5 Photoluminescence of Nanocomposites with *InSe* Lamellar Semiconductors

13.5.1 InSe

The PL spectrum at $T = 80$ K of n–*InSe* crystals is composed of at least two bands with peaks at 1.328 eV (A) and 1.314 eV (B) (Fig. 13.27). The edge band (A) is located in the spectral region of excitons in the state n = 1 (Fig. 13.28) and it can be considered as radiative annihilation of free exciton. The B band prevails in the spectrum. This band is shifted towards lower energies against to direct exciton emission band by 14 meV. The value is equal to the energy of optical phonons (A_{1g} vibration mode) in *InSe* semiconductor with rhombohedral lattice as shown in Fig. 13.27. The good correlation between the energy of optical phonon that are active in the formation of the edge of fundamental absorption band and the energy width between PL bands A and B (Fig. 13.27) indicates that B band is obtained as a result of excitons radiative annihilation with phonons emission of 14 meV. The electrical conductivity of *InSe* semiconductor is dominated by a donor center of small energy located at 23 meV from CB [59].

The stoichiometric *InSe* is a semiconductor with electrical conductivity through electrons. The changing of the type of majority charge carriers occurs as result of doping with small amounts of *Cd* and *Zn* [60, 61]. The doping of *InSe* with *Cd* in

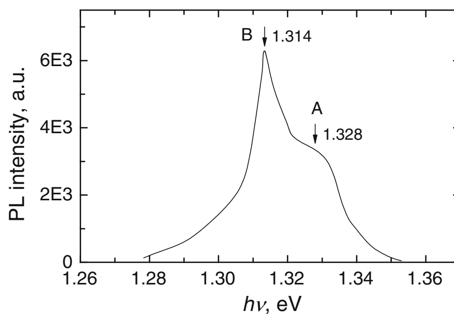

Fig. 13.27 The PL spectrum of n-*InSe* crystals at $T = 80$ K

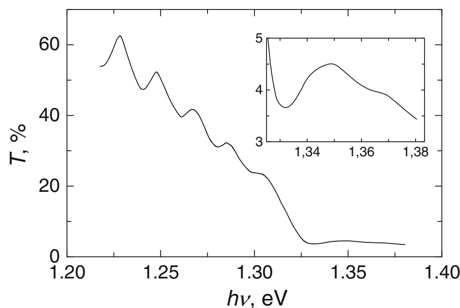

Fig. 13.28 The transmission spectrum in fundamental band edge region of a *InSe* with thickness of 11.2 μm at $T = 80$ K

concentration of 0.1–1.0 at.% changes the diagram of energy levels within bandgap by the formation of a deep acceptor level at 0.45 eV from VB [61]. Also, the *Cd* impurities form levels for holes with energies 0.42 and 0.48 eV from VB [62]. *Cd* in an amount of 0.1–1.0 at.% formes in the *InSe* band gap acceptor electronic states through which nonequilibrium charge carriers' radiative recombination occurs [63]. These recombination energy levels manifest themselves as electronic states of spatial defects induced in *InSe* lamella by splitting of single crystalline blocks [19].

13.5.2 InSe *Intercalated with* Cd

The PL spectra at $T = 80$ K of *InSe* crystals doped with 0.5 at.% *Cd* (a) and 1.0 at.% *Cd* (b) are presented in Fig. 13.29. The *Cd* with the concentration of C ≥ 0.5 at.% forms structural defects in the crystal lattice. This defects shield the excitonic bonds. The PL band caused by luminescencent annihilation of unionized excitons present in the spectrum of undoped *InSe* at 1.328 eV as well as its phonon replica is missing in PL spectra at $T \geq 80$ K. However, the *Cd* impurity atoms form in a new band PL spectra at 1.17–1.27 eV. The maximum of impurity band in PL spectra of *InSe* crystals doped with 0.5 at.% *Cd* is found at energy of 1.215 eV. Since the width of bandgap for *InSe* cat $T = 80$ K is equal to 1.345 eV, the energy of acceptor level formed by *Cd* is equal to 0.13 eV from VB.

As shown in Fig. 13.29a on the wing of PL band at small energies it is present a band with maximum at 1.185 eV. This particularity of PL spectrum is formed as a result of luminescent transitions of nonequilibrium charge carriers from the acceptor level with energy of 0.16 eV. Note that the acceptor level with energy of 0.17 eV from VB were determined in the work of Shigetomi [63] by analyzing the temperature dependence of PL of the *InSe* doped with 5.0 at.% *Cd*.

The increasing of the *Cd* concentration from 0.5 to 1.0 at.% amplifies the band B, which maximum corresponds to photon energy of 1.20 eV. The maximum of band formed by *Cd* impurities at a concentration of 5.0 at.% is shifted to high

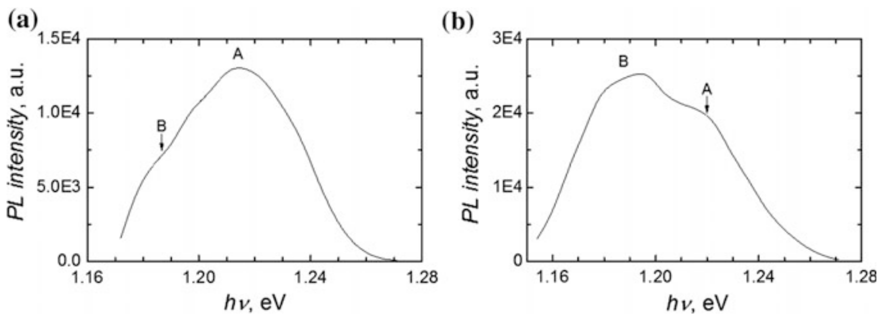

Fig. 13.29 The PL spectra at $T = 80$ K of *InSe* crystals doped with 0.5 at.% *Cd* (**a**) and 1.0 at.% *Cd* (**b**)

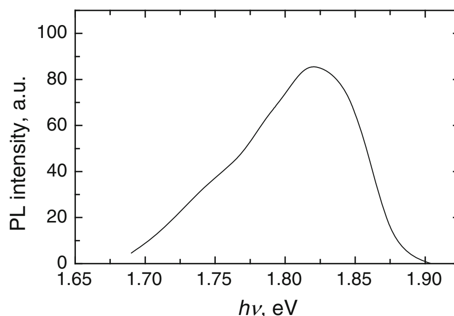

Fig. 13.30 The PL spectrum at T = 293 K of *InSe–Cd*Se micro-crystalline compound obtained by heat treatment at 773 K of *InSe* plates in *Cd* vapor for 3 h

energies by 10 meV in the work of Shigetomi [63]. Thus, we can consider those *Cd* impurity atoms with a concentration up to 1.0 at.% forme in the bandgap of *InSe* two acceptor levels at energies of 0.145 and 0.125 eV from VB.

The PL spectrum at T = 293 K of *InSe–CdSe* microcrystalline composite obtained by heat treatment in *Cd* vapor at 773 K of *InSe* plate for 3 h is shown in Fig. 13.30. The PL band with maximum at 1.83 eV is located at higher energies than the width of bandgap of crystalline compound from composite at T = 293 K: 1.30 eV for *InSe* [64] and 1.80 eV for *CdSe* [36]. The wing from lower energies of PL spectrum is localized in the energy range $h\nu \le 1.80$ eV is formed by radiative recombination of nonequilibrium charge carriers in *CdSe* crystallites from composite. It is well known that the PL spectrum of *CdSe* compound in submicrometric particles represents a Gaussian band with maximum intensity in the wavelength region of 480–620 nm [43, 65, 66]. Thus, we can consider that anti–Stokes PL is determined by the presence of nanometrical *CdSe* crystallites in the composite.

13.5.3 InSe *Intercalated with* Zn

Zinc is one of the chemical elements that is used for doping of p–*InSe* compound [67]. The demand of study of the energy levels diagram formed by this dopant is determined by p–*InSe* perspective usage as photosensitive element in solar cells with high-energy efficiency [68]. The *Zn* forms acceptor levels at 0.16, 0.28, 0.31 eV and the capture level at 0.59 eV from the valence band within the bandgap of *InSe* compound. The energy level at 0.16 eV was determined from the analysis of temperature dependence of the PL impurity band using configurational coordinates model [69]. The levels with energies of 0.28, 0.31 and 0.59 eV were determined from measurements of the Hall effect [60, 70]. The presence of a emission band in the energy range of 1.05–1.28 eV with maximum at 1.17 eV determined by donor–acceptor recombination with *Zn* acceptor level at the energy of 0.13 eV it is characteristic for PL spectra of *InSe* crystals doped with *Zn* [71].

The PL spectrum at T = 80 K of *InSe–ZnSe* composite obtained by heat treatment of *InSe* plates in *Zn* vapor at 783 K for 21 h is shown in Fig. 13.31. The PL

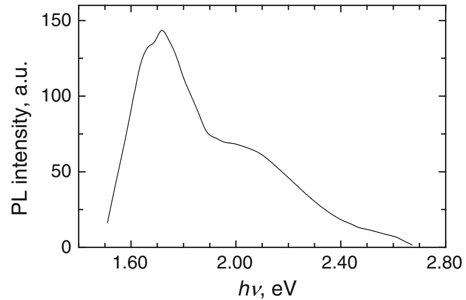

Fig. 13.31 The PL spectrum at $T = 80$ K of *InSe–ZnSe* composite obtained by heat treatment at 783 K of *InSe* plates in *Zn* vapor for 21 h

spectrum is composed of at least three wide bands with maxima respectively at 1.71, 2.10 and 2.58 eV. The width of bandgap of *InSe* compound at $T = 80$ K is equal to 1.342 eV. This value is much smaller than the energy of bands from the spectrum. So, the bands from the PL spectrum (Fig. 13.31) are determined by the processes of luminescent recombination in *ZnSe* crystallites from composite.

The PL spectrum of undoped *ZnSe* crystals at $T = 80$ K contains a band with maximum at 2.76 eV with symmetrical shape and FWHM of ~55 meV. It is considered that this PL band has an excitonic nature [72]. The doping of *ZnSe* crystal with metals from I group (*Cu*, *Ag*, *Au*) leads to the formation of the large number of acceptor levels through which the PL bands are formed in the energy range from 450 to 1000 nm [73].

The temperature dependence of intensity of donor–acceptor recombination bands can be described by the expression (13.3). As shown in Fig. 13.32, the PL thermal quenching in the temperature range of 110–290 K of the band with maximum at energy 1.71 eV is well described by formula (13.3) for thermal activation energy equal to 0.045 eV.

The valence bonds at the edge of *InSe* plates are open, which imposes a much stronger interaction of *Zn* atoms from atmosphere surrounding plates with atoms from…–*Se*–*In*–*In*–*Se*–… packages. The PL spectra at respectively $T = 293$ K (a) and 80 K (b) from…–*Se*–*In*–*In*–*Se*–… planar packages interface are shown in Fig. 13.33a, b.

The PL spectrum of *ZnSe* crystallites from composite at room temperature is composed of two bands: the edge band with maximum at the energy of 2.460 eV and the broadband with maximum at 2.08 eV. The width of bandgap of *ZnSe* crystallite at $T = 293$ and 80 K is equal respectively to 2.680 and 2.793 eV [36]. At the intercalation temperature of 773 K the *Zn* atoms form the stable chemical compounds of *ZnSe* freeing the In atoms that serve as a dopant for both *InSe* and *ZnSe* crystallites from composite. The band from yellow–red spectral region is composed of two subbands with maxima at energies respectively of 2.08 and 1.72 eV. Thus, we can admit that In introduced in *ZnSe* crystallites forms at least three donor levels in his bandgap.

The three bands structure of PL spectrum of *ZnSe* crystallites from *ZnSe–InSe* composite is amplified when the compound is cooled down from 293 to 80 K

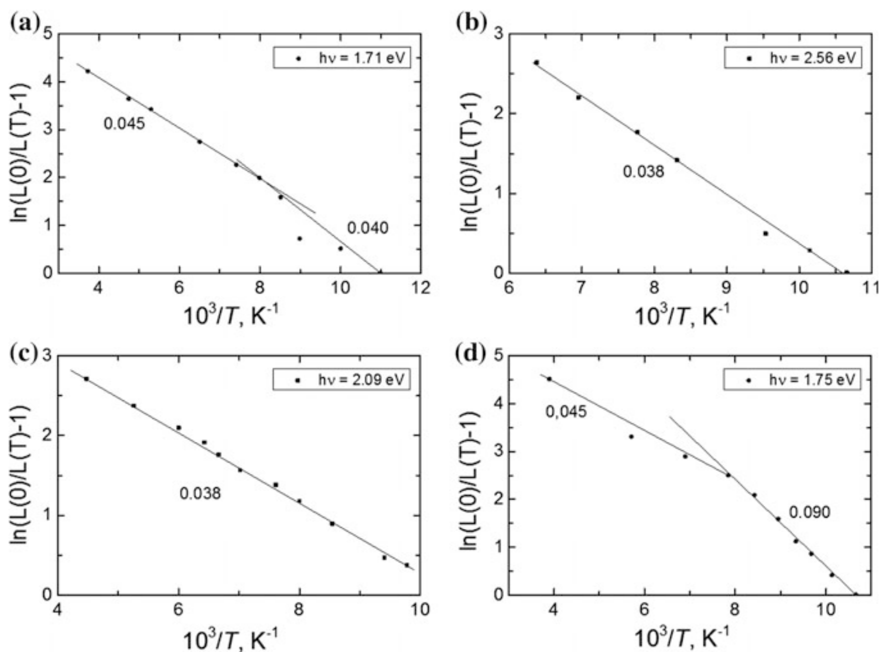

Fig. 13.32 The dependence of the PL peak intensity on the reciprocal temperature for 1.71 eV band from (0 0 0 1) surface of *InSe* plate (**a**) and bands from composite obtained on the *InSe* plate lateral side, with maxima at energies of 2.56 eV (**b**), 2.09 eV (**c**) and 1.75 eV (**d**)

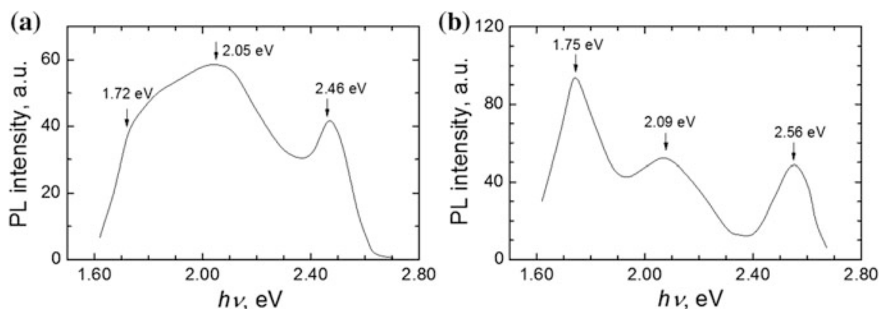

Fig. 13.33 The PL spectra from the lateral side of *InSe* plates that was heat treated at 783 K in *Zn* vapor for 21 h at: T = 293 K (**a**) and 80 K (**b**)

(Fig. 13.33). Three bands are present with maximum at energies of 2.560, 2.090 and 1.750 eV at this temperature. The coefficient of thermal shift of the edge band is equal to $\sim 5 \times 10^{-4}$ eV K^{-1}. This value is in good correlation with thermal shift of bandgap for this compound. The shifting to the lower energies of the bands from the red region of spectrum (2.09 and 1.75 eV) with thermal coefficients much lower

than the shift rate of the width of bandgap of *ZnSe* crystal occurs when the sample's temperature decreases.

At the sample's temperature decrease from 293 to 80 K, the PL bands intensity is reduced more than 60 times. As can be observed from Fig. 13.32, the temperature dependence of the PL intensity of the band with maximum at 1.71 eV (from the (0 0 0 1) surface of *InSe* plate) (Fig. 13.32a) and of those three PL bands of the composite formed on the edge of *InSe* plate with maximum at energies of 2.56 eV (Fig. 13.32b), 2.09 eV (Fig. 13.32c) and 1.75 eV (Fig. 13.32d) are well described by formula (13.3) for PL thermal activation energies of respectively 52, 45 and 38 meV. The PL band from the red region of the spectrum (peak at 1.75 eV), as shown in Fig. 13.32d can be characterized by two thermal activation energies: 90 meV at temperature range of 80–120 K and 45 meV in the temperature range of 120–290 K.

13.6 Conclusions and Generalities

- The *GaS* compound is an n-type semiconductor with indirect bandgap equal to 2.595 eV at $T = 78$ K. The phonons with average energy of 14 meV participate at the formation of the edge of indirect absorption band.
- The PL emission spectra of *GaS* lamella at $T = 78$ K contain a low intensity band close to the edge of indirect absorption band and a band with a slowly asymmetrical contour of donor-acceptor type with the maximum at the energy of 2.32 eV. The doping of *GaSe* crystals with 1 mol% of *Mn* attenuates the band with maximum at the energy of 2.32 eV and forms the characteristic band of *Mn* ions with the maximum at 1.92 eV in *GaS* and *GaSe* lamellar crystals. The PL band with maximum at the energy of 1.92 eV is obtained by the superposition of three Gaussian bands with peaks at 2.040, 1.972 and 1870 eV. The donor-acceptor nature of these bands is proved by the dependence of the PL intensity from the temperature.
- The material composed of *GaS* and *ZnS* nanocrystallites that are photoluminescent in the purple-orange region of the spectrum was obtained by the heat treatment at the temperature of 753 K of *GaS* single crystals in *Zn* vapour. The PL spectrum of *GaS–ZnS* nanocomposite is formed by overlapping of *GaS* and *ZnS* crystallites individual bands.
- The PL spectrum of *GaSe* single crystals at $T = 78$ K is composed of emission bands of localized excitons and their phonon repetitions and the donor-acceptor band with maximum at energy 1.91 eV. The PL spectrum of *GaSe–CdSe* nanocomposite can be presented as band composed of four sub-bands that have the Gauss contour. The PL sub-bands are interpreted as the PL emission of CdSe microcrystallites and nanocrystallites that sizes are from units to tens of nanometers.
- The structure of PL spectrum of *GaTe–CdTe* nanocomposite obtained by heat treatment at 653–833 K was studied. The *GaTe* plates kept for a long time in

normal atmosphere were used as basic material. It was established that the PL activation energy depends weak on the treatment temperature of *GaTe* plates in *Cd* vapour.

- *InSe*−*ZnSe* and *InSe*–*CdSe* nanocomposites are materials that are photoluminescent in the red-NIR region of the spectrum. The presence of antistokes luminescence is determined by the nanometric dimensions of the *ZnSe*, *CdSe* and *InSe* crystallites which serve as components of studied composite materials.

References

1. I. Caraman, E. Vatavu, L. Leontie, M. Stamate, D. Untila, Phys. Status Solidi C **12**, 70 (2015)
2. L. Leontie, I. Evtodiev, N. Spalatu, M. Caraman, S. Evtodiev, O. Racovet, M. Girtan, C. Focsa, J. Alloy. Compd. **584**, 542 (2014)
3. D. Untila, V. Cantser, M. Caraman, I. Evtodiev, L. Leontie, L. Dmitroglo, Phys. Status Solidi C **12**, 65 (2015)
4. G.L. Belenkii, M. O. Godzhaev. Phys. Stat. Sol. (b) **85**, 453 (1978)
5. V. Chiricenco, M. Caraman, I.I. Rusu, L. Leontie, J. Lumin. **101**, 71 (2003)
6. S. Shigetomi, K. Sakai, T. Ikari, Phys. Stat. Sol. (b) **241**, 2607 (2004)
7. S. Shigetomi, T. Ikari, J. Lumin. **118**, 106 (2006)
8. T. Aono, K. Kase, A. Kinoshita, J. Appl. Phys. **74**, 2818 (1993)
9. M. Karabulut, G. Bilir, G.M. Mamedov, A. Seyhan, R. Turan, J. Lumin. **128**, 1551 (2008)
10. J.Z. Wan, J.L. Brebner, R. Leonelli, G. Zhao, J.T. Graham, Phys. Rev. B **48**, 5197 (1993)
11. A. Warrier, A.V.R. Warrier, J. Appl. Phys. **53**, 5169 (1982)
12. V. Capozzi, A. Minafra, J. Phys. C: Solid State Phys. **14**, 4335 (1981)
13. V. Capozzi, Phys. Rev. B **23**, 836 (1981)
14. V. Capozzi, Phys. Rev. B **28**, 4620 (1983)
15. S. Shigetomi, T. Ikari, H. Nakashima, J. Appl. Phys. **73**, 4686 (1993)
16. S. Shigetomi, T. Ikari, J. Appl. Phys. **94**, 5399 (2003)
17. S.I. Lee, S.R. Hahn, C.H. Chung, S.H. Yun, W.T. Kim, Solid State Commun. **60**, 453 (1986)
18. C.H. Chung, S.R. Hahn, H.L. Park, W.T. Kim, S.I. Lee, J. Lumin. **40**, 405 (1988)
19. K. Imai, K. Suzuki, T. Haga, Y. Abe, J. Appl. Phys. **60**, 3374 (1986)
20. N. Spalatu, J. Hiie, V. Valdna, M. Caraman, N. Maticiuc, V. Mikli, T. Potlog, M. Krunks, V. Lughi, Energy Procedia **44**, 85 (2014)
21. S.H. Song, J.F. Wang, G.M. Lalev, L. He, M. Isshiki, J. Cryst. Growth **252**, 102 (2003)
22. G. Colibaba, M. Caraman, I. Evtodiev, S. Evtodiev, E. Goncearenco, D. Nedeoglo, N. Nedeoglo, J. Lumin. **145**, 237 (2014)
23. A. Mycielski, E. Lusakowska, A. Szadkowski, L. Kowalczyk, J. Cryst. Growth **184**, 1044 (1998)
24. M.S. Jin, C.D. Kim, W.T. Kim, J. Korean Phys. Soc. **44**, 920 (2004)
25. N. Okamoto, N. Hara, H. Tanaka, IEEE Trans. Electron Dev. **47**, 2284 (2000)
26. S. Shigetomi, T. Ikari, J. Appl. Phys. **95**, 6480 (2004)
27. S. Shigetomi, T. Ikari, J. Lumin. **113**, 137 (2005)
28. N.M. Gasanly, A. Aydinli, H. Ozkan, C. Kocabas, Solid State Commun. **116**, 147 (2000)
29. Y. Sasaki, C. Hamaguchi, J. Nakai, J. Phys. Soc. Jpn. **38**, 1698 (1975)
30. P.T. Landsberg. Recombination in semiconductors. Cambridge, New York, Port Chester, Melbourne (Cambridge University Press, Sydney, 1991). p. 595
31. I.M. Catalano, R. Cingolani, M. Lepore, Solid State Commun. **60**, 385 (1986)
32. W. Van Gool, A.P. Cleiren, Phil. Res. Rep. **15**, 238 (1960)
33. R.C. Weast. Handbook of Chemistry and Physics. 65. s.l. (CRC Press, 1984), p. 2312

34. G.B. Abdullaev, V.B. Antonov, T.E. Mekhtiev, EYu. Salaev, Sov. J. Quant. Electron. **4**, 80 (1974)
35. W. van Roosbroeck, W. Shockley, Phys. Rev. **94**, 1558 (1954)
36. J. Pankove. Optical Processes in Semiconductors (Mir, Moscow, 1973)
37. Y. Depeursinge, C. Depeursinge, J. Phys. C: Solid State Phys. **12**, 4851 (1979)
38. Y.F. Jellinek, H. Hahn, Z. Naturf. **16**, 713 (1961)
39. J. Krustok, H. Collan, K. Hjelt, J. Appl. Phys. **81**, 1442 (1997)
40. K.R. Le Toullec, N. Piccioli, J.C. Chervin, Phys. Rev. B **22**, 6162 (1980)
41. S. Shigetomi, T. Ikari, N. Nishimura, J. Appl. Phys. **69**, 7936 (1991)
42. S. Shigetomi, T. Ikari, H. Nakashima, Phys. Stat. Sol. (a) **160**, 159 (1997)
43. X. Xu, Y. Wang, T. Gule, Q. Luo, L. Zhou, F. Gong, Mater. Res. Bull. **48**, 983 (2013)
44. E.M. Boatman, G.C. Lisensky, K.J. Nordell, J. Chem. Educ. **82**, 1697 (2005)
45. M. Ya, N.V. Valakh, V.V. Vuychik, S.V. Strelchuk, T.V. Sorokin, S. Shubina, V. Ivanov, P.S. Kop'ev. Semiconductors **37**, 699 (2003)
46. X. Peng, Chem. Eur. J. **8**, 335 (2002)
47. M.A. Eliashevich, *Atomic and Molecular Spectroscopy* (Fizmatgiz, Moscow, 1962)
48. G.B. Abdullaev, G.L. Belenkii, EYu. Salaev, R.A. Suleisianov, Il Nuovo Cimento **38B**, 469 (1977)
49. G. Micocci, A. Serra, A. Tepore, J. Appl. Phys. **82**, 2365 (1997)
50. G. Micocci, A. Serra, A. Tepore, J. Appl. Phys. **81**, 6200 (1997)
51. B. Pajot, *Optical Absorption of Impurities and Defects in Semiconducting Crystals* (Springer, Berlin, 2010)
52. J. Camassel, P. Merle, H. Mathieu, A. Gouskov, Phys. Rev. B **19**, 1060 (1979)
53. N.C. Giles-Taylor, R.N. Bicknell, D.K. Blanks, T.H. Myers, J.F. Schetzina, J. Vac. Sci. Technol. A **3**, 76 (1985)
54. X. Mathew, J.R. Arizmendi, J. Campos, P.J. Sebastian, N.R. Mathews, C.R. Jimenez, M.G. Jimenez, R. Silva-Gonzalez, M.E. Hernandez-Torres, R. Dhere, Sol. Energy Mater. Sol. Cells **70**, 379 (2001)
55. S. Vatavu, H. Zhao, I. Caraman, P. Gaşin, C. Ferekides, Thin Solid Films **517**, 2195 (2009)
56. S. Vatavu, H. Zhao, V. Padma, R. Rudaraju, D.L. Morel, P. Gaşin, Iu Caraman, C.S. Ferekides, Thin Solid Films **515**, 6107 (2007)
57. V. Augelli, C. Manfredotti, R. Murri, R. Piccolo, A. Rizzo, L. Vasanelli, Solid State Commun. **21**, 575 (1977)
58. S. Vatavu, P. Gaşin, Thin Solid Films **515**, 6179 (2007)
59. S. Shigetomi, T. Ikari, Y. Koga, S. Shigetomi, Phys. Stat. Sol. (a) **86**, K69 (1984)
60. G. Micocci, A. Tepore, R. Rella, P. Siciliano, J. Appl. Phys. **71**, 2274 (1992)
61. S. Shigetomi, T. Ikari, Y. Koga, S. Shigetomi. Phys. Stat. Sol. (a) **108**, K53 (1988)
62. G. Micocci, M. Molendini, A. Tepore, F.L. Rella, P. Siciliano, J. Appl. Phys. **70**, 6847 (1991)
63. S. Shigetomi, H. Ohkubo, T. Ikari, J. Phys. Chem. Solids **51**, 91 (1990)
64. M. Di Giulio, G. Micocci, A. Rizzo, A. Tepore, J. Appl. Phys. **54**, 5839 (1983)
65. C.B. Murray, D.J. Norris, M.G. Bawendi, J. Am. Chem. Soc. **115**, 8706 (1993)
66. A.V. Firth, S.W. Haggata, P.K. Khanna, S.J. Williams, J.W. Allen, S.W. Magennis, I.D.W. Samuel, D.J. Cole-Hamilton, J. Lumin. **109**, 163 (2004)
67. A. Chevy, J. Appl. Phys. **56**, 978 (1984)
68. E. Bucher. Physics and Chemistry of Materials with Low-Dimensional Structures, ed. by A. Aruchamy. Photoelectrochemistry and Photovoltaics of Layered Semiconductors (Kluwer Academic Publishers, Dordrecht/Boston/London, 1992), pp. 1–81
69. T. Ikari, S. Shigetomi, Y. Koga, S. Shigetomi. Phys. Stat. Sol. (b) **109**, K81 (1981)
70. S. Shigetomi, T. Ikari, Y. Koga, S. Shigetomi, Jpn. J. Appl. Phys. **20**, L343 (1981)
71. S. Shigetomi, H. Ohkubo, T. Ikari, H. Nakashyma, J. Appl. Phys. **66**, 3647 (1989)
72. P.J. Dean, A.D. Pitt, M.S. Skolnick, P.J. Wright, B. Cockayne, J. Cryst. Growth **59**, 301 (1982)
73. P.J. Dean, B.J. Fitzpatrick, R.N. Bhargava, Phys. Rev. B **26**, 2016 (1982)

Chapter 14
Nanoreliefs Obtained by Various Machining Methods

Laurenţiu Slătineanu, Oana Dodun, Margareta Coteaţă and Irina Beşliu

Abstract The nanoreliefs could be defined as surface asperities having height characteristics lower than one micrometer, in order to be expressed in nanometers. There are various applications that need nanoreliefs and this aspect determined the investigation of the possibilities offered by distinct manufacturing processes of obtaining nanoreliefs. A research concerning the manufacturing methods based on the material removal from workpiece was developed. The analysis revealed that there are machining methods by traditional cutting and nonconventional machining methods that use thermal or electrochemical phenomena in order to remove the material from workpiece. Some essential aspects of such machining methods were highlighted. The factors able to affect the asperities heights were showed. Experimental researches facilitated the identification of mathematical empirical models able to offer supplementary information concerning the influence exerted by some of the process input factors on the surface roughness parameter *Ra*. Surfaces profiles or images were obtained by means of instruments for investigation of the machined surfaces.

14.1 Introduction

In accordance with a proposal formulated in 1997 by T. Masuzawa (University of Tokyo) and K. Tönshoff (Laser Zentrum Hannover), *the micromachining* refers to the obtaining of surfaces having dimensions included in the interval 1–999 µm, by means of distinct machining processes [1]; this could mean that obtaining dimensions between 1 and 999 nm could suggest a domain of *nanomachining*.

By extension, if the parameters able to characterize the relief of machined surface could be expressed by values lower than 1 µm, the so-called *nanoreliefs* or

L. Slătineanu (✉) · O. Dodun · M. Coteaţă
"Gheorghe Asachi" Technical University of Iaşi, Iasi, Romania
e-mail: lslati@yahoo.com; slati@tcm.tuiasi.ro

I. Beşliu
"Ştefan cel Mare" University of Suceava, Suceava, Romania

© Springer International Publishing Switzerland 2016

I. Tiginyanu et al. (eds.), *Nanostructures and Thin Films for Multifunctional Applications*, NanoScience and Technology,
DOI 10.1007/978-3-319-30198-3_14

nanoasperities could be considered. In fact, such a concept is although used to characterize surfaces having very low surface roughness. In the last decades, the researchers highlighted the significance of nanoreliefs for various practical applications.

On the other hand, there is a large set of manufacturing methods. A classification of the manufacturing methods based on changes that affect the workpiece volume and mass [2, 3] shows that there are:

1. Manufacturing methods based *on material removal from workpiece* (*subtractive manufacturing methods*); there is the opinion to attribute to this group the name of *machining methods*, if one accepts that a machining process involves the material removal from workpiece;
2. Manufacturing methods based *on adding material to the workpiece* (*additive manufacturing methods*). This group could include the welding methods or methods able to deposit other materials on the workpiece surface or just in the workpiece surface layer; in the last group, one can include plasma deposition, chemical and electrochemical deposition, laser beam deposition, electron beam deposition, thermal—chemical deposition etc.
3. Manufacturing methods which *do not determine mass changes of workpiece*. One can include here the heat treatments or other manufacturing methods able to generate the change of chemical or physical properties of workpiece material without a significant mass change. For example, in this group, machining methods such are the photoengraving, hardening by plastic deformation, by means of laser beam, plasma beam or electron beam etc. could be included.

Within this work, one takes into consideration especially some subtractive manufacturing methods, as a group characterized by a high weight in machine building. In this way, one can classify the machining methods as follows:

1. *Machining methods by cutting processes;* here, one can take into consideration cutting processes which use metallic tools (turning, milling, drilling etc.) or abrasive particles (grinding, honing, lapping, abrasive jet machining, abrasive water jet machining etc.);
2. *Machining methods based on electrochemical processes* (electrochemical machining, chemical machining);
3. *Machining methods based on thermal processes* (electrical discharge machining, plasma beam machining, laser beam machining, electron beam machining etc.);
4. *Machining methods based on hybrid processes*, characterized by the combination of two or many of the above mentioned machining processes

The nanoreliefs or nanoasperities and the manufacturing methods able to facilitate their obtaining were objectives of research activities.

Thus, Hida et al. proposed a nanofinishing technique based on the use of a microparticle controlled by optical radiation force; in this way, a material removal rate of nanometer order can be achieved and local area of micrometer order can be machined [4].

Chernysh et al. investigated the generation of nanoreliefs on silicon and germanium single crystals by ion irradiation [5]. The atomic force microscopy was used in order to highlight the geometrical characteristics of the nanorelief. The researchers appreciated that the average height of the nanorelief is influenced by the parameters of ion irradiation process.

Jain analyzed a set of nanofinishing techniques, such as abrasive flow machining, magnetorheological finishing, magnetorheological abrasive flow finishing, magnetic abrasive finishing, chemo-mechanical polishing [6]. He considered that these nanofinishing techniques can be applied in order to obtain parts with micrometer or submicrometer form accuracy and surface roughness within nanometer range.

Teplova developed a scientific investigation concerning the possibilities of obtaining nanoreliefs by quasi-plastic machining of hard brittle materials used in electronic industry [7]. She noticed that nanoreliefs having a height of 2–10 nm can be obtained by grinding of diamond workpieces. She appreciated also that in this way, pollutant machining methods like those involving use of aggressive work media could be eliminated.

Metlitskaya et al. studied the formation of wave nanorelief by surface erosion under the action of ion bombardment and using the so-called Bradley-Harper model [8]. They established that the wave nanorelief appears when stability of the plane relief loses is affected, and particularly when the intensity of the flow exceed a certain threshold.

Manna and Molla investigated the influence of some factors corresponding to electrochemical grinding process on surface roughness parameter *Ra* in the case of nanofinishing of test pieces made of Hybrid Al/(Al_2O_3 + ZrO_2)-MMC [9]. They showed that a machined surface characterized by $Ra = 96$ nm can be thus obtained.

14.2 Possibilities of Characterizing Nanoasperities/Nanoreliefs

In machine building, a possible classification of the surface errors takes into consideration the ratio between the pitch and the height of the asperities. Thus, if this ratio between the pitch and the height is lower than 40, the so-called *surface roughness* could be considered.

In order to highlight the characteristics of the nanoasperities, over the years, both profiles sections through such nanoasperities and proper images of the surfaces were investigated.

Initially and just up to the last two decades, especially profile parameters were used and apparata able to offer more complete information concerning a certain machined surface were used in the workshops and laboratories.

There are various parameters which could be determined in order to evaluate the surface roughness. At present, such parameters are classified in the following way:

(a) *peak and valley* or *amplitude parameters* (maximum profile peak height *Rp*, maximum profile valley depth *Rv*, maximum height of the profile *Rz*, mean height of the profile elements *Rc*, total height of profile *Rt* etc.); (b) *roughness parameters based on the mean ordinates value* (arithmetical mean deviation of the assessed profile *Ra*, root mean square deviation of the assessed profile *Rq*, skewness of assessed profile *Rsk*, kurtosis of the assessed profile *Rku* etc.); (c) *spacing parameters* (for example, mean width of the profile elements or mean spacing of the profile irregularities *RSm*); (d) *hybrid parameters* (for example, root mean square slope of the assessed profile *RΔq*); (e) *curves and parameters associated to some curves* (material ratio of the profile *Rmr*(*c*), material ratio curve of the profile—Abbott Firestone curve, profile section height difference *Rδc*, relative material ratio *Rmr*, profile height amplitude curve) etc.

The older preoccupations concerning the identification of some possibilities of highlighting the roughness by considering not only the profile in a certain section, but just 3D evaluation found a first solving in 1991, when the European Commission workshop decided to develop ISO standards able to complete the classic way (2D) of surface roughness evaluation.

In the case of the 3D surface measurement, the main groups of parameters are generally similar to those used in the case of the surface profile evaluation [10].

As above mentioned, the current most used surface roughness parameter is the arithmetical mean deviation of the assessed profile *Ra:*

$$R_a = \frac{1}{l}\int_0^l |z(x)|dx\,(\mu\text{m}), \tag{14.1}$$

where l is the length of assessed profile, $z(x)$—the function corresponding to the surface profile, along the axis *Ox*.

In order to obtain information concerning the nanoasperities, various instruments could be used. Essentially, there are instruments based on a continuous contact of a pin with the investigated surface and instruments which use beams of subatomic particles directed to the surface to be examined; if the instruments that work by contact are known for many years ago, the noncontact instruments were designed and used in the last decades. In the group of noncontact instruments, especially instruments which uses the laser beam or electrons are used. From the instruments able to describe the profile of surface in a certain cross section, by applying many passes along the investigated aria, one can obtain an image of the surface. One can notice that some of these instruments achieve a supplementary magnification of the asperities height; even the image does not respect the real scale of the asperities, one obtains more interesting information about the surface aspect. For example, such an instrument is the atomic force microscope. If one wants to obtain an image of nanoasperities at the same scale for all spatial dimensions, the scanning electron microscope could be used.

14.3 Nanoreliefs Obtained by Mechanical Processes

14.3.1 General Aspects Concerning the Cutting Process and Its Capacity to Generate Nanoreliefs

The cutting process is a machining process in which the material removal from workpiece is achieved by means of cutting tools having cutting edge that generate chips.

The cutting method is considered as a classical machining method, because it is based on the principle of plastic deformation.

Indeed, due to the main cutting motion, by means of its tool face, the cutting tool presses a layer of a certain thickness (corresponding to the so-called depth of cut, a_p) up to the moment when the shearing strength of the workpiece material is exceeded by the exerted pressure and a microcrack is generated (Fig. 14.1). The development of this crack determines the chip generation. Since along the work stroke a single groove could be generated, an additional motion—the feed motion f—is necessary, in order to remove the surplus material on a certain surface of the workpiece.

Practically, these are the main phenomena that determine the generation of the machined surface and of the nanoreliefs appeared on this surface. One can mention also that due to the workpiece material elasticity, after the cutting tool pass, there is an elastic recovery of the workpiece material and this means that the depth of cut a_p measured after the cutting process could be lower than the desired depth of cut. A significant compression of the material detached as chips leads to a length of the chip lower than the length of work stroke able to detach that chip and the thickness t_c of the chip is higher the depth of cut a_p.

The surface layer corresponding to the machined surface includes grains deformed as a consequence of the cutting process and its hardness is different in comparison with the workpiece base material.

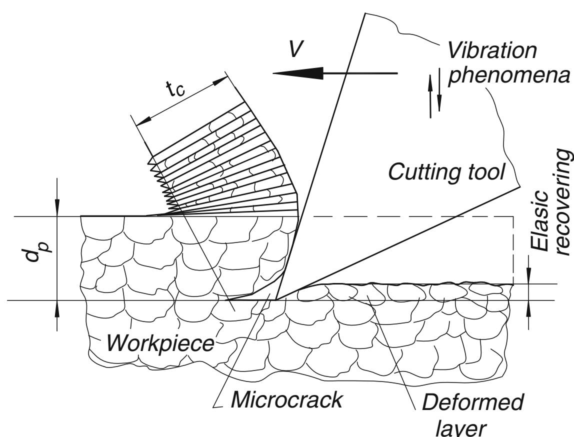

Fig. 14.1 Generation of nanoasperities as a consequence of the turning process

As known, the material corresponding to the grains limits could be a little different if compared with the material found in the grain, due to phenomena developed during the solidifying process of the workpiece metallic material; it is expected that the microcrack generated during the cutting process will correspond, in a certain extent, to this limits between grains. On the other hand, there is the so-called *theory of dislocations*, which takes into consideration the development of the microcracks along the crystals planes in which there are a high number of metallic material imperfections.

As accepted, each cutting process is accompanied by vibration phenomena; in Fig. 14.1, one supposed a tool vibration developed in a direction perpendicularly on the machined surface; in such a case, the vibration will exert a significant influence on the height of the surface nanoasperities.

It one take into consideration the kind of cutting tool and the specific work motions, a large set of machining processes could be highlighted; there are processes of turning, milling, drilling, grinding, honing, lapping etc. Some of these processes, able to generate nanoreliefs, are forwards analyzed.

14.3.2 Nanoreliefs Obtained by Turning

The turning is a cutting process in which the workpiece achieves a main rotation motion, while the cutting tool materializes a feed motion along a direction which is usually placed in the plane of the rotation axis. As one can see, the turning allows obtaining of revolution surfaces (cylindrical, conical, profiled, plane etc.). The active part of the cutting tool has a geometry (angles, nose radius) which are optimized, in order to fulfill distinct criteria (maximum tool life or minimum tool wear, minimum cutting forces, minimum roughness of turned surface, convenient shape of chips generated by turning process etc.). If one takes into consideration just the surfaces to be obtained, one can classify the turning operations in cylindrical or longitudinal turning, plane turning, conical turning, profiled turning etc.

From the point of view of nanoreliefs, a possible classification shows that there are roughing turning, when the surface roughness parameter Ra has sizes equal or higher than 6.3 μm and finishing turning, when one has $Ra \leq 3.2$ μm. More interesting is the case of *fine turning,* which allows obtaining turned surfaces characterized by $Ra < 1$ μm.

The surface generated by the turning process is firstly the result of combining workpiece rotation with linear (usually) feed motion (Fig. 14.2); these motions exert a decisive influence on the surface profile and generate asperities of pitch f, where f is the value of the work feed. Each cutting process is accompanied by vibration phenomena and the immediate consequence of these phenomena is the generation (in case of finishing or fine turning) of other asperities of lower height and approximately pitch f_1 (Fig. 14.1). A supplementary influence could be determined by the inhomogeneity of the workpiece material, by the errors of cutting edge, by the friction phenomena etc.

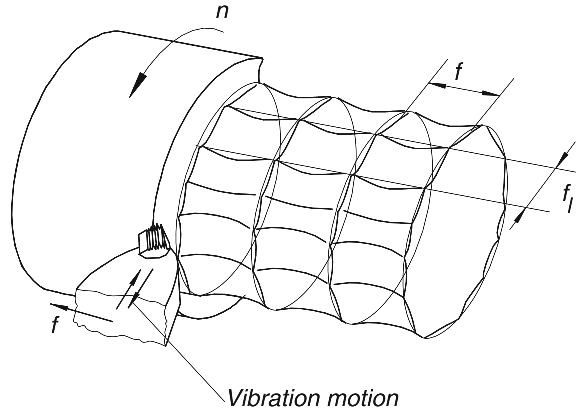

Fig. 14.2 Generation of nanoasperities as a consequence of the turning process

The main groups of factors able to affect the asperities height resulted from the turning process could be:

- Geometry of the active zone of the turning tool (entering angle, end cutting edge angle, back-rake angle, clearance angle, nose radius etc.);
- Parameters which characterize the operating conditions: fed motion speed *f*, cutting speed *v*, depth of cut a_p;
- Characteristics of vibration phenomena (amplitude, frequency, shape of vibration in a graphical representation etc.);
- Physical and mechanical properties of the workpiece material (hardness, ultimate stress, homogeneity etc.), found sometimes in connection with the chemical composition of the workpiece material;
- Rigidity of the machining system including machine tool, cutting tool, workpiece, devices for clamping workpiece and cutting tool;
- Presence and kind of cooling-lubricating fluids;
- Properties of the cutting tool material;
- Size of cutting tool wear etc.

The minimum values of the surface roughness parameter *Ra* obtained by a turning process seems to be *Ra* = 0.1 μm.

Results of research. If one considers the generation of the surface asperities only from geometrical point of view, one can notice that a theoretical relation could be established for the surface roughness parameter *Ra* [2, 3]:

$$R_a = \frac{2r_\varepsilon}{f}\left(r_\varepsilon \arccos\frac{m}{r_\varepsilon} - m\sqrt{1-\frac{m^2}{r_\varepsilon^2}}\right), \tag{14.2}$$

where *m* is the distance which establishes the position of mean line to the tool nose (Fig. 14.3). The theoretical relationship for *m* is:

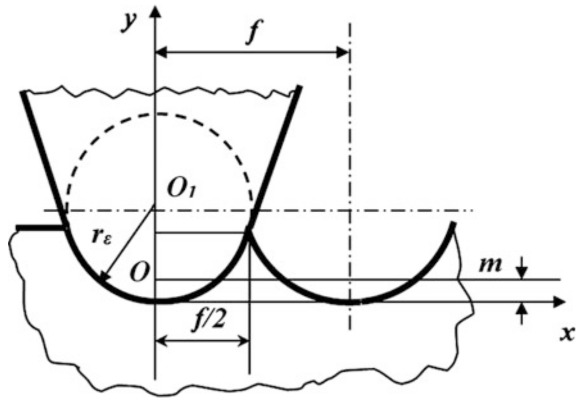

Fig. 14.3 Schematic for the determination of the surface roughness parameter R_a (Slătineanu et al. [3])

$$m = \frac{\sqrt{4r_\varepsilon - f^2}}{4} + \frac{r_\varepsilon^2}{f} arcsin \frac{f}{2r_\varepsilon}. \tag{14.3}$$

Since the theoretical relationship (14.2) established for the surface roughness parameter *Ra* does not directly offer an image about the influence exerted by the input factors r_ε (tool nose radius) and f on the size of the surface roughness parameter *Ra*, sets of values of *Ra* surface roughness parameter were determined for distinct sizes of the input factors r_ε and f. The results were processed by means of specialized software, in order to establish a mathematical power type function, able to better characterize the influence of the input factors on the surface roughness parameter *Ra*. In this way, the following mathematical model [2] was established:

$$R_{at} = 32.77 r_\varepsilon^{-1.011} f^{2.011}. \tag{14.4}$$

The examination of this relationship shows that the feed f exerts a significant influence on the surface roughness parameter *Ra*, because the exponent attached to the feed f in the above written relationship has a higher absolute value, in comparison with the value of the exponent attached to the tool nose radius r_ε.

One can see that the exponents able to highlight the influence exerted by the input factors f and r_ε have values close enough to those existing in a mathematical relation applied sometimes in order to characterize the influence exerted by the same factors on the surface roughness parameter *Ra* [11]:

$$R_a = 0.0000321 \frac{f^2}{r_\varepsilon} \; (\mu\text{m}). \tag{14.5}$$

Experiments were designed and achieved in order to obtain supplementary information concerning the influence exerted by some main factors able to affect the size of turned surface roughness parameter *Ra*. By mathematical processing of the experimental results, empirical mathematical power type functions were

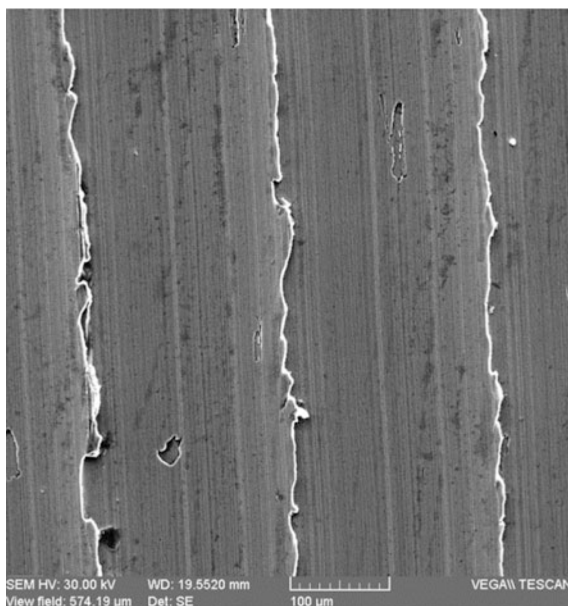

Fig. 14.4 Image of the test piece surfaces obtained by turning (test piece made of carbon steel 1C45, depth of cut a_p = 0.5 mm, longitudinal feed f = 0.2 mm, cutting speed v = 188 m/min, r_ε = 0.4 mm, R_a = 4010 nm, image obtained by means of scanning electron microscope Vega II Tescan LMH, magnification ×500)

determined. For example, in case of turning test pieces made of medium carbon steel 1C45 (containing 0.42 % C, 0.37 % Si, 059 % Mn), the following relationship was established:

$$R_a = 46.25 r_\varepsilon^{-0.468} f^{1.437} v^{-0.173}\ (\mu\text{m}). \tag{14.6}$$

As one can see, there are some differences in comparison with the relations (14.2) or (14.5) established on theoretical way and these differences could be partially justified by the influence exerted by the entire assembly of experimental conditions.

By using the empirical relationship (14.6) or other similar relationships, one can establish that in order to obtain values for the surface roughness parameter *Ra* lower than 1000 nm, and supposing that the tool nose radius is r_ε = 1.2 mm (specific, for example, to finishing turning processes), and turning speed v higher than 100 m/min (in order to avoid the generation of the built-up edge, phenomenon able to increase significantly the asperities height), work feed f lower than 0.12 mm/rev must be used. Very rigid technological systems (lathes, together with tools, workpieces and devices for clamping tools and workpieces) must be used, in order to obtain surfaces characterized by values of surface roughness parameter *Ra* lower than 1000 nm.

In Fig. 14.4, one can see the aspect of nanoreliefs obtained by cylindrical turning of a test piece made of medium carbon steel 1C45; this image was obtained by means of electron scan microscope Vega Tescan II LMH.

The turning speed v exerts a significant influence on the size of surface roughness parameter *Ra* in case of turning workpieces made of carbon steel. One can notice that in the zone of cutting speed v = 20–100 m/min, the generation of the so-called *built-up edge* contributes to the increase of the surface roughness; subsequently, once the increase of the cutting speed over 100 m/min, the built-up edge is not more generated and the surface roughness improves, due to better conditions of chip generation. In this way, one can notice that the increase of turning speed v determines initially a more accentuated and afterwards a low decrease of the surface roughness parameter. This fact was highlighted inclusively by means of the empirical mathematical model (14.6), established for experimental turning speeds v = 102.3–257.1 m/min.

14.3.3 Nanoreliefs Obtained by Abrasive Processes

The abrasive machining processes are based on the material removal from workpiece by the abrasive particles found in motion and pressed on the workpiece surface. In the case of cutting by means of metallic tools, there is the possibility to ensure adequate values for the cutting tool active part geometry and this means that pre-established values are ensured for entering angle, end cutting edge angle, clearance angle, back-rake angle, tool nose radius etc. In the case of abrasive machining, the abrasive particles have dimensions between certain limits, but their positions could be very distinct, so that there is not the possibility to have optimal values for the angles or dimensions corresponding to the cutting zone of each abrasive particle.

If one takes into consideration the possible incorporation of the abrasive particles into an abrasive body, one can notice that there are:

(a) Abrasive machining methods that use abrasive rigid bodies; this is the case of grinding, honing, superfinishing;
(b) Abrasive machining methods that use abrasive flexible tools; one can include in this group abrasive methods like finishing with abrasive flap wheels, with abrasive papers etc. Jain et al. appreciated that this kind of tools are more adequately when the problem of nano-finishing is formulated [12];
(c) Abrasive machining method that use free abrasive particles, found in suspension in a liquid or in a gas or liquid jet.

In all this cases, the particle has a motion in contact with the workpiece surface on which it is also pressed, generating a microcutting process and determining the generation of small chips. One can mention also that not all the abrasive particles found in contact with the workpiece surface are involved in cutting processes; if the abrasive particle geometry is not adequate for generating a cutting process or the force exerted by the particle on the surface layer of the workpiece is not high enough, only a low plastic deformation of the workpiece surface could be remarked. In this way, one can accept that the nanorelief generated by abrasive processes is a

concatenation of small cavities produced by the abrasive particles and zones where only the effects of plastic deformation were developed. One must mention also that each cutting process is accompanied by a plastic deformation of the workpiece material and this means that the machined superficial layer includes a zone with deformed grains.

The main factors able to affect the height of the nanoasperities generated on the surface machined by means of abrasive particles could be:

- Geometric characteristics of the abrasive particles (dimensions, sharp edges, nose radius etc.);
- Properties of the workpiece material (hardness, ultimate stress etc.);
- Forces exerted by the abrasive particles on workpiece surface;
- Speed of relative motion developed between abrasive particles and workpiece surface;
- Characteristics of the abrasive material (hardness, impact resistance, ultimate stress etc.) etc.

The minimum values of the surface roughness parameter *Ra* mentioned in the specialty literature are Ra = 20 nm for honing, Ra = 10 nm for superfinishing, Ra = 13 nm for lapping, Ra = 10 nm for finishing with abrasive papers, Ra = 5 nm for polishing with felt disc Ra = 7.5 nm for magnetic abrasive finishing, Ra = 4 nm for magnetic float polishing with CeO_2, Ra = 0.8 nm for magnetorheological finishing with CeO_2, $Ra < 0.5$ nm for elastic emission machining with ZrO_2 abrasives, Ra = 0.1 nm for ion beam machining [13].

Surface roughness in case of finishing by abrasive jet machining. *The abrasive jet machining* is based on the material removal from the workpiece as a consequence of the effects generated on the workpiece surface by the abrasive grains placed in a high velocity gas stream. Practically, the abrasive particles are transported and directed to the workpiece surface by means of a jet of compressed air (Fig. 14.5).

If an abrasive particle sent perpendicularly on the workpiece surface strikes this surface with a zone which is not proper for developing a cutting process, only

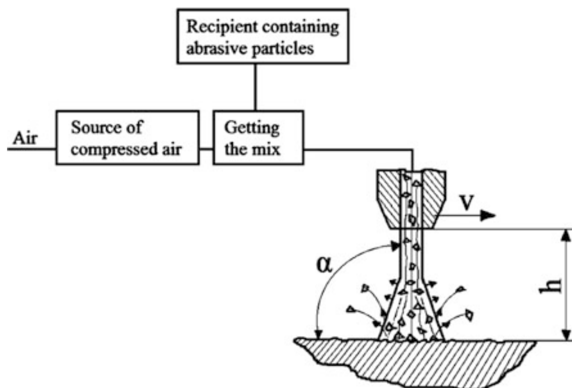

Fig. 14.5 Schematic representation of obtaining abrasive jet (Slătineanu et al. [14])

processes of plastic deformation or fragmentation of the brittle material could be observed. If the abrasive particle strikes the workpiece surface along a perpendicular direction to the surface to be machined and the particle has sharp edges, phenomena of plastic deformation, fragmentation or even breaking of asperities tops could occur. When an abrasive particle is sent along an inclined direction to the workpiece surface and the abrasive particle has active sharp edges, plastic deformation without material removal could be observed or even microcutting processes could develop. In this way, the nanoreliefs of the machined surface are generated.

Research results. Experimental researches developed in order to study the influence exerted by some process input factors on the surface roughness parameter *Ra* in case of test pieces made of medium carbon steel 1C45 ($HB = 210$) led to the following empirical mathematical model:

$$Ra = 1877 g^{0.249} h^{\;0.0955} \alpha^{0.091} \,(\mathrm{nm}), \tag{14.7}$$

where g is the average dimension of abrasive particles, in mm, h—distance between the nozzle and the test piece, in mm, α—inclination angle of the abrasive jet axis to the test piece surface, in degrees.

On can see that in the case of the experimental conditions, the distance h and the inclination angle α practically do not exert influence on the value of the surface roughness parameter *Ra*, while the increase of the average dimension g of the abrasive particles determines the increase of the value corresponding to the surface roughness parameter *Ra*.

In order to obtain finished surfaces characterized by values of the surface roughness parameter *Ra* lower than 1000 nm, by means of the relationship (14.7) one can find that abrasive particles characterized by average dimensions lower than $g = 0.035$ mm must be used.

The aspect of surface obtained by abrasive jet finishing examined by means of scanning electron microscope highlighted the results of impact exerted by the abrasive particles with the workpiece material. The finished surface is the results of complex microcutting and plastic microdeformation of workpiece material (Fig. 14.6).

Surface roughness in case of finishing by means of abrasive flap wheels. The machining scheme valid in the case of finishing of external cylindrical surfaces by means of abrasive flap wheels is presented in Fig. 14.7. One can see that abrasive flaps are attached to a shaft found in rotation motion with a rotation speed n_b. On the other hand, a rotation motion n_w is achieved by the workpiece to be finished, so that the abrasive flaps are obliged to take contact with the workpiece surface. A supplementary feed motion f is necessary to finish a longer surface of the workpiece.

Research results. By mathematical processing of the experimental results corresponding to the abrasive flap wheels finishing, the following empirical model was determined:

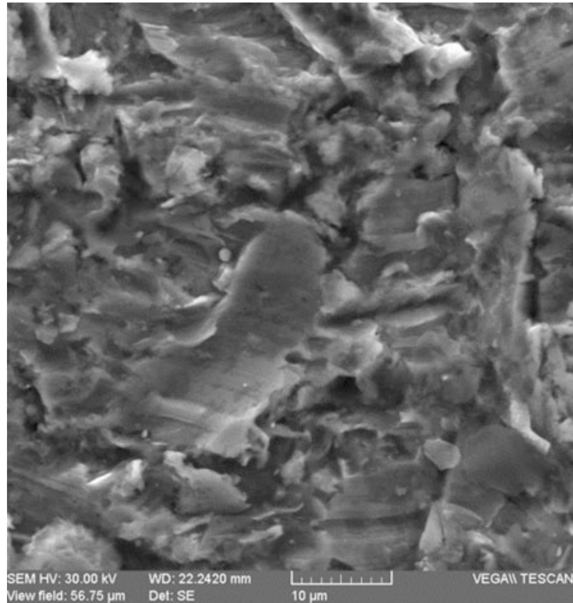

Fig. 14.6 Image of the test piece surfaces obtained by abrasive jet finishing (test piece made of carbon steel 1C45, *Ra* = 1320 nm, image obtained by means of scanning electron microscope Vega II Tescan LMH, magnification ×5000)

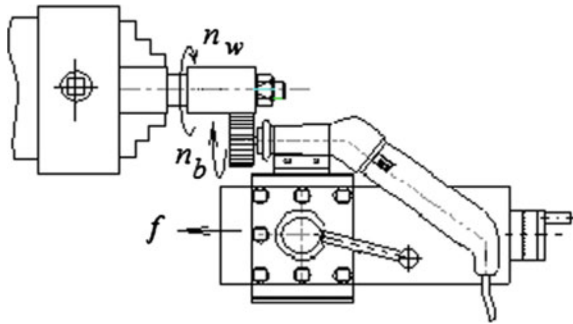

Fig. 14.7 Machining scheme for finishing of cylindrical surfaces by means of abrasive flap wheels (n_w—workpiece rotation motion, n_b—flap wheel rotation motion, f—longitudinal feed motion)

$$R_a = 13530 v_w^{0.352} v_b^{0.770} G^{0.179} f^{0.208}\ (\mathrm{nm}), \tag{14.8}$$

where v_w is the workpiece peripheral speed, in m/s, v_b—abrasive wheel peripheral speed, in m/s, G—abrasive particles (G = 80–180), f—longitudinal feed, in mm/rev. The empirical mathematical model highlights the significant influence exerted by the abrasive wheel peripheral speed v_b, whose increase determines the decrease of the size corresponding to the surface roughness parameter *Ra*.

In Fig. 14.8, an image of a surface finished by means of abrasive flap wheels is presented, while in Fig. 14.9, one can see a profile of such a surface, obtained by means of a surface roughness tester.

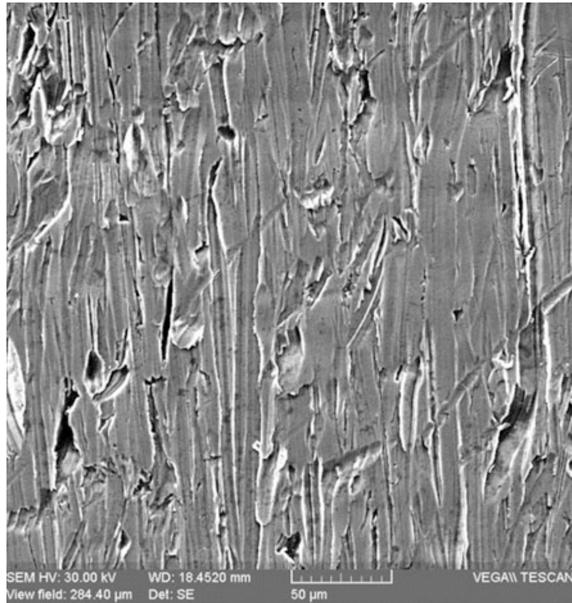

Fig. 14.8 Image of the workpiece surface obtained by abrasive flap wheels finishing (workpiece made of steel 1C45, workpiece peripheral speed v_w = 0.16 m/s, abrasive flap wheel v = 35.2 m/s, longitudinal feed f = 0.03 mm/rev, average particle diameter d = 201 μm, Ra = 407 nm, image obtained by means of scaning electron microscop Vega Tescan II LMH, magnification ×1000)

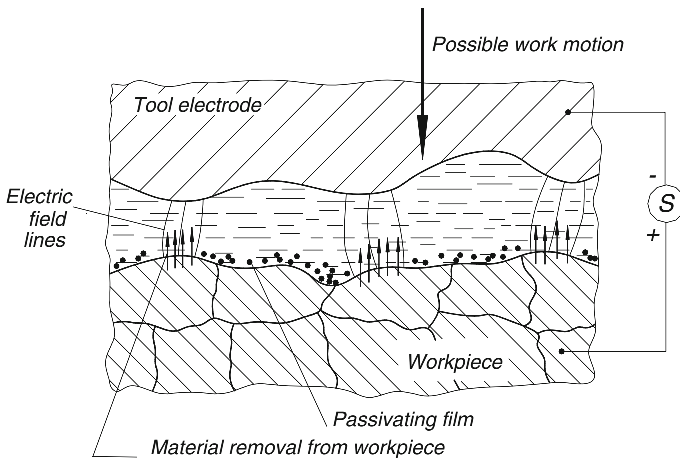

Fig. 14.9 Material removal and nanorelief generation in the case of electrochemical machining process

14.4 Nanoreliefs Obtained by Electrochemical Processes

The electrochemical machining is based on the material removal from workpiece as a consequence of the chemical reactions developed between workpiece material and electrolyte, when there is a tool electrode and both the active surface of tool electrode and surface to be machined of workpiece are immersed in electrolyte. It is necessary also to connect the tool electrode and the workpiece in the circuit of an electric direct current source. The electric circuit is closed by the electrolyte found between the active surface of the tool electrode and the surface to be machined of the workpiece (work gap). If the workpiece anode is affected by a material removal process, at the cathode tool electrode one can notice a process of hydrogen delivering.

As a consequence of the chemical reactions, the products of these reactions can remain near the workpiece surface and, if the products are not removed from work gap, a decrease of the electrolyte concentration occurs and the intensity of the machining process gradually diminishes. On can say that *a passivation phenomenon* develops. In order to ensure the continuity of the electrochemical machining process, distinct actions of removing the consequences of the passivation phenomenon are applied. If one takes into consideration the way of diminishing the results of passivation phenomenon, the following machining methods could be highlighted [1, 2]:

(a) *Machining methods with natural depassivation;* within such machining methods, the generation of the hydrogen bubbles and the bubbles motion to the electrolyte free surface contributes to the electrolyte agitation and to a certain diminishing of the passivation phenomenon intensity, so that the material removal from workpiece could continue. Machining methods such electrochemical polishing, electrochemical pickling etc. are included in this group;
(b) *Machining methods based on a forced circulation of the electrolyte in the work gap*; due to the relatively high speed and pressure of the electrolyte circulation, the passivating film is broken and the process could continue with a high material removal rate. In the group of machining methods involving the forced circulation of the electrolyte in the work gap, machining methods like electrochemical turning, electrochemical drilling, electrochemical milling, electrochemical deburring etc. could be included;
(c) *Hybrid machining methods in which the material removal by electrochemical reactions is supplemented by other traditional or nonconventional processes* that can contribute both to the material removal from workpiece, to stirring electrolyte and to removal of passivating film. Thus, there are machining methods in which the electrochemical process is combined with an abrasive process; for example, such machining methods are the electrochemical grinding, electrochemical honing, electrochemical lapping, electrochemical abrasive sharpening of cutting tools etc. On the other hand, there are hybrid electrochemical discharge machining methods, in which the electrical discharges and eventually supplementary relative motions between the tool electrode and workpiece, found in contact, are applied both for material removal from workpiece and for removal of the passivating film. In this last

group, there are machining methods like electrochemical discharge drilling, electrochemical discharge cutting, electrochemical discharge turning etc.

Among the above mentioned machining methods, the electrochemical polishing and some of the abrasive electrochemical finishing methods (grinding, honing, lapping, superfinishing) are able to generate nanoreliefs.

If one analyses the phenomena which develop in the work gap during the electrochemical machining process and present interest for nanoreliefs generation (Fig. 14.9), one can notice that as the distance between the tool electrode and workpiece diminishes, an electric field of increasing size develops between the close asperities existing on the two surfaces. When the electric field is high enough, chemical reactions are initiated between the electrolyte and the workpiece material. In this way, small quantities of workpiece material are affected by chemical reactions and leave the workpiece.

The process is more intense in those zones where the distance s between the asperities existing on tool electrode and workpiece is lower, in accordance with the theoretical relationship:

$$s = \frac{\left(U - U_{pol}\right)\sigma V_{sp}}{v} \text{ (mm)}, \tag{14.9}$$

where U is the voltage applied to the two electrodes, in V, U_{pol}—voltage, in V, for the two electrodes polarization, σ—the electric conductivity, in ohm^{-1}mm^{-1}), V_{sp}—specific volume of workpiece material, in mm^3/(A · s), and v—electrochemical erosion speed, in mm/s.

This theoretical relation (14.9) shows that a more intense process of material removal develops on the tops of asperities existing on the surface to be machined of the workpiece, where the distance s is lower and the density of the electric field lines is higher.

Research results. The relationship (14.9) is valid when the workpiece material is homogenous; since in the machine building frequently metallic alloys are used, this means that there are at least differences between the chemical compositions of the material found in the metallic grains ant the material found in the boundaries existing among the metallic grains, if one supposes that the material is homogenous in the metallic grains (Fig. 14.9). As a consequence, the electrolyte could react faster or slower with material found in the boundaries, determining a not uniform material removal from the workpiece material and generating asperities of distinct heights.

One can notice that the main factors able to affect the height of the asperities generated on the workpiece surface are the following:

- Chemical compositions and chemical properties of workpiece material and electrolyte;
- Voltage applied to electrodes;
- Concentration, temperature and viscosity of electrolyte and of passivating film generated on the workpiece surface;

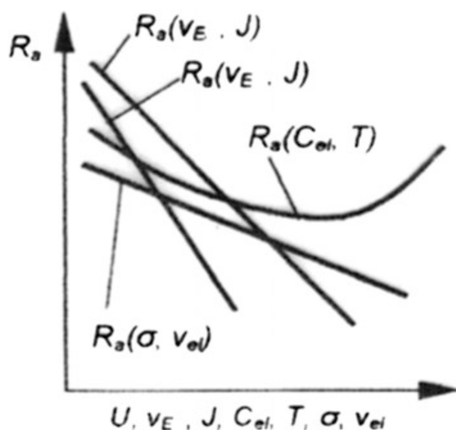

Fig. 14.10 Influence exerted by voltage U, working motion speed v_E, current density J, electrolyte concentration C_{el}, temperature T, conductivity σ and electrolyte circulation speed v_{el} on the surface roughness parameter R_a (after Artamonov [15])

- Initial surface roughness;
- Characteristics of electrolyte circulation near the workpiece surface etc.

In Fig. 14.10, one can see a synthetic representation of the influence exerted by some electrochemical process input factors on the size of the surface roughness parameter *Ra*.

As minimum values of the roughness parameter *Ra* obtained by electrochemical polishing processes, one can mention *Ra* = 80 …100 nm in the case when the initial surface roughness was characterized by *Ra* = 630 …1250 nm and *Ra* = 630–1250 nm, if the initial surface roughness was characterized by *Ra* = 5000–10,000 nm.

In Fig. 14.11, one can see the aspect of the surface obtained by electrochemical machining of a workpiece made of steel 1C45, while in Fig. 14.12 a surface profile obtained by means of a roughness tester is presented.

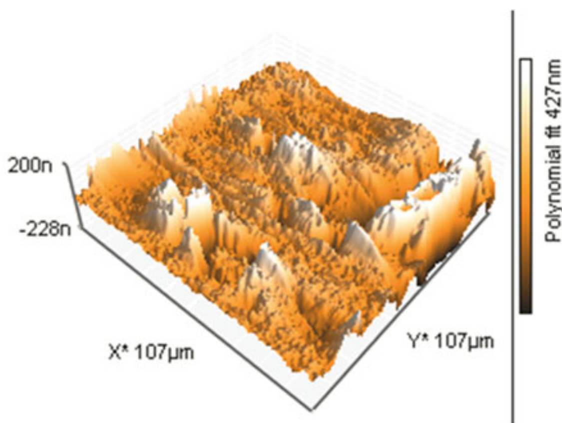

Fig. 14.11 Topography of a surface obtained by electrochemical machining (workpiece made of steel 1C45 electrolyte: aqueous solution of sodium silicate, electrolyte: aqueous solution of soluble sodium silicate, electrolyte density δ = 1.20 g/cm^3, process duration t = 6 min, *Ra* = 710 nm, atomic force microscope EasyScan 2) (Coteaţă [16])

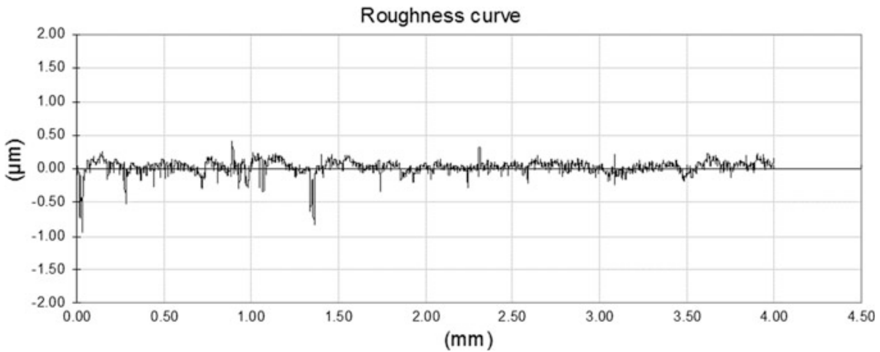

Fig. 14.12 Surface profile obtained by electrochemical machining (worpiece made of a stainless steel containing 0.055 % C, 18.824 % Cr, 0.035 % W, 9.79 % Ni, 1.20 % Mn, U = 35 V, electrolyte: aqueous solution of soluble sodium silicate, electrolyte density $\delta = 1.20$ g/cm^3, process duration t = 6 min, Ra = 70 nm, roughness tester Handysurf E-35A/B) (Coteaţă [16])

14.5 Nanoreliefs Obtained by Thermal Machining Processes

The thermal machining methods are based on the intense heating of the workpiece material, up to temperature when the material from certain workpiece zones is melted and even vaporized. The explosive character of vaporization phenomenon determines the detaching of small quantities of material from the workpiece; subsequently, the circulation of a fluid can contribute to the removing detached material from the work zone.

On can include in the larger group of thermal machining methods *the electrical discharge machining, the plasma beam machining, the laser beam machining, the ion beam machining, the electron beam machining*.

The main factors able to exert influence on the height of nanoreliefs obtained by thermal machining processes could be grouped in the following way:

(1) *Characteristics of thermal flux directed to the workpiece* (intensity, energy density etc.), essentially determined by the heat source and the medium by which the thermal flux is sent to the workpiece;
(2) *Chemical composition and physical properties of the workpiece material* (melting and vaporizing points, thermal conductivity, specific heat etc.);
(3) *Characteristics of the relative motions developed between workpiece and source of thermal flux*;
(4) *Characteristics of the work medium* in which and by which the material detached from the workpiece is removed.

Since there are distinct phenomena used in order to materialize the heat source, there are differences between the results obtained by applying such phenomena in

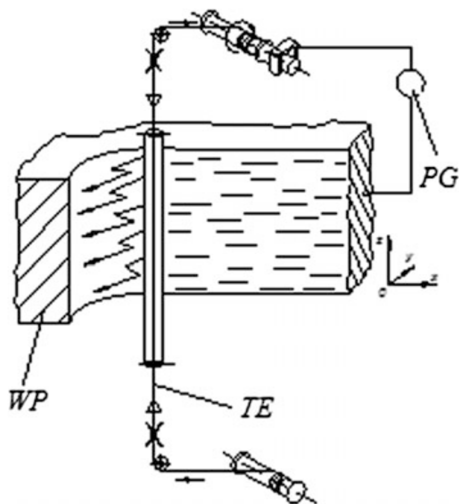

Fig. 14.13 Machining schema valid in case of wire electrical discharge machining: *TE* tool electrode, *WP* workpiece electrode, *PG* pulse generator

order to detach material from workpiece and these differences are reflected also in the different heights of generated nanoasperities.

Thus, in the case of electrical discharge machining, the electrical discharges in pulses are applied in order to determine melting and vaporizing small quantities of workpiece material and the circulation of a fluid (dielectric liquid) contribute to the removal of the detached particles from the work zone (Fig. 14.13). The smallest value of the nanorelief heights obtained by electrical discharge machining was of about 50 nm (*Ra* parameter).

In the case of plasma beam machining, a plasma jet obtained by means of electrical discharges is directed to the workpiece material, determining the melting and vaporizing phenomena and even the removal of the detached material from the machining space. The minimum values of the surface roughness parameter *Ra* in cases of surfaces obtained by plasma beam machining were of about 800 nm.

The laser beam machining uses a high energy laser beam in order to generate the melting and vaporizing phenomena; a gas jet sent along the laser beam axis contributes to the removal of the detached material from the machining space. The minimum values of the surface roughness thus obtained are of about 200 nm (*Ra* parameter).

In the case of electron beam machining, a high intensity electron beam is directed to the workpiece surface, where it generates melting and vaporizing phenomena. Since the machining process develops in vacuumed precincts, the metallic vapors are immediately removed as a consequence of functioning vacuum pumps. The minimum roughness of surfaces machined by means of electron beam is of about $Ra = 80$ nm.

Research results. At present, the most used machining process by thermal erosion is the electrical discharge machining; a version of this machining method uses a wire tool electrode found in a continuous travelling motion from a coil deposit to a coil on which the wire is accumulated; this work motion ensures a continuous compensation of the tool electrode wire and a high machining accuracy (0.0001 mm).

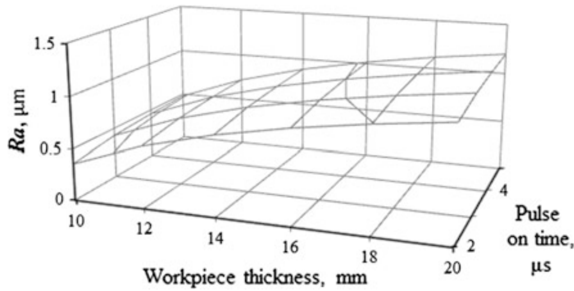

Fig. 14.14 Influence exerted by the workpiece thickness and pulse on time on the *surface roughness* parameter *Ra* (workpiece made of steel 1C45, pulse off time t_b = 7 µs, axial tensile force F_t = 900 gf, button position for current intensity i_a = 1, travelling wire electrode speed v_t = 2500 mm/min)

An empirical mathematical model able to highlight the influence exerted by some factors on the surface roughness parameter *Ra* [17] is:

$$Ra = 2.387 - \frac{14.399}{h} - \frac{0.407}{t_p} - \frac{0.730}{t_b} + \frac{42.406}{Ft} - \frac{0.360}{i_a} + \frac{77.344}{v_t} (\mu\text{m}), \tag{14.10}$$

where h is the workpiece thickness, in mm, t_p—pulse on time, in µs, t_b—pulse off time, in µs, F_t—axial tensile force, in gf, i_a—the position of button which defines the current intensity average amplitude, v_t—travelling wire electrode speed, in mm/min. As one can see, the workpiece thickness h exerts the most significant influence on the value of surface roughness parameter *Ra*. In accordance with the empirical model (14.10), for a workpiece thickness h = 10 mm and considering yet t_p = 2 µs, t_b = 7 µs, F_t = 900 gf, i_a corresponding the setting button position no. 1 and v = 2500 mm/min, one can obtain a machined surface characterized by a value *Ra* = 357 nm.

The graphical representation from Fig. 14.14 illustrates the influence exerted by the workpiece thickness h and the pulse on time t_p on the size of surface roughness parameter *Ra*, in accordance with the empirical mathematical model (14.10).

14.6 Nanoreliefs Obtained by Hybrid Machining Processes

The existence of distinct machining processes determined the researchers to search if combinations of distinct machining processes could be achieved; in this way, machining methods corresponding to combinations of traditional and non-traditional machining processes or just combinations of only nontraditional machining processes were proposed and applied.

In order to highlight the distinct possibilities of combining the traditional and nontraditional machining methods, one can took into consideration the information included in Table 14.1. Although there is a large variety of traditional machining processes by cutting, in Table 14.1 only a generic machining process by cutting was included, since all the cutting methods are based on the same general machining principles (plastic deformation followed by shear). On the other hand, in the case of nonconventional machining processes, many such processes were considered, since they are based on distinct principles.

Research results. The analysis of nanoreliefs could be developed for many combinations of traditional and nontraditional machining processes; in order to give only an example about the generation of nanoreliefs, some information concerning the electrical and electrochemical hybrid machining processes will be included in this subchapter.

As expected, within the hybrid electrochemical discharge machining processes, the machined surface is generated as a result of simultaneous development of electrical discharge machining processes and electrochemical machining processes, respectively, when the tool electrode and workpiece are immersed in a passivating electrolyte. Due to the generation and development of the passivation film on the workpiece surface to be machined as a consequence of chemical reaction developed between electrolyte and workpiece material, distinct ways of breaking and removing the passivating film were studied and used. One of these ways was based on a relative motion and the presence of a pressure between the tool electrode and workpiece; these aspects (relative motion and pressure) ensure conditions for breaking the passivation film and, if the distance between the asperities existing on the tool electrode and workpiece is low enough, electrical discharges could be generated and an additional electrical discharge machining process could develop. Subsequently, the electrochemical processes contribute to the generation and increase of a new passivating film and the process continues in this way, the workpiece material being removed in the desired areas of the workpiece.

The results of the hybrid electrochemical discharge machining process and especially the height of nanoreliefs could be influenced by the following main groups of factors:

- Properties of electrolyte liquid: chemical composition, *pH*, viscosity, electrical conductivity, temperature etc.;
- Parameters of electric current circulation: voltage applied to the electrodes, current density, pulse on time and pulse off time, if electrical pulses are used etc.;
- Properties of workpiece material: physical (melting and vaporizing temperature, electrical conductivity, thermal conductivity etc.) and its chemical composition etc.;
- Factors which characterize the mechanical relations between tool electrode and workpiece: relative speed, contact pressure, the frequency of contact interruptions etc.;

Table 14.1 Hybrid machining processes resulted as combinations of nonconventional machining processes or nonconventional machining processes with traditional machining processes

Machining processes	Traditional machining process	Nonconventional machining processes						
	Cutting	EDM	ECM	CM	PBM	USM	LBM	AMM
Cutting	X				CPB	CUS	CLB	
EDM		X	ECDM			EDMUS	EDMLB	
ECM		ECDM	X			UECM	ECMLB	
CM				X			CMLB	
PBM					X			
USM				CMUS		X		
LBM							X	
AMM								X

EDM Electrical discharge machining, *ECM* electrochemical machining, *CM* chemical machining, *PBM* plasma beam machining, *USM* ultrasonic machining, *LBM* laser beam machining, *AMM* abrasive magnetic machining, *ECDM* electrochemical discharge machining, *CMUS* chemical machining assisted by ultrasounds, *CPB* cutting assisted by plasma beam, *CUS* cutting assisted by ultrasounds, *CLB* cutting assisted by laser beam, *EDMLB* electrical discharge machining assisted by laser beam, *ECMLB* electrochemical machining assisted by laser beam, *CMLB* chemical machining assisted by laser beam

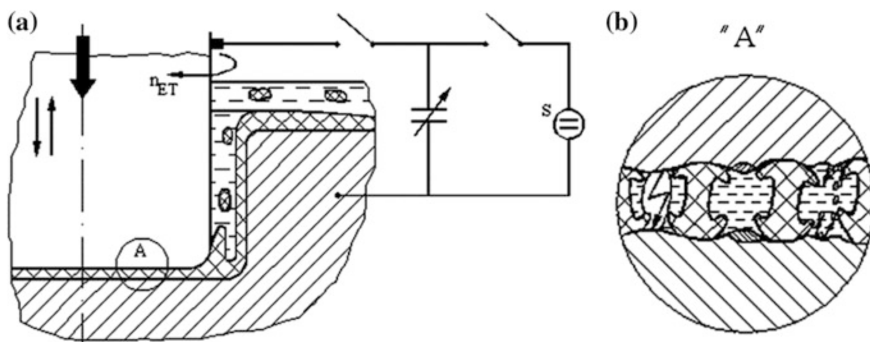

Fig. 14.15 Schematic representation of hybrid electrochemical discharge machining: *a* electrode tool in contact with the workpiece (*S* direct current source, n_{ET} tool electrode rotation motion; *b* detail from the work zone (Coteaţă et al. [18])

- Parameters of electrolyte circulation: speed, pressure, eventually periodical change of pressure etc.

The minimum value for the roughness parameter *Ra* of a surface obtained by electrochemical discharge machining was of about 800 nm.

A schematic representation of the process developed in electrochemical discharge drilling of small diameter holes is presented in Fig. 14.15. The cylindrical tool electrode is connected at the negative pole of direct current source. The tool electrode exerts a pre-established pressure on the workpiece surface and achieves a rotation motion. The electrochemical reactions developed between the workpiece material and the electrolyte (aqueous solution of soluble sodium nitrate) led to the generation of a passivating layer that is removed as a consequence of the pressure and of the relative motion between tool electrode and workpiece. Due to a periodical rectilinear alternative motion achieved by the tool electrode, the material

Fig. 14.16 Aspect of surface obtained by hybrid electrochemical discharge drilling of small diameter holes (workpiece made of high speed steel, tool electrode diameter d_{TE} = 0.5 mm, aqueous solution of soluble sodium silicate, electrolyte density δ = 1.20 g/cm^2, U = 45 V, C = 840 μF, image obtained by means of scanning electron microscope Hitachi S-4800) (Coteaţă [16])

detached as a consequence of chemical reactions and of electrical discharges is removed and gradually the small diameter hole is generated.

Thus, the machined surface appears as a result of both electrochemical reactions and electrical discharges; an aspect of such a surface is presented in Fig. 14.16.

14.7 Conclusions

By analogy with the definition of the nanomachining processes, one can consider that the nanoreliefs could be characterized by heights of the surface asperities lower than one micrometer (1–999 nm). Nowadays, there are various parameters and apparatus which could be used in order to obtain the information concerning the nanoreliefs. These parameters could be evaluated as profile parameters and surface parameters, their mathematical definitions being sometimes similar. A suggestive information about the nanoreliefs could be obtained by means of the apparata able to more magnify the height of the asperities in comparison with the magnification of the studied surface area. If machining methods able to generate nanoreliefs are analyzed, one can take into consideration traditional and nonconventional machining methods. If in the case of traditional machining methods the nanoreliefs are results of plastic deformation and shearing phenomena, in case of nonconventional machining methods, thermal and electrochemical phenomena contributes to the generation of nanoreliefs. Combinations of nonconventional machining methods or of nonconventional and traditional machining methods were also used in order to obtain nanoreliefs. Example of surfaces obtained by turning, abrasive jet finishing, abrasive flap wheel finishing, electrochemical machining, wire electrical discharge machining, hybrid electrochemical discharge drilling of small diameter holes were taken into consideration. In some cases, the experimental results were mathematically processed and empirical models were determined; these empirical models highlight the influence exerted by some process input factors on the size of the surface roughness parameter *Ra*.

References

1. T. Masuzawa, H.K. Tönshoff, Three-dimensional micromachining by machine tools. Ann. CIRP **46**(2), 621–628 (1997)
2. L. Slătineanu, O. Dodun, G. Nagîţ, M. Coteaţă, I.M. Bălan. Theoretical and experimental modelling of the roughness parameter *Ra*. Best of Book 2004, September 22–24, *Valladolid*, 114–125 (2004)
3. L. Slătineanu, G. Nagîţ, O. Dodun, M. Coteaţă, F. Chinesta, A. Gonçalves-Coelho, J. Pamies Teixeira, M. San Juan, L. Santo, F. Santos, *Non-traditional manufacturing processes* (Publishing House Tehnica Info, Chişinău (Republic of Moldova), 2004)
4. K. Hida, T. Miyoshi, H. Takaya, T. Hayashi. Nano-finishing using a micro-particle controlled by optical radiation force. In *Proceedings of JSPE Semestrial Meeting 2006,* JSPE Spring Meeting (2006)

5. V.S. Chernysh, A.S. Patrakeev, E.S. Soldatov, D.V. Petrov, S.V. Alyshev SV. Nanorelief formation under ion irradiation of germanium and silicon surfaces. J. Surf. Investig. X-ray Synchrotron Neutron Techn. **1**(6), 717–721 (2007)
6. V.K. Jain, Abrasive-based nano-finishing techniques: an overview. Mach. Sci. Technol. **12**, 257–294 (2009)
7. T.B. Teplova, Producing nanorelief in machining hard brittle surfaces. Russ. Eng. Res. **29**(8), 853–857 (2009)
8. A.V. Metlitskaya, A.N. Kulikov, A.S. Rudy, Formation of the wave nanorelief at surface erosion by ion bombardment within the Bradley-Harper model. Russ. Microlectron. **42**(4), 238–245 (2013)
9. A. Manna, K.Z. Molla. An Experimental Investigation during Nano Finishing of Hybrid Al/(Al2O3 + ZrO2)-MMC on Developed ECG Setup. in *5th International & 26th All India Manufacturing Technology*, *Design and Research Conference (AIMTDR 2014*), December 12th–14th, 2014, IIT Guwahati, Assam, India, 630-1-630-7 (2014)
10. 3D Surface Measurement. The History, Development, Advantages & Applications (2012). http://www.bruker-axs.com/3d-surface-measurement.html. Accessed 12 Oct 2012
11. G. Boothroyd, W.A. Knight, *Fundamentals of machining and machine tools* (Marcel Dekker Ink, New York and Basel, 1991)
12. V.K. Jain, A. Sidpara, M.R. Sankar, M. Das. Nano-finishing techniques: a review. *Proceedings of the Institution of Mechanical Engineers.* Part C: J. Mech. Eng. Sci. **226**(2), 327–346 (2012)
13. S. Jha, V.K. Jain, Nanofinishing techniques, *Micromanufacturing and nanotechnology* (Springer, Berlin, 2006), pp. 171–195
14. L. Slătineanu, Ş. Potârniche, M. Coteaţă, I. Grigoraş, A.L. Gherman, Roughness at surface abrasive jet machining. Buletinul Institutului Politehnic din Iaşi **57**(4), 220–227 (2011)
15. B.A. Artamonov, A.L. Vishnitskiy, I.S. Volkov, A.B. Glazkov, *'Dimensional electrical machining of metals' (in Russian)* (Vysshaia shkola, Moskow, 1978)
16. M. Coteaţă. Contributions to the study of the machining process by complex, electrical and electrochemical erosion (in Romanian). Doctoral thesis, *"Gheorghe Asachi" Technical University of Iaşi* (2009)
17. O. Dodun, L. Slătineanu, M. Coteaţă, V. Merticaru, G. Nagîţ. Surface Roughness at Wire Electrical Discharge Machining. in *ICAMaT 2014-7th International Conference on Advanced Manufacturing Technologies,* Bucharest (2014)
18. M. Coteaţă, L. Slătineanu, N. Pop, Mass wear of the electrode tool at the electrochemical discharge drilling. Buletinul Institutului Politehnic Iaşi **56**(1), 77–85 (2010)

Chapter 15
Template Assisted Formation of Metal Nanotubes

Ion Tiginyanu, Veaceslav Ursaki and Eduard Monaico

Abstract This chapter provides a review of methods for the production of metal nanotubes and their applications. The importance of nanotemplated growth of nanowires and nanotubes for nanofabrication, and the advantages of nanotubes over nanowires are revealed. Technological approaches for producing various templates, as well as advantages and drawbacks of specific templates, such as ion-track membranes, porous alumina templates, and porous semiconductor templates for nanofabrication are discussed, especially with respect to their suitability for the production of metal nanotubes. Technological methods applied for deposition of metal nanotubes with a focus on electrodepostion and electroless deposition are overviewed for each type of porous templates, and their mechanisms and peculiarities are evidenced. The prospects of application of nanomaterials based on porous nanotemplates in electronics, energy sector, optics, photonics, computers and communications, magnetism and biomedical sciences are explored.

15.1 Introduction

A wide field of potential applications, ranging from electronics, computers and communications to life sciences and biotechnology relies nowadays on the synthesis of functional nanoscale materials and devices. On the other hand, technological development in this area requires wide and intensive research, particularly in miniaturization and preparation of materials with low dimensionality and investigation of their properties which differ strongly from those of bulk materials. The

I. Tiginyanu · V. Ursaki (✉)
Institute of Electronic Engineering and Nanotechnologies "D. Ghitu",
Academy of Sciences of Moldova, Chisinau, Moldova
e-mail: ursaki@yahoo.com

I. Tiginyanu · E. Monaico
National Center for Materials Study and Testing, Technical University of Moldova,
Chisinau, Moldova

© Springer International Publishing Switzerland 2016

I. Tiginyanu et al. (eds.), *Nanostructures and Thin Films for Multifunctional Applications*, NanoScience and Technology,
DOI 10.1007/978-3-319-30198-3_15

strong change in properties of nanoscale materials and devices is induced by the low dimensionality and high surface to volume ratio.

Nanotemplates are widely used in nanofabrication, particularly in the production of large assembles of nanowires and nanotubes of various materials with defined shapes and dimensions [1–4].

Due to their unique properties, metal nanowires and nanotubes, as well as 2D metallo-semiconductor interpenetrating networks are promising for various nano-electronic and optoelectronic applications. Nanowires are used in nanoelectronic devices as interconnects, transparent and flexible electrodes, magnetic devices, chemical and biological sensors [5–10]. The optoelectronic applications of metallic nanowires and nanotubes are based on the extended dielectric/metal interface that can sustain the propagation of electromagnetic waves coupled to collective oscillations of the conduction electrons in the metal, the so called surface plasmon polaritons, allowing the manipulation and transmission of light on the nanoscale [11, 12]. 2D metallo-semiconductor networks are particularly used in sensors involving barrier structures and plasmonic excitations and memory media based on magnetic nanostructures embedded in semiconductor matrices [13–15].

Metallic [2, 3, 16–19] or semiconductor [20–23] nanowires or nanotubes with aspect ratios exceeding sometimes 1000 have been produced by employing the nanotemplate approach.

15.2 Porous Templates for Nanofabrication

Over the last decade, different template-based nanofabrication approaches have been developed which offer the possibility to produce large assembles of nanowires and nanotubes of various materials with defined diameters and lengths [1, 24–28]. Nowadays two types of templates are widely used for nanofabrication purposes, namely porous Al_2O_3 and etched ion track membranes based either on inorganic materials or on organic polymers [25–28]. Both porous Al_2O_3 and etched ion track membranes, however, exhibit high resistivity and therefore they often play a passive role in nanofabrication processes. In particular, templated growth of nanowires via electroplating is provided usually by the metal contact deposited on the back side of the high-resistivity membranes, while electroplating of metal nanotubes requires additional technological steps e.g. chemical modification of the inner surface of the pores prior to electrodeposition which leads to the incorporation of spurious phases in the nanotube walls [26]. Semiconductor nanotemplates which properties can be easily controlled by external illumination, applied electric fields, etc. provide wider possibilities for nanofabrication.

The etched ion track membranes are produced by bombarding thin polymeric films with heavy energetic ions (with specific energies higher than 1 MeV/nucleon) provided, for example, by a cyclotron, followed by chemical etching, which removes the weakened zones with chemical bonds damaged by the heavy ion bombardment. Each ion passing through the polymer foil produces a track, a

cylindrical zone of material with altered properties, which leads to the decomposition of the polymer material. At the step of chemical etching one has to choose carefully the composition of the etching bath and the temperature at which the etching is performed in order to produce pores with the desired shape and size.

The shape and size of the pore are determined by two parameters: v_b the bulk etch rate (etching rate for non-irradiated material) and v_t the track etch rate (the etching rate along the ion track). Typically the etching results in a conical or double conical pore (depending if one or both faces of the foil respectively are exposed to the etching bath) with the opening angle α: $tg\alpha = v_b/v_t$ [4]. In the case of high selectivity etching conditions, i.e. $v_t \gg v_b$ the shape of the pores can be approximated to a cylinder.

One can distinguish several generations of this technology. The so-colled 1st Generation used mainly polycarbonate (PC) and polyethylene terephthalate (PET) polymers that produced 10–20 μm thick microporous membranes with pores between 0.1 and 10 μm that are randomly distributed. This technology was developed in the mid-1980s by Prof. Legras and his team at UCL-POLY [29, 30]. In 1989, a first spinout, Cyclopore, was created.

Since 1996, the ion track technology has progressed considerably, due to the use of new polymers which opened up new possibilities in the control the geometry of the pores and their distribution. This technology, called 2nd Generation, makes use of polyimide (PI), which permits optimal use of the membrane up to 430 °C (PC and PET cannot be used beyond 120 °C). Apart from this, the chemical and mechanical resistance properties of PI are much better, while PI is also a well-known polymer in the field of electronics. On the other hand, PC offers several advantages: possibility to obtain easily both cylindrical or conical pores (the etching selectivity can be tuned on a wide range) and the ease to dissolve the template for direct nanostructures observation. PC dissolves easily in several organic solvents, e.g. dychlormethane. A solution containing 5 M NaOH and 10 % vol. methanol at 50 °C is typically used for producing cylindrical pores, while conical pores are obtained in an aqueous solution containing 9 M NaOH and 50 % methanol at room temperature [4, 31].

The pores of ion track membranes can be filled with metals or other polymers, obtaining therefore nanowires or nanotubes as well as other nanostructures for a broad variety of high-technology applications. The ion track templates offer a few degrees of freedom which makes them very attractive for such applications namely: (i) the possibility of preparing nanopores with the desired shape (cylindrical, conical or double conical); (ii) the possibility of choosing the desired pore density ranging from 1 pore/sample to 10^{10} pores/cm^2 by exposing the polymer foil to the desired ion fluence; (iii) the possibility of choosing the most suited material for the membrane such as polymers (polycarbonate PC, polyethileneterephtalate PET, polyimide PI), glasses, quartz or mica [32].

The method for producing membranes with pore density of 1 pore/sample was developed by the Material Research group at GSI Darmstadt. In order to obtain a single pore is necessary that the sample is hit by only one ion. Thus it is necessary to reduce the flux of heavy ions to approximately 10^3 ions/cm^2 s. A metallic plate

with thickness 0.2 mm with an aperture of 0.2 mm is inserted in front of the sample. A semiconductor detector is placed behind the sample with the purpose to detect each ion passing through the aperture and then through the sample. At such low fluxes the probability of an ion to pass through the aperture is of 1 event/s. This gives enough time to the automated system to switch of the beam using a fast chopper after an ion hit is detected by the detector.

In spite of the progress with ion track membranes, they have an essential drawback that for the preparation of ultra-small structures such as nanowires or nanotubes the first step involves the use of equipment which uses tremendous amounts of energy and has a size of at least several tens of meters namely an ion accelerator. In this sense, porous anodic aluminum oxide (AAO) membranes offer evident advantages. They attracted a remarkable interest due to the pioneer works of Martin [1] and Masuda and Fukuda [33]. Self-organized nanoporous structure with hexagonal ordered morphology were obtained on a highly pure Al surface via electrochemical anodization in acidic medium [34, 35]. Apart from the advantage mentioned above with relation to excluding the need of using an ion accelerator, AAO templates have many advantages over the polycarbonate membranes like high pore density, thermal stability, cost effectiveness and versatility. Pore diameter, length, inter-pore spacing, and pore ordering can be easily tailored by tuning the anodizing parameters such as voltage, time, electrolytes, pH value, and temperature [35].

Different acids like sulfuric acid, oxalic acid and phosphoric acids can be used for anodiziation of Al foils. Usually, sulfuric acid is used for the preparation of AAO templates with small pore diameter ranging from 3 nm to about 50 nm, phosphoric acid is used for obtaining templates with large pore diameter (≥60 nm), and oxalic acid is used to produce AAO templates with medium pore diameter. To obtain highly ordered pores, a two-step anodization was developed. For instance, in the first anodization step the Al foil is anodized at 0 °C and 40 V dc in 0.3 M oxalic acid for about 12 h to form textures on Al surface. The formed aluminum oxide layer is then removed by immersing anodized Al into a mixed solution of 0.4 M chromic acid and 0.6 M phosphoric acid solution at 60 °C. Subsequently, the sample is reanodized for different periods of time under the same anodization conditions as in the first step. Such type of self assembled AAO templates were used to fabricate different types of nanowires and nanotubes by electrochemical deposition method [36–39].

Figure 15.1 illustrates the nano-dimpled surface produced after the alumina membrane that was formed during the first anodization process was etched away. This surface serves as an ideal template for growth of an ordered structure during the second anodization in a two-step anodization process performed in potentiostatic mode at an anodization voltage of 60 V using a 0.3 M oxalic acid electrolyte [27].

Similarly to this 'nano-dimpling' seed-layer used by Sharma et al. [27] for the second anodization, Masuda et al. [40] have demonstrated a greatly improved ordering of the nanoporous structure by using a mechanical deformation pretexturing method on the aluminum foil prior to anodization.

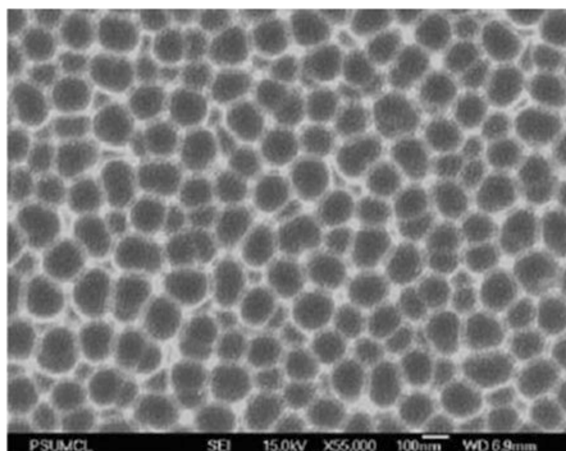

Fig. 15.1 Nano-dimpled aluminum foil after the alumina formed during the first anodization is etched away. Reprinted from Sharma et al. [27]. Copyright (2007) with permission from Springer

Figure 15.2 illustrates ordered arrays of pores with controlled diameter produced in alumina templates [41].

Alumina porous structures produced by two step anodization in a phosphoric acid solution are shown in Fig. 15.3 [42]. The first anodization step is tensiodinamic, while the second step is performed at constant voltage. The first step results in the production of the barrier-type oxide and the initiation of pores, which growth occurs during the second step by a dissolution/precipitation mechanism [43]. The residual metal is dissolved in a 0.1 M CuCl + 20 % HCl (w/w) mixture after the anodization, and the opening of the bottom side of pores is achieved by immersion in an aqueous 1 M NaOH solution at room temperature for 20 min.

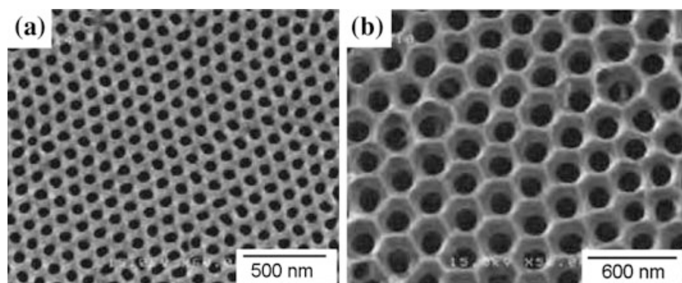

Fig. 15.2 Scanning electron micrographs of AAO templates with different pore sizes of approximately: **a** 60 nm, **b** 120 nm. Reprinted from Chen et al. [41]. Copyright (2010) with permission from American Chemical Society

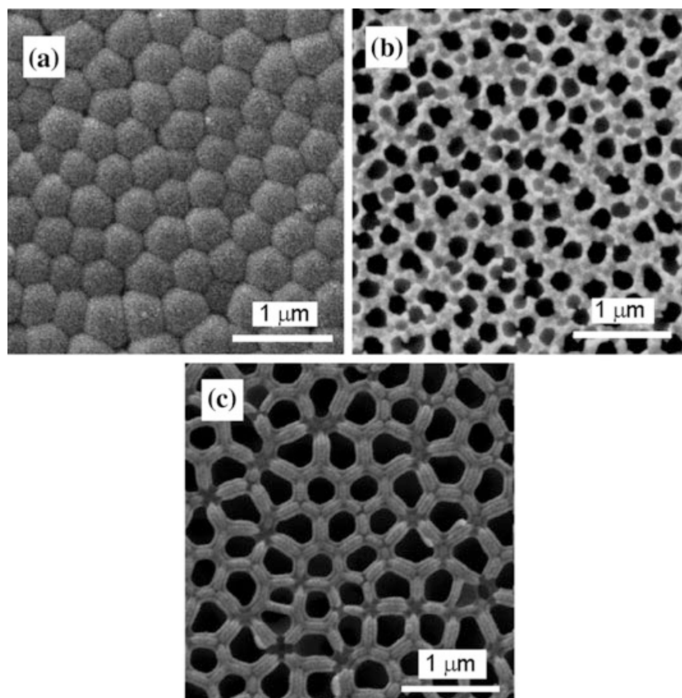

Fig. 15.3 SEM micrographs of an AAM grown in 0.4 MH_3PO_4 at 160 V and T = 10 °C after a tensiostatic charge of 160 C/cm^2: **a** metal-side surface before pore bottom opening; **b** solution side surface; **c** metal-side surface after pore bottom opening. Reprinted from Inguanta et al. [42]. Copyright (2007) with permission from Elsevier

Highly ordered alumina templates with hexagonal morphology have been also realized with a one-step anodization process in 0.4 M aqueous H_2SO_4 electrolyte at constant voltage of 26 V for 23 h using a DC power source at 0 °C [35]. Figure 15.4 shows SEM micrographs of the top and cross sectional surfaces of the produced AAO template at different magnifications. Low magnification top surface image (Fig. 15.4a) shows that the nanopores are very dense and uniform with perfect hexagonal ordering. High magnification image of the top surface (Fig. 15.4b) clearly exhibits the pore ordering and their geometry. Figure 15.4c, d shows the cross-sectional images of AAO template which reveals that the nanopores or nanochannels are very straight and parallel throughout their entire length. The authors have shown how morphology of membranes can be varied by changing anodizing parameters.

As mentioned above, both porous alumina and etched ion track membranes often play a passive role in nanofabrication due to their high resistivity. Over the last years, porous semiconductors have attracted considerable interest from the point of view of manufacturing conductive nanotemplates, especially after the demonstration of the possibility to grow self-organized [44, 45] and single crystalline

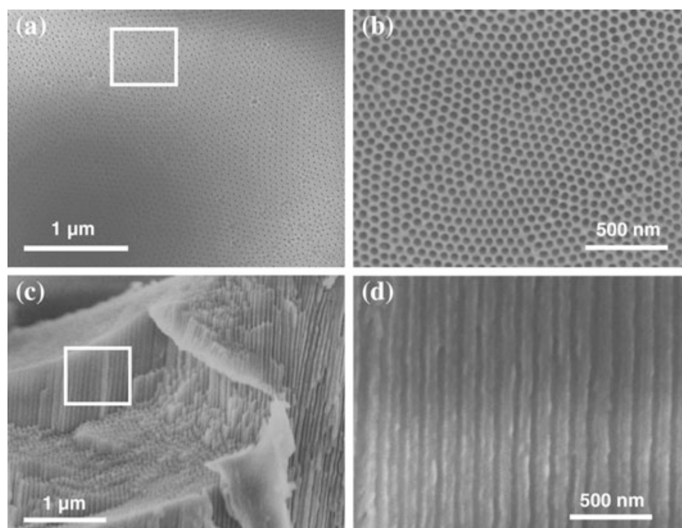

Fig. 15.4 FESEM image of AAO template. **a**, **b** Top surface view at low and high magnification. **c**, **d** Cross-sectional view at low and high magnification. Reprinted from Ali and Maqboo [35]. Copyright (2013) with permission from Springer

two-dimensional hexagonal arrays of pores by anodic etching of n-InP substrates [46–48]. The growth of arrays of parallel pores, although in a less ordered fashion, was demonstrated for CdSe as well [49]. As shown recently [50, 51], InP and CdSe nanotemplates can be produced routinely by anodic etching of crystalline substrates in salty water, the conductivity of the porous InP matrix being as high as to provide excellent conditions for the electrochemical pulsed deposition of Pt nanotubes with diameters as low as 70 nm and length up to 30 µm [51]. The electronic band gap of indium phosphide is 1.3 eV and that of cadmium selenide is 1.7 eV at 300 K, which means that the nanotemplates based on both InP and CdSe are opaque in the visible region of the spectrum. Among III–V and II–VI semiconductors one may consider the wide band gap compounds GaN (Eg = 3.3 eV), ZnO (3.3 eV) and ZnSe (2.7 eV) as good candidates for the fabrication of conductive nanotemplates transparent in the visible region. The morphology of the produced porous semiconductor templates will be shown in the Sect. 15.5.

15.3 Production of Metal Nanotubes in Ion-Track Membranes

Among the methods of filling template pores for nanofabrication are various. However, electrochemical deposition is the most direct approach and a preferred one, since a wide range of materials can be deposited this way [16, 20, 52, 53].

Electrodeposition was employed for the preparation of both metallic and semiconductor nanowires. The first report describing a template preparation of nanowires by electrochemical filling of pores with metals in mica dates back to more than 45 years ago [54, 55]. In contrast to electrochemical deposition which leads in most of the cases to rod-like structures, electroless deposition in nanoporous membranes can be used for the preparation of hollow structures. Therefore, it is suitable for the production of nanotubes [31, 56].

Enculescu published a review paper on nanowires and nanotubes preparation using ion track polymer membranes as templates and their characterization [4]. The first step in preparing nanowires is the deposition of a working electrode on one of the membrane surfaces by depositing a metallic thin film. In order to prepare an electrode with good adhesion to the membrane, a rough surface is preferred. For instance, sputtered deposition is performed for obtaining a gold thin film of approximately 50 nm thickness. Further, a copper layer with the thickness of about 10 μm is electrochemically deposited on top of the gold in order to completely close the pores on the electrode side and to increase the mechanical stability of the system. The sample is introduced in an electrochemical cell with the pores exposed to the deposition solution in the next step. Usually, a potentiostat in a three electrode arrangement is used for the deposition of the wires, and the deposition takes place in three steps. Polarization phenomena occur during the first step performed with higher current in the beginning of the process, while the actual filling of the pores with the material takes place during the second step performed with a relatively steady current. The third step is marked by a strong increase of the current due to the increase in deposition surface when the pores are completely filled and a cap starts to grow on the surface of the membrane. Multilayered wires can be produced by this method. For instance, the deposition of two metals in a layered arrangement can be performed from a single electrolytic bath, if the two metals are chosen in such a way that the difference between their deposition potential is high. Therefore, only the more noble metal is deposited when a lower overvoltage is applied, while an alloy of the two metals is deposited when a higher voltage is applied.

The production of nanotubes by electroless deposition in ion track membrane is based on the feature of the process that the deposition takes place only on the catalytic surface. Therefore, the pore walls can be covered with the desired material avoiding completely filling. As compared to the electroless deposition on macroscopic surfaces, in order to achieve complete tubes, it is necessary to give time to the reactants to reach all over the pore, i.e. the reduction reaction should be slow in order to compensate for the diffusion. To create a large number of catalytic nuclei on the surface, a three step process is employed with a preactivation (for instance with Sn^{2+} ions), and an activation deposition (for instance with Pd) [4]. Such a three step process was applied by Enculescu et al. [32] for the preparation of nano and microtubes of nickel in polycarbonate ion track membranes using the electroless deposition from an acidic bath containing nickel chloride as a source of nickel ions, nickel citrate, sodium hypophosphite and sodium acetate. It was mentioned that the preactivation process is the most important one during the entire deposition, and

this process should be carefully controlled. It was also observed that the deposition takes place in very good conditions when the polymer surface which typically is hydrophobic becomes hydrophilic. The activation occurs during the second step when the template membranes is dipped in a solution containing Pd^{2+} ions and the following reaction takes place: $Sn^{2+} + Pd^{2+} \rightarrow Sn^{4+} + Pd^0$. Palladium colloids are formed on the surface of the samples as a result of this reaction, which constitute the catalyst for the deposition reaction. In commercial electroless metal deposition, a more stable and easier reproducible 2 step process is preferred, which consists in the activation with palladium colloids stabilized by Sn^{4+} ions and afterwards the deposition process.

However, the 3 steps process presents a major advantage for the preparation of very small objects, since the number of Pd nuclei which can be obtained on the surface is one order of magnitude higher than in the 2 steps procedure. This allows the deposition of thinner metal films with higher adhesion to the surface.

The process of metal deposition (for instance Ni) is mainly associated with the reduction of metal ions from the solution in the presence of the catalyst. The main chemical reactions which take place in the deposition process are, for instance:

- the oxidation of the hypophosphite ions in the presence of catalytic surfaces into ortophosphite ions;
- the reduction of metal (Ni) ions.

During the deposition process in the presence of catalytic surface the hypophosphite ions oxidize in ortophosphite ions. The hydrogen atoms which result in this reaction are partially adsorbed onto the catalytic activated surface, where the metal (Ni) reduction reaction takes place, metallic nickel being deposited onto the surface.

In spite of the fact that the electrodeposition process of metal only along the pore walls is not sufficiently controlled relative to an electroless plating method, Motoyama et al. demonstrated that both metal nanowires and nanotubes can be produced by controlling the initial stages of electrochemical growth in PC membranes by using a sputter-deposited Pt–Pd layer as the cathode, which was so thin that the pores at the bottom were opened to pathways for the electrolyte [28]. The growth of Cu nanowires was deduced from the abrupt decrease in the cathodic current during the Cu deposition, which was correlated with the progress of the Cu grain growth and plugging the pores with the coarse Cu grains on the Pt–Pd side. In contrast to this, both nanowires and nanotubes were obtained with electrodeposition of Ni. The observed abrupt decrease in the cathodic current was associated with a nanostructure transition from the tube to the wire occurring at the growth front in this case. The authors mentioned that the important combination of the nanoporous template with a size distribution of metal grains must be emphasized when the nanostructured interface is designed. It was observed that the growth rate of the Ni tubes along the length was one order faster than that for the wall thickening. Therefore, it was found that the Ni nanotube growth lasts for longer deposition times as compared to Cu nanotube, which growth is lost immediately after the beginning of the electrodeposition.

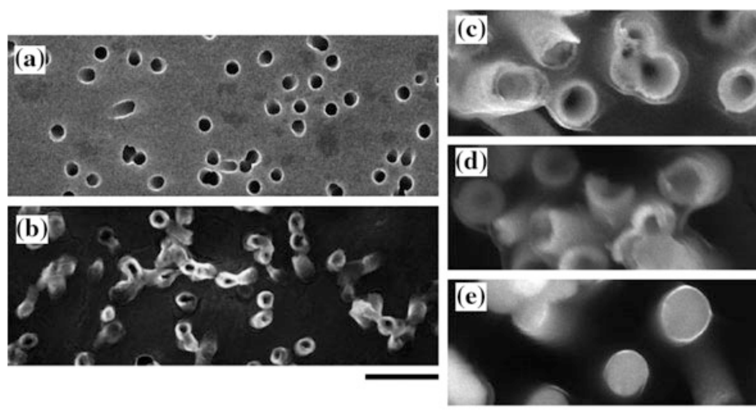

Fig. 15.5 SEM images of the sputter-deposited Pt–Pd layer on the PC membrane template with the pores of 200 nm in diameter (**a**, **b**), and of nanostructures formed at different deposition times (**c**–**e**). *Scale bar* 1.0 μm (**a**, **b**); 200 nm (**c**–**e**). The sputtered side (**a**). The Pt–Pd nanotubes liberated from the PC membrane (**b**). The deposition time for Ni nanostructures is 7 s (**c**); 15 s (**d**); 32 s (**e**). Reprinted from Motoyama et al. [28]. Copyright (2007) with permission from Elsevier

Figure 15.5a shows the Pt–Pd surface on the template membrane with the pores of 200 nm in diameter. It is clearly seen that the pores are not sealed and the original diameter is maintained. The image of the liberated Pt–Pd tubes as the cathode after the dissolution of the membrane with a dichloromethane solution is shown in Fig. 9.5b. The height of the nanotubes is roughly 300–500 nm. The growth of Ni nanostructures into the PC membranes is illustrated in Fig. 15.5c–e after the template membrane was dissolved in dichloromethane. Hollow tubes with wall thicknesses of 20–40 nm are produced at the deposition time of 7 s (Fig. 15.5c), which demonstrates that deposition of nickel occurs only along the pore walls from the edge of the Pt–Pd tubes as the cathode. The Ni tube walls become thicker gradually to reach a thickness of roughly 50 nm at the deposition time of 15 s (Fig. 15.5d). Finally, the top surface no longer shows a hollow cross-section at the deposition time of 32 s (Fig. 15.5e), i.e. nanowires are produced instead of nanotubes.

15.4 Metal Nanotubes in Porous Alumina Templates

Electrochemical deposition is also widely used for the nanofabrication in porous alumina templates. Basically, three kinds of electrochemical deposition methods are applied for filling the pores of AAO template: direct current (DC) electrodeposition [57], pulse electrodeposition (PED) [24], and alternating current (AC) electrodeposition [58].

The preparation of the AAO template for filling with metallic or magnetic materials via DC electrodeposition consists of several steps such as dissolving the

Al substrate in a saturated solution of $HgCl_2$, etched away of the barrier layer using chemical etching, sputtering of a thin metallic contact on one side of AAO which act as a cathode during electrodeposition. Etching away of the barrier layer often leads to the non-uniform widening of pores at the bottom and production of AAO template with different pore diameters at the top and the bottom surface, which ultimately results in non-uniform-diameter nanostructures. Additionally, these steps are time consuming, and the DC electrodeposition in porous AAO without modification of barrier layer is generally unstable and leads to a non-uniform filling of the AAO nanopores due to the cathodic side reaction [24, 35]. The uniformity and

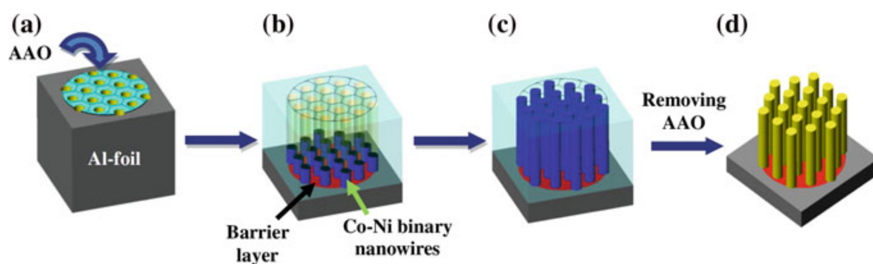

Fig. 15.6 Schematic diagram for co-deposition process of Co-Ni binary nanowires in nanopores of AAO template. **a** AAO template with *circular* shape, **b** filling of nanopores started from Co-Ni binary nanowires at the *bottom* of AAO by exposing circular area to the Co and Ni precursor solution, **c** complete filling of the alumina nanopores from Co-Ni binary nanowires, **d** dissolution of alumina in NaOH to get Co-Ni binary nanowires. Reprinted from Ali and Maqboo [35]. Copyright (2013) with permission from Springer

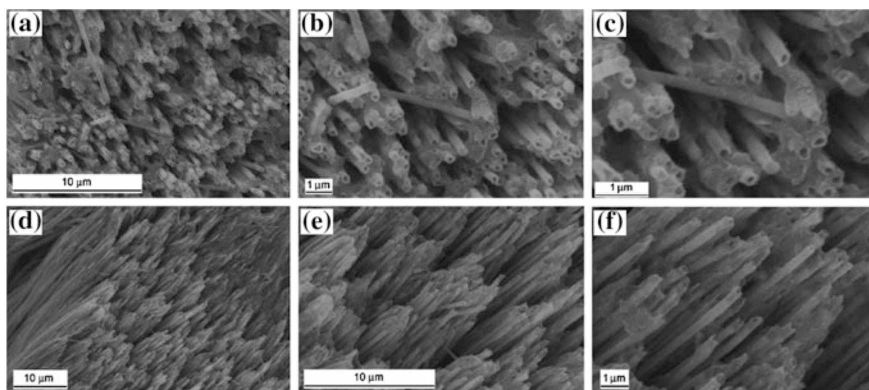

Fig. 15.7 SEM images of iron nanotube arrays: **a** *top view*, magnifying power K5000; **b** *top view*, magnifying power K10000; **c** *top view*, magnifying power K20000; **d** *side view*, magnifying power K2000; **e** *side view*, magnifying power K5000; **f** *side view*, magnifying power K10000. Reprinted from Cao et al. [59]. Copyright (2006) with permission from John Wiley and Sons

pore-filling efficiency increased many folds when the PED method is used compared to DC electrodeposition. However, PED method also needs modification of the barrier layer [24]. In contrast to this, AC electrodeposition is simpler in the sense that it does not need the detachment of AAO template from the Al substrate or modification of the barrier layer. Moreover, since the Al-substrate is not removed, it can be used as cathode during electrodeposition. The AC deposition of Co-Ni binary alloy nanowires without modifying the barrier layer at room temperature was reported by Ali et al. [35]. A schematic diagram of the used metallic deposition is shown in Fig. 15.6.

Cao et al. reported a systematic preparation of well-aligned metal (Fe, Co, Ni) nanotubes into pores of the alumina template and proposed their growth mechanisms. The production of Fe nanotubes is illustrated in Fig. 15.7.

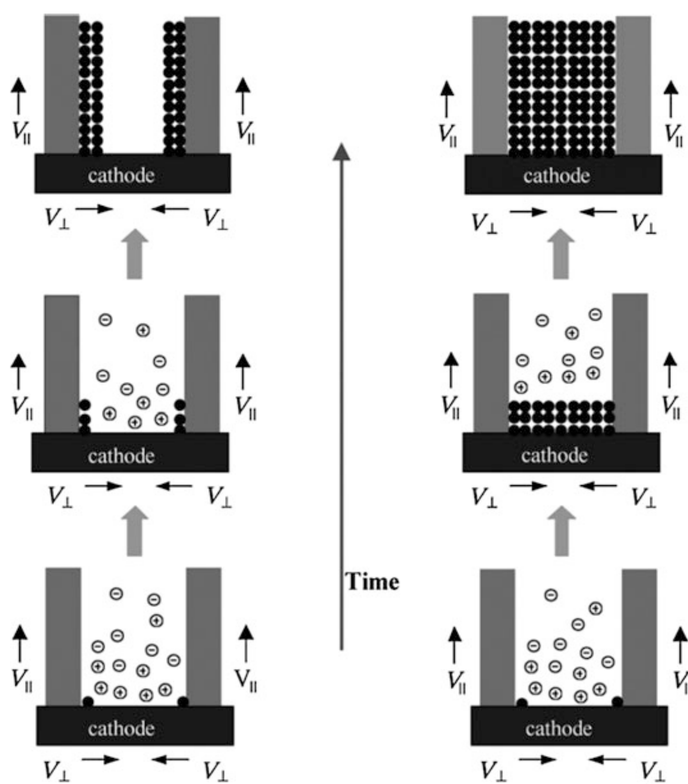

Fig. 15.8 Schematic diagram of the growth mechanism of 1D metal nanostructures via the template-based electrochemical deposition method. **a** Metal nanotube growth steps. **b** Metal nanowire growth steps. Reprinted from Cao et al. [59]. Copyright (2006) with permission from John Wiley and Sons

The schematic diagram of the electrodeposition process proposed by Cao et al. [59] is presented in Fig. 15.8. According to this diagram, the metal ions, surrounded by a hydration layer, move toward the cathode, where they are reduced. The reduction process consists of three steps: (i) the hydration number of metal ions decreases and the metal ions are rearranged in solution near the cathode surface; (ii) metal ions surrounded with partly discarding water molecules are reduced; (iii) adsorbed metal atoms discard the surplus hydration layer, then enter the crystal lattice. According to this growth mechanism of metal nanotubes, the junction between the cathode surface and the bottom edge of the template pore serves as a preferential site for the deposition of metal ions.

Similarly to processes occurring during the preparation of porous membrames, where the shape and size of the pore are determined by the ratio of two parameters: v_b and v_t as described above, the morphology of nanostructures produced into porous alumina template (i.e. nanowires or nanotubes) is determined by two parameters: $v_{||}$ (growth rate parallel to current direction) and $v_{\perp}$ (growth rate perpendicular to current direction). At low current density, these rates are nearly equal each other ($v_{||} \approx v_{\perp}$) and metal atoms fill most of the template pores until the pores are completely filled, wirelike 1D nanostructures being obtained. At high current density, the growth direction parallel to the current direction is the preferential one, which means that $v_{||} \gg v_{\perp}$, and tubular structures are generated.

A similar mechanism was proposed for the growth of Pt nanotubes [60]. Pt nanowires, thick-wall nanotubes and hollow (or thin-wall) nanotubes have been prepared by DC deposition in AAO templates (Fig. 15.9). Nanowires and hollow nanotubes are clearly observed in Fig. 15.9b with a considerable contrast difference, while thick-wall nanotubes can be observed in the middle of Fig. 15.15c. Some of the images showed ruptured parts on nanotubes (left-hand nanotube in Fig. 15.9d). The SEM images of Pt nanowires and nanotubes shown in Fig. 15.9 are well explained according to the above described model (Fig. 15.10a), i.e. nanowires are produced with low-current condition, when Pt metal is relatively slowly electroplated, while nanotubes are obtained with high-current condition, when metal plating starts to generate a tube-like structure from the plasma-sputtered Au on the bottom surface of the AAO membrane and a portion of the inside channel surface. By making use of this model, the authors were able to prepare novel core-shell cable structure of metal alloys (Fig. 15.10b) by stopping the growth of nanotubes of one metal in a high-current-density condition before the surface AAO channels became clogged and subsequently electroplating a second metal within the generated nanotubes at allow current density to fill up the nanotubes.

The growth of metal nanotubes along the pore walls of an AAO membrane by means of of metallic nanoparticles immobilized on the wall surfaces has been also

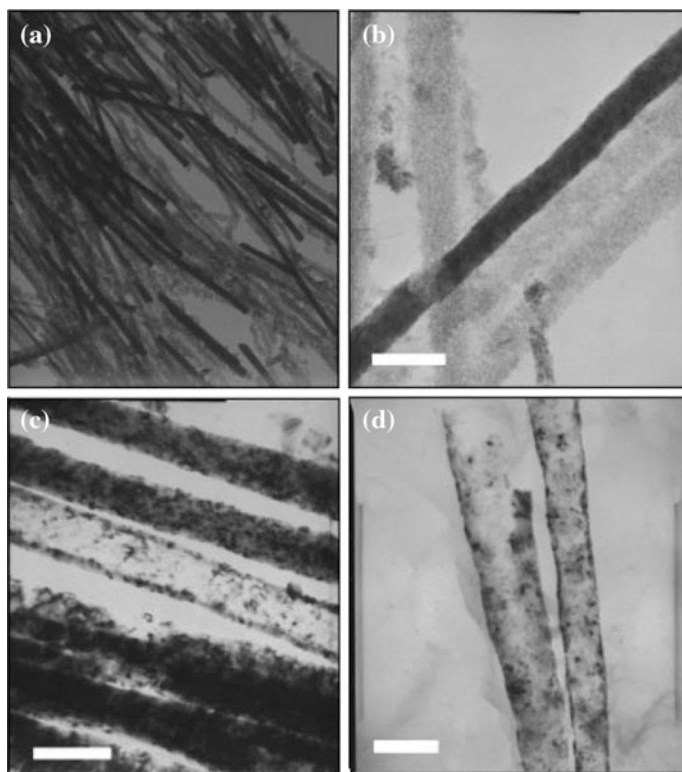

Fig. 15.9 Pt nanowires obtained by the high-current-density plating method. **a** TEM image at low magnification, **b–d** three different kinds of Pt nanostructures (close-packed nanowire, thick-wall nanotube, and hollow nanotube) (*scale bar* is 100 nm). Reprinted from You and Lee [60]. Copyright (2004) with permission from John Wiley and Sons

performed by Lee et al. [61] (Fig. 15.11). Particularly, Ag nanoparticles have been immobilized on the pore walls, followed by the production of Au nanotubes. As described above, the growth of metal nanotubes in this process starts at the base-metal electrode at the bottom of the pores as a result of the nonconducting nature of the nanochannels. The nanotube formation in this electrodeposition process was explained in terms of the relative rates of deposition and the diffusion of metal ions by assuming that the deposition process takes place at the tube tips, and therefore the deposition interfaces and the diffusion layers of metal ions move dynamically with the growth process of the tubes as shown in Fig. 15.11. The conducting path is created by electrodeposition between the tube tip and an isolated Ag nanoparticle, and the deposition interface moves from one isolated nanoparticle to another one via the dynamically created conducting paths.

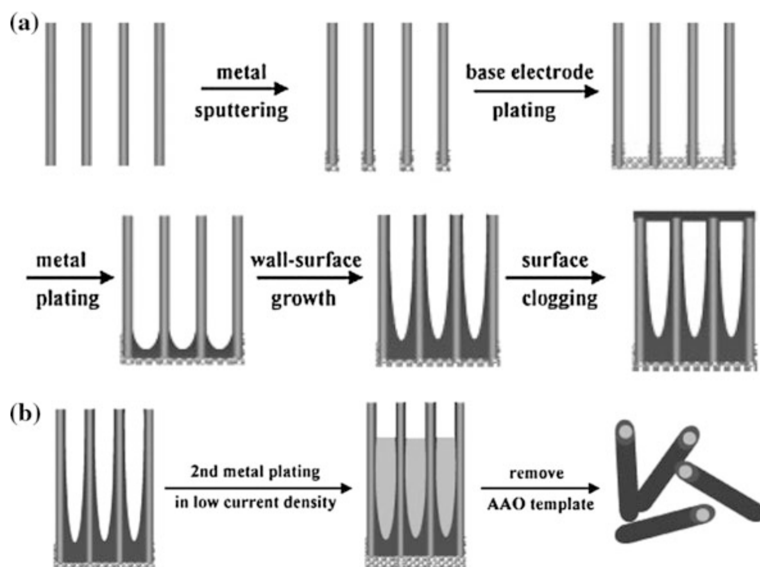

Fig. 15.10 **a** Postulated growth pattern of metal nanostructures by electroplating. **b** Preparation of core-shell nanocable metal alloys by consecutive electroplating at different current densities. Reprinted from You and Lee [60]. Copyright (2004) with permission from John Wiley and Sons

This method results in the production of mixed-metal nanotubes (i.e. Au nanotubes with surfaces decorated with Ag nanoparticles) upon the removal of the oxide matrix. The authors used this method for the preparation of multisegmented metallic nanotubes with a bimetallic stacking configuration along the nanotube axes as shown in Fig. 15.12. It was shown that the design of such multisegmented metallic nanotubes, i.e. the length of each metal segment, can be tuned by controlling the amount of total integrated charges involved in the electrochemical reaction, and such tailoring of the nanotube structure provides fascinating opportunities for engineering the physical properties of nanotube materials.

Apart from electrochemical deposition, electroless deposition can also be employed for the preparation of metal nanotubes into porous alumina templates. Inguata et al. performed nickel electroless deposition from a bath containing Ni sulfate as nickel source and sodium hypophosphite as reducing agent in order to fabricate Ni nanotubes [42]. The surface of pores was sensitized/activated by dipping the membrane alternatively (10 times) in a sensitization solution, containing $SnCl_2$, and in an activation solution containing a Pd salt. The Ni electroless deposition was also performed in five steps, each lasting 4 min, by adding to the same bath the overall quantity of the reducing agent (1.4 g/L). The entire membrane

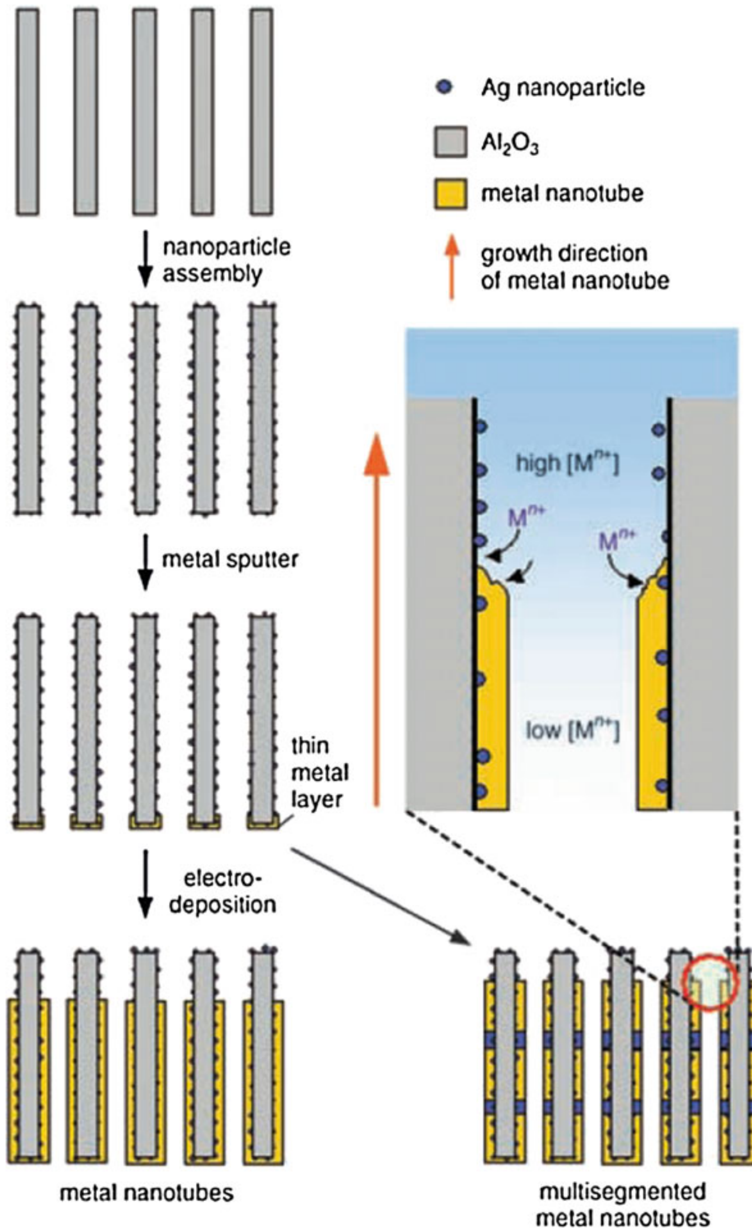

Fig. 15.11 Procedure for the preparation of metal nanotubes and the proposed mechanism of metal nanotube growth (see text). Reprinted from Lee et al. [61]. Copyright (2005) with permission from John Wiley and Sons

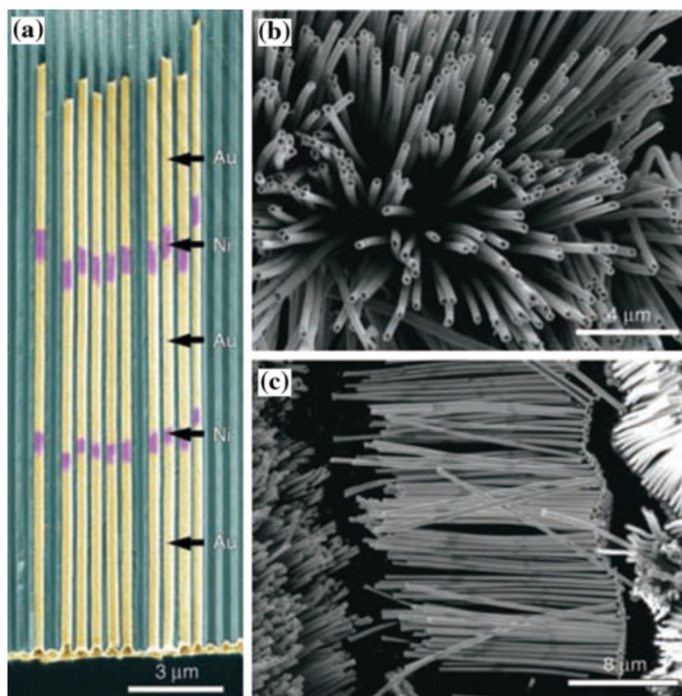

Fig. 15.12 SEM images of multisegmented metal nanotubes with a stacking configuration of Au-Ni-Au-Ni-Au along the nanotube axis. **a** Cross-sectional SEM image of as-prepared metal nanotube–AAO composite, which shows metal nanotubes embedded in an alumina matrix. The signals from Au and Ni are shown in *yellow* and *purple*, respectively. **b**, **c** SEM images of multisegmented metal nanotubes after removal of alumina matrix; part **c** clearly shows the stacking configuration of multisegmented metal nanotubes in which the segments with *bright* and *dark* image contrasts correspond to Au and Ni, respectively. Reprinted from Lee et al. [61]. Copyright (2005) with permission from John Wiley and Sons

surface was covered by Ni spherical grains forming a continuous and dense metal layer after 5 deposition steps as illustrated in Fig. 15.13.

Sung et al. [62] proposed an alternative to electroless and electrochemical deposition method for the production of metal nanotubes in porous alumina templates termed as "two step evaporation method". The method is based on evaporation processes to inject aluminum vapors into the porous template. The aluminum is deposited on the surface of the porous template by vacuum evaporation in the first step, and the deposited aluminum is vaporized and forced to be injected into pores by heating the sample at atmospheric pressure during the second step.

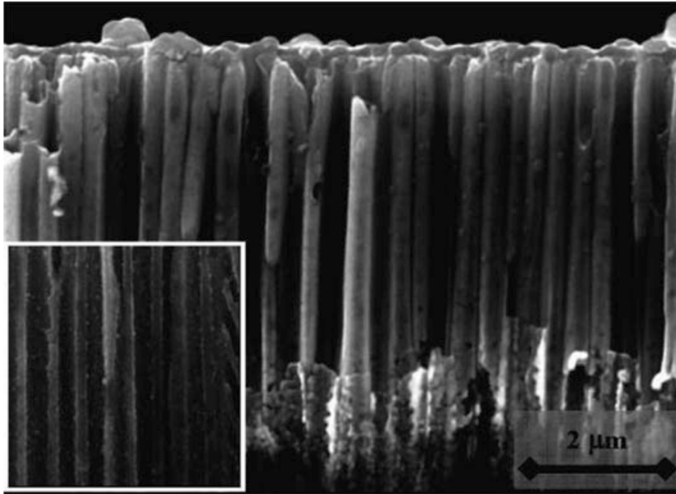

Fig. 15.13 SEM micrograph of the upper part of pores for a commercial AAM after 5 electroless deposition steps. *Inset* is the central part of the channel. Reprinted from Inguanta et al. [42]. Copyright (2007) with permission from Elsevier

15.5 Semiconductor-Metal Nanocomposites on the Basis of Metal Nanotubes Deposited in Semiconductor Templates

As mentioned in the Sect. 15.2, conducting nanotemplates for nanofabrication are produced on semiconductor substrates by anodic etching. The first III–V semiconductor templates, including those with self-organized two-dimensional hexagonal arrays of pores have been prepared on InP substrates. Crystalline (100)-oriented substrates of sulfur doped n-InP with 500 μm thickness and free electron concentration of 1.3×10^{18} cm^{-3} were used for these purposes [51]. Anodic etching was carried out in dark at room temperature in NaCl aqueous solution. It was shown that the diameter of the produced pores is controlled by the concentration of the used electrolyte, pores with diameters of about 70 or 140 nm being obtained with 3.5 or 1.7 M NaCl aqueous solutions, respectively. Figure 15.14a presents a cleavage of a porous sample produced by anodic etching of n-InP substrate in 1.7 M NaCl aqueous solution for 1.5 min, with subsequent removal of the nucleation layer. Anodization of n-InP in aqueous solution of NaCl proves to be an effective approach for the purpose of uniform nanostructuring and fabrication of semiconductor nanotemplates with ordered distribution of pores. These pores are oriented along current lines and they show usually circular shape, independent upon the crystallographic orientation of the substrate. A fascinating property of the current line oriented (CLO) pores is their long-range interaction in the process of formation, leading under certain conditions to self-arrangement in 2D hexagonal close packed

lattice. The CLO pores with transverse dimensions of about 140 nm distributed in 2D hexagonal arrays are clearly seen in Fig. 15.14a.

Nanotubes have been produced into these templates by electroctrochemical pulsed deposition of Pt with the duration of cathodic pulse of 300 μs for Pt deposition in pores with diameters 140 nm, which leads to uniform metal deposition on inner surface of pores (Fig. 15.14b).

Porous ZnSe templates present even more interest, since they are transparent for the visible light due to their larger bandgap. A method has been developed for controlling the conductivity of ZnSe crystals [63], which in its turn determines the diameter of the produced by anodization pores. It is based on doping the samples with Al from a Zn + Al melt. Figure 15.15a illustrates the production of a porous template on 1 mm thick n-ZnSe substrate with free electron concentration of 7×10^{16} cm^{-3}. The anodic etching was carried out in dark at room temperature in a $K_2Cr_2O_7$:H_2SO_4:H_2O electrolyte with the ratio 5:100:10 [64]. Although the formation of uniformly distributed pores exhibiting features of short-range order is

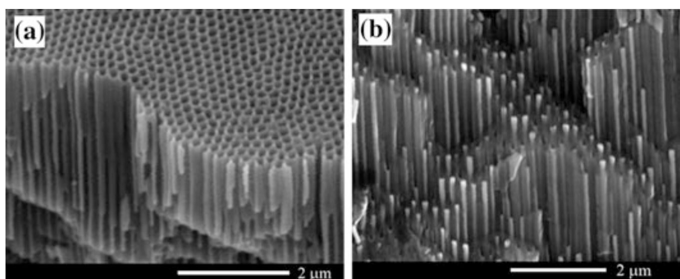

Fig. 15.14 SEM images taken from n-InP template prepared on (100)-oriented substrate with free electron concentration of 1.3×10^{18} cm^{-3} by anodization in 1.7 M NaCl aqueous solution (**a**); and SEM image taken from a cleaved porous template after pulsed electrodeposition of Pt (**b**)

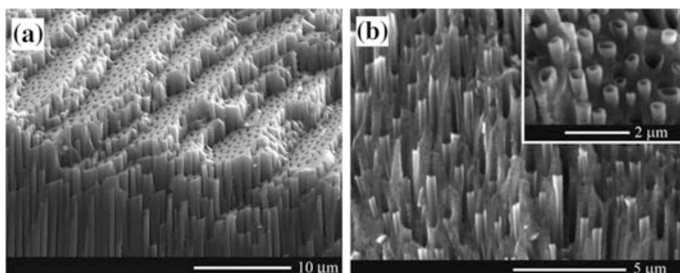

Fig. 15.15 SEM images taken from n-ZnSe template prepared by anodization in a $K_2Cr_2O_7$:H_2SO_4:H_2O electrolyte with the ratio of 5:100:10 (**a**); and SEM image taken from a cleaved template after pulsed electrodeposition of Pt (**b**). The *insert* in (**b**) illustrates a *top view* after the sample was additionally cleaved along a plane nearly perpendicular to the pores

inherent to anodic etching of n-ZnSe, long-range order in pore distribution was not reached. The reason could be the absence of crystallographically oriented pores in ZnSe. It is well known that the long-range order in pore distribution evidenced in n-InP is favored by the network of crystallographically oriented pores initially formed in the nucleation layer [46]. In case this network is well developed, there is a general tendency of current-line oriented pores to form rows oriented along ⟨110⟩ direction.

Pt electroplating in pulsed voltage regime in 20 μm thick porous ZnSe layer with diameters of pores of about 400 nm was carried out at 40 °C for 8 h in a common two-electrode plating cell containing 2 g/l Pt where the porous sample served as working electrode, while a platinum wire was used as counter electrode. During the 200 μs pulse time a cathodic potential of −40 V was applied between the two electrodes to electrochemically reduce the metal species on the inner surface of the porous matrix in contact with the electrolyte. After each pulse a delay time as long as 1 s was used at zero external voltage applied to allow ions to diffuse into pore regions depleted during the deposition pulse. Besides, magnetic stirring was applied to provide recovery of the ion concentration in the electrolyte along the whole depth of pores. As one can see from Fig. 15.15b, electrochemical deposition of Pt resulted in the formation of metal nanotubes with the wall thickness of about 50 nm. Pieces of Pt nanotubes getting out from pores are clearly seen in the cross-sectional view taken from a cleaved sample, see insert in Fig. 15.15b. The quality of nanotubes is indicative of good uniformity of metal deposition on the inner surface of pores.

The possibility to fabricate two-dimensional metallo-semiconductor quasi-periodic structures has been also demonstrated with porous GaP templates [65]. Templates with parallel pores possessing diameters in the micrometer and sub-micrometer ranges have been fabricated by electrochemical etching of commercially available *n*-GaP substrates with (100) orientations and electron concentration of about 10^{17} cm^{-3} in H_2SO_4 aqueous electrolyte.

Figure 15.16a illustrates the morphology of a porous GaP template. Similarly to InP templates, ordered arrays of pores are produced due to self-organization phenomena occurring during the pore growth. The white lines in Fig. 15.16a mark several directions of pore alignment in a porous GaP template. Uniform electroplating of Pt on inner surface of pores was realized in acid platinum bath under pulsed voltage regime, the deposition being performed at 40 °C in a common two-electrode cell where the porous sample served as working electrode and a platinum wire was used as counter electrode. It was found that under pulsed voltage regime it is possible to deposit metal within limited regions in depth of the porous structures, the depth of these regions being mainly dependent upon the ratio between the pulse duration and delay time between pulses. Electroplating starts with the deposition of metal dots, their density increasing with time. Overlapping of neighboring dots leads to the formation of tubular structures, as illustrated in Fig. 15.16b. It was found that the application of short pulses (<0.3 ms) during electroplating results in a predominant deposition of Pt near the bottom of the pores, while longer pulses lead to the predominant deposition near the mouth of the pores. So, the pulse length of 0.3 ms was found to be optimal for a uniform metal

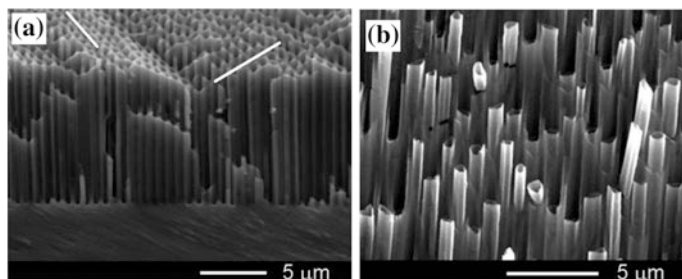

Fig. 15.16 SEM image of a porous GaP template with ordered arrays of pores indicated by *white lines* (**a**) and an image illustrating the formation of Pt cylindrical tubular structures (**b**)

deposition inside the pores of the template, metal tubes with smooth walls with rather good mechanical strength being produced.

Since the GaP template is characterized by ordered arrays of pores, it was found that packs of rows of Pt nanotubes in semiconductor envelope can be easily cleaved from the sample. Actually the semiconductor nanotemplate with the embedded array of metal nanotubes behaves like a layered crystal, the role of individual layers being played by the rows of Pt nanotubes in n-GaP envelopes. The possibility of such a cleavage is important from the point of view of photonic applications of the produces metallized porous GaP templates as discussed in the next section of the paper.

15.6 Applications

As mentioned in the introduction section of this paper, nanomaterials based on porous nanotemplates find wide applications in electronics, optics, computers and communications, magnetism or biomedical sciences. For instance, a device with the metal deposited in a porous semiconductor template can find applications in solid-state electronics, since a system of two interpenetrating networks is formed that has a very large interfacial area [66]. The huge surface of a Schottky contact implies an enormous capacitance, which has been exploited in a variable capacitance device developed on two-dimensional metallo-semiconductor networks prepared by pulsed electrochemical deposition of Pt inside porous GaP membranes with parallel pores possessing diameters in the micrometer and sub-micrometer ranges [65]. The morphology of Pt nanotubes deposited into porous GaP template used for the fabrication of such a device is shown in Fig. 15.17a. As concerns the characteristic sizes of a template for a capacitance semiconductor device, i.e. the pore diameter and the thickness of the skeleton walls, they should be chosen taking into account the value of the depletion region. The operation of the device to be realized is based on the overlapping of the depletion regions in the skeleton walls, starting from a certain applied bias. The rapid change of the device capacitance starts from this voltage and takes place up to the voltage of overlapping the

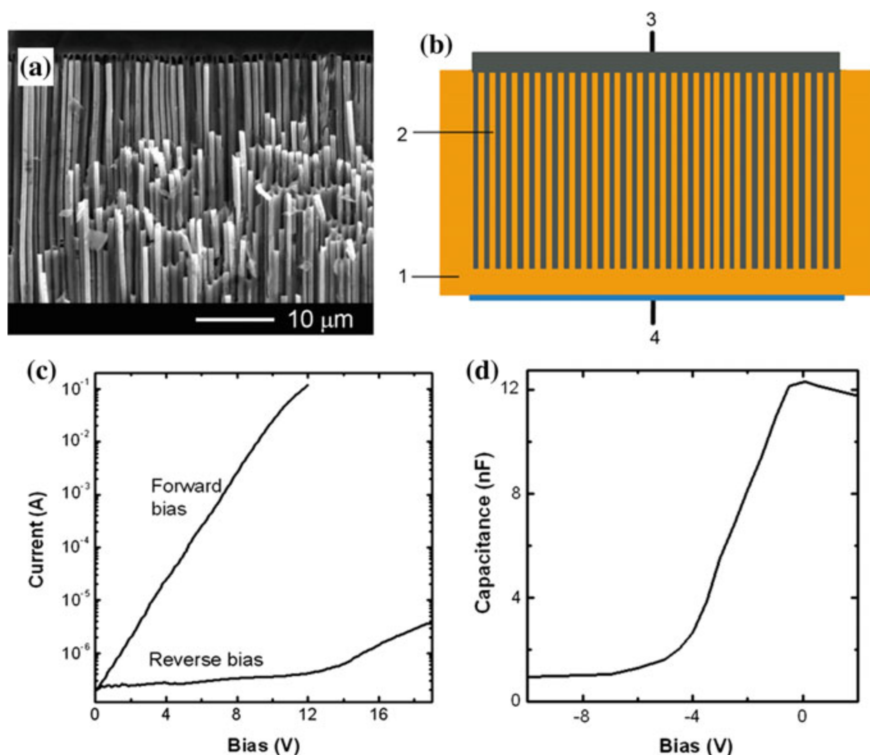

Fig. 15.17 **a** The morphology of Pt nanotubes/porous GaP nanocomposite used for the fabrication of a variable capacitance device. **b** The schematics of the device: *1* GaP substrate; *2* porous GaP template with Pt nanotubes; *3* Pt Schottky contacts deposited inside the pores and on the frontal surface of the template; *4* Ohmic contact. **c** Current-voltage characteristics. **d** Capacitance-voltage characteristics

depletion regions in the whole semiconductor skeleton. Therefore, the width of the walls cannot be less than the double depletion region at zero applied voltage for a given material. The real value of the barrier height in a Pt-*n*-GaP Schottky contact is about 1.1–1.3 eV. One can deduce a width of the depletion region of about 70–80 nm at zero applied voltage in a *n*-GaP specimen with free electron concentration of 10^{17} cm^{-3}. Therefore, the width of the skeleton walls cannot be smaller than 150 nm. The produced templates satisfy these conditions. Figure 15.17b presents the schematics of the device. The GaP porous layer was produced in the depth of 70 μm in a 500-μm thick substrate through an open window with the surface of 0.5 mm^2 on the front side of the GaP wafer. The Schottky contact was formed on the top and inner surfaces of the template, while the ohmic contact was formed on the back side of the substrate through the deposition of In. The current-voltage characteristics of the produced device structure are shown in Fig. 15.17c. The device shows a rectification ratio around 10^5 at the bias of 12 V.

The dependence of the device capacitance upon voltage is presented in Fig. 15.17d. One can see from this characteristic that the capacitance demonstrates a sharp decrease from 12 to 2 nF when the reverse bias is changed from 0.5 to 4 V, it means that the device demonstrates a capacitance density variation as high as 6×10^{-3} picofarad per square micron per volt. This value is much higher than that inherent to a variable capacitance device formed by the diffusion of dopants into a semiconductor material to form a flat p-n junction, or by the deposition of a metal that forms a Schottky contact with a flat semiconductor.

From the point of view of photonic applications, one-dimensional metallo-dielectric multilayer structures prove to be transparent in specific spectral regions and exhibit negative refraction and subwavelength imaging [67, 68]. Two-dimensional metallo-dielectric structures, to which the nanotubes deposited into porous templates belong, are even more prospective for photonic applications, for instance, for the development optical elements based on negative index materials (NIMs). NIMs with $n_{eff} = -1$ ($\varepsilon_{eff} = -1$; $\mu_{eff} = -1$) provide the opportunity for building a "perfect lens" that can focus electromagnetic waves to a spot size much smaller than the wavelength of the radiation [69, 70].

The importance of semiconductor nanotemplates with metal nanotubes grown inside the pores for photonic applications was demonstrated by calculations of some photonic properties. A highly efficient and accurate multiple-scattering approach is usually used to calculate the propagation of electromagnetic waves through the designed structures [71].

In order to investigate the photonic properties of materials assembled from porous templates with metallized pores, a simplified method was used which is based on the analysis of a parameter *f* describing the difference from the point of view of light scattering properties between the investigated material and a similar one with identical geometrical parameters but assembled from rods with the refractive index $n = -1$:

$$f = \max \left| D_m^{ni} - D_m \right|_{10 > m > -10}$$

where D_m^{ni} and D_m are the parameters determining the light scattering properties of the material assembled from rods with $n = -1$ and the investigated material, respectively; *m* is the index of the cylindrical function [71, 72].

The results of calculation of the parameter *f* for a metallized porous GaP template with close packing of pores, i.e. for the diameter of pores equal to the lattice parameter are shown in Fig. 15.18a. Ag was used for metallization since its plasma frequency lies in the near UV spectral range. The optical properties of Ag used in calculations were assumed to be described by the Drude formula with the plasma frequency $\omega_p = 4$ eV and damping parameter $\gamma = 0.01$ eV.

The focusing properties of flat lenses designed from porous GaP templates were studied by calculating the transmitted through the lens electromagnetic power $T = (E/E_0)^2$, where E is the electric field amplitude of the radiation passed through the lens, and E_0 is the electric field amplitude without the lens. In Fig. 15.18b, each

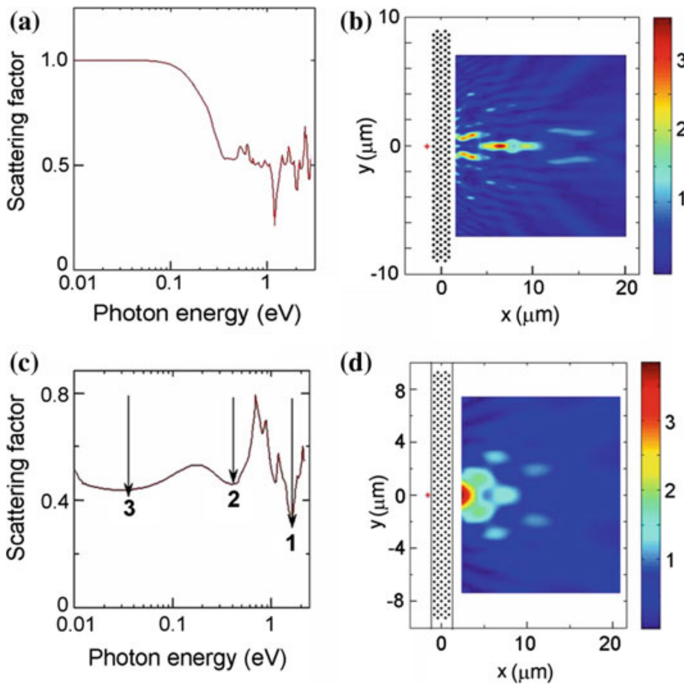

Fig. 15.18 **a** Spectral dependency of the parameter *f* for a porous GaP template with the diameter of pores 500 nm covered by an Ag film with thickness of 44 nm arranged in a *triangular* lattice with the lattice parameter of 500 nm. **b** Focusing properties of a flat lens designed from a porous GaP template as described in (**a**) calculated for the wavelength corresponding to the minimum in the spectral dependency of the *f*-parameter. **c** Spectral dependency of the parameter *f* for a porous GaP template with the diameter of pores 500 nm covered by a metallic film with the thickness of 100 nm and the refractive index n = 100 +200i, arranged in a *triangular* lattice with the lattice parameter of 500 nm; **d** focusing properties of a flat lens designed from a porous GaP template, as described in (**c**), and calculated for the wavelengths corresponding to the minima 2 in the spectral dependency of the *f*-parameter

black point from the flat lens represents a metallized pore, its axis being oriented perpendicularly to the plane of the figure. One can see from Fig. 15.18b that the focusing properties of such a lens are very good.

When investigating the photonic properties of the designed structures at longer wavelengths, one should take into consideration that the dielectric constant of the metal is not appropriately described by the Drude model al long wavelengths where it is characterized by high values of the real and imaginary parts. Having this in mind, calculations have been performed for porous GaP templates with pores covered by a metal with the refractive index n = 100 +200i which is realistic for some metals at low frequencies. As one can see from Fig. 15.18d, this kind of photonic lenses demonstrates also good focusing properties in the infrared spectral range.

Operation of photonic crystal lenses at infrared wavelengths has also been demonstrated on the basis of InP based photonic crystal technological platform including hole and pillar networks fabrication at nanometer scale [73]. Moreover, a two-dimensional device mixing arrays of holes and pillars was evaluated to pave the way for future integrated nanophotonic devices with complex functionalities such as cloaking or routing functions at optical wavelengths [74], detection and/or imaging [75].

It was shown that metallized titania nanotubes are also promising for designing and manufacturing negative index materials [72]. Flat and concave lenses assembled from these nanotubes demonstrate good focusing properties at specific photon energies which are determined by the geometry of nanotubes and features of their spatial distribution. The parameters of the produced TiO_2 nanotubes can be controlled by adjusting the technological conditions of anodizing Ti foils. Particularly, it was shown that the anodization of Ti sheets in an ethylene glycol and HF containing electrolyte allows one to prepare TiO_2 nanotubes with the inner diameter controlled in the range from 10 nm to more than 250 nm through the change of the electrolyte temperature from −20 to +50 °C [76]. Figure 15.19 illustrates the morphology of TiO_2 nanotubes produced at the electrolyte temperature of 0 and +30 °C.

The results of calculation of focusing properties of a concave lens assembled from titania nanotubes (n = 2.6) with the inner diameter of 80 nm and the outer diameter of 160 nm the outer and inner surfaces being covered with an Ag film with thickness of 12 nm are shown in Fig. 15.20.

The focusing properties of flat lenses assembled from metallized titania nanotubes proved to be not so good as those of concave lenses (Fig. 15.21a). However, it was found that these properties can be improved by assembling the flat lens from a superlattice of optimized clusters instead of ordered nanotubes (Fig. 15.21b). A clear superlensing effect is observed with the superlattice of optimized clusters i.e. $S/\lambda^2 < 1$, where S is the surface of the focal spot.

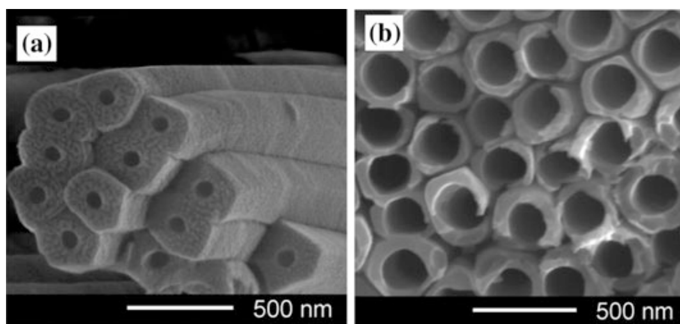

Fig. 15.19 SEM images of TiO_2 NTs prepared by anodization of Ti sheets at the electrolyte temperature of 0 °C (**a**) and +30 °C (**b**)

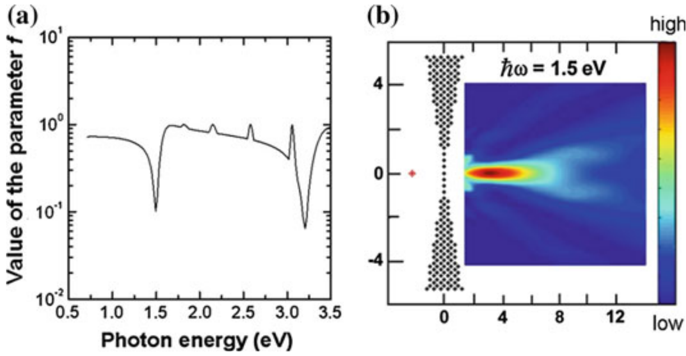

Fig. 15.20 The spectral dependence of the parameter *f* for titania nanotubes with the inner diameter of 80 nm and the outer diameter of 160 nm metallized by an Ag film with thickness of 12 nm (**a**), and focusing properties of a concave flat lens designed from these nanotubes (**b**)

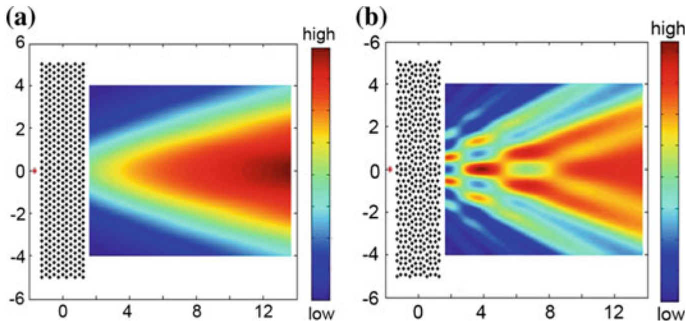

Fig. 15.21 Electric field intensity map of a cross-sectional view of the 2D source–image system when imaging by a photonic crystal flat lens consisting of ordered metallized TiO_2 nanotubes (**a**) and of a superlattice of optimized clusters (**b**)

The prospects for the elaboration of photonic crystal lenses and beam splitters on the basis of two-dimensional metallo-semiconductor structures prepared on porous templates and tubular structures have been also demonstrated on the instance of ZnSe templates [64]. The calculations performed for flat lenses assembled from metallized ZnSe tubes have proved again that focusing properties are better for lenses assembled from superlattices of optimized clusters as compared to those assembled from metallized ZnSe pores ordered in a triangular-lattice. The results of simulations for clusters consisting of metallized ZnSe tubes with parameters indicated in Table 15.1 are shown in Fig. 15.22.

Note that a clear superlensing effect is observed in this case (see Fig. 15.22), i.e., $S/\lambda^2 < 1$. The circles in Fig. 15.22 represent an area with the diameter equal to the wavelength of radiation. As one can see from Fig. 15.22b, these lenses can be used both for focusing or splitting the radiation. Unfortunately, the preparation of ZnSe

Table 15.1 The parameters of two samples assembled from metallized ZnSe tubes

Sample	Inner diameter (nm)	Outer diameter (nm)	Distance between cylinder axis (nm)	Metal film thickness (nm)
#1	40	80	80	6
#2	50	100	100	21

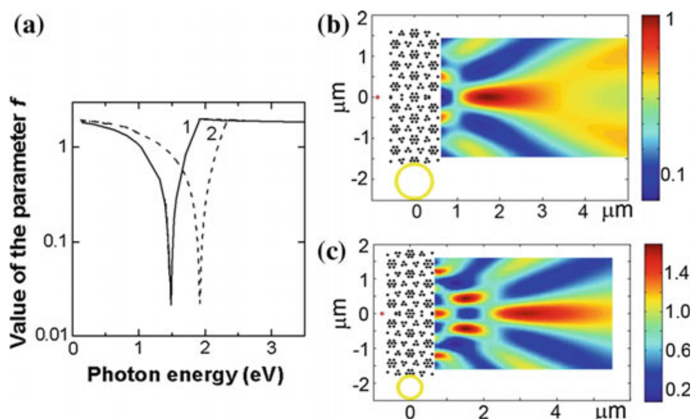

Fig. 15.22 Spectral dependence of the parameter *f* for the sample #1 and #2 (**a**). Electric field intensity map of a cross-sectional view of the 2D source-image system when imaging by a photonic crystal flat lens consisting of clusters of metallized ZnSe nanotubes with parameters indicated in Table 15.1 for sample #1 at the photon energy of 1.48 eV (**b**), and for sample #2 at the photon energy of 1.92 (eV) (**c**)

structures with such morphologies is more complicated from the technological point of view.

A fascinating property of metallized semiconductor templates with ordered arrays of pores from the point of view of photonic applications is the possibility of their cleavage, as discussed in the previous section of the chapter.

Since metallized pores are parallel to the plane of cleavage, both TM and TE polarizations (with the E-field or H-field polarized in the direction of pore axis, respectively) can be easily realized. This is an important advantage as compared to pores oriented perpendicularly to the sample surface, where both the E-field and H-field are always perpendicular to the pore axis for a normally incident light. It was previously shown that photonic crystals exhibiting a photonic bandgap in both TE and TM polarizations are particularly interesting for a better control of light confinement [77].

To avoid the need of cleavage, technological methods have been developed for the preparation of templates with pores oriented parallel to the top surface of the substrate [64]. As shown in Fig. 15.23a, a design was used where some areas of the front surface of the substrate are covered by a photoresist, while other areas are

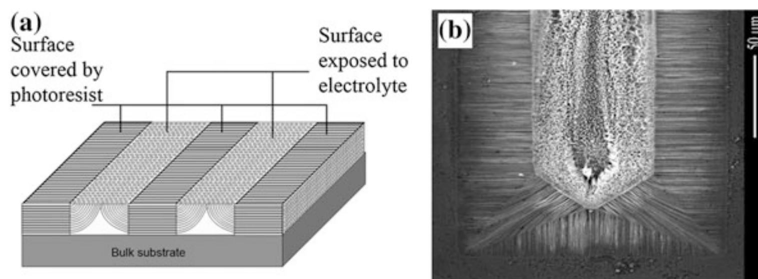

Fig. 15.23 **a** Illustration of the approach for the preparation of porous templates with pores parallel to the *top* surface of the sample. **b** Pt nanotubes deposited in an InP template with pores parallel to the *top* surface

exposed to the electrolyte in the electrochemical etching process. In this case, it is expected that the pores will grow from the surface exposed to the electrolyte initially in a direction perpendicular to the surface. However, with further propagation of pores, they will be deflected in directions parallel to the top surface, and will grow under the regions covered by the photoresist. These nanotemplates are suitable for the electrochemical deposition of metals inside pores, similar to the nanotemplates with pores perpendicular to the surface of the sample. Such kind of InP nanotemplate with Pt nanotubes deposited inside pores is shown in Fig. 15.23b. This approach is also suitable for the preparation of ZnSe templates and composites with pores parallel to the surface.

In a wider context, a range of industries can benefit from the development of metallo-dielectric composites such as transport industry (from the integration in magnetic sensors and radars), telecommunications (from systems of absorption of microwaves), energy sector (from the development of solar cells and fuel cells), as well as the health sector. The electro-deposition offers many advantages in the development of magnetic recording media as compared to other nano-technique, such as Electron Beam Lithography (EBL), Focus ion Beam System (FIB) and Nano-imprint. The dilemma between the grain size of the recording media and the coercivity is the main concern in the development of high information density magnetic recording media. The above mentioned technologies can meet the need of controllable grain size at very high cost. However, even at such cost the nano-fabrication is still not stable for the grain size under and below 100 nm. On the other hand, electro-deposition offers low cost and easy fabrication of nanowires and nanotubes below 100 nm. It is one of few methods that can overcome the geometrical restrictions of inserting metals into very deep nanometric cavities. As compared to nanowires, the interaction between array elements is significantly reduced in nanotubes by controlling the length of nanotubes and wall thickness, resulting in the formation of vortex domain wall in the nanotube arrays. Therefore, nanotubes offer great possibilities for improving the recording density.

Another field of applications of nanotubes and nanowires refers to biomagnetics, such as applications including molecular and cell separation [78–80], drug-delivery

systems [81, 82], biosensing [83–85], studies of cellular function [86, 87], as well as a variety of potential medical and therapeutic applications [86]. Scaffolds made of biodegradable nanowires have been used to repair brain damage and vision in animals, or coax neurons into forming engineered patterns [88, 89].

15.7 Conclusions

This review reveals the importance of nanotemplated growth of nanowires and nanotubes for nanofabrication. Nanowires are easier produced in nanotemplates as compared to nanotubes. However, nanotubes offer a series of advantages for applications. A comparative analysis of various templates evidenced their specific advantages and drawbacks. Basically three types of templates are used: ion-track membranes, porous alumina templates, and porous semiconductor templates. The ion-track membranes produced by bombarding thin polymeric films with heavy energetic ions followed by chemical etching offer advantages of producing nanopores with desired shape and desired density controlled in a wide range over very large surfaces. Cylindrical, conical or double conical pores can be produced in polymeric membranes by choosing two parameters: the bulk etch rate (etching rate for non-irradiated material) and the track etch rate (the etching rate along the ion track). The main drawback of the ion-track membranes is related to employment of very large size and energy consuming equipment, such as ion accelerator, for the preparation of ultra-small structures such as nanowires or nanotubes.

As concerns alumina templates, apart from the advantage of excluding the need of using an ion accelerator, they have many other advantages over the polymeric membranes, such as high pore density, thermal stability, cost effectiveness and versatility. Pore diameter, length, inter-pore spacing, and pore ordering can be easily tailored in alumina templates by tuning the anodizing parameters such as voltage, time, electrolytes, pH value, and temperature. One of the most important advantages of porous alumina templates is associated with self-organization phenomena occurring during electrochemical anodization which results in the production of a hexagonal ordered morphology of pores. Highly ordered pores are usually obtained with a two-step anodization, textures being formed on the Al surface during the first anodization step, while the ordering of pores occurs in the second anodization step. However, ordered pores can also be obtained with one step anodization process performed under specific conditions.

Porous semiconductor templates have attracted considerable interest from the point of view of manufacturing conductive nanotemplates, since both porous alumina and etched ion track membranes have high resistivity, and often play a passive role in nanofabrication. The success with the implementation of porous semiconductor templates in nanofabrication is partially ensured by self-organization phenomena which occur also in semiconductor substrates during anodization, single crystalline two-dimensional hexagonal arrays of pores being formed. The conductivity of semiconductor templates is their major advantage over porous alumina

and etched ion track templates, which requires additional technological steps e.g. chemical modification of the inner surface of the pores prior to electrodeposition which leads to the incorporation of spurious phases in the produced nanotube walls.

Electrochemical and electroless deposition are the main methods user for producing metal nanostructures in all kinds of templates. Electrochemical deposition in etched ion track membranes leads in most of the cases to rod-like structures, while electroless deposition can be used for the preparation of hollow structures. Therefore, it is suitable for the production of nanotubes, since the deposition takes place only on the catalytic surface. To create a large number of catalytic nuclei on the surface, a three step process is employed with a preactivation, and an activation deposition. In spite of the fact that the electrodeposition process of metal only along the pore walls is not sufficiently controlled relative to an electroless plating method, it is in some cases suitable for the production of both metal nanowires and nanotubes by controlling the initial stages of electrochemical growth.

Several kinds of electrochemical deposition methods are applied for filling the pores of porous alumina templates, such as direct current electrodeposition, pulse electrodeposition, and alternating current electrodeposition. Different mechanisms have been proposed for the growth of nanotubes in alumina templates by electrodeposition. According to one of these mechanisms, the morphology of nanostructures produced into porous alumina template is determined by two parameters: growth rate parallel to current direction and growth rate perpendicular to current direction. At low current density, when these rates are nearly equal each other, wirelike 1D nanostructures are obtained. At high current density, the growth direction parallel to the current direction is the preferential one, and tubular structures are generated. According to another mechanism, the growth of metal nanotubes along the pore walls takes place by means of metallic nanoparticles immobilized on the wall surfaces, where the deposition interface moves from one isolated nanoparticle to another one via the dynamically created conducting paths.

Pulse electrodeposition proved to be the most appropriate method for preparation of nanotubes into porous semiconductor templates. It was found that under pulsed voltage regime it is possible to control the metal deposition within limited regions in depth of the porous structures by changing the ratio between the pulse duration and delay time between pulses. A uniform metal deposition inside the pores of the template can be attained by optimizing this parameter, therefore metal tubes with smooth walls of well controlled thickness and rather good mechanical strength being produced.

In semiconductor templates with ordered arrays of pores, it was found that packs of rows of metal nanotubes can be easily cleaved from the sample, and the possibility of such a cleavage is important from the point of view of photonic applications of the produces metallized porous semiconductor templates. The importance of semiconductor nanotemplates with metal nanotubes grown inside the pores for photonic applications was demonstrated by calculations of some photonic properties. The prospects of such metal/semiconductor nanocomposited for the development of beam splitters and focusing elements with a clear superlensing effect have been demonstrated.

Among other application of nanomaterials based on porous nanotemplates, their use in electronics, energy sector, optics, computers and communications, magnetism or biomedical sciences have been demonstrated. In particular, the electro-deposition proved to offer many advantages in the development of magnetic recording media and biomagnetics, such as applications including molecular and cell separation, drug-delivery systems, biosensing, studies of cellular function and therapeutics.

References

1. C.R. Martin, Nanomaterials, a membrane—based synthetic approach. Science **266**, 1961 (1994)
2. A. Fert, L. Piraux, Magnetic nanowires. J. Magn. Magn. Mater. **200**, 338 (1999)
3. I. Enculescu, Z. Siwy, D. Dobrev, C. Trautmann, M.E. Toimil Molares, R. Neumann, K. Hjort, L. Westerberg, R. Spohr. Copper nanowires electrodeposited in etched single-ion track templates. Appl. Phys. A **77**, 751 (2003)
4. I. Enculescu, Nanowires and nanotubes prepared using iob track membrane templates. Digest J. Nanomater. Biostruct. **1**(1), 15–20 (2006)
5. P. Lehana, S. Khan, S. Arya, Int. J. VLSI Signal. Proc. Appl. **1**, 32 (2011)
6. J. Lee, P. Lee, H. Lee, D. Lee, S.S. Lee, S.H. Ko, Nanoscale **4**, 6408 (2012)
7. P.-C. Hsu, S. Wang, H. Wu, V.K. Narasimhan, D. Kong, H.R. Lee, Y. Cui, Nat. Commun. **4**, 2522 (2013)
8. D.A. Dinh, K.N. Hui, K.S. Hui, P. Kumar, J. Singh. Rev. Adv. Sci. Eng. **2**, 324 (2013)
9. Y. Zhang, W. Xu, S. Xu, G. Fei, Y. Xiao, J. Hu, Nanoscale Res. Lett. **7**, 569 (2012)
10. G. Hrkac, J. Dean, D.A. Allwood, Phil. Trans. Phil. Trans. R. Soc. **A369**, 3214 (2011)
11. Y. Bian, Z. Cheng, X. Zhao, L. Liu, Y. Su, J. Xiao, J. Liu, J. Zhu, T. Zhou, J. Lightwave Technol. **31**, 1973 (2013)
12. W.L. Barnes, A. Dereux, T.W. Ebbesen, Nature **424**, 824 (2003)
13. Ch. Valsecchi, Al. G. Brolo. *Langmuir* **29**, 5638 (2013)
14. D.A. Bussian, S.A. Crooker, M. Yin, M. Brynda, Al. L. Efros, V.I. Klimov. Nat. Mater. **8**, 35 (2008)
15. V.A. Vlaskin, R.G. Beaulac, R. Daniel, Nano Lett. **9**, 4376 (2009)
16. M.E. Toimil Molares, V. Buschmann, D. Dobrev, R. Neumann, R. Scholz, I.U. Schuchert, J. Vetter. Single-crystalline copper nanowires produced by electrochemical deposition in polymeric ion track membranes. Adv. Mater. **13**, 62 (2001)
17. T. Ohgai, I. Enculescu, C. Zet, L. Westerberg, K. Hjort, R. Spohr, R. Neumann, J. Appl. Electrochem. **36**, 1157 (2006)
18. W. Schwarzacher, O.I. Kasyutich, P.R. Evans, M.G. Darbyshire, G. Yi, V.M. Fedosyuk, F. Rousseaux, E. Cambril, D. Decanini. J. Magn. Magn. Mater. **198–199**, 185 (1999)
19. L. Gravier, A. Fabian, A. Rudolf, A. Cachin, K. Hjort, J-Ph Ansermet, Meas. Sci. Tech. **15**, 420 (2004)
20. M. Sima, I. Enculescu, T. Visan, R. Spohr, C. Trautmann. Mol. Cryst. Liquid Cryst. **418**, 21 (749) (2004)
21. M. Sima, I. Enculescu, E. Vasile, J. Optoelectron. Adv. Mater. **8**, 825 (2006)
22. T. Ohgai, L. Gravier, X. Hoffer, J-Ph Ansermet, J. Appl. Electrochem. **35**, 479 (2005)
23. D. Xu, Y. Xu, D. Chen, G. Guo, L. Gui, Y. Tang, Chem. Phys. Lett. **325**, 340 (2000)
24. K. Nielsch, F. Müller, A. Li, U. Gösele, Uniform nickel deposition into ordered alumina pores by pulsed electrodeposition. Adv. Mater. **12**, 582 (2000)

25. I.U. Schuchert, M.E. Toimil Molares, D. Dobrev, J. Vetter, R. Neumann, M. Martin. J. Electrochem. Soc. **150**, C189 (2003)
26. W. Lee, R. Scholz, K. Nielsch, U. Gosele, Angew. Chem. Int. Ed. **44**, 6050 (2005)
27. G. Sharma, M.V. Pishko, C.A. Grimes, Fabrication of metallic nanowire arrays by electrodeposition into nanoporous alumina membranes: effect of barrier layer. J. Mater. Sci. **42**, 4738–4744 (2007)
28. M. Motoyama, Y. Fukunaka, T. Sakka, Y.H. Ogata. Electrochim. Acta **53**, 205 (20057)
29. E. Ferain, R. Legras. Heavy ion tracks in polycarbonate. Comparison with a heavy ion irradiated model compound (diphenyl carbonate). Nucl. Instrum. Meth. B **82**, 539–548 (1993)
30. E. Ferain, R. Legras, Track-etched membrane: dynamics of pore formation. Nucl. Instrum. Meth. B **84**, 331–336 (1994)
31. B. Bercu, I. Enculescu, R. Spohr, Nucl. Instrum. Meth. Phys. B **225**, 497 (2004)
32. I. Enculescu, M. Sima, M. Enculescu, E. Matei, M.E. Toimil Molares, Th. Cornelius. Nickel nanotubes prepared by electroless deposition in ion track templates. Optoelectr. Adv. Mater. Rapid Commun. **2**, 133–136 (2008)
33. H. Masuda, K. Fukuda, Ordered metal nanohole arrays made by a two-step replication of honeycomb structures of anodic alumina. Science **268**, 1466–1468 (1995)
34. G. Ali, M. Ahmad, J.I. Akhter, M. Maqbool, S.O. Cho, Novel structure formation in porous anodic alumina fabricated by single step anodization process. Micron **41**, 560–564 (2010)
35. G. Ali, M. Maqboo, Fabrication of cobalt-nickel binary nanowires in a highly ordered alumina template via AC electrodeposition. Nanoscale Res. Lett. **8**, 352 (2013)
36. S. Shamaila, R. Sharif, S. Riaz, M. Khaleeq-ur-Rahman, X.F. Han. Fabrication and magnetic characterization of Co_xPt_{1-X} nanowire arrays. Appl. Phys. A. **92**, 687–691 (2008)
37. S. Shamaila, R. Sharif, S. Riaz, M. Ma, M. Khaleeq-ur-Rahman, X.F. Han, Magnetic and magnetization properties of electrodeposited fcc CoPt nanowire arrays. J. Magn. Magn. Mater. **320**, 1803–1809 (2008)
38. S. Shamaila, R. Sharif, J.Y. Chen, H.R. Liu, X.F. Han, X.F. Magnetic, Field annealing dependent magnetic properties of $Co_{1-x}Pt_x$ nanowire arrays. J. Magn. Magn. Mater. **321**, 3984–3989 (2009)
39. R. Sharif, X.Q. Zhang, S. Shamaila, S. Riaz, L.X. Jiang, X.F. Han. Magnetic and magnetization properties of CoFeB nanowires. J. Magn. Magn. Mater. **310**, e830–e832 (2007)
40. H. Masuda, H. Yamada, M. Satoh, H. Asoh, Appl. Phys. Lett. **71**, 2770 (1997)
41. C.L. Chen, Y.-Y. Chen, S.-J. Lin, J.C. Ho, P.-C. Lee, C.-D. Chen, S.R. Harutyunyan, Fabrication and characterization of electrodeposited bismuth telluride films and nanowires. J. Phys. Chem. C **114**, 3385–3389 (2010)
42. R. Inguanta, M. Butera, C. Sunseri, S. Piazza, Fabrication of metal nano-structures using anodic alumina membranes grown in phosphoric acid solution: tailoring template morphology. Appl. Surf. Sci. **253**, 5447–5456 (2007)
43. K. Shimizu, K. Kobayashi, G.E. Thompson, G.C. Wood, Philos. Mag. A **66**, 643–652 (1992)
44. H. Fujikura, A. Liu, A. Hamamatsu, T. Sato, H. Hasegawa, Jpn. J. Appl. Phys. **39**, 4616 (2000)
45. T. Hirano, A. Ito, T. Sato, F. Ishikawa, H. Hasegawa, Jpn. J. Appl. Phys. **41**, 977 (2002)
46. H. Föll, S. Langa, J. Carstensen, M. Christophersen, I.M. Tiginyanu, Adv. Mater. **15**, 183 (2003)
47. H. Tsuchiya, M. Hueppe, T. Djenizian, P. Schmuki, Surf. Sci. **547**, 268 (2003)
48. S. Langa, M. Christophersen, J. Carstensen, I.M. Tiginyanu, H. Föll, Phys. Status Solidi A **197**, 77 (2003)
49. I.M. Tiginyanu, E. Monaico, V.V. Ursaki, V.E. Tezlevan, R.W. Boyd, Appl. Phys. Lett. **86**, 063115 (2005)
50. I.M. Tiginyanu, E. Monaico, V.V. Ursaki, E. Foca, H. Föll, Electrochem. Solid State Lett. **10**, D127 (2007)
51. I. Tiginyanu, E. Monaico, E. Monaico, Ordered arrays of metal nanotubes in semiconductor envelope. Electrochem. Commun. **10**, 731 (2008)

52. M.E. Toimil Molares, N. Chtanko, T.W. Cornelius, D. Dobrev, I. Enculescu, R.H. Blick, R. Neumann. Fabrication and contacting of single Bi nanowires. Nanotechnology **15**, S 201–S 207 (2004)
53. M. Sima, I. Enculescu, C. Trautmann, R. Neumann, Electrodeposition of CdTe nanorods in ion track membranes. J. Optoelectron. Adv. Mater. **6**, 121–125 (2004)
54. G.E. Possin, Forming very small diameter wires. Rev. Sci. Instrum. **41**, 772 (1970)
55. G.E. Possin. Superconductivity in nearly one-dimensional tin wires. Physica (Utrecht) **55**, 339 (1971)
56. D.T. Mitchell, S.B. Lee, L. Trofin, N. Li, T.K. Nevanen, H. Soderlund, C.R. Martin, J. Am. Chem. Soc. **124**, 11864 (2002)
57. D. Routkevitch, J. Chan, J.M. Xu, M. Moskovits, Electrochem. Soc. Proc. Ser. PV **350**, 97 (1997)
58. A.J. Yin, J. Li, W. Jian, A.J. Bennett, J.M. Xu, Fabrication of highly ordered metallic nanowire arrays by electrodeposition. Appl. Phys. Lett. **79**, 1039 (2001)
59. H. Cao, L. Wang, Y. Qiu, Q. Wu, G. Wang, L. Zhang, X. Liu, Generation and growth mechanism of metal (Fe Co, Ni) nanotube arrays. ChemPhysChem **7**, 1500–1504 (2006)
60. W.-C. You, J.-K. Lee, Field-dependent growth patterns of metals electroplated in nanoporous alumina membranes. Adv. Mater. **16**, 1097–1101 (2004)
61. W. Lee, R. Scholz, K. Nielsch, U. Gosele, A template-based electrochemical method for the synthesis of multisegmented metallic nanotubes. Angew. Chem. **117**, 6204–6208 (2005)
62. D.D. Sung, M.S. Choo, J.S. Noh, W.B. Chin, W.S. Yang, A new fabrication method of aluminum nanotube using anodic porous alumina film as a template. Bull. Korean Chem. Soc. **27**, 1159 (2006)
63. G.N. Ivanova, D.D. Nedeoglo, N.D. Negeoglo, V.P. Sirkeli, I.M. Tiginyanu, V.V. Ursaki, J. Appl. Phys. **101**, 063543 (2007)
64. I.M. Tiginyanu, V.V. Ursaki, E. Monaico, M. Enachi, V.V. Sergentu, G. Colibaba, D.D. Nedeoglo, A. Cojocaru, H. Föll, Quasi-ordered networks of metal nanotubes embedded in semiconductor matrices for photonic applications. J. Nanoelectr. Optoelectr. **6**, 463–472 (2011)
65. I. Tiginyanu, E. Monaico, V. Sergentu, A. Tiron, V. Ursaki, Metallized porous GaP templates for electronic and photonic applications. ECS J. Solid State Sci. Technol. **4**, P57–P62 (2015)
66. D. Vanmaekelbergh, A. Koster, F.I. Marin, Adv. Mater. **9**, 575 (1997)
67. M. Scalora, G. D'Aguanno, N. Mattiucci, M.J. Bloemer, D. de Ceglia, M. Centini, A. Mandatori, C. Sibilia, N. Akozbek, M.G. Cappeddu, M. Fowler, J.W. Haus, Opt. Express **15**, 508 (2007)
68. M. Bloemer, G. D'Aguanno, M. Scalora, N. Mattiucci, D. de Ceglia, Opt. Express **16**, 19342 (2008)
69. J.B. Pendry, Negative refraction makes a perfect lens. Phys. Rev. Lett. **85**, 3966 (2000)
70. D.R. Smith, W.J. Padilla, D.C. Vier, S.C. Nemat-Nasser, S. Schultz, Composite medium with simultaneously negative permeability and permittivity. Phys. Rev. Lett. **84**, 4184 (2000)
71. L.-M. Li, Z.-Q. Zhang, Multiple-scattering approach to finite-sized photonic band-gap materials. Phys. Rev. B **58**, 9587 (1998)
72. V.V. Sergentu, I.M. Tiginyanu, V.V. Ursaki, M. Enachi, S.P. Albu, P. Schmuki. Negative index material lenses based on metallo-dielectric nanotubes. Phys. Stat. Sol. (RRL) **2**, 242 (2008)
73. M. Hofman, G. Scherrer, M. Kadic, X. Melique, W. Smigaj, B. Cluzel, S. Guenneau, D. Lippens, F. de Fornel, B. Gralak, O. Vanbesien, J. Nanomed. Nanotechnol. **4**, 1000185 (2013)
74. G. Scherrer, M. Hofman, W. Smigaj, M. Kadic, T.M. Chang, X. Melique, D. Lippens, O. Vanbesien, B. Cluzel, F. de Fornel, S. Guenneau, B. Gralak, Phys. Rev. B **88**, 115110 (2013)
75. M. Hofman, D. Lippens, O. Vanbesien, Appl. Opt. **49**, 5806 (2010)
76. M. Enachi, I. Tiginyanu, V. Sprincean, V. Ursaki, Self-organized nucleation layer for the formation of ordered arrays of double-walled TiO_2 nanotubes with temperature controlled inner diameter. Phys. Status Solidi RRL **4**, 100–102 (2010)
77. F. Wen, S. David, X. Checoury, M. El Kurdi, P. Boucaud, Opt. Express **16**, 12278 (2008)

78. L.R. Moore, M. Zborowski, L. Sun, J.J. Chalmers, J. Biochem. Biophys. Methods **37**, 11 (1998)
79. J. Escrig, P. Landeros, D. Altbir, E.E. Vogel, J. Magn. Magn. Mater. **310**, 2448 (2007)
80. S.B. Lee, D.T. Mitchell, L. Trofin, T.K. Nevanen, H. Sderlund, C.R. Martin, Science **296**, 2198 (2002)
81. C.R. Martin, P. Kohli, Nat. Rev. Drug Discov. **2**, 29 (2003)
82. H. Hillebrenner, F. Buyukserin, J.D. Stewar, C.R. Martin, Nanomedicine **1**, 39 (2006)
83. D.R. Baselt, G.L. Lee, M. Natesan, S.W. Metzger, P.E. Sheehan, R.J. Colton. Biosens. Bioelectron. **13**, 731 (1998)
84. R. Fan, R. Karnik, M. Yue, D. Li, A. Majumdar, P. Yang, Nano Lett. **5**, 1633 (2005)
85. P. Ball. Nanowire sensors pass drugs test. Nat. Nanozone News (2005)
86. F.J. Alenghat, B. Fabry, K.Y. Tsai, W.H. Goldmann, D.E. Ingber, Biochem. Biophys. Res. Commun. **277**, 93 (2000)
87. R.J. Mannix, S. Kumar, F. Cassiola, M. Montoya-Zavala, E. Feinstein, M. Prentiss, D.E. Ingber, Nature Nanotech. **3**, 36 (2008)
88. K. Bullis, Technol. Rev. **109**, 16 (2006)
89. R.R. Llinas, K.D. Walton, M. Nakao, I. Hunter, P.A. Anquetil, Neuro-vascular central nervous recording/stimulating system: using nanotechnology probes. J. Nanoparticle Res. **7**, 111–127 (2005)

Chapter 16
Thermal Conductivity of Segmented Nanowires

Denis L. Nika, Alexandr I. Cocemasov and Alexander A. Balandin

Abstract In this chapter we present a review of the phonon thermal conductivity of segmented nanowires focusing on the theoretical results for Si and Si/Ge structures with the constant and periodically modulated cross-sections. We describe the use of the face-centered cubic cell and Born-von Karman models of the lattice vibrations for calculating the phonon energy spectra in the segmented nanowires. Modification of the phonon spectrum in such nanostructures results in strong reduction of the phonon thermal conductivity and suppression of heat transfer due to a trapping of phonon modes in nanowire segments. Possible practical applications of segmented nanowires in thermoelectric energy generation are also discussed.

16.1 Introduction

Phonons, i.e. quanta of the crystal lattice vibrations, affect all physical processes in solids [1]. They scatter the electrons and limit the electron mobility near room temperature (RT) and above and influence on the optical properties of crystalline materials. Acoustic phonons are the main heat carriers in insulators and semiconductors. In the long-wavelength limit, acoustic phonons in bulk crystals have nearly linear dispersion, which can be written as $\omega = V_S q$, where V_S is the sound velocity and q is the wavenumber, while the optical phonons are nearly dispersion-less and have a small group velocity $V_G = d\omega/dq$.

Spatial confinement of acoustic phonons in nanostructures affects their dispersion [2–8]. It modifies acoustic phonon properties such as phonon group velocity, polarization, density of states, and changes the way acoustic phonons interact with

D.L. Nika (✉) · A.I. Cocemasov
"E. Pokatilov" Laboratory of Physics and Engineering of Nanomaterials, Department of Physics and Engineering, Moldova State University, Chisinau, Moldova
e-mail: dlnika@yahoo.com

A.A. Balandin
Department of Electrical and Computer Engineering and Materials Science and Engineering Program, University of California - Riverside, Riverside, CA 92521, USA

© Springer International Publishing Switzerland 2016

I. Tiginyanu et al. (eds.), *Nanostructures and Thin Films for Multifunctional Applications*, NanoScience and Technology,
DOI 10.1007/978-3-319-30198-3_16

other phonons, defects and electrons [2–8]. Modification of phonon energy spectra and phonon scattering at the boundaries of nanostructures make the thermal conductivity of nanostructures much lower than the corresponding bulk values [2–8]. It has been demonstrated both experimentally and theoretically that the room temperature (RT) lattice thermal conductivity in freestanding Si nanolayers and nanowires is two orders of magnitude lower than the corresponding bulk value of Si [8–12].

Reduction of size and a corresponding increase in the density of elements on a chip make the task of improving thermal conductivity an important problem in modern electronics [5, 8, 13–15]. An insufficient heat removal from devices implies their overheating, which degrades their performance and limits the operating frequency. On the other hand, decrease of the thermal conductivity may improve the quality of thermoelectrics. The efficiency of the thermoelectric devices is determined by the figure of merit $ZT = S^2\sigma T/(\kappa_{ph} + \kappa_{el})$, where S is the Seebeck coefficient, σ is the electrical conductivity, T is the absolute temperature, κ_{ph} and κ_{el} is the lattice (phonon) and electronic thermal conductivity, respectively. One possible way to increase the figure of merit consists in the achieving low values of thermal conductivity when maintaining good electronic transport characteristics (electrical conductivity and Seebeck coefficient) in phonon-blocking and electron-transmitting nanostructures [5, 8, 16–18].

In spite of the fact that bulk Si is a poor thermoelectric with room-temperature $ZT \sim 0.01$ [19], thin Si, Ge and Si/Ge nanowires (NWs) are considered promising for thermoelectric applications [20–23] owing to the much lower values of the RT lattice thermal conductivity $\kappa_{ph} < 1$ Wm^{-1}K^{-1}. It has been demonstrated experimentally that the good electrical conductivity, as in doped bulk Si, and poor thermal conductivity of Si NWs [20] and rough Si NWs [21] provide relatively high values of $ZT \sim 0.3$–0.6 at RT. These experimental results stimulate theoretical search of one-dimensional Si-based nanostructured materials with the ultra-low thermal conductivity. The reduction of the RT lattice thermal conductivity up to 75 % was theoretically demonstrated in Si/Ge core-shell NWs with Ge thicknesses of several monoatomic layers [24, 25]. The corresponding enhancement of ZT in these NWs was also predicted [26].

In this chapter we review phonon and thermal properties of another kind of semiconductor nanostructures, promising for thermoelectric and thermo-isolating application due to their ultra-low thermal conductivity—referred as *segmented nanowires (SNW)*, i.e. nanowires consisting of segments of different size and/or made of different materials [27–31]. Following our recent publications [27–29] we describe how the thermal flux in segmented Si and Si/Ge nanowires can be suppressed by almost three orders-of-magnitude in comparison with that in bulk Si, and by an order-of-magnitude in comparison with generic Si nanowires. Fabrication of the cross-section modulated SNWs with layer thickness from several monoatomic layers (ML) up to several nanometers is still a technological challenge. However, reports of fabrication of InP, InN/InGaN or metallic SNWs [32–36] suggest that nanostructures considered in this chapter are feasible.

The rest of the chapter is organized as follows. In Sect. 16.2 we describe the theoretical models for phonons and discuss phonon properties of Si and Si/Ge segmented nanowires. In Sect. 16.3 we describe the method of calculation of the thermal conductivity in segmented nanowires and review their thermal properties. We give our conclusions in Sect. 16.4.

16.2 Phonons in Segmented Nanowires

The schemes of a generic rectangular nanowire and considered segmented nanowires are shown in Fig. 16.1: generic NW with the lateral cross-section $d_x \times d_y$ (panel a), Si/Ge SNW with segments dimensions $d_x \times d_y \times l_z^1$ and $d_x \times d_y \times l_z^2$ (panel b), cross-section modulated Si SNW (MSNW) with segments dimensions $d_x^1 \times d_y^1 \times l_z^1$ and $d_x^2 \times d_y^2 \times l_z^2$ (panel c) and cross-section modulated Si/Ge SNW with silicon segments $d_x^1 \times d_y^1 \times l_z^1$ and $d_x^2 \times d_y^2 \times l_z^2$ covered by the Ge shell with thickness d_{Ge} (panel d).

The external surfaces of the considered nanostructures are assumed to be free [37–39]. The X and Y axes of the Cartesian coordinate system are located in the plane of the cross-section of the nanowire and are parallel to its sides, while the axis

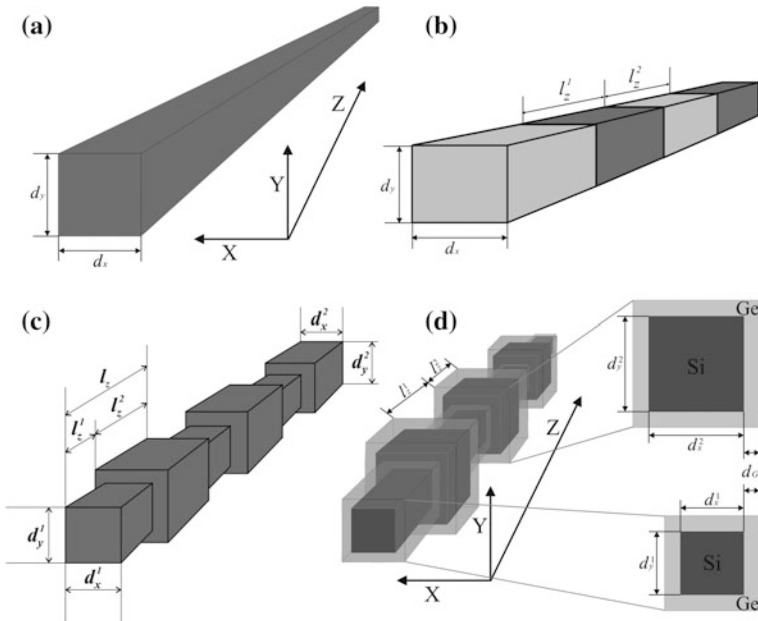

Fig. 16.1 Schematic view of considered generic Si nanowire (**a**), Si/Ge segmented nanowire (**b**) and cross-section-modulated Si (**c**) and Si/Ge (**d**) nanowires. The image was adopted from [27–29] with permission from American Physical Society and American Institute of Physics

Table 16.1 Notations and dimensions of NWs, SNWs and MSNWs under consideration

Nanostructure	Dimensions	Notation in the present work
Si NW	37 ML × 37 ML	Si NW #1
Si NW	14 ML × 14 ML	Si NW #2
Ge NW	37 ML × 37 ML	Ge NW
Si/Ge SNW	37 ML × 37 ML × 6 ML/37 ML × 37 ML × 2 ML	Si/Ge SNW #1
Si MSNW	14 ML × 14 ML × 6 ML/22 ML × 22 ML × 6 ML	Si MSNW #1
Si MSNW	14 ML × 14 ML × 8 ML/22 ML × 22 ML × 8 ML	Si MSNW #2
Si MSNW	14 ML × 14 ML × 8 ML/18 ML × 18 ML × 8 ML	Si MSNW #3
Si MSNW	14 ML × 14 ML × 8 ML/26 ML × 26 ML × 8 ML	Si MSNW #4
Si MSNW	14 ML × 14 ML × 8 ML/30 ML × 30 ML × 8 ML	Si MSNW #5
Si MSNW	14 ML × 14 ML × 8 ML/34 ML × 34 ML × 8 ML	Si MSNW #6
Si MSNW	14 ML × 14 ML × 4 ML/22 ML × 22 ML × 4 ML	Si MSNW #7
Si MSNW	14 ML × 14 ML × 12 ML/22 ML × 22 ML × 12 ML	Si MSNW #8
Si/Ge MSNW	14 ML × 14 ML × 8 ML/22 ML × 22 ML × 8 ML – d_{Ge} = 4 ML	Si/Ge MSNW #1

Z is directed along the axis of the nanowire. We suppose that the length of the nanowire along the axis Z is infinite. The origin of coordinates is at the center of the cross-section of the nanowire. The translation period of SNW/MSNW consists of two segments with dimensions $d_x^1 \times d_y^1 \times l_z^1$ and $d_x^2 \times d_y^2 \times l_z^2$, respectively. The length period of SNW/MSNW is $L = l_z^1 + l_z^2$. The dimensions of nanowires considered in this chapter are presented in Table 16.1.

16.2.1 Face-Centered Cubic Cell Model of Lattice Dynamics in Bulk Crystals

The crystal lattice of silicon or germanium is a diamond-like lattice and it consists of two face-centered cubic sublattices, which are shifted along the main diagonal of a unit cell by 1/4 of its length. In the Face-centered cubic cell (FCC) model two shifted FCC sublattices are considered as a common FCC lattice with the double mass at each lattice node. This simplification neglects the optical phonon modes, but allows expressing three force constants of the model through independent elastic constants of a material. The latter allows one to simulate the acoustic properties of heterostructures consisting of layers with different acoustic properties and various dimensions [40, 41].

In the FCC model all lattice nodes in a bulk crystal are translationally equivalent. The displacement of a lattice atom in the node labeled with the number $\vec{n}$, can be written as

$$\vec{u}(\vec{n};\vec{q},t) = \vec{w}(\vec{q})e^{i(\vec{q}\vec{n}-\omega t)}, \tag{16.1}$$

where $\vec{w}(\vec{q})$ is the time-independent displacement. Because of the equivalence of nodes, the amplitude of their displacements does not depend on the node number: $\vec{n} = \vec{a}_1 n_1 + \vec{a}_2 n_2 + \vec{a}_3 n_3$, where $\vec{a}_1 = \frac{a}{2}(0,1,1)$, $\vec{a}_2 = \frac{a}{2}(1,1,0)$, $\vec{a}_3 = \frac{a}{2}(1,0,1)$ are basis vectors of the face-centered cubic cell, n_1, n_2 and n_3 are integers, and a is the lattice constant: a(Si) = 0.549 nm, a(Ge) = 0.565 nm.

The node displacement in a bulk crystal is described by the equations of motion:

$$m \ddot{u}_i(\vec{n},\vec{q}) = F_i(\vec{n},\vec{q}), \quad i = x,y,z. \tag{16.2}$$

where $F_i(\vec{n},\vec{q})$ is a component of the force acting on the node $\vec{n}$ from the other nodes of the lattice and m is the node mass (double atomic mass in the framework of FCC model). In the harmonic approximation

$$F_i(\vec{n},\vec{q}) = -\frac{\partial V}{\partial u_i(\vec{n},\vec{q})} = -\sum_{\vec{n}',j} \Phi_{ij}(\vec{n},\vec{n}')u_j(\vec{n}',\vec{q}), \tag{16.3}$$

where $\Phi_{ij}(\vec{n},\vec{n}')$ is the three-dimensional matrix of the force constants and V is the potential energy of the lattice.

Taking into account (16.1), one can obtain

$$m\omega^2 w_i(\vec{q}) = \sum_{j=1,2,3,\vec{h}} D_{ij}(\vec{q};\vec{h})w_j(\vec{q}), \tag{16.4}$$

where $D_{ij}(\vec{q};\vec{h}) = \Phi_{ij}(0,\vec{h})e^{i\vec{q}\vec{h}}$ is the dynamic matrix and $\vec{h} = \vec{n}' - \vec{n}$.

We take into account the interaction of the node with the nearest and second-nearest nodes. The interaction with the 12 nearest nodes is centrally symmetric and it is described by one constant α_1^{FCC} [42]. The matrix of the force constants in this case is $\Phi_{il}(\vec{n}',\vec{n}) = -\alpha_1^{FCC}(\vec{n}',\vec{n})h_i^1 h_l^1/(h^1)^2$, where $\vec{h}^1$ indicates the positions of the nearest nodes of the node $\vec{n} = 0$, h_i^1 is the projection of the vector $\vec{h}^1$ on the corresponding coordinate axis X_i. The interaction with the second-nearest nodes is not centrally symmetric and it is described by two constants, α^{FCC} and β^{FCC} [43, 44]. The vector $\vec{h}^2$ describes the position of the 6 s-nearest nodes of the node $\vec{n} = 0$:

$$\begin{aligned}
&\Phi_{ij}(0,\vec{h}^2 = a(\pm1,0,0)) = \delta_{ij}\gamma_{ii},\ \gamma_{11} = \alpha^{FCC};\gamma_{22} = \gamma_{33} = \beta^{FCC} \\
&\Phi_{ij}(0,\vec{h}^2 = a(0,\pm1,0)) = \delta_{ij}\gamma_{ii},\gamma_{11} = \gamma_{33} = \beta^{FCC};\gamma_{22} = \alpha^{FCC} \\
&\Phi_{ij}(0,\vec{h}^2 = a(0,0,\pm1)) = \delta_{ij}\gamma_{ii},\gamma_{11} = \gamma_{22} = \beta^{FCC};\gamma_{33} = \alpha^{FCC}.
\end{aligned} \tag{16.5}$$

Because for every node with the vector $\vec{h}$ there exists a node with the vector $-\vec{h}$, the dynamic matrix is real. Comparing the phonon dispersions $\omega(q)$ for three phonon branches (one longitudinal and two transversal) obtained from (16.4) in the long-wave limit $q \to 0$ with those derived within a continuum approach [39], we established the following relations between the constants α_1^{FCC}, α^{FCC}, β^{FCC} and the elastic moduli of a cubic crystal c_{11}, c_{12} and c_{13}: $\alpha_1^{FCC} = a(c_{12} + c_{44})/2$, $\alpha^{FCC} = a(c_{11} - c_{12} - c_{44})/4$, $\beta^{FCC} = a(c_{44} - c_{12})/8$ [27].

16.2.2 Born-von Karman Model of Lattice Dynamics in Bulk Crystals

The real unit cell structure is taken into account in Born-von Karman (BvK) model of lattice dynamics. For convenience, let's identify the atoms of the first sublattice of diamond—like lattice as the "dark" atoms while the atoms of the second sub-lattice as the "white" atoms as depicted in Fig. 16.2.

The dynamic matrix in BvK model has the form: $D_{ij}(\vec{r}_k, \vec{r}'_k) = \Phi_{ij}(\vec{r}_k, \vec{r}'_k)/\sqrt{m(\vec{r}_k)m(\vec{r}'_k)}$, where $m(\vec{r}_k)$ $[m(\vec{r}'_k)]$ is the mass of the atom at $\vec{r}_k$ $[\vec{r}'_k]$, $\Phi_{ij}(\vec{r}_k, \vec{r}'_k)$ is the matrix of force constants and $\vec{h} = \vec{r}_k - \vec{r}'_k$. For the atom at $\vec{r}_k$, the summation in (16.4) is performed over all the nearest and second-nearest atoms at $\vec{r}'_k$. In the case of silicon or germanium, the atom at $\vec{r}_k$ has 4 nearest neighbors at $\vec{r}'_{k,n} = \vec{r}_k + \vec{h}^I_n$ (n = 1, …, 4) and 12 s-nearest neighbors at $\vec{r}'_{k,n} = \vec{r}_k + \vec{h}^{II}_n$ (n = 1, .., 12). The components of vectors $\vec{h}^I_n$ and $\vec{h}^{II}_n$ are presented in Table 16.2. In our BvK model, the interaction of an atom with its nearest and second-nearest neighbors is described by the following force constant matrices: $\Phi^I_{ij} = (16/a^2)(\alpha\delta_{ij} + \beta(1 - \delta_{ij}))h^I_{n,i}h^I_{n,j}$ for the nearest atoms (n = 1, …, 4) and $\Phi^{II}_{ij} = (4/a^2)(\lambda\delta_{ij}(a^2/4 - h^{II}_{n,i}h^{II}_{n,i}) + \mu\delta_{ij}h^{II}_{n,i}h^{II}_{n,i} + \nu(1 - \delta_{ij})h^{II}_{n,i}h^{II}_{n,j})$ for the second-nearest atoms (n = 1, …, 12), where α, β, μ, λ and ν are the force constants of BvK model,

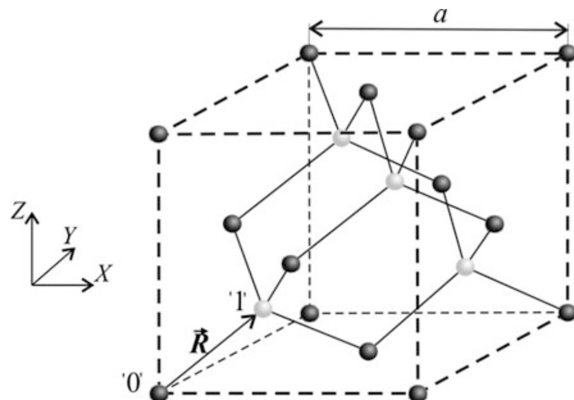

Fig. 16.2 Schematic view of silicon crystal lattice. *White* and *black* atoms show atoms from different face-centered cubic sub-lattices

Table 16.2 Components of the nearest and second-nearest atoms $\vec{r}'_{k,n} = \vec{r}_k + \vec{h}_n^{I(II)}$ in the diamond-type unit cell and a set of the force constants used for Si

Components of vectors $\vec{h}_n^I$ for the selected "white" atom $\vec{r}_k$	Components of vectors $\vec{h}_n^I$ for the selected "dark" atom $\vec{r}_k$	Components of vectors $\vec{h}_n^{II}$ for the selected "white" (or "dark") atom $\vec{r}_k$	Set of five force constants of Si and Ge used for calculation (N/m)
$a/4(1, 1, 1)$; $a/4(1, -1, -1)$; $a/4(-1, 1, -1)$; $a/4(-1, -1, 1)$	$a/4(-1, -1, -1)$; $a/4(-1, 1, 1)$; $a/4(1, -1, 1)$; $a/4(1, 1, -1)$	$a/2(1, 1, 0)$; $a/2(-1, -1, 0)$; $a/2(1, 0, 1)$; $a/2(-1, 0, -1)$; $a/2(0, 1, 1)$; $a/2(0, -1, -1)$; $a/2(-1, 1, 0)$; $a/2(1, -1, 0)$; $a/2(-1, 0, 1)$; $a/2(1, 0, -1)$; $a/2(0, -1, 1)$; $a/2(0, 1, -1)$	Silicon parameters: $\alpha = 54.85$ $\beta = 35.0$ $\mu = 3.8$ $\nu = 2.5$ $\lambda = -4.42$ Germanium parameters: $\alpha = 49.6$ $\beta = 33.0$ $\mu = 3.03$ $\nu = 3.03$ $\lambda = -3.0$

The table is adopted from [28] with permission from American Physical Society

δ_{ij} is the Kronecker's delta and $i,j = x,y,z$. The force constant matrix $\Phi_{ij}(\vec{r}_k, \vec{r}'_k = \vec{r}_k)$ is obtained from the condition that the total force acting on the atom $\vec{r}_k$ at the equilibrium position is equal to 0, i.e. $\Phi_{ij}(\vec{r}_k, \vec{r}'_k = \vec{r}_k) + \sum_{\vec{r}'_k} \Phi_{ij}(\vec{r}_k, \vec{r}'_k \neq \vec{r}_k) = 0$.

By solving the equations of motion (16.4) at Γ and X Brillouin zone points of bulk Si or Ge, we expressed three constants α, μ, and λ of our model through β and the frequencies of the LO and TO phonons at Γ point and the LA phonon at X point:

$$\begin{gathered} \alpha = m\omega_{LO}^2(\Gamma)/8, \\ \mu = m\left(2\omega_{LA}^2(X) - \omega_{LO}^2(\Gamma)\right)/32, \\ \lambda = m\left(4\omega_{TO}^2(X) - 2\omega_{LA}^2(X) - \omega_{LO}^2(\Gamma)\right)/32 - \beta/2. \end{gathered} \tag{16.6}$$

The constants β and ν were treated as fitting parameters and were obtained from the best fit to experimental dispersion curves for bulk Si [45] and Ge [46]. The numerical values of the force constants for Si and Ge are indicated in the last column of Table 16.2.

16.2.3 Lattice Dynamics in Segmented Nanowires

In segmented nanowires, the displacements of the atoms (or nodes of FCC model) belonging to one period are independent, therefore the displacement amplitude $\vec{w}$

depends on the atomic coordinates. The rest of the atomic displacements are equivalent to those in the selected period due to the translational symmetry along the Z-axis. In the case of a generic NW, the translation period consists of two atomic layers of the "dark" atoms and two atomic layers of the "white" atoms (all layers are perpendicular to the Z axis). For SNW/MSNW, the number of atomic layers in the period is determined by L. The displacements of equivalent atoms have the form:

$$\vec{u}(x, y, z + n \cdot L; q_z, t) = \vec{w}(x, y, z; q_z)e^{i(q_z nL - \omega t)}, \tag{16.7}$$

where $\vec{w}(x, y, z; q_z) \equiv \vec{w}(\vec{r}; q_z)$ is the displacement amplitude of the atom with coordinates x, y and z; the period is labeled by an integer n, and q_z is the phonon wavenumber. The equations of motion for the displacement are

$$\omega^2 w_i(\vec{r}_k; q_z) = \sum_{j=x,y,z;\vec{r}'_k} D_{ij}(\vec{r}_k, \vec{r}'_k) w_j(\vec{r}'_k; q_z),\ k = 1, \ldots, N, i = x, y, z, \tag{16.8}$$

where N is the number of atoms in the NW or SNW/MSNW translational period. To calculate the energy spectra of phonons in NWs and SNWs/MSNWs we numerically solve the set of equations (16.8) with free boundary conditions in the XY-plane, i.e. we assume that all force constants outside of the nanowire are equal to 0. The calculations were performed for all q_z values in the interval (0, π/a) for NWs and (0, π/L) for SNWs/MSNWs. Invariance of the set (16.8) with respect to the reflection in the planes of symmetry leads to the following four possible types of solutions [47]:

Dilatational (D): $w_1^{AS}(x_1, x_2); w_2^{SA}(x_1, x_2); w_3^{SS}(x_1, x_2) \rightarrow w_i^D$;

Flexural$_1$ (Flex$_1$): $w_1^{AA}(x_1, x_2); w_2^{SS}(x_1, x_2); w_3^{SA}(x_1, x_2) \rightarrow w_i^{F_1}$;

Flexural$_2$ (Flex$_2$): $w_1^{SS}(x_1, x_2); w_2^{AA}(x_1, x_2); w_3^{AS}(x_1, x_2) \rightarrow w_i^{F_2}$ and

Shear (Sh): $w_1^{SA}(x_1, x_2); w_2^{AS}(x_1, x_2); w_3^{AA}(x_1, x_2) \rightarrow w_i^{Sh}$, where $S(A)$ means the parity of a function with respect to the inversion of the corresponding variable: $f(x_1, x_2) = f(-x_1, x_2) = f(x_1, -x_2) \rightarrow f^{SS}(x_1, x_2)$;
$f(x_1, x_2) = -f(-x_1, x_2) = -f(x_1, -x_2) \rightarrow f^{AA}(x_1, x_2)$ etc.

The energy spectra of dilatational phonons in a homogeneous Si nanowire with the lateral cross-section 37 ML × 37 ML (1 ML = a/4) and Si/Ge segmented nanowire with the same cross-section and 8 atomic layers in the superlattice period (6 silicon atomic layers and 2 germanium atomic layers), calculated in the framework of FCC model, are shown in Fig. 16.3.

The total number of phonon branches of dilatational polarization is equal to 280 for a Si NW #1 and 1120 for a Si/Ge SNW #1. In Fig. 16.3 the phonon branches $\hbar\omega_s(q_z)$ with quantum numbers s = 0, 1, …, 4, 10, 20, 30, …, 100, 200, 300, …, 1100 are shown. The dashed line in Fig. 16.3b shows the maximal phonon energy in a homogeneous Ge nanowire. The maximal phonon frequency of silicon is higher than the maximal frequency of germanium, therefore high-frequency Si-like phonon modes in the Si/Ge SMW #1 are "trapped" in the Si segments and do not spread out in

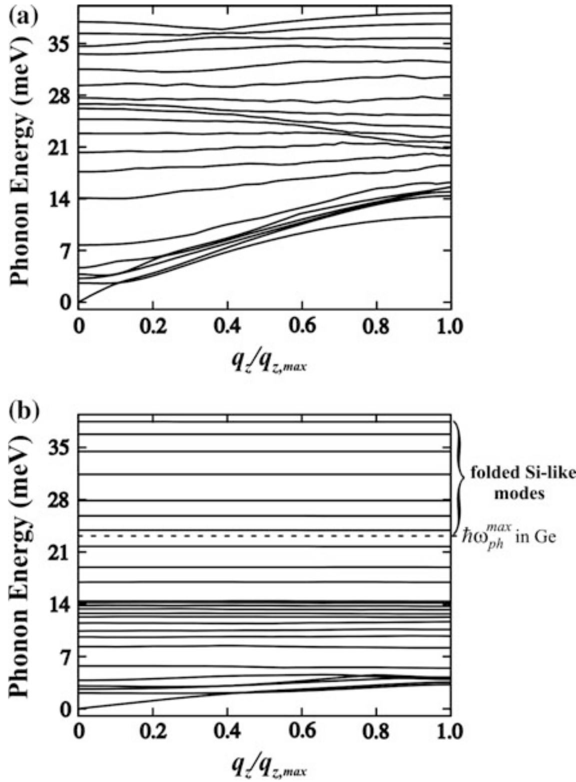

Fig. 16.3 Dilatational phonon energies as a function of the phonon wave vector q in **a** a homogeneous rectangular Si nanowire with the lateral cross-section 37 ML × 37 ML nm. The phonon branches with s = 0 to 4, 10, 30, 50 … 280 are shown; **b** a Si/Ge SNW with the same lateral cross section and 8 atomic layers per superlattice period (2 atomic layers of Ge and 6 atomic layers of Si). The phonon branches with s = 0 to 4, 10, 30, 50 … 190, 200, 300, … 1100, 1120 are depicted. The image is reprinted from [27] with permission from American Physical Society

the Ge segments of the superlattice. These modes will not participate in the processes of heat transfer, i.e. Si/Ge SMWs act as a *phonon filter* removing many phonon modes from thermal transport [27]. Figure 16.3 implies that the velocities of phonon modes with $\hbar\omega > 7$ meV in the Si nanowire are not equal to zero, whereas in a Si/Ge SNW #1, these modes are dispersionless.

The similar phonon trapping effect was also reported for cross-section modulated Si and Si/Ge MSNWs [28, 29]. The phonon branches $\hbar\omega_s(q_z)$ with s = 1, 2, …, 20, 35, 50, 65, …, 1515, 1530 of cross-section modulated Si MSNW #1 are shown in Fig. 16.4. As follows from Fig. 16.4 a great number of phonon modes in the MSNW #1 with energy $\hbar\omega$ > 5 meV are dispersionless and possess group velocities close to zero due to the trapping into the MSNW segments.

The trapping effect is illustrated in Fig. 16.5: the average squared displacements of atoms

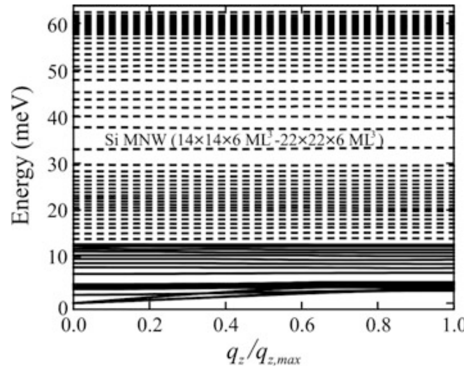

Fig. 16.4 Phonon energies as a function of the phonon wave vector q in Si MSNW with dimensions 14 ML × 14 ML × 6 ML/22 ML × 22 ML × 6 ML. The phonon branches with $s = 1$ to 20, 35, 50, 65, …, 1515, 1530 are depicted. The image is reprinted from [28] with permission from American Physical Society

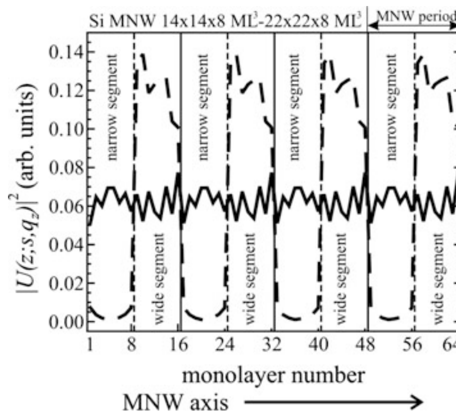

Fig. 16.5 Average squared displacements $|U(z;s,q_z)|^2$ of the trapped ($s = 8$, $q_z = 0.4q_{z,\max}$) (*dashed line*) and propagating ($s = 992$, $q_z = 0.2q_{z,\max}$) (*solid line*) phonon modes in Si MNW with dimensions 14 ML × 14 ML × 6 ML/22 ML × 22 ML × 6 ML. The image is reprinted from [28] with permission from American Physical Society

$$|U(z;s,q_z)|^2 = \begin{cases} \int\limits_{-d_{x,1}/2}^{d_{x,1}/2} \int\limits_{-d_{y,1}/2}^{d_{y,1}/2} |\vec{w}_s(x,y,z;q_z)|^2 dxdy, & \text{if } \; 0 \le z \le l_1 \\ \int\limits_{-d_{x,2}/2}^{d_{x,2}/2} \int\limits_{-d_{y,2}/2}^{d_{y,2}/2} |\vec{w}_s(x,y,z;q_z)|^2 dxdy, & \text{if } \; l_1 < z \le l_2 \end{cases} \tag{16.9}$$

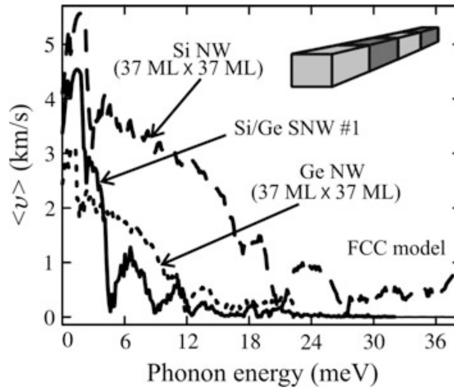

Fig. 16.6 Average phonon group velocity as a function of the phonon energy in Si NW with the lateral cross-section 14 ML × 14 ML and Si MSNW with dimensions 14 ML × 14 ML × 6 ML/22 ML × 22 ML × 6 ML. The image is reprinted from [28] with permission from American Physical Society

in the mode (s = 8, $q_z = 0.4q_{z,max}$) (dashed line) are relatively large in the wide segments of the MSNW and almost vanishing in the narrow segments. Therefore this mode is trapped into the wide segments of the MSNW. For comparison, the average squared displacements of atoms in a propagating phonon mode (s = 992, $q_z = 0.2q_{z,max}$) (solid line), which are equally large in both the wide and narrow MSNW segments, is also shown.

The effect of the phonon deceleration in SNWs and MSNWs is illustrated in Figs. 16.6, 16.7 and 16.8, where we show the average phonon group velocity

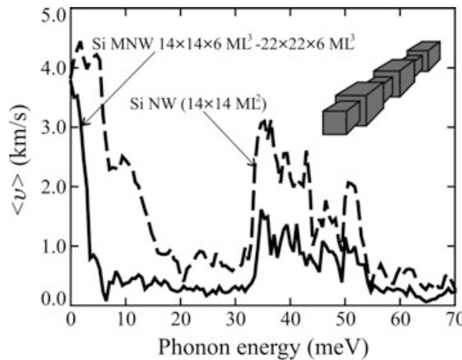

Fig. 16.7 Average phonon group velocity as a function of the phonon energy shown for Si NW with the lateral cross-section area 14 × 14 ML, Si MSNW with dimensions 14 × 14 × 8–22 × 22 × 8 ML and Si/Ge core-shell MSNWs with 14 × 14 × 8–22 × 22 × 8 ML Si core and d_{Ge} = 4 ML. The image is reprinted from [29] with permission from American Institute of Physics

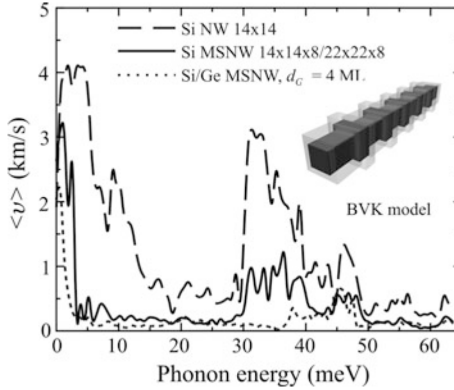

Fig. 16.8 Average phonon group velocity as a function of the phonon energy in Si and Ge homogemeous nanowires with the lateral cross-section 37 ML and in Si/Ge SNW with the same lateral cross-section and 8 atomic layers per superlattice period (2 atomic layers of Ge and 6 atomic layers of Si). The image is reprinted from [27] with permission from American Physical Society

$$\langle v \rangle(\omega) = g(\omega) / \sum_{s(\omega)} (d\omega_s/dq_z)^{-1} \tag{16.10}$$

as a function of the phonon energy for Si NW #2 and Si MSNW #1 (Fig. 16.6); Si NW #2, Si MSNW #2 and Si/Ge MSNW #1 (Fig. 16.7); Si NW #1, Ge NW and Si/Ge SNW #1 (Fig. 16.8). The average phonon group velocity in SNWs and MSNWs is smaller than that in the Si NWs for all phonon energies. As a result, the phonon modes in SNWs and MSNWs carry less heat than those in the NW. The drop in the phonon group velocities in SNWs/MSNWs in comparison with NWs is explained by the trapping effect: the trapped phonon modes represent standing waves existing only in the segments of SNWs/MSNWs.

16.3 Phonon Engineered Heat Conduction of Segmented Nanowires

The phonon thermal flux per unit temperature gradient (referred as thermal flux hereafter) in 1D nanostructures is given by the expression [28, 29]:

$$\Theta = \frac{1}{2\pi k_B T^2} \sum_{s=1,\ldots,3N} \int_0^{q_{z,\max}} \left(\hbar\omega_s(q_z) \upsilon_{z,s}(q_z)\right)^2 \tau_{tot,s}(q_z) \frac{\exp\left(\frac{\hbar\omega_s(q_z)}{k_B T}\right)}{\left(\exp\left(\frac{\hbar\omega_s(q_z)}{k_B T}\right) - 1\right)^2} dq_z. \tag{16.11}$$

Here $\tau_{tot,s}$ is the total phonon relaxation time, s is the number of a phonon branch, k_B is the Boltzmann constant, $\hbar$ is the Planck constant and T is the absolute temperature. The (16.11) is derived from the Boltzmann transport equation (BTE) in the relaxation time approximation [7, 28, 29, 48–50] taking into account 1D density of phonon states [27]. In case of MSNWs the phonon thermal conductivity is related to the phonon thermal flux as:

$$\kappa_{ph} = \frac{l_z^1 + l_z^2}{\left(d_x^1 + 2d_{shell}\right)\left(d_y^1 + 2d_{shell}\right)l_z^1 + \left(d_x^2 + 2d_{shell}\right)\left(d_y^2 + 2d_{shell}\right)l_z^2}\Theta. \quad (16.12)$$

In case of a homogeneous MSNW $d_{shell} = 0$ and (16.12) can be rewritten as: $\kappa_{ph} = \frac{l_z^1 + l_z^2}{d_x^1 d_y^1 l_z^1 + d_x^2 d_y^2 l_z^2}\Theta$. Finally, in case of a homogeneous NW or SNW $d_{shell} = 0$, $d_x^1 = d_x^2 = d_x$ and $d_y^1 = d_y^2 = d_y$, thus (16.12) reduces to: $\kappa_{ph} = \frac{\Theta}{d_x d_y}$.

In Si and Ge nanowires there are two basic mechanisms of phonon scattering: three-phonon Umklapp scattering and boundary scattering [3, 37, 38, 48, 50–54]. According to the Matthiessen's rule, the total phonon relaxation time is given by: $1/\tau_{tot,s}(q_z) = 1/\tau_{B,s}(q_z) + 1/\tau_{U,s}(q_z)$. Here, $\tau_{B,s}$ is the phonon relaxation time for the boundary scattering and $\tau_{U,s}$ is the phonon relaxation time for the Umklapp scattering. The relaxation time of phonons in boundary scattering can be calculated using the following equations [28]:

$$\frac{1}{\tau_{B,s}(q_z)} = \frac{1-p}{1+p}\frac{|\upsilon_{z,s}(q_z)|}{2}\left(\frac{1}{d_x} + \frac{1}{d_y}\right) \quad (16.13)$$

in the case of a NW or SNW,

$$\frac{1}{\tau_{B,s}(q_z)} = \frac{1-p}{1+p}\frac{|\upsilon_{z,s}(q_z)|}{2}\left(\left(\frac{1}{d_x^1} + \frac{1}{d_y^1}\right)\int\limits_{-d_x^1/2}^{d_x^1/2}\int\limits_{-d_y^1/2}^{d_y^1/2}\int\limits_{0}^{l_z^1}|\vec{w}_s(x,y,z;q_z)|^2 dxdydz + \right.$$
$$\left. + \left(\frac{1}{d_x^2} + \frac{1}{d_y^2}\right)\int\limits_{-d_x^2/2}^{d_x^2/2}\int\limits_{-d_y^2/2}^{d_y^2/2}\int\limits_{l_z^1 + a/4}^{l_z^1 + l_z^2}|\vec{w}_s(x,y,z;q_z)|^2 dxdydz\right) \quad (16.14)$$

in the case of a MSNW, and

$$\frac{1}{\tau_{B,s}(q_z)} = \sum_{i=1}^{2} \frac{1}{\tau_{B,s}^i(q_z)},$$

$$\frac{1}{\tau_{B,s}^i(q_z)} = \begin{cases} \frac{1-p}{1+p} \frac{|\upsilon_{z,s}(q_z)|}{2} \left\{ \xi_{core,s}^i(q_z) \left(\frac{1}{d_x^i} + \frac{1}{d_y^i} \right) + \right. \\ \left. + \xi_{shell,s}^i(q_z) \left(\frac{1}{d_x^i + 2d_{shell}} + \frac{1}{d_y^i + 2d_{shell}} \right) \right\}, \text{ if } \xi_{core,s}^i(q_z)/\xi_{shell,s}^i(q_z) \geq \delta, \\ \frac{1-p}{1+p} |\upsilon_{z,s}(q_z)| \frac{\xi_{shell,s}^i(q_z)}{d_{shell}}, \xi_{core,s}^i(q_z)/\xi_{shell,s}^i(q_z) < \delta, \end{cases} \tag{16.15}$$

in the case of a core/shell MSNW, where

$$\xi_{core,s}^i(q_z) = \int_{-d_x^i/2}^{d_x^i/2} \int_{-d_y^i/2}^{d_y^i/2} \int_{(i-1)l_z^1}^{l_z^1+(i-1)l_z^2} |\vec{w}_s(x,y,z;q_z)|^2 dxdydz,$$

$$\xi_{shell,s}^i(q_z) = \int_{-(d_x^i+2d_{shell})/2}^{(d_x^i+2d_{shell})/2} \int_{-(d_y^i+2d_{shell})/2}^{(d_y^i+2d_{shell})/2} \int_{(i-1)l_z^1}^{l_z^1+(i-1)l_z^2} |\vec{w}_s(x,y,z;q_z)|^2 dxdydz - \xi_{core,s}^i(q_z). \tag{16.16}$$

In (16.13)–(16.15), $\upsilon_{z,s}(q_z) = d\omega_s(q_z)/dq_z$ is the phonon group velocity along the nanowire axis, p is the specularity parameter of the boundary scattering. Equations (16.13)–(16.15) provide an extension of the standard formula for the rough edge scattering [3] to the case of a rectangular NW, SNW or MSNW. In (16.14) it was taken into account that a part of the phonon wave corresponding to the mode (s,q_z), concentrated in the MSNW segment $d_x^1 \times d_y^1 \times l_z^1$, scatters on the boundaries of this segment, while the rest of this wave scatters on the boundaries of the segment $d_x^2 \times d_y^2 \times l_z^2$. In (16.15) the parameter δ was introduced in order to classify different phonon modes: core-like, shell-like and propagating. The quantities $\xi_{core,s}^i(q_z)$ and $\xi_{shell,s}^i(q_z)$ show the relative portion of the phonon mode (s, q_z), concentrated in the core or shell of the ith MSNW segment, correspondingly. For core/shell MSNWs it is taken into account that the core-like and propagating modes partially scatter at core/shell interfaces and outer boundaries while shell-like modes with $\xi_{core,s}^i(q_z)/\xi_{shell,s}^i(q_z) < \delta$ scatter only at core/shell interfaces. In this sense, the parameter δ represents a threshold value for a ratio between the integrated phonon amplitudes concentrated in the core $\xi_{core,s}^i(q_z)$ and in the shell $\xi_{shell,s}^i(q_z)$ of ith MSNW segment. For example $\delta = 0.1$ means that in the shell-like modes more than 90 % of lattice vibrations from the ith MSNW segment occur in the shell material, while core region is depleted of phonons. A similar effect of the phonon

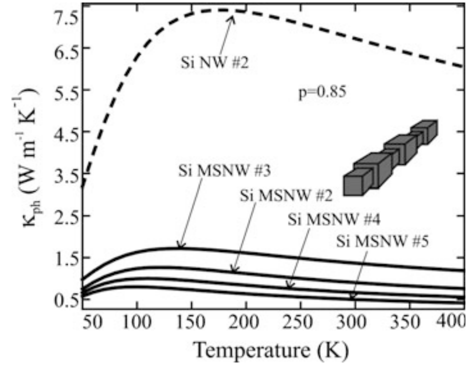

Fig. 16.9 Temperature dependence of the lattice thermal conductivity in Si NW with the cross-section 14 ML × 14 ML and Si MSNW with different dimensions. The image is reprinted from [28] with permission from American Physical Society

depletion was theoretically described by Pokatilov et al. in [55, 56] for the acoustically-mismatched planar heterostructures, where part of the phonons is pushed out into the acoustically softer layers.

The relaxation time of phonons in Umklapp scattering can be calculated using the following formula [28, 29, 51]:

$$\frac{1}{\tau_{U,s}(q_z)} = B_s(q_z)(\omega_s(q_z))^2 T \exp(-C_s(q_z)/T) \tag{16.17}$$

The mode-dependent parameters B_s and C_s in the expressions for the Umklapp scattering in core/shell MSNWs are averaged for the values of the Umklapp scattering parameters in bulk counterparts of the core and shell materials so that $B_s(q_z) = (\xi^1_{core,s}(q_z) + \xi^2_{core,s}(q_z))B_{core} + (\xi^1_{shell,s}(q_z) + \xi^2_{shell,s}(q_z))B_{shell}$ and $C_s(q_z) = (\xi^1_{core,s}(q_z) + \xi^2_{core,s}(q_z))C_{core} + (\xi^1_{shell,s}(q_z) + \xi^2_{shell,s}(q_z))C_{shell}$. The values B_{core}, B_{shell}, C_{core}, C_{shell} can be determined by comparing the calculated thermal conductivity of corresponding bulk material with experimental data. For Si and Ge there were found the following numerical values [28, 57]: $B_{Si} = 1.88 \times 10^{-19}$ s/K, C_{Si} = 137.39 K, $B_{Ge} = 3.53 \times 10^{-19}$ s/K, C_{Ge} = 57.6 K.

In Fig. 16.9, the lattice thermal conductivity of Si NWs and Si MSNWs are plotted as a function of temperature for Si NW #2, as well as for Si MSNWs #2, #3, #4 and #5. The results are presented for a reasonable specularity parameter $p = 0.85$, which was found in [38] from a comparison between theoretical and experimental data for a Si film of 20 nm thickness.

A significant redistribution of the phonon energy spectra and a reduction of the average phonon group velocities in MSNWs strongly suppress their lattice thermal conductivity in comparison with the NW. At room temperature, the ratio between the thermal conductivities in NW and MSNWs ranges from a factor of 5 to 13 depending on the cross-section $S_2 = d_x^2 \times d_y^2$. However, in order to compare more correctly the abilities of MSNWs and NWs to conduct heat one should compare thermal fluxes Θ rather than thermal conductivities κ_{ph} since latter depend explicitly on the dimensions of the nanowires.

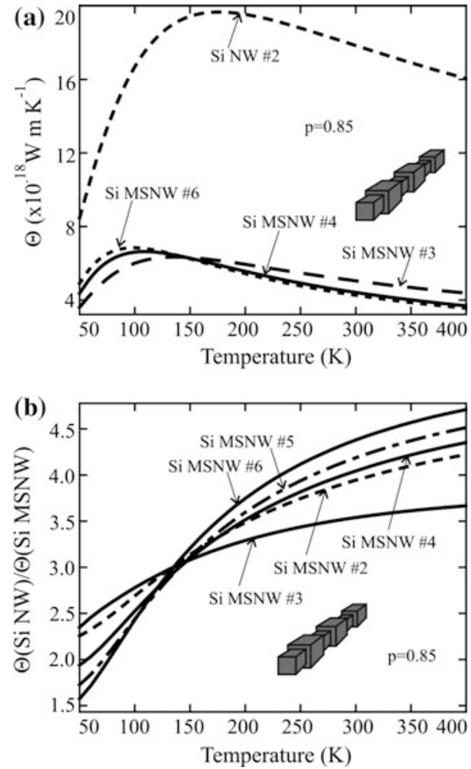

Fig. 16.10 **a** Temperature dependence of the thermal flux for Si NW (*dashed line*) and Si MSNWs with different dimensions. **b** Temperature dependence of the ratio between thermal fluxes in Si NW and Si MSNWs. The image is reprinted from [28] with permission from American Physical Society

In Fig. 16.10a we show the thermal flux for Si NW #2 (upper dashed line) and Si MSNWs #3, #4 and #6 for p = 0.85 as a function of temperature.

The maxima on the thermal flux curves are determined by the interplay between the three-phonon Umklapp and the phonon-boundary scattering. At low temperatures, the boundary scattering dominates; the thermal flux increases with temperature due to the population of high-energy phonon modes and approaches the maximum value when $\tau_U \sim \tau_B$. A further temperature rise leads to an enhancement of the Umklapp scattering and diminution of the thermal flux. An increase of the cross-section of the MSNW wide segments attenuates the phonon-boundary scattering, and the maximum of the thermal flux curves shifts to lower temperatures: from T = 190 K for Si NW #2 to T = 100 K for Si MSNW #6. Therefore, at low temperatures (T < 120 K) the thermal flux reduction is stronger in MSNWs with the smaller cross-sections. A large number of high energy phonon modes in MSNWs are trapped in the wider segments and possess group velocity close to zero. The population of these modes with temperature rise almost does not increase the thermal flux. Thus, at medium and high temperatures the Umklapp-limited thermal flux in MSNWs reduces stronger than that in the NWs without modulation. The ratio of the thermal fluxes in NW and MSNW $\eta = \Theta(\text{Si NW})/\Theta(\text{Si MSNW})$ increases with temperature, and reaches the values of 3.5–4.5 depending on the

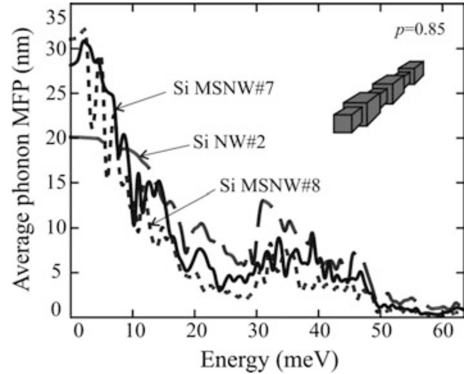

Fig. 16.11 Dependence of the average phonon mean free path on the phonon energy in Si NW (*dashed line*), Si MSNW with N_z = 4 ML (*solid line*) and Si MSNW with N_z = 12 ML (*dotted line*). The image is reprinted from [28] with permission from American Physical Society

MSNW cross-section (see Fig. 16.10b). At temperatures above 150 K the increase of the MSNW cross-section makes the reduction of the thermal flux stronger due to the corresponding rise of the number of the trapped high-energy phonon modes, which do not carry heat in MSNWs. This is distinct from the case of NWs without cross-section modulation. The calculations also showed that the strong modification of the phonon energy spectra and phonon group velocities in MSNWs in comparison with NWs also increases the Umklapp phonon scattering, which is an additional reason for the thermal flux reduction in MSNWs.

An important quantity, which determines the thermal conductivity and thermal flux, is the mode-dependent phonon mean free path (MFP) $\Lambda_s(q_z)$ [58]. Following the Matthiessen's rule the total phonon MFP $\Lambda_s(q_z)$ is given by

$$1/\Lambda_s(q_z) = \sum_{r=B,U} 1/\Lambda_{r,s}(q_z), \tag{16.18}$$

where $\Lambda_{r,s}(q_z) = \tau_{r,s}(q_z) \cdot \upsilon_{z,s}(q_z)$ and $r = B$ stands for phonon-boundary scattering, while $r = U$ for three-phonon Umklapp scattering. The dependence of the average phonon MFP $\langle\Lambda\rangle(\omega) = g(\omega)/\sum_{s(\omega)}(1/\Lambda_s)$ on the phonon energy is presented in Fig. 16. 11 for the Si NW #2 (dashed line) and Si MSNWs #7 (solid line) and #8 (dotted line).

The Umklapp-limited phonon MFPs $\Lambda_{U,s}(q_z)$ in MSNWs are smaller than those in NWs due to both reduced phonon group velocity and stronger phonon scattering. The boundary-limited MFPs $\Lambda_{B,s}(q_z)$ are larger in MSNWs due to the larger average cross-section of MSNW in comparison with that in NW (see (16.14) and (16.15)). As a result, at small energies when the Umklapp scattering is weaker than the boundary scattering $\langle\Lambda\rangle^{MNW} > \langle\Lambda\rangle^{NW}$, while for $\hbar\omega > 5$ meV $\langle\Lambda\rangle^{MNW} \ll \langle\Lambda\rangle^{NW}$. The augmentation of l_z^2 decreases $\langle\Lambda\rangle^{MNW}$ for almost all phonon energies. The energy-averaged phonon MFP calculated from Fig. 16.11 constitutes $\sim$9.25 nm for the Si NW #2, $\sim$8.4 nm for the Si MSNW #7 and $\sim$6.9 nm for the Si MSNW #8. The increase of the MSNW average cross-section at fixed l_z^1 and l_z^2

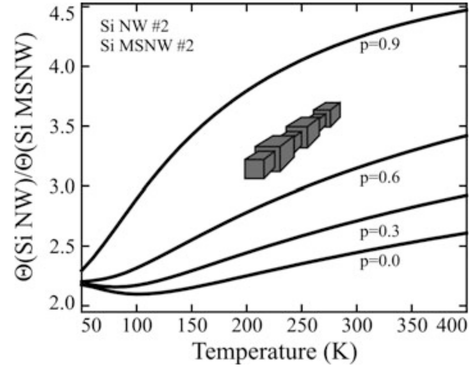

Fig. 16.12 Temperature dependence of the ratio of thermal fluxes in Si NW and Si MSNWs. The results are shown for different values of the specularity parameter $p = 0.0$, 0.3, 0.6 and 0.9. The image is reprinted from [28] with permission from American Physical Society

attenuates boundary scattering and increases the thermal flux. In Fig. 16.12 is shown the dependence of the ratio η of the thermal fluxes in Si NW #2 and Si MSNW #2 on temperature for different values of the specularity parameter $p = 0.0$, 0,3, 0.6, and 0.9.

For the interpretation of the data in Fig. 16.12, authors of [28] were calculated separately the thermal flux Θ_B carried out by the long-wavelength phonon modes (s,q_z), which are mainly scattered at the boundaries and described by the inequality $\tau_U(s, q_z) \geq \tau_B(s, q_z)$, and the thermal flux Θ_U carried out by the rest of the phonons i.e. thermal flux mainly limited by Umklapp scattering processes. The total thermal flux is thus: $\Theta = \Theta_B + \Theta_U$. The calculations showed that for all values of p under consideration, the room temperature thermal flux Θ_B is by a factor of ~ 5 lower in MSNW than that in NW due to the phonon trapping. An increase of p decreases Θ_B and strongly enhances Θ_U in NW due to attenuation of the boundary scattering of the high-energy phonon modes. These phonons in MSNW do not participate in the heat transfer because of their localization in the wider segments. For this reason, the ratio between thermal fluxes in the NW and the MSNW appreciably depends on p: for $p = 0$ $\Theta_U(\text{NW})/\Theta_U(\text{MSNW}) \sim 1$, while for $p = 0.9$ $\Theta_U(\text{NW})/\Theta_U(\text{MSNW}) \sim 3$. As a result, the flux ratio increases with increasing p in a wide range of temperatures from 100 to 400 K. Considering that the room temperature thermal conductivity of the rough Si NWs [59] is already by a factor of 100 lower than the corresponding bulk value, the obtained results suggest that the cross-section modulation of the rough Si NWs will allow for an additional decrease of the thermal conductivity by a factor of 2–2.5 with a subsequent increase of the thermoelectric efficiency ZT.

The dependence of the ratio η of the thermal fluxes in Si NW #2 and Si MSNW 14 ML × 14 ML x N_z/22 ML × 22 ML x N_z on N_z for the temperatures $T = 100$ K, $T = 200$ K, $T = 300$ K and $T = 400$ K and $p = 0.85$ is presented in Fig. 16.13. The calculated points for $N_z = 2, 4, 6, \ldots, 18$ are joined by the smooth curves as guides for an eye.

The overall trend of these curves is determined by the interplay of two effects: (i) phonon trapping, which suppresses the thermal flux and (ii) augmentation of the

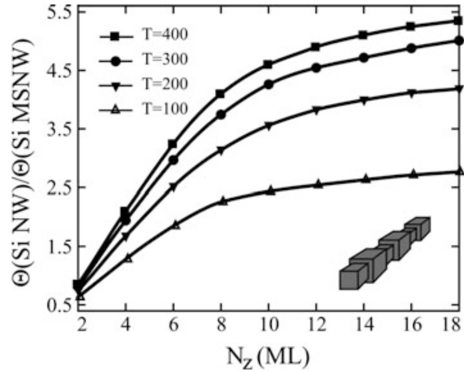

Fig. 16.13 Ratio of thermal fluxes in Si NW and Si MSNWs as a function of N_z. The results are shown for different temperatures $T = 100$, 200, 300 and 400 K. The image is reprinted from [28] with permission from American Physical Society

MSNW average cross-section, which enhances the flux due to the emergence of additional phonon modes for heat propagation and attenuation of the phonon-boundary scattering. In Si MSNW with the ultra-narrow segments $N_z = 2$ ML, the trapping of phonon modes is weak and the thermal flux is larger than that in Si NW ($\eta < 1$). The rise of N_z enhances the trapping, and for all temperatures under consideration the flux ratios rapidly increase with N_z rising up to the values 8 ML to 12 ML, and reach their maximum values at around N_z = 16–18 ML. It is expected that a subsequent rise of N_z should decrease η due to augmentation of the MSNW average cross-section.

In Fig. 16.14 is presented the temperature dependence of phonon thermal conductivity for Si NW #2, Si MSNW #2 and Si MSNWs covered by Ge shell of different thickness d_{Ge}.

Increasing the thickness of Ge shell from 1 to 7 ML leads to a decrease of thermal conductivity of Si/Ge MSNW by a factor of 2.9–4.8 in comparison with that in Si MSNW without Ge, and by a factor of 13–38 in comparison with that in Si NW. The reduction in κ of Si/Ge MSNWs is substantially stronger than that reported for core/shell nanowires without cross-sectional modulation [15, 38, 60–63]. In the core/shell nanowires without modulation, the κ decrease is mainly due to

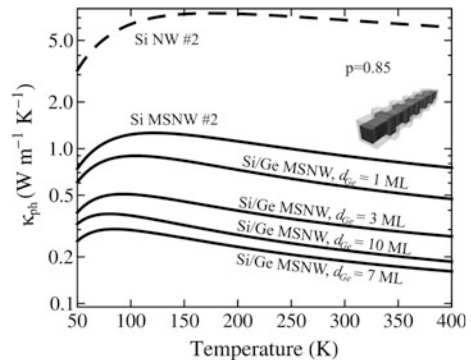

Fig. 16.14 Phonon thermal conductivity as a function of the absolute temperature. Results are presented for Si NW, Si MSNW and core/shell Si/Ge MSNW with different thickness of Ge. The image is reprinted from [29] with permission from American Institute of Physics

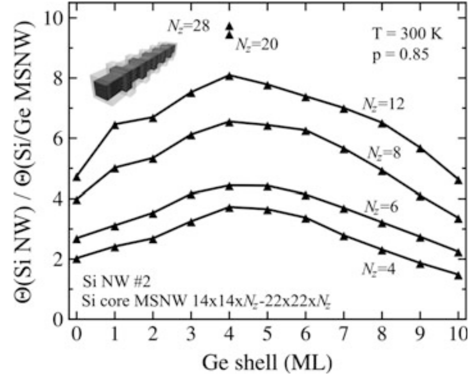

Fig. 16.15 Ratio of thermal fluxes in Si NW and Si/Ge MSNWs as a function of d_{Ge} for different values of N_z. The image is reprinted from [29] with permission from American Institute of Physics

phonon hybridization, which results in changes in the phonon DOS and group velocity. In the core/shell MSNWs, reduction of thermal conductivity is reinforced due to localization of a part of phonon modes in wider MSNW segments. The localization completely removes such phonons from the heat transport.

The dependence of the ratio of thermal fluxes at room temperature for MSNWs and Si NW on d_{Ge} is presented in Fig. 16.15 for $N_z = 4, 6, 8, 12$ ML. Two points for larger $N_z = 20$ ML and 28 ML at $d_{Ge} = 4$ ML are also shown. All curves have a maximum between $d_{Ge} = 3$ ML and $d_{Ge} = 6$ ML. The increase in N_z leads to a shift of the maximum to lower values of $d_{Ge.}$

In order to explain the dependence presented in Fig. 16.15 it was analyzed the frequency-specific thermal flux $\phi(\omega)$, i.e. the integrand in the equation $\Theta = \int_0^{\omega_{\max}} \phi(\omega) d\omega$. The results show that in Si MSNWs without Ge shell, thermal flux is strongly suppressed in comparison with Si NW due to redistribution of phonon energy spectra leading to the reduction of the phonon group velocities and localization of a part of phonon modes in nanowire segments. The influence of Ge shell on the frequency-specific thermal flux of MSNWs is determined by two opposite effects: (i) it reinforces the decrease of the thermal flux in Si/Ge MSNWs as compared with Si MSNWs owing to a stronger decrease of the phonon velocities and stronger phonon localizations; (ii) it increases the thermal flux due to appearance of additional channels for heat transfer through the Ge shell and weakening of the phonon-boundary scattering of propagating and Ge-like phonons. An interplay between two effects explains the non-monotonic dependence of the thermal flux ratio on d_{Ge} shown in Fig. 16.15. The difference between thermal fluxes in MSNWs and NWs becomes larger with growing N_z and reaches maximum value of ~ 10 at $N_z \sim$ 28–32 ML. For $N_z > 32$ ML, thermal flux ratio starts to decrease due to redistribution of the phonon energy spectra and heat conduction through Ge shell.

For ideally smooth interfaces when all phonon scattering events are specular $p = 1$. The value of $p = 0.85$, used in the calculations, corresponds to smooth NW surfaces with root mean square height of interface roughness $\Delta \sim 1$ ML. The Δ was estimated by averaging the mode-dependent specular parameter $\tilde{p}(q, \Delta) = \exp(-2q^2\Delta^2)$ [3, 12, 64, 65] over all q: $p = \int_0^{q_{z,\max}} \tilde{p}(q) dq / q_{z,\max}$. The small

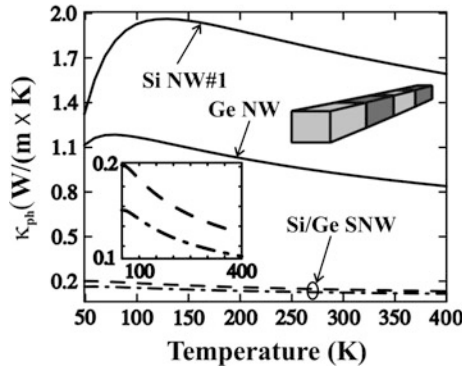

Fig. 16.16 Temperature dependence of lattice thermal conductivity for Si and Ge homogeneous nanowires (*solid lines*) and for Si/Ge SNWs with 12 ML of Si and 4 ML of Ge (*dashed line*) and with 8 ML of Si and 8 ML of Ge (*dash-dotted line*) per period. The image is reprinted from [27] with permission from American Physical Society

roughness of NWs and MSNWs interfaces is beneficial for both maintaining high electron mobility [66, 67] and for suppression of the phonon heat conduction in MSNWs [56]. The increase of p leads to faster growth of the thermal flux in Si NW than in Si MSNWs due to exclusion of high energy phonons in MSNW from heat transfer.

In Fig. 16.16 is plotted the temperature dependence of the phonon thermal conductivity of Si/Ge SNWs with cross-section 37 ML × 37 ML and different lengths of the Si and Ge segments along the wire axis. The results for Si NW #1 and Ge NW with the same cross-section are also presented for comparison. In the temperature range 150–300 K the thermal conductivity in the Si/Ge SNW is 5–6 times lower than that in the Ge nanowire with the same cross section, and 9–11 times lower than that in the Si nanowire.

When the number of atomic layers of Si per period increases from 8 to 12, the properties of the Si/Ge SNW reveal a slight trend towards those of the Si nanowire. Therefore the phonon thermal conductivity of the Si/Ge SNW, containing an equal number of atomic layers of Si and Ge, is lower than that of SNW containing different numbers of atomic layers per period. In [68] it was theoretically shown that the thermal conductivity of SNWs, consisting of different isotopes of silicon is by a factor of 2 smaller than in a Si nanowire. Our results demonstrate an even greater drop in the thermal conductivity in SNW composed of segments from acoustically-mismatched materials due to a stronger localization of phonon modes in the superlattice segments and a stronger decrease of the phonon group velocities. Our findings for the Si/Ge SNWs are in a qualitative agreement with the reduction of the thermal conductivity below the alloy limit predicted for circular Si/Ge SNWs with diameters less than 15 nm [69]. The thermal conductivity down to the sub-1 $Wm^{-1}K^{-1}$ range was achieved in multilayered Ge/Si dot arrays [70]. A similar effect of a strong decrease of the thermal conductivity is demonstrated theoretically

in [71] for Si/Ge 3D-SNWs. The authors of [71] explain the thermal conductivity reduction by a significant decrease of the phonon group velocities and incoherent scattering of phonons.

16.4 Conclusions

We reviewed recent theoretical results on phonon heat conduction in Si and Si/Ge segmented nanowires in the framework of the face-centered cubic cell and Born-von Karman models of lattice dynamics. Trapping of the phonon modes in the nanowire segments, leading to redistribution of the phonon energy spectra, decrease of the phonon group velocities and suppression of the phonon heat conduction are discussed in details. The room temperature heat flux in segmented nanowires can be suppressed by almost three orders-of-magnitude in comparison with that in bulk Si and by an order-of-magnitude in comparison with that in generic Si nanowires. We argue that geometry modulation and acoustic mismatch are highly efficient instruments in engineering phonons in semiconductor segmented nanowires for their thermoelectric and thermal insulator applications.

Acknowledgement DLN and AIC acknowledge the financial support from the Republic of Moldova through the projects 15.817.02.29F and 14.820.18.02.012 STCU.A/5937 and from the Science and Technology Center in Ukraine (STCU, project #5937). The work at the University of California – Riverside was supported by the National Science Foundation.

References

1. M.A. Stroscio, M. Dutta, *Phonons in Nanostructures* (Cambridge University Press, 2001), p. 1
2. A. Balandin, K.L. Wang, Effect of phonon confinement on the thermoelectric figure of merit of quantum wells. J. Appl. Phys. **84**, 6149 (1998)
3. A. Balandin, K.L. Wang, Significant decrease of the lattice thermal conductivity due to phonon confinement in a free-standing semiconductor quantum well. Phys. Rev. B **58**, 1544 (1998)
4. A.A. Balandin, Phonon engineering in nanostructures and nanodevices. J. Nanosci. Nanotechnol. **5**, 1015 (2005)
5. A.A. Balandin, D.L. Nika, E.P. Pokatilov, Phonon engineering in hetero- and nanostructures. J. Nanoelectron. Optoelectron. **2**, 140 (2007)
6. J. Zou, A. Balandin, Phonon heat conduction in a semiconductor nanowire. J. Appl. Phys. **89**, 2932 (2001)
7. N. Mingo, Calculation of Si nanowire thermal conductivity using complete phonon dispersion relations. Phys. Rev. B **68**, 113308 (2003)
8. A.A. Balandin, D.L. Nika, Phononics in low-dimensional materials. Mater. Today **15**, 266 (2012)
9. A. Khitun, A. Balandin, K.L. Wang, Modification of the lattice thermal conductivity in silicon quantum wires due to spatial confinement of acoustic phonons. Superlattices Microstruct. **26**, 181 (1999)

10. D. Li, Y. Wu, P. Kim, L. Shi, P. Yang, A. Majumdar, Thermal conductivity of Si/SiGe superlattice nanowires. Appl. Phys. Lett. **83**, 3186 (2003)
11. W. Liu, M. Asheghi, Thermal conductivity measurements of ultra-thin single crystal silicon layers. J. Heat Transf. **128**, 75 (2006)
12. A.I. Cocemasov, D.L. Nika, Phonons and Phonon Thermal Conductivity in Silicon Nanolayers. J. Nanoelectron. Optoelectron. **7**, 370 (2012)
13. D.G. Kahill, W.K. Ford, K.E. Goodson, G.D. Mahan, A. Majumdar, H.J. Maris, R. Merlin, S. P. Phillport, Nanoscale thermal transport. J. Appl. Phys. **93**, 793 (2003)
14. A. Shakouri, Proc. IEEE **94**, 1613 (2006)
15. A.A. Balandin, Thermal properties of graphene and nanostructured carbon carbon materials. Nat. Mater. **10**, 569 (2011)
16. A. Khitun, A. Balandin, J.L. Liu, K.L. Wang, In-plane lattice thermal conductivity of a quantum-dot superlattice. J. Appl. Phys. **88**, 696 (2000)
17. O.L. Lazarenkova, A. Balandin, Miniband formation in a quantum dot crystal. J. Appl. Phys. **89**, 5509 (2001)
18. D.L. Nika, E.P. Pokatilov, Q. Shao, A.A. Balandin, Charge carrier states and light absorption in the ordered quantum dot superlattices. Phys. Rev. B **76**, 125417 (2007)
19. L. Weber, E. Gmelin, Transport properties of silicon. Appl. Phys. A **53**, 136 (1991)
20. A.I. Boukai, Y. Bunimovich, J. Tahir-Kheli, J.-K. Yu, W.A. Goddard III, J.R. Heath, Silicon nanowires as efficient thermoelectric materials. Nature **451**, 168 (2007)
21. A.I. Hochbaum, R. Chen, R.D. Delgado, W. Liang, E.C. Garnett, M. Najarian, A. Majumdar, P. Yang, Enhanced thermoelectric performance of rough silicon nanowires. Nature **451**, 163 (2008)
22. P.N. Martin, Z. Aksamija, E. Pop, U. Ravaioli, Reduced thermal conductivity in nanoengineered rough Ge and GaAs nanowires. Nano Lett. **10**, 1120 (2010)
23. M. Shelley, A.A. Mostofi, Prediction of high zT in thermoelectric silicon nanowires with axial germanium heterostructures. EPL **94**, 67001 (2011)
24. M Hu, K.P. Giapis, J.V. Goicochea, X. Zhang, and Dimos Poulikakos, Nano Lett. **11**, 618 (2011)
25. D.V. Crismari, D.L. Nika, Thermal conductivity reduction in Si/Ge core/shell nanowires. J. Nanoelectron. Optoelectron. **7**, 701 (2012)
26. X. Chen, Y. Wang, Y. Ma, High thermoelectric performance of Ge/Si core − shell nanowires: first-principles prediction. J. Phys. Chem. C **114**, 9096 (2010)
27. D.L. Nika, E.P. Pokatilov, A.A. Balandin, V.M. Fomin, A. Rastelli, O.G. Schmidt, Reduction of the lattice thermal conductivity in one-dimensional quantum-dot superlattices due to phonon filtering. Phys. Rev. B **84**, 165415 (2011)
28. D.L. Nika, A.I. Cocemasov, C.I. Isacova, A.A. Balandin, V.M. Fomin, O.G. Schmidt, Suppression of phonon heat conduction in cross-section modulated nanowires. Phys. Rev. B **85**, 205439 (2012)
29. D.L. Nika, A.I. Cocemasov, D.V. Crismari, A.A. Balandin, "Thermal conductivity inhibition in phonon engineered core-shell cross-section modulated Si/Ge nanowires. Appl. Phys. Lett. **102**, 213109 (2013)
30. X. Zianni, Diameter-modulated nanowires as candidates for high thermoelectric energy conversion efficiency. Appl. Phys. Lett. **97**, 233106 (2010)
31. X. Zianni, Efficient thermoelectric energy conversion on quasi-localized electron states in diameter modulated nanowires. Nanoscale Res. Lett. **6**, 286 (2011)
32. G.D. Sulka, A. Brzozka, L. Liu, Fabrication of diameter-modulated and ultrathin porous nanowires in anodic aluminum oxide templates. Electrochim. Acta **56**, 4972 (2011)
33. P. Caroff, K.A. Dick, J. Johansson, M.E. Messing, K. Deppert, L. Samuelson, Controlled polytypic and twin-plane superlattices in III–V nanowires. Nat. Nanotechnol. **4**, 50 (2009)
34. L.-T. Fu, Z.-G. Chen, J. Zou, H.-T. Cong, G.-Q. Lu, Fabrication and visible emission of single-crystal diameter-modulated gallium phosphide nanochains. J. Appl. Phys. **107**, 124321 (2010)

35. D.S. Oliveira, J.H.G. Tizei, D. Ugarte, M.A. Cotta, Spontaneous periodic diameter oscillations in inp nanowires: the role of interface instabilities. Nano Lett. **13**, 9 (2013)
36. S.K. Lim, S. Crawford, G. Haberfehlner, S. Gradecak, Controlled modulation of diameter and composition along individual III–V nitride nanowires. Nano Lett. **13**, 331 (2013)
37. D.L. Nika, N.D. Zincenco, E.P. Pokatilov, Lattice thermal conductivity of ultra-thin freestanding layers: face-centered cubic cell model versus continuum approach. J. Nanoelectron. Optoelectron. **4**, 170 (2009)
38. D.L. Nika, N.D. Zincenco, E.P. Pokatilov, Engineering of thermal fluxes in phonon mismatched heterostructures. J. Nanoelectron. Optoelectron. **4**, 180 (2009)
39. D.L. Nika, E.P. Pokatilov, A.A. Balandin, Phonon—engineered mobility enhancement in the acoustically mismatched silicon/diamond transistor channels. Appl. Phys. Lett. **93**, 173111 (2008)
40. E.P. Pokatilov, D.L. Nika, A.A. Balandin, Acoustic phonon engineering in coated cylindrical nanowires. Superlettices Microstruct. **38**, 168 (2005)
41. E.P. Pokatilov, D.L. Nika, A.A. Balandin, Phonon spectrum and group velocities in AlN/GaN/AlN and related heterostructures. Superlattices Microstruct. **33**, 155 (2003)
42. P.N. Keating, Effect of invariance requirements on the elastic strain energy of crystals with application to the diamond structure. Phys. Rev. B **145**, 637 (1966)
43. M. Born, K. Huang, *Dynamic Theory of Crystal Lattices* (Oxford University Press, Oxford, 1954)
44. G. Leibfried, W. Ludwig, in *Theory of Anharmonic Effects in Crystals*, ed. by F. Seitz, D. Turnbull. Solid State Physics, vol. 12 (Academic, New York, 1961)
45. P. Giannozzi, S. de Gironcoli, P. Pavone, S. Baroni, Ab initio calculation of phonon dispersions in semiconductors. Phys. Rev. B **43**, 7231 (1991)
46. G. Nilsson, G. Nelin, Phonon dispersion relations in ge at 80 k. Phys. Rev. B **3**, 364 (1971)
47. E.P. Pokatilov, D.L. Nika, A.A. Balandin, Acoustic-phonon propagation in rectangular semiconductor nanowires with elastically dissimilar barriers. Phys. Rev. B **72**, 113311 (2005)
48. S. Volz, G. Chen, Molecular dynamics simulation of thermal conductivity of silicon nanowires. Appl. Phys. Lett. **75**, 2056 (1999)
49. D.L. Nika, E.P. Pokatilov, A.S. Askerov, A.A. Balandin, Phonon thermal conduction in graphene: Role of Umklapp and edge roughness scattering. Phys. Rev. B **79**, 155413 (2009)
50. D. Donadio, G. Galli, Thermal conductivity of isolated and interacting carbon nanotubes: comparing results from molecular dynamics and the Boltzmann transport equation. Phys. Rev. Lett. **99**, 255502 (2009)
51. N. Mingo, L. Yang, Phonon transport in nanowires coated with an amorphous material: An atomistic Green's function approach. Phys. Rev. B **68**, 245406 (2003)
52. B. Qiu, X. Ruan, Molecular dynamics simulation of lattice thermal conductivity of bismuth telluride using two-body interatomic potentials. Phys. Rev. B **80**, 165203 (2009)
53. A. Ladd, B. Moran, W. Hoover, Lattice thermal conductivity: A comparison of molecular dynamics and anharmonic lattice dynamics. Phys. Rev. B **34**, 5058 (1986)
54. A. Ward, D. Broido, Intrinsic phonon relaxation times from first-principles studies of the thermal conductivities of Si and Ge. Phys. Rev. B **81**, 085205 (2010)
55. E. Pokatilov, D. Nika, A. Balandin, A phonon depletion effect in ultrathin heterostructures with acoustically mismatched layers. Appl. Phys. Lett. **85**, 825 (2004)
56. M.C. Wingert, Z.C.Y. Chen, E. Dechaumphai, J. Moon, J.-H. Kim, J. Xiang, R. Chen, Thermal conductivity of Ge and Ge–Si core-shell nanowires in the phonon confinement regime. Nano Lett. **11**, 5507 (2011)
57. C. Glassbrenner, G. Slack, Thermal conductivity of silicon and germanium from 3°k to the melting point. Phys. Rev. **134**, A1058 (1964)
58. J. Ziman, *Electrons and Phonons: The Theory of Transport Phenomena in Solids* (Oxford University Press, New York, 1960)
59. A. Hochbaum, R. Chen, R.D. Delgado, W. Liang, E.C. Garnett, M. Najarian, A. Majumdar, P. Yang, Enhanced thermoelectric performance of rough silicon nanowires. Nature **451**, 163 (2008)

60. M. Hu, K.P. Giapis, J.V. Goicochea, X. Zhang, D. Poulikakos, Significant reduction of thermal conductivity in Si/Ge core-shell nanowires. Nano Lett. **11**, 618 (2011)
61. E.P. Pokatilov, D.L. Nika, A.S. Askerov, N.D. Zincenco, A.A. Balandin, The size-quantized oscillations of the optical-phonon-limited electron mobility in AlN/GaN/AlN nanoscale heterostructures. J. Phys. Conf. Ser. **92**, 012022 (2007)
62. K. Bi, J. Wang, Y. Wang, J. Sha, Z. Wang, The thermal conductivity of SiGe heterostructure nanowires with different cores and shells. Phys. Lett. A **376**, 2668 (2012)
63. M. Wingert, Z.C.Y. Chen, E. Dechaumphai, J. Moon, J.-H. Kim, J. Xiang, R. Chen, Thermal conductivity of Ge and Ge-Si core-shell nanowires in the phonon confinement regime. Nano Lett. **11**, 5507 (2011)
64. Z. Aksamija, I. Knezevic, Anisotropy and boundary scattering in the lattice thermal conductivity of silicon nanomembranes. Phys. Rev. B **82**, 045319 (2010)
65. Z. Aksamija, I. Knezevic, Lattice thermal conductivity of graphene nanoribbons: Anisotropy and edge roughness scattering. Appl. Phys. Lett. **98**, 141919 (2011)
66. E. Ramayya, D. Vasileska, S.M. Goodnick, I. Knezevic, Electron transport in silicon nanowires: The role of acoustic phonon confinement and surface roughness scattering. J. Appl. Phys. **104**, 063711 (2008)
67. S. Jin, M. Fischetti, T.-W. Tang, Modeling of electron mobility in gated silicon nanowires at room temperature: surface roughness scattering, dielectric screening, and band nonparabolicity. J. Appl. Phys. **102**, 083715 (2007)
68. N. Yang, G. Zhang, B. Li, Ultralow thermal conductivity of isotope-doped silicon nanowires. Nano Lett. **8**, 276 (2008)
69. C. Dames, G. Chen, Theoretical phonon thermal conductivity of Si-Ge superlattice nanowires. J. Appl. Phys. **95**, 682 (2004)
70. G. Pernot, M. Stoffel, I. Savic, F. Pezzoli, P. Chen, G. Savelli, A. Jacquot, J. Schumann, U. Denker, I. Monch, C. Deneke, O.G. Schmidt, J.M. Rampnoux, S. Wang, M. Plissonnier, A. Rastelli, S. Dilhaire, N. Mingo, Precise control of thermal conductivity at the nanoscale through individual phonon-scattering barriers. Nat. Mater. **9**, 491 (2010)
71. J.-N. Gillet, Y. Chalopin, S. Volz, Atomic-scale three-dimensional phononic crystals with a very low thermal conductivity to design crystalline thermoelectric devices. J. Heat Transf. **131**, 043206 (2009)

Chapter 17
THz Devices Based on Carbon Nanomaterials

Mircea Dragoman and Daniela Dragoman

Abstract In this chapter we present a review the terahertz devices based on carbon nanomaterials such as graphene and carbon nanotubes. First, the graphene and carbon nanotube physical properties at high frequencies are described. Then, antennas at terahertz frequencies based on graphene, the generation and detection of terahertz electromagnetic waves are analyzed and different devices and circuits are discussed.

17.1 Introduction

Since the early 90s the research regarding post-CMOS electronics, i.e. the most advanced electronic devices to date, has been enhanced by a new class of materials based on organized aggregation of carbon atoms. Carbon nanotubes (CNTs), discovered in 1991 [1], have been considered as key nanomaterials for the post-CMOS era due to their extremely promising electrical and mechanical properties.

In 2004, the isolation of single atom-sheet matter consisting of carbon atoms, known as graphene, triggered one of the most studied subjects by the physicist' community [2]. Nowadays, graphene is becoming a central subject in electronic engineering [3], as well as many applied areas of physics, such as photonics [4]. THz devices based on CNTs or graphene are at the border between electronics and photonics.

Graphene is the first material in a large class of two-dimensional (2D) materials formed from a single atomic sheet. The exploration of physical properties of graphene

M. Dragoman (✉)
National Institute for Research and Development in Microtechnology, 077190 Bucharest-Voluntari, Romania
e-mail: mircea.dragoman@imt.ro

D. Dragoman
University of Bucharest, 077125 Bucharest-Magurele, Romania

D. Dragoman
Academy of Romanian Scientists, Spalaiul Independentei 54, 050094 Bucharest, Romania

© Springer International Publishing Switzerland 2016

I. Tiginyanu et al. (eds.), *Nanostructures and Thin Films for Multifunctional Applications*, NanoScience and Technology,
DOI 10.1007/978-3-319-30198-3_17

has started by isolating graphene flakes followed by their subsequent transfer on a doped Si/SiO_2 substrate [5]. The transfer method of graphene, grown by the chemical vapor deposition method, on various substrates is the key concept for batch production of graphene monolayers at 4-inch and 6-inch wafer scale, 12-inch wafers being expected only in the next few years [6]. In fact, the discovery of graphene was motivated by the search of a metallic field-effect transistor (FET), which would be much less influenced by electromagnetic radiation than a semiconductor transistor [7].

Searching for the electric field effect (EFE) in common metals was unsuccessful due to the very large number of carriers which needed to be controlled by an electric field. Therefore, other experiments were performed in semimetals such as Bi [8], antimony and graphite, which have a much smaller carrier density compared to a metal [7]. This search was at the origin of the breakthrough that led to the discovery of graphene from graphite. An in-depth review of EFE in various materials is found in [9]. The quest for a metallic transistor was successful in 2012 [10] when an ultrathin Ni film with a thickness of 1–2 nm showed a graphene transistor-like behavior. Further, metallic switches and logic gates were developed based on thin films of 2H-$TaSe_2$, which is a semimetal without bandgap [11]. The EFE is now investigated in other 2D materials, such as black phosphorus [12]. The most advanced device derived from the EFE is the CMOS FET, developed in Si technology, due to its impressive integration capability and reduced consumption. For example, 5.4 billion transistors were recently integrated in a neuromorphic Si chip [13]. The first high-frequency integrated circuit based on graphene—a microwave receiver—has only three transistors [14]. The CNT and graphene are investigated in-depth from the manufacturing point of view and from the experimental and theoretical perspective, in order to achieve large scale production with high reproducibility, controlled chirality, and material purity. A recent review about CNT growth and its ultimate performances and applications is found in [15]. The physical properties of these new nanomaterials determines the macroscopic enhanced or novel electrical behavior of many devices applied in electronics, harvesting, biosensing and photonics [16, 17]. The main physical properties useful for THz electronics of CNTs and graphene are summarized in Tables 17.1 and 17.2.

Carbon electronics is more advanced than graphene electronics—see the review paper [18]. The most prominent success of CNT electronics is a computer having thousands of integrated CNT FET transistors [19]. The CNT computer processor is

Table 17.1 Graphene properties

Parameter	Room temperature values
Mean free path (ballistic transport)	400 nm, even 1 μm for graphene deposited on hexagonal BN
Mobility	40000 cm^2/Vs (intrinsic), but could attain 100000 cm^2/Vs in suspended graphene or in graphene deposited on hexagonal BN
Effective mass of carriers	0 near the Dirac point
Thermal conductivity	5000 W/mK, better than in many metals

Table 17.2 Carbon nanotube properties

Parameter	Room temperature values	Observations
Current density	>10^9 A/cm^2	1000 times larger than in copper
Mobility	10000–50000 cm^{2}V^{-1}s^{-1}	Lower than in graphene
Mean free path (ballistic transport)	300–700 nm in semiconducting CNTs 1000–3000 nm in metallic CNTs	At least three times larger than in the best semiconducting heterostructures

comparable in capabilities to the Intel 4004, which was the first programmable microprocessor and thus the ancestor of microprocessors found today in any computer. Such CNT-based computers could be more energy-efficient than silicon-based computers. In contrast to CNTs, which have a clear perspective for development in digital engineering, graphene electronics is oriented toward high-frequency electronics, since the lack of bandgap in graphene is a serious obstacle towards digital applications.

From all parameters in Tables 17.1 and 17.2, the most important property of graphene and CNTs is the long ballistic transport distances at room temperature. For comparison, the mean free path at room temperature is of only 150 nm in InAs nanowires [20], while the highest mean free path reported in semiconductors at room temperature is found in InSb/AlInSb quantum wells, being of 550 nm [21] at a current density of 10^6 A/cm^2, while in CNTs and graphene at similar or longer mean free paths the current density is higher with two or three orders of magnitudes. This implies that charge carriers in CNTs and graphene travel coherently over hundreds of nanometers at room temperature, without any collision, which explains the high mobilities of these materials.

These facts have important implications for high-frequency devices. More precisely, (i) the large mean free paths allows the fabrication of ballistic high-frequency devices based on CNTs and graphene at room temperature since the minimum features of existing nanolithography such e-beam is below 10 nm, (ii) the cutoff frequency of CNT and graphene ballistic devices are in the THz range since the cutoff frequency $\propto v_F/L$, where L is the mean free path at room temperature and v_F is the Fermi velocity. For example in metallic CNTs the Fermi velocity is 9.3×10^5 m/s while in graphene monolayer this parameter takes a value of about 10^6 m/s.

The knowledge of the electronic band structure of graphene is necessary to understand other properties of CNTs and graphene for THz electronics. The honeycomb structure of carbon atoms, which constitute a graphene layer and can be understood as a superposition of two triangular lattices, is displayed in Fig. 17.1a. The distance between carbon atoms, i.e. the carbon bond length, is of $a = 0.14$ nm and the unit cell is spanned by the two vectors $\boldsymbol{a}_1$ and $\boldsymbol{a}_2$. The reciprocal lattice has also a honeycomb shape. The first Brillouin zone, which is a hexagon with a side length of $4\pi/3\sqrt{3}a$, is displayed in Fig. 17.1b. The non-equivalent points K and K',

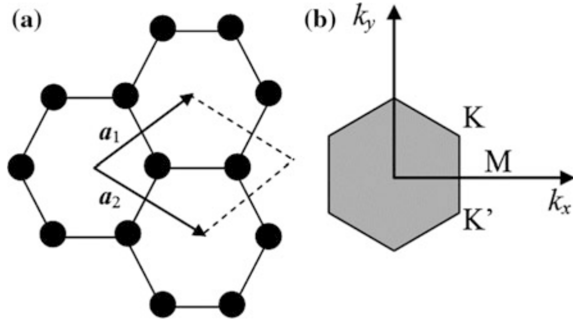

Fig. 17.1 **a** Graphene honeycomb lattice structure and **b** the first Brillouin zone in the reciprocal lattice

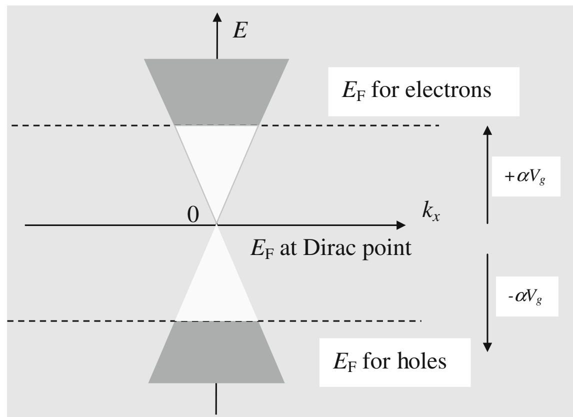

Fig. 17.2 Graphene dispersion relation

called Dirac points, are the most important points in the reciprocal lattice, because the dispersion relation of graphene, given by [22]

$$E(\boldsymbol{k}) = \pm t\sqrt{3 + 2\cos(\sqrt{3}k_y a) + 4\cos(\sqrt{3}k_y a/2)\cos(3k_x a/2)} \tag{17.1}$$

reduces to the linear relation

$$E = \pm\hbar|\boldsymbol{k}|v_{\mathrm{F}} \tag{17.2}$$

near the K and K' points, where $\boldsymbol{k} = \boldsymbol{i}k_x + \boldsymbol{j}k_y$ is the wavenumber measured from K and K', and the positive (negative) sign is assigned to electron (hole) states. The dispersion relation (2) consists of two cones represented in Fig. 17.2.

From Fig. 17.2 we observe that graphene is a semiconductor with no energy gap, because the valence and conduction bands touch at Dirac points. The linear dispersion relation in graphene is not encountered in nature except for photons propagating in a homogeneous medium. Therefore, the graphene dispersion relation is photon-like and graphene can be modeled as a 2D gas of massless carriers. More precisely, graphene is similar to a slow-wave structure, in which the charge carriers

propagate with a velocity $v_F \cong c/300$, which is two orders of magnitude smaller than light velocity of vacuum c. In striking contrast with a semiconductor, the electrons and holes in graphene have identical physical properties, and their selection is done by a gate voltage that shifts the Fermi energy level E_F above and below the Dirac point, where $E_F = 0$. Moreover, via the gate voltage it is possible to tune the carrier density n according to the relation:

$$n = \varepsilon_d V_g / te \cong \alpha V_g \tag{17.3}$$

where ε_d is the dielectric permittivity of the gate dielectric, t is the gate thickness, and V_g is the gate voltage.

A direct consequence of relation (17.3) is the fact that the resistivity and conductivity depend strongly on the gate voltage. Using the Random Phase Approximation (RPA), the conductivity in graphene is given by [23]:

$$\sigma = \begin{cases} 20e^2 n^*/(hn_{imp}), & n - \bar{n} < n^* \\ 20e^2 n/(hn_{imp}), & n - \bar{n} > n^* \end{cases} \tag{17.4}$$

where h is the Planck constant and $\bar{n}$ and n^* are carrier concentrations determined via RPA Boltzmann theory. In the diffusive regime, we learn that charge transport is dominated by scattering from impurities with a concentration n_{imp} of the order of 10^{11} cm^{-2}. In the ballistic transport limit, at the Dirac point, the conductivity is $e^2/(\pi h)$.

Considering now the frequency dependence of the conductivity, it is a sum of frequency-dependent intraband and interband transitions in graphene, $\sigma_1(\omega)$ and $\sigma_2(\omega)$, respectively, as depicted in Fig. 17.3.

$$\sigma(\omega) = \sigma_1(\omega) + \sigma_2(\omega) \tag{17.5}$$

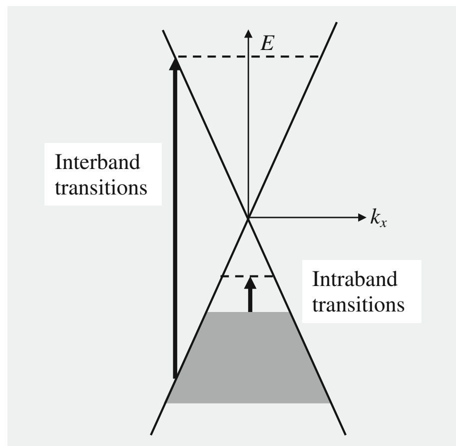

Fig. 17.3 The intraband and interband transitions in graphene

The intraband conductivity is given by:

$$\sigma_1(\omega) = ie^2 E_F / \pi\hbar^2(\omega + i/\tau) \tag{17.6}$$

while the interband term can be expressed as:

$$\sigma_2(\omega) = (ie^2\omega/\pi) \int_0^\infty [f(\varepsilon - E_F) - f(-\varepsilon - E_F)]/[(2\varepsilon)^2 - (\hbar\omega + i\Gamma)]d\varepsilon \tag{17.7}$$

where Γ is the momentum relaxation time, Γ is a broadening parameter and $f(E)$ is the Fermi-Dirac distribution function, which depends on the energy E of charge carriers. For $\tau = 40$ fs and small Fermi energy levels, of 100–200 meV, the intraband transitions and intraband conductivity is dominating up to 1 THz, the interband contributions being rather small or negligible. Beyond 100 THz, and up to the visible spectrum, only the interband transitions are relevant. For $\omega \to \infty$, the optical conductivity attains $e^2/4\hbar$, which leads to 2.3 % absorption in graphene at normal incidence, independent of the wavelength of the electromagnetic radiation. From the formulas (17.6) and (17.7), it can be seen that both intraband and interband conductivities depend on the Fermi energy, and so they can be changed by a gate voltage.

The single-wall CNT is a graphene sheet rolled-up around a chiral vector $\mathbf{C} = n\boldsymbol{a}_1 + m\boldsymbol{a}_2$ with n, m integers, which links two equivalent crystallographic sites. As a result, we have a confinement of carriers in the circumferential direction of the tube, given by the quantization rule:

$$\boldsymbol{k}_\mathrm{c}\boldsymbol{C} = 2\pi j, \tag{17.8}$$

where $\boldsymbol{k}_\mathrm{c}$ is the circumferential component of the wave vector $\boldsymbol{k}$ and $j = 1, 2, 3, \ldots, N$ is an integer. The quantization rule dictates that the allowed energy band structure of the CNT is obtained by cutting the 2D band of graphene into 1D slices. In the vicinity of a K point, for $ka \ll 1$, with $k = |\boldsymbol{k}|$ measured from K, the dispersion relation is linearly dependent on the wave vector k:

$$\omega(k) \cong 3^{1/2} ka/2 + \cdots \tag{17.9}$$

The CNT energy dependence on the wave vector can be expressed as

$$E_{\mathrm{CNT},j} = E_{\mathrm{2D}}(k\boldsymbol{K}_\mathrm{a}/|\boldsymbol{K}_\mathrm{a}| + j\boldsymbol{K}_\mathrm{c}). \tag{17.10}$$

where $\boldsymbol{K}_\mathrm{c}$ is a unit vector along the circumferential direction and $\boldsymbol{K}_\mathrm{a}$ is the reciprocal lattice vector along the axis of the tube. The wave number k takes values in the interval $(-\pi/T, \pi/T)$, where T is the length of the translational vector $\boldsymbol{T}$. The above relation means that we have N discrete values of the CNT wave vector in the $\boldsymbol{K}_\mathrm{c}$ direction, while in the $\boldsymbol{K}_\mathrm{a}$ direction the wave vector is continuous. Thus, N lines of

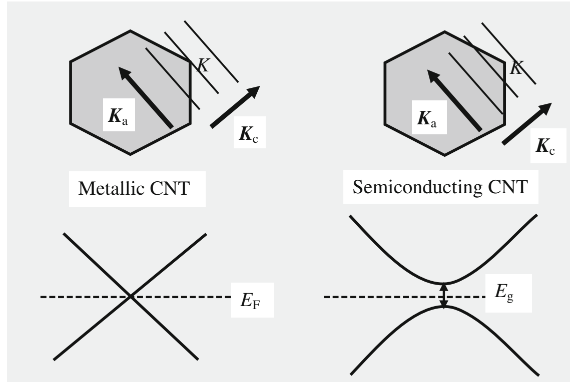

Fig. 17.4 CNT band structure

the form $k\boldsymbol{K}_a/|\boldsymbol{K}_a| + j\boldsymbol{K}_c$ cut the hexagonal Brillouin zone of graphene. We see in Fig. 17.4 that the CNT is metallic-like if the lines cross through the K point, and semiconductor-like otherwise. The CNT is metallic when $n - m = 3i$ and semiconductor when $n - m \neq 3i$, with i an integer. Moreover, at low energies the band structure of a metallic CNT consists of two bands with linear dispersion that intersect at the K point, while for semiconductor CNTs an energy gap E_g opens between the two bands.

The bandgap of the semiconducting CNT is given by:

$$E_g = 4\hbar v_F/3d, \tag{17.11}$$

and takes the value

$$E_g(\text{eV}) \cong 0.9/d(\text{nm}) \tag{17.12}$$

for the Fermi velocity $v_F = 8 \times 10^7$ m/s. Since semiconducting CNTs have diameters of at most few nanometers, their bandgap is in the range 20 meV–2 eV at room temperature.

17.2 Graphene Antennas at THz Frequencies

The graphene antennas are studied because they are able to provide to an antenna tunability and miniaturization. The first THz graphene antenna was reported in [24], where the fact that graphene is a tunable resistance, i.e. its resistance $R(V_g = 0\ \text{V})$ is of the order of 1 kΩ and decreases at tens of ohms for $R(V_g \gg 0\ \text{V})$ or $R(V_g \ll 0\ \text{V})$, was exploited to change the radiation pattern of a dipole or an array of dipoles.

As we have pointed out, in the range 1–30 THz the dominating term of conductivity is the interband conductivity, written in a simpler way as:

$$\sigma_{\text{inter}} = -i(e^2/4\pi\hbar)\ln\left(\frac{2|\mu_c| - \hbar(\omega - i2\Gamma)}{2|\mu_c| + \hbar(\omega - 2i\Gamma)}\right) \tag{17.13}$$

where μ_c is the chemical potential. In principle, the real part of the interband conductivity is much smaller than its imaginary part. On the other hand, both types of conductivity, i.e. interband and intraband, are taken into account in calculating the surface impedance in the THz range, despite the fact that interband conductivity is dominating. We have thus

$$Z_S(V_b) = 1/\sigma(\omega) = R_s(V_b) + jX_s(V_b). \tag{17.14}$$

The simulation data have shown [25] that the surface impedance is primarily reactive (inductive), R_s taking values below 52 Ω, whereas $X_s \gg R_s$ reaches 17–18 kΩ. This result implies that graphene is a high reactive impedance surface (RIS) having certain advantages:

(i) it reduces the lateral lobes
(ii) it enhances the front-to-back ratio of radiated power,
(iii) it minimizes the coupling between the antenna and its image, and assures antenna miniaturization [26].

Moreover, since both conductivity components depend on a gated DC electric field, the surface impedance can be modified by changing this field, graphene being a natural tunable high RIS.

As an example, we consider a gold THz dipole antenna with the length $L = 0.38\ \lambda_0 = 11.25$ μm, the width $W = 1$ μm, a gap of 100 nm and a thickness of 200 nm deposited over a graphene monolayer, which on its turn is transferred onto Si/SiO_2, the SiO_2 having a thickness of 300 nm. The real and imaginary parts of the input impedance of the THz dipole on graphene are displayed in Fig. 17.5. There are many points where $X_s = 0$ or nearly zero.

The radiation pattern at 10 THz was simulated with the CST software, and is represented in Fig. 17.6. The radiation pattern shows no side lobes. The directivity of the antenna is of 6 dBi and its total efficiency is almost 15 %.

We have also analyzed a bow tie antenna with length $L = 0.38\ \lambda_0 = 11.25$ μm, width $W = 1$ μm, and a gap of 100 nm made from gold with a thickness of 200 nm deposited onto graphene on Si/SiO_2. The radiation pattern at 10 THz, represented in Fig. 17.7, shows that the radiation efficiency is 33 % and the directivity is of about 8 dBi. Although it is well known that the bow-tie antenna has two lobes, a single lobe with a high directivity, able to collimate alone the 10 THz radiation without any lens, is evidenced in Fig. 17.7 as a net result of the RIS effect.

The inductive nature of the conductivity (RIS effect) in the THz region implies that TM surface plasmon polariton waves (SPPs) are propagating in graphene at the interface with air [27]. Using graphene on glass, the dimensions of the patch antennas are much smaller than L/λ_0, which is 0.06 for a microstrip patch with a length of 17 μm and width of 10 μm. Thus, SPP, which are occurring in principle at

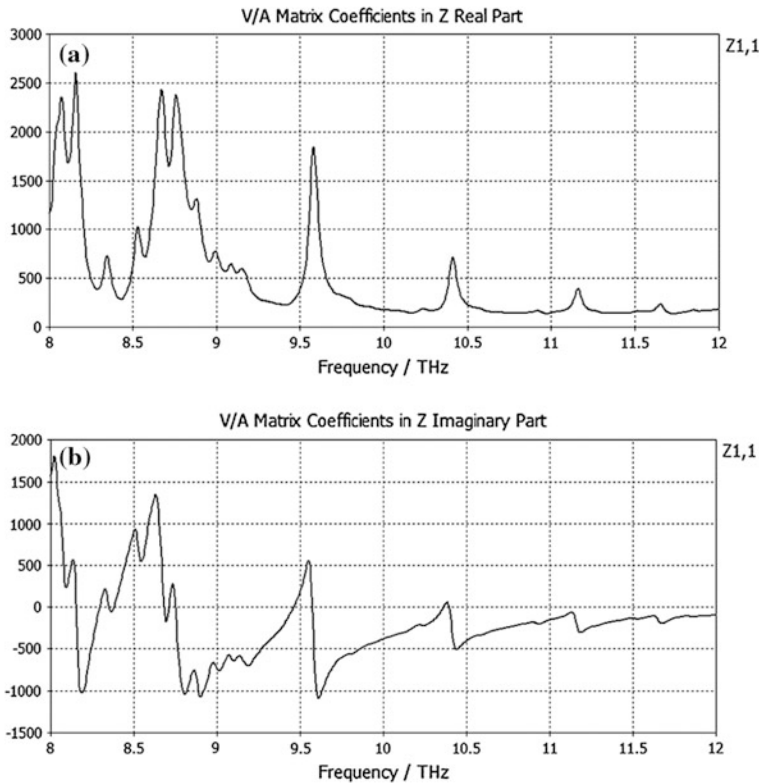

Fig. 17.5 The **a** real and **b** imaginary parts of the input impedance of a dipole on graphene at THz (after Dragoman et al. [25])

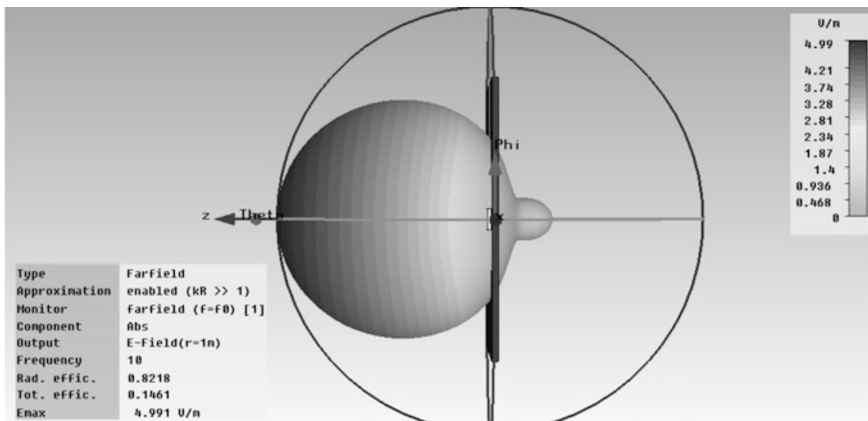

Fig. 17.6 The radiation pattern of a dipole on graphene at 10 THz (after Dragoman et al. [25])

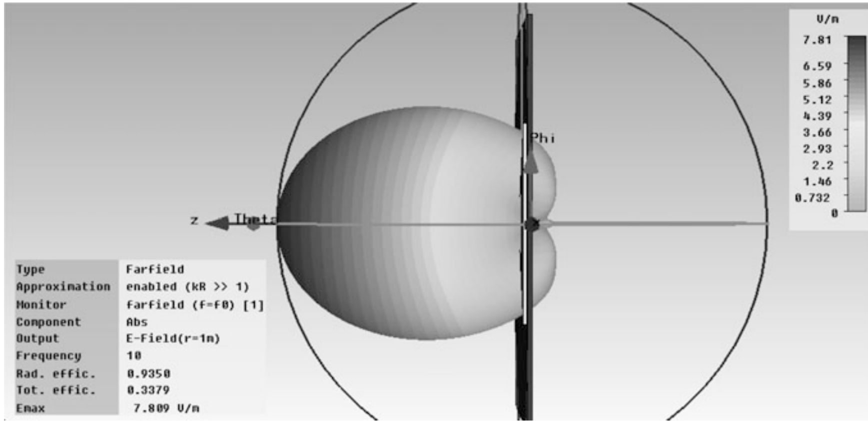

Fig. 17.7 The radiation pattern of a bow tie on graphene at 10 THz (after Dragoman et al. [25])

optical frequencies at metal/dielectric interfaces, are produced at much lower frequencies due to the unique physical properties of graphene. Moreover, the SPP waves in graphene are tunable and display stronger electromagnetic confinement and lower dissipation losses compared to SPP waves in metallic structures.

The SPP graphene antennas are resonant antennas working at the SPP resonance frequency [28] which is given by:

$$M\lambda/2n_{eff} = L + 2\delta L \tag{17.15}$$

where δL is the field penetration outside graphene and the effective index of refraction is:

$$n_{eff} = [1 - 4\mu_0/\varepsilon_0\sigma(\omega)] \tag{17.16}$$

with ε_0 and μ_0 the electric permittivity and magnetic permeability of the vacuum. The dispersion relation of SPPs propagating at the interface between two media with relative electric permittivities ε_{r1} and ε_{r2} can be written as:

$$\varepsilon_{r1}/(k^2 - \varepsilon_{r1}k_0^2)^{1/2} + \varepsilon_{r2}/(k^2 - \varepsilon_{r2}k_0^2)^{1/2} = -i\sigma/\omega\varepsilon_0 \tag{17.17}$$

where $k_0 = \omega/c$. Graphene rings structures are efficient plasmonic antennas at THz frequencies [29]. In this context, the wavenumber and resonant frequency of SPPs in graphene are given, respectively, by:

$$k_{SPP} \approx \hbar\omega^2/(2\alpha E_F c), \tag{17.18}$$

$$\omega_{SPP=}(nE_F/R). \tag{17.19}$$

It can be seen that the main parameters of the SPP wave, i.e. its wavenumber and resonance frequency, depend on the Fermi level, which can be tuned by a gate voltage. Therefore, SPP waves in graphene are tunable.

Emission of electromagnetic radiation via SPP is observed in graphene at impressive high frequencies, of 10^3 THz, and is generated at atomic scale by a point defect leading to SPP resonance at a sub-nanometer scale of about $\lambda/200$. The point defect is generated by replacing two carbon atoms with one Si atom representing a dopant atom, and an additional N atom bonded with the Si atom [30].

17.3 THz Generation Based on Graphene

THz generation using graphene is still in infancy, although some basic experiments have been reported. Most of them are based on the ultrafast excitation using a fs laser and various nonlinear effects in graphene. For instance, suspended graphene in a stripline configuration (see Fig. 17.8) was excited by a fs laser and photocurrents with a duration of maximum 4 ps were produced, corresponding to a spectrum up to 1 THz. The THz radiation is detected by the striplines electrodes, which act as a near-field antenna and as a waveguide up to 1 THz. The stripline has a length of 48 mm. The THz fields are due to build-in fields and a photothermoelectric effect. The THz radiation is collected by a field probe located at 0.3 mm away from graphene. In the graphene-based device, graphene was transferred on a low-temperature (LT) GaAs substrate, such that it spans the two striplines [31]. The graphene was illuminated by a titan-saphire laser with pulse duration of 160 fs and photon energy of 1.59 eV. The entire experimental configuration is a pump-probe set-up with a variable delay stage.

A further development of this approach based on graphene photoconductive switches is a chip containing graphene photoconductive switches for both generation and detection of ps pulses within THz range [31].

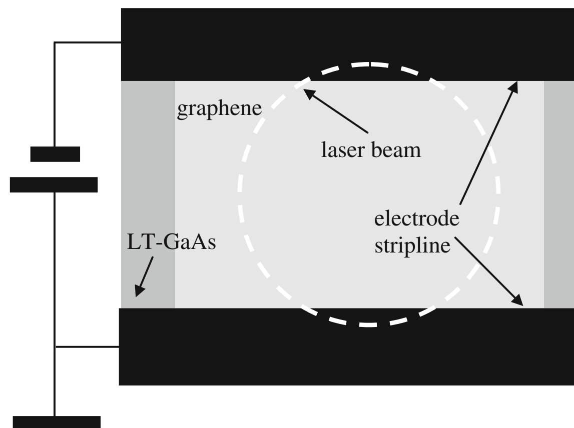

Fig. 17.8 THz generation via suspended graphene using biased striplines

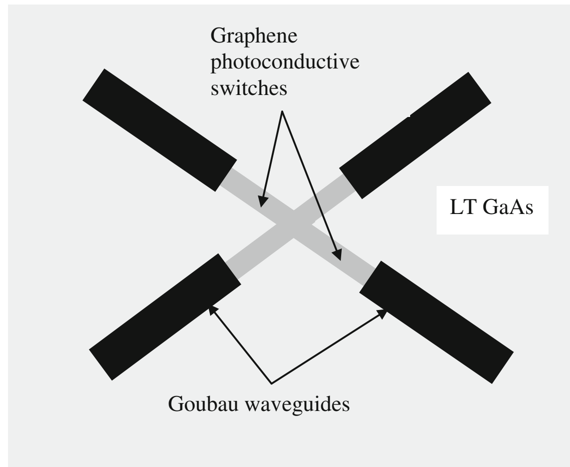

Fig. 17.9 THz generation/detection on chip with photoconductive switches

The photogeneration of charge carriers via visible light absorption encompasses several physical effects in time: (i) ultrafast phenomena are represented by carrier-carrier interactions (10 fs) resulting finally in a Fermi-Dirac distribution function followed by optical phonon scattering at 100 fs time scale with the net result of reducing the energy of hot carriers, (ii) slow phenomena at nanosecond time scale as a result of scattering between electrons and acoustic phonons due to the collisions between hot electrons and the crystalline lattice. None of these processes change the concentration of charge carriers, but both are inefficient, the dominant scattering mechanism being the collision between charge carriers and impurities.

The generation and detection of THz signals comprises several steps: (i) the photoconductive switch is illuminated by a fs laser, (ii) the THz signal is confined within a metal waveguide, and (iii) the interaction between the THz signal and crystalline materials results in absorption at certain resonant frequencies sensed by the second photoconductive switch. The transmitting and the receiving graphene switches are integrated on the same substrate with two planar Goubau waveguides, as depicted in Fig. 17.9.

Another method to generate THz signals is to use the strong nonlinear response in graphene. Third- and second-order optical nonlinearities were used for this aim. Second-order nonlinearities, encompassing difference-frequency and rectification processes, are stronger, but forbidden due to the centrosymmetry of graphene. Thus, an asymmetry is needed to use these strong nonlinearities and this asymmetry is introduced by photoexcitation with femtosecond laser pulses, and linked to in-plane photon wavenumbers. For example, a tilted incidence (e.g. at angles in the □ = 20°–25° range) at the energy $\hbar\omega \gg 2E_F$ introduces the demanded anisotropy.

As it shown in Fig. 17.10 [32], THz generation is produced by the photon drag effect, which implies transfer of light momentum to photogenerated carriers in

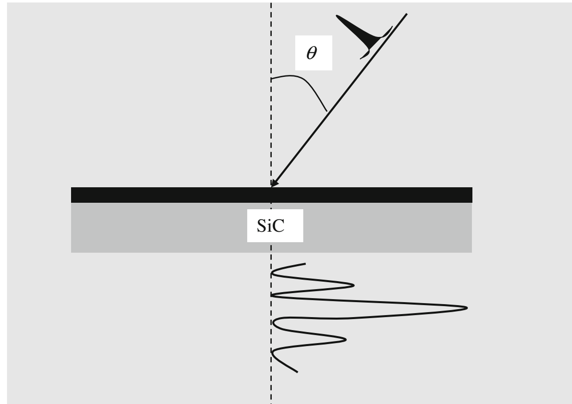

Fig. 17.10 The generation of THz pulses using second-order nonlinearities and the photon drag effect

multilayer graphene. The THz pulse is further transmitted through the SiC substrate and detected via electro-optic sampling.

Presently, THz lasers are designed and first experiments are undertaken to demonstrate that graphene is an amplifier medium for THz frequencies, with a maximum gain achieved so far of 8 cm^{-1} at 4 THz [33].

17.4 THz Detection Based on Graphene and Carbon Nanotubes

THz fields can be detected using graphene FETs with source and drain electrodes in the shape of various metallic antennas. The first experimental demonstration was the detection of a 0.3 THz signal at room temperature using a log-periodic circular-toothed antenna having the source electrode grounded and an outer radius of 322 μm. The channel length of the transistor was 10 μm. The detected signal at the drain contact is given by [34]:

$$\Delta V = (V_a^2/4)[1/\sigma(V_0)][d\sigma(V_g)/dV_g]\big|_{V_g=V_0} \tag{17.20}$$

where the gate voltage is written as $V_g(x,t) = V_0 + V_a \exp(-kx)\cos(\omega t - kx)$.

A bow-tie antenna was further used in the same configuration, i.e. a FET with a graphene channel and with source and drain electrodes in the shape of a bow-tie antenna. This time the channel length was 2.5 μm and the gate width was 2 μm. The THz signals were detected at 0.6 GHz with a noise-equivalent-power (NEP) of 500 $pW/Hz^{1/2}$ and a responsivity of 14 V/W [35]. In Fig. 17.11, we have schematically represented the bow-tie FET THz detector.

A simple logarithmic-periodic antenna, which has in the gap an interdigitated electrode consisting of 4 electrode pairs deposited over a graphene flake, is able also to detect THz radiation pulses (see Fig. 17.12). The THz detector has a rise time of

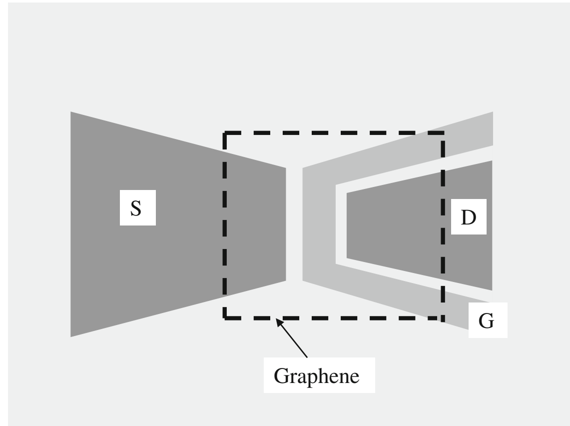

Fig. 17.11 Bow-tie antenna electrodes of a graphene FET for THz radiation

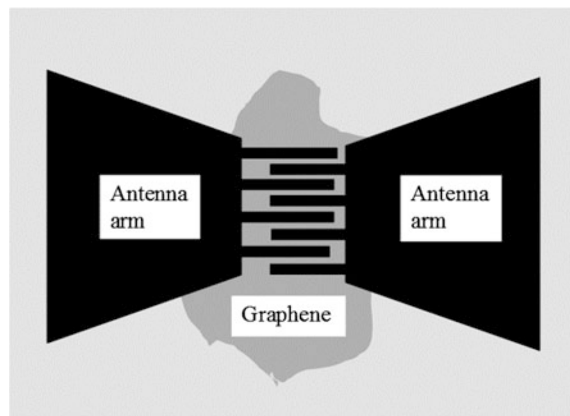

Fig. 17.12 Another graphene-based THz pulse detector

50 fs and is very simple, allowing the study of pulse shapes at the picosecond time scale [36].

Sensitive THz detection was demonstrated recently at room temperature with the help of the photothermoelectric effect in graphene [37]. The graphene has a significant interband absorption at THz. The carrier heat capacity in graphene is considerably reduced compared to bulk materials, implying that a larger temperature gradient is obtained for the same absorbed energy. This photothermoelectric effect has a picosecond time response and can be used for THz detection. Moreover, THz detection at room temperature is possible because the photothermoelectric effect is almost insensitive to temperature.

In experiments, two dissimilar metals distanced at 3 μm are used as electrodes for a graphene monolayer flake (see Fig. 17.13). The dissimilar metals consisting of overlapping regions of Cr and Au are obtained via consecutive and different angle evaporations of these metals. The carriers are heated by the incoming THz radiation, so that, if we consider the contacts as heat sinks, there is a temperature

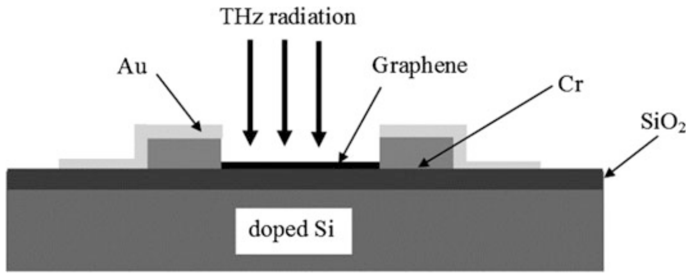

Fig. 17.13 Photothermoelectric THz detection

distribution $T(x)$ along the device. The diffusion of charge carriers produces a potential gradient

$$\nabla V(x) = -S\nabla T(x), \tag{17.21}$$

where S is the Seebeck coefficient of graphene, which is tunable by the backgate voltage and has a very large value [38]. The photodetector response is given by:

$$v = \int_0^L \nabla V(x)dx \tag{17.22}$$

This THz detector has a responsivity of 10 V/W (700 V/W) and a NEP of 1100 pWHz$^{-1/2}$ (20 pWHz$^{-1/2}$) when referring to the incident (absorbed) power.

A review of carbon nanotubes in THz was recently published [39], and the issues reported in this review will not be once again reviewed here. We note, however, that arrays of parallel CNTs were shown recently to behave as THz detectors with a responsivity of 2.5 V/W [40], and to produce THz radiation via optical excitations [41].

17.5 Conclusions

The results obtained in the last few years regarding THz devices based on carbon nanomaterials, and especially graphene, tell us that the famous THz gap will be closed soon by the further development of research in this 2D material. In particular, it is possible that THz graphene transistors that will be developed in few years based on room temperature ballistic transport in graphene will act as THz generators and mixers [42].

References

1. S. Iijima, Helical microtubules of graphitic carbon. Nature **354**, 56–58 (1991)
2. A.K. Geim, Graphene: status and prospects. Science **324**, 1530–1534 (2009)
3. D. Dragoman, M. Dragoman, Transport properties in carbon nanotube and graphene, in *Carbon Nanotubes and Graphene*, ed. by K. Tanaka, S. Iijima (Elsevier, Amsterdam 2014), pp. 151–165
4. F. Xia, H. Wang, D. Xiao, M. Dubey, A. Ramasubramaniam, Two-dimensional material nanophotonics. Nat. Photon. **8**, 899–907 (2014)
5. K.S. Novoselov, A.K. Geim, S.V. Morozov, D. Jiang, Y. Zhang, S.V. Dubonos, I.V. Grigorieva, A.A. Firsov, Electric field effect in atomically thin carbon films. Science **306**, 666–669 (2004)
6. A. Zurutuza, C. Marinelli, Challenges and opportunities in graphene commercialization. Nat. Nanotechnol. **9**, 730–734 (2014)
7. A.K. Geim, nobel lecture: random walk to graphene. Rev. Mod. Phys. **83**, 851–862 (2011)
8. A.V. Butenko, Dm. Shvarts, V. Sandomirsky, Y. Schlesinger, R. Rosenbaum, Hall constant in quantum-sized semimetal Bi films: Electric field effect influence. J. Appl. Phys. **88**, 2634–2640 (2000)
9. C.H. Ahn, A. Bhattacharya, M. Di Ventra, J.N. Eckstein, C.D. Frisbie, M.E. Gershenson, A. M. Goldman, I.H. Inoue, J. Mannhart, A.J. Millis, A.F. Morpurgo, D. Natelson, J.-M. Triscone, Electrostatic modification of novel materialsRev. Mod. Phys. **78**, 1185–1212 (2006)
10. M. Dragoman, G. Konstantinidis, K. Tsagaraki, T. Kostopoulos, D. Dragoman, D. Neculoiu, Graphene-like metal-on-silicon field-effect transistor. Nanotechnology **23**, 305201 (2012)
11. J. Renteria, R. Samnakay, C. Jiang, T.R. Pope, P. Goli, Z. Yan, D. Wickramaratne, T.T. Salguero, A.G. Khitun, R.K. Lake, A.A. Balandin, All-metallic electrically gated 2H-$TaSe_2$ thin-film and logic circuits. J. Appl. Phys. **115**, 034305 (2014)
12. S.P. Koenig, R.A. Doganov, H. Schmidt, A.H. Castro Neto, B. Özyilmaz, Electric field effect in ultrathin black phosphorus. Appl. Phys. Lett. **104**, 103106 (2014)
13. P.A. Merolla, J.V. Arthur, R. Alvarez-Icaza, A.S. Cassidy, J. Sawada, F. Akopyan, B.L. Jackson, N. Imam, C. Guo, Y. Nakamura, B. Brezzo, I. Vo, S.K. Esser, R. Appuswamy, B. Taba, A. Amir, M.D. Flickner, W.P. Risk, R.M.D.S. Modha, A million spiking-neuron integrated circuit with a scalable communication network and interface. Science **345,** 668–673 (2014)
14. S.-J. Han, A. Valdes Garcia, S. Oida, K.A. Jenkins, W. Haensch, Graphene radio frequency receiver integrated circuits. Nat. Comm. **3086** (2014)
15. A. Eatemadi, H. Daraee, H. Karimkhanloo, M. Kouhi, N. Zarghami, A. Akbarzadeh, M. Abasi, Y. Hanifehpourand, S.W. Joo, Carbon nanotubes: properties, synthesis, purification, and medical applications. Nano Res. Lett. **9**, 2–13 (2014)
16. M. Dragoman, D. Dragoman, *Nanoelectronics: Principles and Devices*, 2nd edn. (Artech House, Boston, 2009)
17. D. Dragoman, M. Dragoman, *Bionanoelectronics* (Springer, Heidelberg, 2012)
18. Y. Che, H. Chen, H. Gui, J. Liu, B. Liu, C. Zhou, Review of carbon nanotube nanoelectronics and macroelectronics. Semicond. Sci. Technol. **29**, 073001 (2014)
19. M.M. Shulaker, G. Hills, N. Patil, H. Wei, H.-Y. Chen, H.-S.P. Wong, S. Mitra, Carbon nanotube computer. Nature **501**, 526–530 (2013)
20. S. Chuang, Q. Gao, R. Kapadia, A.C. Ford, J. Guo, A. Javey, Ballistic InAs nanowire transistors. Nano Lett. **12**, 555–558 (2012)
21. A.M. Gilbertson, A. Kormanyos, P.D. Buckle, M. Fearn, T. Ashley, C.J. Lambert, S.A. Solin, L.F. Cohen, Room temperature ballistic transport in InSb quantum well nanodevices. Appl. Phys. Lett. **99**, 242101 (2011)
22. C. Neto, A.H.F. Guinea, N.M.R. Peres, K.S. Novoselov, A.K. Geim, The electronic properties of graphene. Rev. Mod. Phys. **81**, 109–162 (2009)

23. S. Adam, E.H. Hwang, V.M. Galitski, S. Das Sharma, A self-consistent theory of graphene transport, PNAS **104**, 18392–18395 (2007)
24. M. Dragoman, A.A. Muller, D. Dragoman, F. Coccetti, R. Plana, Terahertz antenna based on graphene. J. Appl. Phys. **107**, 104313 (2010)
25. M. Dragoman, M. Aldrigo, A. Dinescu, D. Dragoman, A. Costanzo, Towards a terahertz direct receiver based on graphene up to 10 THz. J. Appl. Phys. **115**, 044307 (2014)
26. H. Mosallaei, K. Sarabandi, Antenna miniaturization and bandwidth enhancement using a reactive impedance substrate. IEEE Trans. Antennas and Propag. **52**, 2403–2414 (2004)
27. M. Tamagnone, J.S.G. Diaz, J.R. Mosig, J. Perruisseau-Carrrier, Analysis and design of terahertz antennas based plasmonic resonant graphene sheets. J. Appl. Phys. **112**, 114915 (2012)
28. M. Dragoman, D. Dragoman, Plasmonics: applications to nanoscale terahertz and optical devices. Prog. Quant. Electron. **32**, 1–41 (2008)
29. P.W. Liu, W. Cai, L. Wang, X. Zhang, J. Xu, Tunablbe teraherz antennas based on graphene ring structures. Appl. Phys. Lett. **100**, 153111 (2012)
30. W. Zhou, J. Lee, J. Nanda, S.T. Pantelides, S.J. Pennycook, J.-C. Idrob, Atomically localized plasmon enhancement in monolayer graphene. Nat. Nanotechnol. **7**, 161–165 (2012)
31. N. Hunter, A.S. Mayorov, C.D. Wood, C. Russell, L. Li, E.H. Linfield, A.G. David, J.E. Cunningham, On-chip picosecond pulse detection and generation using graphene photoconductive switches. Nano Lett. **15**, 1591–1596 (2015)
32. J. Maysonnave, S. Huppert, F. Wang, S. Maero, C. Berger, W. van de Heer, T.B. Norris, L.A. de Vaulchier, S. Dhillon, J. Tignon, R. Ferreira, J. Mangeney, Terahertz generation by dynamical phonon drag effect in graphene excited by femtosecond optical pulses. Nano Lett. **14**, 5797–5802 (2014)
33. T. Otsuji, S.B. Tombet, A. Satou, M. Ryzhii, V. Ryzhii, Terahertz-wave generation using graphene: toward new types of terahertz lasers. IEEE J. Sel. Top. Quant. Electron. **19**, 8400209 (2013)
34. L. Vicarelli, M.S. Vitiello, D. Coquillat, A. Lombardo, A.C. Ferrari, W. Knap, M. Polini, V. Pellegrini, A. Tredicucci, Graphene field-effect transistors as room-temperature terahertz detectors. Nat. Mater. **11**, 865–871 (2012)
35. A. Zak, M.A. Andersson, M. Bauer, J. Matukas, A. Lisauskas, H.G. Roskos, J. Stake, Antenna-integrated 0.6 THz FET direct detectors based on CVD graphene. Nano Lett. **14**, 5834–5838 (2014)
36. M. Mittendorff, S. Winnerl, J. Kamann, J. Eroms, D. Weiss, H. Schneider, M. Helm, Ultrafast graphene-based broadband THz detector. Appl. Phys. Lett. **103**, 021113 (2013)
37. X. Cai, A.B. Sushkov, R.J. Suess, M.M. Jadidi, G.J. Jenkins, L.O. Nyakiti, R.L. Meyers-Ward, S. Li, J. Yan, D.K. Gaskill, T.E. Murphy, H.D. Drew, M.S. Fuhrer, Sensitive room-temperature terahertz detection via the photothermoelectric effect in graphene. Nat. Nanotechnol. **9**, 814–819 (2014)
38. D. Dragoman, M. Dragoman, Giant thermoelectric in graphene. Appl. Phys. Lett. **91**, 203116 (2007)
39. R.R. Hartmann, J. Kono, M.E. Portnoi, Terahertz science and btechnology of carbon nanomaterials. Nanotechnology **25**, 322001 (2014)
40. X. He, N. Fujimura, J.M. Lloyd, K.J. Erickson, A.A. Talin, Q. Zhang, W. Gao, Q. Jiang, Y. Kawano, R.H. Hauge, F. Leonard, J. Kono, Carbon nanotube terahertz detector. Nano Lett. **14**, 3953–3958 (2014)
41. L.V. Titova, C.L. Pint, Q. Zhang, R. Hauge, J. Kono, F.A. Hegmann, Generation of terahertz radiation by optical excitation of aligned carbon nanotubes, Nano Lett. **15** (2015) doi: 10.1021/acs.nanolett.5b00494
42. M. Dragoman, A. Dinescu, D. Dragoman, Negative differential resistance in graphene-based ballistic field-effect transistor with oblique top gate. Nanotechnology **25**, 415201 (2014)

Chapter 18
Abrasive Flow Machining

N. Ionescu, D. Ghiculesc, A. Visan and V. Avramescu

Abstract The chapter presents some elements related to Abrasive Flow Machining (AFM), specifically state of the art, elements of technological system, and construction of equipment as well as experimental results. The technological system comprises machine, tooling, working media, carrier, abrasive grains. This equipment could be the base for further researches in AFM field, comprising two opposed cylinders, which assures extrusion with semisolid abrasive media back and forth through the work piece or through passages formed by the work piece and a fixture. By repeatedly extruding the media from one cylinder to the other, an abrasive action is produced as the media enter a restrictive passage and travel through or across the work piece. In this way, the work piece can be nanofinished under Ra = 0.1 μm.

18.1 Introduction

Within the concerns aiming at developing the non-traditional technologies, a highly efficient ecological procedure emergent nowadays is **A**brasive **F**low **M**achining (AFM), as it is known in the speciality literature [1].

Abrasive Flow Machining finishes surfaces and edges by extruding viscous abrasive media through or across the workpiece. This procedure uses a rheopectical work media having as fundamental feature the increasing of viscosity upon the action of compression forces. Abrasion occurs only where the flow of the media is restricted; other areas remain unaffected. The effect of this nonconventional mechanical machining occurs at nanometer scale, obtaining surface roughness under Ra = 100 nm.

N. Ionescu (✉) · D. Ghiculesc · A. Visan
University Politehnica of Bucharest, Bucharest, Romania
e-mail: ionescu_upb@yahoo.com

V. Avramescu
SC ICTCM SA - Mechanical Engineering and Research Institute, Bucharest, Romania

© Springer International Publishing Switzerland 2016

I. Tiginyanu et al. (eds.), *Nanostructures and Thin Films for Multifunctional Applications*, NanoScience and Technology,
DOI 10.1007/978-3-319-30198-3_18

The studies regarding the abrasive flow machining [2–5] showed that through this finishing procedure it is possible to accomplish operations such polishing, trimming and edge rounding for workpieces within a very wide dimension range, performed in places with difficult access. Using this procedure we can polish orifices of over 0.15 mm, diameter, cavities and complex surfaces in a wide domain of dimensions. A variety of finishing results can be achieved by altering the process parameters. The process can yield production rates of up to hundreds or even thousands of parts per hour.

Since the year 2000, the authors have been developing their own research, which they would publish in several scientific works [2, 6–10]. This chapter presents an original complex abrasive flow machining equipment that was designed by the authors and produced in ICTCM SA of Bucharest. The importance of this work resides in the fact that the implementation of this equipment will allow for, both the industrial application of this technology, and the continuation of AFM research.

18.2 Elements of Technological System at Abrasive Flow Machining

The major elements of an AFM system include the machine, the tooling, and the abrasive media [4].

Machines for abrasive flow machining are available with extrusion pressure ranging from 700 to 22000 kPa with flow rates up to 380 l/min. Control systems can be added to monitor and control additional process parameters, such as temperature, viscosity, wear, and flow speed of the media. AFM system designed for production applications often include part-cleaning and unload/reload stations as well as media maintenance and cooling units. Automated systems can process thousands of parts per day, with processing times typically ranging between 1 and 3 min for each pallet loaded with workpieces.

Tooling holds workpiece in position and directs the abrasive media to the appropriate areas, restricts flow at areas where abrasion is desired and can block flow areas that are to remain unaffected.

The media consist of a pliable polymer carrier and a concentration of abrasive grains. The viscosity of the carrier and the type, concentration, and size of the abrasive grains can be varied to achieve specific results. Higher-viscosity media are nearly solid and are used for uniform polishing or for abrading the walls of large passages. Lower-viscosity media are generally appropriate for radiusing edges and for processing small passages [2].

The carrier is a mixture of a rubberlike polymer and lubricating fluid. By varying the ratio of the polymer and the lubricating fluid, the carrier can have viscosity ranging continuously from very high to very low. One of the solutions used to obtain it is the following [5]: a polymer formed from 22.5 kg of a dimethyl silicone oil, 0.225 kg of $FeCl_3 6H_2O$ (Lewis acid catalyst) and 1.35 kg of pyroboric acid by reaction at a temperature of 200–250 °C with agitation to form a highly

viscous boron-organo silicon heteropolymer. This is reacted with 0.65 kg of NH_4CO_3 to neutralise any acid residue. The resulting material is somewhat brittle, stiff and crumbly. A gel is formed by adding 1.7 kg of aluminium stearate to 20 kg of hydrocarbon at room temperature with stirring. The mixture is then heated to the gelation temperature of 194 °F heated further to 240 °F and held at that temperature for 15 min to form a relatively thick gel. Nine kg of the polymer is mixed with 28 kg of the gel at a temperature of 215 °F. After thorough mixing, the mixture is cooled and kneaded until it becomes homogenous.

The abrasive grains used in AFM are most commonly made of silicon carbide, although boron carbide, aluminium oxide, and diamond can also be used. Particle sizes range from 0.005 to 1.5 mm. The better the starting finish, the smaller the grit sizes used for processing. The larger abrasive cut at a faster rate, while the smaller sizes provide finer finishes and accessibility to small holes. The depth of cut made by the abrasive grains at the surface depends on the sharpness and size of the abrasive grains, the extrusion pressure applied, and the stiffness of the media [6, 11].

18.3 Conceptual Design of the AFM Equipment

Depending on the application, there are several possible alternative solutions of AFM: the AFM process using two opposed cylinders, the orbital movement AFM, the AFM process using one cylinder [4] and the AFM-Sontex Process. Considering the AFM concept, the equipment designed by the authors is based on the AFM technique with two opposed cylinders and a fixture.

This conceptual solution presented in Fig. 18.1 uses two opposed cylinders to extrude semisolid abrasive media back and forth through the passages formed by the workpiece and the tooling [1].

By repeatedly extruding the media from one cylinder to the other, an abrasive action is produced as the media enter a restrictive passage and travel through or across the workpiece. The machining action is similar to a grinding or lapping operation as the abrasive media gently polishes the surfaces or edges. When forced into a restrictive passage, the polymer carrier in the media temporarily increases in viscosity. This holds the abrasive grains rigidly in place. They abrade the passages only when the matrix is in this thicker viscous state. The viscosity returns to normal when the thickened portion of media exits the restrictive passage.

The viscosity and the flow rate of the media affect the uniformity of stock removal and the edge radius size. If the objective of the flow machining involves the uniform polishing of walls within the restricted passages, as in the die polishing, for example, the media chosen should maintain a uniform flow rate as in travels through the passage (Fig. 18.2a). Low flow rates are best for uniform material removal. For deburring or radiusing the edge of a passage, the higher flow rate of lower viscosity media within the passage causes the edges to be abraded more than the passage walls (Fig. 18.2b).

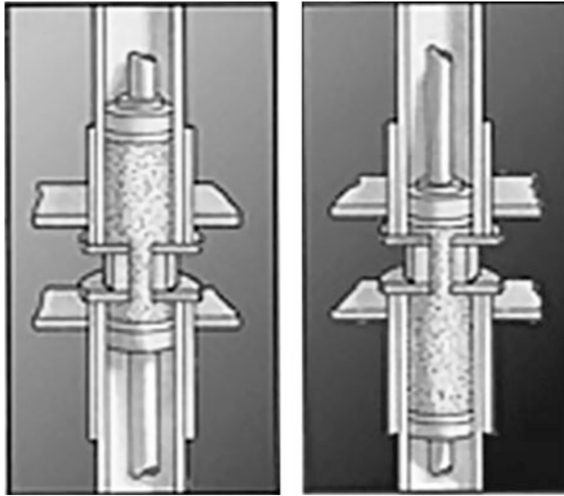

Fig. 18.1 AFM technique using two opposed cylinders (Rhoades [1])

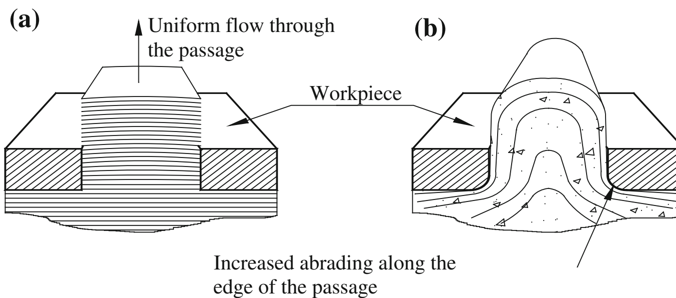

Fig. 18.2 Schematic showing of uniform flow through the passage (a) and the flow pattern of media entering a passage, which generates the machining action used for deburring and radiusing (b)

The flow rate depends on the machine settings, the formulation of the media and the workpiece and tooling configuration.

Considering the conceptual behaviour, the AFM system includes in principle the machine, the tooling, and the abrasive media. **Tooling** holds workpiece in position and directs the abrasive media to the appropriate areas, restricts flow at areas where abrasion is desired and can block flow areas that are to remain unaffected. Between the two cylinders, parts can be positioned, oriented and fixed in view of their machining with or without tooling. **The media** consists of a pliable polymer carrier and a concentration of abrasive grains. The viscosity of the carrier and the type, concentration, and size of the abrasive grains can be varied to achieve specific results. Higher-viscosity media are nearly solid and are used for uniform polishing

or for abrading the walls of large passages. Lower-viscosity media are generally appropriate for radiusing edges and for processing small passages. **The carrier** is a mixture of a rubberlike polymer and lubricating fluid. By varying the ratio of the polymer and the lubricating fluid, the carrier can have viscosity ranging continuously from very high to very low. The abrasive grains used in AFM are most commonly made of silicon carbide, although boron carbide, aluminium oxide, and diamond can also be used, particle sizes depending on desired surface roughness and machining rate to be obtained. The finer the starting surface, the smaller the grit size used for processing. The large size grit provides a faster processing rate, while the smaller sizes provide finer finishes and accessibility to small orifices. The depth of cut made by the abrasive grains at the surface depends on the sharpness and size of the abrasive grains, the extrusion pressure applied, and the stiffness of the media.

The media production is a distinct topic that the authors focused on in collaboration with chemistry professionals, the results being disseminated in a series of works [7–10].

18.4 Detailed Design of the AFM Equipment

The equipment designed by the authors takes over the movement from an outer source (press, planing machine, or other independent mechanism specially designed for this equipment), through the two traverse devices located at the end of rods. Once the movement reaches the two traverse devices, it is conveyed on to the first cylinder through the piston rod and at the same time to the rod of the second cylinder by means of the two exterior actuating rods. The movement from the two pistons rods reaches into the cylinders, where pressure is produced on the working media forcing the latter to pass through the machined part orifices, with the part being placed between the two cylinders. Upon entry into narrow spaces to be processed, the media viscosity increases, and the abrasive particles through interlocking provide the processing of part walls. The two pistons travel simultaneously back and forth. When one piston reaches its maximum travel, the media has passed through the part into the second cylinder and this cylinder piston has reached its minimum travel. This back and forth piston travel sets the medium moving from one position to the other, and performs a processing cycle with the final result being obtained at the end of repeating this cycle several times.

Figure 18.3 shows a general view of the AFM processing equipment and Fig. 18.4, a longitudinal section view through this equipment both in first version.

This equipment was designed by aid of CATIA V5R16 software. To have the assembly design, each element has been designed in turn, according to part class algorithm. The component items of the equipment are as follows: chassis, cylinders, guiding elements, the actuating and supporting rods and the transverse items.

The chassis is the basic structure of the entire assembly. Several manufacturing methods and processes have been considered for the chassis production, such as casting, plastic deformation and welding. Therefore, the chassis (Fig. 18.5),

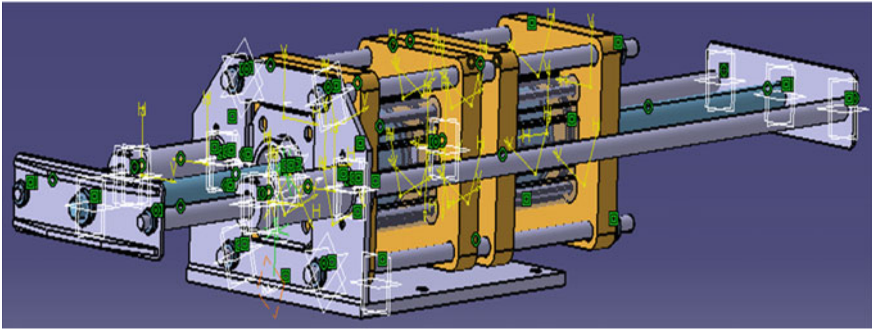

Fig. 18.3 AFM processing equipment

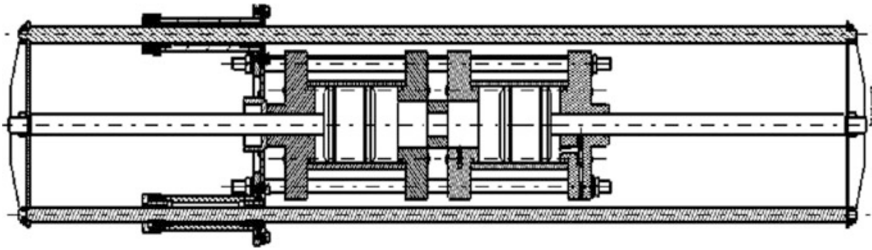

Fig. 18.4 Longitudinal section through the AFM processing equipment

Fig. 18.5 Equipment chassis

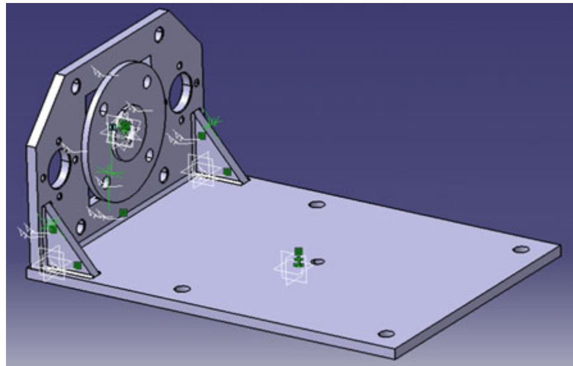

produced in welded construction, comprises two steel plates, 12 mm thick and one flange that allows for cylinder fixing.

The chassis plate is provided with holes that allow for the fixing of equipment and other devices on the machine (Fig. 18.6).

We applied the Finite Element Analysis (Fig. 18.7) to determine the chassis behaviour of the AFM equipment in operation and observe the high stress zones, as

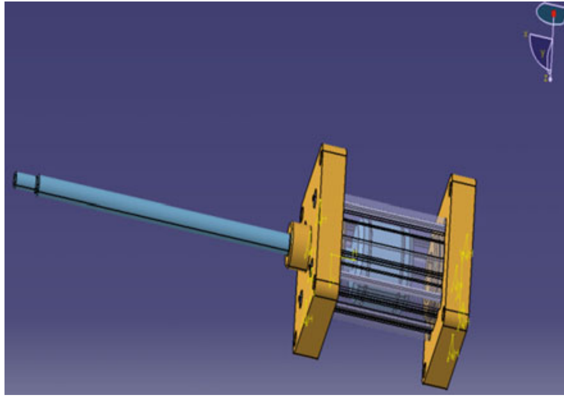

Fig. 18.6 Cylinder

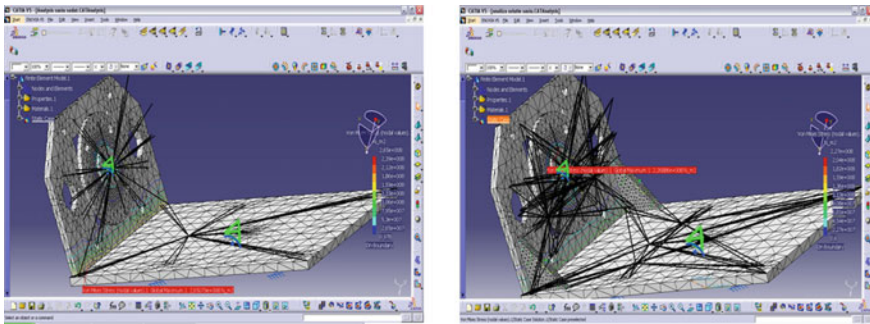

Fig. 18.7 Finite element analysis

well as any low fatigue resistance spots. Several constructive solutions were examined (cast construction, welded construction, different alternative placement of the ribs, etc.), as well as the chassis behaviour under several static loads, at specified stress.

Cylinders presented in Fig. 18.6 are the principal elements of the AFM equipment, performing the extrusion of a semisolid abrasive media through the machined part orifices. The machined part is placed between the two cylinders; the transfer of abrasive media occurs into the part orifice through the inferior flange bore of the first cylinder, then passing through the second cylinder bore gets inside the second cylinder. The abrasive media feeding is provided through the feeding orifice of either the first, or the second cylinder; the abrasive media is discharged through a similar orifice, or by part removal. Either standard cylinders, market cylinders, or cylinders produced according to user requirements can be used, function of operating regimes.

We used Mebis cylinders for the design equipment 1.11-12-63-50. Due to the abrasive media properties, as well as the presence of abrasive particles, the cylinders are subject to inevitable wear leading to equipment output depreciation.

These phenomena will make the object of other detailed individual assessment study, to determine the sealing devices material and cylinder corpus that are susceptible to operate with optimum results.

The guiding elements, the actuating rods and supporting rods are component elements with simple geometry that allow simultaneously actuating and correlating the two cylinders.

The traverse devices are the connecting elements between the actuating rods and the cylinder piston rods. Made of highly resistant materials, with two rigid fixing fins, these transverse devices behave as an interface between the above mentioned elements.

The other equipment for nanofinoshing, by abrasive flow, which is designed by the authors, is a specialised machine—tool, which is intended for nanofinishing the parts with small and complex surfaces. The piece is fixed in a work device, which is specific for each individual part type. The surfaces processing is performed by AFM process with two opposite cylinders and a fixture. The schematic representation of the equipment is shown in Fig. 18.8.

The main components of this equipment are: the frame, the inferior work cylinder, the work blade, the work superior cylinder, the vertical beam, the work head, the control panel and the work device.

The frame is a welded construction with a ribbed structure comprising the electrical and pneumatic installation. There are mounted the tank of the work blade

Fig. 18.8 The schematic presentation of the AFM equipment

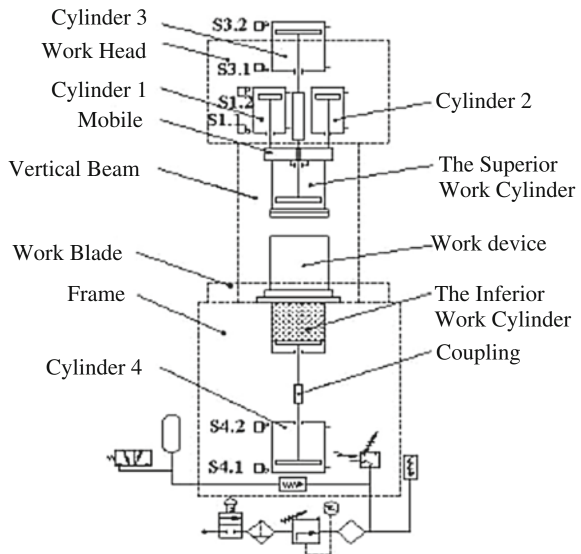

at its upper part of the construction and the control panel on the lateral side of construction.

The inferior work cylinder is fixed inside the frame supported on the work blade plate. This is a work cylinder as it contains the rheopectic abrasive work media and under the action of the pneumatic cylinder 4, entrains the media through the part to the superior work cylinder.

The work blade permits mounting the machined part with or without special orientation device of the media and it provides the real machining area. When a bore is polished, the part can be mounted between the two cylinders without special device. If polishing of exterior surfaces is intended, it is necessary to use a special device that allows the orienting of the media onto these surfaces. The work blade comprises a catch pit provided at the bottom with an electro-insulating plate fixed onto the inferior table of this equipment.

The superior work cylinder has a diameter of 200 mm and the stroke of 125 mm. It is mounted on the superior work table and it is actuated by the pneumatic cylinder 3. Its role is to receive the media from the inferior work cylinder through part and redirect it back to cylinder through part, by several work cycles.

The vertical beam assures the connection between frame and work head and it is a welded construction with a ribbed structure, so that it would provide adequate rigidity of AFM equipment.

The work head is a rigid welded construction, fixed on a vertical beam. It contains the pneumatic cylinder 3 that actuates the superior work cylinder rod, as well as the actuating pneumatic cylinders 1 and 2, with the diameter of 125 mm and travel of 125 mm, which actuates the lowering into work position of the mobile table together with the superior work cylinder. On the superior table, a control rod is mounted, which actuates the micro-switch cams, to perform the up and down work cycles.

The superior work table is in fact a set of three plates: device fixing plate provided with T channels, electro-insulating plate and connecting plate on which 1 and 2 pneumatic cylinder rods, the support columns and the control rod are mounted.

The work device is put inside of the work blade, on the inferior table of the machine. Its role is for positioning, orienting and fixing the piece and also for directing the abrasive fluid to the areas which are to be processed, thus providing the work interstice in the processed areas, so the other surfaces of the part remain unprocessed.

The control panel enables switch on and off the AFM equipment, as well as the operation in two working regimes, manual and automatic.

The main technological and functional characteristics of the equipment for AFM are presented in Table 18.1.

Based on these constructive solutions, the authors have designed produced and homologated a complex high output AFM equipment (Fig. 18.9), with wide machining application range, operating independently [12].

Table 18.1 The main characteristics of the AFM equipment

The work pressure for pneumatic cylinders	>5 bar
The cylinder work head diameter	125 mm
Cylinders diameter for processing	200 mm
The work cylinders diameter	200 mm
The stroke of all cylinders	125 mm
The capacity of the work cylinders	5 L
The rheopectic work average output	60 l/min
The viscosity of work medium	10–12 Poise
The size of the abrasive particles	0,005–1,5 mm
Abrasive material	SiC, Al_2O_3, diamond
The adjustment coverage of the work medium temperature	30–40 °C
The high size of the processed parts (ϕ x H)	200 × 120 mm
The number of work cylinders cycles	20–40 cycles/min
The productivity	10–150 pcs/h
The overall dimension of the device ($L \times l \times H$)	1020 × 840 × 2930 mm
The net mass of the device	1430 kg

The operation cycle of AFM equipment is detailed below. At the beginning of the processing cycles, the superior work table is raised in order to insert the piece in the device. The pneumatic cylinders 1 and 2, which actuate the work table, have their rods retired in order to act the micro switch S1.2 (see Fig. 18.8). The pneumatic cylinder 3 which actuates the superior work cylinder has also its rod retired in order to actuate the micro switch S3.2. The inferior work cylinder, which is placed under the fixed inferior table, where there is the work device, has its rod retired. The rod of the pneumatic cylinder 4 is also retired by means of micro switch S4.1. After the part was introduced in the device, this will be closed by lowering the superior work table. For this, there will be actuated the pneumatic cylinders 1 and 2 and their rods are let down till the micro switch S1.1 is actuated. At the same time, the rod of the cylinder 3 is let down to actuate the micro switch S3.1. In this way the piston of the superior work cylinder is standing down but also is letting down with the table in the same time. After the device is closed, the processing cycles can start. In order that the rheopectic fluid ascends from the inferior work cylinder into the superior cylinder through the processed part, the rod of the cylinder 4 ascends till the micro switch S4.2 is actuated, at the same time with the rod of the cylinder 3 ascending, till the micro switch S3.2 is actuated. The reverse circulation of the work fluid is made by descending the rod of the cylinder 3 till the micro switch S3.1 is actuated, in the same time with the descending of the cylinder 4 rod, till the micro switch S4.1 is actuated. At the end of the work cycles, the rheopectic fluid should be inside of the inferior work cylinder; in this moment it can open the work device by ascending the superior work table. Therefore there is given the command for the ascending of the 1 and 2 cylinders rods from the work head till the micro switch S1.2 is actuated. At the same time, the 3 cylinder rod ascends till the micro switch S3.2 is actuated.

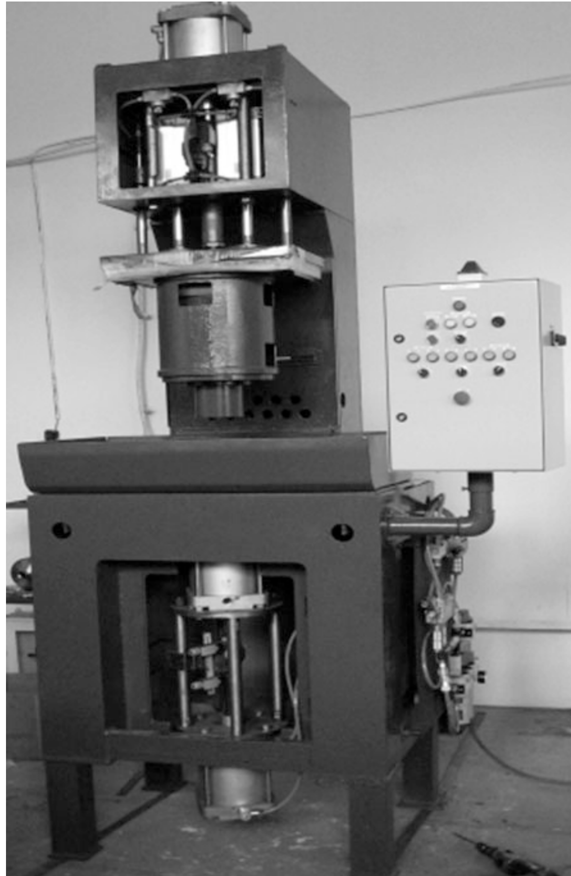

Fig. 18.9 General view of AFM equipment

18.5 Experimental Results

In the frame of this work a main aim is the obtaining the suitable fluids using ecological, safe and efficient materials.

Abrasive fluids (AF) materials

Keeping these criteria we used the following chemicals and materials.

Fluid component

O—oleine contain mainly oleic acid with formula: $\mathbf{CH_3(CH_2)_7CH{=}CH(CH_2)COOH}$;

ODT—diethanolamide of oleic acid containning about 20 % **TEA**—**triethanolamine** $N(C_2H_5OH)_3$ with **OD**—amide, resulting from reaction of condensation of **D-dietanholamine** $\mathbf{HN(C_2H_5)_2}$ with oleic acid, with water elimination as follows:

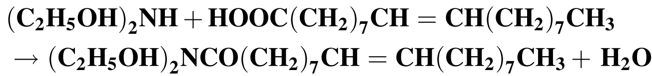

$$(C_2H_5OH)_2NH + HOOC(CH_2)_7CH = CH(CH_2)_7CH_3 \rightarrow (C_2H_5OH)_2NCO(CH_2)_7CH = CH(CH_2)_7CH_3 + H_2O$$

The **ODT** product imparts many useful properties for **AF** fluid like increasing viscosity, emulsifying corrosion inhibition and lubrificating.

O-PPG and **O-MPG** are two esters of acid oleic **o** with polypropylene glycol **PPG** short chain polymer of **mpg** mono propylene glycol of formula:

CH_3-CHOH-CH_2OH.

H_2O—water in some circumstances is an useful additive to enhance the viscosity and reopecticity of the fluid.

Beside of those main components can used also be used other minor additives [6, 11].

Abrasive materials

Abrasive materials used in these preliminary samples of **AF** are for the beginning only three:

(1) **Alumina**, aluminium oxide **Al_2O_3**, fine power grains of 3–70 μm;
(2) **Silicone carbide SiC**, fine power grains of 6–63 μm;
(3) **Silica,** silicium dioxide **SiO_2**, fine power grains of 48 μm;

The hardness values of abrasive powders used are very high in the Mohs scale:

Al_2O_3—9, SiC—9 and **SiO_2—9.**

The highest value in this scale is the hardness 10 for the diamond. In the next extended research we intend also to use other abrasive materials in order to increase the value of the nanofinishing work.

The results obtained are discussed underneath.

Composition of AF samples

Using the chemicals and materials presented above we tried to obtain several abrasive fluids for AFM method.

The mixtures of those components in different ratios, is obtained under high stirring.

The effect of great interest is the reopecticity of the resulted viscous **AF** fluid.

The reopecticity is crucial for nanofinishing, because it means the increase of viscosity of the fluid under mechanical force; the abrasive grains abrade only in this viscous state where they hold rigidly in place.

The viscosity of the fluid returns to initial state when it exits the restrictive passage.

The viscosity and the flow rate of the media affect the uniformity of stock removal and the edge radius size. If the objective of the flow machining involves the uniform polishing of walls within the restricted passages, as in the die polishing, for example, the media chosen should maintain a uniform flow rate as in travels through the passage.

The preliminary abrasive fluid obtained considering the above stated principles are presented the next two tables [11–14]. In Table 18.2, it was used as main component the carboxyamide **OD** with **TEA**—triethanolamine added **ODT.**

Table 18.2 Abrasive fluids (AF), on **ODT** base

Component n/Sample	ODTn (%)	O (%)	Abrasive m (%)	H_2On (%)	PPG (%)	η_i (poise)	Abrasive's nature
1a	25	25	10	40	–	~16	1:1 SiC/Silica
1a'	40	10	10	40	–	~25	1:1 SiC/Silica
1b	20	22	8	46	4	~14	1:1 Silica/Al_2O_3
1b'	20	24	8	46	2	~20	1:1 Silica/Al_2O_3
1c	40	30	10	–	20	~12	Al_2O_3
1c'	40	40	10	–	10	~16	Al_2O_3

Table 18.3 Abrasive fluids (AF), on **O-PPG** base

Component b/Sample	O-PPGv (%)	O (%)	Abrasive c (%)	H_2O (%)	TEA (%)	η_i (poise)	Abrasive's nature
2a	35	20	10	25	10	~12	1:1 SiC/Silica
2a'	35	30	10	15	10	~20	1:1 SiC/Silica
2b	30	20	10	30	10	~10	1:1 Silica/Al_2O_3
2b'	40	25	10	10	15	~25	1:1 Silica/Al_2O_3
2c	25	35	10	20	10	~10	Al_2O_3
2c'	30	35	10	15	10	~15	Al_2O_3

In the Table 18.3, main component the ester **O-PPG** was used.

The next samples of **AF** show a different composition because both main **ODT** components and **O-PPG** were used in all samples and only one abrasive; calcinated alumina with finest grain of 2.9–3.1 μm.

These samples are presented in the Table 18.4.

It must be noticed that the ester **O-MPG** (mono propylene glycol) is very similar with the previous **O-PPG** (polypropylene glycol) used in samples of Tables 18.2 and 18.3 and is easier to obtain at a reproducible chemical structure.

Some illustrative structures of abrasive media with reopectic characteristics obtained in the frame of our researches are presented underneath in Figs. 18.10, 18.11, 18.12, 18.13, 18.14 and 8.15, using Microscop NEOPHOT 32 and Scentis Image Analysis Modules:

Table 18.4 Abrasive fluids (AF), on ODT and MPG base

Component/ Sample	ODT (%)	O (%)	Alumina (%)	PPG (%)	O-MPG (%)	η_i (poise)
F1	30	30	5	10	25	15
F2	25	35	10	5	25	12
F3	25	45	5	–	25	10
F4	25	35	10	–	30	14

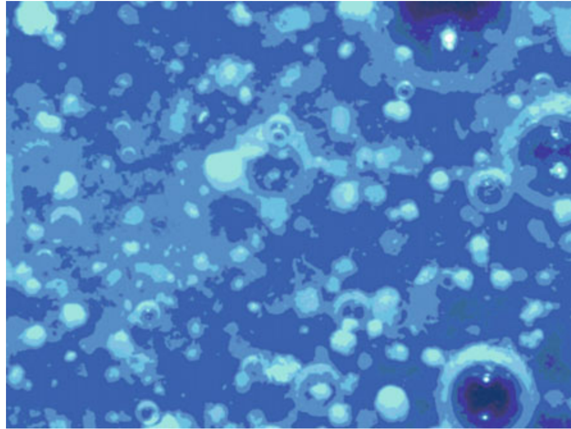

Fig. 18.10 Structure of abrasive media, sample AF 1b—magnitude × 50

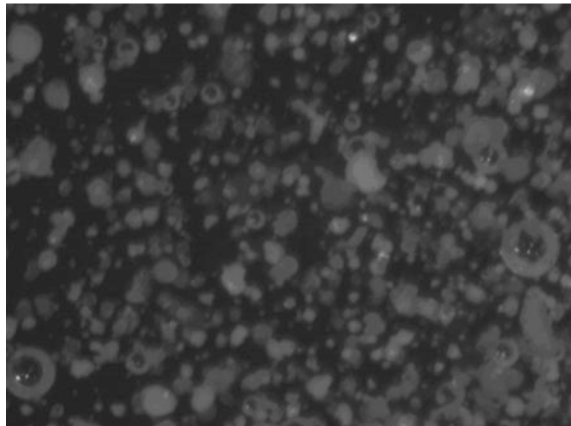

Fig. 18.11 Structure of abrasive media, sample AF 1c—magnitude × 50

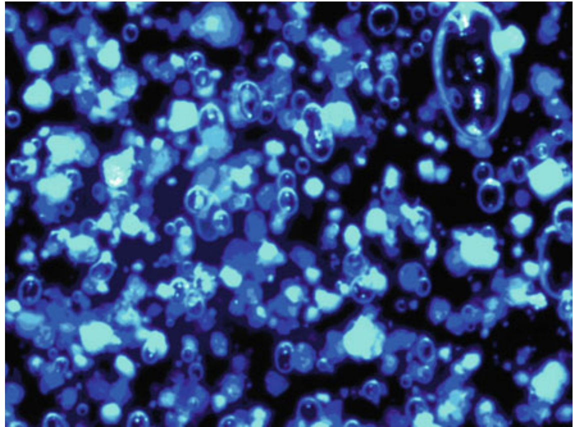

Fig. 18.12 Structure of abrasive media, sample AF 1c′—magnitude × 50

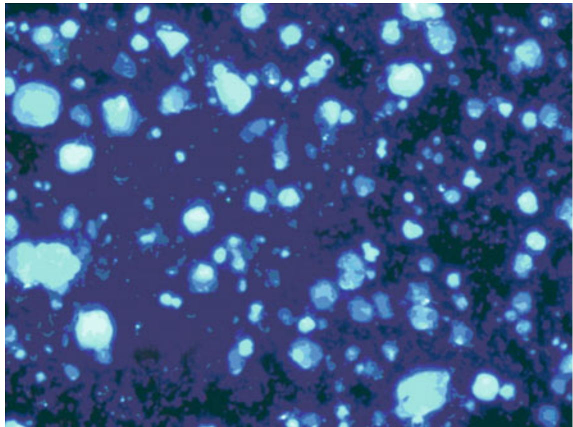

Fig. 18.13 Structure of abrasive media, sample AF 2b—magnitude × 50

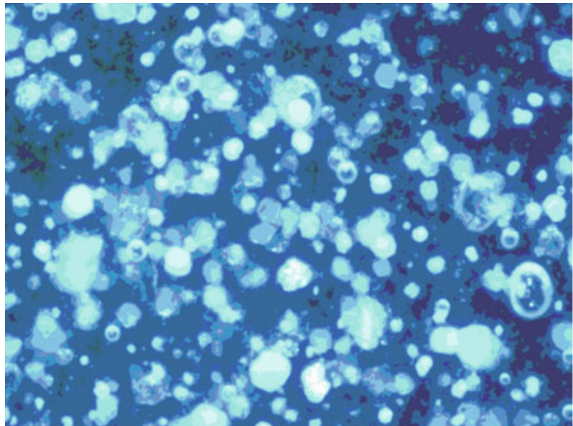

Fig. 18.14 Structure of abrasive media, sample AF 2b′—magnitude × 50

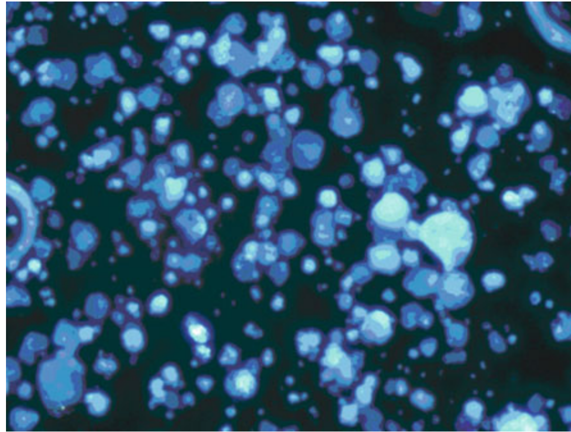

Fig. 18.15 Structure of abrasive media, sample AF 2c—magnitude × 50

Characteristic of abrasive fluids (AF)

Due to the complexity of **AF** samples their characterization is very difficult as well as the correlation of composition with efficiency in the nanofinishing [4].

In this preliminary work the main characteristics of the samples were determined as follows:

Stability and the homogeneity. The stability is good in time between several weeks to several months when the sample does not present the phases separation. After separation the sample returns at initial state. The homogeneity is good by visual observation but in the future a better microscopic analysis of structures will be correlated with the nanofinishing process and geometrical form of passage.

Viscosity is also difficult parameter to determine because, as it is was before explained it is variable during homogenisation due the reopecticity. The values given in the Tables 18.2, 18.3 and 18.4 for initial viscosity are only approximate.

Viscosity dependence with temperature is also very important, because it does be as small as possible. The most of samples are quite stable with the temperature increasing until 70 °C—when they became more fluid but after they return at initial values by decreasing temperature.

Reopecticity is the increase of fluid viscosity under mechanical pressure, it depends essentially of the mechanical parameters of the **AFM** machine and so can be evaluated quantitative during de nanofinishing process.

18.6 Conclusions

Based on the foregoing aspects, we may conclude the following:

1. World-wide the AFM procedure is much utilized for operations such as deburring, polishing and radiusing which find applications in aircraft, cars manufacture, dies and mould manufacture etc.;

2. In spite of the preliminary character of these results they reveal many possible formulations for the abrasive fluid compositions;
3. This will allow choosing the most suitable **AF** fluids for any specific application;
4. The base for the future development of **AFM** nanofinishing unconventional method is ensured by the abrasive fluids as they are here presented.
5. The original AFM equipment designed and produced by the authors permits nanofinishing a wide range of parts in manual or automatic regime;
6. The constructive principle solution used to produce this equipment is based on the placing of the part between two opposite cylinders; the rheopectic abrasive media is moved from one cylinder to another through the part in several work cycles.

References

1. L.J. Rhoades, Abrasive Flow Machining, *ASM Handbook, vol. 16.5 Machining* (ASM International Publ, Materials Park, 1995), pp. 514–519
2. N. Ionescu, A. Vişan, Ecological effects of the application of the abrasive flow machining procedure. Revista de Ecologie Industrială, Nr. **10–12**, pp. 88–91 (2000). ISSN 1224-3183
3. L.J. Rhoades, *Abrasive Flow Machining with an in situ viscous plastic medium* (USA Patent, No, 1990). 5125191
4. L.J. Rhoades, *Reversible Unidirectional Abrasive Flow Machining* (USA Patent, No, 1992). 5070652
5. W. Walch, Abrasive Flow Machining Apparatus and Method, *PCT Patent*, WO 03/035325 (1993)
6. N. Ionescu, A. Vişan, A. Dincă, Superfinisarea suprafeţelor prin curgere abrazivă folosind medii de lucru reopectice, in *Proceedings of the International Conference TEHNOMUS XI*, pp. 427—432, Suceava, May 2001. ISBN 937-9408-96-6
7. V. Avramescu, N. Ionescu, N.E. Avramescu, C. Dogariu, G. Orasanu, A. Visan, A Dimon, Researches regarding modellation and simulation of the nanofinishing process of the complex surfaces using abrasive flow with rheopectic work mediums, in *International Scientific Conference* Balttrib, 2007, Lituania, Kaunas, 22–23 Nov 2007
8. V. Avramescu, N.E. Avramescu, R. Grejdanescu, T.L. Păun, Aspects concerning the nanofinishing process of the complex surfaces by abrasive flowing using rheopectic mediums, in *Proceedings of International Conference WSEAS—CM'2008*, pp. 83–86, Cambridge, UK, 23–25 Feb 2008. ISBN 978-960-6766-38-1
9. V. Avramescu, G. Oraşanu, D. Bobe R. Grejdanescu, C. Orăşanu T.L. Păun, N.E. Avramescu, Technologies and equipments for complex surfaces nanofinishing by abrasive flowing with reopectic work mediums, in *Annals Of The Oradea University, Fascicle of Management and Technological Engineering*, vol VII (XVII), pp. 41–48 (2008)
10. V. Avramescu, R. Grejdanescu, C. Orăşanu, T.L. Păun, G. Orasanu, D. Bobe, N.E. Avramescu, Technologies and equipments for complex surfaces nanofinishing by abrasive flowing with rheopectic work mediums, in *Computational Engineering in Systems Applications, WSEAS International Conference*, pp. 98–103, Heraklion, Grece, 22–25 July 2008. ISBN 978-960-474-000-0
11. R. Grejdanescu, et al., Researches regarding modellation and simulation of the nanofinishing process of the complex surfaces using abrasive flow with rheopectic work mediums, in *International Scientific Conference Balttrib*, *2007,* Lituania, Kaunas, 22–23 Nov. 2007

12. A. Vişan, N. Ionescu, V. Avramescu G. Orasanu, Design and manufacturing an Abrasive Flow Machining Equipment, ModTech International Conference, Chişinău, Mai (2009)
13. R. Grejdanescu et al., Aspects concerning the nanofinishing process of the complex surfaces by abrasive flowing using rheopectic mediums, in *Proceedings of International Conference WSEAS—CM'2008,* pp. 83–86, Cambridge, UK, Feb 23–25 2008. ISBN 978-960-6766-38-1
14. R. Grejdanescu et al., Technologies and equipments for complex surfaces nanofinishing by abrasive flowing with rheopectic work mediums, in *Computational Engineering in Systems Applications, WSEAS International Conference,* pp. 98–103, Heraklion, Grece, 22–25 iulie 2008

Index

0–9
13–38 factor, 525
2.9–4.8 factor, 525
1D nanostructures, 485
3D structures, 92

A
A_2B_6 thin films, 144, 147, 182
Abrasive, 552
Abrasive flap, 458, 459
Abrasive jet, 457, 458, 470
Abrasive machining, 456
Abrasive media, 565
Absorbance, 341
Absorption, 128, 384, 397, 444
Absorption band, 392, 395, 403, 404, 410
Absorption coefficient, 383, 386, 388, 396, 397, 399–401, 408, 422
Absorption mechanism, 389
Absorption spectra, 386, 387, 399–401, 405
Absorption spectrum, 391, 398
Acceptor level, 420, 425, 427, 431, 433, 438, 440
Acoustic modes, 246, 256, 257
Acoustically-mismatched, 527
Activation energy, 122, 345
Active pit model, 18
Adherence, 86, 103
Adhesion to the surface, 481
Adhesives, 103
Adsorbed species, 12
Adsorbed water, 100
Adsorption, 97
Adsorption capacitance, 24
Affinity sensors, 30
AFM image, 356, 373
AIIIBVI, 400, 415
AIIBVI compounds, 346, 348, 395
AIIBVI semiconductors, 416
AIIIBVI semiconductors, 333, 390
Alternating current SECM, 33
Alumina porous structures, 477
Aluminum, 73
Amorphization, 48
Amorphous state, 44, 48, 56, 57, 69, 76
Anatase-like structure, 324
Anisotropic quasi-static direct ME effect, 218
Anisotropy, 335
Annealed, 162, 164, 168, 169, 172, 173, 178, 180
Annealing, 156, 159, 160, 169, 175, 177, 179
Anodic dissolution, 60, 76, 78
Anodic film, 17
Anodization, 477
Antiferromagnet, 308
Antiferromagnetic, 303, 306, 309, 310
Applications, 382
Ar^+ bombardment, 328
Atomic emission analysis, 342
Atomic force scanning electrochemical microscopy, 33
Austenite, 56
Automatic regime, 567

B
Ballistic transport, 535, 547
Band, 271
Bandgap, 101, 129, 275, 278, 285, 387, 388, 397, 403, 420
Beam splitters, 498
Bending modes, 198
Biomagnetics, 500
Biosensing, 501
Biosensors, 29
Blade, 559
Bode plot, 6
Bolt-nut, 102
Boundary, 519

© Springer International Publishing Switzerland 2016
I. Tiginyanu et al. (eds.), *Nanostructures and Thin Films for Multifunctional Applications*, NanoScience and Technology,
DOI 10.1007/978-3-319-30198-3

Boundary conditions, 514
Boundary-limited, 523
Bow-tie antenna, 545
Breaking assembly, 105
Bridgman–Stockbarger, 337
Brillouin zone, 513
BTE, 519
Bulk, 521
BvK, 512

C
Capacitive loop, 19
Capacitor, 6
Carbides, 92
Carbon, 96, 120
Carbon nanotubes, 533
Carrier density, 537
Carrier recombination, 422
Catalytic activity, 318
Cd vapor, 365–367, 402
CdS, 149, 151, 166
CdS thin film, 145, 150, 155, 183
CdTe, 146
CdTe thin film, 147, 149, 151, 166
Cementite, 56
Chalcogenides, 346
Characteristics, 124
Charge carrier, 343, 345, 406
Charge imbalance, 327
Charge transfer resistance, 9
Chemical composition, 87, 91
Chemical corrosion, 60, 77
Chemical etching, 483
Close spaced sublimation (CSS) method, 145, 147, 150, 151, 154–157, 158–160, 162, 163, 180, 181
Clusters, 95, 354, 357, 358, 369, 431
Coating capacitance, 26
Coercivity, 229
Cold electrode, 51
Cold electrode spots, 44, 51–54, 67, 70, 71, 78
Combined, 340
Compact, 95
Comparison, 130
Compensated semiconductor, 344
Composites, 354, 361–363, 370–373, 371, 402, 406, 424, 425, 429, 432, 433, 436–438, 441
Composite materials, 191, 193
Composition, 120
Concentration, 127
Conduction band, 280
Conductive nanotemplates, 478
Conductivity, 115, 120, 343, 537
Confinement, 507
Constant-phase element, 9
Constitutive equations, 199, 200, 218
Cooling, 120
Copper, 73
Core-level peaks, 321
Core-shell, 485
Corrosion rate, 108
Corrosion resistance, 108
Corrosion speed, 60, 61, 69, 76, 77, 79
Coupling coefficients, 229
Coupling constants, 218
Coupling parameter, 203
Covalent bonds, 347
Crystal cuts, 211
Crystal orientation, 212
Crystalline compound, 434
Crystallites, 119, 360, 365, 371, 373, 425, 428, 441, 442
Crystallographic characteristics, 336, 359
Crystals, 337
Cubic structure, 117
Current density, 408
Current-voltage characteristics, 125, 141
Curves, 135
Cutoff frequency, 535
Cutting, 448, 451–453, 456, 467
Cycles, 106
Cylinder, 553, 557

D
Deceleration, 517
Deep acceptor levels, 426
Deformations, 376
Degradation, 99
Dependence, 133
Depletion region, 494
Depth, 92
Detailed design, 555
Detectors, 278
Dielectric permittivity, 205, 207, 393
Diethanolamide, 561
Diffraction, 337, 349, 357, 360, 370
Diffractogram, 55, 57
Diffuse reflectance, 393
Diffusion, 85, 340
Diffusion coefficient, 51, 52, 54
Diffusion impedance, 10
Dilatational, 514
Diluted ferromagnet, 302
Dimensions, 376
Dipolar transitions, 323
Dirac points, 536
Direct exciton, 387
Direct ME effect, 205

Discharge circuit, 45, 46, 59, 61, 78
Dislocation density, 373
Dispersion, 131
Dispersionless, 515
Dissimilar metals, 546
Dissipation, 92
Dissolution of oxygen, 44, 48, 50
Distribution, 351
Donor–acceptor recombination, 442
Donor level, 427
Double-layer capacitance, 12
Durability, 86
Dynamic matrix, 512
Dynamometer, 87

E
EDAX, 120
EDX, 92
Effectiveness of inhibition, 28
Efficiency, 88
Elastic constants, 510
Elastic interaction, 193
Electric field, 90
Electric field effect, 534
Electrical conductivity, 345
Electrical discharge machining, 465, 467
Electrical erosion, 58, 71
Electrical properties, 342
Electrical resistance, 60, 61, 63, 72–74
Electrochemical deposition, 479
Electrochemical discharge machining, 467, 469
Electrochemical dissolution, 108
Electrochemical growth, 502
Electrochemical impedance method, 4
Electrochemical machining, 461–464
Electrodeposition, 481
Electrodeposition process, 485
Electro-erosion, 88
Electroless deposition, 480
Electroless plating, 481
Electrolyte, 108
Electromagnetic induction, 239, 247
Electromechanical (EM) resonance, 229, 231, 240, 241, 244, 248, 249, 254–256, 256, 258
Electromechanical coupling, 195
Electromechanical resonance, 197
Electronic transitions, 389
Elemental composition, 368
Emission mechanism, 420
Energies, 128
Energy levels, 123, 440
Energy spectra, 514
Envelope, 141
Enzymatic sensors, 29
Equipment, 553, 555, 561
Equipment chassis, 556
Equipment industry, 102
Equivalent circuit, 7
Escape depth, 321
Evaporation, 116
EXAFS, 320
Exchange, 268, 290, 291, 293
Exchange bias, 302, 303, 306–308, 310
Exchange coupling, 309
Exchange interaction, 268–270, 272, 274, 281, 283, 287, 290, 291, 293
Exciton, 386, 424
Exciton annihilation, 427
Exciton emission, 417
Exciton radius, 393
Excitonic absorption, 390, 392
Excitonic continuum, 391
Extensional length-resonance, 198
Extrinsic, 121
Extruding, 551

F
Faraday induction, 231, 237, 238
FCC, 510
Field-effect transistor, 534
Films, 115, 116
Flat lenses, 495
Fluids, 561
Focusing properties, 497
Fourier inversion, 319
Free path, 408
Friction, 86
Friction forces, 107
Fullerenes, 99, 100
Fundamental absorption, 399
Fundamental band, 391

G
Gallium oxide, 352
$GaPO_4$, 270
GaSe plates, 353
GaTe plates, 366
Gaussian curves, 436
Generator, 87
Glassy mass, 107
Good agreement, 130
Graphene, 533
Graphite, 89, 98
Graphite film, 85, 90
Grinding, 553
Growth of single crystals, 335
Growth direction, 371
Guiding elements, 558

H
H_2SO_4, 76
Hall effect, 343
Hardness, 85
Harmonic, 511
Heat, 507, 120
Heat treatment, 366, 370, 376, 432, 435
Helmholtz coil, 234–236, 239, 241
Heterojunctions, 318, 406, 408, 409
$Hg_{1-x}Mn_xTe$, 273, 275, 267, 268, 270, 271, 277, 279–281, 284
$Hg_{0.86}Mn_{0.14}Te$, 282
$Hg_{1-x-y}Cd_xMn_yTe$, 267, 272, 273, 279, 292
Holes concentration, 344
Hollow tubes, 482
Homogeneity, 566
Hybrid machining, 461, 468
Hysteresis loop, 302, 306, 307

I
Illumination, 134
Impurities, 438
Impurity band, 418, 432
Increases, 522
Inductor, 6
Infrared (IR), 267, 268, 295, 404
Inhomogeneities, 134
Inner resistance, 105
Interaction, 511
Interband conductivity, 539
Intercalant, 354
Intercalation, 334, 347, 348, 359, 360, 362, 368, 373, 376, 406, 432, 435
Interface, 368, 369, 384
Interface roughness, 526
Interference, 127
Interpenetrating networks, 493
Interplay, 522
Intrinsic, 121
Ionic, 14
Ion track membranes, 474
Ion track technology, 475
Ionization, 44, 47, 49
IR region, 340

K
Kinetic impedance, 10

L
Lamellar semiconductor, 416
Lamellar structure, 335
Laminate composites, 197
Laminate structures, 248
Lapping, 553
Large mean free, 535
Laser, 136
Lateral lobes, 540
Lattice parameter, 117
Layered semiconductors, 376, 382
Lead-free PE compounds, 195
Lead-free PE single-crystals, 219
Lead-free piezoelectrics, 210, 216
Lifetime, 134, 141
$LiNbO_3$, 201, 210, 215
Linear dispersion relation, 536
Liquid phase, 74
Local expansion of the anatase lattice, 329
Local structure, 323
Local surrounding, 329
Localization, 527
Lock-in amplifier, 230, 233, 234, 236, 237, 244, 260
Logarithmic-periodic antenna, 545
Long-range order, 325, 492
Long-wavelength, 524
Low dimensionality, 473
Luminescence, 431
Luminescence centers, 419
Luminescencent transitions, 421
Luminescent emission, 417
Luminescent recombination, 433

M
Machined surface, 45, 46, 48, 50–53, 58, 60, 63, 67, 70
Machinery, 102
Machining methods, 447, 448, 461, 470
Magnetic bias, 231
Magnetic field, 207
Magnetic moment, 306–308
Magnetization, 228
Magnetoelectric (ME) effect, 228
Magnetoelectric effect, 190
Magnetoelectric tri-layers, 210
Magnetostriction, 191, 193, 196, 218
Magnetron sputtering, 303, 304, 319
Mass transfer, 14
Material tensors, 209
Materials, 410
Matthiessen's rule, 519
Maxima, 127
ME charge coefficients, 218
ME coefficient, 215, 233, 235, 238, 250–254, 257–260
ME composite, 210, 231, 228, 242
ME coupling, 193, 209, 218, 228, 229, 238, 250, 251

ME effect, 230, 231, 234, 235, 237, 238, 242, 246, 248, 252, 261
ME voltage coefficient, 203, 204, 212, 218
Mean free path, 523, 534
Mechanical stability, 101
Mechanism, 126
Metal/semiconductor nanocomposited, 502
Metal films, 481
Metal nanotubes, 485
Metal waveguide, 544
Metallic state, 328
Metallized titania nanotubes, 497
Metallo-dielectric composites, 500
Metallo-semiconductor structures, 498
Metals/alloys electrodeposition, 12
Metglas, 197, 204, 209, 218, 251
Metglas alloy, 239, 246
Metglas composite, 240
Metglas/Piezocrystal/Metglas, 218
Micro-composite, 426
Microscope, 93
Miller indices, 118
Minima, 127
Mixed-metal nanotubes, 487
Mixed kinetics, 15
Mobility, 534
Modulated, 509
Molding glass forms, 106
Molecules, 373
Monoclinic, 325
Morphology, 87, 91, 349, 493
Mosaic blocks, 95
Mossbauer spectra, 56, 57
Mott-Schottky plots, 21
MS phase, 228, 240, 246, 248, 254, 259
Multi wall nanotubes, 101
Multiferroic, 190, 192, 228, 238, 242
Multiferroic compounds, 193
Multipart equivalent circuit, 19
Multisegmented metallic nanotubes, 487

N
NaCl, 76
Nanoasperities, 450, 457
Nanochannels, 486
Nanoclusters, 352
Nanocomposite, 377, 382, 410, 421, 439
Nanocrystallites, 430, 444
Nanocrystalline semiconductors, 348
Nanofabrication, 478, 482
Nanofinishing, 567
Nanometric cavities, 500
Nanoparticles, 429
Nano-oxidation, 44, 59
Nanophotonic devices, 497
Nanopores, 475
Nanoporous structure, 476
Nanoreliefs, 447, 449, 451, 452, 458, 461, 467, 470
Nanoscale materials, 474
Nanostructures, 354, 376
Nanotemplates, 474, 501
Nanotubes, 100, 476
Nanowires, 508
Narrow-bandgap, 267
Narrow-gap, 268, 272, 273, 278, 285
Negative index materials, 495
N-TiO_2nanostructured thin films, 144
Norton equivalent circuit, 208
Nucleation layer, 490
Nyquist plot, 5

O
ODT, 563
Ohmic resistance, 6
Oleine, 561
Open circuit potential, 27
Operation cycle, 560
O-PPG, 563
Optical absorption, 388
Optical orientation, 294
Ordered arrays of pores, 493
Ordered distribution of pores, 490
Organic films, 26
Oxidation, 90
Oxide pellicles, 44, 59, 68, 74
Oxygen depletion, 326
Oxygen spectrum, 96
Ozone synthesis, 50, 78

P
Passivation, 109
Passive film, 22
Passive pit model, 18
Passive state, 109
PE coefficient, 242, 243, 248, 252, 254, 257
PE crystal orientation, 219
PE effect, 229, 231, 246, 258
PE phase, 233
PE single crystal, 209
Peaks, 134
Phase composition, 57, 61, 68
Phonon, 395, 423, 444, 507
Phonon emission, 420, 430
Phonon energy, 396
Phonon filter, 515
Phonon repetition, 430
Photocatalysts, 317

Photoconductivity, 134, 282–284, 295, 406
Photoconductivity spectra, 279
Photodetectors, 295
Photoluminescence, 137, 282, 284–289, 416, 436, 439
Photonic applications, 495
Photonic bandgap, 499
Photonic crystal lenses, 497
Photonic crystals, 499
Photoreceivers, 295
Photothermoelectric effect, 546
Photovoltaic device, 143, 145–148, 149–152, 155, 163, 166, 167, 180, 182, 183
Physical, 89
Piezocrystal, 216, 243, 250–254, 258, 259
Piezoelectric, 191
Piezoelectric coefficients, 218
Piezomagnetic, 192
Piezomagnetic coefficients, 206, 218, 229
PL spectrum, 418, 420, 428, 429, 436, 441, 442
Plasma, 88
Plasma channel, 44, 45, 47, 48, 59, 63, 66, 67, 72, 78
Plasma-sputtered, 485
Plating cell, 492
PMN, 210
Pneumatic cylinders, 560
Polycrystalline compound, 423
Polymer, 552
Population, 522
Pore-filling, 484
Pore walls, 486
Porous anodic aluminum oxide, 476
Porous matrix, 492
Porous membrames, 485
Porous oxide capacitance, 20
Porous resistance, 20
Porous semiconductor templates, 479, 501
Potential barrier, 125
Powders, 116
Power, 89
Pre-edge and edge features, 323
Process temperature, 354
Properties, 334, 337
Pulse current generator, 58
Pulse electrodeposition, 502
Pulsed electrical discharge machining (PEDM), 44–50, 52, 53, 57–60, 63–65, 67, 68, 71–73, 75, 76, 78
Pulsed voltage regime, 492
PVD, 329
Pyroelectric effect, 230
Pyrolytic graphite, 92

Q
Quartz, 210
Quasi-static model, 203, 218

R
Radiation efficiency, 540
Radiation pattern, 541
Radiative annihilation, 439
Raman bands, 363
Raman scattering, 341
Raman spectrum, 339
Reactive impedance surface, 540
Recombination, 115, 134, 138, 140, 417
Recombination levels, 421, 424
Rectangular, 509
Redistribution, 521
Reduced mass, 393
Reducing effect, 328
Reduction, 527
Reflectance, 129, 383, 394
Reflection, 127, 357, 363
Reflection spectrum, 397
Refractive index, 130, 384
Relationship, 117
Relaxation time, 137, 519
Reopecticity, 562
Resistance of solution, 25
Resistance to corrosion, 74
Resistivity, 537
Resistor, 6
Resonance mode, 245, 246
Resonant antennas, 542
Resonant mode, 249, 254, 255, 257, 258
Restrictive, 562
RF magnetron sputtering, 149, 168, 169, 172–174, 176, 177
Roosbroeck–Shockley theory, 422
Roughness, 44, 52, 63, 70, 74, 86, 119, 127, 447, 449, 450, 453–455, 457–459, 463, 465, 466, 469
Rupture, 106
Rutile structure, 324

S
Sample, 135, 563
Sandwich, 117
Scanning electrochemical impedance spectroscopy, 31
Scherrer formula, 363
Schottky contact, 494
Screw, 102
Screwing moment, 102
Segmented nanowires, 513
Selenium vacancies, 123

Self-organization phenomena, 501
Self-organized, 490
SEM, 119, 349
Semiconductor $Hg_{1-x}Mn_xTe$, 271
Semiconductor, 269, 270, 278, 281, 286, 290, 295
Semimagnetic, 267, 272, 277, 279, 286, 290, 293–295
Semimagnetic semiconductor, 268, 270, 274, 277, 281, 285, 288, 290, 291, 294, 295
Sensitization solution, 487
Separating graphite structures, 92
Shear mode, 245, 257, 258, 261
Shear rupture, 104
Shear stress, 103, 107
Shock wave, 93
Short-range order, 491
Single crystals, 365
Single oscillator model, 132
Single wall nanotubes, 97
Sixfold coordination, 327
Slope, 133
Slow phenomena, 544
Small radius atoms, 354
Solid ointment, 106
Solubility, 100
Solvents, 100
Specific properties, 390
Spectra, 339
Spectral characteristics, 410
Specularity, 520
Spin-glass, 309, 310
Spots, 51
SQUID magnetometer, 306
Stability, 566
Standing waves, 518
Steel 45, 72
Stoichiometric, 349
Stoichiometric composition, 342
Strain, 206
Stress, 206
Structure, 94, 99, 565
Sub-excitation regime, 47, 49
Superconducting memory, 302
Superconducting spintronics, 301, 310
Superconducting spin-valves, 302
Superconductor-ferromagnet (S-F) heterostructures, 301
Superficial layer, 56, 70
Superlensing effect, 497
Surface impedance, 540
Surface morphology, 353
Surface oxidation, 44, 46, 51, 52, 54, 61, 62, 76, 78, 79
Surface plasmon polariton waves, 540
Surface states, 336, 411
Symmetry, 200, 337
Synthesis, 358

T

Tauc relationship, 129
Technological schemes, 59
Temperature, 98, 135, 566
Temperature dependence, 344
Tensor properties, 201
Tetragonal structure, 324
TGA, 97
Thévenin equivalent circuit, 208
Thermal activation, 442, 444
Thermal conductivity, 521
Thermal flux, 518
Thermal machining, 464
Thermal quenching, 431
Thermal stability, 98
Thermo-chemical treatment, 52, 53
Thermo-physical properties, 45, 46, 62
Thermoluminescence, 139
Thick layer, 406
Thin film, 154
Thin layers, 402
Third- and second-order optical nonlinearities, 544
Threshold, 520
THz generation, 543
Ti^{4+} vacancies, 327
Ti environment, 324
TiO_2nanostructured thin film, 168, 170, 171, 173, 175, 177, 179, 183
Titanium, 73
Tool-electrode, 58, 59, 61, 63, 64, 65, 72, 75
Transmission, 126, 339, 385, 394, 404
Transmission electron microscopy (TEM), 304
Transmission spectrum, 398
Transmittance, 383
Trapped, 514
Trapping, 140
Tri-layered composite, 218, 238, 239, 242, 248, 249, 250, 253, 256–260
Tri-layered composites of Metglas and PE single crystals, 218
Tri-layered ME composites, 212
Tri-layered structure, 203
Triclinic polymorphs, 325
Tube-like structure, 485

Tubular structures, 492
Turning, 452, 453, 455, 456, 470
TWS, 320

U
Ultrafast phenomena, 544
Ultramicroelectrode, 31
Umklapp-limited, 523
Umklapp, 519
Underpotential deposition, 23
UPD shift, 23

V
Vacuum evaporation, 489
Valence band, 280
Valence bonds, 348
Values, 130
Van, 422
Vibration, 339, 362
Vibration modes, 362, 397
Viscosity, 553, 562

W
Warburg impedance, 10
Weak, 525
Wear, 86, 106
Wear resistance, 85
Weight change, 98
W insertion, 327
WO_6 octahedra, 325
Work cylinder, 559
Workpiece, 94
WTS, 320

X
XPS, 68, 96, 319
XPS depth profiles, 322
X-ray diffraction (XRD), 117, 319
XRD lines, 350, 370
XRD pattern, 366

Z
Zeolite crystal channels, 101
Zinc atoms, 123
ZnS, 352
ZnSe, 149, 166
ZnSe buffer thin film, 164
ZnSe thin film, 156, 159, 160, 162, 164
Zn vapors, 363, 369